ADVANCED TECHNOLOGIES IN FLOW DYNAMICS AND COMBUSTION IN PROPULSION AND POWER

EDITED BY: Lei Luo, Bengt Aake Sunden, Songtao Wang and Xiao Liu
PUBLISHED IN: Frontiers in Energy Research

frontiers Research Topics

frontiers

ISSN 1664-8714
ISBN 978-2-88976-723-6
DOI 10.3389/978-2-88976-723-6

About Frontiers

Frontiers is more than just an open-access publisher of scholarly articles: it is a pioneering approach to the world of academia, radically improving the way scholarly research is managed. The grand vision of Frontiers is a world where all people have an equal opportunity to seek, share and generate knowledge. Frontiers provides immediate and permanent online open access to all its publications, but this alone is not enough to realize our grand goals.

Frontiers Journal Series

The Frontiers Journal Series is a multi-tier and interdisciplinary set of open-access, online journals, promising a paradigm shift from the current review, selection and dissemination processes in academic publishing. All Frontiers journals are driven by researchers for researchers; therefore, they constitute a service to the scholarly community. At the same time, the Frontiers Journal Series operates on a revolutionary invention, the tiered publishing system, initially addressing specific communities of scholars, and gradually climbing up to broader public understanding, thus serving the interests of the lay society, too.

Dedication to Quality

Each Frontiers article is a landmark of the highest quality, thanks to genuinely collaborative interactions between authors and review editors, who include some of the world's best academicians. Research must be certified by peers before entering a stream of knowledge that may eventually reach the public - and shape society; therefore, Frontiers only applies the most rigorous and unbiased reviews.
Frontiers revolutionizes research publishing by freely delivering the most outstanding research, evaluated with no bias from both the academic and social point of view. By applying the most advanced information technologies, Frontiers is catapulting scholarly publishing into a new generation.

What are Frontiers Research Topics?

Frontiers Research Topics are very popular trademarks of the Frontiers Journals Series: they are collections of at least ten articles, all centered on a particular subject. With their unique mix of varied contributions from Original Research to Review Articles, Frontiers Research Topics unify the most influential researchers, the latest key findings and historical advances in a hot research area! Find out more on how to host your own Frontiers Research Topic or contribute to one as an author by contacting the Frontiers Editorial Office: frontiersin.org/about/contact

ADVANCED TECHNOLOGIES IN FLOW DYNAMICS AND COMBUSTION IN PROPULSION AND POWER

Topic Editors:
Lei Luo, Harbin Institute of Technology, China
Bengt Aake Sunden, Lund University, Sweden
Songtao Wang, Harbin Institute of Technology, China
Xiao Liu, Harbin Engineering University, China

Citation: Luo, L., Sunden, B. A., Wang, S., Liu, X., eds. (2022). Advanced Technologies in Flow Dynamics and Combustion in Propulsion and Power. Lausanne: Frontiers Media SA. doi: 10.3389/978-2-88976-723-6

Table of Contents

05 ***Effects of Coolants of Double Layer Transpiration Cooling System in the Leading Edge of a Hypersonic Vehicle***
Shibin Luo, Zhichao Miao, Jian Liu, Jiawen Song, Wenxiong Xi and Chaoyang Liu

18 ***Influence of Self-Pulsation on Atomization Characteristics of Gas-Centered Swirl Coaxial Injector***
Chuanjin Jiang, Yuan Xie, Yuchao Gao, Wei Chu, Yiheng Tong, Xiuqian Li and Wansheng Nie

33 ***Improvement of Mixing Efficiency in the Combustion Chamber of a Powder-Fuel Ramjet Engine***
Wenxiong Xi, Jian Liu and Ren Mengfei

49 ***Characteristics of the Waviness End-Face Mechanical Seal in Reactor Coolant Pump Considering the Viscosity-Temperature Effect***
Yu Ma, Ya-Hui Wang, Hai-Chun Zhou and Wen-Tao Su

60 ***Impact Investigation of Stator Seal Leakage on Aerodynamic Performance of Multistage Compressor***
Qi Wang, Zhou Zhang, Qingsong Hong and Lanxue Ren

74 ***Research on the Hole Length Ratio of Fan-Shaped Holes in Flat Plate Film Cooling***
Xun Zhou, Runxuan Qin and Le Cai

86 ***Numerical Study on the Biomimetic Trailing Edge of a Turbine Blade Under a Wide Range of Outlet Mach Numbers***
Fengbo Wen, Yuxi Luo, Shuai Wang, Songtao Wang and Zhongqi Wang

102 ***Maximum Thickness Location Selection of High Subsonic Axial Compressor Airfoils and Its Effect on Aerodynamic Performance***
Chuansijia Tao, Xin Du, Jun Ding, Yizhou Luo and Zhongqi Wang

116 ***Analysis of Tangential Combustion Instability Modes in a LOX/Kerosene Liquid Rocket Engine Based on OpenFOAM***
Kangkang Guo, Boqi Xu, Yongjie Ren, Yiheng Tong and Wansheng Nie

126 ***Flow Conditioning to Control the Effects of Inlet Swirl on Brush Seal Performance in Gas Turbine Engines***
Yuxin Liu, Wenlei Dong, John Chew, Michael Pekris, Benzhuang Yue and Xiaozhi Kong

142 ***Three-Dimensional Numerical Analysis of Longitudinal Thermoacoustic Instability in a Single-Element Rocket Combustor***
Guo Kangkang, Xu Boqi, Ren Yongjie, Tong Yiheng and Nie Wansheng

160 ***Effect of Film Position on the Flow and Heat Transfer Characteristics of Full-Ribbed Rotor Tip***
Haimeng Zhou, Chenglong Wang, Zhiqi Kong, Wei Du and Zhongqi Wang

176 ***Experimental Study on Fuel-Switching of Dual-Fuel Gas Turbine Combustor***
Lin Feng, Yang Qiang, Liu Xiao, LI Ming-jia, Ran Jun-hui and Li Ya-jun

188 ***Combustion Characteristics of Methane-Air Mixtures in Millimeter-Scale Systems With a Cavity Structure: An Experimental and Numerical Study***
Junjie Chen and Tengfei Li

209 ***Unsteady Motion of Shock Wave for a Supersonic Compression Ramp Flow Based on Large Eddy Simulation***
Xing Huang, Li-Xu Wang, Dong-Dong Zhong and Ning Ge

219 ***Active Flow Control Based Bleed in an Axial Compressor Cascade Using Large Eddy Simulation***
Yun Gong, Shaowen Chen, Cong Zeng and Songtao Wang

231 ***Large-Eddy Simulation of the Boundary Layer Development in a Low-Pressure Turbine Cascade With Passive Flow Control***
Pengcheng Yang, Shaowen Chen, Weihang Li and Cong Zeng

243 ***Multi-Objective Optimization of Circumferential Groove Casing Treatment in an Ultra-Highly Loaded Low-Reaction Transonic Compressor Rotor***
Shengli Ding, Shaowen Chen, Songtao Wang and Zhongqi Wang

257 ***Effects of Multiple Injection Strategies on Heavy-Duty Diesel Energy Distributions and Emissions Under High Peak Combustion Pressures***
Zhao Zhang, Haifeng Liu, Zongyu Yue, Yangyi Wu, Xiangen Kong, Zunqing Zheng and Mingfa Yao

272 ***Study on Self-Excited Oscillation Suppression of Supersonic Inlet Based on Parallel Cavity***
FeiChao Cai and Xing Huang

287 ***Viscous Oil Film Thermal Modeling of Hydrostatic Bearings With a Rectangular Microgroove Surface***
Teng Liu, Chentao Li, Runze Duan, Huiru Qu, Faze Chen, Zhenlin Zhou, Jianjun Zhang and Zhanqun Shi

298 ***Parametric Design Optimization of Reverse Thrust Blades and Analysis of Fluid-Solid Coupling***
Yang Huicheng, Yang Qingzhen, Wang Canliang and Bai Jin

309 ***A Numerical Study on Mechanical Seal Dynamic Characteristics Within a Reactor Coolant Pump***
Jun-Li Wang, Xing-Yuan Chen, Maxime Binama, Wen-Tao Su and Jian Wu

326 ***Study on Trajectory Optimization of Hypersonic Vehicle Based on Neural Network***
Feichao Cai and Xing Huang

340 ***Investigations on Spray Characteristics and Self-Pulsation of a Gas-Centered Shear Coaxial Injector***
Gao Yuchao, Chu Wei, Xie Yuan, Jiang Chuanjin, Xu Boqi, Su Lingyu and Tong Yiheng

frontiers in Energy Research

ORIGINAL RESEARCH
published: 09 September 2021
doi: 10.3389/fenrg.2021.756820

Effects of Coolants of Double Layer Transpiration Cooling System in the Leading Edge of a Hypersonic Vehicle

Shibin Luo[1], Zhichao Miao[1], Jian Liu[1], Jiawen Song[1], Wenxiong Xi[1] and Chaoyang Liu[2]*

[1]School of Aeronautics and Astronautics, Central South University, Changsha, China, [2]College of Aerospace Science and Engineering, National University of Defense Technology, Changsha, China

As a promising and efficient active cooling method, double layer transpiration cooling is introduced into the design of the cooling system in the leading edge of a hypersonic vehicle. The physical model is built combined with hypersonic transpiration cooling, film cooling, heat conduction, porous media heat conduction and convection heat transfer. In addition, effects of different kinds of coolants are considered to reveal cooling mechanisms in different operation conditions. A comprehensive turbulence model validation and mesh independence study are provided. Flow characteristics caused by flow impingement, separation, transition and interaction with the cooling flows are displayed and analyzed in the work. When different kinds of coolants supplied at the same mass flow rate, the coolants with low densities, i.e., H_2 and He, have the lowest peak temperature compared with the coolants with large densities, i.e., N_2 and CO_2. The coolants with low densities have a large ejecting velocity which provides large kinetic energy to penetrate deeply in the porous media. In addition, when the ejecting velocity is large enough, a recirculation is formed in front of the leading edge and pushes the high temperature region located in stagnation region away from the leading edge. However, when the coolants are ejected at the same velocity, the coolants with large densities exhibit better cooling performance.

Keywords: transpiration cooling, hypersonic vehicle, leading edge, recirculation, cooling performance

OPEN ACCESS

Edited by:
Lei Luo,
Harbin Institute of Technology, China

Reviewed by:
Xing Yang,
Xi'an Jiaotong University, China
Jin-yuan Qian,
Zhejiang University, China

****Correspondence:***
Jian Liu
jian.liu@csu.edu.cn

Specialty section:
This article was submitted to Advanced Clean Fuel Technologies, a section of the journal Frontiers in Energy Research

Received: *11 August 2021*
Accepted: *30 August 2021*
Published: *09 September 2021*

Citation:
Luo S, Miao Z, Liu J, Song J, Xi W and Liu C (2021) Effects of Coolants of Double Layer Transpiration Cooling System in the Leading Edge of a Hypersonic Vehicle. Front. Energy Res. 9:756820. doi: 10.3389/fenrg.2021.756820

INTRODUCTION

Continuous increase of flight Mach number of the hypersonic vehicle, the total temperature of the freestream increases and the surface aerodynamic heating of the aircraft is furtherly enhanced. To meet the aerodynamic performance, the sharp leading edge shape is adopted, which also leads to strong aerodynamic heating (Boyd & Padilla, 2003; Glass, 2008). The peak of heat flux density at the leading edge of a hypersonic vehicle can reach more than 10 MW/m^2 (Kennedy et al., 2011). The high heat flux density imposed on the leading edge has exceeded the melting point of the materials and led to the damage to the structures. And with the development of hypersonic vehicles in the direction of wide speed range, long flight time, high Mach number, and lightweight, the traditional passive thermal protection technology is unable to meet high heat load (Ji et al., 2021). Therefore, it is urgent

Abbreviations: M, mass flow rate, kg/s; l, length of the leading edge, m; k, thermal conductivity, W/m·K; T, temperature, K; p, pressure, Pa; Dp, average pore diameter, m; K, permeability of porous media, m−2; U, velocity, m/s; x, y, Cartesian coordinate, m; μ, fluid dynamic viscosity, Pa·s; ρ, fluid density, kg/m3; k, thermal conductivity, W/(m.K); ε, porosity; γ, specific heat capacity ratio; 0, stagnation; f, fluid; s, solid; c, coolant; eff, effective; Ma, Mach number

to search for an efficient active cooling technology to protect the leading edge and other high temperature regions of a hypersonic vehicle (Huang et al., 2015).

Transpiration cooling is a kind of active cooling technology that can greatly improve cooling efficiency with limited coolant supply which has the advantage of providing a large quantity of contacting surfaces for solid surfaces and coolant flows. The coolant enters the micro skeleton material of porous media and induces convective heat transfer which has benefits for heat transfer within the porous media. At the same time, a thin film is formed on the solid surface of the material when the coolant flow ejects out and isolates the protected surfaces from the high-temperature mainstream (Luikov, 1963; Glass et al., 2001). Compare with regenerative cooling and film cooling, transpiration cooling can improve respectively the cooling efficiency by 35 and 13% (Landis & Bowman, 1996; Leontiev, 1999). At the same time, transpiration cooling has the advantages of uniform film coverage, low coolant consumption, and high cooling efficiency (Dahmen et al., 2014). At present, transpiration cooling has been applied in the engine combustion chamber, rocket nozzle, nose cone, and leading edge of the reentry aircraft (Soller et al., 2009).

Scholars have carried out some experimental and numerical studies on the application of transpiration cooling in hypersonic vehicles. Shen et al. (2016) carried out transpiration cooling experiments using water as the coolant. The experimental results show that the cooling efficiency is the lowest in the stagnation zone where bears high aerodynamic heating and high stagnation pressure. Jiang et al. (2017) carried out an experimental study on the strut with three different cooling structures in a wind tunnel. The results show that single transpiration cooling structures cannot effectively cool the leading edge of the strut under high injection pressure. Also, the average efficiency of the combination of transpiration cooling and film cooling is higher than that of single transpiration cooling under the same coolant consumption. Connolly (2021) numerically studied the effects of geometric structures on hypersonic transpiration cooling performance under the condition of Ma = 7.5. The results show that the radius of the nosetip has a great influence on the heat flux, while the wedge angle has little effect on the heat flux on the wedge-shaped surface.

Ding et al. (2019) concentrated on the thermal protection of the leading edge of a hypersonic vehicle and proposed a coupled numerical method to calculate the overall cooling effect. Based on the previous studies about double layer cooling structures in a turbine blade, a novel double layer combined cooling (DLCC) conception is proposed by Ding et al. (2020). The coolant is allocated reasonably by adjusting the layout of the film slots, and the feasibility of the film-transpiration combined cooling scheme is verified. The work of Ding et al. (2020) shows that the double layer combined cooling is a very effective active cooling method, which provides a reference for the design of thermal protection system of a hypersonic vehicle. Ding et al. (2020) considered the effects of several discrete film slot layouts on cooling efficiency of the double layer combined cooling structures. The transpiration cooling efficiency is mainly determined by the properties of coolants and main flow, blowing ratio, the geometric structure, and mainstream conditions (Zhu et al., 2018). However, flow structures and heat transfer mechanism of double layer combined cooling conception need to be further studied.

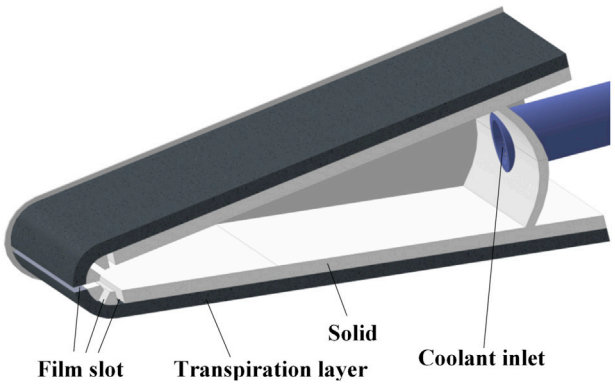

FIGURE 1 | Double layer transpiration cooling in the leading edge of a hypersonic vehicle.

In the previous study, Chauvin and Carter (1955) used gaseous Helium, gaseous Nitrogen, and distilled water as the coolants of transpiration cooling. The results show that the consumption of Helium is less than Nitrogen when the same cooling effect is achieved. Gülhan and Braun (2011) compared the cooling effects of Air, Argon, and Helium at the same blow ratio. The results show that the cooling efficiency of air and Argon is the same, and Helium has better cooling performance under the same blowing ratio.

In the present work, the novel double layer combined cooling structure and transpiration cooling technology is used in the leading edge cooling of a hypersonic vehicle. A model coupled with compressible flow, porous media heat transfer, convective heat transfer, and heat conduction are proposed. The heat transfer and fluid flow characteristics of the transpiration cooling are revealed. Effects of the different coolants and mainstream conditions are considered in this paper. Some suggestions are provided for the application of transpiration cooling in the leading edge of a hypersonic vehicle.

DESCRIPTION OF THE COMPUTATIONAL DOMAIN

Geometrical Model

The design of the geometric model in this work bases on the double layer combined cooling structure at the leading edge of a hypersonic vehicle proposed by Ding et al. (2020). The structure is composed of inner and outer layers, the outer layer is a transpiration cooling layer, and the porous medium material is sintered nickel-based superalloy.

The inner layer is a film slot layer with discrete slots, which is made of high-strength aluminum alloy. Part of the coolant can directly enter the porous media layer through the slots in the two sides, and some coolant can be directly ejected out of the leading edge through the central slot. The pipe at the tail continuously transports coolant into the cooling cavity to realize the thermal protection of the leading edge. The schematic diagram of the structure is shown in **Figure 1**.

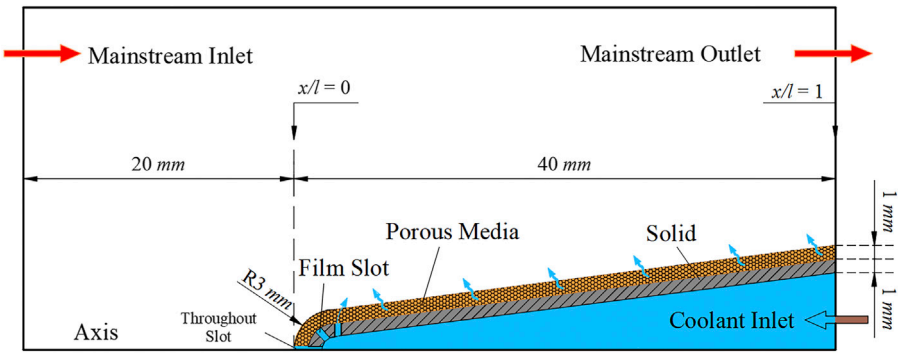

FIGURE 2 | Two-dimensional computational domain used in the present study.

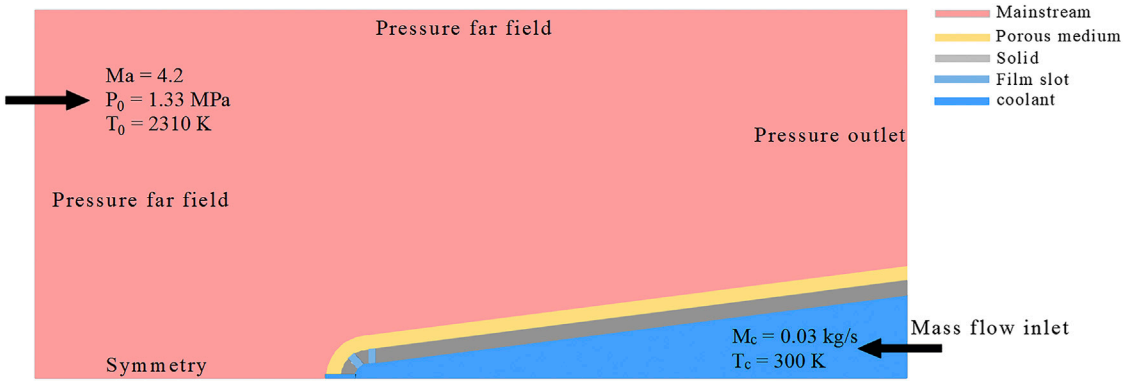

FIGURE 3 | Boundary conditions setting.

TABLE 1 | Conservation equations for different computational domains (Ding et al., 2020).

Computational domain	Conservation equations
Freestream	Continuity equation: $\nabla \cdot (\rho \vec{U}) = 0$
–	Momentum equation: $\nabla \cdot (\rho \vec{U}\vec{U}) = -\nabla p + \nabla \cdot \bar{\bar{\tau}}$
–	Energy equation: $\nabla \cdot [\vec{U}(\rho E + p)\ ] = \nabla \cdot (k\nabla T + \bar{\bar{\tau}} \cdot \vec{U})$
Porous media	Continuity equations: $\nabla \cdot (\varepsilon \rho \vec{U}) = 0$
–	Momentum equation: $\nabla \cdot (\varepsilon \rho \vec{U}\vec{U}) = -\varepsilon \nabla p - (\frac{\varepsilon^2 \mu}{K}\vec{U} + \frac{\varepsilon^3 C_2}{2}\rho\left\|\vec{U}\right\|\vec{U})$, $C_2 = \frac{3.5}{D_p}\frac{1-\varepsilon}{\varepsilon^3}$
–	Energy equation: $\nabla \cdot [\vec{U}(\rho_f E_f + p)\ ] = \nabla \cdot (k_{eff}\nabla T + \bar{\bar{\tau}} \cdot \vec{U})$, $k_{eff} = \varepsilon k_f + (1-\varepsilon)k_s$
Solid	Heat conduction equations: $\nabla \cdot (k_s \nabla T) = 0$

Because the leading edge shape and flow structure characteristics are the same along the spanwise direction, the two-dimensional geometric model is adopted ignoring the three-dimensional effect. In addition, the geometric model and flow field characteristics are symmetric in the spanwise direction, half of the sectional model is selected. The main size of the model is shown in **Figure 2**.

In **Figure 2**, the total length of the leading edge is 40 mm, the wedge angle is 14°, and the radius of the head is 3 mm. The film slot layer and the transpiration cooling layer have the same thickness of 1 mm, and the width of all the discrete slots is 0.5 mm.

The sharp end of the leading edge is the origin. The mainstream flow direction is taken as the positive direction of the *x*-axis, then the positive direction of the *y*-axis is determined.

Computational Domain and Physical Model

In this paper, the computational domain includes hypersonic transpiration cooling, film cooling, heat conduction in the porous

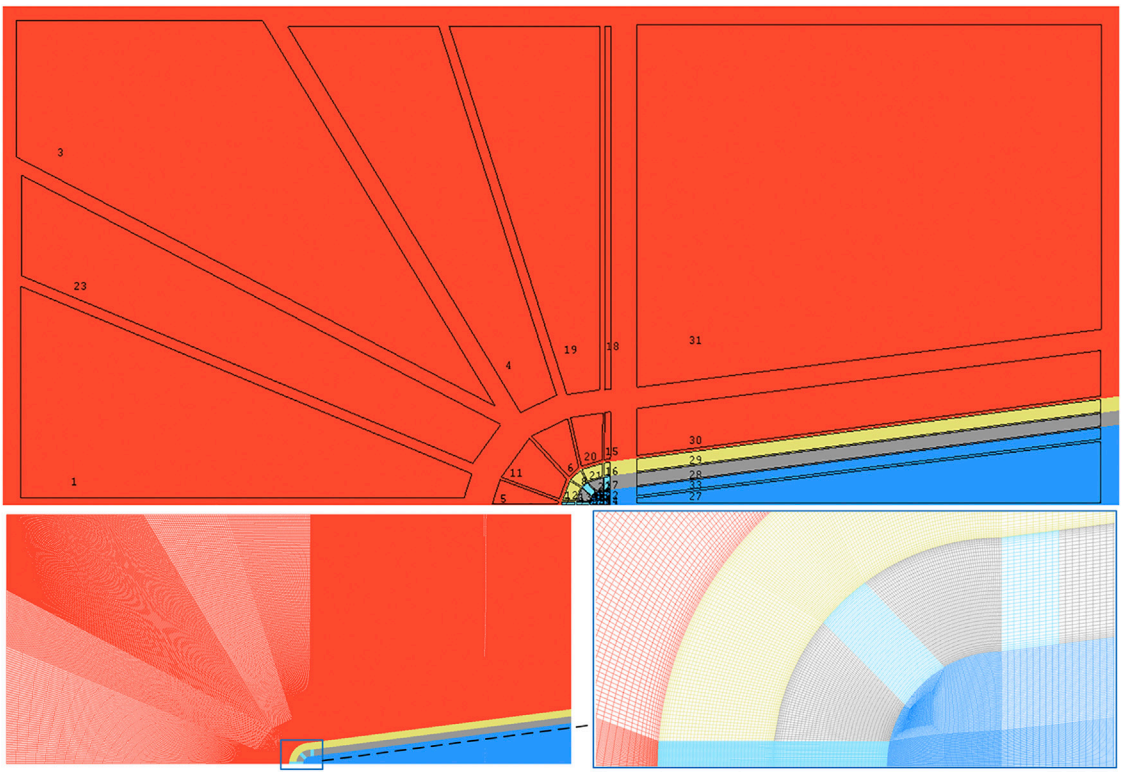

FIGURE 4 | Structured meshes and local mesh details.

media, and convective heat transfer is established. The computational domain is shown in **Figure 3**. **Table 1** shows the governing equations of all the heat transfer processes (Ding et al., 2020).

In **Figure 3**, the coolant is injected from the inlet on the right side, and the mass flow rate is controlled as 0.03–0.05 kg/s. Part of the coolant is ejected out through a throughout slot in the central part and pushes the shock wave away from the outside surface. The other part enters the porous media through the film slot and penetrates through the porous media after fully heat exchange with the solid materials. Then a uniform coolant film forms on the solid surface which separates the high temperature mainstream from the structure surfaces.

TABLE 2 | Boundary conditions.

Boundary conditions	Value
Mainstream Ma	4.2
Mainstream total pressure P_0	1.33 MPa
Mainstream total temperature T_0	2310 K
Specific heat capacity ratio γ	1.4
Coolant mass flow rate M_c	0.03 kg/s
Coolant inlet temperature T_c	300 K
Porosity of porous media	0.33
Viscous resistance of porous media	1.33e + 13
Turbulent intensity	5%
Turbulent viscosity ratio	10
Solid thermal conductivity	202.4 W/(m·K)

COMPUTATIONAL METHOD AND PROCEDURE

Meshing Details

The complete structured meshing of the geometric model is carried out, and the O-block and discrete block strategy are adopted to generate the structured meshes. Because the mesh quality of shock wave boundary layer and outside wall has a great influence on the calculation results, the mesh height of the first layer of the leading edge outside wall is adjusted so that the dimensionless wall y plus value is less than one on the whole outside wall (She and Fan, 2018).

In the contact region of the film slot, porous media, and mainstream are connected by coupled algorithms to realize data transportation. The local details of the meshes are shown in **Figure 4**.

A mesh independence study is performed at mass flow rate of 0.03 kg/s. For the mesh independence study, four kinds of mesh with different numbers of nodes, mesh 1 (284,393), mesh 2 (337,832), mesh 3 (403,417), and mesh 4 (549,667), are generated to calculate the stagnation point temperature of the outside wall. The results calculated by the four kinds of mesh are 2328.0, 2321.6, 2314.2, 2319.1 K. Set the Mesh 3 (Total nodes

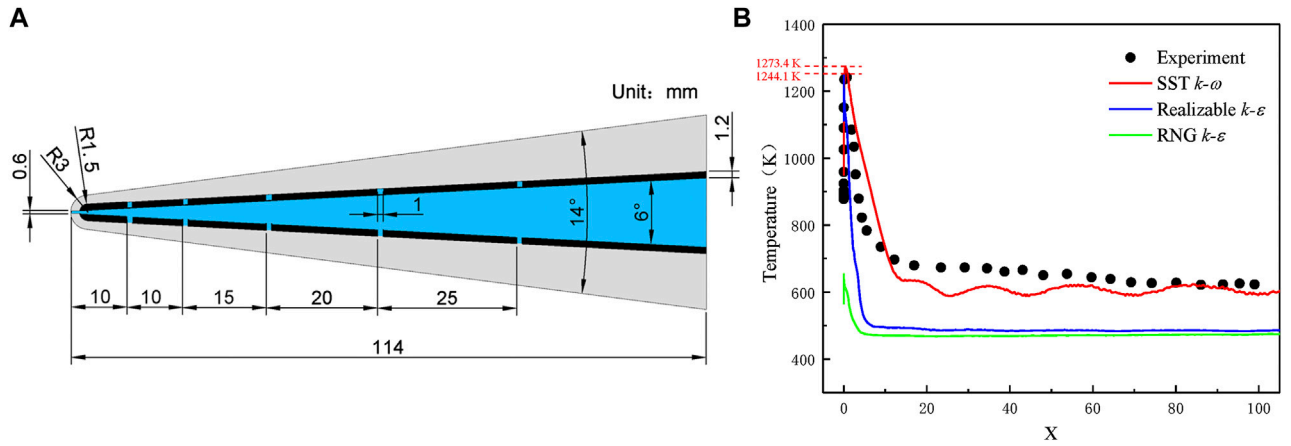

FIGURE 5 | Turbulence model validation. **(A)** The tested model in Ref. (Ding et al., 2020). **(B)** Comparisons of temperature distribution along the leading edge.

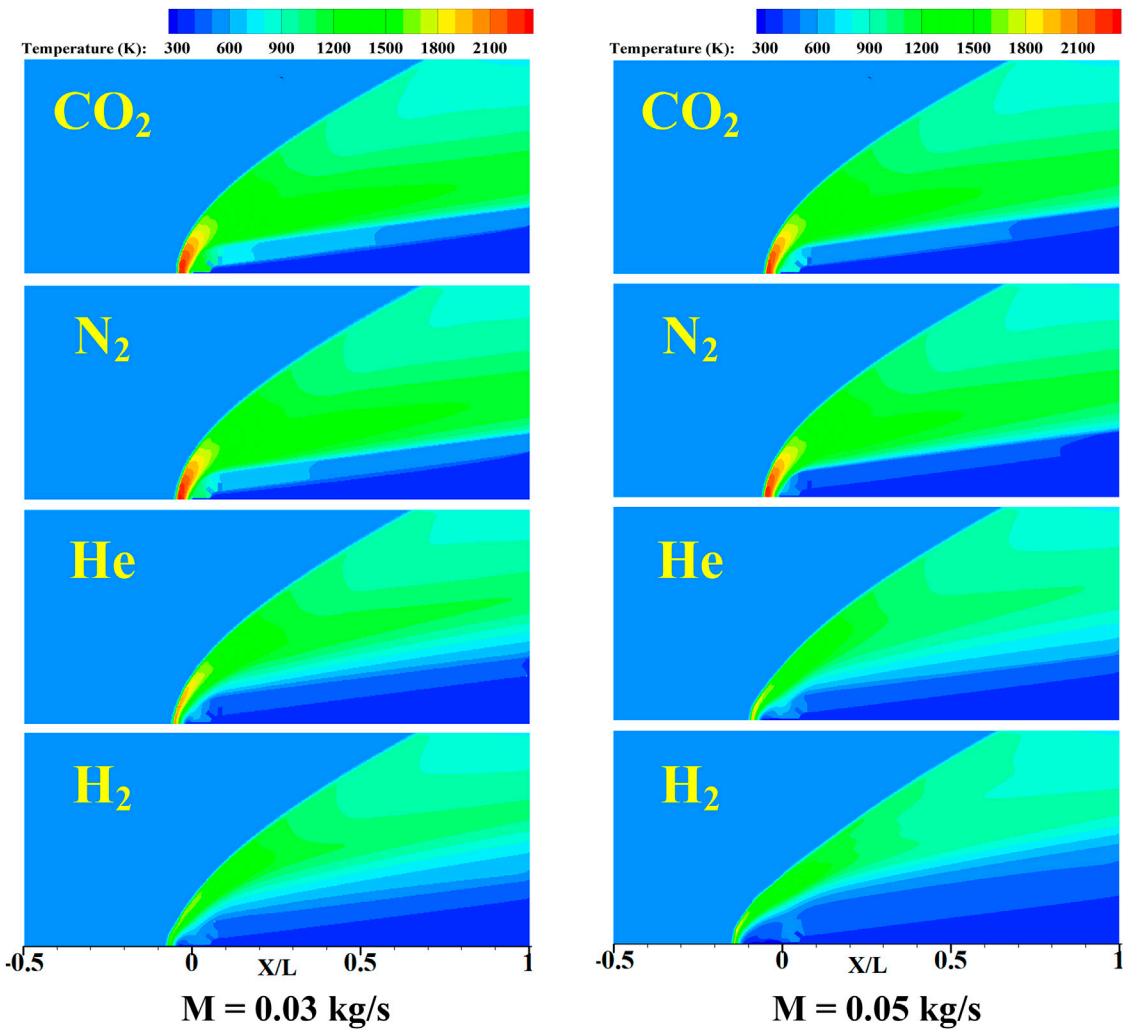

FIGURE 6 | Temperature distributions of the whole domain at coolant mass flow rate = 0.03 kg/s and 0.05 kg/s.

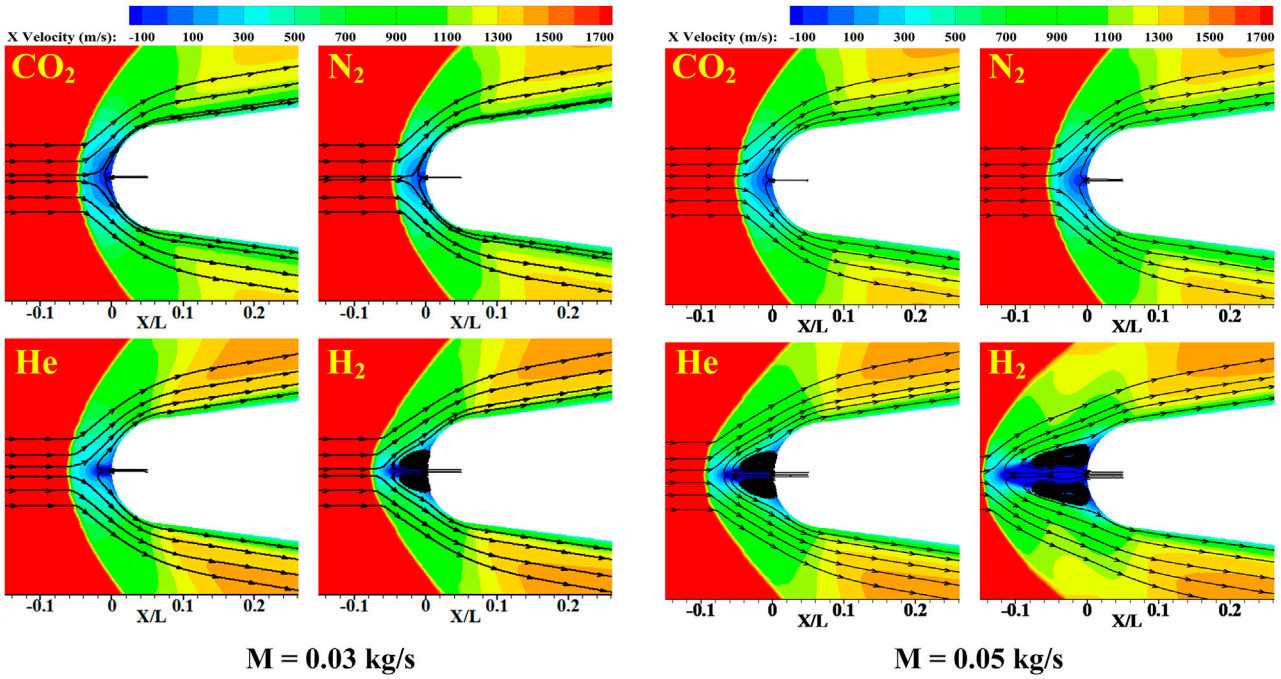

FIGURE 7 | x-velocity distribution and streamlines around the leading edge.

= 403,417) as the baseline. The percentage error of Mesh 1, Mesh 2, and Mesh 4 are +0.6%, +0.32%, and -0.21%, respectively.

According to the calculation results, it can be seen that with the increase of the mesh volume, the difference between the stagnation temperature for different mesh systems becomes smaller. In addition, Mesh 3 is closer to the mainstream temperature and is selected for the lateral calculations.

Boundary Conditions and Solver

The boundary conditions are shown in **Table 2** setting according to the experimental data in references (Shen et al., 2016; Ding et al., 2020) to provide some conveniences for turbulence model validations.

The inlet of the main flow and the upper boundary of the calculation domain is set as pressure far-field, and the outlet of the main flow is set as pressure outlet. The inlet of the coolant is set as mass flow inlet, and the lower boundary of the calculation domain is set as symmetry. The Mach number of the supersonic mainstream is 4.2 with a total pressure of 1.33 MPa and a total temperature of 2310 K. The coolant inlet is set as a constant velocity or mass flow inlet with a flow rate of 0.03–0.05 kg/s, respectively. The temperature of the coolant is set as 300 K. The porosity of porous media is 0.33 and the viscous resistance is $1.33e^{+13}$. The turbulent intensity and viscosity ratio are set respectively as 5% and 10.

The air density of mainstream adopts the ideal gas model and viscosity determined by the Sutherland law. The specific heat, thermal conductivity data of air are obtained from the NIST database and fitted with polynomial functions of temperature (He et al., 2020).

A suitable turbulence model is very important for calculation of complex turbulent flows (Dong et al., 2018). The RANS *k*-ω SST turbulence model is suitable for complex boundary layer and separation flows. Density-based solver and implicit formulation are applied. Second-order upwind scheme is used for the discretization of the continuity, momentum, and energy equations.

The convergence of the calculation is judged by the three aspects below:

1) The absolute criteria are set as 10^{-5} for the continuity, *x*-velocity, *y*-velocity, energy, *k*, and *ω* items.
2) Mass conservation between the inlet and the outlet in the computational domain.
3) The difference of averaged temperature and pressure on the outside wall of the leading edge is less than 0.1% between two iteration steps.

Turbulence Model Validation

To validate the accuracy of the computation model, the experiments in Reference (Ding et al., 2020) is used for validation. The size diagram of the test model is shown in **Figure 5**, and the boundary conditions are set the same with the reference (Ding et al., 2020). The temperature of the outside surface of the porous media is extracted and compared with the experimental results shown in **Figure 5**. Three common turbulence models, i.e., k-ε RNG model, k-ε Reliable model and k-ω SST model, are used for comparisons with the experimental data. It is found that the numerical simulation results predicted by the k-ω SST model are basically consistent with the experimental data in the literature with better treatment of the shear effect of the boundary layer.

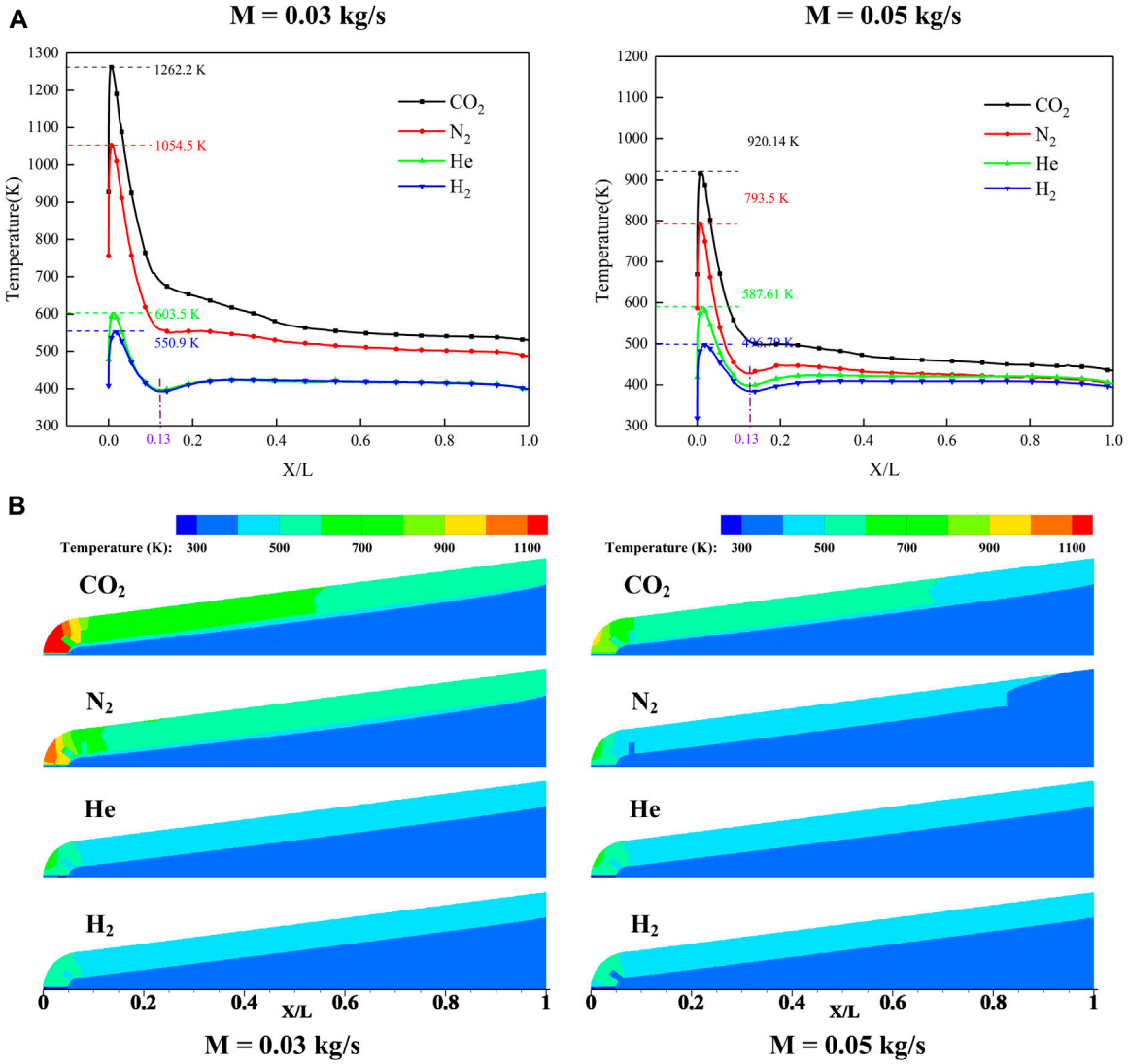

FIGURE 8 | Temperature for different kinds of coolants at M = 0.03 kg/s and M = 0.05 kg/s. **(A)** Temperature contours of the leading edge region **(B)** Temperature distributions along the leading edge surfaces.

Other turbulence models fail to obtain good results and have a large percentage error with experimental values. The trend of the calculated result by the k-ω SST model and experimental result also has good agreements although some deviations can be found in the transition regions. The difference of peak temperature between the calculated results and experimental results is only 29.3K (2.3%). Therefore, the k-ω SST model used in this paper has enough accuracy.

RESULTS AND DISCUSSION

Effects of Different Kinds of Coolants at Same Mass Flow Rate

Figure 6 shows the whole field temperature contours using different kinds of coolants when the mass flow rate of the coolant inlet is set as 0.03–0.05 kg/s. Four kinds of coolants, i.e., CO_2, N_2, He, and H_2 are used, respectively. From the figure, high temperature is found in the region with strong flow impingement and shear flows. With the strong disturbance with the mainstream, bow-shock is formed around the leading edge. After the shock, the temperature is raised around the leading edge and the stagnation region can reach the total temperature of the mainstream. With the coolant ejects from the porous media in the leading edge and temperature of the leading edge is decreased. In the double layer cooling system, the temperature is also decreased along the streamwise direction. However, different kinds of coolants show different cooling abilities even at the same mass flow rate. It can be shown that the coolants with small density have better temperature distribution especially at approaching the stagnation region. It can be attributed to the higher ejecting velocity is obtained by the

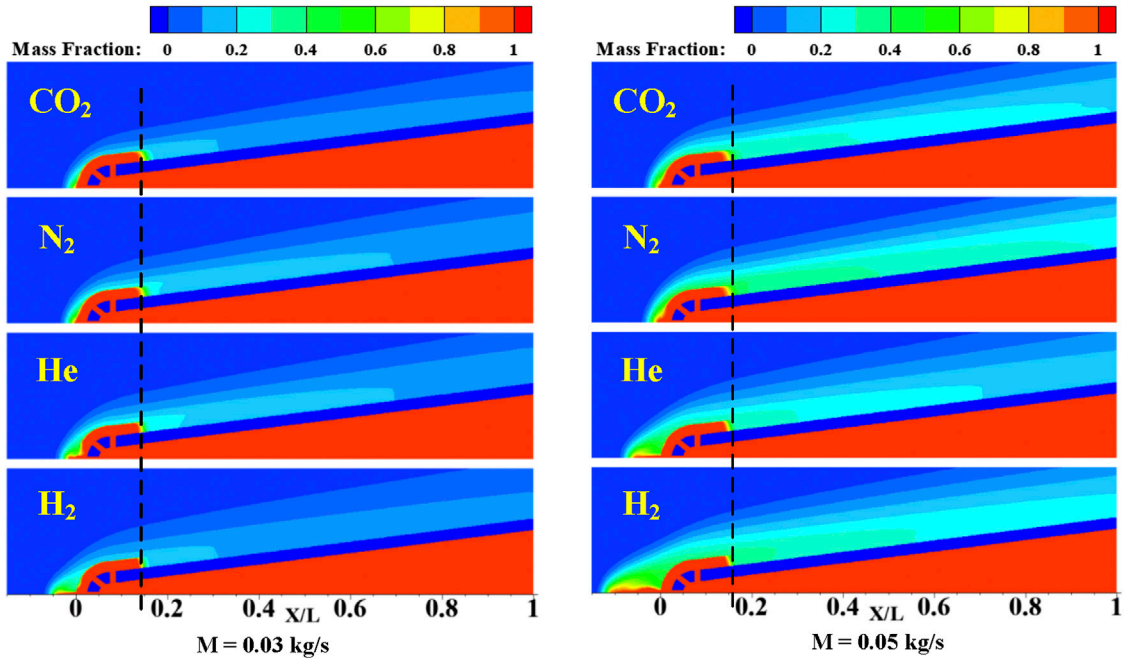

FIGURE 9 | Coolants mass fraction distributions in the computational domain at different mass.

coolants with smaller density at the same mass flow rate. The coolants are arranged from high density to low density in one column. When the coolant mass flow rate at 0.03–0.05 kg/s, the cooling ability of different kinds of coolant is in the order of CO_2 < N_2 < He < H_2.

$$U_c = \frac{M_c}{\rho S} \tag{1}$$

According to **Eq. 1**, when the mass flow rate of coolant is constant, the flow velocity is inversely proportional to the density of the fluid. The densities of the four kinds of coolants, i.e., CO_2, H_2, He and N_2, are 1.797, 0.082, 0.163 and 1.138 kg/m^3, respectively. Under the same mass flow rate, the velocity of the gas with lower density is faster, the bow shock wave is pushed farther away from the head, and an obvious reversed flow region is formed at the stagnation region, which can greatly reduce the temperature.

Figure 7 shows the *x*-velocity and streamlines around the leading edge with different cooling gases at M = 0.03 kg/s and M = 0.05 kg/s. The *x*-velocity also reflects the bow shock generation in the leading edge and has a close correlation with static temperature of the mainstream. The small *x*-velocity means the high static temperature in this region, such as the stagnation region. From the streamline distribution, the strong flow separation and shear flow can be found in the leading edge. When the coolant ejects the cooling hole in the leading edge, the cooling flow interacts with mainstream and is pushed on the leading edge and forms a layer of cooling film. In addition, when the coolant flow ejects at a large velocity, a recirculation region exists in the leading edge region because of the pressure difference and has better thermal protection for the stagnation region. The recirculation region forms a low velocity region and prevents the high temperature mainstream from intruding inside of the leading edge. The largest recirculation region is found in the case of H_2 at the larger mass flow rate of M = 0.05 kg/s.

Figure 8A displays temperature distributions on the leading edge surface for different kinds of coolants at M = 0.03 kg/s and M = 0.05 kg/s. Overall, the temperature on the leading edge surfaces is much lower compared with the mainstream temperature nearby because of the cooling film formed around the leading edge which prevents high thermal load. From the figure, the highest temperature on the leading edge is found in the region close to the stagnation region. Because a straight cooling hole is arranged in the head, the temperature of the leading edge corresponding to the stagnation region is not the highest. When the surface temperature reaches the highest point and it begins to decrease along the streamwise direction and becomes relatively stable after some developments along the streamwise direction. The highest temperature of the leading edge is obtained by the case of CO_2 and the peak temperature is obtained in the order of $T_{CO2} > T_{N2} > T_{He} > T_{H2}$. The phenomenon also has good agreements with the cooling ability in **Figure 6**. The highest peak temperature obtained by the case of CO_2 is 1262.2 K and the lowest temperature is obtained by the case of H_2 with a temperature below than 600 K. The reason for this phenomenon is the larger ejecting velocity and heat capacity of H_2. With the increase of the coolant mass flow rate, the temperature on the leading edge surface is also decreased.

Temperature contours of the leading edge region for different kinds of coolants at M = 0.03 kg/s and M = 0.05 kg/s are displayed

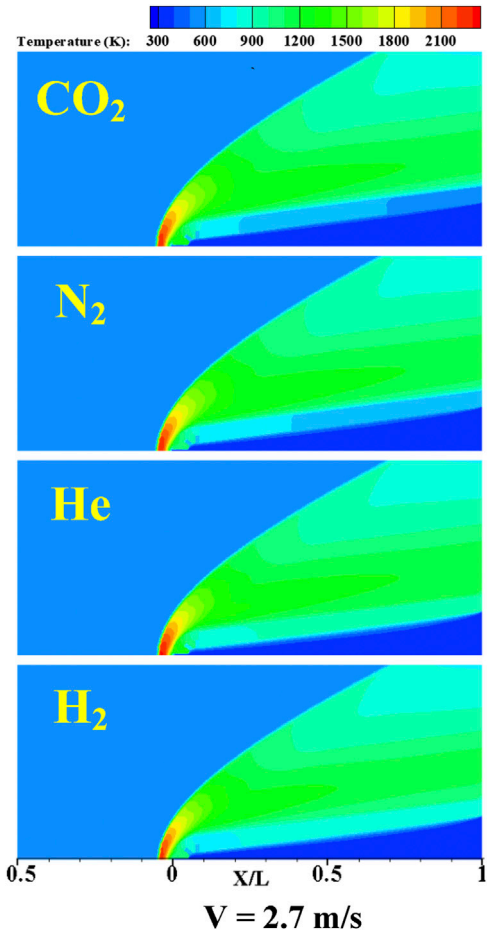

FIGURE 10 | Temperature contours for different kinds of coolants at the same inlet velocity.

in **Figure 8B**. The high temperature is found in the regions close to the stagnation regions where the coolants have difficulties being ejected out. The temperature distribution has the trend of decrease along the streamwise direction and decreases from the inner to the outside. The sharp increase of temperature is found in the region close to the stagnation region and quickly decreases by the cooling effect. From the temperature distribution, it can be noted that double layer transpiration cooling has a great effect on lower down the overall temperature of the leading edge.

Figure 9 presents mass fractions of coolant in the computational domain at different mass flow rates. From the figure, the coolant entering the cooling chamber and ejects out from the stagnation region of the leading edge. When the coolants eject out and form a cooling film along the leading edge surfaces, the coolants spread downstream along the porous media region driven by the pressure differences. It is found that the mass fraction of coolant downstream of porous media is N_2 > He > H_2 > CO_2. The penetration into the porous media is related to the viscosity of the coolant which determines the flow pattern of coolant around the leading edge.

Effects of Different Kinds of Coolants at the Same Inlet Velocity

When the mass flow rate is constant, the ejecting velocity of different coolants is quite different. In the present study, effects of different kinds of coolants at the same inlet velocity are also considered in this paper. Cooling performance of the coolants at the same injection velocity, i.e., 2.7 m/s are compared. The velocity is chosen based on the case of N_2 at the mass flow rate of 0.03 kg/s. Temperature contours for the whole domain using different coolants are provided in **Figure 10**. In the figure, four coolants, i.e., CO_2, N_2, He, and H_2 are used. From the figure, the temperature contours inside the leading edge are similar for all the cases. The solid region of the leading edge is well protected by the coolants. The coolants penetrate into the porous media and decrease local temperature. However, in the case of CO_2 and N_2, the mass flow rates are much larger than the cases of He and H_2 at the same injection velocity. At an inlet velocity of 2.7 m/s, the overall temperature is lower than 900 K in the downstream regions of the leading edge.

Figure 11 displays *x*-velocity contours and streamlines around the leading edge for different kinds of coolants at the same coolant inlet velocity. From the figure, the streamwise clearly presents the bow shock generation and development around the leading edge. Cooling film interacts with the mainstream and protects the surface of the leading edge. In some regions, reversed flows can be found in the head of the leading edge for the cases of CO_2 and N_2 which have large densities. Also, it can be found that the coolants penetrate deeply in the downstream porous media in the cases of CO_2 and N_2 when the coolants have a large density. The coolants with large densities have more strong momentum energy to eject out from the cooling holes and penetrate from the porous media.

Temperatures contours of the leading edge for different coolants are provided in **Figure 12A**. From the figure, the case of N_2 and H_2 has the lowest temperature in the head of the leading edge. For the whole leading edge, the cases of CO_2 and N_2 has relatively low temperature and the coolants have deep penetration downstream. The high density coolants have obvious strengthens when coolants are ejected at the same velocity. However, a relatively large temperature region is found for the case of CO_2.

Figure 12B presents temperature distributions along the leading edge surface at the same coolant inlet velocity. From the figure, the trend of temperature is basically consistent with the results at the same mass flow rate. For the cases with different coolants, the peak temperature of the case of N_2 as the coolant is the lowest. Considering the surface temperature of the whole porous medium regions, the best cooling performance is also provided by coolants using N_2. For the cases of H_2 and He, the peak temperature is more than 1250 K. The case of CO_2 also shows good cooling performance in the downstream region and the surface temperature decreases faster after the peak temperature. However, in the case of CO_2, the head region of the leading edge is relatively high. The worst cooling

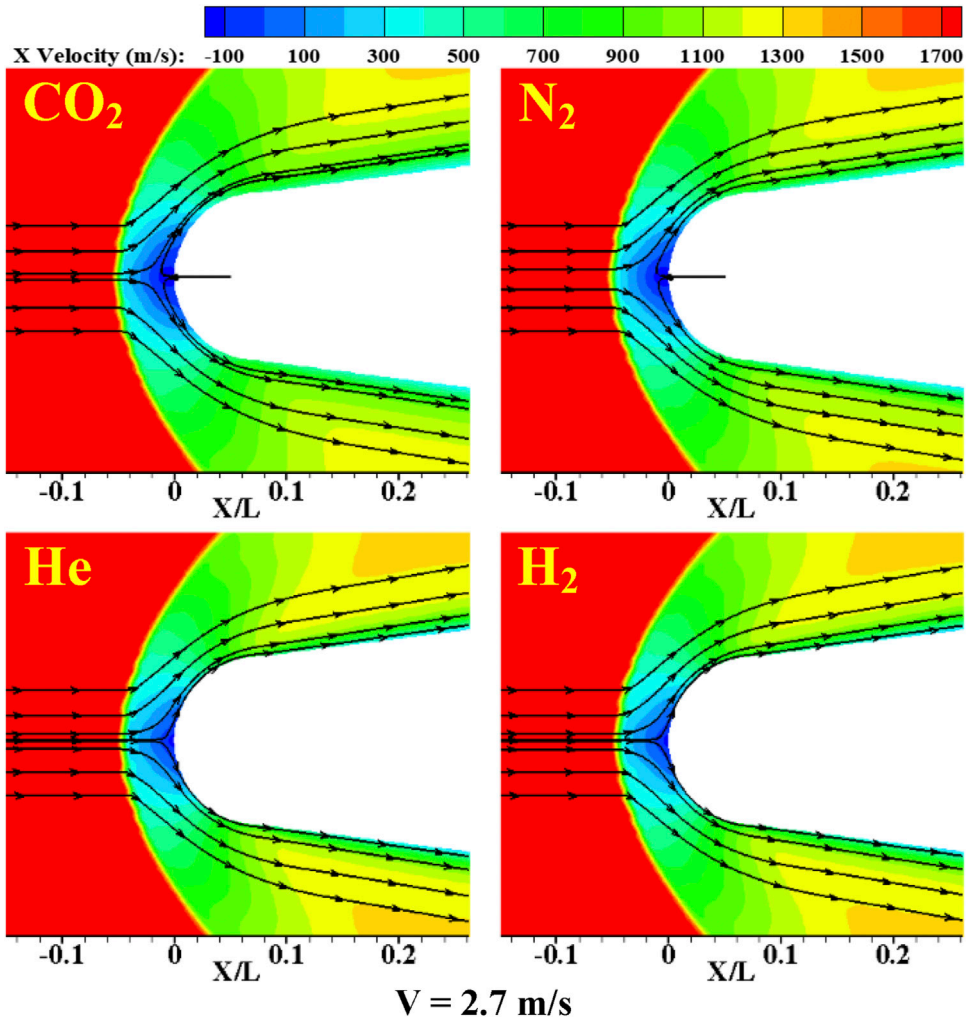

FIGURE 11 | Streamwise velocity and streamlines around the leading edge for different kinds of coolants at the same inlet velocity.

performance is provided by the case of He. Overall, the coolants with large densities have better cooling performance when coolants are ejected at the same velocity.

Figure 13A presents mass fractions distributions of coolant in the computational domain at the same inlet velocity. From the figure, it is clearly shown that the coolants with large densities, i.e., CO_2 and N_2, penetrate deeply in the porous media. The coolants are mainly concentrated in the leading edge region where the cooling holes are located. The mass fraction of in the cases of CO_2 and N_2 in the calculation domain is higher than that case of H_2 and He. **Figure 13B** presents pressure distributions around the leading edge at the same inlet velocity. The pressure in the cooling chamber is large to ensure the coolant can eject out from the porous media in the leading edge region. However, the cases of CO_2 and N_2 are little larger than that of H_2 and N_2. The coolant in the cases of H_2 and He are concentrated upstream of porous media and spread less downstream. However, the cases of CO_2 and N_2 distribute more coolants downstream of porous media which causes the downstream temperature of CO_2 and N_2 lower than that of H_2 and He. The phenomenon is consistent with that founded in **Figure 12**.

CONCLUSION

In the present work, the novel double layer combined cooling structure and transpiration cooling technology is used for the leading edge cooling of a hypersonic vehicle. The physical model built combining with compressible flow, porous media heat transfer, convective heat transfer, and heat conduction are proposed. Heat transfer and fluid flow characteristics of double layer transpiration cooling system are analyzed and

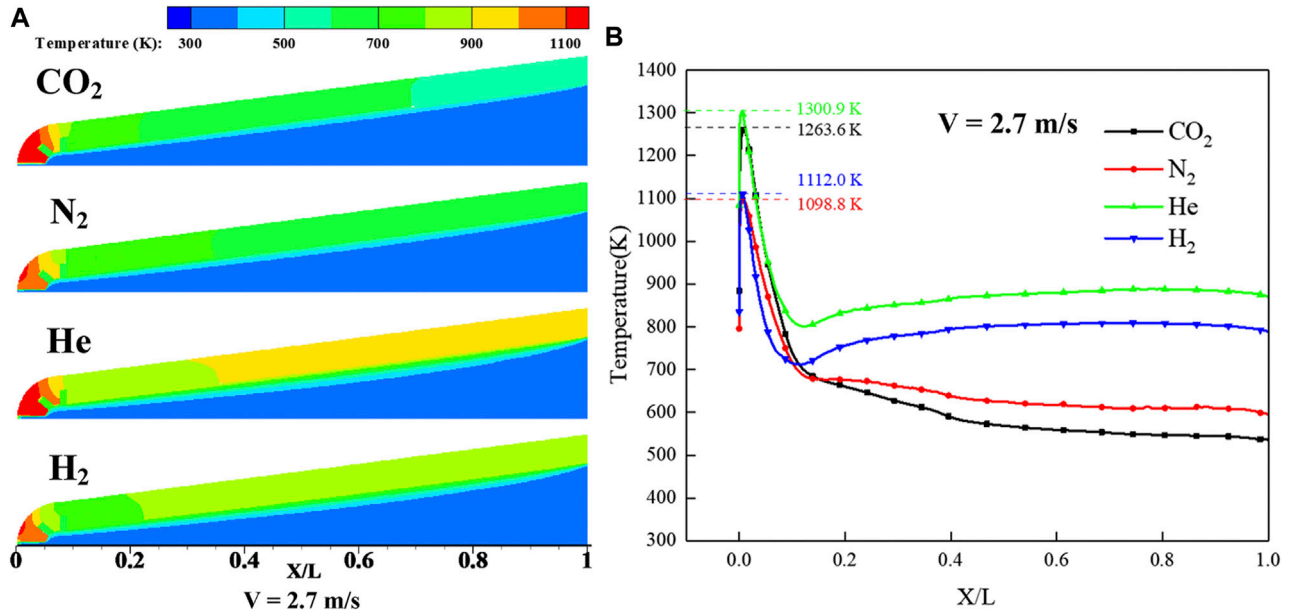

FIGURE 12 | Temperature for different kinds of coolants at the same inlet velocity. **(A)** Temperature contours of the leading edge **(B)** Temperature distributions along the leading edge.

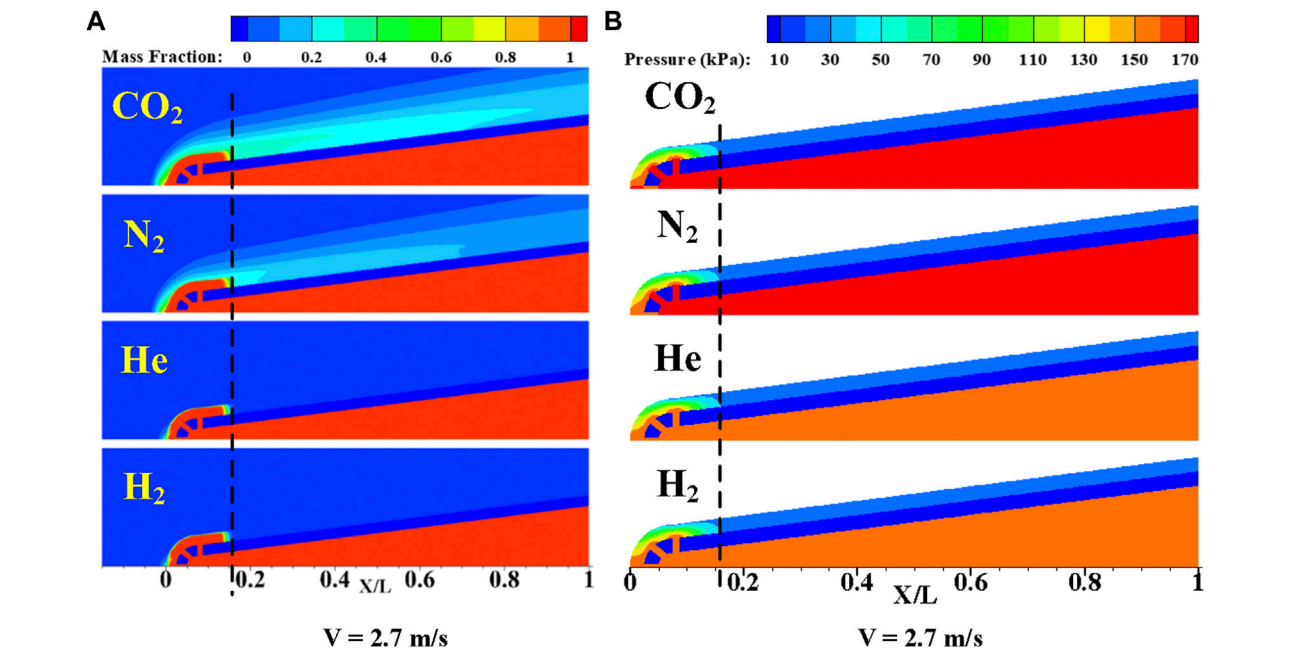

FIGURE 13 | Pressure and mass fraction contours at the same inlet velocity. **(A)** Coolants mass fraction distributions in the computational domain. **(B)** Pressure contours in the leading edge for different kinds of coolants.

revealed. The effects of the coolants and mainstream conditions are considered in this paper. Some conclusions can be obtained from the work.

1) For different kinds of coolants supplied at the same mass flow rate, the coolants with low densities, i.e., H_2 and He, have the lowest peak temperature compared with the coolants with large densities,

i.e., N_2 and CO_2. The coolants with low densities have large eject velocity which provides large kinetic energy to eject out from the leading edge and penetrates deeply in the porous media which well cooling protection downstream. In addition, when the ejecting velocity is large enough, a recirculation which is formed in front of the leading edge pushes the high temperature region located in stagnation regions away from the leading edge.

2) For different kinds of coolants supplied at the ejecting velocity, the coolants with large densities, i.e., CO_2 and N_2, provide good cooling performance considering the whole leading edge region. Compared with the coolant of CO_2, the coolant of N_2 can protect the leading edge better which has a lower temperature in the stagnation region.

DATA AVAILABILITY STATEMENT

The original contributions presented in the study are included in the article/Supplementary Material, further inquiries can be directed to the corresponding author.

AUTHOR CONTRIBUTIONS

SL, ZM, and JL provide research ideas and write the original manuscript. ZM carried out all the calculation work. JS, WX, and CL are responsible for the revision of the paper.

FUNDING

The research work is financially supported by the start-up funds of Central South University (202045012).

ACKNOWLEDGMENTS

This work was supported by the School of Aeronautics and Astronautics, Central South University.

REFERENCES

Boyd, I., and Padilla, J. (2003). "Simulation of Sharp Leading Edge Aerothermodynamics," in 12th AIAA International Space Planes and Hypersonic Systems and Technologies (Norfolk, Virginia: American Institute of Aeronautics and Astronautics). doi:10.2514/6.2003-7062

Chauvin, L. T., and Carter, H. S. (1955). Exploratory Tests of Transpiration Cooling on a Porous 8 Degree Cone at M= 2.05 Using Nitrogen Gas, Helium Gas, and Water as the Coolants. *NACA Res. Memorandum*, L55C29.

Connolly, J. (2021). "Geometry Dependence of Transpiration Cooling for Hypersonic Systems," in AIAA Scitech 2021 Forum (VIRTUAL EVENT: American Institute of Aeronautics and Astronautics) (Reston, Virginia, USA: AIAA). doi:10.2514/6.2021-1519

Dahmen, W., Gotzen, T., Müller, S., and Rom, M. (2014). Numerical Simulation of Transpiration Cooling through Porous Material. *Int. J. Numer. Meth. Fluids* 76, 331–365. doi:10.1002/fld.3935

Ding, R., Wang, J., He, F., Dong, G., and Tang, L. (2019). Numerical Investigation on the Performances of Porous Matrix with Transpiration and Film Cooling. *Appl. Therm. Eng.* 146, 422–431. doi:10.1016/j.applthermaleng.2018.09.134

Ding, R., Wang, J., He, F., Wang, M., Luan, Y., Dong, G., et al. (2020). Numerical Investigation on a Double Layer Combined Cooling Structure for Aerodynamic Heat Control of Hypersonic Vehicle Leading Edge. *Appl. Therm. Eng.* 169, 114949. doi:10.1016/j.applthermaleng.2020.114949

Dong, X., Zhang, Z., Liu, D., Tian, Z., and Chen, G. (2018). Numerical Investigation of the Effect of Grids and Turbulence Models on Critical Heat Flux in a Vertical Pipe. *Front. Energ. Res.* 6, 58. doi:10.3389/fenrg.2018.00058

Glass, D. (2008). "Ceramic Matrix Composite (CMC) Thermal Protection Systems (TPS) and Hot Structures for Hypersonic Vehicles," in 15th AIAA International Space Planes and Hypersonic Systems and Technologies Conference (Dayton, Ohio: American Institute of Aeronautics and Astronautics). doi:10.2514/6.2008-2682

Glass, D. E., Dilley, A. D., and Kelly, H. N. (2001). Numerical Analysis of Convection/Transpiration Cooling. *J. Spacecraft Rockets* 38, 15–20. doi:10.2514/2.3666

Gülhan, A., and Braun, S. (2011). An Experimental Study on the Efficiency of Transpiration Cooling in Laminar and Turbulent Hypersonic Flows. *Exp. Fluids* 50, 509–525. doi:10.1007/s00348-010-0945-6

He, F., Wu, N., Ran, F., and Wang, J. (2020). Numerical Investigation on the Transpiration Cooling of Three-Dimensional Hypersonic Inlet. *Aerospace Sci. Technol.* 106, 106152. doi:10.1016/j.ast.2020.106152

Huang, Z., Xiong, Y.-B., Liu, Y.-Q., Jiang, P.-X., and Zhu, Y.-H. (2015). Experimental Investigation of Full-Coverage Effusion Cooling through Perforated Flat Plates. *Appl. Therm. Eng.* 76, 76–85. doi:10.1016/j.applthermaleng.2014.11.056

Ji, Z., Qin, J., Cheng, K., Liu, H., Zhang, S., and Dong, P. (2021). Design and Performance of a Compact Air-Breathing Jet Hybrid-Electric Engine Coupled with Solid Oxide Fuel Cells. *Front. Energ. Res.* 8, 613205. doi:10.3389/fenrg.2020.613205

Jiang, P.-X., Huang, G., Zhu, Y., Liao, Z., and Huang, Z. (2017). Experimental Investigation of Combined Transpiration and Film Cooling for Sintered Metal Porous Struts. *Int. J. Heat Mass Transfer* 108, 232–243. doi:10.1016/j.ijheatmasstransfer.2016.12.014

Kennedy, P., Donbar, J., Trelewicz, J., Gouldstone, C., and Longtin, J. (2011). "Heat Flux Measurements in a Scramjet Combustor Using Direct Write Technology," in 17th AIAA International Space Planes and Hypersonic Systems and Technologies Conference (San Francisco, California: American Institute of Aeronautics and Astronautics). doi:10.2514/6.2011-2330

Landis, J., and Bowman, W. (1996). "Numerical Study of a Transpiration Cooled Rocket Nozzle," in 32nd Joint Propulsion Conference and Exhibit (Lake Buena Vista, FL, U.S.A.: American Institute of Aeronautics and Astronautics). doi:10.2514/6.1996-2580

Leontiev, A. I. (1999). Heat and Mass Transfer Problems for Film Cooling. *J. Heat Transfer* 121, 509–527. doi:10.1115/1.2826012

Luikov, A. V. (1963). Heat and Mass Transfer with Transpiration Cooling. *Int. J. Heat Mass Transfer* 6, 559–570. doi:10.1016/0017-9310(63)90013-9

She, L., and Fan, G. (2018). Numerical Simulation of Flow and Heat Transfer Characteristics of CuO-Water Nanofluids in a Flat Tube. *Front. Energ. Res.* 6, 57. doi:10.3389/fenrg.2018.00057

Shen, L., Wang, J., Dong, W., Pu, J., Peng, J., Qu, D., et al. (2016). An Experimental Investigation on Transpiration Cooling with Phase Change under Supersonic Condition. *Appl. Therm. Eng.* 105, 549–556. doi:10.1016/j.applthermaleng.2016.03.039

Soller, S., Kirchberger, C., Kuhn, M., Langener, T., Bouchez, M., and Steelant, J. (2009). "Experimental Investigation of Cooling Techniques and Materials for Highspeed Flight Propulsion Systems,"

in 16th AIAA/DLR/DGLR International Space Planes and Hypersonic Systems and Technologies Conference (Bremen, Germany: American Institute of Aeronautics and Astronautics). doi:10.2514/6.2009-7374

Zhu, Y., Peng, W., Xu, R., and Jiang, P. (2018). Review on Active thermal protection and its Heat Transfer for Airbreathing Hypersonic Vehicles. *Chin. J. Aeronautics* 31, 1929–1953. doi:10.1016/j.cja.2018.06.011

Conflict of Interest: The authors declare that the research was conducted in the absence of any commercial or financial relationships that could be construed as a potential conflict of interest.

Publisher's Note: All claims expressed in this article are solely those of the authors and do not necessarily represent those of their affiliated organizations, or those of the publisher, the editors and the reviewers. Any product that may be evaluated in this article, or claim that may be made by its manufacturer, is not guaranteed or endorsed by the publisher.

frontiers in Energy Research

ORIGINAL RESEARCH
published: 28 September 2021
doi: 10.3389/fenrg.2021.760150

Influence of Self-Pulsation on Atomization Characteristics of Gas-Centered Swirl Coaxial Injector

*Chuanjin Jiang, Yuan Xie, Yuchao Gao, Wei Chu, Yiheng Tong *, Xiuqian Li and Wansheng Nie*

Department of Aerospace Science and Technology, Space Engineering University, Beijing, China

There is a lack of understanding of the spray characteristics of gas-centered swirl coaxial (GCSC) injectors during self-pulsation occurs. Therefore, the self-pulsation of a GCSC injector was investigated experimentally in this study. Experiments were conducted at atmospheric pressure with filtered water and dried air supplied through a propellant feed system. A back-lighting high-speed photography technique was used to capture unsteady spray features. A laser-based particle size analyzer (LPSA) was used to measure the size of the droplets in the spray. The effects of recess and gas-liquid ratio on spray self-pulsation were analyzed. It was found that the recess of the injector strongly determines the spray pattern. When spray self-pulsation occurs without recess, both the center and periphery of the spray oscillate. With an increase in the mass flow rate of the gas, the boundary between the center and the periphery of the spray becomes more noticeable. Meanwhile, small droplets in the spray center oscillate, with the periphery of the spray being characterized by a periodic "shoulder." Under the same operating conditions but with a small recess (2 mm), the spray adheres to the injector faceplate. With a larger recess (7 mm), when spray self-pulsation occurs, the spray periodically forms "shoulder" and "neck," similar to the behavior of self-pulsation in a liquid-centered coaxial injector. Therefore, it can be concluded that spray self-pulsation enhances atomization at the center of the spray to a certain extent. However, atomization becomes worse in the periphery with an oscillating spray.

Keywords: gas-centered coaxial swirl injector, self-pulsation, SMD, spray angle, atomization

OPEN ACCESS

Edited by:
Xiao Liu,
Harbin Engineering University, China

Reviewed by:
Jian Liu,
Central South University, China
Peng Cheng,
National University of Defense Technology, China
Yingchun Wu,
Zhejiang University, China

****Correspondence:***
Yiheng Tong
yiheng_tong@sina.com

Specialty section:
This article was submitted to Advanced Clean Fuel Technologies, a section of the journal Frontiers in Energy Research

Received: *17 August 2021*
Accepted: *13 September 2021*
Published: *28 September 2021*

Citation:
Jiang C, Xie Y, Gao Y, Chu W, Tong Y, Li X and Nie W (2021) Influence of Self-Pulsation on Atomization Characteristics of Gas-Centered Swirl Coaxial Injector. Front. Energy Res. 9:760150. doi: 10.3389/fenrg.2021.760150

INTRODUCTION

Combustion instability has permanently restricted the development of liquid rocket engines. When combustion instability occurs, the pressure in the combustion chamber oscillates periodically, and the oscillation frequency ranges from hundreds to thousands or even tens of thousands of Hz (Harrje, 1972; Yuhui, 2001; Zhenguo, 2012). Self-pulsation, accompanied by the periodic oscillation of spray flow and pressure, is an important physical phenomenon of injectors under certain operating conditions. Self-pulsation is generally believed to induce combustion instability (Im et al., 2005; Im and Yoon, 2008; Zhongtao, 2016).

Gas-liquid swirl coaxial injectors have been widely used in liquid rocket engines. The liquid enters the swirling chamber through tangential holes and forms a rotating liquid film under the action of a centrifugal force. The gas passes through the gas channel and interacts with the liquid at the injector orifice to significantly enhance atomization. According to the type and location of the swirling propellant, there are two injector types: liquid-centered swirl coaxial (LCSC) injectors and gas-centered swirl coaxial injectors (Im et al., 2015).

In recent decades, a large number of studies have been carried out on the self-pulsation of LCSC injectors. However, researchers have not reached a consistent conclusion about the effect of self-pulsation on atomization characteristics. Bazarov (Bazarov, 1995; Ismailov and Heister, 2009) believed that the droplet size of a self-pulsation spray is smaller than that of a stable spray under the same operating conditions. From the point of spatial radial distribution of droplet size, the self-pulsation spray is more uniform than the stable spray. Therefore, spray self-pulsation can improve atomization quality and propellant mixing uniformity without causing combustion instability. Zhou (Jin et al., 1996) pointed out that screaming can strengthen atomization when the gas pressure drop is low. However, Im (Im and Yoon, 2008; Im et al., 2009) reported that self-pulsation increases the droplet diameter and weakens the atomization performance of the injector. Furthermore, mass flow pulsation caused by self-pulsation might lead to heat releases and acoustics in the combustion chamber. Thus, this pulsation can amplify unsteady combustion. Kang (Zhongtao et al., 2016) compared a stable spray with a self-pulsation spray and found that the latter could reach a farther radial region. From the perspective of the spatial distribution of the spray, self-pulsation is beneficial for combustion. However, self-pulsation causes the radial distribution of SMD (Sauter mean diameter) to change from an inverted V-shape to a hollow cone, and the SMD generally increases compared with the steady spray. Therefore, self-pulsation is harmful to atomization and must be suppressed.

Compared with the amount of research on LCSC injectors, research on GCSC injectors are few. Lightfoot (Lightfoot, 2005) analyzed the breakup of a liquid film and pointed out that the main breakup modes of liquid film are surface breakup, ribbon formation, perforation, and prompt atomization. Sivakumar (Sivakumar and Kulkarni, 2011) divided spray breakup modes into wave-assisted, perforated sheet, segmented sheet, and pulsation spray regimes. It was found that liquid film maintained an axisymmetric shape when the first two crushing modes appeared. When self-pulsation occurs, the Strouhal number of the spray is almost constant. Xu (Shun, 2016) summed up the method of liquid film breakup as segmented sheet, bubble, pure-pulsating, and perforated sheet breakups, by observing the spray image under conditions with different gas-liquid ratios. Furthermore, he found that self-pulsation led to an increase in the spray angle in the GCSC injector. Meanwhile, the size of droplets in the spray also oscillated severely, as the amount of large droplets increased. Im (Im et al., 2015) compared the GCSC injector to the LCSC injector and found that the GCSC injector spray angle decreased with an increase in the momentum ratio under a low momentum ratio. This is because the interspace gas between the liquid and gas is entrained into the high-velocity gas stream and liquid sheet. Therefore, the external ambient gas pressure was greater than the ambient gas pressure inside the space. Matas (Matas et al., 2014) found that the oscillation frequency of the surface wave of the liquid film is positively correlated with the gas velocity, but has nothing to do with the liquid velocity. Park (Gujeong et al., 2014) pointed out that at the high liquid Reynolds number, the gas Reynolds number has little effect on the spray angle. However, at a low liquid Reynolds number, the gas Reynolds number has a more significant influence on the spray angle. Li (Xuan et al., 2013) investigated that the effect of high pressure on the atomization of GCSC nozzles and found that backpressure causes the spray cone angle to decrease. Joseph (Joseph et al., 2020) conducted that the spray of the GCSC injector is comprised of two different spray patterns: a dense center spray of finer droplets and a rough outer spray. Jeon (Jeon et al., 2011) divided the liquid film breakup mode into internal mixed and external mixed modes. It is believed that when the liquid film is externally mixed, the spray cone angle decreases with an increase in the momentum ratio. However, when the liquid film is internally mixed, the spray angle increases with increasing momentum ratio. Furthermore, when the liquid film is broken inside the injector orifices, the spray angle is the smallest. Increasing the recess results in a reduction in the momentum ratio of the minimum spray angle. Park (Gujeong et al., 2014) pointed out that at a high liquid Reynolds number, the gas Reynolds number has a negligible effect on the spray angle and the thickness of the liquid film. By contrast, at a low liquid Reynolds number, the gas Reynolds number has a significant effect on the spray angle and thickness of the liquid film.

Many studies have shown that recess is an important factor in self-pulsation. A large or small recess weakens self-pulsation; therefore, there exists a specific recess length that leads to the strongest self-pulsation (Bazarov, 1995; Bazarov, 1996; Jin et al., 1996; Jin et al., 1997; Bazarov, 1998). Yang (Yang et al., 2008) proposed the theory of the recess angle, comparing the spray angle of the inner swirl port and the angle of the recess. According to the relative size of the recess angle and the spray angle, he identified three types flow patterns in the recess chamber of the LCSC injector: outer mixing flow, critical mixing flow, and inner mixing flow. Kang (Kang et al., 2016) and Bai (Bai et al., 2018; Bai et al., 2019; Bai et al., 2020) used Yang's theory to develop the mechanism of self-pulsation for LCSC injectors. They believed that when the recess angle of the injector equals the angle of the liquid film, the spray is in a critical mixing mode. Yoon (Yoon et al., 2013) pointed out that the mechanism of self-pulsation is different under different recess lengths. In the case of a small recess ratio, the frequency of self-pulsation increases with the Reynolds number of the gas and liquid and decreases with the recess ratio. The self-pulsation frequency obtained in Yoon's experiments was 2.6–5 kHz. However, with a high recess ratio, the gas and liquid mix might interact with each other in the recess chamber inside the injector. Furthermore, self-pulsation decreases with the liquid Reynolds number, when the characteristic frequency is 0.6–0.8 kHz.

In summary, a large number of studies have been conducted on the self-pulsation of LCSC injectors. However, studies on the self-pulsation of GCSC injectors are a few. Therefore, there is a lack of understanding of the spray characteristics of GCSC injectors when self-pulsation occurs. In this study, the effects of recess and gas-liquid ratio on the spray pattern, spray angle, and droplet size of a GCSC injector were studied experimentally

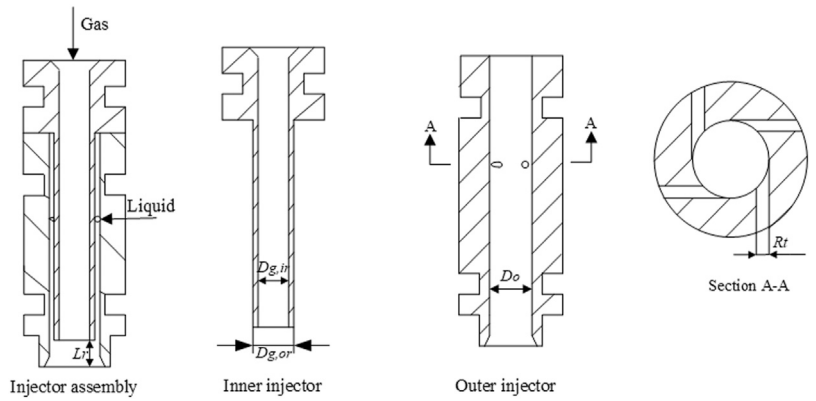

FIGURE 1 | Geometry of the injector.

TABLE 1 | Dimensional parameters of the injector.

Parameters	Values (*mm*)
D_o	5.5
D_g	3.5
h_{gap}	0.5
d_t	0.6
L_r	0, 2, 7

using a high-speed photography system and laser particle size analyzer. Mechanisms of spray self-pulsation in a GCSC injector have also been proposed.

EXPERIMENTAL METHODS

Experimental Facilities

A schematic of the GCSC injector and a detailed view of the injector are shown in **Figure 1**. As shown in **Figure 1**, the coaxial swirl injector is composed of inner and outer injectors. Dried air is injected through an inner injector. The outer injector is a swirl injector, and the liquid (water) enters the swirl chamber through four tangential entries arranged circumferentially. Under centrifugal force, a rotating liquid film is formed, which interacts with the gas at the outlet. The key geometrical parameters of the injector are listed in **Table 1**.

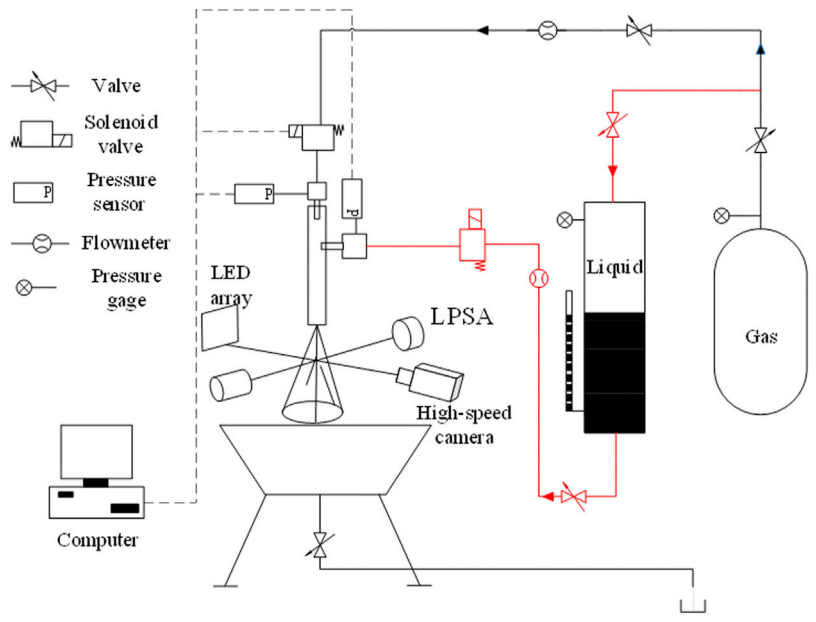

FIGURE 2 | Experimental system.

TABLE 2 | Operating conditions in experiments.

Test NO	mg(g/s)	ml(g/s)	Lr/(mm)	GLR
1	0–6.5	14	0	0–0.46
2	0–11.5	14–30	2	0–0.82
3	0–11.5	17–30	3	0–0.68
4	0–11.5	17–35	7	0–0.58

The experimental apparatus used in this study is shown in **Figure 2** and is composed of a propellant feed system, a GCSC injector, a measurement and control system, an image acquisition system, and a spray collector. Pressure sensors with an accuracy of 0.25% FS (the 4,730 diffused silicon pressure sensors) were used to measure the pressure in the liquid and gas manifold. The liquid mass flow rate was measured using a turbine flow meter (LWGY) with an accuracy of 1% FS. The gas mass flow rate was measured using a Coriolis flow meter (MFC608) with an accuracy of 0.5% FS.

Operating Conditions

In this study, experiments were conducted at atmospheric pressure with filtered water and air supplied through a propellant feed system. The operating conditions of the experiments are shown in **Table 2**.

Experimental Technique

The spray images were collected using a high-speed camera. To obtain clear spray images, a backlighting imaging technology was employed for instantaneous spray images; LED light (Scienploer Light Tech, HLS-30, Maximum power: 250 W)

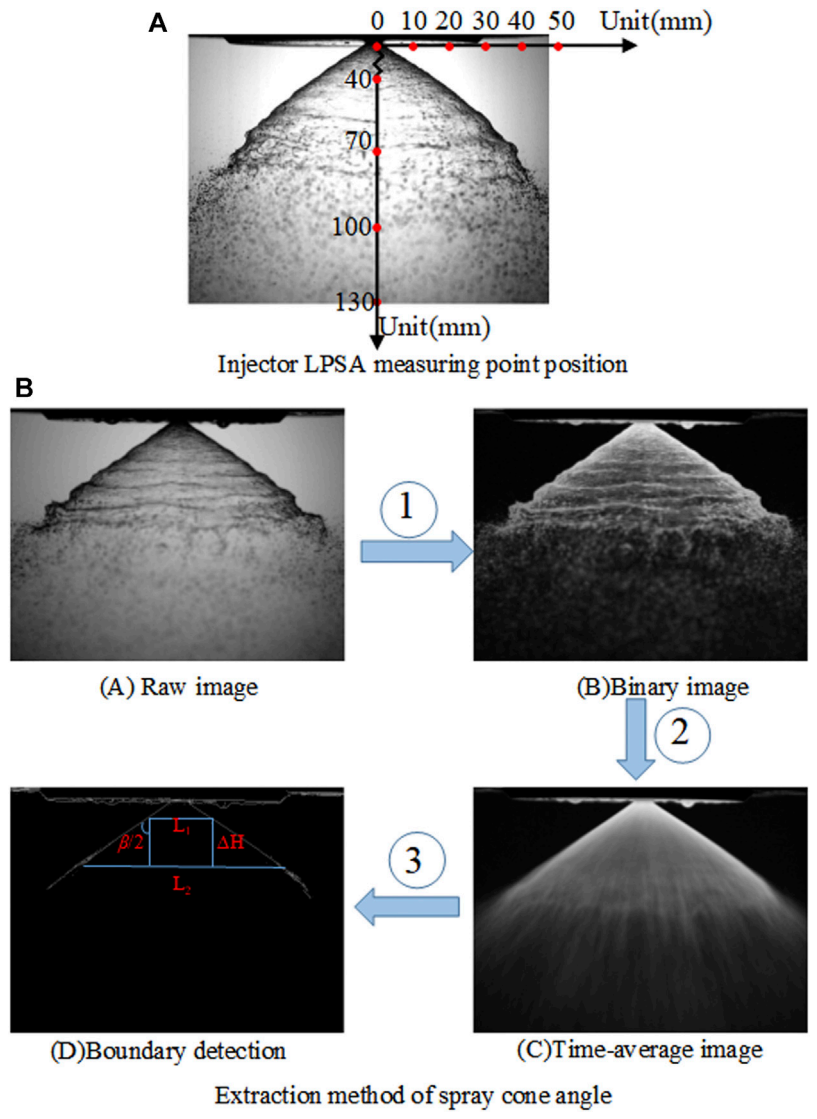

FIGURE 3 | SMD measurement and spray angle extraction method.

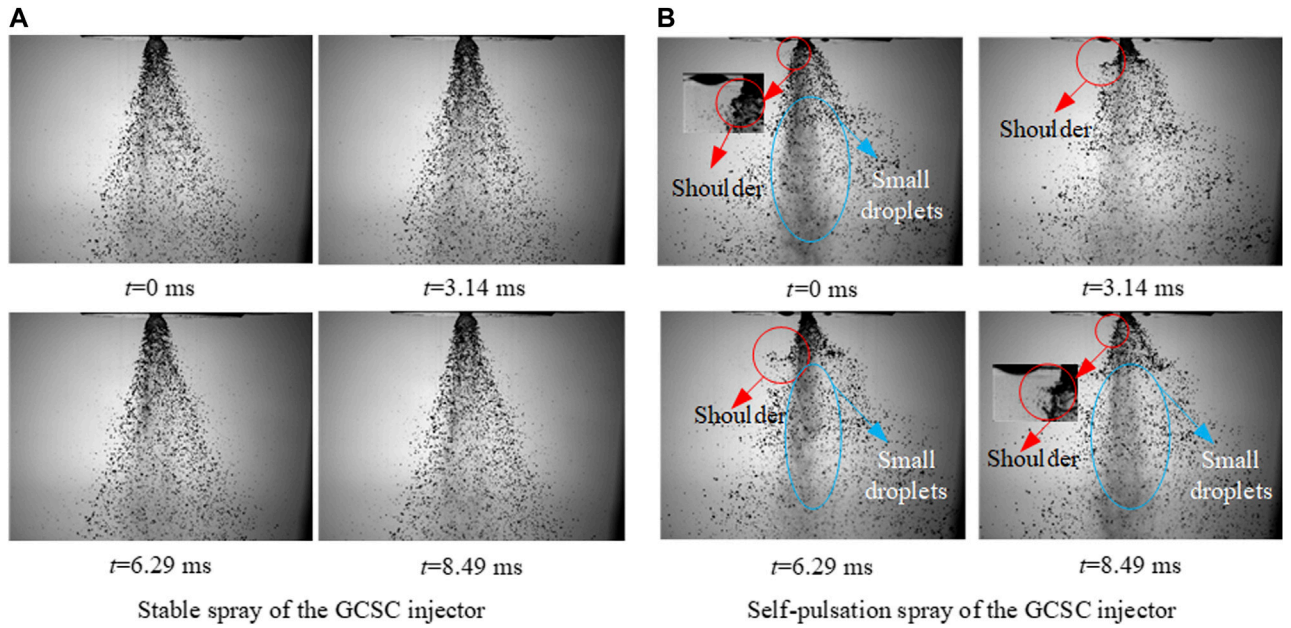

FIGURE 4 | Spray images of the GCSC injector: **(A)** Stable spray of the GCSC injector; **(B)** Self-pulsation spray of the GCSC injector.

was used to illuminate the spray. The resolution of the camera was 800 × 600 pixels with a frame rate of 31,784, and the exposure time was set to 1/478110 s. The droplet diameter was measured using a laser particle size analyzer (Spraylink, Linkoptik, 0.5%). The measurement plane was 130 mm downstream of the injector outlet. Inside this plane, the liquid film was observed to break into droplets. On the measurement plane (as shown in **Figure 3**), the measuring points were distributed along the radial direction with a distance of 10 mm from each other. The laser particle size analyzer collected 40 sets of droplet data within 20 s.

Image Processing

In this study, the spray cone angle was extracted using a method proposed by Daviault (Ramadan et al., 2012). Two straight lines were taken at different distances downstream of the injector outlet to measure the spray width on the two lines (**Figure 3B**). Finally, the spray cone angle is calculated by **Eq. 1**,

$$\frac{\beta}{2} = \arctan\left[\frac{L_2 - L_1}{2\Delta H}\right] \quad (1)$$

Where L_1, L_2 is the width of the spray on the two lines, ΔH is the vertical distance of the two lines, β is spray cone angle. The specific method (as shown in **Figure 3B**) was as follows: first, raw images with and without spray were used to remove the background and then binarize the images without the background information. The threshold was determined by a threshold segmentation algorithm based on iterative computation, and then binarized images were obtained. Consequently, the spray boundary was determined. Then, 2000 images were processed using time-equalized processing. Finally, the spray angle was determined using the method described above. By applying these three steps to a series of spray images, the spray angles for all the operational conditions were obtained. In this paper, the spray angle is extracted from the spray width of four groups of different positions. The measurement results are 112°, 110°, 109°, 115°, and the relative error is about 2%. It can be seen that the spray cone angle will not vary depending on the measurement position. The upper boundary selected in this paper is the injector orifices, and the lower boundary is 30 mm downstream of the injector orifices.

RESULTS AND DISCUSSION

Spray Pattern

Figures 4A,B show the stable and self-pulsation sprays of the GCSC injector, respectively. As seen in **Figure 4A**, the stable spray pattern remains constant over time. However, there are apparent differences between sprays of the GCSC and LCSC injectors. Tiny droplets are found at the center of the stable spray of the GCSC injector because high-speed airflow interacts with the spray and then generates some tiny droplets, because of which the spray appears as a solid cone. The stable spray of the LCSC injector has fewer droplets at the center, and the spray is hollow and conical.

When self-pulsation occurs, the spray oscillates periodically with time. For the self-pulsation spray of the GCSC injector (**Figure 4B**), similar to that proposed by Kang (Zhongtao et al., 2016), a larger liquid film width was defined as “shoulder” in this study. When self-pulsation occurs, “shoulders” are generated periodically at the injector orifice. The film primarily breaks at the shoulder, forming large droplets. In the process of downstream movement, “shoulder” development gradually

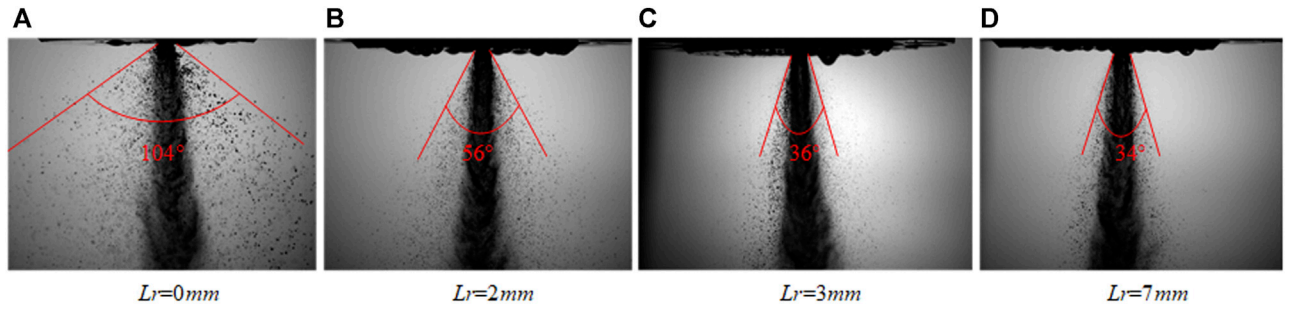

FIGURE 5 | Stable spray patterns with various recess length (m_l = 20 g/s, m_g = 12.6 g/s).

becomes more expansive. At the same time, tiny droplets are periodically generated at the center of the spray. Compared with the "shoulder" droplets, the tiny droplets at the center are smaller and move faster under the action of air flow (**Figure 4B**). In the LCSC injector, the liquid film first breaks up at the second neck, and then the second shoulder begins to break up into liquid filaments. It is worth mentioning that the LCSC injector in a different recess length of its self-pulsation spray will produce a significant "neck" and "shoulder." However, in GCSC injectors, the recess can significantly affect the shape of the spray. Sprays produce distinct "neck" and "shoulder" characteristics only in specific recess, which will be discussed in *Effect of Recess on Spray Pattern Section* of this paper.

Effect of Recess on Spray

Effect of Recess on Spray Pattern

As a crucial geometric structure of the injector, the recess has a significant effect on the spray. **Figure 5** shows a stable spray under different recess lengths with m_l (liquid mass flow rate) = 20 g/s and m_g (gas mass flow rate) = 12.67 g/s. Under the same operating conditions, increasing the recess length would decrease the radial distribution of the stable spray. As a result, the spray is more concentrated, and the entire spray appears as a dense column of liquid. This is because as the recess length increases, the contact area of the gas liquid increases, and the gas-liquid interacts strongly in the recess chamber. As a result, the gas momentum is transferred to the liquid, increasing the axial velocity of the liquid. Therefore, with an increase in the recess length, the droplets diffusing along the radial direction decrease, and the central spray becomes denser. By comparing the sprays with recess lengths of 3 and 7 mm, it was observed that the two sprays had the same morphology under the same operating conditions. This indicates that the momentum exchange between the gas and liquid phases is completed in the recess chamber. Under these conditions, increasing the recess length had little influence on the spray pattern.

The effect of recess on the spray self-pulsation was more significant. **Figure 6A** shows that when recess length is 0 mm, the spray peripheral periodically produces "shoulders," and the center periodically produces tiny droplets. Compared with the "shoulder" droplets, the tiny droplets in the center are comparatively smaller and move faster than those droplets far from the center. When the recess length increased, the droplet adhered to the wall (**Figure 6B**). The spray angle increased instantly, approaching 180°, and many droplets gathered on the injector faceplate. Kim (Kim et al., 2013) also observed an adherent phenomenon in a backpressure environment, but a specific reason was not given. When the recess length was 0 and 7 mm, no adherent phenomenon was observed. Therefore, an adherent phenomenon can be inhibited by increasing or decreasing the recess. This study suggests that the adhesion phenomenon is caused by self-pulsation.

When the recess length increases to 3 and 7 mm (**Figures 6C,D**), the self-pulsation disappears under the same operating conditions. However, this does not mean that the self-pulsation completely disappears under recess length 3 and 7 mm, but only that the operation condition range of the self-pulsation has changed. **Figure 7** shows the self-pulsation spray (m_l = 20 g/s, m_g = 3.6 g/s) with an injector L_r (recess length) = 7 mm. As observed in the figure, the morphology of the self-pulsation changes further. Like the LCSC injector, there are apparent "neck" and "shoulder" structures appearing alternately. There are still much fewer tiny droplets at the center of the spray compared with those under the same operating conditions without recess. When spray self-pulsation occurs with a recess of L_r = 7 mm, the noise produced by the spray was more prominent than that with other recess lengths. A variation in the recess length of the injector would lead to a shift in the self-pulsation operation conditions. This indicates that the self-pulsation mechanisms of the GCSC injector with different recess lengths are entirely different. The mechanisms are discussed in detail in *Mechanism of Spray Self-pulsation Section*.

Effect of Recess on Spray Angle

Recess can improve the mixing efficiency of an injector. **Figures 8A,B** show the variation law of the spray angle of the stable and self-pulsation sprays with the recess lengths. For a stable spray, increasing the recess length leads to a decrease in the spray angle. Because the increase in recess changes the spray morphology (**Figure 5**), the radial distribution of the spray decreases. However, the self-pulsation spray can reach a farther radial region, and thus the spray angle increases. When the recess length was 2 mm, self-pulsation led to the wall adherent phenomenon, and the spray angle was as high as 180°. Therefore, the spray angle first increases and then decreases

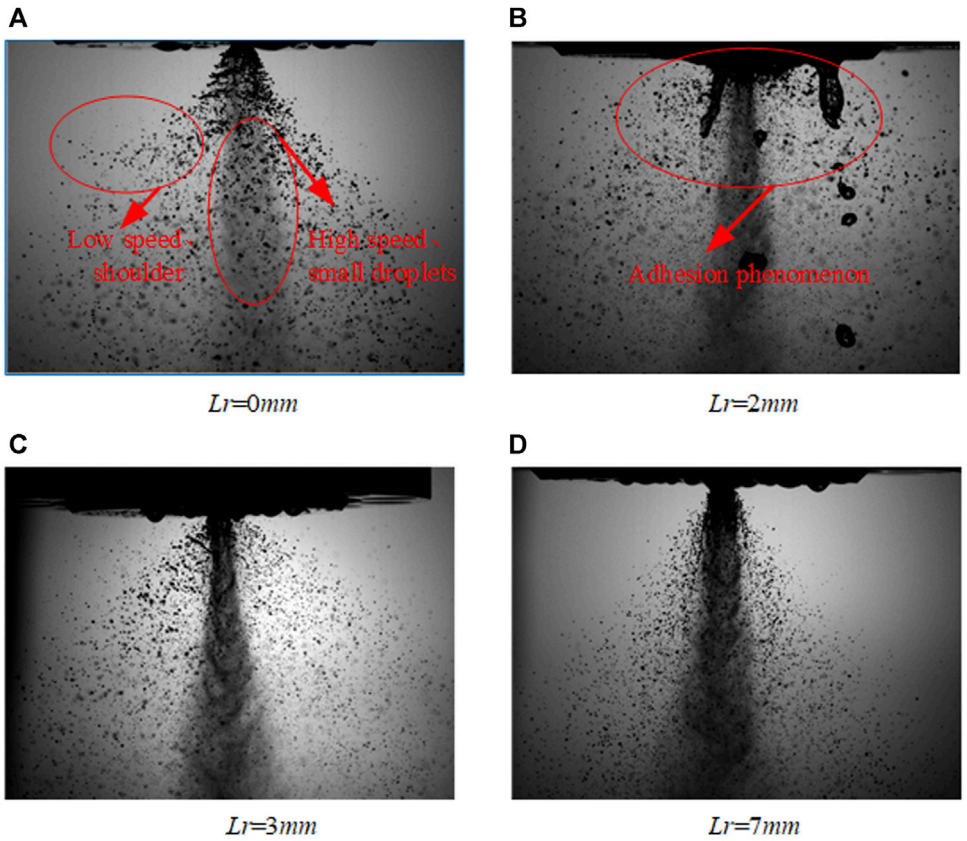

FIGURE 6 | Effect of recess on self-pulsation spray pattern (m_l = 20 g/s, m_g = 6.8 g/s).

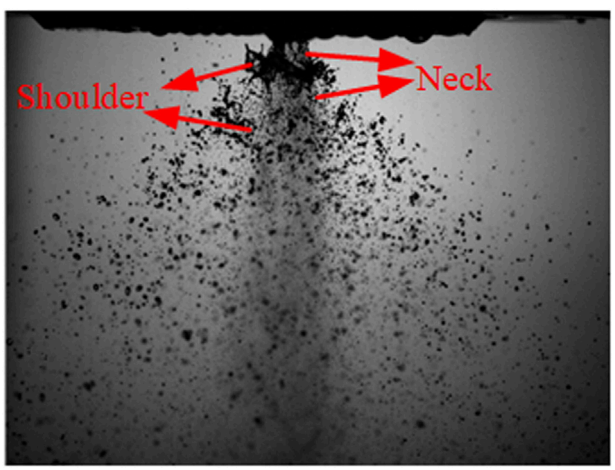

FIGURE 7 | Self-pulsation spray at the recess length of 7 mm (m_l = 20 g/s, mg = 3.6 g/s).

with an increase in recess length. This is because the self-pulsation mechanism of the spray is different under different recesses, which leads to different radial diffusion capacities of the spray.

Effect of Recess on Spray SMD

As shown in **Figure 9**, for both the stable spray (m_g = 0 g/s and m_g = 5.16 g/s) and self-pulsation spray (m_g = 10.3 g/s), increasing the recess is beneficial for improving the atomization characteristics of the injector and reducing the spray particle size. When L_r = 0 mm, self-pulsation causes the SMD distribution to show a single peak distribution. This is because when self-pulsation occurs, a large number of small droplet groups are generated in the spray center, while a large number of large droplet groups are generated on the periphery. Therefore, the SMD increases sharply in the radial direction, the SMD distribution heterogeneity increases rapidly, and the spray quality deteriorates sharply. When the recess length was 2 mm, self-pulsation had little effect on the radial distribution of the SMD. Therefore, under the same operating conditions, increasing the recess length weakens the influence of self-pulsation on the SMD radial distribution of the spray.

Effect of Gas-Liquid Ratio on Spray

Effect of Gas-Liquid Ratio on Spray Pattern

The gas-liquid ratio is an important parameter of operating conditions. When the gas mass flow rate was 0 g/s, the liquid film sheet breakup mode was characterized by a wave-assisted sheet breakup (**Figure 10A**). With an increase in gas flow, gas promotes the development of surface waves. The liquid film

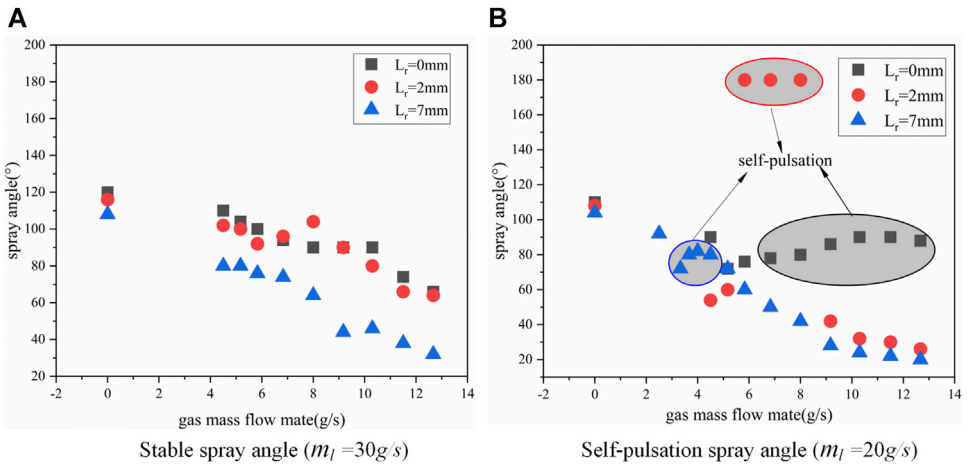

FIGURE 8 | Influence of recess on spray angle. **(A)** Stable spray angle (m_l =30 *g/s*). **(B)** Self-pulsation spray angle (m_l =20 *g/s*).

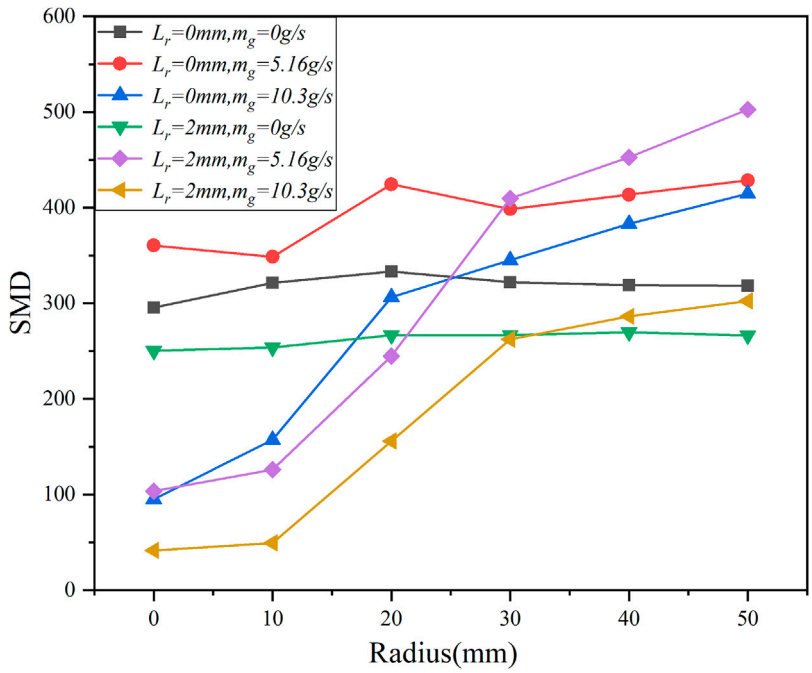

FIGURE 9 | Radial distribution of SMD with different recess lengths.

breaks at a significant wave amplitude on the surface to create holes. Subsequently, the hole gradually developed, causing the liquid film to break, forming a perforated broken hole (**Figure 10B**). The gas flow continued to increase, and the number of holes increased because the hole distribution was extremely uneven, resulting in a sizeable lumpy liquid film. The large lumpy liquid film gradually broke into liquid wire and developed into droplets downstream, forming a segmented sheet breakup (**Figure 10C**). When the gas flow rate continues to increase, the spray will cause violent pulsations. At the same time, there will be screaming, forming a self-pulsation breakup (**Figures 10D–H**). When the gas flow is sufficiently large, the gas has a powerful shearing effect on the liquid film. The liquid film was quickly cut into tiny droplets by airflow at the injector outlet. The spray formed a liquid column consisting of tiny droplets in the center, producing small droplets around it, forming an air-blasted breakup (**Figure 10** (i)).

As shown in **Figure 10**, with the increase in the gas mass flow rate (m_g = 6.8 g/s ~ m_g = 11.5 g/s), the tiny droplets in the center of the self-pulsation spray become dense gradually. This is because with the increase in the gas mass flow rate, the ejection and entrainment ability of the central gas to the droplet is enhanced.

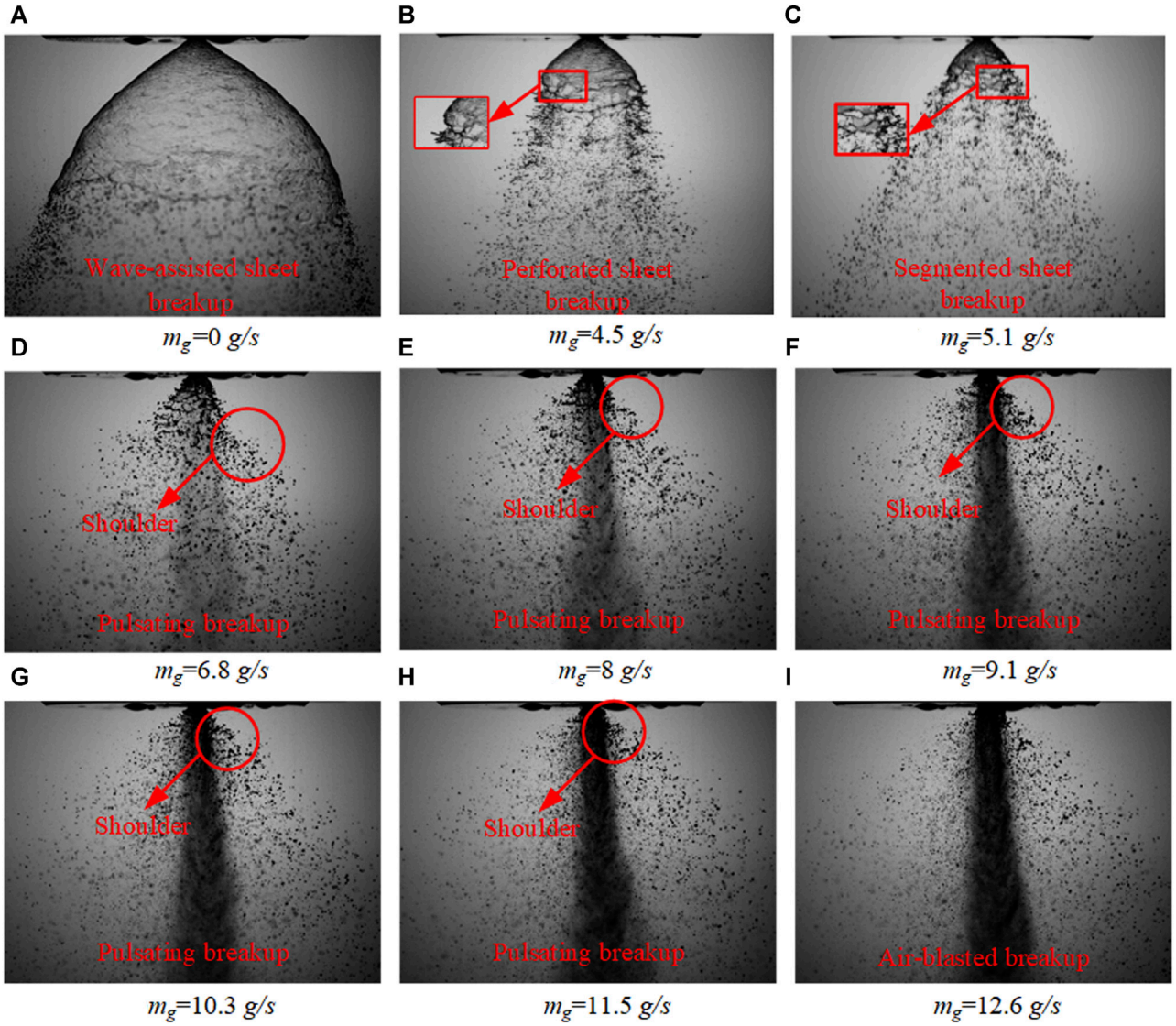

FIGURE 10 | Effect of gas-liquid ratio on spray.

However, as the gas mass flow continued to increase, the self-pulsation phenomenon gradually disappeared. Because the gas-liquid interaction is powerful and the liquid film is quickly broken into tiny droplets, liquid drops are ejected from the injectors, making the formation of bubbles difficult. Thus, it can be seen that the gas flow rate has an essential effect on the self-pulsation of the spray.

Effect of Gas-Liquid Ratio on Spray Angle

Moreover, under the condition of self-pulsation (**Figure 8B**), the spray cone angle first decreased and then increased and then decreased with the increase in gas flow. This is because the periodic oscillation of the spray will make the radial distribution of the liquid film more expansive. Under the condition of no self-pulsation (**Figure 8A**), the spray cone angle generally decreases with an increase in gas flow.

Effect of Gas-Liquid Ratio on Spray SMD

The gas-liquid ratio also had an essential effect on the SMD. As shown in **Figure 11**, increasing the gas mass flow rate worsened the uniformity of the spray particle size distribution. With the increase in the gas mass flow rate (m_g from 0 g/s to 8 g/s), the overall SMD showed an increasing trend caused by the droplet aggregation due to the ejection of the gas. As a result, the overall distribution gradually changed from the inclined "N" shape distribution to the hollow cone distribution in the radial direction. This is because a large number of tiny droplets were entrained to the center of the spray. When the gas mass flow rate is increased to 10.3 g/s, self-pulsation is generated. The overall SMD of the spray is decreased, and the reduction is more obvious in the spray center. It can be seen that the self-pulsation has a strengthening effect on atomization.

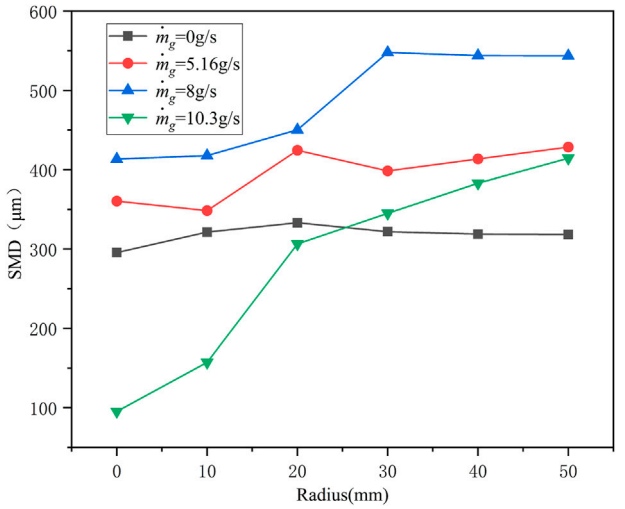

FIGURE 11 | Radial distribution of SMD under conditions with different gas-liquid ratios.

entrained. In this case, the pressure of the outer gas was greater than that of the inside gas. The entrainment ability of the gas in the liquid film was greater than the inertial force of the liquid film. At this moment, the liquid film contracted and produced a bubble-like structure, resulting in an increase in pressure inside the bubble. When the internal pressure of the bubble was greater than its surface tension, the bubble broke, resulting in self-pulsation. Santanu (Sahoo and Gadgil, 2021)classified self-pulsation without recess into two types: large-amplitude pulsation (LAP) and small-amplitude pulsation (SAP).

In this study, the adherent phenomenon was considered to be caused by self-pulsation. **Figure 13A** shows a cycle of the adherent phenomenon. As can be seen from **Figure 13A**, the liquid film contracted and then expanded in one cycle, and the liquid film touched the injector faceplate during expansion. **Figure 13B** shows the formation mechanism of the adherent phenomenon. Compared with no recess, when self-pulsation occurred under a small recess length, the position of the gas-liquid action moved upstream of the spray due to recess. Under

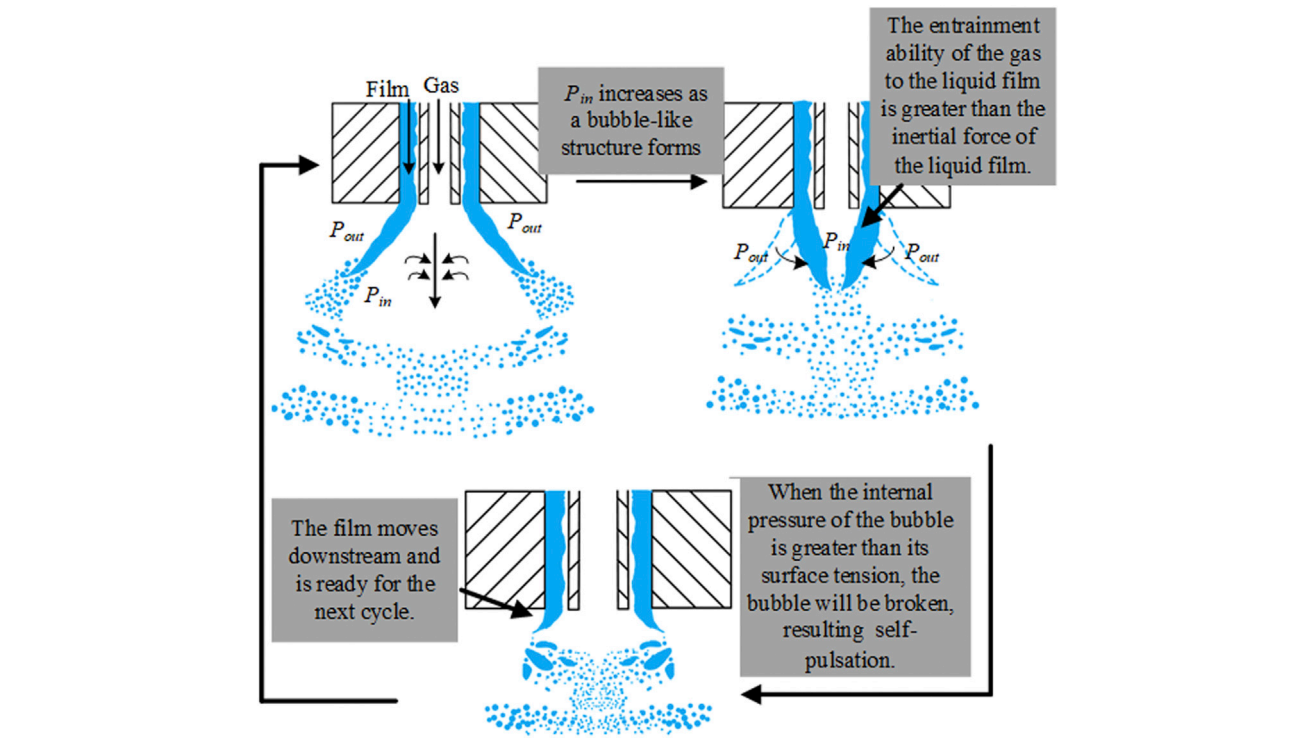

FIGURE 12 | Spray self-pulsation mechanism without recess.

Mechanism of Spray Self-Pulsation

Xu (Shun, 2016) found that the self-pulsation of the injector without recess was mainly caused by the attraction and polymerization of gas to the liquid film (**Figure 12**). When the momentum of gas reached a specific operating condition, the pressure inside the liquid film P_{in} decreased as the gas was the action of the airflow, the amplitude of the dominant surface wave increased. When the entrainment capacity of the gas was greater than the inertial force of the liquid, the liquid film contracted. When the internal pressure of the bubble was greater than its surface tension, the bubble broke at the trough of the dominant surface wave. Moreover, the pressure inside the

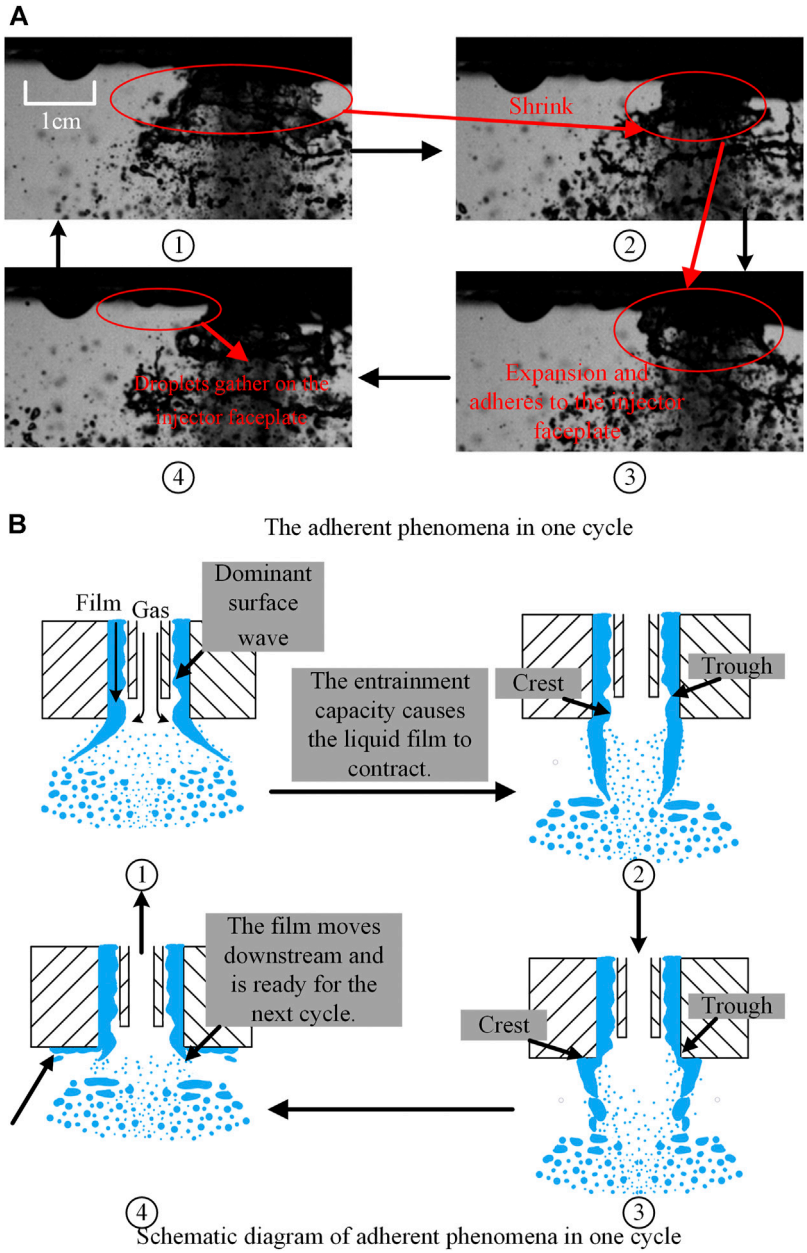

FIGURE 13 | Mechanism of adherent phenomena with small recess. **(A)** The adherent phenomena in one cycle. **(B)** Schematic diagram of adherent phenomena in one cycle.

bubble caused the crest of the liquid film near the injector orifices to impact the injector faceplate, forming adhesion. At $L_r = 2$ mm, when the gas mass flow rate or liquid mass flow rate was increased, the adhesion phenomenon weakened, which is due to the suppression of self-pulsation.

Lightfoot (Lightfoot et al., 2006) detected the gas-liquid shearing of the liquid film in the recess chamber, and shearing occurred in two forms. At a low momentum ratio, the surface waves appeared to grow uniformly. With an increase in the momentum ratio, the gas-liquid shearing effect became stronger. As a result, the thickness of the liquid film was unevenly distributed. The peaks of the surface waves increased and were stripped by the gas. This study considered that uneven surface waves under the injector in a long recess cause spray self-pulsation (**Figure 14A**). Moreover, this surface wave is formed by a strong gas-liquid shearing effect. Therefore, K-H instability is the root cause of spray self-pulsation under a long recess. As the liquid film flows in the recess chamber, the unstable shearing effect of K-H increases as the gas flow increases. This causes the surface wave of the liquid film to gradually change from a uniformly growing form to a form of gas stripping. When surface waves develop to a specific thickness (a more prominent peak is formed),

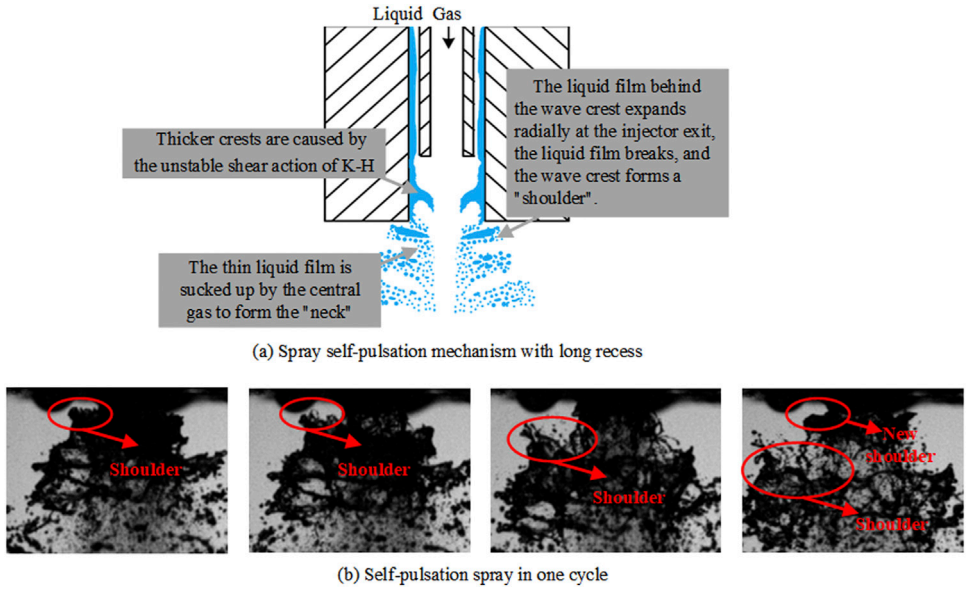

FIGURE 14 | Self-pulsation mechanism with long recess.

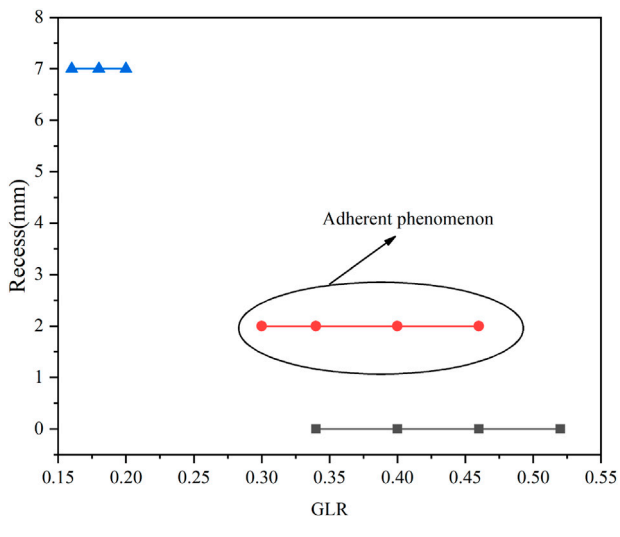

FIGURE 15 | Self-pulsation operating condition range (ml = 20 g/s).

they block the gas passageway. This causes the pressure of the gas passage to increase, pushing the liquid membrane rapidly downstream. When the gas and liquid move to the injector outlet, the liquid film loses wall constraints. Under the action of the central high-pressure gas, radial expansion occurs and breaks in the thinner part of the liquid film, and the thicker liquid film forms the "shoulder". At the same time, the central high-pressure gas pressure is released and rapidly reduced. The thinner liquid film is squeezed to the center less than the external ambient gas pressure, forming a "neck." **Figure 14B** is the image taken in the experiment, It can be seen from figure that the "shoulder" has been formed after the liquid film flows out injector orifice. This is consistent with the self-pulsation mechanism proposed in this study. In the experiment (**Figure 7**), it was found that the "shoulder" liquid flow of the spray was larger and the "neck" liquid flow was small. This is due to the thicker liquid film forming the "shoulder" and the thinner liquid film forming the "neck."

Figure 15 shows the relationship between the operating condition range of the injector self-pulsation and the recess. It can be seen from the figure that when the recess length Lr = 0 mm, the spray produces self-pulsation. Under the same gas-liquid ratio, the recess length increases to 2 mm, and the spray adhesion phenomenon occurs. It is further confirmed that the adhesion phenomenon is caused by self-pulsation. When the recess length Lr = 7 mm, the self-pulsation operating condition range is very different from the range under the small recess length.

CONCLUSION

In the present study, the self-pulsation of a gas-centered swirl coaxial injector was investigated experimentally. The effects of recess and gas-liquid ratio on the spray pattern, spray angle, and droplet size of a GCSC injector were analyzed. The following conclusions can be drawn from this study:

1. Recess has a significant influence on the shape of self-pulsation. Without recess, when spray self-pulsation occurs, both the center and the outside of the spray oscillate. The tiny droplets at the spray center oscillate, with the periphery of the spray being characterized by periodic "shoulder." The spray adheres to the panel plane under the same operating conditions but with a small recess (2 mm). With a long recess (7 mm), when spray self-pulsation occurs, the spray periodically forms "shoulder" and "neck."

2. The gas-liquid ratio is an important parameter of the injection conditions. With an increase in the gas-liquid ratio, the breaking modes of the liquid film are wave-assisted sheet breakup, perforated broken, segmented sheet breakup, self-pulsation breakup, and air-blasted breakup. In particular, with the increase in the gas mass flow rate, the tiny droplets at the center of the self-pulsation spray become dense gradually.
3. During self-pulsation, the spray particle size also oscillates. This will lead to a wider distribution of spray in the radial direction, which enhances the atomization effect of the central spray to a certain extent. The radial distribution of SMD is small at the center, but it increases sharply outward. With an increase in the spray particle size outside, the non-uniformity of the SMD distribution is rapidly increased, and the spray quality deteriorates sharply.
4. Recess determines the injector's self-pulsation mechanism. The mechanism of self-pulsation of the injector without recess is the leading action of the central gas, and the mechanism of self-pulsation of the injector under large recess is the shearing action of the K-H instability on the liquid film.

DATA AVAILABILITY STATEMENT

The original contributions presented in the study are included in the article/Supplementary Material, further inquiries can be directed to the corresponding author.

AUTHOR CONTRIBUTIONS

CJ main contributions were experiments, data processing and writing, YX and YG were the main contributors to the experiment, WC and YT contributed primarily to data processing, XL and WN mainly provided financial support for the experiment.

FUNDING

The authors would like to express their sincere acknowledgments for support from the National Natural Science Foundation of China (Grant Nos. 12002386, 51876219).

REFERENCES

Bai, X., Cheng, P., Sheng, L., Li, Q., Zhang, X., and Kang, Z. (2019). Effects of Backpressure on Self-Pulsation Characteristics of Liquid-Centered Swirl Coaxial Injectors. *Int. J. Multiphase Flow* 116, 239–249. doi:10.1016/j.ijmultiphaseflow.2019.04.017

Bai, X., Li, Q., Cheng, P., Sheng, L., and Kang, Z. (2018). Investigation of Self-Pulsation Characteristics for a Liquid-Centered Swirl Coaxial Injector with Recess. *Acta Astronautica* 151, 511–521. doi:10.1016/j.actaastro.2018.07.002

Bai, X., Sheng, L., Li, Q., Cheng, P., and Kang, Z. (2020). Effects of Annulus Width and post Thickness on Self-Pulsation Characteristics for Liquid-Centered Swirl Coaxial Injectors. *Int. J. Multiphase Flow* 122, 103140. doi:10.1016/j.ijmultiphaseflow.2019.103140

Bazarov, V. (1996). *Influence of Propellant Injector Stationary and Dynamic Parameters on High Frequency Combustion Stability*, 32nd Joint Propulsion Conference and Exhibit, Cleveland, OH.

Bazarov, V. (1998). *Non-linear Interactions in Liquid-Propellant Rocket Engine Injectors*. AIAA/ASME/SAE/ASEE Joint Propulsion Conference and Exhibit. doi:10.2514/6.1998-4039

Bazarov, V. (1995). *Self-pulsations in Coaxial Injectors with central Swirl Liquid Stage, 31st Joint Propulsion Conference and Exhibit, San Diego, CA, USA*. doi:10.2514/6.2014-3411

Gujeong, P., Lee, I., Lee, J., and Yoon, Y. (2014). *Measurement of Film Thickness in Gas-Centered Swirl Coaxial Injectors. 50th AIAA/ASME/SAE/ASEE Joint Propulsion Conference, Cleveland, OH*. doi:10.2514/6.2014-3411

Harrje, D. T. (1972). *Liquid Propellant Rocket Combustion Instability, Scientific and Technical Information Office*. Washington, DC: National Aeronautics and Space.

Im, J.-H., Kim, D., Han, P., Yoon, Y., and Bazarov, V. (2009). Self-Pulsation Characteristics of A Gas-Liquid Swirl Coaxial Injector. *Atomiz Spr* 19, 57–74. doi:10.1615/atomizspr.v19.i1.40

Im, J. H., Cho, S., Yoon, Y., and Moon, I. (2015). Comparative Study of Spray Characteristics of Gas-Centered and Liquid-Centered Swirl Coaxial Injectors. *J. Propulsion Power* 26, 1196–1204. doi:10.2514/1.48436

Im, J. H., Kim, D. J., Yoon, Y. B., and Bazarov, V. (2005). *Self-Pulsation Characteristics of A Swirl Coaxial Injector With Various Injection And Geometric Conditions*. Aiaa/asme/sae/asee Joint Propulsion Conference & Exhibit, Tucson, Arizona. doi:10.2514/6.2005-3749

Im, J. H., and Yoon, Y. (2008). *The Effects of the Ambient Pressure on Self-Pulsation Characteristics of a Gas/Liquid Swirl Coaxial Injector*. AIAA/ASME/SAE/ASEE Joint Propulsion Conference & Exhibit, Hartford, CT. doi:10.2514/6.2008-4850

Ismailov, M., and Heister, S. (2009). *Nonlinear Modeling of Classical Swirl Injector Dynamics*. Aiaa/asme/sae/asee Joint Propulsion Conference & Exhibit, Denver, Colorado.

Jeon, J., Hong, M., Han, Y. M., and Lee, S. Y. (2011). Experimental Study on Spray Characteristics of Gas-Centered Swirl Coaxial Injectors. *J. Fluids Eng.* 133, 121303. doi:10.1115/1.4005344

Jin, Z., Xiaoping, H., Yuhui, H., and Zhenguo, W. (1997). A Study of the Mixing Characteristics of Gas-Liquid Coaxial Swirling Injector of Liquid Rocket Engine. *J National University Defense Tech.* 19, 9–13.

Jin, Z., Xiaoping, H., Yuhui, H., Zhenguo, W., Liangsheng, Z., and Xiaoqing, Y. (1996). AN EXPERIMENTAL STUDY ON ACOUSTIC Characteristics of Gas-liquid Coaxial Injector Of Liquid Rocket Engine. *J Propulsion Technology* 17, 37–41.

Joseph, A., Sakthikumar, R., and Sivakumar, D. J. J. o. F. E. (2020). Experimental Characterization of Sprays in a Recessed Gas-Centered Swirl Coaxial Atomizer. *J. Fluids Eng.* 142, 4. doi:10.1115/1.4045986

Kang, Z., Li, Q., Cheng, P., Zhang, X., and Wang, Z. (2016). Effects of Recess on the Self-Pulsation Characteristics of Liquid-Centered Swirl Coaxial Injectors. *J. Propulsion Power* 32, 1–9. doi:10.2514/1.b35632

Kim, J. G., Han, Y. M., Choi, H. S., and Yoon, Y. (2013). Study on spray Patterns of Gas-Centered Swirl Coaxial (GCSC) Injectors in High Pressure Conditions. *Aerospace Sci. Technol.* 27, 171–178. doi:10.1016/j.ast.2012.08.004

Lightfoot, M. (2005). *Atomization Mechanism of Wall-Bounded Two-phase Flows*.

Lightfoot, M., Danczyk, S. A., and Talley, D. G. (2006). *Atomization in GasCentered Swirl-Coaxial Injectors. ILASS Americas, 19th Annual Conference on Liquid Atomization and Spray Systems, Toronto, Canada, May 2006*.

Matas, J. P., Hong, M., and Cartellier, A. (2014). Stability of a Swirled Liquid Film Entrained by a Fast Gas Stream. *Phys. Fluids* 26, 121303–121366. doi:10.1063/1.4871395

Ramadan, O. B., Matida, E. A., Hughes, P. M., and Hughes], R. J. F. (2012). Atomization Performance of Petroleum Coke and Coal Water Slurries from a Twin Fluid Atomizer. *Fuel* 98, 183–193. doi:10.1016/j.fuel.2012.02.042

Sahoo, S. K., and Gadgil, H. (2021). Dynamics of Self-Pulsation in Gas-Centered Swirl Coaxial Injector. *An Exp. Study J Propulsion Power* 37. doi:10.2514/1.b38043

Shun, X. (2016). *Research on the Dynamic spray Characteristics of the Gas-Centered Swirl Coaxial Injector*. National University of Defense Technology, Changsha.

Sivakumar, D., and Kulkarni, V. (2011). Regimes of spray Formation in Gas-Centered Swirl Coaxial Atomizers. *Exp. Fluids* 51, 587–596. doi:10.1007/s00348-011-1073-7

Xuan, L., Tian, L., Jinli, H., Shaohua, Z., and Xu, X. (2013). *The Preliminary Study of Oxygen-Centered Kerosene-Swirl Coaxial Injector*. Aiaa/asme/sae/asee Joint Propulsion Conference, Cleveland, OH.

Yang, L.-j., Ge, M.-h., Zhang, M.-z., Fu, Q.-f., and Cai, G.-b. (2008). Spray Characteristics of Recessed Gas-Liquid Coaxial Swirl Injector. *J Propulsion Power* 24, 1332–1339. doi:10.2514/1.23977

Yoon, J., Chung, J. M., and Yoon, Y. (2013). *Study on Self-Pulsation Characteristics of Gas/Liquid Shear Coaxial Injector with Annular Liquid Sheets*. Aiaa/asme/sae/asee Joint Propulsion Conference & Exhibit, Atlanta, Georgia.

Yuhui, H. (2001). *Theoretical, numerical Simulation and Experimental Investigations of Combustion Instability in Liquid Rocket Engine*. National University of Defense Technology, Changsha.

Zhenguo, W. (2012). *Modeling and Numerical Simulations of Internal Combustion Process of Liquid Rocket Engines*. National Defense Industry Press, Beijing.

Zhongtao, K., Li, Q., Peng, C., Xinqiao, Z., and Zhen-guo, W. (2016). Effects of Self-Pulsation on the spray Characteristics of gasCliquid Swirl Coaxial Injector. *Acta Astronautica* 127, 249–259. doi:10.1016/j.actaastro.2016.05.038

Zhongtao, K. (2016). *The Unsteady Atomization Mechanism and Combustion Characteristics of Gas-Liquid Swirl Coaxial Injector*. National University of Defense Technology, Changsha.

Conflict of Interest: The authors declare that the research was conducted in the absence of any commercial or financial relationships that could be construed as a potential conflict of interest.

NOMENCLATURE

n Number of tangential holes of external injector

D_o diameter of liquid orifice (mm)

D_g diameter of gas orifice (unit:mm)

h_{gap} gap thickness (unit: mm)

dt diameter oftangential inlet (unit: mm)

L_r recess length (unit:mm)

D_i droplet diameter(unit:mm)

Ni the number of droplets with a diameter of D_i.

m mass flow rate

Subscripts

g gas

l liquid

frontiers in Energy Research

ORIGINAL RESEARCH
published: 06 October 2021
doi: 10.3389/fenrg.2021.756905

Improvement of Mixing Efficiency in the Combustion Chamber of a Powder-Fuel Ramjet Engine

Wenxiong Xi[1], *Jian Liu*[1]* *and Ren Mengfei*[2]*

[1]School of Aeronautics and Astronautics, Central South University, Changsha, China, [2]College of Astronautics, Nanjing University of Aeronautics and Astronautics, Nanjing, China

The challenge of the powder-fuel ramjet is to improve the mixing effect of powder-fuel with oxidizing agents and combustion efficiency. To improve the mixing and combustion efficiency of the powder-fuel ramjet engine, three configurations in head shapes and three exhaust gas inlet patterns of the engine are designed based on a typical powder-fuel ramjet engine combustion chamber. The effect of the head shapes and exhaust gas inlet patterns is analyzed and compared by the three-dimensional numerical simulation method. A comprehensive model validation is built, and the calculation results of the k-ε standard model are compared with the experimental data. The results show that the cylindrical head forms a recirculation zone at the head of the combustion chamber, which leads to powder deposition in the head region of the chamber. The design with the round head and the coned head reduces the recirculation inside the head region, and the exhaust gas from the fuel gas generator has benefits in powder injection and mixing inside the combustion chamber. The exhaust gas inlet of the inclined six hole type has benefits in the mixing of powder and high temperature exhaust gas because it generates strong flow impingement in the core part of the chamber.

Keywords: powder ramjet engine, powder deposition, mixing, flow impingement, pressure loss

OPEN ACCESS

Edited by:
Lei Luo,
Harbin Institute of Technology, China

Reviewed by:
Wei Huang,
National University of Defense Technology, China
Zhiyong Lin,
Sun Yat-sen University, China

***Correspondence:**
Ren Mengfei
15656279836@163.com
Jian Liu
jian.liu@csu.edu.cn

Specialty section:
This article was submitted to Advanced Clean Fuel Technologies, a section of the journal Frontiers in Energy Research

Received: *11 August 2021*
Accepted: *01 September 2021*
Published: *06 October 2021*

Citation:
Xi W, Liu J and Mengfei R (2021) Improvement of Mixing Efficiency in the Combustion Chamber of a Powder-Fuel Ramjet Engine. Front. Energy Res. 9:756905. doi: 10.3389/fenrg.2021.756905

INTRODUCTION

The powder-fuel ramjet engine combines the advantage of the solid ramjet and the liquid ramjet engine and has drawn a lot of attention in recent years. It uses high-energy metal/non-metal powder as fuel for combustion (Woosuk et al., 2018). It obtains high combustion efficiency and an adjustable fuel supplying rate like a liquid ramjet engine. In addition, it has simple structures, high reliability and easy maintenance like a solid ramjet engine. More and more researchers try to use new fuels in ramjets (Singh and Walker, 2015). Metal fuels can achieve large heat release and high specific impulse in the combustion process compared with traditional hydrocarbon fuels (Goroshin et al., 2001).

Compared with a solid ramjet engine, the flow rate of the powder fuel is easier to be adjusted like one kind of fluid fuel (Gong et al., 2017). In addition, due to the high energy density in the metal powder, the engine can obtain high specific impulse. However, it is difficult to achieve a self-sustaining burn depending on metal powder because a combustion environment of high temperature is required for metal powder. Xu et al. (Xu et al., 2019) designed a hybrid powder–solid fuel ramjet (HPSR). Although the problem of the high-temperature combustion environment has been improved in an HPSR, some new problems about combustion efficiency and flame stabilization have to be solved. For Mach numbers in excess of those for which turbojet concepts can be used, subsonic burning ramjet concepts are used until their Mach number limit is reached (Bertin and

Cummings, 2003). Flow structures in a powder-fuel ramjet have changed a lot compared with the traditional scramjet combustor, and the traditional strategy of flame stability needs some modifications (Liu et al., 2020a). Owing to the high combustion requirements of metal particles, some strategies are needed to sustain the combustion, which also brings about other problems such as deposits of combustion products, excessive pressure loss, and low mixing efficiency (Li et al., 2019). These problems can be solved by using a flame stabilizer designed by Hsu et al. (Hsu et al., 1995). However, the design of the flame stabilizer increases the complexity of the structure and reduces reliability.

Many research studies about powder combustion in a powder-fuel ramjet have been performed, including the research centers of NASA and ONERA. Linnell and Miller (2002) analyzed the ramjet with a combustion chamber at a pressure around 250 kPa, and a thrust of 2900 N and specific impulse of 400 s were achieved. Goroshin et al. (1999) found that the combustor operating at fuel-rich conditions has benefits for the combustion stability. An experimental prototype of a powder-fuel ramjet was built and tested in ONERA (A (2002). Ramjet scra, 2002), which laid the foundation for experimental measurements. Miller and Herr (2004) measured effectiveness of these powder-fuel systems, and the related thrust and specific impulse at conditions were obtained. Abbud-Madrid et al. (2001) also tried to use metal and high-energy non-metal powder as engine fuels. It is found that the residual time and powder size can affect the flame shape and the burning rate. Shafirovich et al. (1993)and Shafirovich and Varma (2008) tested the burning of magnesium powder particles with carbon dioxide. It is concluded that magnesium is the most promising fuel with the relatively high-specific impulse and easy inflammability in CO_2. The results also show that the reaction of aluminum and carbon dioxide in the ramjet and turbojet engines is feasible. Recently, boron powder has drawn some attention as the fuel for powder ramjet engines (Abdalla et al., 2020). Gany (2015) has studied the boron powder combustion applied in the ramjet combustors. Regarding the blocking phenomenon caused by the thermodynamic reaction at high temperature and pressure, the blocking phenomenon becomes worse at a high ratio of boron/air. Rashkovskiy (2019) developed the model of the residue formation in the combustion chamber with boron powder propellants. Li et al. (2016) investigated an aluminum powder-fuel ramjet, and they found that the increased mass rate of the fluidization gas improved the mixing efficiency.

Mixed compression inlets and isolators exhibit a series of such interactions at different Mach numbers and boundary layer thicknesses (Gaitonde, 2015). The geometric shape of the combustion chamber has a great influence on the blending efficiency (Chelaru and Mingireanu, 2011). Different powder injection arrangements and air inlet patterns were studied by Stowe et al. (2004), such as the angle between the powder injection and the air inlets, the axial distance from the burner head to the air inlets, and the angle between the two air inlets. The main problem that exists in the powder-fuel ramjet is to enhance the mixing effect of the air and the powder fuel (Huang et al., 2020). It is necessary to search for an optimized shape of the combustion chamber and an improved exhaust injection pattern for a powder-fuel ramjet (Li et al., 2021). Because the research work on powder injection and combustion chamber design is in a preliminary stage, some experience and related parameters of solid fuel injection of a solid rocket ramjet are referred.

From the above, there are limited research studies about the design of the combustion chamber in a powder-fuel ramjet to improve the mixing. In the present work, effects of different designs on the head shapes and inlet patterns are considered. Based on a certain typical powder-fuel ramjet, three configurations in head and three exhaust inlet patterns of the engine are designed. The influence of the structural design is analyzed and compared by the three-dimensional numerical simulation method. The mixing efficiency, pressure loss, and relative density distributions are analyzed to provide some references for the design the combustion chamber. Because of the poor deposition and mixing effect in the head region of a powder fuel ramjet, a parametric study of head shapes and gas inlet patterns is performed to improve the mixing efficiency and avoid deposition. The optimal structure of the combustion chamber is proposed for initial design of a powder-fuel ramjet.

GEOMETRIC MODEL

Combustion Chamber of a Typical Powder-Fuel Ramjet

Based on the aforementioned research works, a typical combustion chamber model of the powder-fuel ramjet is created (**Figure 1**). The oxidizer, air, enters the combustion chamber through two separated air inlets mounted on the combustion chamber along the streamwise direction, shown as air inlet 1 and air inlet 2 in the figure. The air supplied from air inlet 1 makes the air-to-powder ratio close to the equivalent ratio and then meets the requirements of engine startup and ignition (Auerswald et al., 2020). Air from air inlet 2 increases the air-to-powder ratio to improve the specific impulse of the engine and combustion efficiency. There are some exhaust inlets arranged on the head of the combustion chamber. The high-temperature and high-speed exhaust is injected into the combustion through these exhaust inlets. The powder fuel is injected from the central inlet on the head of the chamber by the fluidization gas. The working medium of the fluidization process is air. The fluidizing powder mixes with the exhaust from the exhaust inlet, air from air inlet 1 and air inlet 2 in the combustion chamber.

Computational Domain

From the published articles, some parameters of a solid rocket ramjet are given in **Table 1**. In the table, the geometric configuration of the experimental combustor and test conditions are available. **Figure 2** shows the related geometric parameters of the combustion chamber. The diameter of the combustion chamber is 160 mm (d) with a length of 1,560 mm (l). The simplified engine has six main exhaust nozzles, with a diameter of 16 mm (d_2). They are distributed circumferentially at an angle of 60 degrees. The diameter of the powder inlet is 21 mm (d_1). The lengths of the two rectangular air inlets on the

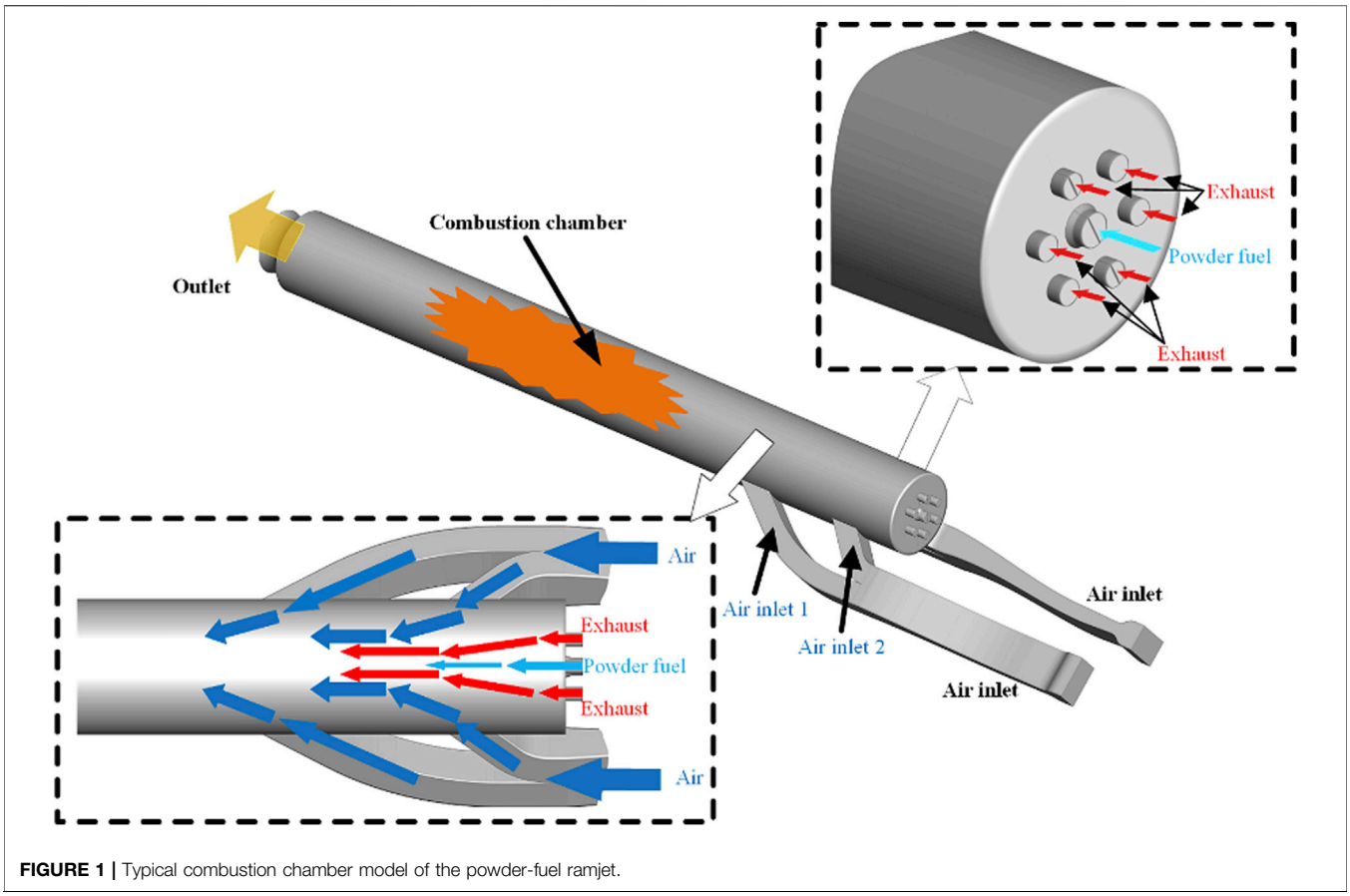

FIGURE 1 | Typical combustion chamber model of the powder-fuel ramjet.

TABLE 1 | Geometric parameters and test conditions of the previous experiments.

Reference	*d* (mm)	Air inlets and type	α (°)	*h* (mm)	Fuel injection type
W.H. and Clark (Clark, 1982)	196.85	2 Circular, 162 deg opposed	60	0.5	In inlets
Choudhury (Choudhury, 1982)	89	4 Circular, cantable	45,75	0.6–4.0	Radial central
Stull et al. (Stull et al., 1983)	150	2 Rectangular ventral	30,45,60	0.4–0.9	In inlets
Dijkstra et al. (Dijkstra et al., 1995)	100	2 Circular ventral	45	0.7	Central nozzle protruding 30 mm
Dijkstra et al. (Dijkstra et al., 1995)	127	2 Circular ventral	45	0.96	Central nozzle protruding 51 mm
Ristori et al. (Ristori et al, 1999)	100	2 Square, opposed	45	0.65–1.35	2 Nozzles, laterally off center
Vigot et al. (Vigot et al., 1991)	85	4 Circular, shifted, deflectors	45–90	0.5	Various
Vigot et al. (Vigot et al., 1991)	168	4 Circular, shifted, deflectors	45–90	0.5	Various
Hsieh et al. (Hsieh et al., 1989)					two dimensional
Schadow (Schadow, 1972)	150	2 Opposed rectangular slits	45	0, Negative	Central nozzle

side wall are 82 mm (l_1) and 52 mm (l_2), respectively. From the top view, the angle between the two air inlets is 90 degrees. To study the influence of the structural shape in the head and exhaust inlet of the combustion chamber on the mixing and engine performance, dome height 1, dome height 2, and the distance between the high-temperature exhaust inlet center and the fuel inlet center are fixed at 110 mm (h_1), 330 mm (h_2), and 37 mm (l_3), respectively.

Based on the traditional design with a cylindrical head and six exhaust inlets type (case A) Chuang et al. (1989), two modified designs varied in head shapes and three exhaust inlet patterns were built aiming at improving the mixing efficiency. The head shapes of case B and case C are designed as a round head type and a coned head type, respectively, as shown in **Figure 3** (case B) and (case C). In **Figure 4**, the high-temperature exhaust inlet is designed as four-hole type in case A1 and eight-hole type in case A2. Case A3 is designed as six inclined holes, with an inclination angle of 30 degrees. The details of the six configurations are described as follows:

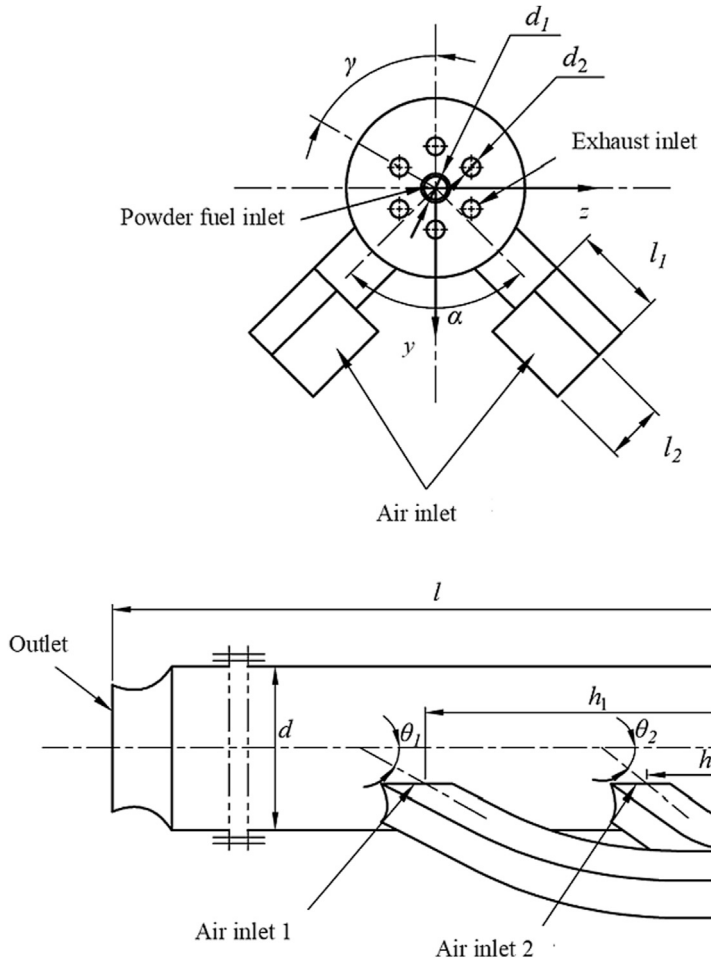

FIGURE 2 | Related geometric parameters of the combustion chamber.

Case A: basic model, cylindrical head, six exhaust inlets. Case B: round head with spherical diameter of 243 mm, six exhaust inlets. Case C: coned head with the inclined contracted angle of 22 degrees, six exhaust inlets

Case A1: cylindrical head, four exhaust inlets

Case A2: cylindrical head, eight exhaust inlets

Case A3: cylindrical head, six inclined exhaust inlets with an inclination angle of 30 degrees

COMPUTATIONAL METHODOLOGY

Governing Equations and Model Validation

In the calculations, three turbulence models are tested and compared. Commercial CFD software ANSYS Fluent 19.0 Liu et al. (2020b) is used for simulation. It uses parallel algorithm to solve the three-dimensional Navier–Stokes equation in a structured multi-block grid system. In order to simulate the compressible flow regime, a density-based solver scheme Roe (2003) is applied.

Murty and Chakraborty (2012) used the k-ε standard model in the study of mixing effects and obtained pretty accurate results. The transport equations of k and ε are shown as following two equations:

$$\frac{\partial}{\partial t}(\rho k) + \frac{\partial}{\partial x_i}(\rho k u_i) = \frac{\partial}{\partial x_j}\left[\left(\mu + \frac{\mu_t}{\sigma_k}\right)\frac{\partial k}{\partial x_j}\right] + G_k + G_b - \rho\varepsilon - Y_M + S_k$$

and

$$\frac{\partial}{\partial t}(\rho\varepsilon) + \frac{\partial}{\partial x_i}(\rho\varepsilon u_i) = \frac{\partial}{\partial x_j}\left[\left(\mu + \frac{\mu_t}{\sigma_\varepsilon}\right)\frac{\partial \varepsilon}{\partial x_j}\right] + C_{1\varepsilon}\frac{\varepsilon}{k}(G_k + C_{3\varepsilon}G_b) - C_{2\varepsilon}\rho\frac{\varepsilon^2}{k} + S_\varepsilon.$$

In the two equations, μ_t is written as follows:

$$\mu_t = \rho C_\mu \frac{k^2}{\varepsilon}.$$

The species transport equation is also used in this article, and this conservation equation takes the following general form:

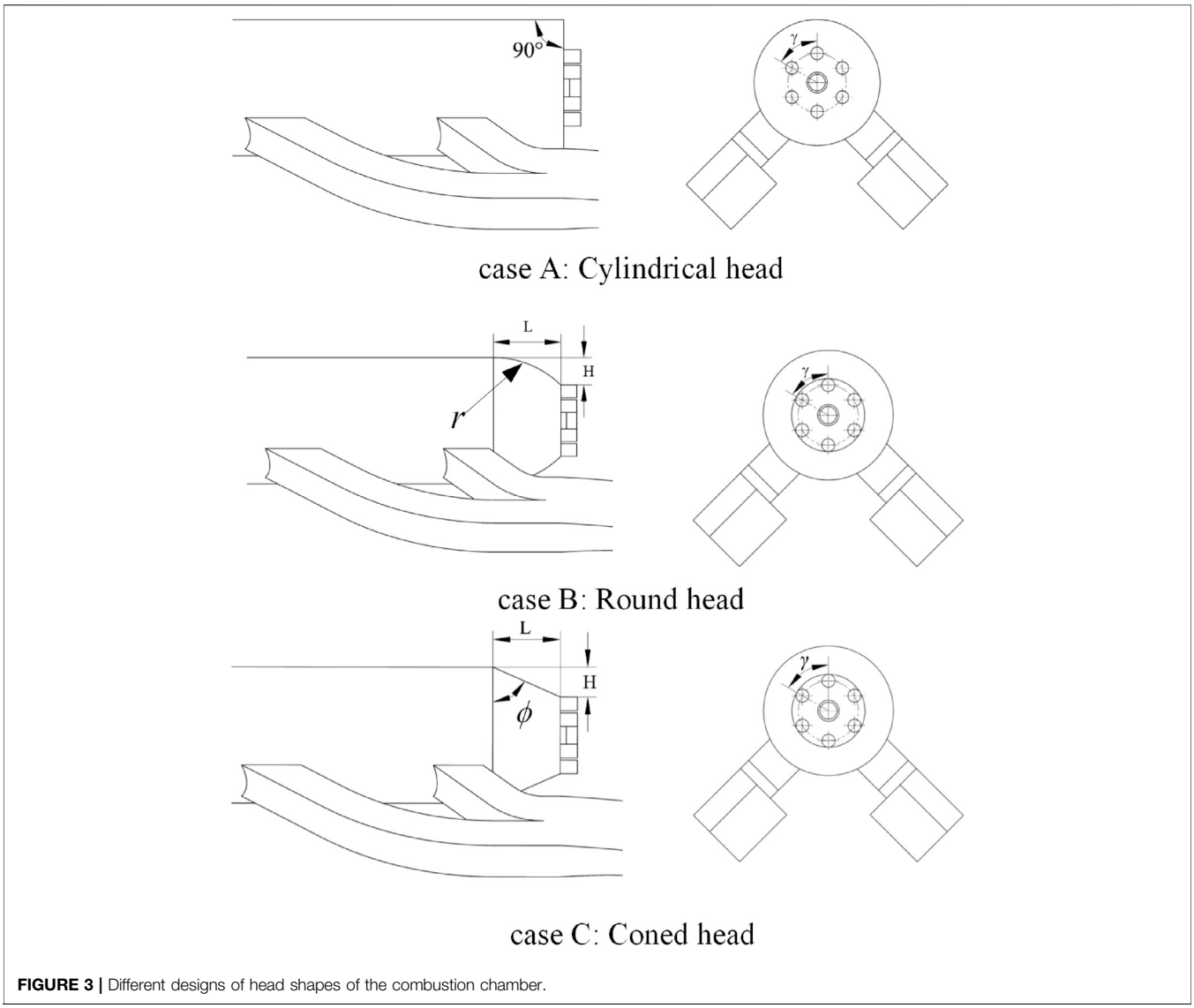

FIGURE 3 | Different designs of head shapes of the combustion chamber.

$$\frac{\partial}{\partial t}\left(\rho Y_i\right) + \nabla \cdot \left(\rho \overline{\boldsymbol{v}} Y_i\right) = -\nabla \cdot \overline{\boldsymbol{J}}_i + R_i + \boldsymbol{S}_i,$$

where R_i is the net rate of production of species i by chemical reaction and S_i is the rate of creation by addition from the dispersed phase plus any user-defined sources.

The k-ε standard turbulence model has been used in this work. The pressure values predicated by the turbulence model and the pressure measured by the experiments in the combustion chamber of the ramjet are compared in **Figure 5**. Obviously, the predicted results by the k-ε standard model have good agreement with the trend with the tested result and the ratio of pressure to total pressure at each pressure measurement locations along the axis in different operation conditions is nearly overlapped. Since the three cross-sectional areas show a trend of increasing and then decreasing, the pressure ratio shows a trend of decrease and then increase. In addition, the results show that the model has good stability and the obtained value has acceptable deviations in a certain range of fluctuations. It should be pointed out that there are some inevitable differences between simulation results and experimental results. For example, the pressure test region has relatively large disturbance by the instruments. However, the fluctuation can be ignored in the simulation process, and the pressure change is not obvious. Therefore, the k-ε standard model has shown enough validations for later calculations.

Boundary Conditions

In the present work, the mixing effect of high-temperature exhaust and the powder is replaced by the mixing of high-temperature exhaust (H_2O and CO_2) with air ejecting from the central inlet. **Table 2** gives the related parameters of air and high-temperature exhaust and the boundary conditions of the work. The assumptions in the calculations are listed as follows.

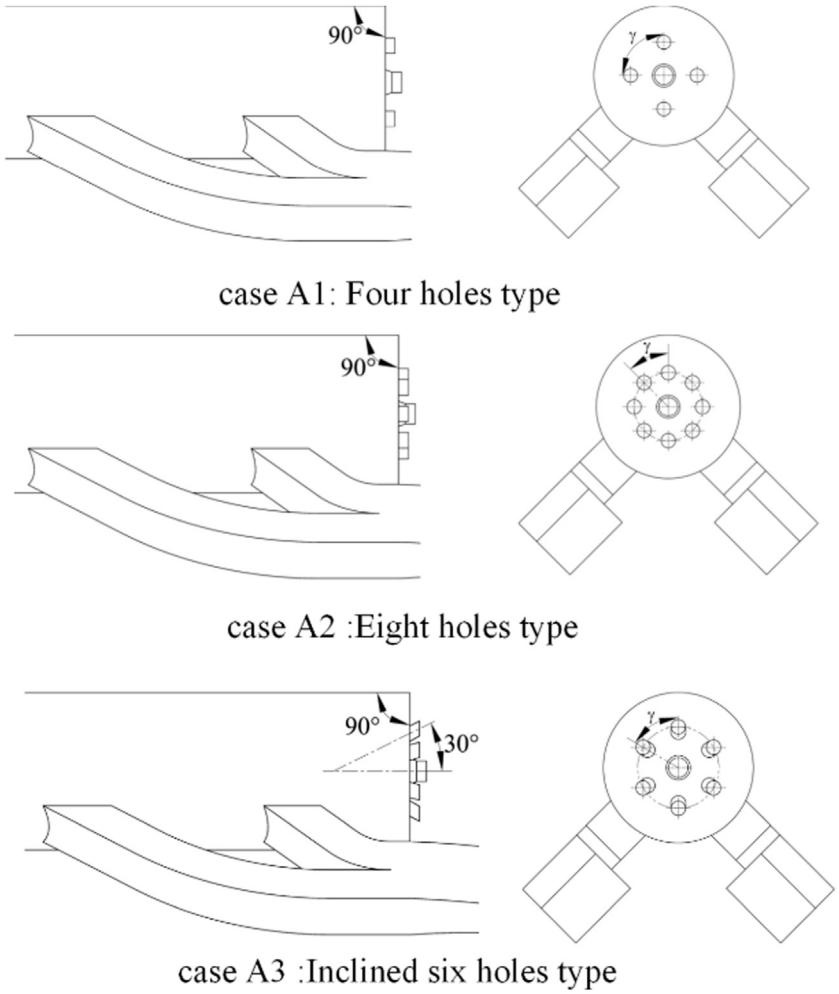

FIGURE 4 | Different designs of exhaust inlet patterns mounted on the combustion chamber.

1) The fluidized gas of powder is assumed as air.
2) The exhaust is assumed as H_2O and CO_2. There are many substances in the high-temperature exhaust, but only the CO_2 and H_2O vapors are considered.
3) The gas in the combustion chamber is adiabatic without heat exchange with the surrounding environment.
4) Gaseous radiation and body force are ignored.
5) High-temperature exhaust is regarded as an ideal gas.

Mesh Generation

In order to reduce the calculation effort, the computational domain is half of the entire domain with the symmetry boundary conditions. The structured meshes are generated to improve the calculation accuracy. The meshes in the head region are dense because the flow structures and mixing effect in this region are complex. The structured meshes in the whole domain and some typical regions are displayed in **Figure 6**.

The computational domain and grid are generated using commercial software ANSYS ICEM 19.0. A multiblock grid approach is used (as shown in **Figure 6**). To ensure the accuracy of the numerical simulation, cells are densely close to the wall surface, the high-temperature exhaust inlet, and the powder inlet. The height of the first cell row is made a value of 0.1 mm near the wall, and the total number of cells is 0.9 million.

Grid Independence Analysis

In order to eliminate the influence of the grid sizes on the calculation results, three different mesh systems are built for the grid independence study, the grids are coarse, medium, and fine, and the number of grids is 0.26, 0.91, and 1.48 million, respectively. For different grid regimes, the concentration distribution of carbon dioxide on the section of the combustion chamber is compared. **Figure 7** shows the concentration distribution of carbon dioxide at each interface of the combustor displayed by the three different grid regimes. The *y-z* cross section at $x/l = 0.25$ is selected from the location of the side wall air inlet mounted the combustion chamber, and the concentration value shows great fluctuation. Therefore, the carbon dioxide concentration in the cross section of the combustion chamber is significantly reduced after $x/l = 0.25$.

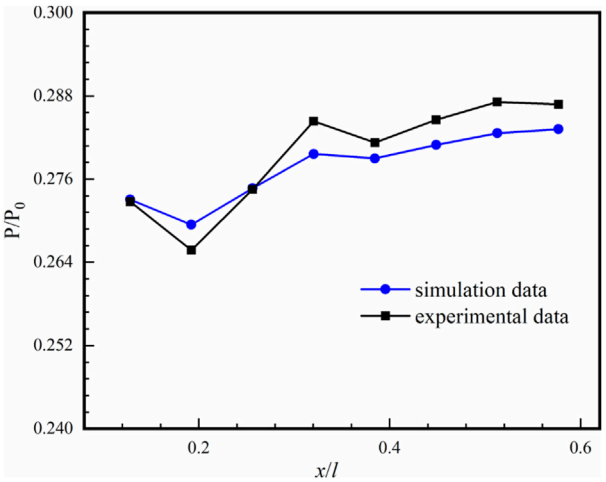

FIGURE 5 | Turbulence model validation: the value of P/P_0 on *y-z* sections along the streamwise direction at different locations between simulation and experimentation.

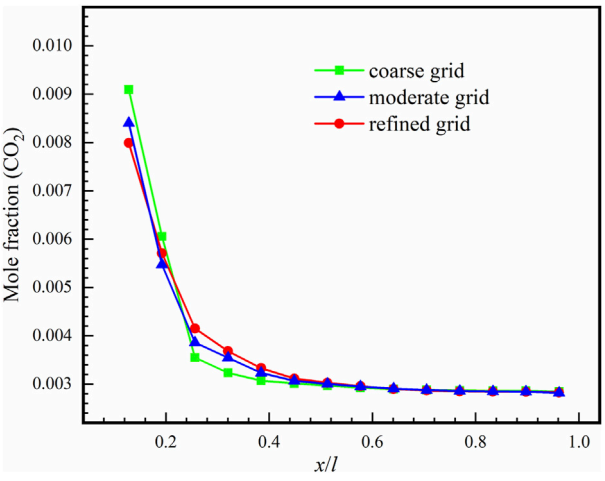

FIGURE 7 | Averaged mole fraction of CO_2 on *y-z* sections along the streamwise direction predicted by different grid regimes.

TABLE 2 | Boundary conditions.

Boundary	Total temperature(K)	Static pressure (kPa)	Mass flow (kg/s)	Outlet pressure (Pa)	Types
Air inlet	806.5	623.1	2.385	—	Mass flow inlet
Exhaust inlet	2,200	26.667	0.104	—	Mass flow inlet
Fuel inlet	806.5	623.1	0.01925	—	Mass flow inlet
Outlet	—	20	—	$2.0x10^4$	Pressure outlet
Wall	—	—	—	—	Wall

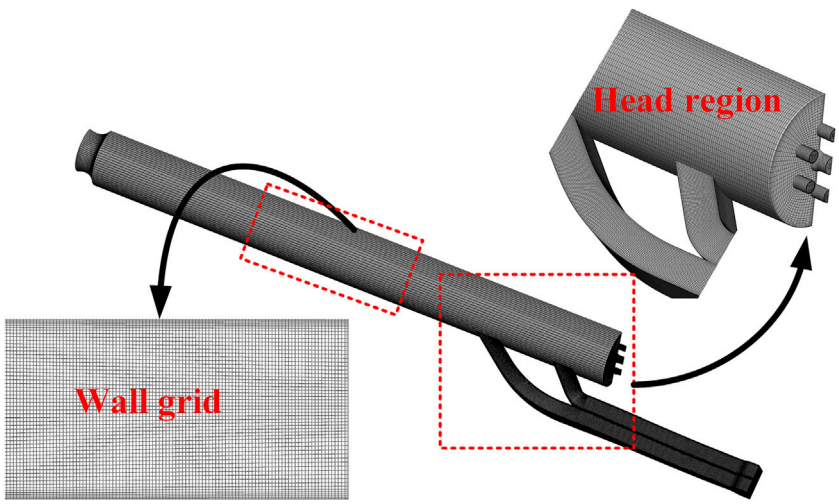

FIGURE 6 | Structured meshes in the typical regions.

From **Figure 7**, the calculated carbon dioxide concentration on the cross section by three grid systems is basically overlapping. The medium grid and fine grid are closer to each other at the separation point. In order to balance the calculation efficiency and accuracy, medium grid is used for subsequent calculation. The average value of y plus calculated on the grid wall is 22, which

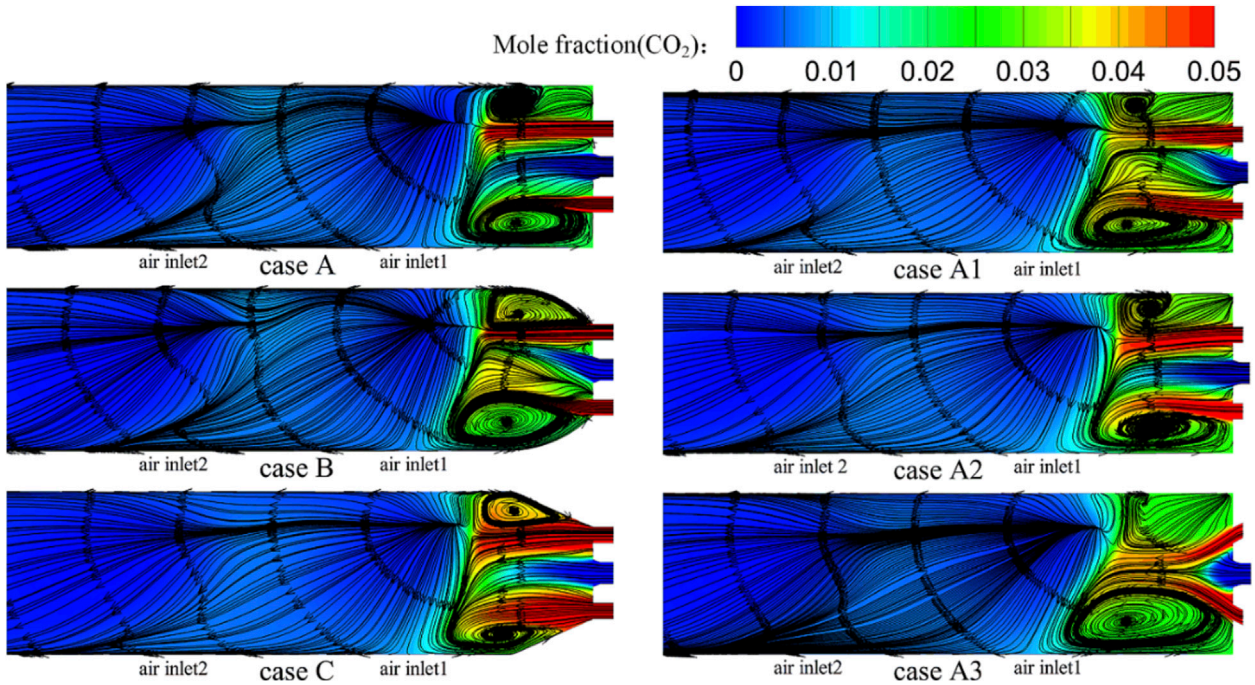

FIGURE 8 | Contours of the mole fraction (CO_2) and streamline distributions on the *x-z*.

is set based on the requirement of the standard *k-ε* turbulence model.

RESULTS AND DISCUSSIONS

In order to study the influence of the head structures and high-temperature exhaust inlet patterns on the performance characteristics of the combustion chamber, the flow field characteristics, the mixing efficiency with the total pressure loss, and the density distribution of the combustion chamber are analyzed and compared.

Flow Field Characteristics

In order to figure out the flow field structures inside the combustion chamber in each design, the streamline distributions of the symmetry plane under various conditions are presented. **Figure 8** shows the contours of the mole fraction (CO_2) and streamline distributions on the *x-z* central sections of the combustion chamber in each case. The high-temperature exhaust at the inlet of the combustion chamber is water vapor and carbon dioxide, and the central fluidizing gas is air. It can be seen that the high-temperature exhaust mixes with the supplied air at air inlet 1 and air inlet 2 in each case, which forms a recirculation zone inside the head of the combustion chamber. In different cases, the scales of the recirculation zone are different. The small recirculation zones cause the powder to gather together and have a negative effect on the operation of the combustion chamber. Moreover, the powder cannot burn totally in the combustion chamber because of the short residence time so that the production of the powder combustion gathers inside the head of the combustion chamber. Compared with case A, case B and case C have similar symmetrical recirculation zones and the scale of the recirculation zones is relatively large, which can cover the powder injection region. In case B and case C, high-temperature exhaust and air are mixed to form a recirculation zone with a symmetrical structure in the head, which increases the stay time of the powder and can easily achieve fully burned. In case A, some metal powder is wrapped in the recirculation zone and cannot be transported to the core combustion region for full combustion. Compared with other cases, the high-temperature exhaust in case B and case C surrounds the powder particles closely to peel off the surface oxide layer and liquid film of the powder particles continuously, which helps the powder particles to burn completely. In case A2 and case A3, it can be seen that increasing the number of high-temperature exhaust inlets is helpful to the fluidization effect of the powder and the formation and extension of the recirculation zone. In case A3, it can be clearly seen that the heightened effect of the recirculation zone is obvious, and the scouring effect of high-temperature exhaust on the core reaction region is improved. When the exhaust and powder fuel are injected at high temperature with a certain angle, the mixing and combustion efficiency of powder and exhaust are stronger than other cases.

Contours of relative density of the mixing exhaust/air on two *y-z* sections (x/l = 0.125 and x = 0.25) for all the cases are displayed in **Figure 9**. The relative density is the ratio of the total density to the air density.

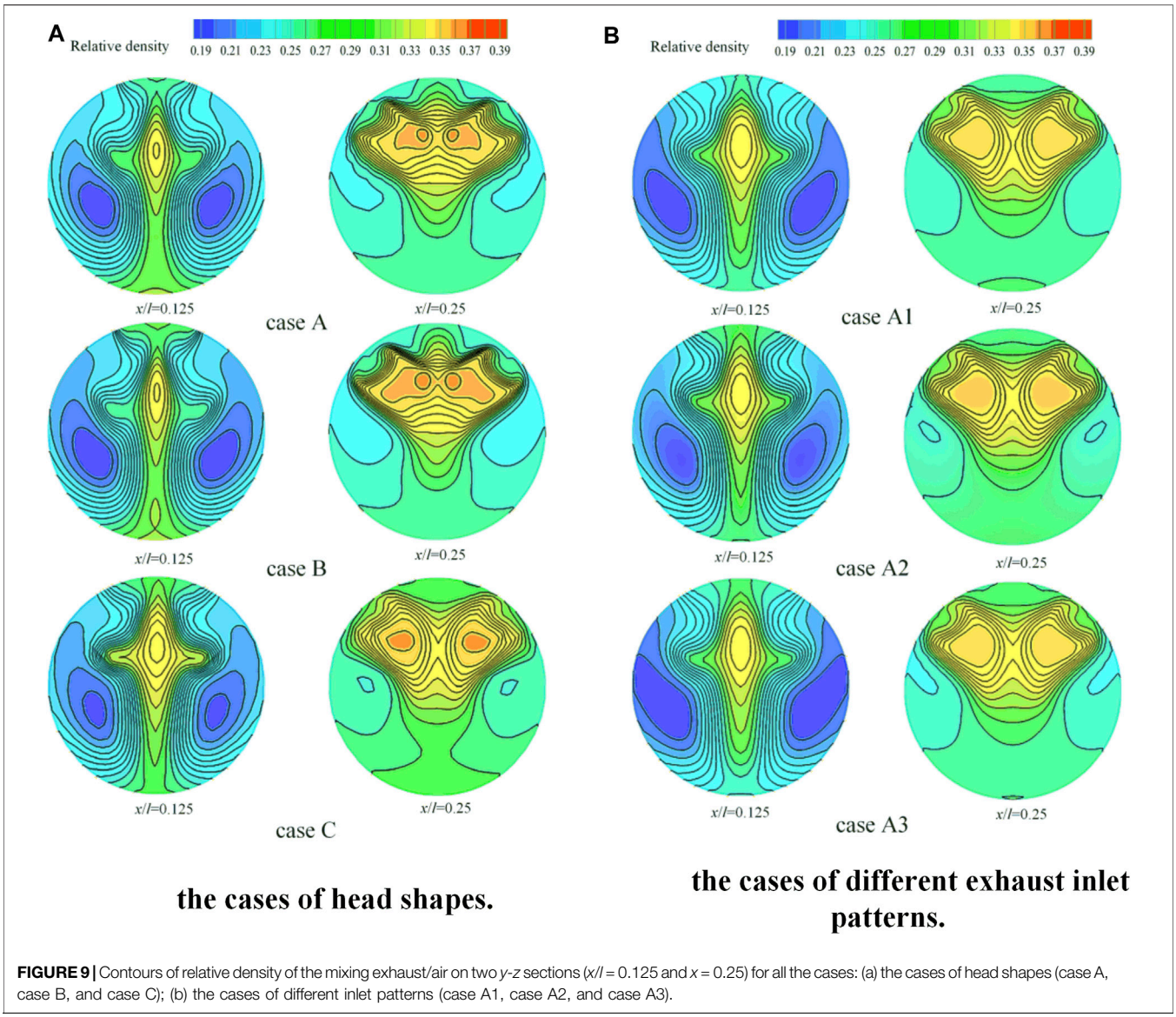

FIGURE 9 | Contours of relative density of the mixing exhaust/air on two *y-z* sections ($x/l = 0.125$ and $x = 0.25$) for all the cases: (a) the cases of head shapes (case A, case B, and case C); (b) the cases of different inlet patterns (case A1, case A2, and case A3).

$$relative\ density = \frac{total\ density}{density_{air}}.$$

The high relative density is found on the middle of the cross section $x/l = 0.125$, and it also distributed two sides in the section of $x/l = 0.25$ for all cases. When the relative density of the certain area is close to 1, it indicates that the density of the area is close to the air. It also means that the mixing degree is better. And the relative density gradient describes the uniformity of the mixing field. From **Figure 9A**, the high relative density is found in small area inside cylindrical head and round head at the section of $x/l = 0.25$. It has disadvantages for the powder mixing with the gases around in the region. On the other side, the relative density distribution of the coned head is uniform with a good mixing efficiency. In addition, a better relative density is obtained in the case with the change of exhaust inlet patterns to the inclined six holes type. In the section of $x/l = 0.125$, a large region with relative high density is found in the coned head shape, which indicates that this design provides a better mixing performance than the other cases.

Pressure distributions on the *x-y* central sections and six *y-z* sections along the streamwise direction for all the cases are shown in **Figure 10**. A region with high static pressure is formed at the region of the two air side inlets. The high-pressure regions in case A and case B are larger than those in case C, which prevents the powder injection and mixing in the combustion chamber. The pressure loss is also shown in this figure, and the coned head type obtains the smallest pressure loss penalty. In case A1 and case A2, there is an obvious decrease in pressure inside the head region, but it is improved in case A3. Therefore, the inclined six holes type, that is, case

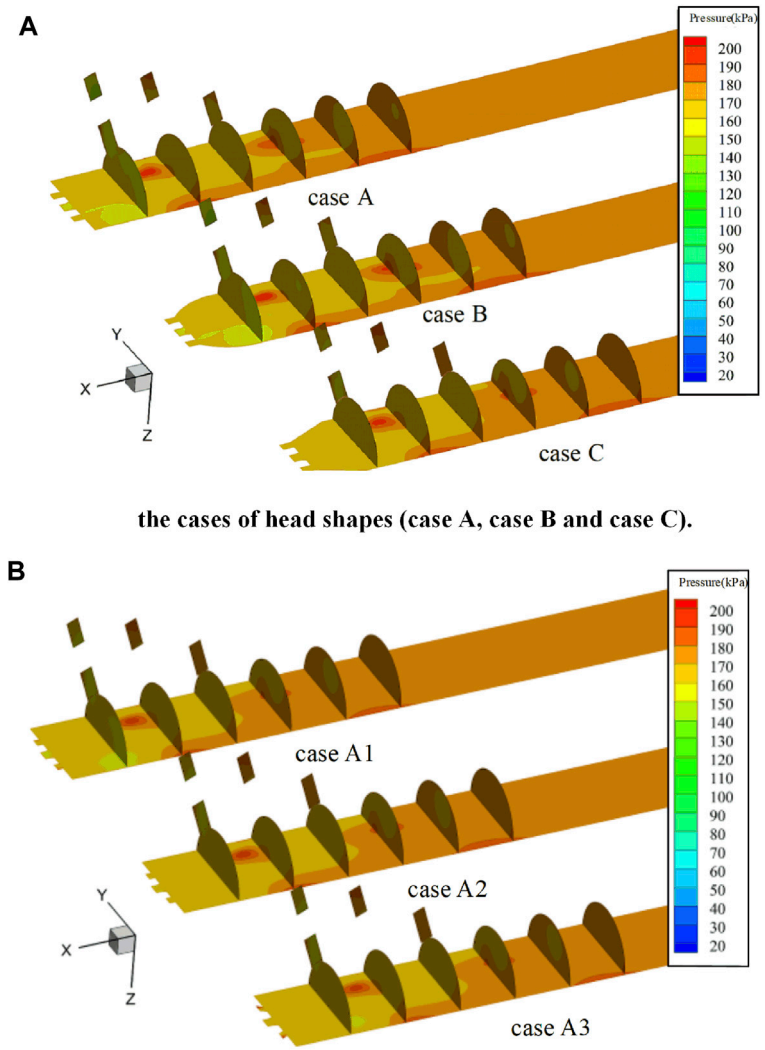

FIGURE 10 | Pressure distributions on the *x-y* central sections and six *y-z* sections along the streamwise direction for all the cases: (a) the cases of head shapes (case A, case B, and case C); (b) the cases of different inlet patterns (case A1, case A2, and case A3).

A3, provides the best powder injection and mixing. Compared with case A1 and case A2, the pressure distribution in case A3 is more uniform.

Mixing Efficiency

In 1992, Lomkov and Kopchenov (Kopchenov and Lomkov, 1992) proposed the definition of a mixing degree in a certain section is defined as follows:

$$D = \frac{\iint \rho u (c - \overline{c})^2 dA}{\overline{c}^2 \iint \rho u dA}.$$

In the formula, D, u, c, and ρ represent component mixing degree, flow velocity, mass concentration, and local density, respectively. A represents area, $\overline{c}$ represents the weighted average mass concentration on the calculated section, and $D = 1$ represents no fuel injection. The mixing efficiency is very low. $D = 0$ means that the components are fully and uniformly mixed. In order to make the mixing efficiency proportional to the mixing degree, the next equation is defined as follows:

$$\eta = 1 - D.$$

In this expression, η is the mixing efficiency and D is the mixing degree.

Figure 11 shows the comparisons of mixing efficiency distributions for all cases. Each datum is obtained by averaging all the results on the *y-z* sections along the streamwise direction. The side wall air inlet 1 and air inlet 2

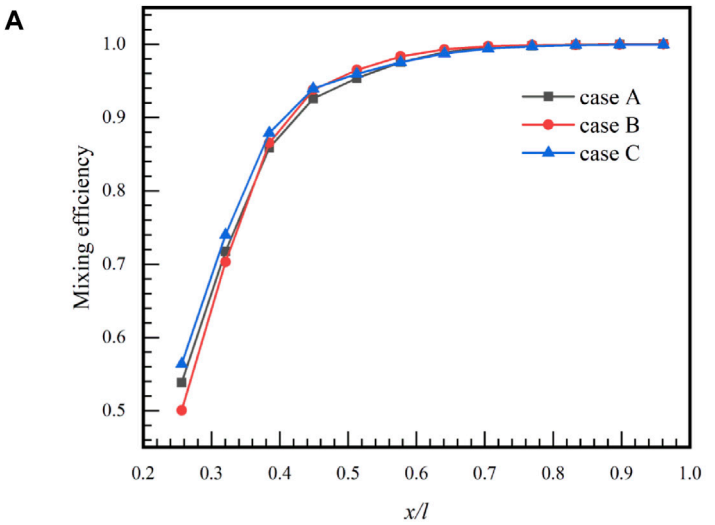

Comparisons of mixing efficiency for case A, case B and case C.

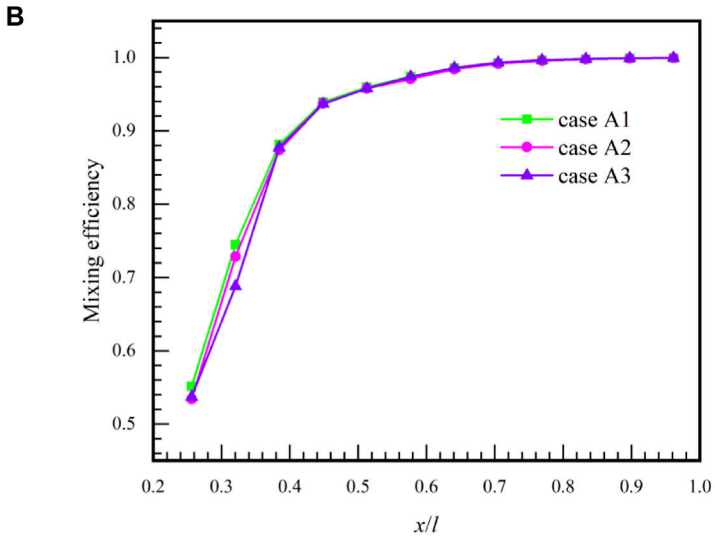

Comparisons of mixing efficiency for case A1, case A2 and case A3.

FIGURE 11 | Comparisons of mixing efficiency distributions for all cases. Each datum is obtained by averaging all the results on the *y-z* sections along the streamwise direction. (a) Comparisons of pressure mixing efficiency for case A, case B, and case C. (b) Comparisons of pressure mixing efficiency for case A1, case A2, and case A3.

cause additional flow mixing in the combustion chamber. The mixing effect is not obvious when the flow is approaching in the combustion chamber. Therefore, the starting point of the distribution in the combustion chamber is set at air inlet 2, and all the six distributions curves obtain the same trend. From **Figure 11**, the mixing efficiency of the process increases continuously in the section of the combustion chamber from air inlet 2. The final value is equal to 1, which means that the mixing efficiency in the combustion chamber gradually reaches the maximum value. However, in the entire flow field, the mixing efficiency of the coned type (case C) combustor shows an advantage at the starting region of the inlet 2 section. At the starting point, the mixing efficiency of the round type (case B) combustor is always lower than the mixing degree of other two cases. The curve of the round head type has presented a rapid increase in the considered range of x direction. This shows that the mixing efficiency of the round head is better than that of the cylindrical type. It can be seen that change in the number and angle of high-temperature exhaust inlets can have great influence on the mixing efficiency, when cases A1, A2, and A3 are compared. It is not obvious that by changing the head structures and the exhaust inlet patterns in the combustion chamber can directly affect the mixing efficiency. In addition, the relationship between pressure loss and mixing efficiency

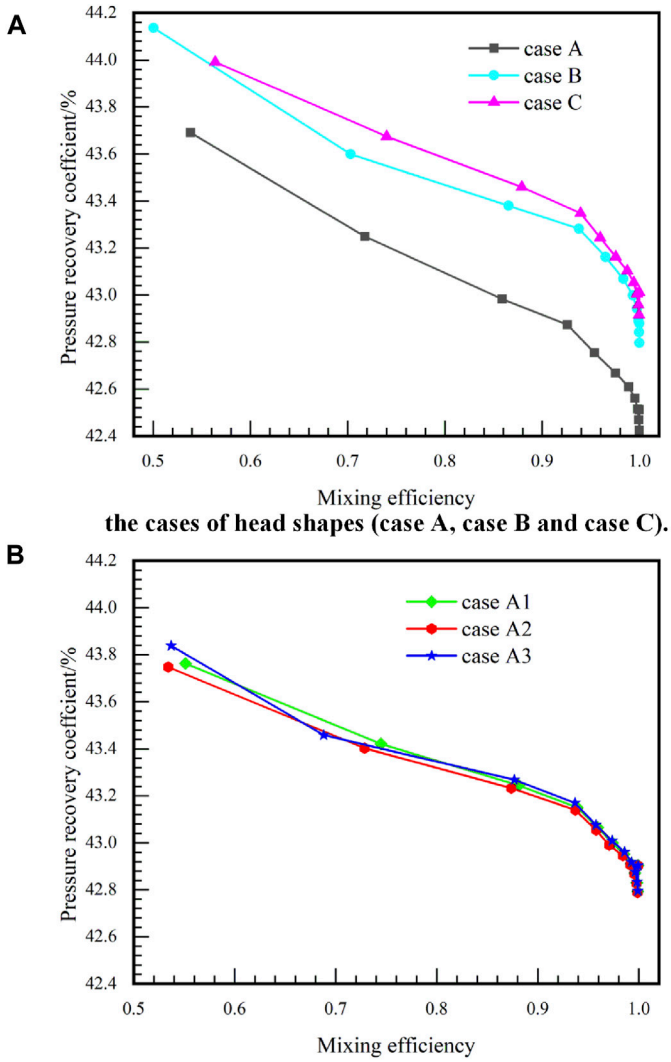

FIGURE 12 | Correlation between pressure recovery coefficients and mixing efficiency on the *y-z* sections along the streamwise direction: (a) the cases of head shapes (case A, case B, and case C); (b) the cases of different exhaust inlet patterns (case A1, case A2, and case A3).

needs to be considered together to determine the mixing performance.

Figure 12 shows correlation between pressure recovery coefficients and mixing efficiency on the *y-z* sections along the streamwise direction. It can be seen from **Figure 12** 1) that the traditional cylindrical head of the combustion chamber gives more total pressure loss under the same mixing efficiency. At this time, the coned head type has improved this problem, and it always has high mixing efficiency than other types. This also indicates that the coned head type has the lowest pressure loss under the same mixing efficiency. It can be seen from **Figure 12** 2) that the three curves of mixing efficiency of case A1, case A2, and case A1 are nearly overlapping. When the head shapes are the round head or coned head, the total pressure loss and mixing efficiency are improved compared with the cylindrical head. In addition, from **Figure 12A**, it can be found that the round head is slightly inferior to the coned head. It can be seen from **Figure 12** 1) and **Figure 12** 2) that as long as the head shape is improved, there is obvious advantages in total pressure loss and mixing efficiency.

Pressure Loss

The pressure loss in the mixing process is an important evaluation factor for the structure design in a combustion chamber. In order to further compare the pressure loss of several cases and evaluate the engine performance, the pressure recovery coefficient in the combustion chamber is calculated.

The total pressure recovery coefficient is expressed as follows:

$$\sigma = \frac{\overline{P}_{0_{out}}}{\overline{P}_{0_{undisturbed}}}.$$

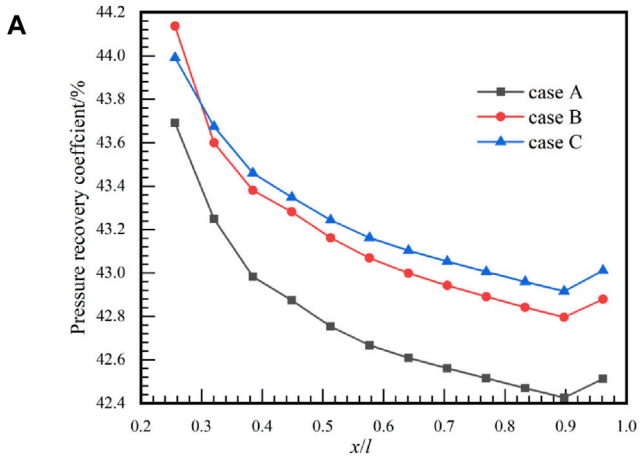

FIGURE 13 | Pressure recovery coefficients distributions for all cases: **(A)** pressure recovery coefficients of different cases of the head shapes; **(B)** pressure recovery coefficients of different cases of the exhaust inlet patterns.

In the formula, σ represents the total pressure recovery coefficient, $\overline{P}_{0_{undisturbed}}$ represents the average total pressure of the undisturbed air flow, and $\overline{P}_{0_{out}}$ represents the average total pressure of the outlet.

The total pressure recovery coefficient of the inlet is defined as: the ratio of the average total pressure of the inlet to the average total pressure of the undisturbed part. It is used to measure the pressure loss of the airflow inside the engine.

The average total pressure (Li et al. 2017) is defined as follows:

$$\overline{P}_0 = \frac{\iint P_0 \rho u dA}{\iint \rho u dA}.$$

In the formula, $\overline{P}_0$ represents the average total pressure; P_0 represents the total pressure, ρ represents the density, u represents the speed along the x axis, and A represents the cross-sectional area.

According to the total inlet pressure recovery coefficient, the pressure recovery coefficient of the combustion chamber is defined. The pressure recovery coefficient is defined as follows:

$$\lambda = \frac{\overline{P}_{0_{section}}}{\overline{P}_{0_{in}}},$$

where λ represents the pressure recovery coefficient of each section of the combustion chamber, $\overline{P}_{0_{section}}$ represents the average total pressure of each section, and $\overline{P}_{0_{in}}$ represents the average total pressure at the inlet.

Figure 13 shows the pressure recovery coefficients distributions for all cases along the axial section. The six curves have the same trend, and the section pressure recovery coefficient shows a gradually decreased trend along the axial direction. It can be seen that the pressure recovery coefficient of case A is always lower than that of other cases in **Figure 13A**. Even compared with case A1, case A2, and case A3, the pressure recovery coefficient of case A is the smallest. It also indicates that

the pressure loss of the combustion chamber with the modified head shapes and exhaust inlet patterns is smaller than that of case A. Among them, case C has the best performance with the largest pressure recovery coefficient compared with other configurations. Therefore, it is more recommended to use a round head or coned head type to improve mixing effect of powder and high temperature exhaust. When the number of high temperature exhaust inlets is changed, the effect of improving the pressure recovery coefficient is not too obvious. It can be clearly seen from **Figure 13** that the cross-sectional pressure recovery coefficient in the final stage has increased. Because the cross section is located in front of the engine throat, the pressure recovery coefficient in this region is increased with the pressure increasing.

SUMMARY AND CONCLUSION

The k-ε standard turbulence model and the three-dimensional component transport model are used in this study, which is selected from a comprehensive turbulence model validation simulating the flow in the powder-fuel ramjet combustion chamber. Different head shapes of combustion chamber and exhaust inlet patterns are designed, aiming at improving the mixing of powder and exhaust in a combustion chamber. The characteristics and flow field structure of the combustion chamber in each case are compared and analyzed. The pressure recovery, mixing efficiency, and the relative density are presented and compared. The conclusions emerged from this study are provided as follows.

1) For the head shape of the combustion chamber, the design with the coned head (case C) and the round head (case B) has benefits in powder injection and mixing inside the combustion chamber compared with the cylindrical head (case A). The cylindrical head forms recirculation located in the corner of the combustion chamber, which easily leads to powder deposition in the head region and then reduces the powder combustion efficiency. However, the design with the coned head has a better mixing effect than the round head.

2) Compared with the cylindrical head, the mixing efficiency of the combustion chamber is improved without increasing the pressure loss penalty in the case of the cylindrical head and the coned head. The best mixing efficiency of the combustion chamber is obtained by the coned head case.

3) The exhaust inlet of eight-hole type (case A2) has advantages in the powder–exhaust mixing compared with the design with four-hole type (case A1) by increasing the area of the mixing region. Compared with the normal cylindrical holes, the inclined inlet injection holes (case A3) can generate stronger flow impingement and flow mixing in the core part of the chamber with reduced pressure loss penalty.

DATA AVAILABILITY STATEMENT

The raw data supporting the conclusions of this article will be made available by the authors, without undue reservation.

AUTHOR CONTRIBUTIONS

WX designed the research. MR processed the corresponding data. MR wrote the first draft of the manuscript. JL helped organize the manuscript. WX revised and edited the final version.

FUNDING

The research work is financially supported by the open cooperative innovation fund of Xi'an Modern Chemistry Research Institute (748030030) and the startup funds of Central South University (202045012).

ACKNOWLEDGMENTS

This work was carried out at the School of Aeronautics and Astronautics at Central South University, China, and College of Astronautics, Nanjing University of Aeronautics and Astronautics China.

REFERENCES

Abbud-Madrid, A., Modak, A., Branch, M. C., and Daily, J. W. (2001). Combustion of magnesium with carbon dioxide and carbon monoxide at low gravity. *J. Propulsion Power* 17 (4), 852–859. doi:10.2514/2.5816C

Abdalla, A. M., Hossain, S., Petra, P. M., Ghasemi, M., and Azad, A. K. (2020). Achievements and trends of solid oxide fuel cells in clean energy field: a perspective review. *Front. Energ.* 14 (2), 359–382. doi:10.1007/s11708-018-0546-2

Auerswald, S., Hoerberg, C., Pflug, T., Pfafferott, J., Bongs, C., and Henning, H. (2020). Experimental Investigation of the Air Exchange Effectiveness of Push-Pull Ventilation Devices. *Energies* 13 (21). doi:10.3390/en13215817

Bertin, J. J., and Cummings, R. M. (2003). Fifty years of hypersonics: where we've been, where we're going. *Prog. Aerospace Sci.* 39 (6-7), 511–536. doi:10.1016/s0376-0421(03)00079-4

Chelaru, T.-V., and Mingireanu, F. (2011). Hybrid rocket engine, theoretical model and experiment. *Acta Astronautica* 68, 1891–1902. doi:10.1016/j.actaastro.2010.12.008

Choudhury, P. R. (1982). Characteristics of a side dump gas generator ramjet. *18th AIAA/SAE/ASME Jt. Propulsion Conf.* doi:10.2514/6.1982-1258

Chuang, C. L., Cherng, D. L., Hsieh, W., Settles, G., and Kuo, K. (1989). Study of flowfield structure in a simulated solid-propellant ducted rocket. *27th Aerospace Sci. Meet.*

Clark, W. H. (1982). Experimental Investigation of pressure oscillations in a side dump ramjet combustor. *J. Spacecraft Rockets* 19 (1), 47–53. doi:10.2514/3.62203

Dijkstra, F., Mayer, A., Wilson, K., Smith, R., and Schadow, K. (1995). Ducted rocket combustion experiments at low gas-generator combustion temperatures. *31st AIAA/ASME/SAE/ASEE Jt. Propulsion Conf. Exhibit.* doi:10.2514/6.1995-2415

Gaitonde, D. V. (2015). Progress in shock wave/boundary layer interactions. *Prog. Aerospace Sci.* 72, 80–99. doi:10.1016/j.paerosci.2014.09.002

Gany, A. (2015). Thermodynamic limitation on boron energy realization in ramjet propulsion. *Acta Astronautica* 98, 128–132.

Gong, L., Chen, X., Yang, H., Li, W., and Zhou, C. (2017). Investigation on the effect of diaphragm on the combustion characteristics of solid-fuel ramjet. *Acta Astronautica* 139, 449–462. doi:10.1016/j.actaastro.2017.07.031

Goroshin, S., Higgins, A. J., and Kamel, M. (2001). Powdered metals as fuel for hypersonic ramjets. *ASEE Jt. Propulsion Conf. Exhibit*. doi:10.2514/6.2001-3919

Goroshin, S., Higgins, A. J., and Lee, J. H. S. (1999). Powdered magnesium - carbon dioxide combustion for Mars propulsion. *35th AIAA/ASME/SAE/ASEE Jt. Propulsion Conf. Exhibit*.

Hsieh, W. H., Chuang, C. L., Yang, A. S., Cherng, D. L., Yang, V., and Kuo, K. K. (1989). Measurement of flowfield in a simulated solid-propellant ducted rocket combustor using laser Doppler velocimetry. *AIAA/ASME/SAE/ASEE 25th Jt. Propulsion Conf.* doi:10.2514/6.1989-2789

Hsu, K. Y., Gross, L. P., Trump, D. D., and Roquemore, W. M. (1995). Performance of a trapped-vortex combustor. *33rd Aerospace Sci. Meet. Exhibit*. doi:10.2514/6.1995-810

Huang, C., Yu, H., and Dai, J. (2020). Mixing and combustion augmentation of the RBCC with different mixer configurations in ejector mode. *Acta Astronautica* 174, 281–293.

Kopchenov, V. I., and Lomkov, K. E. (1992). The enhancement of the mixing and combustion processes in supersonic flow applied to scramjet engine. *28th AIAA/SAE/ASME/ASEE Jt. Propulsion Conf. Exhibit*. doi:10.2514/6.1992-3428

Li, C., Hu, C., Xin, X., Li, Y., and Sun, H. (2016). Experimental study on the operation characteristics of aluminum powder fueled ramjet. *Acta Astronautica* 129, 74–81. doi:10.1016/j.actaastro.2016.08.032

Li, J., Liu, H., Liu, X., Ye, Y., Wang, H., Wang, X., et al. (2021). Development of a simplified n-heptane/methane model for high-pressure direct-injection natural gas marine engines. *Front. Energ.* 15 (2), 405–420. doi:10.1007/s11708-021-0718-3

Li, L.-q., Huang, W., Yan, L., and Li, S.-b. (2017). Parametric effect on the mixing of the combination of a hydrogen porthole with an air porthole in transverse gaseous injection flow fields. *Acta Astronautica* 139, 435–448. doi:10.1016/j.actaastro.2017.07.048

Li, X., Zhang, W., Huang, Z., Ju, D., Huang, L., Feng, M., et al. (2019). Pre-chamber turbulent jet ignition of methane/air mixtures with multiple orifices in a large bore constant volume chamber: effect of air-fuel equivalence ratio and pre-mixed pressure. *Front. Energ.* 13 (3), 483–493. doi:10.1007/s11708-019-0631-1

Linnell, J., and Miller, T. (2002). A preliminary design of a magnesium fueled Martian ramjet engine. *38th AIAA/ASME/SAE/ASEE Jt. Propulsion Conf. Exhibit*. doi:10.2514/6.2002-3788

Liu, C., Sun, M., Wang, H., Yang, L., An, B., and Pan, Y. (2020). Ignition and flame stabilization characteristics in an ethylene-fueled scramjet combustor. *Aerospace Sci. Tech.* 106, 106186. doi:10.1016/j.ast.2020.106186

Liu, D., Chen, Y., and Dai, W. (2020). Acoustic Characteristics of Bi-directional Turbines for Thermoacoustic Generators. *Front. Energ.* 10 (2). doi:10.1007/s11708-020-0702-3

Miller, T., and Herr, J. (2004). Green rocket propulsion by reaction of Al and Mg powders and water. *ASEE Jt. Propulsion Conf. Exhibit*. doi:10.2514/6.2004-4037

Murty, M., and Chakraborty, D. (2012). Effect of injection angle in mixing and combustion characteristics of scramjet combustor. *Int. J. Hypersonics* 2, 15–28.

ONERA (2002). *Ramjet Scramjet & PDE [EB/OL]*. . http://www.onera, source of work.

Rashkovskiy, S. A. (2019). Formation of solid residues in combustion of boron-containing solid propellants. *Acta Astronautica* 158, 277–285. doi:10.1016/j.actaastro.2019.03.034

Ristori, A., Heid, G., Cochet, A., and Lavergne, G. (1999). Experimental and numerical study of turbulent flow inside a research SDR combustor. *35th AIAA/ASME/SAE/ASEE Jt. Propulsion Conf. Exhibit*. doi:10.2514/6.1999-2814

Roe, P. L. (2003). Characteristic-based schemes for the Euler equations. *Annu. Rev. Fluid Mech.* 18 (1), 337–365.

Schadow, K. (1972). Boron combustion characteristics in ducted rockets. *Combustion Sci. Tech.* 5, 107–117. doi:10.1080/00102207208952511

Shafirovich, E., and Varma, A. (2008). Metal-CO2 propulsion for Mars missions: Current status and opportunities. *J. Propulsion Power* 24 (3), 385–394. doi:10.2514/1.32635

Shafirovich, E. Y., Shiryaev, A. A., and Goldshleger, U. I. (1993). Magnesium and carbon dioxide - A rocket propellant for Mars missions. *J. Propulsion Power* 9 (2), 197–203. doi:10.2514/3.23609

Singh, L. A., and Walker, M. L. R. (2015). A review of research in low earth orbit propellant collection. *Prog. Aerospace Sci.* 75, 15–25. doi:10.1016/j.paerosci.2015.03.001

Stowe, R. A., Dubois, C., Harris, P. G., Mayer, A. E. H. J., Dechamplain, A., and Ringuette, S. (2004). Performance prediction of a ducted rocket combustor using a simulated solid fuel. *J. Propulsion Power* 20, 936–944. doi:10.2514/1.2799

Stull, F. D., Craig, R. R., Streby, G. D., and Vanka, S. P. (1983). Investigation of a dual inlet side dump combustor using liquid fuel injection. *AIAA 21st Aerospace Sci. Meet.* doi:10.2514/6.1983-420

Vigot, C., Cochet, A., and Guin, C. (1991). Combustion behavior of boron-based solid propellants in a ducted rocket. *Int. J. Energetic Mater. Chem Prop* 2, 386–401. doi:10.1615/intjenergeticmaterialschemprop.v2.i1-6.230

Woosuk, J., Seungkwan, B., Juhyeon, P., and Sejin, K. (2018). Combustion characteristics of ramjet fuel grains with boron and aluminum additives. *J. Propulsion Power* 34, 1070–1079.

Xu, Y., Jia, R., Medina, H., and Sun, H. (2019). Effect of tangential swirl air inlet angle on the combustion efficiency of a hybrid powder-solid ramjet. *Acta Astronautica* 159, 87–95. doi:10.1016/j.actaastro.2019.03.046

Conflict of Interest: The authors declare that the research was conducted in the absence of any commercial or financial relationships that could be construed as a potential conflict of interest.

Publisher's Note: All claims expressed in this article are solely those of the authors and do not necessarily represent those of their affiliated organizations, or those of the publisher, the editors, and the reviewers. Any product that may be evaluated in this article, or claim that may be made by its manufacturer, is not guaranteed or endorsed by the publisher.

NOMENCLATURE

A area of the selected region (m^2)

c mass concentration

D component mixing degree

d combustor diameter (mm)

d_1 powder fuel inlet diameter (mm)

d_2 high-temperature exhaust inlet diameter (mm)

h_1 dome height 1 (mm)

h_2 dome height 2 (mm)

k turbulent kinetic energy(m^2/s^2)

l combustor length (mm)

l_1 length of air inlet 1 (mm)

l_2 length of air inlet 2 (mm)

l_3 the distance between the exhaust inlet with the fuel inlet (mm)

P_0 total pressure (Pa)

$P_{(\_)\ 0out}$ average total pressure of the inlet air flow $(Pa)_{0undisturbed}$ average total pressure of the undisturbed air flow (Pa)

$P_{(\_)\ 0out}$ average total pressure of the inlet air flow $(Pa)_{0undisturbed}$ average total pressure of the undisturbed air flow (Pa)

R the net rate of production of species

S the rate of creation

u speed along the x axis (m/s)

v speed along the y axis (m/s)

w speed along the z axis (m/s)

x streamwise direction (m)

y spanwise direction (m)

z normal direction (m)

Greek symbols

α air inlet angles (°)

β angle between the high-temperature exhaust inlet and the fuel inlet (°)

γ angle between high-temperature exhaust inlet (°)

ε eddy current dissipation rate

η mixing efficiency

θ_1 angle between air inlet 1 and combustion chamber (°)

θ_2 angle between air inlet 2 and combustion chamber (°)

λ pressure recovery coefficient

μ fluid dynamic viscosity (Pa·s)

ρ fluid density (kg/m^3)

σ total pressure recovery coefficient

ϕ angle of the cone head

Subscripts

0 total

in air inlet

max maximum

out outlet air flow

undisturbed undisturbed air flow

frontiers in Energy Research

ORIGINAL RESEARCH
published: 15 October 2021
doi: 10.3389/fenrg.2021.763074

Characteristics of the Waviness End-Face Mechanical Seal in Reactor Coolant Pump Considering the Viscosity-Temperature Effect

Yu Ma[1], *Ya-Hui Wang*[1], *Hai-Chun Zhou*[2]* *and Wen-Tao Su*[3]*

[1]Sino-French Institute of Nuclear Engineering and Technology, Sun Yat-Sen University, Zhuhai, China, [2]Disease Prevention Department, The Second Hospital Affiliated to Heilongjiang University of Chinese Medicine, Harbin, China, [3]College of Petroleum Engineering, Liaoning Shihua University, Fushun, China

Mechanical seals prevents flow leakages in reactor coolant pumps thus playing an important role in their operational safety. However, their operational performance depends on different parameters, the seal geometrical design and the sealing medium characteristics among others. This study investigates the main performances of the waviness end-face mechanical seal, considering the effect of fluid flow and thermal characteristics. The involved coupled thermal-hydraulic process is simulated using the OpenFOAM, based on the coupled Navier-Stokes and energy balance equations. Study results showed that the viscosity-temperature effect may increase the flow leakage, and decrease both the opening force and the liquid film stiffness. The later may be decreased to negative values under specific conditions. It's therefore generally found that visco-thermal characteristics of the sealing medium may negatively affect mechanical seal's operational stability. On the other hand, from the perspective of liquid film temperature rise, the visco-thermal effect may lead to the regulation of the temperature rise in the liquid film, which improves the mechanical seal's operational safety in some aspects. Through a comprehensive analysis, the optimal structural parameters of the waviness mechanical seal investigated in this study are found to be $h_i = 2.5\mu m$, $\beta = 900\mu rad$ $(R_d\text{-}R_i)/(R_o\text{-}R_i) = 0.2$, $\alpha = 0.8$, and $k = 9$.

Keywords: openFOAM, mechanical seal, viscosity-temperature effect, reactor coolant pump, waviness end-face

OPEN ACCESS

Edited by:
Songtao Wang,
Harbin Institute of Technology, China

Reviewed by:
Lei Tan,
Tsinghua University, China
Yang Xiao,
Xi'an University of Science and Technology, China
Junlian Yin,
Shanghai Jiao Tong University, China

***Correspondence:**
Hai-Chun Zhou
zhc801211@163.com
Wen-Tao Su
suwentao@lnpu.edu.cn

Specialty section:
This article was submitted to Advanced Clean Fuel Technologies, a section of the journal Frontiers in Energy Research

Received: *23 August 2021*
Accepted: *28 September 2021*
Published: *15 October 2021*

Citation:
Ma Y, Wang Y-H, Zhou H-C and Su W-T (2021) Characteristics of the Waviness End-Face Mechanical Seal in Reactor Coolant Pump Considering the Viscosity-Temperature Effect. Front. Energy Res. 9:763074. doi: 10.3389/fenrg.2021.763074

INTRODUCTION

The shaft seal is an isolation device to prevent the leakage of reactor coolant pumps (RCP) (Salant et al., 2018), which is directly related to the safe operation of the nuclear power plant (Nilsson et al., 2009; Baraldi et al., 2011; Feng et al., 2016; Kok and Benli, 2017; Luqman et al., 2019). As one of the key components of shaft seals, the mechanical seal (Harp and Salant, 1998; Clark et al., 2002; Simon, 2018) plays a vital role in the safety and reliability of the entire structure, where different shapes of its end face lead to the different hydraulic effects (hydrodynamic and hydrostatic effects). In comparison with the hydrostatic seals, hydrodynamic seals can reach better performance owing to its hydrodynamic effect (Pascovici and Etsion, 1992; Batten et al., 2008).

Many researches on hydrodynamic seal's structure and operational mechanism have been conducted in the past decades (Stanghan-Batch and Iny, 1973; Wen et al., 2013; Falaleev, 2015;

Han and Tan, 2020). Among others, in order to analyze the pressure and temperature distribution within a mechanical seal, Merati et al. (1999) established a computational model for flow and thermal analysis, which could effectively predict both the flow field characteristics in the seal chamber and the temperature distribution within the stator. On the other hand, wanting to improve the performance of a mechanical seal, Clark et al. (2002) established a coupled thermal-hydraulic model based on the CFD method. Based on the associated model, they proposed some effective measures to improve the cooling effect of the stationary ring's end faces. In the same respect, Danos et al. (2000) established a numerical model for thermo-hydrodynamic lubrication, involving heat transfer analysis through the rings. This model tackled a three-dimensional general case of misaligned faces and a wavy rotor face in a stable dynamic tracking regime. The results showed the influence of different parameters such as the interface geometry, the nature of the lubricant, the fluid flow, the ring materials, and heat transfer conditions on the ring surfaces. Tournerie et al. (2001), analyzing the mechanical seal's thermal behavior, investigated the influence of mechanical seal end-face tilt, where they built a three-dimensional thermal-hydraulic coupling model to study the temperature distribution of the seal ring liquid film, as well as the heat transfer process between seals.

In some cases, complicated conditions should be considered, especially in the special pump types. To say the least, wanting to analyze the applicability of the wave-tilt dam seal, Young et al. (Young and Lebeck, 1989; Young et al., 2003) experimentally studied the characteristics of the wave-tilt dam seal, in which both the hydrostatic and hydrodynamic effects are produced on the radial taper and circumferential waves of the seal, respectively. Due to these properties, this seal can provide sufficient opening force and can be used under complex conditions. In addition to the wave-tilt dam seal, Mayer (Mayer, 1989) proposed a mechanical seal with a deep groove structure on the sealing end face. During this research, the experiment of the end-face mechanical seal of the rectangular deep-buried water cushion body is mainly considered, and its mathematical model for the elastic flow is established using the relaxation iteration method. It was shown that the pressure effect would lead to the wave deformation of the hydropads seal. Djamaï et al. (2010) put forward a numerical model of thermal-fluid analysis in deep groove seal, and the influences of operation and design parameters on sealing performance were analyzed. It was shown that the hydrodynamic effect of the deep groove seal was negligible, while the opening force was mainly provided by the hydrostatic effect.

In addition to the thermal-hydraulic properties, another important property that should be focused on is the thermos-elastic property, which in addition to thermal characteristics, describes the elastic characteristics in the sealing mechanism. To this end, some improved research works involving thermo-elastic properties coupling have been conducted. Among others, Liu et al. (2011); Liu et al. (2015) with a target of studying the sealing mechanism of the wave-tilt dam end-face mechanical seal under different working conditions, established a three-dimensional thermo-elastic coupling model and analyzed the sealing mechanism of the mechanical seal under the starting and stable operating conditions. Peng et al. (2012) established a coupled thermal-fluid-solid model for a convergent double tapered hydrostatic mechanical seal and experimentally investigated the effect of thermo-elastic deformation on the seal performance. Among other parametric studies, Hu et al. (Chandramoorthy, Hadjiconstantinou) studied the effect of speed and closing pressure on the sealing behavior for a grooved end-face seal ring, where the increase of both parameters led to a correspondingly increasing volume leakage rate. As for Gustafsson et al. (2017), the shape of micro-grooves on the end-face of the sealing ring may considerable influence the thermohydrodynamic characterstics of the liquid film in its seal gap region.

Taking from the above presented literature and other works from different sources, it's obvious that previously conducted works have systematically established the analytical method to study mechanical seal operations. Most of the previous works on mechanical seals are mainly based on the bearing lubrication theory, in which the Reynolds equation (Chandramoorthy, Hadjiconstantinou; Gustafsson et al., 2017) is often used as the governing equation to solve the pressure distribution of the liquid film in the seal ring gap. The Reynolds equation is a simplified approximation of the Navier-Stokes equation (Temam, 2001; Pietarila Graham et al., 2008; Sinchev et al., 2018; Danchin and Mucha, 2019) to solve the narrow gap laminar flow. In this approximation, the pressure change along the film thickness direction is neglected by assuming that the thickness of the seal ring gap liquid film is small enough. However, for the complicated mechanical seal conditions (e.g., the wave-tilt dam end-face mechanical seal), the pressure change along the film thickness direction should be considered for more reliable results. When neglecting this pressure change, some errors will be introduced and the numerical solutions may deviate from the real life conditions. This situation requires more accurate equations to describe the fluid flow and heat transfer phenomenon in the mechanical seal. To this end, the Navier-Stokes equations, being a more detailed description than the Reynolds equation, can be considered. Therefore, in the present study, in order to study the waviness end-face mechanical seal more accurately, the coupled Navier-Stokes and Energy equations are used based on the open-source software OpenFOAM to analyze the pressure and temperature distributions (Jasak et al., 2007; Gebreslassie et al., 2013a; Gebreslassie et al., 2013b; Chen et al., 2014). The viscosity-temperature effect (visco-thermal effect) of the sealing medium is also considered to calculate the heat-flow coupling process. Based on this model, the influences of structural parameters on seal performance are studied, and the optimal parameters of the seal design are proposed.

The present article is organized as follows. In *Research Object and Methodology*, both the investigated case and the utilized research methodology are established and explained. This includes the seal geometric model, sealed medium governing equations, the utilized boundary conditions, and the definitions of main sealing performance variables. *Results and Discussion* studies the effects of structural parameters on the sealing

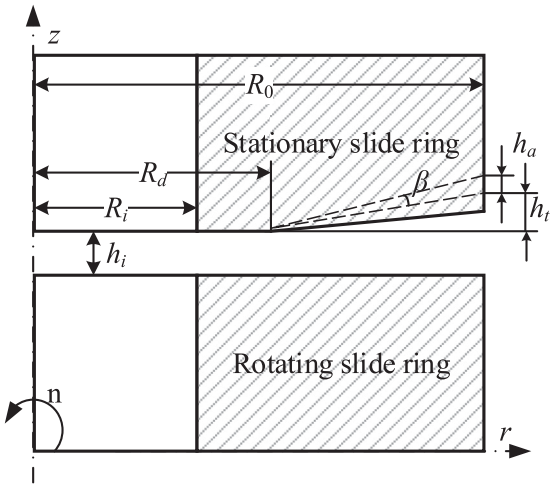

FIGURE 1 | The geometry of the mechanical seal.

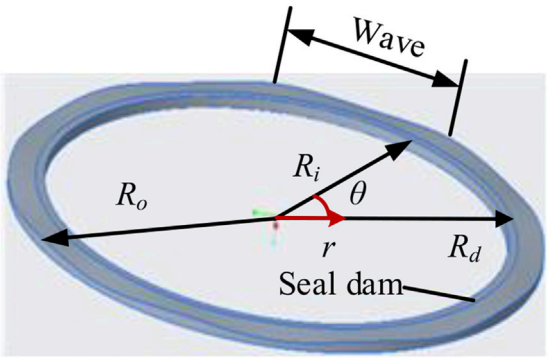

FIGURE 2 | Schematic of the waviness end face.

performances, including the leakage rate, the film opening force, the film stiffness, and the temperature distribution. The main conclusions of this work are given in *Conclusion*.

RESEARCH OBJECT AND METHODOLOGY

Geometric Model

The geometry of the investigated mechanical seal in the RCP is shown in **Figure 1**. It consists of two sliding rings, namely the rotating ring and stationary ring. The inside and outside radius of the seal face are set as R_i = 140.25 mm and R_o = 151.25 mm, respectively. The rotating slide ring rotates counterclockwise at an angular speed of w. Between the rotating and stationary slide rings, the sealed medium (deionizer water is used in this case) flows from the outside zone to the inside chamber via the main leakage path with thickness h_i.

The end face of the rotating slide ring is flat, and its roughness is less than 1 μm. The end face of the stationary slide ring consists of 9 wavinesses and a flat plane, as shown in **Figure 2**. The film thickness between the frictional pair is described as in **Eq. 1** (Liu et al., 2011):

$$h(r,\theta) = \begin{cases} h_i & R_i \le r \le R_d \\ h_i + \tan\beta(r - R_d)(1 - \alpha\cos k\theta) & R_d \le r \le R_o \end{cases}, \quad (1)$$

where h_i, β, r, and θ stand for the thickness of the inner radius, radial angle on the stator face, and the coordinate of radial and rotating directions, respectively. Moreover, R_i, R_d, and R_o are the inner radius, dam radius, and outer radius, respectively. The dimensionless parameter α is defined as shown in **Eq. 2**:

$$\alpha = h_a/h_t \quad (2)$$

h_a and h_t stand for the wave amplitude and taper height of the outer radius; k is the wave number.

Governing Equations

The coupled thermal-hydraulic behavior within the mechanical seal is analyzed using the numerical technique, which starts from the establishment of the governing equations. To simplify the numerical simulation, some basic and reasonable assumptions are applied as follows:

1) The sealed fluid is incompressible since the flow velocity is very small; and the viscosity-temperature effect is considered.
2) Only the steady-state condition under the normal operations is considered, and the seal faces are always parallel to each other.
3) According to the relevant parameters, the Re number is about 210 and the flow factor number is 0.354. Therefore, the fluid film is laminar.
4) The pressure variation in the direction of the fluid film is considered.
5) The cavitation phenomenon is neglected.
6) The seal gap is considered as full-film lubrication, and no face contact happens during the operation.

Under these conditions, the governing equations to describe the lubrication film flow are written as:

$$\nabla \cdot \boldsymbol{u} = 0, \quad (3)$$

$$(\boldsymbol{u} \cdot \nabla)\boldsymbol{u} = -\frac{1}{\rho}\nabla p + \nu\nabla^2\boldsymbol{u}, \quad (4)$$

where $\boldsymbol{u}$ is the fluid velocity, ρ is the density of deionized water, p is the pressure, and ν is the kinematic viscosity.

Due to the very narrow seal gap, the large frictional heat will be produced by viscosity shear force in the process of operation, which will increase the temperature of the fluid film. Therefore, to simulate the temperature field, the energy equation including the dissipation item should be considered as in **Eq. 5** (Shen et al., 2019):

$$\rho c_p(\boldsymbol{u} \cdot \nabla T) = \lambda\nabla^2 T + \Phi, \quad (5)$$

where Φ is the dissipation function, and is defined as shown in **Eq. 6**:

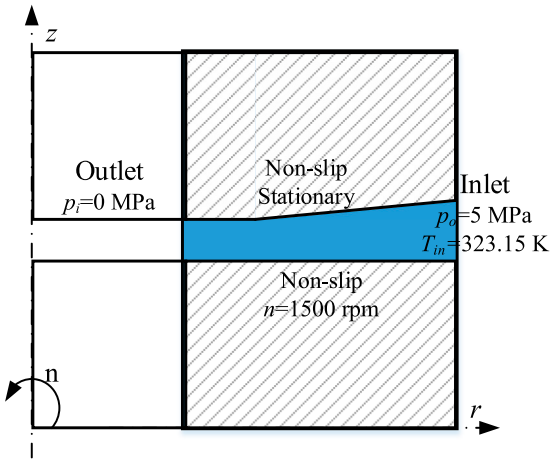

FIGURE 3 | Schematic of the boundary conditions.

$$\Phi = \mu\left[2\left(\frac{\partial u}{\partial x}\right)^2 + 2\left(\frac{\partial v}{\partial y}\right)^2 + \left(\frac{\partial w}{\partial z}\right)^2 + \left(\frac{\partial u}{\partial y} + \frac{\partial v}{\partial x}\right)^2 + \left(\frac{\partial u}{\partial z} + \frac{\partial w}{\partial x}\right)^2 + \left(\frac{\partial v}{\partial z} + \frac{\partial w}{\partial y}\right)^2\right] - \frac{2}{3}\mu\left(\frac{\partial u}{\partial x} + \frac{\partial v}{\partial y} + \frac{\partial w}{\partial z}\right)^2 \tag{6}$$

In this equation, μ is the dynamic viscosity while u, v, and w are the components of fluid velocity $\boldsymbol{u}$ along with the directions of x, y, and z coordinates. When considering the viscosity-temperature effect, the viscosity is strictly dependent on the temperature distribution of the fluid film as shown in **Eq. 7**:

$$\mu = \mu_0 \exp\left[-\beta_0 (T - T_0)\right], \tag{7}$$

where T_0 is the reference temperature and μ_0 is the reference viscosity, β_0 is the parameter that indicates the influence of temperature change on viscosity, namely the viscosity-temperature coefficient.

In this study, the initial operating parameters are kept constant: the viscosity-temperature coefficient keeps β_0 keeps the value of 0.0175 K^{-1}; the reference temperature keeps T_0 stays 323.15K; and the reference viscosity keeps μ_0 stays 0.05494×10^{-3} Pa·s.

Boundary Conditions

The fluid region (blur region) is the area enclosed by the inner and outer boundaries ($r = R_i$, and $r = R_o$) and the upper and lower sealing surfaces, as shown in **Figure 1**. To simulate the behavior of the proposed seal numerically, the boundary conditions should be determined.

The schematic of the boundary conditions is shown in **Figure 3**. For simplification, one of the waviness widths in the circumferential direction is taken, and the periodic cyclic boundaries are applied to the circumferential boundaries, i.e., the front and back boundaries. The considered mechanical seal is an external pressure structure. During the normal operation, the working fluid flows from the external high-pressure side to the internal low-pressure side, i.e., the outer boundary ($r = R_o$) is the inlet pressure boundary with $p_o = 5$ MPa, and the inner boundary ($r = R_i$) is the outlet pressure boundary with $p_i = 0$ MPa. Since there is no slip between the boundary fluid and the sealing surface of the stationary slide ring, the no-slip boundary condition is applied to up and bottom boundaries (i.e., the upper and lower seal surfaces). The rotating speed of the sealing surface of the rotating slide ring is n = 1,500 rpm. The temperature boundary is applied to the inlet boundary, in which the inlet temperature is set as T_{in} = 323.15 K. The zero-gradient boundary of heat transfer is applied to the outlet, up, and bottom boundaries. The tolerance of all the simulations is set as 10^{-6}.

Sealing Performance

To study the characteristics of the waviness end-face mechanical seal in reactor coolant pumps with the viscosity-temperature effect, some typical and concerned parameters are analyzed, including the leakage rate Q, the opening force F_{open} and the liquid film stiffness k_z. The leakage rate is one of the main parameters to ensure the safe and stable operation, which is defined as:

$$Q = \int_0^{2\pi} \int_0^h V_r r dz d\theta, \tag{8}$$

where V_r is the fluid velocity in the radial direction defined as:

$$V_r = \frac{1}{2\mu}\frac{\partial p}{\partial r}(z^2 - zh). \tag{9}$$

The appropriate leakage rate is important to ensure stable and safe operation. On the one hand, too low leakage may lead to the direct wear of seal ring end face, and on the other hand, the excessive leakage may cause seal failure.

Similarly, another important parameter, namely sealing opening force that characterizes the bearing capacity of the liquid film can be obtained by integrating the liquid film pressure along the sealing end face as:

$$F_{open} = \int_0^{2\pi} \int_{R_i}^{R_o} p r dr d\theta \tag{10}$$

Near the steady-state equilibrium position of the liquid film, the increase of opening force caused by a slight axial disturbance is the liquid film stiffness, which can be defined as:

$$k_z = -\frac{\partial F_{open}}{\partial h}\Big|_{h=h_i} \tag{11}$$

RESULTS AND DISCUSSION

This section analyzes the influences of the structural parameters on sealing performance considering the viscosity-temperature effect. The effects of thermo-hydrodynamic lubrication (THD) and hydrodynamic lubrication (HD) are compared and analyzed,

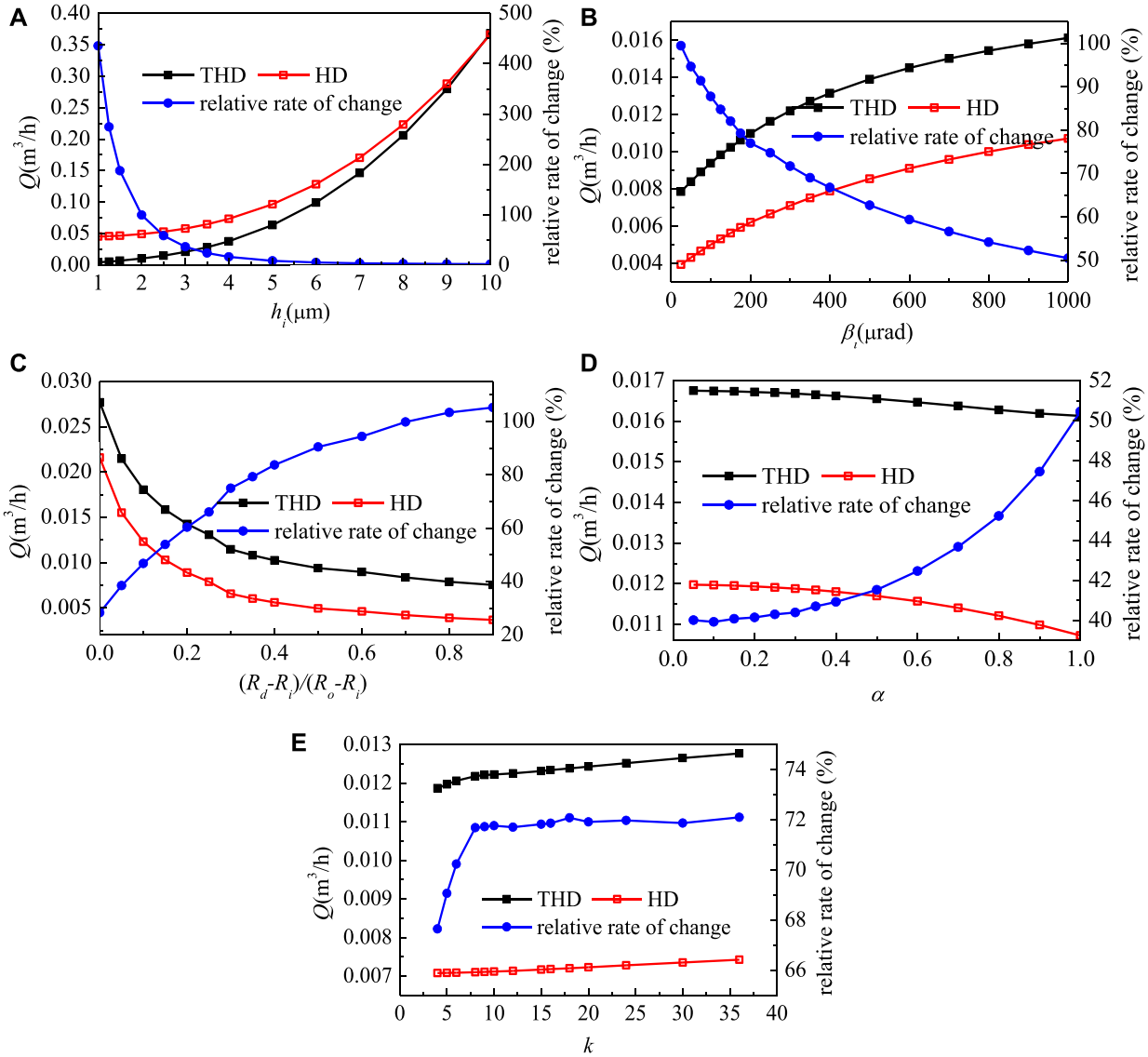

FIGURE 4 | Influence of structural parameters under the viscosity-temperature effect on leakage.

and the optimal design parameters of the waviness mechanical seal are obtained.

Effects of Structural Parameters on the Leakage Rate

Due to the small sealing clearance, when the sealing ring rotates at high speed, the viscous shear friction heat will be generated, which reduces the viscosity and correspondingly, reduces the leakage. **Figure 4** shows the effects of the structural parameters of the waviness end-face mechanical seal on the leakage rate when considering the viscosity-temperature effect. The effect of film thickness on the leakage is shown in **Figure 4A**, in which the relative rate of change is the relative deviations of the HD solutions from the THD solutions. In general, as the film thickness increases, the leakage rates obtained from the THD and HD processes gradually close to each other, since that, as the film thickness increases, the viscous shear friction heat effect decreases correspondingly. When the film thickness is small enough, the HD process will strongly overestimate the leakage rate, while when the film thickness reaching 10 μm, the HD solution is much closed to the THD solution and the relative change rate decreases to 1.75%. These conditions indicate that the viscosity-temperature effect will be obvious when the liquid film is thin and will decrease as the thickness of the liquid film increases. Therefore, from this point of view, the film thickness should be large enough to ensure small viscosity-temperature. However, if the base film is too thick, the leakage will increase and the sealing effect will not be achieved. Therefore, the base film thickness of the seal design should be kept within the appropriate range.

Figure 4B shows the effect of the taper of the stationary slide ring end-face on the leakage. Similar to that of the base film

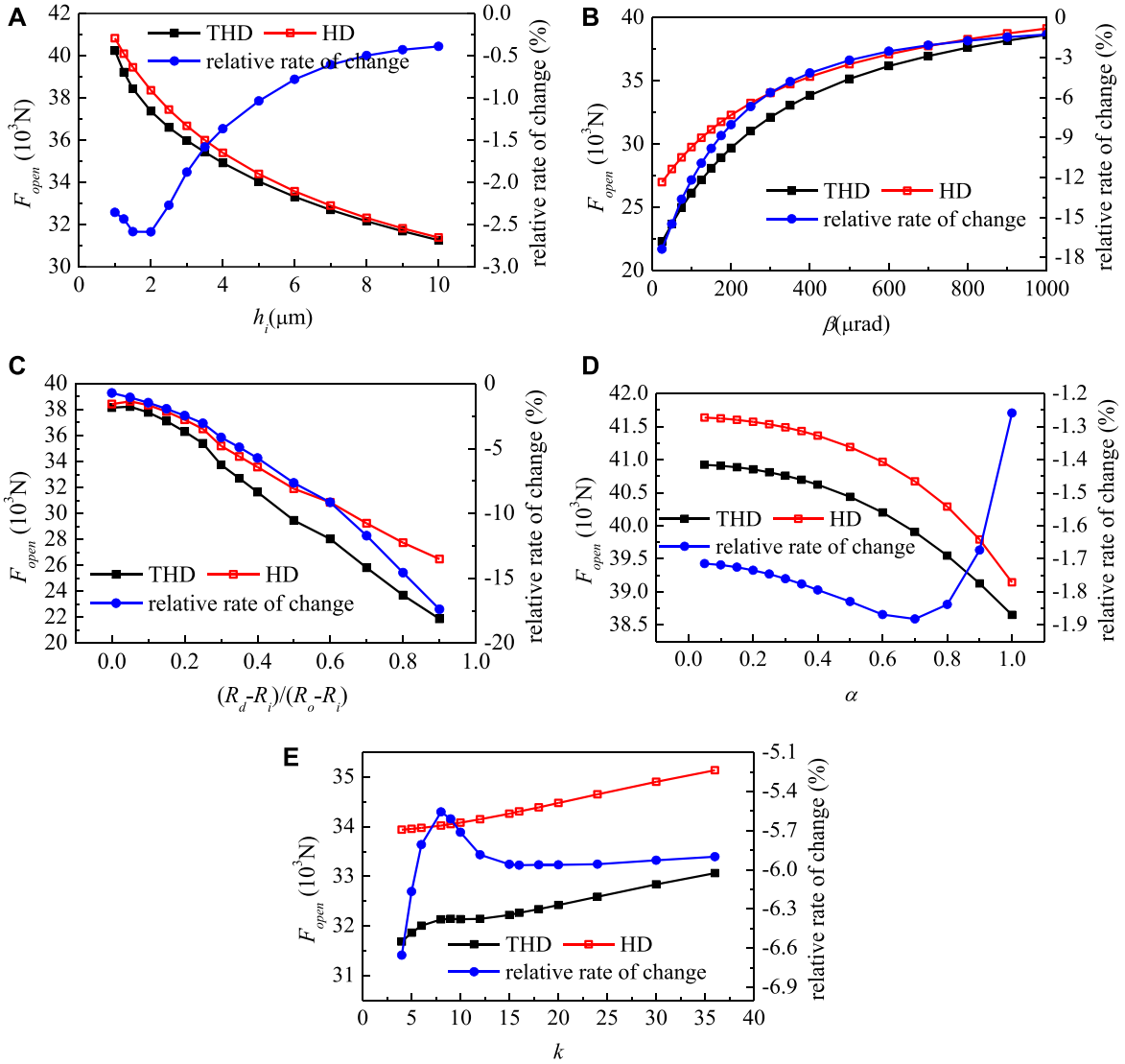

FIGURE 5 | Effect of structural parameters on the opening force under the viscosity-temperature effect.

thickness, as the taper increases, the viscosity-temperature effect on the leakage rate decreases. As the taper increases, the film thickness of the taper zone in the seal clearance increases, and the viscous shear friction heat decreases correspondingly. Considering the viscosity-temperature effect, the relative change rate of the leakage decreases from the maximum of 99.49–50.47% with the increase of the taper, which indicates that the taper should be large enough to reduce the viscosity-temperature effect.

Figure 4C shows the effect of the dam width ratio $(R_d\text{-}R_i)/(R_o\text{-}R_i)$ on the leakage rate. Different from the film thickness and the taper, the leakage rate decreases as the dam width ratio increases, and the relative change rate increases correspondingly. The increase of the dam width ratio directly increases the dam area, which increases the viscous shear friction heat and the temperature rise in the liquid film. Due to this effect, the viscosity-temperature effect of the dam width ratio will increase as the dam-width ration increases. As the dam width ratio increases, the relative change rate of leakage will increase from the minimum 28.27% to the maximum 105.19%. Therefore, to reduce the viscosity-temperature effect, a relatively lower dam width ratio is required.

Figure 4D shows the effect of the dimensionless parameter α on the leakage rate, i.e., the effect of waviness amplitude of stationary slide ring end-face on the leakage rate. The increase of α means the increase of the waviness amplitude, which will reduce the film thickness of the waviness region, and increase the viscous shear friction heat. Therefore, with α increasing, the effect of viscosity-temperature on the leakage increases correspondingly. On the other hand, the decrease in film thickness is still limited due to the increase of waviness amplitude. Therefore, from the point of the relative change rate variation, it does not change much, which varies

between 40.02 and 50.17%. However, from the point of the relative change rate value, the viscosity-temperature effect is still large. **Figure 4E** shows the effect of the wave number on the leakage rate. In general, the variation of wavenumber has little effect on the relative change rate of leakage. The relative change rate of leakage remains between 67.66 and 72.1%.

Effects of Structural Parameters on the Film Opening Force

This part analyzes the influence of the viscosity-temperature effect on the opening force. As the temperature increase, the fluid viscosity will decrease and the viscosity-temperature effect for the waviness end-face mechanical seal will be reduced correspondingly. Meanwhile, the hydrodynamic effect and the hydrostatic effect will be reduced. Therefore, the opening force considering the viscosity-temperature effect (THD solutions) will be less than that without considering the viscosity-temperature effect (HD solutions). **Figure 5** shows the effects of different structural parameters on the opening force, the solutions with and without considering the viscosity-temperature effect are compared with each other. Different from the leakage, the relative change rate is always less than 0, i.e., the opening force with considering the viscosity-temperature effect is lower than that without considering the viscosity-temperature effect.

Figure 5A shows the effect of the base film thickness on the opening force. As the base film thickness increases, the opening force decreases and the relative change rate of the opening force increases first and then decreases. The relative change rate varies from −0.39 to −2.59%. As the base film thickness increases, viscous shear friction heat reduces and the viscosity-temperature effect has less effect on the opening force.

Figure 5B shows the effect of the taper of stationary slide ring end-face on the opening force, in which the opening force increases as the taper increases and the relative change rate decreases as the taper increases. As the taper increases, the film thickness in the waviness region increases and the viscous shear friction heat decreases. Therefore, the effect on the viscosity of the sealing medium reduces. The effect on the opening force and the relative change rate of the opening force will decrease with the increase of taper, which varies from −1.26 to −17.38%.

Figure 5C shows the effect of the dam width ratio on the opening force, in which the opening force decrease as the dam width ratio increases, while the relative change rate increases as the dam width ratio increases. With the increase of the dam width ratio, the dam area increases, the viscous shear friction heat increases, and the influence on the viscosity of the sealing medium increase correspondingly. The increase of the dam width ratio increases the influence of opening force, and the relative change rate of opening force increases from −0.72 to −17.41%.

Figure 5D shows the effect of α on the opening force, in which the opening force decreases as α increases, and the relative change increases first and then decreases. As α increases, the waviness amplitude increases, and the viscous shear friction heat increases, thus the viscosity change increase also. Therefore, with the increase of α, the influence of viscosity-temperature on the opening force increases. When α increases to a certain value, the hydrodynamic effect of the waviness end-face seal becomes strong enough, leading to a decrease in the relative change rate of opening force, from −1.26 to −1.88%.

Figure 5E shows the effect of the wave number on the stationary slide ring end-face on the opening force. The opening force increases as the wave number increases and the viscosity-temperature effect makes the opening force lower. The increase of wave number will make the high-temperature region denser, thus weakening the hydrostatic effect, and the opening force will be relatively small. However, the hydrodynamic effect will be enhanced as the wavenumber increases. The relative change rate of the opening force is not large, which varies between 5.56 and 6.65%.

Effects of Structural Parameters on Film Stiffness

This part studies the influence of structural parameters of the mechanical end-face seal on the fluid film stiffness with considering the viscosity-temperature effect. The film stiffness under different structural parameters is shown in **Figure 6**, with and without considering the viscosity-temperature effect, respectively. To analyze the effect of the viscosity-temperature effect on the fluid film stiffness, the relative change rate of the liquid film stiffness was calculated. The negative sign of the relative change rate indicates the decrease of film stiffness.

Figure 6A shows the effect of film thickness on film stiffness. As the film thickness increases, the stiffness increases first and then decreases, while the relative change rate always decreases. In comparing to the HD results, the stiffness of the THD results is always lower than that of the HD results, due to the viscosity-temperature effect. With the increase of the film thickness, the relative change rate of the film stiffness decreases from −33.39 to −2.7%. This indicated that as the film thickness increases, the effect of the viscosity-temperature effect on liquid film stiffness will decrease. With the increase of the film thickness, the viscous shear friction heat and the weaker the viscosity-temperature effect will reduce.

Figure 6B illustrates the effect of the taper of stationary slide ring on the liquid film stiffness, in which both the film stiffness and the relative change rate increase first and then tend to stable. When considering the viscosity-temperature effect, the liquid film stiffness tends to be lower than that of the HD solutions. This effect will be decreased as the taper increases. As the taper degree decreases, the viscosity-temperature effect generates a more striking impact on the liquid film stiffness, and the liquid film stiffness can be negative, i.e., the opening force increases as h increases. This phenomenon is caused by the generated viscous shear friction heat, which could be very unfavorable for the stable operation of the seal if the taper angle is extremely small. Under the optimal circumstance with the largest taper degree, the relative rate of change can be as low as 44.67%, which could be much better for the stable operation. In consideration of this, credence should be given to a relatively larger taper degree when designing the mechanical seal.

Figure 6C depicts the effect of the dam width ratio on the fluid film stiffness. When the dam width ratio being equal to zero, there is no dam area and the viscosity-temperature effect will increase the liquid film stiffness. However, when the dam area exists, the viscosity-temperature effect, in turn, decreases the film stiffness. As the dam

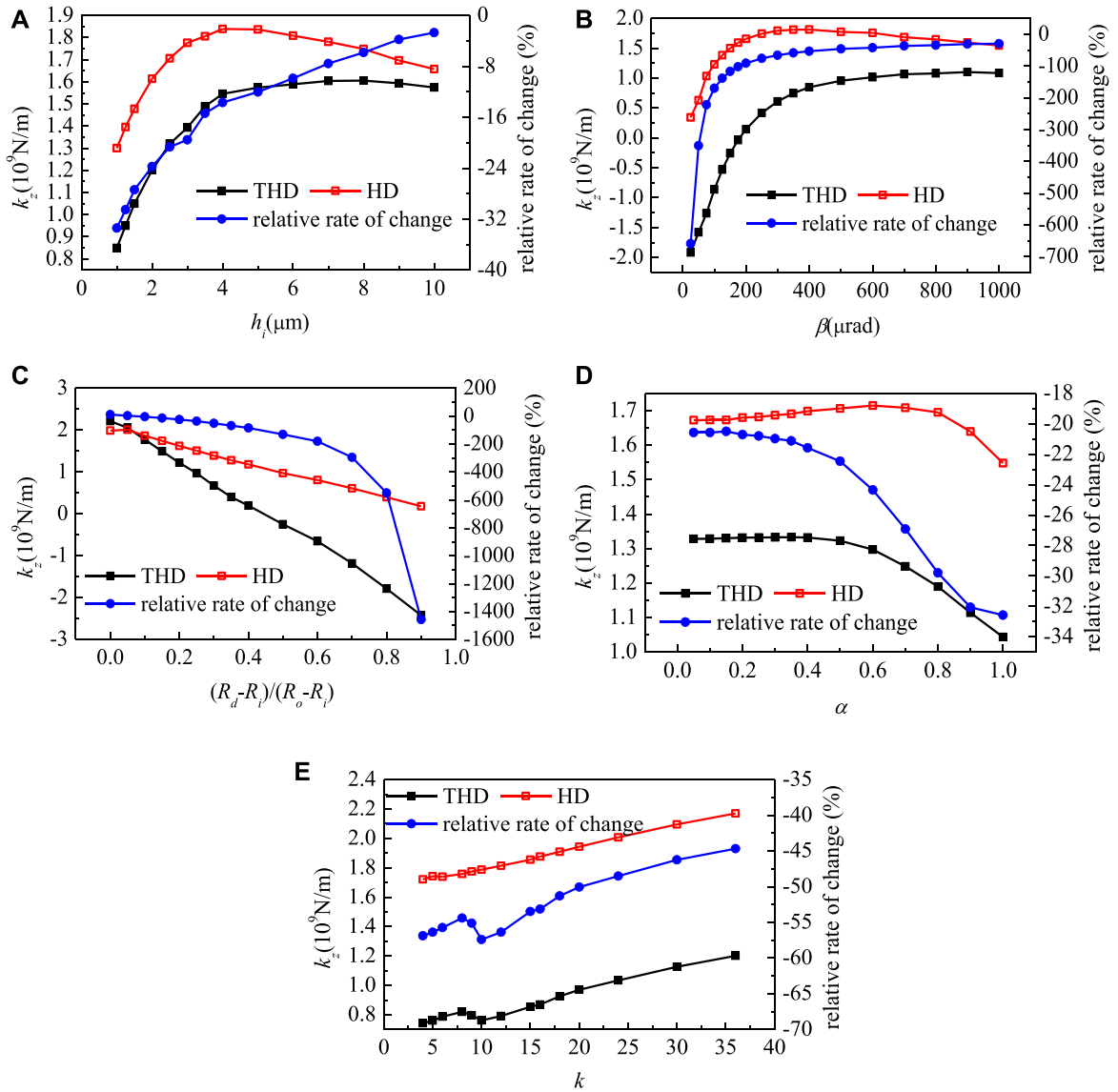

FIGURE 6 | Effect of structural parameters on the fluid film stiffness under the viscosity-temperature effect.

area increases, an increasing amount of viscous shear friction heat is generated, which leads to a non-negligible viscosity-temperature effect on the liquid film stiffness. According to **Figure 6C**, when the dam width ratio is large enough, the film stiffness without considering the viscosity-temperature effect is close to 0 and the film stiffness with considering the viscosity-temperature has a relative larger negative value. The relative change rate of the liquid film stiffness can reach a very large value, which will threaten the operation of the seal. As the dam width shrinks, the relative change rate of the liquid film stiffness can decline to 2.27%. The above result indicates the importance of the small dam width ratio in the design of the mechanical seal.

Figure 6D presents the effect of α on the liquid film stiffness. As α increases, both the stiffness and the relative change rate stabilize first and then decrease. From this picture, one can find that the viscosity-temperature effect will reduce the film stiffness. To be more specific, as α increases, the influence of the viscosity-temperature effect on the liquid film stiffness increases correspondingly. The relative change rate of the liquid film stiffness slightly increases from −20.57 to −32.57%.

Figure 6E shows the effect of the wave number on the liquid film stiffness, in which both the stiffness and relative change rate increase as the wavenumber increases. When considering the viscosity-temperature effect, the film stiffness will be reduced and the relative change rate in different wavenumber can reach 44.67–57.41%. The change of wave number will lead to a higher density of the high-temperature region in the liquid film. It is noteworthy that the changing wavenumber does not lead to a

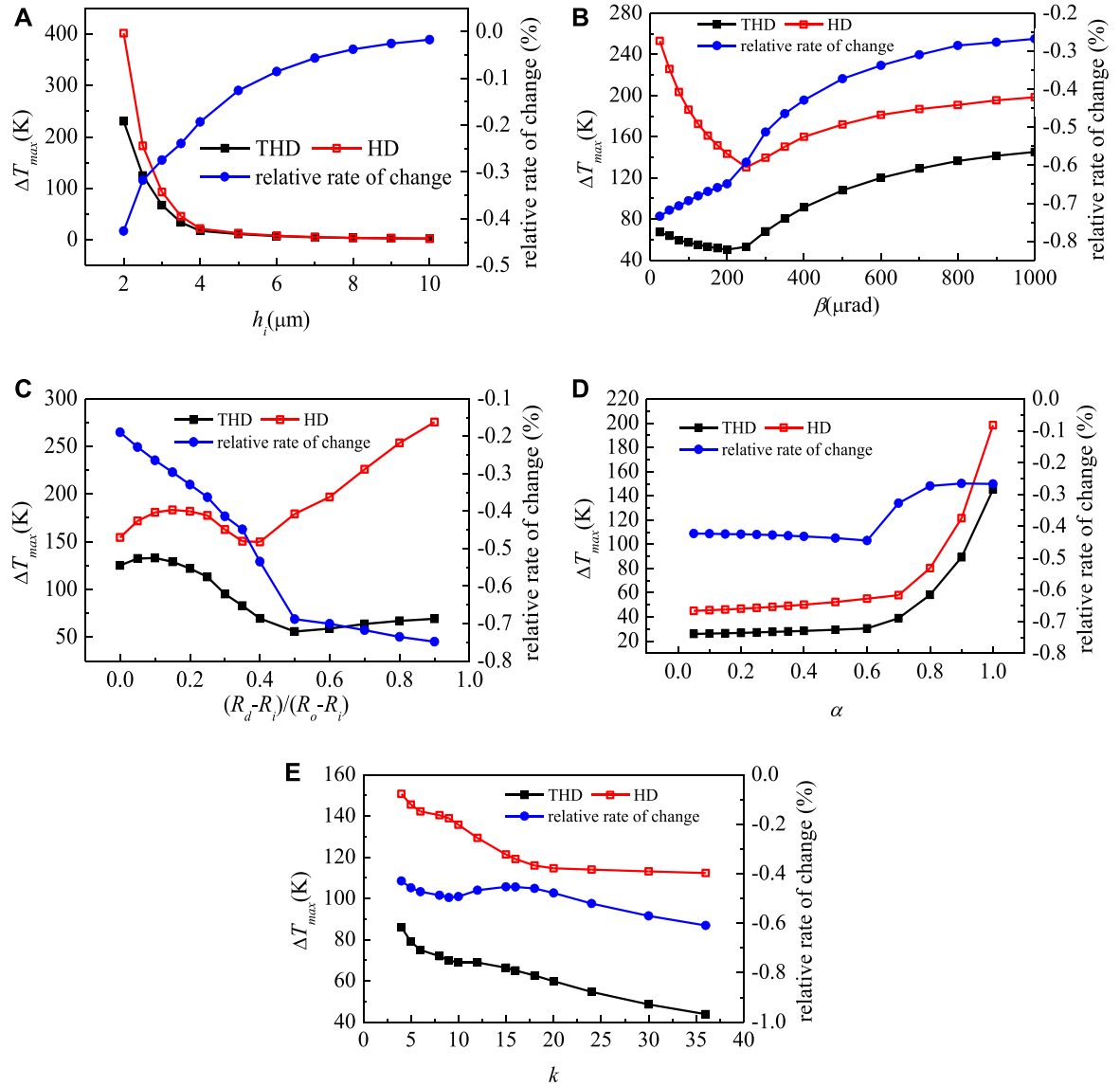

FIGURE 7 | Effect of structural parameters under the viscosity-temperature effect on the maximum temperature difference in the liquid film.

large temperature rise, thus the change of relative change rate is relatively gentle.

According to these analyses, the viscosity-temperature effect should be taken into consideration in analyzing the performance of the waviness end-face mechanical seal. The neglect of the viscosity-temperature effect will lead to the overestimation of the film stiffness, which will destroy the safe and stable operation of the seal. Besides, to control the leakage while ensuring the sufficient bearing capacity and stable operation, it is necessary to set appropriate structural parameters of the waviness end-face mechanical seal in the design. In this case, the mechanical seal with the base film thickness being kept at 2.5 μm, the taper being around 900 μrad, the dam width ratio being around 0.2, α being around 0.8, and the wave number being 9 can be one of the optimal combinations for the best performance.

Effects of Structural Parameters on Film Temperature Distribution

In the final part, the influence of the structural parameters of the waviness end-face mechanical seal on the temperature field of the liquid film is studied. When considering the viscosity-temperature effect, the viscosity of the working fluid decreases as the temperature increases. This property will reduce the generated viscous shear friction heat and suppresses the increase of temperature in turn. According to these characteristics, it can be predicted that the maximum temperature difference in the fluid film with considering the viscosity-temperature effect will be smaller than that without considering the viscosity-temperature effect.

Figure 7A illustrates the effect of the base film thickness on the maximum temperature difference in the liquid film, in which

β = 300 μrad and α = 0.5. In general, as the base film thickness increases, the temperature increase in the fluid film becomes lower. In considering the viscosity-temperature effect, the temperature increases under different base file thicknesses when h_i < 4 μm are always lower than that without considering the viscosity-temperature effect. When h_i > 4 μm, the temperature increases of THD solutions and HD solutions are all the same, since the large film thickness makes the viscosity-temperature effect unobvious. Correspondingly, the relative change rate between THD and HD solutions decreases as the film thickness increases, which agrees with the regulation of temperature increases.

Figure 7D depicts the effect of α on the maximum temperature difference in the liquid film at two stages. Under different α, the maximum temperature difference increases in different trends. When α < 0.6, the maximum temperature increases slowly, and after that, the temperature difference increases sharply. This condition is caused by the increase of α when α is big enough. At large α, the increase in α will cause a high temperature in the wave area of the outer diameter side, which results in a sharp increase in temperature difference. For the safe operation, this sharp increase should be avoided in designing the WTD mechanical seal, which requires that the value of α should be set no more than 0.8. The relative change rate between the THD and HD solutions slightly lowered, and always kept between 0.2–0.5%, indicating that the viscosity-temperature effect has a non-obvious influence under this condition.

Figure 7E shows the effect of the wavenumber of the mechanical seal on the maximum temperature difference in the liquid film. In general, as the wave number increase, the maximum temperature decreases with different trends. It can be found that around k = 9–15, the temperature difference has a plateau period, and then decreases slowly. Therefore, to ensure the relatively small temperature difference and reduce the mechanical difficulty, the wave number can be set as 9. The variation of the relative change rate ranges merely from 0.5 to 0.6%, which is relatively stable.

In short, the consideration of the viscosity-temperature effect in the liquid film of the sealing gap is important in controlling the temperature rise. It is presented in **Figure 7** that, when the base film thickness is greater than 2.5 μm, the taper is greater than 600 μrad, the dam width ratio is less than 0.2, and α is at around 0.8, the viscosity-temperature effect on the temperature rise could be acceptable. Under such circumstances, the mechanical seal is expected to have a better performance.

CONCLUSION

The mechanical seal is one of the main components of the reactor coolant pump (RCP) in the nuclear power plant, whose performance strongly influences the safety and stability of nuclear reactor operation. This work studies the characteristics of the waviness end-face mechanical seal, where, considering both the viscosity dissipation and viscosity-temperature effects, the influence of heat transfer and fluid flow characteristics is revealed. The sealing medium flow is guided by Navier-Stokes and Energy balance equations, the simulations of which are performed using an open-source software OpenFOAM under different conditions. Since the effect of viscous shearing for the utilized fluid medium can result in a huge amount of heat waste in the seal ring, which may end up threatening the seal's normal operations. This study also investigated the liquid film's thermal evolution characteristics. Note also that, in line with the working fluid properties, thermal influence analysis requires the consideration of the liquid film's viscosity characteristics. Concluding remarks on the present study can be summarized as follows:

1) The viscosity-temperature effect can increase the leakage, while this effect decreases the opening force and the liquid film stiffness. In particular, when considering the viscosity-temperature effect, the values of liquid film stiffness may have a negative value. These properties will lead to a higher risk in the safe and stable operation of the mechanical seal. According to these analyses, it can be concluded that the viscosity-temperature effect plays a negative role in the mechanical seal performance, which cannot be ignored in the design of the mechanical seal.
2) From the perspective of liquid film temperature rise, the viscosity-temperature effect can reduce the temperature rise in the liquid film, which improves its safe operations. Based on the above considerations, when designing the waviness mechanical seal, the optimal structural parameters can be set as h_i = 2.5μm, β = 900μrad $(R_d\text{-}R_i)/(R_o\text{-}R_i)$ = 0.2, α = 0.8, and k = 9.

More research endavours are still needed to extend the present study to farther operating conditions where for instance the sealing medium (utilized working fluid in the seal gap) would be changed to other commonly utilized fluids in these system to investigate the associated impact of the sealing performance. Moreover, it will be more informative to explore the eventual changes in flow field characteristics such the pressure and temperature contours using the CFD post-processing component.

DATA AVAILABILITY STATEMENT

The original contributions presented in the study are included in the article/Supplementary Material, further inquiries can be directed to the corresponding authors.

AUTHOR CONTRIBUTIONS

H-CZ provided the background of this work. YM, W-TS and H-CZ contributed to conception and design of the study. YM and Y-HW conducted the computation work and the analysis the work with H-CZ and W-TS. YM wrote the first draft of the manuscript. Y-HW, H-CZ and W-TS revised the manuscript and W-TS submitted it.

FUNDING

This work is supported by National Natural Science Foundation of China (U1830118, 51976043) and LiaoNing Revitalization Talents Program (XLYC2007083), Liaoning BaiQianWan Talents Program (LNBQW2020Q0141).

REFERENCES

Baraldi, P., Compare, M., Despujols, A., and Zio, E. (2011). Modelling the Effects of Maintenance on the Degradation of a Water-Feeding Turbo-Pump of a Nuclear Power Plant. *Proc. Inst. Mech. Eng. O: J. Risk Reliability* 225, 169–183. doi:10.1243/1748006xjrr336

Batten, W. M. J., Bahaj, A. S., Molland, A. F., and Chaplin, J. R. (2008). The Prediction of the Hydrodynamic Performance of marine Current Turbines. *Renew. Energ.* 33. doi:10.1016/j.renene.2007.05.043

Chen, G., Xiong, Q., Morris, P. J., Paterson, E. G., Sergeev, A., and Wang, Y.-C. (2014). OpenFOAM for Computational Fluid Dynamics. *Notices Amer. Math. Soc.* 61, 354–363. doi:10.1090/noti1095

Clark, R., Azibert, H., and Oshinowo, L. (2002). Computer Simulation of Mechanical Seal Leads to Design Change that Improves Coolant Circulation. *Mater. Des.* 23, 113–117. doi:10.1016/s0261-3069(01)00048-6

Danchin, R., and Mucha, P. B. (2019). The Incompressible Navier-Stokes Equations in Vacuum. *Comm. Pure Appl. Math.* 72, 1351–1385. doi:10.1002/cpa.21806

Danos, J. C., Tournerie, B., and Frêne, J. (2000). Notched Rotor Face Effects on Thermohydrodynamic Lubrication in Mechanical Face Seal. *Tribology* 38, 251–259. doi:10.1016/s0167-8922(00)80130-3

Djamaï, A., Brunetière, N., and Tournerie, B. (2010). Numerical Modeling of Thermohydrodynamic Mechanical Face Seals. *Tribology Trans.* 53, 414–425. doi:10.1080/10402000903350612

Falaleev, S. V. (2015). Techniques for Calculating the Hydrodynamic Characteristics of Mechanical Face Seals with Gaps of Complex Forms. *J. Friction Wear*. 36(2):177–183. doi:10.3103/S1068366615020063

Feng, X. D., Dazhuan, W. U., Yang, L. F., and Jia, Y. (2016). Technology for CNP1000 Shaft Sealed Reactor Coolant Pump. *J. Drainage Irrigation Machinery Eng.* 34 (7):553–560. doi:10.3969/j.issn.1674-8530.15.0162

Gebreslassie, M. G., Tabor, G. R., and Belmont, M. R. (2013). Numerical Simulation of a New Type of Cross Flow Tidal Turbine Using OpenFOAM - Part I: Calibration of Energy Extraction. *Renew. Energ.* 50, 994–1004. doi:10.1016/j.renene.2012.08.065

Gebreslassie, M. G., Tabor, G. R., and Belmont, M. R. (2013). Numerical Simulation of a New Type of Cross Flow Tidal Turbine Using OpenFOAM - Part II: Investigation of Turbine-To-Turbine Interaction. *Renew. Energ.* 50, 1005–1013. doi:10.1016/j.renene.2012.08.064

Gustafsson, T., Hakula, H., and Leinonen, M. (2017). Stochastic Galerkin Approximation of the Reynolds Equation with Irregular Film Thickness. *Comput. Math. Appl.* 74, 1590–1606. doi:10.1016/j.camwa.2017.06.012

Han, Y., and Tan, L. (2020). Dynamic Mode Decomposition and Reconstruction of Tip Leakage Vortex in a Mixed Flow Pump as Turbine at Pump Mode. *Renew. Energ.* 155, 725–734. doi:10.1016/j.renene.2020.03.142

Harp, S. R., and Salant, R. F. (1998). Analysis of Mechanical Seal Behavior During Transient Operation. *J. Tribology* 120, 191–197. doi:10.1115/1.2834409

Jasak, H., Jemcov, A., and Tukovic, Z. (2007). OpenFOAM: A C++ Library for Complex Physics Simulations," in International workshop on coupled methods in numerical dynamics, IUC Dubrovnik Croatia, 2007, 1–20.

Kok, B., and Benli, H. (2017). Energy Diversity and Nuclear Energy for Sustainable Development in Turkey. *Renew. Energ.* 111, 870–877. doi:10.1016/j.renene.2017.05.001

Liu, W., Liu, Y., Wang, Y., and Peng, X. (2011). Parametric Study on a Wavy-Tilt-Dam Mechanical Face Seal in Reactor Coolant Pumps. *Tribology Trans.* 54, 878–886. doi:10.1080/10402004.2011.611325

Liu, Y., Liu, W., Li, Y., Liu, X., and Wang, Y. (2015). Mechanism of a Wavy-Tilt-Dam Mechanical Seal under Different Working Conditions. *Tribology Int.* 90, 43–54. doi:10.1016/j.triboint.2015.03.020

Luqman, M., Ahmad, N., and Bakhsh, K. (2019). Nuclear Energy, Renewable Energy and Economic Growth in Pakistan: Evidence from Non-linear Autoregressive Distributed Lag Model. *Renew. Energ.* 139, 1299–1309. doi:10.1016/j.renene.2019.03.008

Mayer, E. (1989). Performance of Rotating High Duty Nuclear Seals. *Lubrication Eng.* 45, 275–286.

Merati, P., Okita, N. A., Phillips, R. L., and Jacobs, L. E. (1999). Experimental and Computational Investigation of Flow and Thermal Behavior of a Mechanical Seal. *Tribology Trans.* 42, 731–738. doi:10.1080/10402009908982276

Chandramoorthy, N., and Hadjiconstantinou, N., *A Reynolds Lubrication Equation for Dense Fluids Valid beyond Navier-Stokes*, E22.

Nilsson, J., Wojciechowski, A., Stromberg, A. B., Patriksson, M., and Bertling, L. (2009). An Opportunistic Maintenance Optimization Model for Shaft Seals in Feed-Water Pump Systems in Nuclear Power Plants. *IEEE Bucharest, Powertech*, 1–8. doi:10.1109/ptc.2009.5281892

Pascovici, M. D., and Etsion, I. (1992). A Thermo-Hydrodynamic Analysis of a Mechanical Face Seal. *Stle Tribology Trans.* 114, 639–645. doi:10.1115/1.2920930

Peng, X. D., Liu, X., Meng, X. K., Sheng, S. E., and Li, J. Y. (2012). Thermo-elasto-hydrostatic Effect Analysis of a Double Tapered Hydrostatic Mechanical Seal in Reactor Coolant Pumps. *Tribology* 32, 244–250. doi:10.1109/APPEEC.2012.6306984

Pietarila Graham, J., Holm, D. D., Mininni, P. D., and Pouquet, A. (2008). Three Regularization Models of the Navier-Stokes Equations. *Phys. Fluids* 20, 035107. doi:10.1063/1.2880275

Salant, R. F., Payne, J. W., Johnson, W. R., and Boles, G. (2018). Simulation of a Hydraulically Controllable Reactor Coolant Pump Seal. *Tribology Int.* 122, 163–168. doi:10.1016/j.triboint.2018.02.024

Shen, S., Qian, Z., and Ji, B. (2019). Numerical Analysis of Mechanical Energy Dissipation for an Axial-Flow Pump Based on Entropy Generation Theory. *Energies* 12, 4162. doi:10.3390/en12214162

Simon, A. (2018). *Robust, Gas-Lubricated Mechanical Seal for Processing Natural Gas*. Sealing Technology. 2018 (5), 5–6. doi:10.1016/S1350-4789(18)30206-X

Sinchev, B., Sibanbayeva, S. E., Mukhanova, A. M., Nurgulzhanova, A. N., Zaurbekov, N. S., Imanbayev, K. S., et al. (2018). Some Methods of Training Radial Basis Neural Networks in Solving the Navier-Stokes Equations. *Int. J. Numer. Meth Fluids* 86, 625–636. doi:10.1002/fld.4470

Stanghan-Batch, B., and Iny, E. H. (1973). A Hydrodynamic Theory of Radial-face Mechanical Seals. *J. Mech. Eng. Sci.* 15, 17–24. doi:10.1243/JMESJOUR197301500502

Temam, R. (2001). *Navier-Stokes Equations: Theory and Numerical Analysis*. Providence, RI: American Mathematical Soc.

Tournerie, B., Danos, J. C., and Frêne, J. (2001). Three-Dimensional Modeling of THD Lubrication in Face Seals. *J. Tribology* 123, 196–204. doi:10.1115/1.1327584

Wen, Q. F., Ying, L., Huang, W. F., Suo, S. F., and Wang, Y. M. (2013). The Effect of Surface Roughness on thermal-elasto-hydrodynamic Model of Contact Mechanical Seals. *Sci. China(Physics,Mechanics Astronomy)*, 56, 112–121. doi:10.1007/s11433-013-5266-3

Young, L. A., Key, B., Philipps, R., and Svendsen, S. (2003). Mechanical Seals with Laser Machined Wavy SiC Faces for High Duty Boiler Circulation and Feedwater Applications. *Lubrication Eng.* 59, 30–39.

Young, L. A., and Lebeck, A. O. (1989). *The Design and Testing of a Wavy-Tilt-Dam Mechanical Face Seal*. Lubrication Engineering, 45 (5), 322–329.

Conflict of Interest: The authors declare that the research was conducted in the absence of any commercial or financial relationships that could be construed as a potential conflict of interest.

frontiers in Energy Research

ORIGINAL RESEARCH
published: 28 October 2021
doi: 10.3389/fenrg.2021.760477

Impact Investigation of Stator Seal Leakage on Aerodynamic Performance of Multistage Compressor

Qi Wang[1,2]*, *Zhou Zhang*[1,2], *Qingsong Hong*[1,2] *and Lanxue Ren*[1,2]

[1]Harbin Marine Boiler and Turbine Research Institute, Harbin, China, [2]National Engineering Laboratory for Marine and Ocean Engineering Power System—Marine Engineering Gas Turbine Laboratory, Harbin, China

In this paper, a numerical model based on the mass flow rate of seal leakage is presented, and a 3D numerical method of a multistage axial compressor with good engineering practicability is established. Validation consists of modeling a nine-stage axial compressor in all operating rotation speeds and calculating results of the performance characteristic curves in good agreement with test data. Comparisons are made against different cases of seal leakage mass flow rate for analyzing the impact of increasing seal leakage on the aerodynamic performance of the multistage axial compressor. The results indicate that the performance of the nine-stage axial compressor is degenerated faster and faster with seal leakage increasing in all operating working points, and the degeneration of performance of this compressor can be evaluated by the relationships of main performance parameters with the mass flow rate of seal leakage. Comparisons of flow distribution in the compressor for different cases of seal leakage also show that stators located in front stages of the multistage axial compressor are affected more seriously by the increasing seal leakage, and it can be confirmed that relatively larger flow losses in front stages bring significant impact on the decay of aerodynamic performance of a multistage axial compressor.

Keywords: numerical model, seal leakage, multistage axial compressor, characteristic curves, different working conditions

OPEN ACCESS

Edited by:
Xiao Liu,
Harbin Engineering University, China

Reviewed by:
Bing Ge,
Shanghai Jiaotong University, China
Bin Jiang,
Harbin Engineering University, China

***Correspondence:**
Qi Wang
overlucked@163.com

Specialty section:
This article was submitted to Advanced Clean Fuel Technologies, a section of the journal Frontiers in Energy Research

Received: *18 August 2021*
Accepted: *22 September 2021*
Published: *28 October 2021*

Citation:
Wang Q, Zhang Z, Hong Q and Ren L (2021) Impact Investigation of Stator Seal Leakage on Aerodynamic Performance of Multistage Compressor. Front. Energy Res. 9:760477. doi: 10.3389/fenrg.2021.760477

INTRODUCTION

A compressor plays a decisive role in the performance of aero-engines and gas turbines as an important core component. Nowadays, the compressor has a higher total pressure ratio, higher efficiency, and larger surge margin than itself in past years. To satisfy the requirement, more advanced aerodynamic design methods need to be developed and used. With the improvement of the compressor performance and aerodynamic design methods, the influence of actual structure on performance has been a key factor during the research of an advanced compressor. While a compressor aerodynamic scheme is designed, the impact level of any actual structure on performance must be thoughtful. It could ensure the performance directly when the designed compressor is applied practically. Up to now, a lot of research studies directed at the actual structure which has great influence on the internal flow of compressor have been carried out, such as the blade fillet (Debruge, 1980; Curlett, 1991; Hoeger et al., 2002), the tip clearance of rotor (Wang et al., 2018), the hub clearance of stator (Lu and Li, 2016), and so on (Khaleghi, 2019). Among them, the seal structure between the stator root and

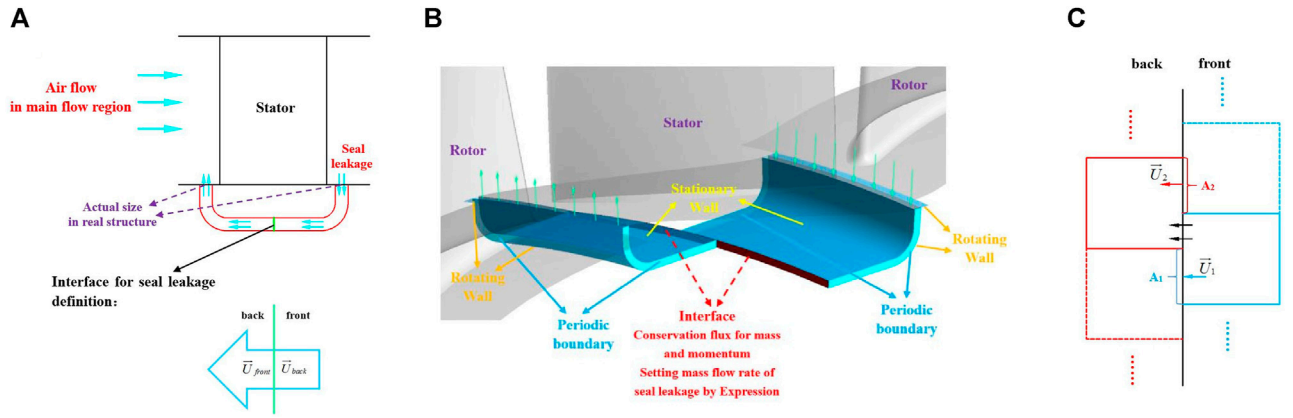

FIGURE 1 | Meridian and Three-dimensional flow model of seal leakage. Meridian flow model for seal leakage at stator root **(A)**, Three-dimensional seal leakage fluid domain model **(B)**, Conservative flux transmissin method through the interface **(C)**.

TABLE 1 | Main parameters of the nine-stage axial compressor.

Parameter at the design point	Value
Corrected rotation speed (rpm)	7,285
Mass flow rate (kg/s)	85.0
Inlet hub ratio	0.371
Inlet aspect ratio	1.443
Inlet tip speed (m/s)	355.6
Inlet relative tip Mach number	0.89

the disk is one of the most important actual structures and has a strong impact on compressor performance.

When the compressor stator has an inner ring, radial clearance must exist between the inner ring of the stator and disk. For this reason, the seal structure is usually used to reduce the air leakage at the radial clearance such as labyrinth seal and brush seal. Because the internal flow of seal cavity is very complex, and it has a strong interaction with the main flow region in the compressor, degeneration of seal effect can lead to the performance reduction of aero-engines and even the accident. Considering the specific fuel consumption, thrust–weight ratio, and reliability, advanced seal technology needs to be invented and used. And a lot of fundamental research studies on the seal effect and leakage flow have been carried out. For many years, the research studies in the field of seal technology mainly centered around theoretical, experimental, and numerical analysis (Wellborn, 2001; wellborn and Okiishi, 1996; Liu et al., 2014; Kong et al., 2017; Kim et al., 2019).

On the contrary, because of many reasons, for example, the seal cavity model is complex and the seal actual radial clearance is varied during the compressor operation, many research studies on seal performance have just been stopped at the principle analysis for seal itself. Few research studies are carried out on the effect of seal engineering application on the aerodynamic performance of a multistage axial compressor. Therefore, a numerical model which can be used to simulate the seal leakage at the stator root is set up based on the commercial code ANSYS CFX in this paper. And the impact of seal leakage at the stator root on the aerodynamic performance of a nine-stage axial compressor is investigated and analyzed.

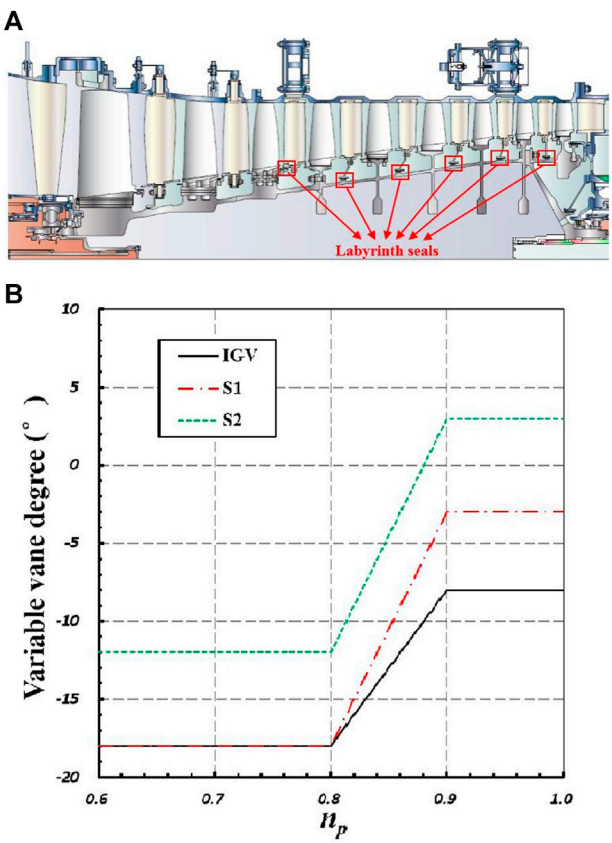

FIGURE 2 | Basic structural parameters of the nine-stage axial compressor. Main structures of the nine-stage axial compressor **(A)**, Variable vane degree related to non-dimensional corrected rotation speed **(B)**.

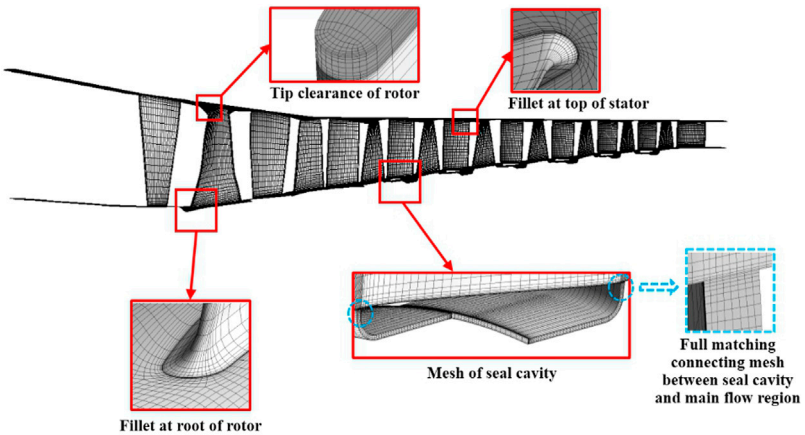

FIGURE 3 | Computational mesh generation of the nine-stage axial compressor.

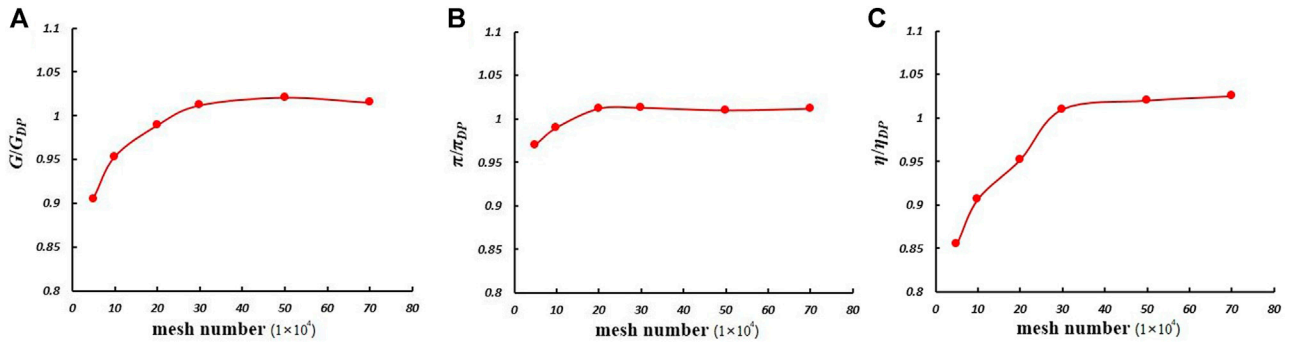

FIGURE 4 | Grid sensitivity analysis for the computational results of total performance parameters. Corrected mass flow **(A)**, Total pressure ratio **(B)**, Isentropic efficiency **(C)**.

NUMERICAL STUDY

Numerical Model for Seal Leakage

The actual seal structure at the stator root is very complex, and the characteristic length in the seal cavity is much less than that in the main flow region. When an actual seal model (the scale is 1:1) is added to the three-dimensional numerical simulation of the multistage axial compressor, more difficulties will be faced and more time will be cost because of the heavy work of geometry modeling and meshing, and these problems may bring a long engineering design cycle. This is very adverse to the engineering application. Moreover, the main mode of action between the seal cavity and the main flow region in the compressor is the level of air leakage. To avoid the above problems, the mass flow rate of seal leakage can be chosen as the key research parameter of the effect of seal engineering application on the aerodynamic performance of a multistage axial compressor, and a simplified numerical model can be set up on this basis.

First, a two-dimensional meridian flow model is set up for seal leakage at the stator root. The meridian flow model can be carried out by the Meridional Techno Effects function in the AutoGrid5 package of NUMECA software. **Figure 1A** shows the schematic diagram of the meridian flow model. In this model, an interface for the definition of leakage needs to be set. Second, based on the two-dimensional meridian flow model, a three-dimensional seal leakage fluid domain model for the numerical simulation of signal blade passage of the multistage axial compressor can be set up. **Figure 1B** shows the three-dimensional seal leakage fluid domain model and the kinds of its boundary conditions which need to be set in ANSYS CFX software.

Through the interface, flux conservation transfer must be ensured. Because the model is a circular periodic symmetric model and the radial heights on either side of the interface are the same, the areas on either side of the interface must be equal. **Figure 1C** shows the flux transmission method through the interface. The flux on the intersection surface will be transported directly to the other side, and the flux $\vec{U}_1$ in the area A1 will be transformed to the flux $\vec{U}_2$ and then be transported into the region of area A2. As the distribution of grid nodes on either side of the interface is different, an interface interpolation algorithm needs to be used to achieve flux conservation transfer. In this paper, two faces on either side of

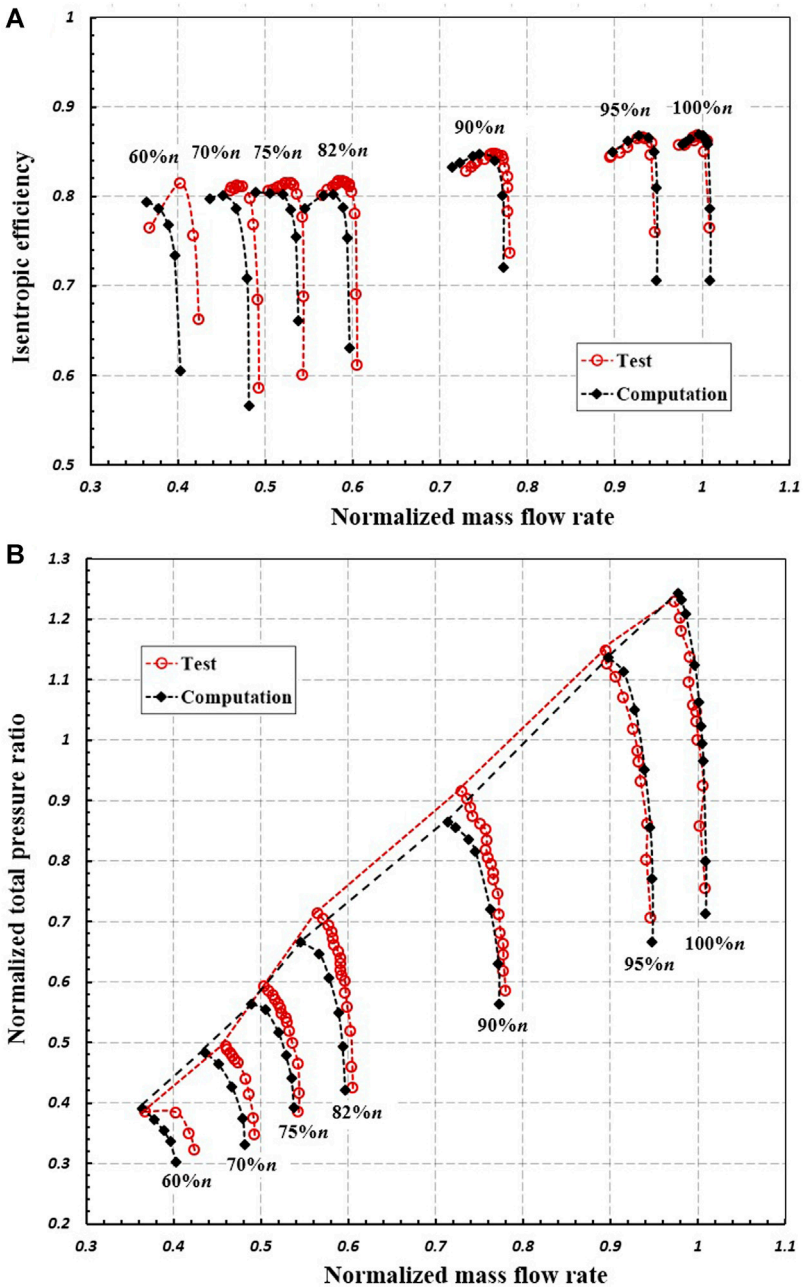

FIGURE 5 | Comparison of characteristic curves for the compressor performance between computation and test. Characteristics of isentropic efficiency relative to normalized mass flow rate **(A)**, Characteristics of normalized total pressure ratio relative to normalized mass flow rate **(B)**.

the interface are intersected using the Sutherland–Hodgman clipping algorithm. This method computes the exact area fractions using polygon intersection and is much faster and more accurate than other methods.

Flux conservation transfer through the interface (from $\vec{U}_{\text{front}}$ to $\vec{U}_{\text{back}}$) can be ensured by the governing equations of mass, momentum, and energy.

The mass control equation is

$$\frac{\partial \rho}{\partial t} + \nabla \cdot \left(\rho \vec{u}\right) = 0. \tag{1}$$

The momentum control equation is

$$\frac{\partial}{\partial t}\left(\rho \vec{u}\right) + \nabla \cdot \left(\rho \vec{u}\vec{u}\right) = -\nabla p + \nabla \cdot \left(\bar{\bar{\tau}}\right) + \vec{F}. \tag{2}$$

For a Newtonian fluid, $\bar{\bar{\tau}}$ can be computed as follows:

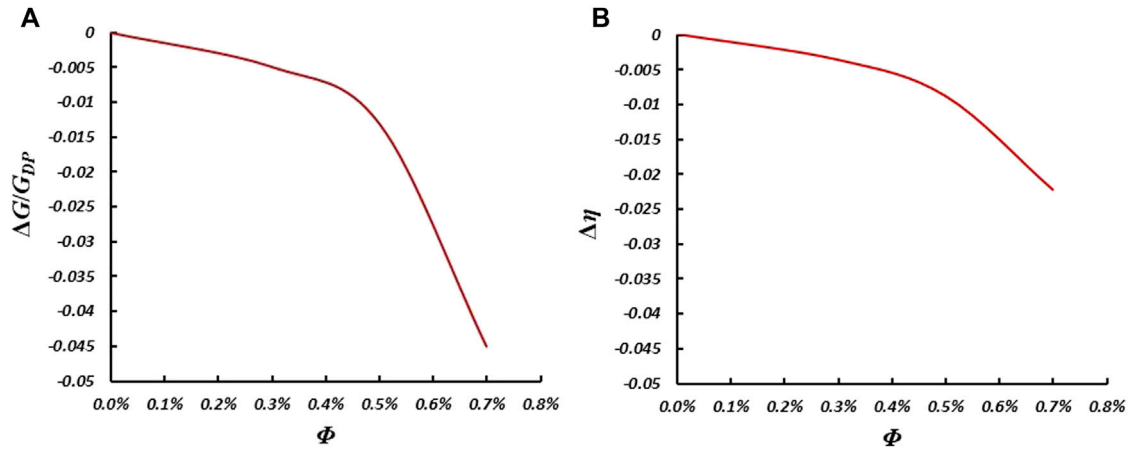

FIGURE 6 | Changing curves of compressor performance parameters related to the seal leakage at design point. $\Delta G/G_{DP}$ related to Φ **(A)**, $\Delta\eta$ related to Φ **(B)**.

$$\bar{\bar{\tau}} = \mu\left[\left(\nabla\vec{u} + \nabla\vec{u}^{T}\right) - \frac{2}{3}\nabla\cdot\vec{u}I\right]. \tag{3}$$

The energy control equation is

$$\frac{\partial}{\partial t}(\rho h_t) + \nabla\cdot\left(\vec{u}(\rho h_t + p)\right) = \nabla\cdot\left(\lambda\nabla T + \left(\bar{\bar{\tau}}\cdot\vec{u}\right)\right) + \vec{u}\cdot\vec{F} + S_h. \tag{4}$$

And h_t can be calculated as follows:

$$h_t = h + \frac{u^2}{2}. \tag{5}$$

Physical Model

In this study, a nine-stage axial compressor is taken as the research object. The mass flow of this compressor exceeds 85.0 kg/s at its design rotation speed of 7285 rpm at the ISO ambient reference condition. The compressor has an inlet hub ratio of 0.371 and an inlet aspect ratio of 1.443. The inlet tip speed and inlet relative tip Mach number of this compressor are 355.6 m/s and 0.89, respectively. **Table 1** shows the parameters of this compressor in detail.

Figure 2A shows the main structures of the nine-stage axial compressor. The compressor consists of 19 blade rows that include one row of the inlet guide vane, nine rows of the rotor blade, and nine rows of the stator blade. It contains three rows of variable stators (IGV, S1, and S2), and they move in the range of 0.82~0.9 n which are controlled by the corrected rotation speed as depicted in **Figure 2B**. From S3 to S8, there are labyrinth seals at the roots of stators.

Numerical Research Method

The steady and viscous three-dimensional numerical simulation of the nine-stage axial compressor is carried out in this study. **Figure 3** shows the computational mesh generation of the compressor. A structure grid is generated in the mesh discretization of computational regions with the AutoGrid5 package of NUMECA software. The O4H grid topology is used in the main flow region of compressor blade passage, and the H grid topology is used in the fluid domain of seal cavity. The tip clearance of rotor is 0.5 mm, and a butterfly mesh topology is used in this region. The fillets at each root of the rotor and top of the stator have the same actual size as the compressor rig. The present simulation uses the commercial code ANSYS CFX to solve the 3D compressible Reynolds-averaged Navier–Stokes equations, which is conducted on a parallel computer. And the standard κ-ε turbulence model is adopted to calculate the turbulence in this study, which is a two-path turbulence model proposed by Launder and Spalding in 1972.

In the process of mesh generation, the dimensionless wall distance parameter y^+ is considered by controlling the distance between the first layer grid nodes adjacent to the wall. The equation of y^+ is as follows:

$$y^+ = \frac{\rho u_\tau y_{wall}}{\mu}, \tag{6}$$

where $u_\tau = \sqrt{\tau_{wall}/\rho}$ is the friction velocity; τ_{wall} is the wall shear stress; y_{wall} is the distance of the first layer grid node adjacent to the wall; and p and μ represent the density and dynamic viscosity coefficient of the fluid.

For meeting the y^+ requirement of the standard κ-ε turbulence model, the height of the first layer of grids is determined as 0.01 mm, and the scalable wall function is used as the wall-function method which can be a consistent solution for any encrypted grid and avoid the deterioration of computed results when $y^+ < 15$ (Chedevergne, 2018).

The leakage mass flow rate at the interface of every seal cavity is determined as the test result of the nine-stage compressor. During the compressor test, the leakage mass flow rate at every seal structure is measured, and the test results are 0.27–0.32% of the mass flow rate at the compressor inlet. For letting it be more convenient to compare the effect of different leakages, the leakage mass flow rate at every seal structure is determined as 0.3% of the mass flow rate at the compressor inlet to simulate the experiment condition.

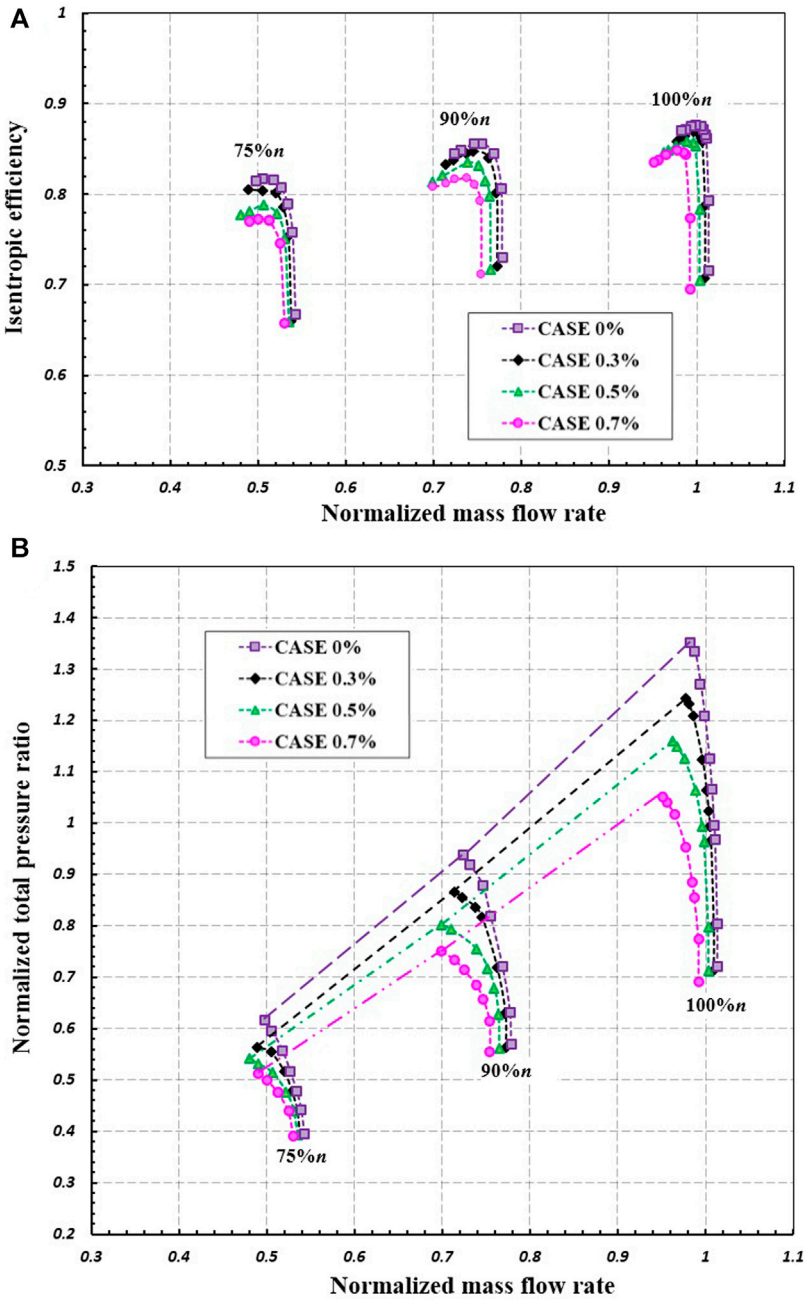

FIGURE 7 | Comparison of characteristic curves for the compressor performance on different cases of seal leakage. Characteristics of isentropic efficiency relative to normalized mass flow rate **(A)**, Characteristics of normalized total pressure ratio relative to normalized mass flow rate **(B)**.

The total pressure and total temperature at the inlet and the circumferential averaged static pressure at the outlet are given in the boundary conditions of the nine-stage axial compressor. The fractional intensity and eddy length scale of inlet turbulence boundary conditions are specified as 0.02 and 0.003 m, respectively. The rotor–stator interface conditions are set as the mixing plane. No slip and adiabatic conditions are specified on the hub, shroud, and blade wall.

Validation of Numerical Method

For proving the applicability of the numerical model to seal leakage and the numerical method in this study, the three-dimensional numerical simulation of the nine-stage axial compressor by the above method is carried out and the boundary conditions are set the same as the compressor test conditions. At the same time, the isentropic efficiency is calculated by the method of compressor test as

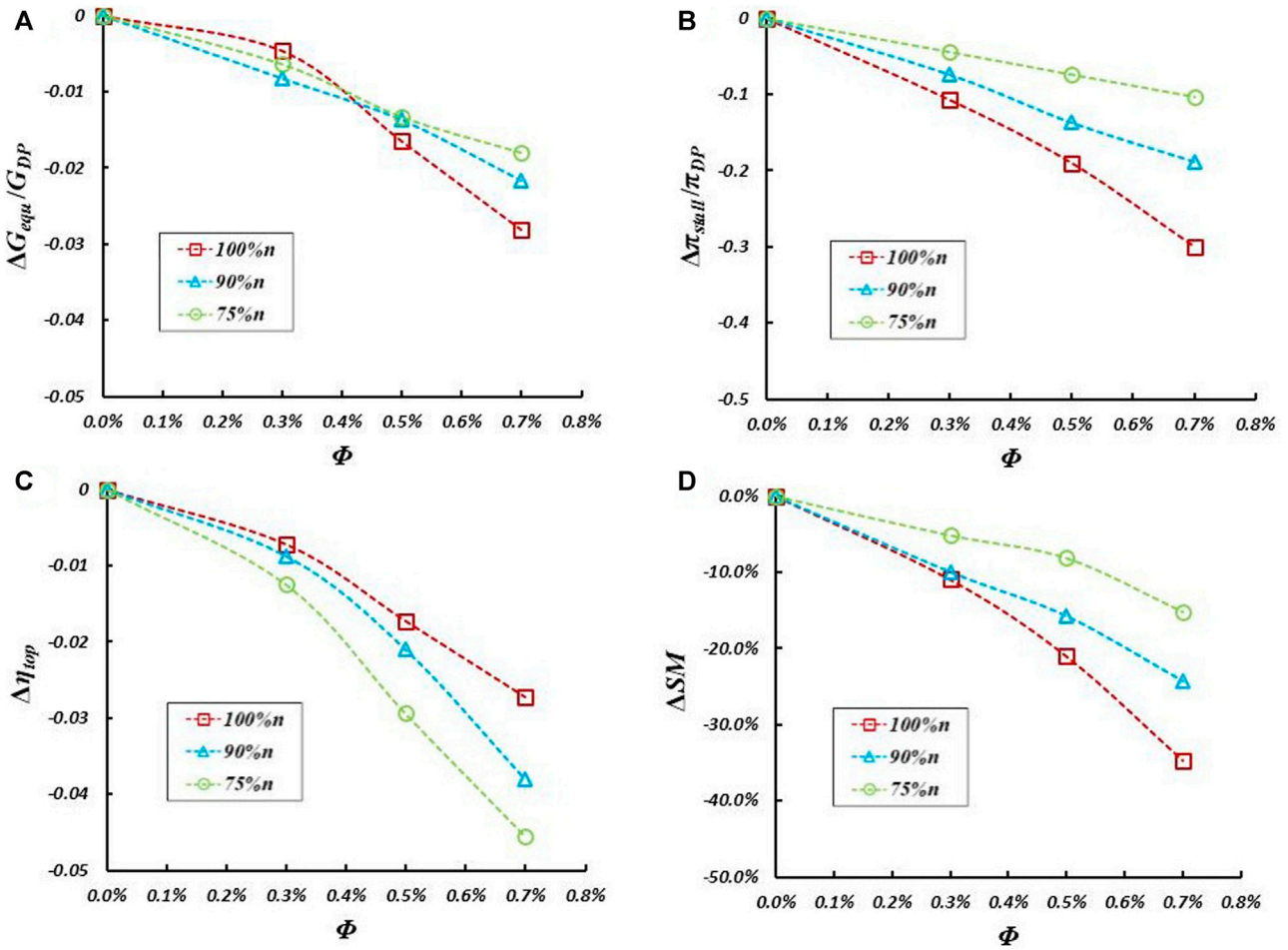

FIGURE 8 | Changing curves of compressor performance parameters related to the seal leakage at different rotation speeds. $\Delta G_{equ}/G_{DP}$ related to Φ **(A)**, $\Delta\pi_{stall}/\pi_{DP}$ related to Φ **(B)**, $\Delta\eta_{top}$ related to Φ **(C)**, ΔSM related to Φ **(D)**.

$$\eta = \frac{\pi^{*\frac{\gamma-1}{\gamma}} - 1}{\theta - 1}, \tag{7}$$

where the value of k can be calculated as follows when the temperature of air is between 242 and 1000 K:

$$\gamma = \frac{B_1 + 2B_2T_{ave} + 3B_3T_{ave}^2 + 4B_4T_{ave}^3 + 5B_5T_{ave}^4}{B_1 - 1.98726 + 2B_2T_{ave} + 3B_3T_{ave}^2 + 4B_4T_{ave}^3 + 5B_5T_{ave}^4}. \tag{8}$$

Here, the values of Bi which are the temperature polynomial coefficients of air thermal properties are shown as follows: $B_1 = 0.72806730 \times 10^{1}$, $B_2 = -0.14341481 \times 10^{-2}$, $B_3 = 0.23482926 \times 10^{-5}$, $B_4 = -0.10484129 \times 10^{-8}$, and $B_5 = 0.12429040 \times 10^{-12}$.

At first, the effect of grid number on the numerical results is evaluated. Different cases of grid number for each blade row are determined as 50 thousand, 100 thousand, 200 thousand, 300 thousand, 500 thousand, and 700 thousand grid cells. The grid sensitivity has been studied by evaluating G/G_{DP}, π/π_{DP}, and η/η_{DP} at the design point of the compressor, as shown in **Figure 4**. According to the results, the compressor performance parameters are considered sufficiently refined to obtain results which are independent of the grid number after each blade row exceeds 300 thousand grid cells. To minimize the computational time, the case of 300 thousand grid cells for each blade row is determined for considering the nine-stage axial compressor in this study.

Figure 5 shows the result comparison of characteristic curves for the compressor performance between computation and test. The computational results are consistent with the test results. At 100%n and 95%n, the values of G, π, and η match with the test results very well. From 60%n to 90%n, the computational results have a few deviations from the test results and the largest deviation appears at 60%n. Nonetheless, the surge line of computational results is very consistent with the test results. According to the comparison, the configurations of the numerical method and grid number in this study are considered sufficiently refined to obtain results.

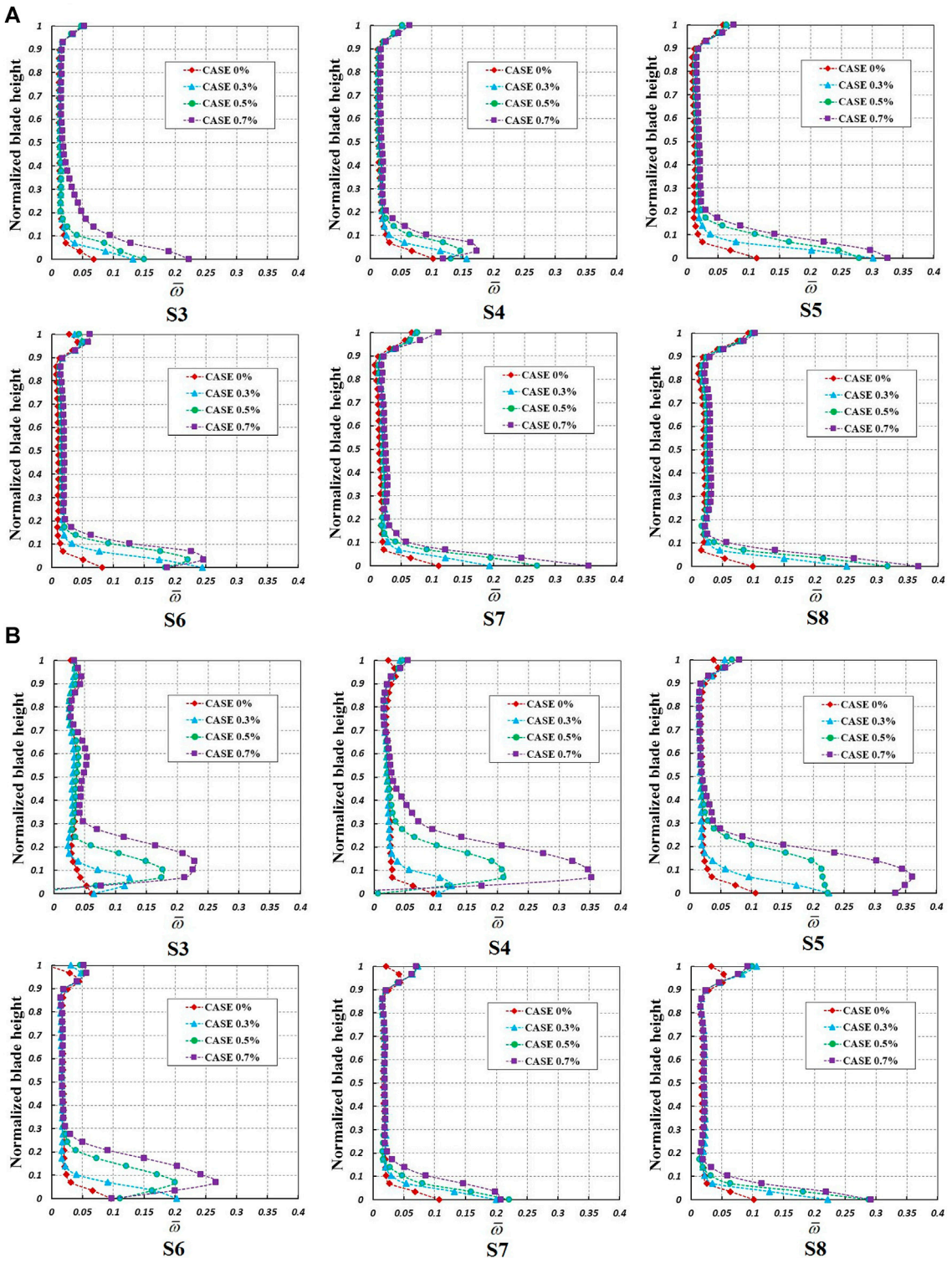

FIGURE 9 | Distribution of $\bar{\omega}$ at each stator along its span at the design point of 100%n **(A)**, The nearest stall point of 75%n **(B)**.

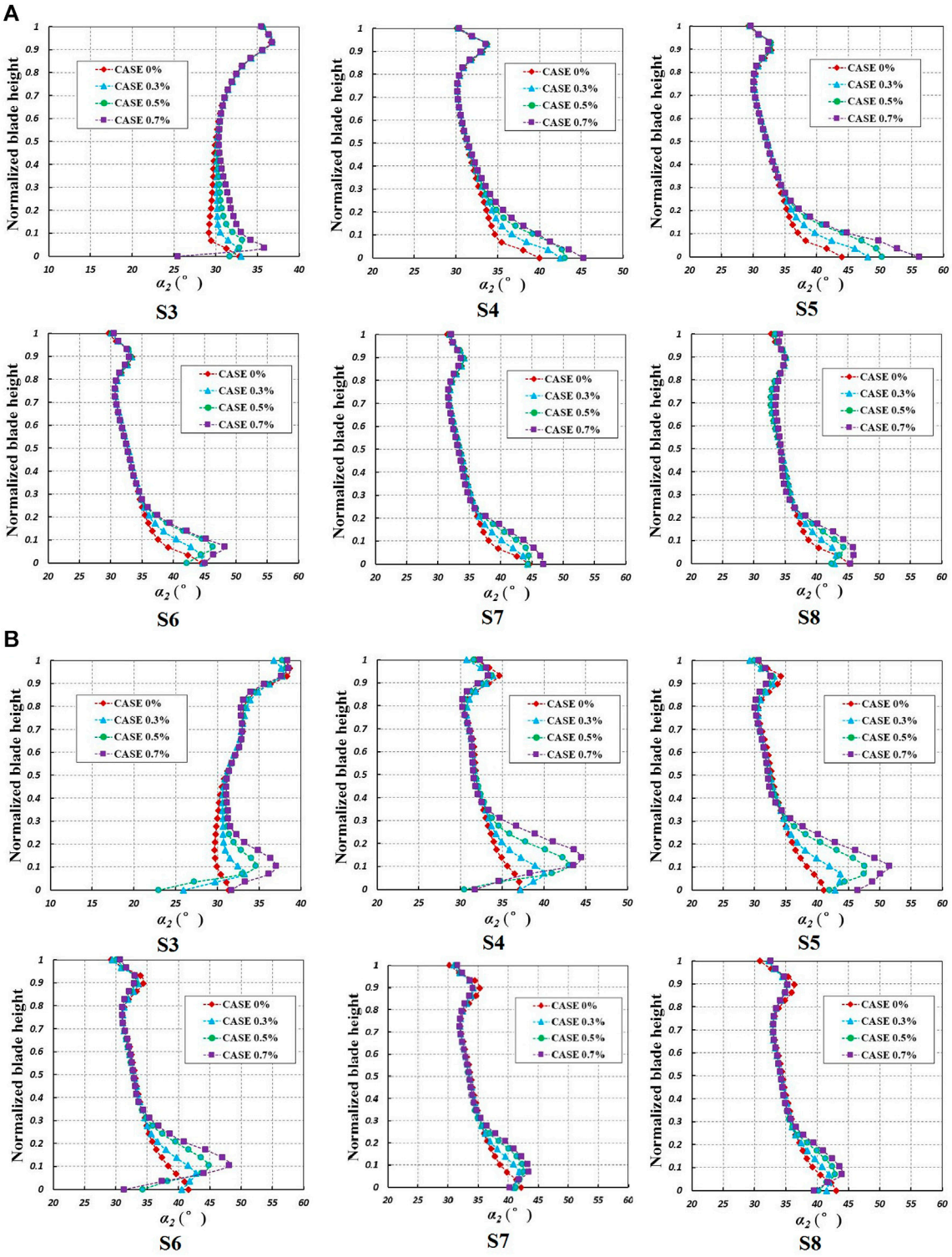

FIGURE 10 | Distribution of α2 at each stator along its span at the design point of 100%n **(A)**, The nearest stall point of 75%n **(B)**.

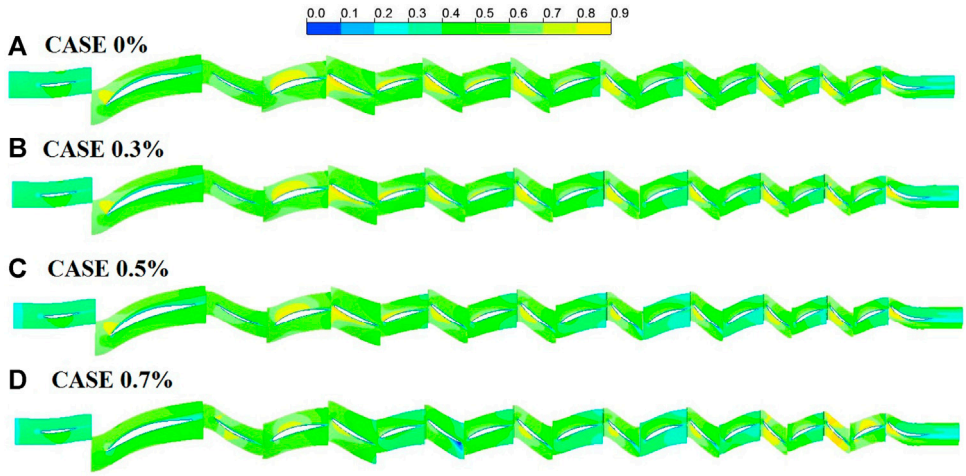

FIGURE 11 | Relative Mach number contours of 10% span at the design point of 100%n. CASE 0% **(A)**, CASE 0.3% **(B)**, CASE 0.5% **(C)**, CASE 0.7% **(D)**.

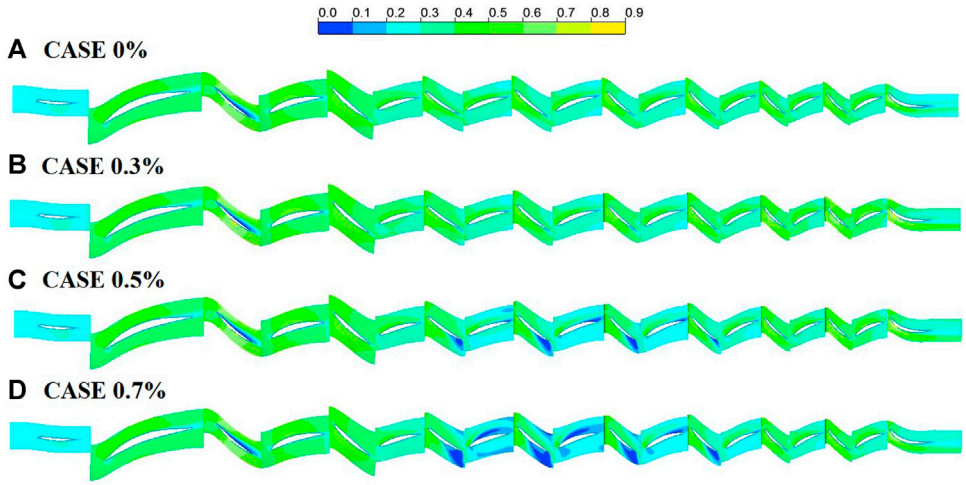

FIGURE 12 | Relative Mach number contours of 10% span at the nearest stall point of 75%n. CASE 0% **(A)**, CASE 0.3% **(B)**, CASE 0.5% **(C)**, CASE 0.7% **(D)**.

RESULTS AND DISCUSSIONS

In this section, different cases of seal leakage for the nine-stage axial compressor are simulated and compared to research the effect on aerodynamic performance. These cases are 0 (no leakage), 0.3, 0.5, and 0.7% of the mass flow rate at the compressor inlet. 75%n, 90% n, and 100%n are selected as the rotation speeds analyzed.

Impact on Overall Performance of Compressor

The computational results of overall performance parameters in different cases of seal leakage at the design point of the compressor are shown in **Figure 6**. In the figure, the changing rules of $\Delta G$and $\Delta\eta$ related to Φ at the design point can be clearly seen. When seal leakage increases, the compressor performance has an apparent decline in the corrected mass flow rate and isentropic efficiency at the same total pressure ratio. The more the seal leakage, the worse the performance of the compressor. With the increase of seal leakage mass flow rate, the decay of compressor performance is getting faster and faster; especially, the seal leakage mass flow rate becomes greater than 0.5% of the inlet mass flow rate.

Figure 7 shows the result comparison of characteristic curves for the compressor performance in different cases of seal leakage. With the increasing seal leakage, the performance of the compressor is degenerated obviously. When the seal leakage increases, the corrected mass flow rate, the self-pressurizing ability, the isentropic efficiency, and the surge margin are fully degenerated.

For investigating the changing multistage compressor performance related to the seal leakage in different rotation speed curves, the variation of equivalent corrected mass flow rate ΔG_{equ} is defined as

$$\Delta G_{equ} = \frac{\sum_{i=1}^{N} \Delta G_i}{N}, \tag{9}$$

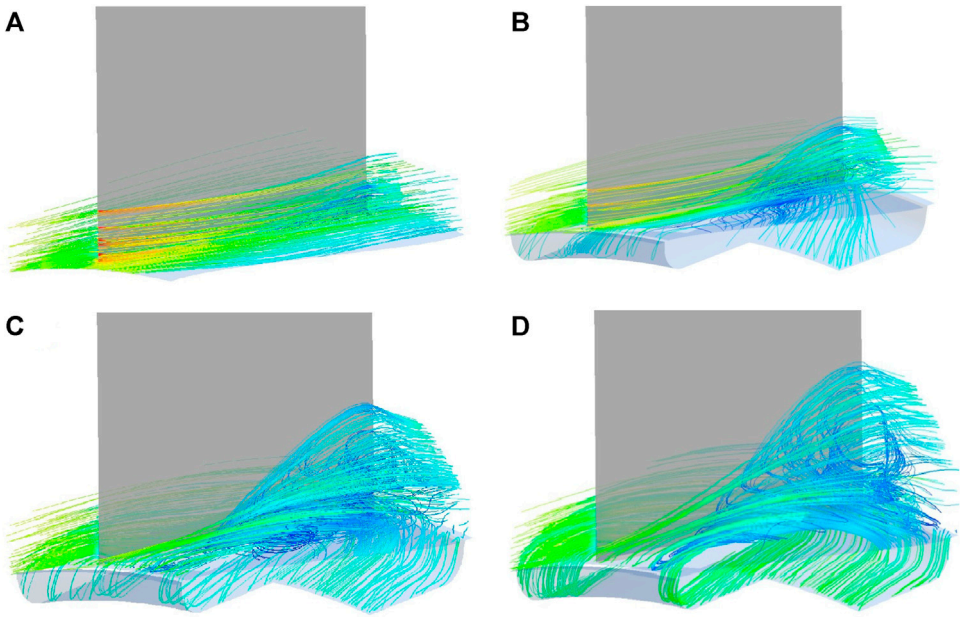

FIGURE 13 | 3D streamlines near the root region of S3 at the nearest stall point of 75%n. CASE 0% **(A)**, CASE 0.3% **(B)**, CASE 0.5% **(C)**, CASE 0.7% **(D)**.

where N is the interpolation point between the choke point and the stall point on each rotation speed curve of this compressor.

The variation of equivalent corrected mass flow rate ΔG_{equ}, the variation of highest total pressure ratio $\Delta\prod$stall, the variation of highest isentropic efficiency $\Delta\eta$top, and the variation of surge margin ΔSM are selected as the main parameters researched in this part. **Figure 8** shows the changing curves of ΔG_{equ}, $\Delta\prod$stall, $\Delta\eta$top, and ΔSMrelated to the seal leakage at different rotation speeds. According to the curves, variations of these main parameters with the mass flow rate of seal leakage at different rotation speeds can be obtained clearly. All of them are degenerated with the increasing seal leakage at each rotation speed. The equivalent corrected mass flow rate ΔG_{equ} has a fast decline at 100%n when the mass flow rate of seal leakage becomes greater than 0.3%, and its decline curves at 90%n and 75%n can be approximated as a linear change. For the highest isentropic efficiency $\Delta\eta$top, a fast decline appears at every rotation speed when the mass flow rate of seal leakage becomes greater than 0.3%, and it decreases faster when the rotation speed becomes lower. The highest total pressure ratio $\Delta\prod$stall and surge margin ΔSM are both changed as linear approximation with the increasing seal leakage at each rotation speed, and they decrease faster when the rotation speed becomes higher.

Analysis of Compressor Internal Flow Distribution

For analyzing the loss situation in stator passage, the total pressure loss coefficient proposed by Lieblein and Roudebush (1956) is used. It is given as

$$\bar{\omega} = \frac{p_1^* - p_2^*}{p_1^* - p_1}, \tag{10}$$

where p_1^* is the total pressure at the cascade inlet of the stator blade, p_2^* is the total pressure at the cascade outlet of the stator blade, and p_1 is the static pressure at the cascade inlet of the stator blade.

Figures 9A,B, respectively, show the distribution along the span of the blade from S3 to S8 at the design point of 100%n and the nearest stall point of 75%n when the mass flow rate of seal leakage changes. As shown in **Figure 9A**, at the design point of 100%n, the total pressure loss of each stator is increased with the increasing seal leakage and the affected region of each stator is mainly under 20% span of blade height. When the mass flow rate of seal leakage becomes 0.7% of the inlet mass flow rate, flow field degradation occurs in S3 passage first, almost 40% span of S3 blade height from the root is affected, and the total pressure loss is obviously increased. It is the main reason which brings the decay of performance when the mass flow rate of seal leakage becomes greater than 0.5% for the nine-stage compressor, as shown in **Figure 6**.

As shown in **Figure 9B**, at the nearest stall point of 75%n, the total pressure loss of each stator is also increased with the increasing seal leakage like the phenomenon at the design point of 100%n. For stators from S3 to S6, when the mass flow rate of seal leakage becomes greater than 0.3%, the total pressure loss near the root of these stators is obviously increased, and the affected blade height of these stators is almost developed near 30% span. When the mass flow rate of seal leakage becomes 0.7% of the inlet mass flow rate, the affected region of S4 is close to 50% span of blade height. The performance degradation of these stators causes the decay of compressor performance and serious stall, so both isentropic efficiency and surge margin of the compressor have a fast decline. As illustrated in **Figures 9A,B**, for the nine-stage compressor, the stators located in front stages are affected more

seriously by the increasing seal leakage than the stators located in back stages wherever the working point of the compressor is.

For further verifying the impact of increasing seal leakage, the distribution of flow angle α2 at each stator outlet along the span of the blade from S3 to S8 at the above two operating points is shown in **Figures 10A,B**, respectively. As illustrated in the figures, the outlet flow angle of each stator is increased with the increasing seal leakage at both the design point of 100%n and the nearest stall point of 75%n. And the phenomenon is consistent with the distribution shown in the above figures. It indicates that the internal flow of each stator passage is affected by the increasing seal leakage. When the seal leakage increases, the flow loss of the stator is increased, and it causes the deviation angle to increase. It influences the flow matching of blade passages, which can obviously cause compressor performance degradation. With the increasing seal leakage, it can also be seen that the stators located in front stages have larger deviation angles than the stators located in back stages of the nine-stage compressor, which is the same as the phenomenon of total pressure loss distribution.

Figures 11, **12**, respectively, show the relative Mach number contours of 10% span on the blade-to-blade surface at the design point of 100%n and the nearest stall point of 75%n when the mass flow rate of seal leakage changes. At the design point, an obvious separation appears at the 10% span of S3 when the mass flow rate of seal leakage becomes 0.7% of the inlet mass flow rate. And at the nearest stall point of 75%n, serious flow separations occur at the 10% span of stators from S3 to S6 when the mass flow rate of seal leakage becomes 0.5% of the inlet mass flow rate, and the separations are developed more seriously when the seal leakage increases to 0.7% of the inlet mass flow rate. The separation vortices choke the whole passage of stators from S3 to S6, and the flow of downstream rotors is affected and separated.

For further analysis of the impact of increasing seal leakage on the details of flow distribution at the stator root, S3 is chosen because it is one of the most serious stators in front stages which is affected by seal leakage. **Figure 13** shows the 3D streamlines near the root region of S3 with the increasing mass flow rate of seal leakage at the nearest stall point of 75%n. The 3D flow details near the space of the stator root region can be clearly seen from the figure. At the stator root region, the air enters the seal cavity from the trailing edge of the stator and flows out from the leading edge. It mixes with the main flow of blade passage, and strong interaction occurs between leakage flow and main flow. With the increasing seal leakage, the interaction becomes stronger and the affected region increases larger. It causes more serious flow separation at the trailing edge of the blade root and aggravates the corner stall of the stator.

CONCLUSION

In this paper, a numerical model which can be used to simulate the seal leakage at the stator root is set up, and it is used in the analysis of the impact of increasing seal leakage on the aerodynamic performance of a nine-stage axial compressor. The performance characteristic parameters of the compressor are calculated, and their changing curves which are related to the mass flow rate of seal leakage are obtained. The flow conditions in the nine-stage compressor for different cases of seal leakage are simulated and compared at the same time. Based on the results, the main conclusions can be made as follows:

1) According to the comparison between computation and test, the engineering practicability and applicability of this numerical model to seal leakage in the multistage axial compressor is proved. Combined with the 3D numerical simulation method which is used in this paper, the aerodynamic performance of the nine-stage axial compressor can be predicted well. The numerical model and method are considered sufficiently refined to obtain results.
2) For a multistage compressor, with the increasing mass flow rate of seal leakage, the performance of the compressor is degenerated faster and faster when its working point is at the design point or others. The flow capacity, working capacity, efficiency, and surge margin of the compressor have an overall decline.
3) According to the internal flow distribution of the nine-stage compressor, when the mass flow rate of seal leakage increases, the stators located in front stages are affected more seriously by the increasing seal leakage than the stators located in back stages of a multistage compressor wherever the working point of the compressor is. Both degradation of flow condition and increase of flow loss in stators located in front stages develop faster with the increasing seal leakage. And this is the main reason that causes the decay of aerodynamic performance of a multistage compressor.

DATA AVAILABILITY STATEMENT

The raw data supporting the conclusions of this article will be made available by the authors, without undue reservation.

AUTHOR CONTRIBUTIONS

QW, ZZ, and QH contributed to conception and design of the study. WQ contributed to the numerical model. ZZ and HQ performed the numerical calculations. LR checked and helped analyze the calculation results. All authors contributed to manuscript revision and read and approved the submitted version.

FUNDING

This study was funded by the National Science and Technology Major Project (2017-II-0006-0019).

ACKNOWLEDGMENTS

The authors would like to acknowledge the support of National Engineering Laboratory for Marine and Ocean Engineering Power System—Marine Engineering Gas Turbine Laboratory.

REFERENCES

Alizadeh, M., Nikkhahi, B., Farahani, A. S., and Fathi, A. (2014). Numerical Study on the Effect of Geometrical Parameters on the Labyrinth-Honeycomb Seal Performance. ASME Paper No. GT2014-25147.

Chedevergne, F. (2018). Analytical wall Function Including Roughness Corrections. *Int. J. Heat Fluid Flow* 73, 258–269. doi:10.1016/j.ijheatfluidflow.2018.08.001

Curlett, B. P. (1991). *The Aerodynamic Effect of Fillet Radius in a Low Speed Compressor cascade*. Cleveland, Ohio: NASA-TM-105347 Lewis Research Center.

Danish, S. N., Qureshi, S. R., Imran, M. M., Khan, S. U.-D., Sarfraz, M. M., El-Leathy, A., et al. (2016). Effect of Tip Clearance and Rotor-Stator Axial gap on the Efficiency of a Multistage Compressor. *Appl. Therm. Eng.* 99, 988–995. doi:10.1016/j.applthermaleng.2016.01.132

Debruge, L. L. (1980). The Aerodynamic Significance of Fillet Geometry in Turbocompressor Blade Rows. *J. Eng. Gas Turb. Power* 102, 984–993. doi:10.1115/1.3230371

Denecke, J., Dullenkopf, K., Wittig, S., and Bauer, H.-J. (2005). *Experimental Investigation of the Total Temperature Increase and Swirl Development in Rotating Labyrinth Seals*. ASME Paper No. GT2005-68677, 1161–1171. doi:10.1115/gt2005-68677

Galindo, J., Tiseira, A., Navarro, R., and López, M. A. (2015). Influence of Tip Clearance on Flow Behavior and Noise Generation of Centrifugal Compressors in Near-Surge Conditions. *Int. J. Heat Fluid Flow* 52, 129–139. doi:10.1016/j.ijheatfluidflow.2014.12.004

Hoeger, M., Baier, R. D., Müller, R., and Engber, M. (2006). "Impact of a Fillet on Diffusing Vane Endwall Flow Structure," in The 11th International Symposium on Transport Phenomena and Dynamics of Rotating Machinery. ISROMAC2006-057, Honolulu, Hawaii, Feb 2006.

Hoeger, M., Schmidt-Eisenlohr, U., Gomez, S., Sauer, H., and Müller, R. (2002). Numerical Simulation of the Influence of a Fillet and a Bulb on the Secondary Flow in a Compressor cascade. *Task Q.* 6, 25–37.

Kumar, S. S., Bhanudasji Alone, D., Thimmaiah, S. M., Mudipalli, J. R. R., Ganguli, R., Kandagal, S. B., et al. (2018). Aerodynamic Characterization of a Transonic Axial Flow Compressor Stage - with Asymmetric Tip Clearance Effects. *Aerospace Sci. Tech.* 82-83, 272–283. doi:10.1016/j.ast.2018.09.001

Khaleghi, H. (2019). Effect of Discrete Endwall Recirculation on the Stability of a High-Speed Compressor Rotor. *Aerosp. Sci. Technol.* 85, 171–179.

Kim, S., Kim, K., and Son, C. (2019). Three-dimensional Unsteady Simulation of a Multistage Axial Compressor with Labyrinth Seals and its Effects on Overall Performance and Flow Characteristics. *Aerospace Sci. Tech.* 86, 683–693. doi:10.1016/j.ast.2019.01.055

Kong, X., Liu, G., Liu, Y., and Zheng, L. (2017). Experimental Testing for the Influences of Rotation and Tip Clearance on the Labyrinth Seal in a Compressor Stator Well. *Aerospace Sci. Tech.* 71, 556–567. doi:10.1016/j.ast.2017.10.003

Liu, G. W., Chen, K., Gang, T., and Zheng, H.-L. (2015). Influences of Pressure Ratio and Reynolds Number on Flow Characteristics of Labyrinth Seal in Compressor Stator Well. *J. Aerosp. Power* 30, 1554–1560. doi:10.13224/j.cnki.jasp.2015.07.003

Launder, B. E., and Spalding, D. B. (1972). *Mathematical Models of Turbulence*. London, UK: Academic Press.

Lieblein, S., and Roudebush, W. H. (1956). Theoretical Loss Relations for Low-Speed Two-Dimensional-cascade Flow. NACA-TN-3662.

Liu, G. W., Kong, X. Z., and Cheng, K. (2014). Numerical Study for Effects of Rotation and Swirl on Labyrinth Sealing in a Compressor Stator Well. *J. Propuls. Technol.* 35, 1687–1693.

Lu, H., and Li, Q. S. (2016). Cantilevered Stator Hub Leakage Flow Control and Loss Reduction Using Non-uniform Clearances. *Aerosp. Sci. Technol.* 51, 1–10. doi:10.1016/j.ast.2016.01.013

Micio, M., Facchini, B., Innocenti, L., and Simonetti, F. (2011). Experiment Investigation on Leakage Loss and Heat Transfer in a Straight through Labyrinth Seal. ASME Paper No. GT2011-46402, 967–979. doi:10.1115/GT2011-46402

Ramakrishna, P. V., and Govardhan, M. (2009). Stall Characteristics and Tip Clearance Effects in Forward Swept Axial Compressor Rotors. *J. Therm. Sci.* 18, 40–47. doi:10.1007/s11630-009-0040-6

Straka, P., and Němec, M. (2016). Influence of the Radial gap under the Stator Blade on Flow Around the Hub-End of the Rotor Blade. *Amm* 821, 120–128. doi:10.4028/www.scientific.net/amm.821.120

Straka, P. (2014). Numerical Simulation of Flow in Hub-gap of Axial Stator Blades. *EPJ Web of Conferences* 67, 1–6. doi:10.1051/epjconf/20146702112

Suder, K. L., and Celestina, M. L. (1996). Experimental and Computational Investigation of the Tip Clearance Flow in a Transonic Axial Compressor Rotor. ASME Paper No. 99-GT-365.

Szwaba, R., Kaczynski, P., and Doerffer, P. (2014). Roughness Effect on Shock Wave Boundary Layer Interaction Area in Compressor Fan Blades Passage. *Aerosp. Sci. Technol.* 37, 130–137.

Taghavi-Zenouz, R., and Ababaf Behbahani, M. H. (2018). Improvement of Aerodynamic Performance of a Low Speed Axial Compressor Rotor Blade Row through Air Injection. *Aerospace Sci. Tech.* 72, 409–417. doi:10.1016/j.ast.2017.11.028

Wang, Z., Lu, B., Liu, J., and Hu, J. (2018). Numerical Simulation of Unsteady Tip Clearance Flow in a Transonic Compressor Rotor. *Aerospace Sci. Tech.* 72, 193–203. doi:10.1016/j.ast.2017.11.012

Waschka, W., Wittig, S., and Kim, S. (1990). Influence of High Rotational Speeds on the Heat Transfer and Discharge Coefficients in Labyrinth Seals. ASME Paper No. GT1990-330. doi:10.1115/90-gt-330

Wellborn, S. R. (2001). Details of Axial Compressor Shrouded Stator Cavity Flows. ASME Paper No. 2001-GT-0495.

Wellborn, S. R., and Okiishi, T. H. (1996). *Effects of Shrouded Stator Cavity Flows on Multistage Axial Compressor Aerodynamic Performance*. NASA-CR-198536.

Zhong, J., Han, S., Lu, H., and Kan, X. (2013). Effect of Tip Geometry and Tip Clearance on Aerodynamic Performance of a Linear Compressor cascade. *Chin. J. Aeronautics* 26, 583–593. doi:10.1016/j.cja.2013.04.020

Zhu, J. Q., and Sun, L.(2005). Experimental Investigation on the Layout of Tip Clearance for an Axial-Flow Compressor Rotor, Paper No. AIAA 2005-808, in 43rd AIAA Aerospace Sciences Meeting, Reno, Nevada, USA,January 2005, pp.1–9. doi:10.2514/6.2005-808

Conflict of Interest: The authors declare that the research was conducted in the absence of any commercial or financial relationships that could be construed as a potential conflict of interest.

GLOSSARY

$\vec{U}_{front}$ flux at the front of the interface in the seal cavity

$\vec{U}_{back}$ flux at the back of the interface in the seal cavity

ρ density (kg/m^3)

$\vec{u}$ velocity (m/s)

t time (s)

p pressure (Pa)

p* total pressure (Pa)

T * total temperature (K)

$\vec{F}$ external body forces (N)

$\overline{\overline{\tau}}$ viscous shear stress tensor (Pa)

μ dynamic viscosity (N s/m^2)

I unit tensor

h_t total enthalpy (J/kg)

h static enthalpy (J/kg)

λ thermal conductivity (W/m K)

S_h heat source (J/kg)

y^+ non-dimensional distance

n corrected rotation speed at the design point (rpm)

n_p non-dimensional corrected rotation speed

η isentropic efficiency

π total pressure ratio, p^*_{out}/p^*_{in}

Θ total temperature ratio, T^*_{out}/T^*_{in}

γ specific heat ratio

G corrected mass flow rate (kg/s)

G_{leak} corrected mass flow rate of seal leakage (kg/s)

Φ leakage as a percentage of the inlet mass flow rate, G_{leak}/G_{in}

SM surge margin, $(G_{op} \cdot \pi_{st})/(G_{st} \cdot \pi_{op}) - 1$

ΔG variation of corrected mass flow rate (kg/s), G–G0

Δη variation of isentropic efficiency, η–η0

Δπ variation of total pressure ratio, π–π0

ΔSM variation of surge margin, SM–SM0

ΔG_{equ} variation of equivalent corrected mass flow rate (kg/s)

$\bar{\omega}$ total pressure loss coefficient

α_2 flow angle at the stator outlet (the angle between the flow direction and the axial direction)

Subscript

in compressor inlet

out compressor outlet

ave average value of the compressor inlet and outlet

0 case of no seal leakage

DP test value of compressor performance parameter at design point

op compressor working point

st compressor stall point

frontiers in Energy Research

ORIGINAL RESEARCH
published: 16 November 2021
doi: 10.3389/fenrg.2021.784654

Research on the Hole Length Ratio of Fan-Shaped Holes in Flat Plate Film Cooling

Xun Zhou, Runxuan Qin and Le Cai*

School of Energy Science and Engineering, Harbin Institute of Technology, Harbin, China

To study the influence of different hole length ratios on the flow structure and film cooling efficiency, a calculation model of fan-shaped hole was constructed and numerically studied. The effect of different hole length ratios on the cooling efficiency under different blowing ratios was compared and analyzed. The results showed that as the blowing ratio increases, the overall average efficiency of most of the hole length ratio cases first increases and then decreases. Only in the case with a cylindrical part length/total length ratio of 0.5 did the efficiency continue to increase. When the blowing ratio is small, the spanwise average efficiency of each hole length ratio case is closer, but the flow structure and efficiency distribution are quite different. For the medium blowing ratio, the overall average efficiency of the small hole length ratio case is higher, and the efficiency decreases as the hole length ratio increases. When the cylindrical part length/total length ratio is further increased to 1, the cooling efficiency region basically converges into a spanwise narrow region. For larger blowing ratio conditions, after 10D after the hole outlet, the case with a cylindrical part length/total length of 0.5 is more efficient.

Keywords: film cooling effectiveness, fan-shaped hole, adiabatic effectiveness, heat transfer characteristics, kidney-type vortices

OPEN ACCESS

Edited by:
Xiao Liu,
Harbin Engineering University, China

Reviewed by:
Jingjun Zhong,
Shanghai Maritime University, China
Jun Li,
Xi'an Jiaotong University, China
Bai-tao An,
Chinese Academy of Sciences (CAS), China

****Correspondence:***
Xun Zhou
zhouxun@hit.edu.cn

Specialty section:
This article was submitted to Advanced Clean Fuel Technologies, a section of the journal Frontiers in Energy Research

Received: *28 September 2021*
Accepted: *21 October 2021*
Published: *16 November 2021*

Citation:
Zhou X, Qin R and Cai L (2021) Research on the Hole Length Ratio of Fan-Shaped Holes in Flat Plate Film Cooling. Front. Energy Res. 9:784654. doi: 10.3389/fenrg.2021.784654

INTRODUCTION

As the turbine inlet temperature increases, the thermal load of the turbine blades increases accordingly, and therefore, higher requirements are put forward for the cooling of the turbine. Film cooling is an important part of gas turbine external cooling. Using a flat film cooling model is very helpful for studying the flow and heat transfer characteristics of film cooling.

Li et al., 2014 used pressure-sensitive paint and particle image velocimetry technology to measure the flow field and temperature field of film cooling of cylindrical holes with composite angles of 0°, 45°, and 90°. It was found that the flow field structure changes greatly when the compound angle changes. Rogers et al., 2017 conducted an experimental study on cross-flow-supplied full-coverage film cooling for a sparse film cooling hole array and found that the adiabatic film cooling effectiveness generally increased with the streamwise position and generally increased as the blowing ratio increased. Luo et al., 2021 studied the application of film cooling to the cooling system of the leading edge of hypersonic aircraft and found that low-density coolant air has the lowest peak temperature

Abbreviations: C, cylindrical part length (mm); D, hole diameter (mm); L, total part length (mm); L_{hole}, hole length (mm); M, blowing ratio,$\rho_c u_c/\rho_\infty u_\infty$; T, temperature (K); V, velocity (m/s); x, y, z, Cartesian coordinates (mm); η, adiabatic cooling effectiveness $(T_{main} - T)/(T_{main} - T_{cool})$; ω, vorticity (s^{-1}); cool, coolant; later, spanwise averaged; total, overall averaged; main, mainstream.

compared with high-density coolant air. El-Gabry et al., 2013 used infrared radiation thermography, liquid crystal thermography, and thermocouples to measure flow field temperature and film cooling efficiency and used hotwire anemometry to measure velocity and turbulence quantities. The velocity vectors and contours at the streamwise planes showed a distinct kidney vortex, and the contours also indicated that the jet was lifted. Johnson et al., 2014 used pressure-sensitive paint technology to measure the adiabatic film cooling efficiency of a row of cylindrical holes and found that, as the density ratio increased, the adiabatic film cooling efficiency also increased. Eberly and Thole, 2014 used time-resolved digital particle image velocimetry technology to measure the flow field of a row of cylindrical film cooling holes and found Kelvin–Helmholtz breakdown in the jet-to-freestream shear layer. Laroche et al., 2021 conducted research on film cooling of flat plates with a 90F0B0 compound angle and used the particle image velocimetry technique to document the velocity field. The temperature field was acquired using the cold wire technique. In the first three rows, the film protection was shown not to be efficient. After four rows, the film builds up, leading gradually to better insulation of the wall. Jeon and Son, 2021 used computational fluid dynamics to study the simplified geometry of an integrated configuration of a ribbed channel, film hole, and mainstream passage and found that the film cooling holes located in the separated flow region of a ribbed channel showed minimum reduction and considerable enhancement in film cooling effectiveness, and internal heat transfer also improved. Tian et al., 2021 conducted a three-dimensional turbine cascade model to analyze particle trajectories at the blade leading edge under film-cooled protection. The deposition mechanism in this research was based on the particle sticking model and the particle detachment model. The numerical results indicated that most of the impact region was located at the leading edge and on the pressure side.

In addition to cylindrical film cooling holes, there are a variety of hole types used in film cooling studies. Wright et al., 2011 used pressure-sensitive paint technology to conduct experimental research on the film cooling efficiency of cylindrical holes, fan-shaped holes, and laidback fan-shaped holes and found that in all hole-type cases, as the freestream turbulence intensity increases, the film effectiveness decreases. As the blowing ratio increases, this effect decreases. Lee and Kim, 2012 carried out a numerical simulation study with a novel film-cooling hole, compared its cooling efficiency with a fan-shaped hole, and found that the novel-shaped hole shows greatly improved lateral spreading of the coolant and cooling performance in terms of the film-cooling effectiveness in comparison with the fan-shaped hole. Issakhanian et al., 2016 proposed a new oval film cooling hole and used magnetic resonance concentration technology to measure the coolant concentration in the 3D test field. The results showed that compared to the round hole, the oval hole reduces the strength of the main counter rotating vortex pair. Ragab and Wang., 2018a, Ragab and Wang., 2018b used infrared cameras and thermocouples to measure the temperature field and found that the newly incorporated fan-shaped film cooling hole had higher film cooling efficiency than cylindrical holes. Lee et al., 2021 experimentally investigated the effect of mainstream velocity on the optimization of a fan-shaped hole on a flat plate and found that the optimized hole showed a 49.3% improvement in the overall averaged film cooling effectiveness compared to the reference hole with DR = 2.0 and M = 2.0. Baek et al., 2021 numerically simulated the film cooling flow with a shaped hole with 15° forward expansion, a 35° inclination angle, and 0° and 30° compound angles with large eddy simulations. The results showed that the turbulence and mixing intensity of the forward expansion hole were weaker and lower than those of the cylindrical hole, respectively. Thus, the film cooling effectiveness of the forward expansion hole was higher. Kim et al., 2021 performed an experimental study to investigate the effects of the arrangement of fan-shaped film cooling holes and the density ratio on the heat transfer coefficient and found that, for the given fan-shaped hole parameters, the effects of the row-to-row distance and hole arrangement were not significant.

Burd et al., 1998 used hot-wire anemometry measurements to measure the average velocity and turbulence intensity of the mixing area of the coolant and free-stream flows in film cooling and found that under low free-stream turbulence conditions, pronounced differences existed in the flow field between L/D = 7.0 and 2.3. These differences became less prominent at high free-stream turbulence intensities. Lutum and Johnson, 1999 conducted an experimental study on the influence of hole length on the cooling efficiency of cylindrical film cooling holes and found that when the hole length is greater than five times the hole diameter, the cooling efficiency is basically not affected. Gritsch et al., 2005 conducted experiments on the film cooling efficiency of three fan-shaped holes with L/D = 7.5, 9.5, and 11.5, and the results showed that the average cooling efficiency of the three cases was not much different. Haydt et al., 2018 used computational fluid dynamics prediction and particle image velocimetry measurement to study the adiabatic film efficiency of 7–7–7 holes with different hole lengths. In this study, the expansion mode was maintained unchanged, and different hole lengths led to different area ratios. The research results show that a larger hole length provides higher effectiveness. Saumweber and Schulz, 2012 conducted an experimental study on the film cooling efficiency of two fan-shaped holes with L/D = 6 and 10 and found that under the small blowing ratio condition, the cooling efficiency of the long hole length case was slightly higher. However, the cooling efficiency of the long hole length case is lower at high blowing ratio conditions.

However, there have been some studies on the hole length of film cooling. In the existing research on the hole length of the fan-shaped hole, the total hole length of the film cooling hole and the area ratio and shape of the hole inlet and outlet were not fixed, which mainly reflects the influence of the change in total hole length and area ratio.

NUMERICAL SIMULATION APPROACH

In this paper, a numerical study was carried out on a flat film cooling model, which is shown in **Figure 1A**. There is only one

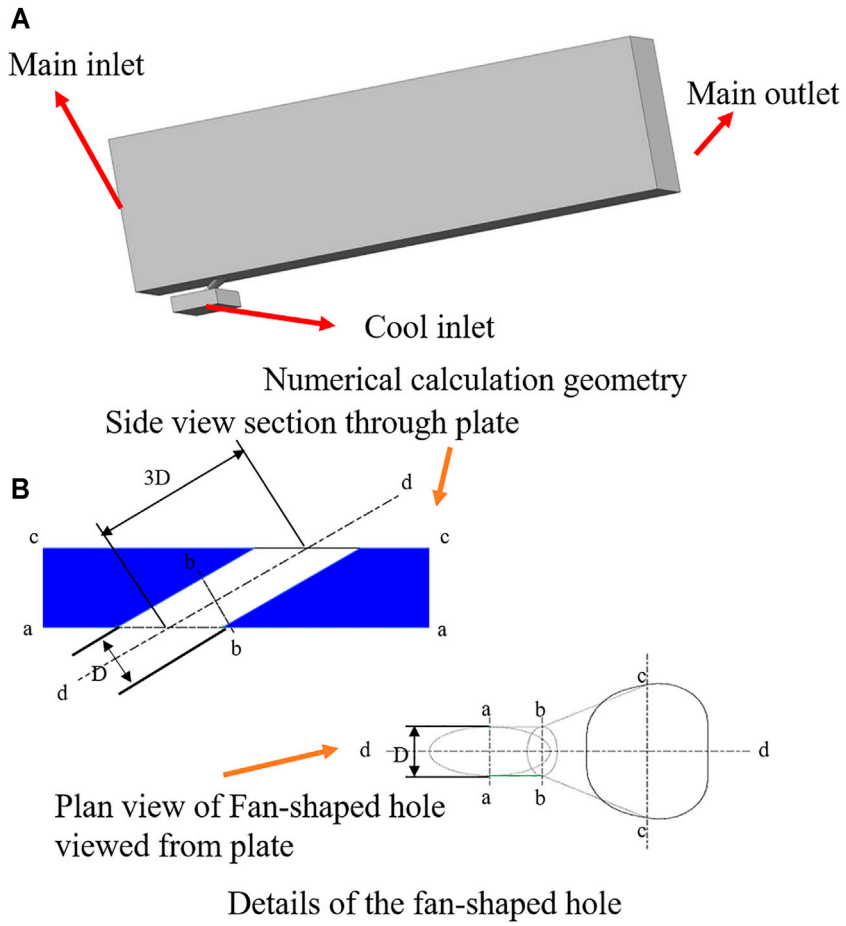

FIGURE 1 | Geometry. **(A)** Numerical calculation geometry and **(B)** details of the fan-shaped hole.

film cooling hole in the flat model, the hole diameter is 5 mm, and the hole inclination angle is 30°. The width of the plate in the spanwise direction is 12D, and the mainstream inlet is set 10D upstream of the hole. To study the long-distance effect of film cooling, the mainstream outlet is at 60D downstream of the hole. The height of the main flow domain is set to 20D to shield the cooling air from the influence of the upper wall of the main flow. The cooling air is provided by the plenum, which is the coolant inlet at one end and the other closed structure, with a width of 6D and a height of 2D. To comment on the influence of cross-flow, the angle between the cold air flow direction and mainstream flow direction is 90°. Except for the mainstream inlet, the mainstream outlet, and the coolant inlet in the domain, the rest of the walls are nonslip frictionless and adiabatic walls. The total temperature at the mainstream inlet is 540 K, the turbulence intensity is 3.6%, and the static pressure at the outlet is 101,325 Pa, while ensuring that the mainstream Mach number is 0.3. For the coolant, the inlet total temperature is 310 K, and the turbulence intensity is 3.6%, which is consistent with the conditions reported in Saumweber et al., 2003. The blowing ratio of the film cooling hole is controlled by specifying the mass flow at the coolant inlet. The working fluid under study is ideal air.

The film cooling holes studied in this research are fan-shaped holes based on the construction method in Saumweber et al., 2003, as shown in **Figure 1B**. In the study, the total hole length is 3D. Under the condition of ensuring that the inlet and outlet of the film cooling hole remain unchanged, the ratio of the hole length of the film cooling hole is controlled by adjusting the position of the interface (b–b plane in the figure) between the cylindrical part and the fan-shaped part. To ensure that the overall layout of the air film holes is a cylindrical fan-shaped structure, and considering the hole inclination angle of 30°, the adjustment space of the interface is limited to at least 1D from the wall in the axial direction of the hole. That is, the b–b plane should be located between the e plane and the f plane in the axial direction of the hole. The cylindrical part length refers to the distance between the b–b plane and the e plane in the axial direction of the hole, while the total part length refers to the distance between the e plane and the f plane in the axial direction of the hole. A total of five cases with a C/L of 0, 0.25, 0.5, 0.75, and 1 were set up. The length of the cylinder part refers to its length in the axial direction of the hole and does not include the length of the restriction section. Even if the cylindrical part length/total length ratio reaches 1, the overall

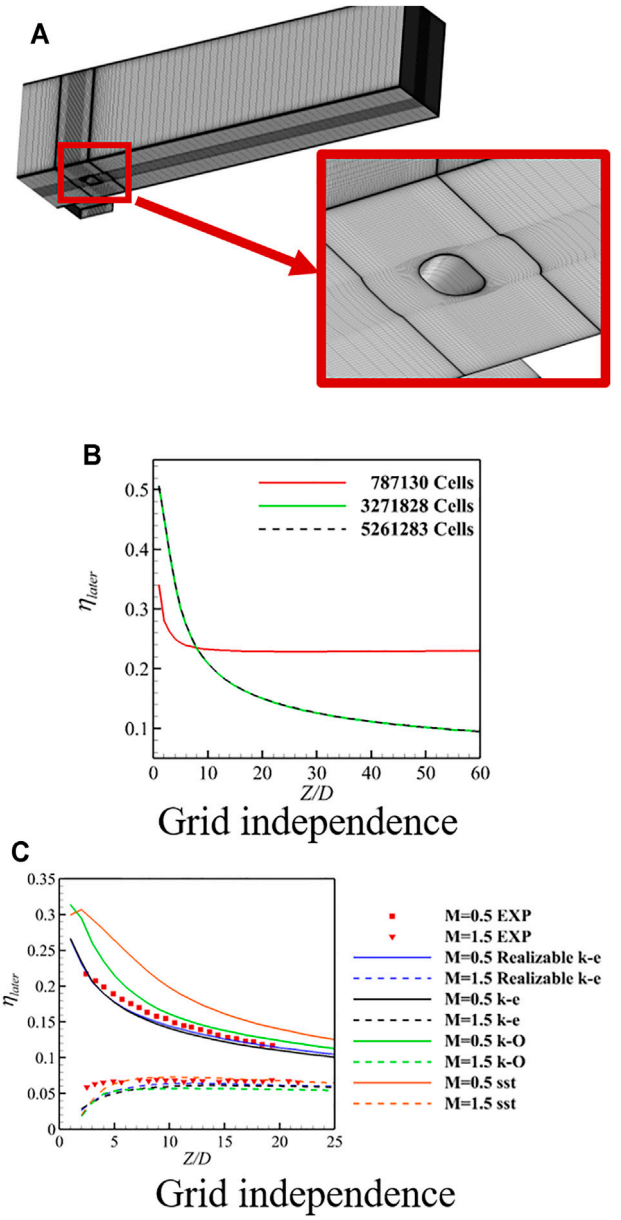

FIGURE 2 | Grid and method information. **(A)** Computational grids, **(B)** grid independence, and **(C)** numerical verification.

structure of the cylinder fan shape and the area ratio of the inlet and outlet remain unchanged. At the same time, to clarify the influence of different blowing ratios, five blowing ratios of 0.5, 1.0, 1.5, 2.0, and 2.5 are set.

The grids used in the calculation are structured grids generated by ANSYS ICEM CFD. To ensure that the value of y^+ on the wall is near 1, a surface layer is provided on all the walls. The fluid domain mesh and details are shown in **Figure 2A**. The original fan-shaped hole is set with three grids of coarse, medium, and fine meshes, with 780,000, 3.27 million, and 5.26 million grids, respectively. The distribution of the spanwise average cooling efficiency in different grid numbers along the flow direction is shown in **Figure 2B**. The difference between the predicted values of the 3.27 million and 5.26 million grids is very small. The two lines representing 3.27 million and 5.26 million in the figure basically coincide. Therefore, the medium-scale grid was selected in the following research.

The overall simulation analysis uses ANSYS Fluent software, the realizable k–e turbulence model to solve the Reynolds averaged Navier–Stokes equations, and selects the enhanced wall treatment to strengthen the simulation of the flow near the wall. The coupled solver is used to enhance the stability and convergence of the solution, and the normalized root mean square convergence criterion of the residuals is <1 F0B4 10^{-6}. In order to verify that the turbulence model selection is reasonable and the simulation method is effective, four turbulence models of standard k–e, k–o, SST, and realizable k–e are selected, and their results are verified with the experimental results in Ref. SAUMWEBER, 2003. **Figure 2C** shows the distribution of the spanwise average cooling efficiency in different turbulence models along the flow direction. When the blowing ratio is 0.5, the predictions of the adiabatic efficiency of the SST and k–o models are too high, the predicted values of the standard k–e and realizable k–e models are almost the same, but the predicted value of the realizable k–e model is closer to the experimental value. When the blowing ratio is 1.5, the predictions of various models for the vicinity of the hole outlet region are relatively low, but the predicted value of the downstream region is only slightly different from the experimental value. On the whole, the numerical results using the realizable k–e model are the closest to the experimental results, so the realizable k–e model was selected in this study as Liu et al., 2015.

RESULTS AND DISCUSSION

According to **Figure 3A**, when the blowing ratio is small, the difference between different C/L cases is smaller, but as the C/L increases, the overall cooling efficiency decreases. As the blowing ratio increases, the difference between the various C/L cases increases. When the blowing ratio increases to 2, as the C/L increases, the overall average cooling efficiency does not simply decrease but first slightly increases and then decreases. According to **Figure 3B**, the two cases with C/L = 0 and 0.25 have similar trends with the blowing ratio. The overall average efficiency continues to rise when the blowing ratio increases from 0.5 to 2 and then decreases slightly when the blowing ratio is larger. For the case with C/L = 0.75, the overall average efficiency still increases first with the increase in the blowing ratio and decreases when the blowing ratio is >2, but the decrease is greater. As C/L = 1, the overall average efficiency first increases and then decreases as the blowing ratio increases, but the inflection point blowing ratio is smaller. The most special one is the case with a C/L of 0.5. In this case, the overall average efficiency continues to increase as the blowing ratio increases. When the blowing ratio is large, the overall average efficiency is higher than the overall average efficiency in the small C/L case.

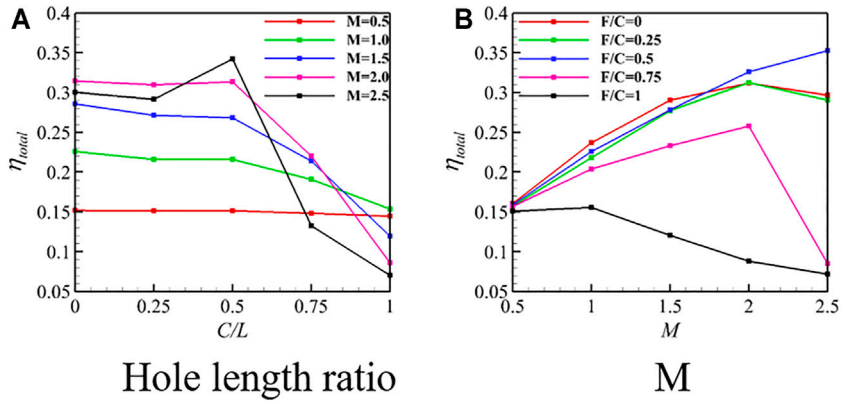

FIGURE 3 | Overall averaged efficiency. **(A)** Hole length ratio and **(B)** M.

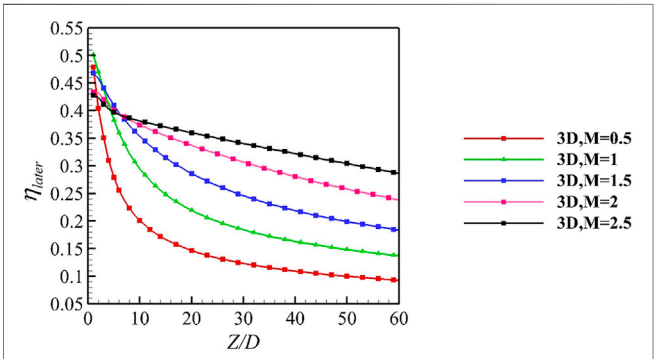

FIGURE 4 | Spanwise average efficiency in C/L = 0.5 case.

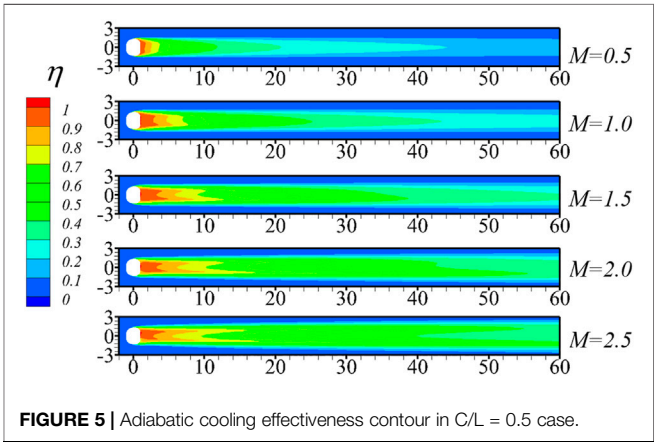

FIGURE 5 | Adiabatic cooling effectiveness contour in C/L = 0.5 case.

Effect of M on the Flow Structure and Film Cooling Efficiency

Take the basic C/L of 0.5 as an example to study the influence of different blowing ratios on the flow structure and film cooling efficiency. As shown in **Figure 4**, under different blowing ratio conditions, the spanwise average cooling efficiency basically decreases along the flow direction. Near the outlet of the film cooling hole, the spanwise average cooling efficiency of different blowing ratios is relatively small, but the spanwise average cooling efficiency first increases and then decreases as the blowing ratio increases. For the area far away from the outlet of the film cooling hole, the M = 0.5 condition has the lowest spanwise average cooling efficiency at each flow direction position. As the blowing ratio increases, the spanwise average cooling efficiency at each flow direction position increases.

As shown in **Figure 5**, when the blowing ratio is 0.5, there is a small area of high cooling efficiency at the outlet of the hole. In the downstream region, which is far away from the hole outlet, the cooling efficiency distribution degenerates to a unimodal distribution. When the blowing ratio increases to 1, the distribution of the high-efficiency zone at the hole outlet becomes a bimodal distribution, and this zone expands significantly in the flow direction. In the downstream region, the cooling efficiency also degrades to a unimodal distribution, but the cooling efficiency is higher than the cooling efficiency at the M = 0.5 condition in the same flow direction, consistent with the trend of cooling efficiency increase in each flow direction position as the blowing ratio increases from 0.5 to 1 in **Figure 4**. When the blowing ratio increases to 2, the distribution of cooling efficiency at the hole outlet is still bimodal, and the range is further expanded. In the downstream region, the cooling efficiency distribution does not degrade to a unimodal distribution but still maintains a bimodal distribution. However, even if the cooling efficiency distribution becomes a bimodal distribution, the high cooling efficiency area covers a wider area in both the flow direction and the spanwise direction than the M = 1.5 condition, indicating that the spanwise average cooling efficiency at the same flow direction is higher. When the blowing ratio is further increased to 2.5, the cooling efficiency distribution maintains a bimodal distribution, but the asymmetry becomes more obvious. In the downstream region, the cooling efficiency at the centerline decays faster along the flow direction compared to the M = 2 condition, and the green area with medium cooling efficiency appears closer to the upstream, so the cooling efficiency is lower.

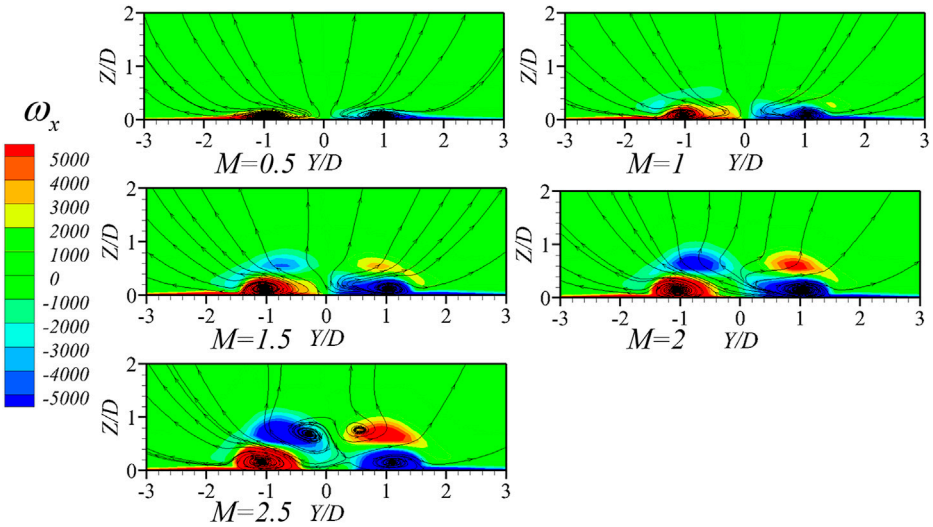

FIGURE 6 | Details of cooling air in C/L = 0.5 case. **(A)** 3D streamlines of cooling air, **(B)** streamline and adiabatic cooling effectiveness contour at d–d plane, and **(C)** X-direction vorticity contour and streamline at X/D = 2 plane.

The details of cooling air flow field are shown in **Figure 6**. According to the 3D streamline and the streamline of d–d plane in the hole, it is found that the adhesion ability of cooling air becomes worse with the increase in blowing ratio. At the same time, the velocity contour on the streamline shows the velocity of cooling air increase. As shown in **Figure 6C**, when the blowing ratio is 0.5, there is a small area with a larger X-direction vorticity at Y = ± 1D. The vorticity directions on both sides of the centerline are opposite. The two-dimensional streamline of the 2D behind the hole plane also shows the existence of vortices here, which are a pair of kidney-shaped vortices with opposite turns. For the convenience of description, they are recorded as vortex pair A. When the blowing ratio increases to 1.5, the area with high X-direction vorticity expands in the tangential direction, and the streamline entrainment scale expands in the tangential direction, reflecting the increase in the strength of vortex pair A. At the same time, a new pair of high X-direction vorticity regions are seen to appear on the upper outside of vortex pair A, but according to the distribution of the streamlines on the tangent plane, this new pair of high X-direction vorticity regions can be judged to be only a strong shear region. When the blowing ratio continues to increase, the high X direction vorticity region corresponding to vortex pair A continues to expand, mainly in the tangential direction. When the blowing ratio expands to 2.5, the high flow vorticity region corresponding to vortex pair A shrinks in the spanwise direction, and the X-direction vorticity near the wall region in the center surface decreases. At the same time, according to the two-dimensional streamline, there is a pair of small vortices in the region of Y = ± 0.3D, but on the one hand, the entrainment range is small; on the other hand, the X-direction vorticity is low. This is a pair of vortices induced by antisymmetric vortex pair A, recorded as vortex pair B. The separation of vortex pair B from the wall makes the fluid movement direction near the center surface change from upward to downward, which means that vortex pair B entrains the mainstream hot air toward the wall, which reduces the overall cooling efficiency.

According to the X-direction vorticity contour on the spanwise plane at 30D behind the hole in **Figure 7**, compared to the M = 2 condition, the strength and range of vortex pair B in the M = 2.5 condition are larger, which makes the film cooling efficiency of the near centerline area in this working condition lower. However, when the blowing ratio is 2.5, vortex pair A not only has a larger range but also has a larger spanwise spacing. It corresponds to the downstream region in **Figure 5**; compared with M = 2, the two high cooling efficiency zones in the M = 2.5 condition have a larger width and a longer spanwise spacing. As a result, the film cooling efficiency here is higher.

Effect of the Hole Length Ratio on the Flow Structure and Film Cooling Efficiency

When the blowing ratio is small, the overall average temperature difference of different C/L cases is small, but the flow field of cooling air in different C/L cases is quite different. The X-direction vorticity and streamline distribution on the spanwise plane at 2D behind the hole in the M = 0.5 condition are shown in **Figure 8**. When C/L is 0, there is a high X-direction vorticity area at Y = ± 1.2D, and the entrainment of the two-dimensional streamlines in the spanwise plane also shows that vortex pair A appears in this area. When C/L increases to 0.25, the high X-direction vorticity area at Y = ± 1.2D increases significantly, indicating that the strength and range of vortex pair A increase. At the same time, streamline entrainment is found at Y = ± 0.2D, but the entrainment range and flow direction vorticity are both small, indicating that vortex pair B exists in this area. When C/L is further increased, vortex pair A obviously converges to the center plane, especially when C/L increases to 0.5, and vortex pair A appears at Y = ± 0.9D. Vortex pair B, originally located in the center plane, basically disappears.

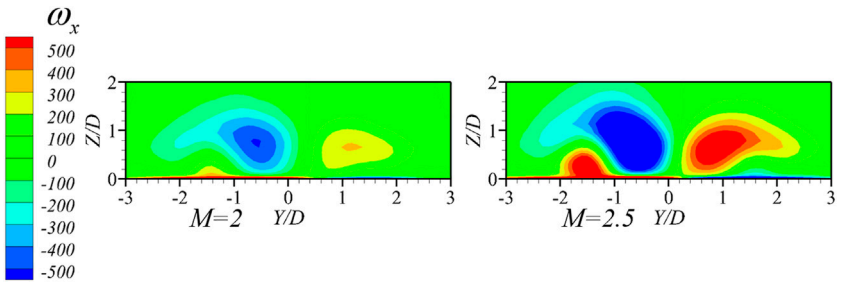

FIGURE 7 | X-direction vorticity contour at X/D = 30 plane in C/L = 0.5 case.

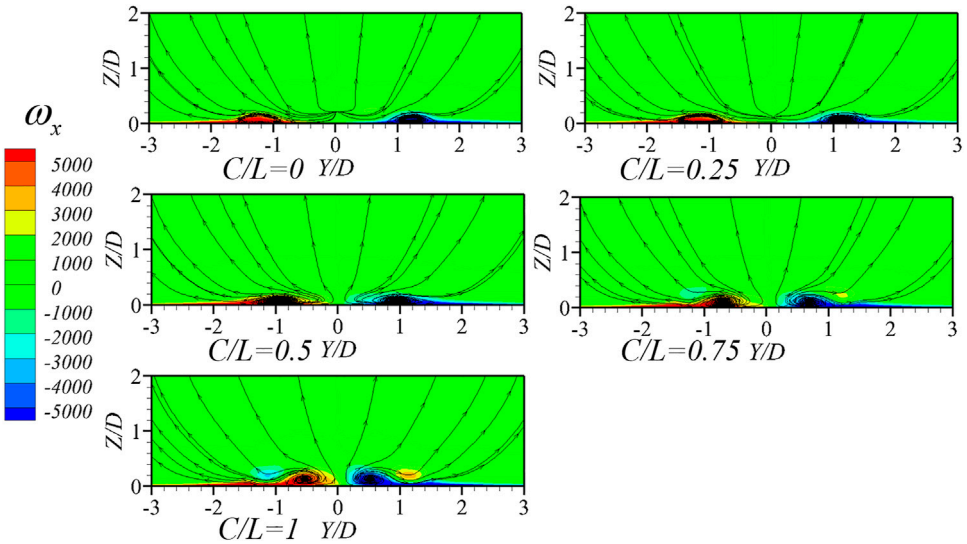

FIGURE 8 | X-direction vorticity contour and streamline at X/D = 2 plane in M = 0.5 condition.

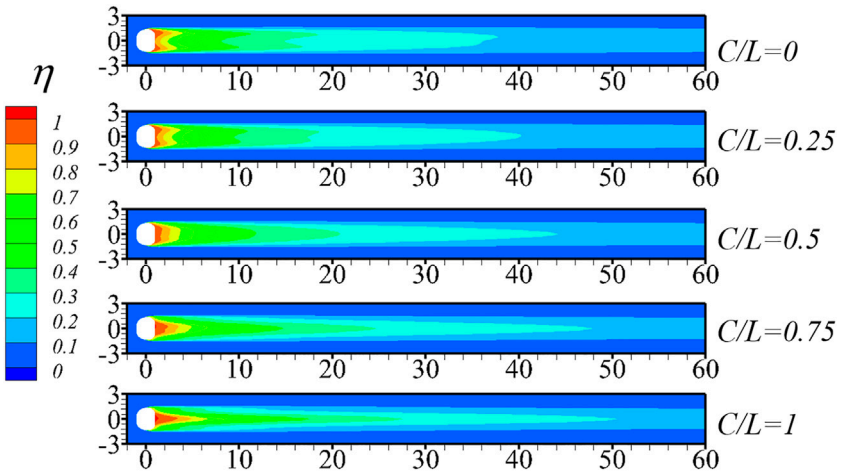

FIGURE 9 | Adiabatic cooling effectiveness contour in M = 0.5 condition.

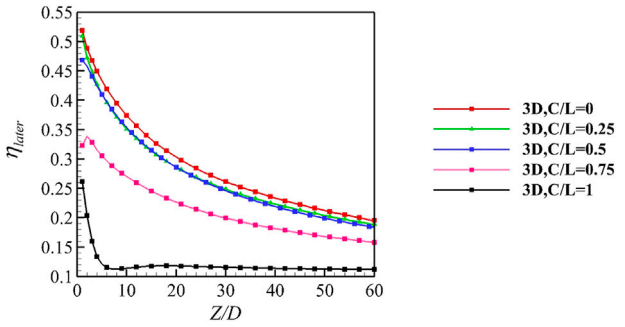

FIGURE 10 | Spanwise average efficiency in M = 1.5 condition.

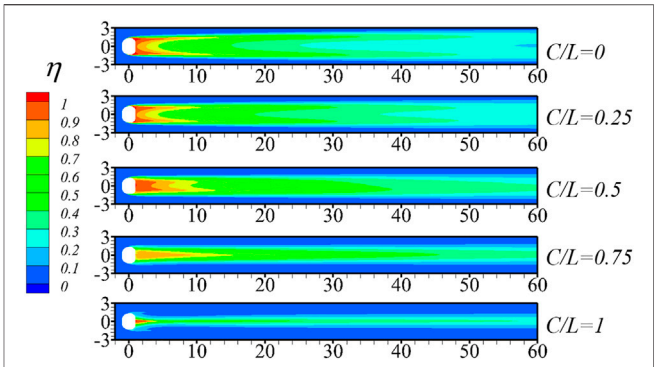

FIGURE 11 | Adiabatic cooling effectiveness contour in M = 1.5 condition.

Due to the different strengths and positions of the vortex pairs in different C/L cases, the cooling efficiency distributions in different cases are also quite different, as shown in **Figure 9**. When the C/L is relatively small, the high-efficiency area near the hole outlet region and the medium-efficiency area (light green area) near 15D behind the hole region are both obvious bimodal modes. When the C/L increases to 0.5, a new high cooling efficiency region appears in the middle of the original spanwise-separated high-efficiency bimodal, and the whole presents a spanwise continuous distribution. The medium efficiency area near 15D behind the hole region also degenerates into a unimodal distribution due to the convergence of vortex pair A. When C/L is further increased to 1, the high cooling efficiency area near the hole outlet region also degenerates into a unimodal distribution, in line with the trend in **Figure 8** that vortex pair A converges toward the center plane as C/L increases.

Under the M = 1.5 condition, the flow direction development of the spanwise average efficiency in different C/L cases is shown in **Figure 10**. On the whole, the spanwise average temperature of the three cases with C/L F0A3 0.5 has a small difference in each flow direction position, and the development trend along the flow direction is also consistent. When C/L is 0.75, the average spanwise efficiency first increases slightly and then decreases with increasing flow distance. The case with a C/L of 1 has the lowest average efficiency at each flow direction position, and the average efficiency drops rapidly from the hole outlet in the flow direction, then rises slightly, and then remains basically unchanged.

Specifically, when the blowing ratio is 1.5, the cooling efficiency contour for different C/L cases is shown in **Figure 11**. When C/L = 0, the high-efficiency area near the hole outlet region has an obvious bimodal mode, and the cooling efficiency still presents a bimodal distribution far from the hole outlet region. When the C/L ratio increases to 0.25, the cooling efficiency double peaks converge in the spanwise direction. Clearly, after 50D of the hole outlet, the original low efficiency area existing near the centerline in the C/L = 0 case disappears. However, at the same time, the cooling efficiency near Y = ± 3D is found to be lower than the cooling efficiency in the C/L = 0 case. When the C/L increases to 0.5, although the high-efficiency area near the hole outlet region still presents a bimodal distribution, the two high-efficiency peaks further converge. Especially in the area from the hole outlet to the 3D behind the hole, the two high-efficiency peaks converge into a continuous high cooling efficiency zone in the spanwise direction. In the downstream region, the cooling efficiency distribution degenerates to a unimodal distribution. When the C/L is further increased to 0.75, the overall cooling efficiency distribution is unimodal. The high cooling efficiency area near the hole outlet region covers only a small area close to the centerline in the spanwise direction and does not exist at the hole outlet in the flow direction. Overall, the distribution of high cooling efficiency area conforms to the trend in **Figure 13** that the average efficiency increases at the outlet of the hole and then decreases downstream. When the C/L increases to 1, the high cooling efficiency area shrinks rapidly after the hole outlet. The area with an obvious cooling effect occupies only a width of approximately 2.5D in the spanwise direction, which is much smaller than other C/L cases. The width of this area is recovered after a slight contraction near 10D after the hole and is basically unchanged farther downstream, in line with the trend in **Figure 10** that the average efficiency of the case is the lowest in all flow directions, and the average efficiency first drops rapidly, then rises slightly, and then remains basically unchanged.

Figure 12 shows the X-direction vorticity and streamline distribution on the spanwise plane at 2D behind the hole in the M = 1.5 condition. When C/L is 0, there is an area of high X-direction vorticity at Y = ± 1.4D, and the entrainment of the two-dimensional streamline in the spanwise plane also shows that vortex pair A appears here. At Y = ± 0.8D, which is closer to the center plane, a pair of high X-direction vorticity areas also appear at approximately 0.5D from the wall, accompanied by the entrainment of two-dimensional streamlines, which is vortex pair B. At the same time, the range of the high X-direction vorticity area and the scale of the streamline entrainment indicate that vortex pair B dominates more. When C/L increases to 0.25, the high X-direction vorticity region corresponding to vortex pair B is significantly reduced, and the streamline entrainment scale is also greatly reduced, indicating that the strength and range of

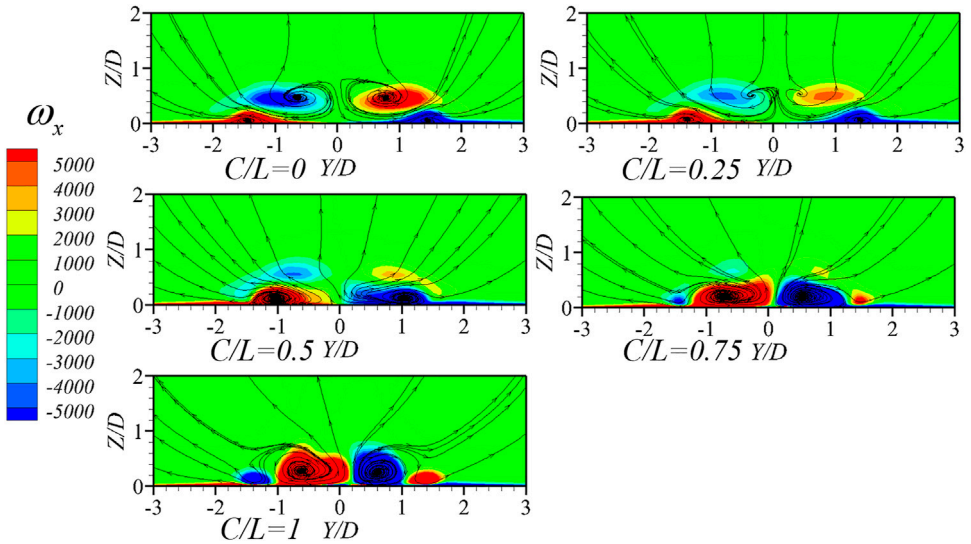

FIGURE 12 | X-direction vorticity contour and streamline at X/D = 2 plane in M = 1.5 condition.

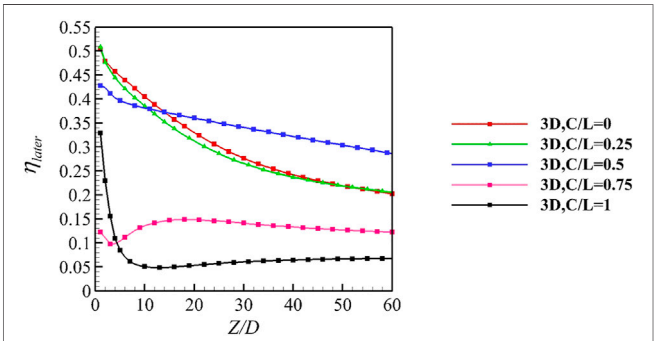

FIGURE 13 | Spanwise average efficiency in M = 2.5 condition.

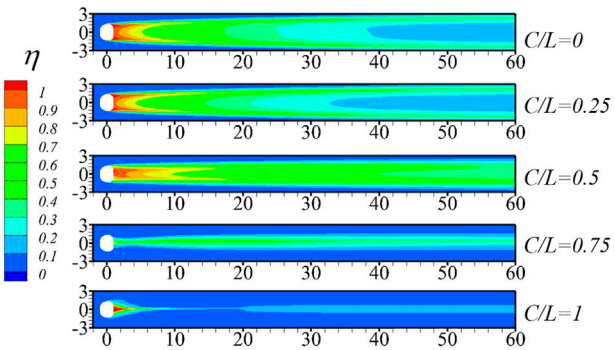

FIGURE 14 | Adiabatic cooling effectiveness contour in M = 2.5 condition.

vortex pair B is significantly reduced compared to the C/L = 0 case. This is the trend in the cooling efficiency contour, and the efficiency near the centerline of the case with a C/L of 0 is lower than the efficiency of the case with a C/L of 0.25.

When C/L increases to 0.5, vortex pair A converges to Y = ± 1D in the spanwise direction. The direction of the streamlines in the near-wall areas on both sides of the centerline is changed upwards, and the mainstream air here is not entrapped and blown toward the wall, as in the small C/L case. The convergence of vortex pair A and the change in flow direction near the centerline explain the difference in the cooling efficiency contour between this case and the small C/L case. With a further increase in C/L, vortex pair A further converges to the centerline so that the high cooling efficiency at the hole outlet is further reduced in the spanwise direction. The high X direction vorticity area of vortex pair A converges in the spanwise direction and expands to 0.5D in the tangential direction, reflecting the increase in the injection momentum of the cooling air. A new high X-direction vorticity area appears outside the high X direction vorticity area of vortex pair A, which is defined as area C. When C/L further increases to 1, vortex pair A further converges to Y = ± 0.6D in the spanwise direction, and the corresponding high X-direction vorticity area expands to 0.7D in the tangential direction. At the same time, the outer high X-direction vorticity area C also converges, and the range is slightly enlarged, indicating that the entrapment effect to the outer mainstream is further enhanced, and the cooling efficiency is greatly reduced.

When the blowing ratio is 2.5, the flow direction development of the spanwise average efficiency in different C/L cases is shown in **Figure 13**. On the whole, the difference in spanwise average efficiency between the two cases with C/L = 0 and 0.25 is smaller in each flow direction, and the development trend along the flow direction is also consistent. In the C/L = 0.5 case, the spanwise average efficiency first rises slightly and then decreases with increasing flow direction distance, but the decline is relatively gentle. In contrast, the spanwise efficiency at 10D behind the hole and downstream region exceeds the C/L = 0 and 0.25 cases. In the cases with C/L ratios of 0.75 and 1, the spanwise average efficiency

dropped rapidly from the hole outlet along the flow direction and then rebounded slightly, but the overall average efficiency was lower than that in the other cases.

The cooling efficiency contours for different C/L cases at the M = 2.5 condition are shown in **Figure 14**. When C/L is 0, the cooling efficiency distribution near the hole outlet region and the downstream region are both obvious bimodal modes. When the C/L increases to 0.25, the high cooling efficiency area is still a bimodal distribution with a larger spacing, but the efficiency in the large spanwise width zone between the two cooling peaks in the downstream region is significantly reduced. Overall, cooling efficiency distribution conforms to the trend in **Figure 13** that the spanwise averaged cooling efficiency of this case in the downstream region is slightly less than the spanwise averaged cooling efficiency of the C/L = 0 case. When C/L increases to 0.5, the bimodal high-efficiency area at the hole outlet converges into a spanwise continuous zone. In the region far away from the hole outlet, the two high cooling efficiency peaks are still discontinuous in the spanwise direction, but the spanwise separation between the two peaks is much smaller than the case with C/L ratios of 0 and 0.25. Therefore, the low cooling efficiency area between the two high cooling efficiency peaks is also smaller, which makes the spanwise average efficiency higher. When the C/L further increases to 0.75, the area with obvious cooling effect shrinks from the outlet in the spanwise direction and then slightly expands at 10D behind the hole, maintaining a unimodal distribution as a whole farther downstream and only occupying approximately 4D in the spanwise direction, conforming to the trend of average efficiency development along the flow direction in **Figure 13**. When C/L increases to 1, the high cooling efficiency area at the hole outlet is slightly expanded, but the area with an obvious cooling effect after 10D behind the hole is narrower in the spanwise direction, only occupying approximately 2.5D in the spanwise direction.

The X-direction vorticity and streamline distribution on the spanwise plane at 2D behind the hole in the M = 2.5 condition are shown in **Figure 15**. When C/L is 0, vortex pair A appears near the wall at Y = ± 1.6D. There is a vortex pair B at Y = ± 0.8D, which is farther from the wall. The range of the high X-direction vorticity area and the scale of the two-dimensional streamline entrainment indicate that vortex pair B dominates in this case. When C/L increases to 0.25, the high X-direction vorticity area corresponding to vortex pair B is found to be closer to the central plane, and the range is slightly expanded, just as shown in the cooling efficiency contour that the efficiency near the central plane is lower than C/L = 0 case. When C/L increases to 0.5, vortex pair A further converges to Y = ± 1D in the spanwise direction, while the scale of vortex pair B shrinks and is farther away from the wall. On the whole, conforming to the trend in the cooling efficiency contour, the two high cooling efficiency peaks converge into a spanwise continuous high cooling efficiency area. As C/L increases to 0.75, vortex pair A converges near the center plane, thereby changing the flow direction at the center plane so that the mainstream here will not be entrained to the wall. The expansion of the high X-direction vorticity area and the increase in the entrainment area of the streamline indicate that the range and strength of vortex pair A have been further increased so that its entrapment effect on the outer mainstream is also further increased so that the cooling efficiency of the outer region is reduced. When C/L increases to 1, the vortex at area C also further increases, which, in contrast, makes the entrainment range of vortex pair A mainstream decrease, which is in line with the trend of increasing cooling efficiency at this flow position.

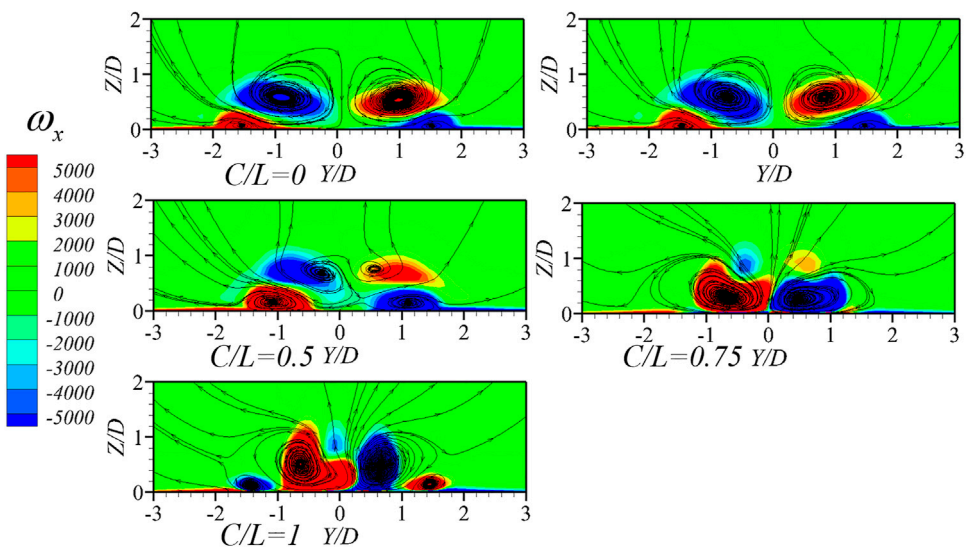

FIGURE 15 | X-direction vorticity contour and streamline at X/D = 2 plane in M = 2.5 condition.

CONCLUSION

The effect of different hole length ratios on cooling efficiency under different blowing ratios was studied by numerical methods. The following were observed.

1) As the blowing ratio increased from small (blow ratio = 0.5) to medium (blow ratio = 1.5), the overall average efficiency of most cylindrical part length/total length ratio cases increased; only in the case with a cylindrical part length/total length ratio of 1 did the overall average efficiency first increase and then decrease. When the blowing ratio was further increased to a larger condition (blow ratio = 2.5), the overall average efficiency continued to increase in only the case with a cylindrical part length/total length ratio of 0.5.
2) When the blowing ratio was small, the spanwise average efficiency of each cylindrical part length/total length ratio case was closer, but the flow structure and efficiency distribution were quite different. As the cylindrical part length/total length ratio increased, the antisymmetric kidney-shaped vortices converged toward the center plane, and the two high cooling efficiency regions at the hole outlet also converged toward the center plane. When the cylindrical part length/total length ratio reached 0.75, the kidney-shaped vortex pair basically converged to the center surface, and the high cooling efficiency area also degenerated into a unimodal distribution;
3) For the medium blowing ratio, the overall average efficiency of the small cylindrical part length/total length ratio case was higher, and the cooling efficiency decreased as the cylindrical part length/total length ratio increased. As the cylindrical part length/total length ratio increased to 0.5, the bimodal distribution separated in the spanwise direction near the hole outlet converged into a continuous bimodal distribution in the spanwise direction. When the cylindrical part length/total length ratio was further increased to 1, the cooling efficiency region basically converges into a spanwise narrow region;
4) For larger blowing ratio conditions, near the hole outlet region, the cooling efficiency of the small cylindrical part length/total length ratio case was higher. As the cylindrical part length/total length ratio increased, the efficiency decreased. When the cylindrical part length/total length ratio increased to 0.75, the cooling efficiency region basically converged into a spanwise narrow region. However, when the cylindrical part length/total length ratio increased to 1, the entrainment of the kidney-shaped vortex to the outer mainstream was restricted, and the average efficiency of the expansion rebounded slightly. After 10D after the hole outlet, the case with a cylindrical part length/total length of 0.5 is more efficient.

DATA AVAILABILITY STATEMENT

The raw data supporting the conclusions of this article will be made available by the authors, without undue reservation.

AUTHOR CONTRIBUTIONS

XZ is responsible for the overall guidance, RQ is responsible for the main calculation and analysis, and LC is responsible for the technical guidance.

ACKNOWLEDGMENTS

The authors acknowledge the financial support provided by the National Science and Technology Major Project of China (2017-III-0009-0035).

REFERENCES

Baek, S. I., Ryu, J., and Ahn, J. (2021). Large Eddy Simulation of Film Cooling with Forward Expansion Hole: Comparative Study with LES and RANS Simulations. *Energies* 14, 2063. doi:10.3390/en14082063

Burd, S. W., Kaszeta, R. W., and Simon, T. W. (1998). *Measurements in Film Cooling Flows: Hole L/D and Turbulence Intensity Effects.*

Eberly, M. K., and Thole, K. A. (2014). Time-Resolved Film-Cooling Flows at High and Low Density Ratios. *J. Turbomach.* 136. doi:10.1115/1.4025574

El-Gabry, L. A., Thurman, D. R., Poinsatte, P. E., and Heidmann, J. D. (2013). Detailed Velocity and Turbulence Measurements in an Inclined Large-Scale Film Cooling Array. *J. Turbomach.* 135. doi:10.1115/1.4023347

Gritsch, M., Colban, W., Schär, H., and Döbbeling, K. (2005). Effect of Hole Geometry on the Thermal Performance of Fan-Shaped Film Cooling Holes. *J. Turbomach.* 127, 718–725. doi:10.1115/1.2019315

Haydt, S., Lynch, S., and Lewis, S. (2018). The Effect of Area Ratio Change *via* Increased Hole Length for Shaped Film Cooling Holes with Constant Expansion Angles. *J. Turbomach.* 140. doi:10.1115/1.4038871

Issakhanian, E., Elkins, C. J., and Eaton, J. K. (2016). Film Cooling Effectiveness Improvements Using a Nondiffusing Oval Hole. *J. Turbomach.* 138. doi:10.1115/1.4032045

Jeon, S., and Son, C. (2021). Comparative Numerical Study of the Influence of Film Hole Location of Ribbed Cooling Channel on Internal and External Heat Transfer. *Energies* 14, 4689. doi:10.3390/en14154689

Johnson, B., Tian, W., Zhang, K., and Hu, H. (2014). An Experimental Study of Density Ratio Effects on the Film Cooling Injection from Discrete Holes by Using PIV and PSP Techniques. *Int. J. Heat Mass Transfer* 76, 337–349. doi:10.1016/j.ijheatmasstransfer.2014.04.028

Kim, Y. S., Jeong, J. Y., Kwak, J. S., and Chung, H. (2021). The Effects of Hole Arrangement and Density Ratio on the Heat Transfer Coefficient Augmentation of Fan-Shaped Film Cooling Holes. *Energies* 14, 186. doi:10.3390/en14010186

Laroche, E., Donjat, D., and Reulet, P. (2021). A Combined Experimental and Numerical Characterization of the Flowfield and Heat Transfer Around a Multiperforated Plate with Compound Angle Injection. *Energies* 14. doi:10.3390/en14030613

Lee, K.-D., and Kim, K.-Y. (2012). Performance Evaluation of a Novel Film-Cooling Hole. *J. Heat Transfer* 134. doi:10.1115/1.4006752

Lee, S. I., Jung, J. Y., Song, Y. J., and Kwak, J. S. (2021). Effect of Mainstream Velocity on the Optimization of a Fan-Shaped Film-Cooling Hole on a Flat Plate. *Energies* 14, 3573. doi:10.3390/en14123573

Li, X., Qin, Y., Ren, J., and Jiang, H. (2014). Algebraic Anisotropic Turbulence Modeling of Compound Angled Film Cooling Validated by Particle Image Velocimetry and Pressure Sensitive Paint Measurements. *J. Heat Transfer* 136. doi:10.1115/1.4025411

Liu, C.-L., Liu, J.-L., Zhu, H.-R., Wu, A.-s., He, Y.-H., and Zhou, Z.-X. (2015). Film Cooling Sensitivity of Laidback Fanshape Holes to Variations in Exit Configuration and Mainstream Turbulence Intensity. *Int. J. Heat Mass Transfer* 89, 1141–1154. doi:10.1016/j.ijheatmasstransfer.2015.06.019

Luo, S., Miao, Z., Liu, J., Song, J., Xi, W., and Liu, C. (2021). Effects of Coolants of Double Layer Transpiration Cooling System in the Leading Edge of a Hypersonic Vehicle. *Front. Energ. Res.* 9. doi:10.3389/fenrg.2021.756820

Lutum, E., and Johnson, B. V. (1999). *Influence of the Hole Length-To-Diameter Ratio on Film Cooling with Cylindrical Holes*.

Ragab, R., and Wang, T. (2018a). An Experimental Study of Mist/Air Film Cooling with Fan-Shaped Holes on an Extended Flat Plate—Part 1: Heat Transfer. *J. Heat Transfer* 140. doi:10.1115/1.4037641

Ragab, R., and Wang, T. (2018b). An Experimental Study of Mist/Air Film Cooling with Fan-Shaped Holes on an Extended Flat Plate—Part II: Two-phase Flow Measurements and Droplet Dynamics. *J. Heat Transfer* 140. doi:10.1115/1.4037642

Rogers, N., Ren, Z., Buzzard, W., Sweeney, B., Tinker, N., Ligrani, P., et al. (2017). Effects of Double Wall Cooling Configuration and Conditions on Performance of Full-Coverage Effusion Cooling. *J. Turbomach.* 139. doi:10.1115/1.4035277

Saumweber, C., and Schulz, A. (2012). Effect of Geometry Variations on the Cooling Performance of Fan-Shaped Cooling Holes. *J. Turbomach.* 134. doi:10.1115/1.4006290

Saumweber, C., Schulz, A., and Wittig, S. (2003). Free-stream Turbulence Effects on Film Cooling with Shaped Holes. *J. Turbomach.* 125, 65–73. doi:10.1115/1.1515336

Tian, K., Tang, Z., Wang, J., Vujanović, M., Zeng, M., and Wang, Q. (2021). Numerical Investigations of Film Cooling and Particle Impact on the Blade Leading Edge. *Energies* 14, 1102. doi:10.3390/en14041102

Wright, L. M., Mcclain, S. T., and Clemenson, M. D. (2011). Effect of Density Ratio on Flat Plate Film Cooling with Shaped Holes Using PSP. *J. Turbomach.* 133. doi:10.1115/1.4002988

Conflict of Interest: The authors declare that the research was conducted in the absence of any commercial or financial relationships that could be construed as a potential conflict of interest.

frontiers in Energy Research

ORIGINAL RESEARCH
published: 17 November 2021
doi: 10.3389/fenrg.2021.789246

Numerical Study on the Biomimetic Trailing Edge of a Turbine Blade Under a Wide Range of Outlet Mach Numbers

Fengbo Wen[1]*, *Yuxi Luo*[1], *Shuai Wang*[2], *Songtao Wang*[1] and *Zhongqi Wang*[1]

[1]School of Energy Science and Engineering, Harbin Institute of Technology, Harbin, China, [2]The 705 Research Institute of China Shipbuilding Industry Corporation, Xi'an, China

This study was carried out to investigate the loss mechanism of a blade with a harbor seal whisker structure on the trailing edge under different Mach numbers. The loss of high-pressure turbine blades with four different trailing edge geometries, including a prototype, an elliptical trailing edge (ETE), a sinusoidal trailing edge (STE), and a biomimetic trailing edge (BTE) at Mach numbers of 0.38–1.21 is studied. The delayed detached-eddy simulation method is used to predict the detailed flow of the four cascades. The result shows that, when the Mach number is less than 0.9, the BTE can effectively reduce the energy loss coefficient compared with the other three cases. As the Mach number increases, the three-dimensional characteristics of the wake behind the BTE weaken. The energy loss coefficient of the blade with the BTE is close to that of the blade with the ETE and STE when the Mach number is greater than 0.9. Besides this, by controlling the wake, the BTE can effectively suppress the dynamic movement of shock waves in the cascade at high Mach numbers.

Keywords: biomimetic trailing edge, turbine blade, Mach number, energy loss, shock wave

OPEN ACCESS

Edited by:
Lipo Wang,
Shanghai Jiao Tong University, China

Reviewed by:
Xiaoqing Qiang,
Shanghai Jiao Tong University, China
Qiang Wang,
North University of China, China
Bin Jiang,
Harbin Engineering University, China

***Correspondence:**
Fengbo Wen
fengbo@hit.edu.cn

Specialty section:
This article was submitted to Advanced Clean Fuel Technologies, a section of the journal Frontiers in Energy Research

Received: *04 October 2021*
Accepted: *19 October 2021*
Published: *17 November 2021*

Citation:
Wen F, Luo Y, Wang S, Wang S and Wang Z (2021) Numerical Study on the Biomimetic Trailing Edge of a Turbine Blade Under a Wide Range of Outlet Mach Numbers. Front. Energy Res. 9:789246. doi: 10.3389/fenrg.2021.789246

INTRODUCTION

Due to the wide application of modern gas turbines, such as power generation, aviation, and in the oil and gas industries, gas turbines are designed to meet different working conditions. As a type of continuous working equipment, the loss reduction of the gas turbine can save energy, and the blade profile optimization is an efficient way to reduce energy loss (Hamakhan and Korakianitis, 2010; Korakianitis et al., 2012; Zhang et al., 2012). For the gas turbine, the blade profile loss consists of boundary layer loss, shock loss, and trailing edge loss due to the mixing processes (Denton, 1993), and trailing edge loss accounts for one third of the total loss in subsonic flow (Mee et al., 1990). The unsteady motion of the vortex shedding from the trailing edge contributes significantly to the wake mixing loss (Lin et al., 2017a), acoustic resonances, and structural vibrations.

The flow of the turbine trailing edge is considered to be a steady process for a long time. With the introduction of flow visualizations, the consistent structure of the turbine trailing edge flow, known as the von Karman vortex street, has been revealed (Sieverding and Manna, 2020). Han and Cox (Han and Cox, 1982) use the kerosene smoke to visualize the three-dimensional structure of the vortices shedding from the turbine trailing edge. The holographic interferometric density measurement technique was adopted by Sieverding et al. (2003) to show the vortices shedding from a high-pressure turbine vane. The base pressure of the trailing edge is measured with pneumatic pressure taps and fast-response sensors. The results reveal the connection between the formation length of the trailing edge vortices and the base pressure coefficient. In the aspect of

numerical simulation, various numerical methods are used to study the wakes of turbine blades. Léonard et al. (2010) compare the ability of Reynolds-averaged Navier–Stokes (RANS), unsteady RANS (URANS), and large eddy simulation (LES) methods to simulate a turbine blade at a high subsonic outlet Mach number. They show that the RANS method cannot depict the unsteady flow of the wake. Although the URANS method can predict the mean trailing edge wake to a certain extent, only the LES method can provide a detailed view of the wake. As a hybrid method, the delayed-detached eddy simulation (DDES) method can accurately predict the wake flow while reducing the computational cost in the boundary layer. Lin et al. (2017b) use a DDES code with a low-dissipation numerical scheme to simulate the flow of a high-pressure turbine stage. They explain the length characteristics of the wake vortices and reveal the transportation of the vortices.

The vortex shedding from the turbine trailing edge causes a high shear rate in the wake, which leads to high entropy generation in the wake. Therefore, controlling the shedding of vortices is an effective way to reduce wake loss. Denton and Xu (Denton and Xu, 1990) find that the base pressure of the trailing edge is closely related to vortices shedding and trailing edge loss, and increasing the base pressure can effectively reduce the loss in the wake. Motallebi and Norbury (Motallebi and Norbury, 1981) experimentally study the effects of base bleed on vortex shedding and base pressure of the blunt trailing edge. Their results show that a small amount of bleed air can shift the motion of the vortices and result in a substantial increase in base pressure. Furthermore, a larger amount of bleed air makes the vortices' motion disappear. Raffel and Kost (Raffel and Kost, 1998) study the coolant ejection of the turbine trailing edge at Ma from 1.01 to 1.45. The results show that the coolant can change the shock system and modify the vortex shedding frequency. Bernardini et al. (2013) study the effect of trailing edge pulsating coolant ejection under supersonic flow. They conclude that the change in the value of the coolant, not the absolute value, affects the shape of the vortex. However, Xu and Denton (Xu and Denton, 1988) point out that, although the introduction of coolant ejection can increase the base pressure, additional losses are introduced by the coolant ejection. On the other hand, elliptic trailing is found to be able to delay the separation of the boundary layer and reduce the loss caused by vortex shedding (El-Gendi et al., 2013). El-Gendi et al. (2010) use the equidistant microtubes that connect the suction side and pressure side at the beginning of the trailing edge to control the wake. They find that the microtubes can reduce the blade profile loss by 3%. Wang et al. (2019) study the effect of the degree of suction-side convexity on the vortex shedding. Through the local spatial-temporal stability analyses, they find that the wake velocity profiles in the near-wake region are more unstable for a fuller suction boundary layer. Besides this, a more convex curvature can suppress the vortex shedding, and the trailing edge loss was lower. Inspired by the whisker of the harbor seal, the authors propose a bionic method to control the vortex shedding at the trailing edge of turbine blades (Luo et al., 2019).

Blind seals and seals living in turbid waters can track their prey by sensing the wakes left by their prey (Dehnhardt et al., 2001; Schulte-Pelkum et al., 2007; Wieskotten et al., 2010). The unique whisker structure of the seal gives the seal the ability to sense the wake. Ginter et al. (2012) provide a detailed description of a harbor seal's whisker structure. Beem and Triantafyllou (2015) experimentally study the vibration of the harbor seal's whisker model under uniform flow and upstream wake. Their results reveal that the whisker of the harbor seals hardly vibrates under uniform flow. While under the upstream wake, the whisker behaves as unique vibrations. Hanke et al. (2010) use experimental and numerical methods to study the wake of a harbor seal's whisker under uniform flow. They indicate that the structure of the harbor seal's whiskers can break the coherence structure of Karman vortices and reduce the vortex-induced vibrations. In the authors' previous research (Luo et al., 2019), the method of using the harbor seal structure to construct a bionic blade trailing edge is proposed. It is proved by DDES numerical simulation that the biomimetic trailing edge (BTE) suppresses the formation of a Karman vortex at the trailing edge when the isentropic exit Mach number is 0.79 and generates small spanwise vortices, which reduces the wake loss.

Actually, at different exit Mach numbers, the patterns of trailing edge vortex shedding are very different. Carscallen et al. (1996) use the ultrashort Schlieren photographs to investigate the wake of a transonic turbine vane at various Ma. They find that the shedding of the von Karman vortex street was intermittent when $Ma < 0.7$ and continuous when $0.7 < Ma < 1.0$. When $Ma > 1.0$, the von Karman vortex street was found to be transient between different shedding patterns. Melzer and Pullan (Melzer, Pullan) study the influence of different blade trailing edge geometries on loss at exit Ma from 0.4 to 0.97. Their experimental results show that the suppression of vortex shedding under transonic conditions can effectively reduce loss. Graham and Kost (Graham and Kost, 1979) measure the loss of two high-turning turbine blades at the outlet Ma from 0.7 to 1.4. Their results show that the loss first increases, then decreases, and then increases with the outlet Ma. Sieverding et al. (1978) measure the performance of various suction-side curvatures of the turbine blade. Their results also show that there is a peak and a valley in the area where the outlet Ma is close to 1.

Although it is proved that the bionic trailing edge can suppress the Karman vortex and reduce wake loss significantly at an exit Mach number of 0.79 in (Luo et al., 2019), as mentioned above, different exit Mach numbers have a great influence on the form of trailing edge vortex for conventional blades, so the important purpose of this paper is to study the influence of the BTE on the wake vortex and the ability to control wake loss under different Mach number conditions (0.38–1.21), especially after the Mach number is greater than 1, and the influence of BTE on the shockwave system and related loss. This study provides an important reference for the application of BTE in turbines under different working conditions.

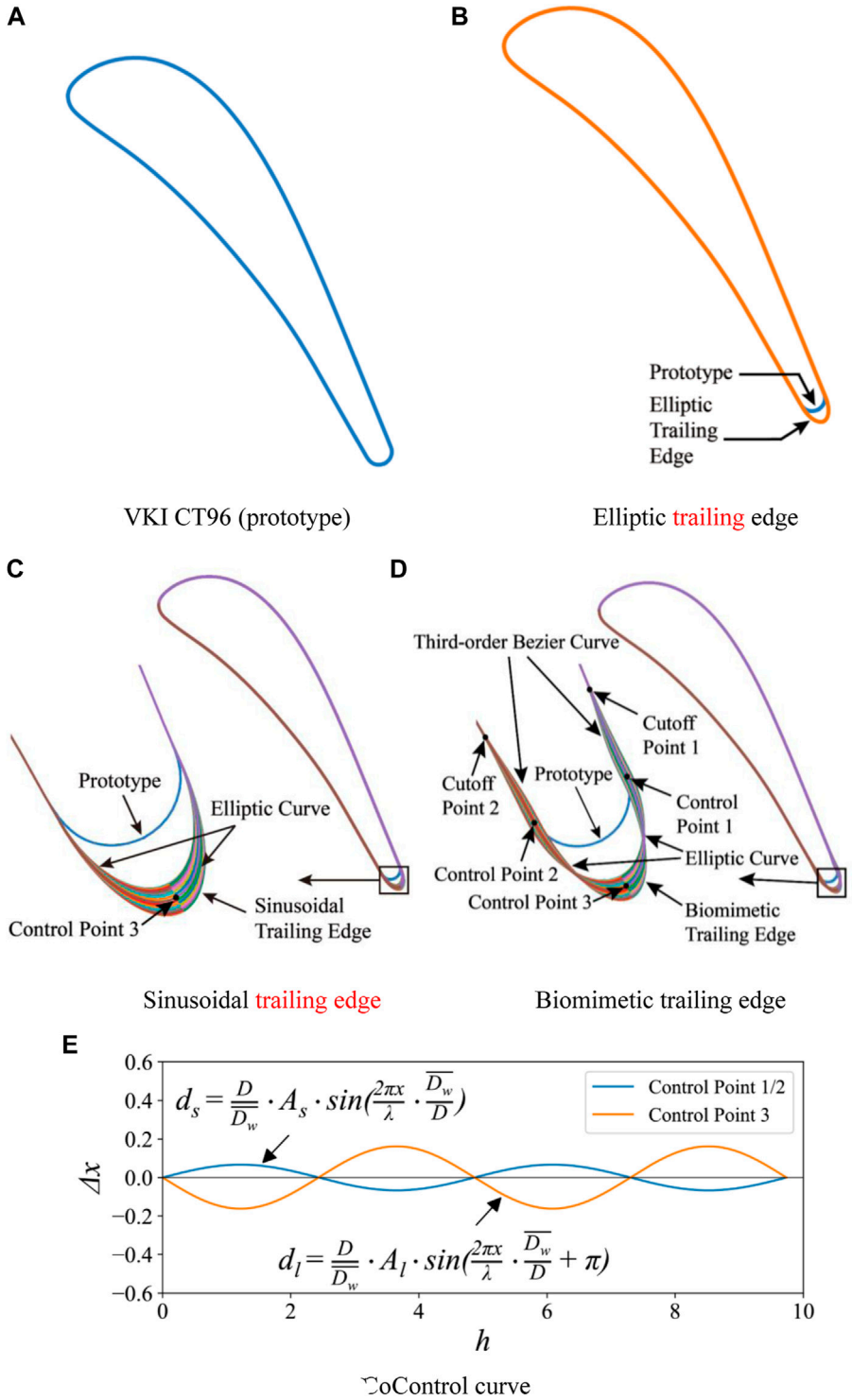

FIGURE 1 | The profiles of the four cases and the generation method of the biomimetic blade. **(A)** VKI CT96 (prototype) **(B)** Elliptic trailing edge. **(C)** Sinusoidal trailing edge **(D)** Biomimetic trailing edge. **(E)** Control curve.

TABLE 1 | VKI CT96 cascade characteristics (Sieverding et al., 2003).

Chord length c	140 mm
Axial chord length c_{ax}/c	0.656
Pitch to chord ratio g/c	0.696
Blade height h	25.528 mm
Trailing edge thickness to chord ratio D/c	0.0531
Trailing edge wedge angle	δ_{te}7.5°
Stagger angle θ	−49.83°

GEOMETRIC MODELS AND NUMERICAL METHODS

Geometric Models

Four turbine blades with different trailing edge geometries are studied in this paper. The prototype blade is a high-pressure turbine guide vane, called VKI CT96 (Sieverding et al., 2003) as shown in **Figure 1A**. The detailed parameters of the VKI CT96 cascade are listed in **Table 1**. The biomimetic blade is designed based on the VKI CT96 profile. Because the biomimetic blade contains the characteristics of ellipse and sine, the profiles with the elliptical trailing edge (ETE) and sinusoidal trailing edge (STE) are also studied in this research as shown in **Figures 1B,C**.

The seal whisker parameters provided by Hanke et al. (2010) are used to generate the biomimetic blade. There are two main features of the whisker: The first is that the cross-section of the beard is elliptical, and the second is that both the major and minor axes of the cross-section ellipse varies sinusoidally along the spanwise direction; the average ratio of major and minor axes is 2:1. Therefore, the ellipse with a 2:1 major and minor axis ratio is selected as the base trailing edge to generate the three-dimensional BTE. The profile of the biomimetic blade is shown in **Figure 1D**. To maintain the thickness of the blade trailing edge, the chord length of the biomimetic blade is slightly extended to achieve the first feature. Besides this, two minor axis endpoints (control points 1 and 2) and one major axis endpoint (control point 3) were selected to change sinusoidally in the spanwise direction. The sine curve corresponding to the three control points is shown in **Figure 1E**. The sine curve expression at control points 1 and 2 is

$$d_s = \frac{D}{\overline{D_w}} \cdot A_s \cdot sin\left(\frac{2\pi x}{\lambda} \cdot \frac{\overline{D_w}}{D}\right), \tag{1}$$

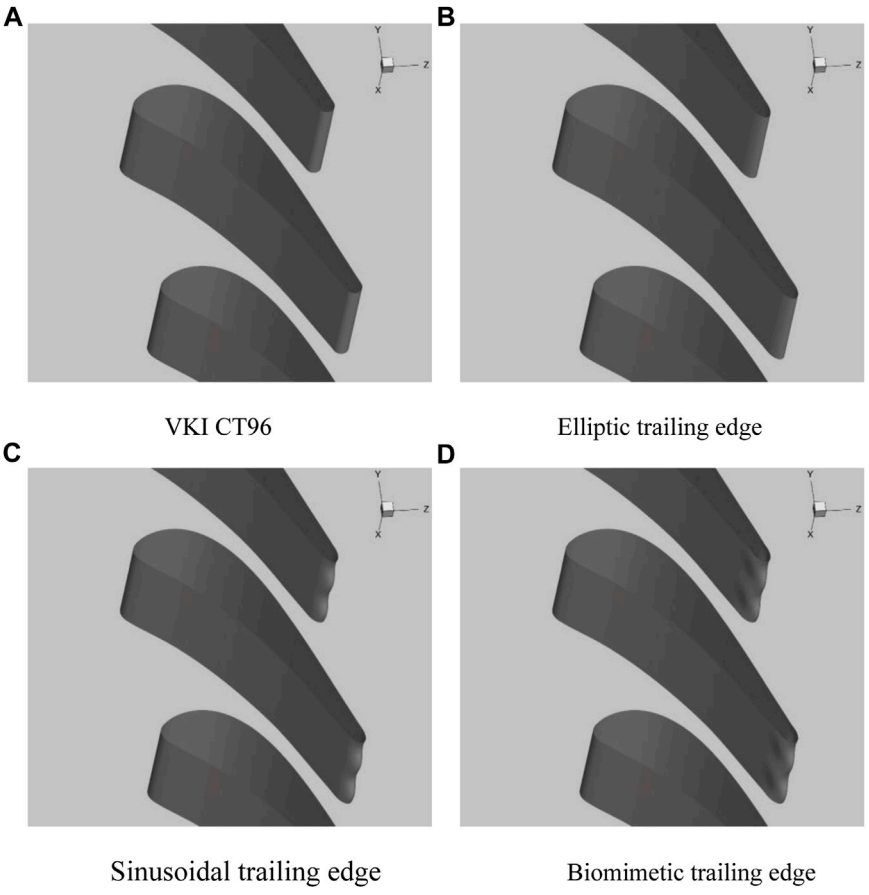

FIGURE 2 | The three-dimensional view of the four cascades. **(A)** VKI CT96 **(B)** Elliptic trailing edge. **(C)** Sinusoidal trailing edge **(D)** Biomimetic trailing edge.

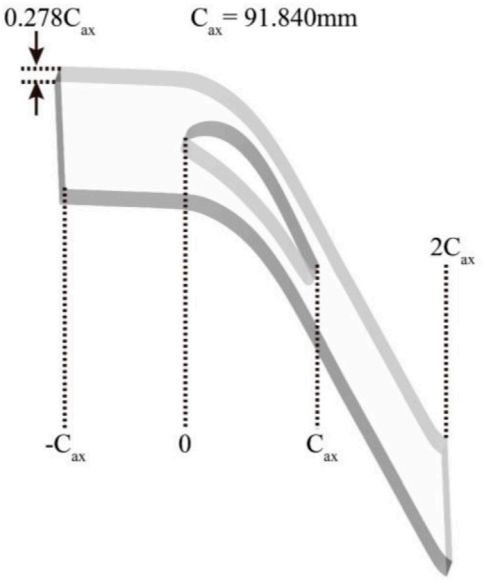

FIGURE 3 | The computational domain.

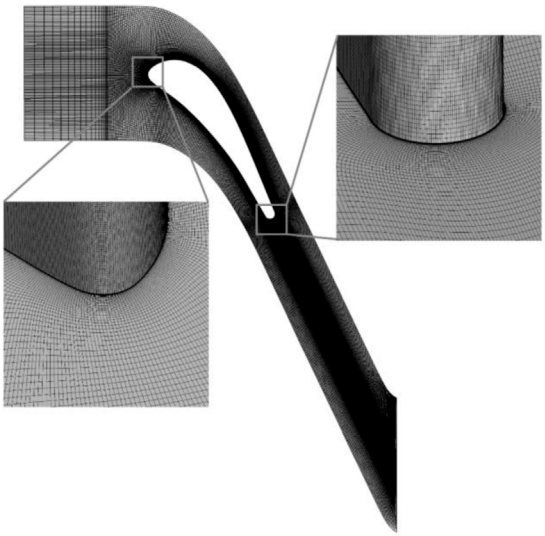

FIGURE 4 | Computational mesh and details at the leading and trailing edges.

where d_s is the difference value of a half minor axis between the BTE and base ellipse at each layer, D is the trailing edge thickness of vane or blade, $\overline{D_w}$ is the mean length of the minor axis of the harbor seal whisker, A_s is the amplitude of the sine curve of the whisker at the minor axis, and λ is the wavelength of the major sine curve. The sine curve expression at control point 3 is

$$d_l = \frac{D}{\overline{D_w}} \cdot A_l \cdot sin\left(\frac{2\pi x}{\lambda} \cdot \frac{\overline{D_w}}{D} + \pi\right), \tag{2}$$

where d_l is the difference value of a half major axis between the BTE and base ellipse at each layer, and A_l is the amplitude of the sine curve of the whisker at the major axis.

The part of the trailing edge is separated from cutoff points 1 and 2, and the blade profile before the cutoff points is unchanged. The third-order Bezier curve is used to connect cutoff points 1 and 2 with control points 1 and 2. Besides this, the elliptical curve is used to connect control points 1 and 2 with control point 3. The biomimetic blade is formed by stacking the profile lines of each layer in the spanwise direction. For the sinusoidal blade, only control point 3 changes sinusoidally in the spanwise direction. The three-dimensional view of the four cascades is shown in **Figure 2**.

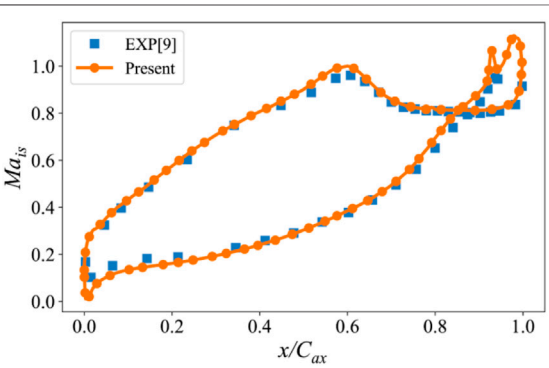

FIGURE 5 | Time-averaged isentropic Mach number.

TABLE 2 | The flow conditions in the experiment (Sieverding et al., 2003).

Inlet total temperature	280 K
Inlet total pressure	140,000 Pa
Inlet turbulence intensity	1%
Outlet isentropic Mach number $Ma_{2,is}$	0.79
Reynolds number Re	2.8×10^6

Numerical Methods

The computational domain is shown in **Figure 3**. The inlet is at one axial chord length upstream of the blade leading edge. The outlet is at one axial chord length downstream of the blade trailing edge. The height of the computational domain is 0.278 times the axial chord length, which is one period of the biomimetic blade. A total of 5.17 million cells are used to discretize this computational domain and the mesh in the region of the leading edge, trailing edge, and the wake are refined as shown in **Figure 4**.

The boundary conditions used in the current simulation are consistent with the experiment of Sieverding et al. (2003) as shown in **Table 2**. The total temperature and total pressure are given at the inlet of the computational domain. The suction and pressure sides of the blade are set as adiabatic and nonslip walls. The pitchwise and spanwise boundaries of

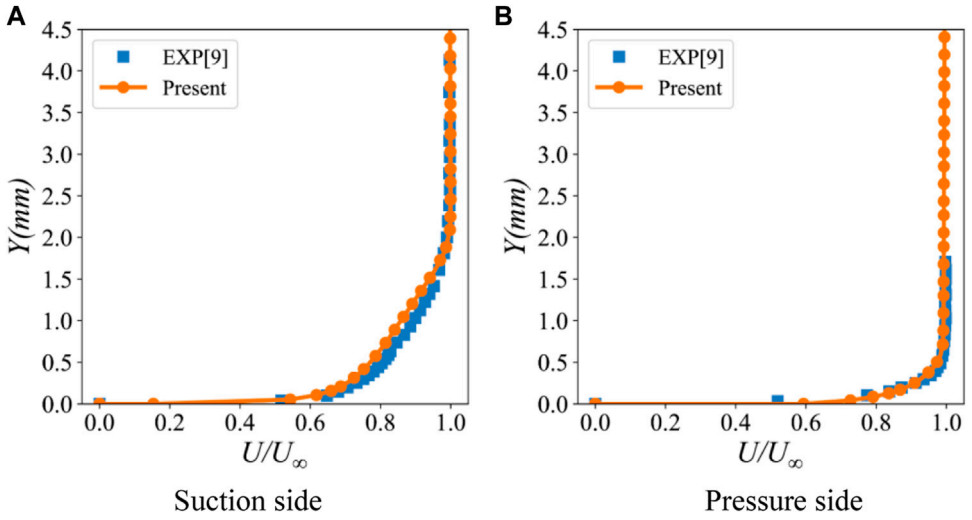

FIGURE 6 | Velocity profiles in the boundary layer at one trailing edge thickness upstream of the trailing edge circle. **(A)** Suction side **(B)** Pressure side.

the computational domain are set to be periodic boundary conditions. To study the loss of the four blades under different Mach numbers, the outlet static pressure was adjusted to change the outlet Mach number.

The commercial software ANSYS FLUENT is used as the solver in the current study. This software is based on the finite volume method. The DDES method is selected to simulate the turbulent flow and $SST - k\omega$ is used to simulate the near-wall region. The pressure-based solver and the coupled algorithm are used to solve the governing equation. The bounded central differencing scheme is selected for spatial discretization and the bounded second-order implicit scheme for transient formulation. The time step is set to 5×10^{-7} s. A total of 50 vortex shedding periods were simulated, of which the first 30 vortex shedding periods are used to converge the flow field, and the last 20 periods were used to count the time-averaged value.

Numerical Validation

The experimental data of Sieverding et al. (2003) is used to verify the validity of the numerical results. All verifications are based on experimental conditions with an outlet Mach number of 0.79. The comparison of experimental and numerical results of isentropic Mach number distribution on the blade surface is shown in **Figure 5**. The results of the DDES method are generally in good agreement with the experimental results. The numerical result at the leading edge has a lower isentropic Mach number, which may be due to the slight difference between the experimental air inlet angle and the numerical simulation.

The comparison of the velocity profile of the boundary layer between the numerical and experimental results is shown in **Figure 6**. The boundary layer velocity profiles are

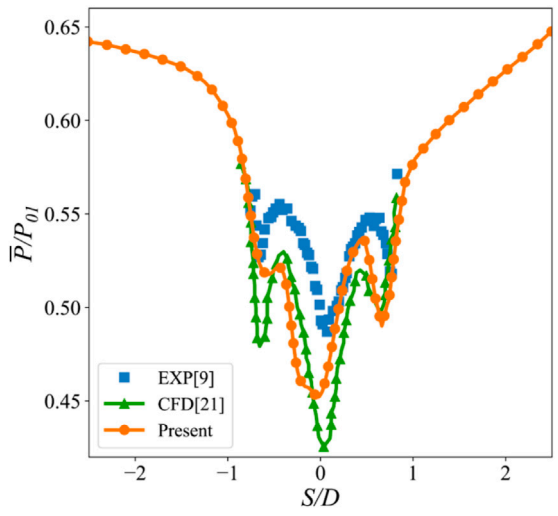

FIGURE 7 | Time-averaged pressure distribution at the trailing edge.

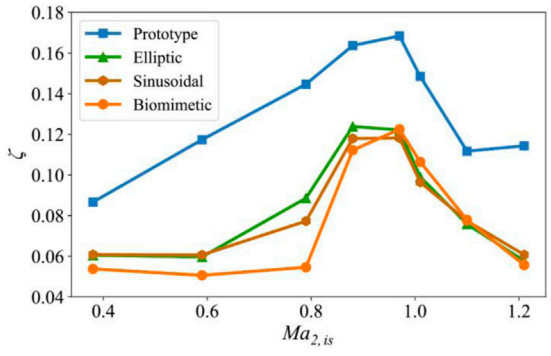

FIGURE 8 | The relationship between the energy loss coefficient of the four blades and the outlet isentropic Mach number.

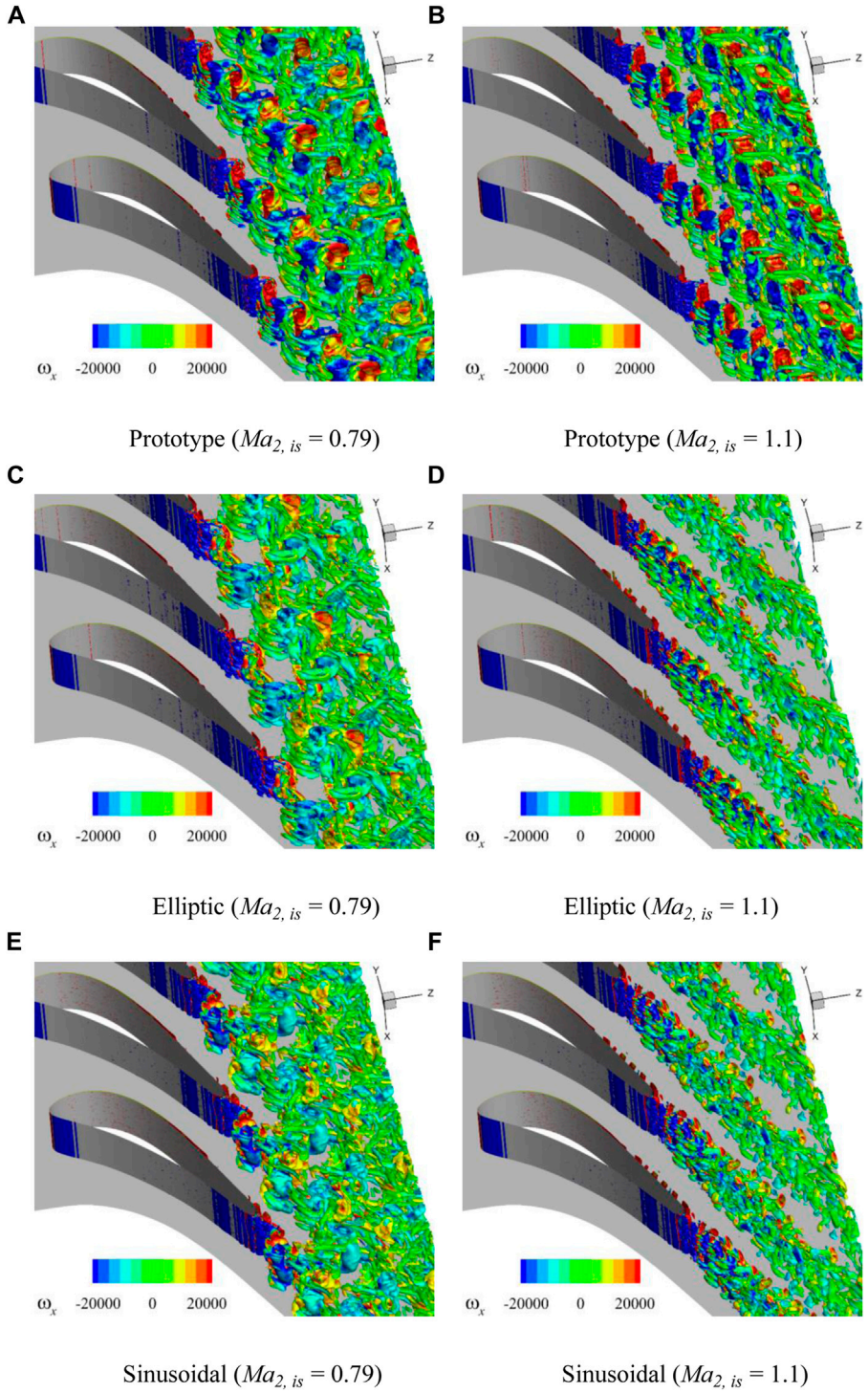

FIGURE 9 | Isosurfaces of Q criterion ($Q = 1 \times 10^7$) for the four profiles under $Ma_{2,is}$ = 0.79 and $Ma_{2,is}$ = 1.1. **(A)** Prototype ($Ma_{2,is}$ = 0.79) **(B)** Prototype ($Ma_{2,is}$ = 1.1). **(C)** Elliptic ($Ma_{2,is}$ = 0.79) **(D)** Elliptic ($Ma_{2,is}$ = 1.1). **(E)** Sinusoidal ($Ma_{2,is}$ = 0.79) **(F)** Sinusoidal ($Ma_{2,is}$ = 1.1). **(G)** Biomimetic ($Ma_{2,is}$ = 0.79) **(H)** Biomimetic ($Ma_{2,is}$ = 1.1).

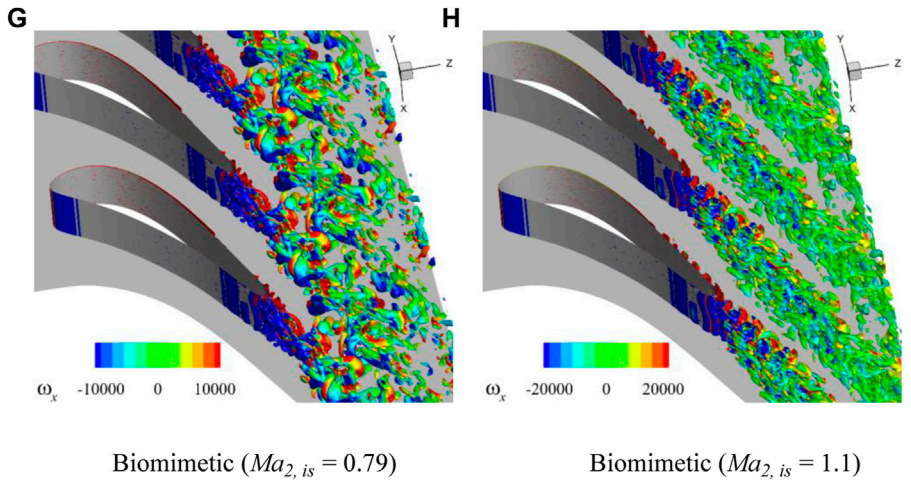

FIGURE 9 | *(Continued)*

measured at one trailing edge thickness upstream of the trailing edge circle. The velocity profile of the boundary layer on the pressure side is in good agreement with the experimental results. The boundary layer velocity profile on the suction side is consistent with the experimental results. The velocity profile in the middle of the boundary layer is slightly different from the experimental results. This may be because the URANS method in the boundary layer has insufficient ability to capture the turbulent flow on the suction side.

The comparison of the time-averaged pressure distribution at the trailing edge is shown in **Figure 7**. There are three local minimum values, respectively, on the suction side, pressure side, and center of the trailing edge. The trend obtained by the current numerical results is consistent with the experimental results, but the pressure distribution is underestimated. This may be due to the insufficient ability of the DDES method to predict near-wall regions with strong separation flows. Compared with the numerical results of El-Gendi et al. (2013), the results obtained by the current DDES method are more consistent with the experimental results. In a word, from the comparison of the numerical and experimental results, the current numerical method is reliable.

RESULTS AND DISCUSSION

Loss Analysis

The energy loss coefficient was used to evaluate the profile loss of the four blades at different Mach numbers. The energy loss coefficient is defined as

$$\zeta = 1 - \eta = 1 - \frac{1 - (P_2/P_{02})^{\frac{\gamma-1}{\gamma}}}{1 - (P_2/P_{01})^{\frac{\gamma-1}{\gamma}}}, \tag{3}$$

where P_2 stands for outlet static pressure, P_{01} and P_{02} represent the stagnation pressure at the inlet and outlet, and γ is the ratio of specific heat. The relationship between the energy loss coefficient of the four blades and the Mach number is shown in **Figure 8**. The outlet isentropic Mach number in the range of 0.38–1.21 is simulated.

For the prototype blade, in the subsonic region, the energy loss coefficient increases with the increase of exit isentropic Mach number and reaches the maximum at the Mach number about 0.97 and then decreases until it reaches the minimum at the Mach number close to 1.1. After that, when the Mach number increases further, the energy loss coefficient increases slightly again, which may be caused by the increase of shockwave loss. The mechanism that the turbine vane has a local maximum in the transonic region is revealed by previous researchers. Before reaching the maximum, the loss is mainly caused by Karman vortex street. When the exit Mach number increases to about 0.97, the trailing shockwave system appears at the trailing edge, and then the origin of the vortex street migrates from the blade trailing edge to a point downstream of the junction of the two trailing edge shear layers (Carscallen et al., 1996). The trailing edge base pressure increases; the wake vortex narrows and becomes weaker. Therefore, although the shockwave brings a certain loss, the loss caused by Karman vortex street dominates and is greatly reduced, so the total loss shows a downward trend.

For the blades with ETE and STE, these two kinds of blades contain part of the characteristics of the harbor seal whisker. In the entire simulated Mach number range, the losses of these two blades are greatly reduced compared to the prototype. The losses of these two blades are close in most ranges except when the Mach number is in the range of 0.6–1.0. In this range, the loss of the blade with the STE is lower. Besides this, the Mach number corresponding to the local maximum of the loss is shifted forward compared with the prototype.

The blade with the BTE contains all the characteristics of the harbor seal whisker. The loss of the blade with the BTE in

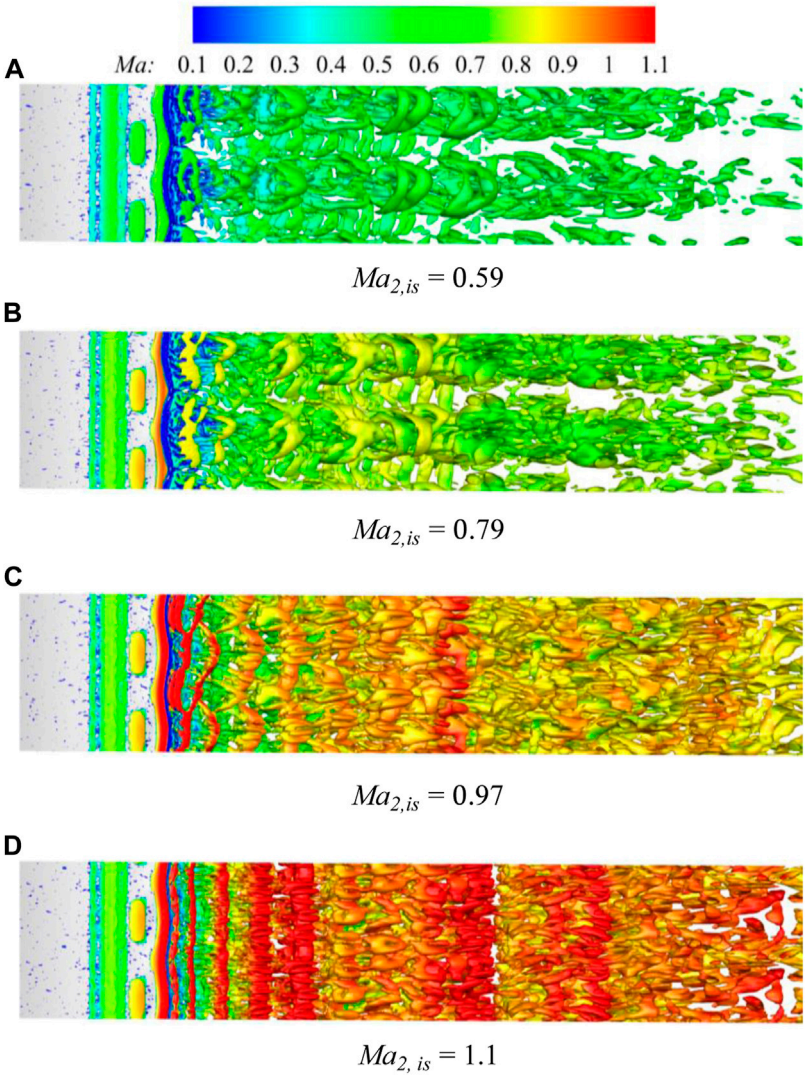

FIGURE 10 | The Q-criterion ($Q = 1 \times 10^7$) isosurface of the BTE dyed with Mach number under different Mach numbers. **(A)** $Ma_{2,is} = 0.59$. **(B)** $Ma_{2,is} = 0.79$. **(C)** $Ma_{2,is} = 0.97$. **(D)** $Ma_{2,is} = 1.1$.

all simulated Mach numbers is greatly reduced compared with the prototype. When the Mach number is less than 0.9, the loss of the blade with the BTE is lower than the blades with the ETE and STE. The Mach number corresponding to the local maximum of the loss of the blade with the BTE is closer to the prototype.

The Wakes at Different Mach Number

To reveal the mechanism of the loss of the four profiles under different Mach numbers, the wake characteristics of these profiles at different outlet Mach numbers are analyzed in this section. The vortex characteristics in the wake are displayed using the Q criterion as shown in **Figure 9**. The wakes at the two typical exit Mach numbers are displayed, and they are $Ma_{2,is} = 0.79$ and $Ma_{2,is} = 1.1$, respectively.

For $Ma_{2,is} = 0.79$, the wake of the prototype is in the form of an obvious Karman vortex street, which is composed of the main and streamwise vortices surrounding the main vortices as shown in **Figure 9A**. For the profile with the ETE, the wake is still in the form of Karman vortex street, but the wake strength is weakened as shown in **Figure 9C**. For the profile with the STE, the wake strength is also weakened compared with the prototype, and the main vortices are distorted in the spanwise direction as shown in **Figure 9E**. For the profile with the BTE, the Karman vortices in the wake are completely suppressed and transformed into small vortices with a three-dimensional structure. Besides this, these vortices dissipate faster as they move downstream.

For $Ma_{2,is} = 1.1$, the turbulence level in the prototype's wake is greatly reduced, and the wake area is narrowed. The energy loss coefficient of the prototype under $Ma_{2,is} = 1.1$ is lower than that

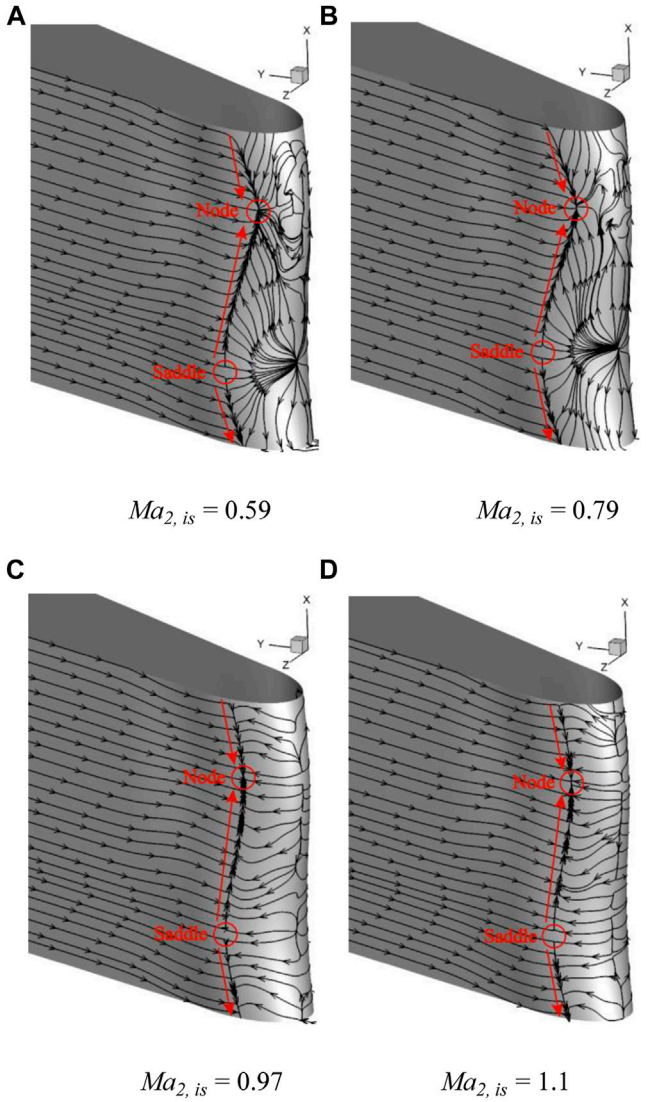

FIGURE 11 | Time-averaged surface streamlines in the trailing edge region of different Mach numbers. **(A)** $Ma_{2,is}$ = 0.59 **(B)** $Ma_{2,is}$ = 0.79. **(C)** $Ma_{2,is}$ = 0.97 **(D)** $Ma_{2,is}$ = 1.1.

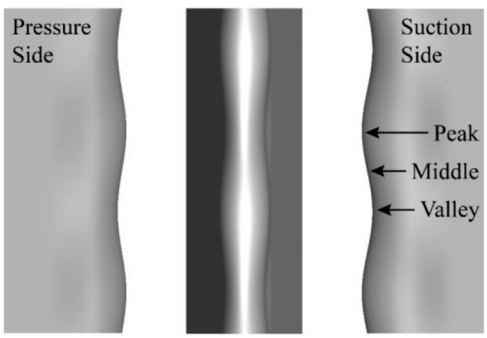

FIGURE 12 | Sections of peak, middle, and valley.

of $Ma_{2,is}$ = 0.79 as shown in **Figure 8**. In this region, the shockwave loss increases with the increase of Mach number, which is discussed in the next section. Therefore, the reduction of the energy loss coefficient between 0.98 and 1.1 is mainly due to the reduction of the wake loss. When $Ma_{2,is}$ = 1.1, the wakes of the profiles with the ETE, STE, and BTE are similar, which is why the energy loss coefficients of the three profiles are close. Compared with $Ma_{2,is}$ = 0.79, the wake behind the ETE and STE is significantly narrower. Besides this, when $Ma_{2,is}$ = 1.1, the strength of the main vortex behind the two trailing edges decreases and dissipates rapidly in the process of moving downstream. The energy loss coefficients of the profiles with these two trailing edges at $Ma_{2,is}$ = 1.1 is lower than $Ma_{2,is}$ = 0.79 as shown in **Figure 8**, which is also caused by the reduced wake loss in this Mach number range. For the profile with all the characteristics of the whisker, when $Ma_{2,is}$ = 1.1, the three-dimensional effect of the BTE is relatively weakened.

To reveal the controlability of the profile with all the characteristics of the whisker under different Mach numbers, we show the Q criterion isosurface under different Mach numbers as shown in **Figure 10**. For $Ma_{2,is}$ = 0.59 and $Ma_{2,is}$ = 0.79, the wake behind the BTE shows an obvious three-dimensional structure as shown in **Figures 10A,B**. In the spanwise direction, the wakes are mainly constrained in the valley area of the BTE. In the process of moving downstream, the wake behind the BTE can be divided into three areas, which are the wake formation, development, and dissipation areas. In the wake formation area, the three-dimensional vortices are mainly shed from the valley of the BTE. Because the fluid behind the trailing edge tends to converge from the peak to the valley, the flow velocity of the fluid in the valley area is higher. This speed difference causes a hairpin vortex to form in the wake development area. The vortex head of the hairpin vortex is in the valley area, and the vortex leg is close to the peak area. When the wake moves further downstream, the vortices transform into small vortices and then dissipate in the wake dissipation area. When the Mach number further increases, the three-dimensional control effect of the BTE on the wake weakens. For $Ma_{2,is}$ = 0.97, the BTE causes the shedding vortices to distort in the spanwise direction as shown in **Figure 10C**. For $Ma_{2,is}$ = 1.1, the three-dimensional control effect of the BTE has almost completely disappeared as shown in **Figure 10D**. The weakening of this three-dimensional effect is the reason why the energy loss coefficient of the BTE is close to that of the ETE and the STE.

To study the flow mechanism of the BTE at different Mach numbers, the time-averaged surface streamlines in the trailing edge region under different Mach numbers as shown in **Figure 11**. For $Ma_{2,is}$ = 0.59 and $Ma_{2,is}$ = 0.79, the fluid in the trailing edge region shows a strong three-dimensional separation pattern. There is a node corresponding to the peak of the BTE, and there is a saddle point at the valley. The reverse fluid shows strong spanwise motion, and they flow from the valley to the node as shown in **Figures 11A,B**. For $Ma_{2,is}$ = 0.97 and $Ma_{2,is}$ = 1.1, the spanwise flow of the reverse fluid almost disappears, and the streamwise distance between the node and

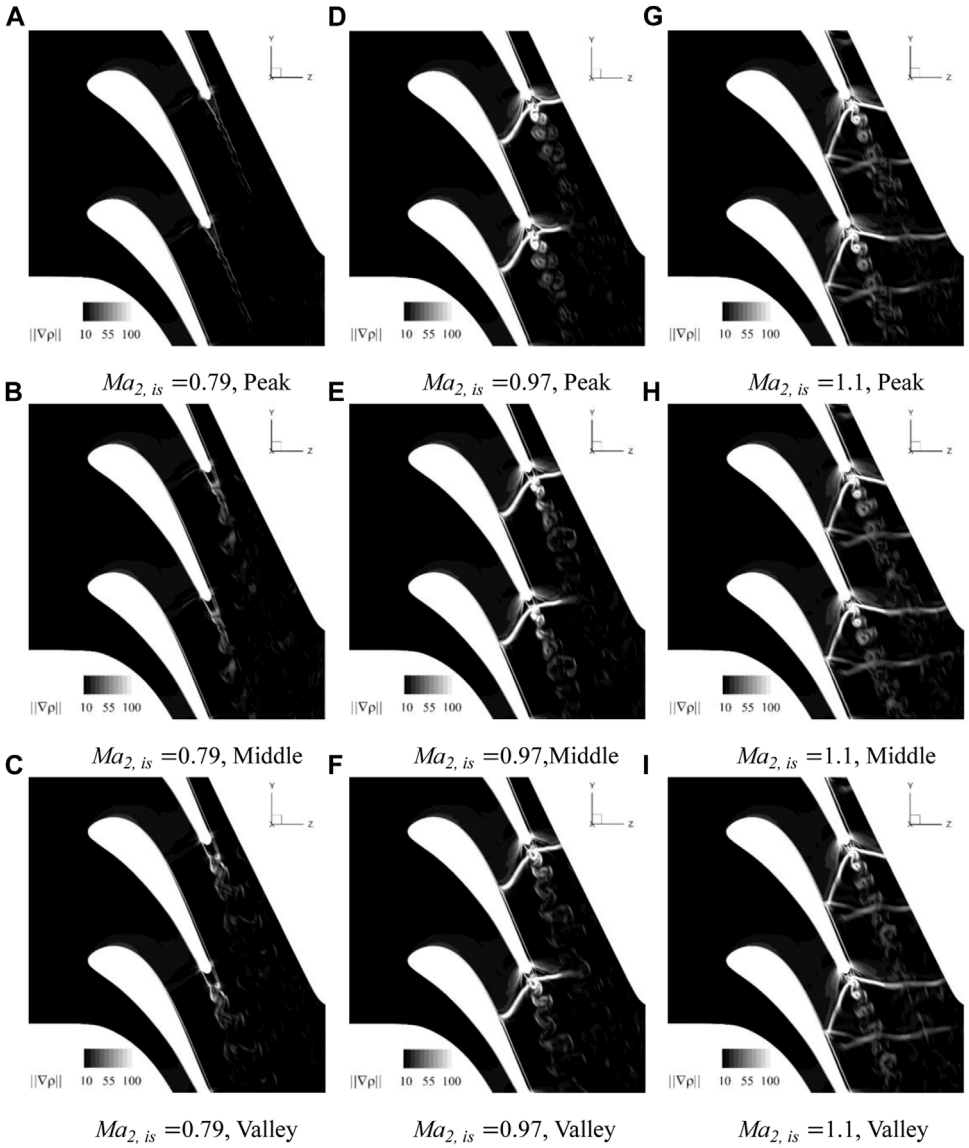

FIGURE 13 | Numerical Schlieren on peak, middle and valley sections at $Ma_{2,is}$ = 0.79, 0.97, 1.1. **(A)** Ma2, is=0.79, Peak **(B)** Ma2, is=0.79, Middle **(C)** Ma2, is=0.79, Valley **(D)** Ma2, is=0.97, Peak **(E)** Ma2, is=0.97, Middle **(F)** Ma2, is=0.97, Valley **(G)** Ma2, is=1.1, Peak **(H)** Ma2, is=1.1, Middle **(I)** Ma2, is=1.1, Valley.

the saddle point is closer as shown in **Figures 11C,D**. The weakening of this three-dimensional separation is the reason for the reduced control effect of the BTE at high Mach numbers. The authors speculate that the reason for the weakening of the three-dimensional separation at high Mach numbers is related to the amplitude of the sine curve of the BTE at control points 1 and 2 as shown in **Figure 1D**, which will be further studied in the future.

Shockwave Analysis

Because the profile of BTE changes along the blade height, to better analyze the shock system and vortex structures on the sections at different spanwise positions, as shown in **Figure 12**, three sections of peak, middle and valley are taken for comparative analysis. In **Figure 13**, contours of density gradient on peak, middle, and valley sections at $Ma_{2,is}$ =0.79, 0.97, 1.1 are shown, and in the next content, they are discussed and analyzed in combination with the flow field of the prototype trailing edge shown in **Figure 14**.

It can be seen from **Figures 13A–C** that, when $Ma_{2,is}$ = 0.79, the trailing edge flow structure is obviously different due to the different trailing edge thickness of each section. From the peak to the valley section, the trailing edge vortex scale increases with the increase of the trailing edge thickness, but there is no stable von Karman vortex street. By comparing the von Karman vortex street at the trailing edge of the prototype shown in **Figure 14**, it can be concluded that, when $Ma_{2,is}$ =

0.79, the BTE has a strong inhibition ability on the von Karman vortex street.

At $Ma_{2,is}$ = 0.79 and $Ma_{2,is}$ = 1.1, as shown in **Figures 13D–I**, a typical swallow tail shock system appears at the trailing edge, which is mainly characterized by the expansion wave system emitted from the separation points on both pressure and suction sides, the subsequent trailing edge shocks and the reattachment shocks (Lakshminarayana, 1996) at the confluence region of the flows from the suction and pressure surfaces, and at this time, the generation position of the trailing edge vortex moves downstream to the confluence region.

When $Ma_{2,is}$ = 0.97, it can be seen from **Figures 13D–F** that the patterns of trailing edge shock system and wake vortex are little different on different sections, the scales of the wake vortex on different sections are only slightly different due to the change of trailing edge thickness. The pressure side reattachment shock propagates toward the suction surface of the adjacent blade without an obvious reflected shockwave. It should be noted that, although the wake vortices on all the sections have certain von Karman vortex characteristics, the pressure side reattachment shock does not bend obviously under the action of wake vortex, which is very different from the prototype shown in **Figure 14B**. The main reason is that, under this Mach number condition, the wake vortex of the BTE is weak and has little effect on the shockwave.

From **Figures 13G–I**, it can be seen that, when $Ma_{2,is}$ = 1.1, the patterns of the trailing edge shock system and wake vortex are basically the same on different sections. The pressure side reattachment shockwave is little affected by the wake vortex and relatively straight. It interacts with the boundary layer on the suction surface of the adjacent blade, and a reflected shockwave is produced. The reflected shockwave propagates downward and interacts with the wake vortex, part of which is reflected from the wake vortex, and the other part penetrates the vortex to form a more complex wave–vortex interaction. The suction side reattachment shockwave is slightly affected by the weak wake vortex, and no reflected shockwave is produced, and it continues to penetrate the vortex and propagate downstream. Comparing **Figure 13H** and **Figure 14C**, it can be seen that the von Karman vortex of the prototype blade has a great impact on the wake flow structure. Even if the shockwave is strong at this time, the von Karman vortex is still in the dominant position. The reflected shockwave on the adjacent blade cannot pass through the wake vortex and is reflected again. The suction-side reattachment shockwave is broken by the vortex and dissipated when passing through the wake, and the unsteadiness of the whole trailing edge region is significantly stronger than that of BTE. It can be concluded that the BTE has a strong ability to suppress the Karman vortex at the trailing edge when $Ma_{2,is}$ is relatively low. After $Ma_{2,is}$ reaches or exceeds 1, the BTE can still weaken the strength of the trailing edge vortex, and then weaken the unsteadiness of the wake flow, which is also verified by numerical Schlieren pictures shown in **Figure 15**.

Figure 15 shows the numerical Schlieren at different times in a cycle when $Ma_{2,is}$ = 1.1, which can show the shock and vortex dynamics in the wake in more detail. We find that the shockwave at the trailing edge of the prototype exhibits periodic motion due to the alternate shedding vortices. Every time the vortex falls off, the turning of the airflow here changes. The vortices falling off the suction side generate a new suction side shockwave, and the phenomena also happens on the pressure side. The suction-side shockwave interferes with the wake during the movement. The pressure-side shockwave interacts with the suction side of the adjacent blade to produce a reflected shockwave, and the reflected wave also moves with the pressure-side shock as shown in **Figure 15A**. However, for the profile with the BTE, the unsteady motion of the shockwave is greatly reduced. The shockwave behind the BTE hardly changes with time as shown in **Figure 15B**. This is because the BTE suppresses the scale and strength of the shedding vortex, which makes the vortex shedding almost have no effect on the shockwave.

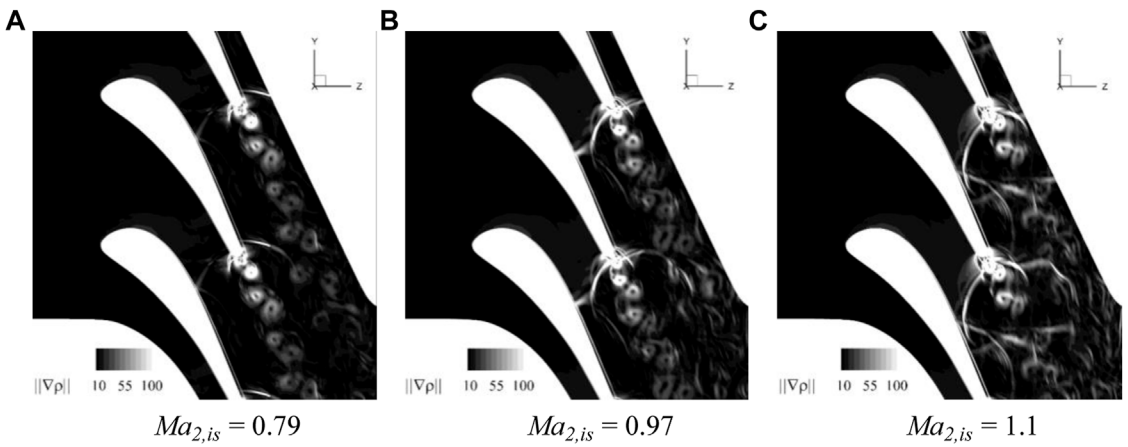

FIGURE 14 | Numerical Schlieren at different Mach numbers for the prototype. **(A)** Ma2,is = 0.79 **(B)** Ma2,is = 0.97 **(C)** Ma2,is = 1.1.

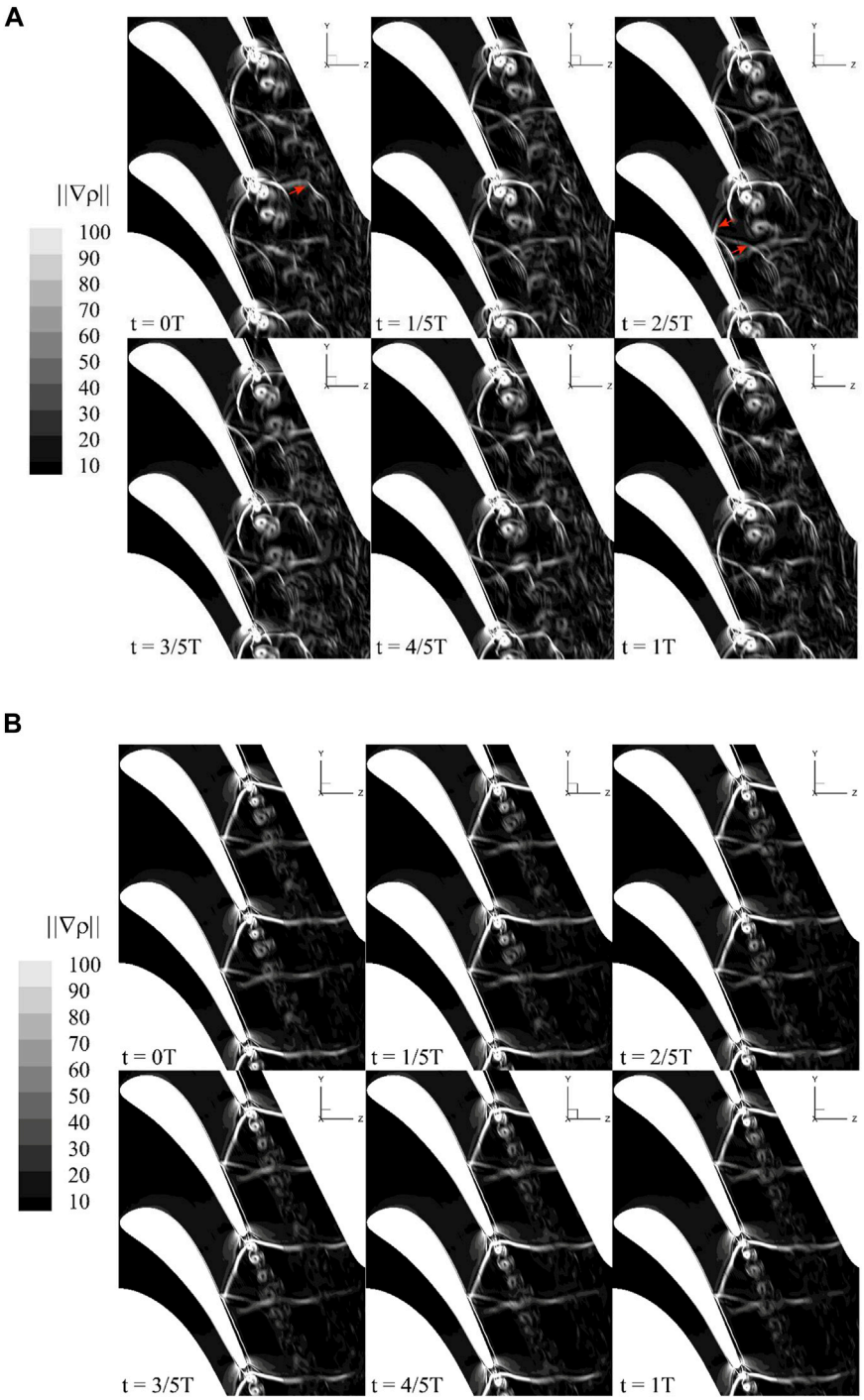

FIGURE 15 | Numerical Schlieren of prototype and BTE at different times when *Ma* = 1.1. **(A)** Prototype **(B)** Biomimetic.

CONCLUSION

The flow of the four blades, including prototype, ETE, STE, and BTE, are simulated at the exit isentropic Mach number of 0.38–1.21. The simulation results of the DDES method are generally in good agreement with the experimental data.

Within the Mach number range of 0.38–1.21, the energy loss coefficients of the four cases all show a trend of first increasing and then decreasing. In addition, the energy loss coefficients of the ETE, STE, and BTE are smaller than that of the prototype in the entire Mach number range. When the Mach number is less than 0.9, the BTE can effectively reduce the energy loss coefficient compared with the other three cases.

With the increase of Mach number, complex shockwave patterns appear in both the prototype and biomimetic cascade. When the exit Mach number approaches or exceeds 1, the trailing edge shock pattern of the BTE is more stable, and the wake vortex is relatively weak, which has little effect on the shockwaves. At $Ma_{2,is}$ = 1.1, the shockwave of the prototype cascade changes periodically with the shedding vortex. However, the BTE suppresses this dynamic movement of the shock wave and the flow unsteadiness in the trailing edge region in the cascade.

DATA AVAILABILITY STATEMENT

The original contributions presented in the study are included in the article/Supplementary Material, further inquiries can be directed to the corresponding author.

AUTHOR CONTRIBUTIONS

FW is the corresponding author of the article, and the main work includes calculation, analysis and article writing. YL's main work includes numerical computation and post-processing. ShW's main work includes numerical computation and post-processing. SoW assists in writing and reviewing the article. ZW reviewed the article and put forward some suggestions for revision.

FUNDING

The authors acknowledge financial support from the Natural Major Science and Technology Project of China (No. 2017-I-0005-0006) and the Outstanding Youth Science Foundation of Heilongjiang Province of China (No. YQ 2020E016).

REFERENCES

Beem, H. R., and Triantafyllou, M. S. (2015). Wake-induced 'slaloming' Response Explains Exquisite Sensitivity of Seal Whisker-like Sensors. *J. Fluid Mech.* 783, 306–322. doi:10.1017/jfm.2015.513

Bernardini, C., Salvadori, S., Martelli, F., Paniagua, G., and Saracoglu, B. H. (2013). Pulsating Coolant Ejection Effects Downstream of Supersonic Trailing Edge. *Eng. Appl. Comput. Fluid Mech.* 7 (2), 250–260. doi:10.1080/19942060.2013.11015468

Carscallen, W., Fleige, H., and Gostelow, J. (1996). Transonic Turbine Vane Wake Flows. in Turbo Expo: Power for Land, Sea, and Air. American Society of Mechanical Engineers (ASME), V001T01A109. doi:10.1115/96-gt-419

Dehnhardt, G., Mauck, B., Hanke, W., and Bleckmann, H. (2001). Hydrodynamic Trail-Following in Harbor Seals (*Phoca vitulina*). *Science* 293 (5527), 102–104. doi:10.1126/science.1060514

Denton, J. D. (1993). The 1993 Igti Scholar Lecture: Loss Mechanisms in Turbomachines. *J. Turbomach.* 115 (4), 621–656. doi:10.1115/1.2929299

Denton, J. D., and Xu, L. (1990). The Trailing Edge Loss of Transonic Turbine Blades. *J. Turbomach.* 112, 277–285. doi:10.1115/1.2927648

El-Gendi, M. M., Ibrahim, M. K., Mori, K., and Nakamura, Y. (2010). Novel Flow Control Method for Vortex Shedding of Turbine Blade. *Trans. Jpn. Soc. Aero. S Sci.* 53 (180), 122–129. doi:10.2322/tjsass.53.122

El-Gendi, M. M., Lee, S. W., Joh, C. Y., Lee, G. S., Son, C. H., and Chung, W. J. (2013). Elliptic Trailing Edge for a Turbine Blade: Aerodynamic and Aerothermal Effects. *Trans. Jpn. Soc. Aero. S Sci.* 56 (2), 82–89. doi:10.2322/tjsass.56.82

Ginter, C. C., DeWitt, T. J., Fish, F. E., and Marshall, C. D. (2012). Fused Traditional and Geometric Morphometrics Demonstrate Pinniped Whisker Diversity. *PloS one* 7 (4), e34481. doi:10.1371/journal.pone.0034481

Graham, C., and Kost, F. (1979). *Shock Boundary Layer Interaction on High Turning Transonic Turbine Cascades*. American Society of Mechanical Engineers (ASME).

Hamakhan, I. A., and Korakianitis, T. (2010). Aerodynamic Performance Effects of Leading-Edge Geometry in Gas-Turbine Blades. *Appl. Energ.* 87 (5), 1591–1601. doi:10.1016/j.apenergy.2009.09.017

Han, L. S., and Cox, W. (1982). A Visual Study of Turbine Blade Pressure-Side Boundary Layers, In Turbo Expo: Power for Land, Sea, and Air. American Society of Mechanical Engineers (ASME), V001T01A020. doi:10.1115/82-gt-47

Hanke, W., Witte, M., Miersch, L., Brede, M., Oeffner, J., Michael, M., et al. (2010). Harbor Seal Vibrissa Morphology Suppresses Vortex-Induced Vibrations. *J. Exp. Biol.* 213 (15), 2665–2672. doi:10.1242/jeb.043216

Korakianitis, T., Hamakhan, I. A., Rezaienia, M. A., Wheeler, A. P. S., Avital, E. J., and Williams, J. J. R. (2012). Design of High-Efficiency Turbomachinery Blades for Energy Conversion Devices with the Three-Dimensional Prescribed Surface Curvature Distribution Blade Design (circle) Method. *Appl. Energ.* 89 (1), 215–227. doi:10.1016/j.apenergy.2011.07.004

Lakshminarayana, B. (1996). *Fluid Dynamics and Heat Transfer of Turbomachinery*. New York: John Wiley & Sons, 567–570.

Léonard, T., Gicquel, L. Y., Gourdain, N., and Duchaine, F. (2010). Steady/unsteady Reynolds-averaged Navier–Stokes and Large Eddy Simulations of a Turbine Blade at High Subsonic Outlet Mach Number. *J. Turbomach.* 137 (4).

Lin, D., Su, X., and Yuan, X. (2017). Ddes Analysis of the Wake Vortex Related Unsteadiness and Losses in the Environment of a High-Pressure Turbine Stage. *J. Turbomach.* 140 (4).

Lin, D., Yuan, X., and Su, X. (2017). Local Entropy Generation in Compressible Flow through a High Pressure Turbine with Delayed Detached Eddy Simulation. *Entropy* 19 (1), 29. doi:10.3390/e19010029

Luo, Y., Wen, F., Wang, S., Zhang, S., Wang, S., and Wang, Z. (2019). Numerical Investigation on the Biomimetic Trailing Edge of a High-Subsonic Turbine Blade. *Aerospace Sci. Tech.* 89, 230–241. doi:10.1016/j.ast.2019.04.002

Mee, D., Baines, N., Oldfield, M., and Dickens, T. (1990). An Examination of the Contributions to Loss on a Transonic Turbine Blade in cascade. In Turbo Expo: Power for Land, Sea, and Air. American Society of Mechanical Engineers, V005T16A012. doi:10.1115/90-gt-264

Melzer, A., and Pullan, G. The Role of Vortex Shedding in the Trailing Edge Loss of Transonic Turbine Blades. *J. Turbomach.* 141 (4).

Motallebi, F., and Norbury, J. F. (1981). The Effect of Base Bleed on Vortex Shedding and Base Pressure in Compressible Flow. *J. Fluid Mech.* 110, 273–292. doi:10.1017/s0022112081000748

Raffel, M., and Kost, F. (1998). Investigation of Aerodynamic Effects of Coolant Ejection at the Trailing Edge of a Turbine Blade Model by Piv and Pressure Measure-Ments. *Experiments in Fluids* 24 (5-6), 447–461. doi:10.1007/s003480050194

Schulte-Pelkum, N., Wieskotten, S., Hanke, W., Dehnhardt, G., and Mauck, B. (2007). Tracking of Biogenic Hydrodynamic Trails in Harbour Seals (phoca Vitulina). *J. Exp. Biol.* 210 (5), 781–787. doi:10.1242/jeb.02708

Sieverding, C., Decuypere, R., and Hautot, P. (1978). Investigation of Transonic Steam Turbine Tip Sections with Various Suction Side Blade Curvatures. *STIN* 80, 26632.

Sieverding, C. H., Richard, H., and Desse, J.-M. (2003). Turbine Blade Trailing Edge Flow Characteristics at High Subsonic Outlet Mach Number. *J. Turbomach.* 125 (2), 298–309. doi:10.1115/1.1539057

Sieverding, C., and Manna, M. (2020). A Review on Turbine Trailing Edge Flow. *Ijtpp* 5 (2), 10. doi:10.3390/ijtpp5020010

Wang, S., Wen, F., Zhang, S., Zhang, S., and Zhou, X. (2019). Influences of Trailing Boundary Layer Velocity Profiles on Wake Vortex Formation in a High-Subsonic-Turbine cascade. *Proc. Inst. Mech. Eng. A: J. Power Energ.* 233 (2), 186–198. doi:10.1177/0957650918779935

Wieskotten, S., Dehnhardt, G., Mauck, B., Miersch, L., and Hanke, W. (2010). Hydrodynamic Determination of the Moving Direction of an Artificial Fin by a Harbour Seal (phoca Vitulina). *J. Exp. Biol.* 213 (13), 2194–2200. doi:10.1242/jeb.041699

Xu, L., and Denton, J. D. (1988). The Base Pressure and Loss of a Family of Four Turbine Blades. *J. Turbomach.* 110 (1), 9–17. doi:10.1115/1.3262174

Zhang, W., Zou, Z., and Ye, J. (2012). Leading-edge Redesign of a Turbomachinery Blade and its Effect on Aerodynamic Performance. *Appl. Energ.* 93, 655–667. doi:10.1016/j.apenergy.2011.12.091

Conflict of Interest: Author SW is employed by The 705 Research Institute of China Shipbuilding Industry Corporation.

The remaining authors declare that the research was conducted in the absence of any commercial or financial relationships that could be construed as a potential conflict of interest.

NOMENCLATURE

Ma = Mach number

D = trailing edge thickness

$\bar{D}$ = mean length of the minor axis

A = amplitude

c = chord length

g = pitch length

h = blade height

P = pressure

T = temperature

Re = reynolds number

Greek symbols

δ = Wedge angle

θ = Stagger angle

λ = wavelength

ζ = energy loss coefficient

η = isentropic efficient

γ = ratio of specific heat

ρ = density

Subscripts

te = trailing edge

ax = axial direction

w = habor seal whisker

l = major axis

s = Minor axis

is = isentropic

1 = static property at cascade inlet

2 = static property at cascade outlet

01 = stagnation property at cascade inlet

02 = stagnation property at cascade outlet

Abbreviations

ETE = elliptic trailing edge

STE = sinusoidal trailing edge

BTE = biomimetic trailing edge

frontiers in Energy Research

ORIGINAL RESEARCH
published: 22 November 2021
doi: 10.3389/fenrg.2021.791542

Maximum Thickness Location Selection of High Subsonic Axial Compressor Airfoils and Its Effect on Aerodynamic Performance

Chuansijia Tao[1], *Xin Du*[1]*, *Jun Ding*[2,3], *Yizhou Luo*[1] *and Zhongqi Wang*[1]

[1]School of Energy Science and Engineering, Harbin Institute of Technology, Harbin, China, [2]Hangzhou Turbine Power Group Co., Ltd., Hangzhou, China, [3]College of Power and Energy Engineering, Harbin Engineering University, Harbin, China

Solidity and camber angle are key parameters with a primary effect on airfoil diffusion. Maximum thickness location has a considerable impact on blade loading distribution. This paper investigates correlations of maximum thickness location, solidity, and camber angle with airfoil performance to choose maximum thickness location quickly for compressor airfoils with different diffusion. The effects of maximum thickness location, solidity, and camber angle on incidence characteristics are discussed based on abundant two-dimensional cascade cases computed through numerical methods. Models of minimum loss incidence, total pressure loss coefficient, diffusion factor, and static pressure rise coefficient are established to describe correlations quantitatively. Based on models, dependence maps of total pressure loss coefficient, diffusion factor, and static pressure rise coefficient are drawn and total loss variation brought by maximum thickness location is analyzed. The study shows that the preferred selection of maximum thickness location can be the most forward one with no serious shock loss. Then, the choice maps of optimal maximum thickness location on different design conditions are presented. The optimal maximum thickness locates at 20–35% chord length. Finally, a database of optimal cases which can meet different loading requirements is provided as a tool for designers to choose geometrical parameters.

Keywords: high subsonic compressor, blade profile, maximum thickness location, solidity, prediction model, database

OPEN ACCESS

Edited by:
Bengt Sunden,
Lund University, Sweden

Reviewed by:
Xiaoqing Qiang,
Shanghai Jiao Tong University, China
Shijun Sun,
Beijing Institute of Technology, China
Xiaoxu Kan,
Shanghai Maritime University, China

***Correspondence:**
Xin Du
xindu@hit.edu.cn

Specialty section:
This article was submitted to Advanced Clean Fuel Technologies, a section of the journal Frontiers in Energy Research

Received: *08 October 2021*
Accepted: *05 November 2021*
Published: *22 November 2021*

Citation:
Tao C, Du X, Ding J, Luo Y and Wang Z (2021) Maximum Thickness Location Selection of High Subsonic Axial Compressor Airfoils and Its Effect on Aerodynamic Performance. Front. Energy Res. 9:791542. doi: 10.3389/fenrg.2021.791542

HIGHLIGHTS

- Performance prediction models containing maximum thickness location is established, which can be used in compressor preliminary design.
- Choice maps of maximum thickness location and solidity are found on three different conditions, where camber angle, diffusion factor, or static pressure rise is constant respectively.
- A database of optimal maximum thickness location is provided for designers to meet different design requests.

1 INTRODUCTION

With the increase of stage loading, the area coverage of boundary layer separation enlarges and disordered vortex structures become more complicated within the flow passage (Sun et al., 2018; Hu

et al., 2021; Ju et al., 2020). To achieve good aerodynamic performance, employing effective flow control approaches is necessary both in rotors and stators for the highly loaded aero-engine compressor (Wang et al., 2021). The low-reaction design method is proposed to simplify the sophisticated flow control strategy (Qiang et al., 2008; Sun et al., 2019; Sun et al., 2020; Sun et al., 2021). For a highly loaded low-reaction stage, both the inlet Mach number and the static pressure rise of the stator significantly increase. In this case, the high subsonic stator airfoil design with high flow turning which can achieve low loss-level, increase efficiency and static pressure rise capability becomes a huge challenge (Zhang et al., 2019).

When inlet Mach number increases to a certain degree, supersonic flow appears at local region of suction surface and brings sharp rise of loss (Shi and Ji, 2021). It is called supercritical flow condition when incoming flow is high subsonic and transonic flow exists in the passage. With shock-free and controlled diffusion features, controlled-diffusion airfoil (CDA) introduced in the early 1980s was originally designed for supercritical cascades (Dunker et al., 1984; Niederdrenk et al., 1987; Elazar and Shreeve, 1990; Steinert et al., 1991; Jiang et al., 2015). As CDA blades were primarily developed for aero-engines but not the optimum solution for heavy-duty gas turbines, Köller et al. (2000) and Kusters et al. (2000) designed a high subsonic compressor airfoil family (Ma ≤ 0.8, $\theta \leq 30^{\circ}$, e/b = 25%). The optimization results demonstrated that the well-controlled front loading airfoil obtained good performance through promoting early transition without strong laminar separation. Besides, it is conducive to reducing the adverse pressure gradient and the loading at the rear region of suction side. Sieverding et al. (2004) transferred and adapted the preceding design system to industrial compressors and the optimized airfoils (Ma = 0.5, e/b = 25%) were generated. The results indicated that as the maximum thickness location moved forward, the peak velocity position on the suction side migrated forwards, and stabilized boundary layer is the reason why front-loading airfoils present good performance. Wang et al. (2020) investigated the evolution of vortex structures and separated flow transition process in front-loaded airfoil through large eddy simulations. As the laminar separation was suppressed on the suction surface of the front-loaded airfoil, the associated vortex dynamics was weakened. Hence, the high level of Reynolds shear stresses recedes.

Although previous conclusions for front-loading airfoils are effective, most optimization research objects are dispersive and lack of revealing the universal rules of parameter selection. When facing different design requirements, it is difficult to achieve a quick front-loading blade profile design. Moreover, these questions must be raised: What kind of flow problems will occur when the maximum thickness position moves forward? Is there a limit to the forward movement of the maximum thickness position? What is the effect of cascade key parameters on the influence brought by forward movement of maximum thickness position? The systematic study of cascade geometrical parameters is helpful to reflect the influence rules of key geometrical parameters on airfoil aerodynamic performance and reveal the flow evolution mechanism. In this situation, it is necessary to build up performance prediction models for supercritical airfoils, which include maximum thickness location and key geometrical parameters. The results of models contribute to revealing the generality of maximum thickness location selection and providing a tool of blade profile selection for mean-line and through-flow design.

For high-load aero-engine compressor design, solidity and camber angle are key geometrical parameters in preliminary design, which have a remarkable influence on flow turning capacity, blade loading, and working range (Howell, 1945; Zweifel, 1945; Carter, 1950; Lieblein et al., 1953; Johnsen and Bullock, 1965; Britsch, 1979). An increase of solidity could achieve high flow turning, but increases the number of blades and profile loss (Sans et al., 2014). To meet the needs of empirical solidity inputs in mean-line and through-flow design, performance prediction models including solidity which can be used in multistage axial flow compressor are needed (Larosiliere et al., 2002; Horlock and Denton, 2005; Burberi et al., 2020). Sans et al. (2014) updated the correlations for controlled diffusion blades and extended their application to the high Mach number flow regimes. Bruna and Cravero chose inlet flow angle, inlet Mach number, AVDR, Reynolds number, and solidity as model parameters to study profile loss (Ma1 = 0.5–0.84, σ = 0.625–2, θ = 37.4°–43.4°) (Bruna et al., 2006). Xu and Du established performance characteristics prediction models for the curved blade containing solidity and camber angle in NACA65 compressor cascade (Ma1 = 0.2–0.6, σ = 1.2–1.8, θ = 30°–60°) (Xu et al., 2018), and integrated aspect ratio into the models in the follow-up research (Xu et al., 2019).

As an attempt to provide a reference for compressor preliminary design, this paper investigates rules of maximum thickness location selection matching cascade key parameters. Several camber angles are selected to investigate different typical flow problems for the generality of the conclusion. The in-house program introduced in reference (Li, 2007) is used for the generation of profiles. The numerical calculation carried out in abundant two-dimensional linear cascades has been successfully applied for performance evaluations and flow phenomena detections. The evolution of performance parameters (ω_o, D_o, and Cp_{2o}) at minimum loss incidence versus geometrical parameters (σ, e/b, and θ) is studied. The flow mechanism leading to the performance differences is analyzed based on the calculated performances and flow details. Then performance parameters are described in function of geometrical parameters. Based on polynomial models, dependence maps ofω_o, D_o, and Cp_{2o} and the effect of e/b on them are discussed. In addition, choice maps of optimal e/b at selected θ, D_o, or Cp_{2o} are presented respectively. Finally, a database of all the optimal e/b is provided for designers with different demands as a tool to choose parameters.

2 INVESTIGATION PROGRAMS AND NUMERICAL METHOD

2.1 Investigation Programs

The investigated blade profile is used in the stator of the second stage of a three-stage compressor. The curve of the camber line is

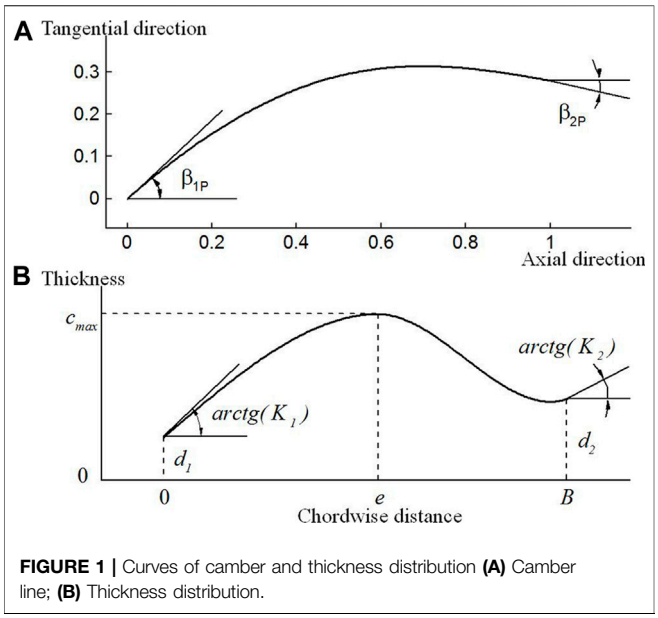

FIGURE 1 | Curves of camber and thickness distribution **(A)** Camber line; **(B)** Thickness distribution.

described by a quartic polynomial and normalized by axial chord length, as shown in **Figure 1A**. It is well controlled to arrange the blade loading chordwise distribution and to alter the deviation angle. Two cubic polynomial curves connected at maximum thickness location are used to describe the thickness distribution, as shown in **Figure 1B**. The d_1, d_2 are the leading edge and trailing edge radius. The variables K_1, K_2 are the rate of thickness changing along the chord at leading edge and trailing edge. The e is the location of maximum thickness, while e/b is normalized by chord.

Geometrical parameters and flow conditions of the cascade are shown in **Table 1**. Maximum thickness and its position are normalized by chord length. Chord length, maximum thickness and inlet curvature of camber line has been optimized in the previous design of blade profile. Cascade geometrical parameters (σ, e/b, and θ) are changed in the ranges which cover the usually used values in industry applications. Effects of e/b and θ on profiles are shown in **Figure 2**. **Figure 3** shows the axial distribution of the thickness and suction side curvature of the blade at $\theta = 40^{\circ}$. As shown in the figure, the curvature of the suction side has a step, whose position is obviously related to e/b. The suction side curvature increases before the step but reduces after it with the forward migration of e/b.

2.2 Numerical Method and Validation

The structured grid is generated by the IGG/AutoGrid5 module of the NUMECA software package. As shown in **Figure 4**, a mixed O-and H-block is used for the computation domain. The inlet of the computational domain is located 100% chord length ahead of the leading-edge. The outlet of the computational domain is set 100% chord length behind the trailing-edge with a buffer zone. The measurement plane location is 40% chord length behind the trailing-edge for complete wake development. The thickness of the first grid layer is 10^{-6} m, and 5×10^{-6} m near the hub and shroud, which can insure $y^{+}<3$ at solid wall in all cases and satisfy the solving demands of the selected turbulence model in this paper.

With such a topology structure, a grid independence study is carried out with different grid nodes number, including seven meshes with respectively from about 45 to 140 thousands cells. As shown in **Figure 5**, when further refining the mesh grid with grid number beyond 100 thousands, the results almost have no modification. Therefore, the spanwise node number adopted is 5 in this study, and the total grid node number is about 109 thousands.

The code solver FINE™ EURANUS is used to solve the Reynolds-Averaged Navier-Stokes equations with finite volume form. The governing equation for the relative velocities in the rotating frame can be expressed as:

$$\frac{\partial \vec{U}}{\partial t} + \nabla \cdot \vec{F}_I + \nabla \cdot \vec{F}_V = \boldsymbol{Q} \tag{1}$$

where $\vec{U}$ is the vector of the conservative variables; $\overrightarrow{F_I}$ is inviscid flux vector; and $\overrightarrow{F_V}$ is viscous flux vector. Their variable forms are given by:

$$\vec{\boldsymbol{U}} = \begin{bmatrix} \bar{\rho} \\ \bar{\rho}\tilde{w}_1 \\ \bar{\rho}\tilde{w}_2 \\ \bar{\rho}\tilde{w}_3 \\ \bar{\rho}\tilde{E} \end{bmatrix} \boldsymbol{F_{Ii}} = \begin{bmatrix} \bar{\rho}\tilde{w}_i \\ \overline{p^*}\boldsymbol{\delta}_{1i} + \bar{\rho}\tilde{w}_i\tilde{w}_1 \\ \overline{p^*}\boldsymbol{\delta}_{2i} + \bar{\rho}\tilde{w}_i\tilde{w}_2 \\ \overline{p^*}\boldsymbol{\delta}_{3i} + \bar{\rho}\tilde{w}_i\tilde{w}_3 \\ \left(\bar{\rho}\tilde{E} + \overline{p^*}\right)\tilde{w}_i \end{bmatrix} - \boldsymbol{F_{Vi}} = \begin{bmatrix} 0 \\ \bar{\tau}_{i1} \\ \bar{\tau}_{i2} \\ \bar{\tau}_{i3} \\ \bar{q}_i + \tilde{w}_i\bar{\tau}_{ij} \end{bmatrix} \tag{2}$$

TABLE 1 | Parameters and flow conditions of research.

Parameters	Value								
Chord b/(m)	0.0242								
Inlet Mach number Ma_1	0.8								
Solidity σ	1.25	1.35	1.46	1.56	1.67	1.76	1.86	1.95	2.05
Inlet Blade angle β_{1p}/(°)	45°		50°			54°		56°	
Outlet Blade angle β_{2p}/(°)	10°								
Camber angle θ/(°)	35°		40°			44°		46°	
Maximum thickness c_{max}	4.5%								
Maximum thickness location e/b	20%		30%		40%	50%		60%	
Inlet curvature of camber kk_1	2.00								

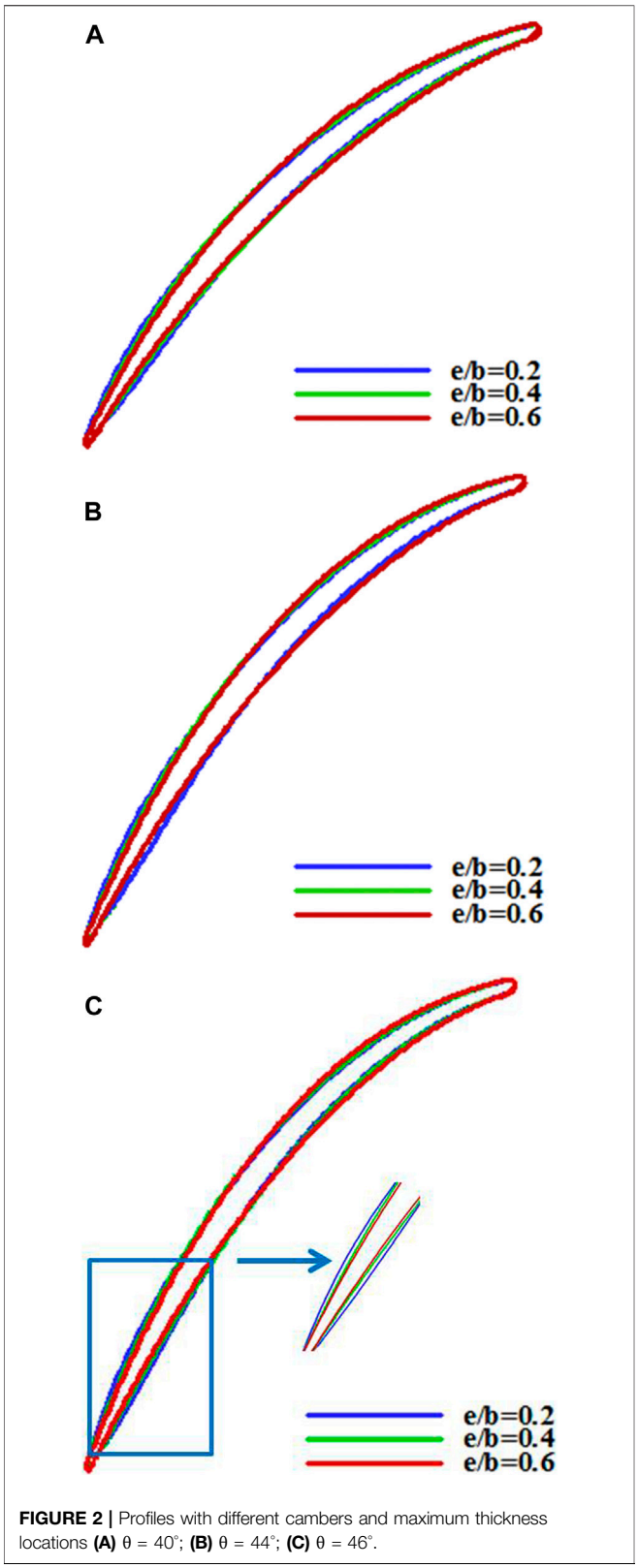

FIGURE 2 | Profiles with different cambers and maximum thickness locations **(A)** θ = 40°; **(B)** θ = 44°; **(C)** θ = 46°.

where the superscripts "-" and "~" are the time average value and density weighted average value, respectively; w_i is the x_i component of the relative velocity; E is the total energy; p^* is the total pressure; δ_{ij} is the Kronecker number; τ_{ij} is the Reynolds stress; and q_i is the heat flux component. The contributions of the Coriolis and centrifugal forces are contained in the source item vector Q, which is given by:

$$Q = \begin{bmatrix} 0 \\ (-\rho)\left[2\vec{\omega} \times \vec{w} + \left(\vec{\omega} \times \left(\vec{\omega} \times \vec{r}\right)\right)\right] \\ \bar{\rho}\vec{w}\nabla\left(\frac{1}{2}\omega^2 r^2\right) \end{bmatrix} \tag{3}$$

where ω is the angular velocity of the relative frame of reference; r is the radius; and $\vec{w}$ is the relative velocity. (NUMECA International, 2015).

The MOGA profile in literature (Song and Ng, 2006) is selected to validate the calculation methods of the two-dimensional cascade. Several turbulence models were adopted to show the effect of turbulence models on the simulation accuracy at Ma = 0.77 in **Figure 6A**. It can be seen that the trend of numerical simulation is basically consistent with experiments. The Spalart-Allmaras turbulence model is employed, as it provides high robustness and good compromise in accuracy for the prediction of complex flows (Spalart and Allmaras, 1994). The simulations are fully turbulent without boundary layer transition effects.

Besides, the space discrete form is TVD of the second-order upwind scheme, and Min-Mod flux limiter is adopted to enhance the scheme stability. The temporal discretization scheme is four-stage Runge-Kutta scheme, with multigrid solver and implicit residual smoothing method to accelerate the residual convergence.

Inlet boundary conditions are prescribed with total pressure (430 kPa), total temperature (440 K) and inflow angle. Free-slip and adiabatic conditions are imposed at the solid walls. Translational periodic boundary condition is used in the pitchwise direction. In the computations, the mass-flow specified at the outlet is modified to achieve the desired inlet Mach number. Non-reflecting boundary condition is used at inlet/outlet planes.

3 RESULTS AND DISCUSSION

Based on Lieblein's definition (Lieblein, 1955), the diffusion factor given in **Eq. 4** is used to assess the loading of blades. In **Eq. 4**,v_1,v_2,Δv_u and σ are inlet velocity, outlet velocity, tangential velocity variation, and solidity. Total pressure loss coefficient (ω) and static pressure rise coefficient (Cp_2) are selected to evaluate airfoil aerodynamic performance. The definitions of ω and Cp_2 are described in **Eq. 5** and **Eq. 6**. Here, $P_1^*$and$P_1$are total and static pressure at the cascade inlet, while$P_2^*$and$P_2$are total pressure and static pressure at the outlet. Mass-weighted averaging is used.

$$D = 1 - \frac{v_2}{v_1} + \frac{\Delta v_u}{2v_1\sigma} \tag{4}$$

$$\omega = \frac{P_1^* - P_2^*}{P_1^* - P_1} \tag{5}$$

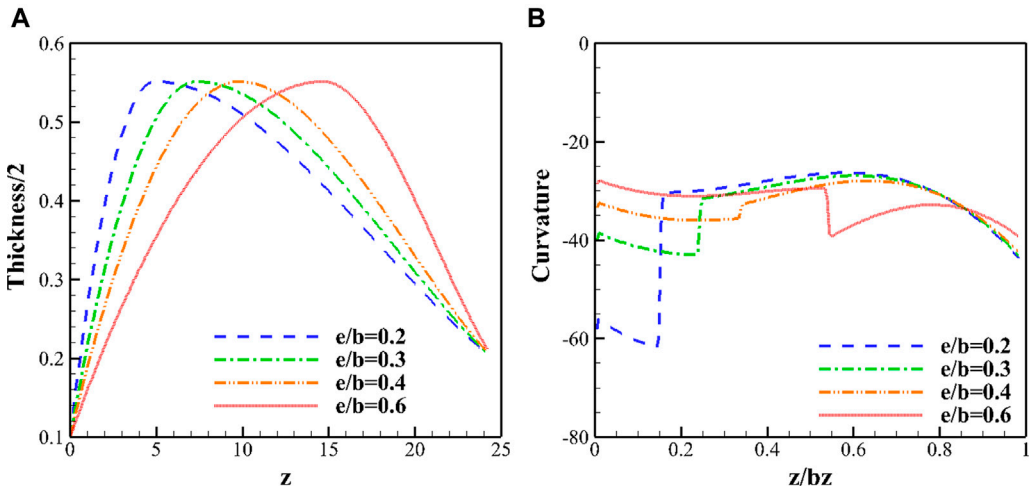

FIGURE 3 | Axial distribution of profile thickness **(A)** and the curvature of suction side **(B)**.

$$Cp_2 = \frac{P_2 - P_1}{P_1^* - P_1} \tag{6}$$

The effect of maximum thickness location (e/b), solidity (σ) and camber angle (θ) on airfoil performance are discussed, including minimum loss incidence (i_o), diffusion factor (D_o), total pressure loss coefficient (ω_o), and static pressure rise coefficient (Cp_{2o}). Minimum loss incidence (i_o) refers to the incidence with minimum loss within the incidence range, while the other three performance parameters are obtained in this case.

3.1 Incidence Characteristics

Figure 7 shows incidence characteristics of total pressure loss coefficient and diffusion factor from negative to positive stall at different solidities ($Ma_1 = 0.8$). It can be seen that as solidity increases, total pressure loss coefficient curves move up and rightwards, and diffusion factor curves migrate rightwards. Obviously, i_o, ω_o and D_o increase with solidity.

Figure 8 shows incidence characteristics of total pressure loss coefficient and diffusion factor with different camber angles ($Ma_1 = 0.8$). It can be seen that as camber angle increases, incidence range shrinks, while both total pressure loss coefficient and diffusion factor curves move up, which means ω_o and D_o increase but i_o changes slightly.

Figure 9 shows incidence characteristics of total pressure loss coefficient and diffusion factor with different maximum thickness locations ($Ma_1 = 0.8$). It can be seen that when maximum thickness location moves upstream, positive incidence range increases and loss reduces, except for **Figures 9A,C**. As e/b increases, i_o and D_o reduce but ω_o increases.

It can be found that solidity (σ), camber angle (θ), and maximum thickness location (e/b) have impacts on two-dimensional cascade incidence characteristics. The trend of optimum incidence performance varying with cascade geometrical parameters will be discussed in detail afterward.

3.2 Parameters on Minimum Loss Condition

3.2.1 Minimum Loss Incidence

Supplementary Figure S10 shows i_o versus σ with different e/b and θ. It can be seen that as σ increases, i_o rises nearly linearly, except for the cases at $e/b = 0.2$, $\theta \leq 40^\circ$. The trend is in accord with the results in reference (Sans et al., 2014). **Supplementary Figure S11** shows i_o versus θ with different σ and e/b. It shows that the evolvement of i_o versus θ is quadratic almost for all e/b and σ. In most cases, i_o decreases slightly with an increasing θ, except for cases at $e/b = 0.2$, $\sigma \geq 1.46$. In these cases, i_o decreases more significantly, which agrees with **Supplementary Figure S10A**. **Supplementary Figure S12** shows i_o versus e/b with different σ and θ. It illustrates that the evolution of i_o with e/b is quadratic, reflecting in two different patterns. In the cases with big θ and small σ, i_o increases firstly and then decreases while e/b is enhanced. In the cases with small θ and big σ, i_o decreases as e/b increases.

3.2.2 Total Pressure Loss Coefficient

Supplementary Figure S13 shows ω_o versus σ with different e/b and θ. It illustrates that ω_o almost increases linearly with σ. It is because that a rise in a number of blades attracts linear increases of profile loss. **Supplementary Figure S14** shows ω_o versus θ with different e/b and σ. As θ rises, ω_o decreases firstly and then increases, which can also be observed in **Supplementary Figure S13**. **Supplementary Figure S15** shows ω_o versus e/b with different σ and θ. It indicates that ω_o decreases firstly and then increases with the rise of e/b, which presents quadratic curves except for some low-load cases. The minimum of ω_o occurs at e/b = 0.2–0.3 and alters with σ and θ.

3.2.3 Diffusion Factor

Supplementary Figure S16 shows D_o versus solidity with different e/b and θ. As solidity is increasing, D_o increases and then keeps constant with a quadratic trend. The influence of σ is very limited. It is because that the rise of i_o with σ causes an increase of blade load correspondingly and compensates for the

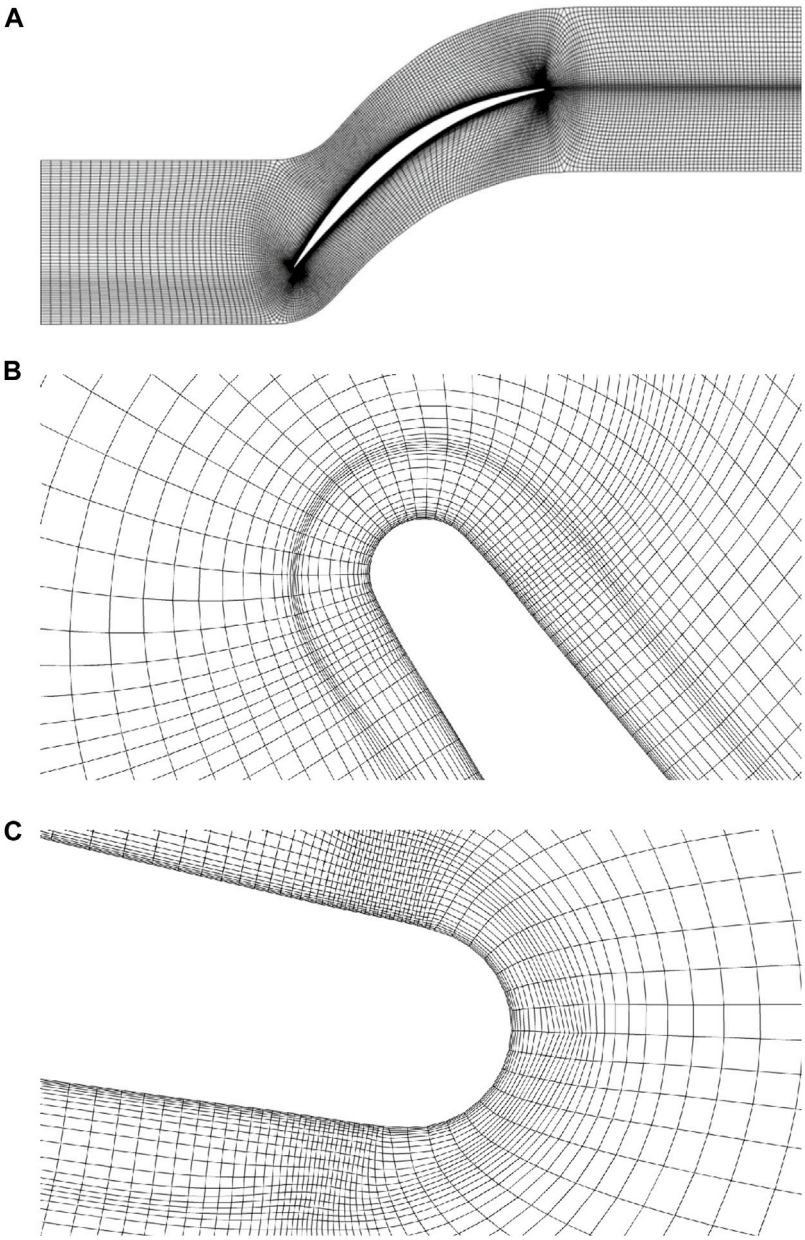

FIGURE 4 | Configuration of calculation mesh grids **(A)** Grids diagram; **(B)** Mesh grids at the leading edge; **(C)** Mesh grids at the trailing edge.

decrease of blade load caused by σ. Another observation is that D_o increases faster for lower cambers at $e/b = 0.2$, which is different from the reference (Sans et al., 2014). It is because that the e/b is different from that of the literature (Sans et al., 2014), while the observation in literature (Sans et al., 2014) agrees with the cases at $e/b \geq 0.3$.

Supplementary Figure S17 shows D_o versus θ with different e/b and σ. D_o increases linearly as θ increases, which is a result of flow turning increase. **Supplementary Figure S18** shows D_o versus e/b with different σ and θ. It can be seen that D_o varies quadratically with e/b, resembling curves of i_o versus e/b in **Supplementary Figure S12**.

3.2.4 Static Pressure Rise Coefficient

Supplementary Figures S19–21 show Cp_{2o} versus σ, θ, and e/b respectively. The trends of Cp_{2o} evolution resemble these of D_o in **Supplementary Figures S16–18**. Besides, it can be noticed that Cp_{2o} is influenced more significantly than D_o by σ.

3.3 Flow Mechanism Analysis of Normal Airfoils

This section aims at revealing how e/b affects the loss-level of the blade and transonic flow of airfoils with normal camber angle ($\theta \leq 40^{\circ}$) without flow separation. Analysis indicates that the related

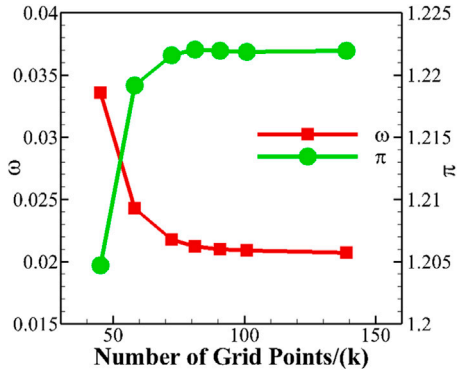

FIGURE 5 | Effect of grid points number on the loss and static preesure ratio.

flow mechanism is the same at $\theta = 35^{\circ}$ and $\theta = 40^{\circ}$. For brevity, the cases with $\theta = 40^{\circ}$ are selected to discuss here. As shown in **Supplementary Figure S22**, the *e/b* can cause a significant influence on velocity distribution at blade surface and load of the blade. With the upstream propagation of *e/b*, the position of suction peak velocity moves forward, and peak velocity increases, which result in the front-loaded velocity distribution. When *e/b* moves forward to a certain extent, the flow after the suction peak decelerates sharply. Besides, suction peak velocity increases with the reduction of solidity, which means a rise in blade loading.

As shown in **Supplementary Figure S23**, the flow separation does not occur in moderate-load blade passage. It can be observed through the flow field that the acceleration in the front portion of the passage amplifies with the upstream propagation of *e/b*. Shock wave generates when *e/b* moves forward to some extent. It indicates that the forward migration of *e/b* induces shock. In conjunction with **Figure 3B**, it can be attributed to that in the flow acceleration region before the shock (before 20% chord), the forward migration of *e/b* causes the increase of the curvature of the suction side, which is conducive to the flow acceleration. By comparing the flow field at different solidities, it can be found that the shock is easy to occur at low σ, which is caused by the increased suction peak velocity. In general, the forward migration of *e/b* and reduction of σ induces the generation of shock.

Supplementary Figure S24 illustrates the velocity gradient on the blade surface, which reflects viscous shear in the boundary layer. It can be seen that in the case without serious shock, the velocity gradient reduces with the forward migration of *e/b* in the most portion (30–80% chord), which indicates the weaker viscous shear. It is the reason why the small *e/b* reduces total pressure loss in the case without shock. By comparing with **Figure 3B**, it can be found that in the deceleration area after the suction peak velocity, the reduction of suction side curvature caused by the upstream propagation of *e/b* contributes to the lower gradient of velocity. In conjunction with analysis of flow field, how the *e/b* alteration influences loss of the blade is demonstrated: in the flow acceleration region before 20% chord, the forward migration of *e/b* induces the generation of shock; while in the deceleration region after the suction peak velocity, the upstream propagation of *e/b* contributes to the weaker viscous shear.

3.4 Flow Mechanism Analysis of High-Load Airfoils

This section illustrates how *e/b* affects the loss of the blade and transonic flow of high-load airfoils with higher camber angle ($\theta \geq 44^{\circ}$) with flow separation. For brevity, the cases with $\theta = 46^{\circ}$ are selected to discuss for the clearer difference. As shown by **Supplementary Figure S25**, the trend of velocity distribution on the blade surface and load of the blade caused by *e/b* and σ are the same as normal airfoils ($\theta \leq 44^{\circ}$, as shown in **Supplementary Figure S22**). The case *e/b* = 0.31 is the optimal *e/b* at $\theta = 46^{\circ}$, σ = 1.25. It should be mentioned that the rise of the camber angle generates a slight drop in suction peak velocity.

Supplementary Figure S26 illustrates the flow field at $\theta = 46^{\circ}$. It can be observed that compared with normal airfoils, flow separation exists at the rear portion of the blade (behind 80% chord). The scale of separation shrinks with the upstream migration of *e/b*. Besides, the effects of *e/b* and σ on

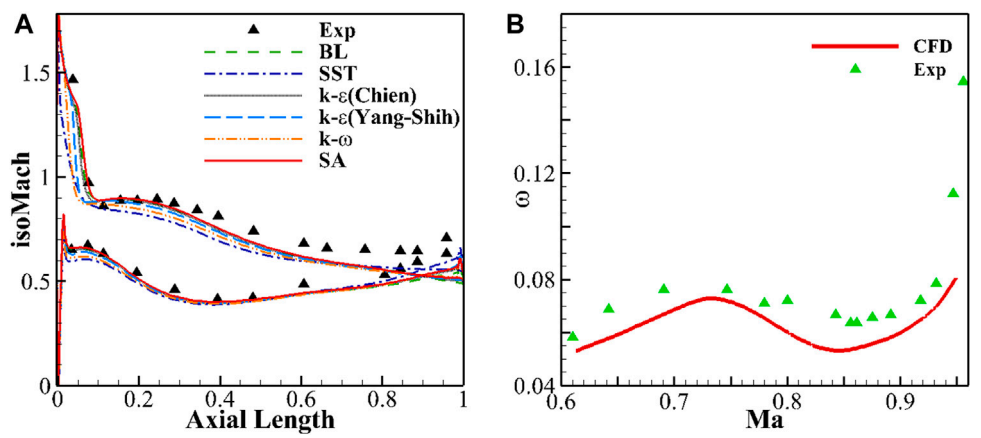

FIGURE 6 | Comparison of numerical and experimental results **(A)** Isentropic Mach distribution of blade surface; **(B)** Total pressure loss versus inlet Mach number.

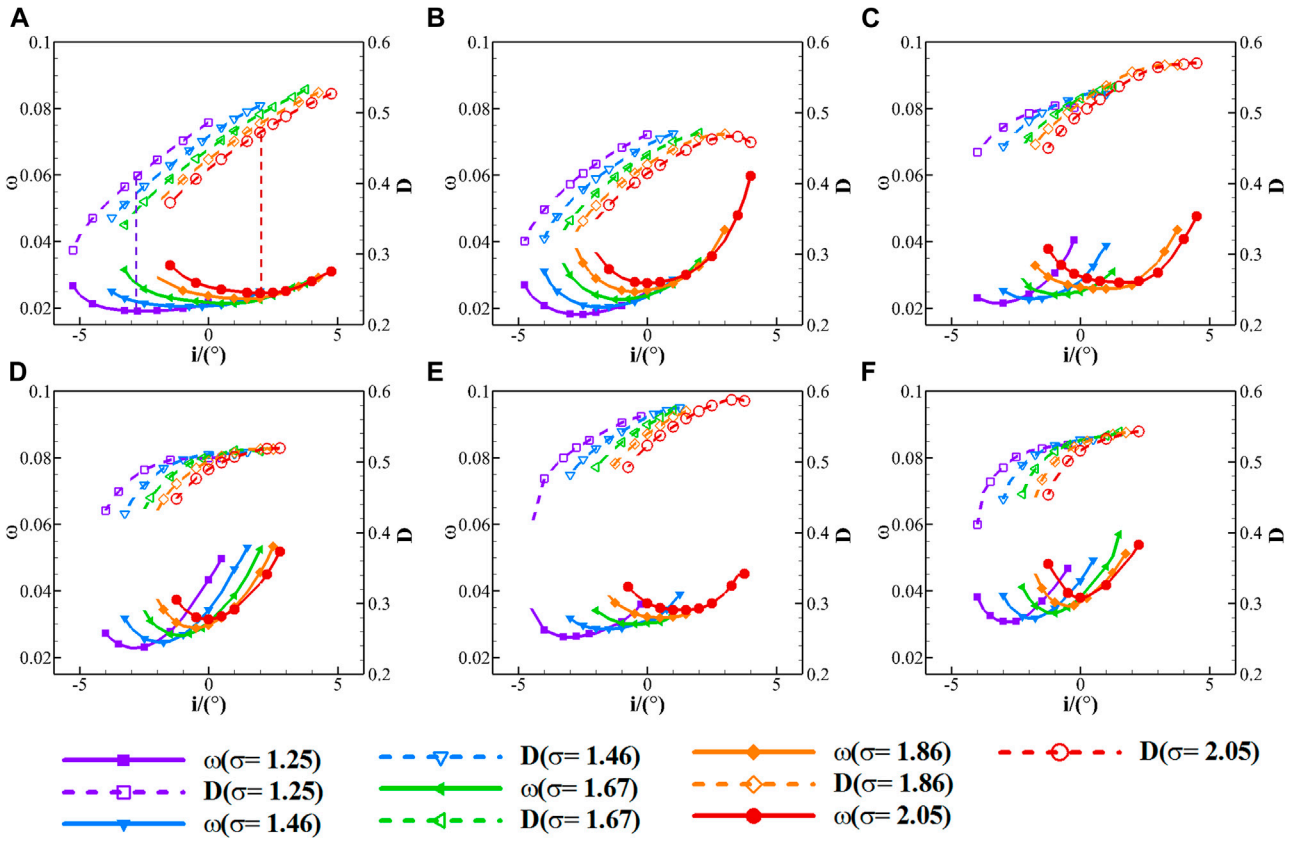

FIGURE 7 | Influence of solidities on incidence characteristics of total pressure loss coefficient and diffusion factor **(A)** e/b = 0.2, $\theta = 40^{\circ}$; **(B)** e/b = 0.6, $\theta = 40^{\circ}$; **(C)** e/b = 0.2, $\theta = 44^{\circ}$; **(D)** e/b = 0.6, $\theta = 44^{\circ}$; **(E)** e/b = 0.2, $\theta = 46^{\circ}$; **(F)** e/b = 0.6, $\theta = 46^{\circ}$.

acceleration flow are the same as that in normal airfoils. It should be noted that the strength of supersonic flow at $\theta = 46^{\circ}$ is weaker than that of $\theta = 40^{\circ}$, which can be attributed to the lower peak velocity in **Supplementary Figure S25**.

The influence of *e/b* on boundary layer behavior is used to explain the reason for loss-level. It can be observed in **Supplementary Figure S27** that the influence of *e/b* on velocity gradient and viscous shear agrees with the trend reflected in **Supplementary Figure S24**. Especially, reverse flow occurs in the area where the velocity gradient is close to zero. At small solidity ($\sigma = 1.25$), the forward migration of *e/b* delays the onset of boundary layer separation.

Supplementary Figure S28 reflects the boundary layer growth before separation. It can be noticed that low *e/b* contributes to the stabilized boundary layer, which reflects in the delay of the onset of rapid growth of boundary layer. The total pressure distribution of blade wake shown in **Supplementary Figure S29** also confirms that the high total pressure loss region of blade wake significantly shrinks with the forward migration of *e/b*. In general, small *e/b* conduces to the drop of the loss (caused by viscous friction) and the separation scale of high-load airfoils, although contributes to the generation of shock.

3.5 Models

Based on the discussion above, it can be inferred that i_o, ω_o, D_o and Cp_{2o} change with σ, θ, and *e/b*, and their correlations can be described by such quadratic multiple regression model as **Eq. 7**. The variable$X = x_i$denotes cascade geometrical parameter (σ, *e/b*, or θ). The variable$N$denotes the number of input parameters (3). The variable$F$denotes performance parameters (i_o, ω_o, D_o, or Cp_{2o}). Variables a、b、c denote model coefficients. The regression models are verified by the coefficient of determination $R^2 \geq 0.96$.

$$F(X) = a_0 + \sum_{i=1}^{N} b_i x_i + \sum_{i=1}^{N} c_i x_i^2 + \sum_{j=2}^{N} \sum_{i=1}^{j-1} c_{ij} x_i x_j \qquad (7)$$

Supplementary Figure S30 shows the comparison of results obtained by models and CFD calculations, in which the horizontal axis and vertical axis represent CFD results and model predicting results. The red lines imply that the results predicted by models are equal to CFD calculations, while blue dots are close to them.

Supplementary Figure S31 shows errors of the model predicting results compared with CFD calculations. The error of minimum loss incidence (Δi_o) is defined as $\Delta i_o = |i_{o,Mod} - i_{o,CFD}|$, in which $i_{o,Mod}$ is estimated by **Eq. 4** and $i_{o,CFD}$ is computed by CFD. It can be observed that Δi_o is no more than $\pm 0.7^{\circ}$. The error of diffusion factor (ΔD_o) is defined as $\Delta D_o = \frac{|D_{o,\ Mod} - D_{o,\ CFD}|}{D_{o,\ CFD}}$, in which $D_{o,\ Mod}$ is estimated by **Eq. 4** and $D_{o,CFD}$ is computed by CFD. It can be observed that ΔD_o is no

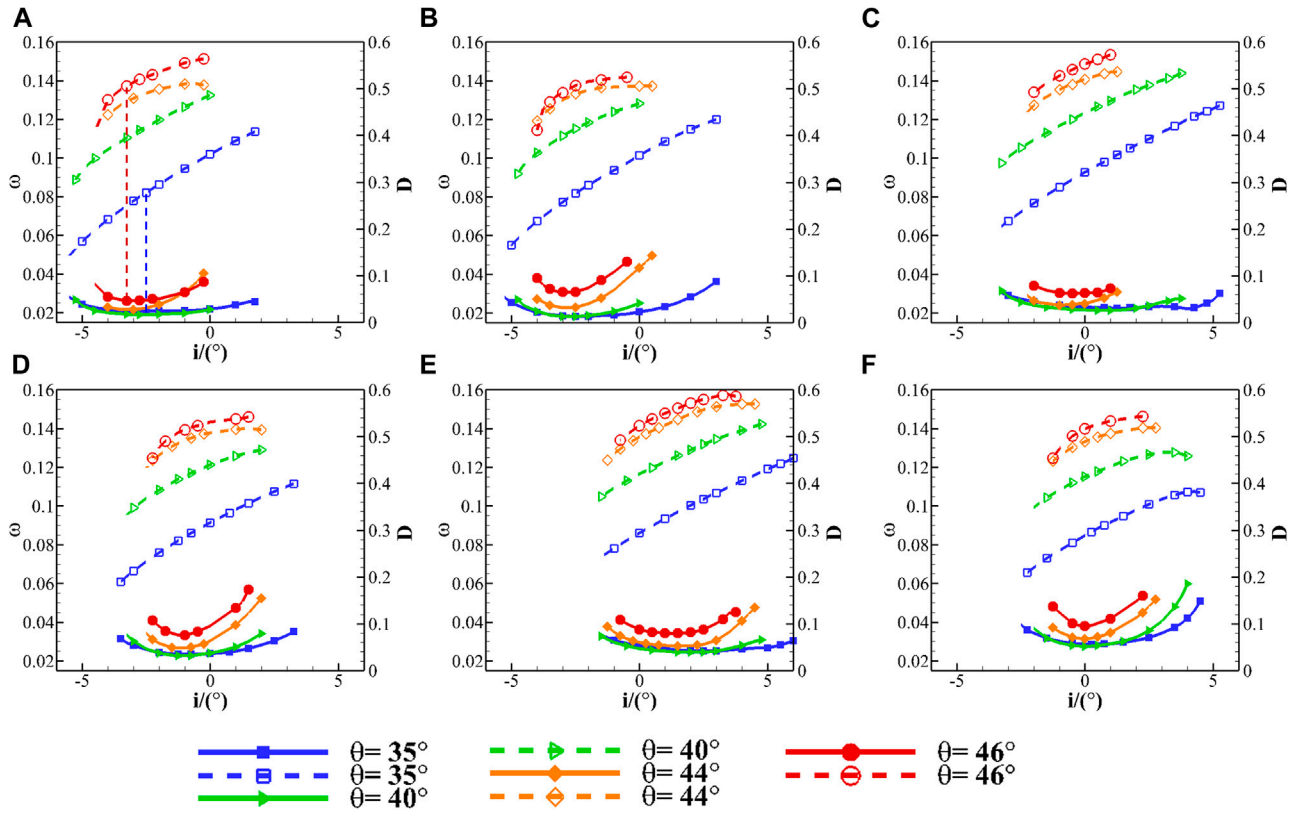

FIGURE 8 | Influence of camber angles on incidence characteristics of total pressure loss coefficient and diffusion factor **(A)** e/b = 0.2, σ = 1.25; **(B)** e/b = 0.6, σ = 1.25; **(C)** e/b = 0.2, σ = 1.67; **(D)** e/b = 0.6, σ = 1.67; **(E)** e/b = 0.2, σ = 2.05; **(F)** e/b = 0.6, σ = 2.05.

more than 5% for most cases. Errors of total pressure loss coefficient ($\Delta\omega_o$) and static pressure rise coefficient (ΔCp_{2o}) are defined in the same way as ΔD_o. In **Supplementary Figures S31C,D**, $\Delta\omega_o$ and ΔCp_{2o} are no more than 8%.

3.6 Application

3.6.1 Loss Variation on Isosurfaces of Camber Angle

The established models help to obtain numerous continuous data in the investigation sample space and to explore the correlations maps of parameters. The distribution of minimum loss (ω_o) is given in **Supplementary Figure S32** when θ is constant. Three axes represent e/b, θ, and σ, while the blue color represents low ω_o. It can be seen in **Supplementary Figure S32** that ω_o rises sharply when θ increases over 44°. For constant θ, the low loss area exists at low σ and upstream e/b. Because the camber angle is determined in premier compressor design, it is necessary to explore the correlations of e/b and σ at selected θ.

Quantitative analysis of total loss variation brought by e/b is necessary in order to evaluate the impact of e/b. It can be found in **Supplementary Figure S32** that for constant θ and σ, the maximum loss is mostly at e/b = 0.6. The total loss variation ($\delta\omega_o$) is defined as $\delta\omega_o = \frac{\omega_{o,e/b=0.6}-\omega_o}{\omega_{o,e/b=0.6}}$. While ω_o is the local total pressure loss coefficient, $\omega_{o,e/b=0.6}$ is the total pressure loss coefficient at e/b = 0.6 with the same σ and θ.

Supplementary Figure S33 displays the distribution of total loss variation ($\delta\omega_o$) caused by the alteration of e/b (θ = 40°), as well as contours of D_o and Cp_{2o}. Three axes of **Supplementary Figure S33** represent σ, e/b, and ω_o, while the red color represents high total loss variation. For each σ, there is a maximum $\delta\omega_o$ (namely, the minimum ω_o) case, whose e/b is called as optimal e/b (e/b_{opt}). Such cases compose the black line named as $(\delta\omega_o)_{\max}$, θ = 40°.

In **Supplementary Figure S33**, contours of D_o and Cp_{2o} at constant θ are displayed under the contour of $\delta\omega_o$. The solid black lines and dashed ones represent contours of D_o and Cp_{2o} respectively. It can be seen that the upstream move of e/b leads to an increase of D_o and Cp_{2o}, which means that the optimum e/b reduces loss and increases diffusion.

All the cases with the maximum of $\delta\omega_o$ composing the surface of e/b_{opt} for selected θ and σ are given in **Supplementary Figure S34**. The points on the surface produce lower loss than those with the same θ and σ but off the surface. It can be observed that e/b_{opt} locates at 25–35% chord. This observation includes but is not limited to the reference (Koller et al., 1999; Kusters et al., 2000; Sieverding et al., 2004).

The distribution of optimal e/b is illustrated in **Supplementary Figure S35**, while $\delta\omega_o$ of e/b_{opt} is shown in **Supplementary Figure S36**. It can be observed that e/b_{opt} moves downstream when θ or σ decreases and the shock generates more easily. It can achieve more than a 10% reduction of total pressure loss at $\theta \geq 44°$.

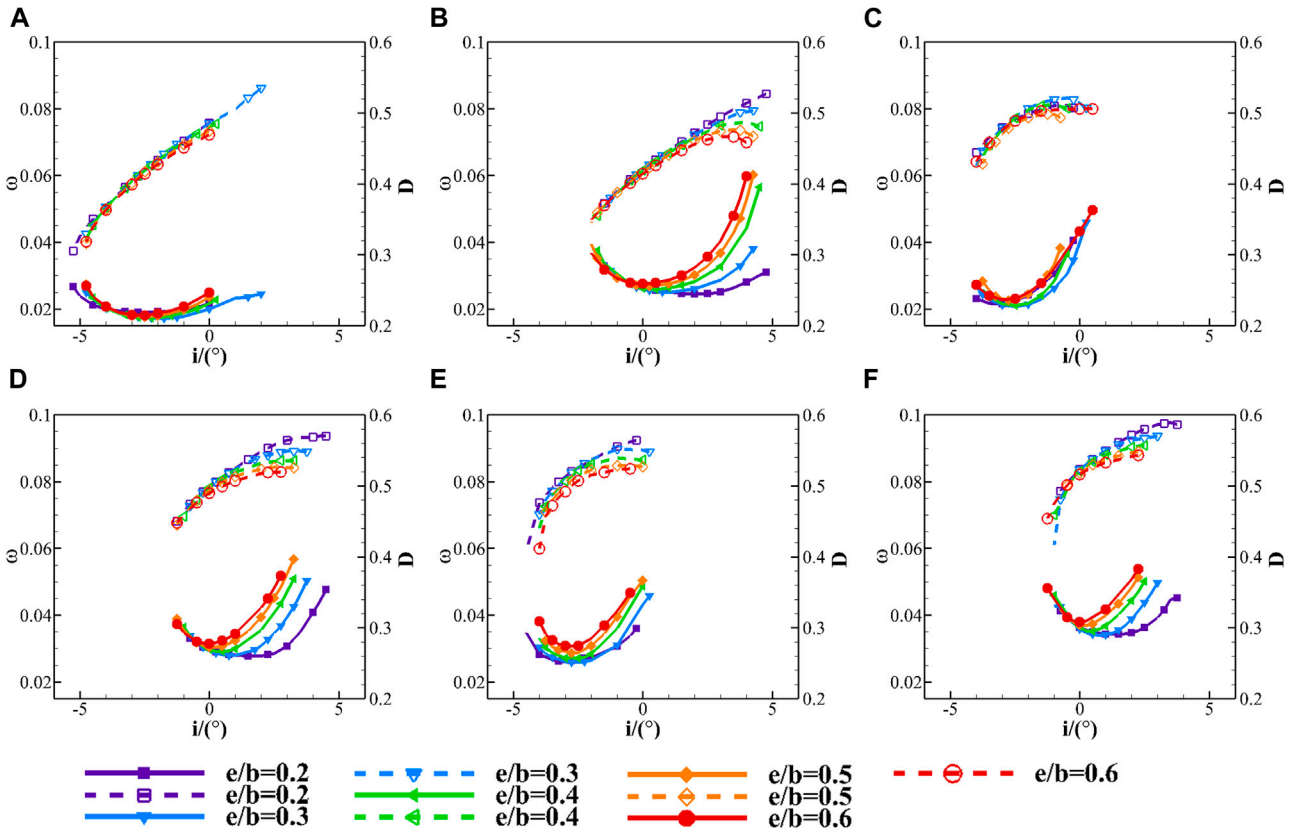

FIGURE 9 | Influence of maximum thickness locations on incidence characteristics of total pressure loss coefficient and diffusion factor **(A)** $\theta = 40^{\circ}$, $\sigma = 1.25$; **(B)** $\theta = 40^{\circ}$, $\sigma = 2.05$; **(C)** $\theta = 44^{\circ}$, $\sigma = 1.25$; **(D)** $\theta = 44^{\circ}$, $\sigma = 2.05$; **(E)** $\theta = 46^{\circ}$, $\sigma = 1.25$; **(F)** $\theta = 46^{\circ}$, $\sigma = 2.05$.

Thus, compared with normal-load airfoils, smaller e/b is preferred to produce excellent aerodynamic performance in high-load cascades, while total loss variation caused by e/b_{opt} is more significant.

The cases with e/b_{opt} ($\theta = 40^{\circ}$ or 46°, $\sigma = 1.25$ or 2.05) in **Supplementary Figure S35** are selected to verify the accuracy of e/b_{opt} predicted by the model. Their velocity distribution and boundary layer behaviors are depicted in details in **Supplementary Figures S22–29**. In conjunction with the previous analysis, it can be found that the e/b_{opt} is the most forward e/b without serious shock loss. Therefore, the preferred selection of e/b for the high subsonic airfoil can be suggested as the most forward e/b with no serious shock loss.

3.6.2 Loss Variation on Isosurfaces of Diffusion Factor

Because diffusion factor indicates blade load, it is necessary to explore correlations of parameters at different D_o. As a result of the predominant effect of θ on D_o, the isosurfaces of D_o in **Supplementary Figure S37** are nearly horizontal and similar to those of θ in **Supplementary Figure S32**.

It can be noticed in **Supplementary Figure S37** that for constants D_o and σ, the maximum loss occurs at $e/b = 0.6$. The $\delta\omega_o$ is still defined as $\delta\omega_o = \frac{\omega_{o,e/b=0.6} - \omega_o}{\omega_{o,e/b=0.6}}$. While ω_o is the local total pressure loss coefficient, $\omega_{o,e/b=0.6}$ is the total pressure loss coefficient at $e/b = 0.6$ with the same σ and D_o.

Supplementary Figure S38 displays $\delta\omega_o$ and ω_o versus σ and e/b when D_o is the constant, as well as contours of Cp_{2o} and θ. At each σ, there is a maximum $\delta\omega_o$ case, whose e/b is the optimal e/b. The black line, named as $(\delta\omega_o)_{\max}$, $D_o = 0.5$, consists of such cases. It can be noticed that e/b_{opt} moves upstream when σ increases.

In **Supplementary Figure S38**, contours of θ and Cp_{2o} are drawn as solid black lines and dashed ones under the contour of $\delta\omega_o$. It can be seen that the upstream move of e/b leads to θ and Cp_{2o} reduction. It means that e/b_{opt} achieves lower ω_o and Cp_{2o} and maintains D_o with lower θ than $e/b = 0.6$ at the same σ.

All the cases with e/b_{opt} at selected σ and D_o among the sample space are given in **Supplementary Figure S39**. The points on the surface produce lower loss than those with the same D_o and σ but off the surface. It can be observed that the e/b_{opt} locates at a 20–35% chord.

3.6.3 Loss Variation on Isosurfaces of Static Pressure Rise Coefficient

The situation where Cp_{2o} is constant is discussed in this part. Because Cp_{2o} rises with the increase of D_o, the isosurfaces of Cp_{2o} in **Supplementary Figure S40** are similar to those of D_o in **Supplementary Figure S37**. Solidity has a significant effect on Cp_{2o}, which causes the difference between isosurfaces of D_o and Cp_{2o}.

Since highest loss occurs at e/b = 0.6 for selected Cp_{2o} and σ, $\delta\omega_o$ is defined as $\delta\omega_o = \frac{\omega_{o,e/b=0.6}-\omega_o}{\omega_{o,e/b=0.6}}$, in which ω_o is the local total pressure loss coefficient and $\omega_{o,e/b=0.6}$is the total pressure loss coefficient at e/b = 0.6 with the same σ and Cp_{2o}.

Supplementary Figure S41 displays $\delta\omega_o$ and ω_o versus σ and e/b when Cp_{2o} is constant, as well as contours of D_o and θ. The black line which is named as $(\delta\omega_o)_{max,\ Cp_{2o}}$ = 0.4 consists of the cases with maximum $\delta\omega_o$ at each σ. At selected Cp_{2o}, the optimal e/b moves forward as σ increases.

In **Supplementary Figure S41**, the solid black lines and dashed ones under the isosurface of Cp_{2o} are contours of θ and D_o. Because θ reduces and D_o increases as e/b decreases, e/b_{opt} achieves lower loss and higher D_o with lower θ than e/b = 0.6 at the same Cp_{2o} and σ.

The cases with e/b_{opt} are given in **Supplementary Figure S42** and produce lower loss than those with the same Cp_{2o} and σ but off the surface. The e/b_{opt} locates at a 20–35% chord.

3.6.4 Database of Optimal Airfoils

All the optimal e/b that can meet the three different kinds of design requirements (selected θ, D_o, or Cp_{2o}) are contained by a database, whose flow chart is shown in **Supplementary Figure S43**. The design requirement is regarded as a restriction, and correlation of optimal e/b, ω_o, D_o, Cp_{2o}, and θ with σ on the line of $(\delta\omega_o)_{max}$ are depicted in maps. According to needed performance parameters (such as ω_o or Cp_{2o}), σ can be chosen appropriately and input. Then corresponding e/b_{opt} and performance parameters (ω_o, D_o, Cp_{2o}) predicted by models are provided as the output.

The program interface of the database is shown in **Supplementary Figure S44**. When the θ input is 44°, maps of e/b_{opt}, ω_o, D_o and Cp_{2o} versus σ are shown below the θ input box in **Supplementary Figure S44A**. It can be seen that as σ increases, e/b_{opt} moves forward, and ω_o, D_o, Cp_{2o} rise. When the desired σ (such as 1.3) is input, corresponding e/b_{opt}, ω_o, D_o and Cp_{2o} are indicated by red stars on the curves, and their values are displayed on the right side. Small σ (for example, σ = 1.25) can be chosen to reduce ω_o, when e/b_{opt} is at 32% chord length. Large σ (for example, σ = 2.05) is available to improve D_o and Cp_{2o}, when e/b_{opt} is at 23% chord length.

The database is also useful when the design goal is to achieve a certain D_o (for example, D_o = 0.45) or Cp_{2o} (for example, Cp_{2o} = 0.4). When D_o is selected, the effects of σ on e/b_{opt}, ω_o, θ and Cp_{2o} are given below the D_o input box in **Supplementary Figure S44B**. It can be seen that as σ increases, e/b_{opt} moves forward, the corresponding θ decreases, while ω_o and Cp_{2o} rise. When Cp_{2o} is selected, the effects of σ on e/b_{opt}, ω_o, θ and D_o are presented below the Cp_{2o} input box in **Supplementary Figure S44C**. As σ increases, e/b_{opt} moves forward, corresponding θ and D_o decrease, and ω_o rises. Therefore, the predetermined Cp_{2o} can be achieved at σ = 1.25 with the lowest ω_o, when e/b_{opt} is at 33% chord length.

4 CONCLUSION

This paper aims to investigate the influence of geometrical parameters (e/b, θ, σ) on the aerodynamic performance (D_o, ω_o, Cp_{2o}) of high subsonic stator airfoil. Numerical investigation indicates that optimization of e/b can lead to a considerable reduction of loss level at minimum loss incidence condition. The key conclusions are as follows:

1) Substantial two-dimensional cascade cases are simulated through validated numerical methods. It is indicated that D_o, ω_o, and Cp_{2o} versus σ are linear, but quadratic versus e/b. D_o and Cp_{2o} versus θ are linear, while ω_o versus θ is quadratic.
2) In the flow acceleration region before the 20% chord, the forward migration of e/b causes the increase of the curvature of the suction side. It is conducive to the flow acceleration and induces the generation of shock. While in the deceleration region after the suction peak velocity, the reduction of suction side curvature caused by the upstream propagation of e/b contributes to the drop of loss and separation scale. Therefore, the preferred selection of e/b can be suggested as the most forward e/b with no serious shock loss.
3) Quadratic multiple regression models of performance parameters are established. The models help to obtain the optimal e/b surfaces at selected θ, D_o or Cp_{2o}. The results show that when e/b_{opt} locates at 20–35% chord, $\delta\omega_o$ is maximum. As θ, D_o, or Cp_{2o} increase, $\delta\omega_o$ becomes more significant. So, the selection of e/b has an important effect on high-load blade profile.
4) A database is established to meet design requests, which provides optimal e/b according to the selected θ, D_o, Cp_{2o} and σ. When θ is selected, maps of performance parameters (ω_o, D_o, Cp_{2o}) versus σ are depicted, according to which σ can be appropriately chosen. When selected σ is input, corresponding optimal e/b and performance parameters predicted by models are presented as the output. The database also helps when the design request is selected D_o or Cp_{2o}.

DATA AVAILABILITY STATEMENT

The original contributions presented in the study are included in the article/**Supplementary Material**, further inquiries can be directed to the corresponding author.

AUTHOR CONTRIBUTIONS

CT provides innovation, numerical simulation experiment, model establishment and writing for this article. XD provides financial support and guidance about the content of the article. JD and ZW contributes similar to XD. YL has engaged in some technical work.

FUNDING

This research is supported by the National Natural Science Foundation of China (Grant No. 51906049), China Postdoctoral Science Foundation (No. 2020M671672) and the National Science and Technology Major Project (No. 2017-II-0007-0021).

SUPPLEMENTARY MATERIAL

The Supplementary Material for this article can be found online at: https://www.frontiersin.org/articles/10.3389/fenrg.2021.791542/full#supplementary-material

REFERENCES

Britsch, W. R. (1979). *Effects of Diffusion Factor, Aspect Ratio and Solidity on Overall Performance of 14 Compressor Middle Stages*. Washington: National Aeronautics and Space Administration.

Bruna, D., Cravero, C., and Turner, M. G. (20062006). The Development of an Aerodynamic Performance Prediction Tool for Modern Axial Flow Compressor Profiles. *Proc. ASME Turbo. Expo* 6, 113–122. doi:10.1115/gt2006-90187

Burberi, C., Michelassi, V., Del Greco, A. S., Lorusso, S., Tapinassi, L., Marconcini, M., et al. (2020). Validation of Steady and Unsteady CFD Strategies in the Design of Axial Compressors for Gas Turbine Engines. *Aerosp. Sci. Technol.* 107. doi:10.1016/j.ast.2020.106307

Carter, A. D. S. (1950). *The Low Speed Performance of Related Aerofoils in Cascades*. A.R.C. Tech. Report, Report No.R.55. Washington: NGTE.

Dunker, R., Rechter, H., Starken, H., and Weyer, H. (1984). Redesign and Performance Analysis of a Transonic Axial Compressor Stator and Equivalent Plane Cascades with Subsonic Controlled Diffusion Blades. *J. Eng. Gas Turbines Power* 106, 279–287. doi:10.1115/1.3239560

Elazar, Y., and Shreeve, R. P. (1990). Viscous Flow in a Controlled Diffusion Compressor Cascade with Increasing Incidence. *J. Turbomach.* 112, 256–265. doi:10.1115/1.2927642

Horlock, J. H., and Denton, J. D. (2005). A Review of Some Early Design Practice Using Computational Fluid Dynamics and a Current Perspective. *J. Turbomach.* 127, 5–13. doi:10.1115/1.1650379

Howell, A. R. (1945). Fluid Dynamics of Axial Compressors. *Proc. Inst. Mech. Eng.* 153, 441–452. doi:10.1243/pime_proc_1945_153_049_02

Hu, H. D., Yu, J. Y., Song, Y. P., and Chen, F. (2021). The Application of Support Vector Regression and Mesh Deformation Technique in the Optimization of Transonic Compressor Design. *Aerosp. Sci. Technol.* 112, 106589. doi:10.1016/j.ast.2021.106589

I. A. Johnsen and R. O. Bullock (Editors) (1965). *Aerodynamic Design of Axial-Flow Compressors* (Washington: Scientific and Technical Information Division, National Aeronautics and Space Administration), 36.

Jiang, B., Zheng, Q., Zhang, H., Zhang, X. L., Chen, Z. L., Qiu, Y., et al. (2015). Advanced Axial Compressor Airfoils Design and Optimization. *Asme. Turbo. Expo. Turbine Tech. Conf. Exposition* 2a, 11. doi:10.1115/gt2015-43846

Ju, Z. Z., Teng, J. F., Zhu, M. M., Ma, Y. C., Qiang, X. Q., Fan, L., et al. (2020). Flow Characteristics on a 4-stage Low-Speed Research Compressor with a Cantilevered Stator. *Aerosp. Sci. Technol.* 105, 106033. doi:10.1016/j.ast.2020.106033

Köller, U., Mönig, R., Küsters, B., and Schreiber, H.-A. (2000). Development of Advanced Compressor Airfoils for Heavy-Duty Gas Turbines - Part I: Design and Optimization. *J. Turbomach.* 122, 397–405. doi:10.1115/1.1302296

Kusters, B., Schreiber, H. A., Koller, U., and Monig, R. (2000). Development of Advanced Compressor Airfoils for Heavy-Duty Gas Turbines - Part II: Experimental and Theoretical Analysis. *J. Turbomach.* 122, 406–414. doi:10.1115/99-GT-096

Larosiliere, L. M., Wood, J. R., Hathaway, M. D., Medd, A. J., and Dang, T. Q. (2002). *Aerodynamic Design Study of Advanced Multistage Axial Compressor*. Washington: National aeronautics and space administration cleveland oh glenn research center.

Li, S. B. (2007). "Design of Highly Loaded Dihedral Stator and Investigation on the Aerodynamic Stage Performance in an Axial Transonic Compressor," Doctor Thesis (China: Harbin Institute of Technology).

Lieblein, S. (1955). *Aerodynamic Design of Axial-Flow Compressors: VI-experimental Flow in Two-Dimensional Cascades*. Cleveland, OH: NACA Research Memorandum, Lewis Flight Propulsion Laboratory.

Lieblein, S., Schwenk, F. C., and Broderick, R. L. (1953). *Diffusion Factor for Estimating Losses and Limiting Blade Loadings in Axial-Flow-Compressor Blade Elements*. Cleveland, OH: NACA Research Memorandum, Lewis Flight Propulsion Laboratory.

Niederdrenk, P., Sobieczky, H., and Dulikravich, G. S. (1987). Supercritical Cascade Flow Analysis with Shock-Boundary Layer Interaction and Shock-free Redesign. *J. Turbomach.* 109, 413–419. doi:10.1115/1.3262121

NUMECA International (2015). *IGG v10.1, User Manual*. Brussels: NUMECA International.

Qiang, X. Q., Wang, S. T., Feng, G. T., and Wang, Z. Q. (2008). Aerodynamic Design and Analysis of a Low-Reaction Axial Compressor Stage. *Chin. J. Aeronaut.* 21, 1–7. doi:10.1016/S1000-9361(08)60001-1

Sans, J., Resmini, M., Brouckaert, J. F., and Hiernaux, S. (20142014). Numerical Investigation of the Solidity Effect on Linear Compressor Cascades. *Proc. Asme. Turbo. Expo. Turbine Tech. Conf. Exposition* 2a, 15. doi:10.1115/gt2014-25532

Shi, H., and Ji, L. (2021). Leading Edge Redesign of Dual-Peak Type Variable Inlet Guide Vane and its Effect on Aerodynamic Performance. *Proc. Inst. Mech. Eng. G: J. Aerospace Eng.* 235, 1077–1090. doi:10.1177/0954410020966168

Sieverding, F., Ribi, B., Casey, M., and Meyer, M. (2004). Design of Industrial Axial Compressor Blade Sections for Optimal Range and Performance. *J. Turbomach.* 126, 323–331. doi:10.1115/1.1737782

Song, B., and Ng, W. F. (2006). Performance and Flow Characteristics of an Optimized Supercritical Compressor Stator cascade. *J. Turbomach.* 128, 435–443. doi:10.1115/1.2183316

Spalart, P. R., and Allmaras, S. R. (1994). *A One-Equation Turbulence Model for Aerodynamic Flows*. Seattle: Rech. Aerospatiale, 5–21.

Steinert, W., Eisenberg, B., and Starken, H. (1991). Design and Testing of a Controlled Diffusion Airfoil Cascade for Industrial Axial Flow Compressor Application. *J. Turbomach.* 113, 583–590. doi:10.1115/1.2929119

Sun, S., Chen, S., Liu, W., Gong, Y., and Wang, S. (2018). Effect of Axisymmetric Endwall Contouring on the High-Load Low-Reaction Transonic Compressor Rotor with a Substantial meridian Contraction. *Aerospace Sci. Tech.* 81, 78–87. doi:10.1016/j.ast.2018.08.001

Sun, S. J., Wang, S. T., and Chen, S. W. (2020). Design, Modification and Optimization of an Ultra-high-load Transonic Low-Reaction Aspirated Compressor. *Aerosp. Sci. Technol.* 105, 105975. doi:10.1016/j.ast.2020.105975

Sun, S. J., Wang, S. T., and Chen, S. W. (2019). The Influence of Diversified Forward Sweep Heights on Operating Range and Performance of an Ultra-high-load Low-Reaction Transonic Compressor Rotor. *Energy* 194, 116857. doi:10.1016/j.energy.2019.116857

Sun, S. J., Wang, S. T., Zhang, L. X., and Ji, L. C. (2021). Design and Performance Analysis of a Two-Stage Transonic Low-Reaction Counter-rotating Aspirated Fan/compressor with Inlet Counter-swirl. *Aerosp. Sci. Technol.* 111, 106519. doi:10.1016/j.ast.2021.106519

Wang, M. Y., Li, Z. L., Yang, C. W., Han, G., Zhao, S. F., and Lu, X. G. (2020). Numerical Investigations of the Separated Transitional Flow over Compressor Blades with Different Loading Distributions. *Aerosp. Sci. Technol.* 106, 106113. doi:10.1016/j.ast.2020.106113

Wang, Z. A., Chang, J. T., Li, Y. F., and Kong, C. (2021). Investigation of Shock Wave Control by Suction in a Supersonic cascade. *Aerosp. Sci. Technol.* 108, 106382. doi:10.1016/j.ast.2020.106382

Xu, W., Du, X., Tao, C., Wang, S., and Wang, Z. (2019). Correlation of Solidity, Aspect Ratio and Compound Lean Blade in Compressor cascade Design. *Appl. Therm. Eng.* 150, 175–192. doi:10.1016/j.applthermaleng.2018.12.167

Xu, W., Du, X., Wang, S., and Wang, Z. (2018). Correlation of Solidity and Curved Blade in Compressor cascade Design. *Appl. Therm. Eng.* 131, 244–259. doi:10.1016/j.applthermaleng.2017.12.003

Zhang, L., Wang, S., and Zhu, W. (2019). Application of Endwall Contouring in a High-Subsonic Tandem cascade with Endwall Boundary Layer Suction. *Aerospace Sci. Tech.* 84, 245–256. doi:10.1016/j.ast.2018.08.041

Zweifel, O. (1945). The Spacing of Turbo-Machine Blading, Especially with Large Angular Deflection. *Brown Boveri Rev.* 32, 436–444.

Conflict of Interest: JD was employed by Hangzhou Turbine Power Group Co., Ltd.

The remaining authors declare that the research was conducted in the absence of any commercial or financial relationships that could be construed as a potential conflict of interest.

Publisher's Note: All claims expressed in this article are solely those of the authors and do not necessarily represent those of their affiliated organizations, or those of the publisher, the editors and the reviewers. Any product that may be evaluated in this article, or claim that may be made by its manufacturer, is not guaranteed or endorsed by the publisher.

GLOSSARY

h/b aspect ratio
h blade height
b chord
R^2 coefficient of determination
kk curvature of camber
D diffusion factor
P* total pressure
T* total temperature
v velocity
c thickness
i incidence angle
Ma Mach number
e/b maximum thickness location
Re Reynolds number
P static pressure
Cp_2 static pressure rise coefficient
β_p blade angle
θ camber angle
ω the total pressure loss coefficient
ΔD errors of diffusion factor
$\delta\omega$ Total loss variation
δD improvement of diffusion factor
δCp_2 improvement of static pressure rise coefficient
$\delta\theta$ improvement of camber angle
Δv velocity-difference
σ solidity
Δi errors of incidence
ΔCp_2 errors of static pressure rise coefficient
$\Delta\omega$ errors of total pressure loss coefficient
o minimum incidence
Mod model
u tangential
1 inlet
2 outlet
max maximum
min minimum

frontiers in Energy Research

ORIGINAL RESEARCH
published: 11 January 2022
doi: 10.3389/fenrg.2021.810439

Analysis of Tangential Combustion Instability Modes in a LOX/Kerosene Liquid Rocket Engine Based on OpenFOAM

Kangkang Guo, Boqi Xu, Yongjie Ren, Yiheng Tong and Wansheng Nie**

Department of Aerospace Science and Technology, Space Engineering University, Beijing, China

Self-excited high frequency combustion instability (HFCI) of first-order tangential (1T) mode was observed in a staged-combustion LOX/Kerosene liquid rocket engine numerically. Two different kinds of 1T patterns, standing wave mode and traveling wave mode, were captured in the present work. In the nominal operation condition, the ratio of oxygen-to-fuel (O/F) was 2.5. Propellant was evenly distributed in all injectors and no HFCI occurred. The chamber pressure obtained from the numerical simulation and experiment showed a good agreement, which validated the numerical model. When the mass flow of fuel for two injectors was modified, severe HFCI occurred. The pressure wave node was located at a fixed diameter, showing a 1T standing wave mode. As the O/F was set 4.4 and the propellant distribution was completely uniform, the numerical result yielded a 1T wave node featured a spinning behavior, which was a traveling 1T wave mode. Once the HFCI arose, no matter what standing mode or spinning mode, the pressure and heat release oscillated totally in phase temporally and coupled spatially. The heat release from combustion was fed into the resonant acoustic mode. This was the thermoacoustic coupling process that maintained the HFCI.

Keywords: combustion instability, LOX/kerosene liquid rocket engine, sprayFOAM solver, ratio of oxygen-to-fuel, thermo-acoustic coupling

OPEN ACCESS

Edited by:
Xiao Liu,
Harbin Engineering University, China

Reviewed by:
Fan Zhag,
Tianjin University, China
Zun Cai,
National University of Defense Technology, China
Wu Yi,
Beijing Institute of Technology, China

****Correspondence:***
Yiheng Tong
yiheng_tong@sina.com
Wansheng Nie
SEUpropulsion@126.com

Specialty section:
This article was submitted to Advanced Clean Fuel Technologies, a section of the journal Frontiers in Energy Research

Received: *07 November 2021*
Accepted: *08 December 2021*
Published: *11 January 2022*

Citation:
Guo K, Xu B, Ren Y, Tong Y and Nie W (2022) Analysis of Tangential Combustion Instability Modes in a LOX/Kerosene Liquid Rocket Engine Based on OpenFOAM. Front. Energy Res. 9:810439. doi: 10.3389/fenrg.2021.810439

INTRODUCTION

HFCI remains an unresolved problem for the development of liquid rocket engines (LREs). Advanced heavy rocket engines are a prominent demand of farther space exploration. However, HFCI still acts as a big obstacle in the way since 1940s (Harrje, 1972; Culick and Yang, 1995). HFCIs have the characteristics of pressure oscillations at frequencies on the order of kilohertz, corresponding to the chamber's resonant acoustic modes. HFCI is extraordinarily destructive, especially the 1T mode, which can destroy the cooling fluid film attached to the chamber wall and further give rise to extensive heat transfer to the injector faceplate and chamber wall (Dranovsky et al., 1994). Therefore, once the HFCI of 1T mode occurs, the combustion chamber would suffer a severe thermal load even completely be destroyed in some extreme conditions. As shown in **Figure 1**, there are three examples that LRE was damaged by HFCI.

Rayleigh Criterion (Rayleigh, 1878; Rayleigh and Nachtrieb, 1957) is a widely accepted and significant consensus used for explaining the maintaining mechanism of thermo-acoustic instability. Rayleigh thought that the time the pressure was at its peak was when heat was added to a system in an oscillatory cycle, as the oscillation would be encouraged and the amplitude would increase; but if the

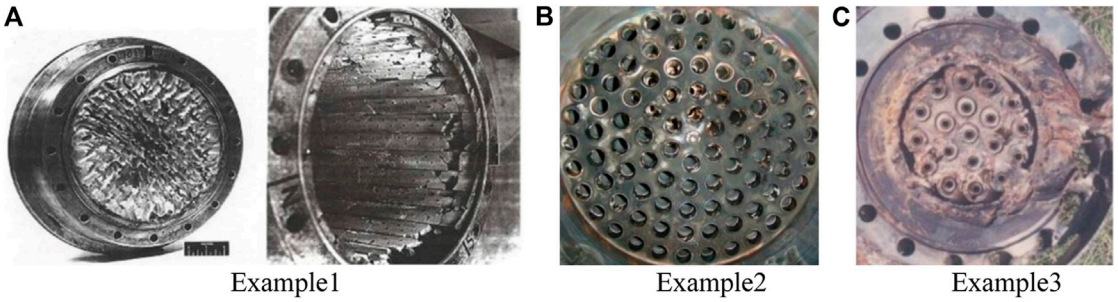

FIGURE 1 | Three damaged LREs caused by HFCI. **(A)** Example1. **(B)** Example2. **(C)** Example1.

heat was extracted from the system when the pressure was at its peak value, the oscillation would be discouraged, and the amplitude would decrease. Almost every LRE suffered from HFCI during its development process, and the deep reason that results in HFCI has not been uncovered until now. Therefore, HFCI should be paid sufficient attention for its theoretical and engineering significance. The most firsthand and effective methods are the full-scale tests. Unfortunately, the full-scale tests are expensive and time-consuming, and thus impractical. When the development of a rocket engine is hampered by HFCIs, the approach usually taken is the trial-and-error procedures, like the development campaigns of F-1 engine of the Apollo project (Oefelein and Yang, 1993). There are over 2,000 full-scale engine tests with approximately 100 diverse injector designs were performed to solve the problems caused by HFCIs.

With the rapid growth of computer processing power, computational fluid dynamics (CFD) has become more prevalent in modeling combustion instabilities. Numerical simulation methods of different levels, from low to high fidelity, have been developed over the last decade. Tremendous efforts have been devoted to building reduced-order models (Frezzotti et al., 2018) and high-fidelity simulation models (Garby et al., 2013; Urbano et al., 2016).

Combined experimental and computational studies have shown a promising path for investigating combustion instabilities. A continuously variable resonance combustor (CVRC), developed at Purdue University specifically for the investigation of longitudinal combustion instability, has been studied both experimentally (Miller et al., 2007; Yu et al., 2012) and numerically (Harvazinski et al., 2015). The results indicated that combustion instability was associated with periodic vortex shedding. Subsequently, a seven-element (Pomeroy and Anderson, 2016; Popov and Sirignano, 2016) and a nine-element (Orth et al., 2018; Gejji et al., 2020) sub-scale rocket combustor was designed to boost self-excited transverse instabilities. In-depth numerical simulations (Tudisco et al., 2016; Harvazinski et al., 2019) based on the experimental setup were performed. It was found that the mass flow rate of the outer injectors was altered by the transverse pressure waves resulting in a sudden heat release, which eventually triggered the transverse combustion instability. A multi-injector cryogenic propellant rocket combustor, characterized by 1T mode self-excited combustion instability, was conducted in the German Aerospace Center (Gröning et al., 2016; Hardi et al., 2016; Armbruster et al., 2020; Klein et al., 2020). Urbano et al. (2016) conducted a corresponding high-fidelity calculation, which is a landmark work for its high accuracy and enormous computing load. Both the experimental analysis and numerical results indicated that the 1T mode thermoacoustic instability was strongly coupled with oxidizer injectors.

In this paper, the HFCI of a Kero/LOX LRE is studied numerically based on OpenFOAM (Open Source Field Operation and Manipulation), and the mechanism of combustion instability is analyzed. Previous experiment research (Bibik et al., 2008a; Bibik et al., 2008b) has indicated that the 1T HFCI mode has two behaviors: standing wave and traveling wave. The work in this paper concentrates on detailing the mechanisms of the two patterns of 1T HFCI mode.

NUMERICAL SIMULATION MODEL

In gas-liquid two-phase spray combustion, the most mainstream methods are Lagrange-drop and Eulerian-fluid (LDEF). In the LDEF frame, the gas phase is processed as a continuous medium while the liquid phase is treated as discrete particles, and the interaction between the gas phase and discrete particle phase is considered. In the current work, the oxidizer is gaseous while the fuel is liquid. Therefore, the gaseous oxidizer is modeled in a Eulerian framework, while the liquid fuel is modeled in a Lagrangian framework. Compressible Reynolds-averaged Navier-Stokes (RANS), the most widely used numerical simulation method in engineering, was adopted in this paper.

Governing Equations and CFD Solver

The CFD calculations were performed based on OpenFOAM, which is an open-source, object-oriented code developed by OpenCFD. In this work, the sprayFoam solver, a spray and combustion code, was used. Eulerian-Lagrangian simulation framework was adopted. The gas phase is solved in an Eulerian framework and governed by Navier-Stokes (N-S) equations with chemical reactions, where the equations are considered to be continuous in space and time. The general form of the governing equation, which is the conservative three-

TABLE 1 | Chemical reaction mechanism.

Reaction	A	E_a	n_{KERO}	n_{O2}
$C_{12}H_{26} + 18.5O_2 \rightarrow 12CO_2 + 13H_2O$	2.587E9	1.256E8	0.25	1.5

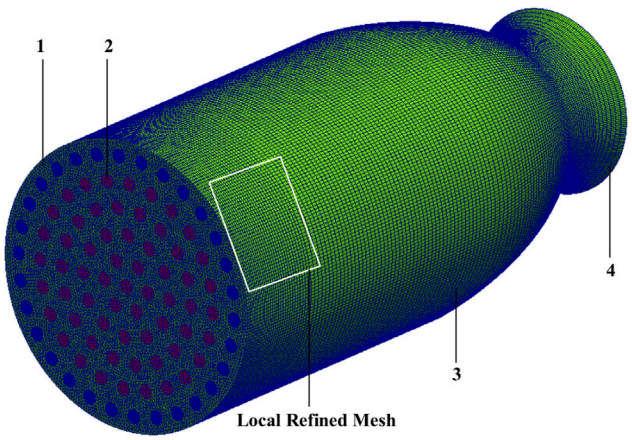

FIGURE 2 | Unstructured mesh.

dimensional N-S equations in a rectangular coordinate system, is given as follows (Veynante and Vervisch, 2002).

$$\frac{\partial \vec{U}}{\partial t} + \frac{\partial\left(\vec{F} - \vec{F}_v\right)}{\partial x} + \frac{\partial\left(\vec{G} - \vec{G}_v\right)}{\partial y} + \frac{\partial\left(\vec{H} - \vec{H}_v\right)}{\partial z} = \vec{J} \quad (1)$$

Where $\vec{U}$ is the conservative variable vector, t is the time variable, $\vec{F}$, $\vec{G}$, $\vec{H}$ and $\vec{F}_v$, $\vec{G}_v$, $\vec{H}_v$ are the convection item vectors and viscous term vectors, respectively, and $\vec{J}$ denotes the source term vector. Equation of components (continuity equation), momentum equation, and energy equation in the directions of x, y, and z are all included by the above equation.

The liquid spray is modeled in a Lagrangian framework. A standard discrete droplet method (DDM) approach is used. To calculate the evolution of the location and velocity components of the parcels, a set of differential equations along the trajectory of each particle is solved. Each parcel stands for a class of identical and non-interacting droplets. To model interaction between discrete droplets and continuous phase, the parcels are tracked through the physical space in a Lagrangian manner based on the mass, momentum, and energy exchange with the gas phase. In the present work, the coneNozzleInjection model served as the injection model, where the atomization cone is set as 90° according to the experimental result. The Rosin-Rammler distribution model, as the most widely used model, was adopted with an average droplet diameter equal to 50 μm. The RanzMarshall model was used to model the droplet heat transfer. Meanwhile, the dispersive and break-up models were not considered.

TABLE 2 | Boundary conditions of internal flow field.

NO	Name	Boundary condition
1	injector inlet	mass flow inlet
2	injector face	no-slip and thermal- isolation wall
3	chamber wall	no-slip and thermal- isolation wall
4	nozzle outlet	pressure outlet

TABLE 3 | Configuration of chamber and initial parameters.

Parameters of Kerosene/LOX LRE	Value
diameter of chamber (mm)	200
diameter of throat (mm)	98
length of chamber (mm)	400
mass flow of fuel (kg/s)	13/10.5
inlet temperature of fuel (K)	450
mass flow of oxidant (kg/s)	32.5/46.2
inlet temperature of oxidant (K)	600
pressure of outlet (pa)	101325
temperature of outlet (K)	300
propellant mixture ratio (O/F)	2.5/4.4

Discretization Scheme and Solution of the Equation

The finite volume method (FVM) was adopted to discretize the governing equation mentioned above. For the strong nonlinear coupling of N-S equations, the coupling between pressure and velocity was modeled by the PIMPLE algorithm (Veynante and Vervisch, 2002). As for the discretization process for viscous terms and convective terms, interface interpolation with second-order precision was achieved with the central difference scheme and Van Leer scheme, respectively. The backward difference scheme with second-order precision is applied for the time term.

Chemical Reaction Mechanism

It is difficult to obtain an accurate chemical reaction process because kerosene is a mixture of hundreds of components. In this paper, $C_{12}H_{26}$ served as the alternative fuel and a single-step global chemical reaction mechanism is adopted to model the chemical reaction process. The chemical reaction rate is calculated by the following equation.

$$K_f = \mathrm{A}e^{-\mathrm{E_a}/T} c_{KERO}^{n_{KERO}} C_{O_2}^{n_{O_2}} \quad (2)$$

Where A is the pre-exponential factor, E_a is the activation energy, T is the temperature with unit K, and c_{KERO} and c_{O_2} denote the molar concentration of kerosene and oxygen with unit mol/cm^3, respectively. The specific chemical reaction mechanism is listed in **Table 1**.

Turbulent Model and Turbulent Combustion Model

Regarding the turbulent model, in consideration of calculated quantity, the standard $k - \varepsilon$ two equations model is chosen. The

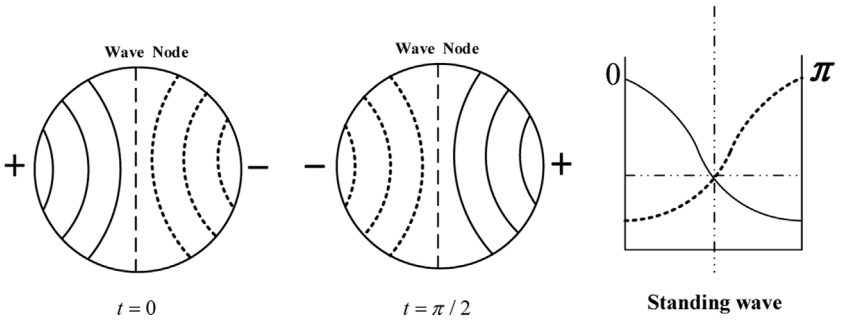

FIGURE 3 | Standing wave 1T vibration mode structure.

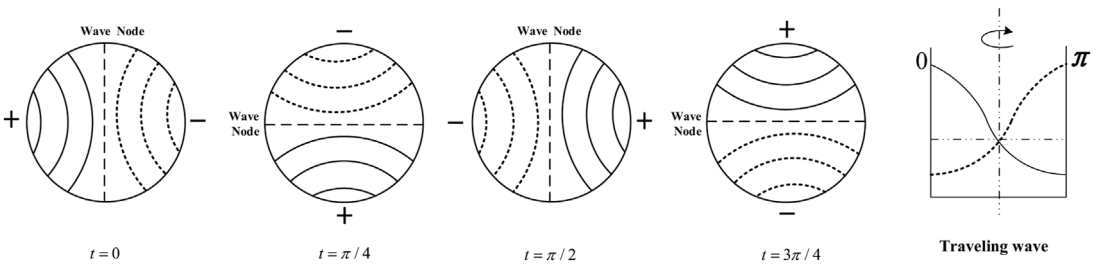

FIGURE 4 | Traveling wave 1T vibration mode structure.

eddy–dissipation (ED) model is selected to model the interaction between turbulence and chemical reactions. The ED model is established based on the Eddy Break-Up (EBU) model (Peters, 2000). In the ED model, it is assumed that the combustion process is mixing-limited and the complex chemical kinetic rates are negligible (Peters, 2000; Veynante and Vervisch, 2002). Undoubtedly, the non-premixed flames for the staged-combustion rocket motor in the present work are mixing-controlled.

Mesh, Boundary Conditions, and Geometry Parameters

Unstructured mesh is used in paper, as is shown in **Figure 2**. The mesh contains about 1.38 million cells, and the region near the injector face is refined, since the chemical reaction takes place in this region. The boundary conditions of the computational domain are listed in **Table 2**. The geometrical parameters of the LRE and initial conditions in this work are detailed in **Table 3**.

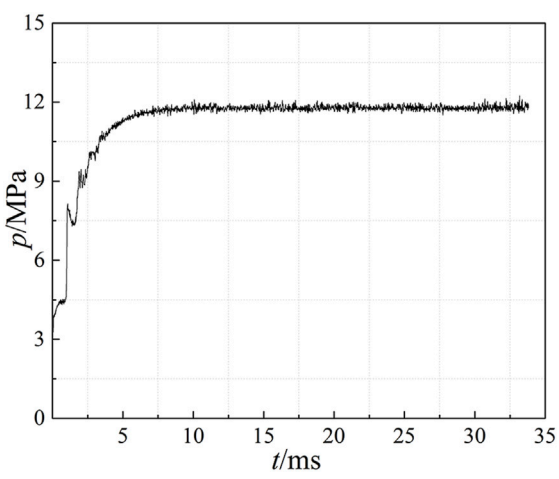

FIGURE 5 | Numerical simulation based on experiment (probe is near the wall and 50 mm downstream from injector faceplate).

COMBUSTION CHAMBER ACOUSTIC THEORY

The LRE chamber can be simplified into a cylinder with two closed sides. The wave equation in the cylinder is given below (Yu et al., 2012).

$$\frac{\partial^2 p'}{\partial t^2} = c^2\left(\frac{\partial^2 p'}{\partial x^2} + \frac{\partial^2 p'}{\partial r^2} + \frac{1}{r}\frac{\partial p'}{\partial r} + \frac{1}{r^2}\frac{\partial^2 p'}{\partial \theta^2}\right) \tag{3}$$

Where p' represent the pressure disturbance, c is chemical equilibrium acoustic velocity, and x, r, θ are the cylindrical coordinates.

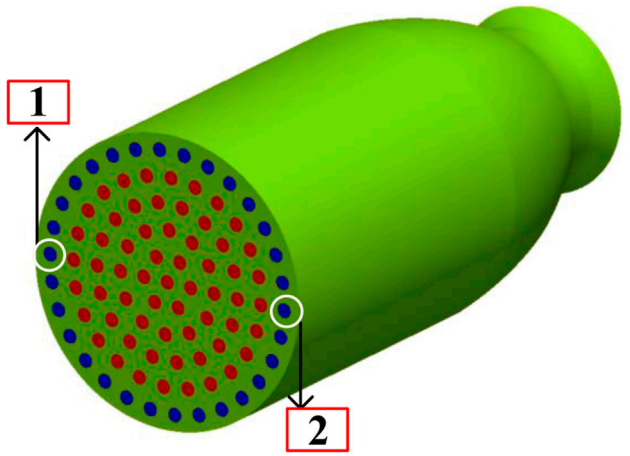

FIGURE 6 | Injectors with uneven distribution of propellant.

The intrinsic acoustic frequency of the combustion chamber is shown as follow (Huzel and Huang, 1992),

$$f_{mnq} = \frac{c}{2}\sqrt{\left(\frac{\alpha_{mn}}{R_0}\right)^2 + \left(\frac{q}{L_0}\right)^2} \quad m, n, q = 0, 1, 2 \ldots\ldots \tag{4}$$

Where α_{mn} represents the transverse eigenvalues, R_0 and L_0 are the radius and length of the chamber, respectively, and m, n, q represent the tangential, radial, and axial directions, respectively.

Theoretically, there are two kinds of solution of tangential acoustic mode, they are standing wave solution and traveling wave solution, shown as **Eqs 5**, **6**, respectively (Yang and Anderson, 1995).

$$p' = A\cos\left(q\pi\frac{x}{L}\right)J_m\left(\pi\alpha_{mn}\frac{r}{R}\right)\cos m\theta\cos\omega t \tag{5}$$

$$p' = A\cos\left(q\pi\frac{x}{L_0}\right)J_m\left(\pi\alpha_{mn}\frac{r}{R_0}\right)\cos\left(m\theta \pm \omega t\right) \tag{6}$$

Where

For the standing wave solution, the nodal diameter is located at a fixed position, and the standing wave 1T mode structure could be demonstrated by **Figure 3**. In the traveling wave solution, the nodal diameter is spinning around the center of the cycle. Its changing process is depicted in **Figure 4**.

ANALYSIS OF NUMERICAL SIMULATION RESULTS

There are three cases being calculated based on the numerical simulation model built in the present work: case1 is based on experimental conditions, while case2 and case3 are aimed at exploring two kinds of 1T HFCI mode.

Validation of Numerical Simulation Model

Under the nominal conditions, the mass flow rates of fuel and oxidizer are 13.0 kg/s and 32.5 kg/s, respectively, resulting in an O/F of 2.5. The chamber pressure under nominal conditions was about 12 MPa in the experimental test. The numerical simulation based on the experimental conditions is carried out. Propellant is evenly distributed to 91 injectors. The pressure-time history is shown in **Figure 5** and the chamber pressure remained at 11.80 MPa, resulting in an error of 1.67% compared with its experimental counterpart. The error is reasonable and the validation of the numerical simulation model can be verified.

Standing Wave Pattern of 1T HFCI

In case2, O/F = 2.5, and the only difference from case1 is that the fuel mass flow rate of No.1 and No.2 injectors in **Figure 6** is changed. Half of the fuel for No.1 injector is allocated to No.2 injector. This non-uniform distribution leads to severe HFCI.

The pressure-time trace and its FFT (Fast Fourier Transform Algorithm) result are given in **Figure 7**. The probe location is 50 mm away from the injector faceplate and near the chamber wall. The dominant frequency is 3524 Hz. In case2, the chemical equilibrium acoustic velocity is 1145.3 m/s, which could be

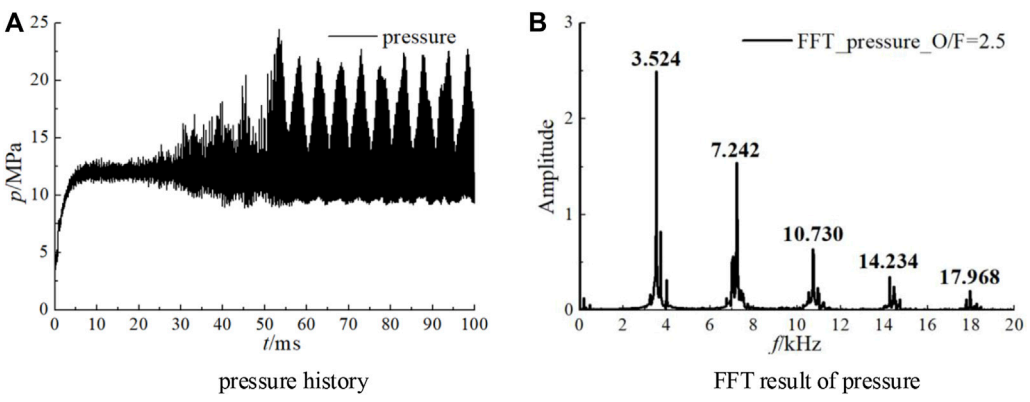

FIGURE 7 | Pressure history and its FFT result of case2 (probe is near the wall and 50 mm downstream from injector faceplate). **(A)** pressure-time trace. **(B)** FFT result of pressure.

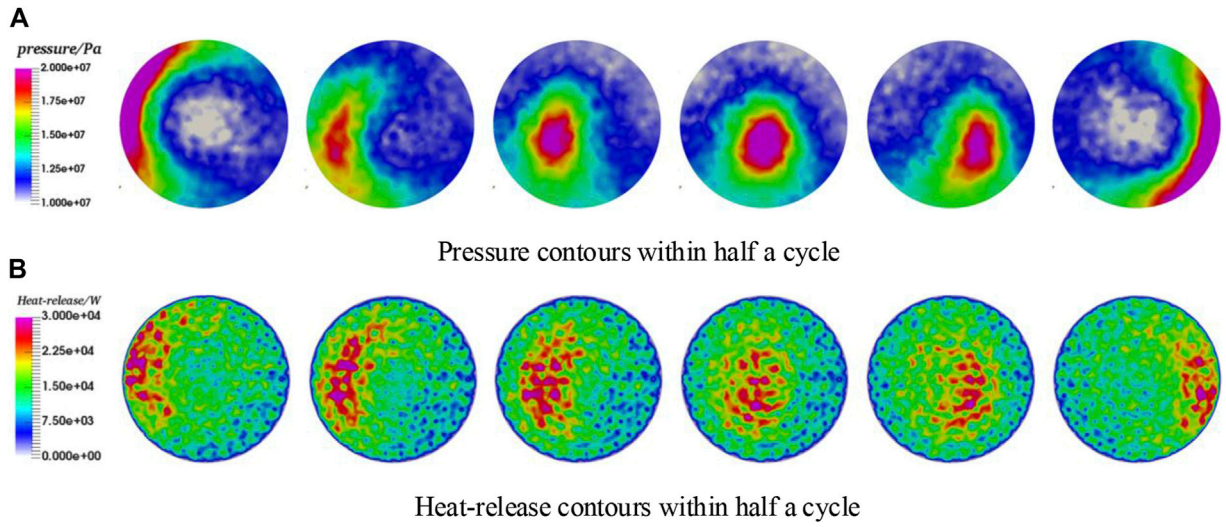

FIGURE 8 | Pressure and heat-release changing process within half a period in case2. **(A)** Pressure contours within half a cycle. **(B)** Heat-release contours within half a cycle.

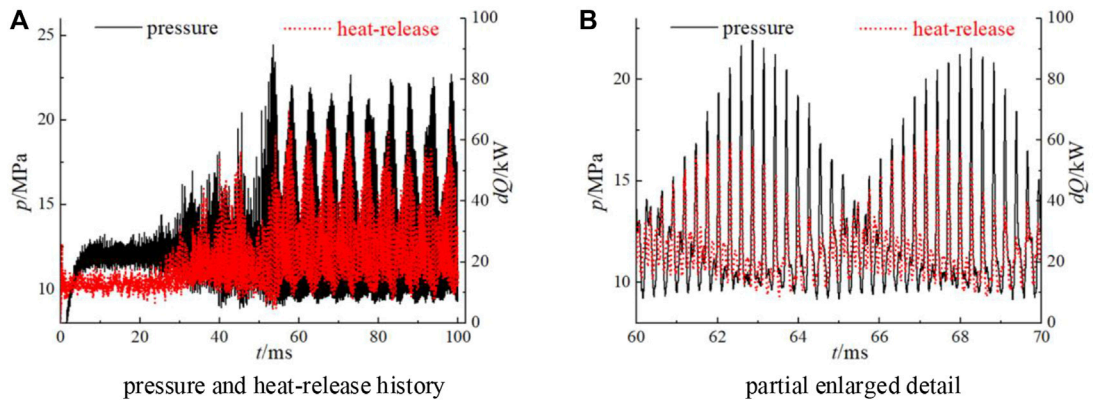

FIGURE 9 | Relationship between pressure and heat-release in case2 (probe is near the wall and 50 mm downstream from injector faceplate). **(A)** pressure and heat-release history. **(B)** partial enlarged detail of **(A)**.

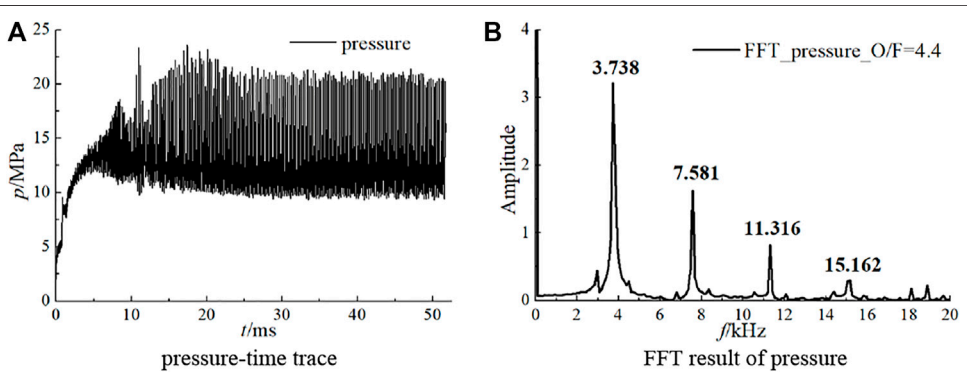

FIGURE 10 | Pressure history and its FFT result of case2 (probe is near the wall and 50 mm downstream from injector faceplate). **(A)** pressure-time trace. **(B)** FFT result of pressure.

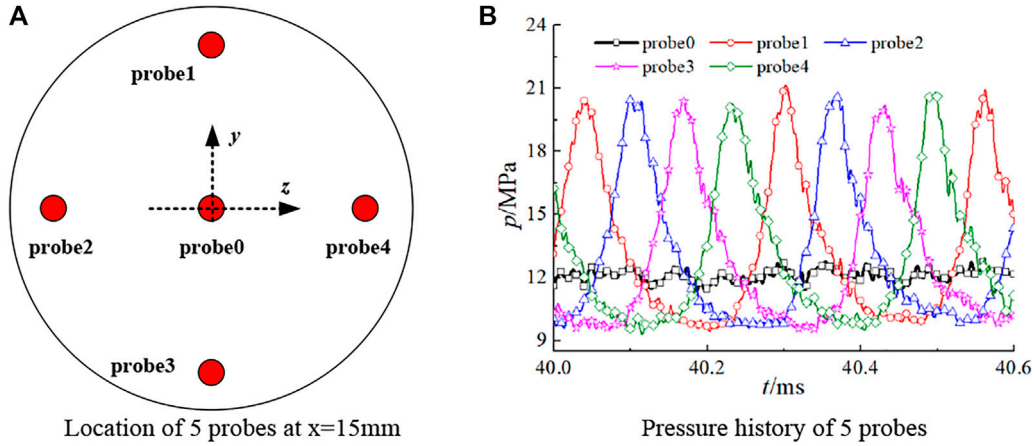

FIGURE 11 | Pressure relationship of 5 probes at cross section x = 50 mm. **(A)** Location of 5 probes at x=15 mm. **(B)** Pressure history of 5 probes.

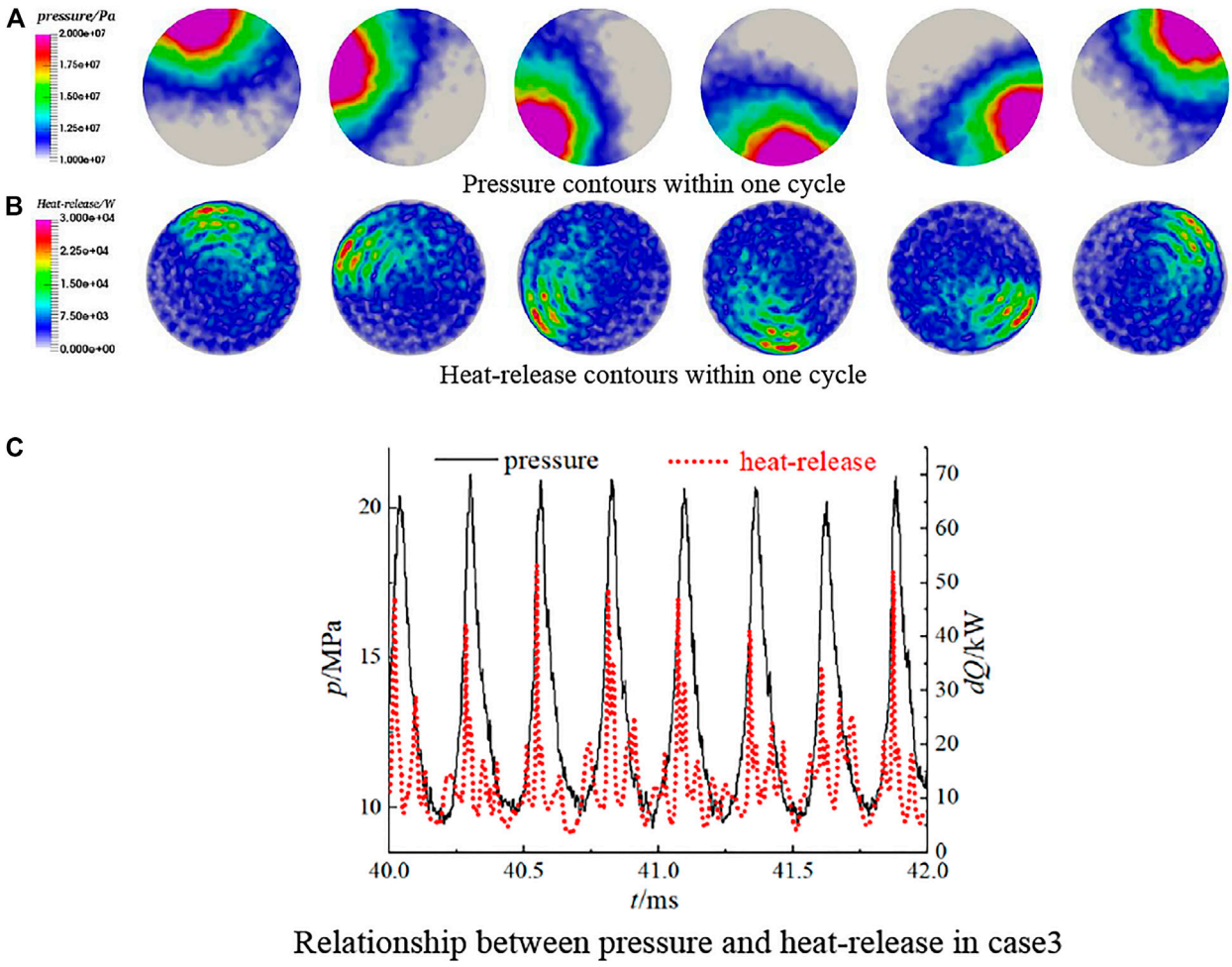

FIGURE 12 | Pressure and heat-release changing process within one cycle in case3. **(A)** Pressure contours within one cycle. **(B)** Heat-release contours within one cycle. **(C)** Relationship between pressure and heat-release in case3.

calculated by CEA (Chemical Equilibrium with Applications) from NASA (McBride and Gordon, 1996). The theoretical intrinsic frequency of 1T mode (according to **Eq. 4**) for case2 is 3729 Hz, and the difference between the numerical result and the theoretical value is 5.5%. Therefore, it is believed that 1T HFCI appears in case2 based on preliminary judgment.

The pressure and heat-release evolution process within half an oscillation cycle in cross-section x = 50 mm are detailed in **Figure 8**. Where there is a pressure peak, there is a heat-release peak, so pressure and heat-release are coupled spatially. Pressure and heat-release peaks move along a diameter line back and forth, and the nodal diameter remains unchanged, so the HFCI is a standing mode in case2.

Figure 9 shows the temporal relationship between pressure and heat-release. Apparently, the pressure and heat-release oscillate in phase. What occurs in case2 is in accordance with the Rayleigh Criterion both spatially and temporally. By means of the pressure and heat-release contours and their temporal relationship, the thermal-acoustic coupling can be demonstrated more clearly.

Traveling Wave Pattern of 1T HFCI

When the value of O/F arrives at 4.4, and all 91 injectors share uniform propellants. A severe HFCI occurs, which is proven to be a traveling wave 1T mode. The pressure-time trace and FFT result are given in **Figure 10**.

Obviously, the pressure-time trace indicates that it is an equal-amplitude oscillation, and the dominant frequency is 3738 Hz. The chemical equilibrium acoustic velocity is 1092.2 m/s, calculated by CEA, so the theoretical 1T frequency is 3556 Hz. The error between the numerical and theoretical values is 4.8%. Therefore, an initial judgment can be made that a 1T mode HFCI occurs when O/F value reaches 4.4.

Five probes in a transverse section (x = 50 mm, 50 mm away from injector faceplate) and their pressure-time traces are shown in **Figure 11**. The pressure of probe0, located at the center of the cycle, remains nearly constant, while the other 4 probes that are near the chamber wall show nearly constant amplitude. Two probes which are 180°apart (probe1 and probe3, probe2 and probe4) have reverse phase: when the pressure value of probe1 reaches the peak of the wave, the pressure value of probe3 nearly arrives at its lowest value. Also, it is clear that the pressure peak successively arrives at probe1→probe2→probe3→probe4→probe1. Therefore, a conclusion can be drawn that it is a spinning 1T HFCI mode and the direction of rotation is counter-clockwise. This conclusion can be proven further by the pressure and heat-release contours at the transverse section (x = 50 mm) within one cycle, and the contours are shown in **Figures 12A,B**.

An important feature is that the peak values of pressure and the heat-release always remain synchronous spatially. The relationship between pressure and heat-release in probe1 is shown in **Figure 12C**, and pressure and heat-release oscillate in phase. Obviously, the pressure and heat-release coupling process drives the HFCI.

CONCLUSION

From the numerical simulation results and analysis above, the following three conclusions were reached:

1. HFCI is sensitive to initial conditions. Compared with case1, a subtle change of propellant distribution in case2 leads to severe HFCI. The only difference between case1 and case2 is the injection distribution, Therefore, the comparison between case1 and case2 could indicate that the subtle change of propellant distribution exerts a significant effect on HFCI. The only difference between case1 and case3 is the operating condition (O/F). Therefore, the comparison between case1 and case3 could indicate that the O/F has a great influence on HFCI.
2. The two different 1T modes were captured numerically: standing mode with a constant nodal diameter and traveling mode with spinning nodal diameter.
3. Whether the 1T HFCI is in standing mode or traveling mode, the pressure and heat-release oscillated in phase both spatially and temporally, which accords with Rayleigh Criterion. It is the coupling process between pressure and heat-release that drives and maintains the thermo-acoustic instability.

DATA AVAILABILITY STATEMENT

The raw data supporting the conclusion of this article will be made available by the authors, without undue reservation.

AUTHOR CONTRIBUTIONS

KG's main contributions were to the numerical simulation model and data processing. BX contributed primarily to data processing and writing the manuscript. YR and YT were the main contributors to the numerical simulation model. WN mainly provided financial support for the numerical simulation.

FUNDING

National Natural Science Foundation of China (Nos 12002386 and 51876219).

ACKNOWLEDGMENTS

The authors would like to express their sincere acknowledgments for the computing resources provided by Beijing Beilong Super Cloud Computing Co., Ltd.

REFERENCES

Armbruster, W., Hardi, J. S., Miene, Y., Suslov, D., and Oschwald, M. (2020). Damping Device to Reduce the Risk of Injection-Coupled Combustion Instabilities in Liquid Propellant Rocket Engines. *Acta Astronautica* 169, 170–179. doi:10.1016/J.ACTAASTRO.2019.11.040

Bibik, O., Lubarsky, E., Shcherbik, D., and Hadjipanayis, M. (2008). *Rotational Traveling of Tangential Wave in Multi-Injectors LRE Combustor Simulator*. Availableat: https://academic.microsoft.com/paper/2471634577/.

Bibik, O., Lubarsky, E., Shcherbik, D., Hadjipanayis, M., and Zinn, B. (2008). *Rotational Traveling of Tangential Wave in LRE Combustor Simulator*. doi:10.2514/6.2008-1001

Culick, F. E. C., and Yang, V. (1995). *Overview of Combustion Instabilities in Liquid-Propellant Rocket Engines*.

Dranovsky, M. L., Yang, V., Culick, F. E. C., and Talley, D. G. (1994). *Combustion Instabilities in Liquid Rocket Engines: Testing and Development Practices in Russia*.

Frezzotti, M. L., Nasuti, F., Huang, C., Merkle, C. L., and Anderson, W. E. (2018). Quasi-1D Modeling of Heat Release for the Study of Longitudinal Combustion Instability. *Aerospace Sci. Techn.* 75, 261–270. doi:10.1016/J.AST.2018.02.001

Garby, R., Selle, L., and Poinsot, T. (2013). Large-Eddy Simulation of Combustion Instabilities in a Variable-Length Combustor. *Comptes Rendus Mécanique* 341, 220–229. doi:10.1016/j.crme.2012.10.020

Gejji, R., Lemcherfi, A. I., Strelau, R., Slabaugh, C. D., and Anderson, W. E. (2020). *Combustion Response of Shear Coaxial Injectors to Transverse Combustion Instabilities*. Orlando, FL: AIAA Scitech 2020 Forum. doi:10.2514/6.2020-0424

Gröning, S., Hardi, J. S., Suslov, D., and Oschwald, M. (2016). Injector-Driven Combustion Instabilities in a Hydrogen/Oxygen Rocket Combustor. *J. Propulsion Power* 32, 560–573. doi:10.2514/1.B35768

Hardi, J., Oschwald, M., Grning, S., Beinke, S., and Knapp, B. (2016). *High Frequency Combustion Instabilities in Liquid Propellant Rocket Engines: Research Programme at DLR Lampoldshausen, Thermoacoustic Instabilities in Gas Turbines and Rocket Engines: Industry Meets AcademiaMunich*. Germany. Availableat: https://www.researchgate.net/publication/312217154.

Harrje, D. T. (1972). *Liquid Propellant Rocket Combustion Instability, SP-194*. Washington, DC United States: NASA Headquarters.

Harvazinski, M. E., Gejji, R., Talley, D. G., Orth, M. R., Anderson, W. E., and Pourpoint, T. L. (2019). *Modeling of Transverse Combustion Instability*. California: AIAA Scitech 2019 ForumSan Diego. doi:10.2514/6.2019-1732

Harvazinski, M. E., Huang, C., Sankaran, V., Feldman, T. W., Anderson, W. E., Merkle, C. L., et al. (2015). Coupling between Hydrodynamics, Acoustics, and Heat Release in a Self-Excited Unstable Combustor. *Phys. Fluids* 27, 045102. doi:10.1063/1.4916673

Huzel, D. K., and Huang, D. H. (1992). *Modern Engineering for Design of Liquid Propellant Rocket Engines*.

Klein, S., Börner, M., Hardi, J. S., Suslov, D., and Oschwald, M. (2020). Injector-coupled Thermoacoustic Instabilities in an Experimental LOX-Methane Rocket Combustor during Start-Up. *CEAS Space J.* 12, 267–279. doi:10.1007/S12567-019-00294-4

McBride, B. J., and Gordon, S. (1996). *Computer Program for Calculation of Complex Chemical Equilibrium Compositions and Applications, NASA-RP-1311*.

Miller, K., Sisco, J., Nugent, N., and Anderson, W. (2007). Combustion Instability with a Single-Element Swirl Injector. *J. Propulsion Power* 23, 1102–1112. doi:10.2514/1.26826

Oefelein, J. C., and Yang, V. (1993). Comprehensive Review of Liquid-Propellant Combustion Instabilities in F-1 Engines. *J. propulsion Power* 9, 657–677. doi:10.2514/3.23674

Orth, M. R., Vodney, C., Liu, T., Hallum, W. Z., Pourpoint, T. L., and Anderson, W. E. (2018). *Measurement of Linear Growth of Self-Excited Instabilities in an Idealized Rocket Combustor*. doi:10.2514/6.2018-1185

Peters, N. (2000). *Turbulent Combustion*. Cambridge University Press.

Pomeroy, B., and Anderson, W. (2016). Transverse Instability Studies in a Subscale Chamber. *J. Propulsion Power* 32, 939–947. doi:10.2514/1.B35763

Popov, P. P., and Sirignano, W. A. (2016). Transverse Combustion Instability in a Rectangular Rocket Motor. *J. Propulsion Power* 32, 620–627. doi:10.2514/1.B35868

Rayleigh, L., and Nachtrieb, N. H. (1957). The Theory of Sound. *Phys. Today* 10, 32–34. doi:10.1063/1.3060230

Rayleigh, L. (1878). The Explanation of Certain Acoustical Phenomena 1. *Nature* 18, 319–321. doi:10.1038/018319a0

Tudisco, P., Ranjan, R., and Menon, S. (2016). *Numerical Investigation of Transverse Forcing in a Multi-Element, Shear-Coaxial, High Pressure Combustor*. California: 54th AIAA Aerospace Sciences MeetingSan Diego. doi:10.2514/6.2016-2155

Urbano, A., Selle, L., Staffelbach, G., Cuenot, B., Schmitt, T., Ducruix, S., et al. (2016). Exploration of Combustion Instability Triggering Using Large Eddy Simulation of a Multiple Injector Liquid Rocket Engine. *Combustion and Flame* 169, 129–140. doi:10.1016/J.COMBUSTFLAME.2016.03.020

Veynante, D., and Vervisch, L. (2002). Turbulent Combustion Modeling. *Prog. Energ. combustion Sci.* 28, 193–266. doi:10.1016/s0360-1285(01)00017-x

Yang, V., and Anderson, W. E. (1995). *Liquid Rocket Engine Combustion Instability*. American Institute of Aeronautics and Astronautics.

Yu, Y. C., Sisco, J. C., Rosen, S., Madhav, A., and Anderson, W. E. (2012). Spontaneous Longitudinal Combustion Instability in a Continuously-Variable Resonance Combustor. *J. Propulsion Power* 28, 876–887. doi:10.2514/1.B34308

Conflict of Interest: The authors declare that the research was conducted in the absence of any commercial or financial relationships that could be construed as a potential conflict of interest.

NOMENCLATURE

$\vec{U}$ conservative variable vector

$\vec{J}$ source term vector

T temperature (unit: K)

c_{KERO} molar concentration of kerosene (unit: mol/cm^3)

c_{O_2} molar concentration of oxygen (unit: mol/cm^3)

p' pressure disturbance (unit: Pa)

C chemical equilibrium acoustic velocity (unit: m/s)

α_{mn} transverse eigenvalues

R_0 radius of the chamber (unit: m)

L_0 length of the chamber (unit: m)

v viscous

KERO kerosene

$\mathbf{O_2}$ oxygen

m tangential directions

n radial directions

l axial directions

frontiers in Energy Research

ORIGINAL RESEARCH
published: 03 February 2022
doi: 10.3389/fenrg.2021.815152

Flow Conditioning to Control the Effects of Inlet Swirl on Brush Seal Performance in Gas Turbine Engines

Yuxin Liu[1], Wenlei Dong[1], John Chew[2], Michael Pekris[2], Benzhuang Yue[1] and Xiaozhi Kong[3]*

[1]Marine Engineering College, Dalian Maritime University, Dalian, China, [2]Naval Architecture and Ocean Engineering College, Dalian Maritime University, Dalian, China, [3]Department of Mechanical Engineering Sciences, University of Surrey, Guildford, United Kingdom

When subject to highly swirling inlet flow, the bristles on the upstream face of a brush seal in gas turbine engines tend to slip circumferentially, which may lead to aeromechanical instability and seal failure. In this article, a new design of the front plate of brush seal, which mitigates this effect, is presented. Angled ribs on the upstream side of the front plate are used to reduce the swirl of the flow impacting on the bristle pack. The effects of the rib geometry, including angle of inclination and height-to-spacing ratio, are investigated using computational fluid dynamics, and a bulk porous medium model of the bristle pack, on a simple seal geometry. Results show that the ribs can effectively regulate the flow upstream of the bristle pack, reducing the swirl and channeling flow radially inward to the sealing section, resulting in decreased circumferential forces on the bristles. Ribs inclined at 20° to the radial direction and with height-to-spacing ratio of 0.4 were selected as the most effective of those investigated for the seal geometry under study. A model of an aeroengine preswirled cooling air chamber was created to give insight into the inlet swirl boundary conditions that a preswirl seal brush seal could be subjected to at a range of leakage flow rates and inlet swirl velocities. The new design and upstream roughness feature substantially reduced inlet swirl velocity incident on the bristle pack. The findings in this work could have a significant impact on brush seal design and, in particular, mitigate a significant operational risk of swirl-induced instability in high-pressure, high-speed shaft seal locations.

Keywords: brush seal, inlet swirl, front plate, ribs, bristle stability

OPEN ACCESS

Edited by:
Lei Luo,
Harbin Institute of Technology, China

Reviewed by:
Shuang Guo,
Dalian University of Technology, China
Gaowen Liu,
Northwestern Polytechnical University, China

****Correspondence:***
Yuxin Liu
yxliu@dlmu.edu.cn

Specialty section:
This article was submitted to Advanced Clean Fuel Technologies, a section of the journal Frontiers in Energy Research

Received: *15 November 2021*
Accepted: *02 December 2021*
Published: *03 February 2022*

Citation:
Liu Y, Dong W, Chew J, Pekris M, Yue B and Kong X (2022) Flow Conditioning to Control the Effects of Inlet Swirl on Brush Seal Performance in Gas Turbine Engines. Front. Energy Res. 9:815152. doi: 10.3389/fenrg.2021.815152

INTRODUCTION

Brush seals are used for sealing between rotating and stationary components in applications with high-speed rotating shafts such as aeroengines. As reported by Chupp et al. (2002), compared to traditional labyrinth seals (Asok et al., 2008), brush seals improve sealing performance by reducing the leakage rate to 10% to 20% that of the latter. However, other performance factors such as wear, stability, and in-service deterioration have, to date, limited the application of brush seals (Aslanzada et al., 2009). Further research and development are needed to understand and improve these aspects so that brush seals can achieve their full potential.

A basic brush seal design includes a front plate, backing ring, and bristle pack, as shown in **Figure 1**. In order to reduce the wear between the bristles and the rotor and make it easier for the bristles to adapt to the radial movement of the rotor, the bristles are typically inclined at 30°–60° (ϕ) to the radial

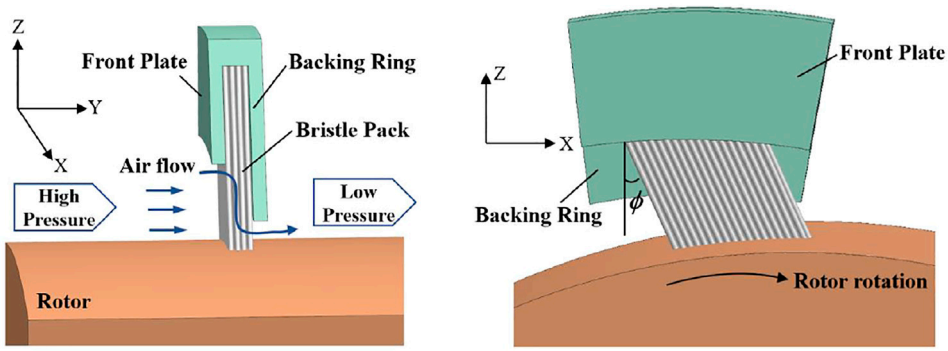

FIGURE 1 | Basic brush seal.

direction in planes of constant axial position. In operation, the bristle tips are often in contact or near-contact with the rotor, due to blowdown of the sealing elements, so that a significant proportion of the leakage flow passes through the bristle pack. The tortuous, narrow flow path between the bristles and the small radial clearance with the rotor, if any, provides resistance to the flow, thereby achieving good sealing performance.

The detailed behavior of the bristle pack in a brush seal depends on complex aeromechanical interactions. Even with known aerodynamic forces, calculation of bristle deflections is a challenging problem. For example, Zhao and Stango (2007) reported that the reaction and frictional forces between bristles and rotor, bristles, and backing plate and between adjacent bristles affect the deformations. The frictional forces cause pack stiffness and hysteresis and are particularly challenging to model accurately. A number of approaches to modeling of mechanical aspects have been presented in the literature. Crudgington et al. (2012) established a three-dimensional (3D) mechanical model to estimate the reaction forces and bristle deflection, showing that hysteresis and aerodynamic loading are the dominant factors for the sealing performance. Guardino and Chew (2004) and Lelli et al. (2006) developed 3D computational fluid dynamics (CFD) and 3D bristle bending models for brush seals, demonstrating the potential to investigate bristle pack deformation under aerodynamic loading. Sun et al. (2016) also developed a 3D coupled CFD-mechanical model and used this to investigate the effects of geometric parameters on the leakage characteristic of brush seals.

For less detailed and more computationally efficient modeling of leakage flow and aerodynamic effects, porous medium representations of the bristle pack are often used within CFD models, Bayley and Long (1993), Wei et al. (2015), and Gresham et al. (2016) introduced a leakage based on a linear porous medium model for comparison with their experimental results. Chew et al. (1995) proposed a nonlinear, anisotropic porous treatment and calibrated the viscous and inertial coefficients with experimental data. Chew and Hogg (1997) further explored the choice of coefficients considering leakage data for a wider set of experiments. Dogu and Aksit (2006) and Dogu et al. (2016) also developed the porous medium method and analyzed the effects of different front plate and bristle geometrical parameters and operating conditions on the leakage flow characteristics of brush seals.

A very limited number of studies have considered brush seal behavior in highly swirling environments. Sharatchandra and Rhode (1996) and Helm et al. (2008) found that brush seals could weaken the swirling flow, which can benefit shaft dynamic stability (Ramakrishna and Govardhan, 2008). However, lift forces are generated on the bristles, and this could cause instability of the upstream bristles and deterioration in performance. Considering possible aerodynamic instability and seal failure, Liu et al. (2020) analyzed the effect of inlet swirl on the bristle deflection using the Surrey University Brush Seal Iterative Simulator, a coupled 3D CFD and mechanical model. Results indicated that slip and possible instability of the upstream bristle row can be correlated with inlet swirl dynamic head. A plane front plate exacerbated this effect. As shown in **Figure 2**, the swirl of the flow entering the pack near the bristle tips increased in the presence of the front plate. It was proposed that introducing roughness elements on the upstream surface of the plate could reduce the swirl of flow impacting on the bristles and thereby improve the stability of the seal.

Based on the conclusions above, this article further explores the use of flow conditioning to mitigate the effects of inlet swirl on seal stability. A porous medium model is adopted for the bristle pack, and a front plate with inclined ribs attached on the upstream face is introduced. The effect of the front plate rib geometry on the velocity field, pressure field, and leakage flow of the brush seal under high swirl conditions is investigated in this study. The optimal rib geometry from the parametric study is then evaluated in a model of a turbine cooling air preswirl chamber.

CFD MODELING

Geometry and CFD Mesh Generation for Parametric Study

A brush seal structure including a front plate equipped with ribs is considered in this article, as presented in **Figure 3**. The geometric parameters are based on the brush seal considered in reference (Liu et al., 2020) and summarized in **Table 1**. In the initial parametric study, the curvature of the shaft and the rotation of the rotor are neglected, assuming also that there is a zero clearance

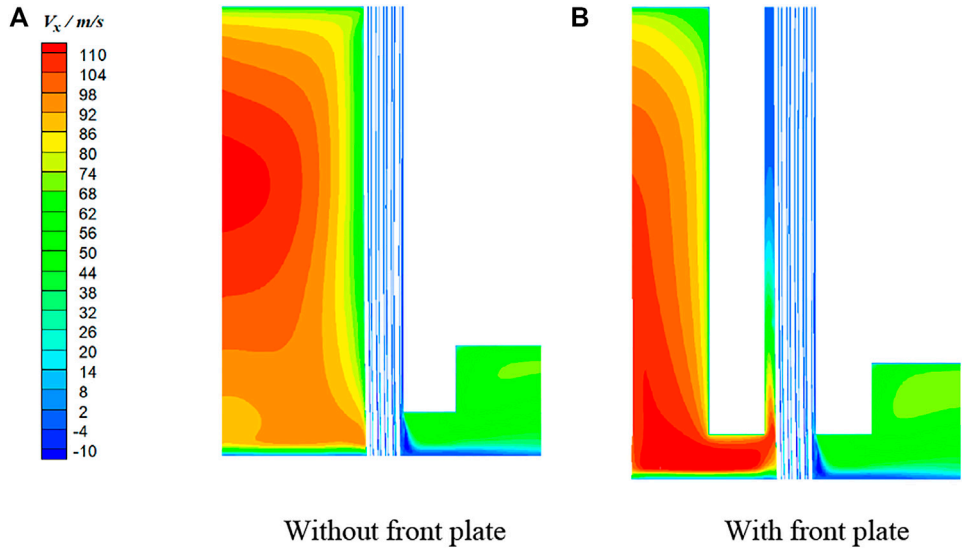

FIGURE 2 | Circumferential velocity contours (SV = 150 m/s): **(A)** without front plate, **(B)** with front plate.

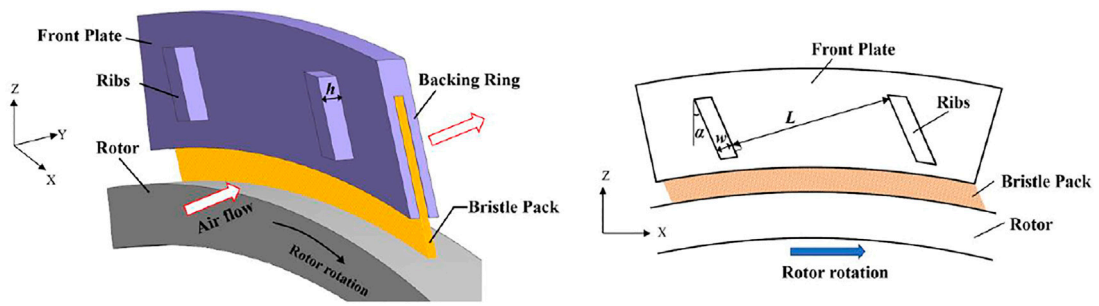

FIGURE 3 | Schematic of a brush seal and front plate with ribs.

TABLE 1 | Brush seal geometry parameters.

No. of axial bristle rows		**10**
Angle of bristles to radial	ϕ	40°
Bristle length	L_b	13.35 mm
Height of bristle overhang	H	1.00 mm
Brush diameter	D	0.10 mm
Clearance between bristles	δ	0.004 mm
Radial clearance between bristle and rotor	Z_{rotor}	0 mm
Rib width	w	2 mm

between the bristle pack and the shaft. As shown in the **Figure 3**, X, Y, and Z coordinates represent the circumferential, axial, and radial directions, respectively, in a finite radius seal, and this terminology is used here despite the neglect of curvature. The model assumes periodicity in the circumferential direction.

The geometric parameters of the ribs include the angle (α), height (h), spacing (L), and width (w), as can be seen in **Figure 3**. The width and height can be nondimensionalized by dividing by the rib spacing. In this way, the determined geometric parameters of ribs can be considered as angle of inclination, height-to-spacing ratio, and width-to-spacing ratio. The angle of inclination relative to the inlet airflow (swirl) direction and the height-to-spacing ratio are expected to strongly affect the flow deflection and degree of separation in the channels between the ribs. Hence, the discussion of the results will focus on these parameters. The base geometry is for ribs with inclination angle to the radial direction of 20°, height-to-spacing ratio of 0.2 (h = 2 mm, L = 10 mm). The values of the geometric parameters considered are summarized in **Table 2**.

Figure 4 shows the calculation domain and mesh for the brush seal with front plate and ribs. ICEM software was used to generate a hexahedral mesh. The mesh is refined through the seal and around the ribs. Further details of the porous medium model used for the bristle pack and boundary conditions are given below. In order to investigate grid dependency, meshes with approximately 6 million, 8 million, and 10 million cells were considered for the base geometry. The applied boundary conditions for the base case are specified in *Numerical Methods and Modeling Assumptions*, including an inlet swirl velocity of 150 m/s. To examine the grid dependence, averaged swirl velocity at specific axial planes and leakage flow rates were examined. **Figure 5**

TABLE 2 | Rib geometry parameters.

Rib width *w*/mm	Angle investigation					*h/L* investigation				
	2									
Angle of ribs to radial α	40°	30°	20°	0°	−20°	20°				
Rib height *h*/mm			2			0.5	1	2	2	
Rib spacing *L*/mm			10			10			5	15
h/L			—			0.05	0.1	0.2	0.4	0.133

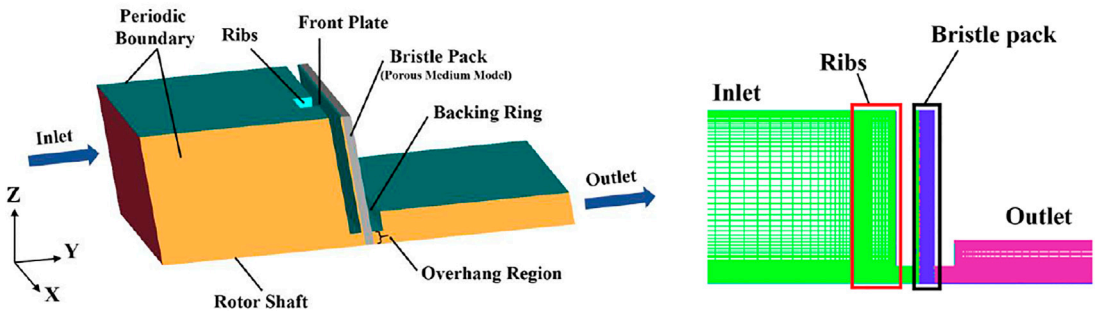

FIGURE 4 | CFD domain and mesh for the base geometry.

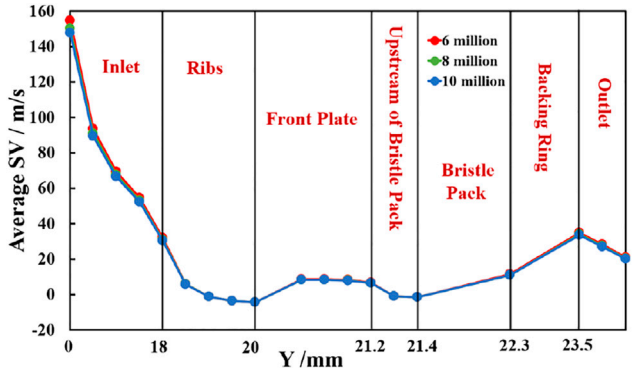

FIGURE 5 | Swirl velocity result for three different meshes.

compares area-averaged swirl velocity for the three meshes. Differences between the meshes are within 3%, and the difference of mass flow rates is less than 0.5%. The 8-million-cell mesh is used for the calculations in the current study.

Numerical Methods and Modeling Assumptions

The commercial CFD software FLUENT was used to obtain 3D, steady numerical solutions of the flow and energy equations using the k-ε turbulence model and second-order upwind spatial discretization. The fluid was modeled as an ideal gas representing air, with specific heat and viscosity given as functions of temperature. At the inlet, boundary conditions of 0.5 MPa total pressure, 300 K total temperature, and 150 m/s circumferential (swirl) velocity were applied. A static pressure of 0.1 MPa was specified at the outlet. Periodic boundary conditions were applied in the circumferential direction, and all further boundaries were assumed to be no-slip and adiabatic. Shaft rotation was not considered in the parametric study but was included in the preswirl chamber application described later. Standard wall functions were used when imposing the no-slip condition on walls, and the equations were solved using the SIMPLE algorithm. The values of y^+ for the walls are in the range of 20–30. The calculations were considered to be converged when the residuals of the continuity equation, energy equation, and turbulence equations had all decreased to 10^{-5} and typical parameters, such as pressure, velocity, and flow rate, no longer changed.

Porous Medium Model

The bristle pack is composed of layers of fine bristles, which are densely packed, typically in a hexagonally close packed arrangement. The airflow passes through the fine gaps between the bristles driven by the pressure difference across the seal. As the main interest here is on the condition of the flow approaching the bristles, rather than the detailed flow within the pack, an approximate treatment of seal flow is used. Following previous studies (Chew et al., 1995; Chew and Hogg, 1997; Zhang

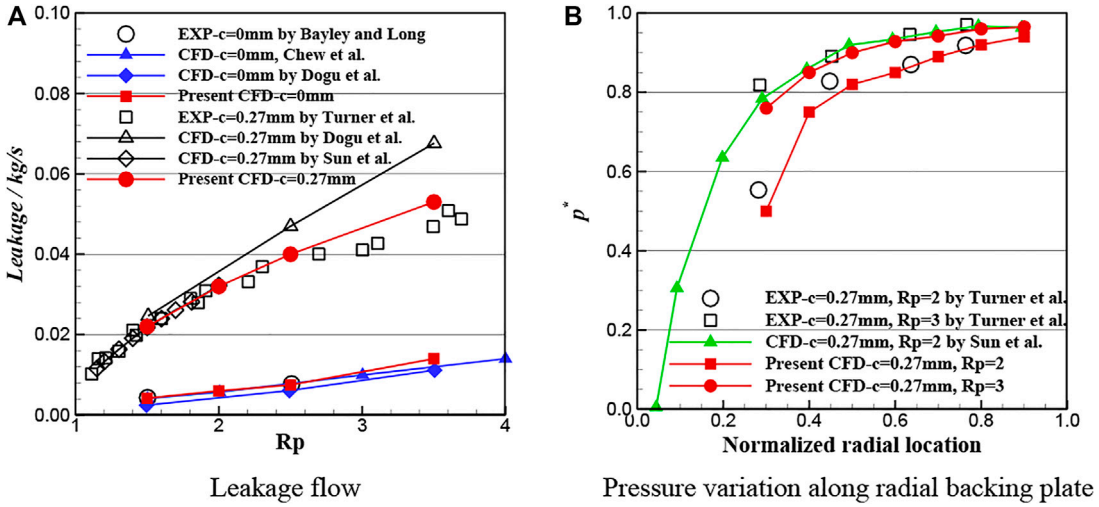

FIGURE 6 | Comparisons of present results with previously published data: **(A)** leakage flow, **(B)** radial pressure distribution on backing plate.

et al., 2017), a nonlinear porosity model is used to simulate the flow through bristle pack by introducing viscosity and inertia losses into the momentum equation, giving

$$\frac{\partial\left(\rho u_i u_j\right)}{\partial x_j} = -\frac{\partial p}{\partial x_i} + \frac{\partial \tau_{ij}}{\partial x_j} + \mathbf{F}_i \tag{1}$$

$$\mathbf{F}_i = -\mathbf{A}_{ij}\mu u_i - 0.5\mathbf{B}_{ij}\rho|\mathbf{u}|\mathbf{u}_i \tag{2}$$

In **Eq. 2**, $\boldsymbol{A}_{ij}$ is the matrix of viscous resistance coefficients, and $\boldsymbol{B}_{ij}$ is the matrix of inertial resistance coefficients. Principal coordinates for the matrices are taken to be z, m, and n. These are the axial direction for the brush seal, parallel to the bristles, and perpendicular to the bristles in an axial plane, respectively. Following reference (Pugachev, 2014), the viscous resistance coefficients a and inertial resistance coefficients b are obtained as follows:

$$a_z = a_n = \frac{66.67\,(1-\varepsilon)^2}{D^2\varepsilon^3} \tag{3}$$

$$a_m = 0.4\varepsilon a_n \tag{4}$$

$$b_z = b_n = \frac{2.33\,(1-\varepsilon)}{D\varepsilon^3} \tag{5}$$

$$b_m = 0 \tag{6}$$

Porosity (ε) refers to the ratio of the void volume to the total volume of the bristle pack in the porous medium and is given by

$$\varepsilon = 1 - \frac{\pi D^2 N}{4w_b \sin\phi} \tag{7}$$

In this equation, N is the number of the bristles per unit circumferential length, D is the diameter of the bristles, w_b is the thickness of the bristle pack, and ϕ is the angle between the bristle and the tangential direction. The expressions for resistance coefficients were validated by experiments in reference (Turner et al., 1998). Based on the geometric parameters in **Table 1**, the porosity of the bristle pack in the current study is 0.192.

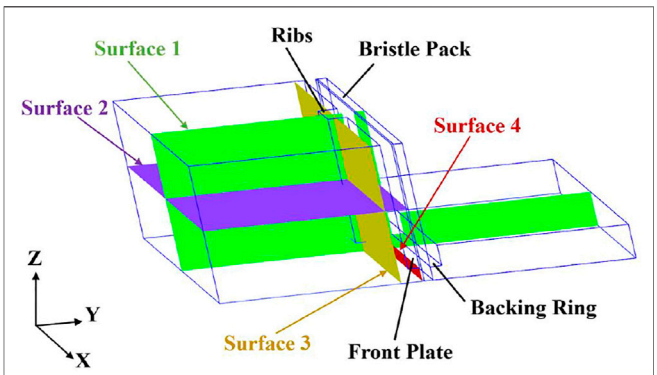

FIGURE 7 | Viewing surfaces for flow visualization.

Numerical Method Validation

Comparisons of results from the present model with Bayley and Long (1993) and Turner et al. (1998), experimental data and previously published modeling results are plotted in **Figure 6**. The calculation model and the boundary conditions for validation were consistent with the experiment (Bayley and Long, 1993; Turner et al., 1998). **Figure 6A** compares the leakage flow for a brush seal with radial clearances $c = 0$ mm, 0.27 mm between the bristle tip and rotor for pressure ratios (Rp) 1 to 4. The nondimensional pressure variation along the radial backing plate, which is defined as $p^* = (p - p_{\text{outlet}})/(p_{\text{inlet}} - p_{\text{outlet}})$, is shown in **Figure 6B**. The calculated leakage and pressure distribution are in good agreement with the experimental data and other workers' numerical results.

PARAMETRIC STUDY

The following subsections discuss the effects of ribs including variations in angle and height-to-spacing ratio on inlet swirl. The flow field upstream of the bristle pack is analyzed with particular

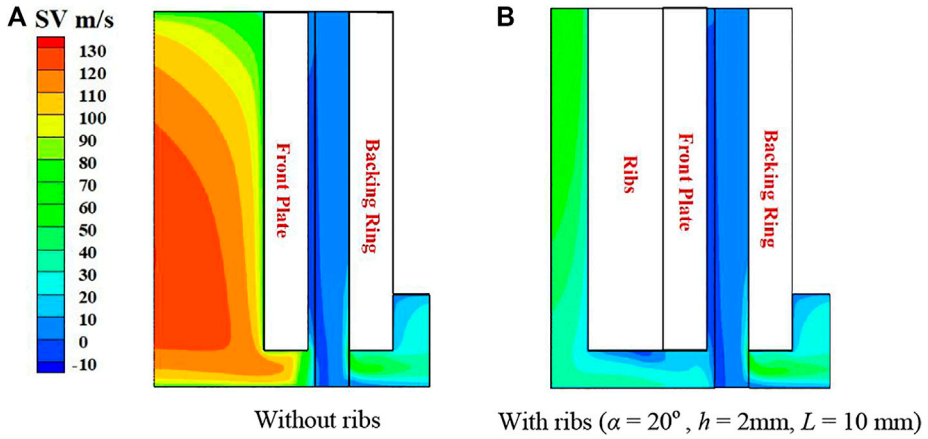

FIGURE 8 | Swirl velocity contours for base geometry on surface 1: **(A)** without ribs, **(B)** with ribs (α = 20°, h = 2 mm, L = 10 mm).

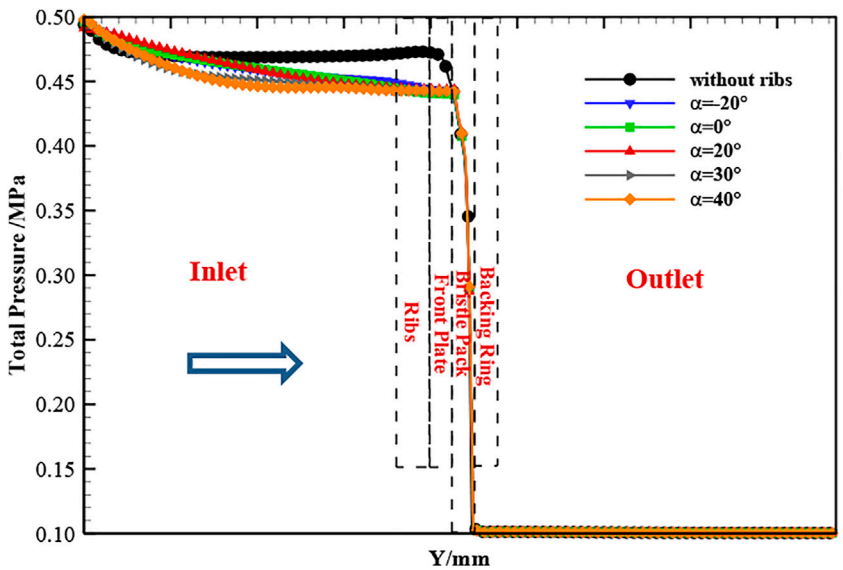

FIGURE 9 | Average total pressure variation with rib angle (h = 2 mm, L = 10 mm).

attention given to the swirl velocity. Predicted leakage flow rates for all cases agreed to be within 1.5%. The four viewing surfaces used to visualize the flow contours and streamlines are shown in **Figure 7**; they are surfaces cutting through the middle of ribs (surfaces 1–3) and 0.2 mm upstream of the bristle pack (surface 4).

Effect of Ribs for Base Geometry

Figure 8 shows swirl velocity contours on surface 1 for the base geometry with and without ribs. The comparison shows that the ribs have a significant effect upstream of the bristle pack, with the ribs reducing swirl velocities considerably. This is expected as the ribs act as roughness elements exerting drag on the flow. The area averaged swirl velocity on surface 4, just upstream of the bristle pack, is reduced from 50.9 to 6.5 m/s due to the presence of the ribs. Thus, the circumferential aerodynamic forces on the bristles, which scale with swirl dynamic head (Liu et al., 2020), are expected to be reduced by a factor of approximately 60.

Effect of the Rib Angle

In order to examine the effect of rib angle on flow, five rib inclination angles (−20°, 0°, 20°, 30°, 40°) were considered. **Figure 9** shows the variation of mass-averaged total pressure distribution along the axial direction for the five rib lay angles and the case without ribs. Approaching the seal, total pressure is significantly reduced for the front plate brush seals with ribs. This is due to the spoiling effect of the ribs, leading to dissipation of the flow kinetic energy. The total pressure variation is similar for the five rib lay angles, with the larger angle cases showing the greater departure from the smooth front plate case. This may be due to

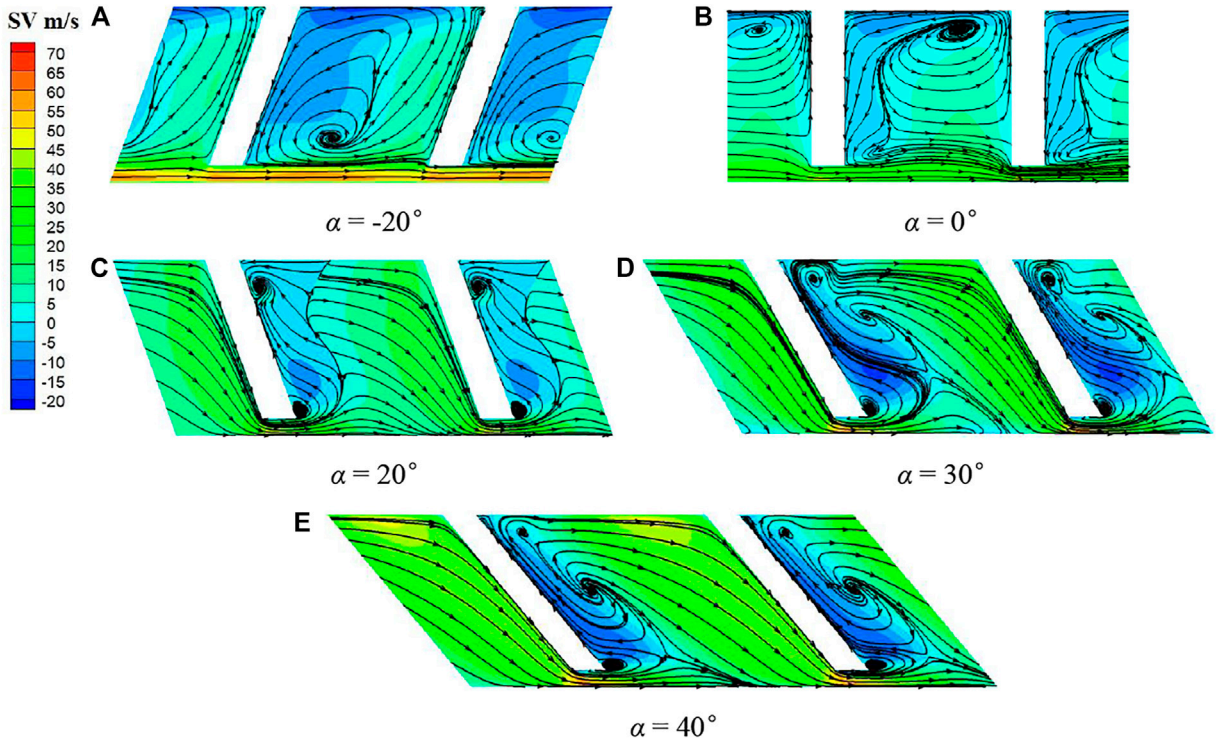

FIGURE 10 | Swirl velocity contours and streamlines on surface 3 (h = 2 mm, L = 10 mm): **(A)** α = –20°, **(B)** α = 0°, **(C)** α = 20°, **(D)** α = 30°, **(E)** α = 40°.

the larger angle ribs inducing more recirculation in the inlet region. As expected, once the flow enters the pack, the effects of inlet swirl rapidly diminish due to the strong resistance to circumferential flow. It is the ratio of tangential to axial aerodynamic force on the upstream bristles that determines circumferential slip and aeromechanical instability (Liu et al., 2020). Although this ratio might be estimated from the porous model, this has not been attempted here as swirl velocity immediately upstream of the bristles is considered sufficient to indicate the performance of the ribs and of the normal aerodynamic force acting to displace the bristles. As shown in the **Figure 9**, the pressure drops rapidly through the bristle pack to the downstream pressure.

Figure 10 shows streamlines and swirl velocity contours on surface 3 for the five rib angles. The cross-flow due to the inlet swirl (from left to right) creates flow separation and vortices between the ribs. For the negative lay angle of –20°, the ribs deflect the flow radially outward, creating an anticlockwise flow in the axial plane. Below the rib bottom where the bristle pack is exposed, swirl velocity is reduced from that without the ribs in **Figure 8**, but it is still substantial. For the radial ribs with lay angle 0°, the outward flow is less extensive. The center of the major circulation between the ribs moves outward and creates a second smaller vortex. There is a significant reduction of swirl near the seal inlet. For positive rib angles, the ribs deflect the flow radially inward toward the seal creating a clockwise flow vortex in the plane. The positive rib angles are clearly more effective in reducing swirl near the shaft and seal inlet. As the rib angle increases, the extent of the radially deflected flow region in this plane also increases, and the swirl velocity beneath the rib tip is seen to increase.

To further illustrate the effect of ribs, contours of swirl velocity on the portion of surface 1 just upstream of the bristle tips, which aligns with the rib centerline where the peak velocities are observed to occur, are shown in **Figure 11**. It can be seen that for α = –20°, 30°, and 40°, the circumferential velocity remains high, although **Figure 10** shows that away from the rib tips swirl velocities for α = 30° and 40° are low. Note also that the contour scale here differs from that in **Figure 8**, and the swirl for all ribbed cases is below that for the plane front plate.

The trends observed above are further illustrated in **Figure 12** and **Table 3**. **Figure 12** plots the area-averaged swirl velocities on planes of constant axial position for the five rib angles and the plane front plate. **Table 3** gives the average and maximum swirl velocities on the plane 0.2 mm upstream of the bristle pack (surface 4). The average and maximum swirls approaching the seal are significantly lower than with the plain front plate for all the ribbed cases. The average swirl velocity changes sharply at the start of the ribbed and front plate axial sections. Once the flow is established downstream of the ribs, the average swirl remains almost constant until the flow enters the bristle pack. The maximum swirl values in **Table 3** confirm that the high local values observed in **Figure 10** for α = 30° and 40° persist close to the bristle pack. The parametric study shows that the 20° angled ribs are most effective in reducing the swirl of the flow onto the bristle pack.

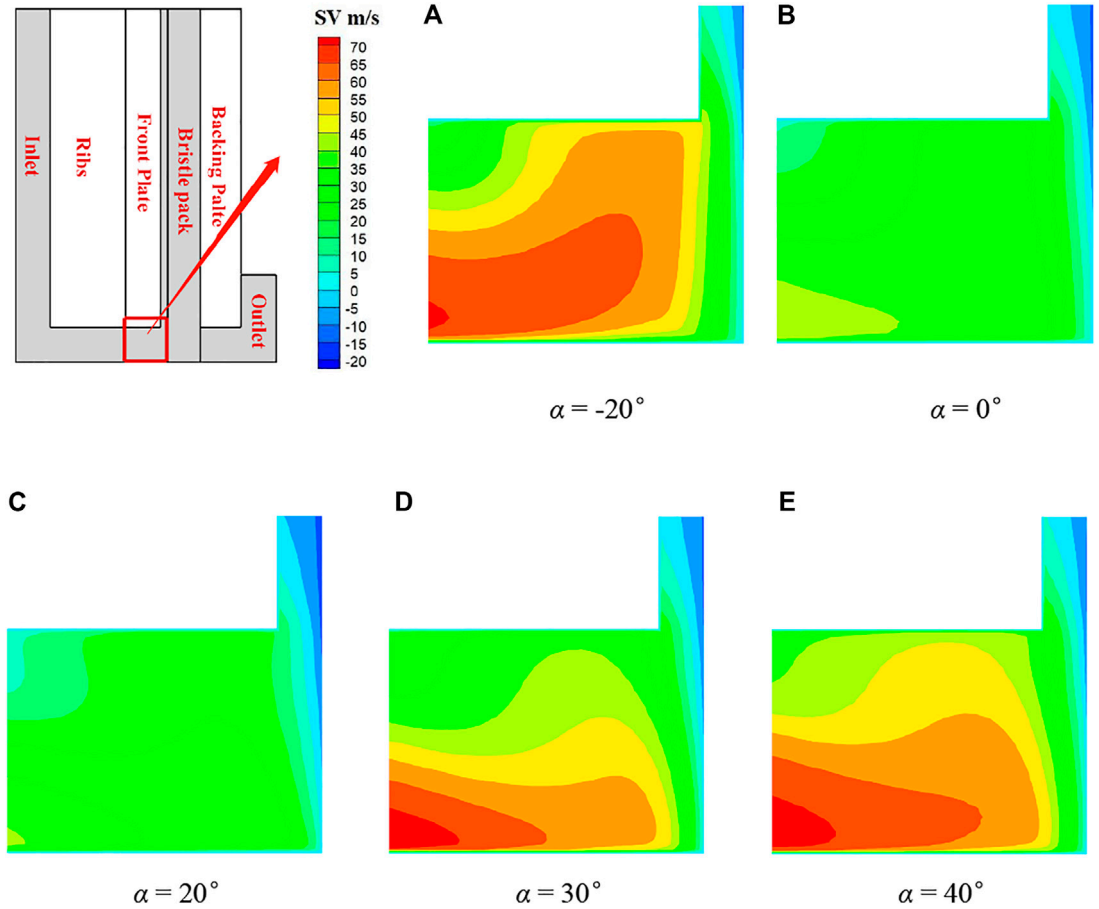

FIGURE 11 | Swirl velocity contours on surface 1 (h = 2 mm, L = 10 mm): **(A)** α = –20°, **(B)** α = 0°, **(C)** α = 20°, **(D)** α = 30°, **(E)** α = 40°.

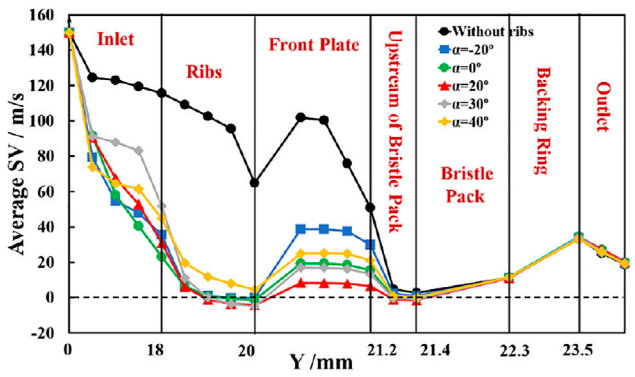

FIGURE 12 | Average swirl velocity variation with rib angle (h = 2 mm, L = 10 mm).

Effect of Rib Height-to-Spacing Ratio

In this section, the rib height-to-spacing ratio was investigated by varying rib height first for the same spacing and then keeping the rib height constant with changing rib spacing. Therefore, the effect of rib height (h = 0.5, 1, 2 mm) on the seal inlet swirl was studied for the rib angle of 20° and rib spacing of 10 mm (h/L = 0.05, 0.1, 0.2). **Figure 13** shows the streamlines and swirl velocity contours on surface 2. As expected, the extent of the separated flow region downstream of the ribs increases with rib height. For h = 2 mm (h/L = 0.2), the flow does not fully reattach between the ribs.

TABLE 3 | Variation of swirl velocity on surface 4 with rib angle.

Angle	SV-avg (m/s)	SV-max (m/s)
Without ribs	50.9	63
–20°	29.9	36.7
0°	15.5	26.1
20°	6.5	19
30°	13.3	39.8
40°	21	40

Figure 14 shows the average swirl velocity with the same overall trends as in **Figure 12**. The average seal inlet swirl is reduced significantly more for h = 2 mm (h/L = 0.2) than at the lower rib heights. **Table 4** gives the average and maximum swirl velocities on the plane 0.2 mm upstream of the bristle pack. Although the effectiveness of the ribs at this angle reduces with

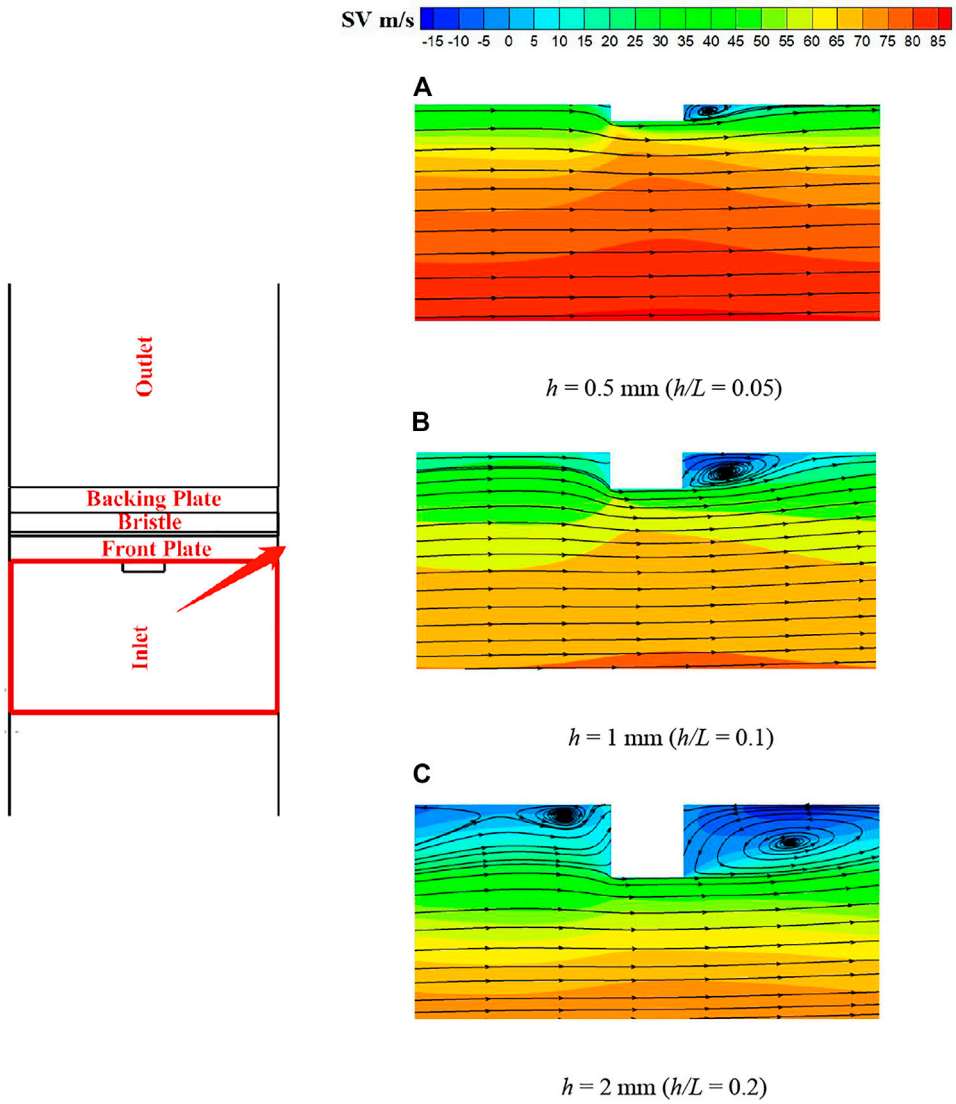

FIGURE 13 | Swirl velocity contours and streamlines on surface 2 (α = 20°, L = 10 mm): **(A)** h = 0.5 mm (h/L = 0.05), **(B)** h = 1 mm (h/L = 0.1), **(C)** h = 2 mm (h/L = 0.2).

decreasing height, the smaller ribs are still as effective in reducing maximum swirl as the 2-mm ribs at higher angles.

Three different rib spacings (L = 5, 10, 15 mm) were considered for ribs with an inclination angle of 20° and a height of 2 mm (h/L = 0.4, 0.2, 0.133). **Figure 15** presents the streamlines and swirl velocity contours on surface 3 for the different spacings. As previously shown, flow separation occurs downstream of the ribs, and at the wider spacings, a local maximum in swirl forms between the tip of the rib and the shaft. At a rib spacing of 5 mm (h/L = 0.4), the airflow between the ribs is more uniformly radially inward, and this produces opposing vortices below the rib tip, with reduced swirl compared to the wider spacings.

Figure 16 shows the average swirl velocity for the three rib spacings. It can be seen that the average swirl in the region between the ribs becomes negative for the rib spacing of 5 mm (h/L = 0.4). This is consistent with the complex flow pattern shown in **Figure 15** and the effects of reduced rib spacing. **Table 5** gives the average and maximum swirl velocities on the plane 0.2 mm upstream of the bristle pack. Both increase with rib spacing. The spacing of 5 mm (h/L = 0.4) shows the best performance of the configurations considered in this study, almost eliminating swirl completely.

Based on **Tables 4** and **5**, the nondimensional averaged and maximum swirl velocity (the ratio of swirl velocity to inlet swirl velocity) on the plane of surface 4 can be plotted against the height-to-spacing ratio h/L of the ribs, as shown in **Figures 17** and **18**, and for an inlet swirl velocity of 150 m/s. Results show that as well as rib angle, h/L can be identified as a key dimensionless parameter in controlling the flow approaching

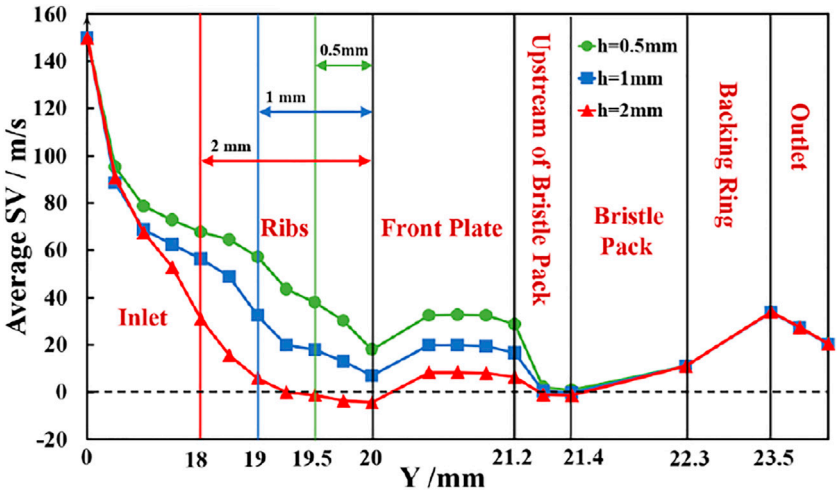

FIGURE 14 | Averaged swirl velocity variation with rib height (α = 20°, L = 10 mm).

TABLE 4 | Variation of swirl velocity on surface 4 with rib height.

Height (mm), *h/L*	SV-avg (m/s)	SV-max (m/s)
0.5, 0.4	28.6	34.6
1, 0.2	16.6	27.3
2, 0.133	6.5	19

the seal. The larger the ratio was, the better the reduction of the swirl flow was. In summary, the geometric parameters of the ribs giving the most effective reduction in inlet swirl are $\alpha = 20°$, $h/L = 0.4$ ($h = 2$ mm and $L = 5$ mm). For this geometry, swirl velocity is significantly reduced or negated as it passes through the separated flow region between the ribs, and a reasonably uniform radial inflow from this region supplies the seal leakage flow.

PRESWIRL CHAMBER APPLICATION

Computational Model

To further evaluate the use of ribs to reduce swirl velocity, an aeroengine preswirled cooling air delivery chamber was modeled incorporating a brush seal with a ribbed front plate in a modified

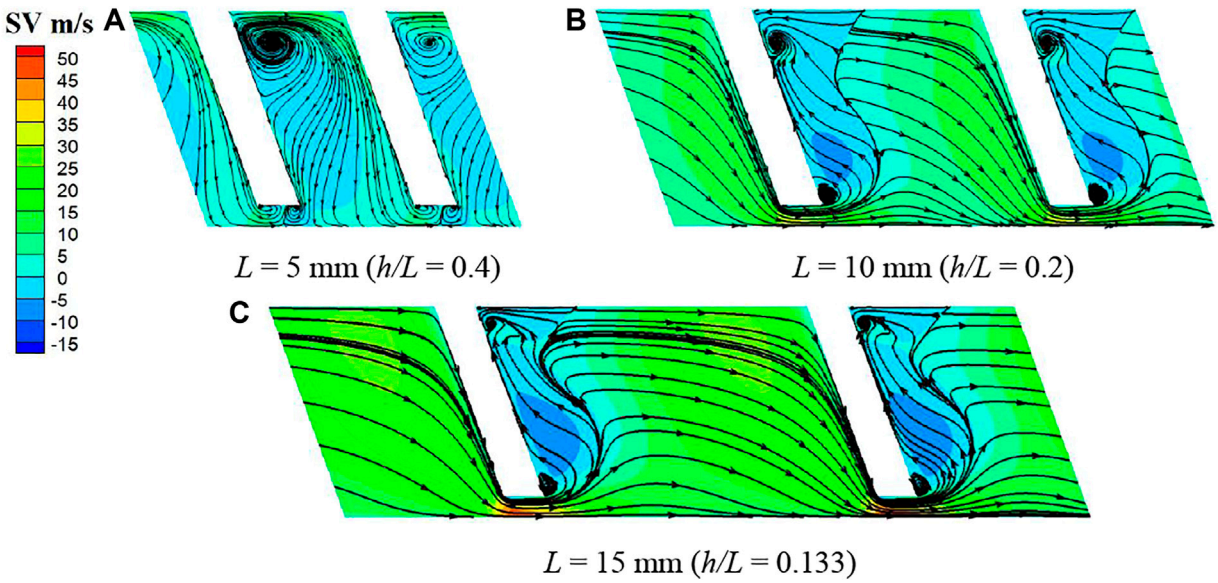

FIGURE 15 | Swirl velocity contours and streamlines on surface 3 (α = 20°, h = 2 mm): **(A)** L = 5 mm (h/L = 0.4), **(B)** L = 10 mm (h/L = 0.2), **(C)** L = 15 mm (h/L = 0.133).

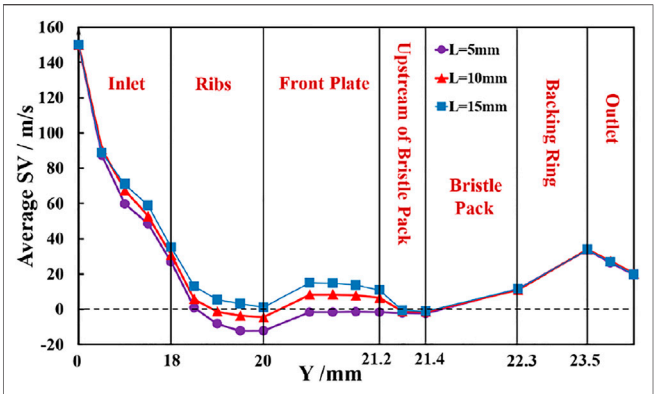

FIGURE 16 | Average swirl velocity variation with rib spacing (α = 20°, h = 2 mm).

TABLE 5 | Variation of swirl velocity on surface 4 with rib spacing.

Spacing (mm), *h/L*	SV-avg (m/s)	SV-max (m/s)
5, 0.4	−1.5	2.6
10, 0.2	6.5	19
15, 0.133	10.9	32

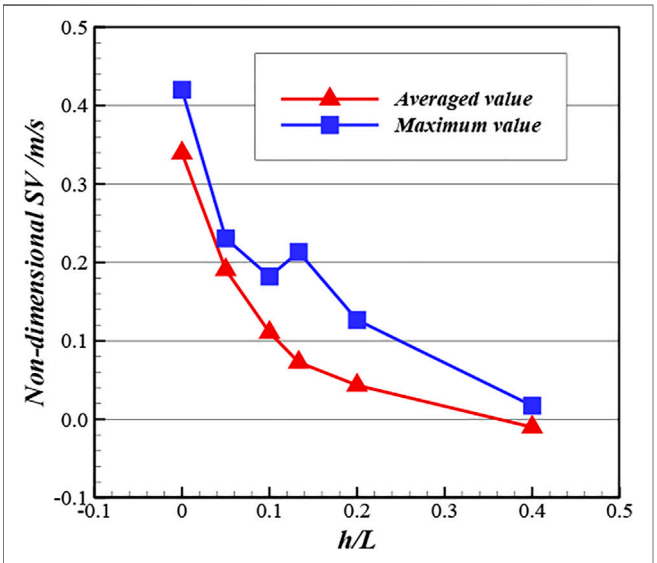

FIGURE 17 | Swirl velocity on surface 4 against *h/L* of ribs.

outer seal position. The model geometry was based on an engine representative preswirl system (Chew et al., 2003; Liu G. et al., 2021; Liu Y. et al., 2021), with the introduction of an outer chamber, and is shown in **Figure 18**. To accommodate the selected design of ribs, circumferential periodicity was assumed for a 2.371° sector. The preswirl nozzles and receiver holes were modeled as slots, inner seal flow was set to zero, and the outer seal was modeled as a brush seal using the porous model with and without front plate ribs. The mid-radial location of preswirl nozzles and receiver holes is 160.5 mm. The radial extent and the axial width ($w_{chamber}$) of the chamber are 28 and 8 mm, respectively. The brush seal geometry and initial choice of porosity were the same as those in the parametric study, as given in **Table 1**. It should be noted that, in this application, the seals are generally designed with a clearance due to the high shaft speeds, to mitigate the risk of heat generation or thermal runaway. Thus, a 0.2-mm radial clearance between rotor and the bristle pack was introduced. The selected front plate design had ribs inclined at 20° to the radial direction, with a height of 2 mm and spacing of 5 mm (h/L = 0.4). The red boundaries in **Figure 18** represent stationary walls, and the blue boundaries represent the rotating walls. The stationary and rotating domains were generated separately and connected by an interface boundary. All domains were meshed by structure meshes, and relatively finer mesh was used for the bristle pack as well as the wall adjacent zones. The mesh had 3.5 million cells with near-wall spacing giving y + values in the range 30–80.

The turbulence characteristics of the flow were modeled using the standard k-ε equations with wall functions on the no-slip boundaries. As for the operating conditions, the total pressure 0.8 MPa was imposed on the preswirl nozzle inlet with swirl velocity 150 m/s, which gives a swirl ratio at nozzle exit around unity. The static pressure at the receiver hole outlet and outer seal outlet was 0.4 MPa, and the rotational speed of the rotating walls and rotational domain was 9,000 rpm (170 m/s at the seal radius) for all simulations. Calculations were considered converged when residuals of continuity, energy and turbulence equations reached 10^{-5}, and the representative flow variables did not change with further iterations.

Results Analysis

Figure 19 shows swirl velocity contours on the periodic plane for the preswirl chamber solutions with and without ribs. Here, the most effective rib design from the parametric study is adopted, and the seal has a 0.2-mm clearance between the bristle pack and the rotor. The ribs on the upstream face of the front plate have little influence on the flow in the preswirl cavity and the swirl at the main cooling flow receiver hole, but clearly modify the flow as it approaches the seal. A further interesting point is that, even without the ribs fitted, the introduction of an outer chamber with stationary walls is effective in reducing swirl of the sealing flow. As confirmed by swirl velocity contours and streamlines just upstream of the seal in **Figure 20**, the ribs substantially reduce the swirl. It can be observed that the flow pattern for the ribbed case is similar to that in **Figure 15A** but with higher swirl beneath the bristle tips that suppresses the vortices shown in **Figure 15**. Effects of the shaft rotation, which were neglected in the parametric study, are seen to be confined to a very thin boundary layer. The average swirl velocity at surface 4 (0.2 mm upstream of the bristle pack) is reduced from 85.2 to 5.4 m/s. Therefore, the circumferential aerodynamic forces loading on the bristles, which scale with swirl dynamic head, will be reduced by a factor of approximately 250.

Further simulations were carried out for a wide range of leakage flow rates (varying porosity and clearance) and at a higher inlet swirl. The results are summarized in **Table 6**. This shows that the ribbed design could reduce the swirl significantly

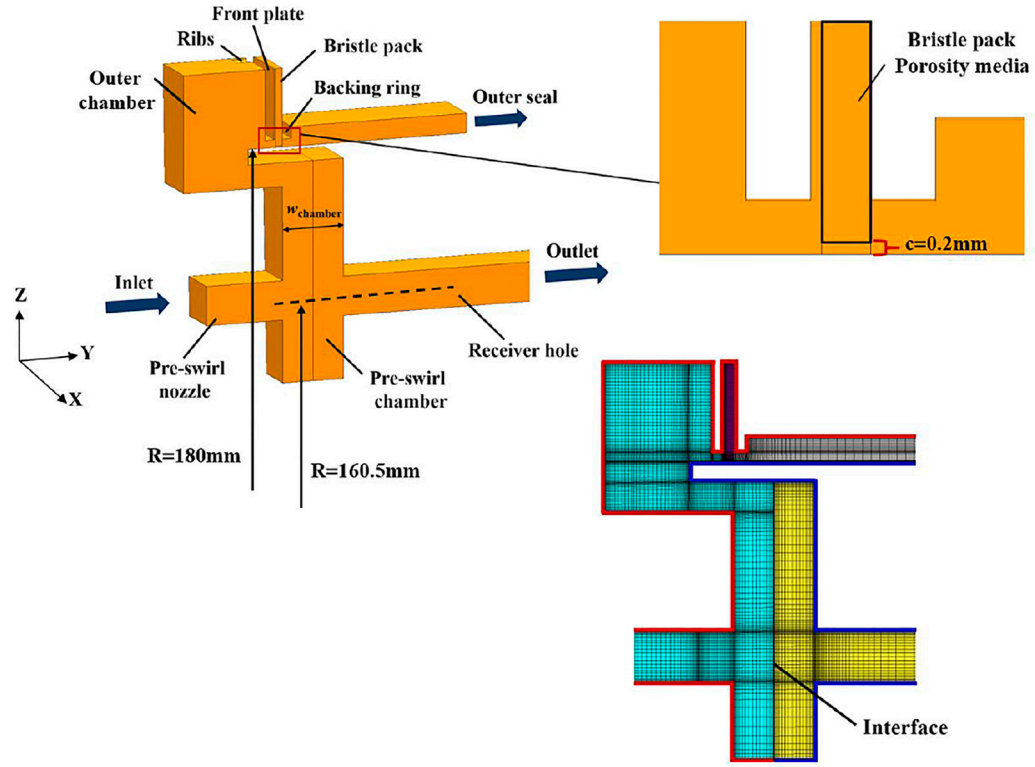

FIGURE 18 | CFD domain and mesh for the preswirl chamber.

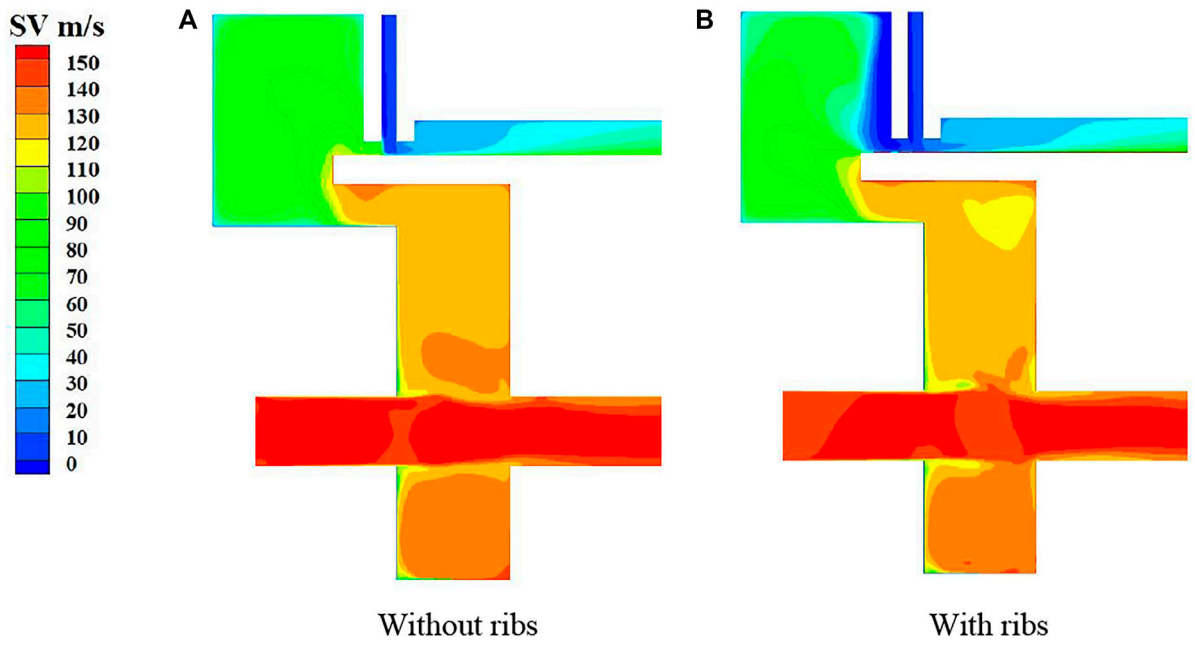

FIGURE 19 | Swirl velocity contours on periodic surface for preswirl chamber applications: **(A)** without ribs, **(B)** with ribs.

when leakage as a percentage of total supplied flow ranges from 0.35% to 5%. With higher inlet swirl velocity (250 m/s), the effect of ribs is still dramatic, reducing the swirl for surface 4 from 158.6 to 3.2 m/s. The data indicate that the effectiveness of the optimized geometry from the parametric study is sensitive to levels of inlet swirl and leakage flow but provides significant swirl

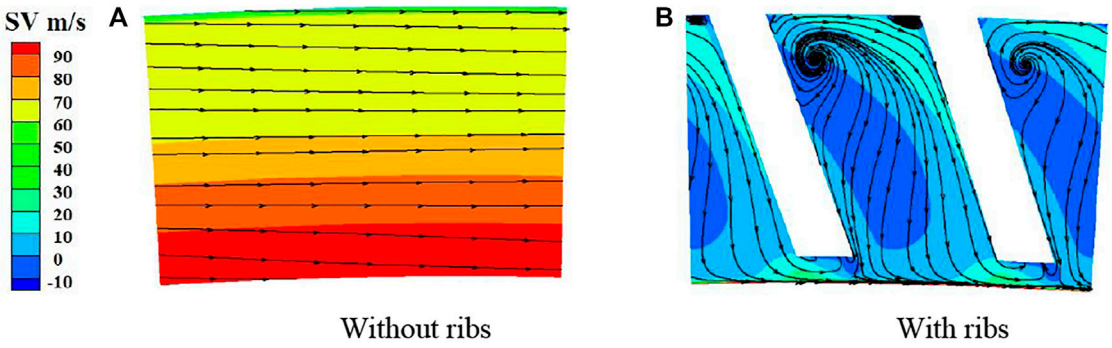

FIGURE 20 | Swirl velocity contours and streamlines on surface 3 for preswirl chamber applications: **(A)** without ribs, **(B)** with ribs.

TABLE 6 | Summary of results for all the conditions considered for the preswirl chamber.

Case	SV_ inlet (m/s)	Ribs	m_leakage (annulus) (kg/s)	m_leakage/ m_total (%)	SV-avg_Surf 4 (m/s)	SV-max_Surf 4 (m/s)	SV_receiver inlet (m/s)
c = 0 mm, ε = 0.192	150	No	0.0264	0.35	51.5	72.9	144.3
		Yes	0.0385	0.51	30.1	82.5	138.0
c = 0 mm, ε = 0.8		No	0.0572	0.75	106.4	122.8	144.3
		Yes	0.0538	0.71	50.1	94.5	146.2
c = 0.2 mm, ε = 0.192		No	0.1080	1.41	85.2	116.8	146.8
		Yes	0.1277	1.66	5.4	46.5	145.7
c = 0.2 mm, ε = 0.8		No	0.3904	4.88	108.4	123.4	149.0
		Yes	0.3878	4.84	37.9	78.6	146.4
c = 0.2 mm, ε = 0.8	250	No	0.2622	4.56	158.6	168.2	247.2
		Yes	0.3047	5.29	3.2	52.5	247.9

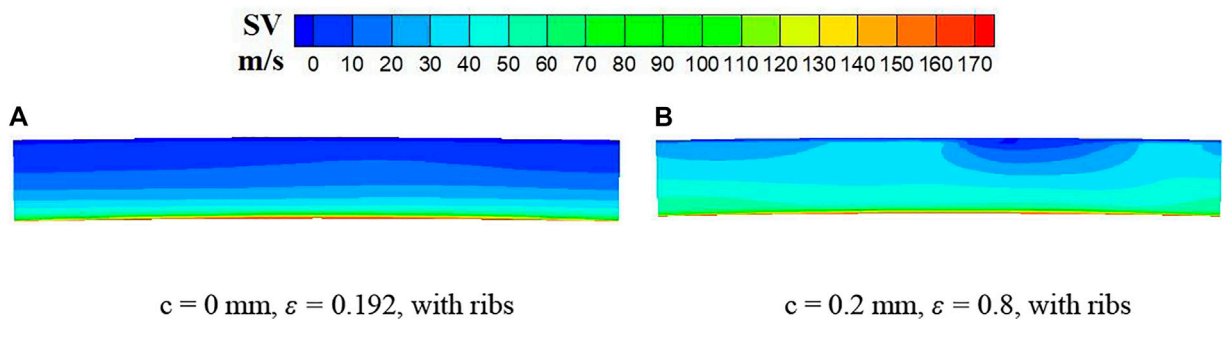

FIGURE 21 | Swirl velocity contours approaching the seal for the lowest and highest leakage flow cases with ribbed front plates (SV = 150 m/s): **(A)** c = 0 mm, ε = 0.192, with ribs, **(B)** c = 0.2 mm, ε = 0.8, with ribs.

reductions in all cases. Thus, inclusion of these parameters in rib optimization studies may give further performance improvements. Considering the maximum swirl velocity at surface 4 for $r > 180.02$ mm (excluding the velocity in the thin boundary on the rotating wall), it can be seen that reasonably uniform flow upstream the bristle pack is achieved. This is further illustrated by the contour plots in **Figure 21**.

The moments on the rotor and stator and the swirl velocity of the blade cooling flow at the receiver affect the system performance. As might be expected, the ribs generally increase the moments slightly. As shown in **Table 6**, the effect on the main cooling air is limited so that an overall benefit from the reduced leakage using brush seals can be maintained.

CONCLUSION

A new design of brush seal front plate has been proposed and analyzed. The plate incorporates ribs that condition the flow entering the bristle pack reducing the flow swirl and hence protect

the bristle from destabilizing aerodynamic forces. The main conclusions are summarized as follows.

1. Angled ribs on the upstream side of the front plate can effectively condition the flow upstream of the bristle pack, reducing swirl and deflecting the flow to feed the seal. This will reduce the circumferential forces impacting on the bristle pack, thereby controlling the bristle slip and instability.
2. Positive rib angles with the flow deflected radially inward toward the seal are clearly more effective in reducing swirl near the shaft and seal inlet. As the positive rib angle increases, the swirl velocity beneath the rib tip is seen to also increase. This could lead to destabilizing aerodynamic forces on the bristles in this region, and the best angle for reducing the swirl flow velocity was found to be approximately 20°.
3. The height-to-spacing ratio of the ribs is another key parameter in controlling the flow approaching the seal. At a rib angle of 20°, ratios ranging from 0 (no ribs) to 0.4 were studied, and the larger the ratio was, the better the reduction of the swirl flow and induction of radial inflow was. Ribs inclined at 20° to the radial direction, with height-to-spacing ratio of 0.4 (height of 2 mm and spacing of 5 mm), showed the best performance in reducing swirl and the most uniform flow in the channel between the ribs.
4. Evaluating the selected design in a CFD model of a turbine cooling preswirl chamber confirmed the expected performance. A number of operating conditions were considered to test the design. In these tests, the leakage flow rate varied from 0.35% to 5% of the supplied coolant flow rate, and the inlet swirl ranged from 150 to 250 m/s. The ribs were found to perform well in reducing swirl (which is expected to improve the seal stability), while having little effect on the preswirl delivery air. Considering the observed reduction in inlet swirl due to the introduction of a seal outer chamber and sensitivities to inlet swirl and leakage rates, inlet swirl reduction might be further improved with additional optimization of the rib and cavity geometry. While the preswirl chamber has provided a useful test case, this sealing geometry can be deployed in other high-value sealing positions where inlet swirl immediately incident on the upstream cover plate region could potentially destabilize the bristle pack.

DATA AVAILABILITY STATEMENT

The raw data supporting the conclusion of this article will be made available by the authors, without undue reservation.

AUTHOR CONTRIBUTIONS

LY, CJ, and PM provide research idea and formal analysis. DW and YB carried out all the calculation work. LY and DW write the original manuscript. CJ, PM, and KX are responsible for the revision of the paper. All authors have read and agreed to the published version of the manuscript.

FUNDING

This research is supported by the National Natural Science Foundation of China (No. 52106040, No. 52006021), China Postdoctoral Science Foundation (No. 2021M700648, No. 2021M690498), Dalian Science and Technology Innovation Fund (No. 2021JJ12GX030) and Natural Science Foundation of Liaoning Province (No. 2020-BS-069).

REFERENCES

Aslan-zada, F. E., Mammadov, V. A., and Dohnal, F. (2013). Brush Seals and Labyrinth Seals in Gas Turbine Applications. *Proc. Inst. Mech. Eng. A: J. Power Energ.* 227 (2), 216–230. doi:10.1177/0957650912464922

Asok, S. P., Sankaranarayanasamy, K., Sundararajan, T., Starwin, P., Kalieswaran, R., and Dinesh, M. (2008). Pressure Drop Characteristics of Water Flow through Static Annular and Triangular Cavity Labyrinth Seals. *Eng. Appl. Comput. Fluid Mech.* 2 (4), 482–495. doi:10.1080/19942060.2008.11015246

Bayley, F. J., and Long, C. A. (1993). A Combined Experimental and Theoretical Study of Flow and Pressure Distributions in a brush Seal. *J. Eng. Gas Turbines Power* 115 (2), 404–410. doi:10.1115/1.2906723

Chew, J., Hills, N., and Khalatov, S. (2003). "Measurement and Analysis of Flow in a Pre-swirled Cooling Air Delivery System," in *ASME Turbo Expo 2003: Power for Land, Sea, and Air* (Atlanta, GA: ASME), 3. doi:10.1115/gt2003-38084

Chew, J. W., and Hogg, S. I. (1997). Porosity Modeling of brush Seals. *J. Tribology* 119 (4), 769–775. doi:10.1115/1.2833883

Chew, J. W., Lapworth, B. L., and Millener, P. J. (1995). Mathematical Modeling of brush Seals. *Int. J. Heat Fluid Flow* 16 (6), 493–500. doi:10.1016/0142-727X(95)00061-T

Chupp, R. E., Ghasripoor, F., Turnquist, N. A., Demiroglu, M., and Aksit, M. F. (2002). Advanced Seals for Industrial Turbine Applications: Dynamic Seal Development. *J. Propulsion Power* 18 (6), 1260–1266. doi:10.2514/2.6061

Crudgington, P., Bowsher, A., Kirk, T., and Walia, J. (2012). "Brush Seal Hysteresis," in 48th AIAA/ASME/SAE/ASEE Joint Propulsion Conference & Exhibit (Atlanta: AIAA). doi:10.2514/6.2012-4003

Dogu, Y., and Aksit, M. F. (2006). Effects of Geometry on Brush Seal Pressure and Flow Fields-Part I: Front Plate Configurations. *J. Turbomach.* 128 (2), 367–378. doi:10.1115/1.2101857

Dogu, Y., Bahar, A. S., and Sertcakan, M. C. (2016). Computational Fluid Dynamics Investigation of brush Seal Leakage Performance Depending on Geometric Dimensions and Operating Conditions. *J. Eng. Gas Turbines Power* 138 (3), 1–13. doi:10.1115/1.403137010.1115/1.4031370

Gresham, T. G., Weaver, B. K., Wood, H. G., and Untaroiu, A. (2016). "Characterization of Brush Seal Permeability," in *ASME Turbo Expo 2016: Power for Land, Sea, and Air* (Seoul, South Korea: ASME), 3. doi:10.1115/GT2016-57910

Guardino, C., and Chew, J. W. (2004). "Numerical Simulation of 3D Bristle Bending in Brush Seals," in *ASME Turbo Expo 2004: Power for Land, Sea, and Air* (Vienna, Austria: ASME), 3. doi:10.1115/GT2004-53176

Helm, P., Pugachev, A., and Neef, M. (2008). "Breaking the Swirl with Brush Seals: Numerical Modeling and Experimental Evidence," in *ASME Turbo Expo 2008: Power for Land, Sea, and Air* (Berlin, Germany: ASME), 3. doi:10.1115/gt2008-50257

Lelli, D., Chew, J. W., and Cooper, P. (2006). Combined Three-Dimensional Fluid Dynamics and Mechanical Modeling of Brush Seals. *J. Turbomach.* 128 (1), 188–195. doi:10.1115/1.2103093

Liu, G., Gong, W., Wu, H., and Lin, A. (2021). Experimental and CFD Analysis on the Pressure Ratio and Entropy Increment in a Cover-Plate Pre-swirl System of Gas Turbine Engine. *Eng. Appl. Comput. Fluid Mech.* 15 (1), 476–489. doi:10.1080/19942060.2021.1884600

Liu, Y., Chew, J. W., Pekris, J., Pekris, M. J., and Kong, X. (2020). The Effect of Inlet Swirl on Brush Seal Bristle Deflections and Stability. *J. Eng. Gas Turbines Power* 142 (7), 071002. doi:10.1115/1.4046696

Liu, Y., Yue, B., Kong, X., Chen, H., and Lu, H. (2021). Design and Performance Analysis of a Vane Shaped Rotating Receiver Hole in High Radius Pre-swirl Systems for Gas Turbine Cooling. *Aerospace Sci. Tech.* 115 (2021), 106807. doi:10.1016/j.ast.2021.106807

Pugachev, A. O. (2014). "Aggregation of Experimental and Theoretical Data for brush Seal Leakage Evaluation," in 50th AIAA/ASME/SAE/ASEE Joint Propulsion Conference (Cleveland, OH: AIAA). doi:10.2514/6.2014-3598

Ramakrishna, P. V., and Govardhan, M. (2009). Aerodynamic Performance of Low Speed Axial Flow Compressor Rotors with Sweep and Tip Clearance. *Eng. Appl. Comput. Fluid Mech.* 3 (2), 195–206. doi:10.1080/19942060.2009.11015265

Sharatchandra, M. C., and Rhode, D. L. (1996). Computed Effects of Rotor-Induced Swirl on Brush Seal Performance-Part 2: Bristle Force Analysis. *J. Tribology* 118 (4), 920–926. doi:10.1115/1.2831629

Sun, D., Liu, N.-N., Fei, C.-W., Hu, G.-Y., Ai, Y.-T., and Choy, Y.-S. (2016). Theoretical and Numerical Investigation on the Leakage Characteristics of Brush Seals Based on Fluid-Structure Interaction. *Aerospace Sci. Tech.* 58, 207–216. doi:10.1016/j.ast.2016.08.023

Turner, M. T., Chew, J. W., and Long, C. A. (1998). Experimental Investigation and Mathematical Modeling of Clearance Brush Seals. *J. Eng. Gas Turbines Power* 120, 573–579. doi:10.1115/1.2818185

Wei, Y., Chen, Z., and Jiao, Y. (2015). Effects of Geometry on Leakage Flow Characteristics of Brush Seal. *J. Harbin Inst. Tech.* 22 (002), 1–7. doi:10.11916/j.issn.1005-9113.2015.02.001

Zhang, Y., Yan, J., and Li, J. (2017). Investigations on Leakage Flow Characteristics of Brush Seal with Consideration of Blow Down Effect. *Lubrication Eng.* 42 (4), 36–42. doi:10.3969/j.issn.0254-0150.2017.04.007

Zhao, H., and Stango, R. J. (2007). Role of Distributed Interbristle Friction Force on Brush Seal Hysteresis. *J. Tribology* 129 (1), 199–204. doi:10.1115/1.2401218

Conflict of Interest: The authors declare that the research was conducted in the absence of any commercial or financial relationships that could be construed as a potential conflict of interest.

Publisher's Note: All claims expressed in this article are solely those of the authors and do not necessarily represent those of their affiliated organizations, or those of the publisher, the editors and the reviewers. Any product that may be evaluated in this article, or claim that may be made by its manufacturer, is not guaranteed or endorsed by the publisher.

NOMENCLATURE

a Viscous resistance coefficient

b Inertial resistance coefficient

D Bristle diameter, m

H Height of bristle overhang, m

h Rib height, m

L Rib spacing, m

L_b Bristle length, m

N Density of the bristles, bristles/mm

p^* Nondimensional pressure = $(p - p_{out})/(p_{in} - p_{out})$

R Radial location, m

SV Swirl velocity, m/s

w Ribs width, m

w_b Thickness of the bristle pack, m

X, Y, Z Circumferential, axial, radial direction, respectively

Z_{rotor} Radial clearance between bristle and rotor, m

α Incline angle of ribs, °

δ Minimum clearance between bristles, m

ε Porosity of the bristle pack

ρ Density of the flow, kg/m^3

ϕ Incline angle of bristle pack, °

Subscripts

m Parallel to the bristles

n Perpendicular to the bristles

z Parallel to the rotating shaft

frontiers in Energy Research

ORIGINAL RESEARCH
published: 04 February 2022
doi: 10.3389/fenrg.2022.835977

Three-Dimensional Numerical Analysis of Longitudinal Thermoacoustic Instability in a Single-Element Rocket Combustor

Guo Kangkang, Xu Boqi, Ren Yongjie, Tong Yiheng and Nie Wansheng*

Space Engineering University, Department of Aerospace Science and Technology, Bei Jing, China

This study numerically investigated the thermoacoustic combustion instability characteristics of a scaled rocket combustor based on a hybrid of the Reynolds-averaged Navier–Stokes and large–eddy simulation method. The turbulence–combustion interactions were treated using flamelet generated manifold approach. An unstable case was simulated with detailed reaction mechanisms (GRI-Mech 3.0). The obtained results agree well with experiment data from Purdue University, in terms of pressure oscillations frequency and power spectral density spectrum. The combustion instability mode was identified to be coupled with the first longitudinal acoustic mode of the combustion chamber by dynamic model decomposition method. According to Rayleigh index analysis, the unstable driving source was found to be located near the combustor step, which was further confirmed by time-averaged flow fields. Detailed three-dimensional vortex ring shedding evolutions at the combustor step were tracked with fine time resolution. Results indicate that the combustion instability arises from periodic vortex ring shedding at the combustor step and interacting with the chamber wall. The unburnt reactants were rolled up by the shedding vortex ring, which would not break up until impact with the chamber wall. Therefore, the mixing performance was significantly enhanced, leading to sudden heat release. Consequently, the thermal energy is added to the acoustic field, and the first longitudinal mode is thus reinforced, giving rise to large amplitude axial velocity oscillations which prompt the generation of the new vortex ring. The results of the present investigation will support the design and development of high-performance rocket engines.

Keywords: combustion instability, numerical simulation, vortex ring shedding, DMD analysis, rocket propulsion

OPEN ACCESS

Edited by:
Xiao Liu,
Harbin Engineering University, China

Reviewed by:
Fan Zhag,
Tianjin University, China
Qingfei Fu,
Beihang University, China
Yang Li,
Northwestern Polytechnical University, China

****Correspondence:***
Ren Yongjie
Spacedreamer@163.com

Specialty section:
This article was submitted to Advanced Clean Fuel Technologies, a section of the journal Frontiers in Energy Research

Received: *15 December 2021*
Accepted: *10 January 2022*
Published: *04 February 2022*

Citation:
Kangkang G, Boqi X, Yongjie R, Yiheng T and Wansheng N (2022) Three-Dimensional Numerical Analysis of Longitudinal Thermoacoustic Instability in a Single-Element Rocket Combustor. Front. Energy Res. 10:835977. doi: 10.3389/fenrg.2022.835977

INTRODUCTION

Combustion instability arising from the coupling between the chamber acoustic resonance modes and pulsated heat release (Lyu et al., 2021), occurs in many applications, especially in high power density engines, such as gas turbines, and rocket engines (Urbano et al., 2016; Ilbas et al., 2021; Jiang et al., 2021). This coupling may induce disturbances inside the combustion chamber, which may cause large amplitude oscillations. Such oscillations can produce high thermal and mechanical stresses on the combustion chamber, leading to performance degradation, mechanical vibrations, or even failure (Franzelli et al., 2010). The present study focused on the combustion instability in a

high-pressure choked combustor, such as a rocket engine. In such engines, high power density presents and the nozzle throat is acoustically choked. As such, even small perturbations can rapidly develop into high-amplitude oscillations. Once unstable combustion appears during the rocket engine development process, it may take significant time and cost to remedy it, as was the case for the well-known Rocketdyne F-1 engine (Oefelein and Yang, 1993).

In most cases, extremely destructive transverse unstable combustion can be suppressed by resonant cavities or baffles (Smith et al., 2010a). However, the transverse modes were treated with careful design, causing longitudinal oscillations with lower frequencies (NguyenTuan et al., 2018). Fundamental comprehension of the combustion instability process has been developed by Rayleigh in the 1870s (Rayleigh, 1878), who demonstrated that the stability of a combustion system can be identified by the sign of the integral value of the product of pressure and heat release rate in an oscillation circle. A positive integral value indicates the driving combustion instability, and vice versa. In practice, the Rayleigh criterion can be described by **Equation 1** (Harvazinski et al., 2013).

$$RI = \frac{1}{t_2 - t_1} \int_{t_1}^{t_2} \frac{\int_\Omega p(t,x) - \bar{p}(x)dx}{\int_\Omega \bar{p}(x)dx} \frac{\int_\Omega q(t,x) - \bar{q}(x)dx}{\int_\Omega \bar{q}(x)dx} dt \quad (1)$$

where RI is the Rayleigh index. $p(x,t)$, and $q(x,t)$ are the local pressure and heat release rate, respectively.

Over the past 2 decades, many investigations have been conducted, both experimentally (Kim et al., 2008; Ruan et al., 2020; Liu et al., 2021a) and theoretically (Culick, 1970; Coates and Horton, 1974; Bhatia and Sirignano, 1991; Sattelmayer, 2003). Typically, the longitudinal combustion instability has mostly been examined systematically at Purdue University (Smith et al., 2006, 2010b; Yu, 2009; Wierman et al., 2012). Various scaled combustors with a single injector have been applied to study the longitudinal combustion instability mechanisms, including the Discretely Variable Resonance Combustor (DVRC (Frezzotti et al., 2014)), Continuously Variable Resonance Combustor (CVRC (Yu et al., 2008)), and Full-Flow Staged Combustor (Lemcherfi et al., 2019). A careful design of the acoustic coupling between the injector and combustion chamber allows exciting unstable combustion easily. In addition, various instability modes have been found in CVRC experiments via continuously changing the oxidizer post length. These experiments provided abundant diagnoses of the combustion flow field, such as dynamic pressure (Sisco, 2007), temperature (Buschhagen et al., 2018), and chemiluminescence (Bedard et al., 2014). The results indicated that the combustion chamber step height and oxidizer post length have a significant influence on combustion instability. However, restricted by high temperature and pressure in the combustion chamber, the experiments show powerless in capturing the detailed flow dynamics inside the chamber.

With recent advancements in computer architectures, it has become popular to study combustion instability through high-fidelity numerical method (Zhao et al., 2019; Xia et al., 2021a; Zhou et al., 2021). Extensive comparisons between numerical simulations and experimental data have been presented in Ref. (Smith, 2010), and the ability of the numerical method to correctly capture the complicated physical behaviors of the combustion chamber has been demonstrated in Refs. (Nozari and Karabeyoğlu, 2015; Duvvuri et al., 2020; Liu et al., 2021b). Numerical studies on combustion instability have been performed using either Large-eddy simulation (LES) or a hybrid Reynolds-averaged Navier-Stokes (RANS)/LES method. Initially, only a 2D axisymmetric model or a section of the combustor (Smith et al., 2010c; Schmitt et al., 2011; Murayama et al., 2018) (in the azimuthal direction) was simulated, and most numerical studies were limited to one- or two-step reaction mechanisms. Such simplifications present several limitations. Firstly, the 3D turbulent mixing is ignored, which is very important for diffusion combustion. Secondly, the vortex stretching/tilting and other vorticity generation mechanisms are neglected. Third, the products in the combustion chamber cannot cross through the axisymmetric line of surfaces, which introduces non-physical boundary conditions. Almost all simulated results have shown that the 2D axisymmetric simulation results agreed only with experiments data qualitatively (Smith et al., 2010b). Compared with experimental results, the unstable combustion frequency is usually overestimated by ≥ 15% (Smith et al., 2010c; Srinivasan et al., 2015), and the amplitude of pressure oscillations is underestimated by up to 40% (Garby et al., 2013). Comparative study of 2D axisymmetric and full 3D numerical simulation of CVRC was conducted by Garby et al. (Fuller, 2019) using dynamic thickened flame and LES models. It was reported that the numerical results of full 3D configuration simulation were more consistent with that of experiments. Furthermore, Harvazinski et al. (Harvazinski et al., 2013) found that the 3D simulation results agreed well with experimental results. Almost all numerical simulations (both axisymmetric and full 3D) overpredict the characteristic frequency.

Most previous studies have treated turbulence chemistry interactions by solving the species transport equations (Smith et al., 2008, 2010a, 2010c; Smith, 2010), leading to not only numerical rigidity but also high computational cost, restricting the reaction mechanisms to one- or two-steps. Harvazinski et al. (Harvazinski et al., 2016) conducted a full 3D numerical simulation with detailed reaction mechanisms (GRI-Mech 1.2), however, the model is significantly expensive compared to the global chemical reaction. Possibly due to inefficient 3D grid resolution, the same oscillation amplitudes were obtained as for the global chemical reaction. Recently, the flamelet progress variable (FPV (Peters, 2000)) approach has been successfully used to predicate unstable combustion in CVRCs (2D axisymmetric) (NguyenTuan et al., 2018). The FPV model has been proven to be much cheaper compared to previous simulations. The reason for its low computational cost lies mainly in the fact that it does not solve the transport equations themselves; instead, the turbulent combustion properties are determined by a series of flamelet libraries or pre-established lookup tables (NguyenTuan et al., 2018). To the best of the author's knowledge, taking computational cost into

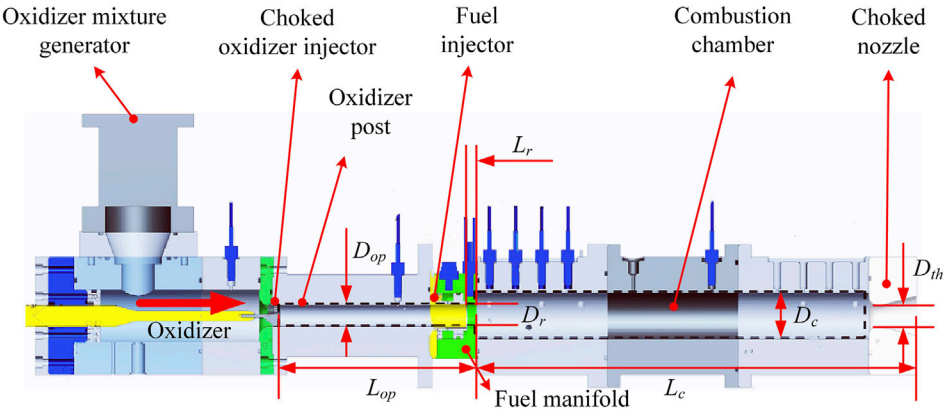

FIGURE 1 | Schematic of the single-element combustor (reproduced from (Yu et al., 2009))

account, previous numerical investigations on CVRCs have been limited by either grid resolution, dimensionality (2D or 3D), or chemical mechanisms (detailed or simplified). A full 3D investigation with a detailed reaction mechanism is required to explore the complete flow dynamics inside a combustion chamber, including vortex shedding and interaction with the chamber wall.

Therefore, to fully characterize the combustion instability mechanisms of CVRC, this study performed a full 3D simulation (with suitable grid resolution) with detailed (GRI Mech 3.0 (Gregory et al., 2018), 53 species and 325 steps) reaction mechanism. This paper is organized as follows. *Combustor Model and Numerical Methods* summarizes the combustor configurations and numerical methods for treating turbulence and chemical reactions. *Result and Discussion* presents the results, detailed discussion, and comparison with existing experiments. Finally, *Conclusion* concludes the paper.

COMBUSTOR MODEL AND NUMERICAL METHODS

Single-Element Combustor

A schematic of the single-element combustor is depicted in **Figure 1**. The combustor is composed of a hot oxidizer mixture generator, oxidizer injector, fuel injector, and dump combustor with a choked nozzle, which has the same configuration as the CVRC developed by Yu et al. (Yu, 2009). The CVRC is named as such because the length of the oxidizer post can be changed continuously. The simulation in this study was performed following the experimental tests of Yu et al. (Yu, 2009; Yu et al., 2009, 2012) to investigate the longitudinal combustion instability in a choked CVRC model. In Yu et al.'s experiments, the oxidizer mixture consists of 52% H_2O and 48% O_2 (by weight) decomposed from the hydrogen peroxide through a catalyst bed. The mixture flows through the oxidizer manifold and was then injected into the oxidizer post through the choked oxidizer injector (**Figure 1**). Gaseous methane (CH_4) was ejected from an annulus consisting of a fuel injector and manifold. The oxidizer and fuel were mixed inside the recess chamber (region between the fuel injector tip and combustor step) and were introduced into the combustion chamber by a shear coaxial injector. The key geometrical parameters of the single-element combustor are listed in **Table 1**.

TABLE 1 | Key geometrical parameters of the single-element combustor.

Parameter	Value (mm)	Parameter	Value (mm)
L_{op}	114.30	L_c	400.00
L_r	10.16	D_{op}	20.47
D_r	23.06	D_c	44.96
Dth	20.80		

The experimental investigations focused on the effects of varying oxidizer post length, which was done both continuously and discretely. The present study aimed to extract the longitudinal combustion instability mechanisms of the combustor model. Therefore, only a fixed oxidizer post length (114.3 mm) was examined. The present study is based on the near most unstable condition in the experiments, corresponding to the geometric configuration detailed in **Table 1**.

Numerical Framework

Turbulence Model

Stress-blended eddy simulation (SBES (Menter, 2016)) is a hybrid RANS/LES turbulence model developed by Ansys Inc., which could provide optimal treatment for the problem of grid-induced separation and switch swiftly from RANS to LES in separating shear layers. The model applies a blending function to automatically switch between RANS and LES models according to local flow characteristics.

Various applications (Yu et al., 2020; Xia et al., 2021b, 2021c) have demonstrated that the SBES method could achieve a satisfactory balance between calculation accuracy and computational expense. Therefore, the SBES method was used to treat turbulence in the present study.

The blending function for SBES is denoted by f_s, and the SBES algorithm for stress-level can be described as:

$$\tau_{ij} = \tau_{ij}^{RANS} f_s + \tau_{ij}^{LES}(1 - f_s) \quad (2)$$

where τ_{ij}^{RANS} and τ_{ij}^{LES} represent the RANS and LES stress tensor, respectively. In this paper, the stress tensor of the RANS part is modeled by the $k-\omega$ shear stress transport (SST) model (Menter, 1994), which works well with the internal flow, while the LES part of the sub-grid scale (SGS) stress was modelled by the sub-grid wall-adapting local eddy-viscosity (WALE (Nicoud and Ducros, 1999)) model.

Turbulent Combustion Model

Premixed and diffusion combustion are the two limits of combustion, respectively. In practice, the fuel and oxidizer generally have been mixed partly before combustion, because of turbulence. When the degree of mixing is not spatially homogeneous, such a combustion mode is called partially premixed combustion. A vigorous interaction between the fuel and oxidizer could develop in the recess region before they enter the combustion chamber. A partially premixed combustion model was thus adopted in this work. The flamelet generated manifold (FGM (Verma et al., 2019; Jurić et al., 2021)) model has previously been applied to treat turbulent chemical processes and has been widely used to treat combustion (Ramaekers, 2011; Verma et al., 2019).

The FGM maps complex, multidimensional chemical reaction information into one or more characteristic variables (such as mixture fraction f, scalar dissipation rate χ, and reaction progress variable c) to achieve dimensionality reduction. This method can reduce the number of transport equations to be solved while considering the detailed chemical reaction mechanism. In this study, a beta-type probability density function (beta PDF (Girimaji, 1991)) FGM table was generated to store precomputed variances of both c and f. The beta PDF FGM could account for turbulent fluctuations and further model the turbulence chemistry interaction. Meanwhile, mean temperature, density, and species fractions could be determined by looking them up in the PDF table with extremely reduced computational cost. Since the turbulent flames in the present work were predominantly non-premixed, the 1-D laminar counterflow diffusion flame was used to generate diffusion FGMs, and detailed theory can be found in reference (Verma et al., 2019). A detailed reaction mechanism (GRI-Mech 3.0) was used to generate the presumed PDF. A set of the mixture fraction space equations are solved to transform laminar counterflow diffusion flame equations from physical space to mixture fraction space. The equations for the species mass fractions are as follows:

$$\rho \frac{\partial Y_i}{\partial t} = \frac{1}{2}\rho\chi \frac{\partial^2 Y_i}{\partial f^2} + S_i \quad (3)$$

and one equation for temperature as follows:

$$\rho \frac{\partial T}{\partial t} = \frac{1}{2}\rho\chi \frac{\partial^2 T}{\partial f^2} - \frac{1}{c_p}\sum_i H_i S_i + \frac{1}{2c_p}\rho\chi\left[\frac{\partial c_p}{\partial f} + \sum_i c_{p,i}\frac{\partial Y_i}{\partial f}\right]\frac{\partial T}{\partial f} \quad (4)$$

where Y_i denotes the mass fraction of the i^{th} species. T, ρ, and f are temperature, density, and mixture fraction, respectively. c_p is the mixture-averaged specific heat. $c_{p,i}$, H_i, and S_i represent the specific heat, specific enthalpy, and reaction rate of i^{th} the species, respectively.

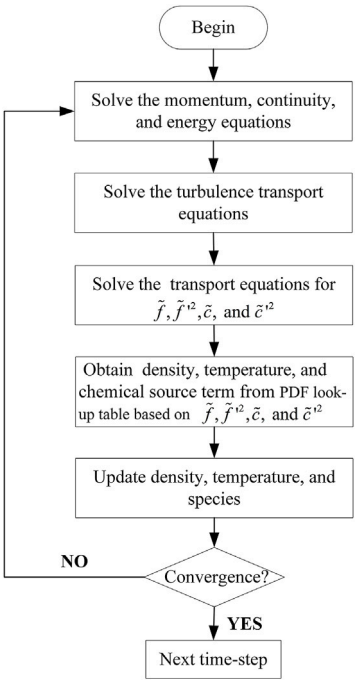

FIGURE 2 | Flowchart of one-time step of the numerical program for the present model (only four specie transport equations were solved, which massively decrease computational cost compared to previous numerical simulations (Smith et al., 2008; Smith et al., 2010a; Smith et al., 2010c; Smith, 2010))

The scalar dissipation χ is defined as

$$\chi = 2D|\nabla f|^2 \quad (5)$$

where D is a diffusion coefficient.

We assumed that the scalar dissipation rate f and reaction progress variable c are independent of each other, so the joint PDF of f and c could be given as:

$$\tilde{P}(f,c) = \tilde{P}(f)\tilde{P}(c) \quad (6)$$

where $\tilde{P}(f)$ (PDF of scalar-dissipation rate) is determined by mean mixture fraction $\tilde{f}$ (Favre mean) and mixture fraction variance $\tilde{f}'$. Similarly, $\tilde{P}(c)$ (PDF of progress variable variance) depends on the mean mixture fraction $\tilde{c}$ and mixture fraction variance $\tilde{c}'$.

Based on the model described above, a detailed chemical reaction mechanism was considered by solving the transport equations of $\tilde{f}$, $\tilde{f}'$, $\tilde{c}$, and $\tilde{c}'$ in a 3D numerical simulation. The detailed theory of the FGM model can be found in Ref. (Verma et al., 2019). The temperature and pressure of the combustion chamber are predicated to be 3000K and 1 MPa. The chamber pressure is much lower than the critical pressure, so, the ideal-gas law is introduced. A flowchart of the overall numerical simulation procedure is illustrated in **Figure 2**.

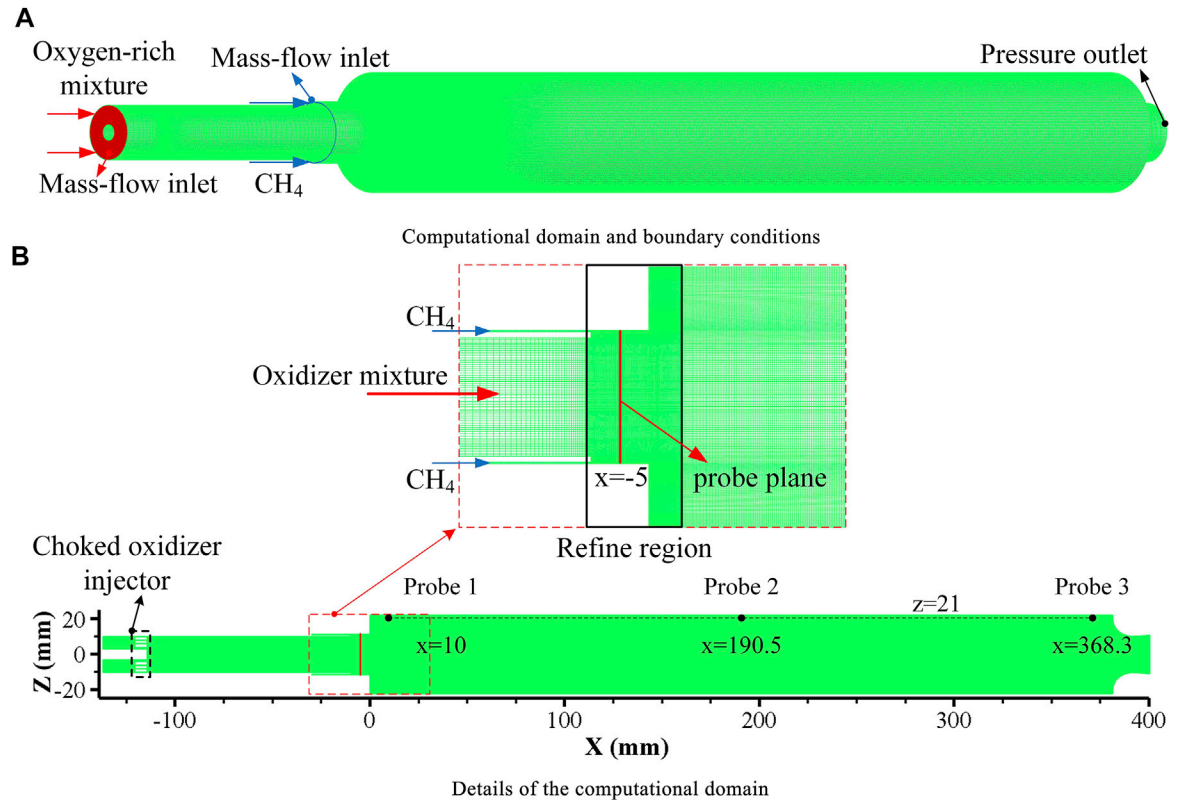

FIGURE 3 | Computational domain and boundary conditions. **(A)** Computational domain and boundary conditions, **(B)** Details of the computational domain.

Computational Domain and Boundary Conditions

As indicated in **Figure 3**, the computational domain consists of the choked oxidizer injector, fuel injector, combustion chamber, and choked nozzle. The oxidizer mixture and fuel inlets were set as constant mass-flow inlets and the mass flow rate of methane and oxidizer are 27.67 g/s and 319.78 g/s respectively. The hot oxidizer (1029K) is composed of 58% water vapor and 42% oxygen by weight. The outlet was set as pressure outlet and the initial pressure is 101,325 Pa. Adiabatic non-slip conditions were adopted for all walls. According to previous research (Yu, 2009; Smith et al., 2010a, 2010b), the combustion instability mechanism of the single-element combustor is expected to be related to the vortex shedding at the combustor step. Consequently, the grids around the combustor step were refined to resolve steep pressure and vorticity gradients, as detailed in the close-up view of **Figure 3B**. After the grid independence study (as illustrated in *Grid Independence Study*), approximately 10.3 million cells were applied to conduct the present study, using 128 processors. The finest grids were located in the refined region and were about 43μm.

To record the signals (e.g., pressure, heat release, velocity) inside the model combustor, three probes were set in the combustion chamber, as depicted in **Figure 3B**. The probe plane, a mass flow rate detection surface (other signals were also recorded) located at x = -5 mm, is displayed in **Figure 3B**. All probes (referred to as probes 1–3) are located at z = 21 mm (very close to the combustion chamber wall) to simulate high-frequency pressure transducers. Probe 2 is in the middle of the combustion chamber to capture the pressure node, and probe 1 is distributed upstream of the chamber. Particularly, probe 3 is set at x = 368.3 mm for comparison with the experiments (Yu, 2009).

Numerical Scheme

The present numerical study was based on a 3D FGM model and performed on *ANSYS Fluent V2020 R1*. Turbulence was solved by SBES method. The SGS model was WALE. Scalar fluxes were discretized in a second-order upwind format. The pressure-implicit with splitting of operators' method (Issa, 1985) was employed to deal with the pressure velocity coupling terms. A bounded-central differencing scheme was applied to discretize the momentum equations. Second-order temporal accuracy was received by applying an implicit dual-time method.

Grid Independence Study

As mentioned above, the present simulation was based on experiments at Purdue University (Yu, 2009). The oxidizer post length was continuously varied in the experiments, and results demonstrated that the limit cycle behavior was quasi-stationary at any given tube length (Yu et al., 2012). Consequently, the present fixed oxidizer post length results

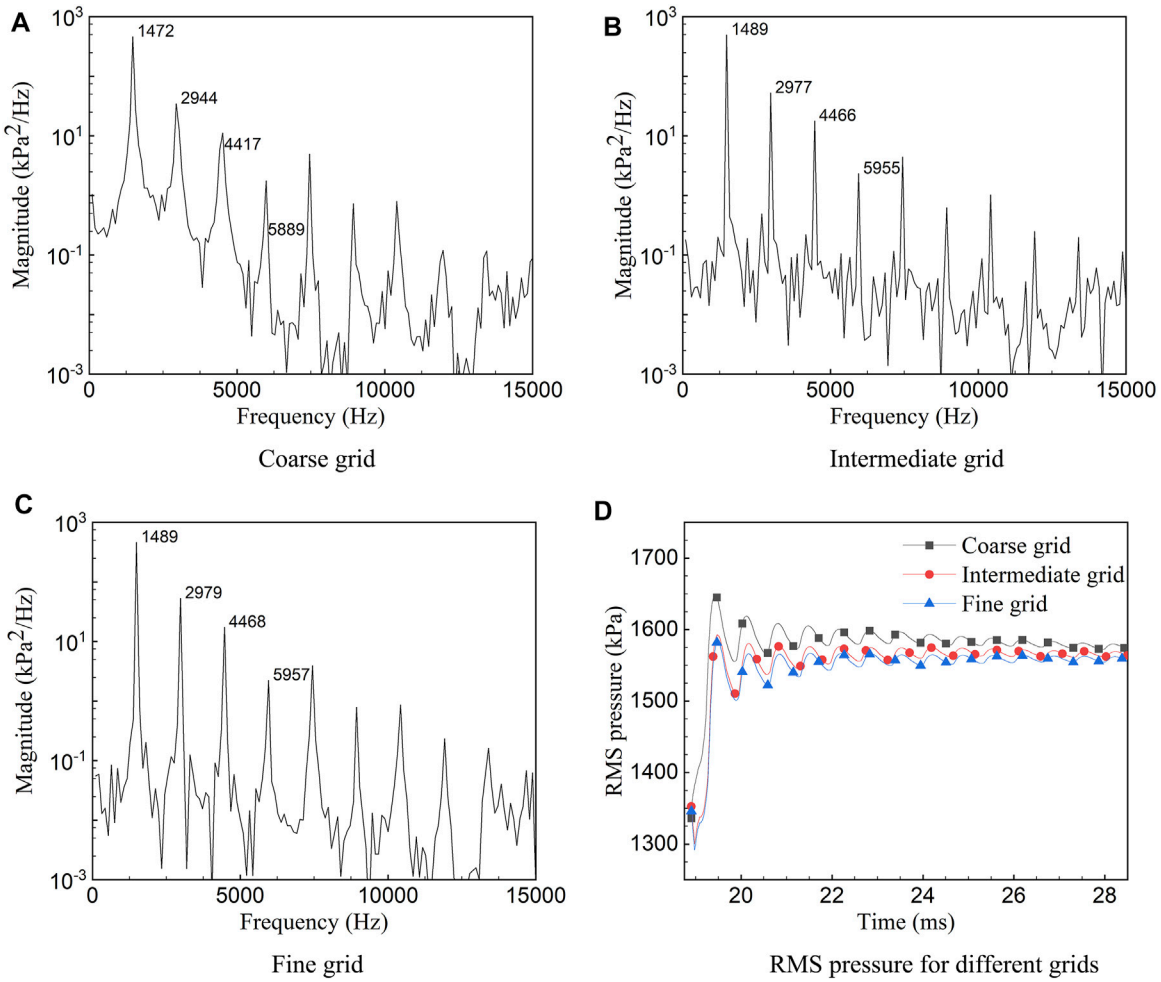

FIGURE 4 | PSD and RMS pressure of various resolution grids. The pressure signals recorded at probe 3 were used for the present analysis. **(A)** Coarse grid (7.7 million cells). **(B)** Intermediate grid (10.3 million cells). **(C)** Fine grid (11.5 million cells). **(D)** RMS pressure for different grids.

can be compared with the experimental results (Yu et al., 2012) to verify the model accuracy. To provide a high temporal resolution, a time step of 2e-7 s was used. Given the limited computing resources, the simulations were performed for no more than 30 *ms*. The following results indicate that the initial transient caused by ignition had been died out and a record length of about 11 *ms* (18.5–29.5 *ms*, probe 3) for statistical analysis.

To ensure appropriate numerical accuracy, a grid independence study was performed on three different levels of mesh resolution. The frequency spectrum is one of the most important characteristics of combustion instability, so it was simulated on all three grids. Meanwhile, the root mean square (RMS) pressure was also evaluated. **Figures 4A–C** present the corresponding power spectral density (PSD) plots for all three grids. The results demonstrate that the deviation of both frequency and magnitude between the intermediate grid and fine grid was almost consistent. The RMS pressures of various grids are displayed in **Figure 4D**. It was found that the solution

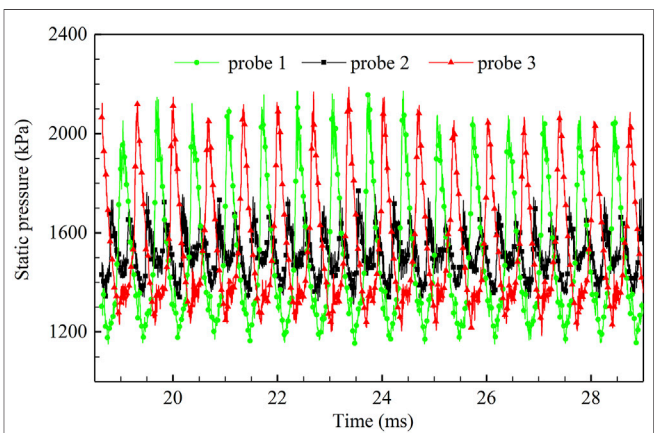

FIGURE 5 | Pressure time traces of probes1, 2, and 3. The amplitude of the pressure time traces at probe 2 is much lower than at probes 1 and 3, and almost peaks twice in one cycle.

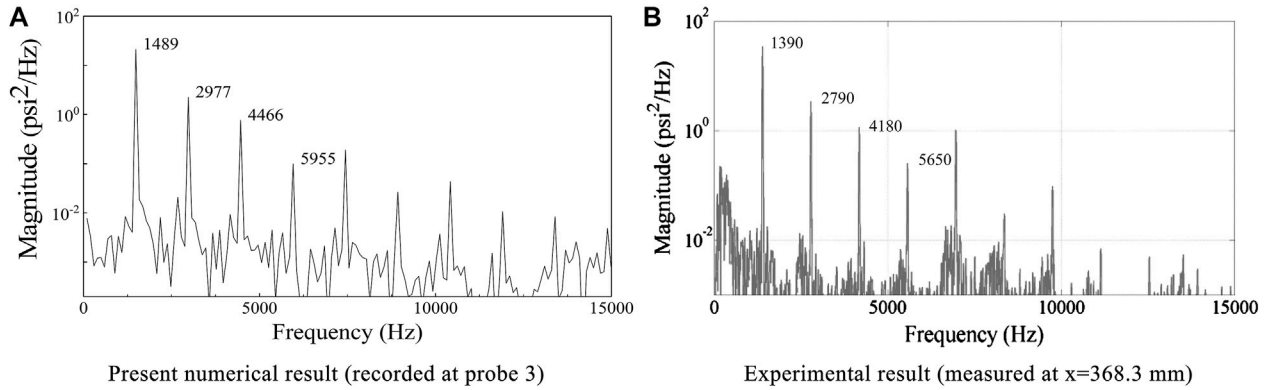

FIGURE 6 | Comparison of PSD analysis between numerical results and experimental (Yu et al., 2012) data. The relative error between computed dominant frequency (1,489 Hz) and experimental result (1,390 Hz) is within 7.2%, and that for pressure oscillations is 19.2%. **(A)** Present numerical result (recorded at probe 3) **(B)** Experimental result (measured at x = 368.3 mm).

starts to converge at the intermediate grid. Thus, given the computational cost and simulation accuracy, the intermediate grid proved suitable for the present study.

RESULTS AND DISCUSSION

Various analysis methods were used to evaluate the computational data, some mainly for identifying the combustion instability mode, and others for investigating the mechanisms of the instability. The results are arranged basically according to the analysis methods and their purposes.

Combustion Instability Mode

Power Spectral Density and Mode Shape

Pressure time traces at probe 1, probe 2 and probe 3 are shown in **Figure 5**. These probes were selected mainly due to their proximity to the predicted locations of pressure anti-nodes (probes 1 and 3) and pressure node (probe 2). The relatively large pressure oscillations would be captured at probe 1 and probe 3 and smaller ones at probe 2. In present study, pressure oscillations were predicted mainly in the longitudinal mode, thereby allowing these probes to accurately identify the dominant unstable behavior. Consistent with expectations, the pressure oscillations at probes 1 and 3 are much larger than that at probe 2, as evident by **Figure 5**. An almost fixed temporal phase difference can be found between probes 1 and 3, and the pressure wave of probe 2 peaks twice in one cycle. The plot also shows that the mean chamber pressure approximately 1.5 MPa, and the experiment (Yu et al., 2012) was designed to be at a target chamber pressure of 1.58 MPa. However, in practice, relatively low combustion efficiencies were achieved resulting in a mean chamber pressure of approximately 1.38 MPa. The slightly higher mean chamber pressure in the present computational may result from the higher combustion efficiencies and lower heat loss (the adiabatic wall). In general, good agreement was achieved with the experiment in the aspect of mean chamber pressure, demonstrating a reasonably accurate evaluation of the global combustion process.

The dominant frequencies can be identified by performing PSD analysis on the pressure time signals. The PSD analysis results are given in **Figure 6A** on a semi-log scale. The *x* axis is the frequency on a linear scale, and the ordinate is the spectral content on a traditional logarithmic scale. Care must be given to the *y* axis, as each major tick denotes an order magnitude of spectral content change. As indicated in **Figure 6**, the present computational PSD results are listed on the left, and the experimental (Yu et al., 2012) results are on the right to further verify the present numerical model. The PSD analysis of **Figure 6A** was based on the pressure signals measured at probe 3, which was in the same location as the pressure signals recorded in the experiment (Yu et al., 2012) (x = 368.3 mm, **Figure 6B**). A dominant frequency of 1,489 Hz, corresponding to the first longitudinal acoustic mode of the combustor, is identified, as evident in **Figure 6A**. Compared with the combustion instability frequency in the experiments (Yu, 2009; Smith, 2010) (the first longitudinal acoustic frequency was 1,390 Hz), the present simulated frequency is slightly higher by less than 7.2%, which is more accurate than in previous numerical studies (Smith et al., 2008, 2010a, 2010c; Smith, 2010). It is worth noting that all walls in the present study were considered adiabatic walls. Therefore, the static temperature and speed of sound in the combustion chamber were higher than those in the experiments. Thus, it is reasonable that the frequency was slightly higher than that in the experiments (Yu, 2009; Smith, 2010). In addition, the plot in **Figure 6A** also suggests that higher harmonics appear in the pressure time signal. Comparing **Figures 6A,B**, not only does the dominant frequency of the present PSD analysis agree well with the experimental results, but also the non-linear harmonic behavior that occurred in the experiment was also captured in the present simulation. In particular, the increasing then decreasing trend between modes 4, 5, and 6 was captured by the simulation. Accordingly, the accuracy of the model in capturing the combustion dynamics of the present combustor has been verified.

To analyze the mode shape inside the combustion chamber, the instantaneous pressure waves of the combustor centerline

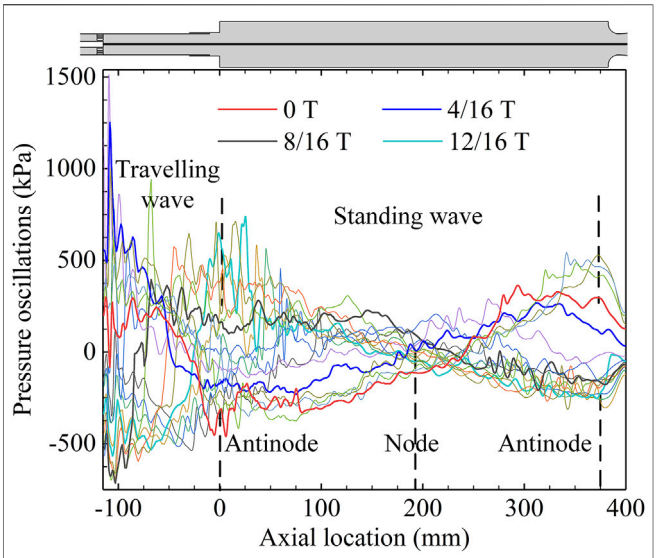

FIGURE 7 | Pressure mode shapes in the model combustor. Oscillating pressure of the centerline (the black line on the top of the plot) over an entire cycle. Only four instantaneous pressure waves are highlighted.

over an entire cycle are plotted in **Figure 7**. The plot not only shows how the pressure changes with time and axial positions inside the combustor but also gives an indication of the pressure oscillation envelope. As shown in **Figure 7**, the maximum values (in the combustion chamber $0 \le x \le 381$) are located at the combustor step and nozzle inlet, and the minimum pressure lies in almost the middle of the combustion chamber, which indicates pressure antinodes at the combustor step and nozzle inlet, and a pressure node near the chamber center. Note that the mode shape in the combustion chamber is different from that in the oxidizer post. The pressure wave in the combustion chamber is more like a standing wave than a traveling wave, although traveling effects are present, while the wave inside the oxidizer post is more similar to a traveling wave. Coupling with the pressure oscillations inside the oxidizer post, the pressure waves propagate upstream and downstream in the combustor model, which may play a crucial role in the combustion instability.

Dynamic Mode Decomposition Analysis

Dynamic mode decomposition (DMD (Tu et al., 2014)) is a purely data-driven matrix decomposition technique that does not rely on any prior physical law and aims to characterize data modes using extracted low-dimensional structures. The temporal and spatial modes of the data sets can be decomposed individually by DMD, which makes the method particularly suitable for analyzing the thermoacoustic instability at specific frequencies (Koizumi et al., 2020). Over the past 10 years, several forms of DMD have been developed, and the version used in this study, named exact DMD, was summarized by Tu et al. (Tu et al., 2014). Detailed mathematical algorithms of exact DMD can be found in Ref (Tu et al., 2014).

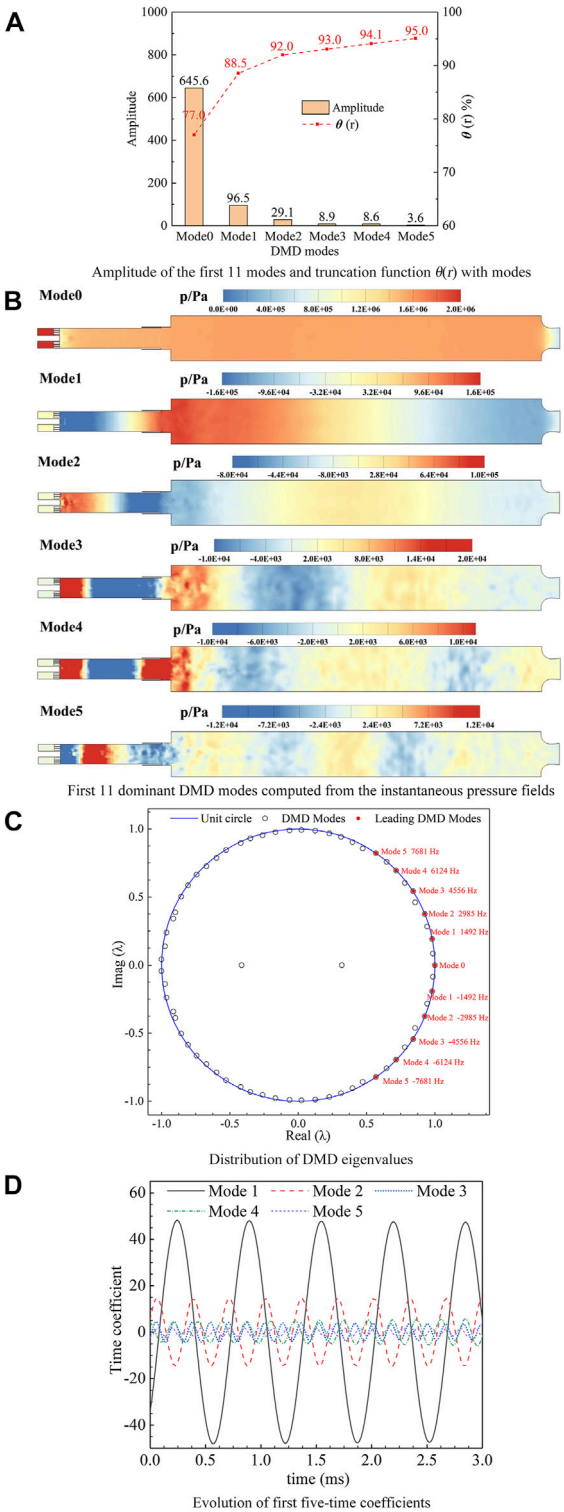

FIGURE 8 | DMD analysis results. **(A)** Amplitude of the first 11 modes and truncation function $\theta(r)$ with modes. **(B)** First 11 dominant DMD modes computed from the instantaneous pressure fields. **(C)** Distribution of DMD eigenvalues. **(D)** Evolution of first five-time coefficients.

A total of 201 snapshots of Y slice from the full 3D high-fidelity pressure fields, corresponding to six cycles have been applied to perform DMD analysis. The snapshots are auto-saved every 100 time-steps in the numerical simulation, where the time resolution is $\Delta t = 2 \times 10^{-5}$ second. This sampling rate can resolve all the major large-scale features associated with flow dynamics. As indicated in **Figure 8B** Mode 0, the DMD analysis suggests a "stationary" mode (Mode 0) which is non-varying in time because of its zero eigenvalue. Therefore, it represents the mean pressure field, and for dynamic stall it has the highest amplitude (Mohan et al., 2015). The other modes appear in pairs and their eigenvalues are complex conjugate, so each pair of modes can be regarded as a single mode with the positive frequency (**Figure 8C**) (Mohan et al., 2015). The truncation function θ(r) is defined as:

$$\theta(r) = \frac{\sum_{i=1}^{j} b(i)}{\sum_{i=1}^{n} b(i)} \tag{7}$$

where $\theta(r)$ is truncation function. $b(i)$ is the amplitude of the ith mode. n is total number of modes, and j represents the first j modes. **Figure 8A** presents the amplitude of the first 11 modes, and the relationships between the mode number and truncation function. As evident in **Figure 8A**, the first 11 modes are enough to make the truncation function up to 95%, which means that the pressure fields can be well reconstructed using the first 11 modes (the deviation from the numerical real pressure field is less than 5%). Therefore, the first 11 modes were selected to realize the pressure field reconstruction (mean field Mode 0, and 5 pairs of conjugate modes, named Mode 1–5).

The first 11 dominant modes are highlighted, corresponding to the modes shown in **Figure 8B**. As **Figure 8D** shows, the oscillation amplitude of the Mode1 (first longitudinal mode) is much higher than that of others, which indicates the dominance of the first longitudinal mode (1,492 Hz). Comparing this with the experimental results (1,390 Hz) demonstrates the reasonable accuracy of the present numerical model. The modes 2, 3, 4, 5 are the 1st, 2nd, 3rd, and 4th harmonics of Mode1, because their frequencies are integer multiples of Model 1 frequency. It is noteworthy that the Model1 suggests large pressure oscillations near the combustor step (**Figure 8B** Model1), which is of great importance to analysis the combustion instability mechanisms Because the amplitudes of the first five-time coefficients remain nearly constant, it can be concluded that the thermoacoustic instability can be maintained during the thermoacoustic coupling process.

Flow Field Snapshots

Instantaneous Flow Fields

Comparing with spectrum analysis, the instantaneous graphs of a specific Y-plane slice make it possible to give a glance at the entire flow field of the combustor. When the time interval between the graphs is small enough, the snapshots can be converted to flow animations, from which the dynamic characteristics can be clearly evaluated, and used to aid interpretation of combustion instability mechanisms. During computations, all data of the entire flow field were auto-saved every 0.02 *ms* for approximately two periods. This frame rate is sufficient (approximately 34 frames per cycle) to produce high-resolution animations, making it possible to track the dynamic characteristics of the flow field in detail. In this section, the instantaneous snapshots at t = 20.8237 *ms* are discussed to gain a global comprehension of the flow field. Second, a series of high-time-resolution images are presented to track the dynamic characteristics of the flow field in detail.

Instantaneous snapshots at a given instance, of pressure, vorticity, mass fraction of CH_4, heat release rate, and temperature are illustrated by **Figure 9**. Taking all plots in **Figure 9** into account, the combustion appears to occur mainly upstream of the combustion chamber, and there seem to be certain relationships between the plots. **Figure 9A** shows a low pressure at the combustor step and relatively high pressure around the nozzle, confirming the first longitudinal acoustic mode. As we can see from **Figure 9B**, vorticity is generated from the choked slot and propagates downstream along with the oxidizer post. Moreover, vorticity also emanates near the combustor step, and the vortices shedding can be easily identified (**Figure 9B**) slightly downstream of the combustor step. Considering **Figures 9B,C** together, the CH_4 appears to be carried by the vortices, which could be accountable for the vorticity and mass fraction of CH_4 being in phase.

The instantaneous flow field snapshots are very important for confirming the reasonableness of the computational results as well as understanding the flow dynamics and combustion instability mechanisms inside the combustor. Therefore, a series of high-time-resolution plots are desirable to track the dynamic characteristics of the flow field in detail.

A series of high-time-resolution flow field snapshots (mass fraction of CH_4, vorticity, heat release, and pressure) are given in **Figure 10**. As shown in **Figure 10** 0T, along with the CH_4 ejecting into the combustion chamber, vortices emerge at the combustor step. The fuel is trapped in the vortices, causing the fairly low propellant mixing efficiency, which further results in a lower heat release rate near the combustor step (**Figure 10** 1/6T). Meanwhile, the pressure plot shows a low pressure near the combustor step and a pressure antinode at the nozzle. With vortices shedding, the fuel is rolled up, expended downstream and on both sides, and the high-pressure waves travel upstream from the nozzle. Further, the vortices impact the combustion chamber wall due to the small step height of the combustor (**Figure 10** 2/6T). The fuel is carried by the vortices and distributed more evenly, as evident by the improved heat release. After the vortices interacts with the chamber wall, the vortices are broken into small vortices, and the mixing efficiency is strongly enhanced, leading to uniform distribution of CH_4, as demonstrated in **Figure 10** 3/6T. The mixing efficiency is greatly enhanced, and the fuel is distributed evenly in the upstream half of the combustor. Consequently, the heat release is increased, and the high-pressure wave propagates further upstream (**Figure 10** 3/6T). As detailed in **Figure 10** 4/6T, the heat release further rises due to the turbulent mixing, and high pressure occurs at the combustor step, demonstrating the spatial coupling between heat release and

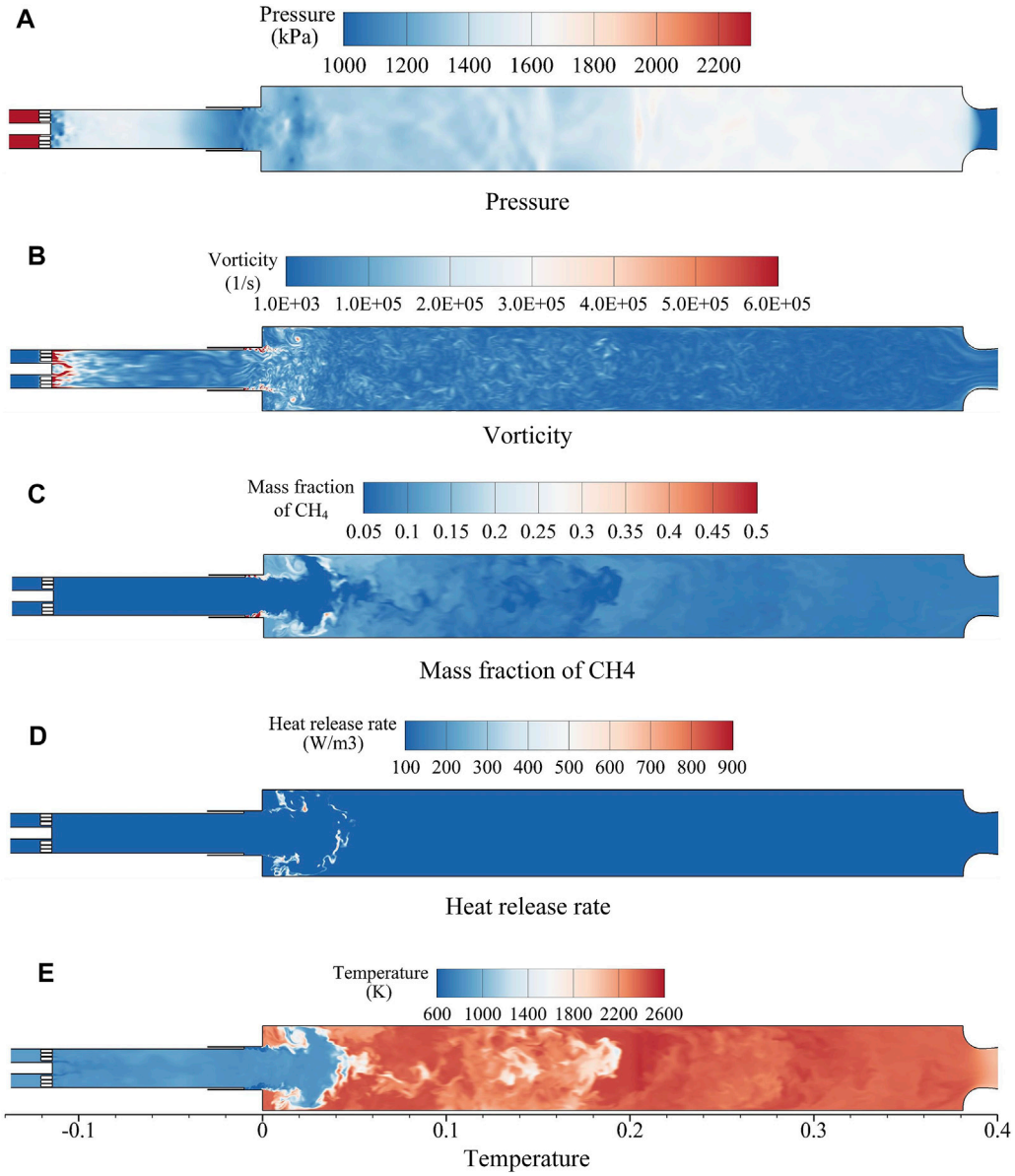

FIGURE 9 | Instantaneous snapshots of **(A)** pressure, **(B)** vorticity, **(C)** mass fraction of CH_4, **(D)** heat release rate, and **(E)** temperature at t = 20.8237 *ms*

pressure. The high pressure propagates upstream into the oxidizer post and downstream to the choked nozzle. Because of the high pressure in the recess region, the propellant cannot eject from the oxidizer post, which is accumulated near the upstream of the recess region, as evident in **Figure 10** 4/6T (plot of CH_4 mass fraction). Inspection of **Figure 10** 5/6T indicates that the pressure near the combustor step gradually dissipates, and the propellant package flows downstream in preparation for the next cycle. It can be deduced that the periodic generation and release of propellant parcels are of great importance in sustaining the combustion instability.

In dump combustors, vortices which play a critical role in combustion process, are generated in the shear layer at the backward-facing step. When the vortex roll-up process is accompanied by interaction with sidewalls, the interface between the fuel/oxidizer mixture and hot combustion products increases, resulting in fine-scaled turbulent mixing improvement and pulsated heat release. To further investigate the unstable vortex shedding behaviors at the combustor step, the Strouhal number (NguyenTuan et al., 2018) is evaluated as follows:

$$S_t = f_v^* D/V \tag{8}$$

where f_v is vortex shedding frequency, D is the flow characteristic length (taken as the recess chamber diameter D_r in the present study), and V is the mean axial velocity at the injector exit. According to Schadow. K. et al. (Schadow and Gutmark, 1992), the preferred Strouhal number in dump

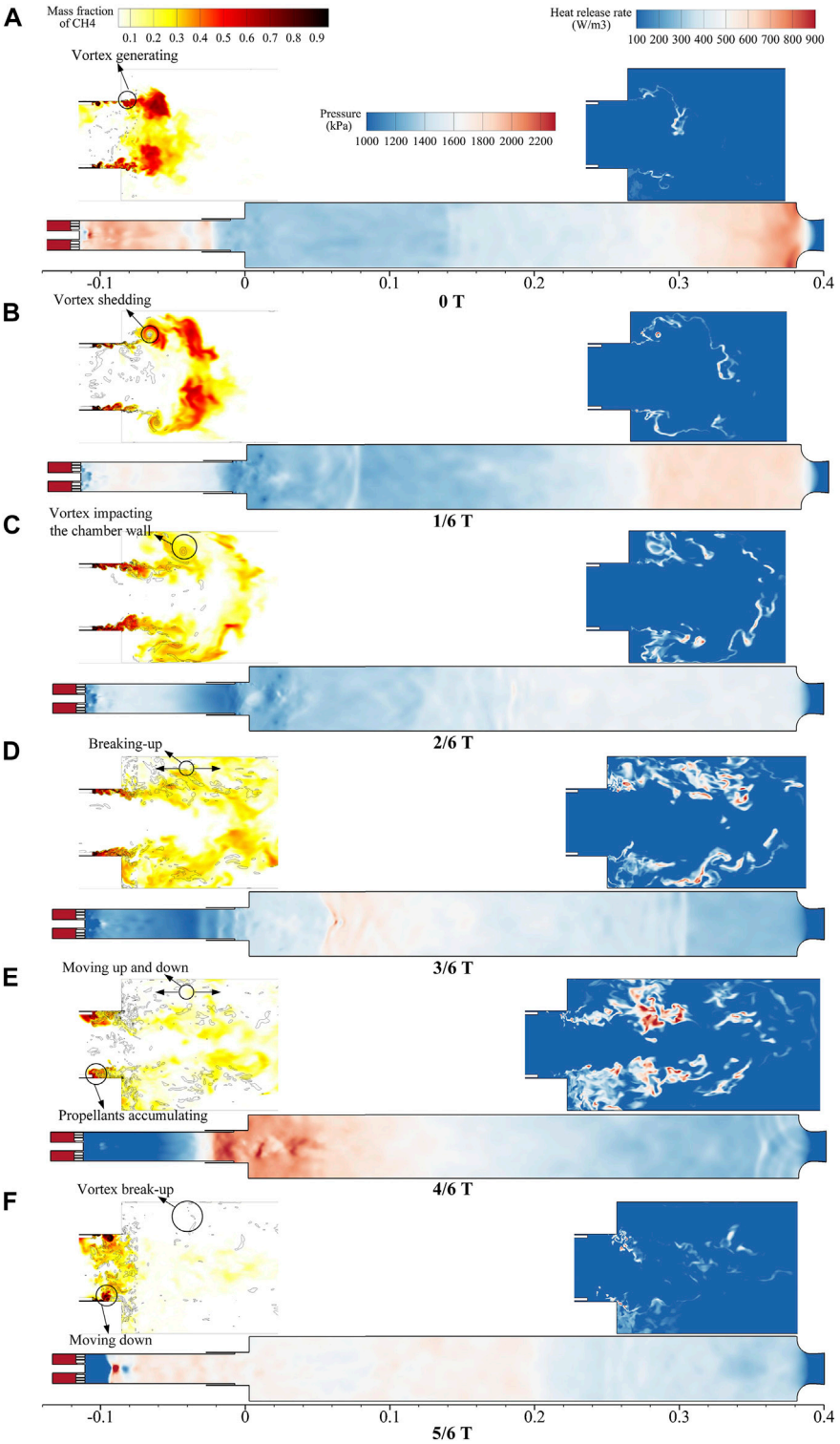

FIGURE 10 | Detailed evolution of flow field in one cycle. The majority of CH_4 and combustion occur upstream of the combustion chamber. Therefore, the flow fields of CH_4 and heat release are shown only upstream of the combustor and scaled by a factor of 2. Black lines in the mass fraction of the CH_4 plot denote vorticity.

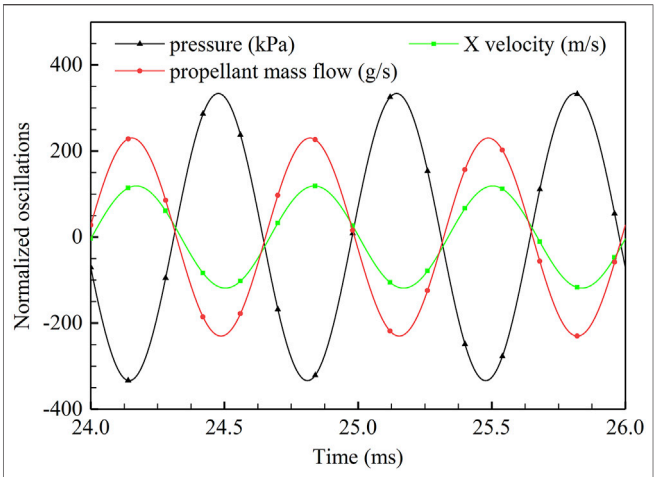

FIGURE 11 | Normalized oscillations of pressure, CH_4 mass fraction, X-velocity, and O_2 mass fraction at probe plane. The signals were band-pass filtered with a center frequency of 1,489 Hz and a bandwidth of 100 Hz.

combustors (such as the one in this study) is between 0.1 and 0.3, which indicates strong mixing at the step. For the present study, the vortex shedding frequency is 1,489 Hz, and the characteristic length is 23.06 mm, giving S_t = 0.172. Moreover, the higher S_t is in the preferred range, the more likely there is to be large coherent vortex structures downstream of the combustor step (NguyenTuan et al., 2018). Thanks to the present full 3D simulation, the vortex shedding dynamics at the combustor step can be tracked carefully.

The pressure waves propagate upstream inside the oxidizer post and downstream in the combustion chamber, leading to high-amplitude axial velocity oscillations, which induce the generation of the new vortex. The signals (the data was band-pass filtered) of the probe plane were recorded as face-averaged and are plotted in **Figure 11**. As can be seen from **Figure 11**, the pressure and axial velocity are almost out of phase. When the high-pressure waves propagate to the probe plane, the flow in the axial direction is blocked, followed by a decrease in axial velocity. Therefore, the propellant accumulates inside the oxidizer post. When the pressure near the probe plane drops, the axial flow is accelerated and the mass flow rate increases, as shown in **Figure 11**. With the acceleration of flow in axial direction, the propellant is injected downstream to the combustion chamber periodically, culminating in pulsated heat release. Pulsation of axial velocity will induce oscillations of the propellant mass flow rate, which is essential for maintaining combustion instability.

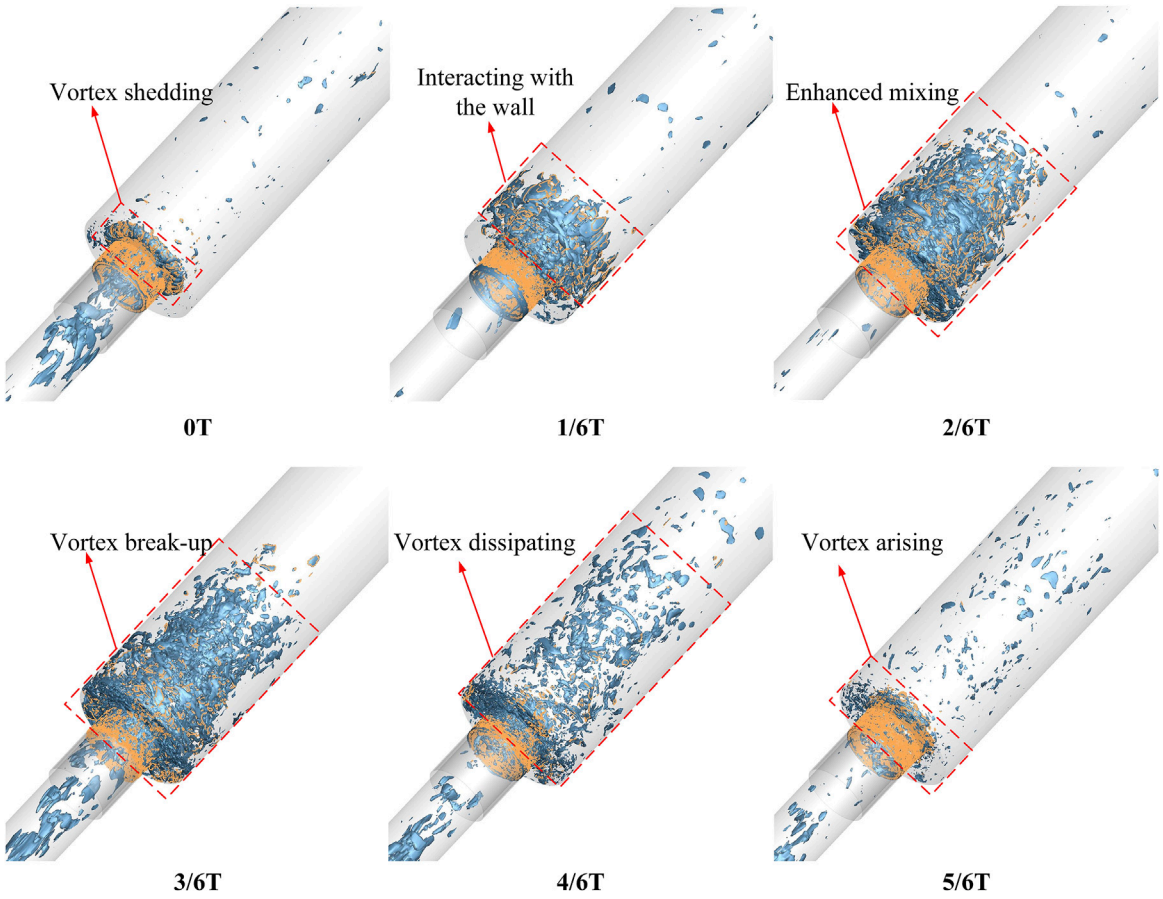

FIGURE 12 | Instantaneous 3D vortex iso-surface (value 2.0e+6*s^{-1}) with CH_4 mass fraction iso-lines (orange line, value 0.4).

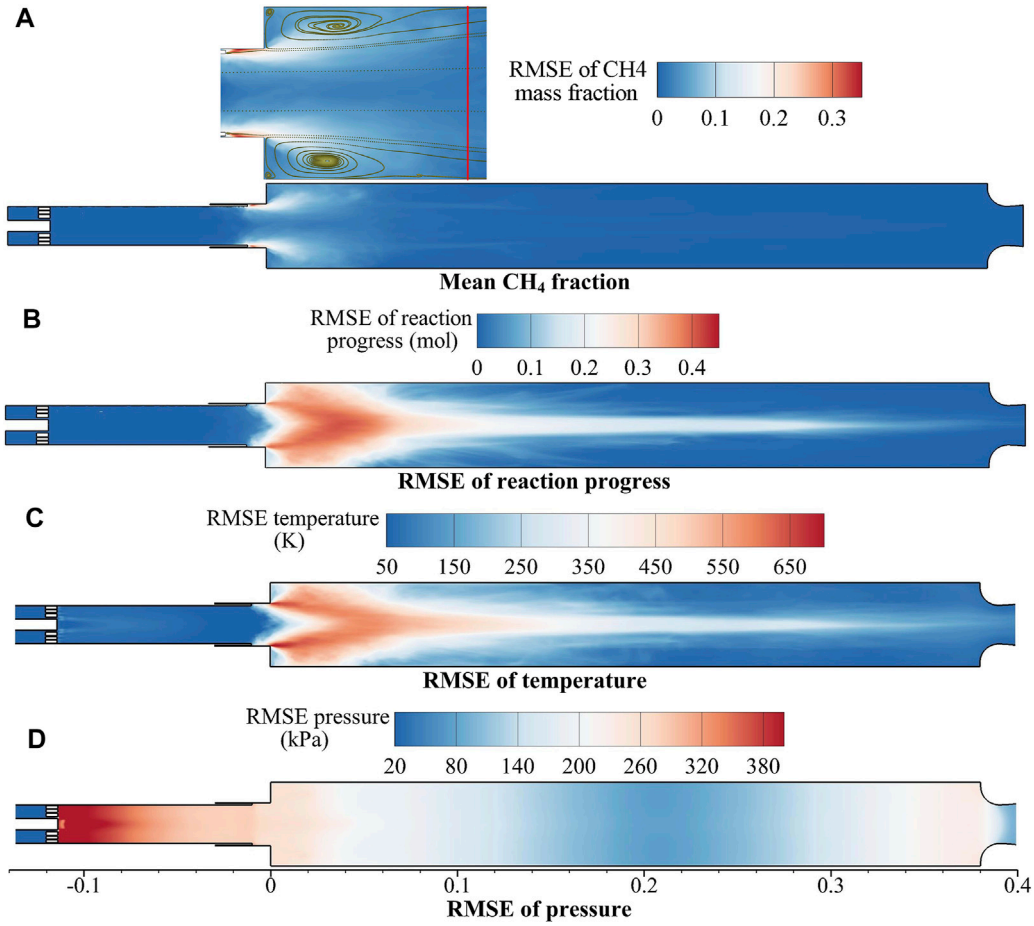

FIGURE 13 | RMSE flow fields **(A)** mass fraction of CH_4, **(B)** reaction progress, **(C)** temperature, and **(D)** pressure.

Benefits from full 3D simulation, the 3D vortex structures, interactions between vortices and CH_4 are presented in **Figure 12**. The results suggest that periodic vortex generating and shedding play a crucial role in driving the combustion instability. As shown in **Figure 12** 0T. 3D vortex ring is identified at the combustor step, because of the oscillated axial velocity, and much gaseous CH_4 is trapped inside the vortex ring. The vortex ring sheds and approaches the combustion chamber wall. Meanwhile, the CH_4 is rolled up by vortex ring. Further, the vortex ring interacts with the combustion chamber wall (**Figure 12** 1/6T). The CH_4 is simultaneously transported to the upstream (large recirculation zone) and downstream. The large vortex ring breaks into small vortices, which massively enhances the mixing performance (**Figure 12** 2/6 T and 3/6T). As such, a large amount of well-mixed propellant is concentrated near the combustor step (large recirculation zone). Combustible gas is consumed quickly, leading to pulsated heat release, causing pressure disturbance near the combustor step, as shown in **Figure 10E**.

Time-Averaged Flow Fields

Although the time-averaged flow field fails to show the dynamic characteristics, it can illustrate the global features of the combustion chamber and help to comprehend the mechanism of the combustion instability. The time-averaged results [root mean squared error (RMSE)] for CH_4 mass fraction, temperature, pressure, and axial (X) velocity are presented in **Figure 13**. The RMSE flow fields indicate the deviations between the measured and true values (estimated with the mean value in the present study). Consequently, the RMSE results can be used to demonstrate the oscillation features of the fields.

As shown in **Figure 13A**, the CH_4 mass fraction oscillates severely near the combustor step. A detailed plot of the CH_4 RMSE around the combustor step is given in the upper left of **Figure 13A** with the streamlines superimposed. The streamlines reveal the recirculation region after the combustor step, accompanied by the reattachment point (as marked by the vertical red line). Comparison of **Figures 13A,B**, and (C) show that the mass fraction of CH_4 and reaction progress oscillate extremely in the recirculation region. Therefore, severe heat release pulsation (corresponding to periodic thermal excitation source) occurs at the combustor step, which results in temperature oscillation, as evident in **Figure 13C**. **Figure 13D** suggests that intensive pressure oscillations occur at the combustor step and nozzle, and

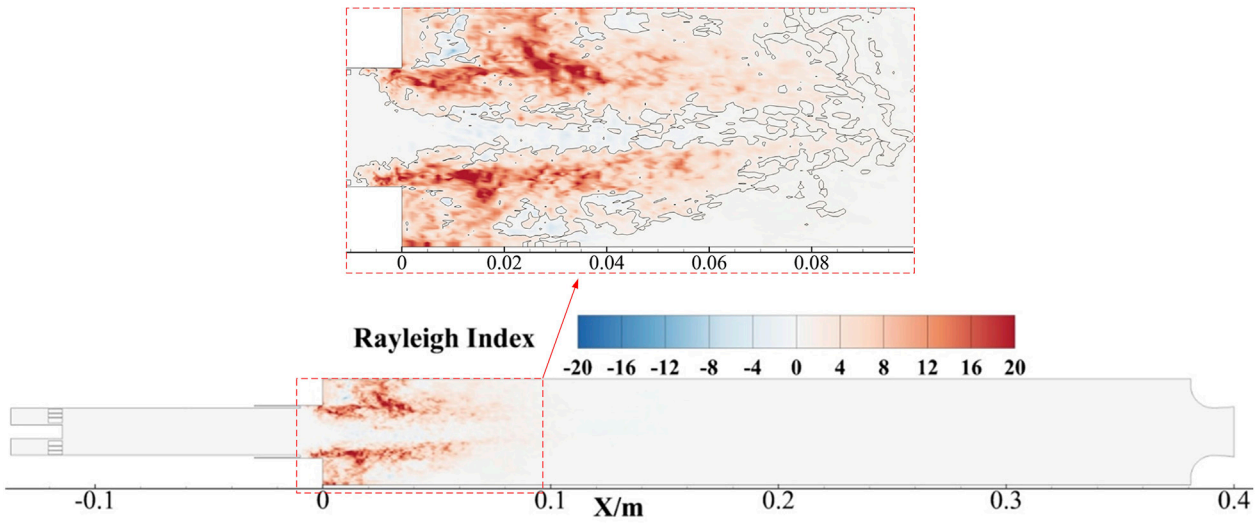

FIGURE 14 | Rayleigh index of the center plane (YZ). A close-up view near the combustor step with zero contours is on the top of the plot.

the pressure varies sightly near the middle of the combustion chamber, confirming the first longitudinal mode of the combustion instability. The pulsated heat release at the combustor step acts as the energy source for the pressure oscillation. Thus, a pressure antinode appears at the combustor step, demonstrating the spatial consistency of heat release and pressure oscillation.

Combustion Instability Mechanism

To further confirm the driving (positive Rayleigh index) and damping (negative Rayleigh index) locations inside the combustion chamber, Rayleigh index analysis is conducted. The definition of Rayleigh index used in the present work was the same as that used by Harvazinski et al. (Harvazinski et al., 2013), which is given by **Eq. 1**.

The Rayleigh index displayed in **Figure 14**, shows the most eye-catching peak near the combustor step. More precisely, the positive Rayleigh index is mainly concentrated in the shear layer and large recirculation zone. The zero contours in the close-up view indicate that there is a negative region near the centerline (oxidizer post), which suggests damping effects in the center of the oxidizer post. These results demonstrate that the primary driving source of the present combustion instability lies at the back step of the chamber. At locations away from the combustor step, the Rayleigh index reduces to zero or even becomes negative, demonstrating the disappearance of driving in these zones. Compared with **Figure 12**, the driving regions almost coincide with the vortex shedding zones, further affirming the vortex shedding driving mechanism of the combustion instability.

Combined with the above analyses, it seems that the self-sustaining combustion instability mechanism in the present combustor model could be described by the mass flow rate of propellant injecting to the combustion chamber, periodic oscillations, and subsequent vortex shedding and interaction with the combustion chamber wall. In terms of the present dump combustion chamber, the periodic vortex shedding appears at the combustor step caused by the pulsated axial velocity. Part of the unburned propellant is trapped in the vortex, and a local flameout state is formed affected by the step velocity gradients. The heat release rate decreases as dose the pressure (**Figure 10B**). Along with the growth of the vortex, the vortex impacts the chamber wall and breaks up into small vortices (**Figure 12**). Propellant mixing is strongly promoted by the vortex break-up, and the reaction progress speeds up, generating a heat release pulsation. The pulsated heat release, just like the periodic thermal energy source, provides energy for combustion instability, leading to acoustic pressure oscillations (**Figure 10**). The energy added to the acoustic field is in phase with the pressure oscillations, which reinforced the acoustic resonance mode. The acoustic resonance causes high-amplitude axial velocity oscillations (mass flow rate oscillations) which induce the generation of the new vortex. The vortex plays a role in delaying the phase of heat release. The propellant is rolled up and carried into the combustion chamber by the vortex and is unable to burn out immediately. A lot of heat will not be released until the vortex impacts the chamber wall. In this way, the phase of heat release is modulated by the vortex shedding to be close to the phase of the pressure, and self-sustaining combustion instability occurs.

CONCLUSION

Based on a hybrid RANS/LES and FGM methods, a comprehensive numerical study was conducted to investigate the unstable combustion characteristics of a CVRC. Severe combustion instability was captured for the combustor. The unstable combustion modes were identified by the PSD and

DMD techniques. Rayleigh index was introduced to evaluate the coupling relationship between pressure and heat release rate. Finally, the combustion instability mechanisms in the CVRC were clarified by tracking snapshots of the flow fields.

The numerical results agree well with experimental results in terms of unstable combustion instability frequency and PSD analysis. The pressure waves propagate upstream to the oxidizer post and downstream to the chamber, arousing axial velocity and mass flow rate of propellant oscillations both in the oxidizer post and combustion chamber. A pressure wave mode, extracted by the DMD method, is coupled with the first longitudinal acoustic mode of the combustion chamber. According to a study of the temporal phase difference, the pressure oscillations and heat release rate are almost in phase at the head of the combustion chamber, and the driving source is mainly located upstream of the chamber, which was further confirmed by the Rayleigh index and time-averaged flow field snapshots.

The flow field evolutions in one cycle were tracked in detail with fine time resolution. 3D vortex ring shedding processes were captured. It was found that the mass flow rate oscillations inside the oxidizer post, along with large vortex ring shedding and interaction with the chamber wall are of great importance in maintaining unstable combustion. The unburnt reactants are rolled up by the vortex. As the vortex ring impacts the chamber wall, it breaks into small vortices, which greatly enhances the turbulent mixing, leading to sudden heat release. The energy added to the acoustic field is in phase with the pressure oscillations, which reinforces the acoustic resonance mode. The acoustic resonance causes high-amplitude axial velocity oscillations (propellant mass flow rate oscillations), which induce the generation of the new vortex.

DATA AVAILABILITY STATEMENT

The raw data supporting the conclusions of this article will be made available by the authors, without undue reservation.

AUTHOR CONTRIBUTIONS

GK mainly contributed to numerical simulation model. RY and XB contributed primarily to data processing and writing. TY contributed primarily to data processing. NW mainly provided financial support for the numerical simulation.

FUNDING

National Natural Science Foundation of China (No. 12002386, 51876219).

ACKNOWLEDGMENTS

The authors would like to express their sincere acknowledgments for support from Department of Aerospace Science and Technology. The authors gratefully acknowledge the computing resources provided by Beijing Beilong Super Cloud Computing Co., Ltd. The company was not involved in the study design, collection, analysis, interpretation of data, the writing of this article or the decision to submit it for publication.

REFERENCES

Bedard, M. J., Sardeshmukh, S. V., Fuller, T., Anderson, W. E., and Tanabe, M. (2014). "Chemiluminescence as a Diagnostic in Studying Combustion Instability in a Practical Combustor," in 50th AIAA/ASME/SAE/ASEE Joint Propulsion Conference, Cleveland, OH, July 28–30, 2014. doi:10.2514/6.2014-3660

Bhatia, R., and Sirignano, W. A. (1991). One-dimensional Analysis of Liquid-Fueled Combustion Instability. *J. Propulsion Power* 7 (6), 953–961. doi:10.2514/3.23413

Buschhagen, T., Gejji, R., Philo, J., Tran, L., Enrique Portillo Bilbao, J., and Slabaugh, C. D. (2018). Experimental Investigation of Self-Excited Combustion Instabilities in a Lean, Premixed, Gas Turbine Combustor at High Pressure. *J. Eng. Gas Turbines Power* 140 (11), 111503. doi:10.1115/1.4039760

Coates, R. L., and Horton, M. D. (1974). Further Considerations on the Interaction of Sound and Flow in Rocket Motors and T-Burners. *Combustion Sci. Technol.* 9 (3-4), 95–102. doi:10.1080/00102207408960343

Culick, F. E. C. (1970). Stability of Longitudinal Oscillations with Pressure and Velocity Coupling in a Solid Propellant Rocket. *Combustion Sci. Technol.* 2 (4), 179–201. doi:10.1080/00102207008952247

Duvvuri, P. P., Shrivastava, R. K., and Sreedhara, S. (2020). Numerical Optimization of a Diesel Combustion System to Reduce Soot Mass and Particle Number Density. *Fuel* 266, 117015. doi:10.1016/j.fuel.2020.117015

Franzelli, B., Riber, E., Sanjosé, M., and Poinsot, T. (2010). A Two-step Chemical Scheme for Kerosene-Air Premixed Flames. *Combustion and Flame* 157 (7), 1364–1373. doi:10.1016/j.combustflame.2010.03.014

Frezzotti, M. L., Terracciano, A., Nasuti, F., Hester, S., and Anderson, W. E. (2014). "Low-order Model Studies of Combustion Instabilities in a DVRC Combustor," in 50th AIAA/ASME/SAE/ASEE Joint Propulsion Conference, Cleveland, OH, July 28–30, 2014. doi:10.2514/6.2014-3485

Fuller, T. (2019). *Dynamic Coupling in a Model Rocket Combustor*. doi:10.25394/PGS.8281850.v1

Garby, R., Selle, L., and Poinsot, T. (2013). Large-Eddy Simulation of Combustion Instabilities in a Variable-Length Combustor. *Comptes Rendus Mécanique* 341 (1), 220–229. doi:10.1016/j.crme.2012.10.020

Girimaji, S. S. (1991). Assumed β-pdf Model for Turbulent Mixing: Validation and Extension to Multiple Scalar Mixing. *Combustion Sci. Technol.* 78 (4-6), 177–196. doi:10.1080/00102209108951748

Gregory, P. S., Golden, D. M., Frenklach, M., Moriarty, N. W., Eiteneer, B., Goldenberg, M., et al. (2018). "GRI-Mech 3.0," Tech. rep., UC Berkeley. Available at: http://combustion.berkeley.edu/gri-mech/(Accessed December 01, 2018).

Harvazinski, M. E., Anderson, W. E., and Merkle, C. L. (2013). Analysis of Self-Excited Combustion Instabilities Using Two- and Three-Dimensional Simulations. *J. Propulsion Power* 29 (2), 396–409. doi:10.2514/1.B34732

Harvazinski, M. E., Talley, D. G., and Sankaran, V. (2016). "Application of Detailed Chemical Kinetics to Combustion Instability Modeling," in 54th AIAA Aerospace Sciences Meeting, San Diego, CA, January 4–8, 2016. doi:10.2514/6.2016-1931

Ilbas, M., Kumuk, O., and Karyeyen, S. (2021). Numerical Study of a Swirl Gas Turbine Combustor for Turbulent Air and Oxy-Combustion of Ammonia/kerosene Fuels. *Fuel* 304, 121359. doi:10.1016/j.fuel.2021.121359

Issa, R. I. (1985). Solution of the Implicitly Discretised Fluid Flow Equations by Operator-Splitting. *JCoPh* 62 (1), 40–65. doi:10.1016/0021-9991(86)90099-9

Jiang, Y., Lee, B.-H., Oh, D.-H., and Jeon, C.-H. (2021). Optimization of Operating Conditions to Achieve Combustion Stability and Reduce NOx Emission at Half-Load for a 550-MW Tangentially Fired Pulverized Coal Boiler. *Fuel* 306, 121727. doi:10.1016/j.fuel.2021.121727

Jurić, F., Stipić, M., Samec, N., Hriberšek, M., Honus, S., and Vujanović, M. (2021). Numerical Investigation of Multiphase Reactive Processes Using Flamelet Generated Manifold Approach and Extended Coherent Flame Combustion Model. *Energ. Convers. Manage.* 240, 114261. doi:10.1016/j.enconman.2021.114261

Kim, H. J., Seo, S., Lee, K. J., Han, Y. M., Lee, S. Y., and Ko, Y. S. (2008). Stability Rating Tests for the Length-Optimization of Baffles in a Liquid Propellant Combustion Chamber Using a Pulse Gun. *Aerospace Sci. Technol.* 12 (3), 214–222. doi:10.1016/j.ast.2007.06.003

Koizumi, H., Tsutsumi, S., Omata, N., and Shimizu, T. (2020). "Thermoacoustic Coupling Mechanism of Combustion Instability in a Continuously Variable Resonance Combustor," in AIAA Scitech 2020 Forum, Orlando, FL, January 6–10, 2020. doi:10.2514/6.2020-1071

Lemcherfi, A. I., Gejji, R., Fuller, T. L., Anderson, W. E., and Slabaugh, C. D. (2019). "Investigation of Combustion Instabilities in a Full Flow Staged Combustion Model Rocket Combustor," in AIAA Propulsion and Energy 2019 Forum, Indianapolis, IN, August 19–22, 2019. doi:10.2514/6.2019-3948

Liu, X., Wang, H., Zheng, Z., and Yao, M. (2021). Numerical Investigation on the Combustion and Emission Characteristics of a Heavy-Duty Natural Gas-Diesel Dual-Fuel Engine. *Fuel* 300, 120998. doi:10.1016/j.fuel.2021.120998

Liu, Y., Li, J., Zhang, T., and Yan, Y. (2021). Active Suppression of Swirl-Stabilized Combustion Instability. *Fuel* 287, 119559. doi:10.1016/j.fuel.2020.119559

Lyu, Z., Jia, X., Yang, Y., Hu, K., Zhang, F., and Wang, G. (2021). A Comprehensive Investigation of LSTM-CNN Deep Learning Model for Fast Detection of Combustion Instability. *Fuel* 303, 121300. doi:10.1016/j.fuel.2021.121300

Menter, F. (2016). Stress-Blended Eddy Simulation (SBES)—A New Paradigm in Hybrid RANS-LES Modeling. *Symp. Hybrid RANS-LES Methods*. doi:10.2514/1.59770

Menter, F. R. (1994). Two-equation Eddy-Viscosity Turbulence Models for Engineering Applications. *AIAA J.* 32 (8), 1598–1605. doi:10.2514/3.12149

Mohan, A. T., Visbal, M. R., and Gaitonde, D. V. (2015). "Model Reduction and Analysis of Deep Dynamic Stall on a Plunging Airfoil Using Dynamic Mode Decomposition," in 53rd AIAA Aerospace Sciences Meeting, January 5–9, 2015, Kissimmee, FL. doi:10.2514/6.2015-1058

Murayama, S., Kinugawa, H., Tokuda, I. T., and Gotoda, H. (2018). Characterization and Detection of Thermoacoustic Combustion Oscillations Based on Statistical Complexity and Complex-Network Theory. *Phys. Rev. E* 97 (2), 022223. doi:10.1103/PhysRevE.97.022223

NguyenTuan, T. M., PopovPavel, P. P., and Sirignano, W. A. (2018). Longitudinal Combustion Instability in a Rocket Engine with a Single Coaxial Injector. *J. Propulsion Power* 34, 354–373. doi:10.2514/1.B36516

Nicoud, F., and Ducros, F. (1999). Subgrid-Scale Stress Modelling Based on the Square of the Velocity Gradient Tensor. *Flow Turbulence and Combustion* 62 (3), 183–200. doi:10.1023/A:1009995426001

Nozari, H., and Karabeyoğlu, A. (2015). Numerical Study of Combustion Characteristics of Ammonia as a Renewable Fuel and Establishment of Reduced Reaction Mechanisms. *Fuel* 159, 223–233. doi:10.1016/j.fuel.2015.06.075

Oefelein, J. C., and Yang, V. (1993). Comprehensive Review of Liquid-Propellant Combustion Instabilities in F-1 Engines. *J. Propulsion Power* 9 (5), 657–677. doi:10.2514/3.23674

Peters, N. (2000). *Turbulent Combustion*. Cambridge: Cambridge University Press. doi:10.1017/CBO9780511612701

Ramaekers, W. (2011). *Development of Flamelet Generated Manifolds for Partially-Premixed Flame Simulations*. Eindhoven, Netherlands: Technische Universiteitndhoven. doi:10.6100/IR716707

Rayleigh (1878). The Explanation of Certain Acoustical Phenomena 1. *Nature* 18 (455), 319–321. doi:10.1038/018319a0

Ruan, C., Chen, F., Yu, T., Cai, W., Mao, Y., Qian, Y., et al. (2020). Experimental Study on Combustion Stability Characteristics in Liquid-Fueled Gas Turbine Model Combustor: Fuel Sensitivities and Flame/flow Dynamics. *Fuel* 265, 116973. doi:10.1016/j.fuel.2019.116973

Sattelmayer, T. (2003). Influence of the Combustor Aerodynamics on Combustion Instabilities from Equivalence Ratio Fluctuations. *J. Eng. Gas Turbines Power* 125 (1), 11–19. doi:10.1115/1.1365159

Schadow, K. C., and Gutmark, E. (1992). Combustion Instability Related to Vortex Shedding in Dump Combustors and Their Passive Control. *Prog. Energ. Combustion Sci.* 18 (2), 117–132. doi:10.1016/0360-1285(92)90020-2

Schmitt, T., Méry, Y., Boileau, M., and Candel, S. (2011). Large-Eddy Simulation of Oxygen/methane Flames under Transcritical Conditions. *Proc. Combustion Inst.* 33 (1), 1383–1390. doi:10.1016/j.proci.2010.07.036

Sisco, J. C. (2007). Measurement and Analysis of an Unstable Model Rocket Combustor. Available at: https://docs.lib.purdue.edu/dissertations/AAI3291091/.

Smith, R., Xia, G., Anderson, W., and Merkle, C. (2010). "Computational Studies of the Effects of Oxidizer Injector Length on Combustion Instability," in 46th AIAA/ASME/SAE/ASEE Joint Propulsion Conference & Exhibit, Nashville, TN, July 25–28, 2010. doi:10.2514/6.2010-6564

Smith, R., Xia, G., Anderson, W., and Merkle, C. (2010). "Extraction of Combustion Instability Mechanisms from Detailed Computational Simulations," in 48th AIAA Aerospace Sciences Meeting Including the New Horizons Forum and Aerospace Exposition, Orlando, FL, January 04–07, 2010. doi:10.2514/6.2010-1152

Smith, R., Ellis, M., Xia, G., Sankaran, V., Anderson, W., and Merkle, C. L. (2008). Computational Investigation of Acoustics and Instabilities in a Longitudinal-Mode Rocket Combustor. *AIAA J.* 46 (11), 2659–2673. doi:10.2514/1.28125

Smith, R. J. (2010). *Computational Investigations of High Frequency Acoustics and Instabilities in a Single-Element Rocket Combustor*. West Lafayette, IN: PhD. Purdue University, 251. Available at: https://docs.lib.purdue.edu/dissertations/AAI3444748/.

Smith, R., Nugent, N., Sisco, J., Xia, G.-P., Sankaran, V., Anderson, W., et al. (2006). "Experimental and Computational Investigation of Combustor Acoustics and Instabilities, Part I: Longitudinal Modes," in 44th AIAA Aerospace Sci. Meet. Exhibit, Reno, Nevada, January 09–12, 2006. doi:10.2514/6.2006-537

Smith, R., Xia, G., Anderson, W. A., and Merkle, C. L. (2010). Computational Simulations of the Effect of Backstep Height on Nonpremixed Combustion Instability. *AIAA J.* 48 (9), 1857–1868. doi:10.2514/1.40385

Srinivasan, S., Ranjan, R., and Menon, S. (2015). Flame Dynamics during Combustion Instability in a High-Pressure, Shear-Coaxial Injector Combustor. *Flow Turbulence Combust* 94 (1), 237–262. doi:10.1007/s10494-014-9569-x

Tu, J. H., Rowley, C. W., Luchtenburg, D. M., Brunton, S. L., and Kutz, J. N. (2014). On Dynamic Mode Decomposition: Theory and Applications. *J. Comput. Dyn.* (1), 391–421. doi:10.3934/jcd.2014.1.391

Urbano, A., Selle, L., Staffelbach, G., Cuenot, B., Schmitt, T., Ducruix, S., et al. (2016). Exploration of Combustion Instability Triggering Using Large Eddy Simulation of a Multiple Injector Liquid Rocket Engine. *Combustion and Flame* 169, 129–140. doi:10.1016/j.combustflame.2016.03.020

Verma, I., Yadav, R., Nakod, P., Sharkey, P., Li, S., and Meeks, E. (2019). "Flamelet Generated Manifold Simulation of Turbulent Non-premixed Bluff Body Flames," in ASME 2019 Gas Turbine India Conference. Volume 2, Chennai, India, December 5–6, 2019. doi:10.1115/GTINDIA2019-2525

Wierman, M., Morgan, C., and Anderson, W. (2012). "Effect of Step Height on Level of Combustion Instability in a Subscale Transverse Rocket Combustor," in 48th AIAA/ASME/SAE/ASEE Joint Propulsion Conference & Exhibit, Atlanta, Georgia, July 30–August 01, 2012. doi:10.2514/6.2012-4205

Xia, C., Brindhadevi, K., Elfasakhany, A., Alsehli, M., and Tola, S. (2021). Numerical Modelling of the Premixed Compression Ignition Engine for superior Combustion and Emission Characteristics. *Fuel* 306, 121540. doi:10.1016/j.fuel.2021.121540

Xia, Y., Sharkey, P., Orsino, S., Kuron, M., Menter, F., Verma, I., et al. (2021). Stress-Blended Eddy Simulation/Flamelet Generated Manifold Simulation of Film-Cooled Surface Heat Transfer and Near-Wall Reaction. *J. Turbomach.* 143 (1), 011008. doi:10.1115/1.4049133

Xia, Y., Stopford, P., Sharkey, P., and Verma, I. (2021). "GT2021-59100 Dynamic Mesh Adaption for Scale-Resolving Reacting Flow Simulations," in Turbo Expo 2021 Turbomachinery Technical Conference & Exposition, June 7–11, 2021. doi:10.1115/GT2021-59100

Yu, X., Verma, I., Zore, K., and Sharkey, P. (2020). "AIAA-2020-0175 SBES/FGM Simulation of Forced Response of a Premixed Blu-Body Stabilized Flame," in AIAA Scitech 2020 Forum, Orlando, FL, January 6–10, 2020. doi:10.13140/RG.2.2.32167.91043/1

Yu, Y. C. (2009). "Experimental and Analytical Investigations of Longitudinal Combustion Instability in a Continuously Variable Resonance Combustor (CVRC),". Available at: https://docs.lib.purdue.edu/dissertations/AAI3378922/.

Yu, Y. C., Sisco, J. C., Rosen, S., Madhav, A., and Anderson, W. E. (2012). Spontaneous Longitudinal Combustion Instability in a Continuously-Variable Resonance Combustor. *J. Propulsion Power* 28 (5), 876–887. doi:10.2514/1.B34308

Yu, Y., Koeglmeier, S., Sisco, J., and Anderson, W. (2008). "Combustion Instability of Gaseous Fuels in a Continuously Variable Resonance Chamber (CVRC)," in 44th AIAA/ASME/SAE/ASEE Joint Propulsion Conference & Exhibit, Hartford,CT, July 21–23, 2008. doi:10.2514/6.2008-4657

Yu, Y., O'Hara, L., Sisco, J., and Anderson, W. (2009). "Experimental Study of High-Frequency Combustion Instability in a Continuously Variable Resonance Combustor (CVRC)," in 47th AIAA Aerospace Sciences Meeting including The New Horizons Forum and Aerospace Exposition, Orlando, FL, January 05–08, 2009. doi:10.2514/6.2009-234

Zhao, D., Gutmark, E., and Reinecke, A. (2019). Mitigating Self-Excited Flame Pulsating and Thermoacoustic Oscillations Using Perforated Liners. *Sci. Bull.* 64 (13), 941–952. doi:10.1016/j.scib.2019.05.004

Zhou, M.-m., Thornock, J., Zhan, Z., Dai, J., Smith, S. T., and Smith, P. J. (2021). Numerical Analysis of Particle Dispersion and Deposition in Coal Combustion Using Large-Eddy Simulation. *Fuel* 304, 121384. doi:10.1016/j.fuel.2021.121384

Conflict of Interest: The authors declare that the research was conducted in the absence of any commercial or financial relationships that could be construed as a potential conflict of interest.

Publisher's Note: All claims expressed in this article are solely those of the authors and do not necessarily represent those of their affiliated organizations, or those of the publisher, the editors, and the reviewers. Any product that may be evaluated in this article, or claim that may be made by its manufacturer, is not guaranteed or endorsed by the publisher.

NOMENCLATURE

c reaction progress variable

c_p mixture-averaged specific heat (unit: J/K)

f mixture fraction

f_s blending function for the SBES

$\dot{m}$ mass flow rate (unit: g/s)

D diameter (unit: mm)

L length (unit: mm)

$P()$ Probability density function

RI Raleigh index

S_t Strouhal number

T temperature (unit: K)

Y species mass fraction

ρ density (unit: kg/m^3)

τ_{ij} stress tensor

$\theta(r)$ truncation function

χ scalar-dissipation rate

Superscripts

$\overline{()}$ time-averaged

$()'$ variance

$\widetilde{()}$ Favre mean

Subscripts

c combustion chamber

i ith species

op oxidizer post

r recess chamber

th nozzle throat

frontiers in Energy Research

ORIGINAL RESEARCH
published: 22 February 2022
doi: 10.3389/fenrg.2022.845350

Effect of Film Position on the Flow and Heat Transfer Characteristics of Full-Ribbed Rotor Tip

Haimeng Zhou[1], *Chenglong Wang*[2]*, *Zhiqi Kong*[3], *Wei Du*[1] *and Zhongqi Wang*[1]

[1]School of Energy Science and Engineering, Harbin Institute of Technology, Harbin, China, [2]Science and Technology on Scramjet Laboratory, National University of Defense Technology, Changsha, China, [3]Beijing Power Machindry Institution, Beijing, China

This article numerically studied the flow and heat transfer characteristics of the full-ribbed fluted tip of a rotor with four types of distribution of cooling films, namely, the mid-arc uniform film at the bottom of the groove, the uniform film on full perimeter ribs, the uniform film on the suction-side rib, and the uniform film on the pressure-side rib. The evolution of secondary flow in the tip clearance under these four conditions was discussed, and the effect of cooling film position on the tip leakage flow and tip heat transfer was also studied. The results showed that films in the ribs were more conducive to lower leakage flow rates and can reduce total energy losses. Adding cooling films on the single-side rib had a better effect on the control of leakage flow rate, with the most significant improvement due to adding cooling films on the suction-side rib. The mid-arc jet at the bottom of the groove can greatly contain the swirl structure in the groove, but it weakened the air sealing effect, which led to a rise in leak flow. The main reason for the swirl structure in the groove was that the leakage flow from the tip of the rotor was blocked by the cold air jet from the cooling films to form a backflow. The vortex inside the groove was the most violent when the air film hole was set on the pressure side, so the loss coefficient was higher, while the vortex inside the groove was the simplest when the cooling film hole was set on the suction side, and the energy loss caused by the vortex inside the groove was the least, and this structure was more favorable to the cooling of the leaf tip. It was also found that the uniformity of the outlet airflow angle distribution improved in the presence of cold air injection on the tip of the rotor.

Keywords: fluted blade tip, blade tip leakage flow, film cooling, rotor, heat transfer

OPEN ACCESS

Edited by:
Xiao Liu,
Harbin Engineering University, China

Reviewed by:
Jie Gao,
Harbin Engineering University, China
Weihua Cai,
Northeast Electric Power University, China

****Correspondence:***
Chenglong Wang
wangchenglonggfkd@163.com

Specialty section:
This article was submitted to Advanced Clean Fuel Technologies, a section of the journal Frontiers in Energy Research

Received: *29 December 2021*
Accepted: *17 January 2022*
Published: *22 February 2022*

Citation:
Zhou H, Wang C, Kong Z, Du W and Wang Z (2022) Effect of Film Position on the Flow and Heat Transfer Characteristics of Full-Ribbed Rotor Tip. Front. Energy Res. 10:845350. doi: 10.3389/fenrg.2022.845350

INTRODUCTION

In the turbine rotor of an aero-engine, the tip clearance must be reserved to prevent friction between the tip of the blade and the magazine. The working environment of the blade tip is severe. In advanced turbines, the gas with higher temperature and pressure further aggravates the operating environment of the tip. According to the research, a 1% increase in tip clearance reduces turbine stage efficiency by about 1%–2% (Bunker, 2006). Therefore, more advanced tip structures need to be applied to control the flow and heat transfer at the tip.

A great deal of research has been done on the aerodynamic and heat transfer characteristics of the rotor tips. Heyes et al. (1992) compared the flow characteristics of leaf tips with suction-side ribs and pressure-side ribs, and found that a ribbed blade tip on the suction side was significantly more effective in reducing leakage losses than a flat blade tip. Nho et al. (2012a) investigated the leakage

flow of the double-notched blade tip structure and flat blade tip structure, and the results showed that the double-notched blade tip structure has less loss in all aspects than that of the flat blade tip structure. Wang et al. (2015) observed the internal flow field of a crowned blade tip by a two-dimensional cascade experiment, which verified the existence of blending losses between the leakage flow and the high-temperature mainstream of the leaf crown structure. Wheeler et al. (2011) investigated the heat transfer characteristics of the static groove blade tip clearance structure using experiments, and measured the heat transfer coefficients at different Reynolds numbers and groove width-to-height ratios, respectively, which showed that the larger the depth of the groove at the tip of the blade, the smaller the heat transfer coefficient, and whether the end wall is rotated or not has little effect on the heat transfer coefficient. Park et al. (2016) studied the heat transfer and flow characteristics of a different number of grooves in a low-speed leaf grille experiment, and the results showed that increasing the number of grooves is beneficial to reduce the total pressure loss coefficient, and the exit loss coefficient becomes smaller with the increase of the number of grooves at the top of the leaf, and adding transverse ribs is beneficial to reduce the heat transfer coefficient at the leading edge of the blade tip. Heyes et al. (1992) investigated the effect of the rib structure of the leaf tip on the leakage flow. The results showed that it is more critical to control the leakage flow than to reduce the loss in the gap. Key and Arts (2006) investigated the leakage flow at high speed in a flat and a notched blade tip structure. The results showed that slight backflow occurs inside the recess, and the recessed tip has a stronger weakening effect on the tip leakage vortex than the flat tip. Hofer and Arts (2009a) experimentally compared the aerodynamic performance of blade tip structures with different rib lengths at transonic speeds with/without cold air injection. Lee et al. (2009) measured the internal flow field and total pressure loss at different gap sizes and different rib heights within the fluted vane tip and concluded that the higher the rib height, the smaller the total loss; the closer the rib heights on both sides, the higher the efficiency; and the lower the pressure-side rib height, the smaller the increase in loss than the lower suction-side rib when the gap sizes are the same. Tallman (2004) studied the ribbed blade tips before and after the improvement by numerical simulation. Mischo et al. (2011) proposed a method to improve the notched blade tip, which can make the return strength of the notch front greatly reduced, and has a good improvement on both the loss in the gap and the heat transfer characteristics of the blade tip. Nho et al. (2012b) experimentally modified the structure of a variety of fluted blade tips and found that the addition of a triangular fluted blade tip structure on the pressure side can reduce the total pressure loss coefficient. Pouagare et al. (1986) first experimentally studied the leakage flow mechanism in the presence of cold air jets, based on a certain blade with a tip clearance of 4% chord length. The results showed that the tip jet was beneficial to weaken the tip leakage flow and improve the tip efficiency. Mercan et al. (2015) performed cold gas jetting along the mid-arc of the rotor tip of a low-pressure turbine and investigated the effect of reduced injection flow on turbine performance. Volino (2017) compared the leakage flow fields of planar and notched blade tips with different injection methods. Injecting cold air at the maximum load position of the planar blade tip can control the leakage flow better. Dey (2001) studied the effect of the leaf tip cold gas injection flow rate on the control effect of leakage flow, and the measurement results showed that the larger the cold gas injection volume, the better the control effect. Rao and Camci (2004a); Rao and Camci (2004b) investigated the leakage flow field and the vortex evolution mechanism for different cold gas flow rates as well as different jet positions when cooling air was injected into the pressure side at two gap sizes. It was shown that the jet can weaken the mixing intensity of the leaky vortex with the upper channel vortex. Hofer and Arts (2009b) investigated the effect of different Re and Ma numbers on the aerodynamic performance of the full circumferential rib tip structure and the suction-side rib tip structure with the addition of cooling gas. Du et al. (2021a); Du et al. (2021b) systematically illustrated the cooling and impact effects of air film pores in the blades. Jin et al. (2019) numerically studied the influence of different arbitrary blade tip shapes on restraining the tip leakage flow in a highly loaded turbine cascade. Kumar et al. (2020) presented the thermomechanical analysis of a typical SGT engine to study the blade tip clearance influenced by the deformation of turbine stage components (turbine rotor and nozzle guide vane (NGV) with integral blade shroud) during transient phases. Guo et al. (2019) studied the blade tip leakage vortex cavitation characteristics for an axial waterjet pump. Luo et al. (2019) numerically investigated the impact of the holes and their location on the flow and tip internal heat transfer in a U-bend channel using topological analysis. Xue and Ng (2018) provided an overview of gas turbine blade tip external cooling technologies, and they also provided an outlook on the future of cooling technology for blade tips. Choi et al. (2021) investigated the wake effects on the HTCDs from the turbine blade tip with different configurations and the corresponding shroud. Du et al. (2019) investigated the aerothermal influences of multi-cavity blade tip, and they pointed out that cavity tip reduces the blade tip heat transfer coefficient. Zhou et al. (2019) investigated the blade tip and casing heat transfer characteristics with cavity and winglet cavity tips. Zhang et al. (2014) investigated the effects of inlet turbulence and the incoming surface layer on heat transfer in leaf tip flow, and found that these two factors had almost no effect on heat transfer at the leaf tip surface. Kwak and Han (2003) studied the heat transfer characteristics of the GE-E3 turbine with cooling gas film holes on the pressure side of the plane blade tip. The results showed that the leakage flow would be blocked by the cooling gas and also weaken the heat transfer coefficient of the blade tip, and the cooling effect of the pressure-side blade tip jet cold gas was not obvious under the small blowing ratio condition. Yang et al. (2006) studied the cooling effect of different cooling air film hole arrangements on a planar leaf tip and analyzed the cooling effect of different film hole arrangement schemes. Bunker and Bailey (2001) measured the heat transfer distribution of ribbed leaf tip structures in a planar cascade and analyzed the effect of different rib heights and different oxidation levels on the heat transfer to the leaf tips. Newton et al. (2006) conducted a comparative analysis of the heat transfer and cooling characteristics of flat blade tips, suction-side ribbed blade tips, and fully ribbed blade tips, and the results showed that notched

TABLE 1 | Geometric parameters of different sections of the rotor.

Parameters	Value (tip-section)	Value (mid-section)	Value (root section)
N	54		
θ_1 (°)	40.7	52.4	60.9
θ2 (°)	–67.4	–66.6	–65.4
L (mm)	43.41	46.83	50.08
H (mm)	46.54	42.47	38.40
D (mm)	16.08	14.42	13.25
A (mm^2)		54,780.5	
θ3 (°)		45	
t (mm)		46.3	
W1 (mm)		1.6	
d (mm)		0.6	

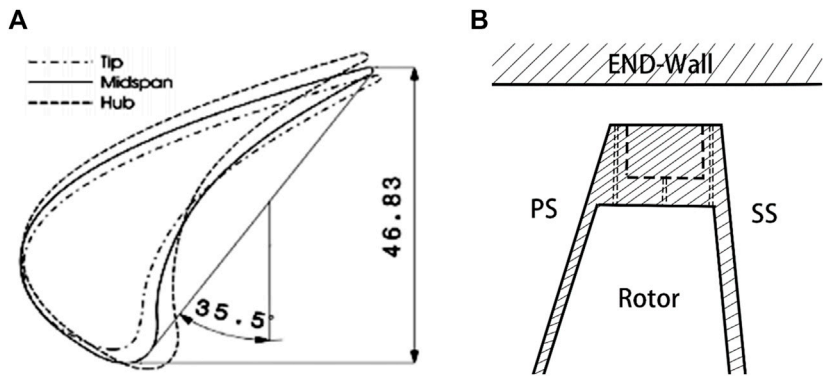

FIGURE 1 | Turbine blade model (Behr, 2007). **(A)** The rotor profile. **(B)** Turbine blade model.

blade tips have lower leakage flow, weaker leakage vortex strength, and lower heat transfer coefficient than flat blade tips, and suction-side ribs increase the leakage flow. Kang and Lee (2016) explored the relationship among leaf tip heat transfer, rib height, and leakage flow intensity and found that the position of the separation and reattachment lines has a great influence on the bottom surface heat transfer distribution. Virdi et al. (2015) investigated the flow and heat transfer characteristics of fluted leaf tips with different clearances under the conditions of transonic motion at the end wall.

From the previous studies, it can be seen that both the ribbed tips and the cooling air injection on the blade tip are effective ways to reduce the blade tip leakage to improve the turbine efficiency and prolong the life of the turbine blades. However, the study of adding cooling air jets at different locations on the ribbed blade tip is not detailed, the flow mechanism and heat transfer characteristics of setting cooling air holes at different locations on the blade tip are not clear, and the vortex evolution process under different conditions has not been studied. Therefore, it is very necessary to study the flow and heat transfer characteristics of the blade tip after adding cooling films at four different locations, analyze the vortex structure inside and outside the notch at the top of the blade, and identify the advantages and disadvantages of each structure by comparing the effect of adding cooling films at different locations on blade tip performance.

DESCRIPTION OF PHYSICAL MODELS

The prototype blade used in this study is the first-stage rotor of the LISA1.5 turbine, which has high power and a low aspect ratio. There are 12 cooling films with a diameter of 0.6 mm at the rotor tip (Behr, 2007). The cooling films eject cold air vertically. The clearance of the blade tip in each case is fixed at $\tau = 1.2$ mm. The geometrical parameters at different cross sections of the blade are shown in **Table 1**. **Figure 1A** shows the rotor blade geometry profile, and **Figure 1B** shows the schematic diagram of the rotor blade tip.

Figure 2 is a schematic diagram of the structure of the four types of fluted tips with cooling films used in this study. The cooling films in Case 1 are located in the middle arc at the bottom of the tip groove. In Case 2, the cooling films are distributed around the entire circumference of the tip rib. The cooling films of Case 3 are all located on the pressure side of the tip rib. The cooling films of Case 4 are all located on the suction side of the leaf tip ribs. Cooling films are evenly arranged in each structure.

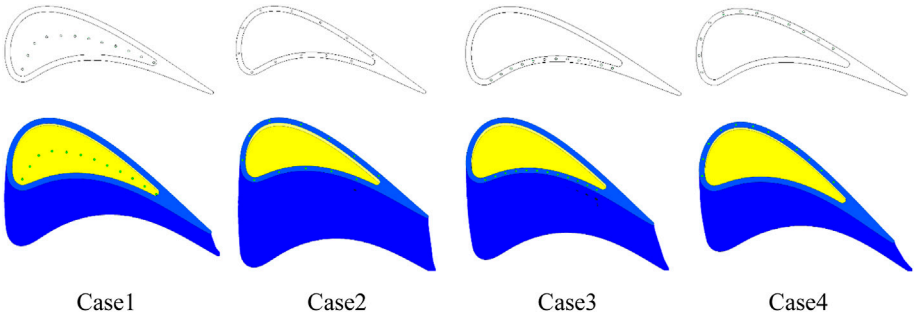

FIGURE 2 | Rotor tip models with different film distributions.

TABLE 2 | LISA1.5 turbine notch blade tip boundary conditions.

Boundary	Parameters	Value
Inlet	T^*_{in}	328.152 K
—	P^*_{in}	138576 Pa
—	Tu_{in}	5%
Outlet	p_{out}	99,975.8 Pa
Blade surface	T_{blade}	Adiabatic
Inlet of cooling air	$T^*_{cool-in}$	164.076 K
—	$P^*_{cool-in}$	145,504.8 Pa

TABLE 3 | Geometric feature configuration of LISA1.5 turbines.

Tip/mid/hub	Stator 1	Rotor	Stator 2
N	36	54	36
θ_1 (°)	0/0/0	40.7/52.4/60.9	−33.0/−35.4/−38.2
θ_2 (°)	72/72/72	−67.4/−66.6/−65.8	66.0/66.0/66.0
L (mm)	49.61/49.71/49.82	43.41/46.83/50.08	72.16/72.04/71.98
A (mm^2)	46,582.8	54,780.5	66,733.0
H (mm)	69.81/63.70/57.60	46.54/42.47/38.40	69.81/63.70/57.60

NUMERICAL METHODOLOGY

Boundary Conditions

The main boundary conditions for the numerical simulation are given in **Table 2**. Except for the inlet and outlet, all the walls are set as the adiabatic no-slip boundary. The total temperature of the inlet is 328.152 K, and the total pressure of the inlet is 328.152 K. The turbulence control is set at about 5%. The static pressure of the outlet is set to 138576 Pa. The inlet total temperature of the cooling films is 164.076 K, and the inlet total pressure of the cooling films is 145,504.8 Pa.

Data Processing

The total pressure loss coefficient (Cpt) is defined by **Eq. 1**:

$$C_{pt} = \frac{(p_0^* - p^*)}{\left(p_0^* - \overline{p_l}\right)}, \tag{1}$$

where p_0^* is the total pressure of the inlet, p^* is the local total pressure, and $\overline{p_l}$ is the average outlet static pressure.

The static pressure coefficient (Cp) is defined as in **Eq. 2**:

$$C_p = \frac{p - p_1}{p_0^* - p_1}, \tag{2}$$

where p is the local static pressure, p_1 is the static pressure at the outlet, andp_0^* is the total pressure at the inlet.

The energy loss coefficient (η_p) of a cascade with cooling air is defined in **Eq. 3**:

$$\eta_p = \frac{(G_r + G_B)0.5c_1^2}{G_r H_r + \sum_i G_{Bi} H_{Bi}}, \tag{3}$$

where G_r is the gas flow rate at the inlet of the cascade, G_B is the total cooling air flow rate through the cascade, c_1 is the average gas flow rate at the outlet, H_r is the available energy of the main airflow, and H_B is the available energy of cooling gas.

H_r and H_B can be calculated according to **Eqs 4**, **5**:

$$H_r = C_{pr} T^*_{r0} \left[1 - \left(\frac{p_1}{p^*_{r0}}\right)^{\frac{k_r - 1}{k_r}}\right], \tag{4}$$

$$H_{Bi} = C_{pB} T^*_{B0i} \left[1 - \left(\frac{p_1}{p^*_{B0i}}\right)^{\frac{k_B - 1}{k_B}}\right], \tag{5}$$

where C_{pr} is the total pressure specific heat capacity of the gas at the inlet andT^*_{r0} is the total temperature of the inlet gas of the cascade. p_1 is the static pressure at the exit of the cascade, p^*_{r0} is the total pressure of the inlet gas, k_r is the inlet gas constant entropy index, C_{pB} is the total pressure specific heat capacity of the cooling air of the cascade, T^*_{B0} is the total temperature of the cooling air of the cascade, p^*_{B0i} is the total pressure of the cooling air at the inlet of the cooling films, andk_B is the constant entropy index of the cooling air.

The heat transfer coefficient (h) is defined as in **Eq. 6**:

$$h = \frac{q}{T_w - T_0}, \tag{6}$$

where q is the local heat flux on the blade surface, T_w is the wall temperature, and T_0 is the incoming flow temperature.

The adiabatic film cooling efficiency (η) is defined as (**Eq. 7**)

$$\eta = \frac{T_{aw} - T_0}{T_c - T_0}, \tag{7}$$

where T_{aw} is the adiabatic wall temperature, T_0 is the incoming flow temperature, and T_c is the cooling air temperature of the inlet.

TABLE 4 | LISA1.5 turbine boundary conditions for numerical verification of aerodynamic characteristics.

Parameters	Value
Ro	2700r/min
Π	1.6
T^*_{in}	328.15 K
P^*_{in}	140000 Pa)
M	11.70 kg/s
D1/D2	660/800 mm

Numerical Verification of Pneumatic Characteristics

The LISA1.5 turbine blades were used for the numerical verification of the aerodynamic characteristics (Behr, 2007); the 3D model for the calculation is obtained by stretching the blade tips of the first-stage static blade (S1), the first-stage dynamic blade(R), and the second-stage static blade (S2). The profile data for the three rows of blades are given in **Table 3**, and the clearance height is set to 0.68 mm. **Figure 3A** shows the geometric profile of the rotor blades, and **Figure 3B** shows the grid schematic of the three rows of blades.

ANSYS CFX is used for numerical calculations. The numerically calculated results were compared with Behr's Behr (2007) experimental data on planar tips. **Table 4** shows the boundary conditions for the numerical calculations. The wall properties of both the blade and the magazine are set to be smooth, adiabatic, and non-slip.

In this article, k-ε, k-ω, and SST turbulence models are selected to verify whether the simulation results meet the research accuracy of turbine blade tip leakage flow.

The comparison between the numerical simulation and experimental results of the total pressure coefficient (*Cpt*) in the radial direction of the stator outlet using different turbulence models is given in **Figure 4**. For the total pressure coefficient at the exit of the first-stage stator, the simulations of the three turbulence models are close to the experimental values. But for the distribution of the total pressure coefficient at the outlet of the first-stage rotor, the calculated results of all three turbulence models are smaller than the experimental values. Overall, the simulated results are slightly different from the experimental values, but the distribution trend and range of the total pressure coefficient of the SST model overlap well. It is indicated that the numerical simulation results of the selected SST turbulence model have some reliability.

Numerical Verification of Heat Transfer Characteristics

A rotor blade tip profile of the GE-E3 turbine is stretched to obtain a 3D model for verification, which is a linear turbine cascade with film cooling. Experimental data from Kwak's planar tip at subsonic speeds were used to verify the credibility of the numerical simulations (Kwak and Han, 2003). The geometric parameters of the computational model are shown in **Table 5**. The tip clearance is 1% of the blade height, the diameter of 13 films are all 1.29 mm, and they are set on the middle arc. In the experiments of Kwak et al., the positioning of the films is not given in detail. Our in-house code was used to determine the location of the films. In our in-house code, we first generate the mid-arc inside the notch at the top of the blade tip, the dimensionless position of the mid-arc near the leading edge is 0, and the dimensionless position of the mid-arc near the trailing edge is 1. The holes on the middle arc are equally distributed. Therefore, it is only necessary to give the number of air films and the dimensionless position of the first and last air films. We obtain the same experimental model as Kwak's model by multiplying and adjusting the two dimensionless positions when the number of air film pores is fixed at 13. The distance between adjacent films

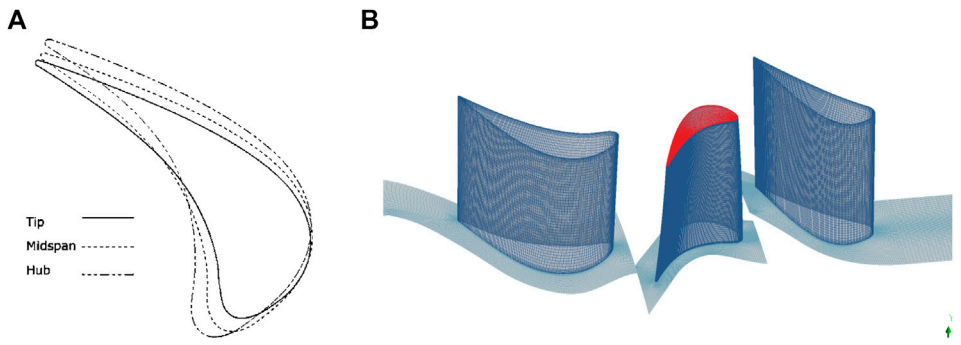

FIGURE 3 | Flat blade tips for numerical verification of aerodynamic characteristics (Behr, 2007). **(A)** The rotor profile. **(B)** Flat leaf tip grid.

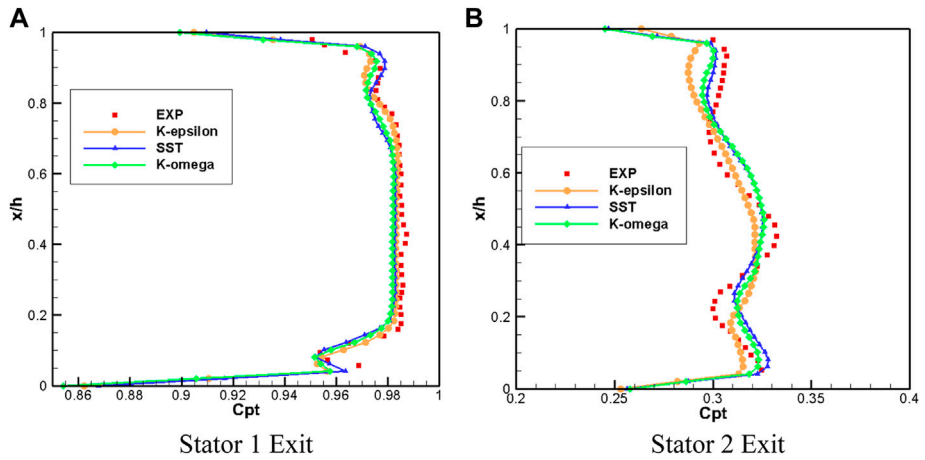

FIGURE 4 | Comparison of numerical simulation results and experimental results (Behr, 2007). **(A)** Stator 1 Exit. **(B)** Stator 2 Exit.

TABLE 5 | Geometric parameters of the fluted tip for verification of heat transfer characteristics.

Parameters	Value
H	122 mm
L	86.1 mm
T	91.5 mm
θ3	32°
T	1.97 mm
H	5.08 mm
W2	2.29 mm
D	1.29 mm

TABLE 6 | Boundary conditions used to verify heat transfer characteristics.

Boundary	Parameters	Value
Inlet	T^*_{in}	297 K
—	P^*_{in}	126900 Pa
—	Tu_{in}	9.7%
Outlet	p_{out}	102700 Pa
Blade surface	T_{blade}	340 K
Inlet of cooling air	$T^*_{cool-in}$	328 K
—	$p^*_{cool-in}$	0.000135 kg/s

is five times the film diameter. The grid field exit length is set to 2.5 times the chord length, the thickness of the first layer of the grid on the wall is 0.000001 mm, the growth ratio of the boundary layer is set to 1.2, and the y + value of the blade surface is controlled at about 1.5. The total number of grids is controlled at about 22 million. **Figure 5A** shows the grid of blade tip with films, and **Figure 5B** shows the schematic diagram of the rotor tip films.

The boundary conditions are shown in **Table 6**. K-ε, SST, and k-ω turbulence models were used for the validation of blade tip heat transfer coefficients and film cooling coverage efficiency. **Figure 6** shows the distribution of heat transfer coefficient (h) and film cooling efficiency (η) compared with the experimental results for the top of the blade tip ribs and the bottom of the notch for the three turbulence models, respectively. The values of heat transfer coefficients simulated by all turbulence models are higher than the experimental results, especially at the top of the ribs and near the trailing edge. The predicted results of the k-ε turbulence model differ significantly from the experimental data; the heat transfer coefficient at the position z1 of the leading edge of the blade is too high. The numerical results of the k-ω turbulence model are close to those of the SST turbulence model; the heat transfer coefficient is high at z2 and z3, respectively. Among the results predicted by the SST turbulence model, position z3 with a high heat transfer coefficient is near the middle of the blade and has the smallest range, which is closest to the experimental value. In addition, all turbulence models overestimate the film cooling efficiency near the cooling film at the bottom of the notch, especially at the leading edge of the blade. The SST turbulence model overestimates η at the suction-side edge of the blade leading edge, but the prediction is more accurate.

RESULTS AND DISCUSSIONS

Pneumatic Performance Analysis

Figure 7 shows the distribution of flow stream and static pressure coefficient (Cp) in the middle section of the blade tip clearance. **Figure 7E** shows the distribution of flow stream and static pressure coefficient of the tip without cooling air condition, which can be used to compare with other cases. The lateral pressure gradient at the fully ribbed fluted blade tip is weakened when cooling air is injected compared to that with no cooling air. The blade tips of the four cooling film distributions all form a low-pressure zone near the suction side at greater than 25% axial position.

Figure 7A shows that the blade tip with the cooling film set in the mid-arc has a larger range of low-pressure zones than the other three types of blade tips. Cooling air is injected vertically into the upper-end wall through the films and creates a small, relatively stable high-pressure zone in the interstitial channel. Influenced by the pressure distribution on the blade surface, the

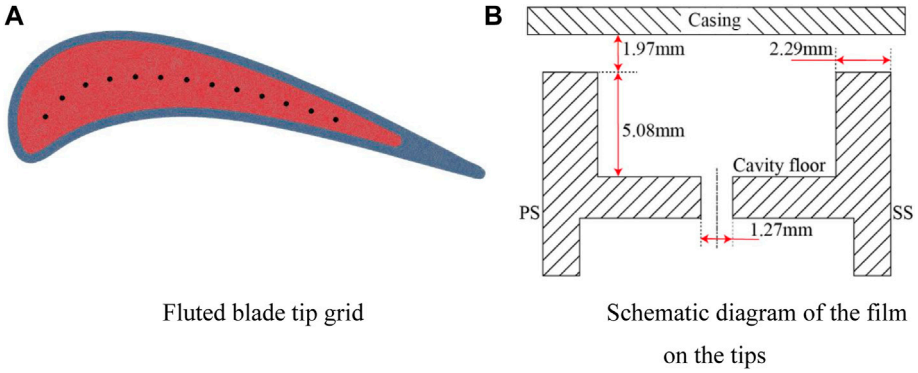

FIGURE 5 | Fluted blade tips for numerical verification of heat transfer characteristics. **(A)** Fluted blade tip grid. **(B)** Schematic diagram of the film on the tips.

pressure is higher in the high-pressure area of the cooling films at the leading edge of the leaf tip, and the pressure is smaller in the high-pressure area closer to the rear.

Figure 7B shows that the airflow from the films strikes the end wall first and enters the leaf tip gap along the pressure side under the influence of the pressure difference. The pressure in the high-pressure region near the pressure-side films is higher than that near the suction-side films.

Comparing **Figures 7A–D**, it was found that among the four tip structures, the pressure-side ribs with added cooling films had the largest airflow folding angle (the angle of deflection of the flow line in the cascade concerning the mainstream flow line). Cooling air injection has a more pronounced impeding effect on the leakage flow of the full circumferential rib tip but not much resistance to the leakage flow of the suction-side rib tip. The position of the reattachment line (RL) and the suction-side leakage flow separation line (LSL) do not change much. **Figures 7C,D** show that the number of streamlines contained in the leaky flow separation line (LSL) is significantly reduced due to the sealing effect of the cooling air jets on the tip ribs on the leaky flow, which indicates that the blade tip structure with films on the ribs reduces the tip leaky flow rate, and the tip structure with films in the suction-side ribs provides better results.

Figure 7D shows that the leakage flow is accelerated twice after passing through the pressure-side ribs and is hit by the cooling airflow on the suction-side ribs at the outlet, resulting in a decrease in the leakage flow rate out of the clearance. The tip leakage flow is no longer observed in the clearance above the suction-side ribs and is replaced by a discrete strip-like leakage flow; this indicates that the ejected cooling air has suppressed most of the leakage flow in the interstitial space, and the main cause of the vortex structure in the blade tip is no longer the blade tip leakage flow but the suction leakage flow formed by the cooling air jet on the suction side.

As a result, the total energy loss at the outlet of a fluted tip structure with air film holes is higher due to the involvement of a small amount of cooling air, but the addition of air film holes can more effectively reduce the tip leakage vortex and leakage flow. The tip with films set in the suction-side ribs has the best control

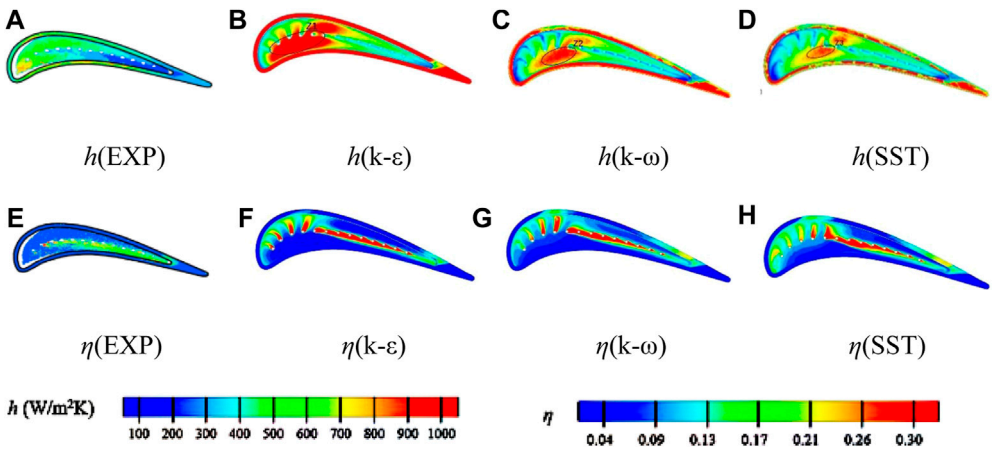

FIGURE 6 | Verification of heat transfer characteristics by numerical simulation (Kwak and Han, 2003). **(A)** *h* (EXP). **(B)** *h* (k-ε). **(C)** *h* (k-ω). **(D)** *h* (SST). **(E)** *η* (EXP). **(F)** *η* (k-ε). **(G)** *η* (k-ω). **(H)** *η* (SST).

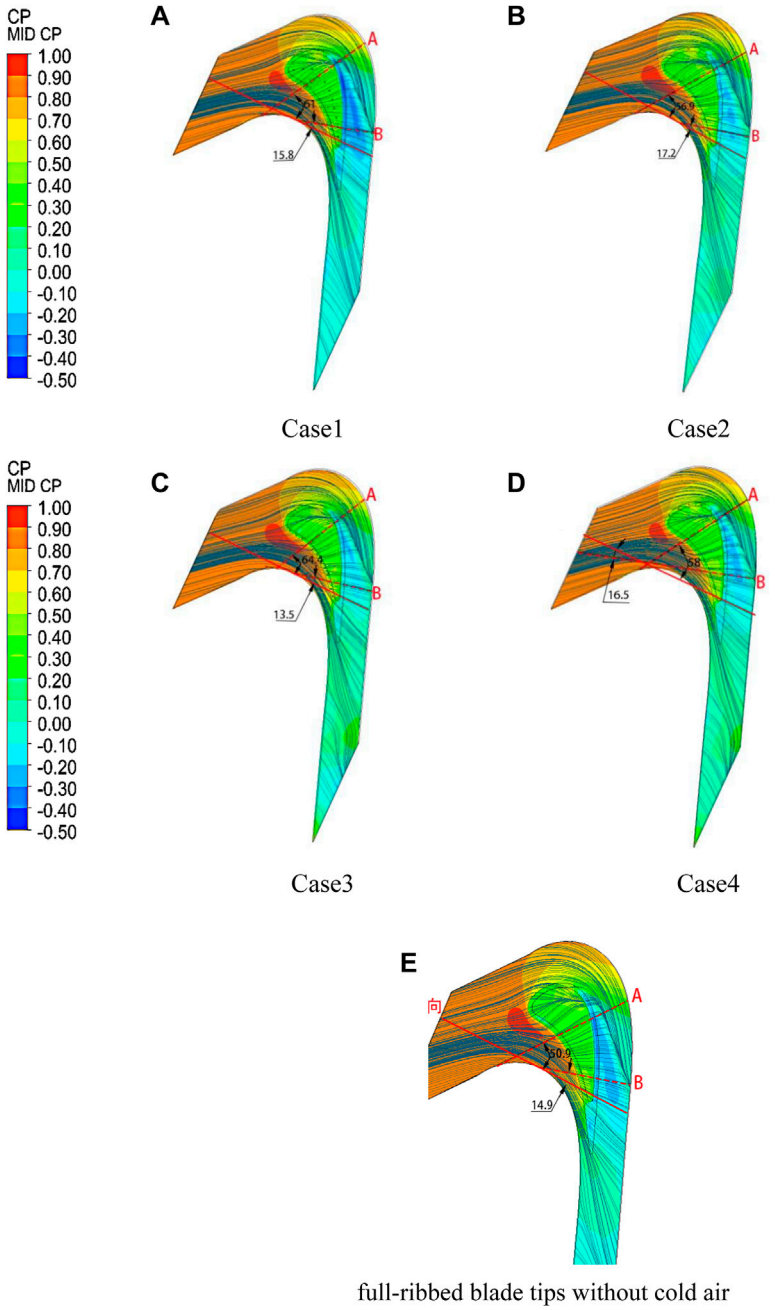

FIGURE 7 | Flowlines and static pressure distribution in the interstitial section. **(A)** Case 1, **(B)** Case 2, **(C)** Case 3, **(D)** Case 4, and **(E)** full-ribbed blade tips without cold air.

effect on the leakage vortex, the leak flow control effect is the worst with films set in the middle arc of the groove bottom, and the blade tip structure with films set in the pressure-side ribs is not conducive to the control of leakage vortices.

As shown in **Figure 7**, two radial sections "A" and "B," which are approximately parallel to the leaf tip leakage flow, are selected to analyze the flow of leakage flow in detail. The position between cross sections "A" and "B" represents the range of the leaf tip leakage area. The solid red line is the axial direction of the blade, and the dashed line is the two cross-sectional positions of "A" and "B."

In the four structures, the angle between section "A" and the axial direction is films set on the pressure-side rib (64.4°) > films set in the middle arc of the bottom of the notch (61.0°) > films set on the suction-side rib (58.0°) > films set on the full circumference rib (56.9°), which indicates that the leakage flow is disturbed by disturbance of the cooling air jet, the flow direction gradually changes, pressure-side rib jets have the greatest effect on flow

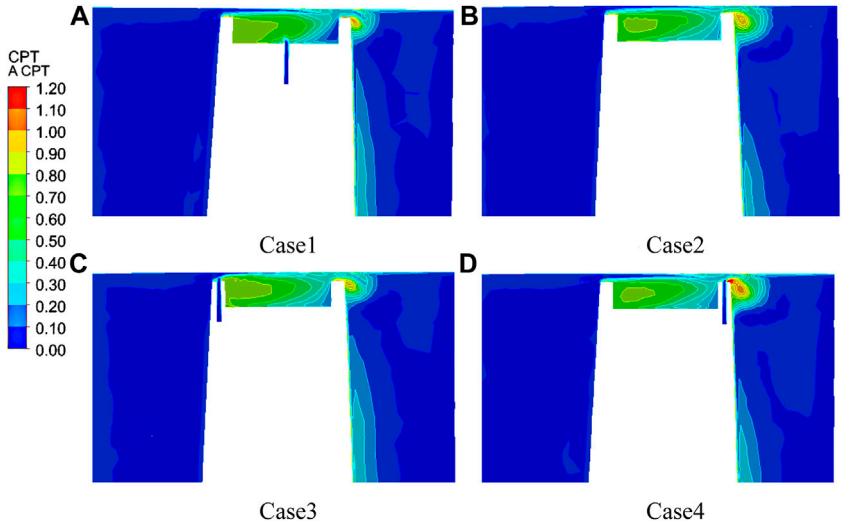

FIGURE 8 | Distribution of the total pressure loss coefficient at cross-section "A" with different distributions of cooling films. **(A)** Case 1, **(B)** Case 2, **(C)** Case 3, and **(D)** Case 4.

direction, and single-side rib jets have less effect on airflow than full circumferential rib jets.

The angle between section "B" and the axial direction is films set on the full circumference rib (17.2°)> films set on the suction-side rib (16.5°)> films set in the middle arc of the bottom of the notch (15.8°)> films set on the pressure-side rib (13.5°), which indicates that the leakage fluid and high-temperature mainstream mixing angle become smaller, and then the leaf tip leakage flow direction is gradually close to the axial direction.

Figure 8 shows the total pressure loss distribution cloud of section "A," which can reflect the flow state of the leakage flow in the complete clearance space of the leaf tip and in the straight leaf grille channel. The leakage flow near the end wall is only subject to wall friction, and the loss is small. It can be seen in section "A" that a part of the leakage flow of the four tip structures produces a vortex in the groove, but the intensity of the vortex in the groove is different.

From **Figure 8A**, it can be seen that when a part of the leakage flow in the recess produces a vortex, cold airflow with certain kinetic energy also joins the vortex structure in the recess in Case 1, which inevitably destroys the separation bubble at the bottom of the groove, preventing the evolution of the vortex structure and forming a low-pressure angle vortex at the intersection of the bottom of the groove and the inner wall of the suction-side ribs; it can also reduce vortex loss in the groove and the exit velocity of the leakage flow, and results in the deflection of the leakage flow on the suction side to the upper side and lower kinetic energy. The leakage vortex size is minimized, and a part of the fluid flowing out of the clearance creates a new vortex in the attachment layer of the upper magazine.

As seen in **Figure 8C**, the pressure-side ribs set with films have a smaller leaky vortex size and a higher leaky vortex nucleus location than the tips of the other three structures, and the airflow hitting the pressure-side ribs is initially blocked, which decelerates into the tip gap when mixed with the cold air injected from the pressure side; it further reduces the leakage flow rate into the gap and also raises the location of the incoming leakage flow upward, which forms the most developed vortex system inside the groove and enhances the mixing effect with the mainstream at the leading edge.

Figure 8D shows that the size of the leaky vortex at the tip is the largest and the position of the vortex nucleus is the lowest in Case 4. When the airflow impacted the pressure side, the leakage flow decelerated for the first time; then under the action of pressure difference, part of the leakage flow entered the groove at a faster speed to form a vortex. As the separation bubble above the ribs on the suction side is destroyed by cold air and the outlet airflow is lifted to the upper magazine by the impact of cold air, the development of the vortex inside the groove is changed and the intensity of the vortex is greatly weakened. When the vortex flows out of the suction side, the cooling air ejected from the films participates in the formation of a leaky vortex-like structure, which results in a larger leaky vortex size.

As shown in **Figure 8B**, the cooling air from both the pressure- and suction-side vents will affect the gap leakage flow, which causes the flow rate to slow down even more and the gap flow to lift further up the magazine.

Figure 9 shows the distribution of the total pressure loss in section "B." It can be found that the size and loss of the leakage vortex in section "B" are higher than those in section "A." It can be seen from **Figure 9C** that in Case 3, the extent and loss of the tip leakage vortex are the largest, the position of the vortex nucleus is downward, and the vortex generated by the partial leakage flow in the groove is lifted upward the largest, which forms a stronger air seal on the blade tip clearance. The leakage flow develops to downstream along the flow direction. The trailing edge of the blade width is smaller, the influence of the suction-side intrusion flow on the vortex in the trailing edge notch becomes larger, the vortex development inside the groove is hindered, and the intensity of the internal vortex is weakened to

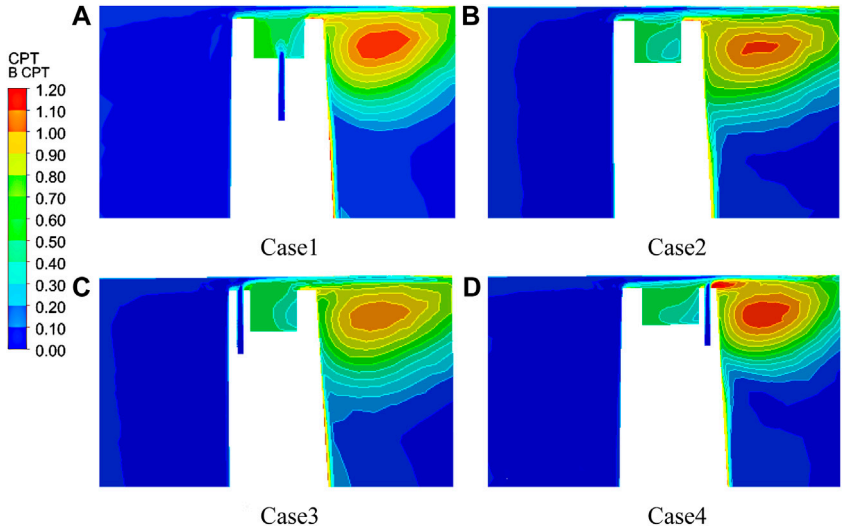

FIGURE 9 | Distribution of the total pressure loss coefficient at cross-section "B" with different distributions of cooling films. **(A)** Case 1, **(B)** Case 2, **(C)** Case 3, and **(D)** Case 4.

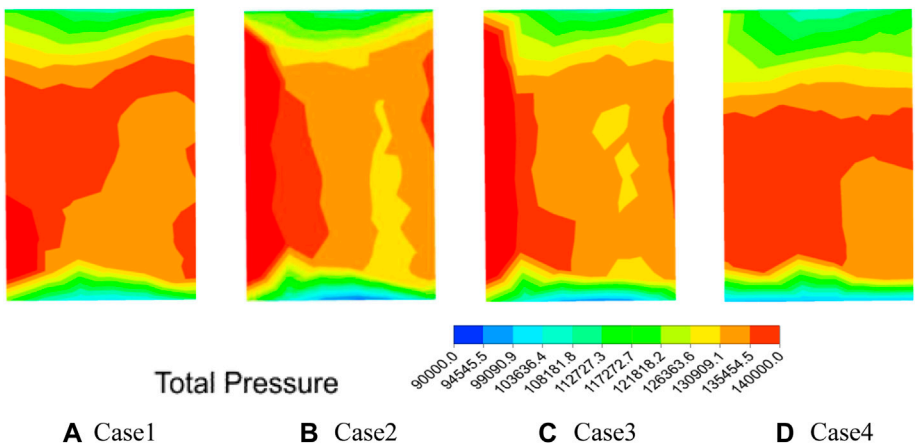

FIGURE 10 | Total pressure distribution at the outlet. **(A)** Case 1, **(B)** Case 2, **(C)** Case 3, and **(D)** Case 4.

varying degrees. From **Figure 9A**, it can be seen that the vortex kinetic energy dissipation in the blade tip is stronger in Case 1. **Figure 9D** shows that a small high-pressure zone is formed above the ribs of the suction side in Case 4; the reason is that the suction-side exit velocity at the trailing edge is larger, the airflow hits the top of the ribs to form a small separation bubble, and the airflow from the suction-side ribs will destroy the separation bubble. At the same time, the cold air was ejected with a certain kinetic energy and mixed with the outlet leakage flow, which makes the suction side of the outlet air velocity greatly reduced, and airflow is lifted; therefore, the smallest leakage vortex size and the highest vortex nucleus are generated at the trailing edge in Case 4, which indicates that this blade structure is conducive to controlling the blade tip leakage flow. From the above discussion, it can be seen that under the fixed gap size, the blade tip structure with films in the bottom mid-arc of the groove and films in the suction-side ribs can effectively reduce the leakage mixing loss, among which the structure of the suction-side ribs with films provides better control of the interstitial flow at the tip.

Figure 10 shows the total outlet pressure distribution under different air film hole setting schemes. The higher the total outlet pressure, the lower the loss. The high-pressure region is the largest in Case 4, which indicates that the jet scheme has the least losses. And the high-pressure area is small in Case 2 and Case 3, which indicates that the tip loss is higher for both types of film distribution.

Figures 11, **12** show the distribution of the total pressure loss coefficient and the outlet airflow angle in the blade height direction, respectively. The total pressure loss coefficients of leaf roots were all close to 0.05. The total pressure loss at the

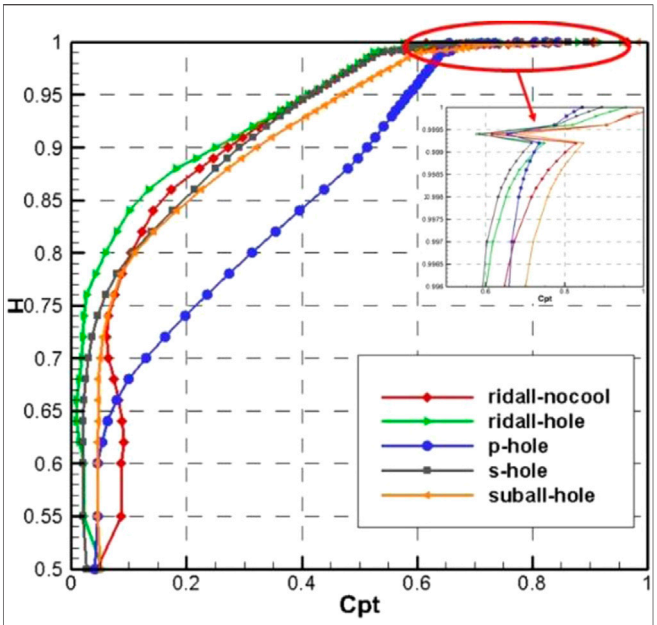

FIGURE 11 | Distribution of the total pressure loss coefficient along with the blade height.

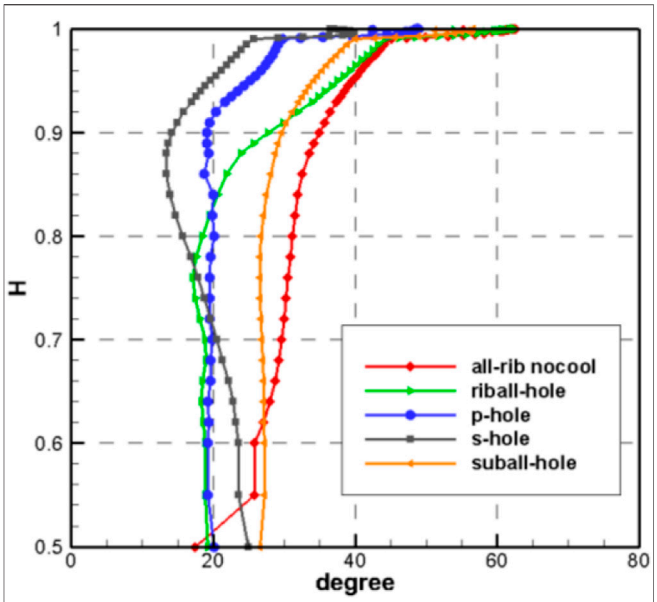

FIGURE 12 | Distribution of the outlet airflow angle along with the blade height.

tip and root is minimal (0.025) in Case 3. Two high-loss areas exist for the four different tip structures: one is the leakage vortex high-loss area of 0.97–0.99 H and the other is the channel vortex high-loss area of 0.84–0.90 H. Both high-loss areas rise along with the blade height with cooling air injection, and the high-loss area becomes smaller than a fluted blade tip without cooling films. Compared to a fluted tip without a cooling film, a fluted tip with cooling films has a reduced channel vortex loss at 0.84–0.90 H. The channel vortex loss is the smallest in Case 2. This indicates no improvement in channel eddy losses in Case 1 and Case 4. The leakage eddy loss is minimized at 0.99 H in Case 4; the high loss area of leaf tip leakage flow is the largest at the tip in Case 1. This indicates that the air film holes on the full circumferential ribs and on the suction-side ribs can significantly reduce not only the channel vortex loss but also the leakage vortex loss, while it also indicates that the air film holes on the pressure-side ribs can reduce the leakage vortex loss but increase the channel vortex loss. The four types of tip structures with cooling films have similar outlet airflow angle distribution trends along with the blade height; the uniformity of the outlet airflow angle distribution is improved with cooling films compared to the fluted tip without cooling films. The uniformity of the outlet airflow angle distribution is better in Case 1 and Case 3.

Figure 13 shows the distribution of streamline in cross-section "A" and cross-section "B," which visualizes the flow of the leakage flow in the impeller and the evolution of the internal vortex system.

From **Figure 13A**, it can be seen that the vortex structure in the recess is contained in the structure of Case 1. Although the mixing of cooling air and high-temperature leakage flow will form film protection at the bottom of the groove, the air sealing effect above the magazine is weakened, which will lead to an increase in the flow of leakage flow into the clearance.

Figures 13B–D reveal that the cooling air injected on the ribs can destroy the separation bubbles above the ribs, and most of the cooling air injected on the pressure-side ribs leaks into the upper channel vortex and evolves further, and the cooling gas injected on the suction-side ribs is influenced by the main flow of the gap exit to participate in the development of the leak-like vortex. This indicates that the air jet on the ribs is beneficial to control the leakage flow rate, especially the suction-side jet has the best effect on the pneumatic sealing of the whole blade tip. By analyzing Case 1–Case 4, the main cause of the internal vortex structure was changed from the tip leakage flow to the return flow after the cooling air jet was engaged. The leakage vortex at the suction side of section "B" is larger than that of section "A" and farther from the suction surface. The gap leakage flow in cross-section "A" is first dissipated by the kinetic energy of a part of the pressure-side rib jet and then disturbed by the return flow of the jet plug on the suction side, creating a medium-sized angular vortex near the pressure side of the groove and a small angular vortex near the suction side of the groove in Case 2. The vortex inside the groove is the least developed in Case 4, which means that the vortex loss in the recess is minimized, and the bottom separation bubble in the recess near the suction side is increased by the influence of the cold air on the suction side, which is more conducive to blade cooling.

As shown in **Figure 14**, for different blade tip clearance under the blade, suction surface and pressure surface limit the flow line distribution. From the left suction-side surface flow line distribution, it can be seen that the leaf tip secondary flow covers nearly a quarter of the channel height near the trailing edge of the blade. The position above the yellow dashed line indicates the area of small vortices caused by the interstitial flow

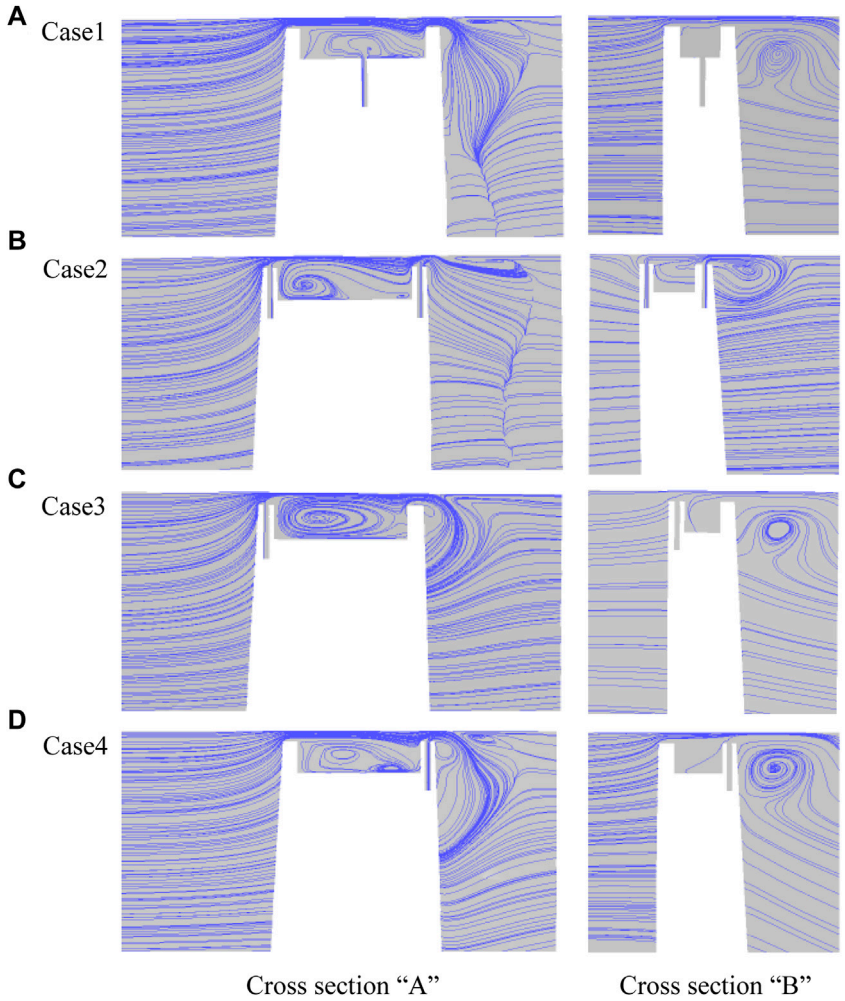

FIGURE 13 | Flowline distribution of "A" and "B" cross sections of fully ribbed leaf tips with different distribution of films. **(A)** Case 1, **(B)** Case 2, **(C)** Case 3, and **(D)** Case 4.

perpendicular to the leaf tip. The red dashed line in the figure shows the reattachment line of the tip leakage vortex (TLV) and the tip channel vortex (TPV), and the green dashed line indicates the separation line of the tip passage vortex (TPV).

As shown in **Figure 14A**, in Case 1, the extent of the separation bubble at the tip of the leaf closest to the suction side is the smallest, and the position of the separation bubble moves up along the flow direction and disappears at the trailing edge. The small vortex region at the tip gradually becomes larger, and the vortex region is lifted upward at the trailing edge. Only in Case 1, the reattachment lines of the tip leakage vortex (TLV) and tip passage vortex (TPV) are shifted upward along the flow direction, and the reattachment lines of the rest of the cases are shifted downward along the flow direction.

As shown in **Figure 14C**, in Case 3, the vortex range in the suction surface is minimal and disappears at the trailing edge of the ribs. The radial extent of the vortex caused by the airflow perpendicular to the gap at the tip of the leaf is minimal. It may be due to the fact that the cold air has some kinetic energy in Case 3, which increases the blocking effect of the clearance entrance.

As shown in **Figures 14B,D**, the range of reattachment line at the tip is wider in Case 2 and Case 4, which suggests that both types of leaf tips can develop a more complete leakage vortex on the suction side, and the flow is more developed downstream, causing the reattachment line to move downstream along the flow direction. The shape of the reattachment line is more moderate in Case 2. The channel vortex separation line is the closest to the top, and the reduction in channel vortex loss is the greatest in Case 4; its channel vortex range is also smaller, and the channel vortex (TPV) separation line near the trailing edge is tilted upward to a greater extent, which indicates that the suction side of the rib tip is conducive to weakening the channel vortex. However, the channel vorticity line of the blade tip with film holes on the full circumference rib and the pressure-side rib is gently inclined upward near the trailing edge, which implies that the channel vortices of these two types of tips are more developed along the flow direction, and the channel vortices of the tips with films on

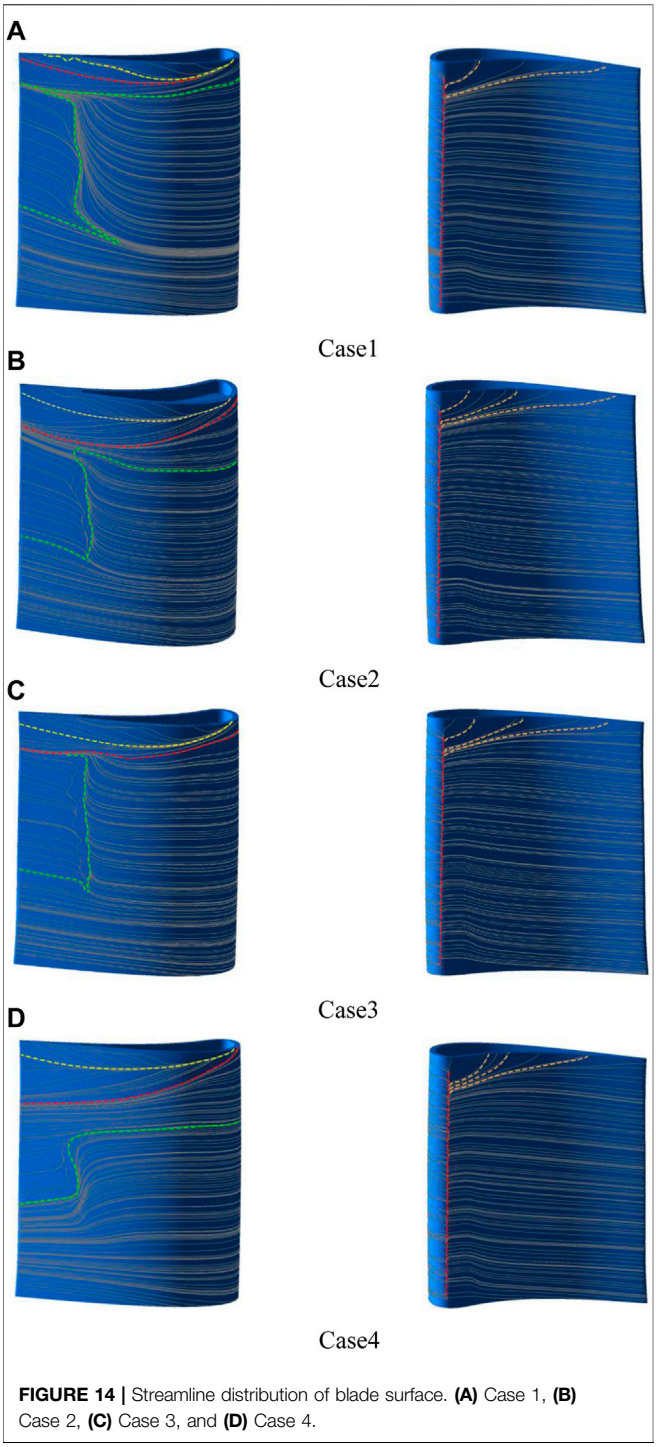

FIGURE 14 | Streamline distribution of blade surface. **(A)** Case 1, **(B)** Case 2, **(C)** Case 3, and **(D)** Case 4.

the pressure-side ribs are the most strongly mixed with the leakage vortices.

The surface flow line on the pressure side shows that after the airflow strikes the end wall, part of the fluid passes laterally through the cascade channel, and the red separation line on the pressure side all moves to the front edge, the moving distances are Case 4, Case 1, Case 3, and Case 2 in the descending order; the greater the distance the separation line moves forward, the more favorable the tip structure is to improve the angle of attack of the incoming flow.

TABLE 7 | Exit aerodynamic parameters of the blade tip with different cooling film distributions.

Tip structure	Energy loss at the outlet	Relative leakage flow (kg/s)
Notched blade tips without cold air	0.124266	0.007744
Case 1	0.123515	0.007788
Case 2	0.139805	0.007343
Case 3	0.139770	0.006936
Case 4	0.123249	0.006685

From the previous discussion, it is clear that the structure of the fluted leaf tip with cold air affects the flow of the leakage stream as well as the development and evolution of the leakage vortex. The variation of leakage vortex and channel vortex losses caused by different cooling film distributions are also different.

Table 7 shows the total energy loss and relative leakage flow of the cascade for different tip configurations, which can more visually compare the impact of different cooling film arrangements on aerodynamic performance. As shown in **Table 7**, the total loss of the fully ribbed fluted tip structure with the addition of cooling air injection is higher than that without cooling air, but the increase in total loss due to cold air is not significant because the proportion of the cooling airflow to the total flow is small. Case 1 has the lowest total pressure loss at the leaf tip, about 0.122515; Case 2 has the highest leaf tip loss, about 0.139805; and Case 4 has lower leaf tip loss than Case 3. The fully ribbed fluted tip structure with cooling air injection has a lower leakage flow than that without cooling air; Case 1 has the highest leakage flow rate of about 0.007788 kg/s; and the leakage flow rate of Case 4 is the smallest, about 0.006685 kg/s.

In summary, the addition of film holes on the ribs is more conducive to reducing the leakage flow rate. In particular, when the number of air film holes is fixed, adding films on the single-side rib has a better control effect on leakage flow, and adding films on the suction-side rib has the most significant improvement effect. Adding films on the arc at the bottom of the groove is beneficial to reduce the energy loss of the blade, but it will increase the relative leakage flow rate. Adding the films to the suction-side rib will not only reduce the total energy loss but also reduce the leakage flow rate.

Heat Transfer Performance Analysis

Figure 15 shows the distribution of film cooling efficiency η at the top of the rib and the bottom of the groove under the four cooling film hole arrangements. While the low-temperature air released from the interior of the blade participates in the evolution of the vortex structure, it also changes the distribution of the tip surface temperature. The films in Case 1 have the largest coverage of the groove, and the film coverage of the tip ribs is very low.

The overall cooling efficiency of the blade tip structure with films added to the ribs is similar and low. In Case 3, the cooling air not only achieves high-intensity cooling on the pressure-side ribs but also can appropriately suppress the heat load of the suction-side ribs. In Case 4, the cooling air not only achieves high-

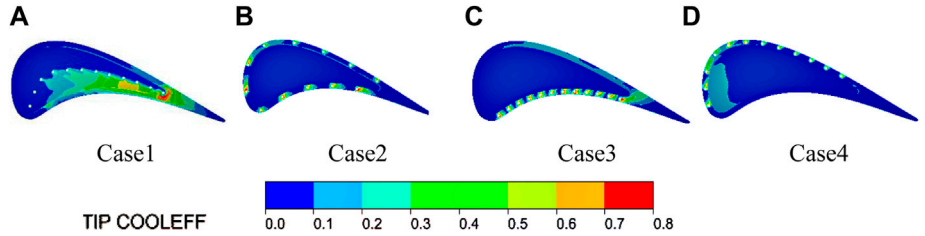

FIGURE 15 | Film cooling efficiency for different air film hole distribution schemes η. **(A)** Case 1, **(B)** Case 2, **(C)** Case 3, and **(D)** Case 4.

intensity cooling on the suction-side ribs, and in the leading edge of the blade notch position, the cold air has a covering effect. After the tip clearance flow is decelerated by the cooling air from the pressure-side ribs at the entrance of the clearance, most of the cooling air mixed with the leakage flow participates in the development of the vortex in the groove cavity, and a small part of the fluid passes through the blade tip to cool the suction-side ribs. In Case 2, the cooling air jet achieves a more comprehensive discretization cooling of the ribs.

CONCLUSION

In this article, the flow and heat transfer characteristics of the fluted blade tip of a rotor were studied under different configurations of cooling films. The effect of the cooling film position on the tip leakage flow and the aerodynamic characteristics of the tip was analyzed. The vortex structure inside the blade tip recess and the development of secondary flow in the clearance were compared for four types of the air film aperture distribution. The main conclusions obtained are as follows:

1) The total loss of the full-ribbed fluted tip structure with the addition of cooling air injection is higher than that without cooling air; however, the proportion of cold airflow to total flow was small, so the increase in total loss due to cooling air is not significant. The total pressure loss for the tip with cooling films added to the arc in the groove is the smallest, the value is approximately 0.122515, the tip with uniform films on full perimeter ribs has the highest loss, and the value of the loss is about 0.139805.
2) The addition of cooling air injection on the ribs was more conducive to reducing the leakage flow rate, the most significant improvement was achieved by adding cooling films to the suction-side ribs, and the leakage flow rate of the tip was about 0.006685 kg/s. The highest leakage flow rate was found for the tip with the cooling film added to the arc in the groove, with a value of 0.007788 kg/s. The swirl structure inside the groove was mainly caused by the return flow of the tip leakage stream from the cooling air jet. The vortex in the groove evolved most intensely when the films on the pressure-side ribs eject cooling air.
3) The uniformity of the outlet flow angle distribution was improved when there was cold air injection. Adding cooling films in the middle arc of the bottom of the groove and on the pressure-side ribs can improve the uniformity of the outlet flow angle distribution better than other structures.
4) The cooling air can effectively cover the groove by adding films in the middle arc of the tip groove. The cooling air can effectively cover the rib when adding cooling films to the ribs, but inside the recess, the cooling air barely covers the bottom.

DATA AVAILABILITY STATEMENT

The original contributions presented in the study are included in the article/Supplementary Material, further inquiries can be directed to the corresponding author.

AUTHOR CONTRIBUTIONS

All authors listed have made a substantial, direct, and intellectual contribution to the work and approved it for publication.

ACKNOWLEDGMENTS

The authors would like to acknowledge the support of the National Natural Science Foundation of China (Number 52076053) and the National Natural Science Foundation of China (Youth Foundation) (Number 12002374).

REFERENCES

Behr, T. (2007). *Control of Rotor Tip Leakage and Secondary Flow by Casing Air Injection in Unshrouded Axial Turbines*. Dresden: Dresden University of Technology. doi:10.3929/ethz-a-005478482

Bunker, R. S., and Bailey, J. C. (2001). "Effect of Squealer Cavity Depth and Oxidation on Turbine Blade Tip Heat Transfer," ASME Article No, GT2000-0155 in ASME Turbo Expo 2000, New Orleans, LA, June, 2001. doi:10.1115/2001-GT-0155

Bunker, R. S. (2006). Axial Turbine Blade Tips: Function, Design, and Durability. *J. Propul. Power* 22, 271–285. doi:10.2514/1.11818

Choi, S. M., Bang, M., Moon, H. K., and Cho, H. H. (2021). Wake Effects on Heat Transfer from a Turbine Blade Tip with Different Configurations and its Corresponding Shroud. *Int. Commun. Heat Mass Transfer* 126, 105333. doi:10.1016/j.icheatmasstransfer.2021.105333

Dey, D. (2001). *Aerodynamic Tip Desensitization in Axial Flow Turbines*. State College: Pennsylvania State University.

Du, K., Li, Z., Li, J., and Sunden, B. (2019). Influences of a Multi-Cavity Tip on the Blade Tip and the over Tip Casing Aerothermal Performance in a High Pressure Turbine cascade. *Appl. Therm. Eng.* 147, 347–360. doi:10.1016/j.applthermaleng.2018.10.093

Du, W., Luo, L., Wang, S., and Sunden, B. (2021). Film Cooling in the Trailing Edge Cutback with Different Land Shapes and Blowing Ratios. *Int. Commun. Heat Mass Transfer* 125, 105311. doi:10.1016/j.icheatmasstransfer.2021.105311

Du, W., Luo, L., Jiao, Y., Wang, S., Li, X., and Sunden, B. (2021). Heat Transfer in the Trailing Region of Gas Turbines - A State-Of-The-Art Review. *Appl. Therm. Eng.* 199, 117614. doi:10.1016/j.applthermaleng.2021.117614

Guo, Q., Huang, X., and Qiu, B. (2019). Numerical Investigation of the Blade Tip Leakage Vortex Cavitation in a Waterjet Pump. *Ocean Eng.* 187, 106170. doi:10.1016/j.oceaneng.2019.106170

Heyes, F. J. G., Hodson, H. P., and Dailey, G. M. (1992). The Effect of Blade Tip Geometry on the Tip Leakage Flow in Axial Turbine Cascades. *J. Turbomach.* 114, 643–651. doi:10.1115/1.2929188

Hofer, T. s., and Arts, T. (2009a). "Aerodynamic Investigation of the Tip Leakage Flow for Blades with Different Tip Squealer Geometries at Transonic Conditions," in ASME Turbo Expo 2009: Power for Land, Sea, and Air, Orlando, FL, June, 2009 (American: American Society of Mechanical Engineers (ASME)), 1051–1061. doi:10.1115/GT2009-59909

Hofer, T. s., and Arts, T. (2009b). "Aerodynamic Investigation of the Tip Leakage Flow for Blades with Different Tip Squealer Geometries at Transonic Conditions," ASME Article No. GT2009-59909 in ASME Turbo Expo 2009, Orlando, FL, June, 2009. doi:10.1115/GT2009-59909

Jin, J., Song, Y., Yu, J., and Chen, F. (2019). Modification and Optimization Strategies for Turbine Arbitrary Blade Tips. *Proc. Inst. Mech. Eng. A: J. Power Energ.* 233, 675–688. doi:10.1177/0957650919826326

Kang, D. B., and Lee, S. W. (2016). Effects of Squealer Rim Height on Heat/mass Transfer on the Floor of Cavity Squealer Tip in a High Turning Turbine Blade cascade. *Int. J. Heat Mass Transfer* 99, 283–292. doi:10.1016/j.ijheatmasstransfer.2016.03.121

Key, N. L., and Arts, T. (2006). Comparison of Turbine Tip Leakage Flow for Flat Tip and Squealer Tip Geometries at High-Speed Conditions. *J. Turbomach.* 128, 213–220. doi:10.1115/1.2162183

Kumar, R., Kumar, V. S., Butt, M. M., Sheikh, N. A., Khan, S. A., and Afzal, A. (2020). Thermo-mechanical Analysis and Estimation of Turbine Blade Tip Clearance of a Small Gas Turbine Engine under Transient Operating Conditions. *Appl. Therm. Eng.* 179, 115700. doi:10.1016/j.applthermaleng.2020.115700

Kwak, J. S., and Han, J.-C. (2003). Heat Transfer Coefficients and Film Cooling Effectiveness on the Squealer Tip of a Gas Turbine Blade. *J. Turbomach.* 125, 648–657. doi:10.1115/1.1622712

Lee, S. W., Moon, H. S., and Lee, S. E. (2009). Tip Gap Height Effects on Flow Structure and Heat/Mass Transfer over Plane Tip of a High-Turning Turbine Rotor Blade. *Int. J. Heat Fluid Flow* 30, 198–210. doi:10.1016/j.ijheatfluidflow.2008.12.009

Luo, L., Zhao, Z., and Kan, X. (2019). On the Heat Transfer and Flow Structures' Characteristics of the Turbine Blade Tip Underside with Dirt Purge Holes at Different Locations by Using Topological Analysis. *J. Turbomach.* 141, 071004. doi:10.1115/1.4042654

Mercan, B., Doğan, E., Ostovan, Y., and Uzol, O. (2015). Effects of Camberwise Varying Tip Injection on Loss and Wake Characteristics of a Low Pressure Turbine Blade. *Int. J. Heat Fluid Flow* 54, 119–130. doi:10.1016/j.ijheatfluidflow.2015.04.008

Mischo, B., Burdet, A., and Abhari, R. S. (2011). Influence of Stator-Rotor Interaction on the Aerothermal Performance of Recess Blade Tips. *J. Turbomach.* 133, 011023. doi:10.1115/1.4001134

Newton, P. J., Lock, G. D., Krishnababu, S. K., Hodson, H. P., Dawes, W. N., Hannis, J., et al. (2006). Heat Transfer and Aerodynamics of Turbine Blade Tips in a Linear cascade. *J. Turbomach.* 128, 300–309. doi:10.1115/1.2137745

Nho, Y. C., Park, J. S., Lee, Y. J., and Kwak, J. S. (2012). Effects of Turbine Blade Tip Shape on Total Pressure Loss and Secondary Flow of a Linear Turbine cascade. *Int. J. Heat Fluid Flow* 33, 92–100. doi:10.1016/j.ijheatfluidflow.2011.12.002

Nho, Y. C., Park, J. S., Lee, Y. J., and Kwak, J. S. (2012). Effects of Turbine Blade Tip Shape on Total Pressure Loss and Secondary Flow of a Linear Turbine Cascade. *Int. J. Heat Fluid Flow* 33, 92–100. doi:10.1016/j.ijheatfluidflow.2011.12.002

Park, J. S., Lee, S. H., Lee, W. S., Chung, J. T., and Kwak, J. S. (2016). Heat Transfer and Secondary Flow with a Multicavity Gas Turbine Blade Tip. *J. Thermophys. Heat Transfer* 30, 120–129. doi:10.2514/1.T4541

Pouagare, M., Weinhold, W., and Weinhold, W. (1986). "Tip Leakage Reduction through Tip Injection in Turbomachines," AIAA-86-1764 in 22nd Joint Propulsion Conference, Huntsville, Alabama, June, 1986. doi:10.2514/6.1986-1746

Rao, N. M., and Camci, C. (2004). "Axial Turbine Tip Desensitization by Injection from a Tip Trench: Part 1 - Effect of Injection Mass Flow Rate," in ASME Turbo Expo 2004: Power for Land, Sea, and Air, Vienna, Austria, June, 2004 (American Society of Mechanical Engineers (ASME)), 1075–1088. doi:10.1115/GT2004-53256

Rao, N. M., and Camci, C. (2004). "Axial Turbine Tip Desensitization by Injection from a Tip Trench: Part 2 - Leakage Flow Sensitivity to Injection Location," in ASME Turbo Expo 2004: Power for Land, Sea, and Air, Vienna, Austria, June, 2004 (American Society of Mechanical Engineers (ASME)), 1089–1098. doi:10.1115/GT2004-53258

Tallman, J. A. (2004). A Computational Study of Tip Desensitization in Axial Flow Turbines Part2: Turbine Rotor Simulations with Modified Tip Shapes. ASME Article No. GT2004-53919. doi:10.1115/gt2004-53919

Virdi, A. S., Zhang, Q., He, L., Li, H. D., and Hunsley, R. (2015). Aerothermal Performance of Shroudless Turbine Blade Tips with Relative Casing Movement Effects. *J. Propul. Power* 31, 527–536. doi:10.2514/1.B35331

Volino, R. J. (2017). Control of Tip Leakage in a High-Pressure Turbine cascade Using Tip Blowing. *J. Turbomach.* 139, 061008. doi:10.1115/1.4035509

Wang, J., Sundén, B., Zeng, M., and Wang, Q. (2015). Film Cooling Effects on the Tip Flow Characteristics of a Gas Turbine Blade. *Propul. Power Res.* 4, 9–22. doi:10.1016/j.jppr.2015.02.003

Wheeler, A. P. S., Atkins, N. R., and He, L. (2011). Turbine Blade Tip Heat Transfer in Low Speed and High Speed Flows. *J. Turbomach.* 133, 41–55. doi:10.1115/1.4002424

Xue, S., and Ng, W. (2018). Turbine Blade Tip External Cooling Technologies. *Aerospace* 5, 90. doi:10.3390/aerospace5030090

Yang, H., Chen, H.-C., and Han, J.-C. (2006). Film-Cooling Prediction on Turbine Blade Tip with Various Film Hole Configurations. *J. Thermophys. Heat Transfer* 20, 558–568. doi:10.2514/1.18422

Zhang, Q., He, L., and Rawlinson, A. (2014). Effects of Inlet Turbulence and End-wall Boundary Layer on Aerothermal Performance of a Transonic Turbine Blade Tip. *J. Eng. Gas Turb Power* 136, 052603. doi:10.1115/1.4026002

Zhou, Z., Chen, S., Li, W., and Wang, S. (2019). Thermal Performance of Blade Tip and Casing Coolant Injection on a Turbine Blade with Cavity and Winglet-Cavity Tip. *Int. J. Heat Mass Transfer* 130, 585–602. doi:10.1016/j.ijheatmasstransfer.2018.10.130

Conflict of Interest: The authors declare that the research was conducted in the absence of any commercial or financial relationships that could be construed as a potential conflict of interest.

GLOSSARY

τ Tip clearance height

n Number of turbine blades

Ro Rotation speed

θ1 Inlet geometric angle

θ2 Outlet geometric angle

L Axial chord length

H Blade height

D Throat diameter

A Throat area

θ3 Inlet angle

t Pitch

W1 Groove width

h Groove depth

d Film diameter

T_{in}^{*} Total temperature of inlet

P_{in}^{*} Total pressure of inlet

Tu_{in} Turbulence of inlet

p_{out} Static pressure of outlet

T_{blade} Blade surface temperature

$T_{cool-in}^{*}$ The total temperature of the cooling air

$P_{cool-in}^{*}$ The total pressure of the cooling air

π Pressure ratio

m Mass Flow

D1 Hub diameter

D2 Tip diameter

W2 Rib width

η Cooling efficiency of film

Cp Static pressure coefficient

RL Reattach line

LSL Leakage flow separation line

TLV Tip leakage vortex

TPV Tip passage vortex

frontiers in Energy Research

ORIGINAL RESEARCH
published: 23 February 2022
doi: 10.3389/fenrg.2021.796220

Experimental Study on Fuel-Switching of Dual-Fuel Gas Turbine Combustor

Lin Feng[1], *Yang Qiang*[1]*, *Liu Xiao*[2], *LI Ming-jia*[1], *Ran Jun-hui*[1] *and Li Ya-jun*[1]

[1]National Engineering Laboratory for Marine and Ocean Engineering Power System—Gas Turbine Lab of Marine Engineering, Harbin Marine Boiler and Turbine Research Institute, Harbin, China, [2]College of Power and Energy Engineering, Harbin Engineering University, Harbin, China

To research the fuel-switching rules for gas turbine dual-fuel combustor, the effects of fuel change rate, fuel compensation rate, permissible fluctuation limit of outlet temperature, and fuel matching on the fuel-switching performance were studied experimentally by using a real dual-fuel gas turbine combustor. The experimental results show that increasing fuel change rate can reduce fuel-switching time, but the influence of fuel viscosity and evaporative atomization combustion hysteresis leads to the increase of outlet temperature amplitude fluctuation. The fuel compensation rate corresponds to the optimal solution for this combustion chamber; when the fuel change rate decreases, the optimal fuel compensation coefficient will be increase. Meanwhile, by increasing the allowable fluctuation range of outlet temperature and reducing the difference of calorific value of natural gas and diesel, the fuel-switching time can be effectively reduced, and the fuel-switching stability can be improved.

Keywords: gas turbine, combustion chamber, dual-fuel, fuel switch, experimental

OPEN ACCESS

Edited by:
Lei Luo,
Harbin Institute of Technology, China

Reviewed by:
Aiguo Liu,
Shenyang Aerospace University, China
Bing Ge,
Shanghai Jiaotong University, China

***Correspondence:**
Yang Qiang
yangqiangturbine@163.com

Specialty section:
This article was submitted to Advanced Clean Fuel Technologies, a section of the journal Frontiers in Energy Research

Received: *16 October 2021*
Accepted: *29 November 2021*
Published: *23 February 2022*

Citation:
Feng L, Qiang Y, Xiao L, Ming-jia LI, Jun-hui R and Ya-jun L (2022) Experimental Study on Fuel-Switching of Dual-Fuel Gas Turbine Combustor. Front. Energy Res. 9:796220. doi: 10.3389/fenrg.2021.796220

INTRODUCTION

With the development of The Times, the engine has new requirements for fuel adaptability. Jatropha oil (Hashimoto et al., 2014), CME (canola methyl ester), DME (dimethyl ether, CH3OCH3) (Lee and Yoon, 2012), and other alternative fuel (Nascimento et al., 2008; Erazo et al., 2010; Jiang and Agrawal, 2014; Li et al., 2019) have received much development and attention. Fuel adaptability has also led to the development of dual-fuel engines (Korakianitis et al., 2011; Lounici et al., 2014; Yang et al., 2014; Sun et al., 2015). As most important component of the dual-fuel gas turbine, the research of dual-fuel combustors focuses on the performance of different fuels and the dynamic dual-fuel switching process; the dual-fuel combustor design objective is to organize the combustion field in the same structure under the condition of single combustion and mixed combustion and realize the stable fuel-switching (Chong et al., 2020).

According to the classification of switching time, dual-fuel switching technology can be divided into stable fuel-switching technology and fast fuel-switching technology. Among them, the stable fuel-switching technology is not sensitive to the time requirement of the gas turbine fuel-switching process, and the key point is to ensure that the performance of the combustion chamber can meet the design requirements during the whole process of fuel-switching, which is difficult to meet the needs of emergencies in actual engineering (Agwu and Valera-Medina, 2020). Fast fuel-switching technology is mainly used to solve the shortage of stable fuel-switching technology and ensure the short fuel-switching time under the premise of

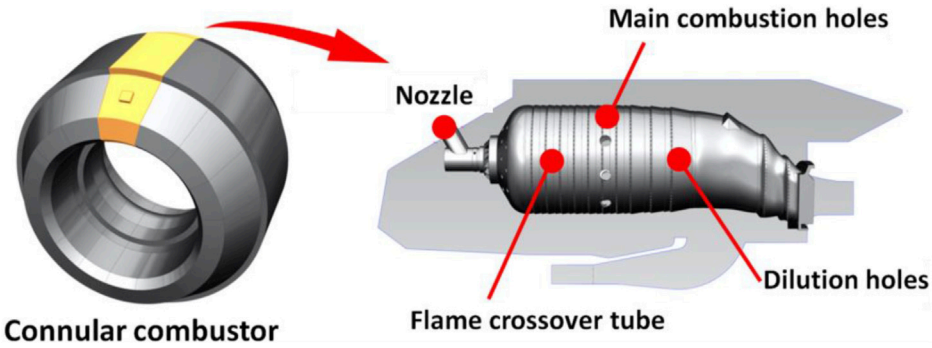

FIGURE 1 | Schematic view of dual-fuel combustor structure.

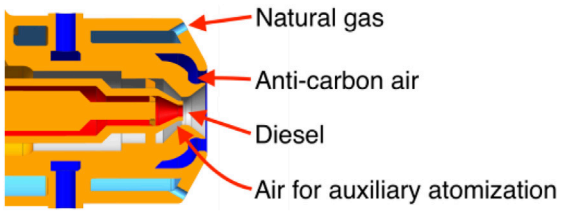

FIGURE 2 | Dual fuel nozzle structure scheme.

continuous and stable operation of the engine. As a non-steady working process of the combustion chamber, the main problems of fast fuel-switching technology are as follows: When the gas turbine is switching between different fuels fastly, the flame in the combustion chamber may be unstable due to the mismatch of the different fuels, leading to ablation of turbine blades or dual-fuel nozzles in the combustion chamber. Sometimes, this situation can also result in combustion chamber blowout or overheating. Therefore, how to shorten the fast fuel-switching time while maintaining the fixed position of flame (or the average temperature at the exit of the combustion chamber) and the stability of the flame (the dynamic pressure value in the combustion chamber) is the key of the research on the fast fuel-switching of the dual fuels combustor.

Around this goal, related scholars and units have also carried out research in different directions. In terms of development of dual-fuel research, structural characteristics and performance indexes of dual-fuel combustors in various manufacturers was introduced (Rokke et al., 2003), and development direction of dual-fuel combustors was indicated. In terms of the simulation of dual-fuel combustor, RANS method was adopted to carry out relevant calculation and analysis for dual-fuel combustor, and a reasonable calculation method of dual-fuel cannular combustor was obtained (Zheng et al., 2010); the simplified mechanism of ammonia/methane co-firing mixing reaction is given (Xiao et al., 2017), which can effectively guide the numerical simulation of combustion chamber. In terms of experimental research, dual-fuel comparison tests were carried out on the MHPS FT8 combustion chamber, and test results show that the combustion chamber performance characteristics are similar under different fuels, but the combustion stability will change to a certain extent during the fuel-switching process (Fox and Schlein, 1990). Dual-fuel

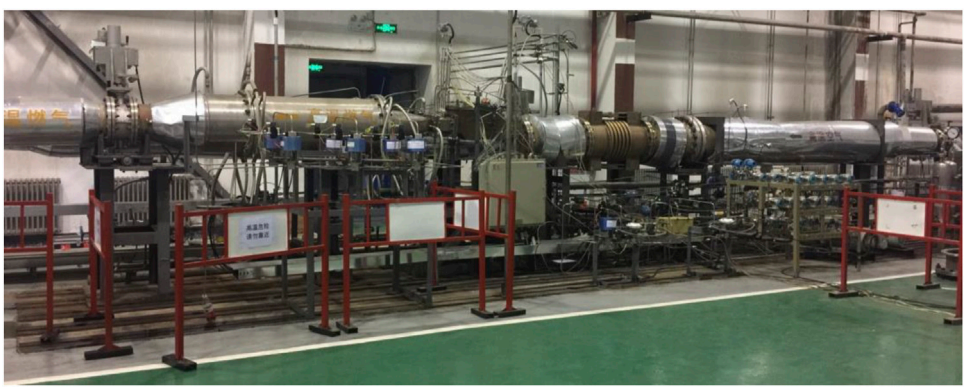

FIGURE 3 | Photograph of the experimental system.

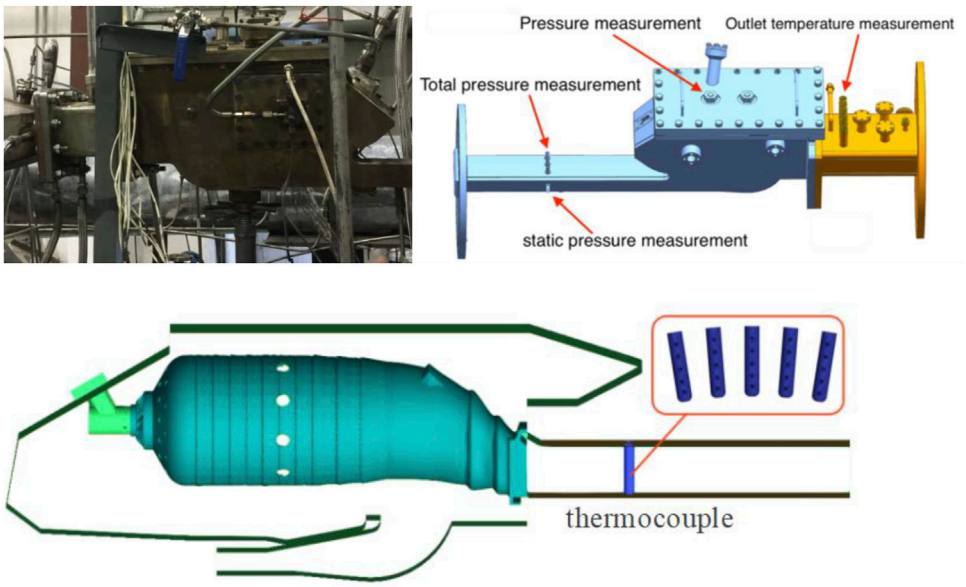

FIGURE 4 | Schematic diagram of the modular combustion test device.

TABLE 1 | Design parameters schedule of the single combustor for test.

Name	Symbol	Unit	Diesel	Nature gas I	Nature gas II
Inlet air mass flow rate	q_{mfM}	kg/h	2,988	2,988	2,988
Inlet air temperature	T_{3M}	K	300	300	300
Inlet air pressure	P_{3M}	MPa	0.4	0.4	0.4
Fuel mass flow rate	q_{mfM}	kg/h	55.0	43.5	52.0

TABLE 2 | Content and scheme combination of dual fuel switch test.

Switching type	Diesel/natural gas change rate, kg/h/s	Outlet temperature fluctuation limit, K	Fuel compensation, kg/h/s	Natural gas type
Natural gas switch to diesel	0.917/-0.725 (Theory switching time, 60 s)	±5	0.1	Natural gas I
	1.834/-1.45 (Theory switching time, 30 s)	±10	0.3	Natural gas II
	3.668/-2.9 (Theory switching time, 15 s)	±20	0.5	
Diesel switch to natural gas	-0.917/0.725 (Theory switching time, 60 s)	±5	0.8	
	-0.458/0.363 (Theory switching time, 120 s)	±10		
	-0.344/0.272 (Theory switching time, 180 s)			

load performance tests were carried out on the Siemens SGT750 gas turbine combustor; the results show that the liquid fuel injection atomization and the change of the calorific value of gas fuel on the performance of dual-fuel combustor is the key direction of dual-fuel combustor research at present (Lindman et al., 2014; Lindman et al., 2017). Dual-fuel load performance tests were also carried out on the 4.2 MW Micro-gas turbine. The test results show that the lean flame stability margin using LBTU (gasifier generated low heating value) gas was more than adequate in relation to load change and fuel changeover requirements. The exhaust gas temperature overall and radial distribution factors have better performance than diesel when using LBTU (Al-Shaikhly et al., 1994), and similar studies are available in the

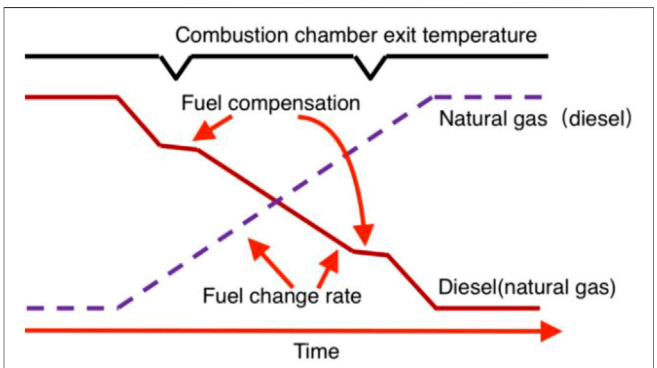

FIGURE 5 | Schematic diagram of dual-fuel switching regulation.

TABLE 3 | Fuel change rate test program.

Test	Diesel change rate kg/h/s	Natural gas change rate kg/h/s	Theory switching time, s
Test 1	+0.917	-0.725	60
Test 2	+1.834	-1.45	30
Test 3	+3.668	-2.9	15
Test 4	-0.344	+0.272	180
Test 5	-0.458	+0.363	120
Test 6	-0.917	+0.725	60

Fuel compensation rate: 0.3 kg/h/s.
Outlet temperature fluctuation limit: ±10K.
Natural gas type: Natural gas I.

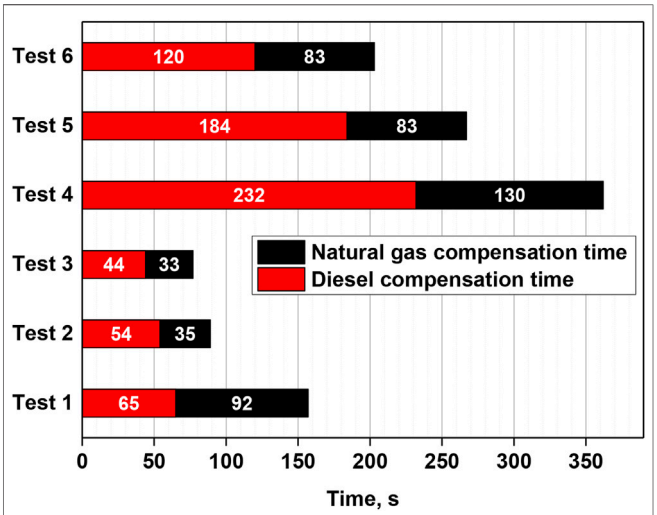

FIGURE 6 | Effects of different fuel change rates on real switching time.

literature (Liu and Sanderson, 2013; Mordaunt and Pierce, 2014).

In general, because fuel-switching involves key equipment selection, control strategy, and user requirements and some other requirements limitations, theoretical calculation and numerical simulation have both limitations. In order to research the influence of relevant parameters on the combustion chamber fuel-switching performance, a type of gas turbine dual-fuel combustion chamber is used to carry out fast fuel-switching test using natural gas and diesel fuel.

RESEARCH HARDWARE

The research object of this paper is a countercurrent annular dual-fuel combustion chamber and it uses diesel and natural gas as fuel. As shown in **Figure 1**, there are 16 liners arranged in an annular way; one row of main combustion holes and one row of mixing holes are arranged on the wall of each liner. Both sides of the liner is provided with a flame crossover tube, and liner cooling is used the film structure.

The dual-fuel nozzle structure is shown in **Figure 2**. The liquid fuel path is located at the center of the nozzle, which adopts the air-assisted atomization structure. The gas fuel path is located in the outer ring of the nozzle, and the injection rules such as injection cone angle and injection velocity are simulated by referring to the liquid fuel atomization.

TEST FACILITY AND METHOD

Test Facility

The test facility is composed of air system, dual-fuel system, ignition system, test device, cooling water system, gas analysis system, exhaust system, measurement system, and control system. The overall appearance of the test facility can be seen in **Figure 3**.

During the test, compressed air enters the test combustion chamber to participate in the combustion, and the high-temperature flue gas after combustion leaves the combustion chamber and enters the exhaust system. The exhaust pipe is cooled by the cooling water, and the high-temperature flue gas is cooled into the exhaust tower and discharged to the atmosphere. The starting ignition system is independently supplied with diesel or natural gas fuel and equipped with an igniter for combustion chamber ignition. The fuel system is divided into natural gas channel and diesel channel, through their respective solenoid valve and pressure regulating valve to transport and regulate fuel. The measurement and control system is responsible for regulating and monitoring the state of the system and is also responsible for measuring the fuel, airflow, temperature, and pressure parameters.

The test device is shown in **Figure 4**. The single-tube molded combustion test device designed to meet the test requirements consists of the test section, the exit measurement section, and the exit transition section. To monitor the inlet and outlet conditions of the combustion chamber, the installation seat of total temperature, total pressure, and static pressure measuring points is arranged at the inlet of the test section, and the installation seat of the outlet temperature thermocouple is arranged at the measurement section. There are 25 thermocouples used to measure the outlet temperature distribution and calculate the OTDF (outlet temperature distribution factor) in this location. The sides of the test device shell are respectively arranged with the igniter equipment seat. Its front end is connected with the air inlet pipe through a connecting flange. Its back end is connected with the outlet measurement section and the transition section in turn, and the transition section is connected with the exhaust pipe.

Test Method

Due to the short-time mixed combustion of the combustion chamber during fuel-switching, testing under rated

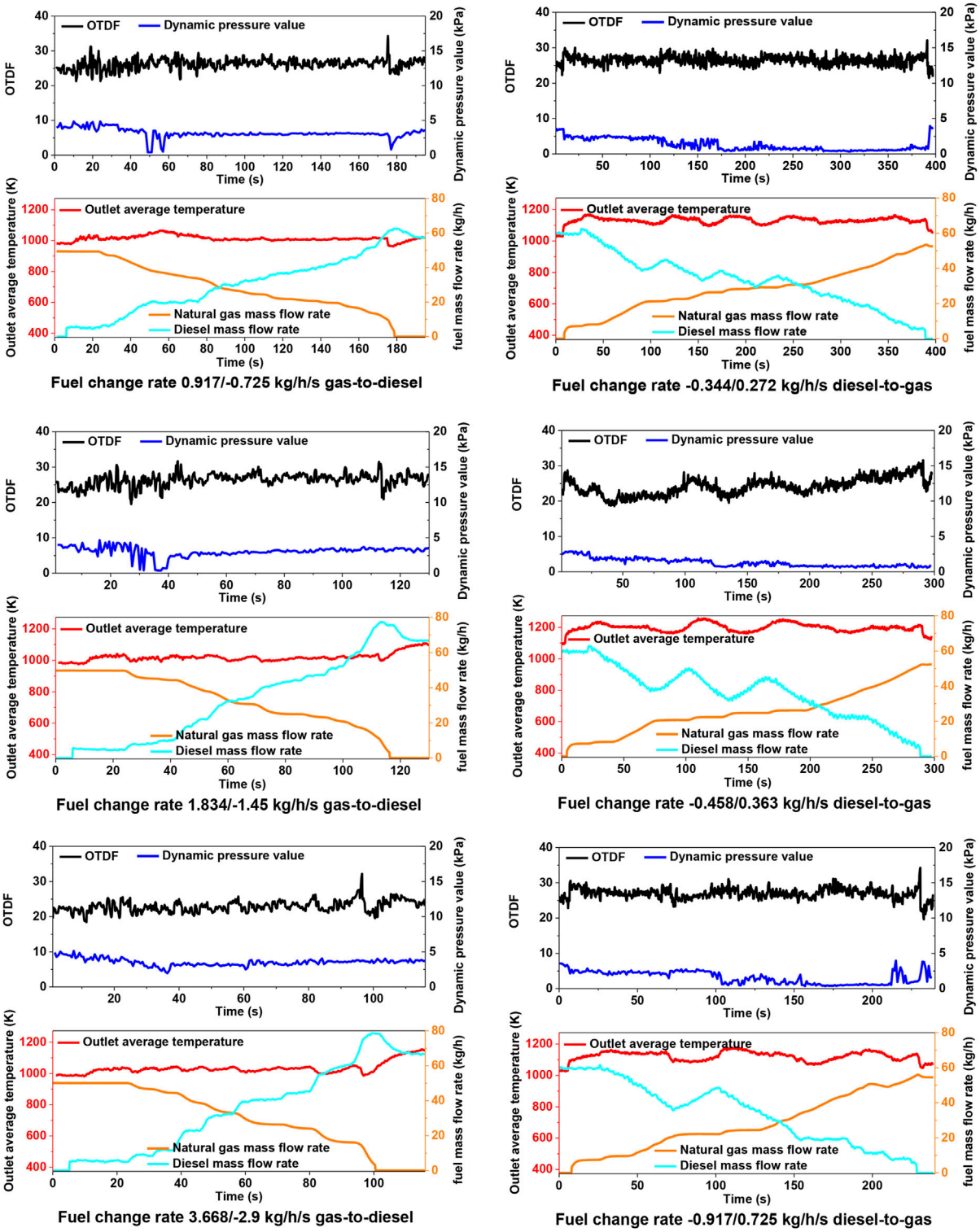

FIGURE 7 | Combustion chamber performance when fuel change rate changes.

TABLE 4 | Fuel compensation coefficient test program.

Test	Diesel change rate kg/h/s	Natural gas change rate kg/h/s	Fuel compensation kg/h/s
Test 1	+1.834	-1.45	0.1
Test 2	+1.834	-1.45	0.3
Test 3	+1.834	-1.45	0.5
Test 4	+1.834	-1.45	0.8
Test 5	-0.458	+0.363	0.1
Test 6	-0.458	+0.363	0.3
Test 7	-0.458	+0.363	0.5
Test 8	-0.458	+0.363	0.8

Outlet temperature fluctuation limit: ±10K.
Natural gas type: Natural gas I.

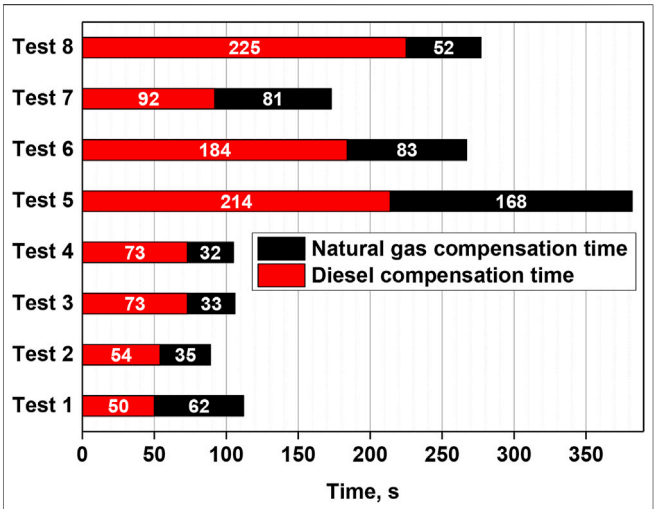

FIGURE 8 | Effects of different fuel compensation coefficient on switching time.

conditions may result in combustion chamber flameout or overtemperature.

To study the rule of fuel-switching and ensure safety, the fuel-switching test was modeled at 0.8Ne, and the inlet air temperature of the combustion chamber was set as the atmospheric ambient temperature. The air and fuel parameters used in the test can be seen in **Table 1**. In the test, to verify the influence of different natural gas calorific value on fuel-switching, N_2 with a volume fraction of 8% was injected into natural gas I and renamed natural gas II.

The fuel-switching test has a combination of multiple parameter changes, which can be seen in **Table 2**. To facilitate the comparative analysis of the fuel-switching time and the change of combustion chamber performance, the test method of changing one of the items and keeping the rest unchanged was adopted.

In the fuel-switching process, the fuel mass flow rate is set according to the average temperature at the exit of the combustion chamber to remain unchanged, that is, the calorific value of fuel input of the combustion chamber remains unchanged during the fuel switching process:

$$q_{mf-oil} H_{oil}^{T_0} = q_{mf-gas\,I} H_{Natural\,gas\,I}^{T_0} = q_{mf-gas\,II} H_{Natural\,gas\,II}^{T_0} \quad (1)$$

where q_{mf-oil} and q_{mf-gas} are the mass flow of diesel and natural gas into the combustion chamber, kg/h, and $H_{oil}^{T_0}$ and $H_{Natural\,gas}^{T_0}$ are the low calorific values of diesel and natural gas at 300K, kJ/kg. In the test, the calorific values of diesel, natural gas I, and natural gas II submitted for inspection are 42700 kJ/kg, 46092 kJ/kg, and 38562 kJ/kg. According to the above setting and data, we can calculate different fuel change rates under different theoretical switching time conditions as **Table 2**.

In **Table 2**, the rate of fuel change the amount of modulated fuel divided by the set-theoretical switching time at a fuel change rate of 0.8Ne. The fuel-switching progress adopts V-type steady-state regulation. The logical diagram is shown in **Figure 5**. The fuel compensation coefficient is also a kind of fuel change rate, which is mainly used to correct the fuel change rate when the combustion chamber exit temperature is not stable.

RESULTS AND DISCUSSION

Rate of Fuel Change

The fuel-switching test was carried out 6 times by changing the rate of fuel/natural gas change. Experiments 1–3 test the switch natural gas-to-diesel, and experiments 4–6 test the switch diesel-to-natural gas. The fuel-switching test scheme is shown in **Table 3**. During the switching process, the real switching time is shown in **Figure 6**; the variation of exit temperature, natural gas flow rate, diesel flow rate, dynamic pressure, and OTDF value can be seen in **Figure 7** during the test.

For the exit temperature of the combustion chamber, the larger fuel change rate will lead to the larger fluctuation range and lower frequency of the exit temperature. As for the OTDF value, it changes with the average temperature at the exit of the combustion chamber. When the temperature increases, the OTDF also increases.

The reason for this phenomenon is that during the fuel-switching process, the flame length in the combustion chamber fluctuates with the fuel amount due to the constant airflow and the unstable fuel amount. The higher internal combustion amount at local time points will inevitably lead to the deterioration of temperature distribution. For this type of combustion chamber, when the gas outlet temperature is increased by 10K, the increased range of OTDF is 1.45–1.93%.

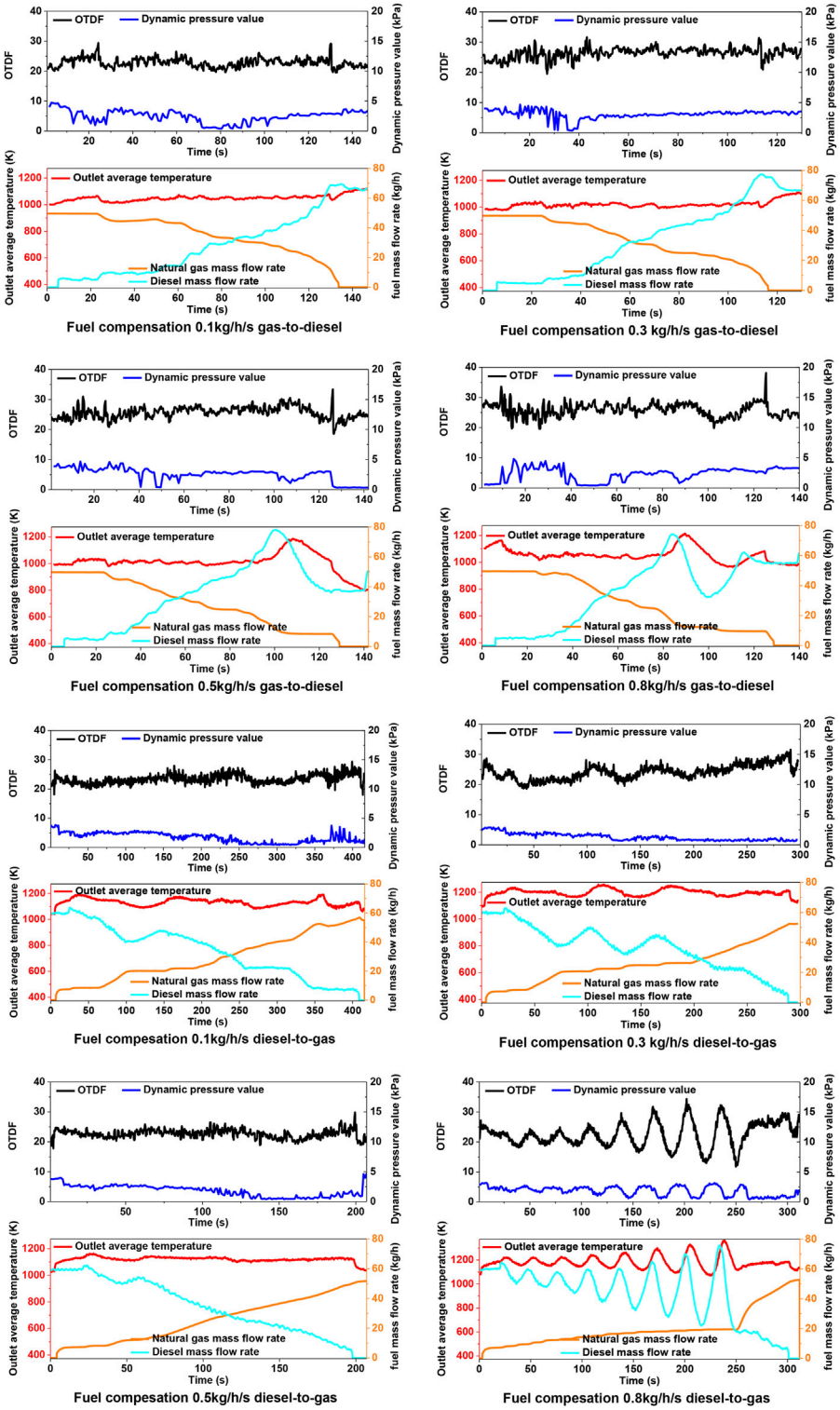

FIGURE 9 | Performance when fuel compensation coefficient changes.

TABLE 5 | Limit outlet temperature fluctuation program.

Test	Diesel change rate kg/h/s	Natural gas change rate kg/h/s	Outlet temperature fluctuation limit, K
Test 1	+1.834	-1.45	±5
Test 2	+1.834	-1.45	±10
Test 3	+1.834	-1.45	±20
Test 4	-0.458	+0.363	±5
Test 5	-0.458	+0.363	±10

Fuel compensation: 0.3 kg/h/s.
Natural gas type: Natural gas I.

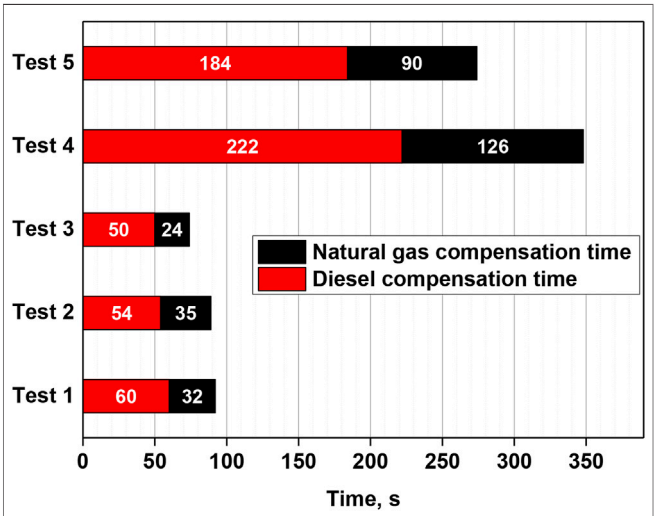

FIGURE 10 | Effects of different temperature fluctuation limitation on switching time.

For the combustion chamber pressure fluctuation, the switching process is not greater than the design value of 4 kPa; When diesel oil switch to natural gas, the pressure fluctuation value shows a slight upward trend in the early stage of fuel-switching, and gradually decreases in the later stage. In general, the pressure fluctuation measured at the main combustion hole of the combustion chamber has little relationship with the fuel change rate, and there is no obvious trend of change.

In order to keep the combustion chamber outlet temperature stable, it is necessary to make fuel compensation during fuel-switching. When diesel compensation is used in the switching process, the largely fuel quantity fluctuation causes the outlet temperature of the combustion chamber to fluctuate greatly. In addition, the diesel fuel compensation process takes longer time than the natural gas compensation process in the fuel-switching process; we also find that the fuel flow at the completion of the switching process is far greater than the design value. The reason is mainly due to the viscosity of diesel and its atomization evaporation process. The response time of the outlet temperature of the combustion chamber has a certain lag when using diesel compensation. It also led to a cyclical oscillation and, in the late switch, caused overshoot and extended the fuel-switching time. We can see that the performance is very obvious in the process of diesel switch to natural gas.

In terms of fuel-switching time, with the increase of fuel change rate, the switching time decreases, which is consistent with the theoretical analysis. However, the actual fuel-switching time of the 6 tests was much longer than the theoretical fuel-switching time, and the time of gas-to-diesel was much lower than that of diesel-to-gas. This reason was also related to the fuel used in fuel compensation, which was consistent with the above reasons.

Fuel Compensation

The fuel-switching test was carried out 8 times by changing different fuel compensation amount in the fuel-switching process. Experiments 1–4 test the switch natural gas-to-diesel, and experiments 5–8 test the switch diesel-to-natural gas. The fuel compensation test scheme is shown in **Table 4**. During the switching process, the influence of fuel compensation amount on switching time is shown in **Figure 8**; the variation of exit temperature, natural gas flow rate, diesel flow rate, dynamic pressure, and OTDF value can be seen in **Figure 9**.

The fuel compensation can also be considered as a kind of fuel change rate regulation in essence. Its difference is the regulation target and regulation range. The rate of fuel change reflects the range of fuel quantity change in the overall fuel-switching process, and the fuel compensation reflects the amplitude limit of fuel quantity change at local time points in the fuel-switching process. The experimental results show that the fuel compensation affects the temperature fluctuation at the outlet of the fuel combustion chamber and fuel-switching time.

We can see from the test data that there is an optimal fuel compensation amount corresponding to the shortest fuel switching time. The fuel-switching time is the shortest when the fuel compensation amount is 0.3 kg/h/s for gas-to-diesel. In the reverse fuel-switching progress, the value is 0.5 kg/h/s. The optimal value of the fuel compensation amount in different fuel-switching processes should be related to the setting of theoretical switching time or fuel change rate. From the test results, the smaller fuel change rate corresponds to a larger value of the optimal compensation coefficient.

At the same time, we can also see from the test results that the fuel-switching time decreases with the increase of fuel compensation amount when the fuel compensation amount is less than the optimal point, and the outlet temperature

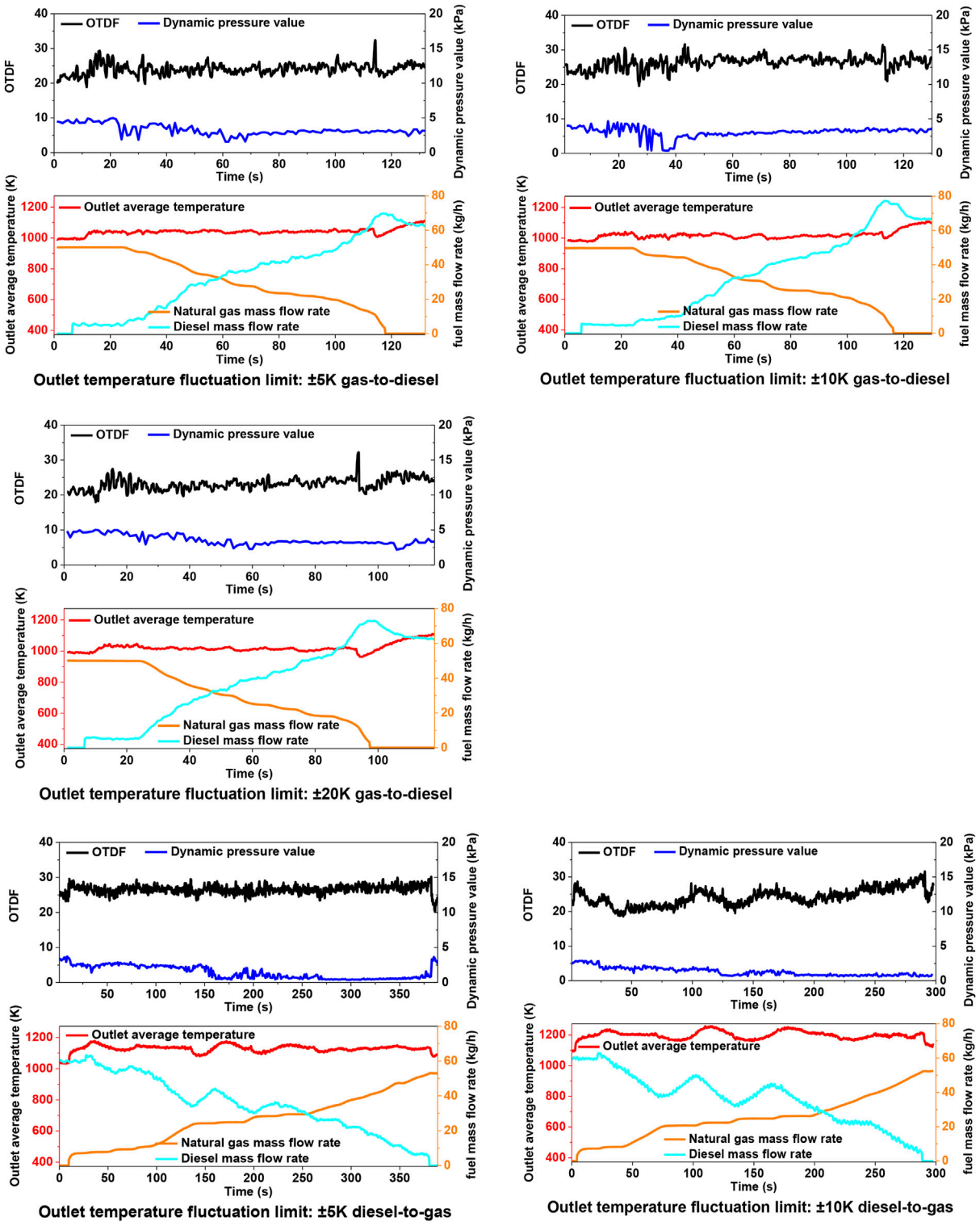

FIGURE 11 | Performance when temperature fluctuation limitation of outlet changes.

TABLE 6 | Fuel change matching test program.

Test	Diesel change rate kg/h/s	Natural gas change rate kg/h/s	Natural gas type
Test 1	+1.834	-1.45	Natural gas I
Test 2	+1.834	-1.45	Natural gas II
Test 3	-0.458	+0.363	Natural gas I
Test 4	-0.458	+0.363	Natural gas II

Fuel compensation:0.3 kg/h/s.
Outlet temperature fluctuation limit: ±10K

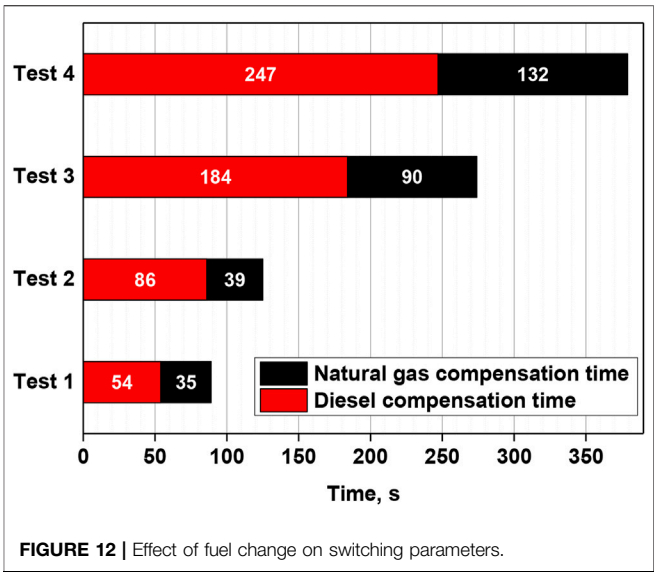

FIGURE 12 | Effect of fuel change on switching parameters.

stability is basically the same. However, when the fuel compensation amount is larger than or equal to the optimal point, the exit temperature of the combustion chamber fluctuates greatly, which is similar to the phenomenon and reasons when the fuel change rate is too large in the above section. When the combustion chamber uses diesel fuel for fuel compensation, the delay of outlet temperature response will still lead to the diesel's flow far beyond the theoretical value, and the restriction of outlet temperature will make the fuel flow adjust to another direction. The cross influence of the two factors will lead to the large fluctuations of the combustion chamber outlet temperature. It can be seen that the fuel compensation amount has a great correlation with the fuel change rate, and there is a more appropriate numerical range under different theoretical switching time.

Limit of Outlet Temperature Fluctuation

The fuel-switching test was carried out 5 times by changing different outlet temperature fluctuation limit in the fuel-switching process. Experiments 1–3 test the switch natural gas-to-diesel, and experiments 4–5 test the switch diesel-to-natural gas. The limit outlet temperature fluctuation test scheme is shown in **Table 5**. During the switching process, the influence of outlet temperature fluctuation limit on switching time is shown in **Figure 10**; the variation of exit temperature, natural gas flow rate, diesel flow rate, dynamic pressure, and OTDF value can be seen in **Figure 11**.

The limit range of combustion chamber exit temperature fluctuation affects the completion time of fuel-switching and the actual fluctuation of combustion chamber exit temperature. When the limit range of combustion chamber outlet temperature fluctuation is narrower, the compensation times will be increased, so that the fuel-switching time will be prolonged, but the volatility of combustion chamber outlet temperature will be more stable.

For dual-fuel combustion chamber, the limit range of outlet temperature fluctuation in the test essentially reflects the variation of gas turbine power. This variation is determined by the actual engineering load requirements. It can be seen that, in order to reduce fuel-switching time, the limit range of temperature fluctuation or the variation range of gas turbine power should be as large as possible within the permitted value.

Fuel Calorific Value Change Matching

The fuel-switching test was carried out 4 times by changing different natural gas type in the fuel-switching process. Experiments 1–2 test the switch natural gas-to-diesel, and experiments 3–4 test the switch diesel-to-natural gas. The different natural gas type test scheme is shown in **Table 6**. During the switching process, the influence of natural gas type on switching time is shown in **Figure 12**; the variation of exit temperature, natural gas flow rate, diesel flow rate, dynamic pressure, and OTDF value can be seen in **Figure 13**.

The test results show that the fuel-switching performance when using natural gas I are better than natural gas II whatever gas-to-diesel or diesel-to-gas fuel-switching process. The reason is that the calorific value of natural gas I is closer to diesel fuel than natural gas II. Better fuel matching (referred to the calorific value of liquid fuel and gas fuel close to each other) is more favorable for dual-fuel combustion chamber switching.

Due to the limitation of the test conditions, more natural gas fuels with different calorific values and different components could not be compared, but it is easy to infer that the specified fuel-switching time must limit the range of fuel calorific value for dual-fuel combustors. Due to the difference of calorific value and components of different fuels, the practical use situation must be considered in the design of dual-fuel combustion chamber.

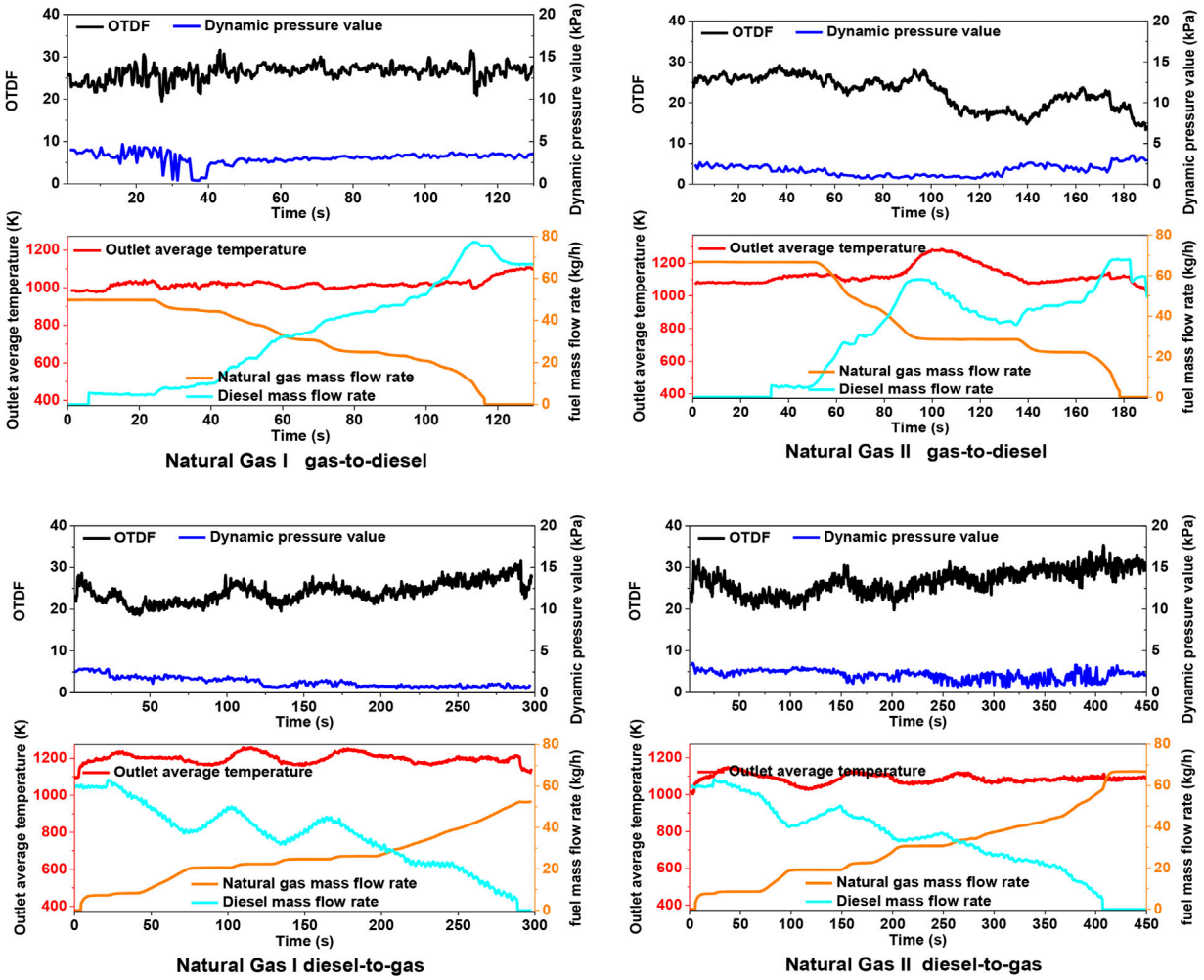

FIGURE 13 | Combustion chamber performance when fuel changes.

CONCLUSION

The fuel-switching performance test of the dual-fuel combustion chamber was carried out on the combustion test facility. The main work and conclusions are as follows:

1) In the fuel-switching test process of the dual fuel combustion chamber, the flame length or OTDF fluctuates just because the unstable fuel quantity and the constant airflow. The instantaneous mismatch between fuel and air flow is the main reason for the fluctuation of outlet temperature.
2) The amount of fuel compensation has a great correlation with the rate of fuel change, and there is a suitable range under different theoretical switching times. For this type of combustion chamber, the optimal fuel compensation is 0.3 kg/h/s when natural gas switches to diesel, and 0.5 kg/h/s when diesel switches to natural gas.
3) The narrower the limit range of combustion chamber outlet temperature fluctuation, the more compensation times will result in the longer fuel-switching time, but the combustion chamber outlet temperature will be more stable.
4) Fuel calorific value difference affects fuel switching time. Lower calorific value difference between gas fuel and liquid fuel will reduce fuel switching time.

DATA AVAILABILITY STATEMENT

The raw data supporting the conclusions of this article will be made available by the authors, without undue reservation.

AUTHOR CONTRIBUTIONS

LF and YG: data curation, writing original draft preparation, and experiment operating. RJ-h and LX: writing, reviewing and editing, validation. LM-j and LY-j: supervision and funding acquisition.

REFERENCES

Agwu, O., and Valera-Medina, A. (2020). Diesel/syngas Co-combustion in a Swirl-Stabilised Gas Turbine Combustor. *Int. J. Thermofluids* 3-4, 100026. doi:10.1016/j.ijft.2020.100026

Al-Shaikhly, A. F., Mina, T. I., and Neergaard, M. O. (1994). "Development of a Dual Fuel LBTU Gas/Diesel Burning Combustion System for a 4.2 MW Gas Turbine," in ASME 1994 International Gas Turbine and Aeroengine Congress and Exposition (New York, NY: American Society of Mechanical Engineers). doi:10.1115/94-gt-438

Chong, C. T., Chiong, M.-C., Ng, J.-H., Tran, M.-V., Valera-Medina, A., Józsa, V., et al. (2020). Dual-fuel Operation of Biodiesel and Natural Gas in a Model Gas Turbine Combustor. *Energy Fuels* 34 (3), 3788–3796. doi:10.1021/acs.energyfuels.9b04371

Erazo, J. A., Jr, Parthasarathy, R., and Gollahalli, S. (2010). Atomization and Combustion of Canola Methyl Ester Biofuel spray. *Fuel* 89 (12), 3735–3741. doi:10.1016/j.fuel.2010.07.022

Fox, T. G., and Schlein, B. C. (1990). Full Annular Rig Development of the FT8 Gas Turbine Combustor. *J. Eng. Gas Turbines Power* 114 (1), 27–32. doi:10.1115/90-gt-029

Hashimoto, N., Nishida, H., and Ozawa, Y. (2014). Fundamental Combustion Characteristics of Jatropha Oil as Alternative Fuel for Gas Turbines. *Fuel* 126. doi:10.1016/j.fuel.2014.02.057

Jiang, L., and Agrawal, A. K. (2014). Combustion of Straight Glycerol With/without Methane Using a Fuel-Flexible, Low-Emissions Burner. *Fuel* 136, 177–184. doi:10.1016/j.fuel.2014.07.027

Korakianitis, T., Namasivayam, A. M., and Crookes, R. J. (2011). Diesel and Rapeseed Methyl Ester (RME) Pilot Fuels for Hydrogen and Natural Gas Dual-Fuel Combustion in Compression-Ignition Engines. *Fuel* 90 (7), 2384–2395. doi:10.1016/j.fuel.2011.03.005

Lee, M. C., and Yoon, Y. (2012). Development of a Gas Turbine Fuel Nozzle for DME and a Design Method Thereof. *Fuel* 102, 823–830. doi:10.1016/j.fuel.2012.05.017

Li, S., Zhang, S., Zhou, H., and Ren, Z. (2019). Analysis of Air-Staged Combustion of NH3/CH4 Mixture with Low NOx Emission at Gas Turbine Conditions in Model Combustors. *Fuel* 237, 50–59. doi:10.1016/j.fuel.2018.09.131

Lindman, O., Andersson, M., Bonaldo, A., Larsson, A., Janczewski, J., and Persson, M. (2017). "SGT-750 Fuel Flexibility: Engine and Rig Tests," in ASME Turbo Expo 2017: Turbomachinery Technical Conference and Exposition. American Society of Mechanical Engineers (Charlotte, NC: American Society of Mechanical Engineers), V04ATA031–V04AT04A. doi:10.1115/gt2017-63412

Lindman, O., Andersson, M., Persson, M., and Munktell, E. (2014). "Development of a Liquid Fuel Combustion System for SGT-750," in ASME Turbo Expo 2014: Turbine Technical Conference and Exposition (Düsseldorf, Germany: American Society of Mechanical Engineers), V04ATA022. doi:10.1115/gt2014-25380

Liu, K., and Sanderson, V. (2013). The Influence of Changes in Fuel Calorific Value to Combustion Performance for Siemens SGT-300 Dry Low Emission Combustion System. *Fuel* 103 (264), 239–246. doi:10.1016/j.fuel.2012.07.068

Lounici, M. S., Loubar, K., Tarabet, L., Balistrou, M., Niculescu, D.-C., and Tazerout, M. (2014). Towards Improvement of Natural Gas-Diesel Dual Fuel Mode: An Experimental Investigation on Performance and Exhaust Emissions. *Energy* 64, 200–211. doi:10.1016/j.energy.2013.10.091

Mordaunt, C. J., and Pierce, W. C. (2014). Design and Preliminary Results of an Atmospheric-Pressure Model Gas Turbine Combustor Utilizing Varying CO2 Doping Concentration in CH4 to Emulate Biogas Combustion. *Fuel* 124 (15), 258–268. doi:10.1016/j.fuel.2014.01.097

Nascimento, M. A. R., Lora, E. S., Corrêa, P. S. P., Andrade, R. V., Rendon, M. A., Venturini, O. J., et al. (2008). Biodiesel Fuel in Diesel Micro-turbine Engines: Modelling and Experimental Evaluation. *Energy* 33 (2), 233–240. doi:10.1016/j.energy.2007.07.014

Røke, P. E., Hustad, J. E., Rø∕kke, N. A., and Svendsgaard, O. B. (2003). "Technology Update on Gas Turbine Dual Fuel, Dry Low Emission Combustion Systems," in ASME Turbo Expo 2003, collocated with the 2003 International Joint Power Generation Conference (Atlanta, GA: American Society of Mechanical Engineers), 97–107.

Sun, L., Liu, Y., Zeng, K., Yang, R., and Hang, Z. (2015). Combustion Performance and Stability of a Dual-Fuel Diesel-Natural-Gas Engine. *Proc. Inst. Mech. Eng. D: J. Automobile Eng.* 229 (2), 235–246. doi:10.1177/0954407014537814

Xiao, H., Howard, M. S., Valera-Medina, A., Dooley, S., and Bowen, P. (2017). Reduced Chemical Mechanisms for Ammonia/Methane Co-firing for Gas Turbine Applications. *Energ. Proced.* 105, 1483–1488. doi:10.1016/j.egypro.2017.03.441

Yang, B., Wei, X., Xi, C., Liu, Y., Zeng, K., and Lai, M.-C. (2014). Experimental Study of the Effects of Natural Gas Injection Timing on the Combustion Performance and Emissions of a Turbocharged Common Rail Dual-Fuel Engine. *Energ. Convers. Manag.* 87, 297–304. doi:10.1016/j.enconman.2014.07.030

Zheng, H., Mu, Y., and He, H. (2010). "Numerical Simulation of Combustion Flows in Dual-Fuel Combustor," in Power and Energy Engineering Conference (APPEEC), 2010 Asia-Pacific. IEEE (Chengdu, China: IEEE), 1–6. doi:10.1109/appeec.2010.5449465

Conflict of Interest: The authors declare that the research was conducted in the absence of any commercial or financial relationships that could be construed as a potential conflict of interest.

frontiers in Energy Research

ORIGINAL RESEARCH
published: 02 March 2022
doi: 10.3389/fenrg.2022.807902

Combustion Characteristics of Methane-Air Mixtures in Millimeter-Scale Systems With a Cavity Structure: An Experimental and Numerical Study

Junjie Chen and Tengfei Li*

Department of Energy and Power Engineering, School of Mechanical and Power Engineering, Henan Polytechnic University, Jiaozuo, China

OPEN ACCESS

Edited by:
Lei Luo,
Harbin Institute of Technology, China

Reviewed by:
Liqiao Jiang,
Guangzhou Institute of Energy Conversion (CAS), China
Wei Du,
Harbin Institute of Technology, China

****Correspondence:***
Junjie Chen
comcjj@163.com
cjj@hpu.edu.cn

Specialty section:
This article was submitted to Advanced Clean Fuel Technologies, a section of the journal Frontiers in Energy Research

Received: *02 November 2021*
Accepted: *21 January 2022*
Published: *02 March 2022*

Citation:
Chen J and Li T (2022) Combustion Characteristics of Methane-Air Mixtures in Millimeter-Scale Systems With a Cavity Structure: An Experimental and Numerical Study. Front. Energy Res. 10:807902. doi: 10.3389/fenrg.2022.807902

The management of internal features of a cavity structure for channels offers the possibility of inherently effective operation within the flammable limits of a combustible fluid stream while preserving high stability for the flame. However, the precise mechanism by which the cavity method generally provides increased flame stability for millimeter-scale systems remains unclear. The combustion characteristics of methane-air mixtures in millimeter-scale systems with a cavity structure were investigated experimentally and numerically to gain a greater understanding of the mechanisms of flame stabilization and to gain new insights into the characteristics of combustion within spaces with extremely small dimensions. The quenching distance was determined both experimentally and numerically. Stable temperature profiles were obtained from thermographic measurements using infrared radiation. The measurements were compared with the model predictions. Subsequent model calculations demonstrate the effects of variations in wall thermal conductivity, heat losses, flow velocity, equivalence ratio, and channel dimensions. Design recommendations were made. The experimental and numerical results indicated that the quenching distance is slightly larger than commonly believed. The cavity structure has little effect on the quenching distance, but can improve the efficiency and performance of the systems considerably. The cavity structure can effectively extend flammability limits, with an increase of about 18% in the operating range defined by the equivalence ratio of the mixture. The length scale of the systems plays a vital role in stabilizing the flame. The thermal conductivity of the solid material is vital in determining the efficiency and performance of the systems. The design with anisotropic thermal conductivity has significant performance advantages. The flow velocity of the fluid and the equivalence ratio of the mixture are important factors affecting the efficiency and performance of the systems.

Keywords: micro-combustion, combustor design, combustion characteristics, methane flames, flame stability, computational fluid dynamics

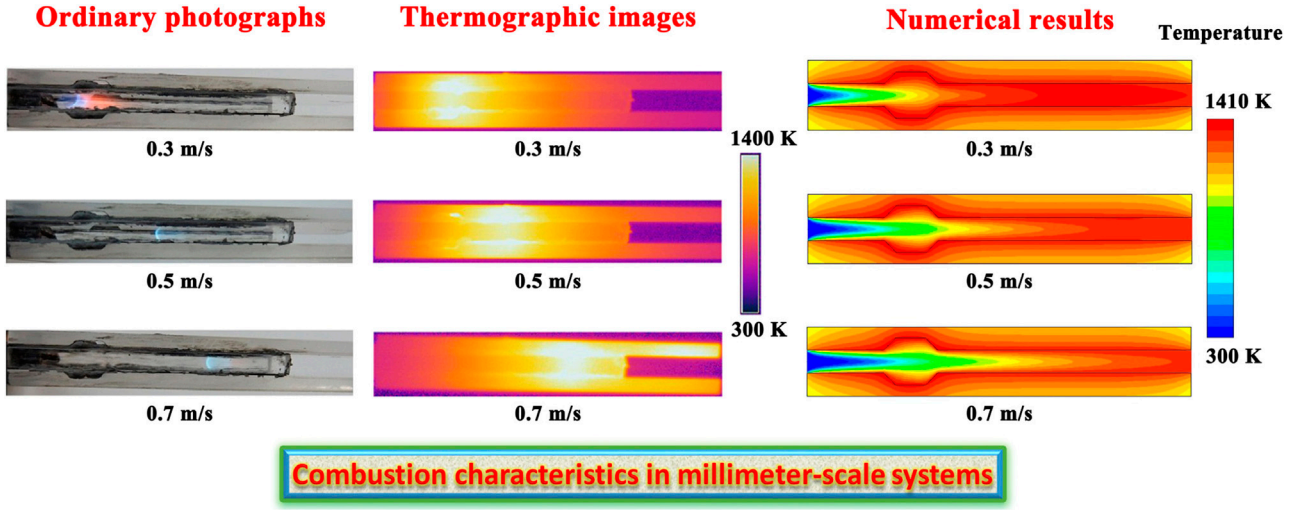

GRAPHICAL ABSTRACT |

HIGHLIGHTS

- The quenching distance is slightly larger than commonly believed.
- The cavity structure has little effect on the quenching distance.
- The length scale of the systems plays a vital role in stabilizing the flame.
- The design with anisotropic thermal conductivity has great performance advantages.
- Important factors affecting performance are determined for the systems.

INTRODUCTION

The trend toward the miniaturization of electromechanical devices and the increased demand for micro-power generation with long-life, low-weight devices have resulted in the development of the field of micro-scale combustion. The concept behind this field is that a miniaturized power-generating system will lead to reduced weight and increased lifetime of an electromechanical device that currently requires batteries for power (Dunn-Rankin et al., 2005; Walther and Ahn, 2011). In addition to the interest in miniaturization, the field is also driven by the potential fabrication of electromechanical devices using micro-system technology or rapid prototyping techniques, with their favorable characteristics for low cost and mass production (Dunn-Rankin et al., 2005; Walther and Ahn, 2011). The field of micro-power generation is still in the feasibility stage. Currently, there is consensus that combustion within a micro-scale space is possible with proper chemical and thermal management (Jiaqiang et al., 2021; Jiaqiang et al., 2022). As the length scale of the devices is reduced, the surface-to-volume ratio increases, which eventually leads to heat loss effects becoming significant at the boundaries or surfaces of the devices (Jiaqiang et al., 2021; Jiaqiang et al., 2022). Significant heat loss effects may become problematic due to flame quenching. Consequently, thermal management becomes essential in order to improve flame stabilization by reducing heat losses.

Flame stabilization is a common problem in combustion systems (Jeong et al., 2017; Grib et al., 2020). A flame will propagate through a fuel-air mixture only when certain conditions prevail. Initially, a minimum percentage of fuel must be present within the fuel-air mixture to make the fuel-air mixture flammable, i.e., the lean flammability limit (Mendiburu et al., 2017; Wang et al., 2021). Similarly, a maximum percentage of fuel must be present within the fuel-air mixture wherein greater than this percentage will prevent burning, i.e., the rich flammability limit (Mendiburu et al., 2017; Wang et al., 2021). The flammability range of a fuel-air mixture is that range of the percentage of fuel within the fuel-air mixture between the lean flammability limit and the rich flammability limit.

One reason that flame stabilization is required in combustion systems is to prevent the flame front from moving upstream from the combustion zone toward the source of fuel, i.e., a flashback (Jeong et al., 2017). During a flashback event, the heat of combustion moves upstream and may damage numerous structures within the fuel and air mixing region of the combustor (Hatem et al., 2018; Zangeneh and Alipoor, 2021). Flashback may occur due to auto-ignition of a fuel-air mixture caused by a residence time of the fuel-air mixture in a region upstream of the combustion zone that exceeds the auto-ignition delay time of that fuel-air mixture at the temperature and pressure of that region.

Flame stabilization also is dependent upon speed of the fuel-air mixture entering the combustion zone where propagation of the flame is desired (Wan and Zhao, 2020a; Choi et al., 2020). A sufficiently low velocity must be retained in the region where the

flame is desired in order to sustain the flame. As is known, a region of low velocity in which a flame can be sustained can be achieved by causing recirculation of a portion of the fuel-air mixture already burned thereby providing a source of ignition to the fuel-air mixture entering the combustion zone (El-Asrag and Menon, 2007; Fugger et al., 2020). However, the fuel-air mixture flow pattern, including any recirculation, is critical to achieving flame stability. Improvements in flame stability would be desirable and may be especially advantageous in applications in which reduced emissions are needed (Cam et al., 2017; Pashchenko, 2020). Various attempts have been made to achieve such improvements. More specifically, various methods have been tried either commercially or experimentally (Bychkov and Liberman, 2000) and many different structures have already been designed (Shanbhogue et al., 2009). The typical method includes the use of recirculation regions to provide a continuous ignition source by mixing the hot combustion products with the cold incoming fuel and air mixture. Structural devices have been commonly employed to establish a recirculation region for improving the stability of the flame during ignition and operation, such as swirlers (Yilmaz et al., 2020), bluff bodies (Jeong et al., 2017; Fugger et al., 2020), cavities (Yilmaz et al., 2017), and rearward facing steps (Yilmaz et al., 2017). The challenge, however, is presented with respect to the structure of a flame stabilizer that ensures high combustion performance, including improved flame stability and acceptable emissions (Khateeb et al., 2020; Khateeb et al., 2021) while reducing capital and operating costs. Consequently, it would be desirable to provide a flame stabilizer for a combustion system, specifically including a combustion chamber structure that enables the system to maintain high stability of the flame under certain conditions while reducing the emission of undesirable products of combustion such as nitrogen oxides, carbon monoxide, and partially oxidized hydrocarbons.

In conventional lean-premixed combustion, a swirler would typically be used to inject the fuel-lean mixture into the combustor (Broda et al., 1998; Kim and Santavicca, 2013). When a swirler is used, the flame is anchored because the swirler induces recirculation of hot combustion products within the combustor (Panda et al., 2019; Han et al., 2020). The recirculating, hot combustion products continuously contact and ignite the incoming fuel-air mixture, thus anchoring the flame in the vicinity of the recirculation zone. An additional effect of the swirler is to direct the incoming fuel-air mixture outwards toward the walls of the combustor, thus rapidly diffusing the mixture into the combustor, making effective use of the combustor's volume (Broda et al., 1998; Kim and Santavicca, 2013). As also is known, adding a swirl component to the flow pattern is beneficial, either axial or radial swirl. The designation of a swirl number for a particular type of swirler is known (Kim and Santavicca, 2013): a swirl number less than around 0.4 indicates a weak swirl and no recirculation is obtained; a swirl number between 0.4 and 0.6 indicates a moderate swirl and no recirculation is obtained but the streamlines diverge; and a swirl number greater than 0.6 indicates a strong swirl and recirculation is obtained.

Another method known for causing recirculation is the placement of a bluff body in the flow path of the fuel-air mixture within the combustion zone (Michaels and Ghoniem, 2018; Morales et al., 2019). A bluff body typically defines a leading edge and a trailing edge, and separation of a mixture passing over the bluff body occurs at the trailing edge of the bluff body thereby forming a wake downstream of the trailing edge. The velocity of the mixture in the wake region is much lower than the velocity of the mixture flowing in the main stream around the bluff body thereby supporting recirculation.

The use of a swirler, a bluff body, or a combination of both to cause recirculation is typical in conventional combustion systems (Tong et al., 2018; Gatti et al., 2019). In a micro-combustion system, however, the use of a swirler is undesirable since all fuel and air would typically be premixed upstream of the combustion system and the combustion reaction takes place in the system with typical lateral dimensions below 1 mm (Ju and Maruta, 2011; Kaisare and Vlachos, 2012). On the other hand, one problem associated with using a bluff body as a flame holder for a micro-combustion system is that the flame is anchored to the flame holder and the excessive heat is life-limiting.

One solution that does not require a swirler or a bluff body is the use of cavities. This approach will become increasingly attractive. A number of different suggestions have been made for facilitating a cavity structure in a micro-combustion system (Wan et al., 2015; Fan et al., 2018; Linhong Li et al., 2019; Zhang et al., 2020a; Zhang et al., 2020b; Xu et al., 2021). The inside surface of a micro-combustion system has a plurality of cavities which are spaced apart from one another. Strong combustion can be initiated in the cavities, and the cavity structure can provide for a more compact primary reaction region and for stable flame holding (Wan et al., 2015; Fan et al., 2018). The cavity structure can also cause an increase in residence time for a portion of the mixture, thereby avoiding instability of the flame. Additionally, the utilization of cavities can initiate recirculation of the fuel and air mixture while promoting micro-scale vortex breakdown and enhancing heat and mass transfer (Wan et al., 2015; Fan et al., 2018; Linhong Li et al., 2019; Zhang et al., 2020a; Zhang et al., 2020b; Xu et al., 2021), therefore making the combustion process more stable. More particularly, this method generally comprises a plurality of cavities arranged on the inside surface of a micro-combustion system, thereby providing increased flame stability for the downstream combustion of the premixed fuel and air stream. A further feature provided by the cavity structure is that hot gas and chemically active species can be more easily transferred into the unreacted inlet gas stream for improved performance. More specifically, the free radicals and heat produced by the reaction process can be transported back upstream in the recirculation region to mix with and initiate combustion of the un-reacted fuel and air mixture. The design, however, is quite complex, and the optimization may account for a plurality of factors including the thermal conductivity of the wall material (Wan et al., 2015), the chemically inert gaseous species (Fan et al., 2018), the shape and configuration of the cavity (Linhong Li et al., 2019), the channel structure of the system (Zhang et al., 2020a), and the synergistic effect of cavities and bluff bodies (Zhang et al., 2020b; Xu et al., 2021). For instance,

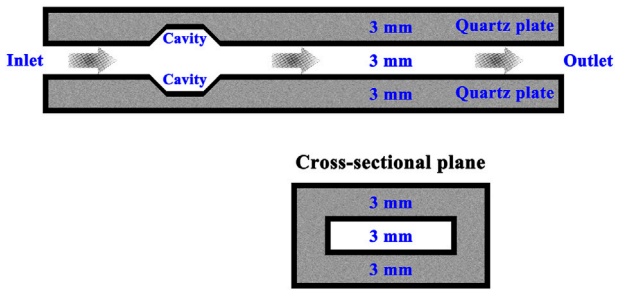

FIGURE 1 | Schematic representation of the system comprising two parallel fused-quartz plates with intersecting trapezoidal cavities. The system is configured for operation with methane.

high thermal conductivity materials confer advantage in terms of improved heat transfer properties, but the cavity structure does not necessarily offer unique performance advantages (Wan et al., 2015). The shape and configuration of the cavities are critical to the function and effectiveness of the structure (Linhong Li et al., 2019). The performance of the system may be largely determined by the structure of the channel, such as an axisymmetric bluff body situated closely behind or in front of a cavity (Zhang et al., 2020a; Xu et al., 2021). For example, the hydrodynamics of the system may be significantly altered by the coupling of cavities with bluff bodies (Zhang et al., 2020a), and bluff bodies can beneficially affect the hydrodynamics involving cavities for use in association with the system (Zhang et al., 2020a; Xu et al., 2021), resulting in significantly greater stability of the flame.

Flame stabilization criteria are even more important when the system operates under small-scale conditions (Wan and Zhao, 2020b; Yakovenko and Kiverin, 2021). It would be especially desirable for combustion systems operating under such conditions to have flame stabilizers that would be highly resistant to external flow field dynamics and perturbations. Under small-scale conditions, efficient methods have been developed for reducing combustion instability, such as a spiral heat exchanger structure (Fan et al., 2017), a counter-flow heat exchanger structure (Zuo et al., 2018; Yan et al., 2019), oxygen enriched air (Qingqing Li et al., 2019), a porous medium for use in thermal recirculation (Yilmaz, 2019), a flame holder design (Wan and Zhao, 2020c), and especially a cavity structure (Wan et al., 2015; Fan et al., 2018). Cavities present unique advantages of the improvement in flame stability. The cavity structure may be advantageously employed for the purpose of miniaturization. More specifically, this approach is particularly advantageous for promoting a stable flame in a micro-combustion system (Ju and Maruta, 2011; Kaisare and Vlachos, 2012). Such a cavity can obstruct a flow path to create a recirculation zone for flame stability (Wan et al., 2015; Fan et al., 2018). This in turn causes an increase in residence time for a portion of the fuel-air mixture. A cavity of a particular configuration provides flame holding and initiates recirculation of the fuel and air mixture in a downstream combustion zone, thereby avoiding any issue from flame stability events as much as possible previously described in the literature (Fan et al., 2017; Zuo et al., 2018; Qingqing Li et al., 2019; Yan et al., 2019; Yilmaz, 2019; Wan and Zhao, 2020c), such as flame quenching (Qingqing Li et al., 2019; Yan et al., 2019) and blowout (Fan et al., 2017; Qingqing Li et al., 2019; Yan et al., 2019; Wan and Zhao, 2020c). In this manner, it is possible to maintain the stability of the flame in a micro-combustion system at a higher level than otherwise obtainable, and to obtain higher performance in operation.

Despite extensive efforts over many years, there remains a need for combustion methods that have high performance and stability at various conditions of operations in millimeter-scale systems with a cavity structure. It is essential to maintain combustion characteristics in such a manner that facilitates flame holding in a reliable manner, and minimizes heat loss while maximizing system efficiency. The flame could optimally be as robust as possible in an effort to maximize the efficiency and performance of the systems (Gupta et al., 2020; Abdallah et al., 2021). A fundamental understanding of the stabilization mechanisms of a flame within very small spaces by the cavity method is of both fundamental and practical significance. However, the precise mechanism by which the cavity method generally provides increased flame stability for millimeter-scale systems remains unclear and warrants further study. While high stability of the flames within the systems is desirable, the efficiency and performance can depend on such factors as the overall design of the system, and the potential role of cavity structure in the stabilization mechanism of the flames is poorly understood.

This study relates to the essential characteristics of combustion in millimeter-scale systems with a cavity structure. The quenching distance was determined both experimentally and numerically, and stable temperature profiles were obtained from thermographic measurements. A computational fluid dynamics model was developed to describe the reactive flow. The model combined a detailed chemical kinetic reaction mechanism and a steady treatment of the fluid mechanics. Numerical simulations were conducted to gain insights into system performance such as flames, temperatures, species concentrations, and reaction rates. Methods of applying a cavity structure to channel walls were developed, which may be utilized with presently existing designs of micro-combustion systems. The factors affecting flame stability and combustion characteristics are determined for the systems. The objective of this study is to investigate the characteristics of combustion in millimeter-scale systems with a cavity structure so as to better understand the stabilization mechanisms of a flame within spaces with extremely small dimensions. Particular focus is placed on determining essential factors for design considerations of millimeter-scale systems with improved flame stability and combustion characteristics, and investigating the potential role of cavity structure in the stabilization mechanism of the flames in order to operate the systems more efficiently.

EXPERIMENTAL METHODS

The system configured to combust methane is illustrated schematically in **Figure 1**. The system comprises two parallel

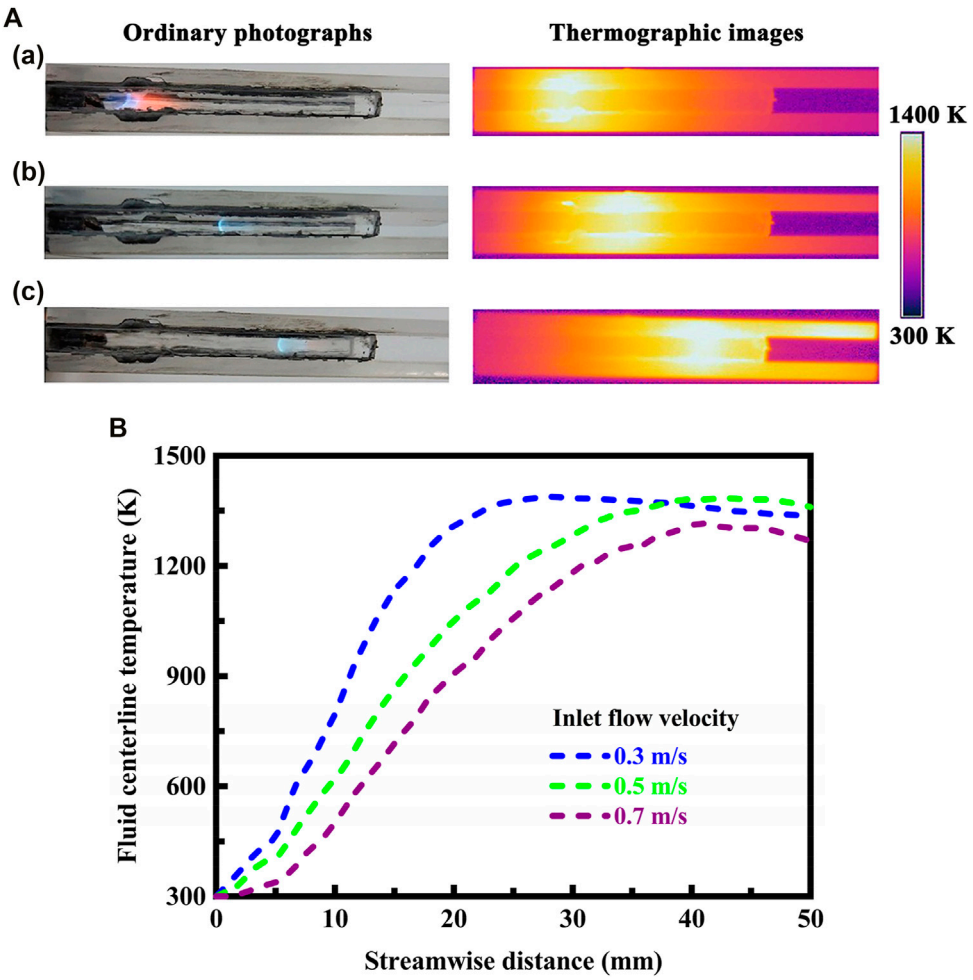

FIGURE 2 | (A) Optical and thermographic images showing laminar premixed methane flames and temperature variation in the system under different flow velocity conditions. The flow velocity of the fluid at the flow inlet is given as follows: (a) 0.3 m/s, (b) 0.5 m/s, and (c) 0.7 m/s. A thermographic camera is used to detect infrared radiation in a way similar to the way an ordinary camera detects visible light. The system is designed in stoichiometric operation; **(B)** Stable fluid centerline temperature profiles determined from thermographic measurements using infrared radiation. The system is designed in stoichiometric operation.

fused-quartz plates that are 50.0 mm in length, 13.0 mm in width, and 3.0 mm in thickness. The thermal conductivity of the plate material is 1.4 W/(m·K), since fused-quartz is a form of silica, also known as silicon dioxide. A flow channel is formed between the two parallel plates. The millimeter-scale channel has a minimum dimension of 5.0 mm or less, and a length that is, far greater than the minimum dimension. The channel can have any length unless restricted by design requirements. The spacing distance between the two parallel plates is 3.0 mm, which defines the characteristic length of the system. This value is chosen primarily because the spacing distance is slightly greater than the critical distance between the two parallel plates through which the methane flame will not propagate (Jarosiński, 1983; Jarosinski, 1986). This critical dimension can be defined as the quenching distance. In practice, the quenching distance is dependent on many factors, for example, the thermal characteristics of the surrounding material, the composition of the fuel stream, and the shape of the channel (Jarosiński, 1983; Jarosinski, 1986). The distance between the two parallel plates varies from 2.0 to 5.0 mm in order to accurately determine the quenching distance for the system at the given reference conditions.

Two trapezoidal cavities are provided in the flow path, as depicted in **Figure 1**, and the flow is subjected to a sudden expansion in the flow channel to induce disturbances in the flow. The cavities are 1.5 mm in height, 4.0 mm in short base length, and 7.0 mm in long base length, with a distance of 10.0 mm from the flow inlet. In addition, the cavities are designed with an angle of 135° relative to the localized horizontal plates at the points of intersection. The cavities have a rectangular cross-section at any selected station along the flow path, and can be adjusted in position with respect to the flow inlet. In order for flame holding to occur, methane and air must be premixed and provided a low velocity region to reside. Therefore, a low flow velocity of the fluid is used at the flow inlet. In most cases, the flow

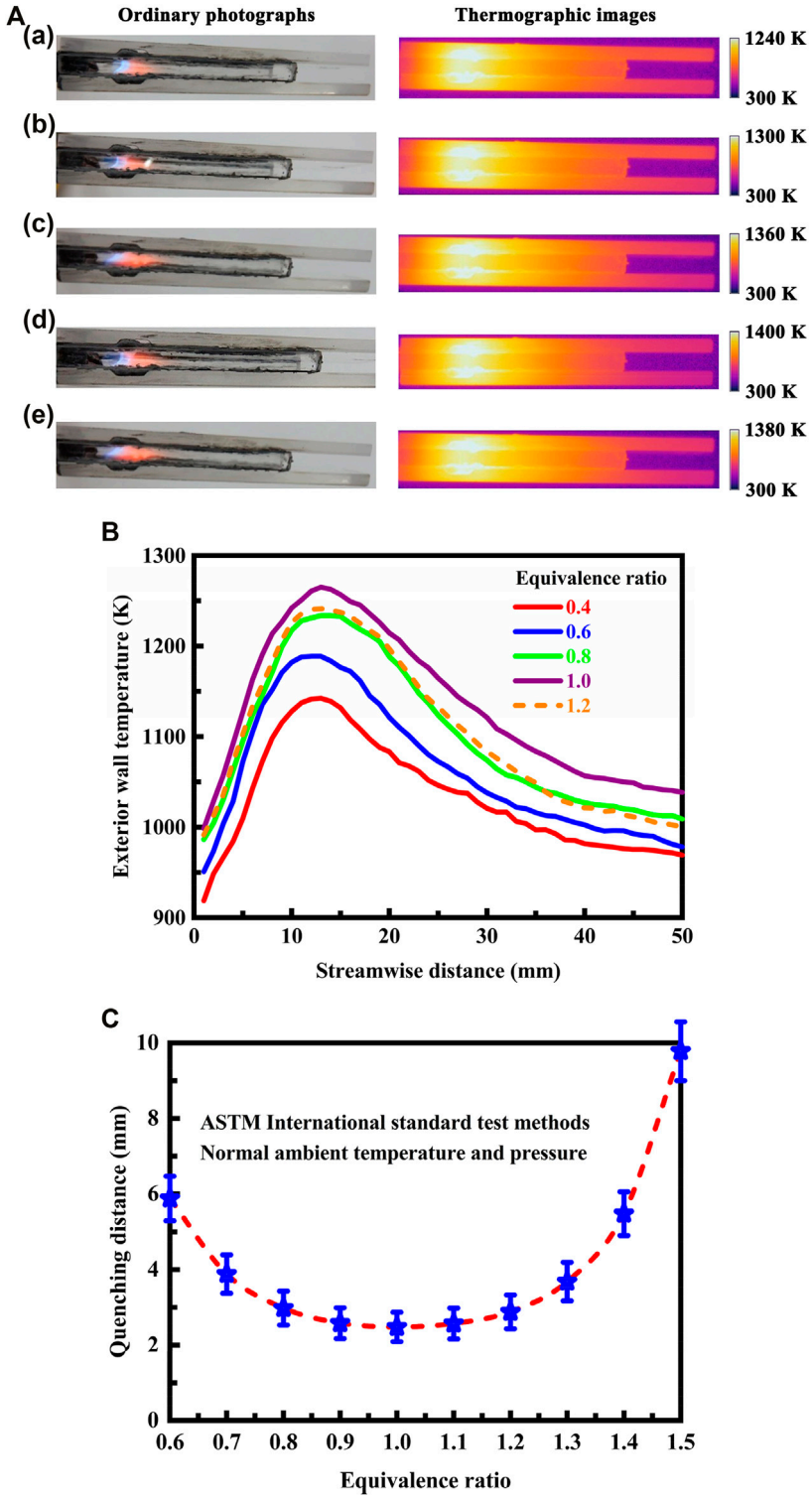

FIGURE 3 | (A) Optical and thermographic images showing laminar premixed methane flames and temperature variation in the system under different equivalent ratio conditions. The equivalent ratio of the mixture at the flow inlet is given as follows: (a) 0.4, (b) 0.6, (c) 0.8, (d) 1.0, and (e) 1.2. The flow velocity of the fluid is 0.3 m/s at the flow inlet; **(B)** Stable exterior wall temperature profiles determined from thermographic measurements using infrared radiation. The flow velocity of the fluid is 0.3 m/s at the flow inlet; **(C)** Effect of equivalence ratio on the quenching distance of the methane flame at normal ambient temperature and pressure. The quenching distance of the methane flame is determined experimentally as described in the *ASTM International* standard test methods (ASTM International, 2016; ASTM International, 2021).

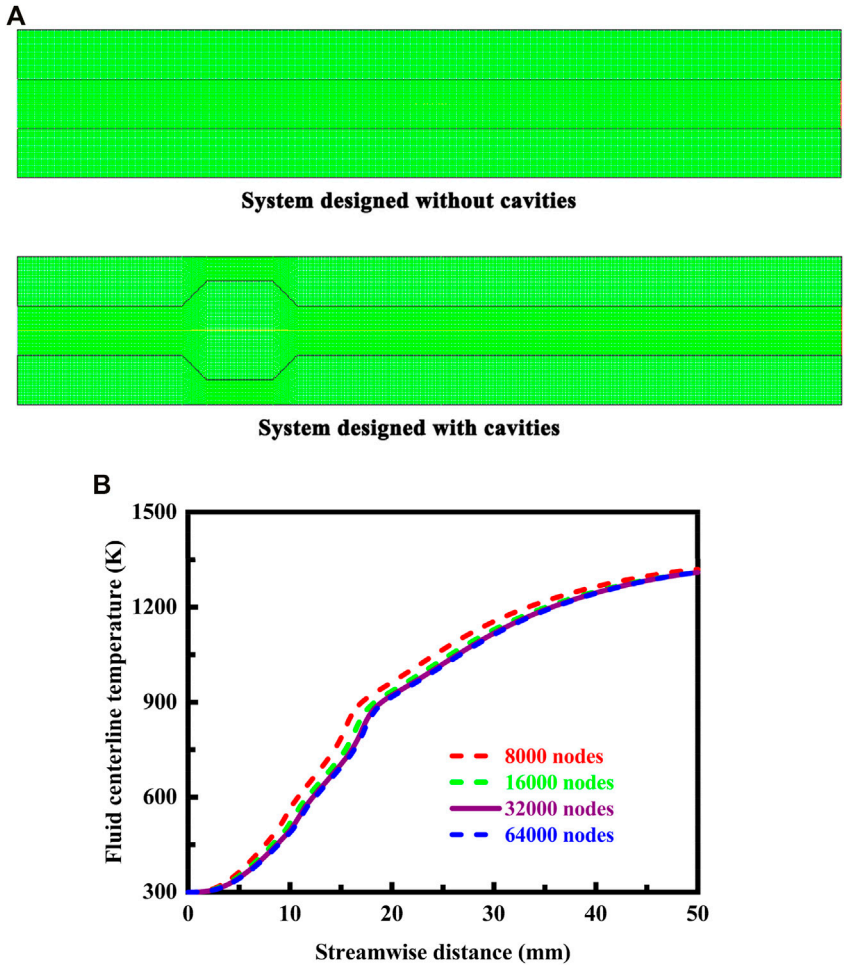

FIGURE 4 | (A) Typical meshes used in computational fluid dynamics simulations for the system designed without cavities and for the system designed with cavities. More nodes are placed around the reaction regions and around the cavity structure; **(B)** Stable fluid centerline temperature profiles for meshes with different nodal densities. The stable temperature profiles are presented along the fluid centerline of the system designed with cavities. Additionally, the flow velocity of the fluid is 0.7 m/s at the flow inlet, and the system is designed in stoichiometric operation.

velocity of the fluid is 0.3 m/s at the flow inlet. A premixed methane-air mixture is fed to the system with a temperature of 300 K. Methane and air are perfectly premixed before they enter the system prior to combustion. The system is designed in stoichiometric operation, because an equivalence ratio of unity is the most reactive mixture composition. Experimental data are therefore obtained based on an initial temperature of 300 K and an equivalence ratio of unity. An ordinary camera is used to form an image using visible light. A thermographic camera is used to create an image using infrared radiation, similar to the ordinary camera that forms an image using visible light. Both emissivity and reflected temperature are adjusted in the thermographic camera to achieve the most accurate thermal image and to determine the corrected temperature. To obtain optimum thermal images, the emissivity of the material surface must be adjusted on the thermographic camera. Correct emissivity adjustment is especially important since the difference in temperature between the measurement environment and the measured object is large. The thermographic camera is precisely calibrated to ensure that the captured pixel values properly correlate to temperatures of the imaged scene. Calibration is performed under controlled conditions with a large number of blackbody reference sources. The thermographic camera is calibrated by the camera manufacturer to factory specifications. Calibration checks are performed by measuring objects with known temperatures and comparing the measured temperatures with the known temperatures. The adjustment to the spacing distance between the two parallel plates is made to determine the flame quenching distance of the system.

The thermographic camera can achieve a resolution of 640 × 480 pixels, and a temperature difference of 1.0 K at the scene induces a maximum temperature difference of 0.02 K at the sensor. The stable fluid centerline temperature profiles are determined from thermographic measurements using infrared radiation, and the thermographic camera is structured to capture

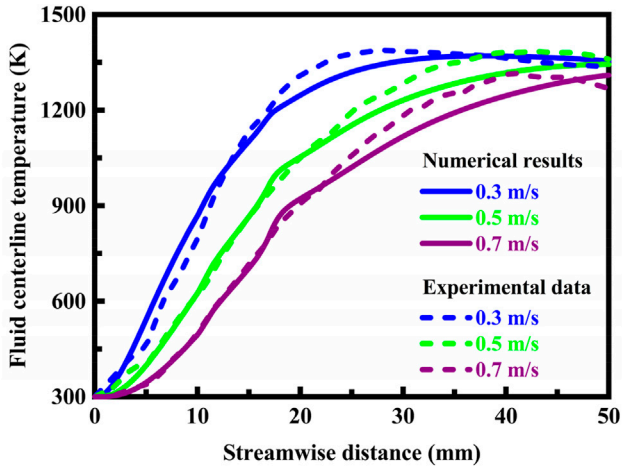

FIGURE 5 | Stable fluid centerline temperature profiles determined from thermographic measurements using infrared radiation and predicted by the model using computational fluid dynamics. The system is designed in stoichiometric operation.

and transmit infrared images of the region of interest and to collect temperature data. The fluid centerline temperature measurement is performed in a direction perpendicular to the direction of the flow of the fluid by the thermographic camera from the sides of the system. The method allows the infrared radiation along the fluid centerline to pass through and be received by the thermographic camera, thereby enabling the fluid centerline temperatures to be measured. To precisely measure the distribution of temperature, the emissivity of each material must be determined accurately. However, it is extremely difficult to determine the emissivity of the flame in the system. The total emissivity of the flame is composed of 2.7, 4.3, and 15.0 μm wavelength bands. The emissivity of the flame is predicted using the Schmidt's theory for the outer region of a flame sheet in thermal equilibrium, followed by an iteration scheme with a wide-band model theory (Schmidt, 1909). More specifically, the empirical correlations suggested by Char and Yeh (1996) are used to predict the cross-section emissivity of the flame by performing a statistical analysis with a dimensionless position parameter. Additionally, both optically thick and optically thin theories are used to make more accurate predictions.

The experiments must be repeated in order to produce data that has acceptable error levels. It is important that the experiments should be repeatable, which is of great importance to the reliability of the experiments and the conclusions supported by the experiments. Experiments are conducted at different times under the same operating conditions, and the number of repetitions of the experiments performed varies from two to six times, depending on the operating conditions applied to the experiments. Such experiments yield almost the same results, which means that the results almost do not change in different trials under the exact same conditions. For example, there is almost no change in temperature while performing the multiple independently-repeated experiments under identical conditions. More specifically, the maximum difference in temperature between different experiments is less than 20 K when the system operates under the same conditions. Error bars can be valuable for understanding the results presented in this study, but they are not shown herein for simplification due to the insignificant difference between the measurement data under the exact same conditions.

EXPERIMENTAL RESULTS AND DISCUSSION

Effect of Flow Velocity

The thermographic images acquired in the infrared spectral region are presented in **Figure 2A** for different flow velocities at the flow inlet, wherein the optical images in the visible spectral region are also presented, thereby allowing for comparisons between different flow velocities in a more intuitive manner. The system is designed in stoichiometric operation. The flow velocity of the fluid varies from 0.3 to 0.7 m/s at the flow inlet. The flow velocity plays a significant role in determining the location of the flame in the system. As the flow velocity increases, the location of the flame moves downstream due to the reduced mean residence time. This means that the location of the flame is very sensitive to changes in the flow velocity, and the flame has a tendency to move downstream when the flow velocity is high, as presented in **Figure 2A**. Additionally, the rate of heat generation within the system increases with increasing the flow velocity. As a result of the competition between the reduced mean residence time and the increased heat generation rate with increasing the flow velocity, the location of the flame shifts downstream within the system. The stable fluid centerline temperature profiles determined from thermographic measurements using infrared radiation are shown in **Figure 2B**. As the flow velocity increases, the location of the peak temperature moves downstream significantly, which shows good agreement with the results obtained for the location of the flame. However, because the location of the flame is determined by the flow velocity being utilized, the system must be specifically configured or designed for use within a particular range of flow velocity. This imposes significant limits on the flow velocities that can be employed.

To understand how to design the system with improved flame stability, it is necessary to determine the quenching distance for the system. The quenching distance varies with mixture composition, thermodynamic conditions, and channel wall characteristics (Jarosiński, 1983; Jarosinski, 1986). The spacing distance between the two parallel plates varies from 2.0 to 5.0 mm to determine the quenching distance. The measurement results indicate that the flame is stable when the spacing distance between the two parallel plates is larger than 2.5 mm, and combustion cannot be sustained when the spacing distance is less than 2.5 mm. Based on this flame stability criteria, the critical value for the quenching distance takes 2.5 mm, which is the minimum allowable distance that ensures flame propagation at the specified composition and thermodynamic conditions. It has been commonly believed that the quenching distance of the methane flame varies from 2.0 to 2.5 mm under stoichiometric

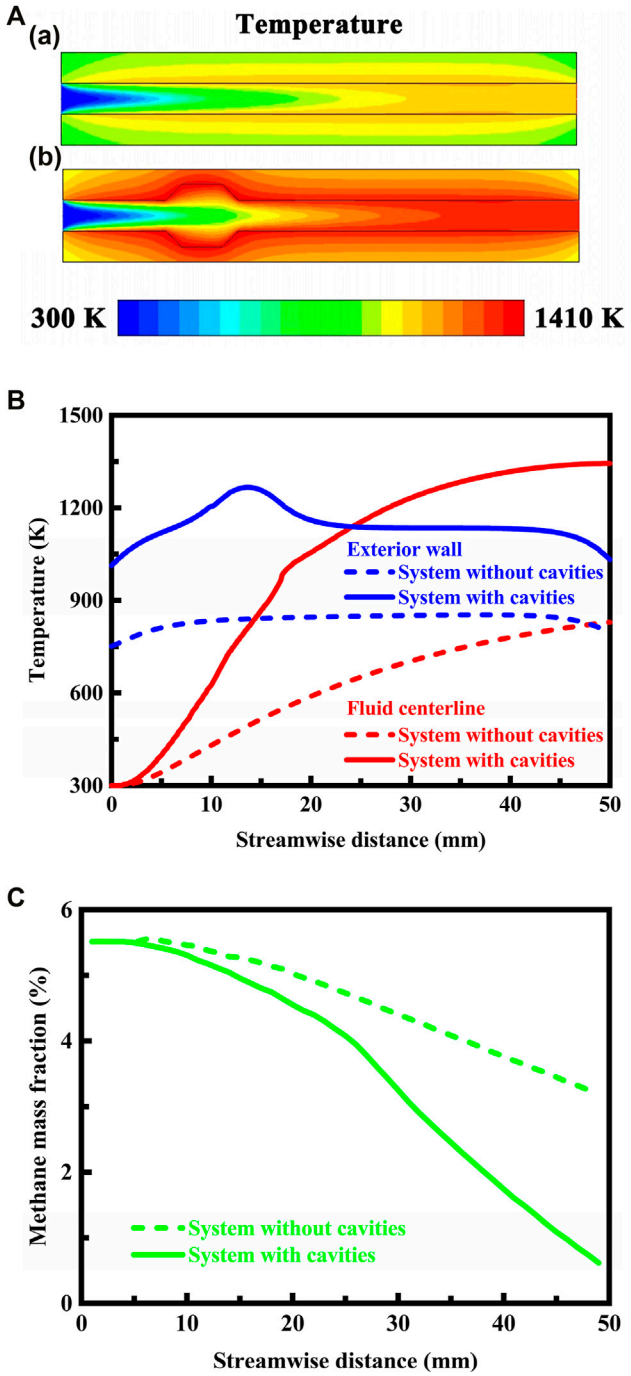

FIGURE 6 | (A) Contour plots of temperature in the system designed in different geometrical configurations. The system is configured (a) without cavities and (b) with cavities. The system is designed in stoichiometric operation, the exterior heat loss coefficient is 20 W/(m^2·K), and the flow velocity of the fluid is 0.3 m/s at the flow inlet. The thermal conductivity of the solid material is 1.4 W/(m·K), which is in consistence with that of the fused-quartz used in the experiments; **(B)** Temperature profiles along the fluid centerline and on the exterior walls of the system designed in different geometrical configurations. The system is designed in stoichiometric operation, the exterior heat loss coefficient is 20 W/(m^2·K), the flow velocity of the fluid is 0.3 m/s at the flow inlet, and the thermal conductivity of the solid material is 1.4 W/(m·K); **(C)** Methane concentration profiles along the fluid centerline of the system designed in different geometrical configurations. The system is designed in stoichiometric operation, the exterior heat loss coefficient is 20 W/(m^2·K), the flow velocity of the fluid is 0.3 m/s at the flow inlet, and the thermal conductivity of the solid material is 1.4 W/(m·K).

conditions, depending on the cavity structure and dimensions. The use of cavities may provide improved flame stability for the downstream combustion of the stream (Wan et al., 2015; Fan et al., 2018; Linhong Li et al., 2019; Zhang et al., 2020a; Zhang et al., 2020b; Xu et al., 2021). However, the quenching distance determined for the system is almost identical to that determined for a smooth system designed without cavities. Therefore, the cavity structure has little effect on the quenching distance.

Effect of Equivalence Ratio

The thermographic images acquired in the infrared spectral region, and the optical images in the visible spectral region, are presented in **Figure 3A** for different equivalence ratios of the mixture at the flow inlet. The stable exterior wall temperature profiles determined from thermographic measurements using infrared radiation are shown in **Figure 3B**. The flow velocity of the fluid is 0.3 m/s at the flow inlet. The equivalence ratio of the mixture varies from 0.4 to 1.2 at the flow inlet.

In all the cases, the mixture is ultimately raised to a temperature at which the combustion reaction occurs in the entire gas stream, as presented in **Figure 3A**. Strong combustion is initiated in the cavities. The cavity structure provides for a more compact primary reaction region and for stable flame holding that is, especially desirable over an extended operating range. This is principally because the structural arrangement increases the intensity of combustion through enhanced heat and mass transfer (Wan et al., 2015; Fan et al., 2018), making the combustion process more stable. A further feature provided by the cavity structure is that some combustion products, such as hot gas and chemically active species, in the primary reaction region are more easily transferred into the unreacted inlet gas stream for improved performance. As a result, the structural arrangement creates small recirculation regions for additional mixing of the hot and chemically reactive combustion products into the incoming channel flow, thereby improving the stability of the flame. Consequently, the utilization of cavities can initiate recirculation of the fuel and air mixture, thereby enhancing heat and mass transfer and providing increased flame stability for the downstream combustion of the premixed fuel and air stream.

The system fueled by methane is capable of operating over a large range of equivalence ratios, such as operation with the mixture that is, as lean as two fifths of stoichiometric fuel, as presented in **Figure 3A**. At the lowest equivalence ratio, the flame is less intense, and the large amount of excess air reduces the peak flame temperature, thus causing a reduction of thermal efficiency. All the mixtures will burn if the fuel concentration lies within the equivalence ratio range. However, the maximum temperature is reached for a stoichiometric mixture, as shown in **Figure 3B**. The

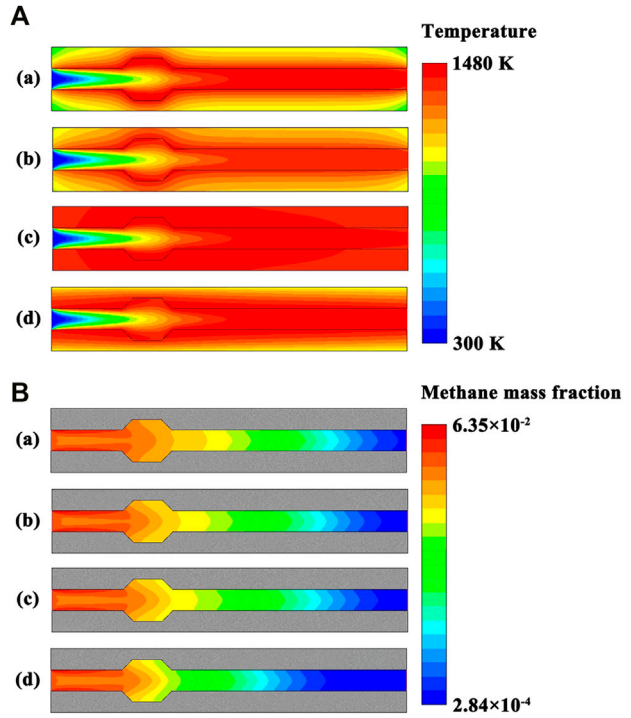

FIGURE 7 | (A) Contour plots of temperature in the system under different thermal conductivity conditions. The thermal conductivity of the solid material is defined as follows: (a) 0.5 W/(m·K), (b) 1.4 W/(m·K), (c) 50 W/(m·K), and (d) 50 W/(m·K) in the longitudinal direction and 0.5 W/(m·K) in the transverse direction. The system is designed in stoichiometric operation, the exterior heat loss coefficient is 20 W/(m^2·K), and the flow velocity of the fluid is 0.3 m/s at the flow inlet; **(B)** Contour plots of methane concentration in the system under different thermal conductivity conditions. The thermal conductivity of the solid material is defined as follows: (a) 0.5 W/(m·K), (b) 1.4 W/(m·K), (c) 50 W/(m·K), and (d) 50 W/(m·K) in the longitudinal direction and 0.5 W/(m·K) in the transverse direction. The system is designed in stoichiometric operation, the exterior heat loss coefficient is 20 W/(m^2·K), and the flow velocity of the fluid is 0.3 m/s at the flow inlet.

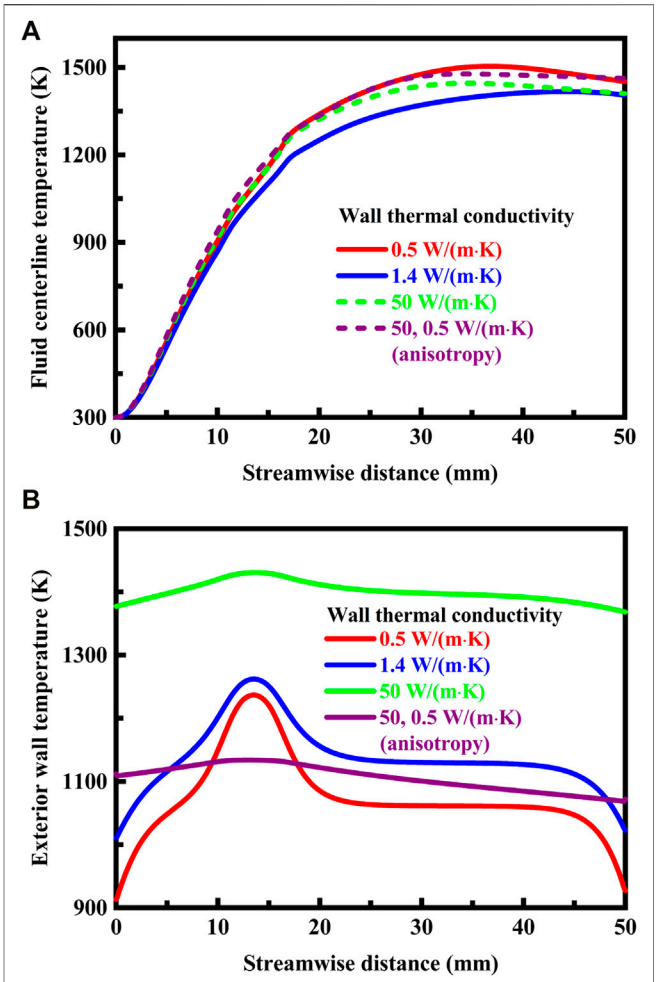

FIGURE 8 | (A) Temperature profiles along the fluid centerline under different thermal conductivity conditions. For the anisotropic solid material, the thermal conductivity is 50 W/(m·K) in the longitudinal direction and 0.5 W/(m·K) in the transverse direction. The system is designed in stoichiometric operation, the exterior heat loss coefficient is 20 W/(m^2·K), and the flow velocity of the fluid is 0.3 m/s at the flow inlet; **(B)** Temperature profiles on the exterior walls under different thermal conductivity conditions. For the anisotropic solid material, the thermal conductivity is 50 W/(m·K) in the longitudinal direction and 0.5 W/(m·K) in the transverse direction. The system is designed in stoichiometric operation, the exterior heat loss coefficient is 20 W/(m^2·K), and the flow velocity of the fluid is 0.3 m/s at the flow inlet.

peak temperature is decreased as the mixture is made fuel-richer or fuel-leaner. The flame is anchored to the duct between the two cavities in all the cases. Consequently, the equivalence ratio has little effect on the location of the flame in the system. In the operation of the system, a back-flow region will be initiated by the cavities due to a sudden change of cross section (Wan et al., 2015; Fan et al., 2018; Linhong Li et al., 2019; Zhang et al., 2020a; Zhang et al., 2020b; Xu et al., 2021), which serves to stabilize the flame for the system. One problem associated with using cavities as a flame holder for the system is that the excessive heat may be life-limiting. Operation will not make the mixture flammable when the mixture is as lean as one fifth of stoichiometric fuel, and therefore the equivalence ratio in this case is less than the lean flammability limit.

The fuel-air mixture will burn only if the concentration of the fuel lies within well-defined lower and upper bounds determined experimentally, referred to as flammability limits. The measurement of flammability limits is performed in order to appropriately design the system and to gain a fundamental understanding of flammability properties of the mixture. However, the characterization of the flammability envelope of the mixture is time consuming and quite difficult through experimental tests. The experimental results indicate that there is a range of methane to air equivalence ratios within which combustion can occur or be sustained within the millimeter-scale systems. The lean and rich flammability limits expressed in terms of the equivalence ratio of the mixture, which define the stable combustion operating range, are 0.38 and 2.2 for the system designed without cavities, and 0.32 and 2.6 for the system designed with cavities. The cavity structure can effectively

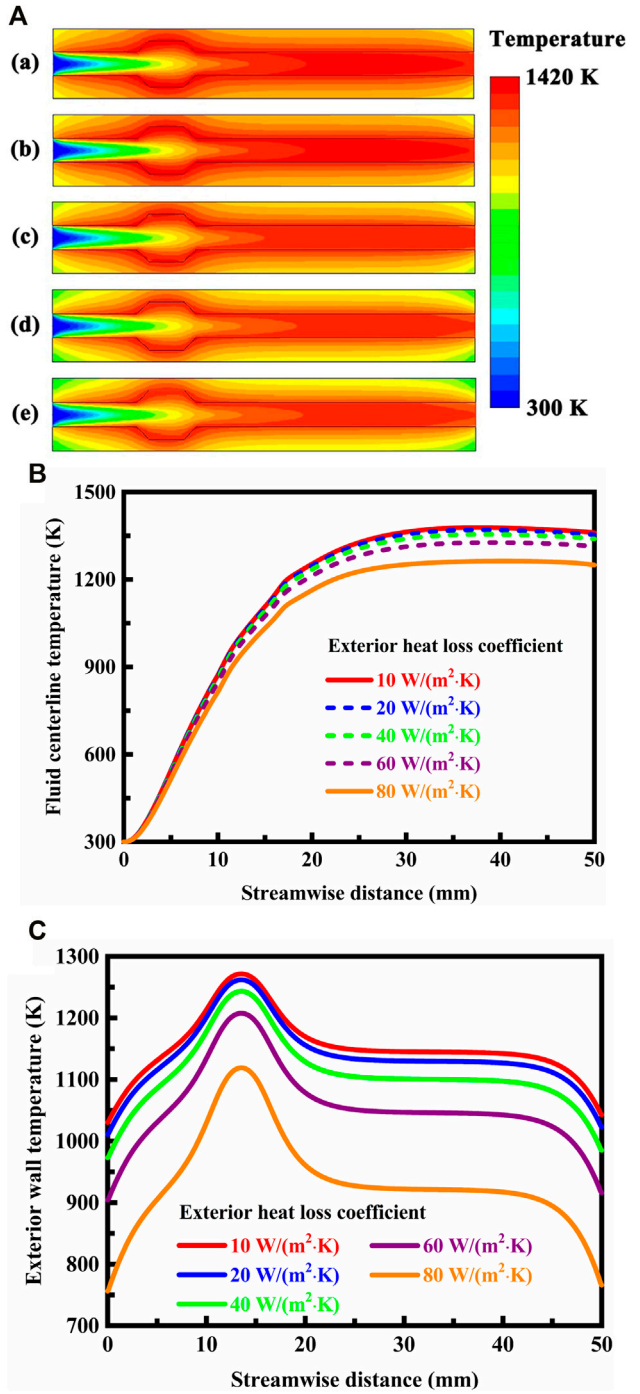

FIGURE 9 | (A) Contour plots of temperature in the system under different exterior heat loss conditions. The exterior heat loss conditions are specified with the exterior heat loss coefficient as follows: (a) 10 W/(m^2·K), (b) 20 W/(m^2·K), (c) 40 W/(m^2·K), (d) 60 W/(m^2·K), and (e) 80 W/(m^2·K). The system is designed in stoichiometric operation, the thermal conductivity is 1.4 W/(m·K) for the solid material, and the flow velocity of the fluid is 0.3 m/s at the flow inlet; **(B)** Temperature profiles along the fluid centerline under different exterior heat loss coefficient conditions. The system is designed in stoichiometric operation, the thermal conductivity is 1.4 W/(m·K) for the solid material, and the flow velocity of the fluid is 0.3 m/s at the flow inlet; **(C)** (*Continued*)

FIGURE 9 | Temperature profiles on the exterior walls under different exterior heat loss coefficient conditions. The system is designed in stoichiometric operation, the thermal conductivity is 1.4 W/(m·K) for the solid material, and the flow velocity of the fluid is 0.3 m/s at the flow inlet.

extend the flammability limits of the mixture, with an increase of about 18% in the operating range defined by the equivalence ratio of the mixture. Consequently, the cavity structure will lead to a wider operating range in terms of the lean and rich flammability limits, with improved flame stability.

The effect of equivalence ratio on the quenching distance of the methane flame is investigated at normal ambient temperature and pressure in order to offer the possibility of inherently safe operation within the flammability limits of the mixture. The results are presented in **Figure 3C**, in which the quenching distance of the methane flame is plotted against the equivalence ratio of the fuel to air. Since the quenching distance of the methane flame depends on a number of factors, such as gas composition, thermodynamic conditions, and channel wall characteristics, it is determined experimentally as described in the *ASTM International* standard test methods (ASTM International, 2016; ASTM International, 2021). The quenching distance is the minimum spacing distance that permits sustained propagation of the methane flame at the specified temperature and pressure conditions. The quenching distance depends heavily on the equivalence ratio of the fuel to air over the entire range of variation, as shown in **Figure 3C**. Additionally, the quenching distance increases with increasing deviation from stoichiometry. Below the quenching distance, ignition of the mixture will not develop into a methane flame. As the spacing distance increases beyond the quenching distance, propagation of the methane flame is possible within the flammability limits.

NUMERICAL MODEL

Description of the System

The system is modeled as two parallel plates and two cavities with dimensions described in detail above. The spacing distance between the two parallel plates is 3.0 mm, unless the context dictates otherwise. To model the combustion reaction of the mixture, the system is simplified as a two-dimensional problem due to the high aspect ratio of the system. It is worth noting that the aspect ratio is the ratio of the height to the width of the channel, and the height is the spacing distance between the two parallel plates. However, to improve the realism of the model and to resolve the combustion problem with greater accuracy (Maruta, 2011; Pashchenko, 2017), further study is needed to perform computational fluid dynamics simulations in three dimensions.

Mathematical Model

The model is implemented in FLUENT (ANSYS, 2018), available from ANSYS Inc., Release 19.2, to obtain the steady-state solution for the reacting flow problem. FLUENT permits modeling of

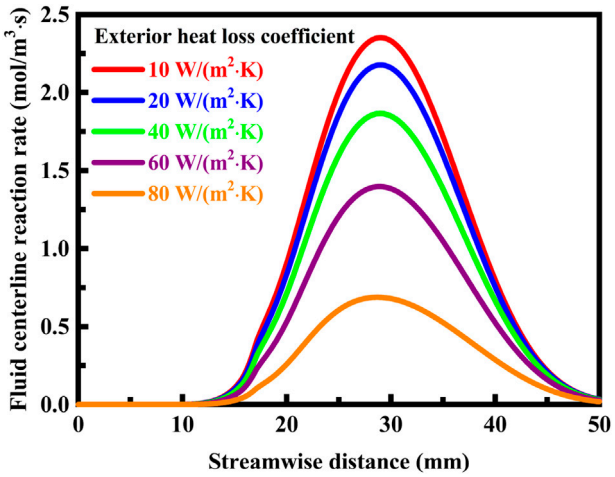

FIGURE 10 | Reaction rate profiles along the fluid centerline under different exterior heat loss coefficient conditions. The system is designed in stoichiometric operation, the thermal conductivity is 1.4 W/(m·K) for the solid material, and the flow velocity of the fluid is 0.3 m/s at the flow inlet.

reacting flow (Wang and Fan, 2021) and related transport phenomena (Yang et al., 2019; Yilmaz, 2019) in the combustion process, and various modes of heat transfer can be modeled (Peng et al., 2019; Zhao and Fan, 2020). The continuity equation is given by

$$\frac{\partial(\rho u_x)}{\partial x} + \frac{\partial(\rho u_y)}{\partial y} = 0, \tag{1}$$

where ρ is the density, u_x is the axial velocity, and u_y is the transverse velocity.

The axial and transverse momentum conservation equations are given by

$$\frac{\partial(\rho u_x u_x)}{\partial x} + \frac{\partial(\rho u_y u_x)}{\partial y} + \frac{\partial p}{\partial x} - \frac{\partial}{\partial x}\left[2\mu\frac{\partial u_x}{\partial x} - \frac{2}{3}\mu\left(\frac{\partial u_x}{\partial x} + \frac{\partial u_y}{\partial y}\right)\right] - \frac{\partial}{\partial y}\left[\mu\left(\frac{\partial u_x}{\partial y} + \frac{\partial u_y}{\partial x}\right)\right] = 0, \tag{2}$$

$$\frac{\partial(\rho u_x u_y)}{\partial x} + \frac{\partial(\rho u_y u_y)}{\partial y} + \frac{\partial p}{\partial y} - \frac{\partial}{\partial y}\left[2\mu\frac{\partial u_y}{\partial y} - \frac{2}{3}\mu\left(\frac{\partial u_x}{\partial x} + \frac{\partial u_y}{\partial y}\right)\right] - \frac{\partial}{\partial x}\left[\mu\left(\frac{\partial u_y}{\partial x} + \frac{\partial u_x}{\partial y}\right)\right] = 0, \tag{3}$$

wherein μ is the dynamic viscosity, and p is the pressure.

The energy conservation equation can be written as follows:

$$\frac{\partial(\rho u_x h)}{\partial x} + \frac{\partial(\rho u_y h)}{\partial y} + \frac{\partial}{\partial x}\left(\rho\sum_{k=1}^{K} w_k h_k V_{k,x} - k_g\frac{\partial T}{\partial x}\right) + \frac{\partial}{\partial y}\left(\rho\sum_{k=1}^{K} w_k h_k V_{k,y} - k_g\frac{\partial T}{\partial y}\right) = 0, \tag{4}$$

wherein h is the enthalpy, w is the mass fraction, k is the thermal conductivity, V is the diffusion velocity, T is the absolute temperature, and K is the total number of chemical species present in the system. Species k is denoted by the subscript k, and the gas mixture is denoted by the subscript g.

For the combustion reaction occurring in the bulk gas phase, the species transport equation can be written as follows:

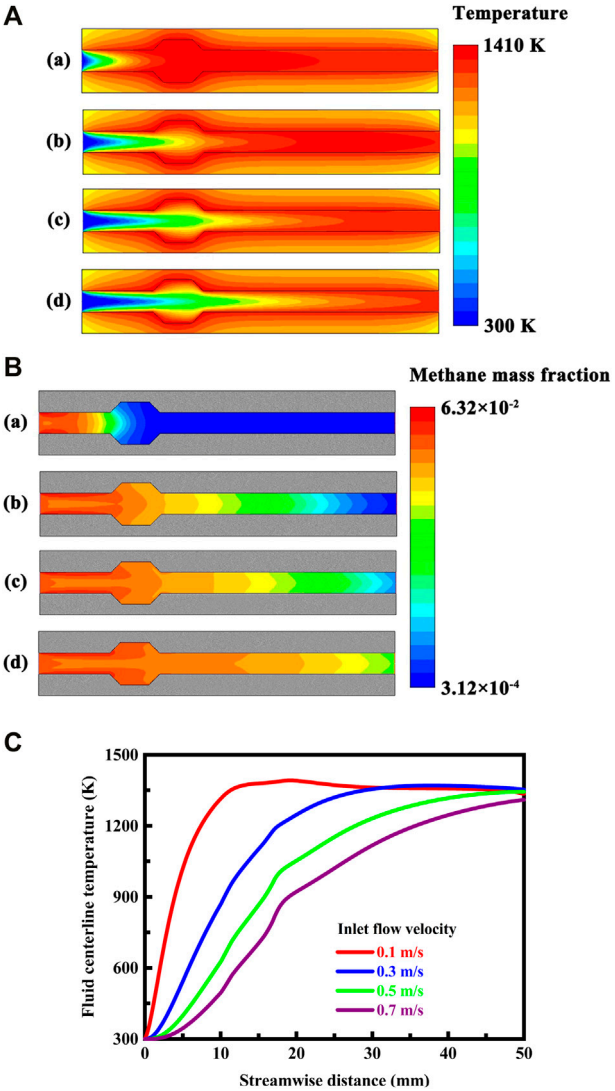

FIGURE 11 | (A) Contour plots of temperature in the system under different flow velocity conditions. The flow velocity of the fluid is defined at the flow inlet as follows: (a) 0.1 m/s, (b) 0.3 m/s, (c) 0.5 m/s, and (d) 0.7 m/s. The system is designed in stoichiometric operation, the exterior heat loss coefficient is 20 W/(m²·K), and the thermal conductivity is 1.4 W/(m·K) for the solid material; **(B)** Contour plots of methane concentration in the system under different flow velocity conditions. The flow velocity of the fluid is defined at the flow inlet as follows: (a) 0.1 m/s, (b) 0.3 m/s, (c) 0.5 m/s, and (d) 0.7 m/s. The system is designed in stoichiometric operation, the exterior heat loss coefficient is 20 W/(m²·K), and the thermal conductivity is 1.4 W/(m·K) for the solid material; **(C)** Temperature profiles along the fluid centerline under different inlet flow velocity conditions. The system is designed in stoichiometric operation, the exterior heat loss coefficient is 20 W/(m²·K), and the thermal conductivity is 1.4 W/(m·K) for the solid material.

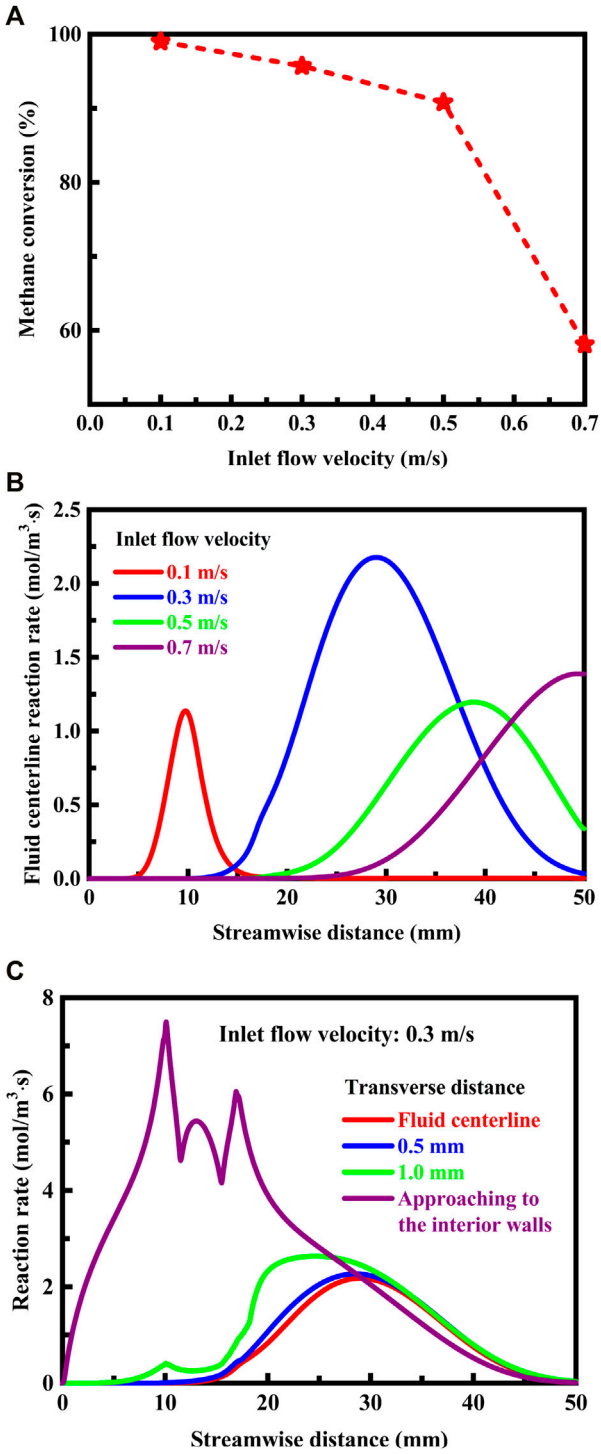

FIGURE 12 | (A) Methane conversion at the flow outlet as a function of the flow velocity of the fluid at the flow inlet. The system is designed in stoichiometric operation, the exterior heat loss coefficient is 20 W/(m^2·K), and the thermal conductivity is 1.4 W/(m·K) for the solid material; **(B)** Reaction rate profiles along the fluid centerline under different inlet flow velocity conditions. The system is designed in stoichiometric operation, the exterior heat loss coefficient is 20 W/(m^2·K), and the thermal conductivity is 1.4 W/(m·K) for the solid material; **(C)** Reaction rate profiles as a function of the

(*Continued*)

FIGURE 12 | streamwise distance at different transverse distances. The flow velocity of the fluid is 0.3 m/s at the flow inlet. The system is designed in stoichiometric operation, the exterior heat loss coefficient is 20 W/(m^2·K), and the thermal conductivity is 1.4 W/(m·K) for the solid material.

$$\frac{\partial(\rho u_x w_k)}{\partial x} + \frac{\partial(\rho u_y w_k)}{\partial y} + \frac{\partial}{\partial x}(\rho w_k V_{k,x}) + \frac{\partial}{\partial y}(\rho w_k V_{k,y}) - \dot{\omega}_k W_k = 0,\ k = 1, \ldots, K, \tag{5}$$

in which $\dot{\omega}$ is the net rate of production, and W is the molecular mass.

The diffusion velocity of gaseous species k arises because of gradients of both temperature and concentration, which can be computed as follows:

$$\vec{V}_k = -D_k \nabla(\ln(w_k \bar{W} W_k^{-1})) + \left(D_k^T W_k (\rho w_k \bar{W})^{-1}\right) \nabla(\ln T), \tag{6}$$

wherein $\vec{V}$ is the diffusion velocity vector, D is molecular diffusivity, D^T is the thermal diffusivity, and $\bar{W}$ is mean molecular mass.

The pressure is represented by the kinetic theory of gases:

$$p = \rho R T \bar{W}^{-1}, \tag{7}$$

where R is the ideal gas constant.

For heat conduction in the solid region, the energy conservation equation is given by

$$\frac{\partial}{\partial x}\left(k_{s,x}\frac{\partial T}{\partial x}\right) + \frac{\partial}{\partial y}\left(k_{s,y}\frac{\partial T}{\partial y}\right) = 0, \tag{8}$$

The solid material is denoted by the subscript s.

At the gas-solid phase boundaries, the energy conservation equation is given by

$$k_{s,y}\left(\frac{\partial T}{\partial y}\right)_{\xi+} - k_g\left(\frac{\partial T}{\partial y}\right)_{\xi-} + \dot{q}_r = 0, \tag{9}$$

wherein $\dot{q}$ is the heat flux. The phase boundaries are denoted by the subscript ξ, and Radiation is denoted by the subscript r.

The equation for exterior heat losses is given by

$$\dot{q} = h_o(T_w - T_e) + \varepsilon F_{w-\infty}\sigma(T_w^4 - T_e^4), \tag{10}$$

in which h_o is the exterior heat loss coefficient, ε is the emissivity factor, F is the view factor, and σ is the Stefan-Boltzmann constant. The walls are denoted by the subscript w, the environment is denoted by the subscript e, and the surroundings are denoted by the subscript ∞. In most cases, the exterior heat loss coefficient is 20 W/(m^2·K), which is a typical example of natural convection.

Numerical Methods

The combustion process is modeled with GRI-MECH 3.0 (Smith et al., 2000), and the detailed mechanism is invariably stiff (Westbrook et al., 2005). The typical meshes used in computational fluid dynamics simulations are illustrated in

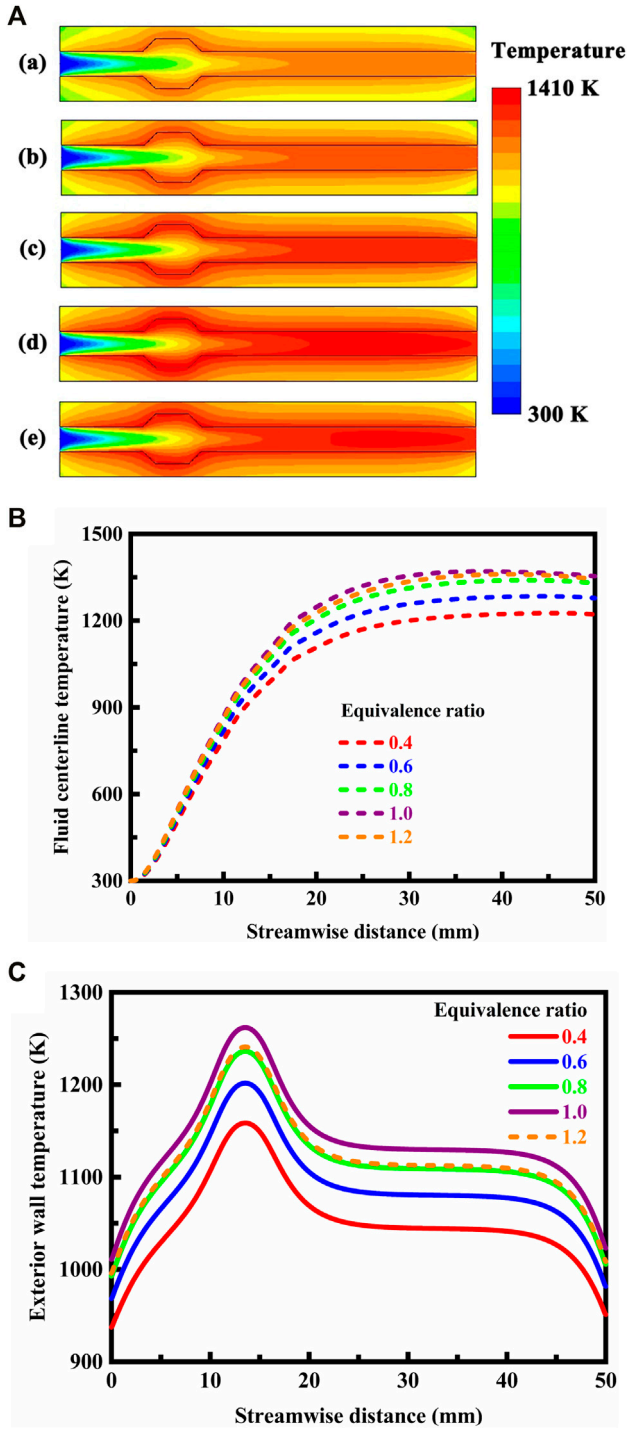

FIGURE 13 | (A) Contour plots of temperature in the system under different equivalence ratio conditions. The composition of the mixture is specified with the equivalence ratio as follows: (a) 0.4, (b) 0.6, (c) 0.8, (d) 1.0, and (e) 1.2. The thermal conductivity is 1.4 W/(m·K) for the solid material, the exterior heat loss coefficient is 20 W/(m^2·K), and the flow velocity of the fluid is 0.3 m/s at the flow inlet; **(B)** Temperature profiles along the fluid centerline under different equivalence ratio conditions. The thermal conductivity is 1.4 W/(m·K) for the solid material, the exterior heat loss coefficient is 20 W/(m^2·K), and the flow velocity of the fluid is 0.3 m/s at the flow inlet; **(C)** Temperature profiles on the exterior walls

(*Continued*)

FIGURE 13 | under different equivalence ratio conditions. The thermal conductivity is 1.4 W/(m·K) for the solid material, the exterior heat loss coefficient is 20 W/(m^2·K), and the flow velocity of the fluid is 0.3 m/s at the flow inlet.

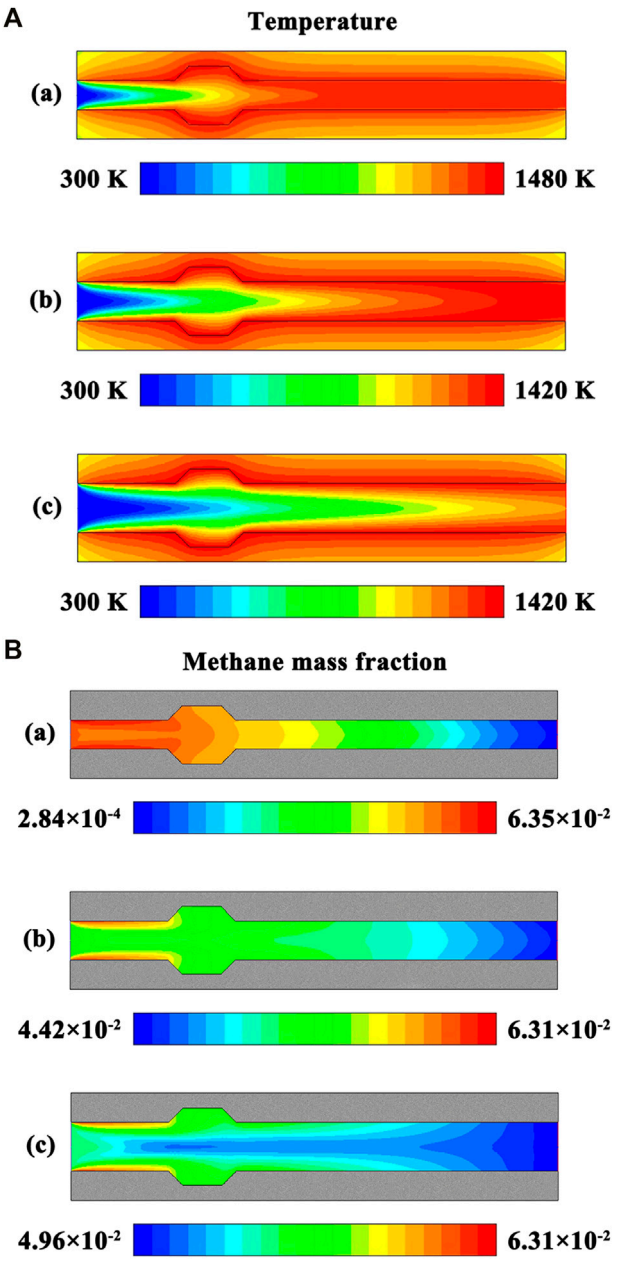

FIGURE 14 | (A) Contour plots of temperature in the system under different channel height conditions. The channel height is specified as follows: (a) 3.0 mm, (b) 4.0 mm, and (c) 5.0 mm. The system is designed in stoichiometric operation, the exterior heat loss coefficient is 20 W/(m^2·K), the thermal conductivity is 1.4 W/(m·K) for the solid material, and the flow velocity of the fluid is 0.3 m/s at the flow inlet; **(B)** Contour plots of methane concentration in the system under different channel height conditions. The channel height is specified as follows: (a) 3.0 mm, (b) 4.0 mm, and (c) 5.0 mm. The system is designed in stoichiometric operation, the exterior heat loss coefficient is 20 W/(m^2·K), the thermal conductivity is 1.4 W/(m·K) for the solid material, and the flow velocity of the fluid is 0.3 m/s at the flow inlet.

Figure 4A for the system designed without cavities and for the system designed with cavities. More nodes are accumulated around the reaction regions and around the cavity structure. In total, the typical mesh consists of 28,000 nodes for the system designed without cavities and 32,000 nodes for the system designed with cavities. A mesh independence test is performed to assure independence of the solution to the combustion problem. The stable temperature profiles along the fluid centerline of the system designed with cavities are presented in **Figure 4B** for meshes with different nodal densities. As the mesh density increases, there is a convergence of the solution. Solutions obtained with a mesh consisting of 32,000 nodes are reasonably accurate. Larger mesh densities, up to 64,000 nodes, offer no obvious advantage. The specific heat of the mixture is defined as a function of composition, and the specific heat of each species is defined as a piecewise-polynomial function of temperature. The solution to the problem is deemed to have converged when the residual is less than 10^{-6} for each of the conservation equations described above.

Validation of the Model

The temperature profiles along the fluid centerline under different flow velocity conditions are presented in **Figure 5**. The temperature profiles are determined from thermographic measurements using infrared radiation and predicted by the model. The system is designed in stoichiometric operation. The model is in reasonable agreement with the experimental measurements.

NUMERICAL RESULTS AND DISCUSSION

Effect of Cavities

The contour plots of temperature in the system are presented in **Figure 6A** in different geometrical configurations. Accordingly, the temperature profiles along the fluid centerline and on the exterior walls are presented in **Figure 6B** for the system designed in different geometrical configurations, and the methane concentration profiles along the fluid centerline are presented in **Figure 6C**. The system is designed in stoichiometric operation. The thermal conductivity of the solid material is 1.4 W/(m·K), which is in consistence with that of the fused-quartz used in the experiments.

There is a sharp rise in temperature caused by the combustion process, which is significantly affected by the geometrical configuration of the system. Specifically, the temperature in the system designed with cavities is much higher than that in the system designed without cavities, as illustrated in **Figure 6A** and shown in **Figure 6B**. The cavities result in a sudden expansion in the flow domain. This sudden expansion of cross section could potentially promote ignition by the flame front propagating through the cavities immediately to upstream of the expansion. Additionally, the sudden expansion of cross section may induce disturbances in the flow region (Pan et al., 2019; Huang et al., 2020) and the cavitated surfaces provide an increased total heat transfer surface area in the region, thereby enhancing heat transfer between the fluid and the solid material and subsequently to the upstream structure of the system by heat conduction through the channel walls. As a result of this combination, the predicted temperature in the system designed with cavities becomes much higher than that in the system designed without cavities. This sharp rise in temperature can raise the flame front speed and therefore may lower the extinction limit temperature and could improve the stability of the flame.

The absence of cavities can lead to sub-optimum combustion. This in turn can be related to, for example, incomplete combustion resulting in poor efficiency, as shown in **Figure 6C**. In contrast, the intensity and efficiency of combustion are enhanced through the use of the cavity structure for the system. More specifically, the system designed with cavities has the advantage of substantially complete conversion of methane at the flow outlet, as shown in **Figure 6C**. The intense combustion activity serves as a mechanism to facilitate the interaction between the hot combustion products and the cold incoming fuel and air mixture, thereby improving the stability of the flame. The importance of enhancing this interaction has been clearly demonstrated in the literature (Wan et al., 2015; Fan et al., 2018). As a result, the cavities can be configured to provide flame holding and initiate recirculation of the fuel and air mixture in a downstream combustion region. This in turn causes an increase in residence time for a portion of the fuel-air mixture, thereby avoiding instability of the flame. The combustion is stabilized because the free radicals and heat produced by the reaction process are transported back upstream in the recirculation region to mix with and initiate combustion of the un-reacted fuel and air mixture. Stable combustion is therefore heavily dependent on the recirculation of the hot and chemically active combustion products back upstream. When the velocity of the recirculated combustion products is increased, the flux of combustion products upstream increases and the combustion process tends to become more stable over a wider range of operating conditions. However, flame holding may cause serious damage to the system, since the increased temperature within the cavities would exceed the design temperature of the wall material.

The use of cavities fundamentally changes the stability of the flame, as discussed above. The efficiency and performance of this system can be further improved, since the number and position of the cavities can vary depending upon the specific application and the fluid used. Additionally, the shape of the cavities can be adapted to further improve the recirculation of the hot and chemically active combustion products and the stability of the flame. Consequently, further optimization steps are required to fully exploit the benefits of the cavity structure while providing efficient and stable combustion. In this manner, it is possible to maintain the stability of the flame within the system at a higher level than otherwise obtainable, and to obtain higher performance in operation.

Effect of Wall Thermal Conductivity

The millimeter-scale system with a cavity structure is designed in stoichiometric operation. In order for flame holding to occur, methane and air must be premixed and provided a low velocity

region to reside. Therefore, a low flow velocity profile is specified at the flow inlet. The contour plots of temperature and methane concentration in the system are presented in **Figures 7A,B**, respectively, under different thermal conductivity conditions. Accordingly, the temperature profiles along the fluid centerline and on the exterior walls are presented in **Figures 8A,B**, respectively, under different thermal conductivity conditions.

The thermal conductivity of the solid material has little effect on temperature of the fluid, as shown in **Figures 7A**, **8A**. This in turn can be related to small differences in methane concentration and conversion, and efficient combustion occurs with the mixture in all the cases, as shown in **Figure 7B**. In contrast, the thermal conductivity of the solid material has a significant effect on the temperature of the channel walls, as shown in **Figures 7A**, **8B**. The wall temperature profile depends heavily upon the thermal conductivity of the solid material. The temperature gradient is steep within the channel walls with a low thermal conductivity. The temperature of the exterior walls typically increases with increase in the thermal conductivity of the solid material, as shown in **Figure 8B**. An important feature of the solid material is that high enough operating temperatures are achievable in the combustion process to permit effective use of the fuel, as shown in **Figure 7B**. A portion of heat of reaction is transferred to the upstream structure of the system by heat conduction through the channel walls and by radiation through the bulk gas phase. This is necessary for ignition and flame stability (Norton and Vlachos, 2003; Norton and Vlachos, 2004). The solid material is advantageously thermally conductive to permit a high wall temperature with more uniform distribution, as shown in **Figures 7A**, **8B**. Higher thermal conductivity levels would be advantageous to the system. For the solid material with a very low thermal conductivity, it is possible to achieve essentially adiabatic combustion in the system. If the thermal conductivity is low enough for the solid material, the maximum temperature might even approach the theoretical adiabatic flame temperature under the specified operation conditions.

The term anisotropy indicated in **Figures 8A,B** is used to describe direction-dependent thermal conductivity of the solid material, and assumes different thermal conductivities in different directions. In this case, the solid material conducts heat in a way that is, anisotropic. For example, the materials used to transfer and reject heat from the heat source in electronics are often anisotropic (Tian et al., 2013; Kang et al., 2018). When the solid material has anisotropic thermal conductivity, heat conduction is anisotropic within the channel walls, as illustrated in **Figure 7A**. Despite the short length of the channel, heat losses to the surroundings may be substantial, but can be reduced by the anisotropic solid material. More specifically, the anisotropic solid material inhibits transverse but allows longitudinal heat conduction, as illustrated in **Figure 7A**. The channel walls permit heat flux in the longitudinal direction to preheat the fluid, yet does not permit heat losses in the transverse direction to the surroundings, which can be accomplished by using anisotropic composite materials (Wan et al., 2017; Wang et al., 2019) or forming vacuum chambers within the channel walls.

Effect of Heat Losses

In practical operation of the system, there may occur considerable heat losses to the environment, resulting in damage to the stability of the flame, and unsatisfactory operation (Fernandez-Pello, 2002; Wan and Fan, 2021). Heat losses from the channel walls may be significant due to the high aspect ratio of the system (Sakurai et al., 2009; Wang et al., 2020). Operation of the system with a low heat loss coefficient is desirable in order to reliably avoid excessive heat losses. To better understand the underlying cause for the stability of the flame, the effect of heat losses on the temperature in the system is evaluated. The contour plots of temperature in the system are presented in **Figure 9A** under different exterior heat loss conditions. Accordingly, the temperature profiles along the fluid centerline and on the exterior walls are presented in **Figures 9B,C**, respectively, under different exterior heat loss conditions.

An increase of the exterior heat loss coefficient leads to a decrease of the temperature in the system, as illustrated in **Figure 9A** and shown in **Figures 9B,C**. As the exterior heat loss coefficient increases, the exterior heat losses are enhanced through the undesirable heat conducting paths. These heat losses result in a drop in the temperature in the system. The change in temperature becomes significant at high exterior heat loss coefficients. The underlying cause is due to the high aspect ratio of the system. When the exterior heat loss coefficient is high, a considerable amount of heat supplied by combustion is dissipated to the surroundings, which could eventually lead to unsatisfactory operation or even failure. At sufficiently high heat-loss conditions, the temperature of the flame becomes sufficiently low that the rate of heat losses to the surroundings exceeds the release rate of combustion heat and the flame can no longer sustain itself within the system. This condition is referred to as the extinction limit of the flame and provides a higher boundary for the exterior heat loss coefficient. The critical exterior heat loss coefficient at which the flame cannot propagate within the system is dependent on several factors, such as the equivalence ratio of the mixture, the thermal conductivity of the solid material, and the flow velocity of the fluid. When a set of specified values are assumed for these factors, the critical exterior heat loss coefficient can be accurately determined. For example, the critical exterior heat loss coefficient is 97 $W/(m^2 \cdot K)$ for the system, when the system is designed in stoichiometric operation, the thermal conductivity is 1.4 W/(m·K) for the solid material, and the flow velocity of the fluid is 0.3 m/s at the flow inlet. The system usually operates dangerously near to the extinction limit. However, the disadvantage associated with the significant heat losses from the system can be fully avoided by the use of a solid material that has anisotropic thermal conductivity. For example, undesirable heat losses are effectively reduced by reducing the transverse thermal conductivity but increasing the longitudinal thermal conductivity, as discussed above.

The reaction rate profiles along the fluid centerline are presented in **Figure 10** under different exterior heat loss conditions. When the exterior heat loss coefficient is low, a desirably high reaction rate level is maintained within the system and the system is capable of dissipating only a small

amount of heat. As the exterior heat loss coefficient increases, the rate of the combustion reaction falls rapidly and the occurring heat losses increase significantly. In the present study, the exterior heat loss coefficient can be equal to or less than 80 W/(m^2·K) without causing the combustion reaction to be quenched, which is higher than that the critical exterior heat loss coefficient determined for a similar system but without cavities (Norton and Vlachos, 2003; Norton and Vlachos, 2004). This is because the utilization of cavities can enhance heat and mass transfer (Wan et al., 2015; Fan et al., 2018; Linhong Li et al., 2019; Zhang et al., 2020a; Zhang et al., 2020b; Xu et al., 2021), thereby providing substantially increased stability for the flame. The system designed with cavities makes possible an operation with very high heat losses, in comparison with that designed without cavities. In the practical design, it is desired to maximize the rate of the combustion reaction without quenching the reaction (Westbrook et al., 1981; Bradley et al., 2020). As the system approaches extinction, the maximum reaction rate decreases, but the reaction region does not shift downstream and is not widely expanded spatially, as shown in **Figure 10**. Interestingly, the location of the flame also does not move downstream with increasing the exterior heat loss coefficient, as illustrated in **Figure 9A**. At a sufficiently high exterior heat loss coefficient, the combustion reaction is quenched, but without leaving the system. Unstable combustion conditions resulting from serious heat losses can be substantially reduced or eliminated by using a solid material that has anisotropic thermal conductivity, as discussed above. This advantageously facilitates the use of the solid material.

Effect of Flow Velocity

Operation conditions in the system are normally dictated by power requirements, which are limited by inlet conditions, such as the flow velocity of the fluid at the flow inlet. The effect of flow velocity is evaluated while maintaining a constant equivalence ratio of the mixture at the flow inlet. The contour plots of temperature and methane concentration in the system are presented in **Figures 11A,B**, respectively, under different inlet flow velocity conditions. Accordingly, the temperature along the fluid centerline is plotted in **Figure 11C** against the streamwise distance at different inlet flow velocity conditions.

The flow velocity plays a significant role in determining the location of the reaction region in the system. As the flow velocity increases, the location of the flame moves downstream significantly, as illustrated in **Figures 11A,B** and shown in **Figure 11C**. The flame is preferentially located as close as possible to the cavities, because vortex breakdown occurs just downstream of the cavities (Krishna and Ravikrishna, 2015; Aravind and Deepu, 2020), thereby enabling flame holding to be achieved in the system. An important metric taken into consideration within the system is the flame which remains stable over a range of flow velocities. At high flow velocities, the flame may blow out of the system, so that no flame exists. The problem of blowout limits the allowable flow velocities in the system. For the system, proper selection of the flow velocity shifts the flame location away from blowout, thereby allowing operation of the system at the desired stable region. The system makes impossible an operation with very high flow velocities, as it usually operates dangerously near to the blowout limit of the flame. Additionally, the front of the flame is widely expanded spatially, as illustrated in **Figures 11A,B**, and the flame is therefore unstable. Consequently, a high flow velocity is to be avoided in order to ensure a stable operation for the system. Care has to be taken here that the flow velocity of the fluid is not too high, so that the flame does not blow out of the system, which is essential for the function of the system.

The conversion of methane at the flow outlet is plotted in **Figure 12A** against the flow velocity of the fluid at the flow inlet. High flow velocities can lead to sub-optimum combustion. This in turn can be related to, for example, incomplete combustion resulting in poor efficiency, as shown in **Figure 12A**. A flow velocity less than 0.5 m/s at the flow inlet ensures good operation performance for the system. Blowout is a particular concern when high flow rates are attempted. The problem of flame blowout has become increasingly severe over a variety of systems (Chang et al., 2020; Wan and Zhao, 2020d), since they are required to achieve better performance and meet severe operability constraints. The reaction rate profiles along the fluid centerline are presented in **Figure 12B** under different inlet flow velocity conditions. When the flow velocity of the fluid is 0.7 m/s at the flow inlet, the position of the maximum reaction rate approaches closely to the flow outlet, and the flame may blow out of the system. The blowout limit is of major importance in operating the system. At flow velocities higher than 0.7 m/s at the flow inlet, stable combustion cannot be achieved in the system. It is therefore not desirable to operate the system in this regime. The rate of the combustion reaction is plotted in **Figure 12C** against the streamwise distance at different transverse distances. The reaction rate approaching to the interior walls is much higher than that in the other regions, and the cavities have a positive effect on the rate of the combustion reaction. Interestingly, the cavity structure results in reaction rate fluctuations under the operation conditions. These reaction rate fluctuations may create significant problems for the operation of the system.

Effect of Equivalence Ratio

The system can be designed for equivalence ratios significantly less or greater than unity. However, the operation of the system is required within the normal limits of flame stability. Methane is therefore present within the fuel-air mixture between the lean flammability limit and the rich flammability limit, and the overall combustion stoichiometry is varied accordingly. The contour plots of temperature in the system are presented in **Figure 13A** under different equivalence ratio conditions. Accordingly, the temperature profiles along the fluid centerline and on the exterior walls are presented in **Figures 13B,C**, respectively, under different equivalence ratio conditions.

Combustion cannot occur or be sustained when the equivalence ratio is 0.2, but the fuel is flammable in the system for equivalence ratios greater than or equal to 0.4, as illustrated in **Figure 13A**. However, methane can be admixed with a larger amount of air so as to maintain the desired flame temperature in the system, for example, equivalence ratios less than or equal to 0.8. In this case, the flame temperature is reduced, and in particular, thermal production of nitrogen oxides is minimal (Miller and Bowman, 1989; Bowman,

1992). At the lower flame temperatures, however, flame stability becomes problematic, as the rate of reaction may be insufficient to prevent localized or global extinction. To increase the temperature, the combustion reaction of methane with air can be enhanced by increasing fuel lean stoichiometry close to the stoichiometric value. More specifically, the temperature increases with increasing the equivalence ratio of the mixture from 0.4 to unity, as shown in **Figures 13B,C**. A fuel-rich or sub-stoichiometric mixture contains less air than the amount theoretically required for complete combustion, and therefore has an equivalence ratio of greater than unity. Lower temperatures are obtained, when the mixture to be combusted is sub-stoichiometric. However, a fuel-rich mixture will make the use of the system absurd due to the increased noxious emissions (Kennedy et al., 2000; Song et al., 2003). Preferentially, the system is designed in stoichiometric operation, because a significantly higher temperature can be reached. Specifically, the maximum temperature occurs at near stoichiometric conditions, as shown in **Figures 13B,C**. The amount of air provided can consume all the fuel completely at an equivalence ratio of unity. As the equivalence ratio of the mixture becomes less than or exceeds unity, the maximum temperature decreases. For example, the maximum temperature is decreased by adding excess air. The maximum temperature becomes sufficiently low under sufficiently fuel-lean conditions, for example, at an equivalence ratio of 0.5. In this case, the rate of heat losses to the surroundings exceeds the release rate of combustion heat and the flame can no longer sustain itself within the system. This condition is referred to as the extinction limit of the flame.

Effect of Channel Height

The system is designed in stoichiometric operation, because an equivalence ratio of unity is the most reactive mixture composition. In order for flame holding to occur, a low flow velocity profile is specified at the flow inlet. The effect of channel dimensions is evaluated to ensure the stable operation of the system and to determine the quenching distance. The contour plots of temperature and methane concentration in the system are presented in **Figures 14A,B**, respectively, under different channel height conditions. The channel height is the spacing distance between the two parallel plates, which is the characteristic length of the system. The channel height varies from 2.0 to 5.0 mm to determine the quenching distance while maintaining a constant thickness of the channel walls. Similarly, the flow rate varies depending upon the channel height while maintaining a constant flow velocity of the fluid at the flow inlet.

As the spacing distance increases, the location of the flame moves towards the channel walls, as illustrated in **Figures 14A,B**. This is because a portion of heat of reaction during the combustion process is transferred to the upstream structure of the system by heat conduction through the channel walls, as discussed above. As the spacing distance increases, the maximum temperature decreases, as illustrated in **Figure 14A**, and incomplete combustion occurs within the system, as illustrated in **Figure 14B**. The length scale of the system is small enough in the transverse direction, when the spacing distance is small. As a result, the heat transfer in the transverse direction greatly affects the temperature profile along the fluid centerline. In this case, the temperature of the fluid is higher than that when the spacing distance is large, and combustion is nearly complete within the system.

As the spacing distance is decreased to 2.7 mm, the flame is very unstable. As the spacing distance is further decreased to 2.5 mm, the flame cannot be sustained and flame extinction typically occurs. Therefore, the quenching distance takes 2.5 mm for the system, which is in consistence with that determined by the experiments, as described above. To make the system operate effectively, there is a need to restrict the channel dimensions above the quenching distance. The flame cannot be sustained when the system operates near the extinction limit. As the spacing distance decreases below the quenching distance, flame propagation is impossible within the millimeter-scale system due to thermal and radical quenching (Jarosiński, 1983; Jarosinski, 1986). The high surface to volume ratio of the system will serve to inherently suppress or partially quench the flame (Popp et al., 1996; Bai et al., 2013). In contrast, the two trapezoidal cavities might mitigate influences of thermal and radical quenching. However, the results presented above indicate that the cavity structure has little effect on the quenching distance.

CONCLUSION

This study was focused mainly upon the essential combustion characteristics of methane-air mixtures in millimeter-scale systems with a cavity structure. Combustion characteristics and system performance were investigated both experimentally and numerically. Stable temperature profiles were obtained from thermographic measurements. Detailed kinetics were used for modeling the system in computational fluid dynamics. Numerical simulations were performed to better understand the stabilization mechanism of a flame within spaces with extremely small dimensions. Of particular concern were the essential factors for design considerations of the millimeter-scale systems with improved flame stability and combustion characteristics. The following major conclusions can be drawn from this study.

- The quenching distance of the methane flame is 2.5 mm for the systems with a cavity structure, which is slightly larger than commonly believed. The cavity structure has little effect on the quenching distance.
- However, the utilization of cavities can improve the efficiency and performance of the systems considerably, including flame stability and temperatures.
- The cavity structure will lead to a wider operating range in terms of the lean and rich flammability limits, with improved flame stability.
- The length scale of the systems plays a vital role in stabilizing the flame within spaces with extremely small dimensions.
- The thermal conductivity of the solid material has a significant effect on the efficiency and performance of the systems. The solid material is advantageously thermally

conductive to permit a high wall temperature with more uniform distribution. The solid material with anisotropic thermal conductivity prevents transverse heat losses but allows longitudinal heat conduction, thereby further improving efficiency and performance for the systems.

- Unstable combustion conditions resulting from serious heat losses can be substantially reduced or eliminated by using a solid material that has anisotropic thermal conductivity. This design has great advantages in improving the efficiency and performance of the systems.
- The flow velocity of the fluid is an important factor affecting the efficiency and performance of the systems. stable combustion is restricted to a relatively narrow range of flow velocities.
- There is necessity of maintaining the fuel-to-air equivalence ratio in the flammable range, and consequently loss of flame stability due to variations in the fuel-to-air equivalence ratio can cause serious problems. Preferentially, the systems are designed in stoichiometric operation.

DATA AVAILABILITY STATEMENT

The raw data supporting the conclusion of this article will be made available by the authors, without undue reservation.

AUTHOR CONTRIBUTIONS

JC contributed to conception and design of the study. JC and TL developed the model and performed the analysis. JC wrote the manuscript. All authors read and approved the submitted version.

FUNDING

This work was supported by the National Natural Science Foundation of China (No. 51506048).

REFERENCES

Abdallah, M. S., Mansour, M. S., and Allam, N. K. (2021). Mapping the Stability of Free-Jet Biogas Flames under Partially Premixed Combustion. *Energy* 220, 119749. doi:10.1016/j.energy.2020.119749

ANSYS (2018). *ANSYS FLUENT User's Guide*. Release 19.2. Canonsburg, Pennsylvania, United States: ANSYS Inc.

Aravind, G. P., and Deepu, M. (2020). Numerical Studies on Convective Mass Transfer Augmentation in High-Speed Flows with Lateral Sweep Vortex Generator and Dimple Cavity. *Int. J. Therm. Sci.* 153, 106379. doi:10.1016/j.ijthermalsci.2020.106379

ASTM International (2016). *ASTM E681-09(2015). Standard Test Method for Concentration Limits of Flammability of Chemicals (Vapors and Gases)*. West Conshohocken, Pennsylvania, United States: ASTM International. ICS Code: 13.300. doi:10.1520/E0681-09R15

ASTM International (2021). *ASTM E582-21. Standard Test Method for Minimum Ignition Energy and Quenching Distance in Gaseous Mixtures*. West Conshohocken, Pennsylvania, United States: ASTM International. ICS Code: 71.100.20. doi:10.1520/E0582-21

Bai, B., Chen, Z., Zhang, H., and Chen, S. (2013). Flame Propagation in a Tube with wall Quenching of Radicals. *Combust. Flame* 160 (12), 2810–2819. doi:10.1016/j.combustflame.2013.07.008

Bowman, C. T. (1992). Control of Combustion-Generated Nitrogen Oxide Emissions: Technology Driven by Regulation. *Symp. (International) Combust.* 24 (1), 859–878. doi:10.1016/s0082-0784(06)80104-9

Bradley, D., Shehata, M., Lawes, M., and Ahmed, P. (2020). Flame Extinctions: Critical Stretch Rates and Sizes. *Combust. Flame* 212, 459–468. doi:10.1016/j.combustflame.2019.11.013

Broda, J. C., Seo, S., Santoro, R. J., Shirhattikar, G., and Yang, V. (1998). An Experimental Study of Combustion Dynamics of a Premixed Swirl Injector. *Symp. (International) Combust.* 27 (2), 1849–1856. doi:10.1016/s0082-0784(98)80027-1

Bychkov, V. V., and Liberman, M. A. (2000). Dynamics and Stability of Premixed Flames. *Phys. Rep.* 325 (4-5), 115–237. doi:10.1016/s0370-1573(99)00081-2

Cam, O., Yilmaz, H., Tangoz, S., and Yilmaz, I. (2017). A Numerical Study on Combustion and Emission Characteristics of Premixed Hydrogen Air Flames. *Int. J. Hydrogen Energ.* 42 (40), 25801–25811. doi:10.1016/j.ijhydene.2017.07.017

Chang, L., Cao, Z., Fu, B., Lin, Y., and Xu, L. (2020). Lean Blowout Detection for bluff-body Stabilized Flame. *Fuel* 266, 117008. doi:10.1016/j.fuel.2020.117008

Char, J.-M., and Yeh, J.-H. (1996). The Measurement of Open Propane Flame Temperature Using Infrared Technique. *J. Quant. Spectrosc. Radiat. Transf.* 56 (1), 133–144.

Choi, J., Rajasegar, R., Mitsingas, C. M., Liu, Q., Lee, T., and Yoo, J. (2020). Effect of Flame Interaction on Swirl-Stabilized Mesoscale Burner Array Performance. *Energy* 2020, 116661. doi:10.1016/j.energy.2019.116661

Dunn-Rankin, D., Leal, E. M., and Walther, D. C. (2005). Personal Power Systems. *Prog. Energ. Combust. Sci.* 31 (5-6), 422–465. doi:10.1016/j.pecs.2005.04.001

El-Asrag, H., and Menon, S. (2007). Large Eddy Simulation of bluff-body Stabilized Swirling Non-premixed Flames. *Proc. Combust. Inst.* 31 (2), 1747–1754. doi:10.1016/j.proci.2006.07.251

Fan, A., Zhang, H., and Wan, J. (2017). Numerical Investigation on Flame Blow-Off Limit of a Novel Microscale Swiss-roll Combustor with a bluff-body. *Energy* 123, 252–259. doi:10.1016/j.energy.2017.02.003

Fan, A., Xiang, Y., Yang, W., and Li, L. (2018). Enhancement of Hydrogen Combustion Efficiency by Helium Dilution in a Micro-combustor with wall Cavities. *Chem. Eng. Process. Process Intensification* 130, 201–207. doi:10.1016/j.cep.2018.06.014

Fernandez-Pello, A. C. (2002). Micropower Generation Using Combustion: Issues and Approaches. *Proc. Combust. Inst.* 29 (1), 883–899. doi:10.1016/s1540-7489(02)80113-4

Fugger, C. A., Gallagher, T. P., Sykes, J. P., and Caswell, A. W. (2020). Spanwise Recirculation Zone Structure of a bluff Body Stabilized Flame. *Combust. Flame* 216, 58–61. doi:10.1016/j.combustflame.2020.02.002

Gatti, M., Gaudron, R., Mirat, C., Zimmer, L., and Schuller, T. (2019). Impact of Swirl and bluff-body on the Transfer Function of Premixed Flames. *Proc. Combust. Inst.* 37 (4), 5197–5204. doi:10.1016/j.proci.2018.06.148

Grib, S. W., Owens, T. C., and Renfro, M. W. (2020). Numerical Analysis of Flame Stabilization for a Steady Premixed Jet in Vitiated Coflow. *Combust. Flame* 221, 201–211. doi:10.1016/j.combustflame.2020.07.040

Gupta, A., Qadri, U. A., Koutita, K., Zadrazil, I., Hussain, T., Balachandran, R., et al. (2020). Experimental Investigation of the Flow in a Micro-channelled Combustor and its Relation to Flame Behaviour. *Exp. Therm. Fluid Sci.* 116, 110105. doi:10.1016/j.expthermflusci.2020.110105

Han, X., Laera, D., Yang, D., Zhang, C., Wang, J., Hui, X., et al. (2020). Flame Interactions in a Stratified Swirl Burner: Flame Stabilization, Combustion Instabilities and Beating Oscillations. *Combust. Flame* 212, 500–509. doi:10.1016/j.combustflame.2019.11.020

Hatem, F. A., Alsaegh, A. S., Al-Faham, M., Valera-Medina, A., Chong, C. T., and Hassoni, S. M. (2018). Enhancing Flame Flashback Resistance against Combustion Induced Vortex Breakdown and Boundary Layer Flashback in Swirl Burners. *Appl. Energ.* 230, 946–959. doi:10.1016/j.apenergy.2018.09.055

Huang, B., Li, H., Xia, S., and Xu, T. (2020). Experimental Investigation of the Flow and Heat Transfer Performance in Micro-channel Heat Exchangers with Cavities. *Int. J. Heat Mass Transfer* 159, 120075. doi:10.1016/j.ijheatmasstransfer.2020.120075

Jarosiński, J. (1983). Flame Quenching by a Cold wall. *Combust. Flame* 50, 167–175.

Jarosinski, J. (1986). A Survey of Recent Studies on Flame Extinction. *Prog. Energ. Combust. Sci.* 12 (2), 81–116. doi:10.1016/0360-1285(86)90014-6

Jeong, C., Bae, J., Kim, T., Yoon, J., Joo, S., and Yoon, Y. (2017). Investigation of Flashback Characteristics Coupled with Combustion Instability in Turbulent Premixed bluff Body Flames Using High-Speed OH-PLIF and PIV. *Proc. Combust. Inst.* 36 (2), 1861–1868. doi:10.1016/j.proci.2016.08.077

Jiaqiang, E., Ding, J., Chen, J., Liao, G., Zhang, F., and Luo, B. (2021). Process in Micro-combustion and Energy Conversion of Micro Power System: A Review. *Energ. Convers. Manage.* 246, 114664. doi:10.1016/j.enconman.2021.114664

Jiaqiang, E., Luo, B., Han, D., Chen, J., Liao, G., Zhang, F., et al. (2022). A Comprehensive Review on Performance Improvement of Micro Energy Mechanical System: Heat Transfer, Micro Combustion and Energy Conversion. *Energy* 239, 122509. doi:10.1016/j.energy.2021.122509

Ju, Y., and Maruta, K. (2011). Microscale Combustion: Technology Development and Fundamental Research. *Prog. Energ. Combust. Sci.* 37 (6), 669–715. doi:10.1016/j.pecs.2011.03.001

Kaisare, N. S., and Vlachos, D. G. (2012). A Review on Microcombustion: Fundamentals, Devices and Applications. *Prog. Energ. Combust. Sci.* 38 (3), 321–359. doi:10.1016/j.pecs.2012.01.001

Kang, D. G., Ko, H., Koo, J., Lim, S. I., Kim, J. S., Yu, Y. T., et al. (2018). Anisotropic thermal Interface Materials: Directional Heat Transfer in Uniaxially Oriented Liquid crystal Networks. *ACS Appl. Mater. Inter.* 10 (41), 35557–35562. doi:10.1021/acsami.8b09982

Kennedy, L. A., Bingue, J. P., Saveliev, A. V., Fridman, A. A., and Foutko, S. I. (2000). Chemical Structures of Methane-Air Filtration Combustion Waves for Fuel-Lean and Fuel-Rich Conditions. *Proc. Combust. Inst.* 28 (1), 1431–1438. doi:10.1016/s0082-0784(00)80359-8

Khateeb, A. A., Guiberti, T. F., Zhu, X., Younes, M., Jamal, A., and Roberts, W. L. (2020). Stability Limits and NO Emissions of Technically-Premixed Ammonia-Hydrogen-Nitrogen-Air Swirl Flames. *Int. J. Hydrogen Energ.* 45 (41), 22008–22018. doi:10.1016/j.ijhydene.2020.05.236

Khateeb, A. A., Guiberti, T. F., Wang, G., Boyette, W. R., Younes, M., Jamal, A., et al. (2021). Stability Limits and NO Emissions of Premixed Swirl Ammonia-Air Flames Enriched with Hydrogen or Methane at Elevated Pressures. *Int. J. Hydrogen Energ.* 46 (21), 11969–11981. doi:10.1016/j.ijhydene.2021.01.036

Kim, K. T., and Santavicca, D. A. (2013). Interference Mechanisms of Acoustic/convective Disturbances in a Swirl-Stabilized Lean-Premixed Combustor. *Combust. Flame* 160 (8), 1441–1457. doi:10.1016/j.combustflame.2013.02.022

Krishna, S., and Ravikrishna, R. V. (2015). Optical Diagnostics of Fuel-Air Mixing and Vortex Formation in a Cavity Combustor. *Exp. Therm. Fluid Sci.* 61, 163–176. doi:10.1016/j.expthermflusci.2014.10.012

Li, L., Yang, W., and Fan, A. (2019). Effect of the Cavity Aft Ramp Angle on Combustion Efficiency of Lean Hydrogen/air Flames in a Micro Cavity-Combustor. *Int. J. Hydrogen Energ.* 44 (11), 5623–5632. doi:10.1016/j.ijhydene.2018.07.162

Maruta, K. (2011). Micro and Mesoscale Combustion. *Proc. Combust. Inst.* 33 (1), 125–150. doi:10.1016/j.proci.2010.09.005

Mendiburu, A. Z., de Carvalho, J. A., Coronado, C. R., and Roberts, J. J. (2017). Flammability Limits Temperature Dependence of Pure Compounds in Air at Atmospheric Pressure. *Energy* 118, 414–424. doi:10.1016/j.energy.2016.12.036

Michaels, D., and Ghoniem, A. F. (2018). Leading Edge Dynamics of Lean Premixed Flames Stabilized on a bluff Body. *Combust. Flame* 191, 39–52. doi:10.1016/j.combustflame.2017.12.020

Miller, J. A., and Bowman, C. T. (1989). Mechanism and Modeling of Nitrogen Chemistry in Combustion. *Prog. Energ. Combust. Sci.* 15 (4), 287–338. doi:10.1016/0360-1285(89)90017-8

Morales, A. J., Lasky, I. M., Geikie, M. K., Engelmann, C. A., and Ahmed, K. A. (2019). Mechanisms of Flame Extinction and Lean Blowout of bluff Body Stabilized Flames. *Combust. Flame* 203, 31–45. doi:10.1016/j.combustflame.2019.02.002

Norton, D. G., and Vlachos, D. G. (2003). Combustion Characteristics and Flame Stability at the Microscale: a CFD Study of Premixed Methane/air Mixtures. *Chem. Eng. Sci.* 58 (21), 4871–4882. doi:10.1016/j.ces.2002.12.005

Norton, D. G., and Vlachos, D. G. (2004). A CFD Study of Propane/air Microflame Stability. *Combust. Flame* 138 (1-2), 97–107. doi:10.1016/j.combustflame.2004.04.004

Pan, M., Wang, H., Zhong, Y., Hu, M., Zhou, X., Dong, G., et al. (2019). Experimental Investigation of the Heat Transfer Performance of Microchannel Heat Exchangers with Fan-Shaped Cavities. *Int. J. Heat Mass Transfer* 134, 1199–1208. doi:10.1016/j.ijheatmasstransfer.2019.01.140

Panda, P. P., Busari, O., Roa, M., and Lucht, R. P. (2019). Flame Stabilization Mechanism in Reacting Jets in Swirling Vitiated Crossflow. *Combust. Flame* 207, 302–313. doi:10.1016/j.combustflame.2019.06.005

Pashchenko, D. (2017). Comparative Analysis of Hydrogen/air Combustion CFD-Modeling for 3D and 2D Computational Domain of Micro-cylindrical Combustor. *Int. J. Hydrogen Energ.* 42 (49), 29545–29556. doi:10.1016/j.ijhydene.2017.10.070

Pashchenko, D. (2020). Hydrogen-rich Fuel Combustion in a Swirling Flame: CFD-Modeling with Experimental Verification. *Int. J. Hydrogen Energ.* 45 (38), 19996–20003. doi:10.1016/j.ijhydene.2020.05.113

Peng, Q., Wu, Y., Jiaqiang, E., Yang, W., Xu, H., and Li, Z. (2019). Combustion Characteristics and thermal Performance of Premixed Hydrogen-Air in a Two-rearward-step Micro Tube. *Appl. Energ.* 242, 424–438. doi:10.1016/j.apenergy.2019.03.137

Popp, P., Smooke, M., and Baum, M. (1996). Heterogeneous-homogeneous Reaction and Transport Coupling during Flame-wall Interaction. *Symp. (International) Combust.* 26 (2), 2693–2700. doi:10.1016/s0082-0784(96)80105-6

Li, Q., Li, J., Shi, J., and Guo, Z. (2019). Effects of Heat Transfer on Flame Stability Limits in a Planar Micro-combustor Partially Filled with Porous Medium. *Proc. Combust. Inst.* 37 (4), 5645–5654. doi:10.1016/j.proci.2018.06.023

Sakurai, T., Yuasa, S., Honda, T., and Shimotori, S. (2009). Heat Loss Reduction and Hydrocarbon Combustion in Ultra-micro Combustors for Ultra-micro Gas Turbines. *Proc. Combust. Inst.* 32 (2), 3067–3073. doi:10.1016/j.proci.2008.06.002

Schmidt, H. (1909). Prüfung der strahlungsgesetze der bunsenflamme. *Annalen der Physik* 334 (10), 971–1028. doi:10.1002/andp.19093341008

Shanbhogue, S. J., Husain, S., and Lieuwen, T. (2009). Lean Blowoff of bluff Body Stabilized Flames: Scaling and Dynamics. *Prog. Energ. Combust. Sci.* 35 (1), 98–120. doi:10.1016/j.pecs.2008.07.003

Smith, G. P., Golden, D. M., Frenklach, M., Moriarty, N. W., Eiteneer, B., Goldenberg, M., et al. (2000). *GRI-MECH 3.0*. Chicago, Illinois, United States: The Gas Research Institute.

Song, K. H., Nag, P., Litzinger, T. A., and Haworth, D. C. (2003). Effects of Oxygenated Additives on Aromatic Species in Fuel-Rich, Premixed Ethane Combustion: A Modeling Study. *Combust. Flame* 135 (3), 341–349. doi:10.1016/s0010-2180(03)00180-9

Tian, X., Itkis, M. E., Bekyarova, E. B., and Haddon, R. C. (2013). Anisotropic thermal and Electrical Properties of Thin thermal Interface Layers of Graphite Nanoplatelet-Based Composites. *Scientific Rep.* 3 (1), 1710. doi:10.1038/srep01710

Tong, Y., Liu, X., Wang, Z., Richter, M., and Klingmann, J. (2018). Experimental and Numerical Study on bluff-body and Swirl Stabilized Diffusion Flames. *Fuel* 217, 352–364. doi:10.1016/j.fuel.2017.12.061

Walther, D. C., and Ahn, J. (2011). Advances and Challenges in the Development of Power-Generation Systems at Small Scales. *Prog. Energ. Combust. Sci.* 37 (5), 583–610. doi:10.1016/j.pecs.2010.12.002

Wan, J., and Fan, A. (2021). Recent Progress in Flame Stabilization Technologies for Combustion-Based Micro Energy and Power Systems. *Fuel* 286, 119391. doi:10.1016/j.fuel.2020.119391

Wan, J., and Zhao, H. (2020). Effect of thermal Condition of Solid wall on the Stabilization of a Preheated and Holder-Stabilized Laminar Premixed Flame. *Energy* 200, 117548. doi:10.1016/j.energy.2020.117548

Wan, J., and Zhao, H. (2020). Anomalous Blow-Off Limit of Methane-Air Premixed Flame in a Micro Preheated Combustor with a Flame Holder. *Int. J. Hydrogen Energ.* 45 (55), 31202–31212. doi:10.1016/j.ijhydene.2020.08.130

Wan, J., and Zhao, H. (2020). Blow-off Mechanism of a Holder-Stabilized Laminar Premixed Flame in a Preheated Mesoscale Combustor. *Combust. Flame* 220, 358–367. doi:10.1016/j.combustflame.2020.07.012

Wan, J., and Zhao, H. (2020). Blowout Limit of Premixed Flame in a Micro Preheated Combustor with a Flame Holder at Different Blockage Ratios. *Int. J. Hydrogen Energ.* 45 (46), 25468–25478. doi:10.1016/j.ijhydene.2020.06.257

Wan, J., Fan, A., Yao, H., and Liu, W. (2015). Effect of thermal Conductivity of Solid wall on Combustion Efficiency of a Micro-combustor with Cavities. *Energ. Convers. Manage.* 96, 605–612. doi:10.1016/j.enconman.2015.03.030

Wan, J., Song, J., Yang, Z., Kirsch, D., Jia, C., Xu, R., et al. (2017). Highly Anisotropic Conductors. *Adv. Mater.* 29 (41), 1703331. doi:10.1002/adma.201703331

Wang, S., and Fan, A. (2021). Combustion Regimes of Syngas Flame in a Micro Flow Reactor with Controlled Temperature Profile: A Numerical Study. *Combust. Flame* 230, 111457. doi:10.1016/j.combustflame.2021.111457

Wang, H., Ding, D., Liu, Q., Chen, Y., and Zhang, Q. (2019). Highly Anisotropic Thermally Conductive Polyimide Composites via the Alignment of boron Nitride Platelets. *Compos. B Eng.* 158, 311–318. doi:10.1016/j.compositesb.2018.09.104

Wang, M., Li, P., and Wang, F. (2020). Dependence of the Blowout Limit on Flow Structure, Heat Transfer, and Pressure Loss in a bluff-body Micro-combustor. *Int. J. Hydrogen Energ.* 45 (38), 19912–19925. doi:10.1016/j.ijhydene.2020.04.113

Wang, D., Qian, X., Ji, T., Jing, Q., Zhang, Q., and Yuan, M. (2021). Flammability Limit and Explosion Energy of Methane in Enclosed Pipeline under Multi-phase Conditions. *Energy* 217, 119355. doi:10.1016/j.energy.2020.119355

Westbrook, C. K., Adamczyk, A. A., and Lavoie, G. A. (1981). A Numerical Study of Laminar Flame wall Quenching. *Combust. Flame* 40, 81–99. doi:10.1016/0010-2180(81)90112-7

Westbrook, C. K., Mizobuchi, Y., Poinsot, T. J., Smith, P. J., and Warnatz, J. (2005). Computational Combustion. *Proc. Combust. Inst.* 30 (1), 125–157. doi:10.1016/j.proci.2004.08.275

Xu, F., Yan, Y., He, Z., Yang, Z., and Zhang, L. (2021). Numerical Study on the Influence of Controllable Flow Ratio on Combustion Characteristics of a Controllable central Slotted bluff Body and Cavity Combined Micro Combustor. *Int. J. Hydrogen Energ.* 46 (9), 6901–6914. doi:10.1016/j.ijhydene.2020.11.117

Yakovenko, I. S., and Kiverin, A. D. (2021). Intensification Mechanisms of the Lean Hydrogen-Air Combustion via Addition of Suspended Micro-droplets of Water. *Int. J. Hydrogen Energ.* 46 (1), 1259–1272. doi:10.1016/j.ijhydene.2020.09.234

Yan, Y., Wu, G., Huang, W., Zhang, L., Li, L., and Yang, Z. (2019). Numerical Comparison Study of Methane Catalytic Combustion Characteristic between Newly Proposed Opposed Counter-flow Micro-combustor and the Conventional Ones. *Energy* 170, 403–410. doi:10.1016/j.energy.2018.12.114

Yang, X., Zhao, L., He, Z., Dong, S., and Tan, H. (2019). Comparative Study of Combustion and thermal Performance in a Swirling Micro Combustor under Premixed and Non-premixed Modes. *Appl. Therm. Eng.* 160, 114110. doi:10.1016/j.applthermaleng.2019.114110

Yilmaz, H., Cam, O., and Yilmaz, I. (2017). Effect of Micro Combustor Geometry on Combustion and Emission Behavior of Premixed Hydrogen/air Flames. *Energy* 135, 585–597. doi:10.1016/j.energy.2017.06.169

Yilmaz, H., Cam, O., and Yilmaz, I. (2020). A Comparison Study on Combustion and Emission Characteristics of Actual Synthetic Gas Mixtures. *Fuel* 263, 116712. doi:10.1016/j.fuel.2019.116712

Yilmaz, H. (2019). Investigation of Combustion and Emission Performance of a Micro Combustor: Effects of bluff Body Insertion and Oxygen Enriched Combustion Conditions. *Int. J. Hydrogen Energ.* 44 (47), 25985–25999. doi:10.1016/j.ijhydene.2019.08.045

Zangeneh, V., and Alipoor, A. (2021). Stability Study of Hydrogen-Air Flame in a Conical Porous Burner. *Energy* 215, 119140. doi:10.1016/j.energy.2020.119140

Zhang, Z., Wu, K., Yuen, R., Yao, W., and Wang, J. (2020). Numerical Investigation on the Performance of bluff Body Augmented Micro Cavity-Combustor. *Int. J. Hydrogen Energ.* 45 (7), 4932–4945. doi:10.1016/j.ijhydene.2019.12.004

Zhang, Z., Wu, K., Yao, W., Yuen, R., and Wang, J. (2020). Enhancement of Combustion Performance in a Microchannel: Synergistic Effects of bluff-body and Cavity. *Fuel* 265, 116940. doi:10.1016/j.fuel.2019.116940

Zhao, M., and Fan, A. (2020). Buoyancy Effects on Hydrogen Diffusion Flames Confined in a Small Tube. *Int. J. Hydrogen Energ.* 45 (38), 19926–19935. doi:10.1016/j.ijhydene.2020.05.010

Zuo, W., Jiaqiang, E., and Han, D. (2018). Numerical Investigations on an Improved Counterflow Double-Channel Micro Combustor Fueled with Hydrogen for Enhancing thermal Performance. *Energ. Convers. Manage.* 159, 163–174. doi:10.1016/j.enconman.2018.01.017

Conflict of Interest: The authors declare that the research was conducted in the absence of any commercial or financial relationships that could be construed as a potential conflict of interest.

Publisher's Note: All claims expressed in this article are solely those of the authors and do not necessarily represent those of their affiliated organizations, or those of the publisher, the editors and the reviewers. Any product that may be evaluated in this article, or claim that may be made by its manufacturer, is not guaranteed or endorsed by the publisher.

frontiers in Energy Research

ORIGINAL RESEARCH
published: 07 March 2022
doi: 10.3389/fenrg.2022.854019

Unsteady Motion of Shock Wave for a Supersonic Compression Ramp Flow Based on Large Eddy Simulation

Xing Huang[1], *Li-Xu Wang*[2], *Dong-Dong Zhong*[2] *and Ning Ge*[2]*

[1]AECC HUNAN Aviation Powerplant Research Institute, Zhuzhou, China, [2]Nanjing University of Aeronautics and Astronautics, Nanjing, China

A large eddy simulation (LES) is conducted to investigate shock wave/turbulent boundary layer interaction in a 24° compression ramp at a high inlet Mach number of *Ma* = 2.9. The recycling/rescaling Method is used as the inflow turbulence generation technique. The shock wave structure and boundary layer flow in the interaction region are studied by flow visualization methods, such as vortex recognition and numerical schlieren. The distributions of turbulent kinetic energy and Reynolds normal stresses at different streamwise locations are analyzed. The results show that a strong anisotropy turbulent flow appears in the reattached boundary layer after the interaction of the shock wave. The large-scale unsteady motion of the separation shock wave is analyzed by using the intermittent factor and power spectrum. It is found that the shock moves around the averaged separation position, and the length scale is equal to 72% of the inlet boundary layer thickness. The power spectrum analysis reveals the existence of low-frequency instability in the separation region.

Keywords: shock wave/turbulent boundary layer interaction, large eddy simulation (LES), low-frequency instability, Görtler-like vortex, power spectrum analysis (PSA)

OPEN ACCESS

Edited by:
Lei Luo,
Harbin Institute of Technology, China

Reviewed by:
Fangfei Ning,
Beihang University, China
Hu Wu,
Northwestern Polytechnical University, China

***Correspondence:**
Ning Ge
gening@nuaa.edu.cn

Specialty section:
This article was submitted to Advanced Clean Fuel Technologies, a section of the journal Frontiers in Energy Research

Received: *13 January 2022*
Accepted: *10 February 2022*
Published: *07 March 2022*

Citation:
Huang X, Wang L-X, Zhong D-D and Ge N (2022) Unsteady Motion of Shock Wave for a Supersonic Compression Ramp Flow Based on Large Eddy Simulation. Front. Energy Res. 10:854019. doi: 10.3389/fenrg.2022.854019

1 INTRODUCTION

The shock wave/turbulent boundary layer interaction (SWBLI) is one of the important physical phenomena in the supersonic flow, which contains complex aerodynamic and thermodynamic problems. The interaction can significantly alter the heat conduction characteristics and produce a strong pressure fluctuation. Although the 2D compression ramp is a simple geometric model in the SWBLI, however the flow phenomena contain boundary layer unsteady flow, separation, reattached flow, and turbulent fluctuation enhancement caused by a strong adverse pressure gradient. The transient flow field presents a highly three-dimensional state (Lee and Wang 1995), and the multiscale interaction produces complex flow structures (Wang 2015). Thus, the simple 2D model is the best model for the validation of the computational fluid dynamics (CFD) method.

In the past, extensive research studies have been conducted on the SWBLI by experimental and numerical methods, but there are still some issues to be explored further. Dolling (Dolling 2001) considered that the low-frequency unsteady flow should be studied for the future in detail. Settles et al. (Settles et al., 1979) conducted a surface oil flow experiment on a compression ramp with an angle of 24°. It was found that the pattern of the "node-saddle point" is alternately arranged near the reattachment line downstream of the ramp, which proves the existence of the streamwise vortex. Smits and Muck (Smits and Muck 1987) used a hot wire anemometer to measure the compression ramp flow and studied the effects of turbulent fluctuation enhancement with three different angles of

the ramp. It was found that when the intensity of the shock wave is sufficiently strong, the unsteady motion of the shock wave will become important due to turbulent fluctuation enhancement. Ganapathisubramani et al. (Ganapathisubramani et al., 2007) used high-speed particle image velocimetry (PIV) technology to measure the compression ramp flow. It was found that the strip-like structures with different momentum exist in the upstream boundary layer, and these strip structures cause a low-frequency pulsation of the separation bubble. Wu et al. (Wu et al., 2013) used nano-tracer planar laser scattering (NPLS) technology to study the laminar/turbulent SWBLI on the supersonic compression ramp; the overall flow field was analyzed and local fine structures were identified.

Yi Zhuang et al. (Zhuang et al., 2018a) have performed an experimental investigation on a compression ramp shock wave/turbulent boundary layer interaction at $Ma = 2.83$. The ice cluster–based planar laser scattering technique was applied to acquire high spatiotemporal resolution images at the center plane. Two-dimensional slices of the coherent vertical structure (CVS) were acquired and extracted from these images with a machine learning–based method. By comparing the features CVS acquired before and after the interaction, the evolution of CVSs in the SWBLI flow was analyzed.

In fact, a large number of experimental studies were carried out at higher Reynolds numbers. But Bookey et al. (Bookey et al., 2005) selected a low-density gas as the working medium to reduce the Reynolds number in the experiment and achieve the numerical simulation (DNS, LES) comparison with experiments. Adams et al. (Adams 2000) used the DNS method to study the supersonic compression ramp flow and found that the Reynolds shear stress after the SWBLI increases more greatly than the Reynolds normal stress. Loginov et al. (Loginov et al., 2006) used the LES method to study the statistical parameter distributions and fluctuation characteristics of the turbulent boundary layer in the compression ramp and compared numerical results with the experimental data. The flow field analysis showed that the large-scale three-dimensional flow structure downstream of the ramp is the principal reason for the spanwise unevenness of the flow field. Wu et al. (Wu and Martin 2008) used the DNS method to study the SWBLI in the compression ramp, with the inlet flow parameters consistent with the experimental conditions given by Bookey et al. (Bookey et al., 2005). By observing the spatiotemporal evolution and using the correlation analysis of the flow field, it was found that the shock wave motion always lags behind the pulsation of the separation bubble. Therefore, a "feedback loop" model consisting of the separation bubble, shear layer, and shock wave system is proposed to explain the mechanism of the low-frequency unsteady motion of the shock wave.

Kenzo S.et al. (Sasaki et al., 2021) have investigated the mechanisms of low-frequency unsteadiness in an impinging shock wave/turbulent boundary layer interaction at a Mach number of $Ma = 2$. The Strouhal number $St = fL/U_\infty$ was used for the space-time spectral analysis to identify the key features of the shock motion, where L is defined as the interaction length and f is the frequency of fluctuation. The dominant frequency in the vicinity of the shock was exhibited by the streamwise evolution of the pre-multiplied spectrum of pressure fluctuations. In the upstream boundary layer, the spectrum presents mainly high-frequency content ($St > 1$) linked to the incoming turbulent eddies. However, in the vicinity of the shock position, a low-frequency broadband range emerges and is centered approximately at $St = 0.03$. As the author pointed out, the large gap between these frequency scales has been reported in previous investigations by Touber and Sandham (Touber and Sandham 2011) and Dupont et al. (Dupont et al., 2006).

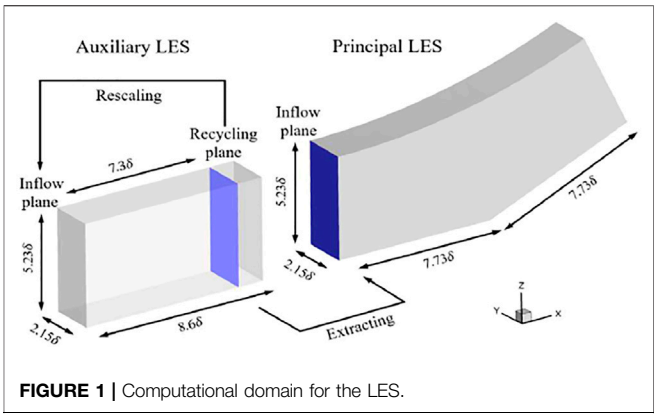

FIGURE 1 | Computational domain for the LES.

In this study, a large eddy simulation is used to study the SWBLI phenomenon of the 24° compression ramp; detailed analysis and discussion are carried out to understand the unsteady features of the shock wave in the SWBLI. The remainder of this manuscript is organized as follows. Section 2 gives a description of the numerical methods and techniques used in this study, including the generation of the inlet turbulent boundary layer, geometric model, and mesh distribution. Section 3 compares the simulation results with experiments and numerical results in the literature to verify the reliability of the program, and the details of the flow field are discussed and analyzed. The last section gives some conclusions of this study.

2 COMPRESSION RAMP AND NUMERICAL METHOD

The work in this study is based on the NUAA-Turbo CFD solver developed by our research group. In the large eddy simulation (LES), the finite volume method is used and the ROE scheme is used for the evaluation of convective fluxes, the WENO_ZQ scheme (Zhu and Qiu 2017) with fifth-order precision for the interface reconstruction, and the sixth-order central difference scheme for the spatial discretization of viscous fluxes. Time discretization uses the Runge–Kutta method with a total variation reduction property of third-order accuracy (Shu and Osher 1989). The dynamic sub-grid scale model is considered, and the sub-grid scale viscosity coefficient is determined with the two consecutive filtering by the method of Germano et al. (Germano 1991).

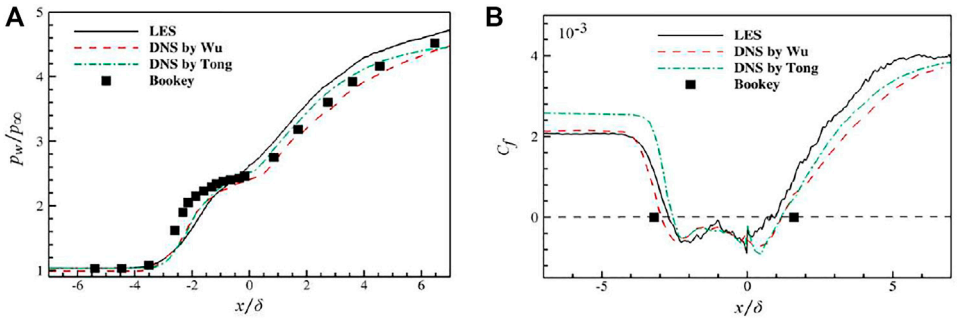

FIGURE 2 | Distribution of averaged wall pressure and skin friction coefficient. **(A)** Averaged wall pressure. **(B)** Averaged skin friction coefficient.

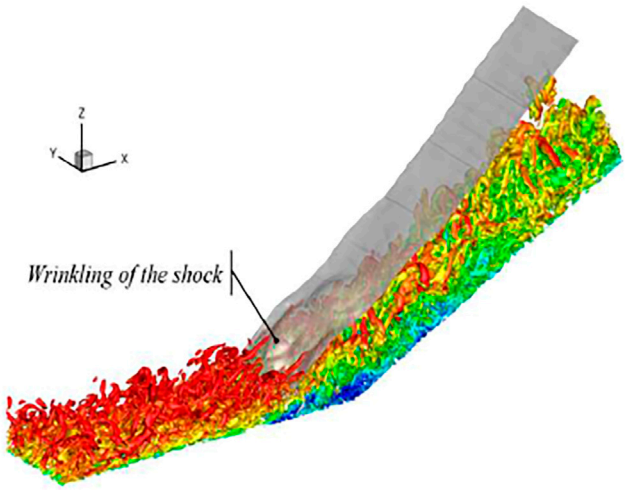

FIGURE 3 | Shock surface wrinkling.

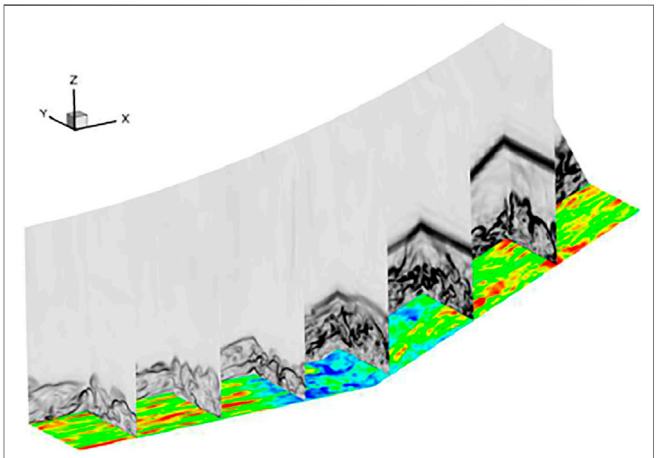

FIGURE 4 | Vortex structure in the interaction region.

The inlet boundary layer thickness δ of the compression ramp is used to make the length scale dimensionless. The computation domain consists of two parts: the flat plane computation domain (auxiliary computation domain) and the 24° compression ramp computation domain (primary computation domain). The "recycling/rescaling" method was used to generate the turbulent boundary layer in the auxiliary computation domain and the computed turbulence information as the inlet boundary condition of the primary computation domain. In the auxiliary computation, the distance from the inlet plane "7.3δ" is set as the recycled plane. The schematic of the computation domain is shown in **Figure 1**. The coordinate system origin is located at the ramp, and the coordinate axes "x, y, and z" indicate the streamwise, spanwise, and normal directions respectively. The upstream and downstream lengths of the ramp are both 7.73δ, the spanwise width is 2.15δ, and the normal height along the wall is 5.23δ. The number of grid points in the three directions is "505 × 89 × 112". The grid is evenly distributed in the spanwise and refined along the streamwise direction at the ramp and in the normal direction to guarantee $z^+ \approx 1$ in the first layer of the grid near the wall. The flow field of the recycled plane in the auxiliary computation domain is extracted as the inlet boundary condition for the primary computation. It is specially noted that when the primary/auxiliary computation domain uses grids of different resolutions, the process of flow field extraction needs to interpolate the variables. For details, this method can refer to Zhong et al., (2021).

For the primary computation domain, the upper boundary of the computational domain and the outlet are set to the subsonic outlet boundary condition. The wall condition of the non-slip isothermal is adopted to the wall, and the wall isothermal temperature is 307 K. The spanwise boundary adopts periodic boundary condition, and the inlet turbulent boundary conditions are dynamically given by the auxiliary computation. For the auxiliary computation, the boundary layer conditions are consistent with the main computation, and the flow Mach number is $Ma = 2.9$, the flow static temperature is 108.1 K, and the flow density is $0.074 kg/m^3$.

In order to verify the reliability of the LES software, the numerical results of the compression ramp will be compared with the experimental results under the same inlet flow conditions.

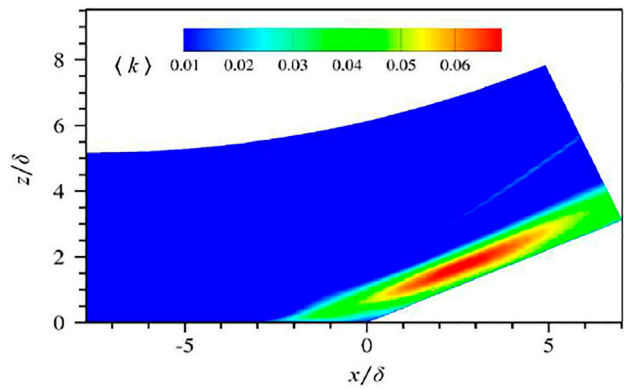

FIGURE 5 | Contour of time-spanwise averaged turbulent kinetic energy.

3 RESULT ANALYSIS AND DISCUSSION

Figure 2 shows the distribution of the averaged wall pressure and skin friction coefficient along the streamwise direction in the primary computation domain, where the DNS results of Wu et al. (Wu and Martin 2008) and Tong et al. (Tong et al., 2017) and the experimental data of Bookey et al. (Bookey et al., 2005) are also presented for the purpose of comparison. By solving the position where the averaged skin friction coefficient C_f is zero, the averaged separation point $x_{sep} = -2.7\delta$ and the re-attachment point $x_{rea} = 0.8\delta$ in the ramp flow are obtained. Overall, the computed pressure distribution and friction coefficient distribution are in good agreement with the experimental values. At upstream of the ramp, it agrees well with the experimental values and DNS results. But it is slightly higher downstream of the ramp. The reason is that the predicted separation region size is slightly smaller and the separated shear layer completes the reattachment process in advance downstream of the ramp; thus, the wall pressure increases rapidly and the range of the pressure platform is shortened.

Figure 3 illustrates the instantaneous flow structure in the compression ramp computation domain. Among them, the quasi-order vortex structure of the turbulent boundary layer is displayed using the Q criterion, and the streamwise direction velocity is used for coloring. The translucent gray surface in the figure is the dimensionless pressure isosurface $p/(\rho_\infty U_\infty^2) = 1.7$, which is used to represent the three-dimensional structure of the separation shock wave. As can be seen in the figure, the flow field in the interaction region has significant three-dimensional characteristics. When a large vortex structure passes through the root of the shock wave, it breaks under the effect of turbulent fluctuation enhancement at the ramp. At the same time, the shock wave deforms at the root, and the shock surface wrinkles along the spanwise direction. While away from the interaction region, the shock wave keeps still the typical two-dimensional structure characteristic.

In order to further illustrate the interaction process between the shock wave and turbulent boundary layer, a slice contour in three directions is used to show the flow field details inside the interaction region, as shown in **Figure 4**. The streamwise and spanwise directions show the numerical schlieren diagram, which is used to show the shock wave, turbulent boundary layer, and flow structure in the separation bubble. It can be seen that the large-scale structure in the interaction region breaks into small-scale structures, which is well agreed with Zhuang Y.et al. (Zhuang et al., 2018b) experimental observation. But, on the slope downstream of the ramp, a large-scale quasi-order structure in the boundary layer is re-established. The instantaneous streamwise direction velocity contour ($y/\delta = 0.02$, approach laminar sublayer) is shown on the slice parallel to the wall. It can be seen that a velocity strip structure alternately arranged along the spanwise direction is observed both upstream and downstream of the ramp in this region. In addition, the flow scale in the separation bubble along the spanwise direction is very different, indicating that the separation bubble is a multiscale flow structure.

3.1 Turbulent Fluctuation

When the flow passes through the interaction region, the turbulent fluctuation is significantly enhanced due to the strong inverse gradient pressure in this region. **Figure 5** is a contour of the time-space averaged turbulent kinetic energy. The definition of turbulent kinetic energy is as follows: $k = (\overline{\rho u'u'} + \overline{\rho v'v'} + \overline{\rho w'w'})/2\rho_\infty U_\infty^2)$. It can be seen from the figure that the intensity of the turbulent kinetic energy after the interaction region rapidly increases and reaches its peak value downstream of the ramp. The increase of the turbulent kinetic energy means significantly that a large number of small-scale structures are generated after the SWBLI.

Figure 6 presents the variation of Reynolds normal stress R_{ii} at different locations in the interaction region. It can be seen that near the ramp ($x = 0.66\delta$), the three Reynolds stress components produce a sharp peak value. As the separated boundary layer reattaches, the Reynolds stress continues to decrease and tends to return to the pre-interaction state at ($x = 2.68\delta$). It is noted that the distribution of Reynolds stress R_{22} in the boundary layer is relatively smooth and appears as a bimodal distribution near the ramp.

3.2 Unsteady Motion of Shock Waves

In order to study the shock wave unsteady motion, intermittent factors are usually used to measure the range of shock wave motion along the streamwise direction. The intermittent factor is defined as the time when the instantaneous wall pressure somewhere in the streamwise direction is greater than the given threshold takes up the proportion of the total flow field time. The computation formula is as follows (Dolling and Or 1985):

$$\lambda = \frac{Time[p_w > (\bar{p}_w + 3\sigma(p_w))]}{Totaltime},$$

where p_w represents the instantaneous wall pressure; $\bar{p}_w$ and $\sigma(p_w)$ represent the average wall pressure of the inlet boundary layer and the standard deviation of the wall pressure, respectively, and the sum of the two is set as the threshold for the computation of the intermittent factor.

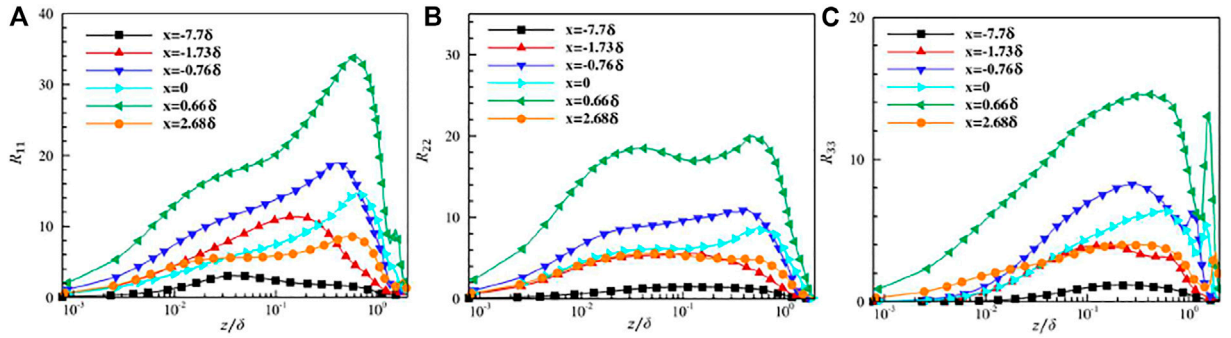

FIGURE 6 | Distribution of Reynolds normal stresses at different streamwise locations. **(A)** Streamwise component. **(B)** Spanwise component. **(C)** Wall-normal component.

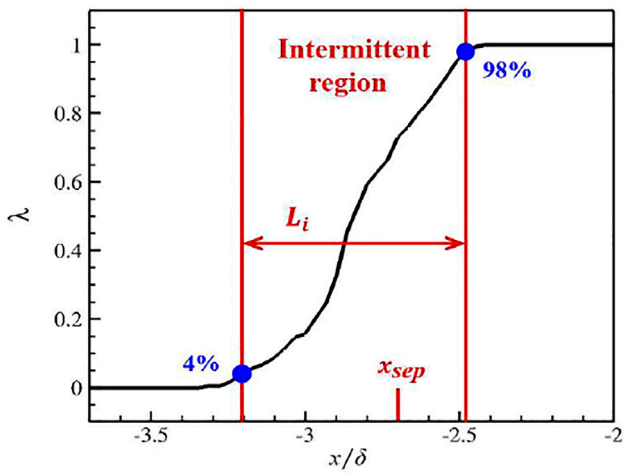

FIGURE 7 | Intermittency factor of the separation shock.

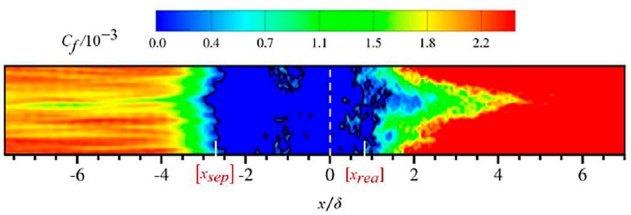

FIGURE 8 | Contour of the time-averaged skin friction coefficient.

Figure 7 exhibits the local distribution of the intermittent factor in the compression ramp. It is known from the definition of the intermittent factor that in the undisturbed upstream boundary layer and downstream region of the ramp, the intermittent factor is always equal to 0 (or 1). However, in the vicinity of the average separation point, the separation shock wave shows a strong unsteady flow characteristic, which is represented by the intermittent factor: $0 < \lambda < 1$. Wu et al. (Wu and Martin 2008) considered that the motion of the shock wave is closely related to the pulsation of the separation bubble. For comparison, the upper and lower limitations of the given intermittent factor are 98 and 4%, respectively, to estimate the streamwise direction range of the shock wave motion as follows: $-3.2\delta \le x \le -2.48\delta$. It can be seen that the flow movement of the separation shock wave in the intermittent region is carried out around the average separation point $(x = -2.7\delta)$. By computation, the length of the intermittent region in this simulation is $L_i = 0.72\delta$ which is slightly smaller than that in the DNS result of the study by Tong et al. (Tong et al., 2017$L_i = 0.72\delta$) $(L_i = 0.72\delta)$

3.3 Görtler Flow Vortex

From the abovementioned analysis, the supersonic compression ramp flow has significant three-dimensional characteristics. Especially on the slope downstream of the ramp, the flow field shows a strong unevenness in the spanwise direction. This phenomenon is closely related to the presence of Görtler flow vortex (Dolling and Or 1985; Grilli et al., 2013).

Figure 8 shows a time-averaged skin friction coefficient contour. The white dashed line represents the location of the ramp. The solid black line in the figure is used to show the separation and reattachment positions of the boundary layer near the ramp defined by the time-averaged friction coefficient equal to 0. It can be observed that the skin friction coefficient of the inlet boundary layer represents a strip pattern alternately arranged which is consistent with the spanwise distribution of the time-averaged separation line. This indicates that the distribution of the separation line is, in a great measure, determined by the skin friction coefficient of the inlet boundary layer. Due to the low-frequency pulsation of the separation bubble, the average reattachment still exhibits strong transient flow characteristics. When the separated boundary layer reattaches, the skin friction coefficient distribution appears as an obvious "V" structure, which is caused by the presence of Görtler vortex pairs. The existence of this "V" structure was also confirmed by Fu-Lin et al., (2016).

The formation of Görtler vortices is related to the curvature of the concave surface. In order to describe the spatial development of the Görtler vortex in detail, **Figure 9** shows the flow field details on six different sections downstream of the average separation

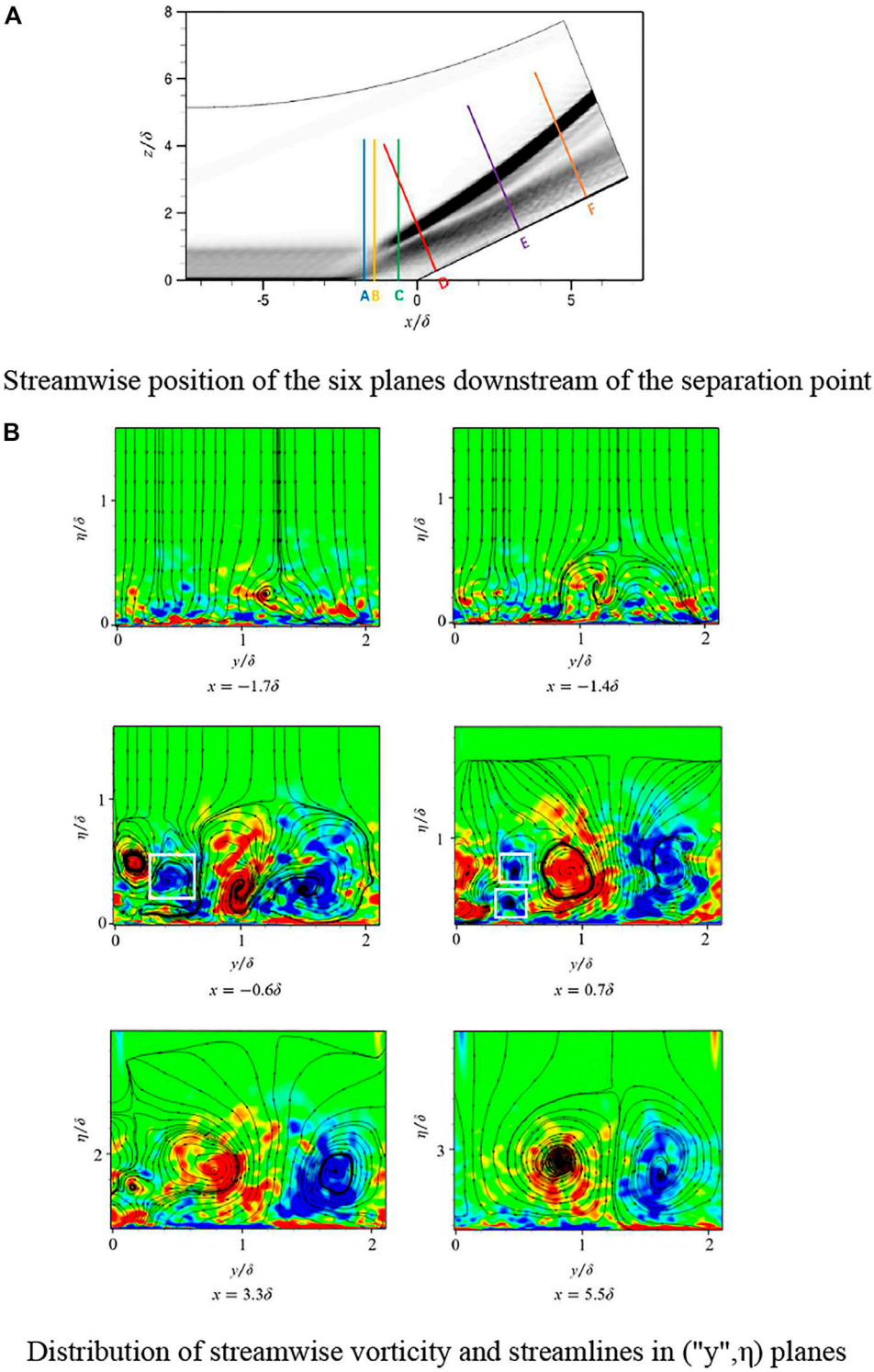

FIGURE 9 | Spatial evolution of Görtler-like vortices in the compression ramp. **(A)** Streamwise position of the six planes downstream of the separation point. **(B)** Distribution of streamwise vorticity and streamlines in ("y",η) planes.

point. These six sections are named A ~ F, corresponding to the streamwise direction positions: -1.7δ, -1.4δ, -0.6δ, 0.7δ, 3.3δ, and 5.5δ, respectively. A schematic diagram of six positions is given in **Figure 9A**, in which the background is space-time–averaged numerical schlieren. **Figure 9B** shows the streamwise direction vorticity ω_x contour, and streamline

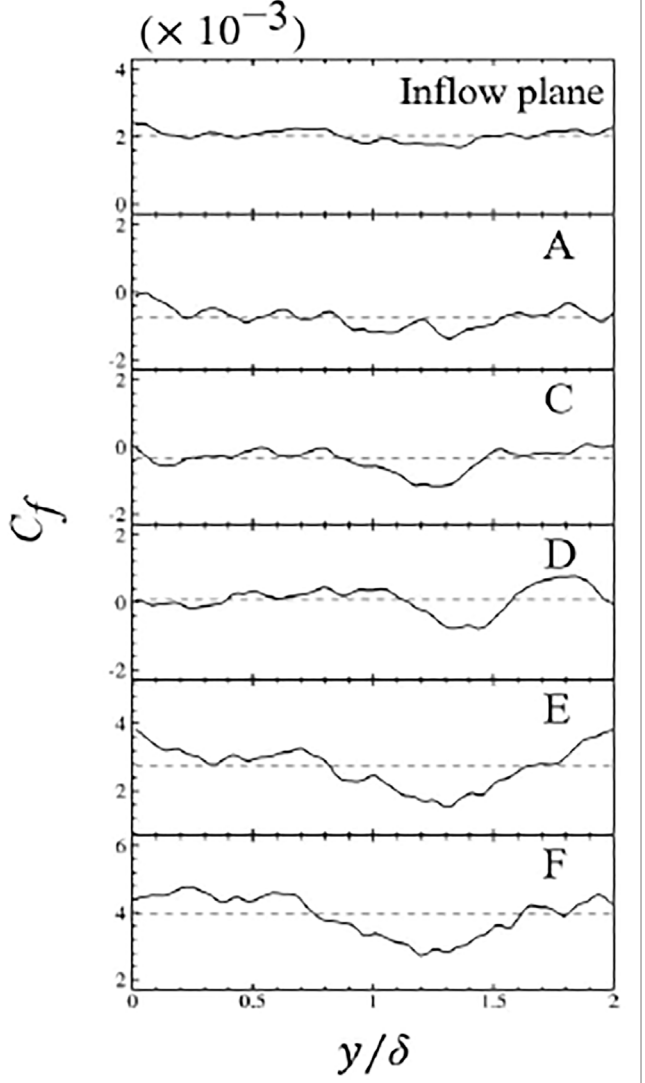

FIGURE 10 | Distribution of the averaged skin friction coefficient in the spanwise direction.

distribution on six sections, where the vorticity contour has a range $-0.5 \leq \omega_x \leq 0.5$. In sections A and B, the streamlines in the near wall region are gradually bent, and a smaller streamwise vortex is formed. When the flow develops to section C, it can be clearly seen in this figure that there is a large pair of vortexes in the streamwise direction **(B)** and a small pair of vortexes in the streamwise direction **(A)**, and the entire boundary layer has a large amount of vortexes in this direction. With the separated boundary layer reattach in the sections D, E and F, the larger pair of the streamwise vortexes gradually occupies almost the entire span width (about 2δ) and appears as a classical kidney eddy structure.

Figure 9B illustrates that it can be estimated that the center of the Görtler vortex pair is located at $y = 1.2\delta$. In general, the position of the Görtler vortex in the spanwise direction changes constantly with time due to the turbulent flow (Floryan 1991), but

Figure 10 shows the time-averaged skin friction coefficient along the span in different sections, including the inlet section of the ramp computation domain and the A, C, D, E, and F sections in **Figure 9** so that the variation of the spanwise distribution of the skin friction coefficient with the development of the flow field can be presented. The dotted line in the figure indicates the time-span–averaged result at this section. At the inlet section, it can be found that the skin friction coefficient along the spanwise direction is not evenly distributed, and a low skin friction coefficient region appears near the spanwise center. Sections A, C, and D are all located in the separation region, so the friction coefficients of these three locations are close to 0. In addition, due to the shock wave/boundary layer interaction and Görtler instability, the skin friction coefficient of these three sections along the spanwise direction shows strong fluctuation. Especially, an obvious low friction coefficient region is formed between $y/\delta = 1 \sim 1.5$. In sections E and F, the amplitude of this low-friction coefficient region is further increased, and a V-shaped distribution is formed. The fluid near the wall converges between the pair of Görtler vortexes and moves toward the outer layer of the boundary layer, locally resulting in a lower friction coefficient. In section F, the skin friction coefficient at the spanwise position $y = 1.2\delta$ reaches a minimum, which is exactly the same as the center position of the Görtler vortex pair. In fact, by observing the friction coefficient distribution at the six different sections, it can be found that the low-friction coefficient region of the inlet section has a high degree of coincidence with the downstream section in the spanwise position. This phenomenon indicates that the spanwise position of the Görtler vortex downstream of the ramp is likely to be affected by the spanwise friction coefficient distribution at the inlet section.

3.4 Low-Frequency Instability

In order to study the low-frequency motion of the separated shock wave, it is necessary to collect the signal of numerical pressure for spectrum analysis. Therefore, 528 wall pressure probes are arranged along the flow direction in the middle section of the calculation domain. The arrangement of these probes is consistent with the grid distribution, that is, one probe is arranged in the center of each wall grid cell. It is worth noting that the signal acquisition process is carried out after the SWBLI flow field is fully established. In order to ensure sufficient time resolution, data recording is carried out every ten time steps in the large eddy simulation, and the physical time interval between two adjacent recording points is $\Delta t = 0.01\delta/U_\infty$. According to the Nyquist sampling theorem, the highest physical frequency that can be captured is $f_s = 1/(2\Delta t) = 50U_\infty/\delta$, which is far greater than the characteristic frequency U_∞/δ of the turbulent boundary layer. Because the low-frequency instability of the SWBLI has a wide frequency range, in order to accurately capture the low-frequency characteristics, the signal acquisition time should cover at least one low-frequency instability period. **Table 1** shows the relevant information of pressure signal acquisition in this large eddy simulation.

Figure 11 presents the variation of wall pressure with time at two different positions upstream of the corner (the corner position is x = 0) in the center plane, and the wall pressure is nondimensionlized by using the inlet pressure P_∞. The blue solid line represents the pressure signal graph collected at the inlet

TABLE 1 | Relevant information of pressure signal acquisition.

Number of data /N	Time span /(δ/U_∞)	Sampling frequency/(U_∞/δ)	Minimum frequency/(U_∞/δ)
40,000	400	50	0.0025

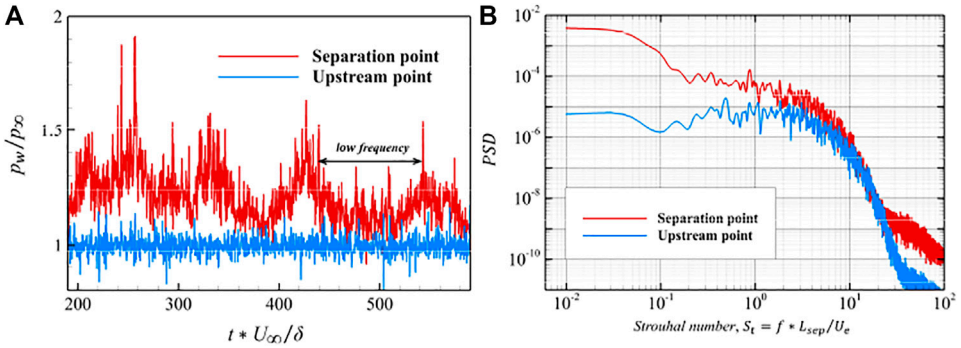

FIGURE 11 | Wall pressure signal **(A)** and power spectrum **(B)**.

turbulent boundary layer, where the pressure fluctuation is not disturbed by the downstream interference area flow. It can be seen that the pressure signal around P_w/P_∞ presents a random fluctuation, and the amplitude of fluctuation is very small. The red solid line indicates the pressure fluctuation with time at the average separation point ($x_{sep} = -2.7\delta$). Compared with the inlet, the pressure signal at the average separation point has larger amplitude of fluctuation due to the interaction between the shock wave and turbulent boundary layer. In addition, from the red solid line, the pressure signal at the separation point not only includes the high-frequency fluctuation but also has the low-frequency fluctuation component as shown in **Figure 11**.

Next, we will make a strict quantitative analysis of the wall pressure fluctuation signal from the perspective of spectral analysis. The Welch method (Barbe et al., 2010) is used to segment the discrete pressure signal, aiming to obtain a smoother and less variance power spectrum density (PSD) curve. In this study, the collected pressure signals are divided into three segments, and the coincidence rate between the segments is 50%. The Hanning window is used to add windows for each segment to improve the variance performance. It should be noted that in the Welch method, the more segmented the data, the smoother the power spectrum curve and the smaller the noise, but at the same time, the resolution of the power spectrum will be affected. Therefore, in the process of data segmentation, we must consider the balance of noise and resolution in the power spectrum curve. **Figure 11B** shows the PSD distribution curve corresponding to the abovementioned two wall pressure signals, where the abscissa is the dimensionless frequency proposed by Dussauge et al. (Dussauge et al., 2006), which is defined as $St = fL_{sep}/U_e$. It can be seen from the figure that the peak value of pressure fluctuation energy in the upstream boundary layer is located in the high-frequency region, while the peak value of pressure fluctuation energy at the average separation point is located in the low-frequency region. **Figure 12** shows the weighted power spectrum density (WPSD) expressed as $WPSD(f) = f*PSD(f)df$. From this figure, we can see more clearly the frequency components of pressure signals at different flow direction positions. For the upstream boundary layer, the fluctuating energy is mainly distributed between $10^0 \sim 10^1$, and the peak frequency is about $St = 3$, which is consistent with the characteristic frequency of the fully developed turbulent boundary layer. For the signal at the average separation point, there is also a wide small peak area in the high-frequency region, which is similar to the WPSD curve obtained in the upstream turbulent boundary layer. At the same time, the red curve shows a more obvious energy peak appearing in the low-frequency region, and the corresponding characteristic frequency is $St = 0.04$, which is completely consistent with the result (0.02–0.05) summarized by Dussauge et al. (Dussauge et al., 2006). In addition, Wang Bo et al. (Wang 2015), Kenzo S. et al. (Sasaki et al., 2021), Tong et al. (Tong et al., 2017), Touber and Sanham (Touber and Sandham 2009), and Pasquariello et al. (Pasquariello et al., 2017) obtained similar results in their respective numerical simulations.

In order to study the distribution of low-frequency instability characteristics in the whole field of the compression corner, **Figure 13** shows the distribution of WPSD on all pressure probes. The white solid line is used to represent the position of the average separation point x_{sep} and the average reattachment point x_{rea} and the white dotted line is used to represent the position of the corner. Once again, it can be clearly seen that the turbulence generation technology in this study does not introduce any low-frequency energy at the inlet. By observing the whole flow field, it is found that this low-frequency instability mainly exists near the average separation point, while in other locations of the flow field, the energy of pressure fluctuation almost exists in the high-frequency range. Especially when the boundary layer is reattached in the downstream, its power spectrum distribution is almost the same as that in the upstream, and the reattached boundary layer shows a

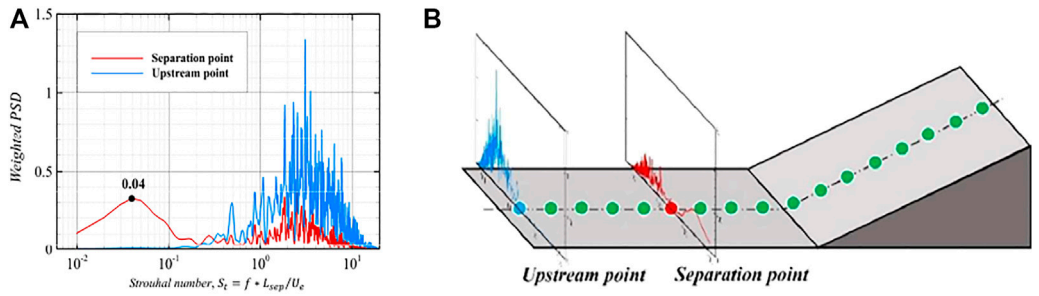

FIGURE 12 | (A) Frequency weighted power spectrum distribution and **(B)** collected positions.

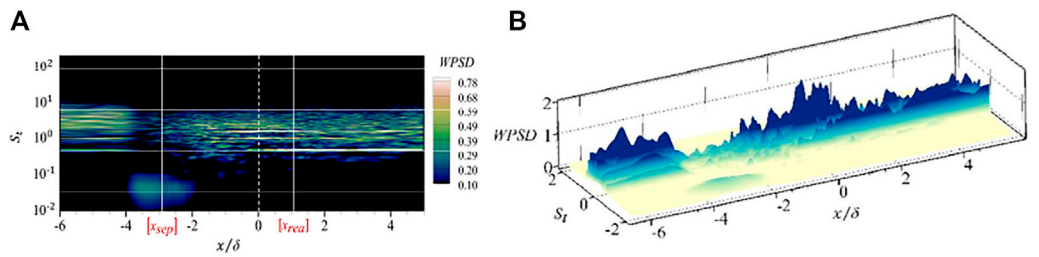

FIGURE 13 | (A) WPSD contour map of the wall pressure signal **(B)** peak map of wall pressure signal.

process of flow recovery. This study considers that this low-frequency motion is caused by the unsteady motion of large-scale separation bubbles. Obviously, the scale of the separation bubble is larger than that of any flow in the boundary layer.

4 CONCLUSION

In this study, a large eddy simulation (LES) is conducted to investigate the shock wave and turbulent boundary layer interaction in a 24° compression ramp with an inflow Mach number of $Ma = 2.9$ and compared with experimental and numerical simulation results in the literature. The shock wave/turbulent boundary layer interaction (SWBLI) was analyzed from two aspects: time domain and frequency domain. The main conclusions are as follows:

The shock wave/turbulent boundary layer interaction represents some flow structure characteristics. When the large scale vortex passes the root of the shock wave, the shock wave surface wrinkles due to the intermittence of the large-scale vortex in the spanwise direction. Under the strong inverse gradient pressure of the compression ramp, the large-scale vortex breaks into a small-scale vortex, the turbulent boundary layer manifests a strong anisotropy characteristic, and the turbulent kinetic energy rapidly increases in the outer layer of the boundary layer downstream of the ramp.

In the region of interaction, the separated shock wave represents an unsteady motion along the streamwise direction. This phenomenon is successfully captured by the intermittent factor. The range of the shock wave motion is $-3.2\delta \le x \le -2.48\delta$, indicating that the unsteady shock wave motion is around the average separation point.

The LES simulation represents a pair of streamwise vortices, called Görtler vortex, occupying almost the entire span width about 2δ on the compression ramp. It is found that the spanwise skin friction coefficient distribution at the inlet of the turbulent boundary layer not only determines the spanwise separation location of the turbulent boundary but also makes the downstream Görtler vortex to be fixed at a certain spanwise position, thus forming a time stable flow structure.

The low-frequency instability in the SWBLI is successfully captured by using the power spectrum analysis method. The corresponding characteristic frequency is $St = 0.04$ near the average separation point. The spectrum analysis indicates that the shock wave motion is related to the pulsation of the separation bubble, while in other locations of flow field, the energy of pressure fluctuation represents almost exclusively the high-frequency characteristics of the fully developed turbulent boundary layer.

DATA AVAILABILITY STATEMENT

The raw data supporting the conclusions of this article will be made available by the authors, without undue reservation.

AUTHOR CONTRIBUTIONS

XH, L-XW, and D-DZ contributed to the conception and design of the study. XH provided an idea scheme; XH, L-XW, and D-DZ coded; XH analyzed; and NG and l wrote the first draft. All authors contributed to manuscript revision and read and approved the submitted version.

REFERENCES

Adams, N. A. (2000). Direct Simulation of the Turbulent Boundary Layer along a Compression Ramp at M = 3 and Re=1685. *J. J. Fluid Mech.* 420 (1), 47–83. doi:10.1017/S0022112000001257

Barbe, K., Pintelon, R., and Schoukens, J. (2010). Welch Method Revisited: Nonparametric Power Spectrum Estimation via Circular Overlap. *J. IEEE Trans. Signal Process.* 58 (2), 553–565. doi:10.1109/TSP.2009.2031724

Bookey, P., Wyckham, C., and Smits, A. (2005). *New Experimental Data of STBLI at DNS/LES Accessible Reynolds Numbers*. Reno: 43rd AIAA Aerospace Sciences Meeting and Exhibit. doi:10.2514/6.2005-309

Dolling, D. S. (2001). Fifty Years of Shock-Wave/boundary-Layer Interaction Research - what Next? *AIAA J.* 39 (8), 1517–1531. doi:10.2514/3.14896

Dolling, D. S., and Or, C. T. (1985). Unsteadiness of the Shock Wave Structure in Attached and Separated Compression Ramp Flows. *J. Experiments Fluids* 3 (1), 24–32. doi:10.1007/BF00285267

Dupont, P., Haddad, C., and Debieve, J. F. (2006). Space and Time Organization in a Shock-Induced Separated Boundary Layer. *J. Fluid Mech.* 559, 255. doi:10.1017/S0022112006000267

Dussauge, J. P., Dupont, P., and Debiève, J. F. (2006). Unsteadiness in Shock Wave Boundary Layer Interactions with Separation. *J. Aerospace Sci. Tech.* 10 (2), 85–91. doi:10.1016/j.ast.2005.09.006

Floryan, J. M. (1991). On the Görtler Instability of Boundary Layers. *J. Prog. Aerospace Sci.* 28 (3), 235–271. doi:10.1016/0376-0421(91)90006-P

Fu-Lin, Ton., Tang, Zhi-Gong., and Xin-Liang, Li. (2016). Direct Numerical Simulation of Shock-Wave and Transitional Boundary Layer Interaction in a Supersonic Compression Ramp. *J. Chin. J. Aeronautics* 37 (12), 3588–3604. doi:10.7527/S1000-6893.2016.0096

Ganapathisubramani, B., Clemens, N., and Dolling, D. (2007). *Effects of Upstream Coherent Structures on Low-Frequency Motion of Shock-Induced Turbulent Separation*. Reno: 45th AIAA Aerospace Sciences Meeting and Exhibit. doi:10.2514/6.2007-1141

Germano, M. (1991). A Dynamic Subgrid-Scale Eddy Viscosity Model. *Phys. Fluids A* 3, 1760–1765. doi:10.1063/1.857955

Grilli, M., Hickel, S., and Adams, N. A. (2013). Large-Eddy Simulation of a Supersonic Turbulent Boundary Layer over a Compression–Expansion Ramp. *J. Int. J. Heat Fluid Flow* 42 (8), 79–93. doi:10.1016/j.ijheatfluidflow.2012.12.006

Lee, C. B., and Wang, S. (1995). Study of the Shock Motion in a Hypersonic Shock System/turbulent Boundary Layer Interaction. *Experiments in Fluids* 19 (3), 143–149. doi:10.1007/BF00189702

Loginov, M. S., Adams, N. A., and Zheltovodov, A. A. (2006). Large-eddy Simulation of Shock-Wave/turbulent-Boundary-Layer Interaction. *J. J. Fluid Mech.* 565 (1), 135–169. doi:10.1017/S0022112006000930

Pasquariello, V., Hickel, S., and Adams, N. A. (2017). Unsteady Effects of Strong Shock-Wave/Boundary-Layer Interaction at High Reynolds Number. *J. J. Fluid Mech.* 823 (1), 617–657. doi:10.1017/jfm.2017.308

Sasaki, K., Barros, D. C., Andre, V., and Cavalieri, G. (2021). Causality in the Shock Wave/turbulent Boundary Layer Interaction. *J. Phys. Rev. Fluids* 6 (6), 064609. doi:10.1103/PhysRevFluids.6.064609

Settles, G. S., Fitzpatrick, T. J., and Bogdonoff, S. M. (1979). Detailed Study of Attached and Separated Compression Corner Flowfields in High Reynolds Number Supersonic Flow. *AIAA J.* 17 (6), 579–585. doi:10.2514/3.61180

Shu, C. W., and Osher, S. (1989). Efficient Implementation of Essentially Non-oscillatory Shock-Capturing Schemes. *J. J. Comput. Phys.* 77 (2), 439–471. doi:10.1016/0021-9991(88)90177-5

Smits, A. J., and Muck, K.-C. (1987). Experimental Study of Three Shock Wave/Turbulent Boundary Layer Interactions. *J. Fluid Mech.* 182 (182), 291. doi:10.1017/S0022112087002349

Tong, F., Yu, C., and Tang, Z. (2017). Numerical Studies of Shock Wave Interactions with a Supersonic Turbulent Boundary Layer in Compression Corner: Turning Angle Effects. *J. Comput. Fluids* 149, 56–69. doi:10.1016/j.compfluid.2017.03.009

Touber, E., and Sandham, N. D. (2009). Large-Eddy Simulation of Low-Frequency Unsteadiness in a Turbulent Shock-Induced Separation Bubble. *J. Theor. Comput. Fluid Dyn.* 23 (2), 79–107. doi:10.1007/s00162-009-0103-z

Touber, E., and Sandham, N. D. (2011). Low-order Stochastic Modelling of Low-Frequency Motions in Reflected Shockwave/boundary-Layer Interactions. *J. Fluid Mech.* 671, 417. doi:10.1017/S0022112010005811

Wang, Bo. (2015). *The Investigation into the Shock Wave/boundary-Layer Interaction Flow Field Organization*. Changsha: Graduate School of National University of Defense Technology.

Wu, M., and Martin, M. P. (2008). Analysis of Shock Motion in Shockwave and Turbulent Boundary Layer Interaction Using Direct Numerical Simulation Data. *J. J. Fluid Mech.* 594 (594), 71–83. doi:10.1017/S0022112007009044

Wu, Yu., Shi-He, Yi., and Chen, Zhi. (2013). Experimental Investigations on Structures of Supersonic Laminar/turbulent Flow over a Compression Ramp. *J. Acta Phys.* 62 (18), 308–319. doi:10.7498/aps.62.184702

Zhong, Dong-Dong., WangXu, Li., and Ge, Ning. (2021). Reflected Shock/Boundary Layer Interaction Structure Analysis Based on Large Eddy Simulation. *Chin. J. aeronautics* 34 (5), 364–372. doi:10.1016/j.cja.2020.12.009

Zhu, J., and Qiu, J. (2017). A New Type of Finite Volume WENO Schemes for Hyperbolic Conservation Laws. *J. Sci. Comput.* 73 (2-3), 1338–1359. doi:10.1007/s10915-017-0486-8

Zhuang, Yi., Tan, Hui-Jun., Li, Xin., Guo, Yun-Jie., and Sheng, Fa-Jia. (2018). Evolution of Coherent Vertical Structures in a Shock Wave/turbulent Boundary-Layer Interaction Flow, Phys. *Fluids* 30, 111702. doi:10.1063/1.5058278

Zhuang, Yi., Tan, Hui-Jun., Li, Xin., Sheng, Fa-Jia., and Zhang, Yu-chao. (2018). Görtler-like Vortices in an Impingingshock Wave/turbulent Boundary Layerinteraction Flow. *Phys. Fluids* 30, 061702. doi:10.1063/1.5034242

Conflict of Interest: Author XH was employed by the company AECC HUNAN Aviation Powerplant Research Institute.

The remaining authors declare that the research was conducted in the absence of any commercial or financial relationships that could be construed as a potential conflict of interest.

frontiers in Energy Research

ORIGINAL RESEARCH
published: 15 March 2022
doi: 10.3389/fenrg.2022.853280

Active Flow Control Based Bleed in an Axial Compressor Cascade Using Large Eddy Simulation

Yun Gong, Shaowen Chen, Cong Zeng and Songtao Wang*

Engine Aerodynamics Research Center, School of Energy Science and Engineering, Harbin Institute of Technology, Harbin, China

The performance of the compressor is of great importance in developing advanced engine technology, and it dramatically influences the cycle efficiency and safety of the engine. The compressor bleed requires a part of the main flow extraction from the passage, and the removal of the airflow plays an essential role in the performance of the compressor. The influence of the constant suction and pulsed suction on the flow structures and the aerodynamic performance in a compressor cascade, and the control mechanisms are numerically studied using large eddy simulation. At a suction mass flow rate of 0.25% of the main flow rate, constant suction leads to a 9.36% reduction in C_{pt}, while pulsed suction gains 24% more benefit in C_{pt} reduction on the basis of the constant suction with an excitation frequency of 100 Hz. It indicates that the pulsed suction has more significant potential to control the loss generation in the compressor. Afterward, the flow field of the baseline, constant suction, and pulsed suction are compared to find out the flow control mechanisms of the constant suction and pulsed suction. Two different formation mechanisms of the passage vortex are found due to the excitation effect of the pulsed suction. Besides, the results of proper orthogonal decomposition and dynamic mode decomposition show that the pulsed suction can simplify and stabilize the compressor flow field, which could lead to a further benefit in C_{pt}.

Keywords: axial compressor, flow control, constant suction, pulsed suction, large eddy simulation

OPEN ACCESS

Edited by:
Xiao Liu,
Harbin Engineering University, China

Reviewed by:
Zhiyuan Cao,
Northwestern Polytechnical University, China
Shijun Sun,
Beijing Institute of Technology, China

****Correspondence:***
Shaowen Chen
cswemail@hit.edu.cn

Specialty section:
This article was submitted to Advanced Clean Fuel Technologies, a section of the journal Frontiers in Energy Research

Received: *12 January 2022*
Accepted: *07 February 2022*
Published: *15 March 2022*

Citation:
Gong Y, Chen S, Zeng C and Wang S (2022) Active Flow Control Based Bleed in an Axial Compressor Cascade Using Large Eddy Simulation. Front. Energy Res. 10:853280. doi: 10.3389/fenrg.2022.853280

INTRODUCTION

The compressor is one of the critical components of the engine, and it plays a crucial role in guaranteeing the cycle efficiency and safety of the engine. The compressor in the modern aeroengine is often designed with high loading to reduce the weight of the engine or increase the pressure before the burner. However, this may induce more serious flow separation within the compressor and further leads to the efficiency or stability loss of the compressor. A lot of work has been done on the flow field details in the high-loading compressor (Gbadebo et al., 2005; Gbadebo et al., 2008; Lei et al., 2008; Wei et al., 2013; Zambonini et al., 2017). Besides, the passive flow control methods, such as lean or sweep blade (Denton and Xu, 2002; Zhang et al., 2018), end-wall contouring (Heinichen et al., 2011; Sun et al., 2018; Sun et al., 2019), and vortex generator (Evans and Hodson, 2010), have been widely investigated to improve the compressor performance. Compared with the passive ones, the active flow control methods (Kerrebrock et al., 1997; Kerrebrock et al., 2008; Jabbal et al., 2013) can adjust according to the operating condition of the compressor; hence, they may be applied as more flexible in many cases, especially for some highly maneuverable aircraft.

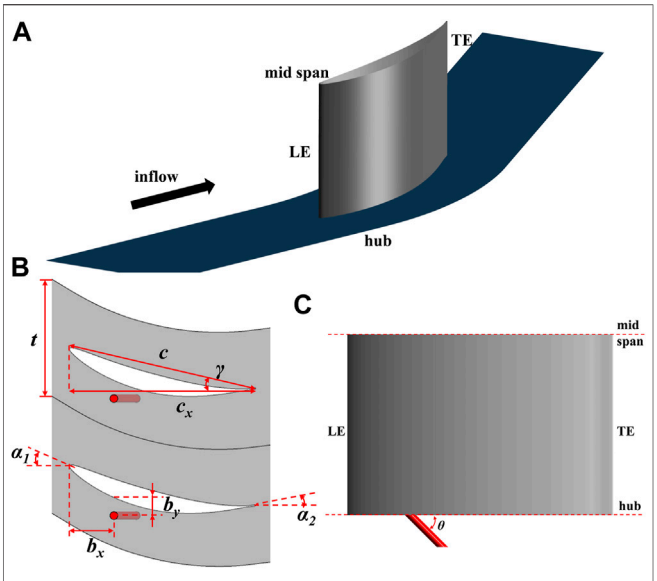

FIGURE 1 | Schematic diagram of the calculation model. **(A)** Calculation model display; **(B)** the definition of the symbols; **(C)** the inclination angle define the hole.

TABLE 1 | Key geometric parameters of the model.

Parameters	Values
c_x	117 mm
C	120 mm
T	74 mm
H	160 mm
Γ	12.4°
α_1	32.123°
α_2	−7.877°
Θ	45°
b_x	29.5 mm
b_y	11 mm

The compressor suction, which was first proposed by Kerrebrock et al. (1997) and Kerrebrock et al. (2008) in an aspirated compressor, is one of the extensively used flow control methods. Afterward, the influence of the suction mass flow rate and the location (Leishman et al., 2007; Gummer et al., 2008) where the suction is installed on the performance of the compressor efficiency are investigated numerically or experimentally. The results indicate that the compressor suction is an efficient flow control method in managing the flow field where the flow separation exists. Compared with the steady flow control methods, the unsteady flow control methods, such as the synthetic jet (Zheng et al., 2005; Zheng et al., 2006; De Giorgi et al., 2012; Jabbal et al., 2013), pulsed jet (Seifert et al., 1993; Schatz and Thiele, 2001) and pulsed suction (PS) (Cerretelli and Kirtley, 2009; Hecklau et al., 2010; Hecklau et al., 2011a; Hecklau et al., 2011b; Zhang and Chen, 2021), are thought to have much more potential in alleviating the compressor flow separation and enhancing the compressor efficiency.

The compressor bleed system is an inevitable component of the aeroengine, and it bleeds air from the compressor to provide turbine cooling air, pressurize the cabin, and guarantee stage matching (Leishman et al., 2007). The removal of the air can enhance the compressor performance after a well-designed arrangement of the bleed configuration (Gummer et al., 2008). Based on the requirements of the compressor bleed and the application of the end-wall flow extraction, an experimental investigation has been performed by us (Zhang and Chen, 2021) to validate the effect of the PS control on a high-loading compressor cascade, and the results indicate that the PS has a better efficiency improvement than the constant suction (CS). Two reasons make the PS much more efficient, and one is that the PS has a larger suction momentum than CS when retaining the same suction flow rate, and the second is the introduction of the pulsed excitation that may create additional vortex structures, which can energize the boundary layer. However, the flow control mechanism of the PS in-depth has not been fully demonstrated yet due to the limitation of the test techniques.

A more detailed and higher-resolution result is required to study the vortex structures of the flow field under the influence of the CS and PS, as well as the controlling mechanism, and this can be achieved through the application of the large eddy simulation (LES) method (Tucker, 2011a; Tucker, 2011b). As the name indicates, the LES method can resolve the large-scale eddies (the size of eddies larger than the grid scale), while the remaining small-scale eddies are predicted through subgrid scale (SGS) models. Because of its advantage in high-resolution result resolving, the LES methods have been used in the works of Gao et al. (2015), Leggett et al. (2018), and Decaix et al. (2015) to find the mechanisms of the flow in depth. The LES is applied on a compressor cascade by Gao et al. (2015), and it is found that the unsteadiness of the compressor corner separation is contributed by an aperiodic shedding of the hairpin vortices. Therefore, to find out the flow field-controlling mechanism of the CS and PS, the LES method is thought to be a good choice.

Based on our former experimental work in Zhang and Chen (2021), the LES is used in this study to provide more detailed information on the flow structures. The comparison of the flow field details of the baseline, the CS, and PS configurations, as well as the flow control mechanism of the CS and PS, are the main scope of this paper. The article is organized into four sections. The first section is a brief comparison of the three configurations, followed by a detailed flow field analysis and the vortex structure description. Then the influences brought by the CS and PS are discussed. Finally, the flow field is decomposed with the help of proper orthogonal decomposition (POD) and dynamic mode decomposition (DMD) to shed more light on the mechanism of the PS and its advantage in compressor flow field controlling.

NUMERICAL METHOD

An NACA65 blade profile is used to perform the investigation in the present article. **Figure 1** shows the calculation model, and a detailed information is given in **Table 1**. The present blade profile has a 2D diffusion factor of 0.408. The inlet is extended one c_x upstream to reduce the numerical effect of the inlet boundary,

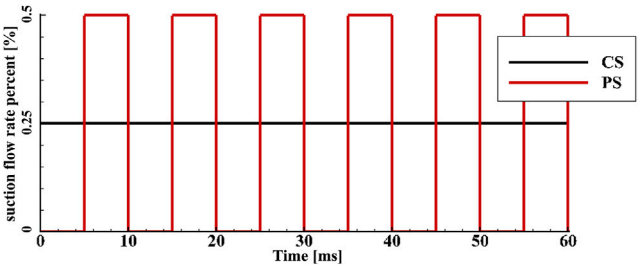

FIGURE 2 | Variation of the bleed rate for the constant suction (CS) and pulsed suction (PS) configuration.

and the outlet is extended one and a half c_x to allow full development of the wake. In order to reduce the computer resource and time cost, only one blade passage is simulated in the present investigation because of the periodicity of the compressor. In addition, according to the previous results (Zhang et al., 2018), the flow field in the upper half passage and lower half passage are the same at the present boundary condition; hence, only half of the blade passage is simulated.

In this paper, three configurations are calculated, the baseline configuration, the CS configuration, and the PS configuration, and the calculation model is shown in **Figures 1B**, C. The suction hole with a diameter of 5 mm is located 25% c_x downstream of the blade leading edge and 11 mm away from the blade suction surface, as shown in **Figure 1B**, and the suction hole position is decided based on our experimental investigation, which can be found in Zhang and Chen (2021). The suction hole has an inclination angle of 45° with the axial direction, as can be seen in **Figure 1C**. The suction mass flow rate is 0.25% of the main flow rate, and the PS configuration has an excitation frequency of 100 Hz, and the variation of the bleed flow rate along the time is displayed in **Figure 2**.

The mesh is generated in ANSYS ICEM CFD with an O4H topology, and the meshing scheme is displayed in **Figure 3**. The grid near the solid wall is refined, and the height of the first layer is 7×10^{-6} m (corresponding to the average value of y^+ to be about 0.4). The maximum stream-wise and span-wise grid sizes are strictly controlled to meet the requirements of the calculation method, and the corresponding Δx^+ and Δz^+ are less than 30 and 20, respectively. Besides, in order to guarantee the precision of the data transfer between the suction hole grid and the main blade passage grid, the grid is refined with an O-type grid and the connection between them are fully matching. Finally, the quantity of the grid nodes is 64 million for the baseline configuration and 74 million for the CS and PS configurations.

The finite-volume-based code ANSYS CFX is used in the present paper to perform the calculation. The second-order backward Euler method is applied as the transient scheme, and the advection scheme is high resolution. The total pressure and flow angle condition are specified at the inlet, and an inlet boundary layer is set. The Mach number at mainstream is 0.1, and the corresponding Reynolds number is about 260,000 based on the blade chord. Besides, the average static pressure condition is specified at the domain outlet. All

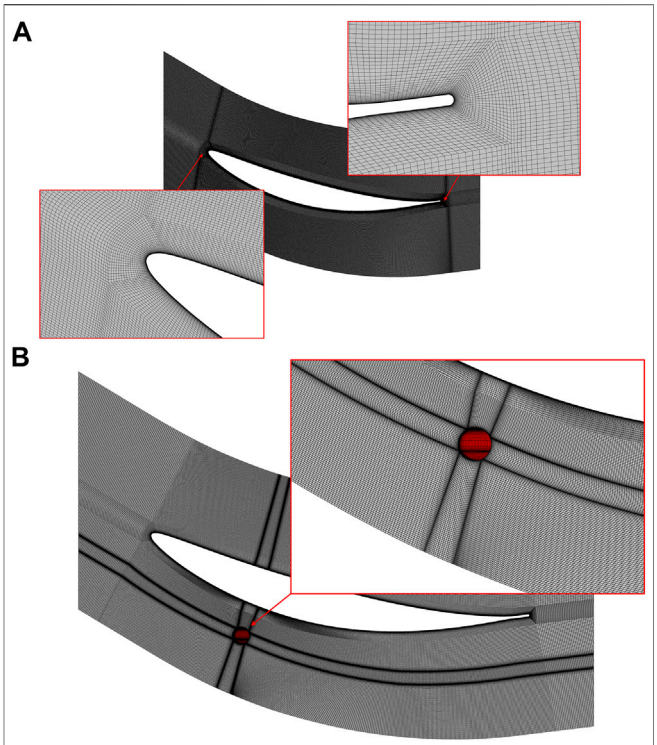

FIGURE 3 | Grid scheme for the baseline, CS, and PS configurations. **(A)** Baseline. **(B)** CS and PS.

walls in the calculation domain are no-slip and adiabatic, including the blade and hub. The symmetry condition is applied at mid-span, and two sides of the domain are periodic interface. In the present paper, the ability of the hole-type suction control method at a high-load state of the compressor is of great interest and worthy of more attention; hence, 8° of the incidence is used to investigate the flow control performance at the large incidence condition.

The LES method is used in this paper with the wall-adapting local eddy-viscosity (WALE) SGS model, which is developed by Nicoud and Ducros (1999) and extensively used in many works (Wei et al., 2013; Zambonini et al., 2017). A RANS resolution is obtained first with turbulence model of SST k-ω and transition model of γ-θ, to be the initial flow field of the LES calculation and compared with the results of LES and experiment data afterward. The LES time step is 1×10^{-5} s, corresponding to the Courant number of about 1, and the inner iteration subtime step is 4. The time duration of airflow from the blade leading edge to the trailing edge is defined as one flow-through time, and 10 flow-through times are required to clear the initial flow field effect, and another 10 flow-through times are needed to obtain the transient results. All the abovementioned processes require at least 240 h for one configuration running on 444 CPU cores to obtain the final results.

The comparison between RANS, LES, and the measurement data in Zhang and Chen (2021) are used to validate the reliability and feasibility of the calculation model in the present study, and the total pressure loss coefficient distribution along the span is

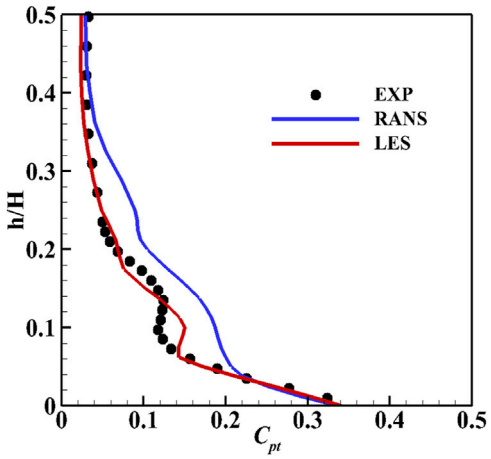

FIGURE 4 | Comparison of C_{pt} distribution along the spanwise.

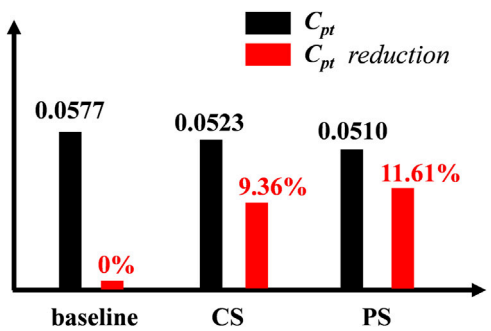

FIGURE 5 | C_{pt} and C_{pt} reduction percent for the baseline, CS, and PS.

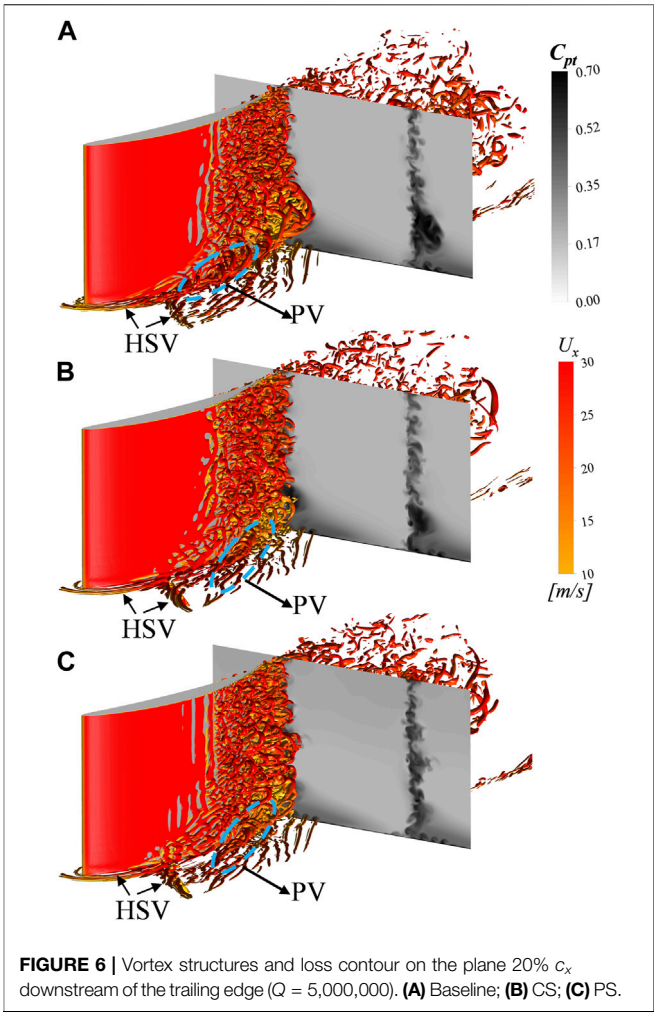

FIGURE 6 | Vortex structures and loss contour on the plane 20% c_x downstream of the trailing edge (Q = 5,000,000). **(A)** Baseline; **(B)** CS; **(C)** PS.

displayed in **Figure 4**. The total pressure loss coefficient is defined in **Eq. 1** as follows:

$$C_{pt} = \frac{p_{01} - p_0}{p_{01} - p_1} \tag{1}$$

where p_0, p represent the total pressure and static pressure, respectively, and subscript 1 denotes the parameter of mainstream flow at the inlet. It is evident that the LES result is consistent with the experiment result, and it predicts a better trend of the loss distribution than the RANS one, especially in the region between 10% and 30% blade span where the large flow separation exists. This indicates that the LES used here is adequate to support the present investigation.

RESULTS AND ANALYSIS

Overall Performance Comparison

The loss in the compressor is of great interest, and it determines the effectiveness of a flow control method. Therefore, the time-averaged total pressure loss at the plane 20% c_x downstream the trailing edge of three configurations are compared in **Figure 5**. It can be seen that the CS and PS configurations reduce the C_{pt} by 9.36% and 11.61%, respectively, based on that of the baseline configuration. Compared with the CS, the PS has 24% more ability in reducing the C_{pt} of the compressor cascade. To have deep knowledge of the flow control mechanism of the PS, the detailed flow fields are compared and analyzed in the following part.

The Q criterion derived from the second invariant of the velocity gradient tensor is used to identify the vortex structures in the compressor flow field, and the function used to calculate the Q value is given below (Hunt et al., 1988),

$$Q = \frac{1}{2}\left(\Omega_{ij}\Omega_{ij} - S_{ij}S_{ij}\right) \tag{2}$$

where Ω_{ij} is an anti-symmetric tensor of the rotation rate, and S_{ij} is a symmetric tensor of the strain rate. The Q is thought to be a balance between the rotation rate and strain rate of the control volume.

$$\Omega_z = \frac{1}{2}\left(\frac{\partial u}{\partial y} - \frac{\partial v}{\partial x}\right) \tag{3}$$

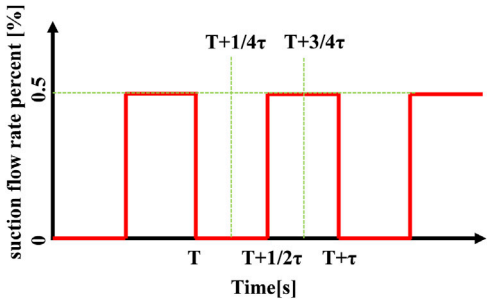

FIGURE 7 | Time definition in a pulse periodicity.

Figure 6 displays the vortex structures in the compressor cascade identified by the *Q* iso-surface and the loss contour on the plane 20% c_x downstream of the blade trailing edge of the three configurations. In the baseline in **Figure 6A**, it is obvious that the passage vortex (PV) arises from the joint point of the suction leg of the horseshoe vortex (HSV) and the pressure one from the adjacent blade, and the PV rolls up and interacts with the vortex structures from the blade suction surface as flowing downstream and leading to further total pressure loss generation. The loss caused by the vortex interaction contributes a considerable part of the total loss, which can be inferred from the loss contour downstream the blade. In **Figure 6B** of the CS configuration, however, both the suction leg and pressure leg of the HSV are removed by the suction hole, and the arising of the PV is contributed by the remaining part of the transverse flow near the endwall. In this case, the size of the PV is significantly reduced compared with that of the baseline, and the total pressure loss attributed to the PV is decreased accordingly. Besides, the interaction between the PV and the separation flow from the blade suction surface is attenuated, and this leads to a further reduction in the C_{pt}. Therefore, the corner separation of the CS configuration is alleviated, and the loss downstream of the blade is reduced accordingly. As for the PS configuration in **Figure 6C**, in addition to the reduction in the PV size, the loss has a significant reduction compared with the CS configuration, which indicates that the PS has more significant potential in flow control of the compressor flow separation than the CS. In the following section, the detailed flow field of the three configurations will be analyzed and compared to clarify how the PS influences the compressor flow field and the controlling mechanism of the PS.

Control Mechanism of the Pulsed Suction

Figure 8 displays the top–down view of the instantaneous vortex structures at five different instantaneous times in a pulse periodicity, and the time definition is given in **Figure 7**; τ denotes the time duration of a pulse. When t = T in **Figure 8A**, the suction hole is in a state in which the previous pulse is ended and another pulse is prepared to start, and the size of the PV, as well as its interaction with the separated flow from the blade suction surface, is small under the influence of the previous pulse, as marked by the black rectangle in **Figure 8A**. When t = T + 1/4τ in **Figure 8B**, there is no flow bled into the suction hole, and in this case, the pressure leg of the HSV and the suction one converge near the position of the suction hole and give rise to the PV afterward. The PV interacts with the separated flow from the blade suction surface and induces more serious flow separation and higher total pressure loss. The PV and separated flow at the blade suction corner develop and entrain the ambient air into the vortices and result in higher loss as flowing downstream, as displayed in the rectangle colored blue in **Figure 8C**. When t = T + 3/4τ in **Figure 8D**, the pressure leg of the HSV, as well as the suction one, are bled into the suction hole, which postpones the arising of the PV. It can be observed that the vortex structures near the suction hole are greatly alleviated, and the vortex size spanwise and pitchwise are restricted; hence, the local flow field can be improved accordingly. In this case, the remaining part of the transverse

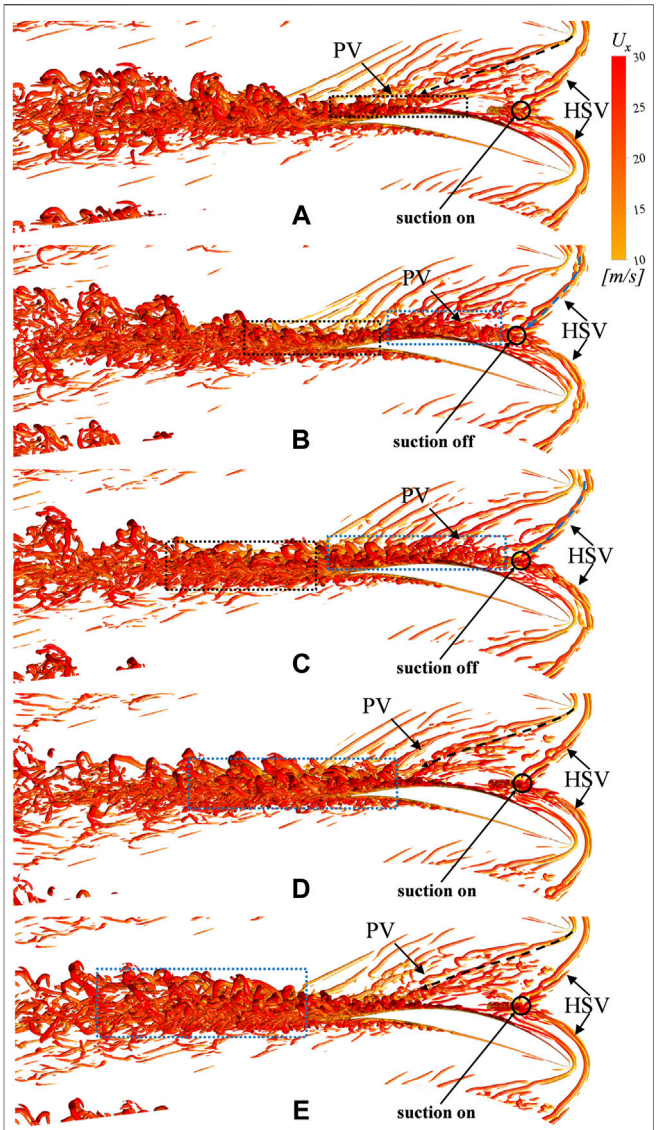

FIGURE 8 | Top–down view of the instantaneous vortex structures for the PS configuration (*Q* = 5,000,000). **(A)** t = T; **(B)** t = T + 1/4τ **(C)** t = T + 1/2τ; **(D)** t = T + 3/4τ; **(E)** t = T + τ.

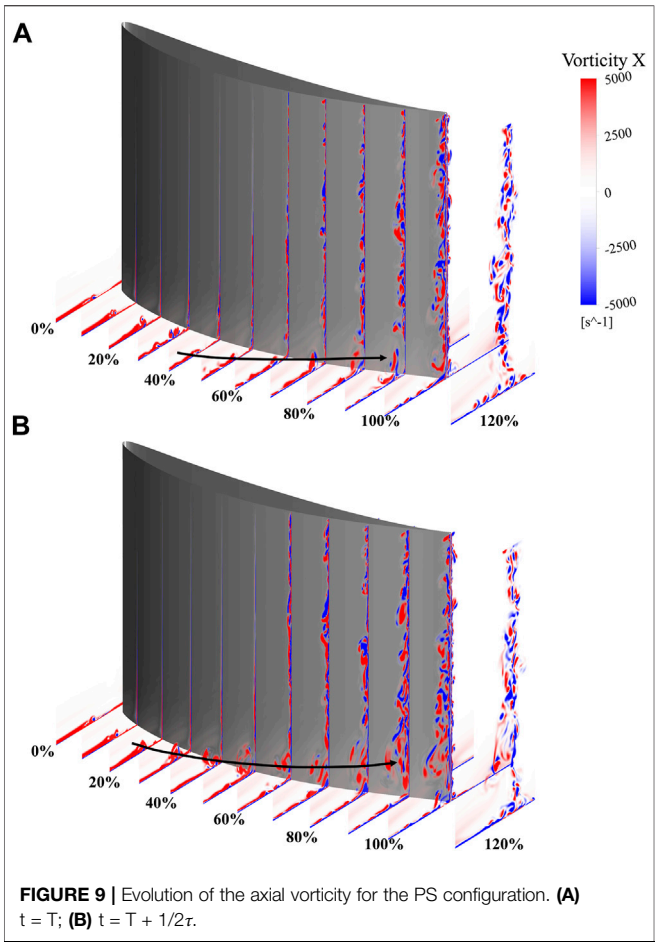

FIGURE 9 | Evolution of the axial vorticity for the PS configuration. **(A)** t = T; **(B)** t = T + 1/2τ.

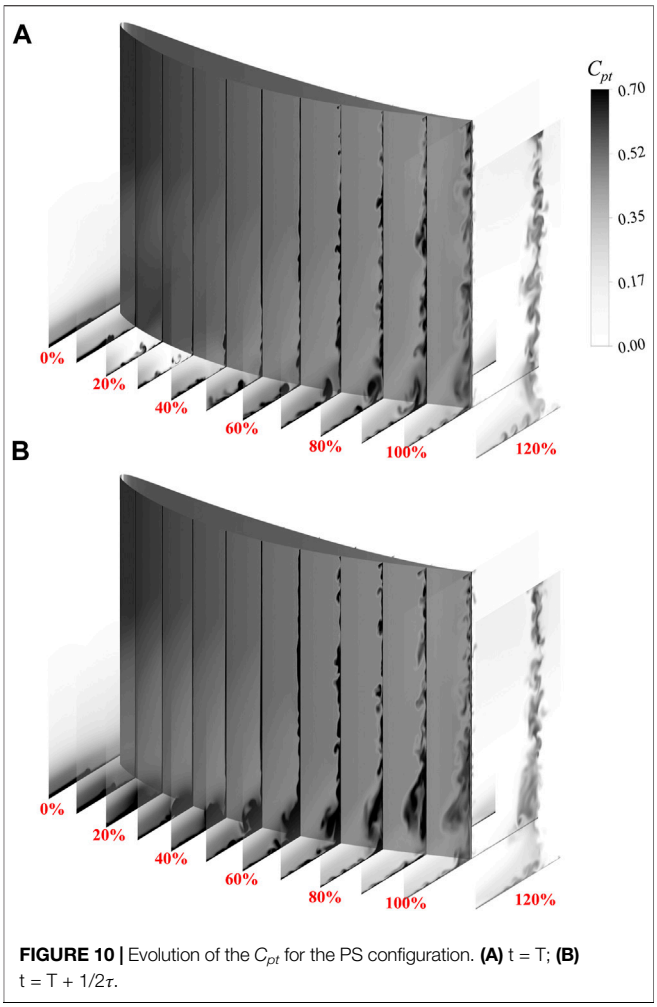

FIGURE 10 | Evolution of the C_{pt} for the PS configuration. **(A)** t = T; **(B)** t = T + 1/2τ.

flow near the endwall accumulates near the blade suction corner and gives rise to the PV, as is shown by the black dotted line. Compared with the position where the PV forms in **Figure 8B**, it is indicated that the formation of the PV is significantly moving downstream, which reduces the vortex structure size both spanwise and pitchwise, and the interaction between the PV and the separated flow from the blade suction surface is weakened; hence, the corresponding loss generated is reduced under the influence of the PS.

Figure 9 displays the evolution of the axial vorticity of the PS configuration, and the results at time T and T + 1/2τ are shown, corresponding to two different states of the suction hole in a pulse periodicity, and the contour of the C_{pt} can be seen in **Figure 10**. When t = T in **Figure 9A**, it can be known that the boundary layer near the endwall from the far upstream, as well as the transverse flow upstream of the suction hole, is removed by the suction hole; hence, the arising of the PV is interrupted. The formation of the PV, which is induced by the accumulation of the transverse flow near the endwall downstream of the suction hole, could be observed and indicated by the black curve. Combined with the contour of the loss evolution in **Figure 10A**, it can be known that less loss will be generated by the PV in this case, and its interaction with the blade suction surface flow separation will be attenuated accordingly, which contributes to the improvement of the compressor flow field. When t = T + τ in **Figure 9B**, the pressure leg of the HSV, colored red, and the suction leg of the HSV, colored blue, converge and give rising to the PV, as indicated by the black curve. The PV interacts with the blade suction surface flow at 60% c_x downstream of the leading edge and breakdown, causing a high level of total pressure loss, as shown in **Figure 10B**.

Figure 11 displays the three-dimensional instantaneous vortex structures in a pulse periodicity of the PS configuration. Combined with the analysis in **Figure 8**, it can be indicated that the compressor flow field is alternatively dominated by two different kinds of PV formation mechanisms under the influence of the PS. One of the PV formations is induced by the pressure leg and suction leg of the HSV, with large size, and results in a higher loss, as shown in **Figures 11B, C**. The other one is induced by the remaining part of the transverse flow near the endwall downstream of the suction hole, and due to the removal of most of the inlet boundary layer by the suction hole, the size of the PV is significantly reduced, and this leads to less loss. Though the suction hole can only affect the flow field near it, the formation mechanism of the PV downstream the suction hole is distinct, and in this way, the PS can have a more profound influence on the

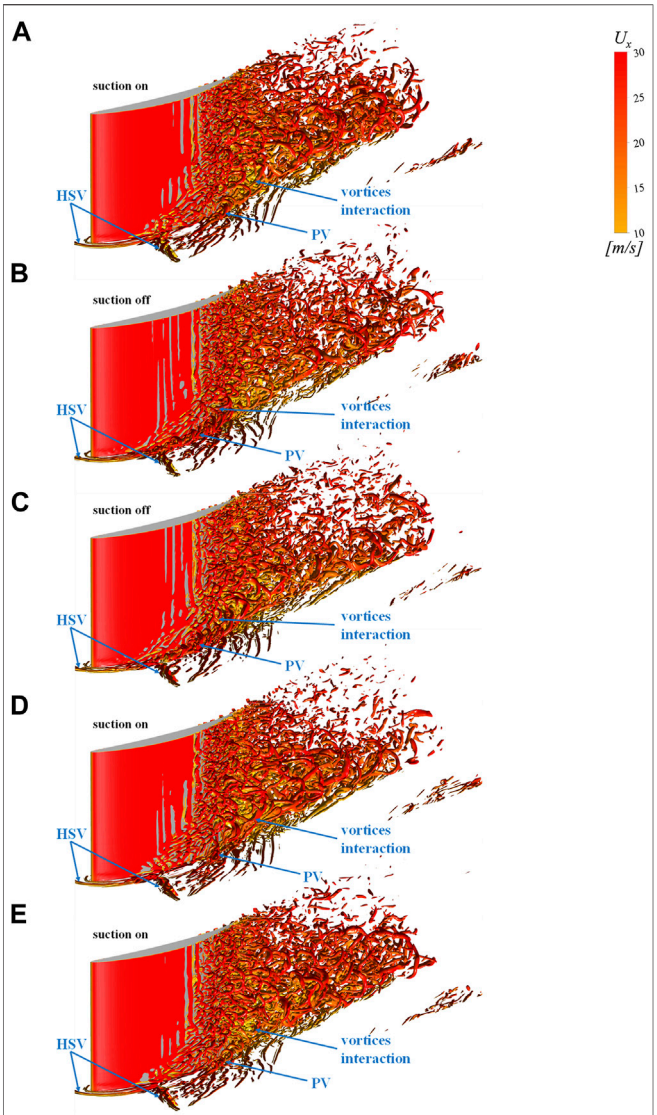

FIGURE 11 | Instantaneous vortex structures for the PS configuration (Q = 5,000,000). **(A)** t = T; **(B)** t = T + 1/4τ **(C)** t = T + 1/2τ; **(D)** t = T + 3/4τ; **(E)** t = T + τ.

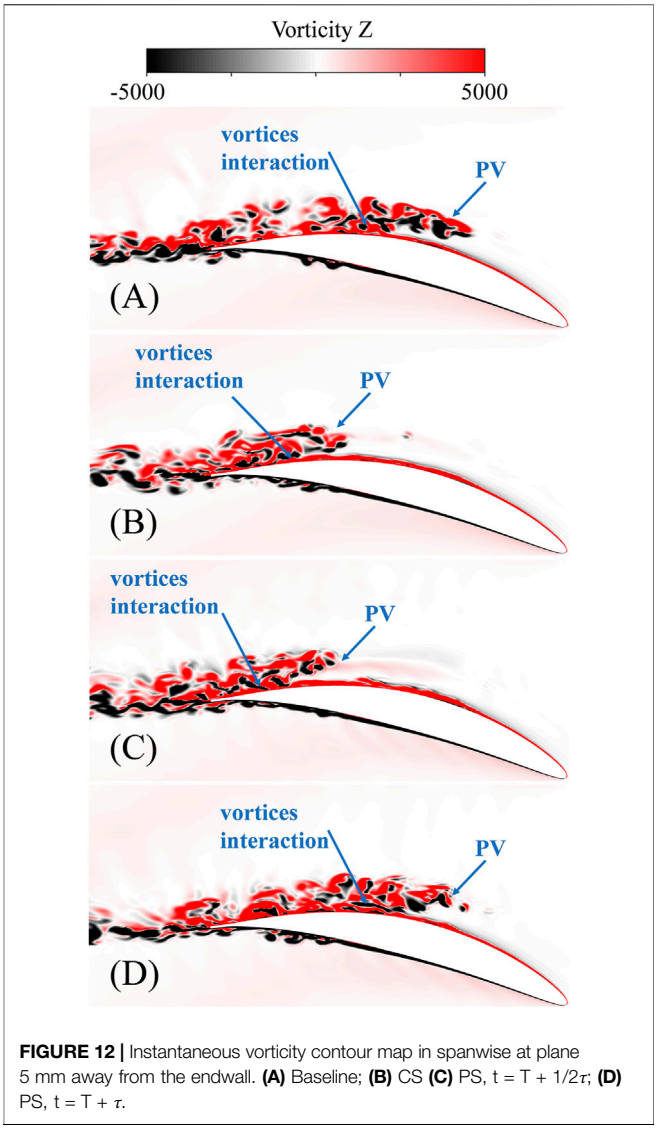

FIGURE 12 | Instantaneous vorticity contour map in spanwise at plane 5 mm away from the endwall. **(A)** Baseline; **(B)** CS **(C)** PS, t = T + 1/2τ; **(D)** PS, t = T + τ.

whole compressor flow field through the alternating transformation of two kinds of the PV formation mechanisms. Besides, the blade suction surface will be influenced by the periodic impingement of the PV, and the periodic perturbation of the PV will promote the momentum transport between the separated flow and the main flow, thus, leading to a further benefit in C_{pt}.

The instantaneous contour maps of the spanwise vorticity evolution of three configurations are given in **Figure 12**, and the contour maps at the plane at 5 mm away from the endwall are displayed. In the baseline in **Figure 12A**, the PV, which is derived from the convergence of the pressure leg (colored in red) and suction leg (colored in black) of the HSV, interacts with the flow on the blade suction surface at 55% c_x downstream the blade leading edge at the plane 5 mm away from the endwall. The vortices breakdown and result in higher loss as it flows downstream afterward. For the CS configuration, however, the interaction of the PV and the blade suction surface flow moving downstream at 73% c_x downstream the blade leading edge at the plane 5 mm away from the endwall. This indicates fewer vortex interactions and less loss generation compared with the baseline. For the PS configuration, there are two distinct flow patterns according to the opening or closing state of the suction hole, and one flow pattern is similar to that of the baseline, and the other one is similar to that of the CS configuration. These two flow patterns are alternately changed as the suction hole opens up and closes off, and this may transfer the excitation frequency of the suction hole to the whole compressor flow field, especially at the blade corner region where the PV and separated flow dominated, and reordered the local flow field; hence, the PS would have a better control performance than the CS at the same suction rate. To have better knowledge of the frequency information of the flow field, especially at the corner separated flow region, the fast Fourier transform (FFT) is applied to the local velocity at point A

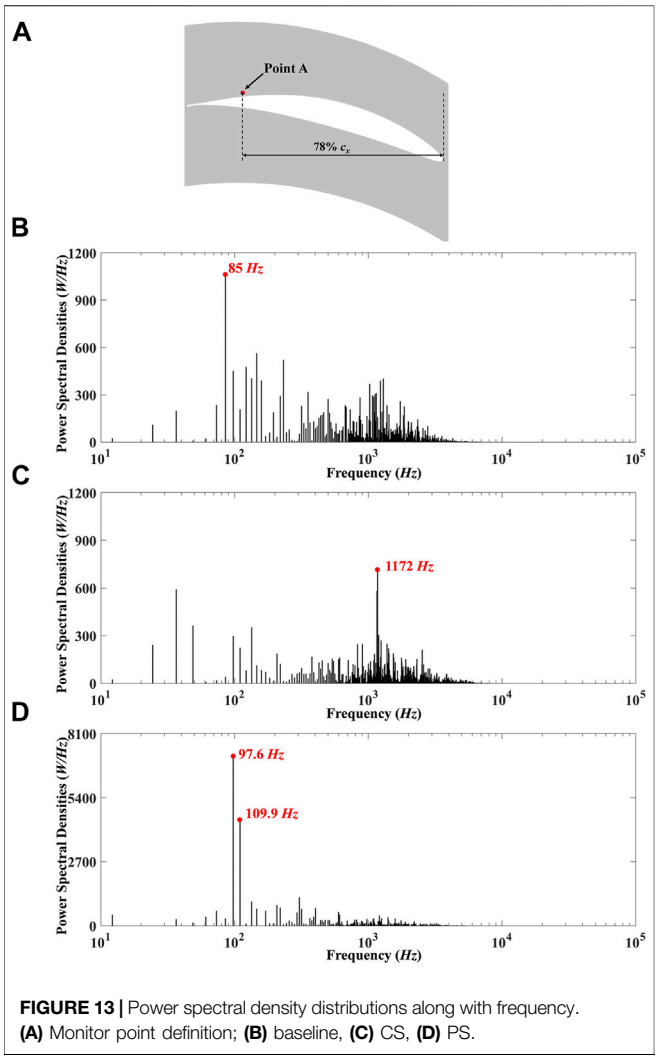

FIGURE 13 | Power spectral density distributions along with frequency. **(A)** Monitor point definition; **(B)** baseline, **(C)** CS, **(D)** PS.

(marked in **Figure 13A**), and the results are shown in **Figure 13**. **Figure 13** shows the power spectral density (PSD) distribution along with the frequency of three configurations, and it can be seen that the baseline, as shown in **Figure 13B**, has a dominant frequency of 85 Hz, and the PSD in this frequency is no more than 1,200 W/Hz. In **Figure 13C** of CS configuration, the dominant frequency was replaced by 1,172 Hz with a lower PSD of about 700 W/Hz. In PS configuration in **Figure 13D**, however, there are two frequencies (97.6 and 109.9 Hz) with large PSD, which means these two frequencies dominate the local flow field, and combined with the frequency of the PS, it can be inferred that the PS can reorder the flow field even at far downstream the suction hole through managing two kinds of the PV formation.

Proper Orthogonal Decomposition and Dynamic Mode Decomposition Analysis

The POD method can decompose the main flow structure in the flow field according to the proportion of the energy, and it not only helps in analyzing a specific mode structure independently but also removes the minor structures through reconstructing the flow field with the first few modes. The POD is based on the snapshots of the instantaneous results in this paper, and the data proceeding process is listed as follows, and detailed information can be found in Shi et al. (2019).

(1) The decomposition of the variables and reorder.

$$X(x,t) = X(x) + X'(x,t) \tag{4}$$

$$\boldsymbol{X_i} = \left[X_1'(x,t), X_2'(x,t), ..., X_N'(x,t)\right]^T \tag{5}$$

$$\boldsymbol{X} = [\boldsymbol{X_1}, \boldsymbol{X_2}, ..., \boldsymbol{X_N}] \tag{6}$$

$X(x,t)$ and $X(x)$ represent the transient and time-averaged velocity, and $X'(x,t)$ is the variation value. $\boldsymbol{X_i}$ denotes the velocity vector at t_i, and $\boldsymbol{X}$ is the velocity matrix.

(2) Build a covariance matrix **R** with the velocity matrix $\boldsymbol{X}$.

$$\mathbf{R} = \boldsymbol{X}^T\boldsymbol{X} \tag{7}$$

(3) Solve the eigenvalues $\boldsymbol{\lambda}$ and eigenvector $\boldsymbol{V}$ of the covariance matrix **R**.

$$\mathbf{R}\boldsymbol{V} = \boldsymbol{\lambda}\boldsymbol{V} \tag{8}$$

(4) Solve the basis vectors of the flow field.

$$\boldsymbol{\phi} = \boldsymbol{U}\boldsymbol{V} \tag{9}$$

(5) Reconstruct the flow field.

$$\boldsymbol{X_i} = \sum \alpha_j * \boldsymbol{\phi}_j \tag{10}$$

where α_j is the time coefficient of the mode j.

$$\alpha_j = \boldsymbol{X_i} * \boldsymbol{\phi}_j \tag{11}$$

The interaction between the PV and the separated flow from the blade suction surface can be obviously observed on the spanwise plane 10 mm away from the endwall; therefore, the axial velocity of the spanwise plane 10 mm away from the endwall is extracted to perform the POD. **Figure 14** shows the energy captured of the POD modes and the contour map of the first five orders of modes for the CS and PS configurations. Compared with the energy captured of the two configurations in **Figure 14A**, it can be seen that the PS increases the energy percent of the low-order modes, which indicates that the flow structures represented by the low-order modes have more ability to dominate the local flow field; hence, the flow field becomes simpler than that of the CS configurations. Besides, compared with the CS configuration in **Figure 14B**, it can be seen that the scale of the flow structures of the PS configuration in **Figure 14C** is larger, and the flow structures represented by the modes are much simpler compared with that of the CS configuration. Besides, it can be inferred that the CS only decreases the size of the vortex structures while keeping the disorder of the flow field unchanged. The PS, however, could also reorder the

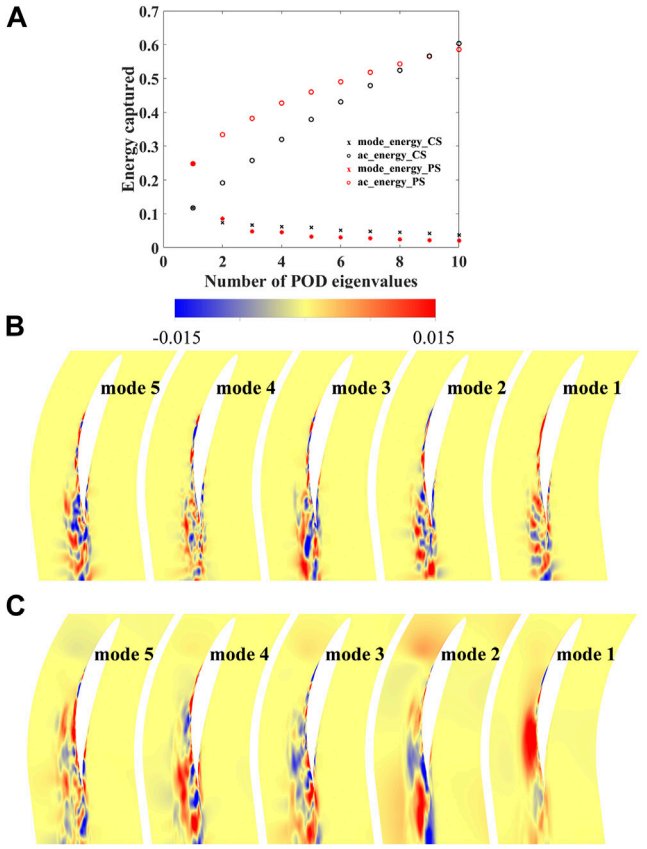

FIGURE 14 | Energy captured of the proper orthogonal decomposition (POD) modes and the contour map of the first five order modes. **(A)** Energy captured of the POD modes; **(B)** CS; **(C)** PS.

compressor flow field and make the flow field simpler, which could lead to a further reduction in the C_{pt}.

The DMD is a method that decomposes the flow field into different dynamic modes with distinct frequencies, and the stability of the modes, as well as the flow structures they represent, can be analyzed according to the eigenvalues. Unlike the POD method, the DMD can decompose the flow field from the order of time, and the calculation process is listed as follows (detailed information can be found in Schmid, 2010):

(1) Define velocity matrix $\boldsymbol{X}$ and $\boldsymbol{Y}$.

$$\boldsymbol{X} = [\boldsymbol{X_1}, \boldsymbol{X_2}, ..., \boldsymbol{X_{N-1}}] \tag{12}$$

$$\boldsymbol{Y} = [\boldsymbol{X_2}, \boldsymbol{X_2}, ..., \boldsymbol{X_N}] \tag{13}$$

where $\boldsymbol{X}$ and $\boldsymbol{Y}$ are the velocity matrix consisting of velocity data at different snapshots.

(2) Singular value decomposition of the velocity matrix $\boldsymbol{X}$.

$$[\boldsymbol{U}, \boldsymbol{S}, \boldsymbol{V}] = \mathrm{svd}(\boldsymbol{X}) \tag{14}$$

$\boldsymbol{U}$ and $\boldsymbol{V}$ are the singular value decomposition basis vectors of the $\boldsymbol{X}$ and $\boldsymbol{S}$ containing the information of the singular value.

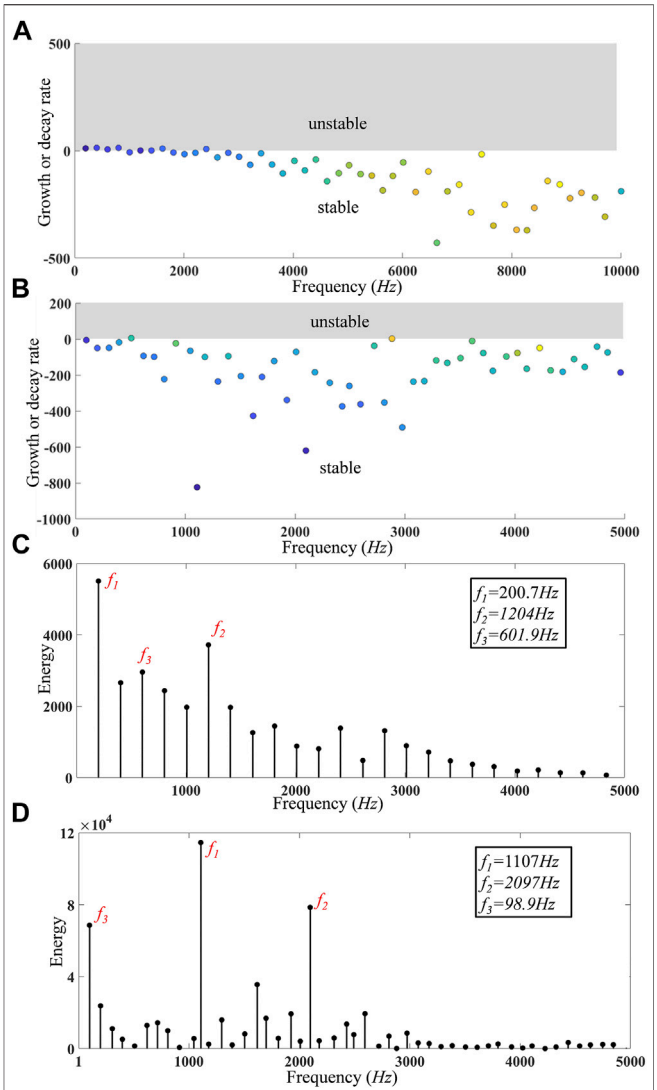

FIGURE 15 | Frequency spectra and the energy distribution of the CS and PS configurations. **(A)** Frequency spectra for the CS configuration; **(B)** frequency spectra for the PS configuration; **(C)** energy distribution for the CS configuration; **(D)** energy distribution for the PS configuration.

(3) Calculate the approximation matrix $\tilde{\mathbf{A}}$ using the vectors $\boldsymbol{U}$, $\boldsymbol{S}$, and $\boldsymbol{V}$ achieved from the last step.

$$\tilde{\mathbf{A}} = \boldsymbol{U}^T * \boldsymbol{Y} * \boldsymbol{V} * \boldsymbol{S}^{-1} \tag{15}$$

The matrix $\mathbf{A}$ is a transformation matrix that can achieve $\boldsymbol{Y}$ from $\boldsymbol{X}$, and $\tilde{\mathbf{A}}$ is an approximation of $\mathbf{A}$.

(4) Solve the eigenvectors and eigenvalues of the matrix $\tilde{\mathbf{A}}$.

$$[\boldsymbol{\Omega}, \boldsymbol{\Lambda}] = \mathrm{eig}\left(\tilde{\mathbf{A}}\right) \tag{16}$$

$\boldsymbol{\Omega}$ and $\boldsymbol{\Lambda}$ are the eigenvectors and eigenvalues, respectively.

(5) Calculate the DMD modes

$$\phi = Y^{*}V^{*}S^{-1}{}^{*}\Omega \quad (17)$$

ϕ is the matrix that contains the DMD modes.

The axial velocity of the spanwise plane 10 mm away from the endwall is extracted to perform the DMD. **Figure 15** is the frequency spectra and the energy distribution for the CS and PS configurations, and the abscissa is the frequency calculated from the image part of the continuous-time eigenvalues, and the ordinate is the growth or decay rate (positive indicates unstable characteristics and negative indicates stable characteristics) of the characteristics represented by the modes for **Figures 15A**,B. The modes are divided into stable and unstable ones according to the DMD eigenvalues, and if the real part of the eigenvalue is positive, the corresponding flow structures represented by the mode is unstable, and vice versa. It can be known from **Figure 15A** that some modes (especially the low-frequency ones) of the CS configuration are unstable (concentrated on the low frequency modes), presented as the positive value of the growth rate. For the PS configuration in **Figure 15B**, however, all the modes are stable, which indicates the flow field can be stabilized under the effect of the pulsed excitation. For example, the boundary layer on the blade suction surface will be much easier to separate from the solid wall under the influence of a small fluctuation if the flow is in an unstable state. For the same reason, the results of DMD with stable modes, such as the PS results, will lead to less flow separation and a reduction in C_{pt}. From the energy distribution at each mode in **Figures 15C,D**, it can be observed that three dominant modes occupied most of the energy in the PS configuration, and the effect of other modes are weakened. The frequencies of the dominant modes are 1,107, 2,097, and 98.9 Hz, respectively, and all these frequencies correspond to the excitation frequency and its frequency multiplication of the excitation frequency. It can be inferred that the flow field in the PS configuration is reordered and stabilized compared with that of the CS configuration; hence, the compressor performance could be improved, and the loss generation is reduced accordingly.

CONCLUSION

Based on the actual application of the bleed in aeroengine, and considering the removal of the airflow from the blade passage, an LES study of the effectiveness of the PS method for the compressor flow separation control was conducted herein. Three configurations (the baseline, CS, and PS) were used, and their flow details, including the vortex structures identified by the Q criterion, the C_{pt}, and the evolution of the vorticity and loss were displayed. Afterward, the POD and DMD methods were applied to analyze the flow field on the order of space and time, respectively. The following conclusions are drawn from the current investigation.

(1) At a suction flow rate of 0.25% of the main flow rate, the CS reduces C_{pt} by 9.36% based on the baseline, while the PS gains 24% more benefit on the basis of the CS and leads to a reduction in C_{pt} by 11.61% with an excitation frequency of 100 Hz, which indicates that the PS has more significant potential in reducing the total pressure loss in the compressor cascade.

(2) For the CS configuration, the reduction in the loss benefits from the reduction in the PV size in the compressor cascade. The formation of the PV is contributed by the transverse flow near the endwall at the existence of the suction hole, and the size of the PV is decreased due to the removal of the HSV. The interaction between the PV and the separation flow from the blade suction surface is postponed and attenuated; hence, the loss generation is reduced accordingly.

(3) For the PS configuration, two different PV formation mechanisms are found in the compressor cascade. The PV either arising from the HSV or contributed by the transverse flow near the endwall alternately forms, and the frequency is approximately equal to the excitation frequency according to the FFT results. The periodic perturbation of the PV promotes the momentum transport between the separated flow and the main flow, thus, leading to a further benefit in C_{pt}.

(4) The PS not only reduces the size of the PV but also simplifies and stabilizes the compressor flow field by introducing an excitation frequency. Compared with the CS, the proportion of energy occupied by each POD mode is transferred to lower-order modes, and the flow structures represented by lower-order POD modes become simpler in PS configuration. All DMD modes in the PS configuration are stable, which could contribute to a further loss reduction.

DATA AVAILABILITY STATEMENT

The original contributions presented in the study are included in the article/supplementary material, Further inquiries can be directed to the corresponding author.

AUTHOR CONTRIBUTIONS

YG and SC provided the research ideas and wrote the original manuscript. YG and CZ carried out all the calculation work. YG, SC, and SW were responsible for the revision of this paper.

FUNDING

This work is supported by the National Natural Science Foundation of China (Grant Nos. 52076052 and 51776048) and National Science and Technology Major Project of China (Grant Nos. Y2019-VIII-0013-0174).

REFERENCES

Cerretelli, C., and Kirtley, K. (2009). Boundary Layer Separation Control with Fluidic Oscillators. *ASME J. Turbomach.* 131, 041001. doi:10.1115/1.3066242

De Giorgi, M. G., Traficante, S., De Luca, C., Bello, D., and Ficarella, A. (2012). "Active Flow Control Techniques on a Stator Compressor Cascade: A Comparison between Synthetic Jet and Plasma Actuators," in ASME Turbo Expo 2012: Turbine Technical Conference and Exposition, Copenhagen, Denmark, June 11–15, 2012. ASME Paper. GT-2012-69535. doi:10.1115/GT2012-69535

Decaix, J., Balarac, G., Dreyer, M., Farhat, M., and Münch, C. (2015). RANS and LES Computations of the Tip-Leakage Vortex for Different gap Widths. *J. Turbulence* 16, 309–341. doi:10.1080/14685248.2014.984068

Denton, J. D., and Xu, L. (2002). "The Effects of Lean and Sweep on Transonic Fan Performance," in ASME Turbo Expo 2002: Power for Land, Sea, and Air, Amsterdam, The Netherlands, June 3–6, 2002. ASME Paper GT2002-30327. doi:10.1115/GT2002-30327

Evans, S., Hodson, H., Hynes, T., Wakelam, C., and Hiller, S.-J. (2010). Controlling Separation on a Simulated Compressor Blade Using Vortex-Generator Jets. *J. Propulsion Power* 26, 819–827. doi:10.2514/1.45518

Gao, F., Ma, W., Zambonini, G., Boudet, J., Ottavy, X., Lu, L., et al. (2015). Large-Eddy Simulation of 3-D Corner Separation in a Linear Compressor cascade. *Phys. Fluids* 27, 085105. doi:10.1063/1.4928246

Gbadebo, S. A., Cumpsty, N. A., and Hynes, T. P. (2008). Control of Three-Dimensional Separations in Axial Compressors by Tailored Boundary Layer Suction. *ASME J. Turbomach.* 130, 2179–2194. doi:10.1115/1.2749294

Gbadebo, S. A., Cumpsty, N. A., and Hynes, T. P. (2005). Three-Dimensional Separations in Axial Compressors. *ASME J. Turbomach.* 127, 331–339. doi:10.1115/1.1811093

Gümmer, V., Goller, M., and Swoboda, M. (2008). Numerical Investigation of End wall Boundary Layer Removal on Highly Loaded Axial Compressor Blade Rows. *ASME J. Turbomach.* 130, 011015. doi:10.1115/1.2749297

Hecklau, M., Van Rennings, R., Zander, V., Nitsche, W., Huppertz, A., and Swoboda, M. (2011a). Particle Image Velocimetry of Active Flow Control on a Compressor cascade. *Exp. Fluids* 50, 799–811. doi:10.1007/s00348-010-0895-z

Hecklau, M., Wiederhold, O., Zander, V., King, R., Nitsche, W., Huppertz, A., et al. (2011b). Active Separation Control with Pulsed Jets in a Critically Loaded Compressor Cascade. *AIAA J.* 49, 1729–1739. doi:10.2514/1.J050931

Hecklau, M., Zander, V., Peltzer, I., Nitsche, W., Huppertz, A., and Swoboda, M. (2010). "Experimental AFC Approaches on a Highly Loaded Compressor cascade," in *Active Flow Control* II. Editor R King (Berlin, Heidelberg: Springer-Verlag Berlin Heidelberg), 171–186. doi:10.1007/978-3-642-11735-0_12

Heinichen, F., Gümmer, V., Plas, A., and Schiffer, H.-P. (2011). Numerical Investigation of the Influence of Non-axisymmetric Hub Contouring on the Performance of a Shrouded Axial Compressor Stator. *CEAS Aeronaut. J.* 2, 89–98. doi:10.1007/s13272-011-0007-7

Hunt, V. D., Wray, A. A., and Moin, P. (1988). *Eddies, Streams, and Convergence Zones in Turbulent Flows.* Washington D.C: Studying Turbulence Using Numerical Simulation Databases-I1, 193–232. doi:10.1007/978-1-4613-1063-1_7

Jabbal, M., Liddle, S., Potts, J., and Crowther, W. (2013). Development of Design Methodology for a Synthetic Jet Actuator Array for Flow Separation Control Applications. *Proc. Inst. Mech. Eng. G: J. Aerospace Eng.* 227, 110–124. doi:10.1177/0954410011428256

Kerrebrock, J. L., Epstein, A. H., Merchant, A. A., Guenette, G. R., Parker, D., Onnee, J.-F., et al. (2008). Design and Test of an Aspirated Counter-Rotating Fan. *ASME J. Turbomach.* 130, 021004. doi:10.1115/1.2776951

Kerrebrock, J. L., Reijnen, D. P., Ziminsky, W. S., and Smilg, L. M. (1997). "Aspirated Compressors," in International Gas Turbine and Aeroengine Congress and Exposition Conference, Orlando, FL, June 2–5, 1997. doi:10.1115/97-GT-525

Leggett, J., Priebe, S., Shabbir, A., Michelassi, V., Sandberg, R., and Richardson, E. (2018). Loss Prediction in an Axial Compressor cascade at Off-Design Incidences with Free Stream Disturbances Using Large Eddy Simulation. *ASME J. Turbomach.* 140, 071005. doi:10.1115/1.4039807

Lei, V.-M., Spakovszky, Z. S., and Greitzer, E. M. (2008). A Criterion for Axial Compressor Hub-Corner Stall. *ASME J. Turbomach.* 130, 031006. doi:10.1115/1.2775492

Leishman, B. A., Cumpsty, N. A., and Denton, J. D. (2007). Effects of Bleed Rate and Endwall Location on the Aerodynamic Behavior of a Circular Hole Bleed Off-Take. *ASME J. Turbomach.* 129, 645–658. doi:10.1115/1.2752191

Nicoud, F., and Ducros, F. (1999). Subgrid-Scale Stress Modelling Based on the Square of the Velocity Gradient Tensor. *Flow, Turbul. Combust.* 62, 183–200. doi:10.1023/A:1009995426001

Schatz, M., and Thiele, F. (2001). "Numerical Study of High-Lift Flow with Separation Control by Periodic Excitation," in 39th aerospace sciences meeting and exhibit, Reno, NV, January 8–11, 2001. AIAA-2001-0296. doi:10.2514/6.2001-296

Schmid, P. J. (2010). Dynamic Mode Decomposition of Numerical and Experimental Data. *J. Fluid Mech.* 656, 5–28. doi:10.1017/S0022112010001217

Seifert, A., Bachar, T., Koss, D., Shepshelovich, M., and Wygnanski, I. (1993). Oscillatory Blowing: A Tool to Delay Boundary-Layer Separation. *AIAA J.* 31, 2052–2060. doi:10.2514/3.49121

Shi, L., Ma, H., and Wang, L. (2019). Analysis of Different POD Processing Methods for SPIV-Measurements in Compressor cascade Tip Leakage Flow. *Energies* 12, 1021. doi:10.3390/en12061021

Sun, S., Chen, S., Liu, W., Gong, Y., and Wang, S. (2018). Effect of Axisymmetric Endwall Contouring on the High-Load Low-Reaction Transonic Compressor Rotor with a Substantial Meridian Contraction. *Aerospace Sci. Technol.* 81, 78–87. doi:10.1016/j.ast.2018.08.001

Sun, S., Wang, S., Chen, S., Tao, C., Cai, L., and Chen, J. (2019). The Impact of Various Forward Sweep Angles on the Performance of an Ultra-High-Load Low-Reaction Transonic Compressor Rotor. *Appl. Therm. Eng.* 150, 953–966. doi:10.1016/j.applthermaleng.2019.01.045

Tucker, P. G. (2011a). Computation of Unsteady Turbomachinery Flows: Part 1-Progress and Challenges. *Prog. Aerospace Sci.* 47, 522–545. doi:10.1016/j.paerosci.2011.06.004

Tucker, P. G. (2011b). Computation of Unsteady Turbomachinery Flows: Part 2-LES and Hybrids. *Prog. Aerospace Sci.* 47, 546–569. doi:10.1016/j.paerosci.2011.07.002

Wei, M., Xavier, O., Lipeng, L., and Francis, L. (2013). Intermittent Corner Separation in a Linear Compressor cascade. *Exp. Fluids* 54, 1546. doi:10.1007/s00348-013-1546-y

Zambonini, G., Ottavy, X., and Kriegseis, J. (2017). Corner Separation Dynamics in a Linear Compressor cascade. *J. Fluids Eng.* 139, 061101. doi:10.1115/1.4035876

Zhang, H., Chen, S., Gong, Y., Wang, S., and Wang, Z. (2018). Combined Application of Negative Bowed Blades and Unsteady Pulsed Holed Suction in a High-Load Compressor in Terms of Aerodynamic Performance and Energy Efficiency. *Appl. Therm. Eng.* 144, 291–304. doi:10.1016/j.applthermaleng.2018.08.046

Zhang, H., and Chen, S. (2021). Pulsed Suction Control in a Highly Loaded Compressor Cascade with Low Suction Flowrates. *ASME J. Turbomach.* 143 (6), 1–39. doi:10.1115/1.4050112

Zheng, X.-Q., Zhou, X.-B., and Zhou, S. (2005). Investigation on a Type of Flow Control to Weaken Unsteady Separated Flows by Unsteady Excitation in Axial Flow Compressors. *ASME J. Turbomach.* 127, 489–496. doi:10.1115/1.1860572

Zheng, X., Zhou, S., Hou, A., Jiang, Z., and Ling, D. (2006). Separation Control Using Synthetic Vortex Generator Jets in Axial Compressor Cascade. *Acta Mech. Sin.* 22, 521–527. doi:10.1007/s10409-006-0042-5

Conflict of Interest: The authors declare that the research was conducted in the absence of any commercial or financial relationships that could be construed as a potential conflict of interest.

NOMENCLATURE

c chord

c_x axial chord

t pitch

α_1 inlet metal angle

α_2 outlet metal angle

x axial direction

y pitch direction

z span direction

U velocity

ω vorticity

τ pulse periodicity

p_0 total pressure

p static pressure

ρ density

i incidence

θ inclination angle

γ stagger angle

H span height

LE leading edge

TE trailing edge

PV passage vortex

HSV horseshoe vortex

BL baseline

CS constant suction

PS pulsed suction.

frontiers in Energy Research

ORIGINAL RESEARCH
published: 22 March 2022
doi: 10.3389/fenrg.2022.853166

Large-Eddy Simulation of the Boundary Layer Development in a Low-Pressure Turbine Cascade With Passive Flow Control

Pengcheng Yang, Shaowen Chen, Weihang Li and Cong Zeng*

Engine Aerodynamics Research Center, Harbin Institute of Technology, School of Energy Science and Engineering, Harbin, China

The boundary layer development on a low-pressure turbine blade surface modified by recessed dimples, U-grooves, and rectangular grooves has been investigated through the large-eddy simulations. The simulations are performed at a Reynolds number of 50,000 (based on the inlet velocity and axial chord length) and extremely low freestream turbulence conditions. The characteristic parameters of the boundary layer are used to estimate the development of the boundary layer, and spectral analysis has also been performed to identify the dominant frequency of shedding vortices. The results of simulations indicate that three surface modifications all reduce the profile losses by restraining the separation bubble size. However, the grooves and dimples show different mechanisms in inhibiting laminar separation. Grooves tend to promote the formation of spanwise vortices, which is more difficult to break into turbulence. A high-speed shedding vortex is induced by the particular 3D structure of dimple, and its shedding frequency is nearly twice the Kelvin–Helmholtz (K-H) instability frequency. The interaction between the shedding vortices and the K-H vortices promotes the breakdown process of the spanwise vortices, which leads to an earlier transition of the boundary layer at a low disturbance level. The current study reveals the different mechanisms of dimples and grooves and shows the great potential of dimples for flow control in low-pressure turbines. Besides, the flow structures inside the dimples with adverse pressure gradients are also explored.

Keywords: dimple, low-pressure turbine, laminar separation, spectral analysis, flow control, LES

OPEN ACCESS

Edited by:
Xiao Liu,
Harbin Engineering University, China

Reviewed by:
Shaobing Han,
Dalian Maritime University, China
Shijun Sun,
Beijing Institute of Technology, China
Yanfeng Zhang,
Institute of Engineering Thermophysics (CAS), China

****Correspondence:***
Shaowen Chen
cswemail@hit.edu.cn

Specialty section:
This article was submitted to Advanced Clean Fuel Technologies, a section of the journal Frontiers in Energy Research

Received: *12 January 2022*
Accepted: *01 March 2022*
Published: *22 March 2022*

Citation:
Yang P, Chen S, Li W and Zeng C (2022) Large-Eddy Simulation of the Boundary Layer Development in a Low-Pressure Turbine Cascade With Passive Flow Control. Front. Energy Res. 10:853166. doi: 10.3389/fenrg.2022.853166

INTRODUCTION

Modern aircraft are designed to have a higher cruising altitude and better engine performance with a larger thrust-to-weight ratio to have a better stealth performance and reduce energy consumption. However, these would lead to the low Reynolds number operation conditions and higher loading of the blade in a low-pressure turbine (LPT), respectively (Houtermans et al., 2004; Praisner et al., 2008; Ji et al., 2021). These characteristics of the LPT stage make the boundary layer on the aft portion of the blade suction side remain laminar and suffer greater

Abbreviations: Cx, axial chord length (unit: mm); $\overline{C_p}$, time-averaged wall-pressure coefficient; $\overline{P_{in}}$, time-averaged static pressure of inlet; x, streamwise coordinate (unit: mm); $\overline{V}_{in}$, time-averaged velocity at the inlet (unit: m/s); DC, dimple center; DE, dimple edge; $\overline{C_f}$, time-averaged wall-skin friction coefficient; $\overline{f_{wall}}$, time-averaged wall shear stress (unit: Pa); δ^*, displacement thickness; θ, momentum thickness; H, shape factor; C_{pt}, total pressure loss coefficient; f, frequency (unit: Hz).

pressure gradients. Hence, it is easier to separate from the wall (Volino, 2008). The separation would lead to significant efficiency losses of the engine, as has been described by Lyall et al. (2011). Therefore, exploring proper methods to solve this problem is significant to improving the engine performance.

A mass of active and passive flow control strategies have been implemented to delay or prevent the boundary layer separation on the LPT blade's suction side (Sondergaard, 2008). Passive flow control is generally implemented by geometry modification of blade surfaces such as recessed grooves, dimples, turbulent trips, and micro-riblets and changing roughness (Lake et al., 1999; Lake et al., 2000; Volino, 2003; Robarge et al., 2004; Montis et al., 2011). Compared with the active control method, the passive way is cheaper and easier to apply in a real engine which is independent of extra energy and device.

Dimples have been employed primarily on golf ball surfaces for drag reduction and were mainly developed for blade cooling in the turbine stage (Bearman and Harvey, 1976; Hwang et al., 2008). The recessed dimples are used to prevent the laminar separation in the LPT blade by Lake et al. (1999)firstly. In their research, three surface treatments including recessed V-grooves, dimples, and trips have been studied experimentally. The dimples which refer to Bearman and Harvey's testing about golf ball dimples have a depth-to-diameter ratio of 0.009, the depth is 1.59 mm, and it is a single row with a spanwise spacing of 22.2 mm. The results have shown that blades with dimple cavities have superior performance for all Reynolds numbers, whereas V-grooves and trips increase the loss generated at higher Reynolds numbers. Inspired by Lake's findings, Rouser (2002) and Casey et al. (2004) pushed the study further. The flow control effect of three different configuration patterns: a single row with different dimple spacing and axial locations, multiple rows of dimples, and asymmetric dimples, is explored by them. These studies suggested that the best location of a single dimple row is near the separated point. However, adding the second row of dimples and asymmetric dimples has no significant improvement on blade performance. In order to further understand the relationship between dimple parameters and flow structures inside the dimples, numerous numerical studies have been performed systematically on a flat plate model with recessed dimples by Vincent and Mapple (2006). They claimed that the flow structure in and around a dimpled cavity is determined by the boundary layer thickness and the dimple size. Moreover, the potential benefits of dimples emerge only when the high-speed shedding exists downstream of the dimples. These studies have demonstrated the capability of the dimple to diminish the adverse effects of laminar flow separation. Furthermore, surface grooves also have been used to inhibit laminar separation, such as rectangular grooves (Volino, 2003) and U-shaped grooves (Robarge et al., 2004), which have taken a good effect too.

It has been noticed that the extent of the laminar separation is mainly affected by the flow state of the separated shear layer since the turbulent boundary layer has stronger momentum exchange than the laminar one and thus is less easy to separate. At low Reynolds numbers, the transition of the separated shear layer may or may not lead to reattachment to the surface, resulting in a short or long laminar separation bubble (LSB). With the development of high-resolution numerical simulation and experimental methods, researchers gain more details about the dynamics of the laminar separation bubble. Most of the previous studies that focused on separation bubbles were performed on a flat plate with an adverse pressure gradient, which was mainly developed by Gaster and Grant (Yarusevych et al., 2008). The transition process of separated boundary layer induced by a change of surface curvature was investigated by Yang and Voke (2001) using a large-eddy simulation method. They claimed that the free shear layer is inviscidly unstable, and the spanwise two-dimensional vortices roll up in the bubble due to the Kelvin–Helmholtz mechanism. With the growth of the three-dimensional motions, spanwise vortices are distorted and break into hairpin vortices further downstream, leading to reattachment and a fully established turbulent boundary layer. The experimental investigation to identify the coherent structures formed within a laminar separation bubble was carried out by Kurelek et al. (2016). They also concluded that the transition process is directly related to the breakdown of the shear-layer vortices in the aft portion of the separation bubble. The research studies performed by Yang et al. and Kurelek et al. are both under quite small freestream turbulence conditions. However, the transition process within the LSB is significantly affected by the freestream turbulence intensity (FSTI). The different dynamics of the transition process in LSBs under the level of freestream turbulence with intensities of 0.1 and 1.45% at separation was presented by McAuliffe and Yaras (2007). They described the breakdown of the spanwise vortices caused by the small-scale fluctuations within the braid region between spanwise vortices under a lower-disturbance environment. At a higher FSTI, spanwise vortices are replaced by streamwise streaks which are caused by "Klebanoff modes" (K-modes). These streaks were primarily identified by Klebanoff and have been observed in extensive numerical simulations and experiments by other researchers. The combined effect of K-H and K-mode instability mechanisms was elucidated by Hosseinverdi and Fasel (2019): K-H instability is the dominant mechanism at lower FSTI conditions, while the K-mode instability becomes the dominant one as the FSTI increases.

The present study is conducted to understand the effect of LPT blade surface modification on the boundary layer development in the laminar separation bubble. Three surface modification strategies, including recessed dimples, recessed U-grooves, and rectangular grooves, were applied to eliminate the laminar separation on the aft portion of a highly loaded LPT blade suction side. Large-eddy simulations were employed to gain more details of the flow field. First, the different boundary layer developments of the three modified surfaces were compared. Then, the flow structure within the dimple cavities and the interactions between shedding vortices generated by dimples and separation bubbles were demonstrated.

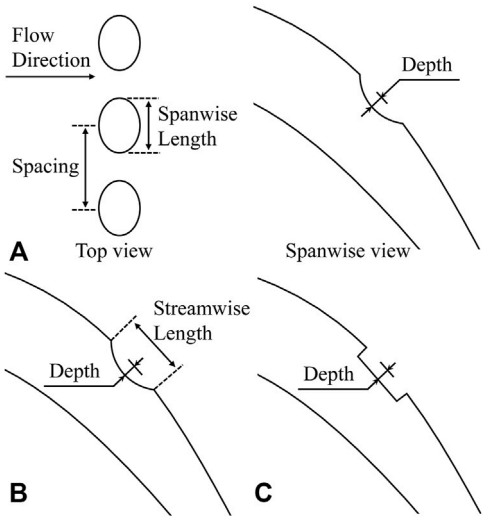

FIGURE 1 | Dimple and groove geometry: **(A)** dimple; **(B)** U-groove; **(C)** rectangular groove.

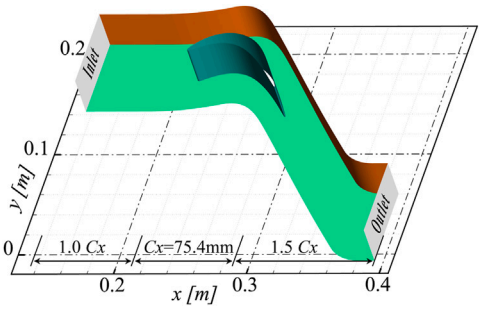

FIGURE 2 | Schematic of the computational domain.

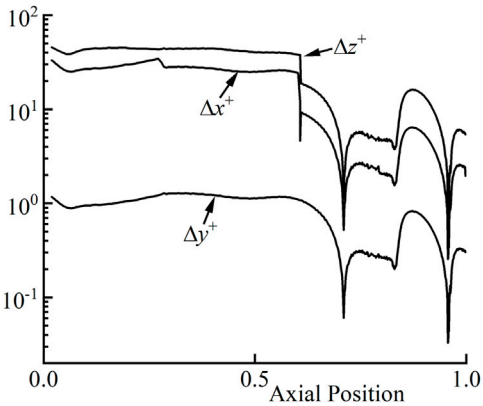

FIGURE 3 | Grid resolution in wall units.

NUMERICAL METHOD

Geometry

The well-known Pratt and Whitney experimental LPT Pak-B blades with and without modified surface are both investigated in this paper. The Pak-B airfoil, which has been widely studied, is a highly loaded and mid-loaded airfoil with Z_w = 1.08, where Z_w is the Zweifel lift coefficient (Mahallati et al., 2013). Under low Reynolds number conditions, profile losses of this airfoil increase dramatically due to boundary layer separation on the aft portion of the suction surface, which has been confirmed by many researchers (Lyall et al., 2011; Mahallati et al., 2013). In the present study, the blade size is scaled with a factor of 0.45, and the scaled blade's axial chord length (Cx) is 75.4 mm. The blade angle is 30° of the inlet and 60° of the outlet. The spanwise extent of the blade is approximately 0.4 Cx, which is deemed sufficient to allow for the natural development of large-scale three-dimensional transient features as the flow transitions to a turbulent state in the separated shear layer (Rizzetta and Visbal, 2003).

Three surface modifications, including recessed dimples, recessed U-grooves, and rectangular grooves, have been used to eliminate the adverse impact on aerodynamics caused by laminar separation. The surface geometries are shown in **Figure 1** schematically. According to the previous studies (Lake et al., 1999; Rouser, 2002; Casey et al., 2004), the best location of a single dimple row is near the separation point. (Once the dimple is placed downstream the separation point, the low-speed fluid inside the bubble would lead to a reduction in flow advection into the cavity, thus restricting the impact of the dimple on the flow field.) Furthermore, larger turbulence losses will be produced by the earlier boundary layer transition when the dimple is further upstream of the separation point, which eventually results in only a slight change in losses. The single row of dimples is placed at the natural, expected separation location of 70% axial chord length. Dimples are recessed into the blade to a depth of 1.6 mm using a ball with a diameter of 11.6 mm. The depth-to-diameter ratio is 0.14. Since the blade surface is curved, the resulting dimple edge is elliptical and has a streamwise length of 7 mm and spanwise length of 8 mm. The spacing of the dimple center is 10 mm. The recessed U-groove is designed to have the same shape as the dimple center on the spanwise vertical plane and to be located in 70% axial chord length. Rectangular grooves with 1.6 mm depth and 7 mm streamwise length are also investigated for comparison.

Details of Numerical Simulation

The separation bubble on the Pak-B blade suction surface is investigated using large-eddy simulation in the present study. The large eddies which contain most of the turbulent kinetic energy (TKE) are calculated explicitly, while the smaller ones, which tend to be more isotropic and homogeneous, are modeled in LES. The Reynolds number based on the inlet velocity and axial chord length is 50,000. The freestream turbulence intensity is extremely low because the turbulence generators are not used at the inlet of the fluid domain. The schematic of the computational domain is shown in **Figure 2**. In order to eliminate the influence of inlet and outlet boundaries on the solution, the computational domain extended 1.0 Cx and 1.5 Cx in upstream and downstream

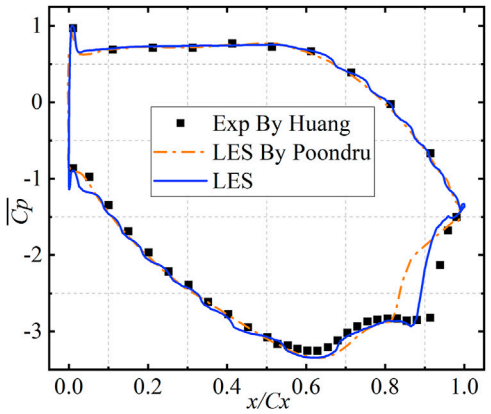

FIGURE 4 | Time-averaged and spanwise-averaged wall-pressure coefficient distribution compared with experimental data by Huang and LES data by Poondru.

directions. A structured multi-block mesh topology method is employed to discretize the spatial domain, and approximately 7×10^6 cells are used. The flow field near the blade surface is resolved *via* an O-type mesh, which ensures the grid orthogonality of the blade wall and can predict the flow in the boundary layer more precisely. **Figure 3** shows the grid resolution in wall units along the blade suction surface. The dimensionless scale of the grid in wall units is $25< \Delta x^+ <30$, $1< \Delta y^+ <1.5$, $35< \Delta z^+ <45$, which is consistent with that in some published studies (Roberts and Yaras, 2005; Cui et al., 2016). The mesh grid is refined in the aft portion of the suction surface where separation occurs, thus having a higher grid resolution to obtain separated flow details.

All simulations are performed using the RANS results as the initial conditions. The governing equations are closed using the WALE (wall-adapted local eddy-viscosity) sub-grid scale model, which has been extensively used in LES. The discretization of spatial derivatives is based on central differencing, and the implicit second-order accurate backward Euler integration is used to advance the solution in time. The total pressure and static pressure distributions specified on the inlet and outlet boundaries are related to the experimental values. The domain is bounded by a symmetric boundary condition in the spanwise direction. Only one single blade passage is calculated in pitch-wise, and the domain is bounded by a periodicity boundary condition. A no-slip wall condition is imposed on the blade surface. The time-step size in the simulations is 8×10^{-6}, yielding a Courant number of 1.0 based on the node spacing and the freestream velocity. Four inner iterations are found to be sufficient to converge the solution to a low magnitude of residuals under the time-step size. With the initial flow field, the solutions are allowed to develop for thirteen through-flows to achieve the convergence, and approximately 10,000 time-steps are required. The time-averaged statistics are then collected for three through-flow periods.

Validation

One of the challenges for numerical simulation in the LPT turbine is to predict the laminar separation bubble precisely. In **Figure 4**, the time- and spanwise-averaged static pressure coefficient ($\overline{C_p}$) distribution on the blade surface is compared between the current study, LES by Poondru, and experimental results by Huang (2005) and Poondru (2008). x/Cx is the relative position along the flow direction. $\overline{C_p}$ is defined as

$$\overline{C_p} = \frac{\bar{P} - \overline{P_{in}}}{0.5\rho \overline{V_{in}^2}}, \tag{1}$$

where $\bar{P}$ and $\overline{P_{in}}$ are the time-averaged local wall pressure and inlet static pressure and $\overline{V_{in}}$ is the time-averaged velocity of inlet. The separation and reattachment locations of the bubble can be inferred from the distribution of $\overline{C_p}$, although the real situation is time-variant. The wall pressure in the fore portion of the bubble almost remains constant because the fluid close to the wall is virtually stationary, thus resulting in a "plateau" of pressure on the surface. The calculated results are in good agreement with the experimental results except for the separated region. LES by Poondru predicted an early reattachment and therefore had a higher blade loading. The current simulation shows a better result than the LES by Poondru, but still slightly earlier reattachment than the experimental results is predicted. Furthermore, **Figures 5A,B** compare the time- and spanwise-averaged velocity profiles inside the bubble at different locations. In the aft portion of the separation bubble, velocity profiles calculated by current LES

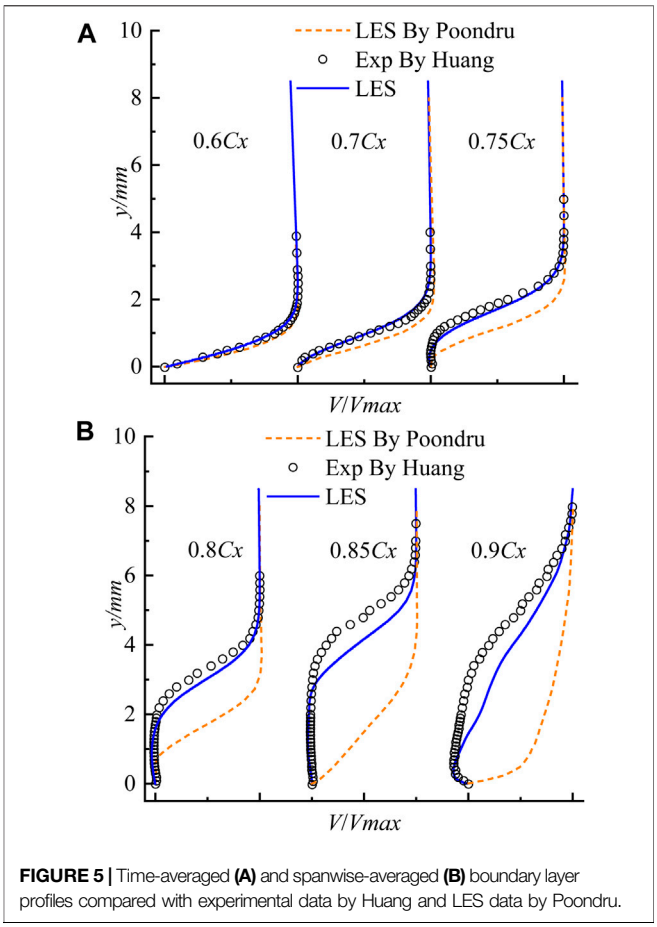

FIGURE 5 | Time-averaged **(A)** and spanwise-averaged **(B)** boundary layer profiles compared with experimental data by Huang and LES data by Poondru.

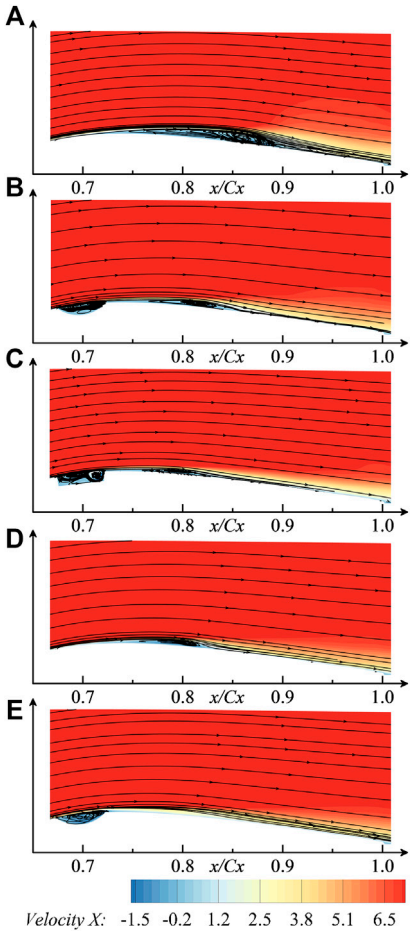

FIGURE 6 | Contours of time- and spanwise-averaged streamwise velocity: **(A)** baseline; **(B)** U-groove; **(C)** rectangular groove; **(D)** DE plane; **(E)** DC plane.

deviate slightly from the experimental data because of the increasing complexity of the flow field. However, since the research is conducted by comparing different cases, it is believed that the results here are acceptable.

RESULTS AND DISCUSSION

In this section, the results calculated from the LES of separated boundary layers on the LPT blade surface for several passive control strategies: recessed dimples, recessed U-grooves, and recessed rectangular grooves, are carefully compared under investigated conditions. For the current investigation, these modified surface structures have the same axial position, maximum engraved depth, and almost the same width in the streamwise direction. A detailed analysis of recessed dimples based on the instantaneous flow structures and spectral analysis is then carried out to explore how the engraved dimples affect the boundary layer development on the LPT blade suction surface.

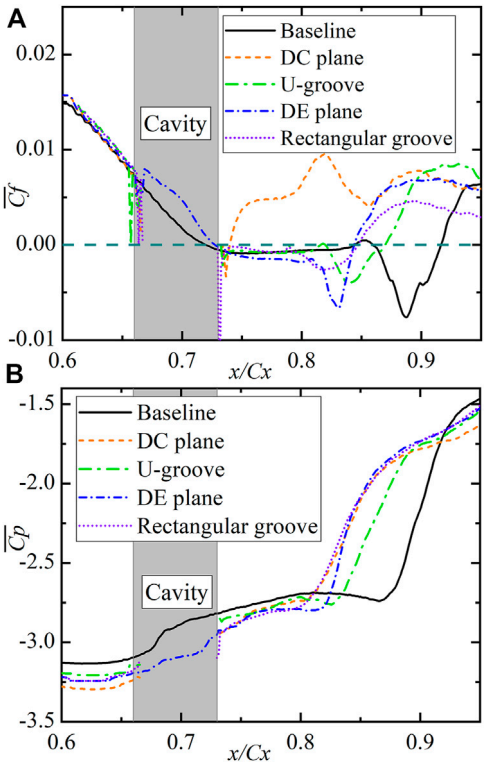

FIGURE 7 | Time- and spanwise-averaged **(A)** wall-skin friction coefficient and **(B)** wall-pressure coefficient distribution for various surfaces.

Comparison of Boundary Layer Developments Between Dimples and Grooves

Time-Averaged Flow Field

Velocity and Wall Coefficients

The time-averaged development of the boundary layer, which is obtained by calculating the arithmetic average of the results of nearly 3,000 time-steps, is discussed for different surface treatments. **Figure 6** shows the contours of time-mean and spanwise-averaged streamwise velocity on spanwise vertical surfaces. Two spanwise vertical planes are selected on the dimpled surface for discussion: vertical plane located in the dimple center and dimple edge (between two dimples), which is represented as DC (dimple center) and DE (dimple edge). The reason for doing this is that dimples are 3D structures and have a different effect along the spanwise direction. Spanwise averaging has been done for the other cases to make the results more reliable. As shown in **Figure 6**, a large low-speed fluid region exists on the surface without modifications due to the severe separation of the boundary layer. When the surface is recessed by dimples, U-grooves, and rectangular grooves, the low-speed region of fluid is reduced significantly. Especially on the DC plane, the low-speed region is almost eliminated. In order to gain more details about the separation bubble, the predicted distribution on the aft portion of the suction surface of time- and spanwise-averaged wall-pressure coefficients and wall-skin

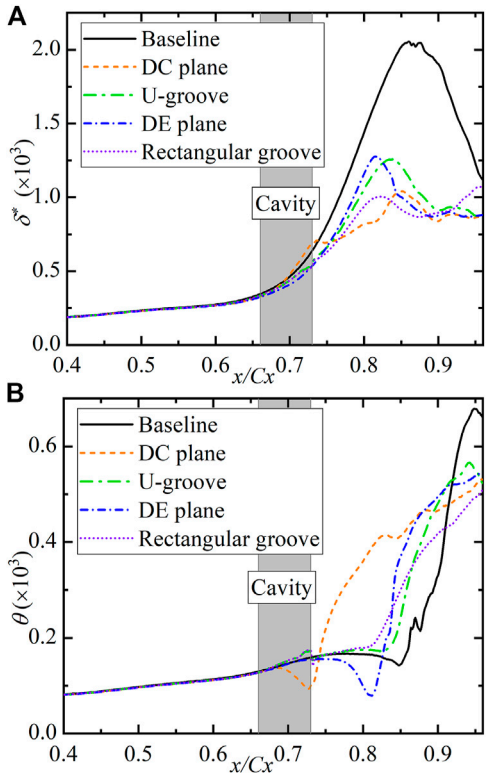

FIGURE 8 | Time- and spanwise-averaged **(A)** displacement thickness and **(B)** momentum thickness distribution for various surfaces.

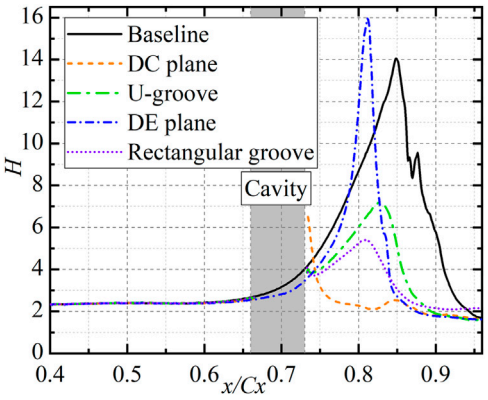

FIGURE 9 | Time- and spanwise-averaged shape factor distribution for various surfaces.

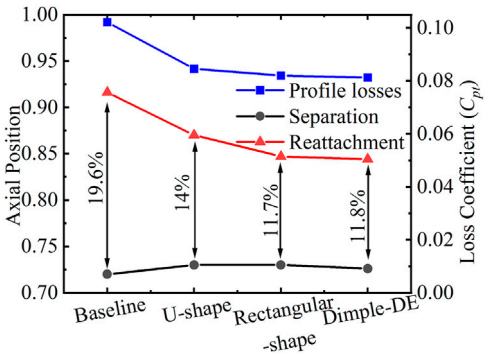

FIGURE 10 | Separation bubble length and the correlated profile losses for various surfaces.

friction coefficients, $\overline{C_p}$ and $\overline{C_f}$, is plotted in **Figure 7** for LES with different cases. $\overline{C_f}$ is defined as

$$\overline{C_f} = \frac{\overline{f_{wall}}}{0.5\rho\bar{V}_{in}^2}, \tag{2}$$

where $\overline{f_{wall}}$ is the time-averaged wall shear stress along the flow direction. The gray area in the pictures is the portion in which the blade surface is concaved. As shown in **Figure 7A**, all the surface treatments make the mean reattachment point, at which $\overline{C_f}$ changes from negative to positive, move upstream significantly. The separation location, at which $\overline{C_f}$ changes from positive to negative, is located at 0.72Cx for the unmodified surface and is not clear for recessed ones because of the existence of cavities. However, the boundary layer just downstream of the cavities has been separated from the wall, and a sharp decrease of $\overline{C_f}$ exists due to the strong local inverse-flow induced by the cavities. Another sharp decrease of $\overline{C_f}$ happens in the aft portion of the separation bubble, which is referred to as the reverse-flow region. The dimpled surface shows the best performance in reducing the separation bubble size in the streamwise direction. On the DC plane, the separation bubble is nearly eliminated except for a small inverse-flow area, while on the DE plane, the boundary layer separates later and reattaches to the surface earlier. As for the rectangular grooves, the right angle at the downstream side leads to a stronger reverse flow on the blade surface. Thus, $\overline{C_f}$ decreases more dramatically than that in the dimples and U-grooves. Its reattachment point is slightly downstream of the point on the DE plane. However, the integral influence of U-grooves on the profile losses is not better than that of dimples, which has been shown later. The U-grooves make the reattachment point move upstream but not as much as the others. It is worth mentioning that the intensity of inverse-flow inside the separation bubble with U-grooves and rectangular grooves is lower than that on the DE plane, although the bubble length is larger in the streamwise direction. The pressure distribution has also been significantly changed due to the earlier reattachment, as shown in **Figure 7B**. The pressure recovered earlier, and the blade loading increased slightly as the separation is restrained.

Shape Factor, Displacement, and Momentum Thickness

The height of the separation bubble in the direction normal to the wall has changed differently from the bubble length along the streamwise direction. The streamwise variation of the displacement thickness, δ^*, and the momentum thickness, θ, is also plotted in **Figures 8A,B** to get further insight into the development of the boundary layer for different cases.

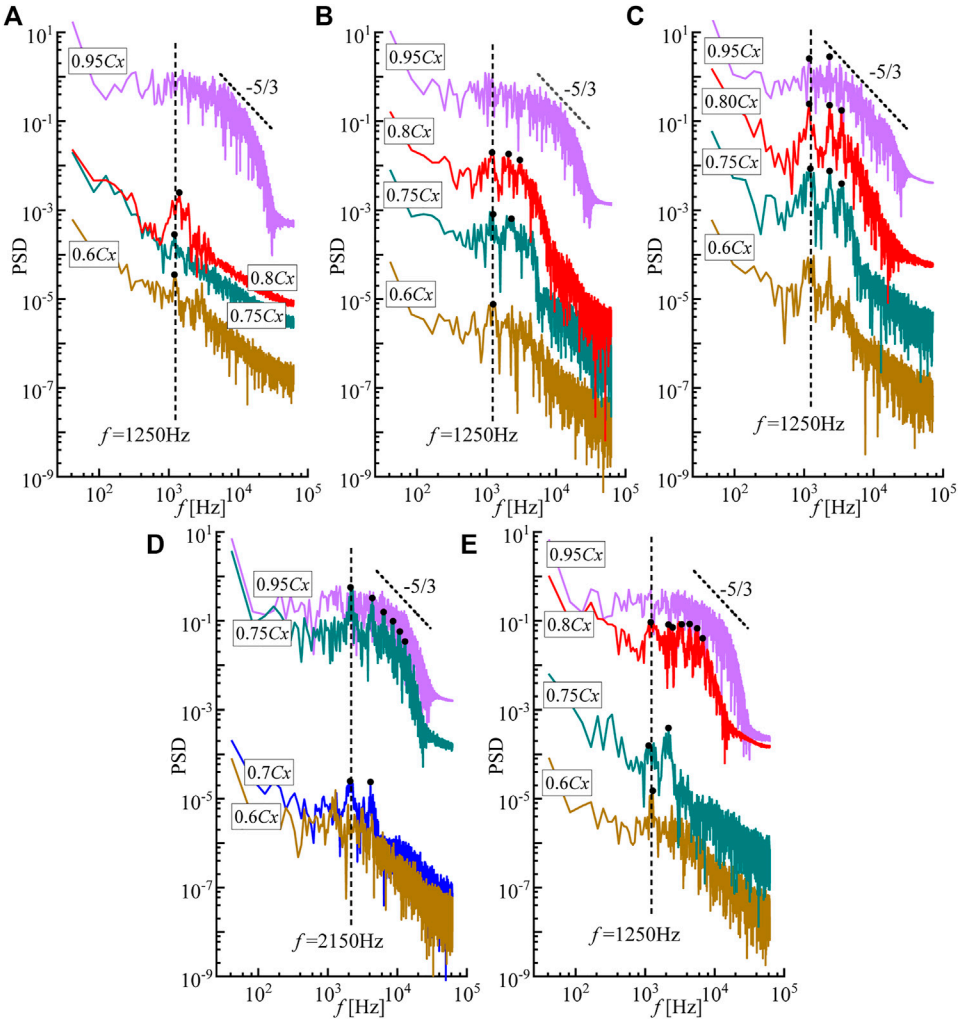

FIGURE 11 | Power spectral of streamwise velocity fluctuations for all cases at various axial positions: **(A)** baseline; **(B)** U-shape; **(C)** rectangular shape; **(D)** DC plane; **(E)** DE plane.

The displacement thickness varies slowly before separation and increases rapidly since the separation occurs. The surface without modification has the maximum value of displacement thickness, which indicates that the height of the separation bubble is the largest. All surface treatments significantly reduce the height of the separation bubble. However, the rectangular grooves and U-grooves are found to be more effective in reducing the thickness of the separation bubble compared to the dimples. The separation bubble on the surface recessed by rectangular grooves is much smaller in the direction normal to the surface than that on the DE plane, although the bubble is a little longer along the streamwise direction. A similar trend is obtained when the separation bubbles on the U-grooved and DE surfaces are compared. A serious mass deficit is observed although the boundary layer is attached to the DC plane, which might be caused by the thick boundary layer. The momentum thickness distribution in **Figure 8B** decreases first and then increases right downstream of the separation point. The decrease and rapid growth of θ would presumably be corresponding to the dead air region and reverse-flow region in the separation bubble because of the different flow rates. For all modified surfaces, the formation of the reverse-flow regions in the time-averaged result moves upstream, representing the shear layer rolls up earlier in a transient sense. A similar relationship between the rapid growth of momentum thickness and reverse-flow region formation was also observed by Hosseinverdi and Fasel (2019).

Furthermore, the transition process of the boundary layer plays a crucial role in the formation of a separation bubble. The shape factor H, which is plotted in **Figure 9**, is a useful parameter for empirically estimating the boundary layer's state on separation and transition. It is calculated by the ratio of δ^* to θ. For all the cases in the present study, the boundary layer has a shape factor of approximately 2.5 before the separation point, which is the expected value for the laminar boundary layer. The shape factor begins to grow rapidly when the separation occurs,

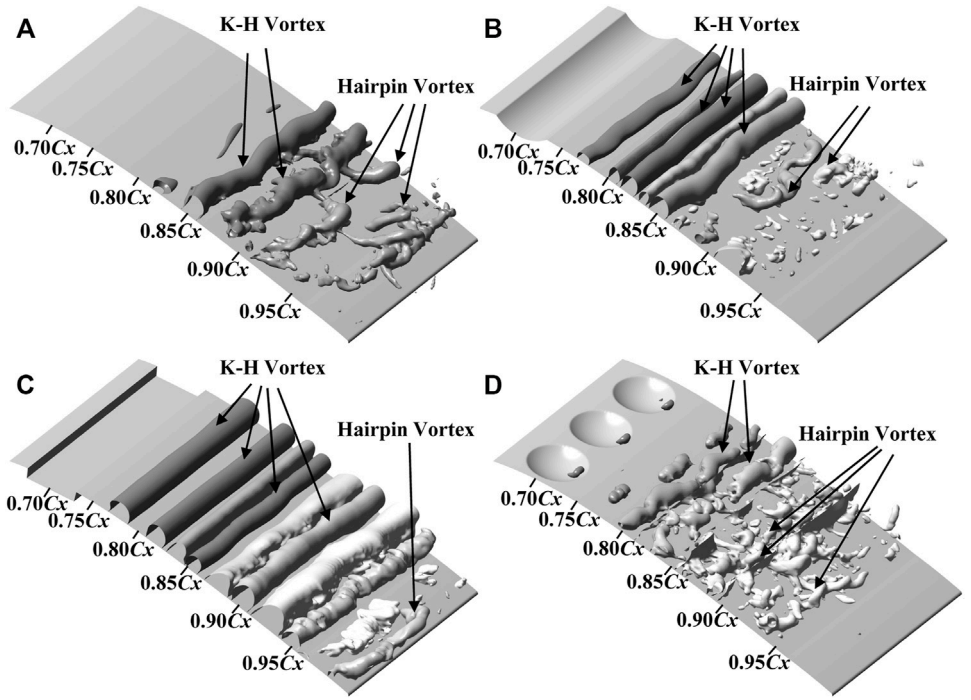

FIGURE 12 | Vortex structures in the separation bubble identified by pressure iso-surfaces: **(A)** baseline; **(B)** U-shape; **(C)** rectangular shape; **(D)** dimple.

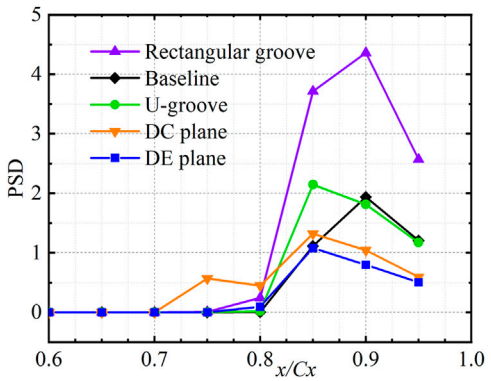

FIGURE 13 | Growth rate of most-amplified disturbances.

owing to the increase of displacement thickness and the slight reduction of momentum thickness. The typical value of shape factor when separation occurs is 3.5 for the laminar boundary layer. With the recovery of the momentum thickness caused by the reverse flow, the shape factor decreases gradually. The separation and reattachment points estimated empirically by the shape factor are almost consistent with those in the analysis above for all cases. All the surface treatments make the boundary layer transition earlier except for rectangular grooves. The boundary layers on the DE and DC planes eventually recover to a fully turbulent shape at the same position after reattachment, with a shape factor smaller than 2 in the current study. The boundary layer on the U-grooved surface transforms into fully established turbulence later. The rectangular grooves, however, fail to accelerate the transition of boundary layer although a smaller separation bubble is produced.

Overall Performance

Profile losses in a low-pressure turbine blade could be increased significantly due to the separation bubble. **Figure 10** shows the variation of profile losses as the bubble length (BL) varies for different surface modifications. The loss coefficient used here is defined as

$$C_{pt} = \frac{P_{0,in} - P_{0,out}}{0.5\rho V_{in}^2}, \tag{3}$$

where $P_{0,in}$ and $P_{0,out}$ are the time-averaged inlet and outlet total pressure. By reducing the separation bubble size, all modifications significantly reduce the profile losses, which shows a close relationship between separation and losses. The recessed dimples show the best performance in reducing the profile losses by 20.4% under the investigated Reynolds number and turbulence intensity conditions. The results indicate that the dimples are more useful in inhibiting separation in an overall sense due to the 3D effect of dimples, although the height of the separation bubble on the DE plane is much larger than that on the surface recessed by rectangular grooves. The rectangular grooves and U-grooves reduce the profile losses by 18.9 and 16.2%, respectively. It can be concluded that the dimples have the greatest potential in inhibiting flow separation compared with rectangular grooves and U-grooves when they are located at the

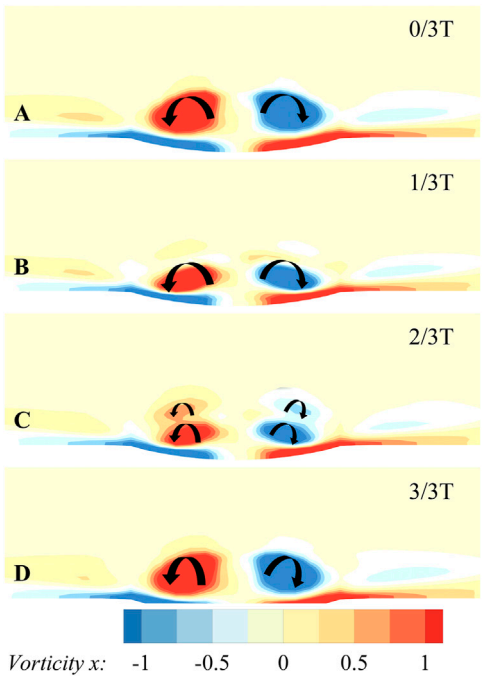

FIGURE 14 | Streamwise vorticity contours at the dimple trailing edge during one shedding periodicity.

same position and have a similar maximum depth and streamwise length. Furthermore, the dimples are unlikely to have the unacceptable penalties at high Reynolds number conditions, while the U-grooves and rectangular grooves have been proved to produce significantly higher losses at higher Reynolds numbers (Lake et al., 2000; Volino, 2003; Robarge et al., 2004). The blade recessed by dimples also tends to have higher strength than that recessed by spanwise grooves.

Spectral Analysis and Instantaneous Vortex Structures

An overall understanding of the time-averaged development of the boundary layer has been obtained above. In this section, the spectral analysis is performed, and the instantaneous vortex structures inside the boundary layer are presented for discussion. The authors tried to get a detailed insight into the laminar–turbulent transition process to explain why these surface modifications can reduce the separation bubble size.

The rapid growth of disturbance inside the separated shear layer would lead to the laminar–turbulent transition, which is essential to the separation bubble size. Under low freestream turbulence conditions, inviscid Kelvin–Helmholtz (K-H) mode has been proved to be the dominant instability during the transition process of the separated boundary layers by numerous studies (Yang and Voke, 2001; Kurelek et al., 2016; McAuliffe and Yaras, 2007; Hosseinverdi and Fasel, 2019). With the growth of unstable fluctuations due to K-H instability, the shear layer rolls up, resulting in the formation of spanwise vortices (K-H vortices). The distortions and breakdown to small-scale turbulent structures of spanwise vortices then occur due to the small-scale turbulence activity (McAuliffe and Yaras, 2007). The Fourier spectra of the streamwise velocity fluctuations for all cases are presented in **Figure 11** for several streamwise locations near the bubble. The data are obtained along with the separated shear layer where the large wall-normal velocity gradient exists. The related vortex structures are identified in **Figure 12** by the pressure isocontours. For the unmodified surface, the boundary layer is laminar, and the inner disturbance is quite low at the locations before separation, as shown in **Figure 11A**. As the boundary layer develops, the disturbances are amplified, and a dominant frequency peak appears at around 1250 Hz, which represents the typical K-H instability frequency. This frequency could be confirmed through the Strouhal number, $Sr_\theta = f\theta/\Delta U$, where f is the unstable frequency, θ is the boundary layer momentum thickness at the separation point, and ΔU is the streamwise velocity at the separation point (McAuliffe and Yaras, 2005). The dominant instability Strouhal number observed in the present simulation is 0.0109, and it is in good agreement with the typical Sr range obtained by many researchers for K-H instability, including 0.005–0.011 by Yang and Voke, 0.010–0.014 by Talan and Hourmouziadis (2002), and 0.011 by McAuliffe and Yara (at low freestream turbulence conditions).

Growth of the most-amplified instability frequency results in the formation of spanwise quasi-two-dimensional vortices, as shown in **Figure 12A**. Further downstream, the spanwise vortices are distorted and break into turbulence very quickly over a short streamwise distance with the appearance of typical hairpin-like structures. Another evidence of the breakdown to turbulence is the frequency content redistribution over a much wider range, as observed in **Figure 11A**. The dominant frequency peak disappears, and fully developed turbulence has been established at 95% axial length position as confirmed by the classical spectrum slopes based on Kolmogorov's theory for isotropic turbulence. Compared with the unmodified surface, the boundary layer becomes more unstable when it crosses over the surface of U-grooves and rectangular grooves, and the inner disturbance grows more rapidly, as shown in **Figures 11B,C**. The most-amplified fluctuation frequency occurs at the fundamental frequency 1,200 Hz, which is almost the same as the K-H instability frequency in the present study. As a result, the spanwise vortices roll up much earlier than on the unmodified surface, as shown in **Figures 12B,C**. However, the spanwise vortices have the intensified vortex intensity and exist over a much longer streamwise distance than on the smooth wall before the breakdown, which means the U-grooves and rectangular grooves have no significant effect in promoting the transition process. Especially, for the rectangular grooves, the spanwise vortices persist further downstream to 95% axial chord length due to a greater disturbance amplitude caused by the sharp edge. It can be concluded that the grooves lead to the stronger K-H instability waves, resulting in the earlier formation and shedding of spanwise vortices with intensified vortex intensity. The intensified spanwise vortices increase the momentum transfer process in the wall-normal direction, and a reattachment region exists downstream of the vortex. The shedding of spanwise vortices results in the periodic

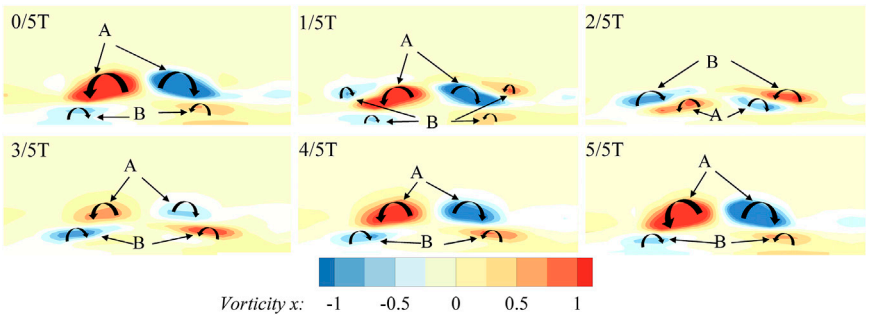

FIGURE 15 | Streamwise vorticity contours downstream the dimple trailing edge in one cycle of vortex shedding.

separation and reattachment of the boundary layer, and it shows a larger reattachment area in a time-averaged sense.

Nevertheless, the dimples show a completely different mechanism in reducing the laminar separation than the grooves. As shown in **Figure 11D**, PSD peaks at around the frequency of 2,150 Hz and at the subharmonic frequencies start to become visible at the 75% chord length location on the DC plane. The typical K-H instability frequency peak is not observed. Spectra of the streamwise velocity pertaining to the boundary layer on the DC plane indicate the existence of the high-frequency shedding vortices downstream of the dimple structure. The shedding vortices could also be identified in **Figure 12D** by the pressure isocontours. The boundary layer on the DC plane is almost attached in a time-averaged sense due to the high-frequency shedding vortices. On the DE plane, however, **Figure 11E** shows a dominant instability frequency at 1,166 Hz representing the typical instability frequency in the present study, which indicates the existence of the K-H vortices. As time proceeds further, disturbances in this frequency band are amplified, following a subharmonic growth. It is worth noting that another frequency peak appears near 2,100 Hz at 80% axial chord length. This could be the development of shedding vortices generated by the dimples along the spanwise direction, as shown in **Figure 12D**. The interaction between the higher-frequency shedding vortices and the low-frequency shedding K-H vortices results in a rapid breakdown of K-H vortices, causing an earlier transition of the laminar boundary layer into the turbulent one. Thus, the separation is inhibited significantly. The particularly three-dimensional structure of dimples makes it possible to promote the earlier boundary layer transition *via* a minor modification on the surface. The growth rate of most-amplified disturbances at various locations is also compared in **Figure 13**. The dimples lead to a lower level of disturbance than the others while the transition process is finished earlier. This may also be the reason why the dimples have a better performance at higher Reynolds numbers than the grooves.

The different mechanisms between dimples, U-grooves, and rectangular grooves show the excellent performance of dimples in restraining the laminar flow separation under low freestream turbulence conditions. The following section describes the influence of several dimple parameters on the flow control effect and investigates the flow structures inside the dimple.

Flow Structure Inside the Dimple

High-frequency shedding vortices downstream of the recessed dimples have been observed *via* the spectral analysis above. Due to the existence of front steps in the trailing edge of the cavities, the fluid flowing through the concave surfaces flows back into the cavities leading to the formation of vortices. However, unlike the U-grooves and rectangular grooves, the bending of dimple edge in the spanwise direction makes the vortex lean toward the streamwise direction. The fluid is accumulated from the spanwise sides to the dimple center, and a pair of counter-rotating streamwise vortices appear in the aft portion of the dimples. The dominant streamwise vortex pair is observed in the present study and many previous studies (Ligrani et al., 2001; Won et al., 2005). The temporal variation of the computed streamwise dimensionless vorticity distribution on the plane perpendicular to the flow direction near the trailing edge of the dimples is shown in **Figure 14** for one whole period of the shedding vortices. It can be seen that a filling/dumping or "breathing" cycle similar to that described in Vincent and Mapple's research (Vincent and Mapple, 2006) exists obviously inside the dimples. The intensity of the dominant streamwise vortex pair decreases and increases periodically, just like "breathing," which is related to the shedding of vortices. The streamwise vortex pair becomes smaller with the shedding of vortices, as shown in **Figure 14B**. However, as time proceeds further, the small vortices generated at the downstream side of dimples gradually converge to the trailing edge of dimples. A new counter-rotating streamwise vortex pair appears at the trailing edge as presented in **Figure 14C**. These two pairs of streamwise vortices then merge into a stronger vortex pair, as shown in **Figure 14A,D**. In addition, the shedding vortex structures also have changed when they depart the dimple as shown in **Figure 15**. The dimensionless vorticity distribution on the plane downstream the dimples is presented in **Figure 15** for a complete vortex shedding period. Two alternating streamwise vortex pairs (A and B) are observed in the figures. The stronger one, A, represents the shedding of dominant streamwise vortex pair, while the other indicates the shedding of vortex pairs induced by dominant vortices inside the dimples.

Furthermore, the flow structures inside the dimples are significantly affected by the adverse pressure gradient since the dimples are placed behind the maximum velocity point on the suction side. More fluid flows back into the dimples, and the streamwise vortices inside the dimples are intensified. Meanwhile, the two counter-rotating vortices coalesce on the dimple trailing edge, and a small scale of spanwise vortex appears at the dimple center as shown in **Figure 12D**. The spanwise vortex connects the streamwise vortex pair: A and B, forming a shedding structure. The shedding structures are associated with the adverse pressure gradient closely. The existence of the adverse pressure gradient makes the streamwise vortex pair B be deflected to the spanwise direction gradually and finally interacts with the spanwise vortices rolled up on both sides.

CONCLUSION

The boundary layer developments on the blade suction surfaces modified by the recessed dimples, recessed U-grooves, and recessed rectangular grooves have been investigated through large-eddy simulation under low Reynolds number and low freestream turbulence conditions. The mechanisms of grooves and dimples associated with the inhibition of laminar separation are demonstrated in the present study.

The dimples show the best performance in reducing profile losses by restraining the separation bubble size. The overall profile losses are reduced by 20.4% with dimples, 18.9% with rectangular grooves, and 16.2% with U-grooves. Under low freestream turbulence conditions, the transition process in a separation bubble is dominated by Kelvin–Helmholtz instability, which results in the formation of spanwise vortices. The spanwise vortices are then distorted and broken into fully turbulent structures. Grooves and dimples show different mechanisms for restraining the separation bubble size. Stronger K-H vortices are induced by grooves of U-shape and rectangular shape, resulting in a larger reattachment area downstream the vortex. However, the intensified spanwise vortices are more difficult to break down to turbulence. As for the rectangular grooves, the turbulent boundary layer is fully established near the trailing edge. A high-speed shedding vortex has been observed downstream the dimple center with a shedding frequency twice the K-H instability frequency through the spectral analysis and pressure isocontour. The interaction between high-speed shedding vortices and spanwise vortices leads to an earlier breakdown to turbulence with a lower level of disturbances. The earlier transition makes the separated boundary layer reattach further upstream, thus reducing the profile losses. The lower level of disturbances caused by dimples also makes the persistent high performance of LPT at a higher Reynolds number possible.

Furthermore, the dimples require a minor surface treatment on the blade surface than the grooves. It could be concluded that dimples have the greatest potential than the grooves in reducing the profile losses due to the unique 3D structures. This study provides further insight into why dimples are better than grooves as a flow control technology in low-pressure turbine blades, and it is meaningful for the development of new passive flow control technologies.

The flow structures inside the dimples are also investigated. A dominant counter-rotating streamwise vortex pair forms in the aft portion of the dimple. When subjected to an adverse pressure gradient, the flow structure inside the dimple is significantly different from that under the condition of the positive pressure gradient. The dominant counter-rotating vortices coalesce at the dimple trailing edge and then shed from the dimples alternatively with another pair of counter-rotating vortices induced by itself. The streamwise vortices then deflect in the spanwise direction and finally interact with the spanwise vortices.

DATA AVAILABILITY STATEMENT

The raw data supporting the conclusions of this article will be made available by the authors, without undue reservation.

AUTHOR CONTRIBUTIONS

PY and SC pushed forward this research topic and were responsible for manuscript writing. WL contributed to the numerical simulation. CZ provided significant help in data processing.

FUNDING

This work is supported by the National Natural Science Foundation of China (Grant Nos. 52076052 and 51776048) and National Science and Technology Major Project of China (Grant Nos. Y2019-VIII-0013-0174).

REFERENCES

Bearman, P. W., and Harvey, J. K. (1976). Golf ball Aerodynamics. *Aeronaut. Q.* 27 (2), 112–122. doi:10.1017/s0001925900007617

Casey, J., King, P., and Sondergaard, R. (2004). "Parameterization of Boundary Layer Control Dimples on a Low Pressure Turbine Blade," in *40th AIAA/ASME/SAE/ASEE Joint Propulsion Conference and Exhibit*. Fort Lauderdale, Florida: American Institute of Aeronautics and Astronautics, 3570. doi:10.2514/6.2004-3570

Cui, J., Nagabhushana Rao, V., and Tucker, P. (2016). Numerical Investigation of Contrasting Flow Physics in Different Zones of a High-Lift Low-Pressure Turbine Blade. *J. Turbomach.* 138 (1), 011003. doi:10.1115/1.4031561

Hosseinverdi, S., and Fasel, H. F. (2019). Numerical Investigation of Laminar-Turbulent Transition in Laminar Separation Bubbles: the Effect of Free-Stream Turbulence. *J. Fluid Mech.* 858, 714–759. doi:10.1017/jfm.2018.809

Houtermans, R. G., Coton, T., and Arts, T. (2004). Aerodynamic Performance of a Very High Lift Low Pressure Turbine Blade with Emphasis on Separation Prediction. *J. Turbomach.* 126 (3), 406–413. doi:10.1115/1.1748416

Huang, J. (2005). *Separation Control over Low Pressure Turbine Blades Using Plasma Actuators*. South Bend, Indiana: University of Notre Dame. [dissertation]. [South Bend].

Hwang, S. D., Kwon, H. G., and Cho, H. H. (2008). Heat Transfer with Dimple/protrusion Arrays in a Rectangular Duct with a Low Reynolds Number Range. *Int. J. Heat Fluid Flow* 29 (4), 916–926. doi:10.1016/j.ijheatfluidflow.2008.01.004

Ji, Z., Qin, J., Cheng, K., Liu, H., Zhang, S., and Dong, P. (2021). Design and Performance of a Compact Air-Breathing Jet Hybrid-Electric Engine Coupled with Solid Oxide Fuel Cells. *Front. Energ. Res.* 402. doi:10.3389/fenrg.2020.613205

Kurelek, J. W., Lambert, A. R., and Yarusevych, S. (2016). Coherent Structures in the Transition Process of a Laminar Separation Bubble. *AIAA J.* 54 (8), 2295–2309. doi:10.2514/1.j054820

Lake, J., King, P., and Rivir, R. (2000). "Low Reynolds Number Loss Reduction on Turbine Blades with Dimples and V-Grooves," in *38th Aerospace Sciences Meeting and Exhibit*. Reston, Virginia: American Institute of Aeronautics and Astronautics, 738. doi:10.2514/6.2000-738

Lake, J., King, P., and Rivir, R. (1999). "Reduction of Separation Losses on a Turbine Blade with Low Reynolds Numbers," in *37th Aerospace Sciences Meeting and Exhibit*. Reston, Virginia: American Institute of Aeronautics and Astronautics, 242. doi:10.2514/6.1999-242

Ligrani, P. M., Harrison, J. L., Mahmmod, G. I., and Hill, M. L. (2001). Flow Structure Due to Dimple Depressions on a Channel Surface. *Phys. Fluids* 13 (11), 3442–3451. doi:10.1063/1.1404139

Lyall, M. E., King, P. I., Sondergaard, R., Clark, J. P., and McQuilling, M. W. (2011). An Investigation of reynolds Lapse Rate for Highly Loaded Low Pressure Turbine Airfoils with Forward and Aft Loading. *Turbo Expo. Power Land, Sea, Air* 54679, 865–876. doi:10.1115/gt2011-46328

Mahallati, A., McAuliffe, B. R., Sjolander, S. A., and Praisner, T. J. (2013). Aerodynamics of a Low-Pressure Turbine Airfoil at Low Reynolds Numbers—Part I: Steady Flow Measurements. *J. Turbomach.* 135 (1). doi:10.1115/1.4006319

McAuliffe, B. R., and Yaras, M. I. (2005). Separation-bubble-transition Measurements on a Low-Re Airfoil Using Particle Image Velocimetry. *Turbo Expo. Power Land, Sea, Air* 47268, 1029–1038. doi:10.1115/gt2005-68663

McAuliffe, B. R., and Yaras, M. I. (2007). Transition Mechanisms in Separation Bubbles under Low and Elevated Freestream Turbulence. *Turbo Expo. Power Land, Sea, Air* 47934, 1063–1076. doi:10.1115/gt2007-27605

Montis, M., Niehuis, R., and Fiala, A. (2011). Aerodynamic Measurements on a Low Pressure Turbine cascade with Different Levels of Distributed Roughness. *Turbo Expo. Power Land, Sea, Air* 54679, 457–467. doi:10.1115/gt2011-45015

Poondru, S. (2008). *Large-Eddy Simulation and Active Flow Control of Low-Reynolds Number Flow through a Low-Pressure Turbine Cascade*. Cincinnati, Ohio: University of Cincinnati. [dissertation].

Praisner, T. J., Grover, E. A., Knezevici, D. C., Popovic, I., Sjolander, S. A., Clark, J. P., et al. (2008). Toward the Expansion of Low-Pressure-Turbine Airfoil Design Space. *Turbo Expo. Power Land, Sea, Air* 43161, 1323–1331. doi:10.1115/gt2008-50898

Rizzetta, D., and Visbal, M. (2003). "Numerical Investigation of Transitional Flow through a Low-Pressure Turbine cascade," in *33th AIAA Fluid Dynamics Conference and Exhibit*. Orlando, Florida: American Institute of Aeronautics and Astronautics, 3587. doi:10.2514/6.2003-3587

Robarge, T., Stark, A., Min, S. K., Khalatov, A., and Byerley, A. (2004). "Design Considerations for Using Indented Surface Treatments to Control Boundary Layer Separation," in *42th AIAA Aerospace Sciences Meeting and Exhibit*. Reno, Nevada: American Institute of Aeronautics and Astronautics, 425. doi:10.2514/6.2004-425

Roberts, S. K., and Yaras, M. I. (2005). Large-eddy Simulation of Transition in a Separation Bubble. *Turbo Expo. Power Land, Sea, Air* 47268, 1049–1055. doi:10.1115/gt2005-68666

Rouser, K. P. (2002). *Use of Dimples to Suppress Boundary Layer Separation on a Low Pressure Turbine Blade*. Ohio: Wright-Patterson Air Force Base. [master's thesis]..

Sondergaard, R. (2008). "LPT Flow Control at AFRL," in *38th Fluid Dynamics Conference and Exhibit*. Seattle, Washington: American Institute of Aeronautics and Astronautics, 4156. doi:10.2514/6.2008-4156

Talan, M., and Hourmouziadis, J. (2002). Characteristic Regimes of Transitional Separation Bubbles in Unsteady Flow. *Flow, turbulence and combustion* 69 (3), 207–227. doi:10.1023/A:1027355105017

Vincent, R., and Mapple, R. (2006). "CFD Investigation of Laminar Flow over a Dimpled Surface Indentation," in *36th AIAA Fluid Dynamics Conference and Exhibit*. San Francisco, California: American Institute of Aeronautics and Astronautics, 3912. doi:10.2514/6.2006-3912

Volino, R. J. (2003). Passive Flow Control on Low-Pressure Turbine Airfoils. *J. Turbomach.* 125 (4), 754–764. doi:10.1115/1.1626685

Volino, R. J. (2008). Separated Flow Measurements on a Highly Loaded Low-Pressure Turbine Airfoil. *Turbo Expo. Power Land, Sea, Air* 43161, 1427–1437. doi:10.1115/gt2008-51445

Won, S. Y., Zhang, Q., and Ligrani, P. M. (2005). Comparisons of Flow Structure above Dimpled Surfaces with Different Dimple Depths in a Channel. *Phys. Fluids* 17 (4), 045105. doi:10.1063/1.1872073

Yang, Z., and Voke, P. R. (2001). Large-eddy Simulation of Boundary-Layer Separation and Transition at a Change of Surface Curvature. *J. Fluid Mech.* 439, 305–333. doi:10.1017/s0022112001004633

Yarusevych, S., Kawall, J. G., and Sullivan, P. E. (2008). Separated-shear-layer Development on an Airfoil at Low Reynolds Numbers. *AIAA J.* 46 (12), 3060–3069. doi:10.2514/1.36620

Conflict of Interest: The authors declare that the research was conducted in the absence of any commercial or financial relationships that could be construed as a potential conflict of interest.

frontiers in Energy Research

ORIGINAL RESEARCH
published: 23 March 2022
doi: 10.3389/fenrg.2022.853360

Multi-Objective Optimization of Circumferential Groove Casing Treatment in an Ultra-Highly Loaded Low-Reaction Transonic Compressor Rotor

Shengli Ding, Shaowen Chen, Songtao Wang and Zhongqi Wang*

School of Energy Science and Engineering, Harbin Institute of Technology, Harbin, China

This study concerns a multi-objective optimization of circumferential single grooved casing treatment for a low-reaction transonic rotor with ultra-high loading. The axial location, width and depth of the groove are investigated as design variables. The optimization problem seeks to fully extend the operation range of the rotor while minimizing efficiency degradation. Artificial neural network of radial basis function is applied to construct the surrogate model. The optimal groove configuration was determined using non-dominated sorting genetic algorithm II (NSGA II) in conjunction with technique for order preference by similarity to ideal solution (TOPSIS). Detailed analysis of flow field reveals that two flow features involving stability enhancement for the low-reaction rotor are the inhibition of shock/vortex interaction in the rotor tip region and the reduction or elimination of double-leakage tip gap flow. The blocking region located right downstream of the interface between the tip leakage flow and the main flow is decreased due to the tip unloading effect and recirculation flow induced by the groove. Additionally, the efficiency improvement can be observed as the intensity of tip leakage vortex decreases. Based on the single groove optimization, the prospect of a particular multiple groove casing configuration consisting of component grooves with varied geometrical dimensions is also discussed in the paper. The simulation results indicate that the new-type multiple groove configuration is more advantageous to the rotor's performance.

Keywords: highly-loaded transonic compressor, casing treatment, optimization design, stability, aerodynamic performance

OPEN ACCESS

Edited by:
Chungen Yin,
Aalborg University, Denmark

Reviewed by:
Xinrong Su,
Tsinghua University, China
Jie Gao,
Harbin Engineering University, China

****Correspondence:***
Shaowen Chen
cswemail@hit.edu.cn

Specialty section:
This article was submitted to Advanced Clean Fuel Technologies, a section of the journal Frontiers in Energy Research

Received: *12 January 2022*
Accepted: *02 March 2022*
Published: *23 March 2022*

Citation:
Ding S, Chen S, Wang S and Wang Z (2022) Multi-Objective Optimization of Circumferential Groove Casing Treatment in an Ultra-Highly Loaded Low-Reaction Transonic Compressor Rotor. Front. Energy Res. 10:853360. doi: 10.3389/fenrg.2022.853360

Abbreviations: C_a, Axial tip chord length; η, Adiabatic efficiency; π^*, Total pressure ratio; m, Mass flow rate; $\vec{X}$, Vector of design variables; $\vec{W}$, Vector of relative velocity; $\vec{\zeta}$, Vector of absolute vorticity; C_p, Static pressure coefficient; ρ, Density; ρ_{ref}, Reference density; V_{rad}, Radial velocity; U_{tip}, Tip speed; $m_{injection}$, Injection flow rate from casing treatment; m_{inlet}, Rotor inlet mass flow rate; ξ, Loss coefficient; CT, Casing treatment; CTB, Bottom surface of casing treatment; L, Lower bound; NS, Near stall condition; P_t, Total pressure; S, Surface; SC, Smooth casing; T, Total temperature; U, Upper bound; V_n, Normal velocity; ζ_n, Absolute vorticity coefficient; ω, Rotor angular velocity; k, Adiabatic index; 1, Rotor inlet; 2, Rotor outlet.

INTRODUCTION

Increasing the overall pressure ratio is an efficient way to increase the cycle efficiency and energy utilization of a gas turbine. In the case of limited blade speed, increasing the pressure rise per stage will require a higher stage loading. Kerrebrock et al. (1997) pioneered the application of boundary layer aspiration to compressor design. A fully aspirated transonic compressor stage, with aspiration on both the rotor and stator, was designed to experiment. The compressor stage achieved a total pressure ratio of 3.4 at a tip speed of 457 m/s. In comparison to conventional stages, the work capacity can be doubled while maintaining acceptable through-flow efficiency. Unfortunately, as a high-speed rotating component, the aspiration slots on the rotor have the potential for an unfavorable influence on blade mechanical strength, severely limiting the engineering application of the aspiration technique. To address this issue, Hu et al. (2014) proposed an unconventional design strategy: a low-reaction aspirated transonic compressor. By increasing the meridional velocity downstream of the passage shock, the rotor could achieve a higher loading coefficient and avoid large-scale flow separation without using aspiration. As a result, the boundary layer aspiration was limited to the stator. It is worth noting, however, that the difficulty of aerodynamic design for the low-reaction compressor rotor is significantly increased due to the lack of active flow control techniques.

Also, higher compressor loading tends to sacrifice safe operating range. There is a conflict between increasing aerodynamic loading and maintaining adequate stall margin. Numerous studies have established the critical role of rotor tip leakage flow and its associated vortex in stall onset (Adamczyk et al., 1993; Hewkin-Smith et al., 2019; Zhu et al., 2021). Owing to the presence of passage shock, the tip leakage behavior in transonic compressors is much more complicated. Experimental and numerical results from Suder and Celestina (1996) revealed that the interaction of the passage shock and the tip leakage vortex (TLV) may primarily contribute to the stall of a transonic rotor. Increased rotor loading can enhance shock/vortex interaction. Casing treatment has been developed as a viable method for mitigating the adverse impacts of tip leakage flow. In general, casing treatment can be broadly divided into two categories in accordance with its structure: circumferential grooves (Shabbir and Adamczyk, 2005; Mustaffa and Kanjirakkad, 2021) and axial slots (Djeghri et al., 2015; Ba et al., 2020). Both configurations exhibit excellent stability enhancement capability, but they permanently alter the shape of the casing and have a continuous influence on the flow field near the rotor tip throughout the operating range, frequently resulting in efficiency penalties (Sun S et al., 2019). Grooved casing treatment has received particular attention due to the benefits of reduced impact on efficiency and ease of manufacture.

Several parametric studies on the grooved casing treatment for transonic compressors have been conducted. The underlying flow mechanisms are gradually uncovered in the process. Rabe and Hah (2002) investigated the effect of groove depth on stability using a combination of numerical simulations and experiments. It was discovered that both shallow and deep grooves had a positive effect on stall margin. The decrease in the incidence angle is thought to be the main factor in stall margin improvement. On the other hand, Muller et al. (2007) observed that shallow grooves were less effective than deep grooves at extending the stall margin but were more conducive to improving peak efficiency. The calculated Mach number distributions near the casing showed that the interaction between the leakage flow and the recirculation flow of grooves reduced tip blockage, preventing the leakage flow from forward spillage and postponing the stall onset.

More recently, Mustaffa and Kanjirakkad. (2021) numerically investigated the impact of groove axial location on NASA rotor 37. To qualify the near casing blockage in transonic rotors, a novel blockage parameter was proposed. The results indicated that the

TABLE 1 | Main parameters of the investigated compressor rotor at PE.

Parameter	Value
Tip speed (m/s)	370
Aspect ratio	0.8
Hub to tip ratio	0.7
Tip camber angle (°)	54.4
Tip relative Mach number	1.22
Mean flow coefficient	0.53
Mean loading coefficient	1.01
Rotor total pressure ratio	2.65
Rotor adiabatic efficiency	0.9253
Axial tip chord (m)	0.0686
Tip clearance (mm)	0.6

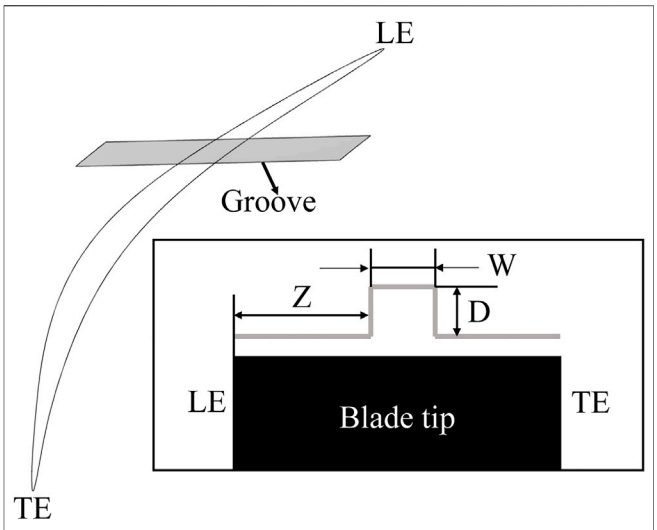

FIGURE 1 | Parameterization of grooved casing treatment.

TABLE 2 | Ranges of groove parameters.

Parameter	Min (% C_a)	Max (% C_a)
Groove depth: D	1.25	20
Groove width: W	2	25
Groove location: Z	0	30

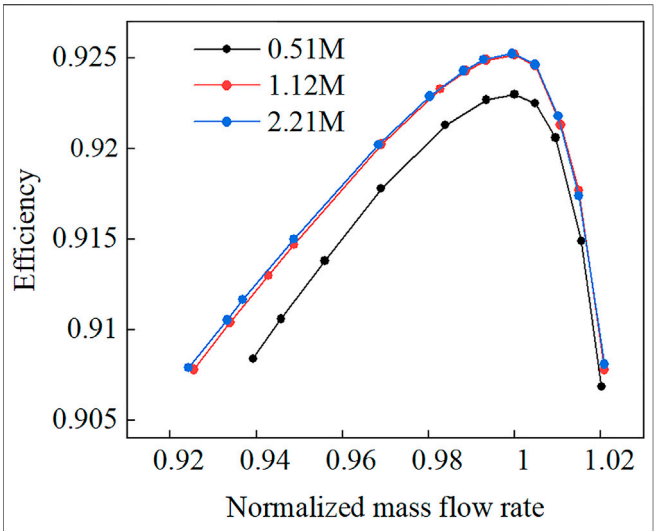

FIGURE 2 | Comparison of overall performance with different meshes.

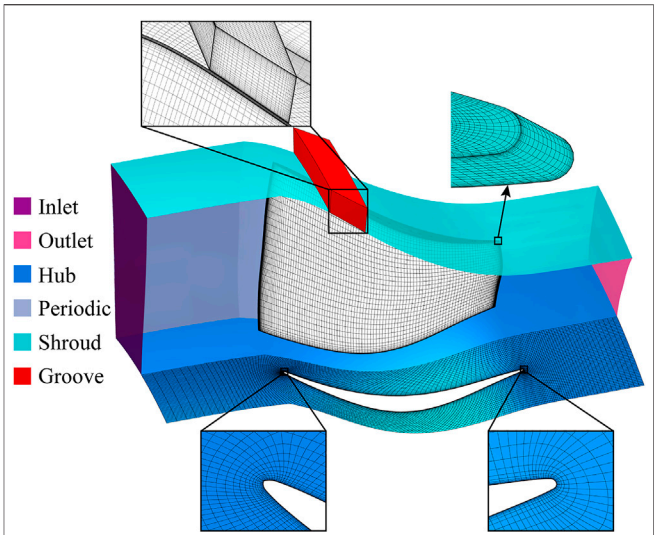

FIGURE 3 | Schematic diagram of the total computational domain.

maximum stall margin increment could be achieved when the groove was located upstream of the peak tip blockage location. It was explained that it is more beneficial to eliminate the front portion of the peak blockage than to reduce the peak blockage itself. Sakuma et al. (2014) also regarded NASA rotor 37 as the research object and studied the influences of groove axial location and depth. The results indicated that the best gain in stall margin occurred at the 20% point of the axial tip chord length (C_a), and that the stability-enhancing effect could be enhanced further by deepening the groove. The groove was concluded to significantly reduce the leakage flow momentum, resulting in the deflection of the TLV and movement of the blocking region. Through numerical studies, Mirzabozorg et al. (2017) examined the effects of varying the width and the axial location of the casing groove. They reported that as groove width varied, the effects of groove location on stall margin and performance followed different laws. Narrow grooves near the leading edge and medium-width grooves increased flow stability by reducing the size of the vortex breakdown region and delaying separation on the blade suction side near the casing. Wide grooves harmed stall margin and performance.

Despite these parametric studies on casing groove, the design criterion for casing groove is still unclear. In practice, the selection of groove geometrical parameters is heavily reliant on the designer's experience, which undoubtedly complicates the search for the optimal design. In the wake of developments in computational fluid dynamics and machine learning techniques, several optimization investigations into casing grooves have been launched in recent years. Choi et al. (2010) optimized casing grooves for a transonic rotor using groove depth and width as variables, with the goal of maximizing stall margin. Kim et al. (2011) performed a multiple-objective optimization of casing grooves with a focus on enhancing stall margin and peak efficiency. Zhao et al. (2014) optimized the effect of casing grooves on NASA rotor 37 based on radial basis function neural network (RBFNN) and a multi-objective evolutionary algorithm. In order to improve stability and design performance, Song et al. (2019) developed a grooved casing treatment optimization method integrated with three-dimensional blade design. These optimization studies were conducted on multiple grooves, using identical and equally spaced casing grooves. In particular, Qin et al. (2014) performed optimization of a six-groove configuration with independent depths. They also pointed out that each groove should ideally have a different width, if computing resources permit.

Houghton and Day (2012) argued that the effects of multiple grooved casing treatment were not simply an accumulation of the individual grooves' effects. Huang et al. (2008) and Choi et al. (2010) found that the groove near the trailing edge was superfluous for stability enhancement. The research of Mirzabozorg et al. (2017) demonstrated that the stall margin improvement of a multiple groove configuration is comparable to that of the upstream single groove. These findings indicate that there are some shortcomings in previous multiple groove optimization studies in which the geometry of each component groove is identical and changes synchronously. During the optimization process, some grooves may be redundant, and the effectiveness of some specific grooves can be hindered.

Besides, in all the studies on casing treatment reviewed here, the subjects were mostly compressors with moderate loading. To date, a detailed research on highly loaded compressor is rare in open literature.

This study presents numerical investigations of grooved casing treatment for a highly loaded low-reaction transonic compressor rotor. A multi-objective optimization is conducted to obtain the best stability-enhancing effect of single circumferential groove while maintaining rotor efficiency. The flow mechanisms governing the grooved casing treatment acting on the rotor are also explored and analyzed. Hence, owing to the presented work, the best values of groove parameters can be revealed,

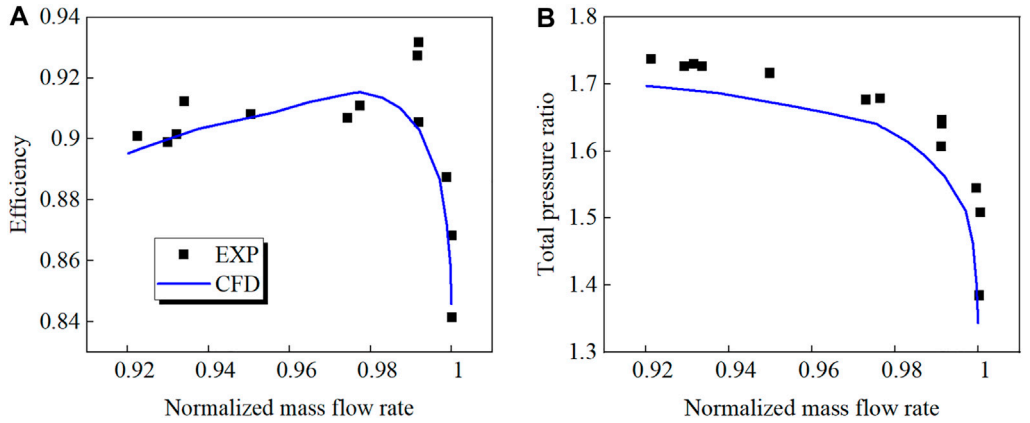

FIGURE 4 | Comparison of measured and predicted characteristic lines. **(A)** Efficiency **(B)** Total pressure ratio.

providing design guidelines for promoting the effectiveness of grooved casing treatment in highly loaded compressors. Finally, an unconventional form of multiple grooved treatment is presented and evaluated on the basis of the optimized single groove design.

MODEL SPECIFICATIONS

The investigated rotor comes from a low-reaction transonic aspirated compressor stage. The design methodology of the unconventional compressor is elaborated in reference (Hu et al., 2014). With the help of this design philosophy, the compressor can achieve an ultra-high loading coefficient with excellent through-flow capacity. The main characteristics of the compressor rotor are summarized in **Table 1**. The rotor can achieve a total pressure ratio of 2.65 at a tip speed of 370 m/s when operating at peak efficiency (PE).

With respect to the casing treatment design, the parameterization is illustrated in **Figure 1**. D, W, and Z represent the depth, width, and axial location of the casing groove, respectively, and are all normalized using the axial tip chord length. The parameter ranges are presented in **Table 2**, which are derived from previous studies on the grooved casing treatment in low-reaction transonic compressors (Zhu et al., 2020) as well as preliminary calculations.

NUMERICAL SCHEMES

Computational Scheme

Three-dimensional steady-state simulations are performed using the commercial code EURANUS. The Reynolds-averaged Navier-Stokes equations are discretized using the cell-centered control volume method. The Spalart–Allmaras turbulence model (Spalart and Allmaras, 1992) is used to evaluate the eddy viscosity as it has been proved to commendably capture tip flow structures in transonic compressors by numerous studies (Ren and Gu, 2016; Sun X et al., 2019; Wang et al., 2019).

Total pressure (101325 Pa), total temperature (288.15 K) and inflow angles are taken as the inlet boundary condition. The static pressure condition is imposed with simple equilibrium distribution law at the outlet. As for the solid walls, no-slip and adiabatic conditions are employed. The characteristic lines are obtained by gradually increasing the static pressure at the outlet. The last operating point where the flow parameters exhibit stable periodic fluctuations is set as the near stall (NS) point. When approaching the PE point and stall limit, the step size of the static pressure at the outlet is adapted to 100 Pa, which corresponds to 0.1% of the inlet total pressure.

Grid Strategy

Calculations are carried out using a single blade passage. The blade passage domain is generated by the O4H grid. The rotor tip gap is constructed using a combination of O-type and H-type grids. Within the gap, there are 25 spanwise grid points that efficiently capture tip leakage flow. When calculating the case with casing groove, an additional H-block mesh is used to discretize the groove domain. The full non-matching connecting technique is employed to connect the blade passage and groove region. This technique ensures satisfactory interpolation accuracy and is thus widely used in casing treatment studies (Mao and Liu, 2020; Zhu and Yang, 2020). Furthermore, the minimum grid spacing is set to 3×10^{-6} m to meet the y+ at most solid walls less than 2. The mesh independent results for the smooth casing are shown in **Figure 2**. The mesh density is varied between 0.51 million and 2.21 million elements. The numerical results are almost identical when the mesh number exceeds 1.12 million. To optimize the computing accuracy and speed, the mesh with 1.12 million grids is chosen for further analysis in this investigation. Then, the grid number of the casing groove is fixed at 0.2 million, beyond which overall performance, stall margin, and tip leakage flow rate remain nearly constant. An overview of the total computational domain is shown in **Figure 3**.

Assessment

In order to demonstrate the reliability and feasibility of the present numerical method, NASA Rotor 67 (Strazisar et al.,

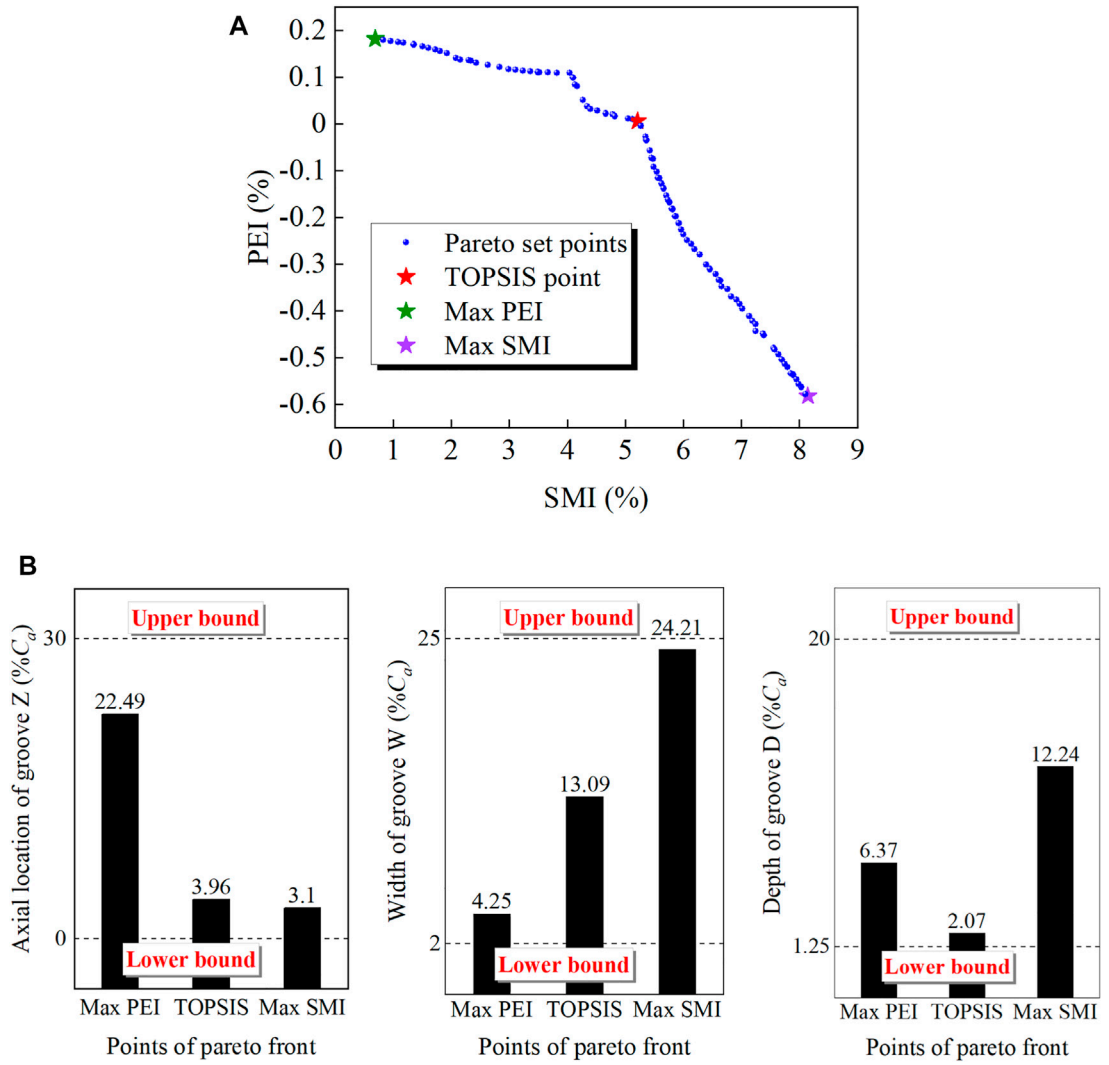

FIGURE 5 | Pareto front and geometric parameters of typical points. **(A)** Pareto front of objective functions **(B)** Geometric parameters of typical points.

TABLE 3 | Ranges of casing groove parameters.

Design	SMI (%) (model)	SMI (%) (CFD)	η_{pe} (%) (model)	η_{pe} (%) (CFD)
Max PEI point	0.691	0.989	92.693	92.705
TOPSIS point	5.281	5.834	92.529	92.533
Max SMI point	8.139	7.65	91.942	91.954

1989) is selected for CFD validation. As with the model studied in this work, NASA Rotor 67 is also a low aspect-ratio, transonic rotor, and the stall inception is triggered by the interaction between the passage shock and the TLV. The numerical settings and grid distribution are consistent with that of the investigated rotor. The experimental and calculated data for Rotor 67 are compared in **Figure 4**, where the abscissa is normalized with the respective choke flowrates for each. The adiabatic efficiency and total pressure ratio are defined as the equations below:

$$\eta = \frac{\left(\frac{P_{t,2}}{P_{t,1}}\right)^{\frac{k-1}{k}} - 1}{\frac{T_2}{T_1} - 1}$$

$$\pi^* = \frac{P_{t,2}}{P_{t,1}}$$

As can be seen from **Figure 4**, the dimensionless flowrate at the NS point predicted by the numerical calculation is 0.92, which is very close to the experimentally measured dimensionless flowrate at the NS point of 0.921. It is demonstrated that the numerical simulation could adequately predict the near stall flowrate. The calculated total pressure ratio curve is underestimated slightly in comparison to the experimental results, within an error of 2.5%. Furthermore, the calculated efficiency is nearly consistent with the experimental data. The efficiency values predicted by simulation at the PE and NS points are 1.75% and 0.6% lower than the experimental results,

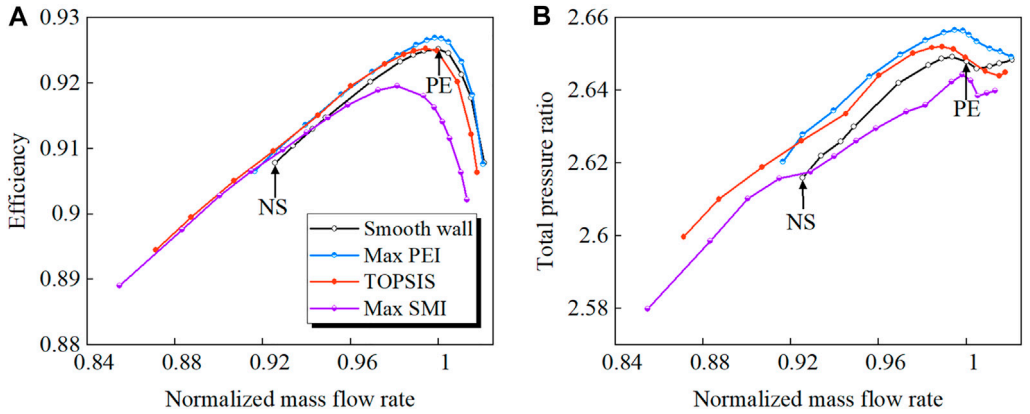

FIGURE 6 | Characteristic lines of rotor with and without casing treatment. **(A)** Efficiency **(B)** Total pressure ratio.

respectively. On the whole, the selected CFD method is capable of predicting the transonic rotor's performance and stable operating range with reasonable accuracy.

MULTI-OBJECTIVE OPTIMIZATION

Peak efficiency and stall margin improvements (PEI and SMI, respectively) are selected as objective functions in order to achieve the optimal effect of casing treatment. SMI is the percentage reduction in mass flow rate at NS produced by the casing treatment, as defined in reference (Houghton and Day, 2012). The two objective functions are calculated using equations:

$$\mathrm{PEI} = (\eta_{\mathrm{PE}})_{\mathrm{CT}} - (\eta_{\mathrm{PE}})_{\mathrm{SC}}$$

$$\mathrm{SMI} = \frac{(m_{\mathrm{NS}})_{\mathrm{SC}} - (m_{\mathrm{NS}})_{\mathrm{CT}}}{(m_{\mathrm{NS}})_{\mathrm{SC}}}$$

Furthermore, two optimization constraints are set: one is the boundaries imposed on the decision variables (*see* **Table 2**), and the other is that the variation in mass flowrate at PE is less than 2%. The second constraint is used to restrict the performance variation within a certain range after applying the casing treatment. Mathematically, the optimization procedure can be expressed as follows.Maximize:

$$\mathrm{f}_1\left(\vec{X}\right) = \mathrm{SMI}, \mathrm{f}_2\left(\vec{X}\right) = \mathrm{PEI}$$

Subject to:

$$(X_{\mathrm{i}})_{\mathrm{L}} < X_i < (X_{\mathrm{i}})_{\mathrm{U}},\ \mathrm{i} = 1, 2, 3$$

$$0.98 \cdot (m_{\mathrm{PE}})_{\mathrm{SC}} < (m_{\mathrm{PE}})_{\mathrm{CT}} < 1.02 \cdot (m_{\mathrm{PE}})_{\mathrm{SC}}$$

The optimal Latin hypercube sampling method (OLHS) (Keane et al., 2008) is used for the design of experiment. 28 groove configurations are calculated to generate the database for the surrogate model. In comparison to the traditional Latin hypercube sampling technique, the OLHS method ensures that a design has adequate space filling qualities. RBFNN is employed to construct the surrogate model, which is frequently used to approximate nonlinear relationships and build nonlinear mappings between input and output variables, because it can project low-dimensional linear data into high-dimensional nonlinear data. Additionally, it has a high rate of learning convergence. RBFNN has been successfully applied to the prediction of compressor operating range and performance in recent literature (Vuong et al., 2021). The precision of the surrogate model was evaluated by means of k-fold cross validation.

Non-dominated sorting genetic algorithm II (NSGA II) is adopted to find the optimal solutions. NSGA II (Deb et al., 2002) is a classical multi-objective evolutionary algorithm, which reduces the complexity of non-dominated sorting genetic algorithm and has high operation speed as well as good nature of the constringency of the solution set. It is an effective method for solving multi-objective functions and should be suitable to this investigation. To begin with, a parent population of size N is created. Through crossover and mutation operations, new individuals with higher quality than the previous generation are generated. This process is iterated so that the population always evolves towards the optimal direction from generation to generation. A Pareto-optimal solution set of objective functions is finally obtained when the algorithm terminates. One hundred populations combined with 600 generations are applied in this optimization.

RESULTS AND DISCUSSION

Multi-Objective Optimization

As depicted in **Figure 5A**, the pareto front is provided as the multi-objective optimization results. It can be seen from the distributions of the pareto front that SMI and PEI present a negative relationship. Consequently, the designer should make a compromise between the capacity of stability extension and the impact on adiabatic efficiency for casing treatment and select one point from the pareto set. Technique for order preference by similarity to ideal solution (TOPSIS) (Behzadian et al., 2012), one

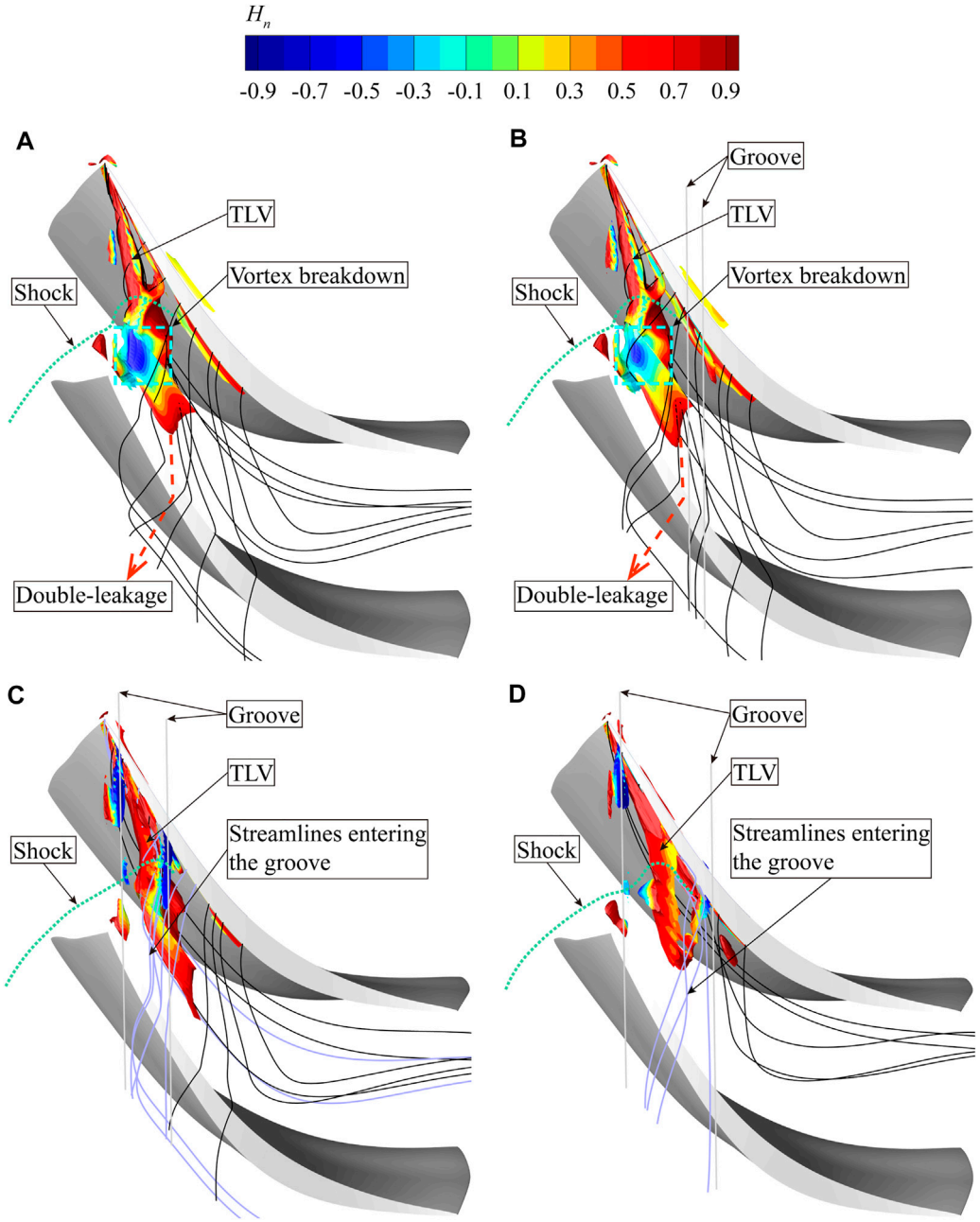

FIGURE 7 | Tip vortex structures with and without casing treatment at NS, captured by Ω method. **(A)** Smooth casing **(B)** Max PEI point **(C)** TOPSIS point **(D)** Max SMI point.

of the most commonly used methods in multi-objective decision analysis, is employed to search the optimal design point. Due to the high through-flow efficiency and limited stall margin for the investigated rotor, prior consideration is given to the stability enhancement capacity of casing treatment in decision-making. Hence, the final optimal solution is obtained by setting a weight ratio of 7:3 for SMI and PEI, which is denoted as the TOPSIS point in **Figure 5A**. In addition, the points corresponding to the maximum values of SMI and PEI are also displayed.

Table 3 compares the surrogate model predictions with the numerical calculation values. The results demonstrate once again the effectiveness and applicability of this surrogate model. **Figure 5B** shows the design variable values of the three typical points. It is found that widening the groove increases the stall margin but degrades peak efficiency. The groove close to the leading edge provides a substantial increase in the stall margin, and the optimum groove in terms of peak efficiency improvement is located around 20% C_a. However,

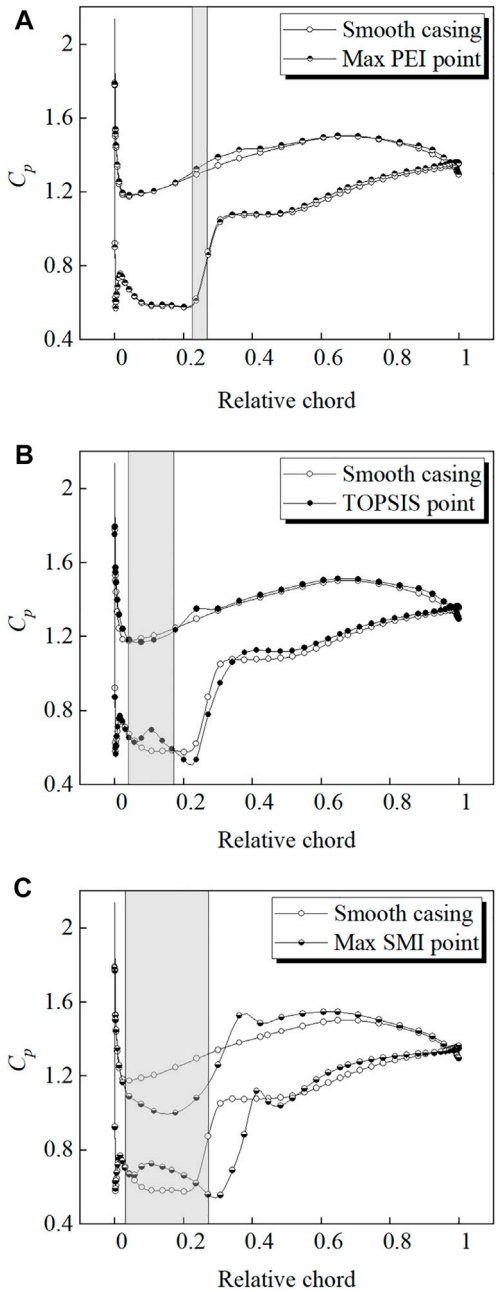

FIGURE 8 | Surface static pressure coefficient distribution at 98% span. **(A)** Max PEI point **(B)** TOPSIS point **(C)** Max SMI point.

no clear pattern was found for the influence of groove depth on the rotor performance. The TOPSIS point is a shallow groove with a depth close to the lower limit of the value range, while the max SMI point is in the middle of the value range, and the max PEI point has a depth in between. According to the casing groove research by Mao et al. (2018), the optimum depth was different for the various locations. Therefore, it can be speculated that the depth has certain correlation with other design variables for the low reaction rotor.

Figure 6 compares the characteristic lines derived from simulations with and without casing treatment. As can be seen from the figure, the max PEI configuration can improve the efficiency and total pressure ratio over the entire flow range, but only slightly increase the stall margin. For the max SMI point, the stall margin can be increased by about 7.65%, but the total pressure ratio and efficiency decrease, and the flowrate reduction at PE approaches the prescribed constraint. The optimal design derived from TOPSIS combines the advantages of the two design cases, without degrading the rotor performance and with a remarkable increase in operating range. As to the aerodynamic performance and stability synthetically, the optimum design is an excellent choice.

Flow Mechanisms of Applying Casing Treatment

Changes in Blade Tip Flow Field at NS

In order to elucidate the underlying mechanism by which casing treatment affects stability, this section will focus on the flow fields at NS. **Figure 7** shows the vortex structures in the tip region. The passage shock is outlined with a green dotted line. A new vortex identification method is used to visualize the tip vortices, that is the objective Ω method (Liu et al., 2019). Compared to other vortex identification methods such as the Q criterion and the λ2 criterion, the Ω method has advantages in terms of definite physical meaning and normalization (values range from 0 to 1). Vortices are colored with normalized helicity H_n, defined as:

$$Hn = \frac{\vec{W} \cdot \vec{\zeta}}{\left|\vec{W}\right|\left|\vec{\zeta}\right|}$$

The stability enhancement effect can be intuitively reflected by the nature of TLV. For the smooth casing, the TLV expands sharply both in the radial and tangential directions after passing through the passage shock, and the normalized helicity value along the TLV fluctuates dramatically. These flow features mark the onset of TLV breakdown. Vortex breakdown is always accompanied by reverse flow generation and induces serious tip blockage. Additionally, abundant double leakage fluid is formed as the TLV impinges on the pressure side of the adjacent blade. The double-leakage fluid has a high jet angle relative to the main flow, further resulting in the blocking of the flow in the tip region. For the max PEI point, the groove is located far downstream from the onset of vortex breakdown and therefore has little influence on the development of the TLV. One can see that the TLV breakdown still occurs, but to a lesser extent than with the smooth casing. By contrast, the original vortex breakdown region is covered by the TOPSIS and max SMI configurations, so that the flow structures in the tip region are powerfully influenced. Despite the fact that the vortex structure has been complicated due to the aspiration and injection of the groove, the TLV no longer breaks down. In addition, the double-leakage is well suppressed. The double-leakage flow downstream of the groove is almost totally removed. Under the groove, the fluid enters the groove (purple streamlines) and passes through the blade tip almost in the tangential direction. Its flow angle with

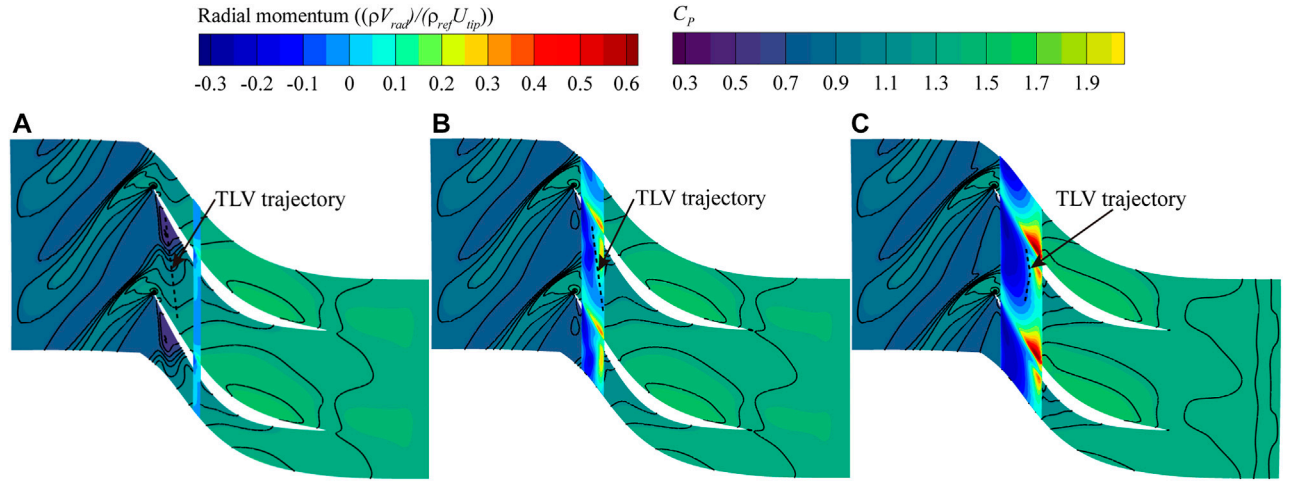

FIGURE 9 | Radial momentum at groove bottom surface and C_p distributions at 98% span. **(A)** Max PEI point **(B)** TOPSIS point **(C)** Max SMI point.

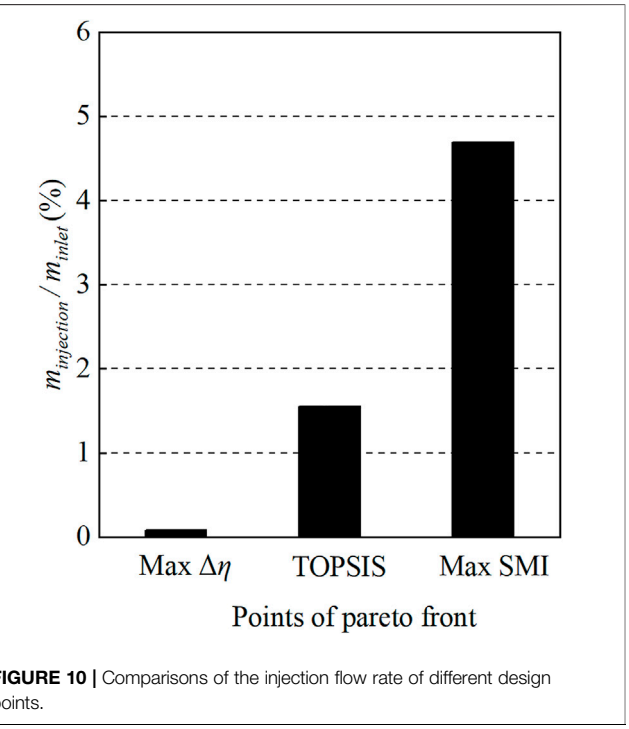

FIGURE 10 | Comparisons of the injection flow rate of different design points.

respect to the blade tip camber is considerably smaller than that of the double-leakage flow occurring in the smooth casing case at the same location. As a result, the fluid through the groove has a smaller jet angle with respect to the main flow, resulting in a reduction in tip blockage and mixing loss. The above effects contribute to stability enhancement.

Tip leakage flow is driven by the pressure difference between the blade tip pressure side and the suction side. Given that the TLV breakdown occurs close to the leading edge, it is reasonable to speculate that this portion of the leakage flow plays a prominent role in the vortex breakdown and stall inception. In **Figure 8**, the surface static pressure coefficient distribution at 98% span is compared between grooved and smooth casing conditions. The pressure coefficient is determined by normalizing the rotor inlet total pressure. It can be seen that at the TOPSIS and max SMI points, the leading edge loading decreases obviously under the groove. The groove is equivalent to increasing the tip gap size in the corresponding region, which increases the radial pressure gradient and causes a decreased pressure difference across the blade tip. The decrease in tip loading indicates that the intensity of tip leakage flow is reduced, and so is the swirl strength of TLV. The TLV breakdown is less likely to occur due to the weakened vortex strength. One can also observe that the pressure on the pressure side just downstream of the groove rises. Sakuma et al. (2014) pointed out that the leakage flow downstream of the groove is disturbed by the leakage flow under the groove, which causes the leakage flow to stagnate and results in the pressure increase. As for the max PEI point, the tip loading exhibits a different pattern of variation, with the load below the groove rising instead. This is due to the double-leakage flow is interfered by the flow under the groove on the pressure side.

In addition to the unloading effect, the recirculation flow of the groove also strongly affects the tip flow field. **Figure 9** shows the radial momentum distribution at the bottom surface of groove. The static pressure coefficient contours at 98% span are also shown in the figure. The trajectory of TLV can be traced by the static pressure troughs. It can be seen that the positive radial momentum zone is located near the blade pressure side, corresponding to the leakage flow being aspirated into the groove. At the TOPSIS and max SMI points, the groove is located above the passage shock, which enhances the driving force of the recirculation, and the flow near the suction side after the shock is also inhaled into the groove. The flow inside the groove appears to be reinjected into the tip passage along the

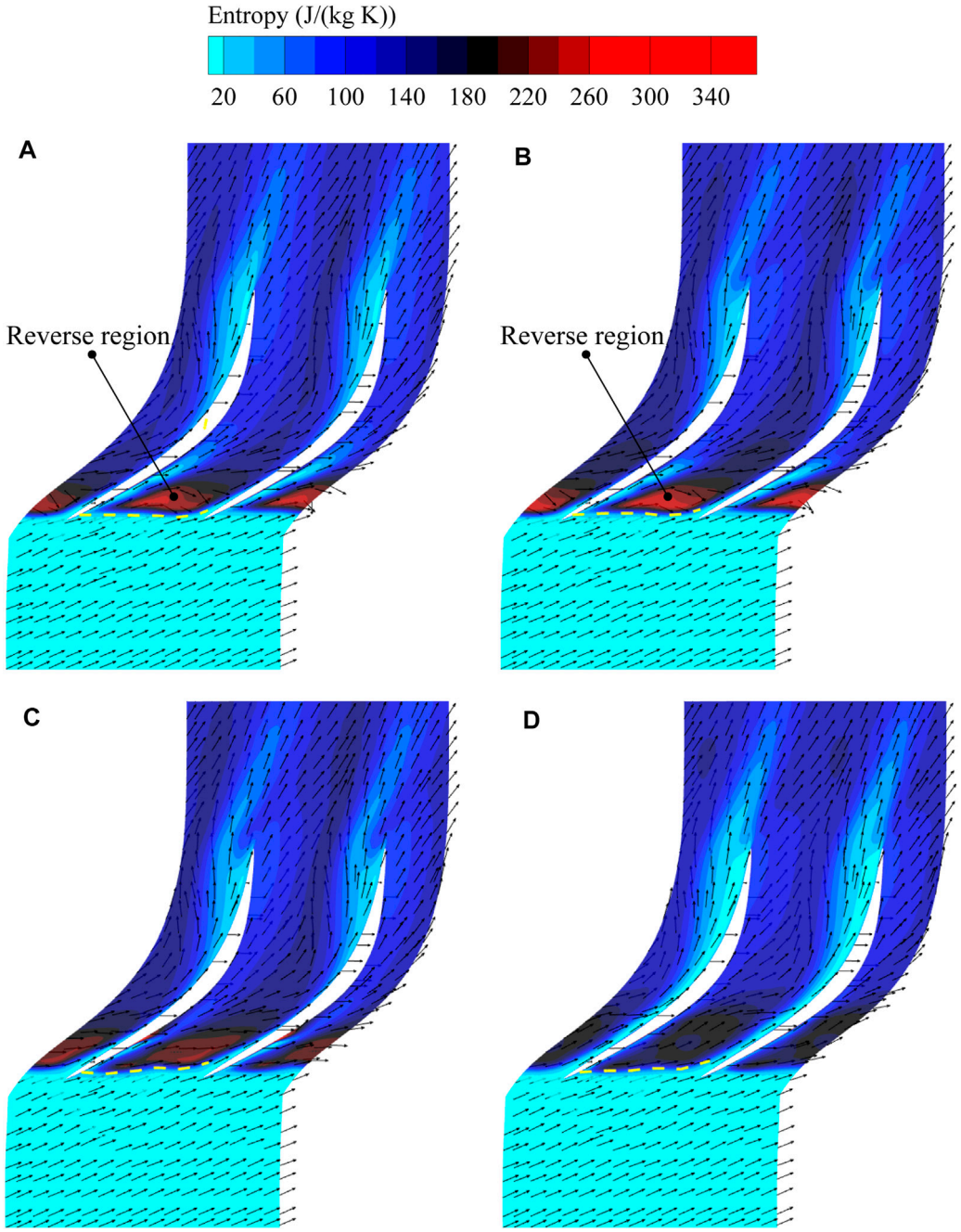

FIGURE 11 | Entropy contours and velocity vectors at 98% span. **(A)** Smooth casing **(B)** Max PEI point **(C)** TOPSIS point **(D)** Max SMI point.

trajectory of TLV. Typically, a low pressure region can be found upstream of the passage shock near the blade suction side. Abundant leakage fluid flows towards this region, causing the blocking of the flow and the roll up of TLV. The recirculation flow energizes the low pressure region. So that, the roll up of TLV is delayed and the starting point of the TLV trajectory is shifted downstream. Meanwhile, the passage shock moves downstream as the tip blockage is reduced. But for the max PEI point, the flow exchange between the groove and the tip region is negligible and has no perceptible impact on the TLV and the shock position. To quantify the capacity of recirculation flow among different configurations, the injection flow rate from the groove is given in **Figure 10**. This can partly explain why the max SMI point is the best in terms of stability enhancement.

From the perspective of dynamics, the momentum balance between main flow and tip leakage flow is a key factor affecting

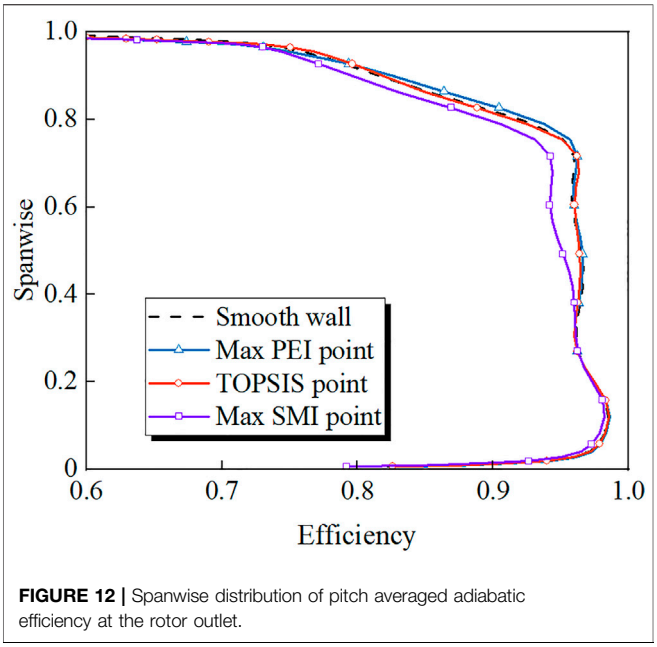

FIGURE 12 | Spanwise distribution of pitch averaged adiabatic efficiency at the rotor outlet.

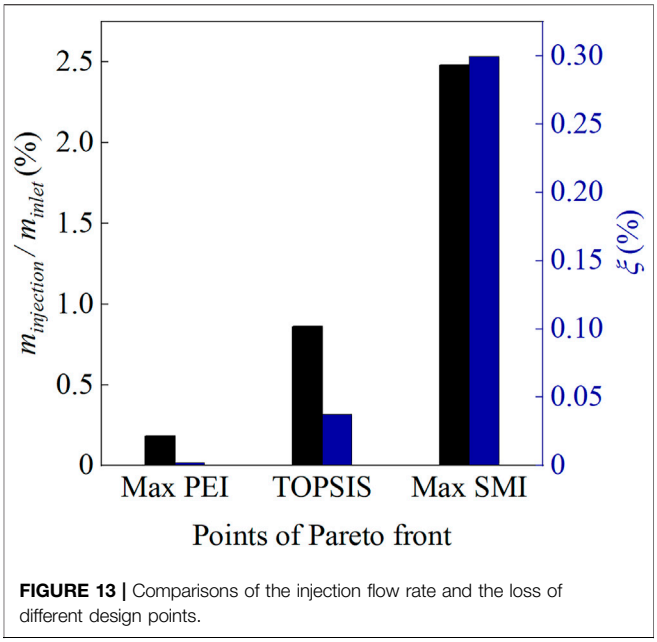

FIGURE 13 | Comparisons of the injection flow rate and the loss of different design points.

the compressor stability (Vo et al., 2008). Numerous researchers have demonstrated that stall is initiated when the main flow/tip leakage flow interface spills out of the blade leading edge, both computationally (Mao and Liu, 2020; Zhu et al., 2020) and experimentally (Hah et al., 2010; Cameron et al., 2013). **Figure 11** shows the entropy contours and velocity vectors at 98% span. The interface can be identified by a very high entropy gradient region, which is denoted by a yellow dotted line. From the comparison, one can see that the increase in stall margin presents a positive correlation with the distance that the interface is pushed downstream. For the smooth casing, a reverse flow region with high entropy values is located right downstream the interface. This region is formed as a result of the TLV/shock interaction, and hinders the flow to pass through the tip passage smoothly. With the blocking of the reverse flow region, the interface is nearly pushed out of the leading edge plane. In the two configurations with higher SMI, the flow in this region is deflected in the axial direction, and the entropy value is reduced. The max SMI point shows a higher extent of flow deflection, indicating a better flow capacity in the tip region.

Casing Treatment Impacts at PE

The impact of casing treatment on compressor efficiency is mainly reflected in two aspects. First, the flow exchange between the casing treatment configuration and the tip passage will cause the efficiency to degrade. On the other hand, the control of tip leakage flow by the casing treatment will reduce the flow loss, thereby increasing the efficiency. This section will focus on the flow characteristics under the action of casing treatment at PE.

Figure 12 presents the spanwise distribution of the pitch averaged adiabatic efficiency at the rotor outlet. The max PEI point increases the efficiency in the region above the 70% span because of the effective suppression of tip leakage flow, and has little impact on the efficiency in the lower span. The TOPSIS point preserves closely the radial efficiency distribution of the smooth casing, indicating that there exists a balance between the loss generation and reduction induced by the casing treatment. For the max SMI point, the efficiency is evidently reduced above the 30% span, which suggests that the recirculation flow brings about extensive additional loss, not limited to the tip region.

Figure 13 shows the injection mass flow rate and the internal flow loss for the three casing treatment configurations. According to the definition in reference (Zhu and Yang, 2020), the internal flow loss of the groove is calculated as follows:

$$\xi = \frac{\iint_{S_{CTB}} \rho P_t V_n dS}{\iint_{S_1} \rho P_t V_n dS}$$

One can see from the figure that the injection flow of the three configurations appears different varies compared to that under condition NS: the max PEI configuration increases, but the other two configurations decrease. This is because the groove of the max PEI point is located above the intersection point of the passage shock with the blade suction side at PE. The driving force for the recirculation flow is enhanced. But even so, the injection flow rate is still very small compared with the other two configurations, so the additional mixing loss near the blade tip is minimal. Meanwhile, the flow loss inside the groove is nearly negligible for the maximum PEI configuration, but significantly greater for the other two configurations.

The contours of the pitch averaged absolute vorticity coefficient near the blade tip for each casing condition are shown in **Figure 14**. The absolute vorticity coefficient is defined as follows:

$$\zeta_n = \frac{\left|\vec{\zeta}\right|}{2\omega}$$

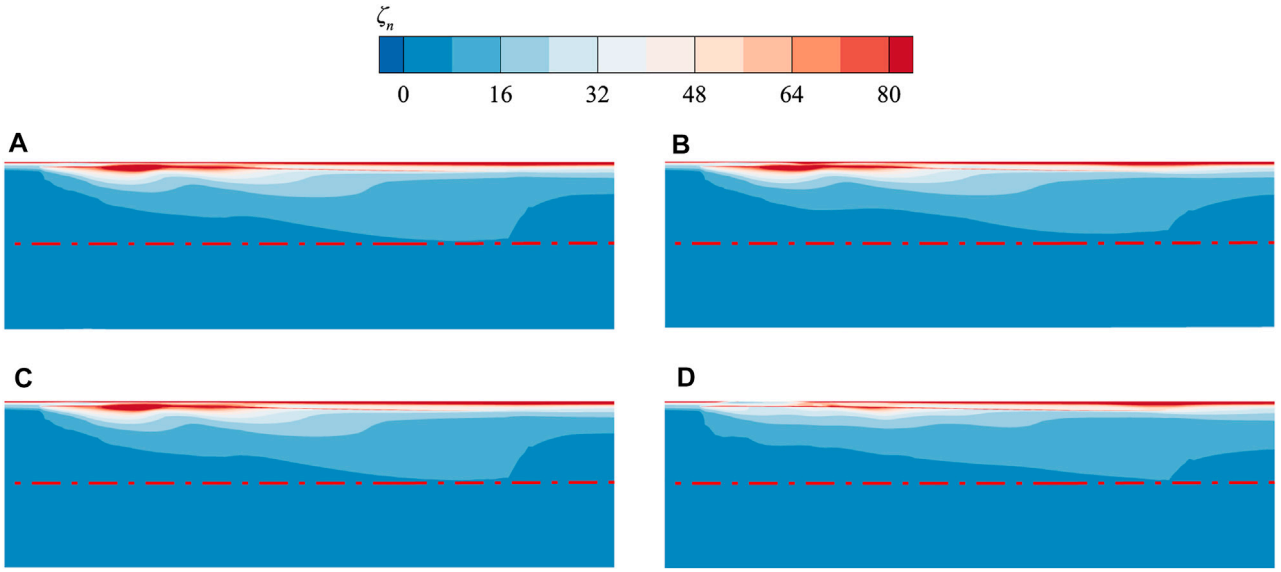

FIGURE 14 | Pitch-averaged absolute vorticity coefficient contours near the tip region. **(A)** Smooth casing **(B)** Max PEI point **(C)** TOPSIS point **(D)** Max SMI point.

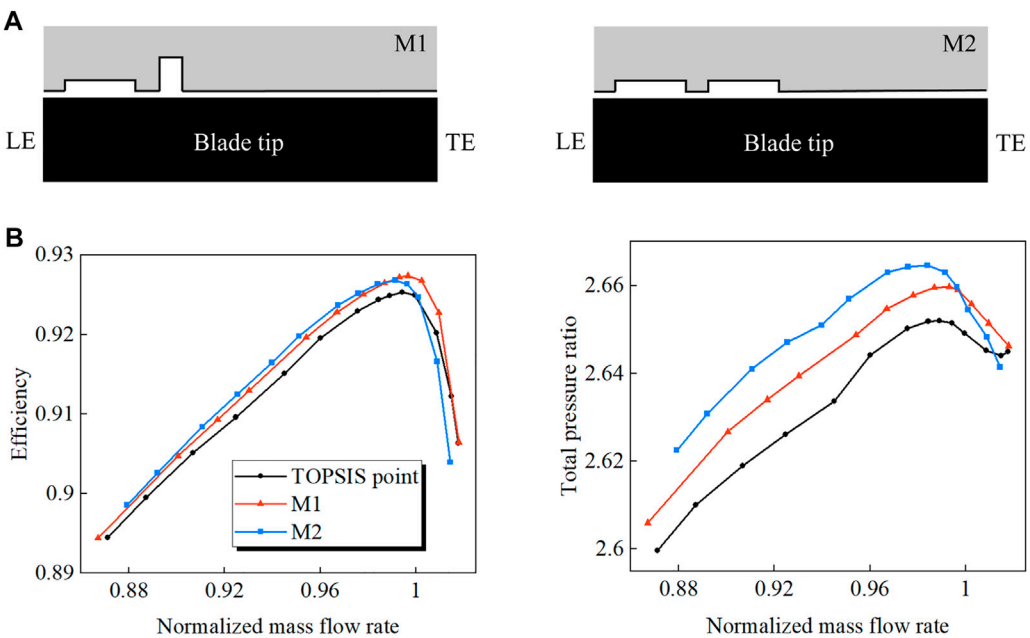

FIGURE 15 | Schematic diagram and characteristic lines of the multiple-groove casing treatments. **(A)** Groove schematic **(B)** Characteristic lines.

The red dash-dotted line in the figure represents the lower boundary of the high absolute vorticity region in the smooth casing condition. As expected, the high vorticity region is reduced at the max PEI point. In order to quantify the intensity of TLV, the integral of the pitch averaged absolute vorticity at the meridional plane is calculated. The integral values of the max PEI, TOPSIS, and SMI points are 0.0629, 0.0633, and 0.0632, respectively. Compared to the smooth casing condition with an integral value of 0.0637, the three casing treatments all decrease the intensity of TLV, with the max PEI point having the greatest reduction. Given that the additional loss caused by the flow exchange between the groove and the tip passage is relatively small, the efficiency for the max PEI point is improved accordingly.

Multiple Grooves

As mentioned in the literature review, almost all previous research on multiple grooved casing treatment has used identical component grooves, but it seems there is no evidence

to prove that such a design is necessary. In this section, a novel multiple-groove casing treatment design strategy, which is composed of component grooves with varied geometrical dimensions, is introduced and discussed. Since the behavior of tip leakage vortex changes drastically as it moves downstream within the blade passage, it is logical to allow the geometrical dimensions of each individual groove in multiple grooved casing treatments to vary.

First, the grooves of the optimal design point (TOPSIS point) and the max PEI point are combined into one multiple-groove casing treatment, named M1. For comparison, the downstream groove of M1 is replaced by an identical groove as that of the TOPSIS point to assemble into another multiple-groove casing treatment, denoted by M2. The two multiple-groove casing treatments are shown schematically in **Figure 15A**. The performance curves of M1 and M2 are compared against the TOPSIS point in **Figure 15B**. It is found that the peak efficiency of both multiple-groove treatments is higher than that of the TOPSIS point, especially for M1. The SMI of M1 is comparable to that of the TOPSIS point. For M2, however, the SMI is 0.9% lower than the TOPSIS point. A similar phenomenon was also observed in Houghton's research when the third groove was added to the two-groove treatment. The contrast shows that varying the groove geometrical dimensions may be necessary in some cases of multiple-groove casing treatments.

CONCLUSION

In the presented work, a multi-objective optimization is conducted to maximize the effect of the single grooved casing treatment on an ultra-highly loaded low-reaction transonic rotor. The flow behaviors that lead to performance changes have been carefully analyzed. There is also discussion of an unconventional form of multiple grooved casing treatment. The main conclusions are summarized as follows:

(1) An optimized groove configuration that increases the rotor stall margin by about 5.8% is obtained without efficiency degradation and distinctive characteristic changes. The groove located around the leading edge has good stability-enhancing performance, and the groove located around 20% C_a is beneficial to the peak efficiency. Wide grooves tend to achieve a higher SMI, but have a greater risk of a serious decline in aerodynamic performance. In addition, there seems to be certain correlation between depth and other parameters.
(2) In the investigated highly-loaded transonic rotor, the breakdown of TLV is observed at the NS point. The flow blockage near the leading edge caused by the vortex breakdown and double-leakage flow is responsible for the flow instability of the transonic rotor. The tip flow filed analysis shows that the optimized grooved casing treatment can suppress the shock/TLV interaction and double-leakage flow. The presence of casing groove generates the radial migration of tip leakage flow, resulting in the tip unloading and aspiration-injection effects. Influenced by the above effects, the swirl strength of TLV is decreased while the roll up of TLV is delayed. Thus, the TLV has a diminished chance of breaking down under the action of the passage shock. As the shock/vortex interaction is weakened, the flow capacity near the tip region is enhanced, which can be observed from the removal of the reverse flow region located downstream of the main flow/tip leakage flow interface. Consequently, the interface is pushed downstream and the tip stall is eventually postponed.
(3) The groove helps to mitigate the intensity of the tip leakage vortex and thus the associated blockage. When the additional loss induced by the flow exchange between the groove and the tip passage is relatively small, the peak efficiency of the rotor can be improved.
(4) Two kinds of multiple-groove casing treatment have been tested. The first treatment consists of component grooves with varied geometrical dimensions, which achieves a comparable SMI as the single groove and has higher peak efficiency. The second treatment is a conventional design with identical grooves, which causes a decrease in stall margin compared to the single groove. The results reflect that a change in the groove geometrical dimensions along the blade chord is required to control rationally different portions of tip leakage flow for the investigated rotor.

DATA AVAILABILITY STATEMENT

The original contributions presented in the study are included in the article/Supplementary Material, further inquiries can be directed to the corresponding author.

AUTHOR CONTRIBUTIONS

SD provides innovation, numerical simulation experiment, model establishment and writing for this article. SC provides financial support and guidance about the content of the article. SW and ZW engage in some technical work.

FUNDING

This work is supported by the National Natural Science Foundation of China (Grant Nos. 52076052 and 51776048) and National Science and Technology Major Project of China (Grant Nos. Y2019-VIII-0013-0174).

REFERENCES

Adamczyk, J. J., Celestina, M. L., and Greitzer, E. M. (1993). The Role of Tip Clearance in High-Speed Fan Stall. *J. Turbomach.* 115 (1), 28–38. doi:10.1115/1.2929212

Agha Seyed Mirzabozorg, M., Bazazzadeh, M., and Hamzezade, M. (2017). Numerical Study on the Effect of Single Shallow Circumferential Groove Casing Treatment on the Flow Field and the Stability of a Transonic Compressor. *Jafm* 10 (1), 257–265. doi:10.18869/acadpub.jafm.73.238.26480

Ba, D., Zhang, Q., Du, J., Li, Z., Zhang, H., and Nie, C. (2020). Design Optimization of Axial Slot Casing Treatment in a Highly-Loaded Mixed-Flow Compressor. *Aerospace Sci. Tech.* 107, 106262. doi:10.1016/j.ast.2020.106262

Behzadian, M., Khanmohammadi Otaghsara, S., Yazdani, M., and Ignatius, J. (2012). A State-Of The-Art Survey of TOPSIS Applications. *Expert Syst. Appl.* 39 (17), 13051–13069. doi:10.1016/j.eswa.2012.05.056

Cameron, J. D., Bennington, M. A., Ross, M. H., Morris, S. C., Du, J., Lin, F., et al. (2013). The Influence of Tip Clearance Momentum Flux on Stall Inception in a High-Speed Axial Compressor. *J. Turbomach.* 135 (5), 051005. doi:10.1115/1.4007800

Choi, K.-J., Kim, J.-H., and Kim, K.-Y. (2010). Design Optimization of Circumferential Casing Grooves for a Transonic Axial Compressor to Enhance Stall Margin. ASME Paper GT2010-22396. doi:10.1115/GT2010-22396

Deb, K., Pratap, A., Agarwal, S., and Meyarivan, T. (2002). A Fast and Elitist Multiobjective Genetic Algorithm: NSGA-II. *IEEE Trans. Evol. Computat.* 6 (2), 182–197. doi:10.1109/4235.996017

Djeghri, N., Vo, H. D., and Yu, H. (2015). *Parametric Study for Lossless Casing Treatment on a Mixed-Flow Compressor Rotor*. ASME Paper GT2015-42750. doi:10.1115/GT2015-42750

Hah, C., Voges, M., Mueller, M., and Schiffer, H.-P. (2010). *Characteristics of Tip Clearance Flow Instability in a Transonic Compressor*. ASME Paper GT2010-22101. doi:10.1115/GT2010-22101

Hewkin-Smith, M., Pullan, G., Grimshaw, S. D., Greitzer, E. M., and Spakovszky, Z. S. (2019). The Role of Tip Leakage Flow in Spike-type Rotating Stall Inception. *J. Turbomach.* 141 (6), 061010. doi:10.1115/1.4042250

Houghton, T., and Day, I. (2012). Stability Enhancement by Casing Grooves: The Importance of Stall Inception Mechanism and Solidity. *J. Turbomach.* 134 (2), 021003. doi:10.1115/1.4002986

Huang, X., Chen, H., and Fu, S. (2008)., *CFD Investigation on the Circumferential Grooves Casing Treatment of Transonic Compressor*. ASME Paper GT2008-51107. doi:10.1115/GT2008-51107

Keane, A., Forrester, A., and Sobester, A. (2008). *Engineering Design via Surrogate Modelling: A Practical Guide*. Chichester: Wiley.

Kerrebrock, J. L., Reijnen, D. P., Ziminsky, W. S., and Smilg, L. M. (1997). *Aspirated Compressors*. ASME Paper 97-GT-525. doi:10.1115/97-GT-525

Kim, J.-H., Choi, K.-J., Husain, A., and Kim, K.-Y. (2011). Multiobjective Optimization of Circumferential Casing Grooves for a Transonic Axial Compressor. *J. Propulsion Power* 27 (3), 730–733. doi:10.2514/1.50563

Liu, J.-m., Gao, Y.-s., Wang, Y.-q., and Liu, C. (2019). Objective omega Vortex Identification Method. *J. Hydrodyn.* 31 (3), 455–463. doi:10.1007/s42241-019-0028-y

Mao, X., and Liu, B. (2020). Investigation of the Casing Groove Location Effect for a Large Tip Clearance in a Counter-rotating Axial Flow Compressor. *Aerospace Sci. Tech.* 105, 106059. doi:10.1016/j.ast.2020.106059

Mao, X., Liu, B., Tang, T., and Zhao, H. (2018). The Impact of Casing Groove Location on the Flow Instability in a Counter-rotating Axial Flow Compressor. *Aerospace Sci. Tech.* 76, 250–259. doi:10.1016/j.ast.2018.01.037

Mustaffa, A. F., and Kanjirakkad, V. (2021). Single and Multiple Circumferential Casing Groove for Stall Margin Improvement in a Transonic Axial Compressor. *J. Turbomach.* 143 (7), 071010. doi:10.1115/1.4050444

Mu¨ller, M. W., Schiffer, H.-P., and Hah, C. (2007). *Effect of Circumferential Grooves on the Aerodynamic Performance of an Axial Single-Stage Transonic Compressor*. ASME Paper GT2007-27365. doi:10.1115/GT2007-27365

Qin, N., Carnie, G., Wang, Y., and Shahpar, S. (2014). Design Optimization of Casing Grooves Using Zipper Layer Meshing. *J. Turbomach.* 136 (3), 031002. doi:10.1115/1.4024650

Rabe, D. C., and Hah, C. (2002). *Application of Casing Circumferential Grooves for Improved Stall Margin in a Transonic Axial Compressor*. ASME Paper GT2002-30641. doi:10.1115/GT2002-30641

Ren, X., and Gu, C. (2016). A Numerical Study on the Tip Clearance in an Axial Transonic Compressor Rotor. *Appl. Therm. Eng.* 103, 282–290. doi:10.1016/j.applthermaleng.2016.04.082

Sakuma, Y., Watanabe, T., Himeno, T., Kato, D., Murooka, T., and Shuto, Y. (2014). Numerical Analysis of Flow in a Transonic Compressor with a Single Circumferential Casing Groove: Influence of Groove Location and Depth on Flow Instability. *J. Turbomach.* 136 (3), 031017. doi:10.1115/1.4025575

Shabbir, A., and Adamczyk, J. J. (2005). Flow Mechanism for Stall Margin Improvement Due to Circumferential Casing Grooves on Axial Compressors. *J. Turbomach.* 127 (4), 708–717. doi:10.1115/1.2008970

Song, W., Zhang, Y., Chen, H., and Deng, K. (2019). Transonic Compressor Blade Optimization Integrated with Circumferential Groove Casing Treatment. *J. Turbomach.* 141 (3), 031015. doi:10.1115/1.4041699

Spalart, P., and Allmaras, S. (1992). *A One-Equation Turbulence Model for Aerodynamic Flows*. AIAA Paper No. 92-0439. doi:10.2514/6.1992-439

Strazisar, A. J., Hathaway, M. D., Suder, K. L., and Wood, J. R. (1989). *Laser Anemometer Measurements in a Transonic Axial Flow Compressor rotorNASA Report No*. NASA TP-2879.

Suder, K. L., and Celestina, M. L. (1996). Experimental and Computational Investigation of the Tip Clearance Flow in a Transonic Axial Compressor Rotor. *J. Turbomach.* 118 (2), 218–229. doi:10.1115/1.2836629

Sun, S., Wang, S., Chen, S., Tao, C., Cai, L., and Chen, J. (2019). The Impact of Various Forward Sweep Angles on the Performance of an Ultra-high-load Low-Reaction Transonic Compressor Rotor. *Appl. Therm. Eng.* 150, 953–966. doi:10.1016/j.applthermaleng.2019.01.045

Sun, X., Dong, X., and Sun, D. (2019). Recent Development of Casing Treatments for Aero-Engine Compressors. *Chin. J. Aeronautics* 32 (1), 1–36. doi:10.1016/j.cja.2018.11.005

Vo, H. D., Tan, C. S., and Greitzer, E. M. (2008). Criteria for Spike Initiated Rotating Stall. *J. Turbomach.* 130 (1), 011023. doi:10.1115/1.2750674

Vuong, T.-D., Kim, K.-Y., and Dinh, C.-T. (2021). Recirculation-groove Coupled Casing Treatment for a Transonic Axial Compressor. *Aerospace Sci. Tech.* 111, 106556. doi:10.1016/j.ast.2021.106556

Wang, W., Lu, J.-l., Luo, X.-q., and Chu, W.-l. (2019). Coupling Method of Stability Enhancement Based on Casing Treatments in an Axial Compressor. *Aerospace Sci. Tech.* 95, 105449. doi:10.1016/j.ast.2019.105449

Yingjiao, H., Songtao, W., Longxing, Z., and Jun, D. (2014). Aerodynamic Design of a Highly Loaded Supersonic Aspirated Axial Flow Compressor Stage. *Proc. Inst. Mech. Eng. A: J. Power Energ.* 228 (3), 241–254. doi:10.1177/0957650913515668

Zhao, Q., Zhou, X., and Xiang, X. (2014). Multi-objective Optimization of Groove Casing Treatment in a Transonic Compressor. *Proc. Inst. Mech. Eng. Part A: J. Power Energ.* 228 (6), 626–637. doi:10.1177/0957650914532266

Zhu, G., and Yang, B. (2020). Optimization of Slots-Groove Coupled Casing Treatment for an Axial Transonic Compressor. *J. Turbomach.* 142 (8), 081003. doi:10.1115/1.4046047

Zhu, M., Teng, J., and Qiang, X. (2021). Unsteady Near-Stall Flow Mechanisms in a Transonic Compressor Rotor at Different Rotating Speeds. *Aerospace Sci. Tech.* 119, 107124. doi:10.1016/j.ast.2021.107124

Zhu, W., Cai, L., Wang, S., and Wang, Z. (2020). Numerical Investigation of Circumferential Groove Casing Treatment in a Highly-Loaded Low-Reaction Transonic Compressor Rotor. *J. Therm. Sci.* 29 (4), 916–927. doi:10.1007/s11630-019-1180-y

Conflict of Interest: The authors declare that the research was conducted in the absence of any commercial or financial relationships that could be construed as a potential conflict of interest.

frontiers | Frontiers in Energy Research

ORIGINAL RESEARCH
published: 14 April 2022
doi: 10.3389/fenrg.2022.857077

Effects of Multiple Injection Strategies on Heavy-Duty Diesel Energy Distributions and Emissions Under High Peak Combustion Pressures

Zhao Zhang, Haifeng Liu, Zongyu Yue, Yangyi Wu, Xiangen Kong, Zunqing Zheng and Mingfa Yao*

State Key Laboratory of Engines, Tianjin University, Tianjin, China

OPEN ACCESS

Edited by:
Xiao Liu,
Harbin Engineering University, China

Reviewed by:
Choongsik Bae,
Korea Advanced Institute of Science and Technology, South Korea
Amin Paykani,
University of Hertfordshire, United Kingdom

***Correspondence:**
Haifeng Liu
haifengliu@tju.edu.cn

Specialty section:
This article was submitted to Advanced Clean Fuel Technologies, a section of the journal Frontiers in Energy Research

Received: *18 January 2022*
Accepted: *22 March 2022*
Published: *14 April 2022*

Citation:
Zhang Z, Liu H, Yue Z, Wu Y, Kong X, Zheng Z and Yao M (2022) Effects of Multiple Injection Strategies on Heavy-Duty Diesel Energy Distributions and Emissions Under High Peak Combustion Pressures. Front. Energy Res. 10:857077. doi: 10.3389/fenrg.2022.857077

Peak combustion pressures (PCP) are increased in heavy-duty diesel engines to obtain higher thermal efficiency. Fuel injection strategy has been a major measure to improve the combustion and emissions of diesel engines. But most existing work of multi-injection strategies was not limited by PCP or was conducted under lower PCP (~15 MPa). In this study, an experimental study is conducted to further improve the understanding of injection strategies on engine performance under a relative higher peak combustion pressure at 20 MPa. The four tested injection strategies are single main injection, pilot-main injection, main-post injection, and pilot-main-post injection. The effects of PCP on brake thermal efficiency (BTE) and other engine performances are also investigated under the same NO_x emissions conditions. Results indicate that more advanced injection timing can obtain higher BTE, while the injection pressure has less effects on BTE as it is higher than 120 MPa. For double-injection, the smaller interval on pilot-main or main-post and the less pilot or post mass improves BTE and emissions. The PCPs are linearly correlated to the BTE, peak average temperature, and peak pressure rise rate (PRR), and the increment of BTE, peak average temperature, and peak PRR are about 0.3%, 30 K, and 0.1 MPa/CA for every 1 MPa increase in PCP, respectively. This also means that the improvement on BTE by the increase of PCP imparts greater thermal and mechanical loads on engine materials and components. At 20 MPa PCP, based on the optimized injection strategies, the BTE of all four strategies is about 42.8%, and the peak PRR of all four strategies is about 0.8 MPa/CA. At a given NO_x emission of 17.4 g/kWh and approximate 20 MPa PCP, all four injection strategies have minor effects on distribution of fuel energy and emissions. Therefore, it can be concluded that the injection strategies have fewer effects on BTE and emissions at the higher peak combustion pressure of 20 MPa; the main purpose of injection strategies is to reduce the peak PRR or reach the potentially required temperature for aftertreatment devices.

Keywords: diesel engine, multiple injection strategies, peak combustion pressure, combustion, emissions

INTRODUCTION

Major global markets have greenhouse gas (GHG) and criteria pollutant regulations in place (Jin et al., 2021). Because of stricter regulations for heavy-duty (HD) commercial vehicles, the first European HD GHG targets will require a fleet averaged reduction in CO_2 of 30% by 2030 as compared to a 2019 baseline (Joshi, 2021). In the meantime, the discussions have already started in Europe on the next level of regulations beyond Euro 6 emissions (Joshi, 2019). Since the internal combustion engine will continue to be the predominant drive source for heavy long-distance transport in the foreseeable future, increasing the engine efficiency and reducing exhaust emissions will make a significant contribution to achieving the above targets (Horvath et al., 2020).

Fuel injection strategy has been a major measure to improve the performance and emissions of diesel engines (Mohan et al., 2013). Roh et al. (2015) investigated the effects of pilot injection on combustion and emissions on a diesel engine. They revealed that the highest pressure and NO_x emissions of pilot injection are significantly decreased when compared to the single injection cases. The main reason for the decreased pressure and NO_x emissions was caused by the shorter ignition delay. Li et al. (2015) presented the effect of multiple injections on particulate matter and reported that the amount of particulate matter decreases with the decrease in the diffusion combustion zone when pilot injection is applied. Lee et al. (2015) revealed the application of multiple injection and EGR to a diesel engine powered by JP-8 fuel. Results showed PM and NO_x emissions could be reduced by half when using JP-8 without decreasing the thermal efficiency. Horibe et al. (2018) applied multiple injection to decrease cooling loss under the condition of high injection pressure, and varied the number of injection stages and the split ratio. Therefore, thermal efficiency was improved owing to the combined split-main injection, increased injection pressure, and advanced injection timing. Park et al. (2018) revealed that, when the injection pressure was increased without changing the injection timing in split injection, brake specific fuel consumption (BSFC) deteriorated due to the increase of dwell duration. The increased injection interval led to deterioration of BSFC, the increase of HC and NO_x emissions, and the significant reduction of soot and CO emissions. In addition, the fixed injection interval with a retardation of injection timing improved the BSFC, increased soot emissions, and decreased the NO_x, HC, and CO emissions. Based on the above analysis, injection timing around top dead center (TDC) and a short injection interval, with not too high injection pressure, improve the BSFC and emission characteristics in split-injection diesel combustion. Osada et al. (2012) improved the thermal efficiency by using closed post injection. The timing of the post injection was advanced as far as possible, and the amount of post injection was set approximately at 20% of the main injection amount. Horibe et al. (2012) also found that advanced post injection slightly improved thermal efficiency. Martin et al. (2016) studied optimization strategy of post injections to decrease soot emissions from a light-duty diesel engine. Results identified two distinct regimes of post injection strategies that decreased soot emissions. For the long-dwell regime, the post mass was the critical factor in achieving soot reduction, whereas in the close-coupled regime, the post interval was the critical factor.

Engine manufacturers applied one of the measures, which was injection strategies, to meet the US Department of Energy (DOE) goal of demonstrating 55% brake thermal efficiency (BTE) on a HD engine. Zukouski et al. (2015) carried out an expanded range of start of injections with rail pressure sweep at each start of injection, and revealed the highest BTE within an optimal 50% of the mass fraction burned window. O'Connor et al. (2017) evaluated a number of single and multiple injection strategies varying injection timing and injection quantity, focusing on the combustion and injection strategy optimization, coupling 3-D computational fluid dynamics with 1-D engine modeling. Results indicated a maximum BTE up to 54.2% at brake specific NO_x of 8 g/kWh, with selected engine operating conditions at brake torque 1550 Nm and engine speed 900 rpm. Kocher (2017) reported that, by adjusting the fuel injection rate to obtain a 2 CA earlier peak heat release rate, the closed-cycle efficiency improved about 0.3%.

It is found that most existing work which applied multiple injection strategies was not limited by the peak combustion pressure (PCP). The injection strategy is related to the PCP, and increasing PCP has enabled increased diesel engine BTE (Megel et al., 2011; Koeberlein, 2014). If the peak combustion pressure at the beginning of expansion is increased, this adds positive area to the p-V diagram which more than offsets a slight increase in the (negative) work required during compression (Heywood, 2018). Therefore, a larger fraction of fuel energy at beginning of expansion is transferred to the piston as work, and the brake thermal efficiency was improved. Factually, HD diesel had steadily increased from approximately 38% BTE and 10 MPa PCP in the mid-1980s to approximately 45% BTE and 17 MPa PCP in 2000. From 2000 to 2010, PCP increased continually but BTE fell first and increased as a result of technologies employed to satisfy new emissions regulations, most notably exhaust gas recirculation (EGR) (Stanton, 2013). For example, a 15 L 354 kW diesel engine (Displacement: 15 L, Power: 354 kW) operated at 42% BTE and 19 MPa PCP in 2010 (U.S. Department of Energy, 2013). From 2010 to 2020, although the PCP did not increase significantly, the BTEs of some

TABLE 1 | The experimental engine specifications.

Parameters	Units	Values
Engine displacement	L	7.7
Compression ratio	-	17.5
Bore × Stroke	mm	110 × 135
Max torque/speed	Nm/rpm	1450/1100–1700
Rated power/speed	kW/rpm	257/2200
Turbocharger system	-	Exhaust gas turbocharger, Wastegate
Air-air intercooler		
Number of valves	-	4
Number of nozzle holes	-	8
Nozzle diameter	mm	0.153
Included spray angle	°	147

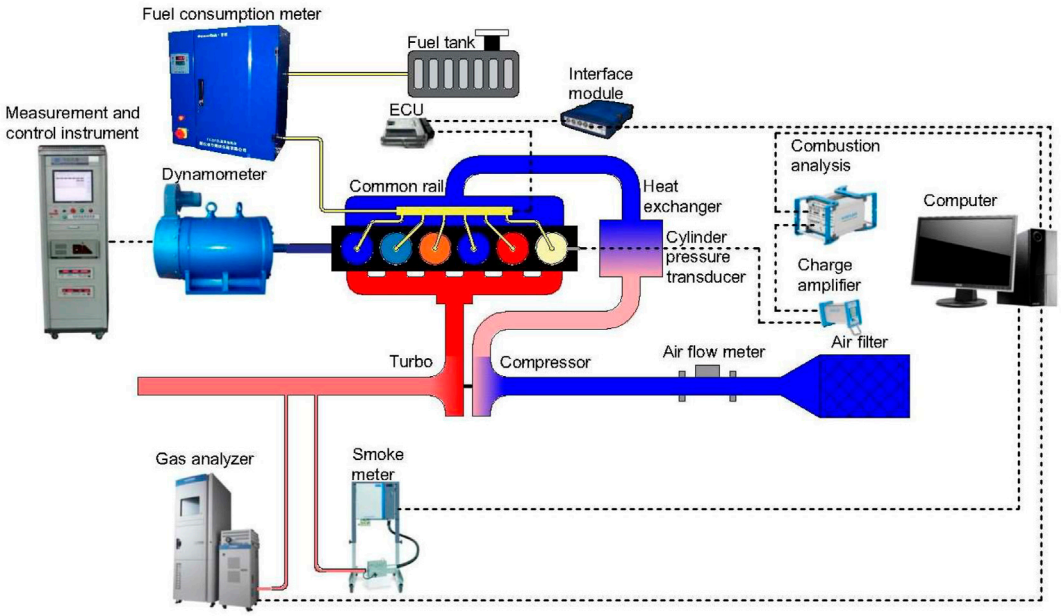

FIGURE 1 | The schematic diagram of the experimental setup.

prototypes were improved to 50% by optimization. The targets from the DOE report are 50% BTE and 25 MPa PCP in 2025, 55% BTE and 27.5 MPa PCP in 2040, and 60% BTE and 30 MPa PCP in 2050 (U.S. Department of Energy, 2013).

The materials used in HD diesel components have their mechanical loading limits (Pierce et al., 2019); an example of recently gray cast iron HD diesel head was designed for 25 MPa PCP (Megel et al., 2011). The injection strategies can improve the performance at the PCP limitation. Suh (2011) revealed that maximum apparent heat release rate (AHRR) of two pilot injections was decreased to 47.2% compared to that of single injection at 5 MPa PCP. It was also found that two pilot injections improved combustion efficiency. Furthermore, in multiple injection strategy, less HC emissions and more CO formation were observed during combustion process, and remarkable simultaneous reduction of soot emissions up to 25% and NO_x emissions up to 58.7% could be achieved in low compression ratio engine. Babayev et al., 2019a compared the different injection strategies with the total injection quantity kept relatively constant under 15 MPa PCP. The results proved that the isobaric combustion concept could achieve gross indicated efficiencies close to or higher than those of a conventional diesel combustion (CDC) cycle. Furthermore, the results revealed that heat transfer losses could be reduced by over 20% with an isobaric cycle. The NO_x emissions were significantly lower for the isobaric combustion. Meanwhile, the soot, CO, and HC emission levels were proven to be fairly similar to those of the conventional diesel combustion. Babayev et al., 2019b also focused on understanding the effect of different injection strategies on the emissions, heat release, and thermal efficiency of isobaric combustion at 15 MPa PCP. At high PCPs, isobaric combustion cycle was capable of achieving efficiencies equal to those of the CDC cycle. However, it

TABLE 2 | Uncertainties of measured parameters.

Measured parameters	Property	Sensitivity	Uncertainties (%)
Engine torque	0–2100 Nm	±2.8 Nm	0.2
Engine speed	0–7000 r/min	±1 r/min	0.01
Intake pressure	0–1000 kPa	±0.5% kPa	0.1
Intake temperature	223.15–573.15 K	±0.05% K	0.35
Exhaust temperature	223.15–1073.15 K	±0.05% K	0.35
Airflow meter	0–1200 kg/h	±1.75 kg/h	0.5
Fuel flow meter	0–150 kg/h	±0.01 kg/h	1
In-cylinder pressure	0–250 bar	16 pC/bar	0.4
Soot emissions	0–8.08 FSN	0.001 FSN	3
NO_x emissions	0–10, 000 ppm	±1 ppm	0.5
HC emissions	0–50, 000 ppm	±1 ppm	0.5
CO emissions	0–50, 000 ppm	±1 ppm	0.5

TABLE 3 | Injection settings.

Type	Injection pressure (MPa)	Pilot-main interval (CA)	Pilot mass (mg)	Main timing (CA ATDC)	Main-Post interval (CA)	Post mass (mg)
Single main injection	120	-	-	−14~−6	-	-
	100–180	-	-	−11	-	-
Pilot-main injection	160	30–5	10	−12~−10	-	-
	160	5	2–10	−12~−10	-	-
Main-post injection	160	-	-	−13~−12	6–14	30
	160	-	-	−12	6	10–30
Pilot-main-post injection	160	5	2	−12~−4	6	10

had much higher exhaust enthalpy, lower PCPs, and heat transfer losses. NO_x formation was only a function of the total injection duration. CO, HC, and soot were formed during the first injection, then oxidized during the subsequent injections. CO, HC, and soot formation rate increased again during the late injections. Nyrenstedt et al. (2020) performed injection strategy experiments with an equivalent HD diesel optical engine around 7 MPa PCP. Three injection strategies built two isobaric heat release cases and an isochoric heat release case. Results found that in the isobaric cases, liquid fuel was injected into burning gases. This resulted in shorter ignition delays and thus a poor mixing level. The lack of air/fuel mixing was clearly the main factor contributing to the high soot emissions observed in isobaric combustion. By tracking the chemiluminescence, the lower heat losses of the isobaric strategy were further explained. Unlike the single injection, multiple injections helped to contain the hot gases away from the walls. However, the opposite effects were also found from the high thermal radiation caused by the extensive soot formation. Ramadan et al. (2020) focused on the effect of fuels on the multiple-injection equivalent HD diesel optical engine which had 7 MPa PCP. The research revealed that isobaric combustion could be achieved even with high octane number fuels such as isooctane. The dwell time between injections was much larger for isooctane, which allowed enhanced mixing of the air with fuel jets and thereby a partially premixed combustion behavior. Tang et al. (2020) evaluated the fuel spray characteristics of the four-consecutive-injections strategy which used in high-pressure isobaric combustion of about 3.2 MPa PCP at TDC. The high-speed imaging of the liquid-phase spray revealed that a short injection dwell reduced the hydraulic delay of the injector, resulting in an increase in both the injection duration and the peak liquid-phase penetration length. Goyal et al. (2020) studied the effect of compression ratio, EGR, and engine speed on CDC and two isobaric combustion cases, by using multiple injection strategies. The high-pressure isobaric combustion (IsoH) and low-pressure isobaric combustion (IsoL) were maintained at PCP of 6.8 and 5 MPa, respectively. From the compression ratio comparison results, it was found that a higher compression ratio resulted in increased gross indicated efficiency and decreased exhaust losses. The NO_x emissions were also increased with decreased soot concentration at the lower compression ratio. Irrespective of EGR rates and engine speed, it was found that IsoH had similar or higher gross indicated efficiency than CDC with the lowest efficiency for IsoL. At a given engine speed, lower EGR rates resulted in lower soot, CO, and HC emissions with higher NO_x emissions. However, with decreased engine speed, HC and CO emissions were highly unchanged.

Based on the aforementioned studies, it is found that multiple-injection can effectively control the in-cylinder

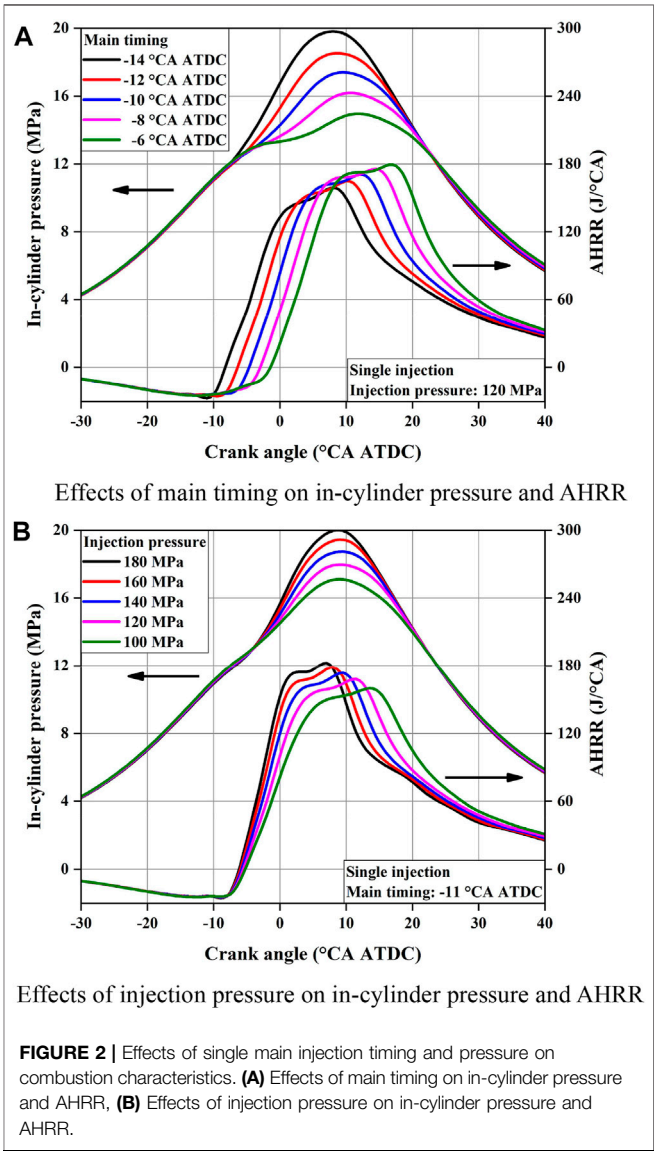

FIGURE 2 | Effects of single main injection timing and pressure on combustion characteristics. **(A)** Effects of main timing on in-cylinder pressure and AHRR, **(B)** Effects of injection pressure on in-cylinder pressure and AHRR.

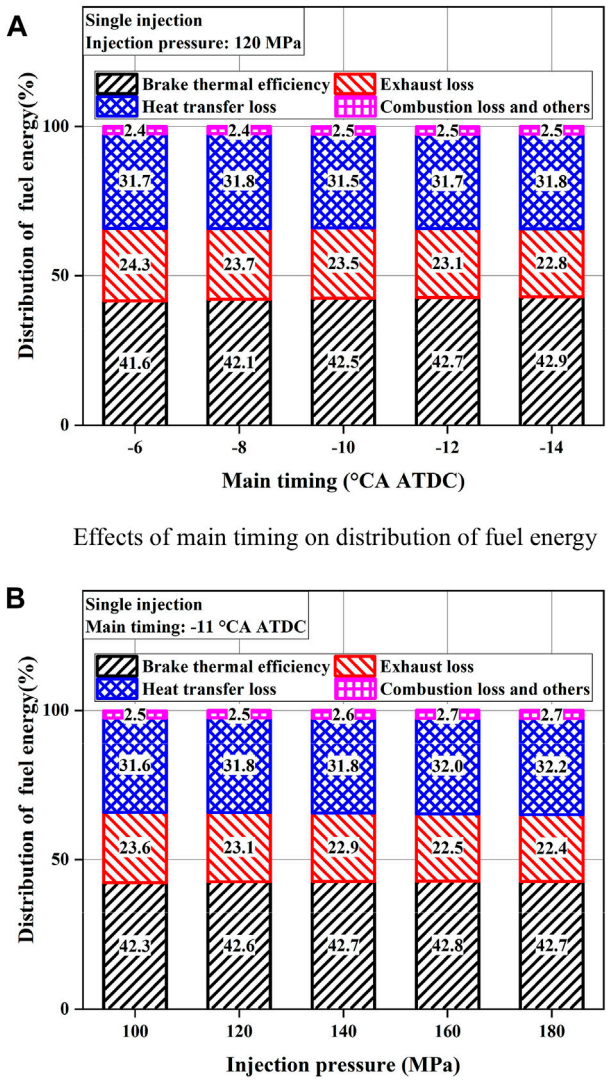

FIGURE 3 | Effects of single main injection timing and pressure on distribution of fuel energy. **(A)** Effects of main timing on distribution of fuel energy, **(B)** Effects of injection pressure on distribution of fuel energy.

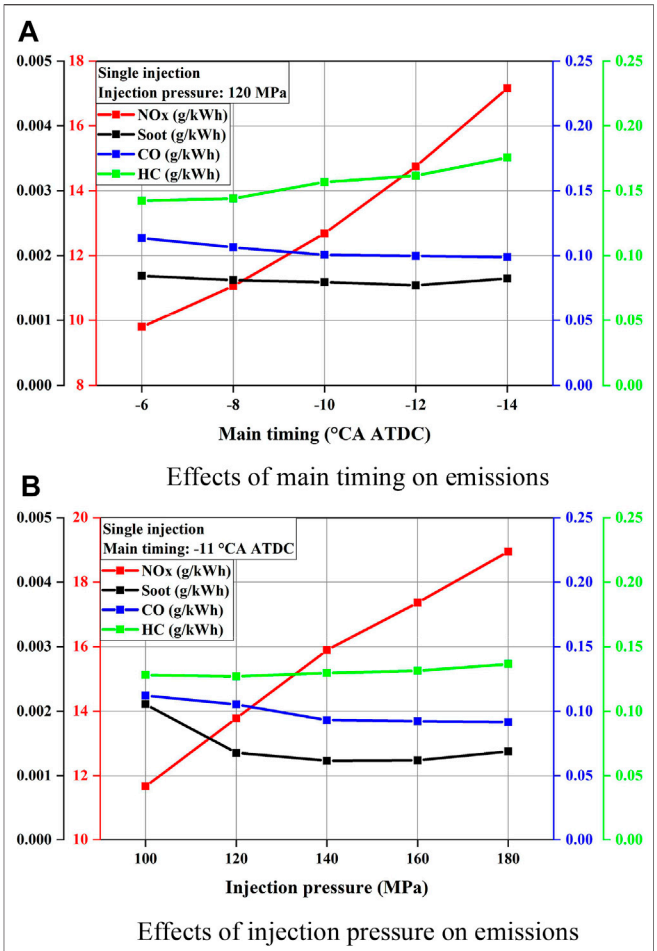

FIGURE 4 | Effects of single main injection timing and pressure on emissions. **(A)** Effects of main timing on emissions. **(B)** Effects of injection pressure on emissions.

combustion, so as to obtain higher thermal efficiency and lower emissions. However, the studies on multiple-injection were mainly conducted under lower PCP at 15 MPa in the previous works. In future, PCPs should be increased further in heavy-duty diesel engines in order to obtain enhanced thermal efficiency. Therefore, in the current study, first of all, for further improve the understanding of injection strategies on higher PCP, the PCP is limited to 20 MPa to investigate the effects of multiple-injection on combustion and emissions. Secondly, the current study will clarify the relationship between PCPs and the engine performance, such as BTE, peak average temperature, and peak pressure rise rate. Finally, an optimized injection strategy is proposed at 20 MPa. The current work can provide a valuable reference on the utilization of injection strategies on diesel engine under higher combustion pressure conditions.

EXPERIMENTAL METHODOLOGY

Engine Setup

All experiments were carried out on an inline and 6-cylinder heavy-duty diesel engine equipped with a Bosch commercial common rail fuel-injection system. The detailed specifications of the engine are listed in **Table 1**. The schematic of the experimental setup is presented in **Figure 1**. The original engine can meet the Euro VI emission regulations by using a high-pressure EGR, a selective catalytic reduction (SCR), a diesel oxidation catalyst (DOC), and a diesel particulate filter (DPF). The EGR, SCR, DOC, and DPF were removed and all the emissions were the raw emissions in this experiment.

The in-cylinder pressure was measured by a pressure transducer (Kistler 6125C) coupled with a corresponding

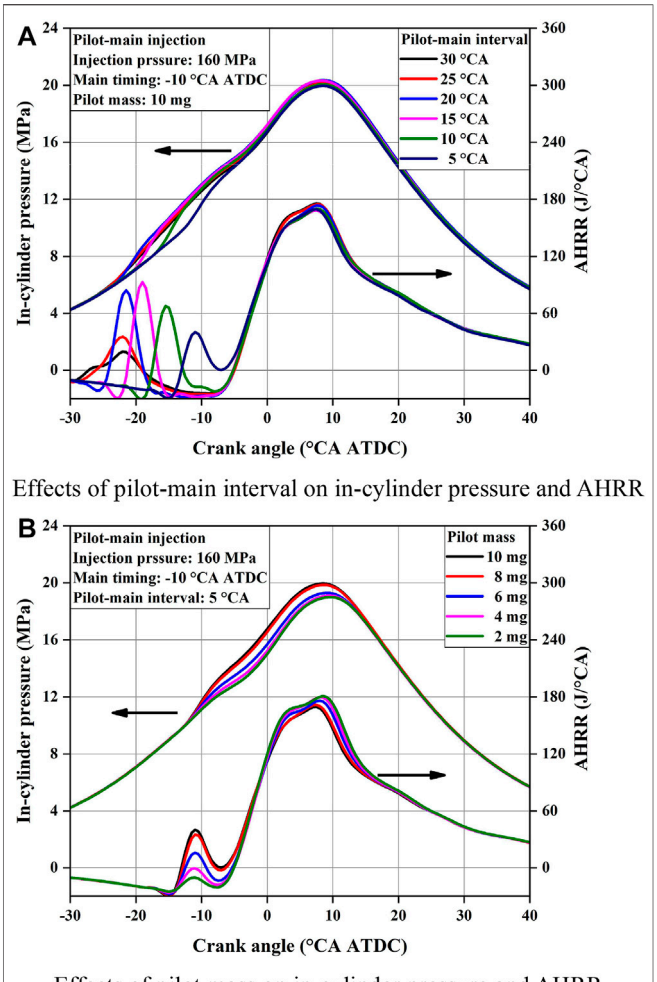

FIGURE 5 | Effects of pilot-main interval and pilot mass on combustion characteristics. **(A)** Effects of pilot-main interval on in-cylinder pressure and AHRR. **(B)** Effects of pilot mass on in-cylinder pressure and AHRR.

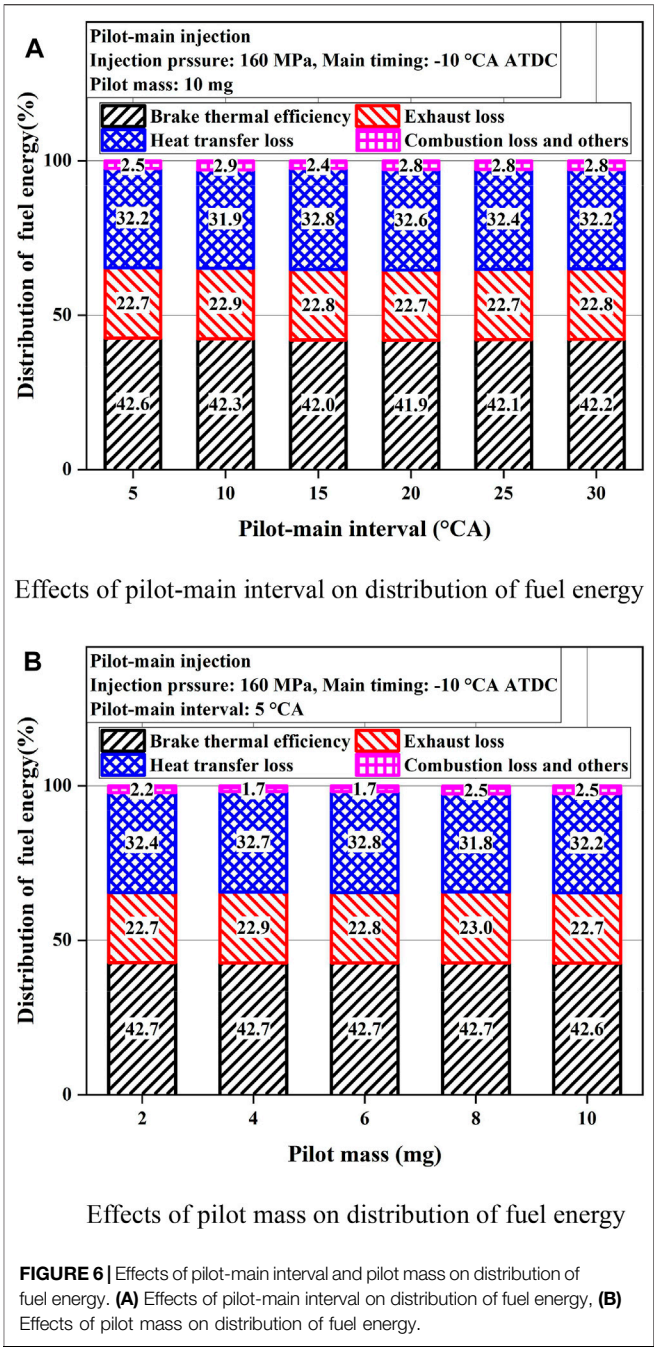

FIGURE 6 | Effects of pilot-main interval and pilot mass on distribution of fuel energy. **(A)** Effects of pilot-main interval on distribution of fuel energy, **(B)** Effects of pilot mass on distribution of fuel energy.

charge amplifier (Kistler 5011B10) and a data acquisition system. The acquisition of cylinder pressure data of 100 consecutive engine cycles was triggered by the optical crank angle encoder (Kistler 2614A4) with a resolution of 0.5 CA. The AHRR values were calculated by the model which has been applied in previous studies (Liu et al., 2013; Zheng et al., 2015a; Zheng et al., 2015b). The average temperatures were calculated using measured in-cylinder pressure and trapped mass with ideal law assumption. Exhaust smoke was measured with a filter paper smoke meter (AVL 415S). Furthermore, the gaseous emissions, including NO_x, HC, and CO, were measured by an exhaust emission analyzer (HORIBA MEXA7100DECR). During the experiment, the temperature of cooling water and intake air were controlled at 85 ± 2°C and 50 ± 2°C, respectively. At each test point, the engine ran for several minutes until the controlled measurement parameters were stable, then the performance, emissions, and combustion pressures were measured and recorded. The uncertainties of the measurement instruments are shown in **Table 2**, which are from the manufacturer specification.

Test Methods

In this work, the operating condition of 1.5 MPa brake mean effective pressure (BMEP) and 1500 rpm engine speed was selected to represent the frequently used operating and the optimal economic area of the diesel engine. The injection settings are listed in **Table 3**. The maximum of the main injection timing of each type was the limit value with the PCP constraint of 20 MPa. In the case of single main injection timing, the injection timing was retarded from −14 CA after top dead center (ATDC) (2 CA interval), and the injection

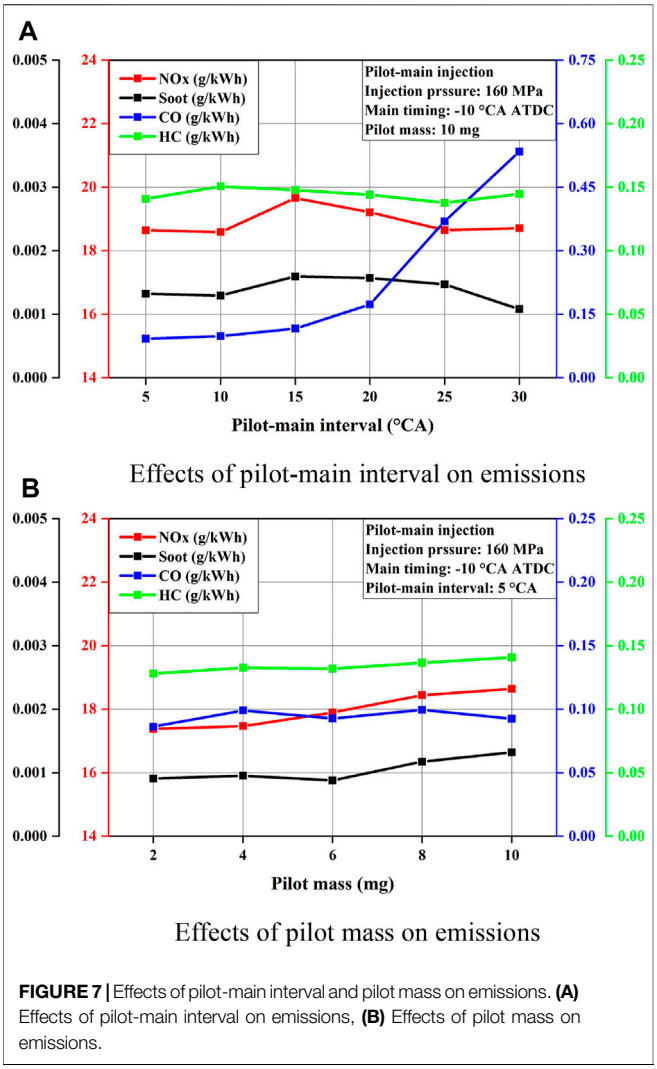

FIGURE 7 | Effects of pilot-main interval and pilot mass on emissions. **(A)** Effects of pilot-main interval on emissions, **(B)** Effects of pilot mass on emissions.

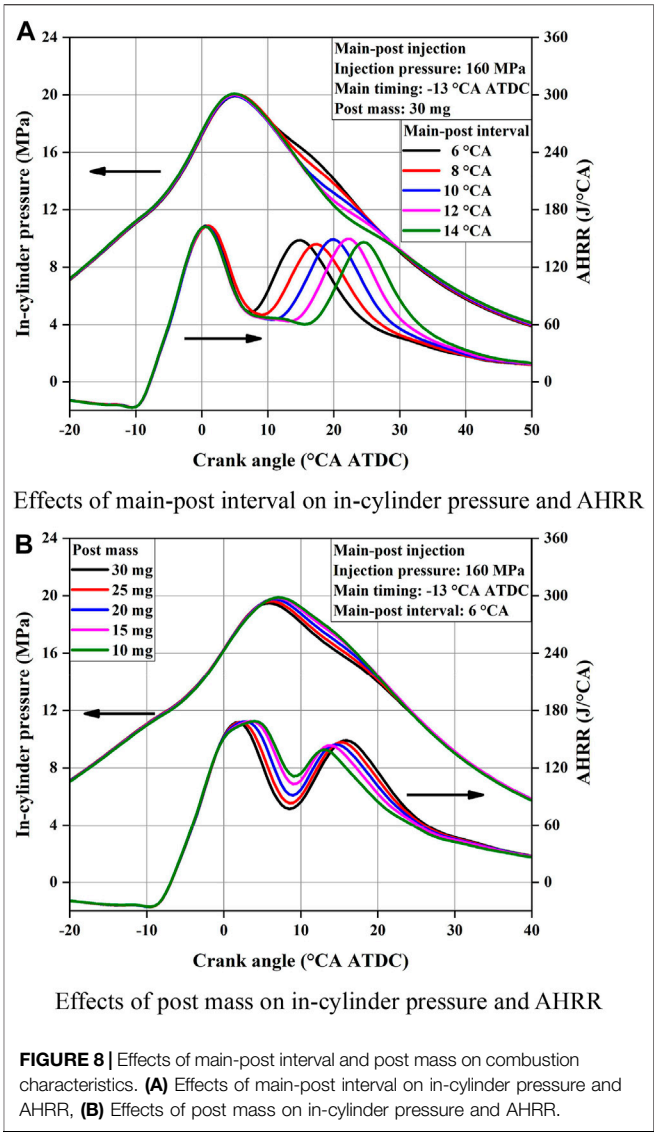

FIGURE 8 | Effects of main-post interval and post mass on combustion characteristics. **(A)** Effects of main-post interval on in-cylinder pressure and AHRR, **(B)** Effects of post mass on in-cylinder pressure and AHRR.

pressure was 120 MPa, which was from the original injection map at this operating condition. In the case of single main injection pressure, the injection pressure was decreased from 180 MPa (20 MPa interval), which was the maximum injection pressure of the fuel-injection system. The injection pressure of following cases was 160 MPa with the highest BTE of the single main injection pressure cases. In the case of pilot-main interval, the interval was deceased from 30 CA (5 CA interval), and the pilot mass was 10 mg. In the case of pilot mass, the pilot mass was decreased from 10 mg (2 mg interval), and the pilot-main interval was 5 CA with the highest BTE of pilot-main interval cases.

In the case of main-post interval, the interval was increased from 6 CA (2 CA interval), which was the minimum main-post interval, and the post mass was 30 mg. In the case of post mass, the post mass was decreased from 30 mg (5 mg interval), and the main-post interval was 6 CA with the highest BTE of main-post interval cases. In the case of pilot-main-post injection, the injection parameters were of the optimum value with the highest BTE of previous cases except main timing, and the main timing was retarded from −12 CA ATDC (2 CA interval).

Distribution of Fuel Energy Analysis Method

The fuel energy (Q_{fuel}) is divided into four parts: brake power, exhaust loss (η_{ex}), heat transfer loss (η_{cool}), and combustion loss and others (η_{misc}). Brake power (P_e) is the usable power delivered by the engine to the load. Energy of exhaust gas (Q_{ex}) is the energy taken away by the exhaust gas, and is calculated based on exhaust temperature. Heat transfer loss includes coolant and oil thermal losses, etc. Combustion loss and others include total combustion and mechanical losses. Combustion loss (η_{comb}) is calculated based on unburned HC, CO, and H_2. Mechanical losses (η_m) are the ratio of mechanical losses power and fuel energy. BTE (η_{et}),

exhaust loss, heat transfer loss, combustion loss, and others are respectively defined as

$$\eta_{et} = \frac{P_e}{Q_{fuel}} \quad (1)$$

$$\eta_{ex} = \frac{Q_{ex}}{Q_{fuel}} \quad (2)$$

$$\eta_{mics} = \eta_{comb} + \eta_m \quad (3)$$

$$\eta_{cool} = 1 - \eta_{et} - \eta_{ex} - \eta_{mics} \quad (4)$$

The detailed calculations of each loss can be found in Ref. (Taymaz, 2006; Heywood, 2018).

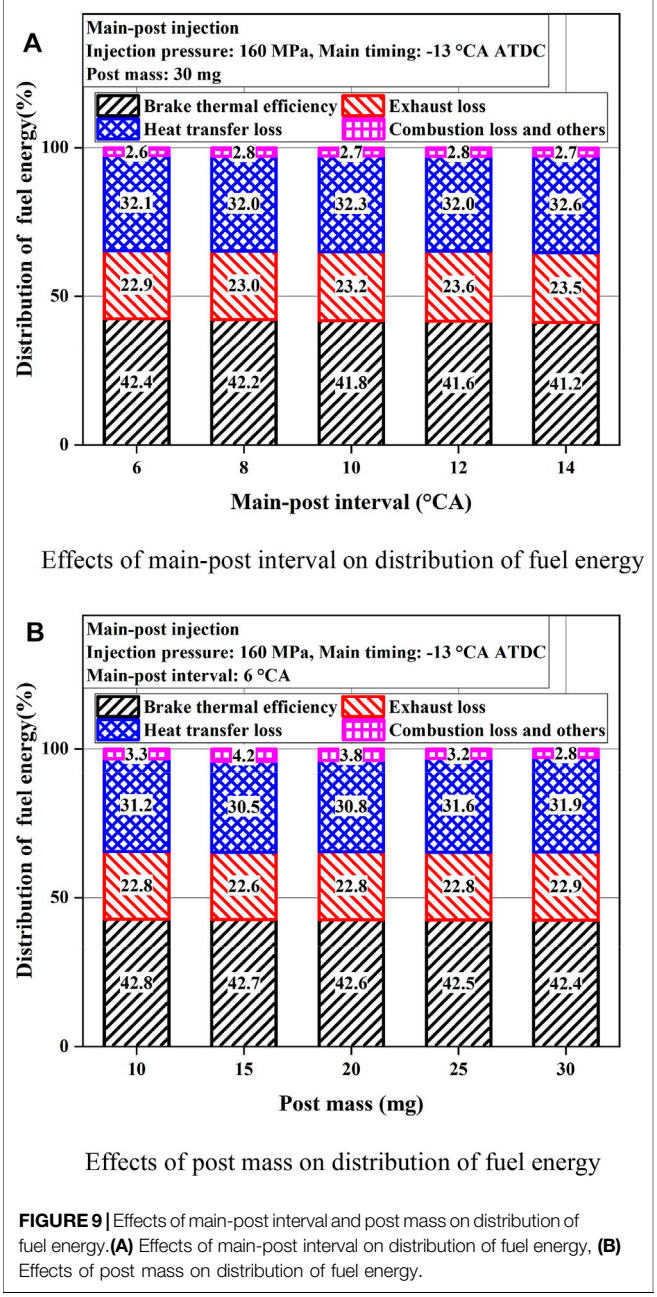

FIGURE 9 | Effects of main-post interval and post mass on distribution of fuel energy. **(A)** Effects of main-post interval on distribution of fuel energy, **(B)** Effects of post mass on distribution of fuel energy.

RESTULTS AND DISCUSSION

Effects of Single Main Injection on Performance Under 20 MPa Peak Combustion Pressure

Figure 2 shows the effects of single main injection timing and pressure on combustion characteristics, respectively. As the main timing retards, the start of combustion delays and the peak combustion pressure decrease. As the injection pressure increases, the injection duration is shortened and the fuel atomization is improved. The peak AHRR and combustion phasing determine the peak combustion pressure. As the injection pressure increases, the combustion phasing is advanced and the peak AHRR is increased, which results in the increase and advance of combustion pressure. Overall, the main injection timing has larger effects on in-cylinder pressure than injection pressure.

Figure 3 shows the effects of single main injection timing and pressure on distribution of fuel energy, respectively. As the main

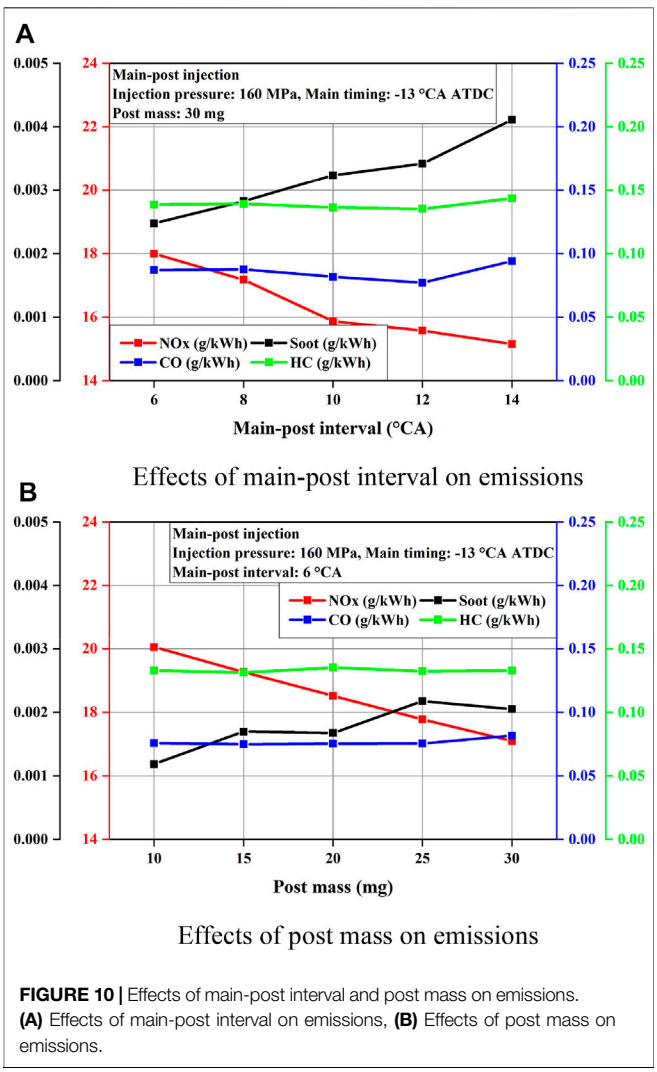

FIGURE 10 | Effects of main-post interval and post mass on emissions. **(A)** Effects of main-post interval on emissions, **(B)** Effects of post mass on emissions.

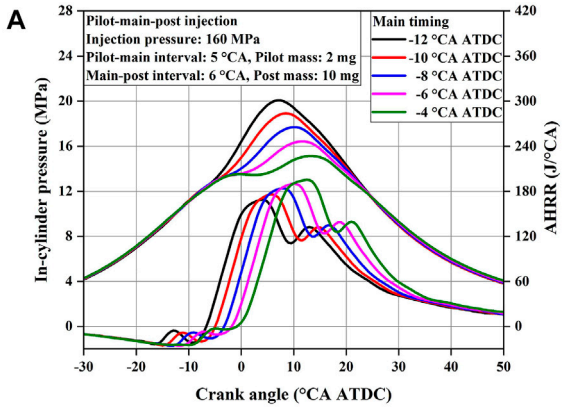

Effects of pilot-main-post injection on in-cylinder pressure and AHRR

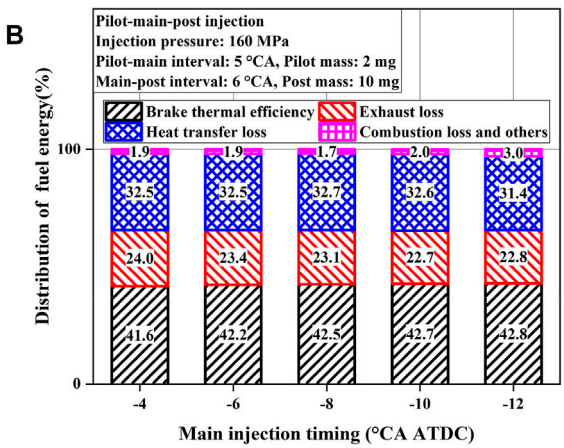

Effects of pilot-main-post injection on distribution of fuel energy

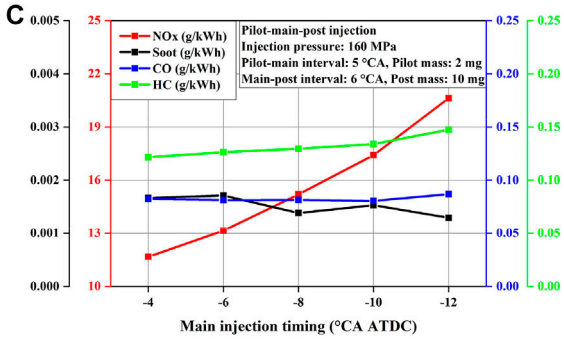

Effects of pilot-main-post injection on emissions

FIGURE 11 | Effects of pilot-main-post injection on combustion and emissions. **(A)** Effects of pilot-main-post injection on in-cylinder pressure and AHRR, **(B)** Effects of pilot-main-post injection on distribution of fuel energy. **(C)** Effects of pilot-main-post injection on emissions.

timing advances, the higher combustion pressure gradually increases BTE, the combustion phasing is nearer to TDC, and exhaust loss decreases gradually; the similar AHRR profiles determine basically unchanged heat transfer and combustion loss. As the injection pressure increases, the combustion pressure and mechanical losses are increased, which offset each other, and finally the BTE first increases and then decreases. With the increase of injection pressure, the combustion phasing is nearer to TDC and exhaust loss decreases gradually, the in-cylinder average temperature increases, and the heat transfer loss increases. The fuel pump work increases, and the mechanical losses increases. It should be noted that BTEs are similar above 120 MPa and all BTEs are between 42.6 and 42.8%. In general, more advanced injection timing can obtain higher BTE, while the injection pressure has fewer effects on BTE as it is higher than 120 MPa.

Figure 4 shows the effects of single main injection timing and pressure on emissions, respectively. As the injection timing advances, the combustion phasing is nearer to TDC and in-cylinder combustion pressure is increased, NO_x emissions increase, while CO emissions decrease slightly. More fuel spray impinges on the combustion chamber walls due to earlier injection timings, resulting in the increase of HC emissions. The constant ignition delay leads to the basically unchanged soot emissions. As the injection pressure increases, in-cylinder combustion temperatures and pressures are increased, CO and NO_x emissions trend is the same as that of the main timing. The improvement of spray atomization leads to the decrease of soot emissions and the shortening of ignition delay leads to the increase of soot emissions, which offset each other, and finally soot emissions first decrease and then increase. It is also because more fuel spray impinges on the combustion chamber walls, leading to slightly higher HC emissions, but the effects on HC emissions are less than those of the injection timings.

Effects of Pilot-Main Injection on Performance Under 20 MPa Peak Combustion Pressure

Figure 5 shows the effects of pilot-main interval and pilot mass on combustion characteristics, respectively. As the interval increases, the pilot-injection timing advances and, accordingly, the AHRR profiles of pilot injections are advanced, while the peak AHRR of pilot injections first increases and then decreases. When the interval is larger, the timing of pilot injection is too early, the in-cylinder temperatures and pressures are lower, and combustion volume is also larger, thus the combustion rates and peaks of AHRR for pilot injection are lower. Due to the fact that the in-cylinder temperature and pressure at 30 CA interval pilot injection are too low, the combustion phasing of pilot injection is similar at 30 and 25 CA interval. When the interval is smaller, in-cylinder temperatures and pressures are increased, the ignition delay of pilot injection is shorter, and peak AHRR of pilot injection is also lower. Therefore, at a given interval of 15 CA, the peak of AHRR for pilot-injection is the highest. Even if the AHRRs of pilot-injections present a large difference, the AHRR profiles of main injections are less affected by the interval. In-cylinder pressure of compression stroke is changed slightly as the peak AHRR of pilot injection changes, but the pilot mass is smaller and the in-cylinder pressure of expansion stroke is basically unchanged with the increased interval. In **Figure 5B**, as the pilot mass increases, the peak AHRR of pilot injection is increased, in-cylinder temperatures and

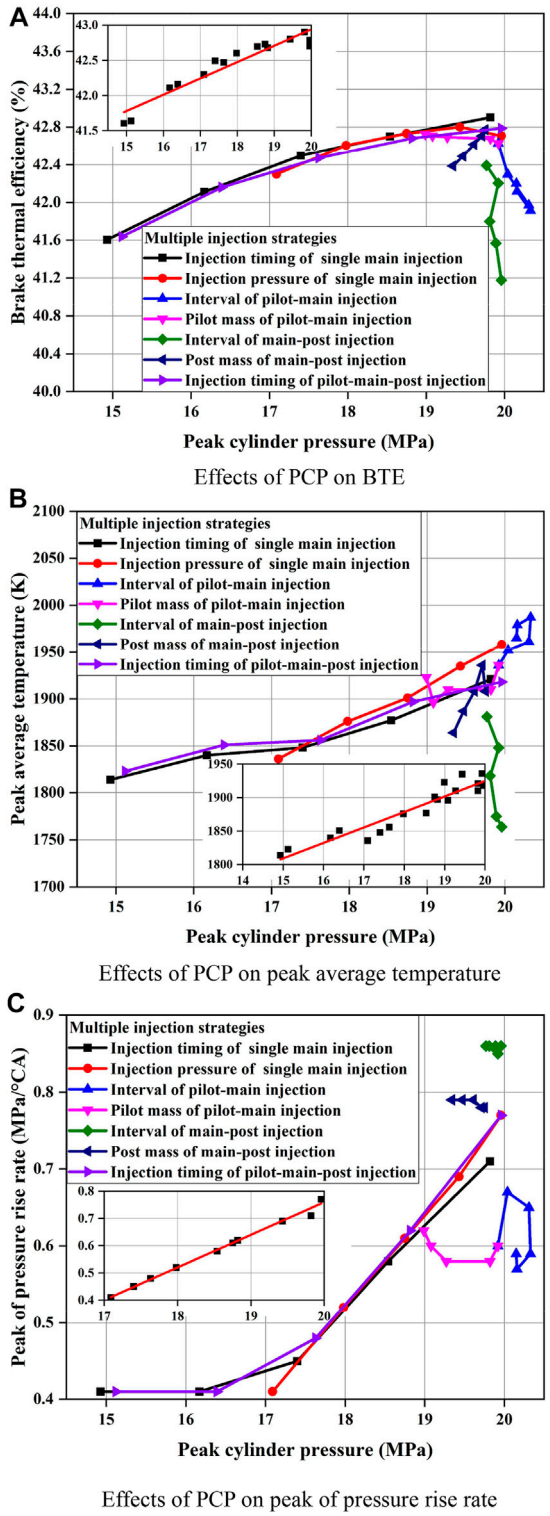

FIGURE 12 | Effects of PCP on performance. **(A)** Effects of PCP on BTE, **(B)** Effects of PCP on peak average temperature, **(C)** Effects of PCP on peak of pressure rise rate.

pressures are higher, the ignition delay of main injection is shorter, and finally results in the decreased peak AHRR of main injection. In-cylinder pressure of compression stroke is increased, which leads to the increase of PCP in expansion stroke. Overall, pilot mass has larger effects on in-cylinder pressure than pilot-main interval.

Figure 6 shows the effects of pilot-main interval and pilot mass on distribution of fuel energy, respectively. In **Figure 6A**, the higher combustion pressure of pilot injection at compression stroke decreases BTE, which also leads to higher combustion temperature of compression stroke, and finally heat transfer loss increases. In general, the smaller pilot-main interval improves BTE. As the pilot mass increases, although the combustion pressure and temperature of expansion stroke increase, the combustion pressure and temperature of compression stroke also increase, which offset each other, and finally results in the basically unchanged distribution of fuel energy.

Figure 7 shows the effects of pilot-main interval and pilot mass on emissions, respectively. The higher peak AHRRs of pilot injection as shown in **Figure 5A** result in slightly more NO_x emissions at 15 and 20 CA intervals. The higher operating load and the smaller pilot mass make the interval have minor effects on HC and soot emissions. The CO emissions increase rapidly as the interval is larger than 15 CA. The AHRRs of main injection are basically unchanged and larger interval decreases the combustion temperature of pilot injection; the generated CO cannot be further oxidized to CO_2, and enters the clearance area, resulting in the increase in CO emissions. As the pilot mass increases, the combustion pressure and temperature increase, which leads to the increase of NO_x emissions. Due to the lower combustion temperature of pilot injection, as the pilot mass increases, the HC and soot emissions of incomplete combustion increase, while the main injection mass decreases, the AHRR of main injection decreases, which are not conducive to HC and soot oxidation, and both emissions increase slightly. Overall, both pilot-main interval and pilot mass have minor effects on emissions; the smaller pilot-main interval and the less pilot mass can improve emissions to some extent.

Effects of Main-Post Injection on Performance Under 20 MPa Peak Combustion Pressure

Figure 8 shows the effects of main-post interval and post mass on combustion characteristics, respectively. As the interval increases, the AHRR profiles of post injections are retarded and the AHRR profiles of main injections and the peaks of AHRR for post injections are basically unchanged. The combustion phasing of post injection retards and is farther to TDC, which results in the basically unchanged AHRR profiles of main injection. Due to the in-cylinder pressure and temperature of main injection being relatively higher, the peaks of AHRRs for post injections are less affected by the main-post interval. As the interval increases, the combustion pressure of post injection is decreased slightly, and the combustion pressure of main injection is basically unchanged. As the post mass increases, the peak AHRR of post injection is increased slightly and the peaks of AHRR for post injections are retarded due to the longer post injection duration. More post mass makes the heat release

TABLE 4 | The highest BTE injection settings at 20 MPa PCP.

Type	Injection pressure (MPa)	Pilot-main interval (CA)	Pilot mass (mg)	Main timing (CA ATDC)	Main-Post interval (CA)	Post mass (mg)
Single main injection	160	-	-	−12	-	-
Pilot-main injection	160	5	2	−12	-	-
Main-post injection	160	-	-	−12	6	10
Pilot-main-post injection	160	5	2	−12	6	10

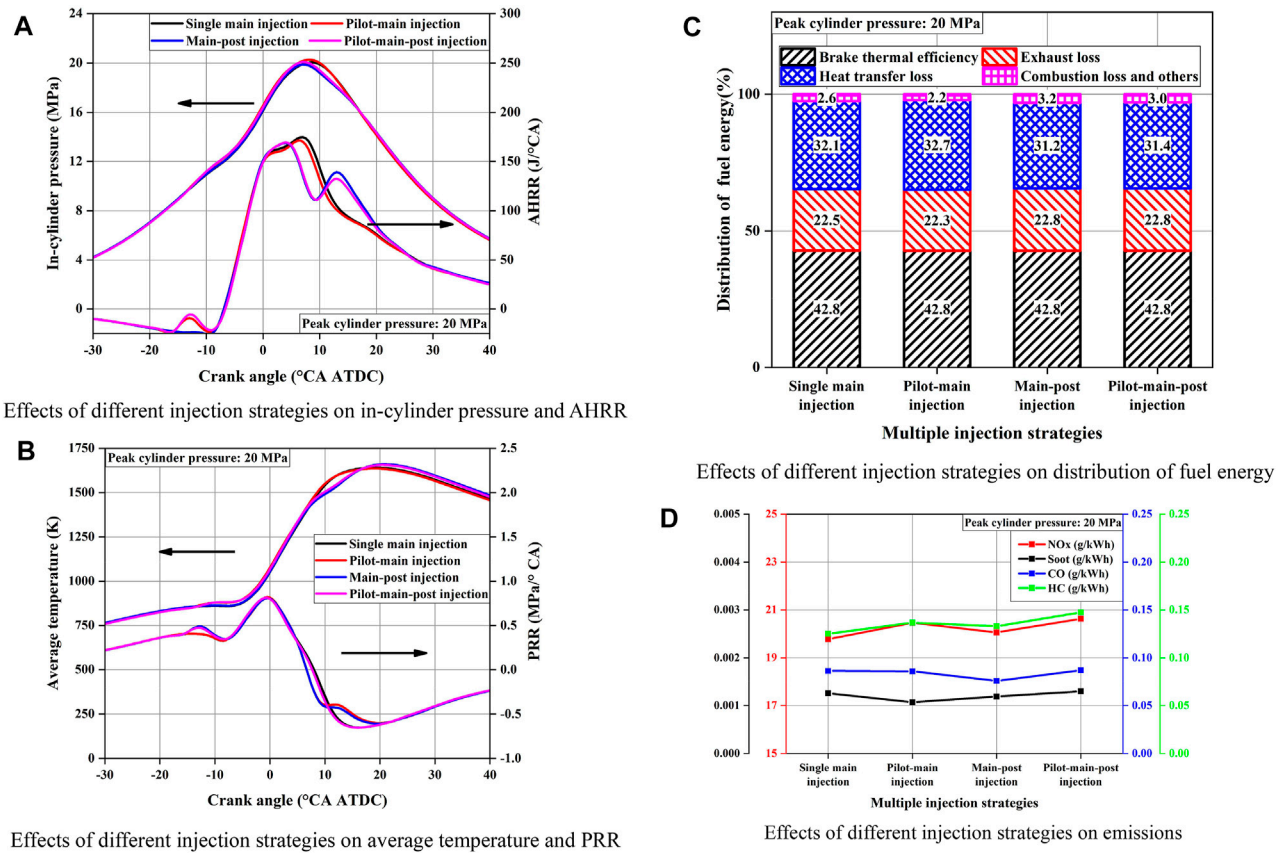

FIGURE 13 | Effects of different injection strategies on performance at 20 MPa PCP. **(A)** Effects of different injection strategies on in-cylinder pressure and AHRR, **(B)** Effects of different injection strategies on average temperature and PRR, **(C)** Effects of different injection strategies on distribution of fuel energy, **(D)** Effects of different injection strategies on emissions.

TABLE 5 | The injection settings at a given NO_x emission of 17.4 g/kWh and approximate 20 MPa PCP.

Type	Injection pressure (MPa)	Pilot-main interval (CA)	Pilot mass (mg)	Main timing (CA ATDC)	Main-Post interval (CA)	Post mass (mg)
Single main injection	160	-	-	−11	-	-
Pilot-main injection	160	5	2	−10	-	-
Main-post injection	160	-	-	−10	6	10
Pilot-main-post injection	160	5	2	−10	6	10

of post injection farther to TDC, results in more exhaust and heat transfer loss, and the heat release of main injection decreases, resulting in lower PCP. In general, post mass has larger effects on PCP than main-post interval.

Figure 9 shows the effects of main-post interval and post mass on distribution of fuel energy, respectively. As the interval increases, combustion phasing of post injection retards and is farther to TDC, and the combustion becomes less isochoric with

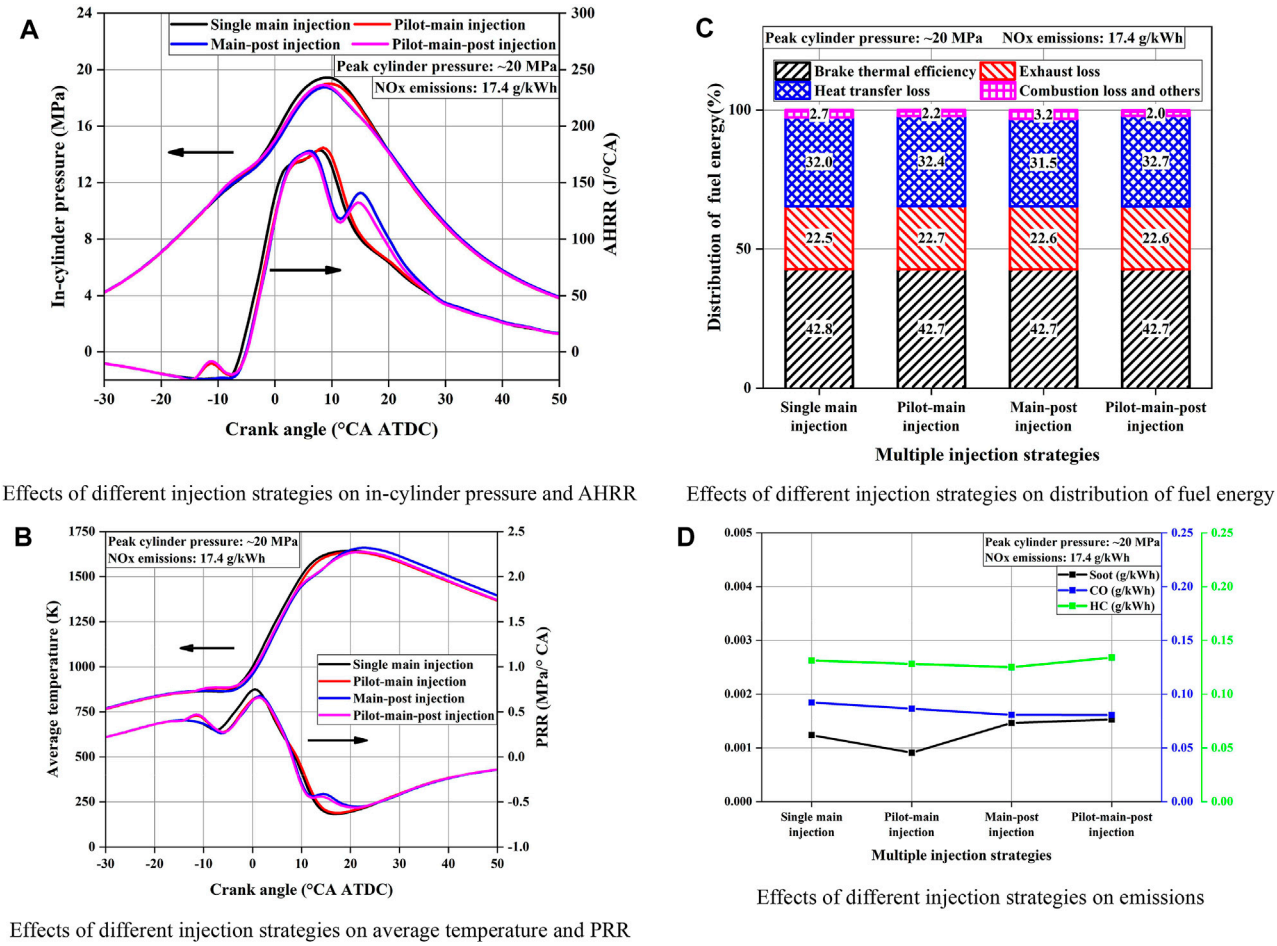

Effects of different injection strategies on in-cylinder pressure and AHRR

Effects of different injection strategies on distribution of fuel energy

Effects of different injection strategies on average temperature and PRR

Effects of different injection strategies on emissions

FIGURE 14 | Effects of different injection strategies on performance at a given NOx emission of 17.4 g/kWh and approximate 20 MPa PCP. **(A)** Effects of different injection strategies on in-cylinder pressure and AHRR, **(B)** Effects of different injection strategies on average temperature and PRR, **(C)** Effects of different injection strategies on distribution of fuel energy, **(D)** Effects of different injection strategies on emissions.

the increase of combustion duration, which leads to the reduction in BTE and the increment of exhaust and heat transfer loss. As the post mass increases, the combustion pressure of main injection is slightly decreased, which results in the decrease of BTE. Meanwhile, the combustion duration is prolonged, which leads to the increased heat transfer loss. Overall, main-post interval has larger effects on distribution of fuel energy than post mass. The smaller main-post interval and the less post mass can improve BTE.

Figure 10 shows the effects of main-post interval and post mass on emissions, respectively. As the interval increases, although the combustion duration is prolonged, the combustion temperature of post injection is decreased, which results in the decrease of NO_x emissions and increase of soot emissions. Both CO and HC emissions are basically unchanged because of the higher in-cylinder pressure and temperature produced by the main injection combustion. The CO and HC emissions are slightly increased at 14 CA interval due to its too low combustion temperature of post injection. As the post mass increases, the combustion duration is also prolonged, but the combustion temperature and pressure of main injection are decreased, which also results in the decrease of NO_x emissions and the increase of soot emissions. Similar to the effects of post interval, both CO and HC emissions are also basically unchanged with the variation of post mass. In general, both main-post interval and post mass have minor effects on emissions of CO and HC emissions, but can reduce NO_x emissions and increase soot emissions.

Effects of Pilot-Main-Post Injection on Performance Under 20 MPa Peak Combustion Pressure

Figure 11 shows the effects of pilot-main-post injection on combustion and emissions. Compared with single main injection, the AHRR profiles of pilot and post injection are added to the AHRR profile of main injection. Similar to single main injection, as injection timing advances, the start of combustion is farther to TDC, and the in-cylinder temperature

and the peak AHRR decrease. But the combustion phasing is nearer to TDC, which leads to the increased combustion pressure. The higher combustion pressure increases BTE, the combustion phasing is nearer to TDC, and exhaust loss decreases gradually; the similar AHRR profiles are determined to be basically unchanged in heat transfer and combustion loss. The combustion phasing is nearer to TDC and in-cylinder combustion pressure is increased, which results in the increased NO_x emissions. More fuel spray impinges on the combustion chamber walls due to earlier injection timings; thus, HC emissions increase slightly. The constant ignition delay and post mass lead to the basically unchanged soot and CO emissions.

Effects of Peak Combustion Pressure on Performance

Figure 12 shows the effects of PCP on performance. The local graphs only include the linear correlation points of different injection strategies. Overall, the increase of PCP is accompanied by the increase of BTE, peak average temperature and PRR. This also means that the improvement on BTE by the increase of PCP imparts greater mechanical and thermal loads on engine components and materials. **Figure 12A** shows that the PCP and BTE are linearly correlated under some injection strategies and the increment of BTE is about 0.3% for every 1 MPa increase in PCP. However, as the interval of pilot-main injection or main-post injection changes, or the post mass of main-post injection changes, they have very large effects on BTE. It can be seen that the PCP of the three injection strategies is about 20 MPa, but the BTE changes greatly. That is to say, at approximately 20 MPa PCP, calibrating the interval of pilot-main injection can make the diesel engine have relatively low PRR as shown in **Figure 12C**. Calibrating the interval and post mass of main-post injection can make the diesel engine have relatively low peak average temperature and thus lower NO_x emissions as shown in **Figure 12B**. Furthermore, the post mass needs to be further reduced to improve BTE. Therefore, the three injection strategies need to be optimized to compromise the above performance and BTE at approximately 20 MPa PCP. Generally, PCP and peak average temperature of the other injection strategies are linearly correlated. The increment of peak average temperature and peak PRR are about 30 K and 0.1 MPa/CA for every 1 MPa increase in PCP.

Effects of Different Injection Strategies on Performance at 20 MPa Peak Combustion Pressure

The highest BTE of different injection strategies is obtained by calibrating the interval and mass in **Table 3**, but the maximum of the main injection timing of each type was the limit value with the PCP constraint of 20 MPa. **Table 4** shows the highest BTE injection settings of different injection strategies at 20 MPa PCP. **Figure 13** shows the effects of injection strategies in **Table 4** on combustion and emissions. Different injection strategies have different characteristics of AHRR profiles. But the in-cylinder pressure profiles are basically the same. The main injection mass of single main injection and pilot-main injection is larger, and the combustion pressure of single main injection and pilot-main injection is slightly higher than that of main-post injection and pilot-main-post injection after PCP. The peak PRR of all four strategies is about 0.8 MPa/CA. The peak combustion temperature of all four strategies is similar. The BTE of all four strategies is 42.8% at 20 MPa PCP. Main-post injection and pilot-main-post injection prolong the combustion duration due to the post injection, which leads to the increased exhaust loss. Single main injection and pilot-main injection increase the higher combustion temperature duration due to larger main injection mass, which results in the increased heat transfer loss. Higher operating load and smaller pilot or post mass make different injection strategies have minor effects on emissions at 20 MPa PCP.

Compared with other emissions, NO_x emissions are increasingly difficult to reduce. Therefore, the effects of different injection strategies on combustion and emissions are studied at the same as NO_x emissions. **Table 5** shows the injection settings at a given NO_x emission of 17.4 g/kWh and approximately 20 MPa PCP. **Figure 14** shows the effects of injection strategies in **Table 5** on combustion and emissions. Single main injection reaches the highest PCP and the combustion phasing is slightly advanced. The combustion pressure of single main injection and pilot-main injection is also slightly higher than that of main-post injection and pilot-main-post injection after PCP. The peak combustion temperature of all four strategies is also similar. The peak PRR of single main injection is slightly higher than the other three strategies. All four injection strategies have minor effects on distribution of fuel energy and emissions. Overall, regardless of keeping the same PCP or same NO_x emissions at approximately 20 MPa combustion pressure, all four injection strategies have minor effects on performance.

CONCLUSION

In this study, an experimental study was conducted to further improve the understanding of injection strategies on engine performance under a relative higher peak combustion pressure at 20 MPa. The operating condition of 1.5 MPa BMEP and 1500 rpm engine speed was selected to represent the frequently used operating and the optimal economic area of the diesel engine. Four strategies of single main injection, pilot-main injection, main-post injection, and pilot-main-post injection were operated. The main conclusions can be summarized as follows.

(1) More advanced injection timing can obtain higher BTE, while the injection pressure has fewer effects on BTE as it is higher than 120 MPa. For double-injection, the smaller interval on pilot-main or main-post and the less pilot or post mass improves BTE and emissions. At approximately 20 MPa PCP, calibrating the interval of pilot-main

injection can make the diesel engine have relatively low PRR. Calibrating the interval and post mass of main-post injection can make the diesel engine have relatively low peak average temperature and thus lower NO_x emissions. Furthermore, the post mass needs to be further reduced to improve BTE. Therefore, the three injection strategies need to be optimized to compromise the above performance and BTE at approximately 20 MPa PCP.

(2) The PCPs are linearly correlated to the BTE, peak average temperature, and peak PRR. The increment of BTE, peak average temperature, and peak PRR are about 0.3%, 30 K, and 0.1 MPa/CA for every 1 MPa increase in PCP, respectively. This also means that the improvement on BTE by the increase of PCP imparts greater thermal and mechanical loads on engine materials and components.

(3) At 20 MPa PCP, based on the optimized injection strategies, the BTE of all four strategies is about 42.8%, and the peak PRR of all four strategies is about 0.8 MPa/CA. At a given NO_x emission of 17.4 g/kWh and approximately 20 MPa PCP, all four injection strategies have minor effects on distribution of fuel energy and emissions. These show that all injection strategies have fewer effects on BTE and emissions at 20 MPa PCP.

The results demonstrated that all injection strategies have less effect on BTE and emissions at 20 MPa PCP, but the pilot-main injection and main-post injection are still effective measures to control combustion noise, mechanical load, heat load, and post-treatment temperature. However, in order to improve BTE, further experimental and numerical investigations are required to deeply examine the impacts of the higher PCP conditions (>30 MPa), higher injection pressure (>300 MPa), and more flexible injection strategy on combustion and emissions.

DATA AVAILABILITY STATEMENT

The original contributions presented in the study are included in the article/Supplementary Material, further inquiries can be directed to the corresponding author.

AUTHOR CONTRIBUTIONS

ZhZ: writing and editing. HL: review. ZY: methodology and validation. YW: investigation. XK: data curation. ZuZ: editing. MY: review and supervision.

FUNDING

This work was supported by the National Natural Science Foundation of China (NSFC) by No. 51976134 and Tianjin Science Fund for Distinguished Young Scholars by No. 20JCJQJC00160.

REFERENCES

Al Ramadan, A. S., Nyrenstedt, G., Ben Houidi, M., and Johansson, B. (2020). Optical Diagnostics of Isooctane and N-Heptane Isobaric Combustion. Technical Paper. 2020-01-1126. Warrendale: SAE. doi:10.4271/2020-01-1126

Babayev, R., Ben Houidi, M., Andersson, A., and Johansson, B. (2019a). Isobaric Combustion: A Potential Path to High Efficiency, in Combination with the Double Compression Expansion Engine (DCEE) Concept. Technical Paper. 2019-01-0085. Warrendale: SAE. doi:10.4271/2019-01-0085

Babayev, R., Houidi, M. B., Shankar, V. B., Aljohani, B., and Johansson, B. (2019b). Injection Strategies for Isobaric Combustion. Technical Paper. 2019-01-2267. Warrendale: SAE. doi:10.4271/2019-01-2267

Goyal, H., Dyuisenakhmetov, A., Houidi, M. B., Johansson, B., Badra, J., Cenker, E., et al. (2020). The Effect of Engine Speed, Exhaust Gas Recirculation, and Compression Ratio on Isobaric Combustion. *SAE Int. J. Engines* 13, 603–615. doi:10.4271/03-13-05-0038

Heywood, J. B. (2018). *Internal Combustion Engine Fundamentals*. second edition. New York: McGraw-Hill Education.

Horibe, N., Bao, Z., Taguchi, T., Egoshi, K., Kawanabe, H., and Ishiyama, T. (2018). Improvement of Thermal Efficiency in a Diesel Engine with High-Pressure Split Main Injection. Technical Paper. 2018-01-1791. Warrendale: SAE. doi:10.4271/2018-01-1791

Horibe, N., Tamura, I., Hamada, T., Liu, L., and Ishiyama, T. (2012). Smoke-Reduction Effect of after Injection in Combination with Pilot Injection. *Trans. Soc. Automotive Eng. Jpn.* 43, 1039–1044. doi:10.11351/jsaeronbun.43.1039

Horvath, A., Seitz, H. F., Gelter, J., and Raser, B. (2020). The Future Heavy-Duty Engine - Basic Engine Concept for Maximum CO2 Reduction. *MTZ Worldw* 81, 68–72. doi:10.1007/s38313-020-0276-9

Jin, C., Ampah, J. D., Afrane, S., Yin, Z., Liu, X., Sun, T., et al. (2021). Low-Carbon Alcohol Fuels for Decarbonizing the Road Transportation Industry: A Bibliometric Analysis 2000-2021. *Environ. Sci. Pollut. Res.* 29, 5577–5604. doi:10.1007/s11356-021-15539-1

Joshi, A. (2019). Review of Vehicle Engine Efficiency and Emissions. Technical Paper. 2019-01-0314. Warrendale: SAE. doi:10.4271/2019-01-0314

Joshi, A. (2021). Review of Vehicle Engine Efficiency and Emissions. Technical Paper. 2021-01-0575. Warrendale: SAE. doi:10.4271/2021-01-0575

Kocher, L. (2017). *Cummins 55% Brake Thermal Efficiency Project, Project ACS098*. Washington, DC: presentation at the US Department of Energy Annual Merit Review.

Koeberlein, D. (2014). *Technology and System Level Demonstration of Highly Efficient and Clean, Diesel Powered Class 8 Trucks*. Washington, DC: Cummins SuperTruck program.

Lee, J., Lee, J., Chu, S., Choi, H., and Min, K. (2015). Emission Reduction Potential in a Light-Duty Diesel Engine Fueled by JP-8. *Energy* 89, 92–99. doi:10.1016/j.energy.2015.07.060

Li, X., Guan, C., Luo, Y., and Huang, Z. (2015). Effect of Multiple-Injection Strategies on Diesel Engine Exhaust Particle Size and Nanostructure. *J. Aerosol Sci.* 89, 69–76. doi:10.1016/j.jaerosci.2015.07.008

Liu, H., Li, S., Zheng, Z., Xu, J., and Yao, M. (2013). Effects of N-Butanol, 2-butanol, and Methyl Octynoate Addition to Diesel Fuel on Combustion and Emissions over a Wide Range of Exhaust Gas Recirculation (EGR) Rates. *Appl. Energ.* 112, 246–256. doi:10.1016/j.apenergy.2013.06.023

Martin, J., Sun, C., Boehman, A., and O'Connor, J. (2016). Experimental Study of Post Injection Scheduling for Soot Reduction in a Light-Duty Turbodiesel Engine. Technical Paper. 2016-01-0726. Warrendale: SAE. doi:10.4271/2016-01-0726

Megel, M., Westmoreland, B., Jones, G., Phillips, F., Eberle, D., Tussing, M., et al. (2011). Development of a Structurally Optimized Heavy Duty Diesel Cylinder Head Design Capable of 250 Bar Peak Cylinder Pressure Operation. *SAE Int. J. Engines* 4, 2736–2755. doi:10.4271/2011-01-2232

Mohan, B., Yang, W., and Chou, S. K. (2013). Fuel Injection Strategies for Performance Improvement and Emissions Reduction in Compression

Ignition Engines-A Review. *Renew. Sustainable Energ. Rev.* 28, 664–676. doi:10.1016/j.rser.2013.08.051

Nyrenstedt, G., Al Ramadan, A., Tang, Q., Badra, J., Cenker, E., Ben Houidi, M., et al. (2020). Isobaric Combustion for High Efficiency in an Optical Diesel Engine. Technical Paper. 2020-01-0301. Warrendale: SAE. doi:10.4271/2020-01-0301

O'Connor, J., Borz, M., Ruth, D., Han, J., Paul, C., Imren, A., et al. (2017). Optimization of an Advanced Combustion Strategy towards 55% BTE for the Volvo SuperTruck Program. Technical Paper. 2017-01-0723. Warrendale: SAE. doi:10.4271/2017-01-0723

Osada, H., Aoyagi, Y., and Shimada, K. (2012). Diesel Combustion Improvement Using High Boost, Wide Range and High Rate EGR in a Single Cylinder Engine (Third Report). *Trans. Soc. Automotive Eng. Jpn.* 43, 855–861. doi:10.11351/jsaeronbun.43.855

Park, S., Kim, H. J., Shin, D. H., and Lee, J.-T. (2018). Effects of Various Split Injection Strategies on Combustion and Emissions Characteristics in a Single-cylinder Diesel Engine. *Appl. Therm. Eng.* 140, 422–431. doi:10.1016/j.applthermaleng.2018.05.025

Pierce, D., Haynes, A., Hughes, J., Graves, R., Maziasz, P., Muralidharan, G., et al. (2019). High Temperature Materials for Heavy Duty Diesel Engines: Historical and Future Trends. *Prog. Mater. Sci.* 103, 109–179. doi:10.1016/j.pmatsci.2018.10.004

Roh, H. G., Lee, D., and Lee, C. S. (2015). Impact of DME-Biodiesel, Diesel-Biodiesel and Diesel Fuels on the Combustion and Emission Reduction Characteristics of a CI Engine According to Pilot and Single Injection Strategies. *J. Energ. Inst.* 88, 376–385. doi:10.1016/j.joei.2014.11.005

Stanton, D. W. (2013). Systematic Development of Highly Efficient and Clean Engines to Meet Future Commercial Vehicle Greenhouse Gas Regulations. *SAE Int. J. Engines* 6, 1395–1480. doi:10.4271/2013-01-2421

Suh, H. K. (2011). Investigations of Multiple Injection Strategies for the Improvement of Combustion and Exhaust Emissions Characteristics in a Low Compression Ratio (CR) Engine. *Appl. Energ.* 88, 5013–5019. doi:10.1016/j.apenergy.2011.06.048

Tang, Q., Sampath, R., Sharma, P., Nyrenstedt, G., Al Ramadan, A., Ben Houidi, M., et al. (2020). Optical Study on the Fuel Spray Characteristics of the Four-Consecutive-Injections Strategy Used in High-Pressure Isobaric Combustion. Technical Paper. 2020-01-1129. Warrendale: SAE. doi:10.4271/2020-01-1129

Taymaz, I. (2006). An Experimental Study of Energy Balance in Low Heat Rejection Diesel Engine. *Energy* 31 (2-3), 364–371. doi:10.1016/j.energy.2005.02.004

U.S. Department of Energy (2013). *WORKSHOP REPORT:Trucks and Heavy-Duty Vehicles Technical Requirements and Gaps for Lightweight and Propulsion Materials*. Washington, DC: U.S. Department of Energy.

Zheng, Z., Li, C., Liu, H., Zhang, Y., Zhong, X., and Yao, M. (2015a). Experimental Study on Diesel Conventional and Low Temperature Combustion by Fueling Four Isomers of Butanol. *Fuel* 141, 109–119. doi:10.1016/j.fuel.2014.10.053

Zheng, Z., Yue, L., Liu, H., Zhu, Y., Zhong, X., and Yao, M. (2015b). Effect of Two-Stage Injection on Combustion and Emissions under High EGR Rate on a Diesel Engine by Fueling Blends of Diesel/gasoline, Diesel/n-Butanol, Diesel/gasoline/n-Butanol and Pure Diesel. *Energ. Convers. Management* 90, 1–11. doi:10.1016/j.enconman.2014.11.011

Zukouski, R., Cigler, J., and Han, G. (2015). *SuperTruck Advanced Combustion Development at Navistar. Presentation at the 2015 DOE Annual Merit Review*. Washington, DC.

Conflict of Interest: The authors declare that the research was conducted in the absence of any commercial or financial relationships that could be construed as a potential conflict of interest.

Publisher's Note: All claims expressed in this article are solely those of the authors and do not necessarily represent those of their affiliated organizations, or those of the publisher, the editors and the reviewers. Any product that may be evaluated in this article, or claim that may be made by its manufacturer, is not guaranteed or endorsed by the publisher.

frontiers | Frontiers in Energy Research

ORIGINAL RESEARCH
published: 19 April 2022
doi: 10.3389/fenrg.2022.884540

Study on Self-Excited Oscillation Suppression of Supersonic Inlet Based on Parallel Cavity

FeiChao Cai[1]* *and Xing Huang*[2]

[1]School of Power and Energy, Northwestern Polytechnical University, Xi'an, China, [2]AECC HUNAN Aviation Powerplant Research Institute, Zhuzhou, China

Aiming at the problem of self-excited oscillation in a supersonic inlet, the oscillation suppression of parallel cavities in a shock system is studied. Based on the shock dynamic model, the theoretical calculation model of parallel cavity under dynamic shock is established, and the effects of cavity volume and oscillation frequency on shock oscillation flow field parameters are analyzed. On this basis, an integrated numerical model including cavity and inlet and outflow fields is established, and the effects of cavity on the inlet flow field parameter distribution and parameter oscillation are compared by using unsteady numerical calculation algorithm. The theoretical calculation results show that the parallel cavity can reduce the amplitude of flow field pressure oscillation, and increasing the cavity volume is beneficial to suppress parameter oscillation. The unsteady numerical calculation of three groups of working conditions shows that the cavity changes the amplitude of parameter oscillation, and the high amplitude frequency point also decreases compared to the model without cavity. Through the alternating change of pressure between the channel and cavity during the movement of the shock wave, the cavity gas filling and overflow dampen the shock wave forward and pressure change of the mainstream, so as to suppress the self-excited oscillation.

Keywords: parallel cavity, supersonic inlet, self-excited oscillation, suppression, unsteady flow

OPEN ACCESS

Edited by:
Lei Luo,
Harbin Institute of Technology, China

Reviewed by:
Dan Zhao,
University of Canterbury, New Zealand
Raffaello Mariani,
Royal Institute of Technology, Sweden

***Correspondence:**
FeiChao Cai
caifeichao@nwpu.edu.cn

Specialty section:
This article was submitted to Advanced Clean Fuel Technologies, a section of the journal Frontiers in Energy Research

Received: *26 February 2022*
Accepted: *21 March 2022*
Published: *19 April 2022*

Citation:
Cai F and Huang X (2022) Study on Self-Excited Oscillation Suppression of Supersonic Inlet Based on Parallel Cavity. Front. Energy Res. 10:884540. doi: 10.3389/fenrg.2022.884540

INTRODUCTION

The flow field of a supersonic inlet is very complex. For a supersonic inlet or hypersonic inlet, an isolation section with equal cross section is usually set after the compression section to stabilize the shock system (Curran et al., 1996). At higher flight speeds, the Mach number of the flow in front of the positive shock in the inlet increases, the interference between the shock and the boundary layer intensifies, and the local separation induced by the shock makes the positive shock evolve into an oblique shock train (Rybalko et al., 2012; Tan et al., 2012). As the back pressure of the inlet increases, the shock train moves forward to the isolation section gradually, and the shock wave changes from symmetrical to asymmetrical and continues its entire movement (Tian et al., 2014). The research shows that even if the back pressure of the inlet remains constant, the shock position will move forward and backward, presenting a state of "self-excitation oscillation" (Meier et al., 1990), which may change the parameters of flow field pressure and flow rate and may cause the structure flutter of the inlet or the pressure oscillation of the inlet/combustion chamber, which will affect the combustion stability (Matsuo et al., 1999; Huang et al., 2018). Therefore, the study of shock wave unsteady oscillation is of great significance for engine design.

A lot of theoretical modeling and research work has been carried out for the shock oscillation phenomenon in a supersonic inlet. Ikui et al. (1974) believed that shock oscillations were caused by the propagation of turbulence pulsation from the upstream of shock waves to the downstream, and the oscillation frequency was related to the Helmholtz resonance frequency and pipeline resonance frequency in the experimental state. Hankey and Shang (1980) deduced the formula of pipe resonance frequency, which can estimate the acoustic resonance frequency under different test conditions. Piponniau et al. (2009) proposed a shock wave separation oscillation frequency model with high reliability through theoretical analysis based on the principle of flow conservation inside and outside the boundary layer separation envelope. Li et al. (2017) established a model of front movement of shock train in a complex background wave system by a theoretical method, predicted the forward propagation process of shock train, and achieved good results. Xu et al. (2019) improved the minimum contraction ratio analysis method of the equivalent throat through the supersonic free interaction theory and predicted the conversion law between the shock train jump and slow movement with reference to the Kantrowitz limit. In addition, based on the test and simulation methods, the pressure fluctuation and energy conversion process of the shock train (Sugiyama et al., 2008; Wang and Zhang, 2010; Li et al., 2012), variation characteristics of flow field parameters of self-excited and forced oscillations (Xiong et al., 2017a; Xiong et al., 2017b; Zhang and Yan, 2021), and the shock wave forward propagation rule (Xu et al., 2015; Lu et al., 2019) have been extensively studied. In addition, there are also relevant studies on the coupling between flow and combustion oscillations (Chen and Zhao, 2018; Zhao et al., 2018). These works provide a reference for understanding the dynamic behavior of shock waves by studying the behavior of shock wave oscillations in a complex flow field.

At present, the research on shock wave oscillation of a supersonic inlet mainly focuses on mechanism analysis, prediction model establishment, flow process research, and so on. On the suppression of shock oscillation in inlets, Herrmann et al. (2013) and Huang et al. (2020) have studied the inlet with a boundary layer suction device, which shows that the suction device has an influence on the process of shock oscillations and the changes of pressure parameters and will restrict the shock position in a certain state. Li (2019) studied the control algorithm under an unstable shock train from the aspect of an engine design by studying the characteristics of shock oscillations. In addition, in order to solve the problem of the local shock wave oscillation in a compressor, Ma (2019) used local boundary layer suction to control the oscillation amplitude and achieved good results in a certain range. Most of these research works control the local flow through the boundary layer overflow, so as to weaken the shock oscillation process. In general, research work on shock wave vibration suppression methods in the supersonic state is relatively less.

In this article, the shock wave oscillation suppression of a supersonic inlet is studied by parallel passive cavities in the isolation section. A theoretical model is established to analyze the feasibility of parallel cavity to suppress the oscillation of main flow parameters. The coupled self-excited oscillation process between the inlet and cavity is calculated based on the numerical method. Then, the effects of parallel passive cavities on the suppression of parameter fluctuations and the convection field in the process of inlet self-excited oscillation are analyzed.

CALCULATION MODEL

Inlet Geometry

Based on the inlet in Reinartz et al. (2003), the cavities are closed in parallel in the isolation section and are connected to the main flow channel through slots. The calculation model is shown in **Figure 1**. The inlet includes a supersonic compression section, an isometric straight throat section, and an expansion section. The parameter inlet height H_1 = 29 mm, compression angle δ_1 = 20.5 degrees, lower lip distance from the leading edge point L_1 = 35 mm, length of the isolation section L_2 = 79.4 mm, height H_2 = 15 mm, and the other main parameters are the same as in Reinartz et al. (2003).

This article studies the influence and suppression of cavity on vibration. Considering the realizability of the structure, the cavity is located in the region composed of the upper wall of the inner channel and the outer wall of the inlet. Due to the nonuniformity of pressure distribution in the isolation section and the shock surface moving back and forth in the isometric section during oscillation, the cavity is divided into five equal volume parts and connected to the isolation section through a gap with a width of 0.75 mm. Cavity height H_4 is used as a variable parameter to change the volume of the cavity. L_4 is the width of the cavity, and its value is 6.61 mm.

Numerical Method and Verification

According to the basic model of the inlet shown in **Figure 1** (Reinartz et al., 2003), the numerical model is established. The boundary conditions of the model include the pressure far-field conditions at the inlet of the external flow field, the pressure outlet conditions at the outlet of the inlet, and the adiabatic wall conditions at the inner and outer walls of the inlet. The finite volume method is used to solve the inlet flow field. The diffusion and convection terms in the control equation are discretized by the second-order central difference scheme and second-order upwind scheme, respectively. The coupled implicit method is used to solve the control equation. Since the SST $k-\omega$ model can simulate separated flow with a strong adverse pressure gradient, it is widely used in simulation calculation (Ma et al., 2017; Zhang and Yan, 2021). Therefore, the SST $k-\omega$ model is adopted in this article.

A grid scale has an important influence on shock wave resolution. In order to compare the influence of the different grid precision on the flow field calculation, three different grid number models are established, and 150,000 (Coarse), 300,000 (Middle), and 600,000 (Fine) grids are generated by local encryption and other measures.

The numerical calculation was carried out for the working condition of Ma2.41. The total inlet temperature is 305 K, the total pressure is 540 kPa, and the angle of attack of the inlet is

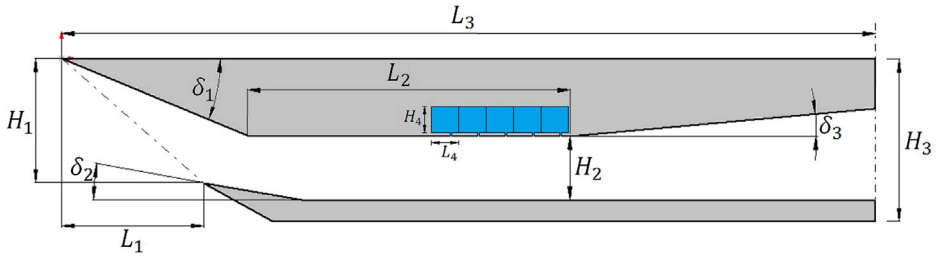

FIGURE 1 | Schematic of the calculation model.

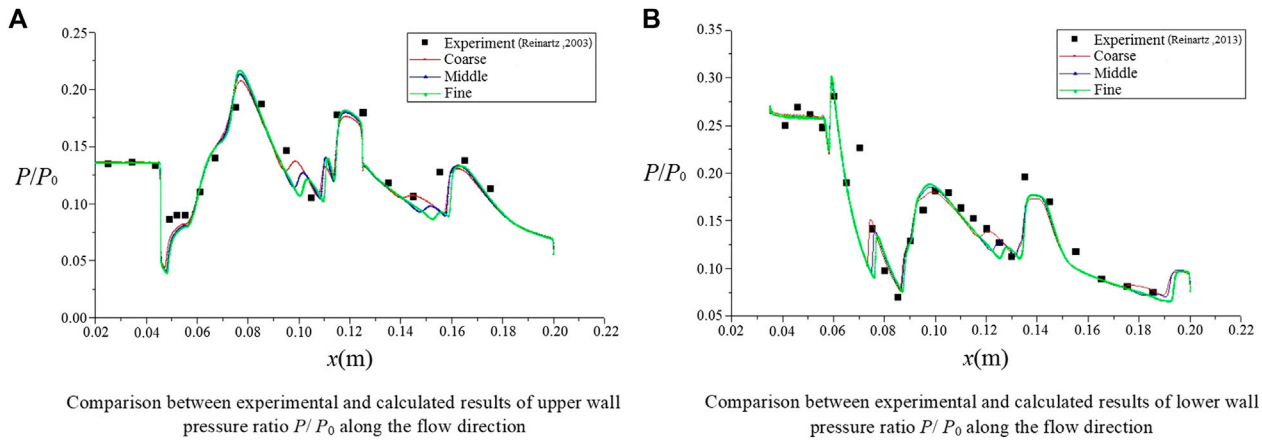

FIGURE 2 | Comparison of wall pressure distribution.

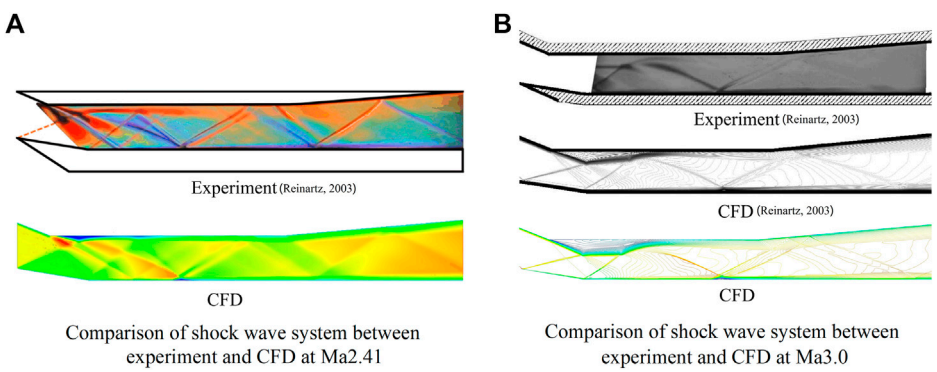

FIGURE 3 | Comparison of the inlet flow field.

-10^0. The calculation conditions are in accordance with the test conditions in Reinartz et al. (2003). During the calculation, the integral value of the wall pressure of the inner channel is monitored and the flow change at the outlet ensured such that the relative amount of parameter change is within 0.2%, within 1,000 iteration steps, so as to ensure the convergence of the calculation process.

From the comparison of the pressure distribution in **Figure 2**, the variation trends of the upper and lower wall pressures of the three grid models with different precisions are basically the same. There is a slight difference in the local pressure jump caused by the shock wave, that is, the position resolution of the shock wave is different. The Middle model and Fine model are relatively close in the local position of the pressure jump. Compared with the test

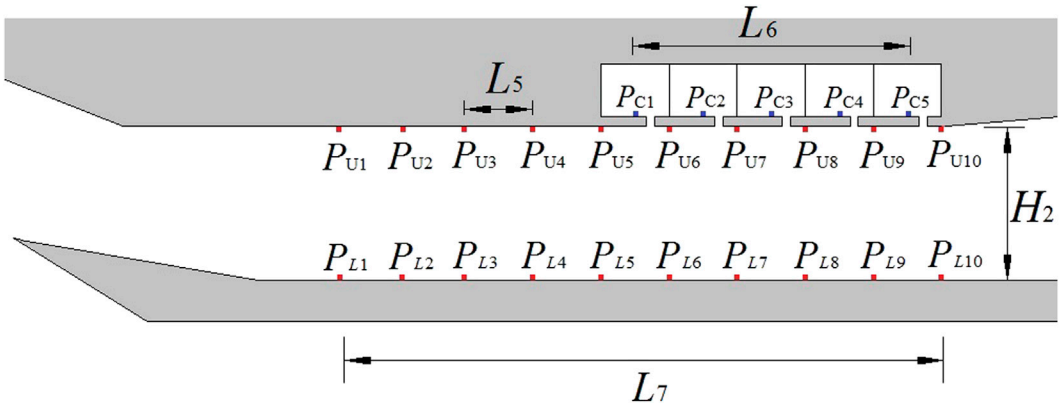

FIGURE 4 | Location of sampling points.

results, the calculation results are in good agreement with the pressure change process of the test points. For the three groups of models, the pressure on the inner wall is integrated respectively. The errors of the Coarse model and Middle model relative to the Fine model are 2.87 and 0.79%, respectively. In general, the different simulation models have good accuracy.

The shock train at two Mach numbers calculated by the Middle model is compared with the experimental schlieren (Reinartz et al., 2003) in **Figure 3**. It can be seen from **Figure 3A** that when Ma_∞ = 2.41, the shock wave reflected by the lower lip intersects with the upper wall surface after the turning point of the compression surface, resulting in a local expansion wave and the local separation of the boundary layer due to the incidence of the oblique shock wave. The interaction and reflection of the shock and expansion waves in the isolation section and the expansion section, and the changes and flow characteristics of these complex wave systems are close to the experimental schlieren. From the comparison of the results of Ma_∞ = 3.0, the separation zone with a large range of the upper wall turning zone reflected in the simulation results in this article is consistent with the simulation and test results in Reinartz et al. (2003), and the expansion flow and reflected wave system after the separation zone are also the same as those of the referenced study.

The comparison with the experimental results shows that the numerical modeling method is feasible. The results of the Middle model in this article are close to those of the Fine model, but the number of grids is reduced by half. Considering the trade-off between computational efficiency and accuracy, the Middle model with 300,000 medium number of grids is used for calculation and analysis.

Sampling Location and Calculation Strategy

In the unsteady calculation, sampling points are set to monitor the pressure change process, including the upper and lower walls of the isolation section and the cavity area. As shown in **Figure 4**, there are a total of 20 sampling points in the isolation section. The sampling points P_{U1}–P_{U10} on the upper wall are evenly distributed at an interval of L_5 = 6.61 mm from the end point of the equal–straight isolation section to the front. The sampling points, numbered P_{C1}–Pc_5, are located near the midpoint of the lower wall of the cavity. The length of the cavity sampling area L_6 = 26.44 mm, and the length of the isolation section sampling area L_7 = 59.49 mm.

For the model with cavity, during the numerical calculation, the gap between the cavity and the mainstream is closed first, and the initial flow field is calculated by the steady method, then by the unsteady method. After 2–3 shock oscillation cycles, the cavity pressure is initialized with the mainstream pressure at the gap between the cavity and mainstream, the flow velocity in the cavity is set to zero, and the calculation is further iterated until the calculation process is stable.

THEORETICAL MODELING AND ANALYSIS

Shock Dynamics Model

Using the theoretical method, a shock dynamic model is established for the channel with equal cross section. For the two configurations, the change law of the flow field parameters when the outlet backpressure oscillates is analyzed to compare the influence of the cavity on the parameter oscillation.

1) Constant Cross-Section Channel Shock Dynamics Model

The theoretical model adopts the constant cross-section channel (Model Basic), the positive shock is located at position 1 in the channel, and the inlet and outlet of the channel are numbered 0 and 2, respectively. Taking the shock surface as the boundary, the pipeline is divided into upstream area U and downstream area D, as shown in **Figure 5** (Model Basic). In Model B with cavity, cavity C is located on the upper side of the downstream area D and connected through the main flow of the gap, as shown in **Figure 5** (Model Cavity).

According to the pressures P_{1U} and P_{1D} before and after the shock surface 1 and the flow velocity Ma_{1U} before the shock, the

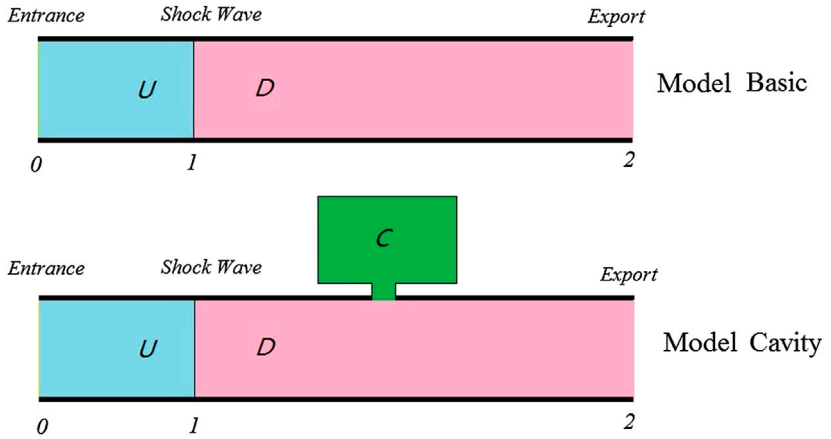

FIGURE 5 | Theoretical calculation model of shock wave motion.

motion velocity $\dot{x}_1$ of the shock surface is calculated as follows (Pan and Shan, 2011):

$$\dot{x}_1 = a_{1U}\left(Ma_{1U} - \sqrt{\frac{P_{1D}}{P_{1U}}\frac{k+1}{2k} + \frac{k-1}{2k}}\right). \tag{1}$$

Set: $Ma_M = Ma_{1U} - \dot{x}_1/a_0$, where a_0 is the sound velocity in front of the shock wave.

The relationship between the flow downstream of the moving shock wave Ma_{1u} and the forward moving speed of the shock wave Ma_{1u}, the parameter Ma_M, and the moving speed $\dot{x}_1$ is:

$$\dot{m}_{1D} = \dot{m}_{1U}\left(1 + \frac{1}{a_{1U}Ma_{1U}}\frac{2\left(Ma_M^2 - 1\right)}{2 + (k-1)Ma_M^2}\dot{x}_1\right). \tag{2}$$

The volume change rate of downstream control volume V_D after the shock wave is:

$$\dot{V}_D = -A\dot{x}_1. \tag{3}$$

For the downstream control body D, the relationship between the inlet and outlet flow and the volume V_D, density ρ_D, and its rate of change is:

$$\dot{m}_{1D} - \dot{m}_2 = V_D\dot{\rho}_D + \rho_D\dot{V}_D. \tag{4}$$

In addition, according to the ideal gas equation, the density change rate is:

$$\dot{\rho}_D = \frac{M}{RT_D}\dot{P}_D. \tag{5}$$

Combining **Formulas 4** and **5**, the flow formula becomes:

$$\dot{m}_{1D} - \dot{m}_2 = V_D\frac{M}{RT_D}\dot{P}_D + \frac{MP_D}{RT_D}\dot{V}_D. \tag{6}$$

According to the above formula, the change rate of downstream control body D pressure is calculated as:

$$\dot{P}_D = \left((\dot{m}_{1D} - \dot{m}_2) - \frac{MP_D}{RT_D}\dot{V}_D\right)\frac{RT_D}{V_DM}. \tag{7}$$

For the upstream controlled body U, the upstream pressure change rate is:

$$\dot{P}_U = \left((\dot{m}_0 - \dot{m}_{1U}) - \frac{MP_U}{RT_U}\dot{V}_U\right)\frac{RT_U}{V_UM}. \tag{8}$$

According to the volume change rate $\dot{V}_U$ of the upstream control body, the shock wave motion speed $\dot{x}_1$, and the parameters of the inlet 0 section, the inlet and outlet flow rates $\dot{m}_0$ and $\dot{m}_{1U}$ of the control body are calculated, and the upstream pressure change rate $\dot{P}_U$ is calculated according to **Formula 8**.

In addition, it also includes the relationship between aerodynamic parameters and their differential values:

$$P_D = \int \dot{P}_D dt\, V_D = \int \dot{V}_D dt\, \rho_D = \int \dot{\rho}_D dt. \tag{9}$$

For the equations composed of the above formulas, the change process of the upstream and downstream parameters and the change of the shock surface position x can be calculated by a simultaneous solution.

2) Computational model with cavity

In the Model Cavity with a cavity, when the pressure in the downstream D area changes, due to the pressure imbalance in the cavity C and D areas, there will be a flow into or out of cavity C under the action of the pressure difference, and the flow in C cavity is close to the stagnation, i.e., $T_C \approx T_0^*$. The cavity volume V_C is a constant value, and the relationship between the flow entering the C cavity $\dot{m}_C$ and the pressure differential $\dot{P}_C$ is:

$$\dot{m}_C = V_C\dot{\rho}_C = V_C\frac{M}{RT_0^*}\dot{P}_C. \tag{10}$$

According to the flow balance relationship, **Formula 4** is transformed into:

$$\dot{m}_{1D} - V_C \frac{M}{RT_0^*}\dot{P}_C - \dot{m}_2 = V_D\dot{\rho}_D + \rho_D\dot{V}_D. \tag{11}$$

Further deformation obtains the pressure change rate $\dot{P}_D$ downstream of the shock wave as:

$$\dot{P}_D = \left((\dot{m}_{1D} - \dot{m}_2) - \frac{MP_D}{RT_D}\dot{V}_D\right)\Big/\left(\frac{MV_D}{RT_D} + \frac{MV_C}{RT_0^*}\right). \tag{12}$$

Since the airflow velocity in the cavity is close to stagnation, the total pressure is taken as pressure P_D in the mainstream area, and the static pressure is the cavity pressure P_C. According to the relationship between the total pressure p^*, static pressure p, and Mach number, the flow Mach number in the gap Ma_{Fx} can be calculated as:

$$Ma_{Fx} = \sqrt{\left(\left(\frac{P}{P^*}\right)^{-\frac{k-1}{k}} - 1\right)\Big/0.2}. \tag{13}$$

When $P_C > P_D$, **Formula 13** is transformed into:

$$Ma_{Fx} = \sqrt{\left(\left(\frac{P_D}{P_C}\right)^{-\frac{k-1}{k}} - 1\right)\Big/0.2}. \tag{14}$$

When $P_C < P_D$, **Formula 13** is transformed into:

$$Ma_{Fx} = \sqrt{\left(\left(\frac{P_C}{P_D}\right)^{-\frac{k-1}{k}} - 1\right)\Big/0.2}. \tag{15}$$

The velocity coefficient λ_{Fx} and flow function $q(\lambda_{Fx})$ are calculated according to the gap flow Ma_{Fx} as:

$$\lambda_{Fx} = \sqrt{1.2Ma^2/(1 + 0.2Ma^2)},$$
$$q(\lambda_{Fx}) = 1.2^{2.5}\lambda_{Fx}\left(1 - \frac{0.4}{2.4}\lambda_{Fx}^2\right)^{2.5}. \tag{16}$$

The flow through the gap is:

$$\dot{m}_C = 0.0404\frac{P_C}{\sqrt{T_0^*}}q(\lambda_{Fx})A_{Fx}$$

or:

$$\dot{m}_C = 0.0404\frac{P_D}{\sqrt{T_0^*}}q(\lambda_{Fx})A_{Fx}. \tag{17}$$

According to $\dot{m}_C$, the cavity pressure change rate $\dot{P}_C$ is calculated as:

$$\dot{P}_C = \dot{m}_C KRT_0^*/V_C. \tag{18}$$

By combining the above parameters, the variation of the downstream parameters of the shock wave with a cavity can be solved.

TABLE 1 | Comparison of calculation parameters of different models.

Parameters	Shock theory			Dynamic model		
Ma_U	1.50	2.50	3.50	1.50	2.50	3.50
P_U (Pa)	54,885	26,436	15,249	54,945	26,465	15,266
P_D (Pa)	134,936	188,357	215,396	135,073	188,564	215,633
Ma_D	0.7011	0.513	0.4512	0.7011	0.513	0.4512

Case Analysis

1) Static parameter calculation

Using the established shock wave dynamic model, the theoretical parameters at different inlet velocities are calculated. The total inlet temperature is 502.088 k and the inlet flow is 3.092 kg/s. The steady-state parameters before and after the shock wave are calculated according to the above inlet conditions, which are compared with the shock wave theory in **Table 1**. It can be seen that the parameters calculated by the shock dynamic model in the *Shock Dynamics Model* section are consistent with the results calculated by the shock theory.

For the velocity of Ma25, the initial values of pressure P_U before shock, pressure P_D after shock and cavity pressure P_C are set to be −10%, −10% and 10% different from the theoretical steady-state value respectively. The steady-state parameters are calculated based on the dynamic model, and the time step is 0.5×10^{-6} s. **Figure 6** shows the dynamic change process of the pressure before and after the shock wave. The pressure P_U before the shock wave has a certain overshoot in the rising process and can quickly stabilize to the steady-state value. The initial values of pressures P_D and P_C after the shock wave are quite different and gradually tend to be consistent with time and remain at the theoretical steady-state value, and the adjustment time from the initial value to parameter stability is about 0.01 s. The calculation results show that the dynamic model can converge to the theoretical steady-state value under large initial value deviation.

The comparison between the two theoretical methods shows the feasibility of the dynamic calculation model.

2) Theoretical analysis of cavity effect on oscillation

Based on the shock wave dynamics model, the influence of the cavity on the parametric oscillation during shock **oscillation** is analyzed. Since there is no self-excited oscillation in the theoretical model, in order to simulate the oscillation process of the shock wave, a certain frequency and amplitude of back pressure P_2 is applied at the outlet:

$$P_2(t) = P_0 + KP_0\sin(\omega t). \tag{19}$$

The dynamic response of flow field parameters is calculated for different cavity volume ratios V_C/V_D. In the calculation example, the analysis is carried out for the working condition of $Ma_0 = 2.5$, taking the amplitude $K = 0.1$, the frequency $\omega = 100$, and P_0 = 26,465 Pa. The calculation results are compared in **Figure 7**.

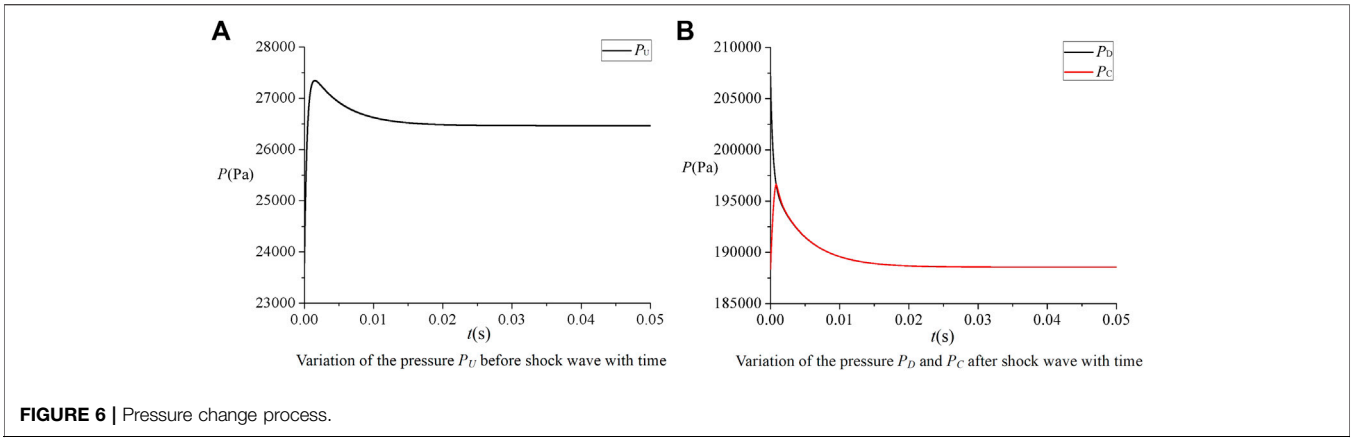

FIGURE 6 | Pressure change process.

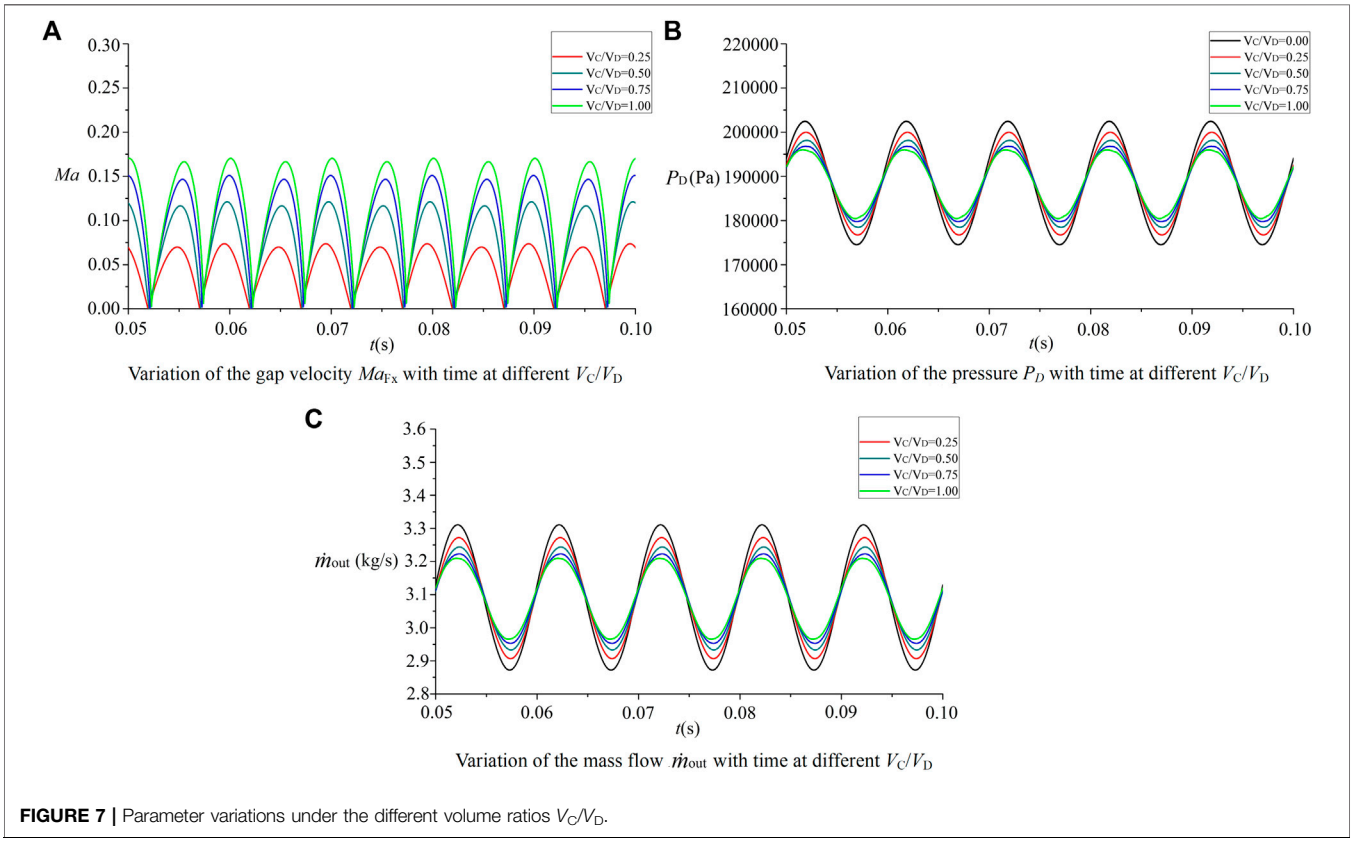

FIGURE 7 | Parameter variations under the different volume ratios V_C/V_D.

As can be seen from **Figure 7**, when the outlet back pressure P_2 fluctuates, after the stable process is established, the pressure and flow change periodically with the same frequency of the back pressure. Due to the periodic change of pressure P_2, the shock wave moves back and forth under the action of the back pressure. After the shock wave, the volume of the control body D area changes, resulting in the change of the pressure P_2 in the mainstream area, which in turn causes the flow velocity Ma_{Fx} in the gap entering the cavity to fluctuate. The value of the Mach number is a positive value. In one cycle, the airflow experiences the process of entering cavity C and entering the main channel D, and the oscillation frequency of the Mach number doubles in value.

Comparing the calculation results of different volume ratios V_C/V_D, it can be seen that under the same back pressure condition, with the increase of the cavity volume, the mainstream can continue to fill when entering the cavity, which hinders the change trend of the mainstream pressure P_D, and the fluctuation amplitude of pressure P_D and flow $\dot{m}_{out}$ decreases. At the same time, after the amplitude of pressure P_D decreases, the pressure difference between the main flow and cavity decreases, and the Mach number Ma_{Fx}

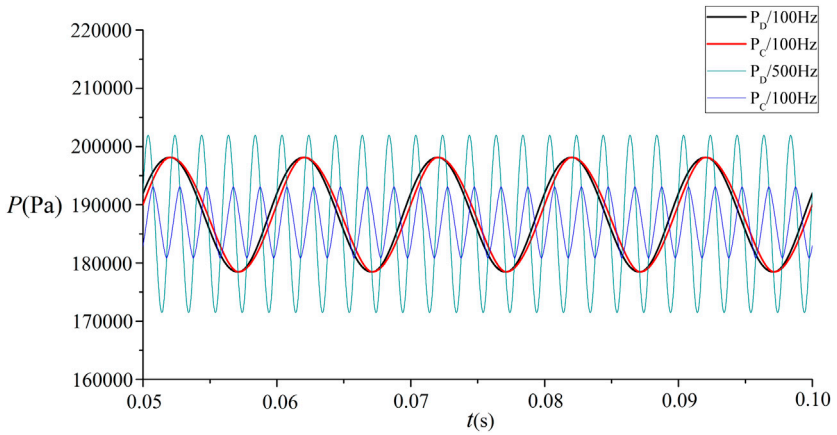

FIGURE 8 | Pressure comparisons under different back pressure variation frequencies.

of the gap flow also decreases. From the calculation results, compared with the scheme without cavity, the pressure P_D and outlet flow $\dot{m}_{out}$ at V_C/V_D = 0.5 decrease to 71.62 and 72.09%, respectively.

For the state of V_C/V_D = 0.5, two different back pressure pulsation frequencies were selected, and the changes in pressure P_D and P_C were compared to study the influence of the oscillation frequency. From the 100-Hz curve, the variation rules and amplitudes of the cavity pressure P_C and the flow channel pressure P_D are basically the same, while the cavity pressure curve slightly lags behind the pressure change of the main flow channel, which indicates that the pressure difference between the two cavities is small. Under the action of the maximum pressure difference, the maximum value of the gap flow velocity does not exceed *Ma*0.15.

When the oscillation frequency of back pressure P_2 is increased to 500 Hz, the amplitude of the mainstream pressure P_D increases compared with 100 Hz, while the amplitude of the cavity pressure P_C decreases, as shown in **Figure 8**. In the process of repeated filling of air flow in the mainstream and cavity, the change of flow pressure through the gap needs a certain time history. When the frequency increases, the dynamic process time of air flow entering or exiting the cavity is relatively shorter. In one cycle, the amplitude of cavity pressure P_C does not increase to the same as that of the mainstream, and the pressure of the mainstream begins to decrease again. Therefore, P_C is significantly smaller than P_D in the mainstream area, and the cavity pressure P_C has a phase difference of about half a cycle relative to the channel pressure P_D. Compared with the results of 100 Hz, there is a significant difference between the two cases. Due to the changes in the internal and external pressure difference and phase change, the Mach number of the gap is relatively higher. The calculation shows that the maximum velocity of the gap reaches Ma_{Fx} = 0.36.

Based on the above theoretical model analysis, when the shock position and pressure after the shock change, a parallel cavity is added in the downstream area of the shock, and due to the change of the relative pressure between the main stream and cavity, the air flows between the cavity and main stream, which can weaken the parameter change amplitude in the oscillation process of the shock to a certain extent and inhibit the shock oscillation. Through analysis, the volume of the cavity and frequency of parameter oscillation have an impact on the effect of oscillation suppression. Increasing the volume of the cavity can "accommodate" or "release" more air flow when the mainstream pressure increases or decreases, so as to hinder the change of parameters. At a lower frequency, the air can flow between the cavity and mainstream for more time, so as to improve the effect of parameter change suppression.

SIMULATION AND ANALYSIS OF SHOCK DYNAMIC PROCESS

The theoretical analysis shows that the cavity can restrain the parameter fluctuation. In practice, when the outlet pressure remains constant, it will also produce a certain range of self-excited oscillation, which will cause the fluctuation of flow, pressure, and other parameters, as well as the forward and backward movement of the shock. Moreover, due to the gas viscosity and wall boundary layer, the coupling with the compression wave system of the inlet will produce strong shock/boundary layer interference, and the unsteady motion of the shock train adds to the complexity of the flow. In the process of shock wave oscillation, when the shock wave moves forward and backward, it may also cross the gap of the cavity. The filling process of the cavity will be very complex, which is difficult to analyze by these theoretical methods. Therefore, the unsteady numerical calculation method is used for research.

Calculation Condition and Time Step

According to the calculation model shown in **Figure 1**, the self-excited oscillation processes under two different cavity volumes are calculated and compared with the results without cavity. The calculation conditions are listed in **Table 2**. The difference

TABLE 2 | Computational model.

Model	Parameter H_4 (mm)
A	0
B	8
C	16

between the three models lies in the numerical difference of cavity height H_4 (as shown in **Figure 1**).

In the shock wave oscillation simulation of the inlet, the calculation is carried out for the state of incoming flow Ma_∞ = 3.0 and back pressure ratio P_{out}/P_∞ = 9.0. Other parameters of the inlet are consistent with those in Reinartz et al. (2003). The selection of the time step has a very important impact on unsteady calculation and is related to the frequency of shock oscillation and grid scale. There are enough iterative steps in one cycle to ensure the convergence of calculation results. When determining the time step, on the one hand, a larger time step is started with initially and the value of the time step is then reduced until the calculated shock oscillation frequency analysis result has nothing to do with the step; on the other hand, according to the spectrum analysis, the shock wave oscillation frequency is about 400 Hz and the iteration step in one cycle is guaranteed to be 5,000 steps; through the analysis, the iterative step size of 0.5×10^{-6} s is taken in this article.

Flow Parameter Comparison and Analysis

According to the working conditions in **Table 2**, the variation laws of outlet flow $\dot{m}_{out}$ and pressure at typical sampling points are compared. According to the calculation results in **Figure 9**, when the back pressure is fixed, the outlet flow of the inlet of the different models oscillates and the amplitude and frequency of the flow curve oscillation of the three models are different.

The flow fluctuation range of Model A is 5.79–9.42 kg/s, and the maximum variation amplitude exceeds ± 30% relative to the steady-state value, with a large fluctuation and jump. The periodicity of the flow curve change is poor, and the peak value of different cycles is also different. Model B has a smaller cavity added, and the flow curves of the different cycles are relatively consistent. In each cycle, it includes the process of rapid rise and rapid decline, and the outlet flow fluctuates in the range of 6.13–9.37 kg/s. Numerically, it is slightly smaller than the fluctuation range of Model A, but due to the differences between the different cycles of Model A, the flow fluctuation of Model B in some cycles is greater than that of Model A. The vibration amplitude of the flow curve of Model C is relatively reduced, and the consistency of the curve change is also good. The variation range of the outlet flow is 7.04–8.82 kg/s.

FFT analysis on the flow curve was performed to analyze the spectral characteristics. From the comparison in **Figure 9B**, it can be seen that the two frequencies with larger amplitudes of the flow curve of Model A are 408 and 466 Hz, respectively, and there are two frequency ranges with larger amplitudes, 300–550 and 1100–1400 Hz, respectively. It shows the complexity of the shock oscillation process. The frequency corresponding to the maximum amplitude of Model B is 411 Hz, and the maximum amplitude at this frequency is significantly higher than that of Model A. In addition, there are also larger amplitudes at the two frequency points of 823 and 1230 Hz. Model C is relatively high at the four frequency points of 377, 758, 1140, and 1510 Hz, but it is lower than the maximum amplitude of Model A, which indicates that the cavity has a certain influence on the amplitude and frequency of the flow. This indicates that under the action of the cavity, the flow curve changes from multiple frequency points of Model A to three and four main frequency points of Model B and Model C, respectively. The main frequency points decrease and the curve changes periodically. From the perspective of the amplitude, although it increases at some frequencies, the total oscillation energy decreases due to the decrease of frequency points. The fundamental frequencies of the three models are close, and Model C with a larger cavity volume has a better suppression effect on the flow oscillation.

According to the simulation calculation, the shock wave oscillation in the inlet is mainly in the middle and rear of the isolation section. For sampling points 4, 7, and 10, the pressure fluctuation process is compared in **Figure 10**.

From the pressure changes of the sampling points P_{U4} and P_{L4} in **Figure 10**, the sampling points are close to the front of the isolating section. In Model A without a cavity, the pressure

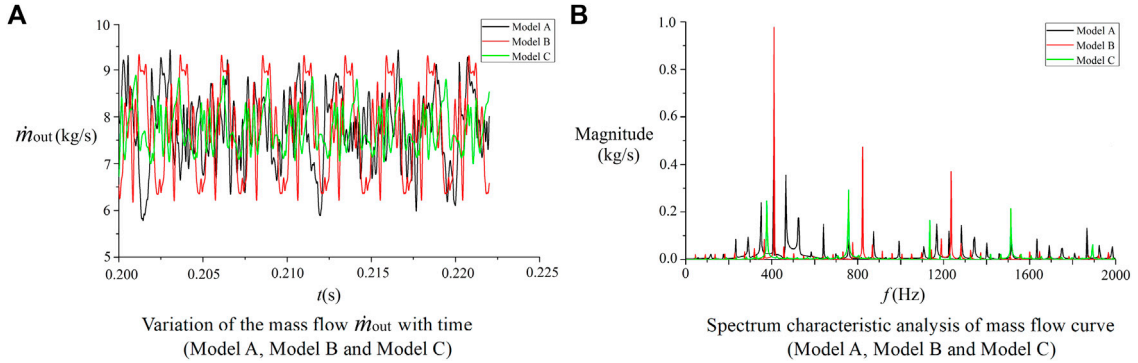

FIGURE 9 | Variation of the mass flow of outlet.

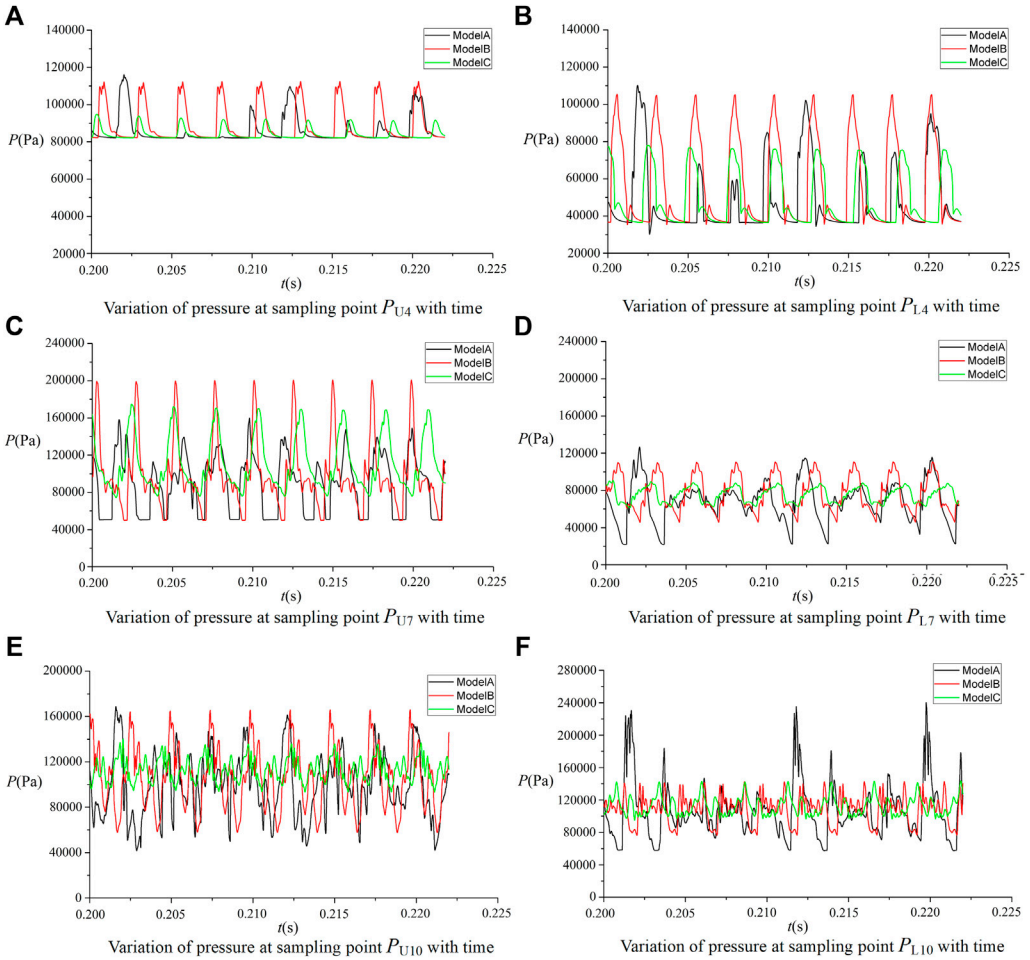

FIGURE 10 | Variation of the pressure at different sampling points.

fluctuations are nonperiodic, and there are small peaks between larger peaks. This indicates that the leading edge of the separation shock only moves forward to this sampling position for part of the time during the oscillation process. The periodicity of the pressure oscillation in Model B is obvious. The frequency of the pressure oscillation on the upper and lower walls is the same. Due to the asymmetry of the shock wave in the flow field, the pressure values are different at the same sampling position. The amplitude of the sampling point P_{L4} on the lower wall is higher than that of P_{U4}. The volume of the Model C cavity increases, the amplitude of the pressure oscillation at the sampling point P_{U4} is significantly reduced, and the amplitude of the sampling point P_{L4} on the upper and lower walls also drops to about half of that of Model B. The peaks and constants appear alternately in the pressure curve, indicating that the shock wave moves forward before sampling point 4 for a part of the time, and moves backward after the sampling point for a part of the time. Due to the increase in the volume of the cavity of Model C, for the system composed of the inlet and the cavity, it is equivalent to increasing the overall space volume. According to the acoustic theory, the acoustic oscillation frequency decreases. According to the spectrum analysis, the main frequencies of pressure oscillations of Model B and Model C are 411 and 372 Hz, respectively, which are close to the results of the spectrum analysis of the outlet flow.

When comparing the pressure curve at sampling point 7 in **Figures 10C,D**, although the pressure oscillations at sampling points P_{U7} and P_{L7} on the upper and lower walls of Model A also show a certain periodicity, the change process, however, between curves is different. The curve of the sampling point P_{U7} contains the change process of the alternating ratio between the peak and the constant value, and the peak also shows the process of rapid rise and fall; the P_{L7} curve of the sampling point on the lower wall has no constant value part and only contains alternating large and small amplitudes. The amplitudes of Model B under different cycles are basically the same. The amplitude of the sampling point P_{U7} on the upper wall is larger than that in Model A, but the oscillation amplitude of P_{L7} on the lower wall is smaller than that in Model A. The oscillation amplitude of Model C is significantly

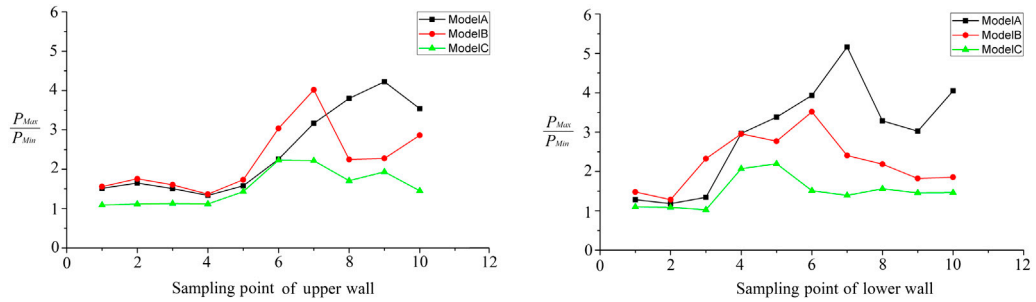

FIGURE 11 | Comparison of the maximum amplitude at sampling points.

reduced, and the sampling point amplitude is about half that in Model B.

The sampling point 10 is located behind the parallel cavity, and the cavity in this region interacts with the airflow in the inlet. As can be seen from **Figure 10E**, the pressure oscillation range of P_{U10} on the upper wall of Model A is large, and the large amplitude oscillation and small amplitude oscillation of P_{L10} on the lower wall occur alternately. The cavity volume of Model B is small, the amplitude of P_{U10} on the upper wall is slightly less than that of Model A, and the amplitude of pressure fluctuation at the sampling point P_{L10} is consistent and significantly reduced in different periods. After the cavity volume further increases, the pressure curve fluctuation of Model C at sampling points P_{U10} and P_{L10} decreases significantly when compared with that of Model A.

Comparing the calculation results in **Figure 10** with those in the *Theoretical Modeling and Analysis* section, it can be seen that the interference of the shock boundary layer cannot be considered in the process of theoretical analysis, and the periodicity of the parameter change is good. In the actual inlet, due to the shock boundary layer's interference, coupled with the shock oscillation process, the shape of the parameter change curve is more complex. However, the results of the theoretical model and inlet numerical calculation show that the parallel cavity can reduce the amplitude of pressure oscillation at different sampling points and inhibit the shock oscillation process.

The pressure fluctuation amplitude ratio P_{Max}/p_{Min} was compared at different sampling points. From the comparison as shown in **Figure 11**, the amplitudes before the sampling point P_{U4} on the upper wall and sampling point P_{L2} on the lower wall are relatively small. In the rear part of the isolation section, the pressure of Model A oscillates greatly, with a maximum amplitude ratio exceeding 5. Compared with Model A, the maximum pressure amplitude of Model B increased at points P_{U4}–P_{U7} on the upper wall, and decreased after P_{U8}; the lower wall decreased significantly from P_{L4} onward. The pressure does not oscillate before P_{U1}–P_{U5} on the wall of Model C, while the amplitude ratio is within 2 between P_{U6} and P_{U10}. Among the sampling points on the lower wall, the amplitude ratio of P_{L4} and P_{L5} is about 2, and the amplitude ratio of the other sampling points does not exceed 1.5. Compared with the case that the maximum amplitude ratio of Model A without cavity exceeds 5, the Model C cavity significantly reduces the pressure amplitude ratio at the sampling point, especially the influence of the lower wall is more obvious, which shows that the cavity can significantly reduce the pressure oscillation.

Flow Field Characteristic Analysis

According to different calculation models, the variations of the flow field in the process of inlet self-excited oscillation is analyzed.

Figure 12 shows the Mach number distribution of the typical flow field in the inlet. It can be seen that under the action of back pressure, the positive shock evolves into a complex wave system which includes the expansion wave, oblique shock, local separation, and shock reflection. There is a strong shock wave/boundary layer interference in the flow field, resulting in the local separation, It includes the R_1 separation zone generated by the interference of the shock wave reflected from the lower lip after the turning point of the compression surface, the R_2 separation zone generated by the interference of the shock train and the boundary layer on the lower wall, and the R_3 separation zone developed from the inlet along the wall under the adverse pressure gradient of the expansion section. The positions and scales of these separation regions change in a large range with the self-excited oscillation in the inlet and are coupled to oscillate with the flow field parameters such as the outlet flow rate and the pressure at the sampling point.

It can be seen from the results of **Figure 10** that there is a clear difference in the amplitude of sampling points between Model B and Model C. Comparing the pressure of the corresponding cavity sampling point with that in **Figure 13**, the pressure oscillation frequency of the cavity is close to that of the mainstream sampling point. At the same sampling point, the pressure oscillation amplitude of Model C is small. From the analysis of the consistency of pressure oscillation at different sampling points, the amplitude and phase of the pressure curve oscillation of each sampling point in Model B are basically consistent. The sampling points P_{C1} and P_{C2} of Model C have large pressure amplitudes, but other points have relatively small amplitudes, which correspond to the small pressure amplitudes of sampling points 6–8 in the mainstream area. Moreover, there is an obvious phase difference between the different sampling points of Model C.

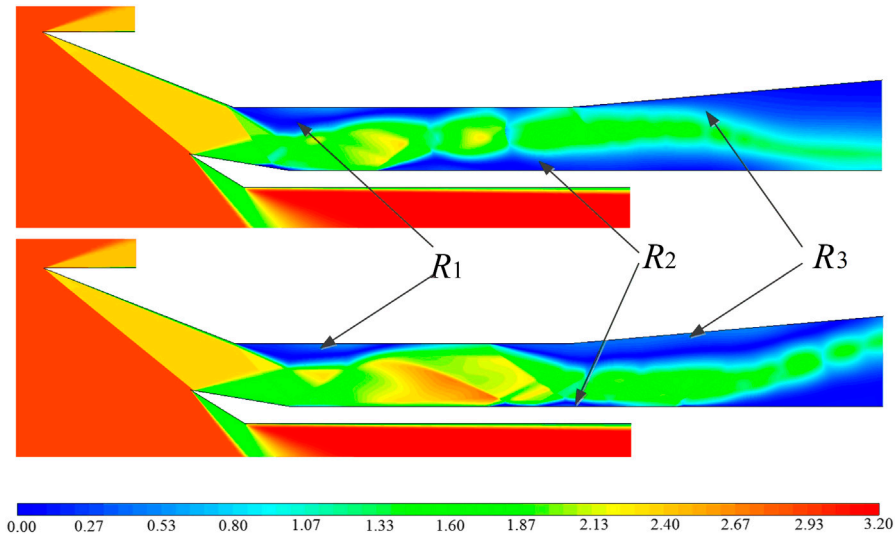

FIGURE 12 | Typical Mach number contours of Model A at different times.

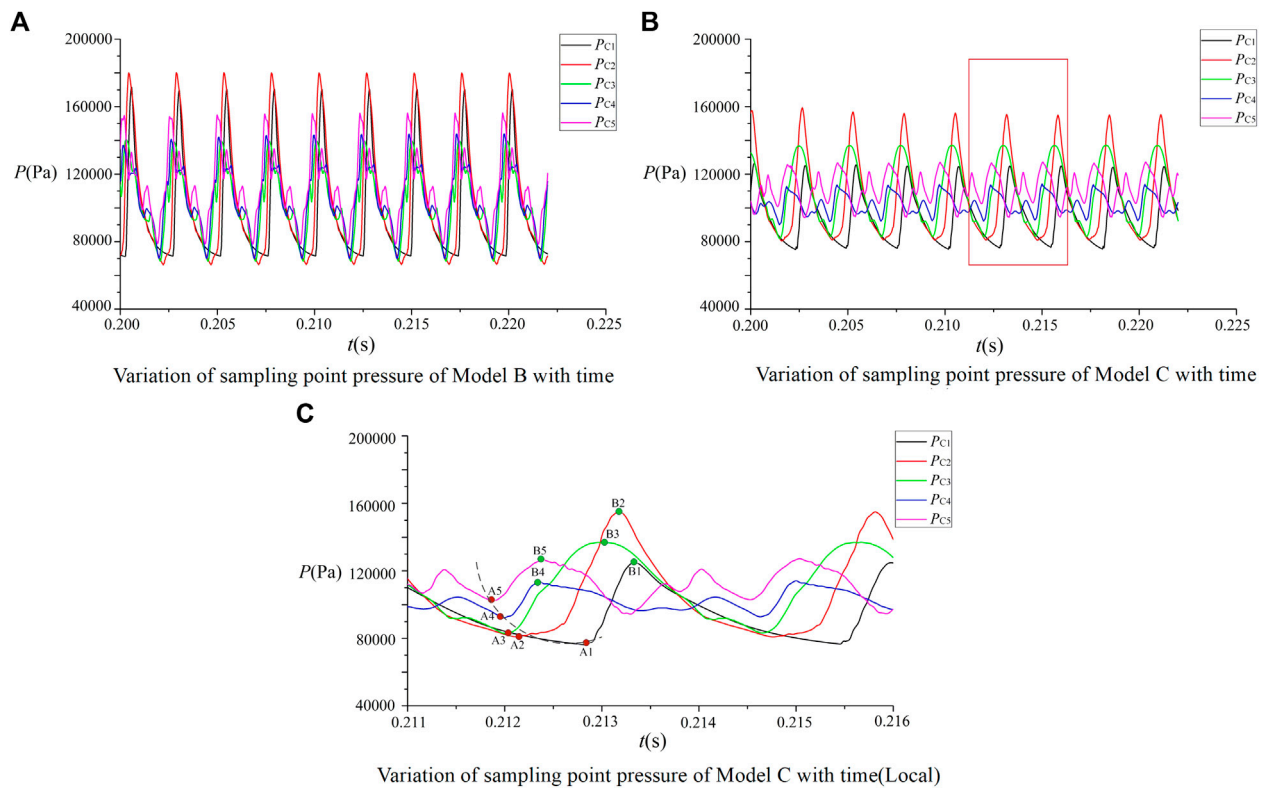

FIGURE 13 | Variation of pressure at cavity sampling point.

The pressure change process in the cavity of Model C was further analyzed. From the local pressure curve, as shown in **Figure 13C**, the amplitude of the sampling point P_{C2} is the largest. Combined with the Mach number analysis of the flow field in **Figure 14**, this sampling point is located in the leading edge of the shock system, where the shock wave swept across this

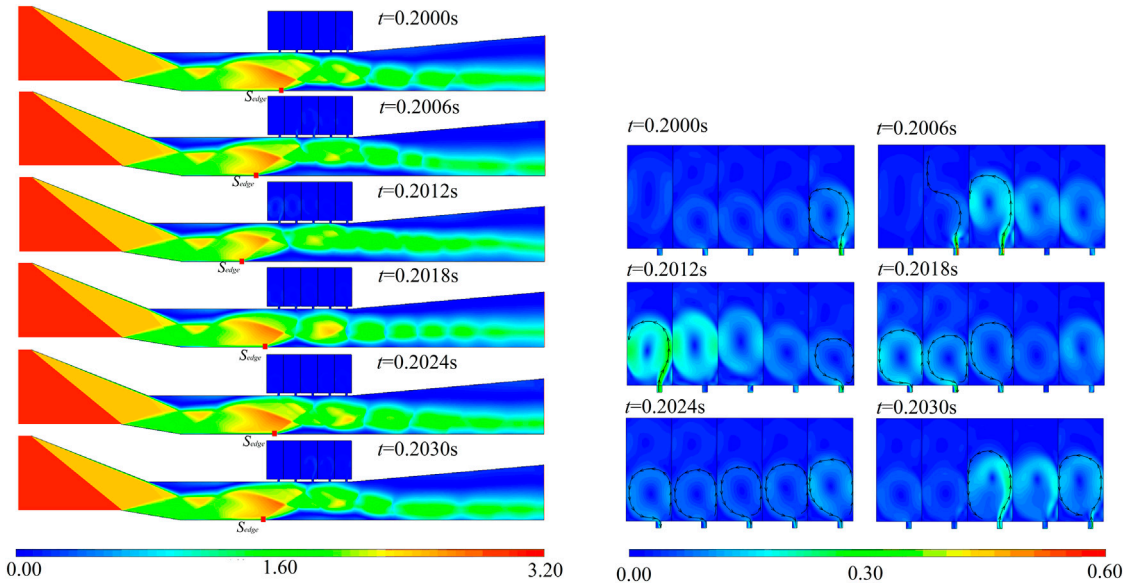

FIGURE 14 | Mach number contours of Model C.

position repeatedly in the process of periodic movement. The large fluctuation of pressure before and after the shock wave causes the pressure in the cavity to change under the alternating low–high–low pressure environment of the mainstream, where the pressure amplitude of the sampling point change is larger and the pressure amplitude of the P_{C2} point changes more than two times. The pressure waveforms of the different sampling points also change. Among them, P_{C1}–P_{C3} basically show a relatively regular periodic change process, while the pressure waveforms of P_{C4} and P_{C5} superimpose more frequencies in one cycle.

Comparing the change processes of the different curves, it can also see that there are obvious phase differences between the different sampling points. The pressure troughs of different curves develop from point A_5 to point A_1, which takes about 1 ms, indicating that the shock wave moves forward in the region of the sampling point. When the mainstream pressure increases, the pressure difference within the cavity increases, the air flow fills the cavity, and the sampling point curve rises. The relationship between the internal and external pressure differences at the different sampling points is different, and the time and value of the pressure curve reaching the peak value are also different. After this, the leading edge of the shock wave moves backward; the cavity pressure, filled by the high pressure after the shock wave, is higher than the pressure of the main stream before the shock wave; the air flow enters the main stream from the cavity; and the pressure at the sampling points P_{C1}–P_{C5} begins to decrease. The periodic motion of the shock wave causes the periodic fluctuation of the main flow and cavity pressure.

Analyzing the Mach number change of the flow field in **Figure 14**, it can be seen that there are still some fluctuations in the flow field after the shock wave system in the isolator, corresponding to the separation areas of R_1 and R_2 in **Figure 12**. In one cycle, the leading edge S_{edge} of the separation zone R_2 moves back and forth within a certain range, and the range of R_2 also changes, but its range of change is significantly reduced compared to the two typical flow fields in **Figure 12**. At the same time, after the parallel cavity, the R_3 separation zone from the outlet to the inlet of the expansion section basically does not cross the straight section and continues to develop. Due to the movement of S_{edge}, the reflected shock generated by the compression of the main stream by the lower separation bubble will be reflected to the upper wall to produce a certain separation zone, but this separation zone is relatively small and does not develop greatly in scale, and the leading edge of the upper wall of the shock wave system lags behind the leading edge of the lower wall.

Combined with the local velocity and streamline of the cavity in **Figure 14**, at $t = 0.200$ s, the leading edge of the shock string is located in the middle of the isolator section, and the pressure of the inlet channel is higher than that of the fifth cavity, so air flow is injected into the cavity through the gap. As the shock wave moves forward, the inflation process of cavity 5 in space–time with $t = 0.206$ s is basically completed. When the leading edge of the shock wave crosses the second and third cavities, high-pressure air flow enters the two cavities. When $t = 0.206$ s, cavity 1 begins to be filled with mainstream gas. At the same time, due to the front movement of the shock wave, the pressure after the shock wave decreases relatively, and cavity 5 begins to exhaust to the mainstream area after the pressure is higher than the mainstream. After this, the leading edge of the shock wave begins to move backward, the mainstream pressure as the back pressure of the cavity drops sharply, and the cavity overflows into the mainstream. The periodic movement before and after the shock wave also leads to the periodic filling process of the cavity.

This filling process has time differences between the different cavities, and there is a phase difference corresponding to the pressure curve, as shown in **Figure 14**.

Through the above analysis, the cavity is equivalent to the pressure comparison device relative to the mainstream. When the shock wave moves forward and the pressure increases, the air flow enters the cavity, which "hinders" the trend of shock wave moving forward to a certain extent; when the shock wave moves backward, the movement of the shock wave is also restrained by the deflation process. Therefore, the pressure oscillation process of the cavity in the inlet increases the aerodynamic damping, so as to reduce the shock amplitude and the change of flow field parameters, which is consistent with the analysis of the theoretical model.

CONCLUSION

In this article, the self-excited oscillation of a supersonic inlet is studied, and the dynamic theoretical model of shock oscillation is established. The variation laws of parameter oscillation and flow field under three different models are compared through numerical simulation. The results show that:

1) based on the shock dynamic model, the theoretical model and numerical simulation model of shock oscillation analysis are established. The comparison with the shock theory and public reference shows that the theory and numerical modeling method in this article are feasible.
2) the theoretical model analysis of different volume cavities and shock oscillation frequencies shows that increasing the volume of parallel cavities can reduce the parametric oscillation amplitude. According to the example analysis, when the cavity volume is 0.5 times the volume of the pipeline downstream of the shock wave, the oscillation amplitudes of the downstream pressure P_D and flow $\dot{m}_{out}$ decrease to 71.62 and 72.09% of those without the cavity, respectively.
3) in the actual viscous flow field, the shock wave system produces self-excited oscillation, the leading edge separation point moves in a large range, the flow field pressure and outlet flow produce large amplitude oscillation, and the corresponding Mach number distribution also produces asymmetric changes. The analysis of the outlet flow curve shows that the parameter oscillation has many frequency points with large amplitude.
4) the parallel cavity has an effect on the outlet flow and the pressure at the sampling point. The parameters of the two parallel cavity models in this article change periodically. The cavity volume of Model C is relatively large, the pressure oscillation amplitude at the sampling point decreases from more than 5 to less than 2 of Model A without cavity, and the amplitude of parameter oscillation decreases significantly.
5) from the comparative analysis of the flow field, when the shock wave moves back and forth, the leading edge repeatedly sweeps the parallel cavity. Under the alternating change of internal and external pressure, the air flow in the cavity is filled repeatedly, which hinders the main flow of the inlet to a certain extent, thus inhibiting the parameter oscillation process.

The research results of this article show that it is a feasible technical way to suppress the change of self-excited oscillation parameters of the inlet to a certain extent by paralleling the cavity in the isolator.

DATA AVAILABILITY STATEMENT

The original contributions presented in the study are included in the article/Supplementary Material, further inquiries can be directed to the corresponding author.

AUTHOR CONTRIBUTIONS

In this article, FC established the shock dynamic model, carried out theoretical analysis, verified the numerical calculation method, and completed the calculation of unsteady shock oscillation in the inlet. XH completed the sorting and analysis of some calculation results.

REFERENCES

Chen, S., and Zhao, D. (2018). Numerical Study of Guide Vane Effects on Reacting Flow Characteristics in a Trapped Vortex Combustor. *Combustion Sci. Techn.* 190 (10-12), 2111–2133. doi:10.1080/00102202.2018.1492568

Curran, E. T., Heiser, W. H., and Pratt, D. T. (1996). Fluid Phenomena in Scramjet Combustion Systems. *Annu. Rev. Fluid Mech.* 28 (1), 323~360. doi:10.1146/annurev.fl.28.010196.001543

Hankey, W., and Shang, J. (1980). Analysis of Self-Excited Oscillations in Fluid Flows." in 13th Fluid and PlasmaDynamics Conference, Snowmass, CO, July 14–16. doi:10.2514/6.1980-1346

Herrmann, D., Siebe, F., and Gülhan, A. (2013). Pressure Fluctuations (Buzzing) and Inlet Performance of an Airbreathing MissileBuzzingand Inlet Performance of an Airbreathing Missile. *J. Propulsion Power* 29 (4), 839–848. doi:10.2514/1.b34629

Huang, H. X., Tan, H. J., and Zhuang, Y. (2018). Progress in Internal Flow Characteristics of Hypersonic Inlet/Isolator. *J. Propulsion Techn.* 39 (10), 2252–2273. doi:10.13675/j.cnki.tjjs.2018.10.010

Huang, R., Li, Z. F., and Nie, B. P. (2020). Shock Train Oscillations in a Two-Dimensional Inlet/Isolator with Suction. *J. Propulsion Techn.* 41 (4), 767–777.

Ikui, T., Matsuo, K., Nagai, M., and Honjo, M. (1974). Oscillation Phenomena of Pseudo-shock Waves. *Bull. JSME* 17 (112), 1278–1285. doi:10.1299/jsme1958.17.1278

Li, N., Chang, J., Yu, D., Bao, W., and Song, Y. (2017). Mathematical Model of Shock-Train Path with Complex Background Waves. *J. Propulsion Power* 33 (2), 468–478. doi:10.2514/1.b36234

Li, N. (2019). *Investigation of the Shock Train Instability and Control Method in Scramjet*. Harbin: Harbin Institute of Technology. doi:10.27061/d.cnki.ghgdu.2019.000250

Li, Z. F., Gao, W. Z., and Li, P. (2012). Experimental Investigation on the Shock Wave Oscillation Behaviors in a Two-Dimensional Hypersonic Inlet Flow. *J. Propulsion Techn.* 33 (5), 676~682.

Lu, L., Wang, Y., and Fan, X. Q. (2019). Investigation of Shock-Train Forward Movement in Mixer of RBCC. *J. Propulsion Techn.* 40 (1), 69~75. doi:10.13675/j.cnki.tjjs.170736

Ma, G. F., Xie, W., and Lin, Y. (2017). Pseudo-shock Characteristics in the Two-Dimensional Supersonic Inlet Diffuser. *J. Aerospace Power* 32 (8), 1950~1961.

Ma, L. C. (2019). *Study on the Effect of Suction Structure and Parameters on the Boundary Layer Oscillation Suction*. Harbin: Harbin Institute of Technology. doi:10.27061/d.cnki.ghgdu.2019.002664

Matsuo, K., Miyazato, Y., and Kim, H.-D. (1999). Shock Train and Pseudo-shock Phenomena in Internal Gas Flows. *Prog. Aerospace Sci.* 35 (1), 33–100. doi:10.1016/s0376-0421(98)00011-6

Meier, G. E. A., Szumowski, A. P., and Selerowicz, W. C. (1990). Self-Excited Oscillations in Internal Transonic Flows. *Prog. Aerospace Sci.* 27 (2), 145–200. doi:10.1016/0376-0421(90)90004-4

Pan, J. S., and Shan, P. (2011). *Fundamentals of Das Dynamics*. Beijing: National Defense Industry Press.

Piponniau, S., Dussauge, J. P., Debiève, J. F., and Dupont, P. (2009). A Simple Model for Low-Frequency Unsteadiness in Shock-Induced Separation. *J. Fluid Mech.* 629, 87–108. doi:10.1017/s0022112009006417

Reinartz, B. U., Herrmann, C. D., Ballmann, J., and Koschel, W. W. (2003). Aerodynamic Performance Analysis of a Hypersonic Inlet Isolator Using Computation and Experiment. *J. Propulsion Power* 19 (5), 868–875. doi:10.2514/2.617710.2514/2.6177

Rybalko, M., Babinsky, H., and Loth, E. (2012). Vortex Generators for a Normal Shock/Boundary Layer Interaction with a Downstream Diffuser. *J. Propulsion Power* 28 (1), 71–82. doi:10.2514/1.5704610.2514/1.b34241

Sugiyama, H., Tsujiguchi, Y., and Honma, T. (2008). Structure and Oscillation Phenomena of Pseudo-Shock Waves in a Straight Square Duct at Mach 2 and 4."in 15th AIAA International Space Planes and Hypersonic Systems and Technologies Conference, Dayton, OH, April 28–May 1, 2008. doi:10.2514/6.2008-2646

Tan, H. J., Sun, S., and Huang, H. X. (2012). Behavior of Shock Trains in a Hypersonic Inlet/Isolator Model with Complex Background Waves. *Exp. Fluids* 53 (6), 1647–1661. doi:10.1007/s00348-012-1386-1

Tian, X, A., Wang, C, P., and Cheng, K. M. (2014). Experimental Investigation of Dynamic Characteristics of Oblique Shock Train in Mach 5 Flow. *J. Propulsion Technol.* 35 (8), 1030~1039. doi:10.13675/j.cnki.tjjs.2014.08.004

Wang, C. P., and Zhang, K. Y. (2010). Shock Train Oscillation and Wall Pressure Fluctuation in Internal Flow. *J. Experiments Fluid Mechanic* 24 (5), 57–62. doi:10.3969/j.issn.1672-9897.2010.05.012

Xiong, B., Wang, Z.-G., Fan, X.-Q., and Wang, Y. (2017a). Experimental Study on the Flow Separation and Self-Excited Oscillation Phenomenon in a Rectangular Duct. *Acta Astronautica* 133, 158–165. doi:10.1016/j.actaastro.2017.01.009

Xiong, B., Wang, Z. G., and Fan, X. Q. (2017b). Characteristics of Forced Normal Shock-Train Oscillation in Isolator. *J. Propulsion Techn.* 38 (1), 1~7. doi:10.13675/j.cnki.tjjs.2017.01.001

Xu, K., Chang, J., and Li, N. (2019). Experimental Investigation of Mechanism and Limits for Shock Train Rapid Forward Movernt. *Expermental Therm. Fluid Sci.* 98, 336~345. doi:10.1016/j.expthermflusci.2018.06.015

Xu, K., Chang, J., Zhou, W., and Yu, D. (2016). Mechanism and Prediction for Occurrence of Shock-Train Sharp Forward Movement. *AIAA J.* 54 (4), 1403–1412. doi:10.2514/1.J054577

Zhan, W. J., and Yan, H. (2021). Numerical Study of Effects of Steady and Oscillating Back-Pressure on Shock Train in an Isolator. *J. Popul. Techn.* 42 (5), 980–990. doi:10.13675/j.cnki.tjjs.190671

Zhao, D., Gutmark, E., and de Goey, P. (2018). A Review of Cavity-Based Trapped Vortex, Ultra-compact, High-G, Inter-turbine Combustors. *Prog. Energ. Combustion Sci.* 66 (may), 42–82. doi:10.1016/j.pecs.2017.12.001

Conflict of Interest: The authors declare that the research was conducted in the absence of any commercial or financial relationships that could be construed as a potential conflict of interest.

Publisher's Note: All claims expressed in this article are solely those of the authors and do not necessarily represent those of their affiliated organizations, or those of the publisher, the editors, and the reviewers. Any product that may be evaluated in this article, or claim that may be made by its manufacturer, is not guaranteed or endorsed by the publisher.

frontiers | Frontiers in Energy Research

ORIGINAL RESEARCH
published: 27 April 2022
doi: 10.3389/fenrg.2022.891380

Viscous Oil Film Thermal Modeling of Hydrostatic Bearings With a Rectangular Microgroove Surface

Teng Liu[1,2], Chentao Li[1], Runze Duan[3], Huiru Qu[3], Faze Chen[2], Zhenlin Zhou[1], Jianjun Zhang[1] and Zhanqun Shi[1]*

[1]School of Mechanical Engineering, Hebei University of Technology, Tianjin, China, [2]School of Mechanical Engineering, Tianjin University, Tianjin, China, [3]School of Energy and Environmental Engineering, Hebei University of Technology, Tianjin, China

The thermal effect of the viscous oil film of hydrostatic bearings is the key factor causing bearing errors, and the hydrostatic bearing working surface with microgroove structures can potentially inhibit the thermal effect and effectively ensure the bearing accuracy. In this study, a modeling method for oil film heat generation of hydrostatic bearings with a rectangular microgroove working surface is established, and the influence of microgroove design scales onto oil film heat generation is studied. First, the flowing field numerical simulation model of the hydrostatic bearing oil film is established and verified by the published analytical model. Based on the simulation method, oil film flowing behaviors of hydrostatic bearings with a rectangular microgroove working surface are studied. Then, by combining the analytical calculation of viscous heat generation of the hydrostatic oil film and its flowing field simulation, a modified oil film thermal modeling of hydrostatic bearings with the rectangular microgroove working surface is established. On this basis, the influence of the microgroove design scale onto oil film heat generation is studied. It can be concluded that with the appropriate scales of the rectangular microgroove, the working surface with microgrooves can reduce the average velocity of the viscous flow field of the hydrostatic bearing oil film and restrain its energy loss and heat generation.

Keywords: hydrostatic bearing, oil film, viscous heat generation, microgroove structure surface, numerical simulation

OPEN ACCESS

Edited by:
Xiao Liu,
Harbin Engineering University, China

Reviewed by:
Iskander Tlili,
Monastir, Tunisia
Luo Xie,
Northwestern Polytechnical University, China

****Correspondence:***
Runze Duan
duanrunze@hebut.edu.cn

Specialty section:
This article was submitted to Advanced Clean Fuel Technologies, a section of the journal Frontiers in Energy Research

Received: *07 March 2022*
Accepted: *28 March 2022*
Published: *27 April 2022*

Citation:
Liu T, Li C, Duan R, Qu H, Chen F, Zhou Z, Zhang J and Shi Z (2022) Viscous Oil Film Thermal Modeling of Hydrostatic Bearings With a Rectangular Microgroove Surface. Front. Energy Res. 10:891380. doi: 10.3389/fenrg.2022.891380

INTRODUCTION

A hydrostatic bearing is the core component of high-precision mechanical equipment such as ultra-precision CNC machine tools, precision experimental instruments, and space simulators. The thermal effect of its viscous oil film is the key factor leading to lubrication failure and accuracy instability of hydrostatic bearings, which seriously restricts the quality improvement of high-end precision machinery products (Liu et al., 2017).

Since the carrying capacity of hydrostatic bearings is achieved based on the formation of a high-stiffness viscous oil film with a 20-micron thickness (less than the viscous bottom layer thickness of pressure oil) (Liu et al., 2017), although hydrostatic bearings have a high operation accuracy and bearing capacity (Kim et al., 2015), the heat generation problem of the viscous oil film is also serious (Liu et al., 2018). Generally, an oil film temperature rise (Liu et al., 2016) can cause its viscosity decrease and lead to an increase in the contact probability between bearing working surfaces and the occurrence of "shaft scraping" and other malignant accidents. Moreover, part of the oil film heat generation can also be transmitted to the bearing structure and cause its thermal deformation, thus

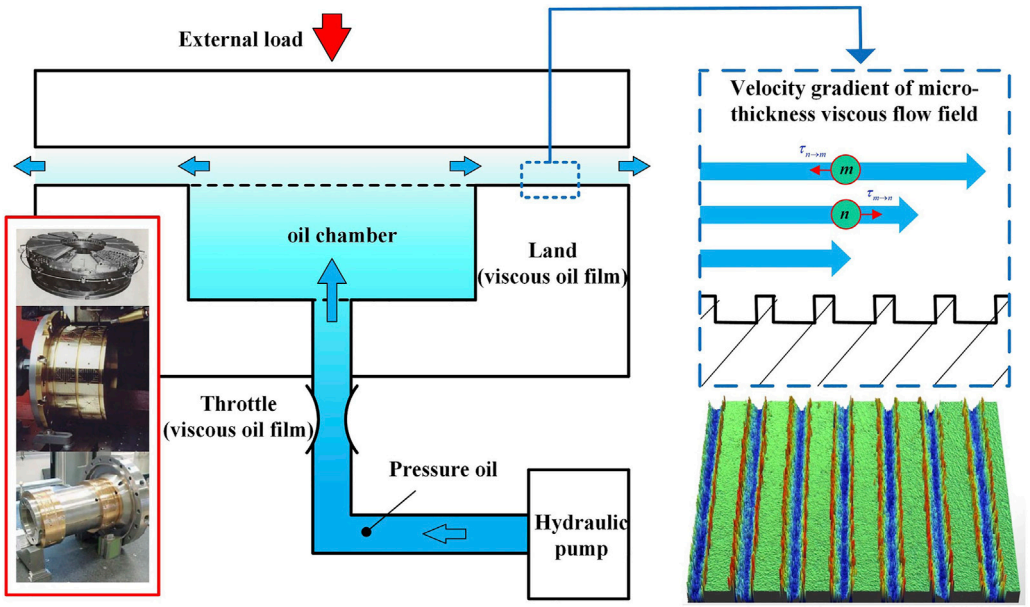

FIGURE 1 | Microgroove working surface of the hydrostatic bearing.

disturbing the bearing accuracy stability (Liu et al., 2016). As shown in **Figure 1**, a microgroove working surface can potentially inhibit heat generation of the viscous oil film and effectively avoid bearing failure caused by the heat effect of the hydrostatic oil film by improving its mechanical properties such as lubrication and adhesion of the working surface of the hydrostatic bearing (Tang et al., 2010).

For the oil film heat generation investigations of hydrostatic bearings under the influence of the microgroove working surface, many scholars have carried out the following relevant research studies by the analytical method and numerical simulation method.

Some scholars have studied the thermal effect mechanism modeling of hydrostatic bearings. Liu et al. (2015) constructed an analytical model of viscous oil film heat generation on a smooth working surface and applied the calculation results as the thermal load of the oil film into the thermo-fluid-solid coupling numerical simulation model of the hydrostatic bearing. Thus, its working conditions–thermal characteristics prediction model was constructed, and the influence mechanism of temperature rise on the viscosity and stiffness of the hydrostatic oil film was revealed. Yu et al. (2018), Yu et al. (2019) studied the thermal deformation characteristics of friction pairs of hydrostatic bearings by using the thermal-fluid-solid coupling numerical simulation method in order to solve the problems of uneven deformation and bearing capacity reduction caused by oil film temperature rise. The mechanism of friction damage of the hydrostatic bearing is revealed, which provides a theoretical basis for performance optimization of the hydrostatic thrust bearing. Tang et al. (2016) studied the influence of the thermal effect on the hydrostatic slipper bearing capacity of the axial piston pump, and the results showed that the slipper bearing capacity increases dramatically with decreasing thermal equilibrium clearance. Zhang et al. (2019), based on the finite volume method, studied the temperature rise and viscosity variation of oil films under the high-speed operation of hydrostatic bearings, revealed the thermal rule of hot oil carrying (HOC), and defined the factor of HOC. In order to study the influence of different viscosity characteristics on the thermal characteristics of fan-shaped oil pads, Huang et al. (2019) compared and analyzed the oil chamber pressure and oil film temperature rise under the temperature–viscosity and pressure–viscosity characteristics based on Fluent software, and the results showed that the temperature–viscosity effect had a greater impact on the thermal characteristics of the oil film than the pressure–viscosity effect. Research studies on the thermal effect mechanism modeling of hydrostatic bearings are mostly based on the assumption of a smooth working surface, while the mechanism of flow and viscous heat generation of hydrostatic bearings on a microstructure working surface is not clear at present.

Other scholars have studied the working surface texture and microstructure characteristics of hydrostatic bearings and their influence. Wang et al. (2016) analyzed the influence of roughness, hydrodynamic, and thermodynamic coupling factors on the pressure distribution and bearing capacity of oil pads of circular hydrostatic bearings based on Christensen's stochastic model of rough surfaces. Kumar and Sharma (2017) studied the combined influence of couple stress lubricants, tilt between bearing pad surfaces, surface roughness, and other factors on hydrostatic bearing performance. Stokes's microcontinuum theory and numerical simulation method are used to study the influence of bearing clearance and bearing bush surface inclination on the performance of hydrostatic bearings. Liu and Hu (2018) studied the influence mechanism of different oil supply pressures, oil groove depth, and surface roughness on

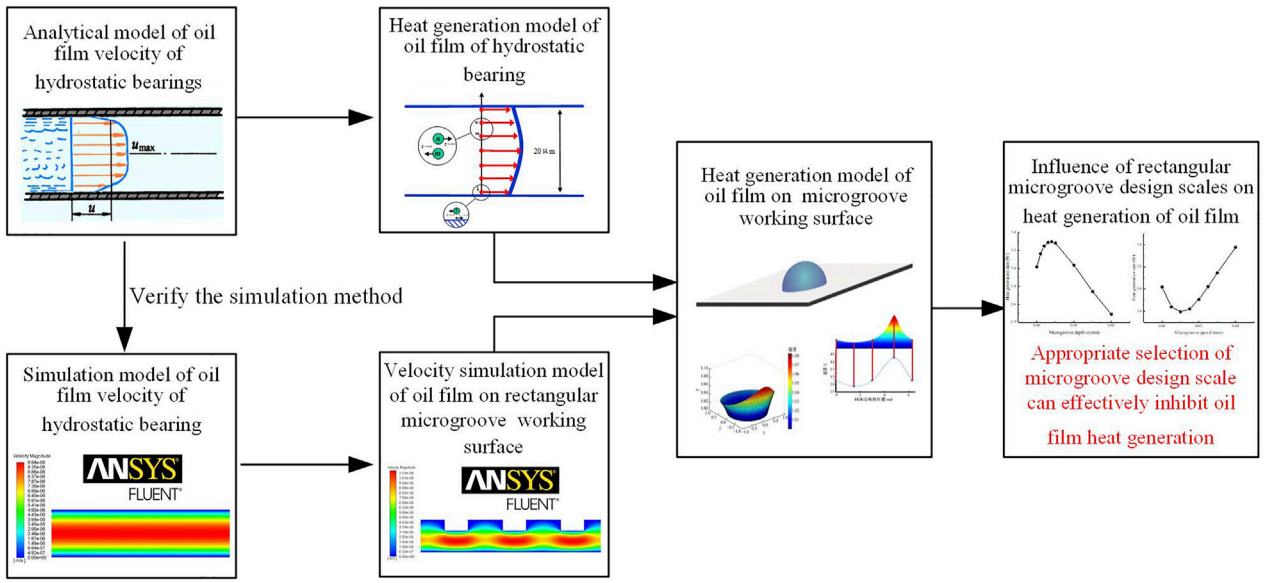

FIGURE 2 | Research method of the influence of rectangular microgroove design scale variation on oil film heat generation.

dynamic and static characteristics of hydrostatic bearings of the precision turntable by using the thermal-fluid-solid coupling numerical simulation method. Comparative analysis shows that the proposed model is more accurate than the traditional model. Lin et al. (2018) studied the influence mechanism of bearing surface texture on characteristics of journal displacement and eccentricity of hydrostatic sliding bearings by using the fluid-solid coupling numerical simulation method. The results showed that the circumferential position of surface texture has an obvious influence on bearing capacity. The research on the surface texture and microstructure morphology of hydrostatic bearings focuses on the analysis of the influence on bearing dynamic/static characteristics, bearing capacity, and other aspects, but the influence on the viscous thermal effect of the hydrostatic bearing fluid layer is not clear.

To sum up, most of the research studies on the modeling of the thermal effect mechanism of hydrostatic bearings are based on smooth working surface conditions, and most of the research studies on the microgroove working surface of hydrostatic bearings focus on the influence mechanism and improvement of bearing dynamic/static characteristics and bearing capacity. However, the effect mechanism of the functional surface of the microgroove on oil film heat generation of hydrostatic bearings is not clear.

In this study, an oil film heat generation model of a hydrostatic bearing with a microgroove working surface is established by combining the analytical model of viscous oil film flow and the numerical simulation of the flow field. The purpose is to explore the influence of surface microgroove design scale variation on hydrostatic bearing oil film velocity gradient and heat generation inhibition and to provide theoretical support for the hydrostatic bearing microgroove oil film heat generation inhibition surface design method. As shown in **Figure 2**, the heat generation analytical model of the oil film of hydrostatic bearings is first derived. Meanwhile, the finite element method is used to simulate the flow field of a two-dimensional (2D) simplified model of the oil film of hydrostatic bearings, and the numerical simulation model is established and its validity is verified by an analytical model. On this basis, the flow field simulation of the oil film of the hydrostatic bearing with the rectangular microgroove working surface is carried out by using the verified effective numerical simulation method. Combined with the heat generation analytical model of the hydrostatic bearing oil film, the heat generation model of the hydrostatic bearing oil film on the rectangular microgroove working surface is established. On this basis, the influence of rectangular microgroove design scales on oil film heat generation is studied.

MODELING METHOD OF OIL FILM HEAT GENERATION FOR HYDROSTATIC BEARINGS

As shown in **Figure 3**, there is an annular oil sealing working face on the oil chamber of the hydrostatic bearing, and the oil film flow field on it can be considered as a viscous fluid flowing in the two-plane gap h. Along the oil sealing working face, the oil film's physical parameters, load conditions, and flow characteristics can be seen as constant values, and the length is short in the X-direction, so the flow field can be considered asinfinitely wide in the Z-direction; then, $\frac{\partial P}{\partial z} = 0$, $v_z = 0$. Therefore, the flow model of the viscous fluid in parallel plane clearance can be simplified to a plane flow problem (Zhong and Zhang, 2007), based on which a 2D oil film model can be established. Pressure oil flows along the X-direction, the inlet pressure is P_{in}, the outlet

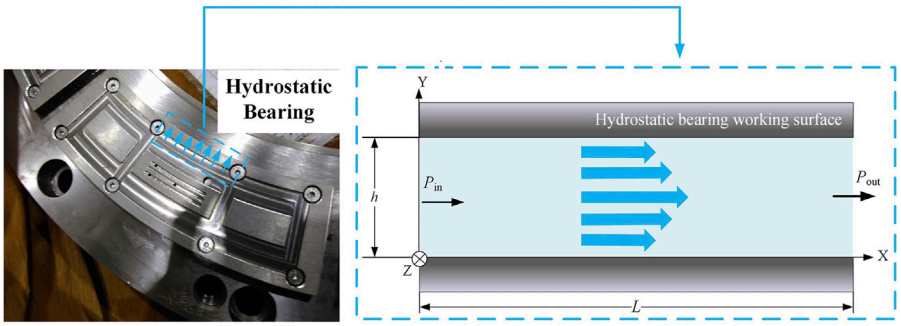

FIGURE 3 | Oil film of the hydrostatic bearing.

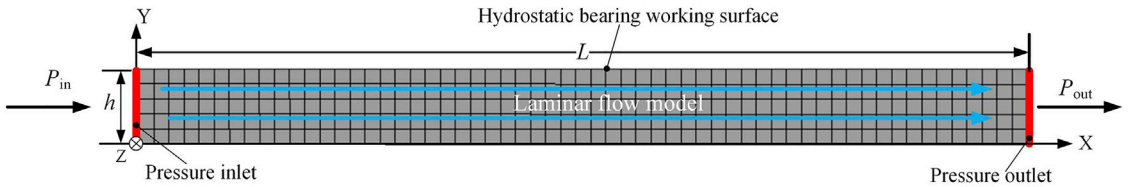

FIGURE 4 | Finite element simulation model of the oil film of the hydrostatic bearing.

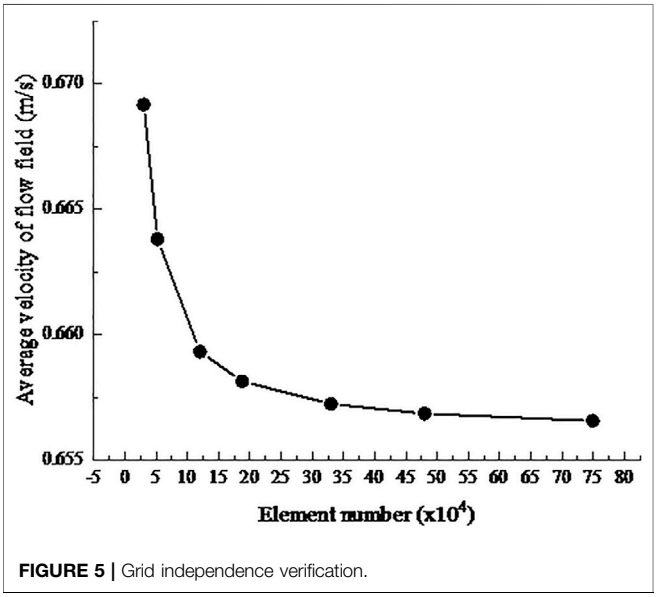

FIGURE 5 | Grid independence verification.

pressure is P_{out}, the flow field length is L, and the oil film thickness is h.

Since the thickness of the viscous oil film of the hydrostatic bearing is less than the thickness of the viscous bottom layer of pressure oil, the flow can be considered laminar flow (Ji and Chen, 2012). Liu et al. (2015) established the calculation method of frictional heat generation of viscous fluids in parallel plane clearance:

$$H = h_w \rho g Q \tag{1}$$

where $h_w = \frac{1}{\rho g}(P_{in} - P_{out})$, so the oil film heat generation rate of the hydrostatic bearing can be expressed as

$$H = (P_{in} - P_{out}) \cdot Q = \Delta P \cdot Q \tag{2}$$

SIMULATION MODELING METHOD FOR THE OIL FILM FLOW FIELD OF THE HYDROSTATIC BEARING WITH A SMOOTH WORKING SURFACE

Simulation Modeling Method

Based on the main design parameters of the oil film on an oil sealing working face of the hydrostatic bearing, the fluid-structure coupling numerical simulation of the hydrostatic bearing oil film is carried out in ANSY-FLUENT, and the analysis type is set as 2D, as shown in **Figure 4**. Set the upper and lower sides as walls, and set the left and right sides as inlets and outlets, respectively. The model is meshed and the flow of pressure oil in the gap is simulated in Fluent. Since the thickness of the oil film (2×10^{-2} mm) is less than the thickness of the viscous bottom layer of hydraulic oil, the flow is laminar flow, so the viscous flow model of pressure oil is set as a laminar flow model. The flow is caused by a pressure difference, so the pressure inlet is set as 1.5 MPa, the pressure outlet is set as 0 MPa, and other boundary conditions remain default. The length of the pressure oil flow direction (X-direction) is 6 mm, and the direction of oil film thickness is the Y-direction. As the temperature rise of the oil film of hydrostatic

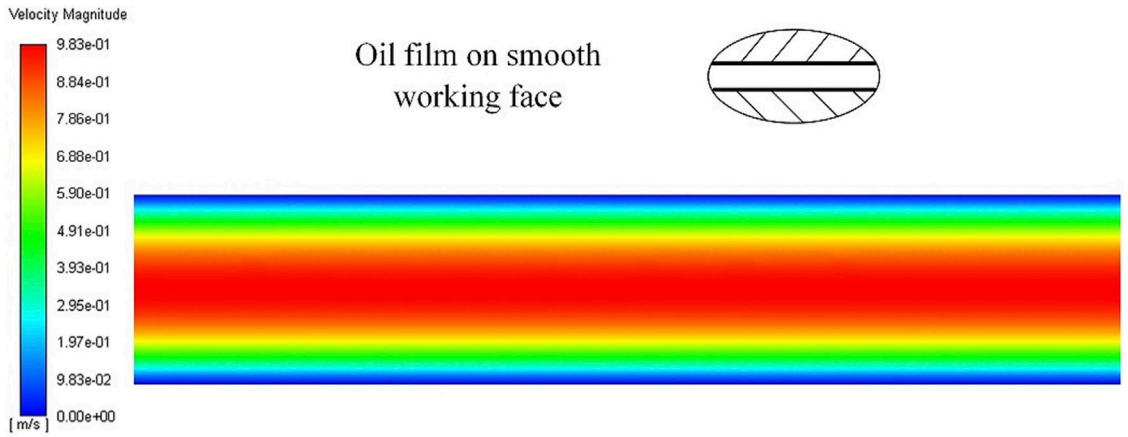

FIGURE 6 | Simulation results of the oil film velocity field of the hydrostatic bearing with a smooth working surface.

TABLE 1 | Comparison of average velocity obtained by flow field simulation and analytical calculations under different working conditions.

Working conditions	Average Velocity		Relative Errors (%)
	Flow field Simulation $\bar{v}$	Analytical calculation v	
P_{in} = 4 MPa P_{out} = 2 MPa $h = 2 \times 10^{-2}$ mm	0.877461 m/s	0.874891 m/s	0.29
P_{in} = 1.5 MPa P_{out} = 0 MPa $h = 2.5 \times 10^{-2}$ mm	1.026911 m/s	1.025262 m/s	0.16
P_{in} = 1.5 MPa P_{out} = 0 MPa $h = 2 \times 10^{-2}$ mm	0.658139 m/s	0.656168 m/s	0.30
P_{in} = 1.5 MPa P_{out} = 0 MPa $h = 1.5 \times 10^{-2}$ mm	0.371119 m/s	0.369094 m/s	0.55

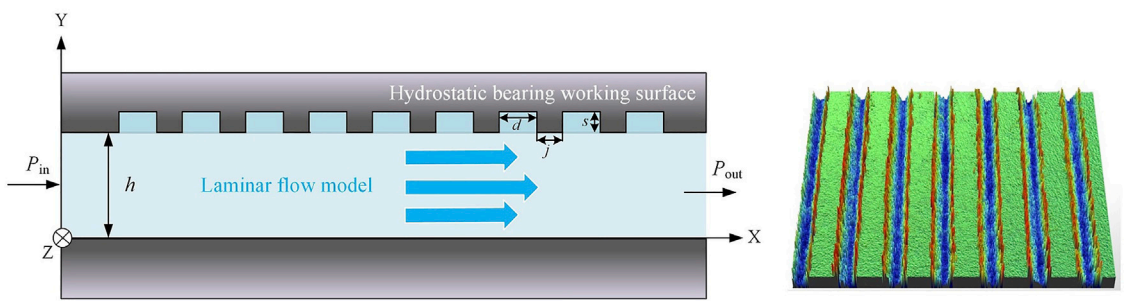

FIGURE 7 | Geometric model of the oil film of the hydrostatic bearing with a rectangular microgroove working surface.

bearings at a low speed (100 r/min) and a light load (less than 10 t) is no more than 3°C (Zhang et al., 2020), the temperature rise has little influence on the viscosity of pressure oil, so the viscosity of hydraulic oil η can be regarded as a constant value of 1.27×10^{-2} Pa s, and the pressure oil density ρ is 865 kg/m^3.

Grid Independence Verification

As shown in **Figure 5**, seven grids with different sizes of 2×10^{-3} mm, 1.5×10^{-3} mm, 1×10^{-3} mm, 8×10^{-4} mm, 6×10^{-4} mm, 5×10^{-4} mm, and 4×10^{-4} mm are selected for verification for the 2D simplified oil film model. As can be seen from the chart, when the element number reaches 1.2×10^5, the average velocity of the oil film flow field tends to be stable, and the relative error of the calculation results of two adjacent element sizes drops below 0.18%, which can be ignored. With the consideration of the simulation quality and efficiency, the element size is selected as 8×10^{-4} mm, the element number is 1.875×10^5, and the element quality and aspect ratio of the grid reached 0.995 and 1.0037, respectively. The grid quality meets the requirements.

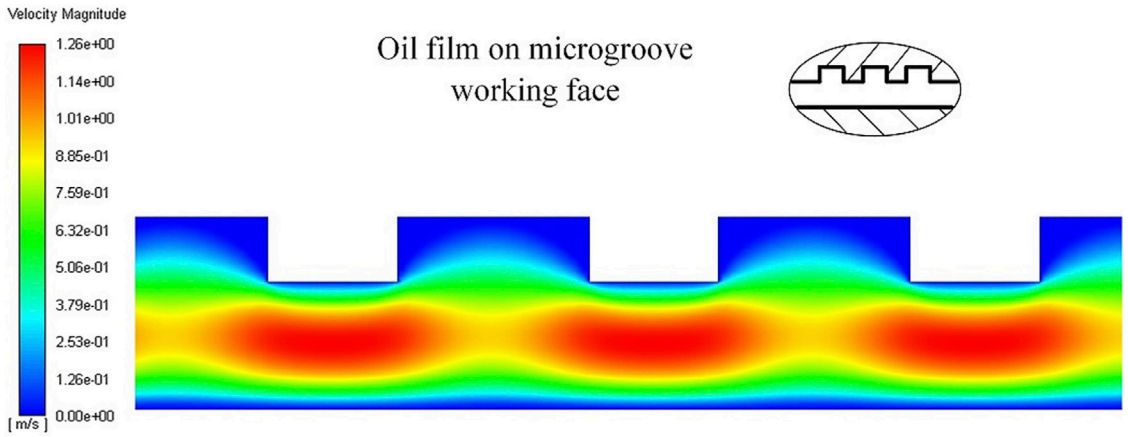

FIGURE 8 | Simulation results of the oil film velocity field of the hydrostatic bearing with a rectangular microgroove working surface.

TABLE 2 | Design scales of the rectangular microgroove (depth variation) and heat generation rate of the corresponding oil film.

Depth *s* (mm)	Span *d* (mm)	Spacing *j* (mm)	Heat Generation *H* (W)
0	0.03	0.02	3.0173
0.001	0.03	0.02	3.1630
0.002	0.03	0.02	3.2481
0.003	0.03	0.02	3.2890
0.004	0.03	0.02	3.2972
0.005	0.03	0.02	3.2815
0.010	0.03	0.02	3.0356
0.015	0.03	0.02	2.7412
0.020	0.03	0.02	2.4885

Reliability Verification of the Simulation Modeling Method

The reliability of the numerical simulation method above can be verified by comparing the simulation results of the oil film flow field with the calculation results of the flow analytical model established by Zhong and Zhang (2007).

Figure 6 shows the simulation results of the oil film velocity field of the hydrostatic bearing with a smooth working surface. The velocity along the flow direction is almost constant. Perpendicular to the flow direction (along the thickness direction), the flow velocity decreases from the middle of the flow field to the wall surface and presents a symmetrical distribution on the middle line of oil film thickness, that is, the flow velocity presents a symmetrical distribution trend of "large in the middle and small on both sides" along the thickness direction. This is consistent with the conic curve distribution corresponding to the flow velocity distribution equation (Zhong and Zhang, 2007), which lays a foundation for verifying the reliability of the simulation method. The average velocity can be obtained by calculating the area-weighted average of the flow field.

For the oil film of the hydrostatic bearing with a smooth working surface, it can be considered as a viscous fluid flowing in the double smooth plane gap h, and its flow rate Q_{smooth} is (Zhong and Zhang, 2007):

$$Q_{\text{smooth}} = \frac{Wh^3}{12\eta L}\Delta P \tag{3}$$

Thus, the average flow velocity of the flow field can be calculated:

$$v = \frac{Q_{\text{smooth}}}{Wh} = \frac{h^2}{12\eta L}\Delta P \tag{4}$$

Table 1 lists the comparison of the average velocity obtained by flow field simulation and analytical calculations under different working conditions for the oil film model of the hydrostatic bearing. The relative errors of both are less than 0.55%, which can be considered basically consistent, proving the reliability of the oil film flow field simulation method of hydrostatic bearings established above.

SIMULATION MODELING METHOD FOR THE OIL FILM FLOW FIELD OF THE HYDROSTATIC BEARING WITH A SMOOTH WORKING SURFACE

Simulation Modeling Method for the Oil Film Flow Field of the Hydrostatic Bearing With a Rectangular Microgroove Working Surface

As shown in **Figure 7**, based on the simulation method above, the geometric model of the oil film of the hydrostatic bearing with a rectangular microgroove working surface is established. First, the design dimensions of microgrooves are defined: the microgrooves on the working surface of hydrostatic bearings are processed by laser, and their cross-section shape along the Z-direction is rectangular. The side length of the rectangle along the flow direction is defined as

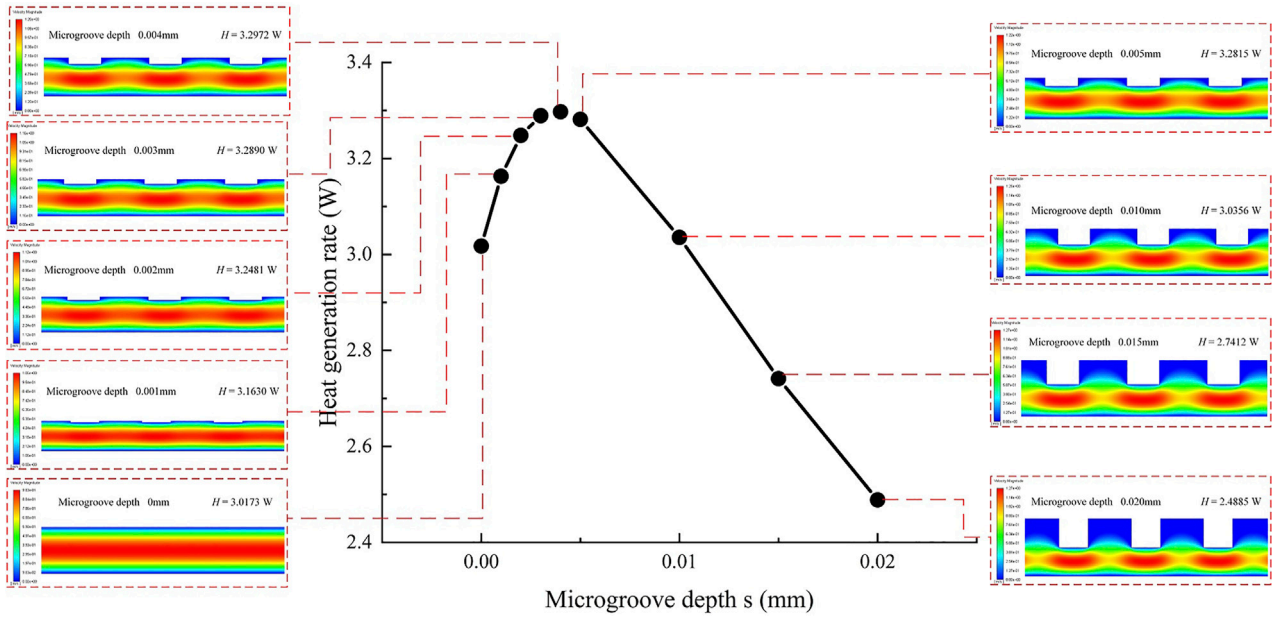

FIGURE 9 | Effect of depth variation of the rectangular microgroove on heat generation rate of the oil film.

TABLE 3 | Design scales of the rectangular microgroove (span variation) and heat generation rate of the corresponding oil film.

Depth *s* (mm)	Span *d* (mm)	Spacing *j* (mm)	Heat Generation *H* (W)
0.008	0	0.02	3.0173
0.008	0.005	0.02	2.8408
0.008	0.010	0.02	2.7965
0.008	0.015	0.02	2.8218
0.008	0.020	0.02	2.9055
0.008	0.025	0.02	3.0222
0.008	0.030	0.02	3.1462
0.008	0.040	0.02	3.3765

microgroove span d, the side length perpendicular to the flow direction is defined as microgroove depth s, and the distance between two adjacent edges with the smallest distance is defined as microgroove spacing j. On this basis, the design dimensions of rectangular microgrooves are empirically determined: depth s = 0.008 mm, span d = 0.03 mm, and groove spacing j = 0.02 mm.

Figure 8 shows the simulation results of the oil film velocity field of the hydrostatic bearing with a rectangular microgroove working surface. It can be seen that due to the existence of microgrooves, the velocity distribution of the oil film flow field is different from that of smooth working surface hydrostatic bearings. Along the flow direction, the velocity near the midline of thickness shows a periodic peak value and decreases in all directions with the peak value as the center, forming a periodic "velocity peak" which is located between the two microgrooves. Along the thickness direction, the velocity distribution is no longer symmetric about the thickness midline.

Modeling Method for Oil Film Heat Generation of Hydrostatic Bearings With a Rectangular Microgroove Working Surface

For the oil film of the hydrostatic bearing with a smooth working surface, the heat generation model can be established by substituting **Eq. 3** into **Eq. 2**:

$$H_{\text{smooth}} = \Delta P \cdot Q_{\text{smooth}} = \frac{Wh^3}{12\eta L}(P_{\text{in}} - P_{\text{out}})^2 \tag{5}$$

Similarly, the flow field simulation modeling method above is applied to the oil film of the hydrostatic bearing with a rectangular microgroove working surface. The area-weighted average of the flow field can be calculated to obtain the average flow rate, and then the flow rate Q_{micro} of the flow field can be calculated:

$$Q_{\text{micro}} = \bar{v} \cdot Wh \tag{6}$$

Since the flow is equal everywhere in the flow field, h is taken as the oil film thickness at the position without a microgroove for easy calculations.

By substituting **Eq. 6** into **Eq. 2**, the heat generation rate of the oil film can be calculated as

$$H_{\text{mirco}} = \Delta P \cdot Q_{\text{micro}} = (P_{\text{in}} - P_{\text{out}}) \cdot \bar{v} \cdot Wh \tag{7}$$

Here, the numerical simulation method and analytical modeling method are combined to establish the oil film heat generation model of the hydrostatic bearing with a rectangular microgroove working surface.

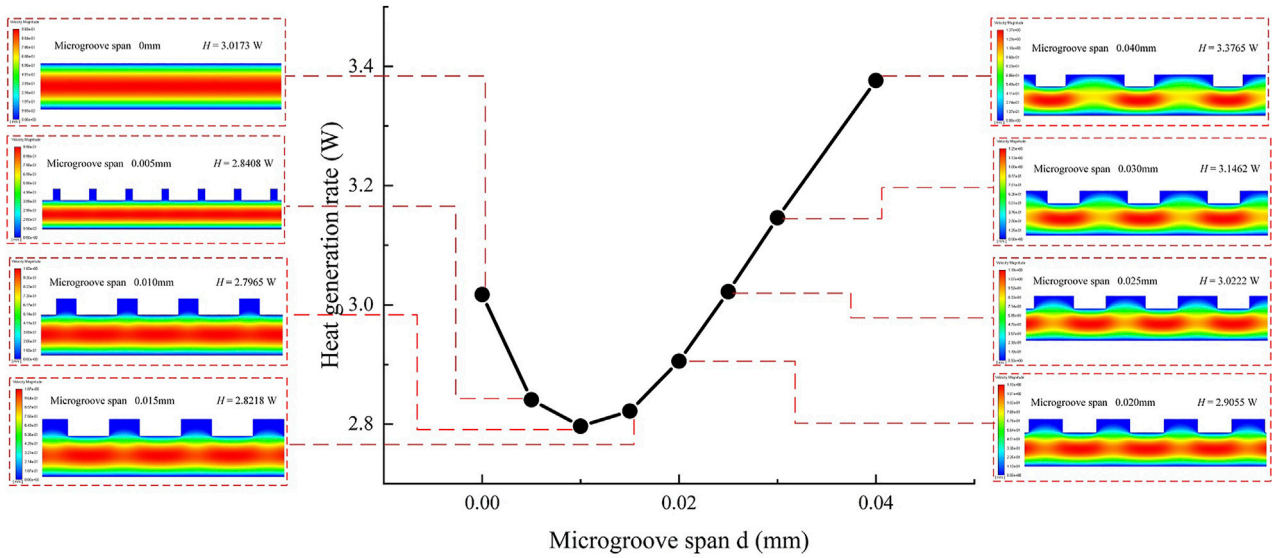

FIGURE 10 | Effect of span variation of the rectangular microgroove on heat generation rate of the oil film.

TABLE 4 | Design scales of the rectangular microgroove (spacing variation) and heat generation rate of the corresponding oil film.

Depth *s* (mm)	Span *d* (mm)	Spacing *j* (mm)	Heat Generation *H* (W)
0.008	0.03	0.005	3.3111
0.008	0.03	0.010	3.2510
0.008	0.03	0.015	3.1908
0.008	0.03	0.020	3.1462
0.008	0.03	0.040	3.0820
0.008	0.03	0.080	3.0406
0.008	0.03	0.160	3.0241
0.008	0.03	0.320	3.0196

EFFECT OF RECTANGULAR MICROGROOVE DESIGN SCALES ON HEAT GENERATION OF THE OIL FILM

On the basis of the numerical simulation method above and the heat generation modeling method, the control variable method is adopted to simulate the effect of design scale variation on oil film heat generation by constantly changing the design scales of microgrooves. In addition, the heat generation rate of the oil film of the hydrostatic bearing with the rectangular microgroove working surface is compared with that of the hydrostatic bearing with a smooth working surface to determine the design scales of the microgroove with heat generation inhibition functions.

Influence of Microgroove Depth Variation on Heat Generation of the Oil Film

Table 2 lists design dimensions of rectangular microgrooves of several groups. The microgroove span and spacing remain constant, and the depth increases by 0.001 mm from 0 and 0.005 mm from 0.005 mm. With the consideration of the actual processing difficulty and the relationship between microgroove depth and oil film thickness, the maximum microgroove depth is restricted to 0.02 mm because the oil film thickness is 0.02 mm. The corresponding heat generation rates are calculated and recorded in the table.

Figure 9 reveals the influence rule of depth variation of rectangular microgrooves on the heat generation rate of the oil film. The abscissa of the curve shows that in the design scales of the microgroove, depth *s* is a variable, and the other two quantities remain constant. The ordinate of the graph represents the heat generation rate of the oil film at this design scale. The simulation results corresponding to each data point are leaded by dotted lines and displayed intuitively on both sides of the curve. As the depth of the microgroove increases from 0, the heat generation rate of the oil film increases first and then decreases. When the depth increases to 0.01 mm, the heat generation rate approaches the value of the oil film on the smooth working surface and continues to decrease with the depth increase. When the depth is less than 0.004 mm, the shallow microgroove does not hinder the flow but affects the flow velocity gradient and increases the heat generation rate. On the contrary, when the depth is greater than 0.004 mm, the microgroove produces local liquid resistance, the flow velocity decreases, and the heat generation rate decreases. However, as the depth increases to 0.010 mm or more, part of the viscous fluid remains in the microgroove, which slows down the flow rate and decreases the heat generation rate significantly. In this case, the microgroove working surface has a thermal inhibition effect compared to the oil film on the smooth working surface.

Influence of Microgroove Span Variation on Heat Generation of the Oil Film

In **Table 3**, the microgroove depth and spacing remain constant, and the span increases gradually by an increment of 0.005 mm. In order to study the influence of microgroove span in a larger range,

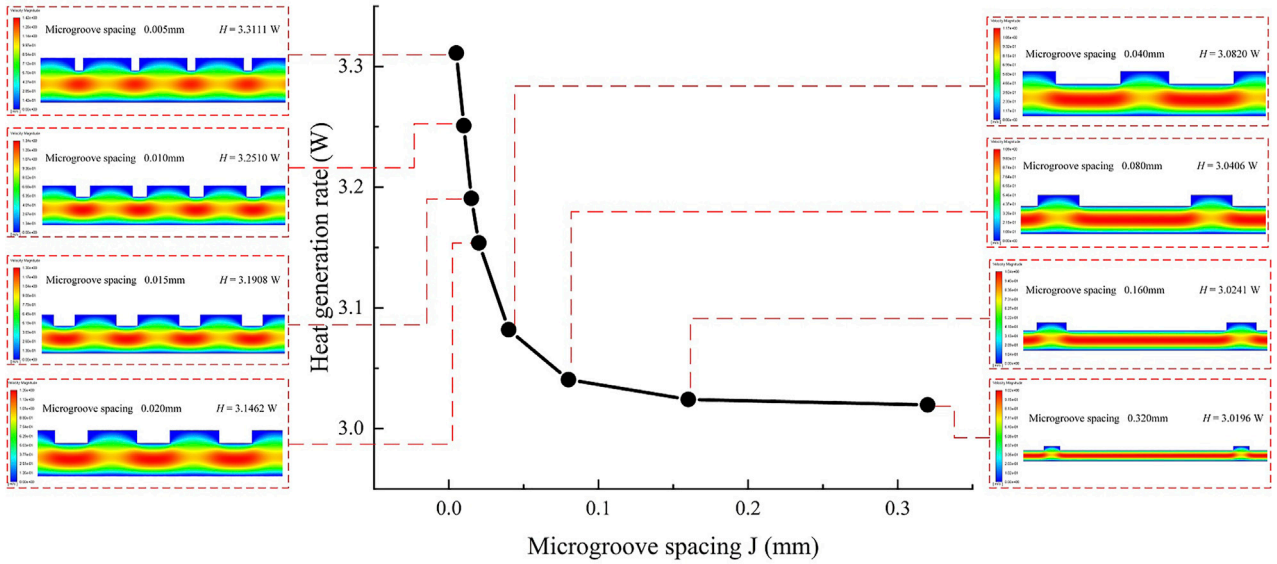

FIGURE 11 | Effect of spacing variation of the rectangular microgroove on heat generation rate of the oil film.

the span increases gradually by 0.01 mm after increasing to 0.03 mm.

The influence of span variation of the rectangular microgroove onto the heat generation rate is shown in **Figure 10**. The abscissa of the graph indicates that span *d* is a variable, and the remaining two quantities in the design scale remain constant. The ordinate of the graph represents the heat generation rate of the oil film at this design scale. As the microgroove span increases from 0, the heat generation rate of the oil film decreases first and then increases, and the turning point is 0.01 mm. After the span increases to 0.025 mm, the heat generation rate of the oil film approaches the value of the oil film on the smooth working surface and continues to increase. When the span is less than 0.01 mm, compared with the oil film on a smooth working surface, the microgroove produces local liquid resistance, which reduces the flow rate and heat generation rate. At this time, the microgroove working surface has the effect of heat generation inhibition. As the span of the microgroove gradually increases, the viscous fluid gradually flows fully in the groove, local liquid resistance decreases, the flow rate increases, and the heat generation rate begins to rise. When the span is larger than 0.025 mm, the microgroove begins to promote the flow and the heat generation rate continues to increase. At this time, the working surface of the microgroove no longer inhibits the heat generation.

Influence of Microgroove Spacing Variation on Heat Generation of the Oil Film

In **Table 4**, the depth and span of microgrooves remain unchanged, and the spacing increases gradually with an increment of 0.005 mm and presents a multiple growth after increasing to 0.02 mm so as to study the influence of spacing changes in a wider range on oil film heat generation.

Figure 11 shows the influence of spacing variation of rectangular microgrooves on the heat generation rate. The abscissa of the graph indicates that spacing *j* is a variable, and the remaining two quantities in the design scale remain constant. The ordinate of the graph represents the heat generation rate of the oil film at this design scale. As the distance between rectangular microgrooves increases from 0.005 mm, the heat generation rate continues to decrease and is always greater than the value of the oil film on the smooth working surface. It can be seen that compared with the oil film on the smooth working surface, the microgroove working surface of these design scales not only does not produce a heat generation inhibition effect but also promotes the flow and heat generation of the viscous fluid. However, with the increase of spacing, the number of grooves in the same process decreases, the decreasing rate of heat generation slows down, and the influence of microgrooves weakens. When the spacing increases to 0.32 mm, the heat generation rate of the oil film is close to the value of the oil film on the smooth working surface because the distribution of microgrooves is sparse enough to approximate the situation of the smooth working surface.

According to the above study, as the design scale of the microgroove changes, the working surface will affect the flow velocity gradient of the oil film flow field, making its heat generation rate greater or less than the value of the oil film on the smooth working surface, that is, to promote or inhibit the heat generation of the oil film. Therefore, with the appropriate scales of rectangular microgrooves, the working surface with microgrooves can reduce the average velocity of the viscous flow field of the hydrostatic bearing oil film and restrain its energy loss and heat generation.

CONCLUSION

In this study, the flow field simulation modeling method of the oil film of the hydrostatic bearing is established and verified by the analytical model. The method is applied to the oil film model of the hydrostatic bearing with a rectangular microgroove working surface, and the flow characteristics and velocity distribution of the oil film flow field are analyzed. Combined with the heat generation modeling method of the hydrostatic bearing oil film on the smooth working surface, the heat generation model of the hydrostatic bearing oil film on the rectangular microgroove working surface is established. On this basis, the influence of three design dimensions, namely, the depth, span, and spacing of rectangular microgrooves, on the heat generation of the oil film of hydrostatic bearings with a rectangular microgroove working surface is analyzed, and the conclusions are as follows:

1) The oil film simulation modeling method of hydrostatic bearings proposed in this study is verified and reliable. It can accurately calculate the average velocity of the oil film flow field, and the heat generation model established on this basis is reliable.

2) Compared with the oil film on the smooth working surface of the hydrostatic bearing, the working surface with appropriate rectangular microgroove design scales can reduce the average velocity of the oil film flow field and inhibit the energy loss and heat generation effect of the oil film.

3) Based on the method in this study, the design scale of microgrooves with heat generation inhibition effects can be obtained from the research results. Design scale range with heat generation inhibition effect: depth 0.010–0.020 mm and span 0–0.025 mm. With the increase of microgroove spacing, the heat generation rate decreases continuously and the working surface has no heat generation inhibition effect. The research results have a guiding significance for the design of microgroove working surfaces of the hydrostatic bearings with heat generation inhibition functions.

RESEARCH PROSPECT

The study of the oil film heat generation mechanism of hydrostatic bearings with a microgroove working surface can provide theoretical support for the design of microgroove working surfaces with heat generation inhibition functions. This research can be widely applied to the improvement of the key performance of high-end precision machinery, which is of great significance to the development of high-end manufacturing, national defense technology, aerospace, and other strategic fields, and has a broad application prospect.

DATA AVAILABILITY STATEMENT

The raw data supporting the conclusion of this article will be made available by the authors, without undue reservation.

AUTHOR CONTRIBUTIONS

TL and RD provide research ideas and guidance for CL and HQ. CL and HQ carried out all the calculation work and wrote the original manuscript. FC and ZZ are responsible for the revision of the paper. JZ and ZS designed the logical structure of the whole manuscript.

FUNDING

This study was supported by the National Natural Science Foundation of China (No. 52005152), the Natural Science Foundation of Hebei, China (No. E2021202117), the National Natural Science Foundation of China (No. 52105477), and the National Natural Science Foundation of China (No. 51875166).

REFERENCES

Huang, Z., Chen, L., Jia, Z. J., and Wang, L. P. (2019). Study on Thermal Characteristics of CNC Hydrostatic Turntable Oil-Film Considering Viscosity Effects. *J. Univ. Electro. Sci. Tech.* 48, 627–632. doi:10.3969/j.issn.1001-0548.2019.04.022

Ji, B., and Chen, J. (2012). *ANSYS ICEM CFD Mesh Division Technology Examples*. Beijing: China Water Resources and Hydropower Press, 78–82.

Kim, B.-S., Bae, G.-T., Kim, G.-N., Moon, H.-M., Noh, J.-P., and Huh, S.-C. (2015). A Study on the thermal Characteristics of the Grinding Machine Applied Hydrostatic Bearing. *Trans. Can. Soc. Mech. Eng.* 39, 717–728. doi:10.1139/tcsme-2015-0057

Kumar, V., and Sharma, S. C. (2017). Study of Annular Recess Hydrostatic Tilted Thrust Pad Bearing under the Influence of Couple Stress Lubricant Behaviour. *Int. J. Surf. Sci. Eng.* 11, 344–369. doi:10.1504/IJSURFSE.2017.10008356

Lin, Q., Bao, Q., Li, K., Khonsari, M. M., and Zhao, H. (2018). An Investigation into the Transient Behavior of Journal Bearing with Surface Texture Based on Fluid-Structure Interaction Approach. *Tribol. Int.* 118, 246–255. doi:10.1016/j.triboint.2017.09.026

Liu, C., and Hu, J. (2018). A FSI-thermal Model to Analyze Performance Characteristics of Hydrostatic Turntable. *Indu. Lubr. Tribol.* 70, 1692–1698. doi:10.1108/ILT-09-2017-0250

Liu, T., Gao, W., Tian, Y., Mao, K., Pan, G., and Zhang, D. (2015). Thermal Simulation Modeling of a Hydrostatic Machine Feed Platform. *Int. J. Adv. Manuf. Technol.* 79, 1581–1595. doi:10.1007/s00170-015-6881-0

Liu, Z. F., Zhan, C. P., Cheng, Q., Zhao, Y. S., Li, X. Y., and Wang, Y. D. (2016). Thermal and Tilt Effects on Bearing Characteristics of Hydrostatic Oil Pad in Rotary Table. *J. Hydrodyn.* 28, 11. doi:10.1016/S1001-6058(16)60662-5

Liu, Z., Wang, Y., Cai, L., Zhao, Y., Cheng, Q., and Dong, X. (2017). A Review of Hydrostatic Bearing System: Researches and Applications. *Adv. Mech. Eng.* 9, 168781401773053. doi:10.1177/1687814017730536

Liu, P., Chen, W., Su, H., and Chen, G. (2018). Dynamic Design and thermal Analysis of an Ultra-precision Flycutting Machine Tool. *Proc. Inst. Mech. Eng. B: J. Eng. Manuf.* 232, 404–411. doi:10.1177/0954405416645257

Tang, Y., Zhou, M., Han, Z. W., and Wan, Z. P. (2010). Recent Research on Manufacturing Technologies of Functional Surface Structure. *JME* 46, 93–105. doi:10.3901/jme.2010.23.093

Tang, H.-s., Yin, Y.-b., Zhang, Y., and Li, J. (2016). Parametric Analysis of thermal Effect on Hydrostatic Slipper Bearing Capacity of Axial Piston Pump. *J. Cent. South. Univ.* 23, 333–343. doi:10.1007/s11771-016-3078-0

Wang, Y., Zhao, Y., Cai, L., Liu, Z., and Cheng, Q. (2016). Effects of thermal and Hydrodynamic Characteristics of Heavy-Duty Rotary Table on the Hydrostatic Circular Pads. *J. Vibroeng.* 18, 4193–4206. doi:10.21595/jve.2016.17079

Yu, X., Zuo, X., Liu, C., Zheng, X., Qu, H., and Yuan, T. (2018). Oil Film Shape Prediction of Hydrostatic Thrust Bearing under the Condition of High Speed and Heavy Load. *Ind. Lubr. Tribol.* 70, 1243–1250. doi:10.1108/ILT-07-2017-0220

Yu, M., Yu, X., Zheng, X., and Jiang, H. (2019). Thermal-fluid-solid Coupling Deformation of Hydrostatic Thrust Bearing Friction Pairs. *Ind. Lubr. Tribol.* 71, 467–473. doi:10.1108/ILT-07-2018-0262

Zhang, Y., Kong, P., Feng, Y., and Guo, L. (2019). Hot Oil Carrying Characteristic about Hydrostatic Bearing Oil Film of Heavy Vertical Lathe in High Speed. *Indu. Lubr. Tribol.* 71, 126–132. doi:10.1108/ILT-03-2018-0091

Zhang, Y. Q., Feng, Y. N., Ni, S. Q., and Luo, Y. (2020). Temperature Rise Characteristics of Beveled Oil Pad Hydrostatic Bearing under the Influence of Hot Oil Carrying. *J. Huazhong Univ. Sci. Tech. Nat. Sci.* 48, 122–127. doi:10.13245/j.hust.200721

Zhong, H., and Zhang, G. (2007). *Design Manual for Hydrostatic Bearings*. Beijing: Electronic Industry Press, 6–9.

Conflict of Interest: The authors declare that the research was conducted in the absence of any commercial or financial relationships that could be construed as a potential conflict of interest.

Publisher's Note: All claims expressed in this article are solely those of the authors and do not necessarily represent those of their affiliated organizations or those of the publisher, the editors, and the reviewers. Any product that may be evaluated in this article or claim that may be made by its manufacturer is not guaranteed or endorsed by the publisher.

frontiers | Frontiers in Energy Research

ORIGINAL RESEARCH
published: 28 April 2022
doi: 10.3389/fenrg.2022.860337

Parametric Design Optimization of Reverse Thrust Blades and Analysis of Fluid-Solid Coupling

Yang Huicheng, Yang Qingzhen, Wang Canliang and Bai Jin*

School of Power and Energy, Northwestern Polytechnical University, Xi'an, China

The parametric design method of equal and unequal thickness reverse thrust blades is studied based on the cubic Bessel curve controlled by four control points. In order to improve the aerodynamic performance of the thrust reverser and reduce the structure weight, the geometry shape of the blade in the three-dimensional thrust reverser cascade assembly was optimized by using a genetic algorithm based on BP artificial neural network, and the fluid-structure coupling and modal analysis of the optimized thrust reverser cascade were carried out. The results show that: compared with the benchmark model, the thrust reverses of the optimized equal thickness and non-equal thickness blades are increased by 15.64 and 12.71%, respectively, and the flow rate increases by 11.32 and 13.52%, respectively; based on the optimized blade profile, increasing the number of stiffeners is more efficient than increasing the thickness of cascade assembly in the area of reducing the maximum stress and strain; Increasing the number of stiffeners and the thickness of cascade assembly can improve the first-order natural vibration frequency of the cascade assembly.

Keywords: reverse thrust blades, parametric design optimization, BP artificial neural networks, genetic algorithm, fluid-solid coupling

OPEN ACCESS

Edited by:
Lei Luo,
Harbin Institute of Technology, China

Reviewed by:
Qingjun Zhao,
Institute of Engineering Thermophysics (CAS), China
Jian Liu,
Central South University, China

****Correspondence:***
Yang Huicheng
yanghc@mail.nwpu.edu.cn

Specialty section:
This article was submitted to Advanced Clean Fuel Technologies, a section of the journal Frontiers in Energy Research

Received: *22 January 2022*
Accepted: *08 April 2022*
Published: *28 April 2022*

Citation:
Huicheng Y, Qingzhen Y, Canliang W and Jin B (2022) Parametric Design Optimization of Reverse Thrust Blades and Analysis of Fluid-Solid Coupling. Front. Energy Res. 10:860337. doi: 10.3389/fenrg.2022.860337

INTRODUCTION

The thrust reverser device can shorten the aircraft's landing distance, reduce the use of the brake device, prolong the life of the brake components, and enhance the ability of the aircraft to cope with emergencies, adverse weather conditions, and short runways (Reemsnyderj and Sagerser, 2015; Hall et al., 2006)'(Hall et al., 2006; Reemsnyderj and Sagerser, 2015). However, using a thrust reverser will lead to an increase in engine weight and fuel consumption rate. For cascade thrust reverser, the cascade is the core component to change the airflow direction and generate thrust. The aerodynamic performance of the blade in cascade directly affects the thrust reverser efficiency and thrust reverser. Therefore, the blade profile design is critical for cascade thrust devices. Improving the aerodynamic performance of the thrust device and reducing the structural weight is also an essential part of the research on the thrust reverser device.

Many scholars have done much work and made some progress in the research of thrust reversers. J. Butterfield et al. (Butterfield et al., 2003; Butterfield et al., 2004) established a multidisciplinary and multi-objective optimization design method with aerodynamics, structure, machining and cost control. He Yan et al. (He and Liu, 2010a; He and Liu, 2010b) studied the effects of two-dimensional blade parameters on the thrust reverser efficiency and flow coefficient. Zhou Li et al. (Zhou et al., 2015) systematically studied the effect of cascade installation angle on the performance of thrust devices. Chen Jun et al. (Chen et al., 2019) analyzed the effect of main cascade geometry parameters

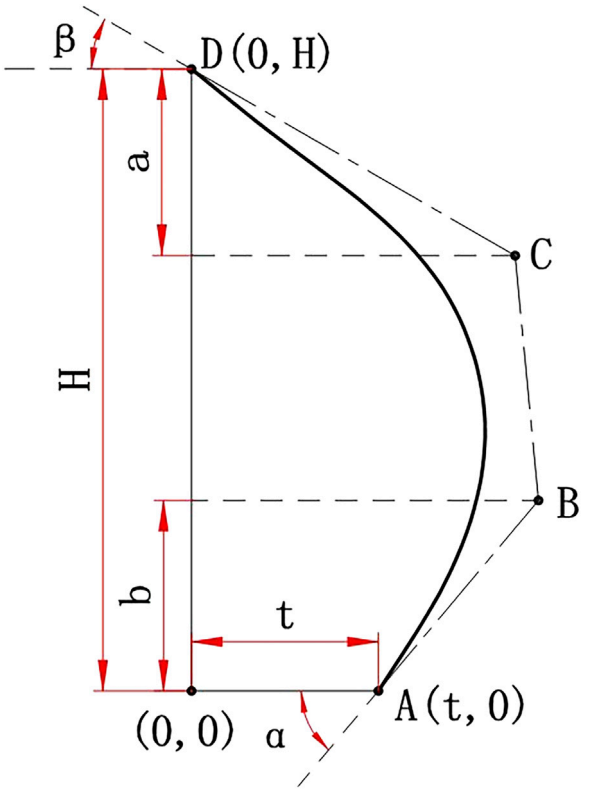

FIGURE 1 | Parametric representation of blade profile.

on the performance of thrust reversals. Zhang Yunhao et al. (Zhang and Eriqitai, 2012) did the aerodynamic/structural coupling analysis of the cascade of the thrust reverser, studied the influence of the cascade parameters on the thrust reverser efficiency, and the influence of blade number and stiffener number on maximum stress value and maximum deformation of a cascade. Compared with the research on two-dimensional blades in cascade thrust reverser devices, the parametric design optimization of three-dimensional equal thickness and unequal thickness thrust blades and their research on thrust performance is still insufficient at present. At the same time, the influence on the structural characteristics of thrust reverser cascade thickness has not been reported. Therefore, it is necessary to carry out research on parametric design optimization of thrust reverser blades and the structural characteristics of the optimized thrust reverser cascade.

In this paper, the blade profile of the cascade thrust reverser is designed by using the Bézier curve and the parameterized design idea. In order to improve the reverse thrust under the design condition, the blade shape is optimized by the genetic algorithm based on BP artificial neural network developed by the research group. Based on the optimal blade profile, the strength and stiffness of a single cascade with a different number of stiffeners and different thicknesses are checked by the unidirectional fluid-solid coupling analysis method and the modal analysis of cascade components is carried out.

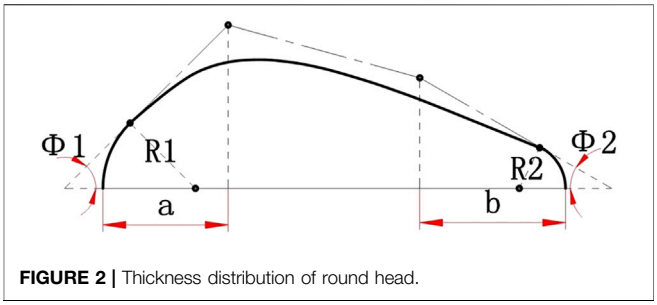

FIGURE 2 | Thickness distribution of round head.

BLADE PARAMETERIZATION METHOD

Blade of Equal Thickness

The traditional equal thickness blade comprises two arcs and a straight line. The geometric meaning of each parameter is evident, which can be generated directly by a geometric method. However, this method has limitations on the range of parameters, and only the first derivative of the profile curve is continuous. The aerodynamic performance of the blade profile is poor. Therefore, this paper uses the Bézier curve to describe the blade shape.

In order to meet the requirements of calculation accuracy and optimization efficiency, a cubic Bezier curve consisting of four control points is used to generate the blade. The disadvantage of this method is that the geometric meaning of design parameters (the x-coordinate, y-coordinate of the control point) is not apparent. The parameters such as inlet airflow angle and outlet airflow angle, which significantly influence blade performance, can not be given directly. To this end, as shown in **Figure 1**, two parameters are added, and the control point coordinates of the Bézier curve are converted into blade

TABLE 1 | Control point coordinates of thickness distribution law of Bézier curve.

	X-Coordinate	Y-Coordinate
Control point 1	$R_1\,(1 - sin\Phi_1)$	$R_1 \cos \Phi_1$
Control point 2	$R_1\,(1 - sin\Phi_1)$	$R_1 \cos \Phi_1 + a \tan \Phi_1$
Control point 3	$1 - R_2\,(1 - sin\Phi_2) - b$	$R_2 \cos \Phi_2 + b \tan \Phi_2$
Control point 4	$1 - R_2\,(1 - sin\Phi_2)$	$R_2 \cos \Phi_2$

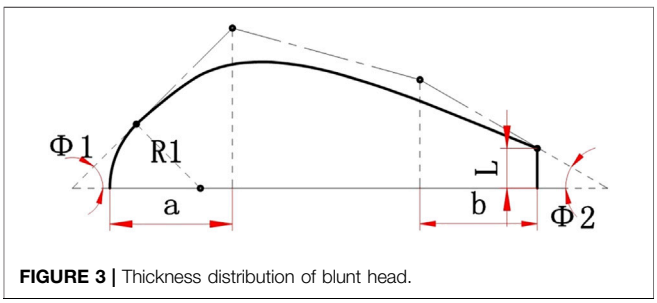

FIGURE 3 | Thickness distribution of blunt head.

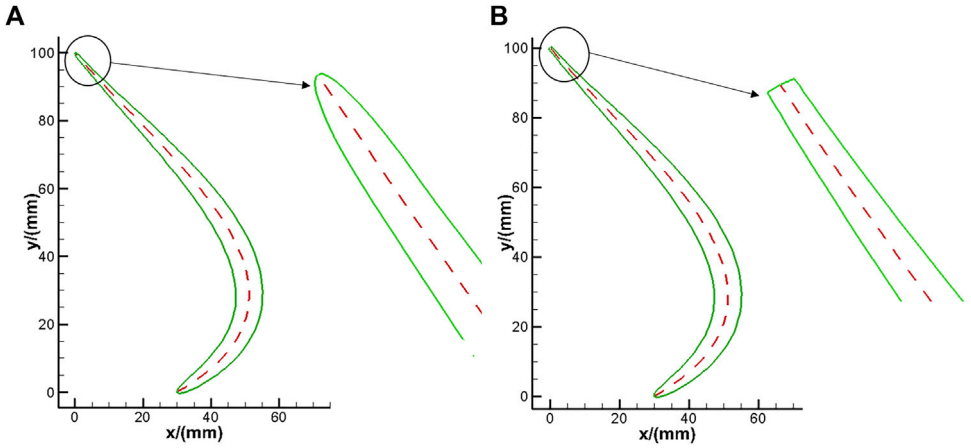

FIGURE 4 | The unequal thickness blade generated by the thickness distribution law of the round head. **(A)** round head **(B)** blunt head.

parameters with obvious geometric significance by using six design parameters.

The meanings of the parameters in **Figure 1** are as follows:

1) The inlet airflow angle α of the blade;
2) The outlet airflow angle β of the blade;
3) The relative position a of the Y coordinate of the point C;
4) The relative position b of the Y coordinate of the point B;
5) The blade-height H;
6) The axial spacing t between the upper and lower ends of the Blade.

The coordinates of the control points A, B, C, and D can be obtained from these six control parameters. Thus, the Bézier curve can be determined.

Blades of Unequal Thickness

Although the blade with equal thickness is easy to process, further aerodynamic performance improvement is neglected. In contrast, blades with different thicknesses can have a better aerodynamic shape, reducing the front and back edges of the blade to the obstruction of airflow.

Using the method of generating equal thickness blades described above generates the mid-arc of unequal thickness blades. Then the thickness distribution law of the blade is generated by using the Bézier curve, and the thickness law is attached to the middle arc to generate unequal thickness blades. As shown in **Figure 2**, the following six parameters are selected as design parameters:

1) Leading edge radius R1;
2) Trailing edge radius R2;
3) Leading edge angle Φ_1;
4) Trailing edge angle Φ_2;
5) The relative position a of the Y coordinate of the second control point
6) The relative position b of the Y coordinate of the third control point.

It is easy to know the coordinates of the control points of the Bézier curve (see **Table 1**), then the Bézier curve can be determined. That is, the thickness distribution law of the blade can be determined.

Sometimes the trailing edge of the blade is not circular but blunt. As shown in **Figure 3**, similar to the above round head thickness law generated, only the parameter of the trailing edge angle Φ_2 should be changed to the thickness L of the blade trailing edge, and the other five parameters should remain unchanged.

The coordinates of the two control points on the left of the Bézier curve are the same as above. The third control point coordinates are (1-b, $L/2 + b\tan\Phi_2$) and the fourth control point coordinates are (1, L/2).

After the thickness distribution law of the blade is determined, the blade with unequal thickness can be generated by superimposing it on the middle arc. **Figure 4** show two kinds of typical unequal thickness blades with a round head and blunt head and their local enlargement of trailing edge. It can be seen from the figure that the trailing edge of the blade with unequal thickness generated by the law of round generated by the law of is relatively smooth, while the trailing edge of the blade with unequal thickness generated by the thickness law of generated by the law of blunt head thickness has prominent sharp angles. Although it is not smooth, it is easy to manufacture the blade.

BLADE OPTIMIZATION

Optimistic Method

Taking the minimum value of function $y = x_1^2 - x_1x_2 + x_2^2$, $x_1, x_2 \in [-0.8, 0.8]$ as an example, the pseudo-parallel multi-population niche genetic algorithm with elitism preservation strategy based on BP artificial neural network is verified to test the nonlinear mapping ability, generalization ability of BP

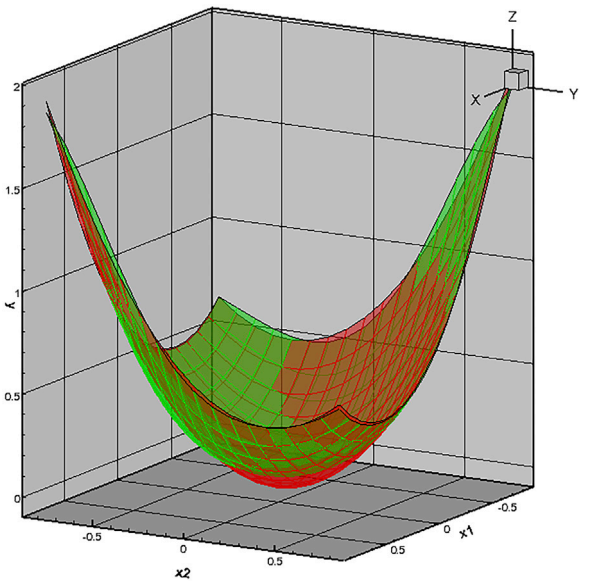

FIGURE 5 | Comparison between actual surface and fitting surface.

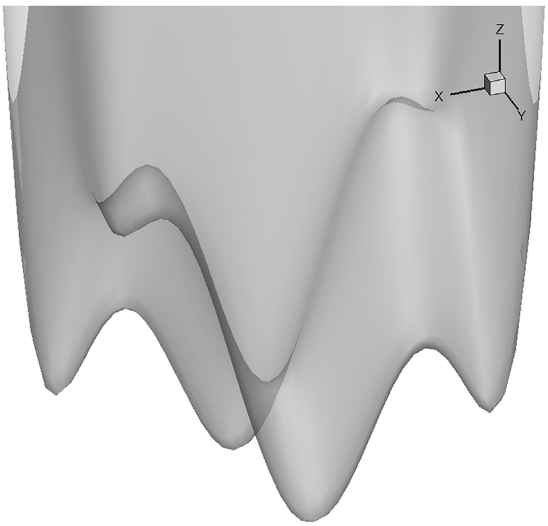

FIGURE 6 | Six-peak humpback function.

artificial neural network and the optimization ability of pseudo-parallel multi-population niche genetic algorithm with elitism preserving strategy. The uniform design U_{17} (17^{16}) (Fang, 1994; Zeng, 1994) is selected to arrange sampling.

As shown in **Figure 5**, it can be seen from the comparison results that the Bp artificial neural network designed by this algorithm meets the accuracy requirements at the sample points and has good generalization ability at non-sample points, which can accurately fit the surface. At the same time, the genetic algorithm finally obtains the minimum value of the function at (0.0003128, 0.008446), where the minimum value is 0.0324, while the actual minimum value of the function is at (0, 0) where the minimum value is 0. The results show that the optimization algorithm used in this paper has good optimization ability, and the minimum surface value in the definition domain can be estimated only through 17 sample points.

In order to verify the ability of the pseudo-parallel multi-population niche genetic algorithm with elite preservation strategy for the multi-peak function, the global minimum of six-peak value hump function $\min f(x, y) = (4 - 2.1x^2 + \frac{x^4}{3})x^2 + xy + (-4 + 4y^2)y^2\,(-3 \le x \le 3, -2 \le y \le 2)$ is solved as an example, the optimization algorithm used in this paper is further verified.

As the name suggests, the six-peak humpback function has six local minimum points (shown in **Figure 6**), the genetic algorithm finally gets the global minimum points (−0.0898, 0.7126), and (0.0898, −0.7126) with a minimum value of −1.031628. The error between the minimum fitness value of the genetic algorithm and the actual value is less than 10^{-5}, which shows that the optimization algorithm used in this paper has a better optimization ability.

Geometric Models and Numerical Methods

As shown in **Figure 7**, the CFM-56 engine, for example, each side of the thrust reverser has six cascades, which are not precisely the same.

In order to simplify the calculation, it is considered that the 12 cascades are the same and surrounded by 360°. The initial blade shapes of each cascade are: inlet angle $\alpha = 50^{\circ}$, outlet angle $\beta = 30^{\circ}$, leading edge radius R1 = 40 mm, trailing edge radius R2 = 30 mm, blade height H = 100 mm, the axial distance between the upper and lower end of blade t = 45 mm. The blade profile was designed by the parametric method described above, and the blade in the cascade can be obtained by stretching the profile. In order to use the periodic boundary condition conveniently in the flow-field calculation, half of the adjacent cascade is selected, and the stiffeners are surrounded in the middle. The final single cascade and its calculation area are shown in **Figure 8**.

As shown in **Figure 9**, the calculation area has meshed. The mesh encryption was carried out near the wall to ensure that the y+ of the boundary layer mesh is close to 1, and 0.83 million, 1.24 million and 3.01 million meshes are used to verify the mesh independence. Finally, 1.24 million meshes are selected as the calculation mesh. Numerical simulation of cascade flow-field using Fluent software. The three-dimensional steady Reynolds-averaged Navier-Stokes equation is selected as the control equation, while the density-based implicit algorithm is used to solve the equations, and the turbulence model is the SST $k - \omega$ model. When the residual falls below 10–4, the calculation is considered convergent. The inlet of the bypass duct is set as a pressure inlet, with a total pressure of 16 4002 Pa and a total temperature of 335.8 K. The far field is set as the pressure farfield boundary condition, the total pressure is 101,325 Pa, the total temperature is 288 K, and the airflow Mach number is set to 0.2. In addition, the walls are set as non-slip and adiabatic wall boundaries.

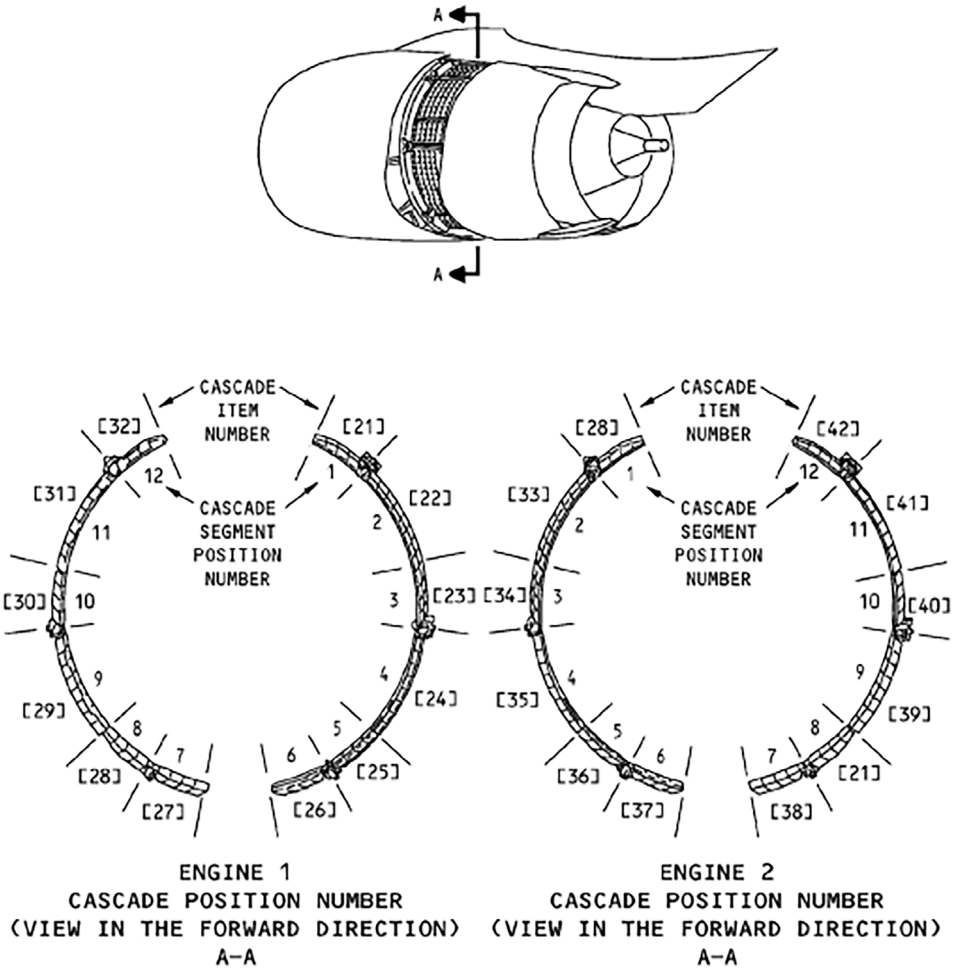

FIGURE 7 | Cascade assembly of CFM56.

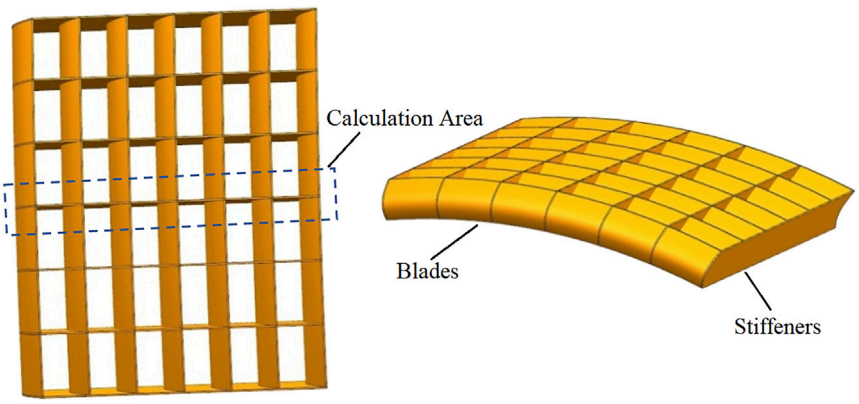

FIGURE 8 | Simplified single cascade and calculation area.

Optimized Results

The blade height H is a crucial design variable of the thrust cascade, and its size affects the thickness of the cascade, which is not used as an optimization variable here. The x coordinates of the four control points of the Bessel curve are used as the optimization variables to study the blades with equal thickness

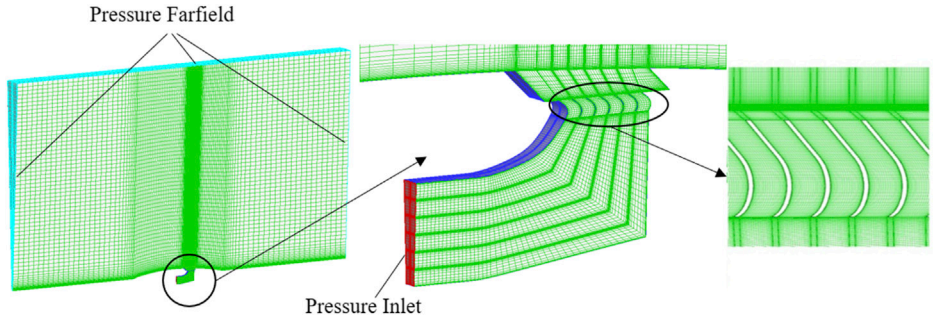

FIGURE 9 | Grid diagram of cascade calculation area.

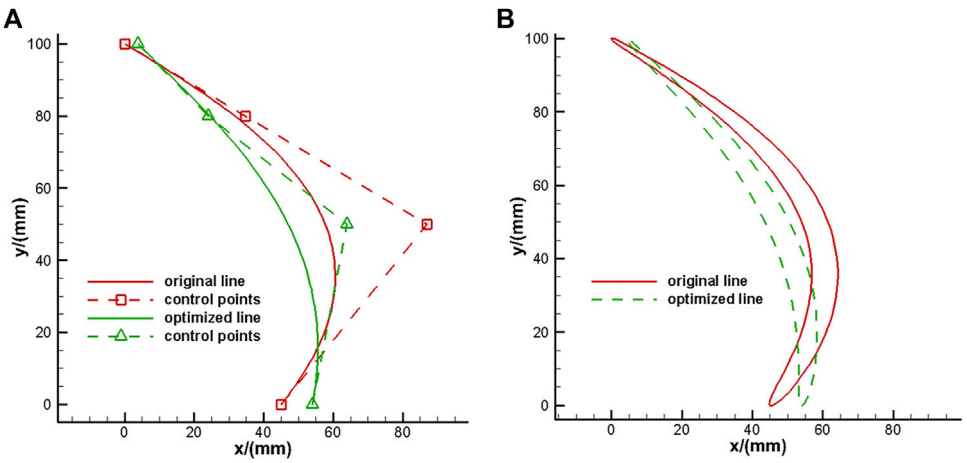

FIGURE 10 | Blade comparison. **(A)** Blades of equal thickness **(B)** Blades of unequal thickness.

and those with unequal thickness. The control point X coordinate of the initial leaf type is selected as the initial value of optimization, and the range of the X coordinate is preliminarily limited, as shown in **Table 2**. The flow field is calculated to obtain the aerodynamic performance parameters of different thrust devices. The optimization algorithm in this paper is used to optimize the design (Trelea, 2003; Han, 2006).

TABLE 2 | X-coordinate optimization range of control points (mm).

	Initialization Value	Minimum Value	Maximum Value
Control point 1	45	35	55
Control point 2	87	60	114
Control point 3	35	22	48
Control point 4	0	−8	8

Blades of Equal Thickness

The blade with equal thickness of the thrust reverser was optimized, and the optimal control point coordinates of the equal thickness blade are (3.918, 100), (24, 80), (64, 50), (54, 0). The comparison of the blade shape between the optimal individual and the benchmark model is shown in **Figure 10**.

The aerodynamic parameters of the optimum individual are shown in **Table 3**.

When the cascade spacing remains unchanged, the effective area at the cascade outlet increases with the optimal individual outlet flow angle, and the flow increases when the cascade outlet velocity does not change much. At the same time, the outlet area

TABLE 3 | Performance comparison of equal thickness blade.

	Reverse Thrust (N)	Flow Rate (kg/s)
Optimum individual	59619	323.92
Relative benchmark model improvement	15.64%	11.32%

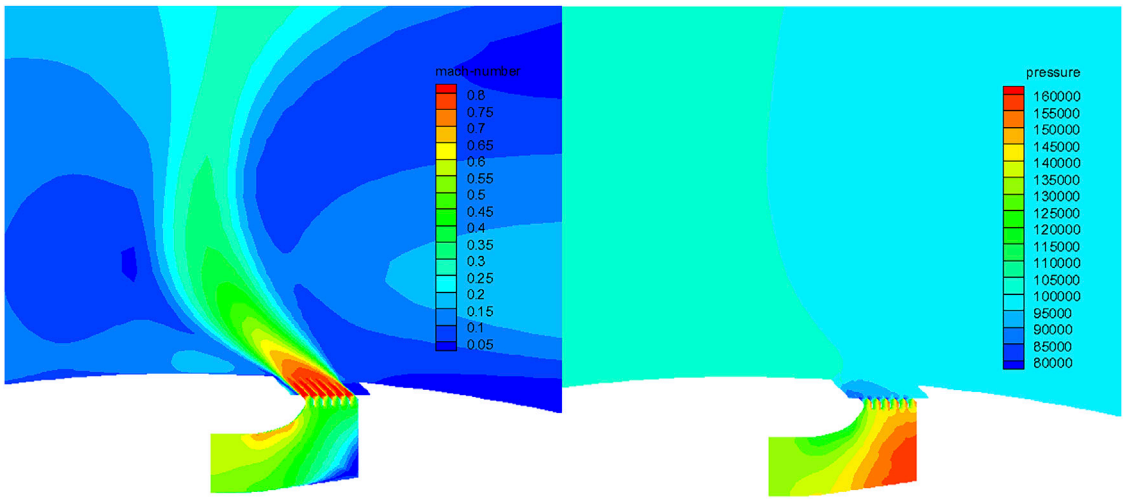

FIGURE 11 | Mach number distribution and static pressure distribution of optimal individual of equal thickness blade.

TABLE 4 | Performance comparison of unequal thickness blades.

	Reverse Thrust (N)	Flow Rate (kg/s)
Optimum individual	59831	331.17
Relative benchmark model improvement	12.71%	13.52%

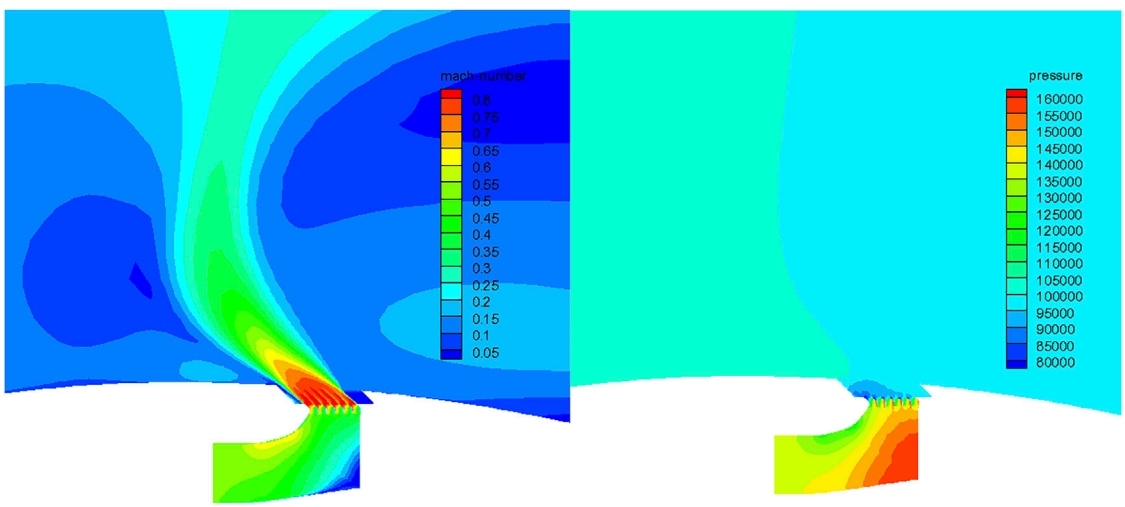

FIGURE 12 | Mach number distribution and static pressure distribution of the optimal individual of unequal thickness blades.

increases and the flow increases, but the inlet area of the bypass does not change, which will lead to the increase of the Mach number of the inlet airflow of the bypass. Therefore, there is a local high Mach number region appears in the upper wall of bypass in the Mach number distribution diagram in **Figure 11**, and accordingly, a corresponding low-pressure region appears in the static pressure diagram.

On the other hand, the increase of the outlet airflow angle will reduce the axial velocity of the outlet. That is, the direction of the outlet airflow is more deviated from the axial direction. Under the combined action of flow rate and outlet axial velocity, the optimal individual thrust reversals reach the maximum.

Blades of Unequal Thickness

The same method was used to optimize the design of the blade with unequal thickness of the thrust device. The coordinates of the control points for the optimal blade shape of the blade with different thicknesses are (4.259, 100), (24, 80), (64, 50), (54, 0).

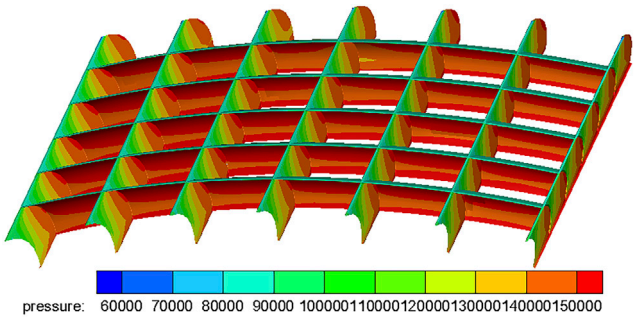

FIGURE 13 | The pressure distribution of the cascade.

The comparison of blade shape between the optimal individual and the benchmark model is shown in **Figure 10**.

The aerodynamic parameters of the optimum individual are shown in **Table 4**.

The Mach number distribution and static pressure distribution of the optimal individual are shown in **Figure 12**. It can be seen from the figure that there is a local high Mach number region on the upper wall of the bypass. Accordingly, there is a low-pressure region in the static pressure diagram. Similar to the thrust cascade with the same thickness blade, the optimal individual thrust reversals reach the maximum under the combined action of flow rate and outlet axial velocity.

The optimization results show that compared with the initial thrust device, the thrust reversals of equal thickness and non-equal thickness are increased by 15.64 and 12.71%, respectively, and the flow rate is increased by 11.32% 13.52%, respectively.

ANALYSIS OF STRUCTURAL CHARACTERISTICS

Taking cascades with the optimal equal thickness blade as an example, the one-way fluid-structure coupling analysis is carried out through the ANSYS Workbench, and the pressure distribution calculated by the flow field is loaded onto the cascades. The strength and stiffness of the cascades with different stiffeners and thicknesses are checked, and the modal analysis is carried out (Butterfield et al., 2006).

Fluid-Structure Coupling Analysis

In order to study the effect of the number of stiffeners on the strength and stiffness of a single cascade assembly, the number of stiffeners was changed to 5, 6, 7 (see **Figure 8**). The blade and stiffener are both equal thickness, and the thicknesses are divided into 3 and 4 mm to study the effect of thickness on the strength and stiffness of cascade assembly (Butterfield et al., 2006).

The pressure distributions on the cascades and the stiffeners are obtained by calculating the flow field of the cascades using the above method, as shown in **Figure 13**. It is also considered that the front and rear ends of the cascades are supported by a strong structure and treated as a fixed boundary condition. Moreover, the stiffeners on both sides of the cascades are supported by solid

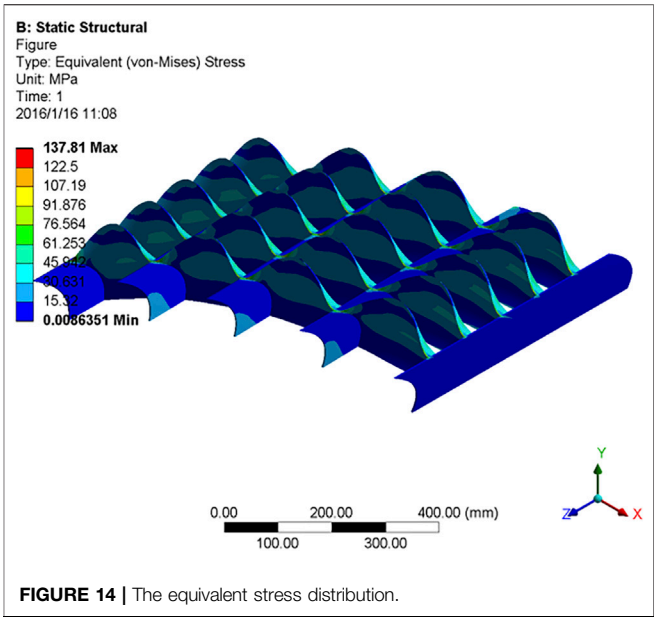

FIGURE 14 | The equivalent stress distribution.

TABLE 5 | The maximum stress of each model (MPa).

Thickness (mm)	Five stiffeners	Six stiffeners	Seven stiffeners
4	137.81	122.09	103.91
3	176.79	147.54	127.89

structures with significant stiffness. In order to simplify the calculation, fixed constraints are also applied. In addition to the surface with fixed constraints, the pressure distribution calculated by the flow field must be loaded on the other surfaces.

After setting constraints and loading pressure, the cascade's equivalent stress and total deformation can be solved. Since the airflow temperature at the backstepping cascade is low, the influence of thermal stress on the strength analysis of the cascade is ignored in this paper. Material is defined as structural steel, density $\rho = 7850kg/m^3$, elastic modulus $E = 2 \times 10^{11}Pa$, Poisson's ratio $\nu = 0.3$, tensile yield limit strength $\sigma_s = 2.5 \times 10^8 Pa$, tensile ultimate strength $\sigma_b = 4.6 \times 10^8 Pa$ (Lu et al., 2017; Liu et al., 2019).

The equivalent stress distribution is shown in **Figure 14** (taking five stiffeners with a thickness of 4 mm as an example). In the figure, the maximum stress value is located at the connection between the blade and the stiffener, while the stress value on the stiffener is minimal. At the same time, since the blades and stiffeners are of equal thickness, the corner at the joint is prone to stress concentration, so the improvement of these places should be considered first in structural optimization.

The maximum stress values of each model are shown in **Table 5**.

As shown in **Table 5**, the highest maximum stress value is the thickness of 3 mm, five stiffener cascade assembly, and lowest for the cascades with 4 mm thickness and seven stiffeners. It shows that increasing the thickness of blades and stiffeners and increasing the number of stiffeners can effectively reduce the

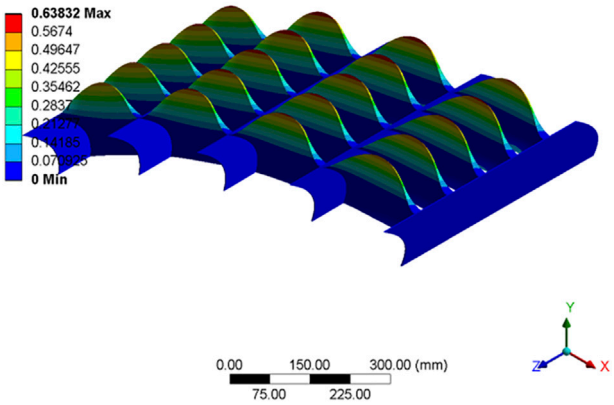

FIGURE 15 | The total deformation distribution.

TABLE 6 | Maximum deformation of each model (mm).

Thickness (mm)	Five stiffeners	Six stiffeners	Seven stiffeners
4	0.42409	0.27698	0.22941
3	0.63832	0.46823	0.34806

maximum stress value of cascade assembly, and the maximum stress values of each model are lower than the tensile yield ultimate strength of the material of 250 MPa.

The total deformation distribution of each model is shown in **Figure 15** (five stiffeners, thickness 3 mm, for example), where the deformation is overstated for clarity. It can be seen from the figure that the main deformation area occurs in the blade part between every two stiffeners, and the closer to the middle part, the greater the deformation. The deformation on the reinforced ribs is small. In this paper, structural steel is selected as the material, and its elastic modulus is relatively large, so the deformation is small.

The maximum deformation of each model is shown in **Table 6**.

As shown in **Table 6**, it can be seen that the highest maximum deformation is the thickness of 3 mm, five stiffener cascade assembly, and lowest for the cascades with 4 mm thickness and seven stiffeners. It shows that the maximum deformation of the cascade assembly can be effectively reduced by increasing the thickness of the blade and the stiffeners and increasing the number of the stiffeners.

Increasing the number of stiffeners or the thickness of the cascades assembly can undoubtedly improve the strength and stiffness of the cascade assembly, but it also leads to an increase in the weight of the thrust reverser device. The mass of each model is shown in **Table 7**.

As can be seen from **Table 7**, increasing the number of stiffeners or the thickness of the cascade assembly will increase

TABLE 7 | Mass of the cascade assembly (Kg).

Thickness (mm)	Five stiffeners	Six stiffeners	Seven stiffeners
4	24.1333	25.8821	27.7126
3	17.4348	18.6267	19.8182

TABLE 8 | Decrease in maximum stress due to increase in unit mass (MPa/Kg).

Thickness (mm)	Five stiffeners	Six stiffeners	Seven stiffeners
4	5.8192	6.4754	7.0910
3	—	24.5407	20.5169

TABLE 9 | Decrease in maximum deformation due to increase in unit mass (mm/Kg).

Thickness (mm)	Five stiffeners	Six stiffeners	Seven stiffeners
4	0.031982	0.042776	0.039786
3	—	0.142705	0.121784

the mass of the cascade assembly. At the same time, it can be found that, compared with increasing the number of stiffeners, the mass increase caused by increasing the thickness of the cascade component is more prominent. By comparing **Table 5** and **Table 6**, it can be identified that increasing the number of stiffeners has a higher efficiency-cost ratio than increasing the thickness of cascade assembly. Therefore, in practical application, the cascade assembly can be designed "Thin and dense" to reduce the weight and improve the economy.

In order to explain this problem quantitatively, the cascades assembly with five stiffeners and a thickness of 3 mm are taken as the benchmark to obtain the decrease of the maximum stress value and the maximum deformation caused by the increase of unit mass of other cascade assemblies, as shown in **Table 8** and **Table 9**.

Table 8 intuitively shows that increasing the number of stiffeners is more effective than increasing the thickness of cascade assembly in reducing the maximum stress value.

As shown in **Table 9**, compared with increasing the thickness of the cascade assembly, increasing the number of stiffeners has a higher efficiency-cost ratio in reducing the maximum deformation.

When the limit load is used as an external load on a structure, the safety factor of the general aircraft must be greater than 1.5. Therefore, in the numerical example selected in this paper, Considering the structural weight and structural safety factor of the engine thrust reverser device, the cascade assembly with seven stiffeners and a thickness of 3 mm can significantly reduce the maximum stress and maximum deformation while only bringing a slight structural weight increase. This cascade assembly has the best performance.

TABLE 10 | The first-order natural frequency of each model (Hz).

Thickness (mm)	Five stiffeners	Six stiffeners	Seven stiffeners
4	509.33	660.12	821.96
3	413.94	530.13	651.37

Modal Analysis

After the modal analysis of the cascade with flow-field pressure applied (Miao, 2019; Zhang et al., 2019), the first-order natural frequencies of each model are obtained, as shown in **Table 10**.

As can be seen from **Table 10**, the cascade assembly with a thickness of 3 mm and five stiffeners has the lowest first-order natural frequency; The highest first-order natural frequency is the cascade assembly with a thickness of 4 mm and seven stiffeners. It shows that increasing the thickness of the blade and the number of stiffeners improves the stiffness of cascade assembly and then improves the first-order natural frequency of cascade assembly.

CONCLUSION

In this paper, a cubic Bézier curve controlled by four points was selected for the parametric design of the blades of cascade thrust reverser device with equal thickness and unequal thickness. On this basis, the genetic algorithm based on Bp artificial neural network is used to optimize the geometric shape of the designed blade, and the structural statics analysis and modal analysis were carried out on the optimized cascade assembly of the thrust reverse device. The results show that:

1) When the cascade spacing remains unchanged and the cascade outlet velocity does not change much, the flow increases with the optimal individual outlet flow angle. On the other hand, the increase of outlet flow angle will reduce the outlet axial velocity when the outlet Mach number changes little. Under the combined action of flow and outlet axial velocity, the optimal individual thrust reverser reaches the maximum.
2) Compared with the benchmark model, the reverse thrust of the optimized blades with equal thickness and non-equal thickness increase by 15.64 and 12.71%, respectively, and the flow rate increases by 11.32 and 13.52%, respectively.
3) The blade strength meets the design requirements, and the number of stiffeners in reducing the maximum stress and deformation has a higher efficiency-cost ratio than increasing the thickness of the cascade assembly. Considering the thrust reverse device's structural weight and safety factor, the cascade assembly with a thickness of 3 mm and seven stiffeners has the best performance in the selected examples.
4) Increasing the number of stiffeners and the cascade assembly's thickness can increase the cascade assembly's stiffness and the first-order natural frequency of its vibration.

DATA AVAILABILITY STATEMENT

The raw data supporting the conclusion of this article will be made available by the authors, without undue reservation.

AUTHOR CONTRIBUTIONS

YH, YQ, and WC provide research ideas. YH write the original manuscript. YH and WC carried out all the calculation work. BJ and YQ are responsible for the revision of the paper.

FUNDING

The research work is financially supported by the fundamental research funds for the central universities (31020190MS708). This work was carried out at the School of Power and Energy, Northwestern Polytechnical University, China.

REFERENCES

Butterfield, J., Yao, H., Benard, E., Price, M., Cooper, R., Monaghan, D., et al. (2003). *Investigation of Weight Reduction in a Thrust Reverser Cascade Using Aerodynamic and Structural Integration [R]*. Norfolk: AIAA, 2003–1576.

Butterfield, J., Yao, H., Curran, R., Price, M., Armstrong, C., Raghunathan, S., et al. (2004). *Integration of Aerodynamic, Structural, Cost and Manufacturing Considerations during the Conceptual Design of a Thrust Reverser Cascade [R]*. Reno: AIAA, 2004–2282.

Butterfield, J., Yao, H., Curran, R., Price, M., Armstrong, C., and Raghunathan, S. (2006). Integrated Methods for the Design of a Thrust Reverser Cascade. *J. Propulsion Power* 22 (4), 862–871. doi:10.2514/1.14446

Chen, J., Han, L., and Shan, Y. (2019). Study on Reverse Thrust Performance in Cascade Thrust Reverser[J]. *Aeronaut. Comput. Tech.* 49 (02), 34–36+42.

Fang, K. (1994). *Uniform Design and Uniform Design table[M]*. Beijing: Science Press.

Hall, S., Cooper, R., and Raghunathan, S. (2006). "Fluidic Flow Control in a Natural Blockage Thrust Reverser[C]," in 3rd AIAA Flow Control Conference.

Han, L. (2006). *Course of Artificial Neural Network[M]*. Beijing: Beijing University of Posts and Telecommunications Press.

He, Y., and Liu, Y. (2010a). Effect of Blade Exit Angle and Pressure Ratio on Cascade Thrust Reverser Performance[J]. *Sci. Technol. Eng.* 10 (02), 458–465.

He, Y., and Liu, Y. (2010b). Effect of Blade Solidity and Pressure Ratio on Cascade Thrust Reverser Performance[J]. *Aeroengine* 36 (02), 16–21.

Liu, G., Yang, S., Wen, L., and Sun, Y. (2019). Static Analysis of Compressor Blade Based on Inverse Modeling [J]. *J. Mech. Eng.* 2019 (01), 50–53+56.

Lu, L., Qi, W., and Wang, L. (2017). Structural Designs and Statics Analysis of 2 MW Wind Turbine Blade[J]. *Mater. Sci. Technol.* 25 (03), 69–76.

Miao, Y. (2019). *Fault Mechanism Anasysis of Fan Blade Based on Fluid-Structure Coupling[D]*. Beijing: Beijing University of Technology.

Reemsnyderj, D. C., and Sagerser, D. A. (2015). Reverse Thrust Performance of a Variable-Pitch Fan Engine at Forward Velocity[J]. *J. Aircraft* 16 (12), 848–855.

Trelea, I. C. (2003). The Particle Swarm Optimization Algorithm: Convergence Analysis and Parameter Selection. *Inf. Process. Lett.* 85 (6), 317–325. doi:10.1016/s0020-0190(02)00447-7

Zeng, S. (1994). *Uniform Design and its application[M]*. Liao Ning: Liaoning People's Press.

Zhang, L., Liu, Y., Chun, L., and Deng, Y. (2019). Mechanical Performance Analysis of Wind Turbine Blade Web Based on Bionic Design [J]. *J. Eng. Therm. Energ. Power* 34 (09), 141–147.

Zhang, Y., and Eriqitai, Q. (2012). Aerodynamic and Structural Coupling Design for Cascade Configuration of Thrust Reverser[J]. *J. Shenyang Univ. Technol.* 34 (01), 56–62.

Zhou, L., Wang, Z., Ren, Y., and Liu, Z. (2015). Influence of Cascade Inlet Installation Angle on Performance of Blockerless Thrust Reverser[J]. *J. Eng. Thermophys.* 36 (12), 2589–2593.

Conflict of Interest: The authors declare that the research was conducted in the absence of any commercial or financial relationships that could be construed as a potential conflict of interest.

Publisher's Note: All claims expressed in this article are solely those of the authors and do not necessarily represent those of their affiliated organizations, or those of the publisher, the editors and the reviewers. Any product that may be evaluated in this article, or claim that may be made by its manufacturer, is not guaranteed or endorsed by the publisher.

frontiers | Frontiers in Energy Research

ORIGINAL RESEARCH
published: 05 May 2022
doi: 10.3389/fenrg.2022.879198

A Numerical Study on Mechanical Seal Dynamic Characteristics Within a Reactor Coolant Pump

Jun-Li Wang[1,2], *Xing-Yuan Chen*[1], *Maxime Binama*[1], *Wen-Tao Su*[1]* *and Jian Wu*[2]

[1]College of Petroleum Engineering, Liaoning Shihua University, Fushun, China, [2]School of Energy Science and Engineering, Harbin Institute of Technology, Harbin, China

Unstable flow within a reactor coolant pump (RCP)'s mechanical seal may cause the change of its sealing parameters, possibly threatening RCP's safe operations. In this study, based on the moving grid technology, a 3D fluid–structure interaction analysis model is established, where the influence of parameters such as the inlet pressure fluctuation, closing force fluctuation, and speed fluctuation on mechanical seal performance characteristics within an RCP is numerically studied. Study results have shown that when pressure and closing force fluctuations are applied, the static ring displacement, the inlet-to-outlet temperature difference, and the leakage difference show similar variational rules. In addition, it is found that the sealing parameters are more sensitive to the step form of fluctuation. When the step change of 4% closing force was applied, the static ring displacement was more than 36.7%, the change of the temperature difference between inlet and outlet zones exceeded 53.5%, and the leakage difference was more than 127.2%. The change of speed has also been found to significantly affect the temperature difference between the RCP mechanical seal's inlet and outlet, but the effect on the leakage and opening force was negligible.

Keywords: mechanical seal, dynamic characteristics, reactor coolant pump, numerical analysis, moving grid technology

OPEN ACCESS

Edited by:
Xiao Liu,
Harbin Engineering University, China

Reviewed by:
Tang Xuelin,
China Agricultural University, China
Lei Tan,
Tsinghua University, China
Jin-Hyuk Kim,
Korea Institute of Industrial Technology, South Korea

***Correspondence:**
Wen-Tao Su
suwentao@lnpu.edu.cn

Specialty section:
This article was submitted to Advanced Clean Fuel Technologies, a section of the journal Frontiers in Energy Research

Received: *19 February 2022*
Accepted: *29 March 2022*
Published: *05 May 2022*

Citation:
Wang J-L, Chen X-Y, Binama M, Su W-T and Wu J (2022) A Numerical Study on Mechanical Seal Dynamic Characteristics Within a Reactor Coolant Pump. Front. Energy Res. 10:879198. doi: 10.3389/fenrg.2022.879198

INTRODUCTION

The reactor coolant pump is one of the most critical equipment and the only rotating equipment in the primary circuit of the pressurized water reactor nuclear power plant, which transports and pressurizes the working fluid of the primary circuit (Liu et al., 2019). The reactor coolant pump works under high-temperature and high-pressure conditions, in a radioactive environment with high technical requirements. Nuclear material leakage is one of the biggest hidden dangers of nuclear power plants. **Figure 1A** schematically shows the main components of a reactor coolant pump. The shaft seal is composed of three similar mechanical seals in series. A single mechanical seal is mainly composed of a stationary ring and rotating ring, as shown in **Figure 1B** (Su et al., 2020). For the sake of addressing some of the operational problems such as wear, elastic deformation, and thermal deformation, the design of the sealing end face geometry involves some radial and circumferential deviations. The deviation from the plane in the radial direction is called taper, and the deviation from the plane in the circumferential direction is called waviness. The radial taper directly determines the load supported by hydrostatic pressure, which determines the thickness and performance of the film. Waviness has a great impact on hydrodynamic lubrication and can produce strong hydrodynamic pressure carrying capacity (Lebeck, 1991; Cochain, 2018), which makes the seal produce sufficient opening force and is used for the sealing of

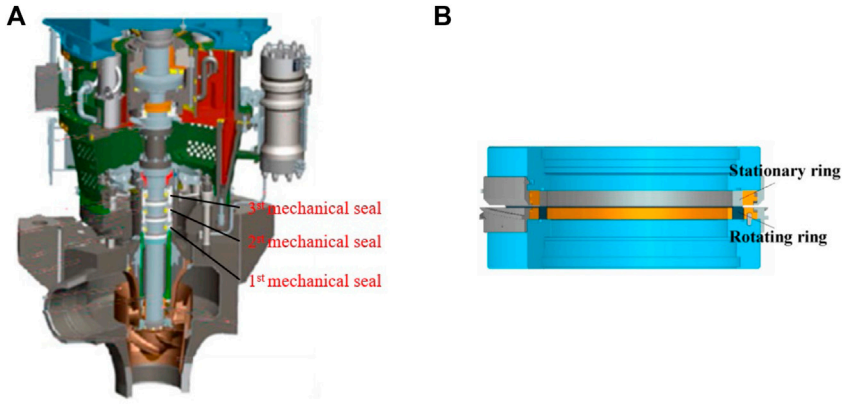

FIGURE 1 | Illustrations of **(A)** the typical reactor coolant pump and **(B)** the mechanical seal assembly structure (Su et al., 2020).

high-parameter machinery such as reactor coolant pump. Many scholars have conducted a large number of studies on the mechanical seal of reactor coolant pumps, including the influence of structural parameters on mechanical seal performance (Liu et al., 2011), the problem of work–heat conversion and heat conduction considering viscosity–temperature effect (Brunetière and Modolo, 2009; Ma et al., 2021), the multiphase flow caused by cavitation (Liu et al., 2015), the fluid–solid thermal coupling problem considering mechanical stress and thermal stress (Liao et al., 2011), and manufacture and experiment of mechanical seal (Feng et al., 2020; Guang and Ma, 2021). These studies mainly focus on the steady-state process of the flow field inside the mechanical seal of the reactor coolant pump. However, the reactor coolant pump presents strong unsteady characteristics during startup (Gao et al., 2013) and sliding (Lu et al., 2019), and the parameters such as speed, head, and temperature change drastically. Even under rated operating conditions, unstable vortex and vortex shedding inside the reactor coolant pump will also cause severe pressure pulsation and unit vibration (Ni et al., 2017; Ni et al., 2020; Zhou et al., 2021). The rotating speed of the reactor coolant pump, temperature of sealing medium, pressure pulsation, and vibration of unit will affect the mechanical seal.

In recent years, unsteady flow field characteristics in reactor coolant pumps' mechanical seals have increasingly attracted the attention of scholars. Liu et al. (2013) established a three-dimensional theoretical model to study the influence of the initial position and velocity of the static ring on the dynamic performance of the waveform end mechanical seal of the reactor coolant pump and found that the amplitude of the static ring was an important parameter affecting the performance of the rotating ring. Falaleev and Vinogradov (2015) established a dual-mass dynamic model applicable to the mechanical seal end face and analyzed the dynamic characteristics of seal theoretically and experimentally. Migout et al. (2015) studied the influence of rising inlet water temperature on mechanical seal through numerical simulation. Their results showed that the mechanical seal oscillated when the inlet water temperature was raised to 170°C, with a minimum film thickness change of 25% and a more significant flow rate change, but the liquid film temperature change was not significant. Chávez and De Santiago (2020) conducted an experimental study on the mechanical seal and obtained the pressure response function under 5–440 Hz excitation by pressure sensor measurement. In addition, the numerical predictions of the pressure response function were conducted at two different static supply pressures and two different dynamic pressures. These predictions indicate that the static supply pressure has no effect on the dynamic pressure response function and that the dynamic response is linear with respect to the dynamic input pressure. Luo et al. (2020) studied the relationship between fault degree and dynamic characteristics of a reactor coolant pump by theoretical analysis and numerical simulation. Their results showed that extrusion failure is more likely to occur when the liquid film thickness is too large or too small, and the opening force is both affected by the lubrication state of the liquid film and the degree of sealing extrusion failure. With the increase in rotating speed, leakage failure may occur in the seal, and the fluctuation of leakage growth reflects the severity of the failure. Blasiak and Zahorulko (2016) used numerical methods to solve the nonlinear Reynolds equation and the motion equation of the static ring and then comparatively studied the characteristics of four mechanical seals with different end faces. The results showed that for some specific conditions, the sharp increase in angular vibration amplitude leads to the contact of rotating and static rings, and the reasonable selection of parameters can significantly reduce the amplitude of stator angular vibration. Chen et al. (2017) used numerical methods to study the disturbance behavior of gas film thickness and pressure of mechanical seals with or without angular excitation, where it was found that the dynamic wedge clearance with a fixed angle between sealing surfaces would be formed under the action of angular excitation. Li et al. (2020) established a 3-DOF dynamic model considering the cavitation effect, extrusion effect, and end face contact, where the dynamic response of a spiral groove liquid film seal under three impacts (pressure change, shaft drift, and shaft bending) was studied. The results showed that the mechanical seal can keep the hydrodynamic lubrication state without surface contact when the pressure Gaussian pulse changes. But it will cause excessive

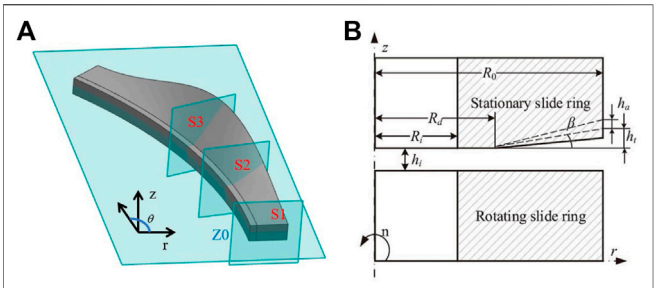

FIGURE 2 | Illustrations of **(A)** the geometry of the wave-tilt-dam mechanical seal and **(B)** schematic of the mechanical seal (Liu et al., 2011).

leakage when the axial drift and bending impact conditions occur. Badykov et al. (2018) took the mechanical secret recipe with rotary grooves as the research object and introduced the fluid–structure coupling simulation method, where the Reynolds average Navier–Stokes equation and the rigid body motion dynamics equation were solved. They investigated the response of the stationary ring and the change of film thickness under different excitation signals applied by the rotating ring.

It can be seen from the aforementioned research status and associated analysis that although some scholars have carried out research on the dynamic characteristics of mechanical seals, there are few studies on mechanical seals that require higher safety performance and working ranges such as reactor coolant pumps. Moreover, many studies have only focused on the theoretical analysis of simplified models. Therefore, in this study, the dynamic characteristics of a waveform end face mechanical seal in a reactor coolant pump are numerically studied by unsteady computational fluid dynamics. The rigid body dynamic equations and Navier–Stokes equations were numerically solved by fluid–structure coupling method, and the dynamic grid technology was introduced to deal with the dynamic motion of the rotating ring. The inlet pressure fluctuation, closing force fluctuation, and mechanical seal dynamic characteristics of reactor coolant pump during the start–stop process were studied. This study and associated findings considerably contribute to an in-depth understanding of mechanical seal operating mechanism and associated design optimization within reactor coolant pumps.

First, based on the dynamic grid technology, the three-dimensional fluid–structure coupling model of the mechanical seal of the reactor coolant pump is established, and the grid independence is verified. Then, the effects of inlet pressure and closing force fluctuations on the mechanical seal's performance characteristics and the internal flow field structure are analyzed. Finally, the influence of speed change on the mechanical seal performance of the reactor coolant pump is studied.

THEORETICAL MODEL

Geometry Model

The mechanical seal is composed of a rotating ring, a sealing cavity, and a fixed static ring. The end face of the rotating ring is processed into a flat plane, while the surface of the static ring is processed into a convergent end face with a taper or amplitude. Static and dynamic pressure effects occur when the sealing medium flows through the gap between dynamic and static rings.

Figure 2 shows a wave–tilt–dam mechanical seal structure diagram. The thickness of liquid film in the gap of the sealing ring can be expressed by the following formula:

$$h = \begin{cases} h_i & R_i \le r \le R_d \\ h_i + (r - R_d)(1 - \alpha \cos k\theta) \tan\beta & R_d \le r \le R_o \end{cases} \quad (1)$$

where R_o and R_i are the outer and inner diameters of the sealing ring, respectively; R_d is the turning radius; r is the radius at any point; β is the taper of the stator face; the tangent of β can be expressed as $\tan\beta = h_t/(R_o - R_d)$, in which h_t is the taper height of outer radius; k is the wavenumber; and the dimensionless parameter $\alpha = h_a/h_t$ is set to 0 when there is no wave on the face and to 1 when the wave amplitude is equal to the taper height of outer radius, in which h_a is the wave amplitude. The basic geometric parameters are given in **Table 1** and are taken from a previous work (Liu et al., 2011).

Seal leakage is one of the key parameters that represent the mechanical seal's performance. For the fluid mechanical seal, if the leakage is too small, the end faces of the seal ring may directly contact, thus causing the wear of the seal ring. If the leakage is too large, the seal fails. In numerical simulation, the leakage is calculated by monitoring the flux at the outlet, that is, $r = R_i$:

$$M = \int_0^{2\pi} \int_0^h r\rho V_r \mathrm{d}z\mathrm{d}\theta \quad (2)$$

Sealing opening force represents the bearing capacity of the liquid film in the seal ring clearance, and it can be obtained by integrating the liquid film pressure along the end face of the seal:

$$F_{open} = \int_0^{2\pi} \int_{R_i}^{R_0} r p \mathrm{d}r\mathrm{d}\theta \quad (3)$$

The temperature of the sealing medium has a significant effect on the mechanical seal of a reactor coolant pump. Too high working medium temperature would cause vaporization of the liquid film, which leads to the vibration of the sealing surface during operation, and subsequent sealing failure. High working medium temperature would also cause thermal deformation of the sealing ring, thus increasing the friction, and further deterioration of the working environment. The temperature of the working medium increases gradually along the flow direction,

TABLE 1 | Geometric parameters of hydrostatic seal (Liu et al., 2011).

Parameter	Value
Outer diameter R_o (mm)	151.25
Inner diameter R_i (mm)	140.25
Turning radius R_d (mm)	142.25
Taper β (μrad)	650
Wave number k	9
Amplitude h_a (μm)	3.5
Speed n (rpm)	1,500

so the maximum temperature usually occurs at the outlet. In this study, the average temperature difference between the seal's outlet and the inlet zones is used as one of the parameters to measure the performance of mechanical seals, which is defined as follows:

$$\Delta T = \bar{T}_{outlet} - \bar{T}_{inlet} \tag{4}$$

Governing Equations

For the unsteady flow of incompressible Newtonian fluid, its governing equation includes the following:

Continuity equation:

$$\nabla \cdot \boldsymbol{u} = 0 \tag{5}$$

where $\boldsymbol{u}$ is velocity vector.

Momentum equation:

$$\frac{\partial \boldsymbol{u}}{\partial t} + \nabla \cdot (\boldsymbol{u}\boldsymbol{u}) = -\frac{1}{\rho}\nabla p + \nu \nabla^2 \boldsymbol{u} \tag{6}$$

where p is the pressure, ρ is density, t is time, and ν is kinematic viscosity.

Energy equation:

$$c_p \frac{\partial (\rho T)}{\partial t} + c_p \nabla \cdot (\rho \boldsymbol{u} T) = \lambda \nabla^2 T + \Phi \tag{7}$$

where $\boldsymbol{c_p}$ is specific heat capacity, $\boldsymbol{\lambda}$ is the heat conduction coefficient of the sealing medium, and Φ is the dissipation function, or otherwise, the heat from end face viscous shear friction. The latter is expressed as follows:

$$\Phi = \mu_m \left[\nabla \boldsymbol{u}_m + (\nabla \boldsymbol{u}_m)^T\right] \odot \nabla \boldsymbol{u}_m \tag{8}$$

The stator moves rigidly along the axial direction, and the equation of motion is as follows:

$$m\ddot{z} + F_{open} + F_{close} = 0 \tag{9}$$

where m is the static sub-mass; F_{open} is the opening force, which is positive along the positive direction of z-axis; and F_{close} is the opening force, which is negative along the z axis.

Boundary Conditions

During the operation, the rotating ring rotates, and the static ring is fixed with the sealing cavity. Therefore, the static ring surface is set with no slip boundary condition, while the rotating ring is set with a rotating speed of 1,500 rpm. The inlet and outlet boundary conditions are set to pressure inlet and pressure outlet, respectively. When the inlet pressure fluctuation is not considered, the total inlet pressure is 5 MPa, and the outlet static pressure is set as 101325 Pa. The total inlet temperature is set to 323.15 K. Due to the fact that the geometric model of the investigated mechanical seal's wavy end face has periodicity, a period is selected in the calculation, leading to a periodic boundary condition with a period of 40° (Su et al., 2020).

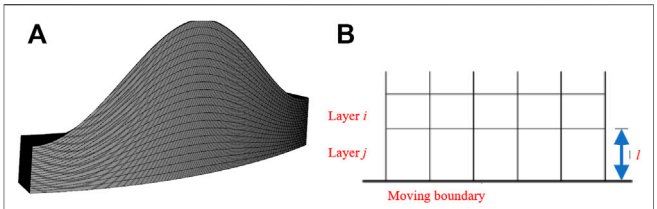

FIGURE 3 | Schematic diagram of grid **(A)** computational domain grid and **(B)** dynamic layer grid update method.

Numerical Method

In this study, numerical simulations are performed with Fluent software. The finite volume method is used to discretize the equations in time and space. The SIMPLE algorithm is used to decouple pressure and velocity. The second-order discrete scheme is used for the spatial discretization of pressure field, while the second-order upwind discrete scheme is applied to both the momentum and energy equations. Only the laminar flow calculation model is considered. The equation of motion is solved by using the Newmark-β method. For unsteady calculation, different time steps are selected to calculate the mechanical seal without disturbance. When the time step was 4×10^{-6} s, the Courant–Friedrichs–Lewy (CFL) number in most areas of the computational domain is less than 1, so the time step of unsteady calculation was set as 4×10^{-6} s, and the residual error of each time step was reduced to 10^{-4} or the calculation was completed at 50 iterations.

Ansys Fluent's dynamic mesh method module provides three features, namely, smoothing, layering, and remeshing, which are respectively, applied to different situations. The core of the layering method is to split (or merge) after stretching (or compressing) to realize the motion of the boundary. There are two methods of updating the grid: one is based on the mesh height and the other based on the mesh ratio. The process involved in the height-based dynamic layer update method is as follows: First, it is assumed to exist at an ideal height l_i on the motion boundary that needs to be updated. The boundary movement eventually leads to the grid being stretched or compressed. As shown in **Figure 3A**, when the mesh height $l > (1 + \varepsilon_s)l_i$, the mesh is divided into two grids. On the other hand, when the border height $l < (1 + \varepsilon_c)l_i$, the grid merges with the next grid. The ε_s and ε_c are compression and separation factors, respectively. The ratio-based dynamic layer update method is suitable for situations where the same layer mesh is inconsistent because the motion boundary is irregular. Similar to the height-based dynamic layer grid update, this method follows the ratio between adjacent layer grids between different locations when updating the grid. In this study, the mesh was separated and merged based on the mesh height, and the maximum mesh height could not exceed 1.4 times the original height during the mesh update process.

In the numerical simulation, the grid independence was verified by changing the number of axial, radial, and circumferential grids, as shown in **Table 2**. In this study, wave–tilt–dam mechanical seals with a base film thickness of

TABLE 2 | Grid number in different examples.

Case	Axial	Radial	Circumferential	Grid number (×10^4)
1	5	125	160	10
2	10	250	240	60
3	15	375	320	180
4	20	500	400	400
5	25	625	480	750

5 μm are selected for the grid independence verification. **Figure 4** shows the evolution of both inlet-to-outlet temperature difference and leakage with the increasing grid number. It can be seen that for both cases as the grid number increases, both the inlet-to-outlet temperature difference and leakage go through a brief steep variation before stabilizing for a wider range of grid numbers. When the computational domain grid increases from 4 million to 7.5 million, inlet-to-outlet temperature and leakage change by 0.13 and 0.14%, respectively. Therefore, the grid of 4 million nodes has been selected for further numerical calculations under different working conditions.

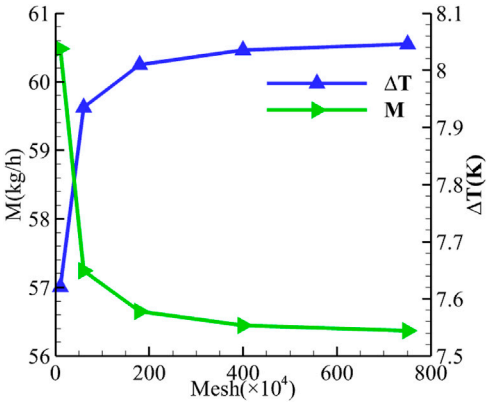

FIGURE 4 | Variation of M and ΔT as the mesh increases.

RESULTS AND DISCUSSIONS

In this research, typical wave–tilt–dam mechanical seals are used to study the effect of three operating conditions, namely, the fluctuating inlet pressure, fluctuating closing force, and changing rotational speed on the mechanical seal's operating characteristics under start–stop circumstances. Based on the steady-state calculation results of the wave–tilt–dam mechanical seal with a 5-μm-base film thickness, the unsteady state calculation was conducted. The dynamic characteristics of the mechanical seal were studied by deliberately inflicting different disturbances, and the influence laws were mainly explored through the selected parameters such as leakage, base film thickness, and inlet-to-outlet temperature difference. The disturbance modes mainly included the sinusoidal and step change modes of fluctuated parameters. The unfluctuated parameters remained unchanged. When a sinusoidal disturbance was applied, the calculation was conducted for seven cycles, with a 300-Hz fluctuation frequency. On the other hand, when a step disturbance was applied, the calculation was run until the stabilization of the main testing parameters (leakage, inlet-to-outlet temperature difference, and liquid film thickness) and then put to stop.

Influence of Inlet Pressure Fluctuation on Mechanical Seal Dynamic Characteristics

Two forms are adopted for inlet pressure fluctuation, where sinusoidal fluctuation is shown as follows:

$$p_{in} = \begin{cases} p_0 & t = 0, \\ p_0 + a p_0 \sin(2\pi t f) & t > 0, \end{cases} \tag{10}$$

where p_{in} is the inlet pressure during unsteady calculation; p_0 is the inlet pressure in steady-state calculation; a is the fluctuation amplitude, where 4, 6, 8, and 10% are selected for this study; and f is the fluctuation frequency, which is selected as 300 Hz for this study.

Step fluctuation is shown as follows:

$$p_{in} = \begin{cases} p_0 & t = 0, \\ p_0 + a p_0 & t > 0, \end{cases} \tag{11}$$

where a is the fluctuation amplitude, and 4, 6, 8, and 10% are selected for this study.

Figure 5 shows the variation patterns of performance parameters such as static ring displacement, inlet-to-outlet temperature difference, and the outlet flow rate with time under sinusoidal fluctuations of different amplitudes. For the static ring displacement, the results show that when the inlet pressure fluctuation amplitude is 10%, the maximum static ring displacement appears at t = 1.504 ms, while the maximum displacement increases by 32.27% compared with the thickness of the base film. The displacement change from the fourth peak to the fifth peak is no more than 0.3%, so the fluctuation region can be considered stable, and the corresponding time is 11.580 ms. The average frequency between the fourth peak and the seventh peak is 300 Hz, which is equal to the pressure fluctuation frequency. The displacement fluctuation amplitude is 18.93% of the base film thickness, and the offset distance is 0.1417 μm. When the fluctuation amplitude of inlet pressure was 4%, it showed a similar pattern. However, its fluctuation amplitude decreased, while the maximum displacement increased by 10.78% compared with the initial test value. The fluctuation amplitude in stable fluctuation was 6.90%. When the amplitude of inlet pressure fluctuation was 6 and 8%, the displacement fluctuation was between the aforementioned two conditions.

For the inlet-to-outlet temperature difference, when the inlet pressure fluctuation amplitude is 10%, the minimum inlet-to-outlet temperature difference appears at the moment t = 2.212 ms, which is 0.708 ms later than the maximum displacement moment. At this moment, the inlet-to-outlet temperature difference is 5.341 K, representing a 33.54% decrease as compared to the initial moment, and the

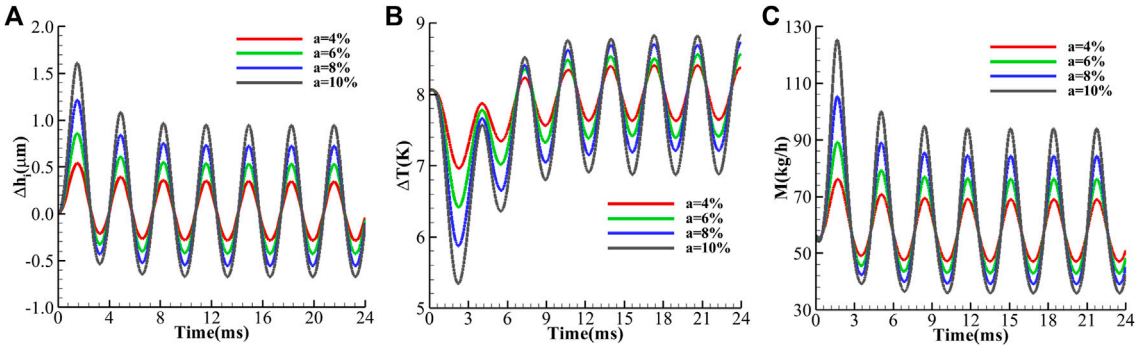

FIGURE 5 | Variation of parameters with time **(A)** static ring displacement, **(B)** inlet-to-outlet temperature difference, and **(C)** the leakage.

displacement change from the fourth valley to the fifth valley is no more than 0.3%. It can be considered that the fluctuation region is stable, and the corresponding time is 12.262 ms. When the fluctuation is stable, the fluctuation amplitude is 14.63%, and the offset is 7.85 K, which is lower than the inlet-to-outlet temperature difference at the initial moment. When the inlet pressure fluctuation amplitude is 4%, the inlet-to-outlet temperature difference is 6.96 K, and the initial moment decreases by 13.33%. It is worth noting that the inlet-to-outlet temperature difference corresponding to low pressure fluctuation is always higher than that corresponding to high pressure fluctuation in the period from t = 0 to T = 6.700 ms, which is different from the variation law of static ring displacement.

For leakage, when the amplitude of inlet pressure fluctuation is 10%, the maximum leakage appears at t = 1.664 ms, which is 0.160 ms later than the maximum displacement moment. The maximum leakage increases by 122.10% as compared to the initial value. The displacement changes from the fourth peak value to the fifth peak value are no more than 0.3%. Therefore, the fluctuation region can be considered stable. The corresponding time, fluctuation amplitude, and deviation distance are 11.748 ms, 66.72%, and 65.07 kg/s, respectively. This deviation distance is higher than the initial leakage. When the fluctuation amplitude of inlet pressure was 4%, it showed a similar pattern, but its fluctuation amplitude decreased, the maximum leakage increased 34.74% compared with the initial test value, and the fluctuation amplitude in stable fluctuation was 22.31%. When the amplitude of inlet pressure fluctuation is 6 and 8%, the leakage fluctuation is between the previous two situations, and its fluctuation frequency is 300 Hz. It is worth noting that in the period from t = 0 to T = 0.468 ms, the leakage is lower than that at the initial test time, and the flow decreases with the increase in pressure fluctuation. The trough value appears at t = 0.240 ms, and the lowest value decreases by 4.25% compared with the initial time.

Through the analysis of the main performance parameters of the mechanical seal of the reactor coolant pump, it can be seen that when the sinusoidal pressure fluctuation is applied, the sealing performance parameters exhibit unstable fluctuations for a period of time, followed by stable fluctuations. The fluctuation intensity is much higher than the disturbance intensity, and they tend to deviate from the initial values. In addition, the fluctuation amplitude of leakage is not proportional to the fluctuation amplitude of static ring displacement. The fluctuation range of leakage is much larger than that of static ring displacement, indicating that the change of the static ring position changes not only the liquid film flow area but also the liquid film flow field distribution.

In order to further analyze the flow field of the sealing liquid film, the distribution law of physical quantity in section Z0 = 4 μm (as shown in **Figure 2A**) at typical time was analyzed. **Figure 6** shows the pressure distribution variation of Z0 at different times when the pressure fluctuation amplitude is 4 and 10%. The results show that the high-pressure region appears in the static loop peak region at the initial moment, and the pressure changes greatly from the turning radius to the outlet, while the pressure change is not obvious near the entrance. In the region of the static ring trough however, the pressure changes drastically near the entrance. When t = 0.24 ms, the pressure near the turning radius of the static loop trough decreases compared with the initial moment, and the pressure decrease degree increases with the inlet pressure fluctuation range. At this moment, the leakage reaches the maximum value, and the pressure near the turning radius of the static ring trough increases, while the pressure gradient tends to be uniform. At t = 23.52 ms, representing the moment when the leakage fluctuates steadily, the leakage is at its lowest value, while pressure near the turning radius of the static ring trough decreases as compared to the initial moment. The low-pressure zone occupies most of the area, and the pressure gradient near the entrance rises. It can therefore be seen that inlet pressure fluctuations mainly affect the pressure distribution rule at the static ring trough, where with the increase in inlet pressure fluctuation amplitude, the pressure fluctuation at the static ring trough becomes larger. However, this has little influence on the pressure distribution at the crest.

Figure 7 shows the temperature distribution variation of Z0 at different times when the pressure fluctuation amplitude is 4 and 10%. It is shown that a low-temperature region appears in the static ring peak region, while the high-temperature region appears between the static ring peak and the trough near the exit. At t = 0.24 ms, the temperature drops slightly as compared to the initial time. At t = 1.68 ms however, it decreases significantly, with the increase in the inlet pressure fluctuation range. At t = 23.52 ms, although the leakage reached the trough value, the temperature did not reach the peak value, and the temperature distribution was similar to the initial time. This indicates that the increase in fluid

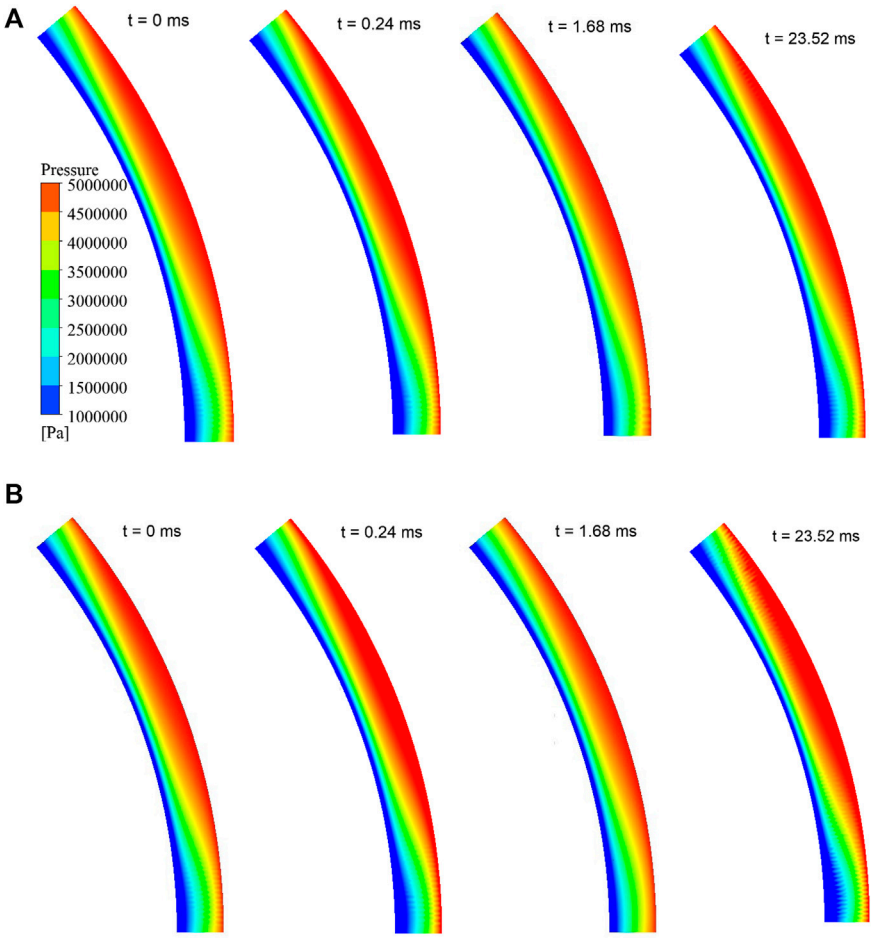

FIGURE 6 | Pressure distribution varies with time **(A)** *a* = 4% and **(B)** *a* = 10%.

flow does not immediately take away the heat generated; there is a delay effect, and the decrease in flow does not immediately "accumulate" the heat and cause the temperature to increase.

Figure 8 shows the velocity distribution change law on Z0 in different times for pressure fluctuation amplitudes of 4 and 10%. It can be seen that high-speed zones appear in the initial times on the static ring wave area, and the velocity gradient near the turning radius is bigger. Low-speed areas appear in the static ring trough area with the almost uniform distribution, leading to a smaller velocity gradient. At t = 0.24 ms, there is no significant difference in velocity distribution mode compared to the initial time. At t = 1.68 ms however, the velocity increases significantly compared with the initial moment and increases with the increase in the inlet pressure fluctuation range. At t = 23.52 ms, the velocity decreases significantly, leading to a corresponding increase in the velocity gradient near the turning radius of the static ring crest. A large velocity change occurs before and after the turning radius. When a = 10%, the flow rate is lower (smaller velocity), and the velocity gradient at the turning radius is larger.

In order to further study the relationship between the flow change, static ring displacement, and velocity change, **Figure 9** has been used to show the radial velocity distribution contour diagram of different circumferential sections. In this figure, the S1 section is at $\alpha = 0^{\circ}$, corresponding to the static ring trough. The S3 section is at $\alpha = 20^{\circ}$, corresponding to the static ring peak. The S2 section is at $\alpha = 10^{\circ}$, thus being between the S1 and S3 (as shown in **Figure 2A**). It is shown that the radial velocity of the circumferential section increases gradually from the static ring trough to the static ring peak at the initial moment. For S1 and S2 sections, the velocity distribution is uniform, while it increases slightly in the exit section. For the S3 section, the velocity increases significantly in the exit section. This feature is more pronounced in the vicinities of the rotating ring. When t = 0.24 ms, the static ring moves up as a result of a slight increase in the base film thickness. The cross-sectional velocity in the S3 section is also found to increase, while that in the S1 section decreased. In addition, the velocity of the inlet section is higher than that of the outlet section, which is more obvious when a = 10%. This, in other words, implicates the existence of large pressure fluctuations. This situation can also be seen from **Figure 4C**. It indicates that the leakage does not increase with the increase in the thickness of the base film, mainly due to the decrease in the cross-sectional velocity at S1.

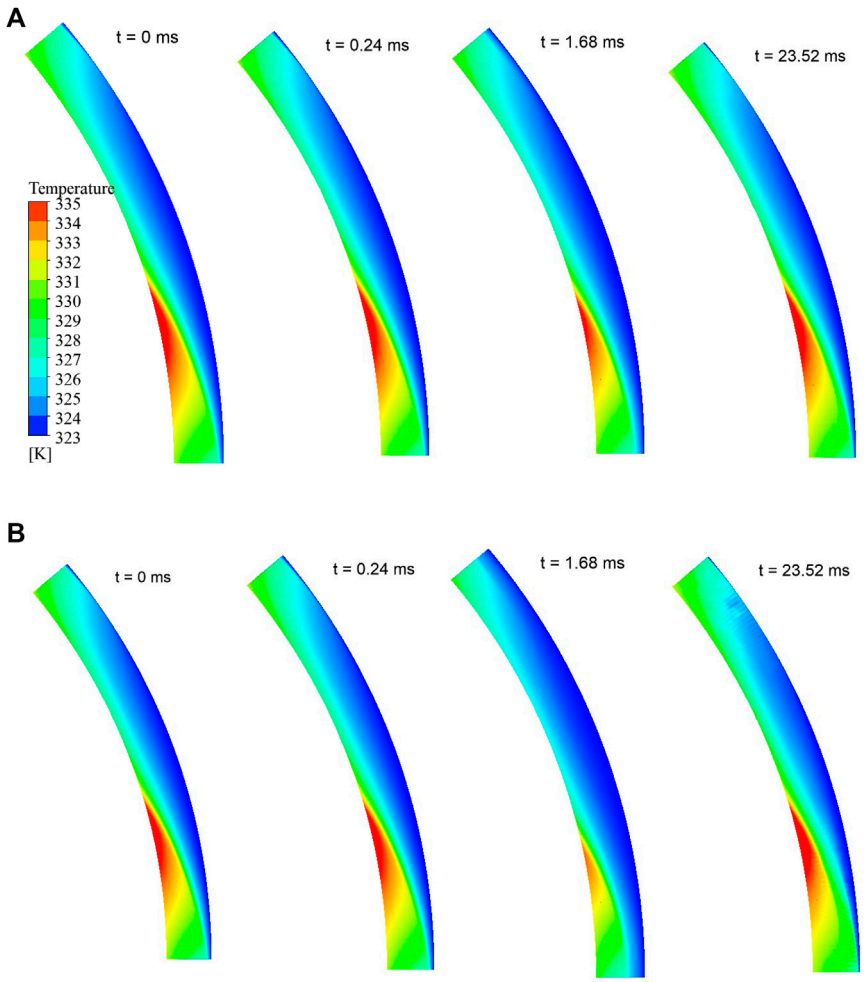

FIGURE 7 | Temperature distribution varies with time **(A)** *a* = 4% and **(B)** *a* = 10%.

When t = 1.68 ms, the static ring moves up further, the thickness of the foundation film increases further, and the velocity in S1, S2, and S3 sections increases significantly. This corresponds to **Figure 4C**, when t = 1.68 ms, the leakage is much higher than the initial moment, and when a = 10%, the leakage increases by 122.10%. However, the increase in base film thickness is only 30.96%, which indicates that the increase in leakage is the result of both the increase in base film thickness and radial velocity simultaneously. When t = 1.68 ms, the static ring moves down, the thickness of the base film decreases, and the radial velocity of each section decreases (the leakage decreases).

Figure 10 shows the evolution of main performance parameters with time, considering different inlet pressure's step fluctuations. Study findings, as presented in this figure, show that the growth of static ring displacement and leakage in the early stage is rapid, followed by a slowly ascending trend. But there has been a brief leakage decrease at the beginning of time (close to t = 0.1 ms), followed by a steep ascent. As for the inlet-to-outlet temperature difference, a rapid descent is recorded within the time interval from 0.2 to 2.8 ms, although there have been slight differences in evolutional trends for different step fluctuations. For the 10% step disturbance, static ring displacement exceeded 99.57%, the change of inlet-to-outlet temperature difference exceeded 75.94%, and leakage change was as high as 572.06%. For the 4% step disturbance, static ring displacement exceeded 34.56%, the change of inlet-to-outlet temperature difference exceeded 52.35%, and leakage change exceeded 126.55%. It therefore can be seen that even a small step disturbance would inflict a great impact on the sealing performance.

Influence of Closing Force Fluctuation on Dynamic Characteristics of Mechanical Seals

For the fluctuation of closing force, two pressure fluctuation forms are adopted, whose sinusoidal fluctuation is shown as follows:

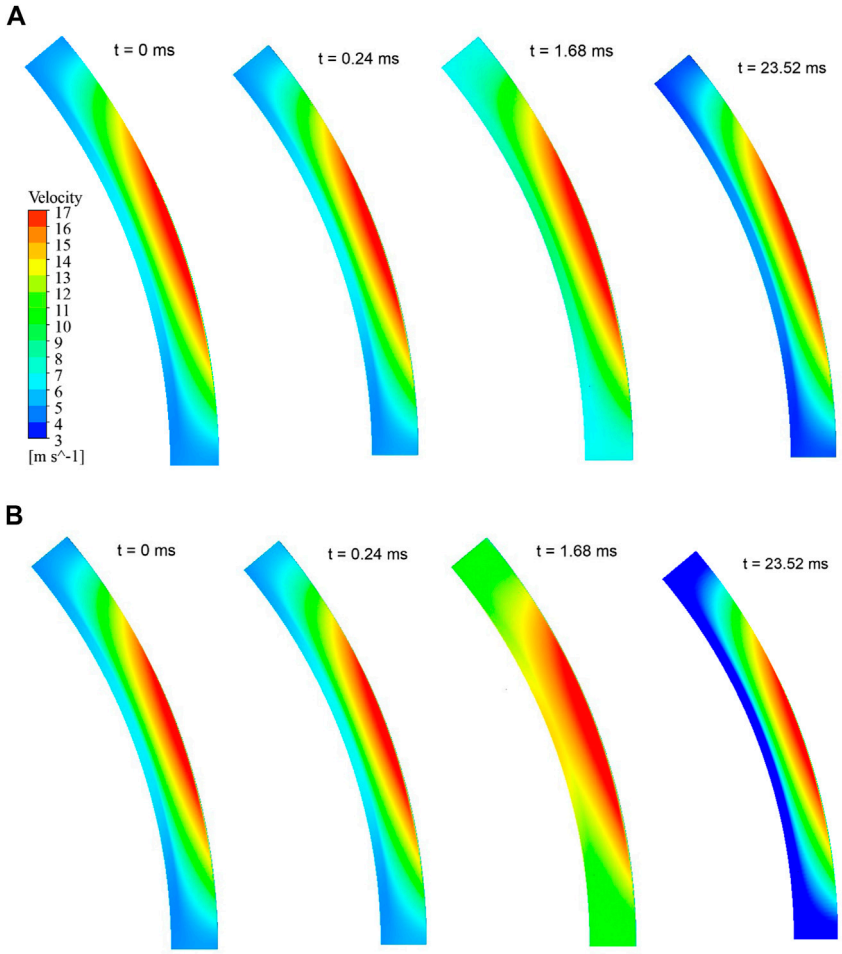

FIGURE 8 | Velocity distribution varies with time **(A)** a = 4% and **(B)** a = 10%.

$$F_{close} = \begin{cases} F_0 & t = 0, \\ F_0 + aF_0 \sin(2\pi t f) & t > 0, \end{cases} \tag{12}$$

where F_{close} is the closing force in unsteady calculation; F_0 is the closing force in steady calculation; a is the fluctuation amplitude where 4, 6, 8, and 10% are selected fluctuation amplitudes in this study; and f is the fluctuation frequency, which is selected as 300 Hz.

Step fluctuation is shown as follows:

$$F_{close} = \begin{cases} F_0 & t = 0, \\ F_0 + aF_0 & t > 0, \end{cases} \tag{13}$$

where a is the fluctuation amplitude, and 4, 6, 8 and 10% are selected for this study.

Figure 11 shows the change law of main performance parameters with time, under different closing force fluctuation amplitudes. The results show that for the static ring, when a 10% closing force fluctuation is applied, the static ring's maximal displacement is recorded at t = 1.500 ms. The maximum displacement increased by more than 33.66% compared with the initial film thickness, which was very similar to the peak time when the inlet pressure fluctuated, but the static ring displacement was slightly larger than the inlet pressure fluctuation displacement (32.27%). Similarly, the variation of static ring displacement from the fourth peak to the fifth peak is no more than 0.3%, and the corresponding time is 11.576 ms. The subsequent static ring displacement fluctuation amplitude is 19.54% of the initial film thickness, and the offset is 0.1591 μm, which are larger than the amplitude and offset of inlet pressure fluctuation. When the amplitude of closing force fluctuation decreases from 8% to 6–4%, the intensity of displacement fluctuation decreases accordingly.

For the inlet-to-outlet temperature difference, when the inlet pressure fluctuation amplitude is 10%, the minimum temperature difference appears at the moment t = 2.252 ms, 0.752 ms later than the maximum displacement moment, and the temperature difference at this moment decreases 33.21% compared with the initial moment. In the stable fluctuation, the fluctuation amplitude is 13.95%, and the deviation distance is 7.86 K. The temperature fluctuation range is smaller, and the deviation distance is closer to the initial temperature. When the amplitude of closing force fluctuation is 4%, the minimum

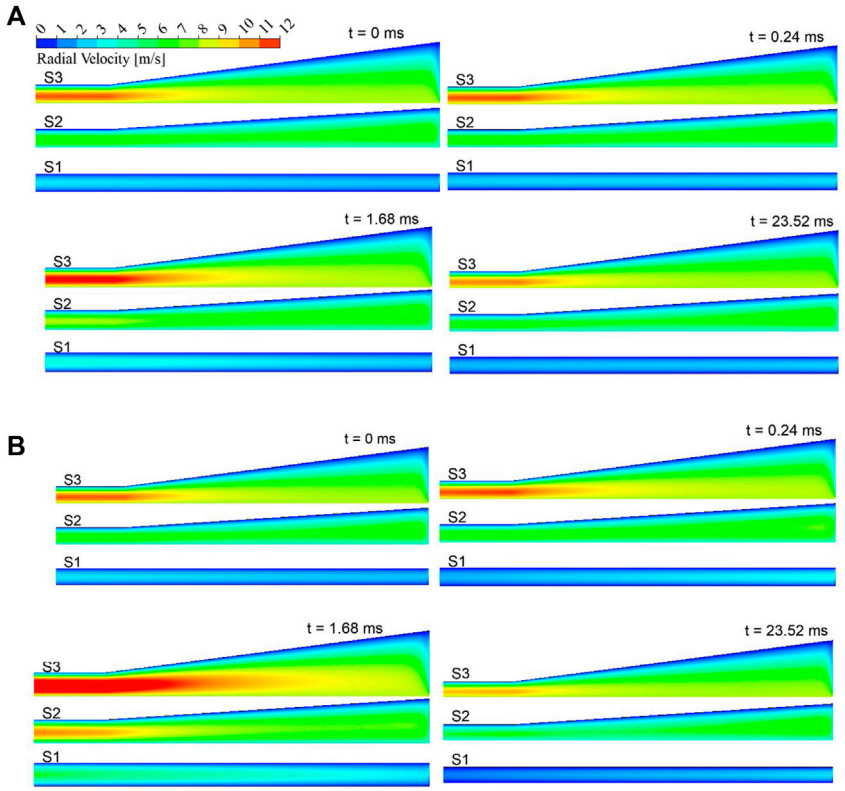

FIGURE 9 | Radial velocity distribution varies with time **(A)** *a* = 4% and **(B)** *a* = 10%.

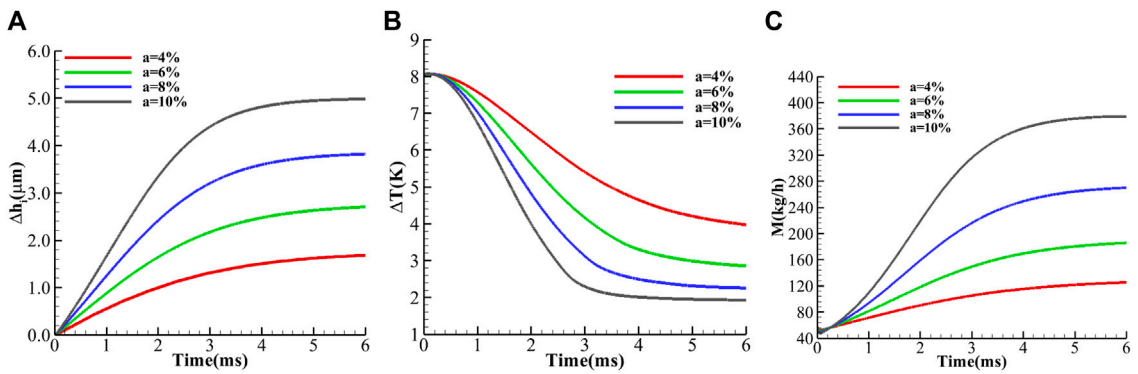

FIGURE 10 | Variation of parameters with time **(A)** static ring displacement, **(B)** inlet-to-outlet temperature difference, and **(C)** the leakage.

temperature difference is 6.99 K, which is 13.06% lower than the initial time. It is noteworthy that the temperature difference corresponding to the fluctuation of low closing force is always higher than that corresponding to the fluctuation of high closing force in the period from t = 0 to t = 6.780 ms, which is different from the variation law of static ring displacement.

For leakage, when the fluctuation amplitude of closing force is 10%, the maximum leakage appears at t = 1.760 ms, 0.260 ms later than the maximum displacement moment. The maximum leakage increases 129.05% compared with the initial value, and the displacement change from the fourth to the fifth peak is no more than 0.3%. So the fluctuation region can be considered stable. The corresponding time is 11.824 ms, the fluctuation amplitude is 72.63%, and the deviation distance is 65.59 kg/s, which is higher than the initial leakage. When the amplitude of closing force fluctuation is 4%, it shows a similar pattern, but its fluctuation amplitude decreases. The maximum leakage increases by 36.36% compared with the initial test value, and the

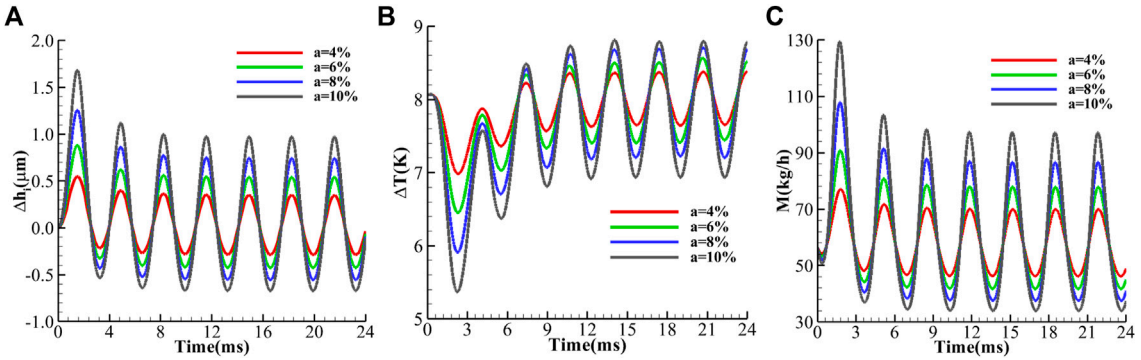

FIGURE 11 | Variation of parameters with time **(A)** static ring displacement, **(B)** inlet-to-outlet temperature difference, and **(C)** the leakage.

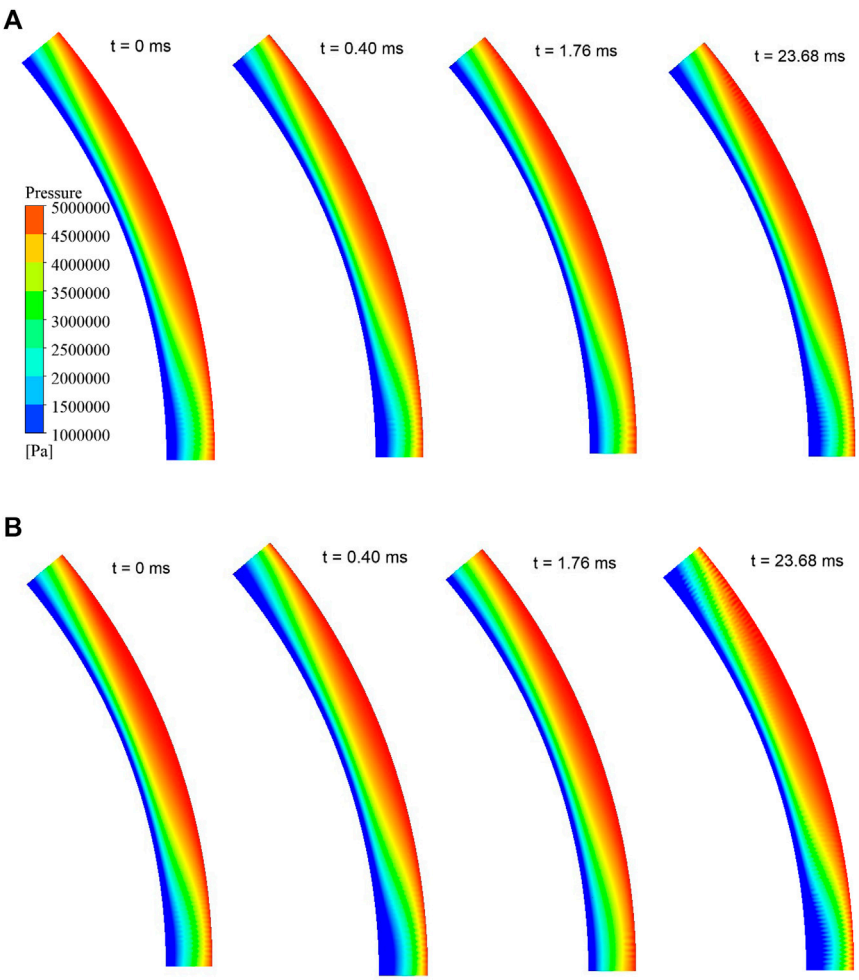

FIGURE 12 | Pressure distribution varies with time **(A)** *a* = 4% and **(B)** *a* = 10%.

fluctuation amplitude in stable fluctuation is 24.12%. When the amplitude of inlet pressure fluctuation is 6 and 8%, the leakage fluctuation is between the aforementioned two situations. It is worth noting that in the period from t = 0 to t = 0.680 ms, the leakage is lower than that at the initial test time, and the flow decreases with the increase in closing force fluctuation. The

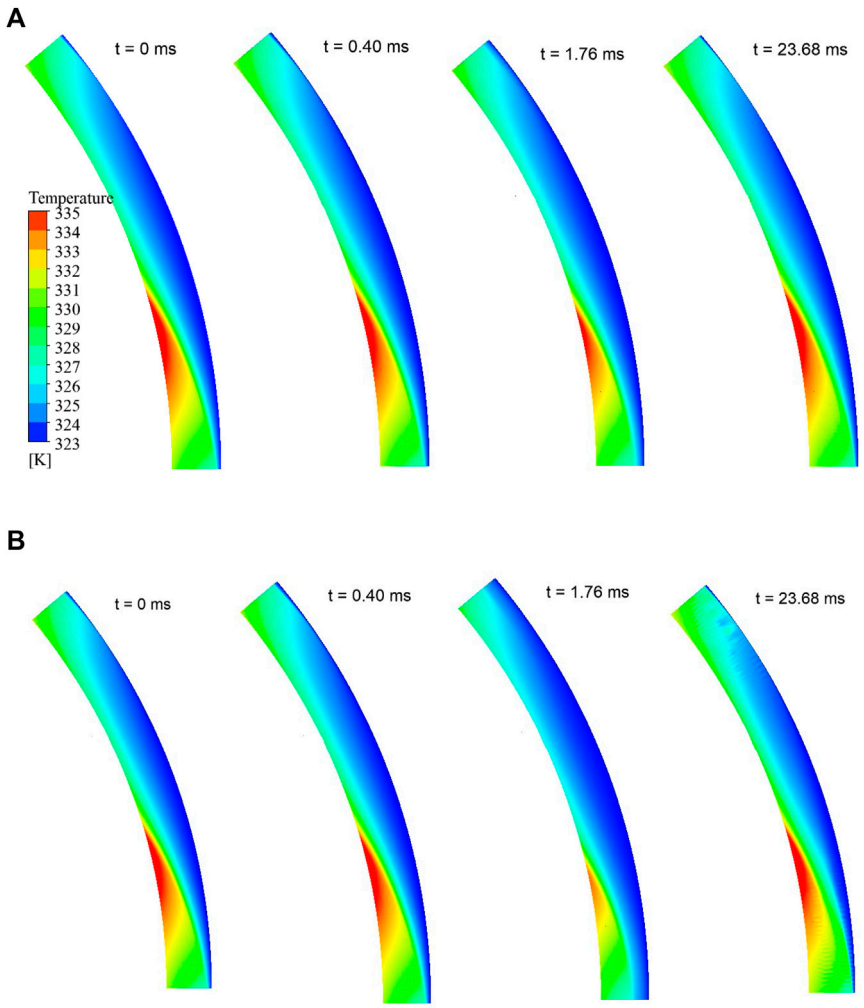

FIGURE 13 | Temperature distribution varies with time **(A)** *a* = 4% and **(B)** *a* = 10%.

trough value appears at t = 0.400 ms, and the lowest value decreases by 10.06% compared with the initial time.

Through the analysis of the main performance parameters of the reactor coolant pump's mechanical seal, it can be seen that when the sinusoidal closing force fluctuation is applied, the sealing performance parameters have distribution rules similar to that when the sinusoidal inlet pressure fluctuation is applied. But the fluctuation degree of both the static ring displacement and leakage are more severe, while the fluctuation degree of the inlet-to-outlet temperature difference is reduced. The time delay of maximum leakage and minimum inlet-to-outlet temperature difference is more obvious than that of the maximum static ring displacement. In addition, compared with sinusoidal inlet pressure fluctuation, the time of phenomenon of flow increases in a very short time after applying closure force disturbance, and the valley flow decreases significantly.

In order to further analyze the flow field of the sealing liquid film, the distribution law of physical quantities in section Z0 = 4 μm (as shown in **Figure 2A**) at typical times was analyzed. **Figure 12** shows the pressure distribution variation rule of Z0 at different times when the fluctuation range of closing force is 4 and 10%. The distribution rule is similar to that when the inlet pressure fluctuation is applied. At the initial moment, a high-pressure region appears in the static loop peak region, and the pressure change from the turning radius to the outlet is quite large, while it is not obvious near the entrance. In the region of the static ring trough however, the pressure is found to drastically change, especially near the entrance. When t = 0.40 ms, the pressure near the turning radius of the static loop trough decreases as compared to the initial moment, where the decreasing pace increases with the inlet pressure fluctuation range. This goes hand in hand with the leakage characteristics at t = 0.40 ms, as presented in **Figure 10C**. When t = 0.40 ms, the leakage reaches the maximum value, and the pressure near the turning radius of the static ring trough increases, while the pressure gradient tends to be uniform. At t = 23.68 ms, corresponding to the trough moment when the leakage fluctuates steadily, the leakage is the lowest at this moment,

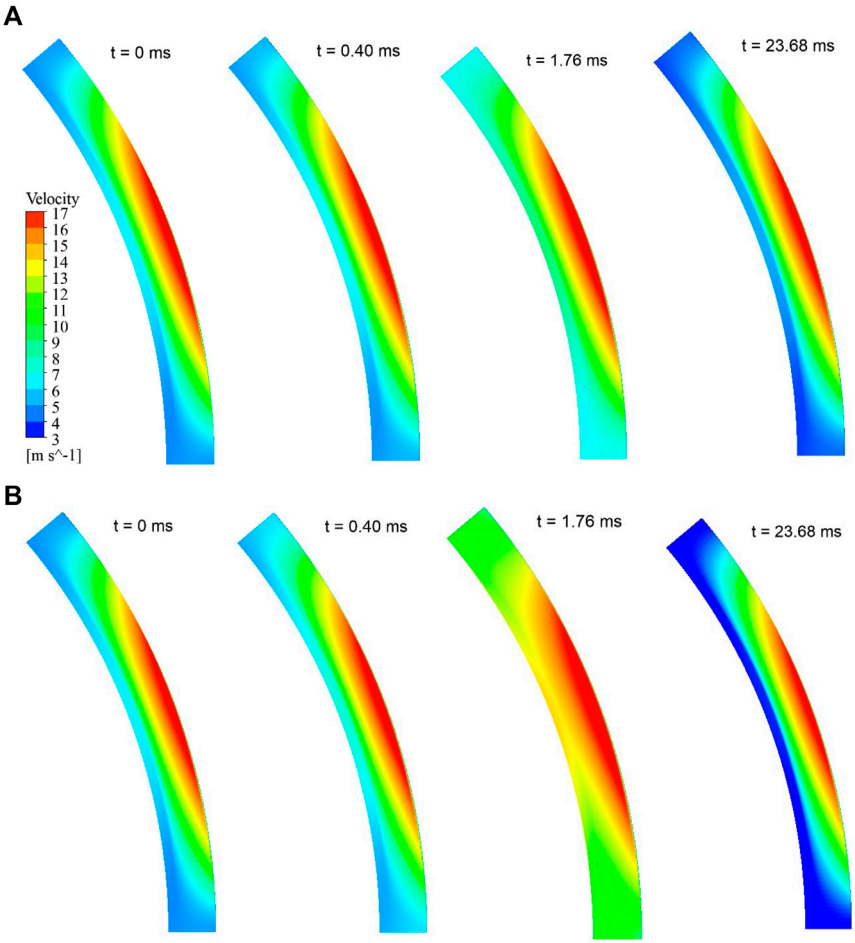

FIGURE 14 | Velocity distribution varies with time **(A)** *a* = 4% and **(B)** *a* = 10%.

and the pressure near the turning radius of the static ring trough decreases compared with the initial moment. The low-pressure area occupies most of the area, and the pressure gradient near the entrance rises. It can be seen that the fluctuation of the closing force mainly affects the pressure distribution law at the static ring trough, where the same pressure fluctuation at the static ring trough increases with the inlet pressure fluctuation amplitude, and has little influence on the pressure distribution at the peak.

Figure 13 shows the temperature distribution variation of Z0 at different times when the applied fluctuation amplitude of closing force is 4 and 10%. The low-temperature region appears in the static ring peak region, while high-temperature region appears between the static ring peak and the trough near the exit. At t = 0.40 ms, the temperature drops slightly compared with the initial time. At t = 1.76 ms, the temperature decreased significantly with the increase in the inlet pressure fluctuation range. At t = 23.68 ms, although the leakage had reached the trough value, the temperature did not reach the peak value. The temperature distribution was similar compared with the initial time, and the value was the same. This indicates that the increase in fluid flow does not immediately take away the heat generated, and there is a delay effect. Moreover, the decrease in flow does not immediately "accumulate" the heat and cause the temperature to increase.

Figure 14 shows the velocity distribution change law at Z0 in different times, for the closing force fluctuation amplitudes of 4 and 10%. Study results show that high-speed zones appear at the initial time in the static ring wave area, and the velocity gradient near the turning radius is bigger. The low-speed zone, on the other hand, appear in the static ring trough area with a somewhat uniform distribution (velocity gradient is smaller). At t = 0.40 ms, there is no significant difference in the velocity distribution mode as compared to the initial time. At t = 1.76 ms, the velocity obviously increases with the closing force fluctuation range. At t = 23.68 ms, the velocity decreases significantly compared with the initial moment, leading to a subsequently large velocity gradient near the turning radius of the static ring crest. Large velocity change is found occur before and after the turning radius. When a = 10%, the flow rate is lower, corresponding velocity is also smaller, and the velocity gradient at the turning radius is larger.

The relationship between flow change, static ring displacement, and velocity change is further studies using the radial velocity distribution cloud diagram of different circumferential sections, as shown in **Figure 15**. The results

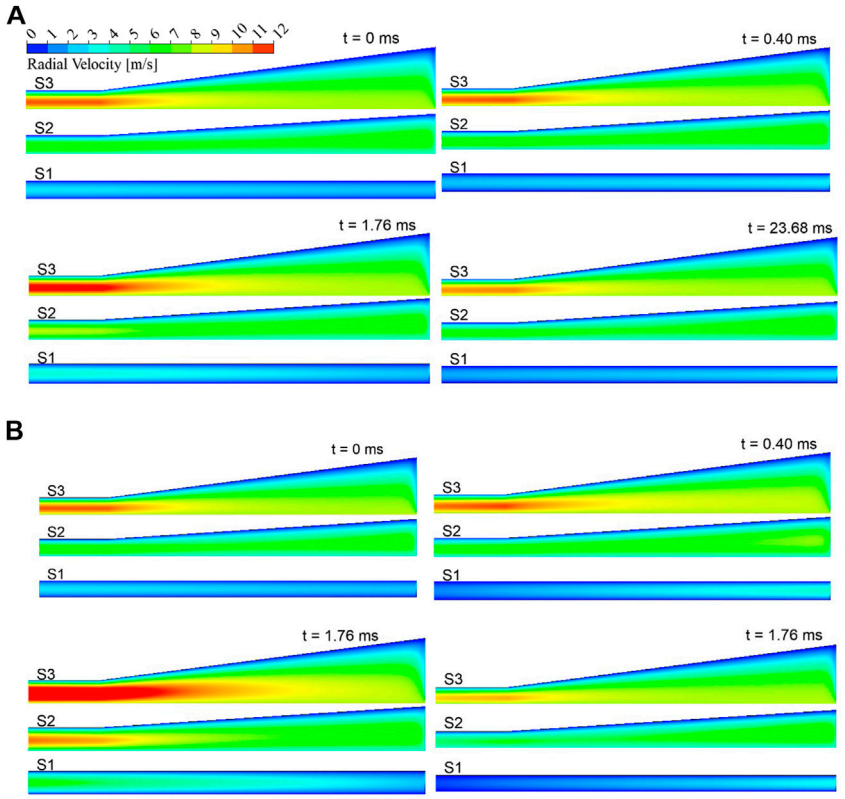

FIGURE 15 | Radial velocity distribution varies with time **(A)** *a* = 4% and **(B)** *a* = 10%.

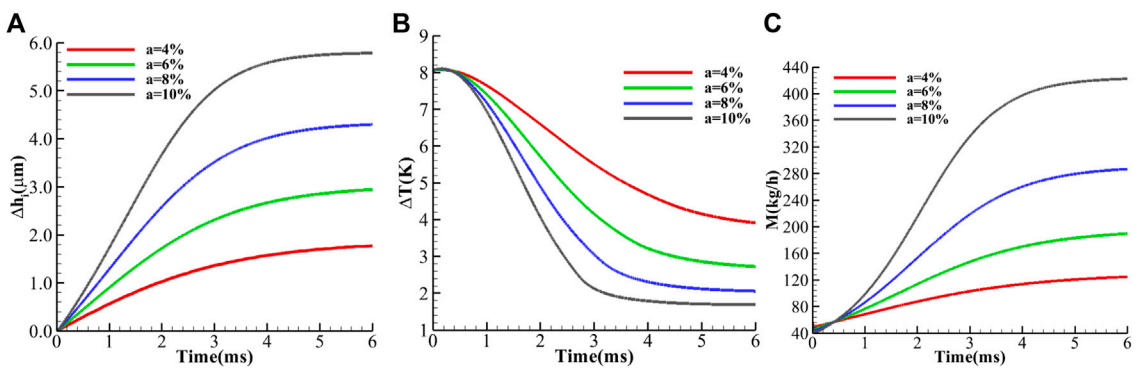

FIGURE 16 | Variation of parameters with time **(A)** static ring displacement, **(B)** inlet-to-outlet temperature difference, and **(C)** the leakage.

show that the radial velocity at the circumferential section increases gradually from the static ring trough to the static ring peak at the initial moment. For S1 and S2 sections, the velocity distribution is uniform, while it slightly increases in the exit section. For the S3 section, the velocity increases quickly, especially in the exit section, where high-velocity zones are predominantly located in the vicinal area to the rotating ring region. When t = 0.40 ms, the static ring moves up, the thickness of the base film slightly increases and the cross-sectional velocity of S3 increases; while the velocity in the S1 cross section decreases. In addition, the velocity of the inlet section is higher than that of the outlet section, which is more obvious when a = 10%., implicating that the pressure fluctuation is large. This corresponds to **Figure 10C** where when t = 0.240 ms, the leakage is lower than the initial moment, indicating that the leakage does not increase with the increase in foundation film thickness, mainly due to the velocity decrease in the S1 cross section. When t = 1.76 ms, the static ring moves up further, the thickness of the base film increases further, and the velocity of S1, S2, and S3 sections all increase significantly, which corresponds to

TABLE 3 | Performance of two kinds of speed.

Parameter (rpm)	ΔT(K)	m (kg/h)	F_{open} (kN)
0	1.183	56.643	34.703
500	2.026	56.616	34.693
1,000	4.381	56.560	34.668
1,500	8.036	56.445	34.631
2000	12.720	56.440	34.624

Figure 10C; when t = 1.76 ms, the leakage is much higher than the initial moment. When a = 10%, the leakage increases as high as 129.05%. The increase in base film thickness is only 33.66%, which indicates that the increase in leakage is the result of a simultaneous increase in both the base film thickness and radial velocity. When t = 1.76 ms, the static ring moves down, the thickness of the base film decreases, the radial velocity of each section decreases, and the leakage consequently decreases.

In general, when the closing force and inlet pressure fluctuations are applied, the distribution law of the liquid film flow field is similar for both cases, but there is a slight difference in terms of numerical values.

Figure 16 shows the variation rules of main performance parameters under different step fluctuations of closing force. It is shown that at t = 6.0 ms, the performance parameters are all stable. On the other hand, from t = 0 ms, both the static ring displacement and leakage are found to increase rapidly in the early stage, while they tend to slow down in the later stage. But the leakage decreases in a very short period of time at the beginning. The rapid change of the inlet-to-outlet temperature difference mainly occurs in the middle stage, and the change is slow afterward. Under a 10% step disturbance, static ring displacement is more than 115.82%, the change of inlet-to-outlet temperature difference is more than 78.98%, and leakage change is as high as 649.19%. Even for a step disturbance as low as 4%, static ring displacement is more than 36.74%, the change of inlet-to-outlet temperature difference is more than 53.50%, and the leakage change is more than 127.22%. It can therefore be seen that even a small step disturbance will have a great impact on the sealing performance. In addition, the change caused by the closing force fluctuation, in terms of static ring displacement, inlet-to-outlet temperature difference, and leakage, is larger than that caused by the inlet pressure fluctuation.

Influence of Speed Fluctuation on Dynamic Characteristics of Mechanical Seals

It is also necessary to study the influence of speed fluctuation on the mechanical seal performance of a reactor coolant pump. **Table 3** shows the steady-state calculation results under different rotational speeds. With the increase in the rotational speed, the leakage decreases gradually, but the change range is very small. Even if the rotational speed reaches 133%, the leakage only decreases by 0.36%. Similarly, the opening force decreases gradually with the increase in the rotational speed. When the rotational speed reaches 133%, the opening force decreases by 0.23%. When the rotational speed is 1500 rpm, the inlet-to-outlet temperature difference is 8.036 K. With the rotational speed decreasing from 1500 to 0 rpm, the inlet-to-outlet temperature difference decreases by 85.28%. When the speed is 133% of the normal rated speed, the inlet-to-outlet temperature difference increases by 58.29% compared with that at the normal rated speed. When the moving ring is stationary, that is, the rotation speed is 0 rpm, the inlet-to-outlet temperature difference is 1.183 k, indicating that there is a shear force in the flow direction of the liquid film, but the shear force in the flow direction is small, and the temperature difference between the inlet and outlet is small. With the increase in rotational speed, the tangential shear force increases gradually. When the speed reaches the rated speed, the tangential shear force is much larger than the flow direction shear force, and the fluid temperature increases rapidly.

In order to further study the temperature of the liquid membrane as the rotational speed change, **Figure 17** shows the Z0 cross-sectional temperature distribution under different

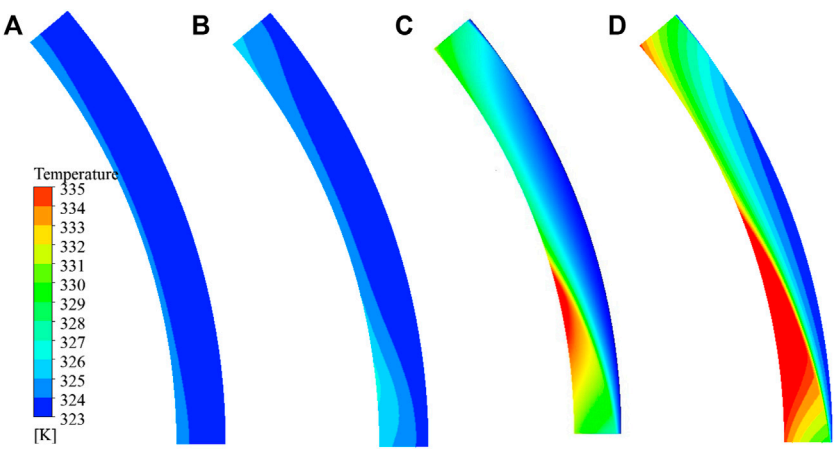

FIGURE 17 | Temperature distribution at different speeds **(A)** 0 rpm, **(B)** 500 rpm, **(C)** 1500 rpm, and **(D)** 2000 rpm.

speeds. The results show that as the speed increases, the cross-sectional temperature is gradually increased, and the temperature distribution is uneven. When the rotational speed is 0 rpm, the temperature distribution of Z0 cross section is relatively uniform, and the temperature at the exit is slightly elevated. With the increase in the speed, the temperature of the inlet is gradually increased, and the temperature at the outlet is gradually increased, but the temperature rise at the peak is small, the temperature rise in the wave valley is large, and the inlet temperature distribution is unevenly distributed. This is due to the thickness of the liquid membrane at the imported peak, the fluid cutting shear is weak, and the temperature rise is not obvious.

CONCLUSION

In this study, the waveform end face mechanical seal of a reactor coolant pump is taken as the research object. A three-dimensional thermal fluid–structure coupling analysis model is established, and the dynamic grid technology is introduced. Then, the effect mechanism of three parameters, namely, the inlet pressure fluctuation, closing force fluctuation, and speed fluctuation on the seal performance characteristics, is numerically studied. This study's main concluding remarks are drawn as follows:

1) When sinusoidal pressure fluctuation is applied, the sealing performance parameters appear unstable for a period of time then present almost stable fluctuations. The fluctuation intensity is much higher than the disturbance intensity, and the fluctuation deviates from the initial value. When a 10% fluctuation is applied, there are significant changes in static ring displacement, inlet-to-outlet temperature difference, and leakage, where their respective peak values change by 32.27, 33.54, and 122.10%, as compared to the initial test state. The change of the static ring position changes not only the liquid film flow area but also the liquid film flow field distribution. The peaks of inlet-to-outlet temperature difference and leakage were 0.708 and 0.160 ms later than that of the static ring displacement, respectively. In addition, seal parameters are more sensitive to step form fluctuations, where, for instance, an applied step fluctuation as small as 4% results in static ring displacement that exceeds 34.56%, temperature difference exceeding 52.35%, and leakage beyond 126.55%.
2) When the sinusoidal form of closing force fluctuation is applied, the static ring displacement, inlet-to-outlet temperature difference, and leakage change show similar distribution rules as when the sinusoidal form of inlet pressure fluctuation is applied. However, the static ring displacement and leakage fluctuation degree are more severe, and the fluctuation degree of inlet-to-outlet temperature difference decreases. The time delay of maximum leakage and minimum temperature difference is more obvious than that of maximum displacement. In addition, the change of static ring displacement, inlet-to-outlet temperature difference, and leakage caused by step fluctuation of the closing force is larger than that caused by the step fluctuation of inlet pressure. When a 4% step disturbance is applied, the static ring displacement is over 36.74%, the temperature difference is over 53.50%, and the leakage goes beyond 127.22%.
3) The effect of speed change on the reactor coolant pump mechanical seal's inlet-to-outlet temperature difference is remarkable, whereas its impact on leakage and opening force is negligible. It is found that when the speed is decreased from 1500 to 0 rpm, the inlet-to-outlet temperature difference decreases by 85.28%; where, on the other hand, the leakage and opening force increase by 0.35 and 0.21%, respectively.

DATA AVAILABILITY STATEMENT

The original contributions presented in the study are included in the article/Supplementary Material, further inquiries can be directed to the corresponding author.

AUTHOR CONTRIBUTIONS

J–LW: conceptualization, methodology, software, formal analysis, and writing—original draft. X–YC: methodology, software, formal analysis, and writing—original draft. MB: methodology, formal analysis, and writing—review and editing. WS: conceptualization, methodology, formal analysis, writing—review and editing, supervision and, funding acquisition. JW: methodology, formal analysis, and supervision.

FUNDING

This work is supported by the National Natural Science Foundation of China (51976043), LiaoNing Revitalization Talents Program (XLYC2007083), Liaoning BaiQianWan Talents Program (LNBQW2020Q0141), and Talent scientific research fund of LSHU (2020XJJL-010).

REFERENCES

Badykov, R., Falaleev, S., Wood, H., and Vinogradov, A. (2018). "Gas Film Vibration Inside Dry Gas Seal Gap," Global Fluid Power Society PhD Symposium GFPS, Samara, Russia, 1–6. doi:10.1109/GFPS.2018.8472383

Blasiak, S., and Zahorulko, A. V. (2016). A Parametric and Dynamic Analysis of Non-contacting Gas Face Seals with Modified Surfaces. *Tribology Int.* 94, 126–137. doi:10.1016/j.triboint.2015.08.014

Brunetière, N., and Modolo, B. (2009). Heat Transfer in a Mechanical Face Seal. *Int. J. Therm. Sci.* 48 (4), 781–794. doi:10.1016/j.ijthermalsci.2008.05.014

Chávez, A., and De Santiago, O. (2020). Determining a Pressure Response Function of the Hose and Sensor Arrangement for Measurements of Dynamic Pressure in a Dry Gas Seal Film. *Tribol Int.* 143, 106007.

Chen, Y., Jiang, J., and Peng, X. (2017). Dynamic Characteristics and Transient Sealing Performance Analysis of Hyperelliptic Curve Groove Dry Gas Seals. *Tribology Int.* 116, 217–228. doi:10.1016/j.triboint.2017.07.017

Cochain, J. (2018). *Numerical and Experimental Study of Misaligned and Wavy Mechanical Face Seals Operating under Pressure Pulses and Pressure Inversions*. Université de Poitiers.

Falaleev, S. V., and Vinogradov, A. S. (2015). Analysis of Dynamic Characteristics for Face Gas Dynamic Seal. *Proced. Eng.* 106, 210–217. doi:10.1016/j.proeng.2015.06.026

Feng, X., Su, W., Ma, Y., Wang, L., and Tan, H. (2020). Numerical and Experimental Study on Waviness Mechanical Seal of Reactor Coolant Pump. *Processes* 8, 1611. doi:10.3390/pr8121611

Gao, H., Gao, F., Zhao, X., Chen, J., and Cao, X. (2013). Analysis of Reactor Coolant Pump Transient Performance in Primary Coolant System during Start-Up Period. *Ann. Nucl. Energ.* 54, 202–208. doi:10.1016/j.anucene.2012.11.020

Guang, F., and Ma, X. (2021). Positioning Accuracy Determination of the Servo Axes for Grinding Wavy-Tilt-Dam Seals Using a Four-Axis Grinder. *Micromachines* 2, 388. doi:10.3390/mi12040388

Lebeck, A. O. (1991). *Principles and Design of Mechanical Face Seals*. John Wiley & Sons.

Li, Y., Hao, M., Sun, X., Li, Z., Wang, Y., Xu, L., et al. (2020). Dynamic Response of Spiral Groove Liquid Film Seal to Impact Conditions. *Tribology Int.* 141, 105865. doi:10.1016/j.triboint.2019.105865

Liao, C., Huang, W., Suo, S., Liu, X., and Wang, Y. (2011). Fluid-solid strong-interaction Model of Mechanical Seals in Reactor Coolant Pumps. *Sci. China Technol. Sci.* 54 (9), 2339–2348. doi:10.1007/s11431-011-4427-8

Liu, M., Tan, L., and Cao, S. (2019). Theoretical Model of Energy Performance Prediction and BEP Determination for Centrifugal Pump as Turbine. *Energy* 172, 712–732. doi:10.1016/j.energy.2019.01.162

Liu, W., Liu, Y., Huang, W., Suo, S., and Wang, Y. (2013). Effect of Disturbances on the Dynamic Performance of a Wavy-Tilt-Dam Mechanical Seal. *Tribology Int.* 64, 63–68. doi:10.1016/j.triboint.2013.02.021

Liu, W., Liu, Y., Wang, Y., and Peng, X. (2011). Parametric Study on a Wavy-Tilt-Dam Mechanical Face Seal in Reactor Coolant Pumps. *Tribology Trans.* 54 (6), 878–886. doi:10.1080/10402004.2011.611325

Liu, Y., Liu, W., Li, Y., Liu, X., and Wang, Y. (2015). Mechanism of a Wavy-Tilt-Dam Mechanical Seal under Different Working Conditions. *Tribology Int.* 90, 43–54. doi:10.1016/j.triboint.2015.03.020

Lu, Y., Zhu, R., Wang, X., An, C., Zhao, Y., and Fu, Q. (2019). Experimental Study on Transient Performance in the Coasting Transition Process of Shutdown for Reactor Coolant Pump. *Nucl. Eng. Des.* 346, 192–199. doi:10.1016/j.nucengdes.2019.03.007

Luo, Y., Fan, Y., Han, Y., Zhang, W., and Acheaw, E. (2020). Research on the Dynamic Characteristics of Mechanical Seal under Different Extrusion Fault Degrees. *Processes* 8 (9), 1057. doi:10.3390/pr8091057

Ma, Y., Wang, Y., Zhou, H., and Su, W. (2021). Characteristics of the Waviness End-Face Mechanical Seal in Reactor Coolant Pump Considering the Viscosity-Temperature Effect. *Front. Energ. Res.* 9. doi:10.3389/fenrg.2021.763074

Migout, F., Brunetière, N., and Tournerie, B. (2015). Study of the Fluid Film Vaporization in the Interface of a Mechanical Face Seal. *Tribology Int.* 92, 84–95. doi:10.1016/j.triboint.2015.05.029

Ni, D., Yang, M., Zhang, N., Gao, B., and Li, Z. (2017). Unsteady Flow Structures and Pressure Pulsations in a Nuclear Reactor Coolant Pump with Spherical Casing. *ASME. J. Fluids Eng. May* 139 (5), 051103. doi:10.1115/1.4035638

Ni, D., Zhang, N., Gao, B., Li, Z., and Yang, M. (2020). Dynamic Measurements on Unsteady Pressure Pulsations and Flow Distributions in a Nuclear Reactor Coolant Pump. *Energy* 198, 117305. doi:10.1016/j.energy.2020.117305

Su, W.-T., Li, Y., Wang, Y.-H., Zhang, Y.-N., Li, X.-B., and Ma, Y. (2020). Influence of Structural Parameters on Wavy-Tilt-Dam Hydrodynamic Mechanical Seal Performance in Reactor Coolant Pump. *Renew. Energ.* 166, 210–221. doi:10.1016/j.renene.2020.11.123

Zhou, Q., Li, H., Pei, L., and Zhong, Z. (2021). Research on Non-uniform Pressure Pulsation of the Diffuser in a Nuclear Reactor Coolant Pump. *Nucl. Eng. Techn.* 53 (3), 1020–1028. doi:10.1016/j.net.2020.08.007

Conflict of Interest: The authors declare that the research was conducted in the absence of any commercial or financial relationships that could be construed as a potential conflict of interest.

frontiers | Frontiers in Energy Research

ORIGINAL RESEARCH
published: 13 May 2022
doi: 10.3389/fenrg.2022.884624

Study on Trajectory Optimization of Hypersonic Vehicle Based on Neural Network

Feichao Cai[1]* *and Xing Huang*[2]

[1]School of Power and Energy, Northwestern Polytechnical University, Xi'an, China, [2]AECC HUNAN Aviation Powerplant Research Institute, Zhuzhou, China

For the horizontal take-off hypersonic cruise aircraft, research on the combined design method of multi-section was carried out, the main design parameters of different sections were analyzed, the parametric design model of the flight path was established, and the characteristics of the typical flight path were studied. On this basis, the calculation of sample points was carried out, and a prediction model of aircraft range and flight time based on the design parameters of the four main flight sections was established based on the neural network method. The genetic algorithm is used to optimize the flight path of the prediction model with the range as the objective function. The research results show that the neural network prediction model based on the parametric design of the trajectory can predict random sample points better than the trajectory model For the prediction of random sample points, compared with the calculation results of the trajectory model, the maximum errors of the flight range and flight time are within 0.82% and 0.45%. The prediction model is optimized with the flight range as the objective function, and the relative error between the optimal range and the trajectory model under the corresponding section parameters is less than 0.2%, which shows that the model established in this paper can better predict the range and flight time according to the section design parameters. Parametric modeling and neural network optimization are feasible methods for aircraft trajectory design and section parameter optimization.

Keywords: hypersonic, flight trajectory, neural network, genetic algorithm, optimization

OPEN ACCESS

Edited by:
Lei Luo,
Harbin Institute of Technology, China

Reviewed by:
Tugrul Oktay,
Erciyes University, Turkey
Parvathy Rajendran,
Universiti Sains Malaysia Engineering Campus, Malaysia

***Correspondence:**
Feichao Cai
caifeichao@nwpu.edu.cn

Specialty section:
This article was submitted to Advanced Clean Fuel Technologies, a section of the journal Frontiers in Energy Research

Received: *26 February 2022*
Accepted: *08 April 2022*
Published: *13 May 2022*

Citation:
Cai F and Huang X (2022) Study on Trajectory Optimization of Hypersonic Vehicle Based on Neural Network. Front. Energy Res. 10:884624. doi: 10.3389/fenrg.2022.884624

1 INTRODUCTION

Due to the outstanding tactical and technical advantages of hypersonic vehicles, they have received extensive attention. The horizontal take-off and landing of a high-speed cruise aircraft is usually powered by an air-breathing combined engine. During the climb, the acceleration and climb ability of the aircraft are affected and constrained by the dynamic characteristics, and the change in the flight profile will affect the engine performance. At the same time, the aerodynamic performance of the full mission profile is highly coupled with the engine performance (Wei, 2022). Therefore, flight profile design and optimization are very important for aircraft/engine matching and the overall technical scheme of aircraft (Mei et al., 2019), which is one of the research hotspots.

Trajectory optimization of a hypersonic vehicle involves many constraints and is a complex nonlinear multi-constraint optimal control problem (Gath and Calise, 1999), which is quite difficult and challenging to solve. Aiming at the trajectory optimization of the aircraft, research based on the trajectory model is carried out. By establishing the calculation model of the flight process, the

influence law of the parameters of different flight sections is analyzed, and the scheme design and optimization are carried out. Lu et al. (2010) proposed a trajectory design method for the climbing phase of a rocket-based combined cycle (RBCC) engine cruise vehicle based on the Mach number dynamic pressure reference curve, but did not adopt the optimization method and did not obtain the optimal solution. Based on the relationship between flight dynamic pressure and design dynamic pressure in flight, Olds and Budianto (1998) put forward three methods to realize isodynamic pressure trajectory control. The climbing trajectory is designed by establishing the Mach number dynamic pressure reference curve of RBCC aircraft and iterating the angle of attack tracking reference curve by dichotomy. Jia and Yan (2015) proposed a climbing trajectory design method for horizontal take-off aspirated combined power aircraft. The climbing trajectory is divided into three sections: take-off climbing section, isodynamic pressure section, and equal heat flow section. Constraints such as overload, dynamic pressure, and heat flow are considered respectively. The constraint boundary of trajectory design and the climbing trajectory design method of three flight sections are given in the altitude-velocity profile. The tracking guidance law of the reference trajectory is designed by using the feedback linearization method. Zhang et al. (2014) adopt the integrated analysis method of aircraft/engine, divide flight sections into different tasks in design and evaluation, and select optimization parameters through scheme comparison. These designing methods can realize the design of the trajectory, but the optimization process is mainly based on models and experience.

Trajectory optimization based on optimization theory or intelligent algorithms is another technical way. From the perspective of algorithms, trajectory optimization problems can be divided into indirect methods and direct methods (Liu, 2017). With the advancement of computer technology, direct method has become a more popular method for solving nonlinear multi-constraint trajectory optimization problems. Extensive research has been carried out on this key problem, and many research results have been obtained (Zhang, 2013; Gandhi and Theodorou, 2016). Among them, the Gauss pseudo spectral method is a direct collocation method based on global interpolation polynomials that has high computational efficiency. Therefore, it is favored by researchers and is the focus of current research (Reddien, 1979; Benson et al., 2006; Tao, 2017). In addition, as a branch of the direct method, the global pseudo spectral method has developed very rapidly, such as the adaptive pseudo spectral method, which is applied to the optimal control problem (Darby et al., 2011) and trajectory piecewise optimization (Zhao and Zhou, 2013), and the improved hp-adaptive pseudo spectral method rising section prediction based on trajectory division into multiple subintervals (Liu et al., 2016). Some scholars have also conducted comparative studies on different improved pseudo spectral methods (Narayanaswamy and Damaren, 2020). Although the pseudo spectral method is widely used in trajectory optimization, the pseudo spectral method is only a transformation method and is often used together with optimization algorithms such as sequential quadratic programming (SQP) (Cui et al., 2020). Compared with traditional algorithms such as the gradient method and dynamic programming method, modern revelation algorithms have gradually become a hot spot in recent years, including particle swarm optimization algorithms and genetic algorithms, which have been applied to many fields such as aerospace (Antunes and Azevedo, 2014; Ahuja and Hartfield, 2015). The numerical optimization algorithm in the study by Zhang (2017) is established under the framework of the particle swarm optimization algorithm. The concepts of Pareto optimal solution and congestion distance are introduced to describe the optimal solution relationship and optimization processing logic in the numerical optimization process of the algorithm, and the corresponding evaluation indexes are used to measure the quality of the optimal solution set. Zheng et al. (2018) took the RBCC hypersonic cruise vehicle as the research object, and proposed a nested optimization strategy of "particle swarm optimization algorithm and pseudo spectral method" for its climb-cruise global trajectory optimization problem. Because the genetic algorithm can be applied to different complex optimization systems, Patrón and Botez (2015) used the genetic algorithm to obtain the minimum fuel consumption flight trajectory, including the longitudinal and lateral directions for the cruise section of the long-distance aircraft. Li et al. (2012) used genetic algorithms to optimize the climbing and cruise range of RBCC hypersonic missiles. This research work has greatly promoted the development of aircraft trajectory optimization.

As a predictive modeling method, neural networks have the advantages of nonlinear fitting, and can improve the accuracy through training, realize the nonlinear approximation of high-dimensional complex mapping (Li et al., 2006), and have been applied in flow solution and flow field reconstruction (Xie et al., 2018; Wang et al., 2021), and trajectory prediction (Zheng et al., 2020). Zhang and Li (2020) optimize the initial weight and threshold in the BP neural network by constructing a GA-BP neural network and comprehensively considering the behavioral characteristics such as longitude and latitude, speed and heading, so as to realize the prediction of ship track. Ma et al. (2020) used a depth network to study trajectory generation for hypersonic vehicles. Oktay et al. (2018) carried out the optimization of the tilt stability and maximum lift drag ratio of variable UAVs, using a neural network. These studies show that neural networks can be applied to trajectory prediction.

At present, the research on aircraft trajectory optimization is relatively in-depth, and the trajectory optimization design is mostly combined with the control system design (Qian, 2021; Tang et al., 2021). For example, in the optimization process, the angle of attack is the main variation, so as to reflect the guidance and control process (Zhou et al., 2020; Zhu et al., 2020). These methods are more suitable for the improvement of flight profiles and control laws in detailed design. Compared with optimization theory and intelligent algorithms, the segment parameters of model-based trajectory design have obvious physical significance. Through the analysis of segment design parameters, it can reflect the influence of different segment parameters on the flight process, help study the coupling law

between engine performance and flight profile, and is very suitable for the preliminary design and demonstration of the trajectory. Based on the characteristics of multi parameter nonlinear influence of hypersonic vehicles, based on section analysis and parametric modeling, this paper constructs the climbing section by section, divides the climbing process into different control law processes, and studies the main influence parameters of different sections. Based on the sample calculation in the flight envelope, the nonlinear combined neural network between the section design parameters and the flight distance and flight time is established, and then the optimization algorithm is used to predict and optimize the overall trajectory parameters of the hypersonic vehicle, which provides a method for the trajectory optimization of hypersonic vehicles.

2 TRAJECTORY CALCULATION MODEL

2.1 Aircraft Centroid Motion Model

Aircraft trajectory calculations include dynamic and kinematic models. The equations describing the motion parameters of the aircraft centroid include:

$$\begin{cases} \dot{R} = V\sin\gamma \\ \dot{\theta} = \dfrac{V\cos\gamma\sin\psi_V}{R\cos\phi} \\ \dot{\phi} = \dfrac{V\cos\gamma\cos\psi_V}{R} \\ \dot{V} = \dfrac{P\cos\alpha\cos\beta - D}{m} - g\sin\gamma \\ \dot{\gamma} = \dfrac{1}{mV}\left[P\left(\sin\alpha\cos\gamma_V + \cos\alpha\cos\beta\sin\gamma_V\right) + L\cos\gamma_V - Z\sin\gamma_V\right] - \dfrac{g}{V}\cos\gamma \\ \psi_V = -\dfrac{1}{mV\cos\gamma}\left[P\left(\sin\alpha\sin\gamma_V - \cos\alpha\sin\beta\cos\gamma_V\right) + L\sin\gamma_V + Z\cos\gamma_V\right] \end{cases}, \tag{1}$$

where R is the distance from the aircraft to the earth's center, V is the aircraft speed, θ and ϕ are the longitude and latitude of the aircraft, respectively, γ is the trajectory inclination, ψ_V is the trajectory deflection angle, γ_V is the speed inclination angle, α and β are the attack angle and sideslip angle of the aircraft respectively, L, D, Z, and P are lift, drag, lateral force, and engine thrust, respectively.

The aerodynamic force acting on the aircraft is the functional relationship of flight speed Ma, height H, attitude angles α, β, etc., and control surface deflection angles δ_x, δ_y, δ_z, etc., which can be expressed as:

$$C_{L,D,Z} = f\left(Ma, H, \alpha, \beta, \delta_x, \delta_y, \delta_z\right), \tag{2}$$

In addition, the trajectory calculation also needs the geometric relationship between the angles in **formula (1)**, atmospheric model, a control system loop model, etc.

2.2 Flight Section Model

For hypersonic vehicles, they go through different flight stages, from ground zero speed take-off to high-altitude high-speed cruise. According to the flight characteristics of different stages, the trajectory can be divided into different sections. Typical sections include:

(1) Program flight section

At the initial stage of takeoff and climb, the aircraft can fly according to a certain law of trajectory parameters. The flight program can construct different modes according to different parameters, such as the change of angle of attackα, the law of altitude H, etc. A typical variation law according to the trajectory inclination γ is:

$$\frac{d\gamma}{dt} = \begin{cases} C_1 & 0 < t < t_1 \\ -C_2 & t_1 \le t < t_2 \end{cases}. \tag{3}$$

Among them, C_1 and C_2 can be taken as constants. Under this law, the aircraft takes off from the horizontal state, gradually decreases after reaching the maximum trajectory inclination, and finally turns into the level flight state.

If the height change rate is taken as the parameter, set the height change rate as a function of time, that is:

$$\frac{dH}{dt} = f(t). \tag{4}$$

$f(t)$ can be a constant value or the law of time. When the climbing ability is insufficient or you want to obtain a large acceleration rate, it can fly at constant altitude and the climb rate is zero, that is:

$$\frac{dH}{dt} = 0. \tag{5}$$

(2) Variable acceleration flight

According to the performance of the engine, the acceleration rate $\dot{V}$ is taken as the control variable in the climbing process. The higher the thrust of the engine, the greater the acceleration rate that can be achieved, otherwise the acceleration rate is reduced. Acceleration rate as a function of time is achieved for a specific flight section:

$$\frac{dV}{dt} = f(t, H, Ma). \tag{6}$$

If the acceleration rate is set to be constant, that is, a constant acceleration rate climb, that is:

$$\frac{dV}{dt} = C. \tag{7}$$

(3) Isodynamic pressure flight

Isodynamic pressure flight is a common flight mode of aircraft, which can coordinate between acceleration rate and climb rate under the constraint of structural load. That is:

$$\begin{cases} \dfrac{dQ}{dt} = 0 \\ Q_0 = C \end{cases}. \tag{8}$$

(4) Cruise flight

When the aircraft reaches the predetermined cruise flight state, the flight altitude and speed remain constant. it is necessary to control the engine thrust through speed feedback and the balance relationship between aerodynamic force and moment to realize cruise flight. During cruise flight, the following requirements are met:

$$\begin{cases} \dfrac{dH}{dt} = 0 \\ \dfrac{dV}{dt} = 0 \\ H = H_C \\ V = V_C \end{cases}. \tag{9}$$

In the above formula, H_C is the cruise altitude and V_C is the cruise speed.

(5) Transition Process Control

During flight, there will be differences in parameters between different sections. During the section conversion, the parameter PID feedback control is used to realize the smooth transition. For example, when transitioning from the constant acceleration phase to constant dynamic pressure flight, take Q^* as the expected dynamic pressure value by controlling the change of trajectory inclination $\Delta\gamma$ adjust the dynamic pressure. Construct the following model:

$$\Delta\gamma^* = K_1(Q - Q^*) + K_2\dot{Q} + K_3\int (Q - Q^*)dt. \tag{10}$$

(6) Engine thrust

The main flight processes of horizontal take-off high-speed aircraft include ground take-off acceleration climb, constant speed cruise, return and other processes. In the climbing process, it is expected to climb at a large acceleration, and the engine works according to the maximum state, including:

$$P = P_{Max}(H, Ma, Q, \varepsilon). \tag{11}$$

Where H, Ma, Q, and ε are flight altitude, Mach number, dynamic pressure, and fuel gas ratio, respectively, and P_{Max} is the thrust value under the maximum condition of the engine.

During cruise flight, the engine works in a throttling state, and the change in thrust can be calculated according to the feedback of a predetermined speedMa^*, and then the thrust can be adjusted through fuel supply. The thrust adjustment of the cruise section adopts the following form:

$$\Delta P = K_1(Ma - Ma^*) + K_2 Ma. \tag{12}$$

(7) Constraints

During the flight, the flight profile, trajectory parameters, attitude angle, etc. will change. According to the design scheme, during the trajectory calculation, it is necessary to restrict the variation range of multiple parameters, mainly including:

Attack angle constraint: $\alpha \in [\alpha_{Min}, \quad \alpha_{Max}]$.

Dynamic pressure constraint: $Q \in \frac{1}{2}\rho V^2 \in [Q_{Min}, \quad Q_{Max}]$.

Flight profile constraints: $Ma \le Ma_{Max}$; $H \le H_{Max}$.

Overload restraint: $N_y \le N_{yMax}$; $N_z \le N_{zMax}$.

Aerodynamic thermal restraint (Jia and Yan, 2015):

$$\dot{q} \le \frac{C_1}{\sqrt{R_d}}\left(\frac{\rho}{\rho_0}\right)^{0.5}\left(\frac{V}{V_C}\right)^{3.15} \le \dot{q}_{Max}. \tag{13}$$

The above constraints affect each other, so they are balanced according to certain strategies during flight.

2.3 Flight Section Design Parameter Analysis

For the flight process of horizontal take-off and landing on a high-speed cruise, the flight trajectories of different flight sections can be constructed. According to the model characteristics of different flight sections, the parameters affecting the flight process are extracted, and the parameter selection needs to be analyzed from the aspects of simplicity and sensitivity. Taking the longitudinal plane flight process as an example, this paper uses a typical four-section trajectory model for analysis. Since the range and flight time are mainly related to the climb and cruise process, the fuel threshold required for the return process is set in the calculation, and the return landing process is no longer compared. The main parameters are listed in **Table 1**, and the trajectory is shown in **Figure 1**.

The typical flight sections described above have a total of 11 parameters. By changing the parameter values and combining the constraints, different flight trajectories can be obtained. Obviously, in the flight profile, there are many parameters affecting the flight process, and there is a complex mutual coupling relationship between them.

Analyzing all parameters would greatly increase the difficulty of analyzing and optimizing the design. In practice, different parameters have different effects on flight trajectory. Through the analysis of a typical trajectory, four parameters are selected as the main variables for the trajectory analysis and optimization design for the flight mission with a certain cruise altitude and speed, including the flight time of the acceleration section T_{A}, the acceleration section acceleration $\dot{V}_{BSet}$, the acceleration section end speed V_{BEnd}, and the dynamic pressure Q_{Cset} in the climb section.

2.4 Numerical Calculation Method

The trajectory calculation model is a system of differential equations, and the fourth-order Runge-Kutta method is adopted for the differential equations. Let the initial value problem be expressed as follows:

$$y' = f(t, y), \quad y(t_0) = y_0,$$
$$y_{n+1} = y_n + \frac{h}{6}(k_1 + 2k_2 + 2k_3 + k_4). \tag{14}$$

TABLE 1 | Parameters of flight section.

Section	Number	Parameter value
I: Programme	A1	Trajectory inclination acceleration rate C_{A1}
	A2	Trajectory inclination reduction rate C_{A2}
	A3	Time of trajectory inclination increase T_{A1}
	A4	Trajectory inclination reduction time T_{A2}
	A5	Total time of program section T_A
II: Constant acceleration	B1	Expected acceleration $\dot{V}_{BSet}$
	B2	Speed at the end of acceleration section V_{BEnd}
III: Constant dynamic pressure	C1	Predetermined dynamic pressure Q_{Cset}
	C2	Speed at the end of constant dynamic pressure section Ma_{Cset}
IV: Cruise	D1	Cruise altitude H_{Dset}
	D2	Cruise speed Ma_{Dset}

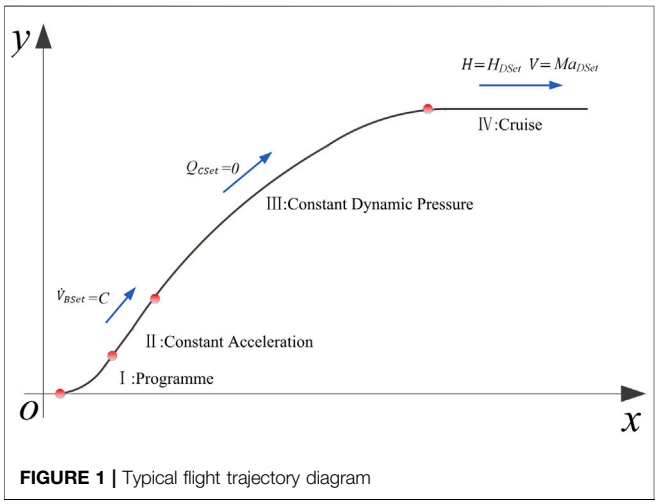

FIGURE 1 | Typical flight trajectory diagram

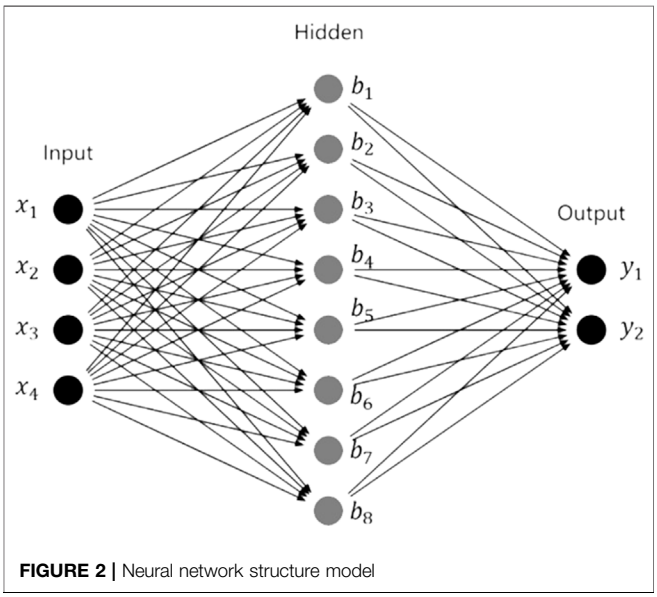

FIGURE 2 | Neural network structure model

Here:

$$k_1 = f(t_n, y_n),$$
$$k_2 = f\left(t_n + \frac{h}{2}, y_n + \frac{h}{2}k_1\right),$$
$$k_3 = f\left(t_n + \frac{h}{2}, y_n + \frac{h}{2}k_2\right),$$
$$k_4 = f(t_n + h, y_n + hk_3).$$

The trajectory is solved by integrating on the time axis.

3 MODELING AND OPTIMIZATION METHOD

3.1 Neural Network Modeling Method

The BP neural network is a nonlinear parameter modeling method. Its most obvious feature lies in the error back-propagation learning algorithm it adopts, and it can adjust the weight coefficients of each layer network in the model in real time through continuous learning. When the total weight and fuel are constant, the variables of trajectory analysis and optimal design are used as input values, and the range R_D and flight time T_D are output values to establish a prediction model for the overall parameters of the trajectory. Since the input data of the neural network is given 4 parameters, the input layer has four nodes. The hidden layer is 1, the number of neurons is 8, and the output layer has two nodes. The adopted neural network structure is shown in **Figure 2**.

The input of the h neuron in the hidden layer is:

$$a_h = \sum_{i=1}^{4} \omega_{ih} x_i, \tag{15}$$

where ω_{ih} represents the weight of the i input neuron in the input layer to the h neuron in the hidden layer.

The activation function passing through the hidden layer is the *tansig* function, and the expression is:

$$f(x) = \frac{2}{1 + e^{-2x}} - 1. \tag{16}$$

Thus:

$$b_h = f(\alpha_h - \gamma_h), \tag{17}$$

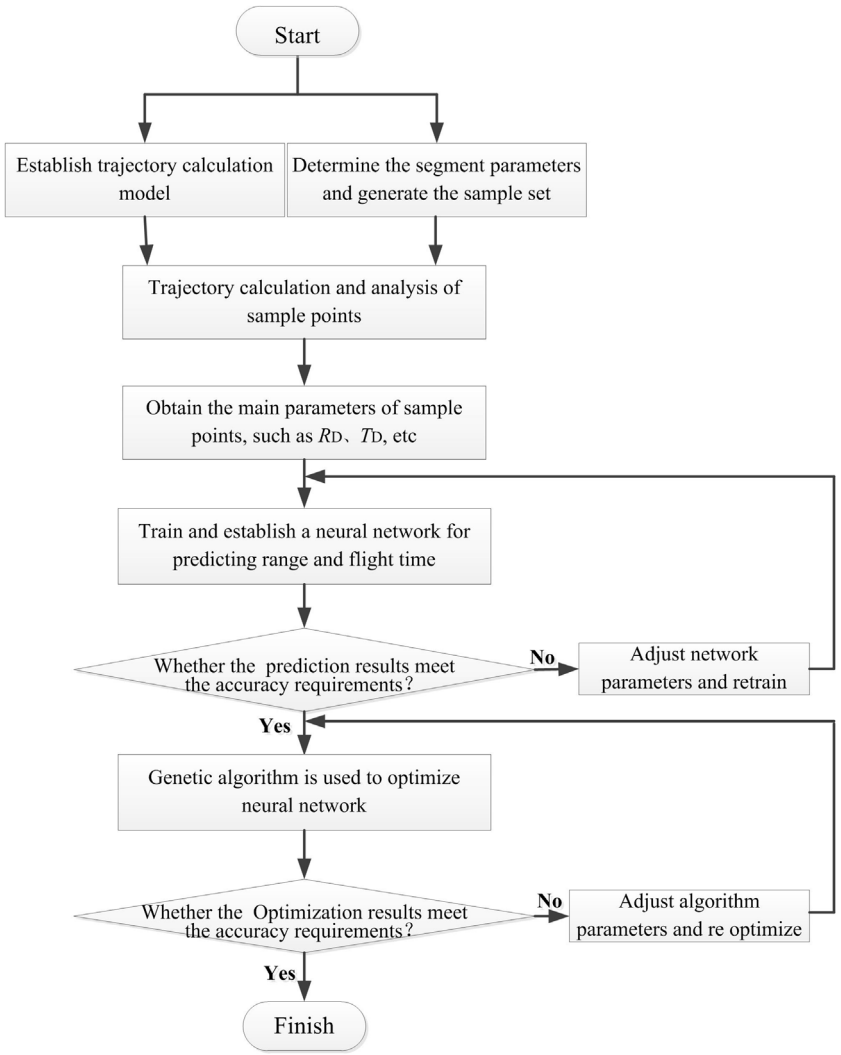

FIGURE 3 | Modeling and analysis process

where γ_h represents the threshold of the h neuron in the hidden layer.

The input of the j neuron in the output layer is:

$$\beta_j = \sum_{h=1}^{8} v_{hj} b_h, \tag{18}$$

where v_{hj} represents the weight from the h neuron in the hidden layer to the j output in the output layer.

The activation function of the output layer is the *purelin* function, and the expression is:

$$f(x) = x. \tag{19}$$

Thus, the output of the neural network is:

$$\tilde{y_j} = f\left(\beta_j - \theta_j\right), \tag{20}$$

where θ_j represents the threshold of the j neuron in the output layer.

Establish loss function:

$$J = \frac{1}{2}\sum_{j=1}^{2}\left(\tilde{y_j} - y_j\right)^2, \tag{21}$$

where y_j is the target output and $\tilde{y_j}$ is the output of the neural network.

By optimizing the input weights of neurons in each layer to minimize the loss function, the output of the neural network is close to the target output as much as possible, and the training model is obtained. Finally, the training model is used for prediction.

3.2 Optimization Algorithm

Based on the establishment of a parametric prediction model, optimization analysis can be carried out. There are many optimization design methods. Among them, the genetic algorithm, as a global optimization design method, has better

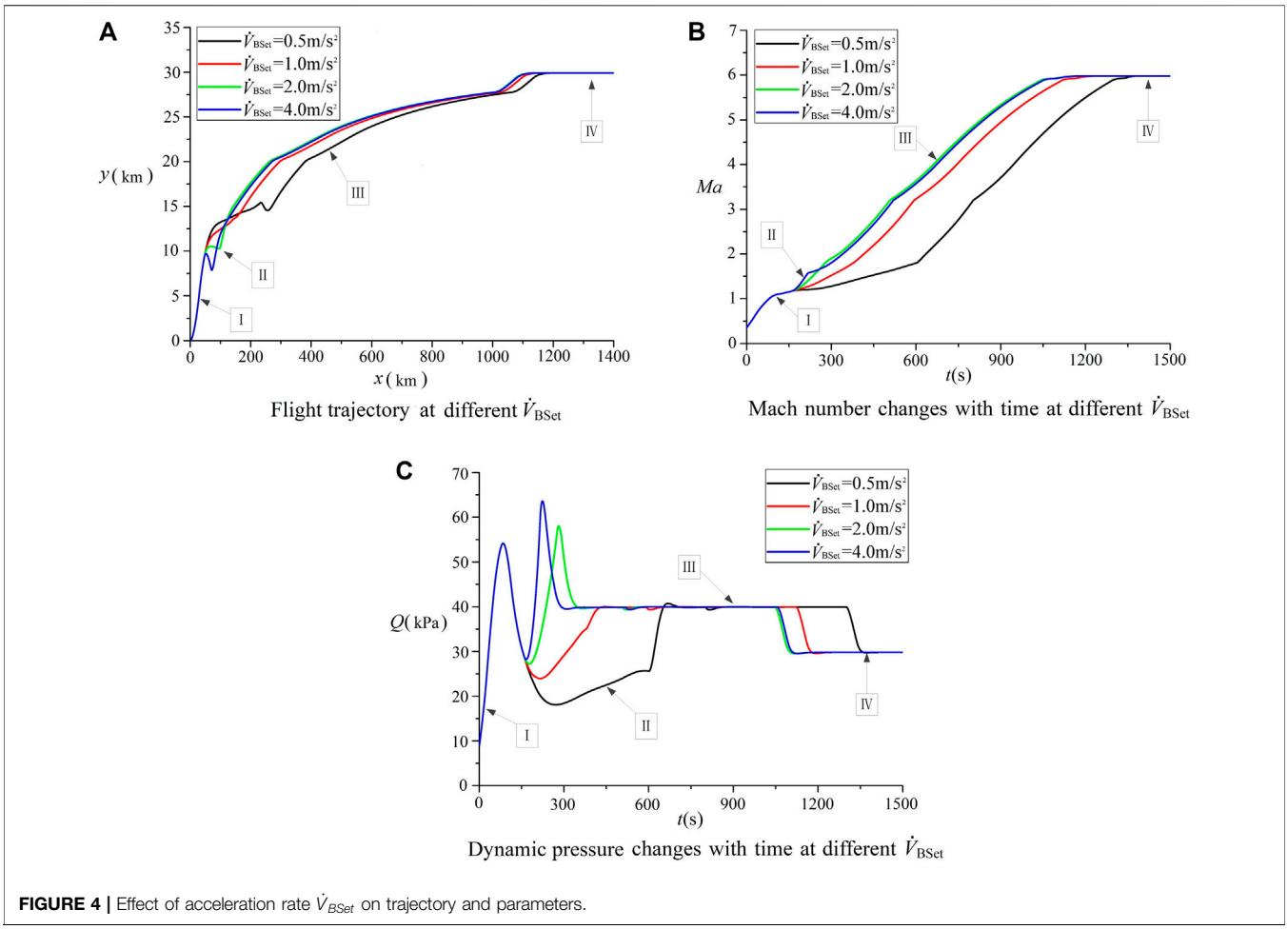

FIGURE 4 | Effect of acceleration rate $\dot{V}_{BSet}$ on trajectory and parameters.

optimization accuracy for nonlinear high-dimensional functions. In this paper, a genetic algorithm is used to optimize the neural network.

3.3 Modeling and Analysis Process

Through the combination of flight sections and parametric modeling, the trajectory optimization of the aircraft is transformed into the established neural network model and the process of optimization. The process of simulation calculation and modeling is as follows:

Step 1. Determine the model's input and output parameters and sample points

According to the flight section analysis of the aircraft, taking the four main parameters that affect the flight section as the input and the range R_D and flight time T_D as the output, the functional relationship is established as follows:

$$\begin{aligned} R_D &= f_R\left(T_A, \dot{V}_{BSet}, V_{BEnd}, Q_{CSet}\right), \\ T_D &= f_T\left(T_A, \dot{V}_{BSet}, V_{BEnd}, Q_{CSet}\right). \end{aligned} \tag{22}$$

According to the working envelope of the aircraft, the analysis sample points for modeling are determined through experimental design or parameter combination. For the four parameter combinations in this paper, a total of 420 sample points are taken.

Step 2. Trajectory calculation of sample points

For the sample points, carry out the trajectory calculation in the flight process according to the trajectory calculation model established in **Section 2**, and obtain the sample values of the range R_D and flight time T_D.

$$\begin{cases} R_{D0} = f_{R0}\left(T_A, \dot{V}_{BSet}, V_{BEnd}, Q_{CSet}\right) \\ R_{D1} = f_{R1}\left(T_A, \dot{V}_{BSet}, V_{BEnd}, Q_{CSet}\right) \\ \cdots\cdots \\ R_{Dm} = f_{Rm}\left(T_A, \dot{V}_{BSet}, V_{BEnd}, Q_{CSet}\right) \end{cases} \quad \begin{cases} T_{D0} = f_{T0}\left(T_A, \dot{V}_{BSet}, V_{BEnd}, Q_{CSet}\right) \\ T_{D1} = f_{T1}\left(T_A, \dot{V}_{BSet}, V_{BEnd}, Q_{CSet}\right) \\ \cdots\cdots \\ T_{Dm} = f_{Tm}\left(T_A, \dot{V}_{BSet}, V_{BEnd}, Q_{CSet}\right) \end{cases} . \tag{23}$$

Step 3. Establish neural network model based on sample points

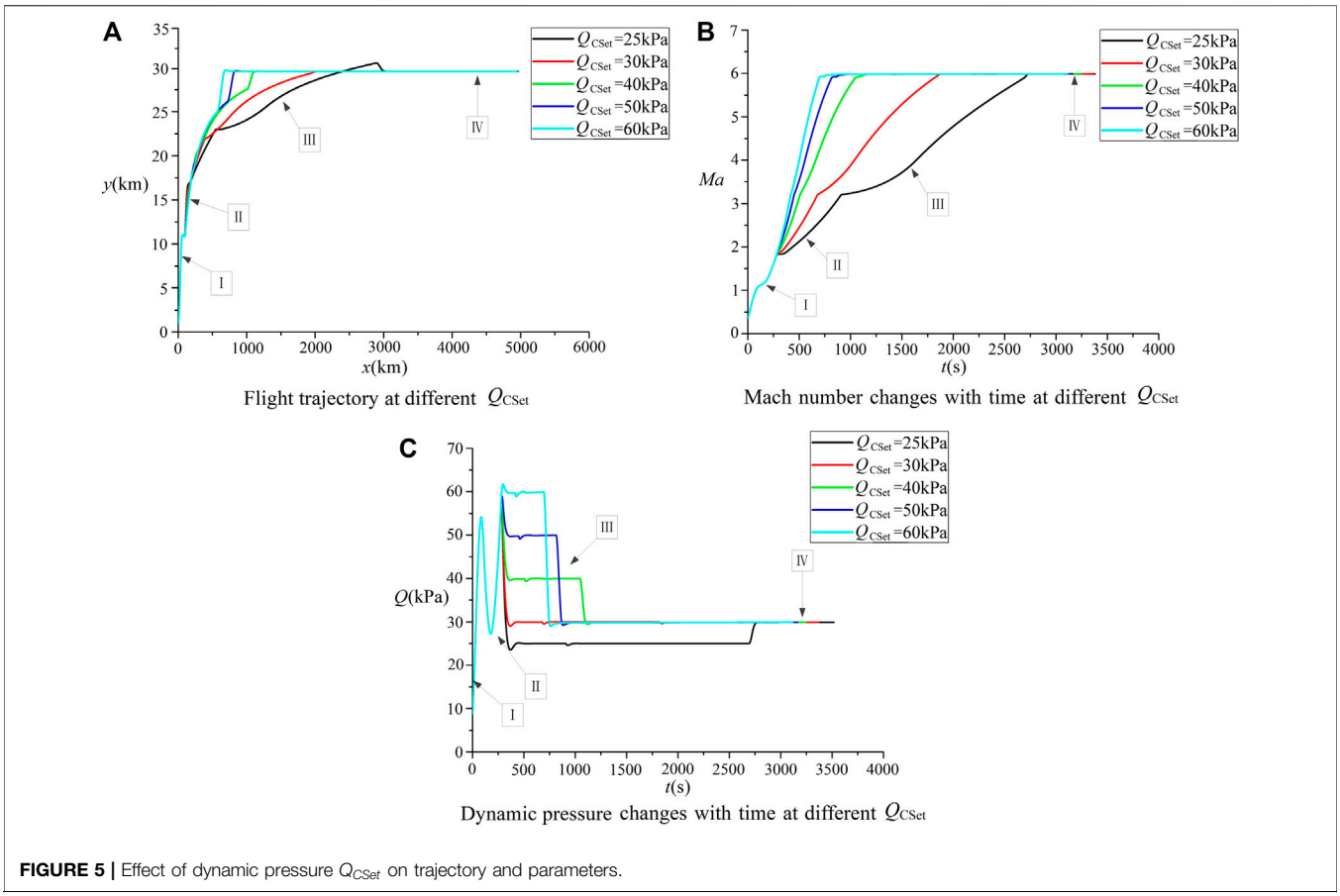

FIGURE 5 | Effect of dynamic pressure Q_{CSet} on trajectory and parameters.

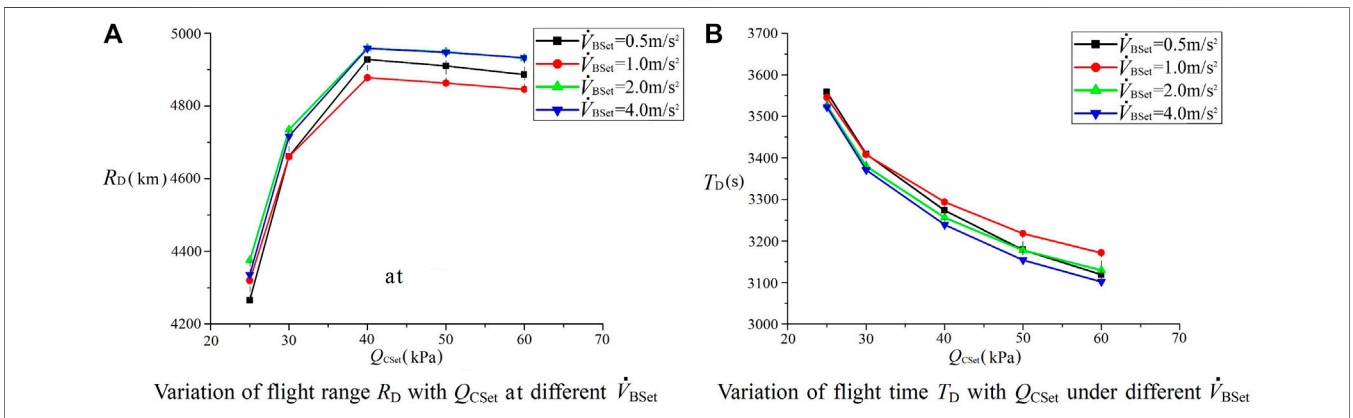

FIGURE 6 | Influence of parameters on overall parameters.

Based on the trajectory calculation results of sample points, the neural network is trained to obtain the functional model between section parameters and range R_D and time T_D. On this basis, the established neural network model is used to predict the random sample points in the flight envelope. After comparing with the trajectory calculation results, the feasibility and accuracy of the model are analyzed.

Step 4. Model optimization

According to the established neural network model, the optimization of the neural network is carried out by using a

TABLE 2 | Experimental and verification scheme.

Experiment serial number	Training set	Test set
1	s1, s2, s3	s4
2	s1, s2, s4	s3
3	s1, s3, s4	s2
4	s2, s3, s4	s1

genetic algorithm with flight range R_D as the optimization objective function. The trajectory calculation is carried out by using the segment parameter value corresponding to the best advantage obtained by optimization. The difference between the optimized value and the calculated value of range and time under the same segment parameters is compared, the feasibility of the optimization result is evaluated, and the characteristics of the optimized trajectory are analyzed.

In the calculation process, the neural network modeling and optimization algorithm parameters can be adjusted according to the verification of the model. The overall modeling and calculation process is shown in **Figure 3**.

4 TRAJECTORY CALCULATION AND ANALYSIS

Trajectory calculation is carried out for the parameter combination of sample points. Among the four parameters selected in this paper, the acceleration rate $\dot{V}_{BSet}$ and dynamic pressure Q_{Cset} have a great influence on the middle of the climb, which is mainly analyzed.

4.1 Influence of Acceleration Rate $\dot{V}_{BSet}$ on Trajectory

For parameters T_A = 160s, speed V_{BEnd} = Ma1.8, and climb dynamic pressure Q_{Cset} = 40kPa, four different climb rates are

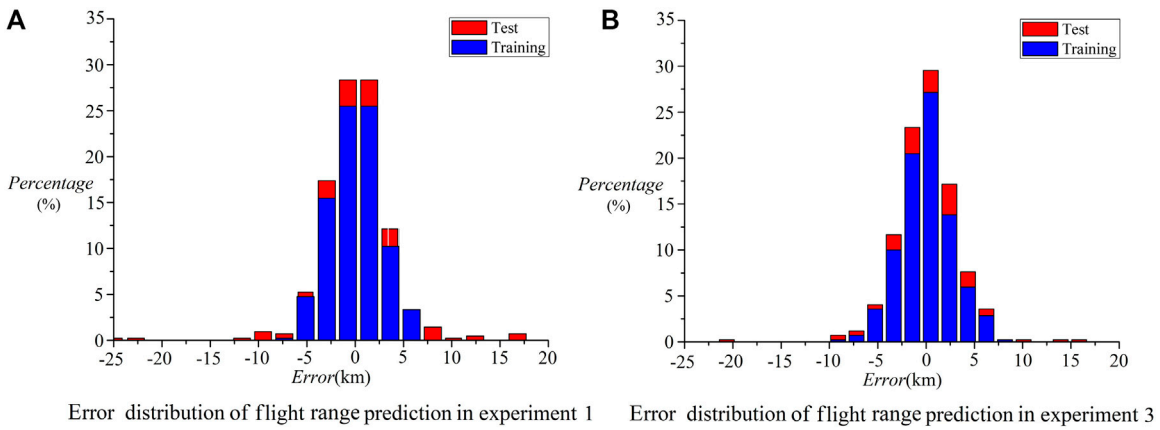

FIGURE 7 | Range R_D prediction results.

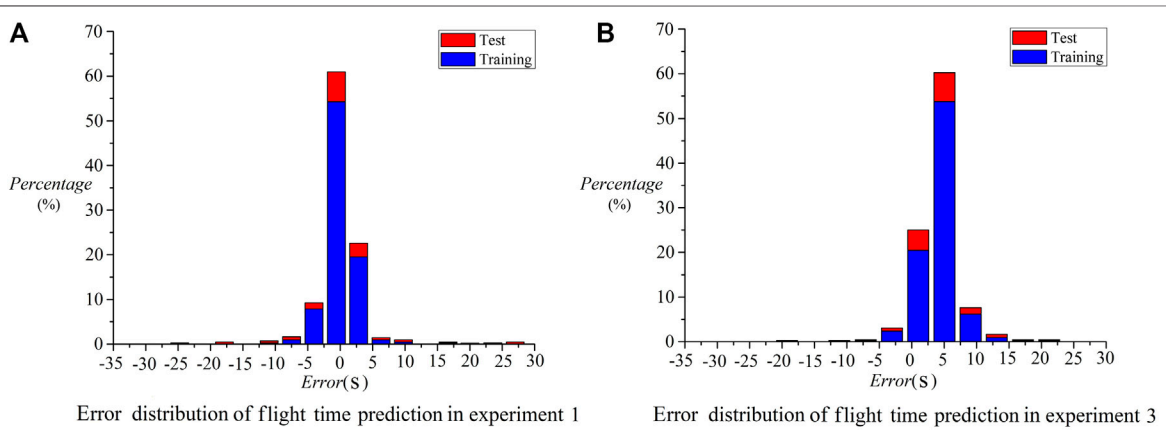

FIGURE 8 | Flight time T_D prediction results.

TABLE 3 | Range and flight time prediction results.

Condition	T_A(s)	$\dot{V}_{BSet}$ (m/s^2)	V_{BEnd} (Ma)	Q_{CSet} (kPa)	$R_{D(BP)}$ (km)	$R_{D(Tra)}$ (km)	Error (%)	$T_{D(BP)}$ (s)	$T_{D(Tra)}$ (s)	Error (%)
1	130	2.4	1.6	35	4902.02	4896.38	0.115	3299.03	3300.57	-0.047
2	90	3.2	1.4	50	4890.86	4885.06	0.119	3133.13	3119.13	0.4488
3	168	1.6	1.7	53	4940.83	4927.74	0.266	3180.49	3171.99	0.268
4	160	0.8	1.3	26	4382.07	4346.47	0.819	3522.28	3522.89	-0.017
5	190	2.2	1.5	29	4647.79	4644.59	0.069	3426.20	3418.99	0.2109
6	110	3.8	1.6	29	4637.02	4627.56	0.204	3397.19	3386.42	0.318
7	150	2.8	1.9	37	4917.70	4925.80	-0.16	3260.34	3261.60	-0.039
8	120	3.5	1.2	58	4922.90	4919.39	0.071	3101.65	3096.20	0.176
9	170	1.9	1.6	40	4939.34	4956.98	-0.36	3267.73	3267.02	0.0217
10	130	1.8	1.8	32	4812.04	4806.08	0.124	3341.99	3341.07	0.0275

TABLE 4 | Main parameters of genetic algorithm.

Parameter	Value
Group size	200
Crossover probability	0.8
Mutation probability	0.05
Maximum evolutionary algebra	500

TABLE 5 | Optimization calculation results.

T_A(s)	$\dot{V}_{BSet}$ (m/s^2)	V_{BEnd} (Ma)	Q_{CSet} (kPa)	R_D (km)	T_D(s)
134.23	2.378	1.205	40.877	4991.40	3247.24

used to calculate flight paths. The results are compared in **Figure 4**.

Before 160 s, the aircraft climbs according to the law of trajectory inclination. The flight Mach number continues to increase, and the dynamic pressure first increases and then decreases. The change is related to the inclination design in the program section. When compared with the trajectory of the climb section in **Figure 4A**, combined with the analysis of Mach number and dynamic pressure change, when the acceleration is $\dot{V}_{BSet}$ 0.5 m/s^2, the flight speed of **Section 2** increases slowly. Under the maximum thrust of the engine, the climb rate of the aircraft is high, that is, the increase rate of height is large, so the dynamic pressure decreases rapidly in the initial stage, as shown in **Figure 4C**. Due to the low acceleration rate, when the flight time is 602.4 s, the speed reaches *Ma*1.8 and turns to **Section 3** dynamic pressure flight. In this process, maintain a low dynamic pressure of about 20–25 kPa. Due to the long flight time of **Section 2**, the overall acceleration and climb time increases significantly, and the aircraft enters the cruise flight in 1300 s.

When the acceleration $\dot{V}_{BSet}$ of the constant acceleration section increases to 1 m/s, the climb rate of **Section 2** decreases, the slope of the Mach number curve increases (**Figure 4B**), and the corresponding dynamic pressure also increases. Through calculation, the flight speed reaches Ma1.8 when the time is 377.9 s, and it turns to **Section 3** constant dynamic pressure climb. Compared with the condition of acceleration of 0.5 m/s^2, the overall climbing time is significantly reduced, and it enters the cruise flight state at 1122 s.

When the acceleration of **Section 2** is further increased, the climb rate of the aircraft is reduced under a certain thrust, and the kinetic energy is increased rapidly by reducing the increasing trend of potential energy. As shown in the trajectory curve in **Figure 5A**, when$\dot{V}_{BSet} = 2m/s^2$, the constant acceleration section is approximately level flight, and when the acceleration is further increased to 4 m/s^2, a local dive is required to achieve a rapid increase in speed. From the change process of Mach number, when $\dot{V}_{BSet} = 2m/s^2$, the flight speed reaches Ma1.8 at277.9 s and turns into a constant dynamic pressure flight section; when $\dot{V}_{BSet} = 4m/s^2$, the flight speed is about Ma1.57 at 217.1 s, but the flight dynamic pressure has exceeded the set maximum dynamic pressure constraint value, so the flight speed is directly transfer to **Section 3**. From the perspective of dynamic pressure changes, after the acceleration rate exceeds 2 m/s^2, the dynamic pressure of **Section 2**

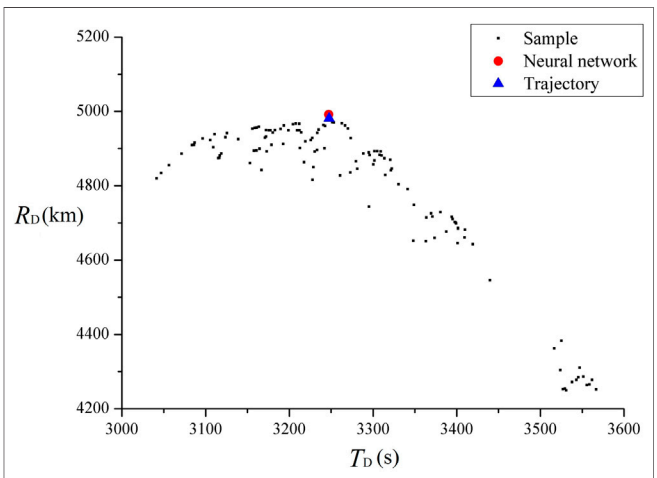

FIGURE 9 | Comparison between optimization results and sample points.

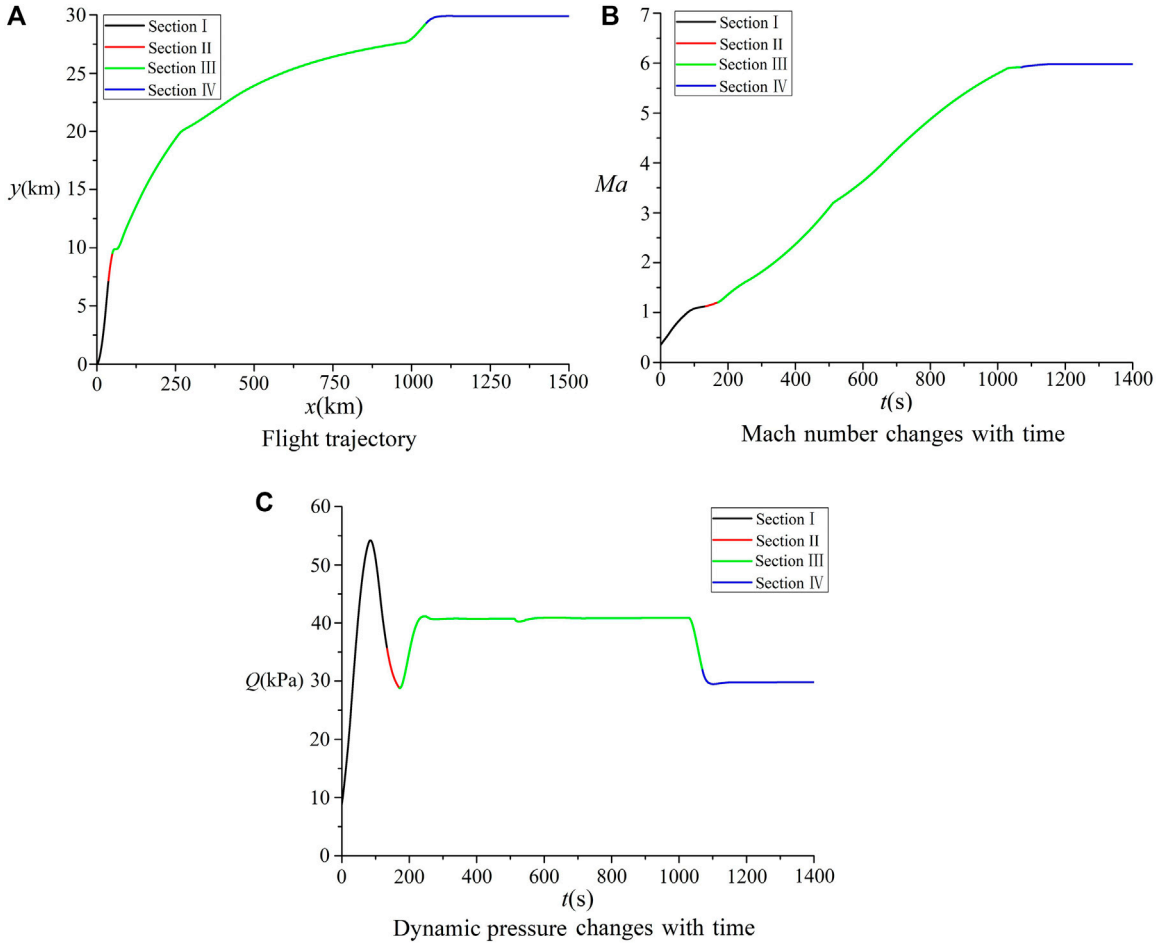

FIGURE 10 | Parameter variation of the optimized trajectory.

increases, and the maximum dynamic pressure exceeds the preset dynamic pressure value of **Section 3**. When transitioning to **Section 3**, the climb rate of the aircraft increases and the acceleration rate decreases until the dynamic pressure is restored. Decrease to the preset dynamic pressure value of **Section 3**, and then maintain the isodynamic pressure to fly. Because the acceleration time is shorter when the acceleration rate is large, the time to enter the cruise flight is also relatively early.

4.2 Influence of Dynamic Pressure Q_{CSet} on Trajectory

For parameters T_A = 160s, speed V_{BEnd} = Ma1.8, and acceleration $\dot{V}_{BSet} = 2m/s^2$, four different climb rates are used to calculate flight paths. The results are compared in **Figure 4**. The flight trajectory under four groups of dynamic pressure Q_{CSet} is calculated.

From the change of parameters in **Figure 5A, B**, the flight dynamic pressure increases, the speed increases faster and the climbing time decreases. When Q_{CSet} = 25kpa, the acceleration process is the longest. Due to the low dynamic pressure flight, the engine thrust is low and the climbing process is slow. It takes about 2693 s to reach the predetermined cruise flight state. With the increase of flight dynamic pressure, the engine thrust increases, and the climbing speed of the aircraft also increases. When the dynamic pressure is 60 kPa, the predetermined cruise parameters can be reached in 650 s, and the aircraft will turn to **Section 4**. From the trajectory in **Figure 5A**, in addition to the difference in climbing time and distance due to the cruise dynamic pressure setting of about 30 kPa and the climbing trajectory according to the dynamic pressure of 25 kPa, the maximum altitude has been higher than the cruise altitude before turning into cruise flight, and the flight altitude needs to be reduced when turning into **Section 4**. When the dynamic pressure during climbing is greater than 40 kPa, it needs to transition to the cruise altitude through further climbing because it is greater than the set cruise dynamic pressure. Under the given flight strategy, the dynamic pressure of **Section 1** is first high and then low (**Figure 5C**). The dynamic pressure has achieved a good transition in the process of change, and there is no serious parameter overshoot and fluctuation.

Corresponding to the changes in trajectory and Mach number, when turning to cruise flight, the dynamic pressure transits from the climb phase to the cruise dynamic pressure.

According to the ballistic simulation of the above typical state, the range and flight time under different combinations of parameters are extracted, which are compared with **Figure 6**.

From **Figure 6A**, the dynamic pressure Q_{CSet} of **Section 3** has a great impact on the range. The range is significantly smaller under the low dynamic pressure of 25 kPa, which is due to the long climbing time and more total fuel consumption. When the dynamic pressure value of **Section 3** is about 40 kPa, the range is the largest. If the dynamic pressure value is further increased, the range will be slightly reduced. From the influence of acceleration$\dot{V}_{BSet}$, the influence under different dynamic pressures is different. When the flight dynamic pressure of **Section 3** is 25 kPa, the range with an acceleration rate of 0.5 m/s^2 is the smallest, while the range with an acceleration rate of 2 m/s^2 and 4 m/s^2 is the largest. When the dynamic pressure is 40kPa, the range with an acceleration rate of 2 m/s^2 is the largest and the range with an acceleration rate of 1 m/s^2 is the smallest, which indicates that there is an interactive relationship between the design parameters of the flight section.

From **Figure 6B**, the dynamic pressure of **Section 3** has a monotonic effect on the flight time. As the dynamic pressure Q_{CSet} increases, the flight time decreases. Compared with the influence of dynamic pressure, the influence of acceleration rate on flight time is relatively small. When the dynamic pressure is 60 kPa, the difference in flight time under different acceleration rates is less than 70 s.

5 PREDICTION MODELING AND OPTIMIZATION

5.1 Neural Network for Predict R_D and T_D

According to the calculation results of sample points, a neural network prediction model corresponding to four parameters, flight range, and flight time is constructed. In the process of parameter construction, through the optimization of neural network model parameters, the main parameters are as follows:

1) Number of hidden layers is 1
2) Number of neurons in hidden layer is 8
3) Learning rate is 0.01
4) Minimum training error is 0.00000 1
5) Training times: 1,000

In order to better test the prediction effect of the algorithm model, the experimental scheme of cross validation is adopted. The data is randomly divided into four subsets, which are recorded as S_1, S_2, S_3, and S_4. Select S_1, S_2, S_3, and S_4 as the test sets, respectively, and select the other three subsets as the training set to establish the model. The experimental and verification scheme are shown in **Table 2**.

The neural network is trained according to the test and verification scheme given in **Table 2**. The R_D and T_D training and prediction results of the two sets of trials are compared in **Figure 7** and **Figure 8**. From the results, the training model's error in the sample prediction value of the flight range is mainly concentrated in ±10 km, and the value error of the flight time prediction value is mainly between ±5 s. The error value of individual test sample points is relatively large, but the relative error is not high, indicating that the neural network has better accuracy.

The random state test is carried out for the established prediction model. **Table 3** shows the range and flight time calculated by using neural network and trajectory model, respectively, under the randomly selected 10 groups of parameter combinations. From the comparison of results, the maximum error between the range prediction value $R_{D(BP)}$ and the trajectory calculation value $R_{D(Tra)}$ is in condition 4. The relative error of the two algorithms is less than 0.82%, and the error of other conditions is less than 0.3%. The maximum relative error between the predicted value $T_{D(BP)}$ of flight time and the calculated value $T_{D(Tra)}$ of trajectory is within 0.45%. It can be seen that the neural network prediction model has high accuracy.

5.2 Parameter Optimization

The aircraft's range is an important indicator of the overall design. In the trajectory design, overload, attack angle, dynamic pressure, etc. have been reflected in the flight model as constraints, so the range R_D is used as the objective function of trajectory optimization.

A genetic algorithm is used to optimize the overall parameters of the established neural network prediction model. The main parameters of the algorithm refer to the values in the study by Cheng and Wang (2011), and the settings are listed in **Table 4**:

In order to test the influence of genetic algorithm parameters, the group sizes of 50, 100, 150, 200, and 250 are taken, and the optimal value of R_D obtained by optimization varies from 4991.40 to 4992.26 km; Take five groups of mutation probability of 0.05, 0.10, 0.15, 0.20, and 0.25. The variation range of R_D is 4991.40–4992.78 km, and its relative variation value is very small. For the training model, the change of algorithm parameters is not sensitive to the optimization results, so it can be carried out according to the parameter values in **Table 4**.

Based on the parameter settings in **Table 4**, a total of 138 steps are iterated, and the calculated results are listed in **Table 5**. From the optimization results, the flight pressure is close to 40 kPa, which is similar to the ballistic characteristics analysis results in **Section 4**.

The optimal value in **Table 5** is used as the input parameter for trajectory calculation. Under this condition, the flight time of the aircraft is 3247.60 s and the range is 4981.15 km. The result of the trajectory calculation is basically consistent with the time prediction value in **Table 4**. The range value is slightly smaller, and the relative error is 0.2058%. Comparing the overall parameters of the sample points, the optimized results, and the optimal point of trajectory calculation in **Figure 9**, it can be seen that the optimized result range R_D is the best, and the flight time T_D is at the middle level of the sample points.

The trajectory and parameter changes in the optimized state are shown in **Figure 10**. From the analysis of the flight process, since the end speed of **Section 2** is Ma1.205, the proportion of this section in the climb process is relatively small, and it is transferred to **Section 3** isodynamic flight when the flight altitude is about

8.7 km. During the whole climbing process, the flight speed continued to increase, and the acceleration in the isodynamic pressure section was large. After the change of dynamic pressure, the maximum value is about 55 kPa, which does not exceed the upper and lower limits of constraints, and the parameter changes are within a reasonable range.

6 CONCLUSIONS

In this paper, research on the parametric modeling of the trajectory is carried out for hypersonic vehicles. Based on the calculation results of the sample points, a neural network model for predicting the flight range and flight time is established, and the genetic algorithm is used to optimize the flight range prediction model. The research has the following conclusions:

(1) The flight process of hypersonic aircraft is complex, and the parameters between each section are mutually constrained. Parametric modeling can be achieved, by designing the flight process as a combination of typical sections and extracting the parameters that affect the sections.
(2) From the influence of typical parameters, the flight dynamic pressure Q_{CSet} is more sensitive to the parameters of the climbing section and the range of the aircraft. When the dynamic pressure is lower than 30 kPa, the climb time will be significantly increased, the fuel will be consumed, and the range will be significantly reduced; when the dynamic pressure is higher than 50 kPa, the range will also decrease.
(3) Based on the sample points, a BP neural network for predicting the range and flight time was established, and the random state test was used. The errors of the range R_D and flight time $T_{D,}$ relative to the calculation results of the trajectory model were within 0.82% and 0.45%, respectively, indicating that the established model has good prediction ability for overall parameter value of the aircraft trajectory.
(4) The genetic algorithm is used to optimize the prediction model, and the error of R_D between the optimization point and the trajectory calculation result is about 0.2% with the maximum range as the objective function. The flight process in the optimized state has a good balance between the flight range and the flight time.

By parametric modeling of the flight section of the hypersonic vehicle and optimization based on the range prediction model, the optimization of the complex flight process can be realized, and it is easy to extend to the modeling process of more parameters and section combinations.

DATA AVAILABILITY STATEMENT

The original contributions presented in the study are included in the article/Supplementary Material, further inquiries can be directed to the corresponding author.

AUTHOR CONTRIBUTIONS

In this article, FC establishes the trajectory calculation model and the neural network model for parameter prediction and carries out the trajectory optimization calculation and analysis. XH completed the calculation and characteristic analysis of the sample trajectory.

REFERENCES

Ahuja, V., and Hartfield, R. J. (2015). Optimization of Scramjet Combustor Geometries Using Genetic Algorithms. *J. Propulsion Power* 31 (5), 1481–1485. doi:10.2514/1.b35397

Antunes, A. P., and Azevedo, J. L. F. (2014). Studies in Aerodynamic Optimization Based on Genetic Algorithms. *J. Aircraft* 51 (3), 1002–1012. doi:10.2514/1.c032095

Benson, D. A., Huntington, G. T., Thorvaldsen, T. P., and Rao, A. V. (2006). Direct Trajectory Optimization and Costate Estimation via an Orthogonal Collocation Method. *J. Guidance, Control Dyn.* 29 (6), 1435–1440. doi:10.2514/1.20478

Cheng, J. N., and Wang, H. P. (2011). Hybrid Genetic Algorithm Global Optimization of Configuration Design for Ballistic Missiles. *Flight Dynamic* 29 (3), 44–47. doi:10.13645/j.cnki.f.d.2011.03.023

Cui, N. G., Guo, D. Z., and Li, K. Y. (2020). A Survey of Numerical Methods for Aircraft Trajectory Optimization. *Tactical Missile Tech.* 5, 37–51. doi:10.16358/j.issn.1009-1300.2020.1.536

Darby, C. L., Hager, W. W., and Rao, A. V. (2011). Direct Trajectory Optimization Using a Variable Low-Order Adaptive Pseudospectral Method. *J. Spacecraft Rockets* 48 (3), 433–445. doi:10.2514/1.52136

Gandhi, M., and Theodorou, E. (2016). "A Comparison between Trajectory Optimization Methods: Differential Dynamic Programming and Pseudospectral Optimal Control," in Proceeding of the AIAA Guidance, Navigation, and Control Conference, San Diego, California, USA, January 2016. doi:10.2514/6.2016-0385

Gath, P., and Calise, A. (1999). Optimization of Launch Vehicle Ascent Trajectories with Path Constraints and Coast Arcs. *J. Guidance, Control Dyn.* 24, 296–304. doi:10.2514/6.1999-4308

Jia, X. J., and Yan, X, D. (2015). Ascent Trajectory Design Method for Air-Breathing Powered Propulsion System. *J. Northwest. Polytechnical Univ.* 33 (1), 104–109. doi:10.3969/j.issn.1000-2758.2015.01.022

Li, Y. I., Tong, H., Song, G., and Dong, L. I. (2006). Application of Neural Network in Calculation of Aircraft's Flight Track Simulation. *J. Naval Aeronaut. Eng. Inst.* 21 (5), 541–544. doi:10.3969/j.issn.1673-1522.2006.05.012

Li, X., Liu, C. A., Wang, Z. J., and Zhang, H. J. (2012). Trajectory Optimization for Maximizing Cruise Range of Air-Breathing Hypersonic Missile. *Acta Armamentarii* 33 (3), 290–294.

Liu, R. F., Yu, Y. F., and Yan, B. B. (2016). Ascent Phase Trajectory Optimization for Hypersonic Vehicle Based on Hp-Adaptive Pseudospectral Method. *J. Northwest. Polytechnical Univ.* 34 (5), 790–797. doi:10.3969/j.issn.1000-2758.2016.05.008

Liu, X. (2017). *Research on Trajectory Optimization and Guidance for Hypersonic Cruise Vehicles*. Wuhan: Huazhong University of Science and Technology.

Lu, X., He, G. Q., and Liu, P. J. (2010). Ascent Trajectory Design Method for RBCC-Powered Vehicle. *Acta Aeronautica Et Astronautica Sinica* 31 (7), 1331–1337.

Ma, T. R., Sheng, Y. Z., and Zhang, X. P. (2020). "The Trajectory Generation via Deep Neural Network for Hypersonic Vehicle," in Proceeding of the 9th International Symposium on Computational Intelligence and Industrial Applications (ISCIIA2020), Beijing, China, Oct.31-Nov.3.

Mei, Y. X., Feng, Y., Wang, R. S., Wu, L. N., and Sun, H. F. (2019). Fast Optimization of Reentry Trajectory for Hypersonic Vehicles with Multiple

Constraints. *J. Astronautics* 40 (7), 758–767. doi:10.3873/j.issn.1000-1328.2019.07.004

Narayanaswamy, S., and Damaren, C. J. (2020). Comparison of the Legendre-Gauss Pseudospectral and Hermite-Legendre-Gauss-Lobatto Methods for Low-Thrust Spacecraft Trajectory Optimization. *Aerospace Syst.* 3, 53–70. doi:10.1007/s42401-019-00042-w

Oktay, T., Arik, S., Turkmen, I., Uzun, M., and Celik, H. (2018). Neural Network Based Redesign of Morphing UAV for Simultaneous Improvement of Roll Stability and Maximum Lift/drag Ratio. *Aircraft Eng. Aerospace Tech.* 90, 1203–1212. doi:10.1108/aeat-06-2017-0157

Olds, J., and Budianto, I. (1998). "Constant Dynamic Pressure Trajectory Simulation with POST," in Proceeding of the 36th AIAA Aerospace Sciences Meeting and Exhibit, Reno,NV,U.S.A., January 1998. doi:10.2514/6.1998-302

Patrón, R. S. F., and Botez, R. M. (2015). Flight Trajectory Optimization through Genetic Algorithms for Lateral and Vertical Integrated Navigation. *J. Aerospace Inf. Syst.* 12 (8), 533–544. doi:10.2514/1.i010348

Qian, S. Y. (2021). *Trajectory Planning and Reentry Guidance for Boost-Glide Vehicle*. Harbin: Harbin Institute of Technology.

Reddien, G. W. (1979). Collocation at Gauss Points as a Discretization in Optimal Control. *SIAM J. Control. Optim.* 17 (2), 298–306. doi:10.1137/0317023

Tang, X. J., Li, Z. T., and Zhang, H. B. (2021). Ascent Guidance Method for Combined-Cycle Vehicle Based onReceding Horizon Pseudo-spectral Optimization. *J. Ballistics* 33 (4), 1–8. doi:10.12115/j.issn.1004-499X(2021)04-001

Tao, C. (2017). Trajectory Optimization and Tracking Controller Based on Gauss Pseudo Spectral Method for Hypersonic Vehicle. *J. Syst. Simulation* 29 (4), 865~872+879. doi:10.16182/j.issn1004731x.joss.201704022

Wang, T. S., Sun, Z. G., Huang, Z., and Xi, G. (2021). Reconstruction of Fluid Flows Past Airfoils Using Neural Network. *J. Eng. Thermophys.* 42 (5), 1205–1212.

Wei, Y. Y. (2022). Major Technological Issues of Aerospace Vehicle with Combined-Cycle Propulsion. *Aerospace Tech.* 1, 1–12. doi:10.16338/j.issn.2097-0714.20220601

Xie, Y., Franz, E., Chu, M., and Thuerey, N. (2018). TempoGAN: A Temporally Coherent, Volumetric GAN for Super-resolution Fluid Flow. *ACM Trans. Graphics* 37 (4), 951–9515. doi:10.1145/3197517.3201304

Zhang, D. Q., Song, W. T., Chai, Z., Liu, L. L., and Meng, P. P. (2014). Aircraft/engine Performance Integrate Analysis on Combined Cycle Engine. *J. Aerospace Power* 32 (10), 2498–2507. doi:10.13224/j.cnki.jasp.2017.10.024

Zhang, T. (2013). *Research on Trajectory Optimization of Air-Breathing Hypersonic Vehicle*. Harbin: Harbin Institute of Technology.

Zhang, W. D. (2017). *Reentry Trajectory Planning and Attitude Control for Hypersonic Glide Vehicles*. Harbin: Harbin Institute of Technology.

Zhang, X., and Li, G. R. (2020). Prediction Model of Ship Trajectory Based on GA-BP. *J. Guangzhou Maritime Univ.* 28 (4), 15–18.

Zhao, J., and Zhou, R. (2013). Reentry Trajectory Optimization for Hypersonic Vehicle Satisfying Complex Constraints. *Chin. J. Aeronautics* 26 (6), 1544–1553. doi:10.1016/j.cja.2013.10.009

Zheng, X., Liu, Z. S., Yong, Y., Lei, J. C., and Li, Z. X. (2018). Research on Climb-Cruise Global Trajectory Optimization for RBCC Hypersonic Vehicle. *Missiles and Space Vehicles* 2, 1–8. doi:10.7654/j.issn.1004-7182.20180201

Zheng, T. Y., Yao, Y., and He, F. H. (2020). Trajectory Estimation of a Hypersonic Flight Vehicle via L-EKF. *J. Harbin Inst. Tech.* 52 (6), 160–170. doi:10.11918/202003094

Zhou, H. Y., Wang, X. G., Zhao, Y. L., and Cui, N. (2020). Ascent Trajectory Optimization for a Multi-Combined-Cycle-Based Launch Vehicle Using a Hybrid Heuristic Algorithm. *J. Astronautics* 40 (1), 61–70. doi:10.3873/j.issn.1000-1328.2020.01.008

Zhu, R. Y., Qi, Z., Wang, L. S., Miao, M., Bai, G. H., Wang, C., et al. (2020). Trajectory Optimization Design of Morphing Vehicle. *Tactical Missile Tech.* 5, 157–164. doi:10.16358/j.issn.1009-1300.2020.1.085

Conflict of Interest: The authors declare that the research was conducted in the absence of any commercial or financial relationships that could be construed as a potential conflict of interest.

frontiers | Frontiers in Energy Research

ORIGINAL RESEARCH
published: 30 May 2022
doi: 10.3389/fenrg.2022.887368

Investigations on Spray Characteristics and Self-Pulsation of a Gas-Centered Shear Coaxial Injector

Gao Yuchao, Chu Wei, Xie Yuan, Jiang Chuanjin, Xu Boqi, Su Lingyu and Tong Yiheng**

Department of Aerospace Science and Technology, Space Engineering University, Beijing, China

The spray characteristics of a gas-centered shear coaxial injector under different conditions and recess ratios (RR) were studied through experiments and numerical simulations. The numerical study was carried out based on the coupled level set and volume-of-fluid (CLSVOF) method and the adaptive mesh refinement (AMR) method. The results indicated that without recess, the spray angle first stayed almost constant and then dropped linearly with an increase in the gas mass flow rate ($\dot{m}_g$) when holding the liquid mass flow rate ($\dot{m}_l$) constant. In contrast, with recess, the spray angle was found to increase with $\dot{m}_g$, which could be attributed to the secondary expansion of the central gas flow. Under specific conditions, self-pulsation occurred and was accompanied by a loud scream. The frequency of the self-pulsation increased with both $\dot{m}_g$ and $\dot{m}_l$. Moreover, the self-pulsation frequency decreased with RR. Meanwhile, the mechanism of self-pulsation was initially explored through numerical simulation. It was concluded that self-pulsation was caused by the surface tension and the pressure difference between the inside and outside of the liquid sheet, together with the central airflow impact extrusion.

Keywords: gas-centered shear coaxial injector, self-pulsation, frequency, recess ratio, spray angle, numerical simulation

OPEN ACCESS

Edited by:
Xiao Liu,
Harbin Engineering University, China

Reviewed by:
Wu Yi,
Beijing Institute of Technology, China
Yingchun Wu,
Zhejiang University, China
Jiaqi Zhang,
National University of Defense Technology, China

****Correspondence:***
Su Lingyu
sulingyu77@163.com
Tong Yiheng
yiheng_tong@sina.com

Specialty section:
This article was submitted to Advanced Clean Fuel Technologies, a section of the journal Frontiers in Energy Research

Received: *01 March 2022*
Accepted: *19 April 2022*
Published: *30 May 2022*

Citation:
Yuchao G, Wei C, Yuan X, Chuanjin J, Boqi X, Lingyu S and Yiheng T (2022) Investigations on Spray Characteristics and Self-Pulsation of a Gas-Centered Shear Coaxial Injector. Front. Energy Res. 10:887368. doi: 10.3389/fenrg.2022.887368

1 INTRODUCTION

Liquid rocket engines are the heart of liquid propellant rockets and are highly valued in many countries. The interaction between gases and liquids significantly enhances the atomization performance of gas–liquid coaxial injectors; therefore, these injectors are widely used in bipropellant liquid rocket engines (Kang et al., 2018).

In an experimental study of liquid-centered shear coaxial injectors, Hardalupas and Whitelaw (1994) found that atomization could be enhanced by reducing the diameter of the liquid injector. Yang and Fu (2012) found that recession could confine the airflow to limited space and enhance the gas–liquid interaction and thus could significantly improve the atomization performance. Hautman et al. (1993) conducted an experimental study on liquid-centered swirl coaxial injectors and found that the spray angle decreased with $\dot{m}_g$ and ambient pressure and subsequently increased with $\dot{m}_l$. The droplet Sauter mean diameter (SMD) demonstrated a single-peak distribution along the radial direction while decreasing along the axial direction downstream. Yang et al. (2006) investigated the effect of recess lengths on the SMD of a liquid-centered swirl coaxial injector. They also proposed the concept of recessed angle. Accordingly, the flow inside the recess chamber was classified into three modes: external mixing, critical mixing, and internal mixing flows. SMD was minimized when the flow was in the critical mixing flow mode. Kulkarni et al. (2010) found that a low Weber number (We) liquid sheet was more sensitive to gas than a high We number liquid sheet for a gas-centered

swirl coaxial injector, with a more obvious variation in the spray angle and breakup length of the low We number liquid sheet. Based on experimental data, Siddharth et al. (2017) found that: 1) the addition of swirl flow in the gas contributed to the breakage of the liquid sheet and 2) the breakup length of the liquid sheet in the counter-swirl air flow (opposite to the direction of liquid sheet rotation) was shorter than that in the co-swirl air flow.

Despite the numerous advantages of a gas-liquid coaxial injector, it can generate self-pulsation under certain structures and conditions, and the accompanying periodic pulsations of spray flow and pressure (Bazarov and Yang, 1998; Eberhart et al., 2012) may cause combustion instability in the thrust chamber, which could further result in combustion instability in liquid rocket engines. Nunome et al. (2007) and (Nunome et al., 2009) experimentally investigated the change in the liquid-centered shear coaxial injector spray from the stable to self-pulsation state and concluded that the recess of the inner injector was the key parameter to inducing injector self-pulsation. They found that there was a critical parameter F_{cr}, at which, when $Re_l/(Re_g)^{0.5} < F_{cr}$, self-pulsation could occur. Tsohas and Heister (2011) studied the internal flow of a recessed chamber during injector self-pulsation using two-dimensional simulation. They found that vortex shedding at the injector, the acoustic instability of the liquid injector, and vortex shedding at the injector outlet could result in self-pulsation. (Kim and Heister (2004) and Kim et al. (2005) conducted a three-dimensional simulation study of the flow inside the injector recess chamber and found that the pulsation frequency and amplitude could be increased by increasing the gas-liquid density and velocity ratios; the amplitude could also be increased by decreasing the jet diameter and increasing the recess length. Kelvin–Helmholtz (K-H) instability on the jet surface was assumed to cause self-pulsation of the injector. Self-pulsation of liquid-centered swirl coaxial injectors was first studied experimentally and theoretically by Bazarov et al. (1995), Bazarov (1998), and Bazarov and Yang (1998). It was concluded that self-pulsation was caused by the time-lag feedback between the rotating liquid sheet and the annular airflow and that self-pulsation can enhance the effect of atomization and mixing to a certain extent. The most important parameter affecting self-pulsation was the recess length. Eberhart et al. (2013) and Eberhart and Frederick (2017) found that the unstable frequency and wave velocity measured at a steady spray were consistent with those measured at self-pulsation in an analysis of proper orthogonal decomposition. Therefore, it was speculated that the occurrence of self-pulsation could be attributed to K-H instability. Chu et al. (2021) investigated the effect of backpressure on the self-pulsation of an injector using three-dimensional numerical simulation and found that: 1) with an increase in the backpressure, the mass flow rate distribution in the radial direction changed from a double peak to a single peak and 2) the central mass flow rate was increased by backpressure and $\dot{m}_g$, while the peripheral mass flow rate decreased. The increase in backpressure could suppress the self-pulsation effect and accelerate the breakage of the liquid sheet; the frequency of self-pulsation increased with an increase in back pressure (or $\dot{m}_g$). Xu. (2016) conducted experiments to further study the phenomenon of self-pulsation in gas-centered swirl coaxial injectors and summarized the conditions of self-pulsation and the range of $\dot{m}_g$ and $\dot{m}_l$. They concluded that self-pulsation was generated by the increase in gas momentum to overcome the inertial potential energy of the liquid sheet, which could further cause periodic aggregation and expansion of the liquid sheet in the outlet.

In recent decades, the study of the gas-liquid coaxial injector spray and self-pulsation characteristics has gradually intensified. The influences of injector structural parameters, injection conditions, back pressure, and other factors on the spray angle, breakage length, droplet SMD, and other spray characteristics were studied using theoretical, experimental, and simulated methods. However, few studies have been published that report on the spray and self-pulsation characteristics of gas-centered shear coaxial injectors. Therefore, in this study, the spray characteristics and self-pulsation of gas-centered shear coaxial injectors under different conditions and recess ratios were investigated by experiments and numerical simulations based on CLSVOF and AMR. Due to the limitation of experimental equipment, the SMD of droplets in this study was not measured. The latest results of particle measurement by Huang et al. (2022) and Wu et al. (2022) provide a reference for the follow-up work.

2 EXPERIMENTAL METHODS

2.1 Experimental System

The experimental system was composed of four parts: 1) a propellant feed system, 2) a measurement and control system, 3) an image acquisition system, and 4) a bench system, as shown in **Figure 1A**. The propellant feed system was composed of a high-pressure gas source, gas conduit, liquid conduit, propellant tank, and other components. To achieve a smooth flow supply to the liquid injector, the propellant (water) storage tank was pressurized with compressed air. Meanwhile, the air was delivered by a high-pressure gas source to the gas injector through the conduit *via* the pressure-reducing valve. The pressure of the liquid and gas manifolds was measured and recorded using a pressure sensor: OHR-M2G-2-L-C-0-1.6 MPa with an accuracy of 0.5% FS. The mass flow rates of the water and pressurized air were measured and recorded using an LWGY turbine flowmeter and a Coriolis mass flowmeter (MFC608), with an accuracy of 0.5% FS, respectively. The in-line image acquisition system was composed of a high-speed camera, shading plate, and rectangular LED background light source (HLS-30, power: 250 W). The distance of each component could be adjusted to ensure a fine spray transient image. During the experiments, the recording rate of the camera was set as 31,862 fps, the exposure time was 1/95,586 s, and the resolution of the transient image was 800 × 600 pixels.

2.2 Geometries of the Injector and Experimental Operating Conditions

A gas-centered shear coaxial injector was studied in the experiment, as shown in **Figure 1B**, in which the outer injector was a coaxial annular aperture, and the inner injector

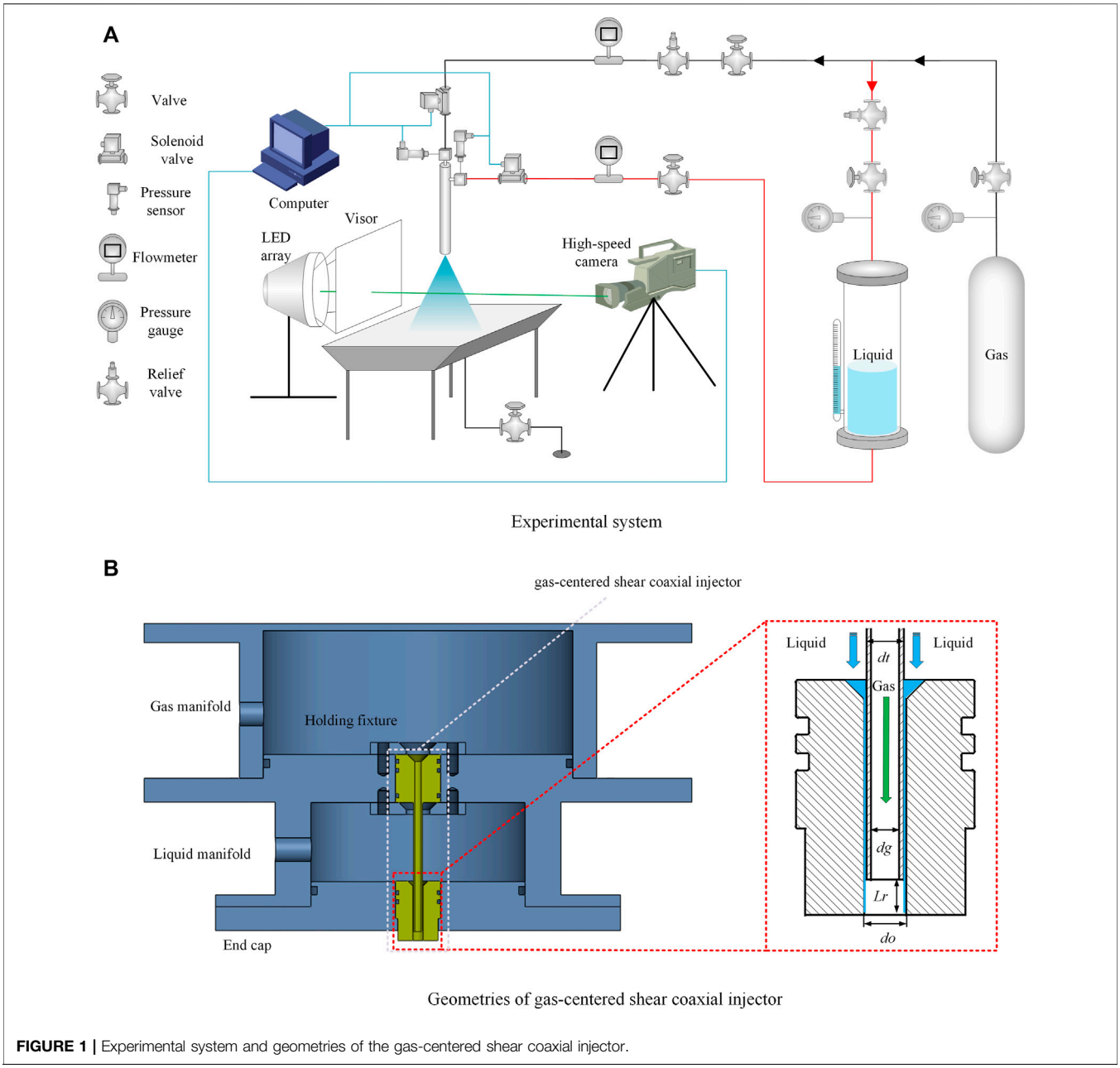

FIGURE 1 | Experimental system and geometries of the gas-centered shear coaxial injector.

was a central circular hole. The liquid fuel entered the injector through the coaxial annular aperture, and the gaseous oxidizer was fed through the central hole. They interacted with each other after spraying out from the injector. For the recessed injector, the gaseous oxidizer was ejected from the inner injector and expanded to compress the liquid fuel; thus, the oxidizer and fuel were initially mixed inside the recess chamber. The liquid fuel was jetted from the outer injector to form a liquid sheet near the injector outlet and then was broken into liquid blocks and droplets after a certain distance (breakup length) downstream. Recess is an important parameter which determines propellants' mixing efficiency and even flame stability (Xu, 2016). Three injectors with different recess lengths were applied in the experiment. The recess length was the distance from the outlet section of the inner injector to the outlet section of the outer injector (Chu et al., 2021), as shown in **Figure 1**. The key

TABLE 1 | Geometrical parameters of the injector.

Parameter	Value
d_g	3.00
d_t	4.00
d_o	4.50
L_r	0, 3.75, 15.00
RR	0, 1.25, 5.00

TABLE 2 | Parameters of working conditions.

Parameter	Oxidizer	Fuel
Simulated medium	Compressed air	Filtered water
$\dot{m}$ (g/s)	4–25	30–120

geometrical parameters of the injector are listed in **Table 1**, and the RR is defined as follows:

$$RR = \frac{L_r}{d_g}.$$

In this study, the spray characteristics and self-pulsation of the gas-centered shear coaxial injector under different working conditions and recess ratios were mainly explored. To ensure the comprehensiveness of the experimental study, the operating conditions in the present experiments were denser, as shown in **Table 2**, whereas the errors of the gas and liquid mass flow rates were less than 4.2 and 6.7%, respectively. The $\dot{m}_l$ is set from 30 *g/s* to 120 *g/s* with a step of 10 *g/s*, and $\dot{m}_g$ increased from 4 *g/s* to 25 *g/s* with a step of 1 *g/s*.

2.3 Image Processing

To obtain the spray angle, self-pulsation frequency, and other information, 2000 images were taken for each working condition and processed by the in-home code.

2.3.1 Acquisition of the Spray Angle

The extraction of the spray angle was performed using the clustering method. First, all the spray images were processed to obtain the time-averaged image; second, the weighted image was obtained by the background, and a time-averaged image was multiplied with the weighted image to eliminate the effect of uneven illumination; third, the time-weighted filtering image was obtained by Gaussian filtering, which was followed by the calculation of the average grayness of each class based on the K-means segmentation algorithm (Arthur and Vassilvitskii, 2007) to obtain the background image classification, and moreover, the background binary image was obtained by morphological filtering. The boundary coordinates were found to extract the spray boundaries, calculating the left and right boundaries of the spray to fit the straight lines l_1 and l_2. Due to the spray being completely broken and unfolded only in the downstream direction and to avoid the interference of the background (as marked by the red circle in **Figure 2A**), the fitted straight line was taken in the 50–75% interval downstream of the spray. Finally, the included angle between the two fitting lines was calculated by the program formula to obtain the spray angle, as shown in the following equation:

$$l_1: y_1 = k_1 x + b_1, \alpha_1 = arctan\, k_1, \quad (1)$$

$$l_2: y_2 = k_2 x + b_2, \alpha_2 = arctan\, k_2, \quad (2)$$

$$\alpha = 180^\circ - |\alpha_1 - \alpha_2|. \quad (3)$$

2.3.2 Acquisition of the Self-Pulsation Frequency

The self-pulsation frequency was obtained by first subtracting the background to obtain the grayscale image after background removal, followed by the binarization of the image after background removal, which was then processed to obtain the binarized image. At a certain distance from the injector outlet, a measurement line was selected (which is 2 mm below the injector for this study), and the spray width information reflected by the

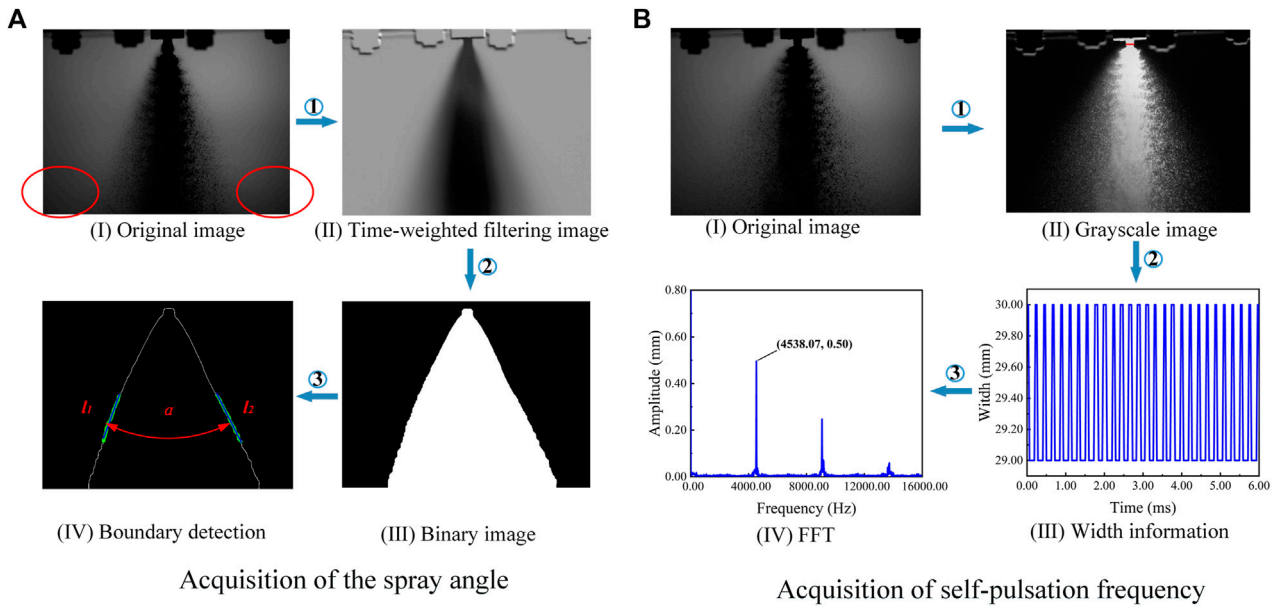

FIGURE 2 | Acquisition of the spray angle and self-pulsation frequency.

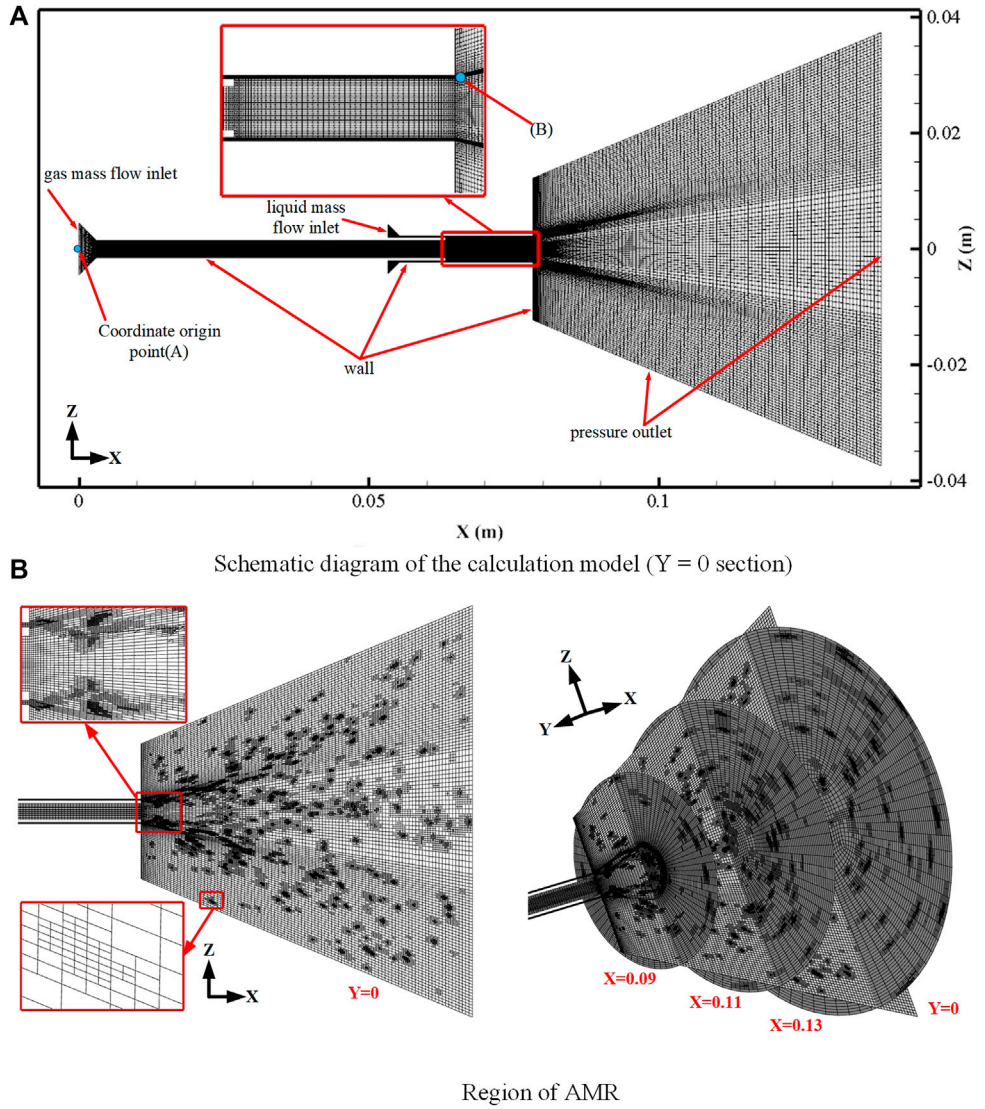

FIGURE 3 | Schematic diagram of the calculation model and region of AMR.

white area on the measurement line was extracted to obtain the spray width of each image. Finally, the frequency involved in the self-pulsation of the spray was obtained by the time series of the spray width subjected to a fast Fourier transform (FFT) (Xu, 2016), as shown in **Figure 2B**.

3 THEORY AND MODEL OF NUMERICAL SIMULATION

3.1 Governing Equations

The governing equations include the mass, momentum, and energy conservation equations, which are described by the governing equations of fluid motion. Incompressible fluid treatment should be conducted if the flow velocity of the liquid is low. Moreover, the incompressible gas treatment should be conducted when the flow velocity of the gas is lower. However, the density change can no longer be neglected if the flow velocity of the gas is larger ($M_a > 0.15$) (Luo, 2017). In that case, it should be treated as a compressible fluid, that is, the energy equation should be considered.

Conservation of mass equation: $\frac{\partial \rho}{\partial t} + \nabla \cdot (\rho U) = 0$.

Conservation of momentum equation: $\frac{\partial}{\partial t}(\rho U) + \nabla \cdot (\rho UU) = -\nabla p + \nabla \cdot (\bar{\bar{\tau}}) + \rho g + F$.

Conservation of energy equation: $\frac{\partial}{\partial t}(\rho E) + \nabla \cdot [U(\rho E + p)] = \nabla \cdot (k_{eff}\nabla T - \sum_j h_j J_j + (\bar{\bar{\tau}}_{eff} \cdot U)) + S_h$.

Whereas:

$$\bar{\bar{\tau}} = \mu\left[(\nabla U + \nabla U^T) - \frac{2}{3}\nabla \cdot UI\right],$$

$$E = h - \frac{p}{\rho} + \frac{U^2}{2}.$$

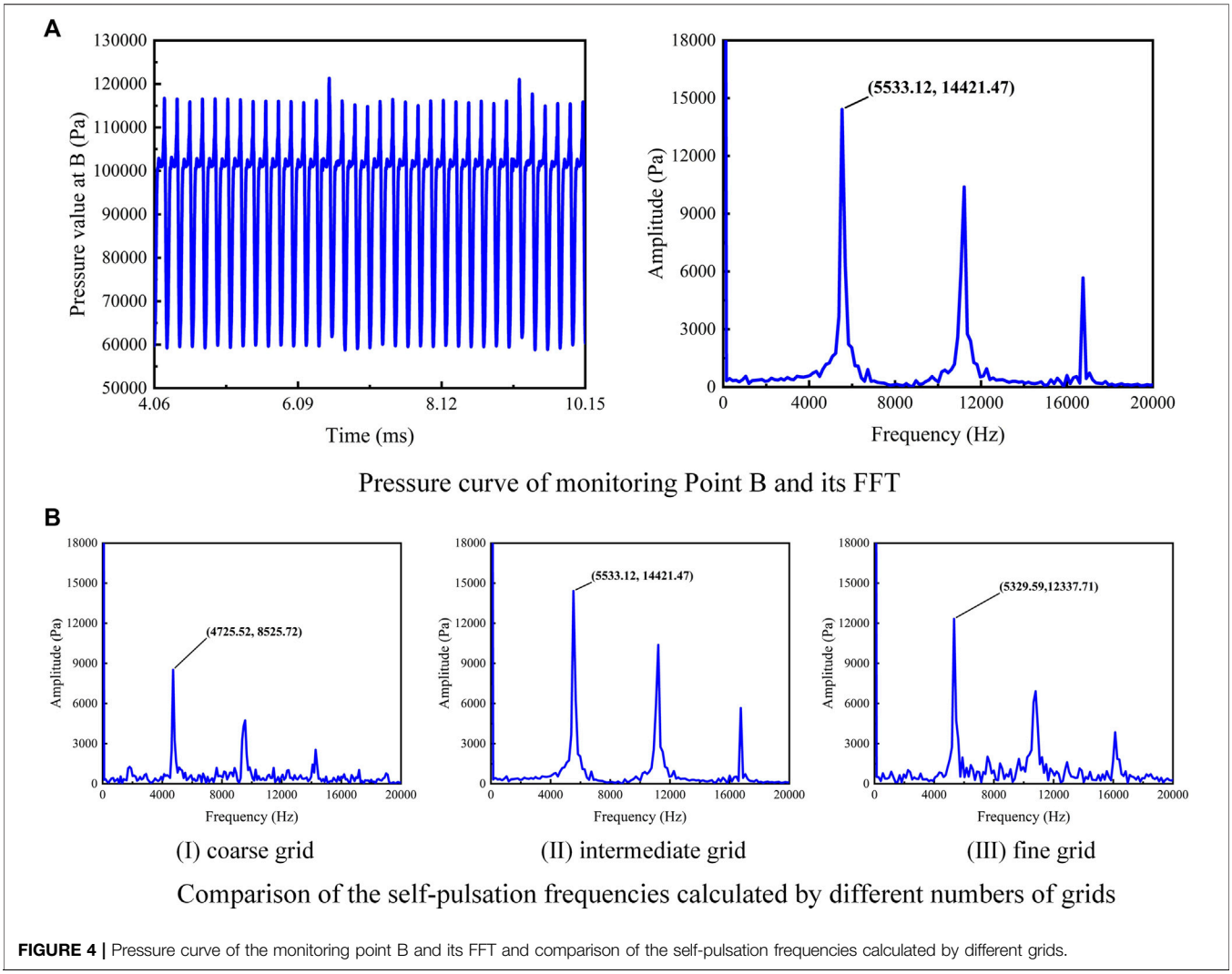

FIGURE 4 | Pressure curve of the monitoring point B and its FFT and comparison of the self-pulsation frequencies calculated by different grids.

3.2 Turbulence Model and the Gas–Liquid Interface Capturing Method

The realizable *k-ε* model was chosen as the turbulence model, for which the constraint on the Reynolds stress was satisfied. Therefore, it can be kept consistent with the real turbulent flow in terms of the Reynolds stress. One of the advantages of this feature in the calculation is that the diffusion velocity of planar and circular jets can be simulated more accurately. Meanwhile, the calculated results could be more consistent with the real situation in problems such as the calculation of rotating flow, calculation of the boundary layer with a directional pressure gradient, and separation flow calculation.

The volume-of-fluid (VOF) method can 1) easily calculate complex phase interface change processes, 2) capture the particularly sharp phase interfaces, and 3) have good volume conservation and other advantages. Its disadvantages are that it may have difficulty in accurately calculating the curvature and physical quantities related to curvature, which results in an increase in the use of computational cost to capture the phase interface location in detail if the encryption of the grid at the phase interface becomes necessary. The level set method has the following advantages: 1) it can accurately calculate the curvature and curvature-related physical quantities, which does not need to reconstruct the interface; 2) it has stronger topological description ability, and 3) the phase interface calculated based on the level set method is smoother than that using the VOF method. Its disadvantage is that it faces difficulty in accurately simulating sharp interfaces with relatively poor volume conservation. CLSVOF combined the VOF method with the level set method, which has the advantages of those two methods. CLSVOF has an excellent capture of the phase interface in two-phase flow simulations (Wang et al., 2016).

The realizable *k-ε* model and the controlling equations of the CLSVOF are described in detail in the literature (Chu et al., 2020).

Owing to the multiscale characteristics of the atomization phenomenon, to fully collect the motion and breakage details of the liquid film and reduce the numerical errors in the numerical solution, the AMR method, which was based on the gradient of

TABLE 3 | Simulation working conditions.

RR	$\dot{m}_l$ (g/s)	$\dot{m}_g$ (g/s)	Case code
0	40	4	Case 0-40-4
	60	4	Case 0-60-4
		7	Case 0-60-7
		8	Case 0-60-8
		25	Case 0-60-25
	80	4	Case 0-80-4
		5	Case 0-80-5
	120	4	Case 0-120-4
1.25	60	4	Case 1.25-60-4
		15	Case 1.25-60-15
5	60	15	Case 5-60-15

the liquid volume fraction (α), was used in this study to encrypt the mesh to accurately track the gas–liquid interface (Wang et al., 2021), as shown in **Figure 3B**. Refinement is realized when the following conditions are satisfied:

$$h|\nabla\alpha| > \varepsilon',$$

where h is the grid scale, and ε' is a constant with a small value. Here, $\varepsilon' = 0.05$. In other words, the grids at the gas–liquid interface are refined. The mesh refinement interval was 10 time steps with three refinement levels.

3.3 Computational Model

A schematic representation of the calculation model is illustrated in **Figure 3A**. It has a gas injector bore diameter of 3 mm and a liquid injector bore diameter of 4.5 mm, among which the vertically downward direction was the positive X-axis, the coordinate origin was located at the center A (0, 0, 0) of the gas injector inlet, and the pressure monitoring point was located at Point B (80.2, 2.25, 0).

The inlet boundary condition of the mass flow rate was applied to the inlet of the gas and liquid, the outlet boundary was set as the pressure outlet boundary, and the wall surface was a non-slip wall boundary. The gas was simulated using air, and the liquid was simulated using water. The pressure discretization method (PRESTO) and the pressure-velocity coupling method (PISO) were applied. Furthermore, the second-order upwind scheme discretization was applied in the momentum and other equations, and the phase interface reconstruction technique (Geo-Reconstruct) was used. Moreover, the simulation accuracy of the wall part was improved by non-equilibrium wall functions. At the initial moment, all the fluid in the calculation region was air. The compressibility of air was considered, and its viscosity was calculated using the Sutherland method, as shown in the following equation:

$$\frac{\mu}{\mu_0} = \left(\frac{T_L}{T_{L0}}\right)^{3/2} \frac{T_{L0} + B}{T_L + B},$$

where B ≈ 110.4 K. The equation is applicable to air over a fairly large range ($T_L < 2000$ K).

For the acquisition of the self-pulsation frequency in the simulation, first, the pressure pulsation curve of monitoring point B (Case 0-80-5) was monitored, and then, its frequency was obtained through FFT (Chu et al., 2021), as shown in **Figure 4A**.

3.4 Simulation Working Condition

The effects of different recess ratios and gas-liquid mass flow rates on the spray characteristics were studied. The simulation working conditions are listed in **Table 3**.

3.5 Grid Independence

Case 0-80-5 was selected for the grid independence study. Three different grids, which initially (before AMR) contain 330,000 (coarse), 630,000 (intermediate), and 930,000 (fine) grids, respectively, were utilized to check the dependence of the grid size. The pressure pulsation frequency at the monitoring point B on basis of those three grids is plotted in **Figure 4B**. Compared with the self-pulsation frequency based on experimental data (5,286 Hz), the frequency errors obtained from the coarse grid calculation (10.6%) were greater than those obtained from the intermediate (4.7%) and fine grid calculations (0.8%). To reduce the calculation cost and ensure its accuracy, an intermediate grid was used for the calculation in this study.

4 RESULTS AND DISCUSSION

4.1 Spray Angle

For injector without recess, the spray angle first stayed almost constant with the variation of $\dot{m}_g$ ($4 \leq \dot{m}_g \leq 6$). However, as $\dot{m}_g$ continued to increase, the spray angle dropped linearly. On the other hand, for injectors with recess (RR = 1.25 and RR = 5), the spray angle got larger with $\dot{m}_g$. Holding $\dot{m}_l = 60\ g/s$, spray images and the changes of spray angles versus $\dot{m}_g$ are shown in **Figures 5A,B**, respectively. Here, the gas–liquid ratio (GLR) of mass flow rates is defined as follows:

$$GLR = \frac{\dot{m}_g}{\dot{m}_l}.$$

For an injector without recess, self-pulsation occurred at a low GLR (the details of self-pulsation are described in **section 4.2**). The spray pulsations in the radial direction led to an increase in the radial distribution of the droplets, resulting in an enlarged spray angle. The self-pulsation phenomenon of the spray was enhanced with the increasing GLR ($0.07 \leq GLR \leq 0.10$). However, because the spray pulsations were very intense, the increase in the spray angle was not particularly significant. In other words, the spray angles stayed almost constant. When the GLR continued to increase, the axial velocity of the central airflow increased sharply, and the strong ejecting effects of the central airflow made the liquid film outlet completely broken. At the same time, the strong ejecting effects made the liquid converge toward the axis, which resulted in the spray angle dropping linearly. Even though there were still self-pulsations in the first working conditions (0.10 <

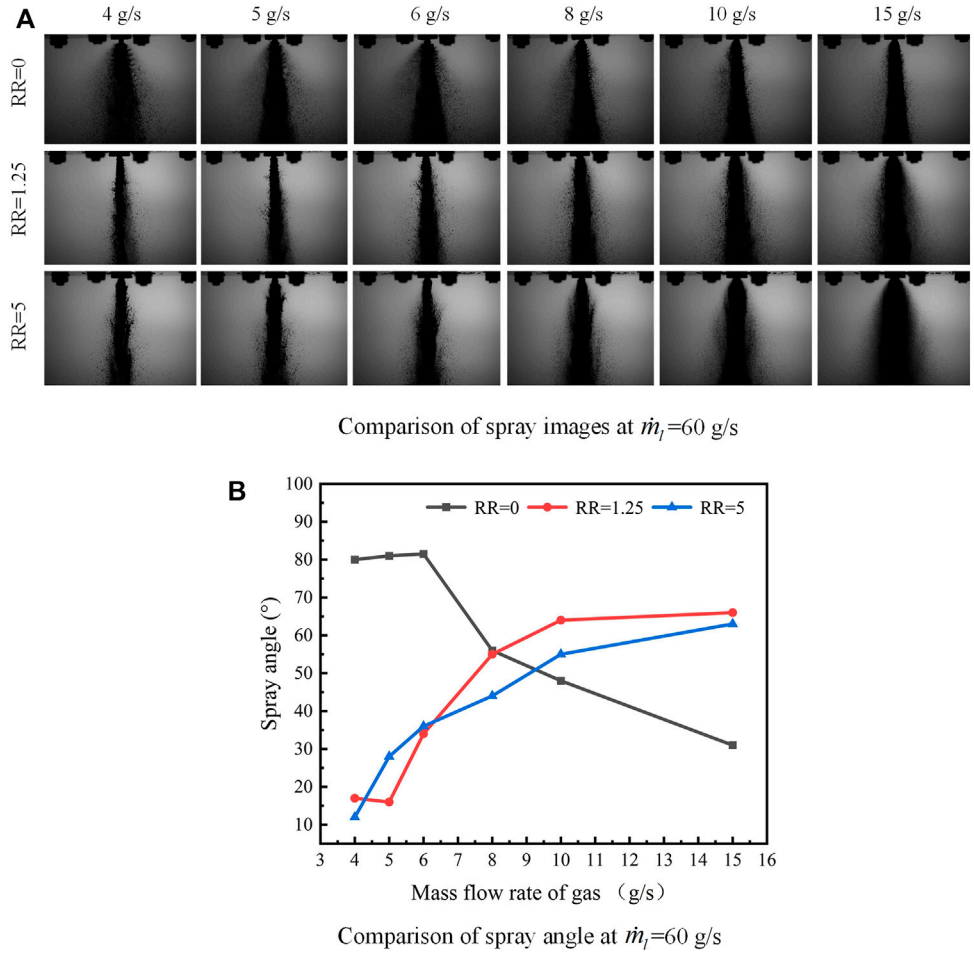

FIGURE 5 | Comparison of spray images and the spray angle at $\dot{m}_l$ = 60 g/s.

GLR≤0.17), the promotion effect of spray pulsation on the spray angle was inferior to the weakening effect of ejecting effects on the spray angle. Meanwhile, the promotion effect of the expansion of the central airflow outlet on the spray angle was inferior to the weakening effect of ejecting effects on the spray angle. A larger GLR led to a stronger ejecting effect of the central airflow and hence minimizes the spray angle.

In the current study, the Mach numbers at the outlet of the gas injector were greater than 0.15. In other words, the gas could not be treated as an incompressible flow. The gas expanded at the injector outlet, and the liquid sheet was directly affected by the gas flow. For the injector with recess, the center gas experienced two expansions, as shown in **Figure 6A**. The first expansion occurred in the recess chamber after the center gas flowed out of the inner injector. Thereafter, the gas got expanded once more downstream of the outlet of the outer injector. However, for the injector without recess, the center gas flow experienced only one expansion at the outlet of the inner injector.

Under conditions with a low GLR (0.07 ≤ GLR<0.13), spray self-pulsation was found for injectors with recess. However, spray angles for those injectors were relatively smaller than those for injectors without recess. It was concluded that the radial diffusion of the liquid film is limited by the recess chamber wall. At the same time, recess can lead to a strong gas–liquid interaction. In other words, the central airflow has strong momentum transfer to the liquid film in the recess chamber. These reduced the radial velocity of the liquid film at the injector outlet, which resulted in a reduction in the spray angle. With the increase in RR, the recess chamber wall limited the radial diffusion of the liquid film for a longer time, and the acting time of the central airflow with the liquid sheet was longer. The radial velocity of the liquid sheet was reduced more significantly, thus further reducing the spray angle. However, with an increase in the GLR, the secondary expansion of the central airflow at the outlet of the outer injector became more and more significant. The expansion gas transferred a greater radial velocity to the liquid sheet, which resulted in an increase in the radial velocity of the liquid sheet and a subsequent increase in the spray angle. However, under a low GLR, the secondary expansion of the central airflow was insignificant and contributed little to the radial velocity of the liquid sheet. Moreover, the above-mentioned observations were confirmed

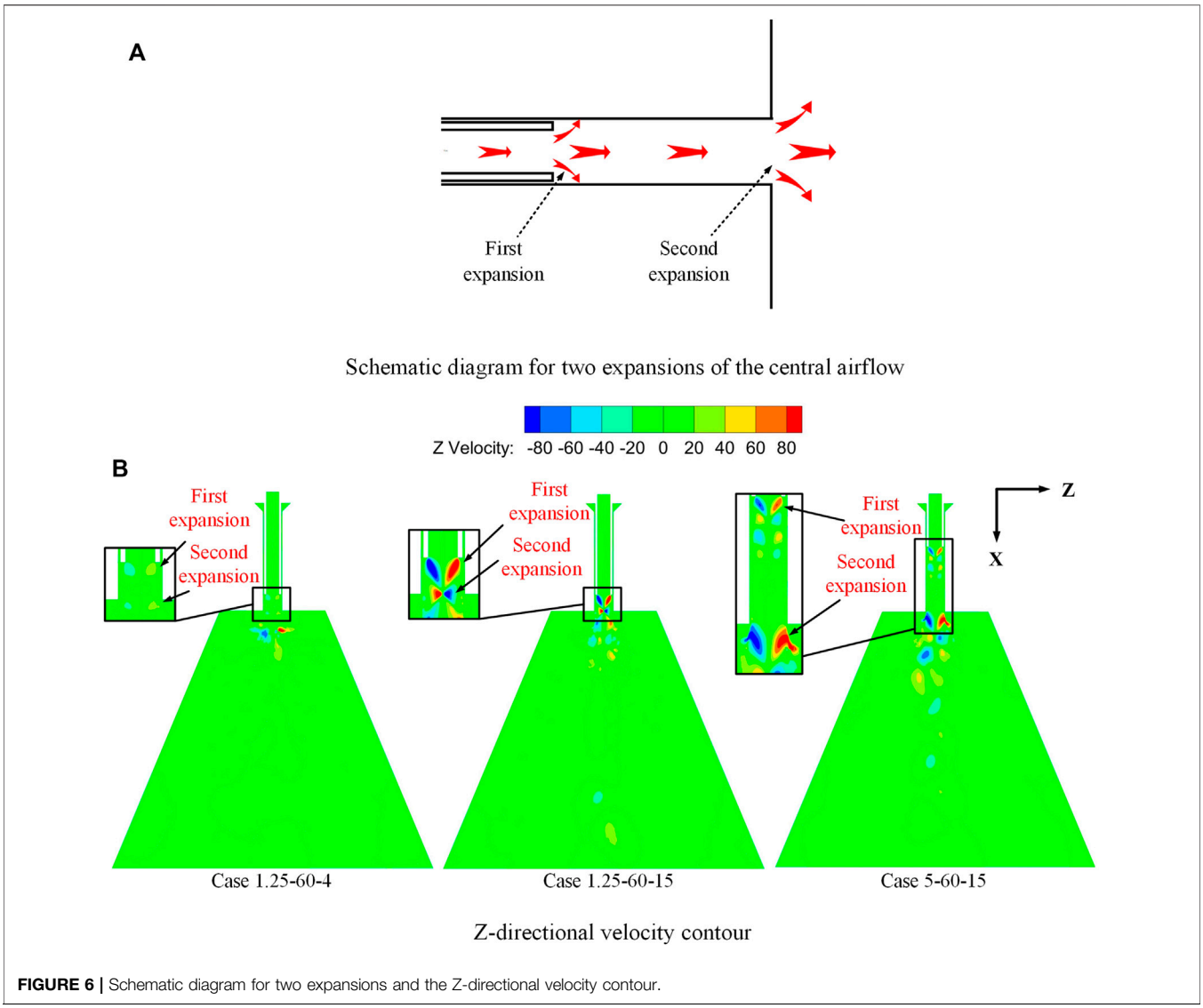

FIGURE 6 | Schematic diagram for two expansions and the Z-directional velocity contour.

through simulation. The Z-directional velocity contours for case 1.25-60–4, case 1.25-60–15, and case 5-60–15 are shown in **Figure 6B**. The two airflow expansions related to case 1.25-60-4 were minimal, whereas the two airflow expansions related to case 1.25-60-15 and case 5-60-15 were significant.

4.2 Self-Pulsation Phenomenon Without Recess

When conducting the experiment under specific working conditions, the injector produced a self-pulsation phenomenon, accompanied by a loud scream, and the self-pulsation frequency increased with $\dot{m}_g$, as shown in **Figure 7A**. However, for a constant $\dot{m}_l$ (such as $\dot{m}_l$ = 80 g/s = 80 g/s), when $\dot{m}_g$ reached a critical value (here $\dot{m}_g$ = 8 g/s), the self-pulsation phenomenon disappeared.

Similar results were obtained from the simulation calculations. As shown in **Figure 7B**, under $\dot{m}_l$ = 60 *g/s* and the gas mass flow rates at 4, 7, 8, and 15 *g/s*, the experimental images are compared with the simulated spray images. A comparison between the experimental and simulated frequencies is shown in **Table 4**. The error between the simulated and experimental frequencies was relatively small, verifying the reliability of the simulation model. The gas–liquid interface in the simulation was represented by the iso-surface with α= 0.25 (Li et al., 2019).

When $\dot{m}_g$ was small, the self-pulsation phenomenon was caused by the gas–liquid interaction at the injector outlet. The self-pulsation spray was formed in the shape of a "Christmas tree". Moreover, the structure of the spray comprised "shoulder" and "neck" sections, which appeared alternately to form the self-pulsation phenomenon of the spray. As shown in **Figure 7B**, the spray pulsations were violent near the injector outlet, whereas the downstream pulsation was weakened. In other words, the self-pulsation phenomenon had a greater impact on the spray characteristics near the injector outlet and less impact on the downstream. With an increase in $\dot{m}_g$, the central airflow of the

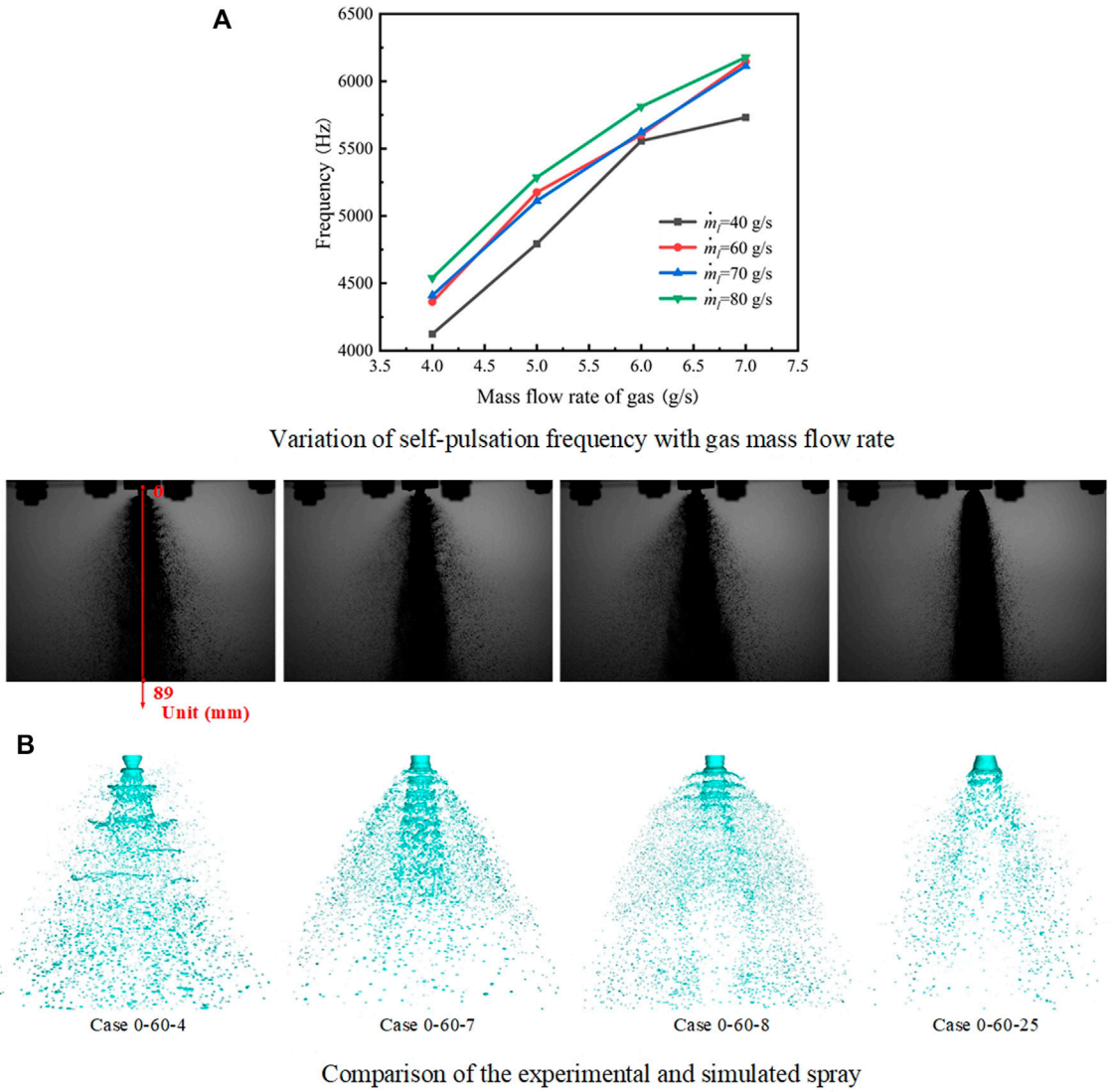

FIGURE 7 | Variation of the self-pulsation frequency with $\dot{m}_g$ and comparison of the experimental and simulated spray.

ejector function was enhanced, the spray gradually gathered toward the axis, and the intensity of the pulsations and breakages of the liquid sheet increased. When $\dot{m}_g$ reached a certain value and above, the self-pulsation phenomenon disappeared, and strong aerodynamic fragmentation of the annular aperture liquid sheet was observed.

Meanwhile, a consistent pattern was observed in the experimental and simulation results; the frequency of self-pulsation increased with $\dot{m}_l$ at a constant $\dot{m}_g$. The variation in the self-pulsation frequency with $\dot{m}_l$ for fixed gas mass flow rates and the comparison between the experimental and simulated frequencies are shown in **Figure 8A**. A comparison between the experimental and simulated spray images for $\dot{m}_g = 4g/s$ and liquid mass flow rates of 40, 60, 80, and 120 g/s is shown in **Figure 8B**. The minimum error between the simulated and experimental frequencies was 0.80%, and the maximum error was 9.79%.

Analysis suggests that the injector self-pulsation resulted from the combined action of the pressure difference between the inside and outside of the liquid sheet, the surface tension of the liquid sheet, and the impact extrusion of the central airflow. For example, in case 0-60-4, the liquid sheet flowed out from the outer annular aperture injector outlet at 1/4T. The airflow in the center of the annular liquid film was fast, while the airflow outside the annular liquid film was approximately in a static state, as shown in **Figure 9A**. In accordance with the Bernoulli equation, the outer pressure of the liquid sheet was demonstrably higher than the inner pressure. Owing to the action of the pressure difference between the inside and outside of the liquid sheet, the liquid film of the annular

TABLE 4 | Comparison of experimental and simulation frequencies.

Case code	Experimental frequency (Hz)	Simulation frequency (Hz)	Error
Case 0-60-4	4,363	4,614	5.75%
Case 0-60-7	6,146	6,412	4.33%
Case 0-60-8	6,720	6,668	0.08%
Case 0-60-25	0	0	0

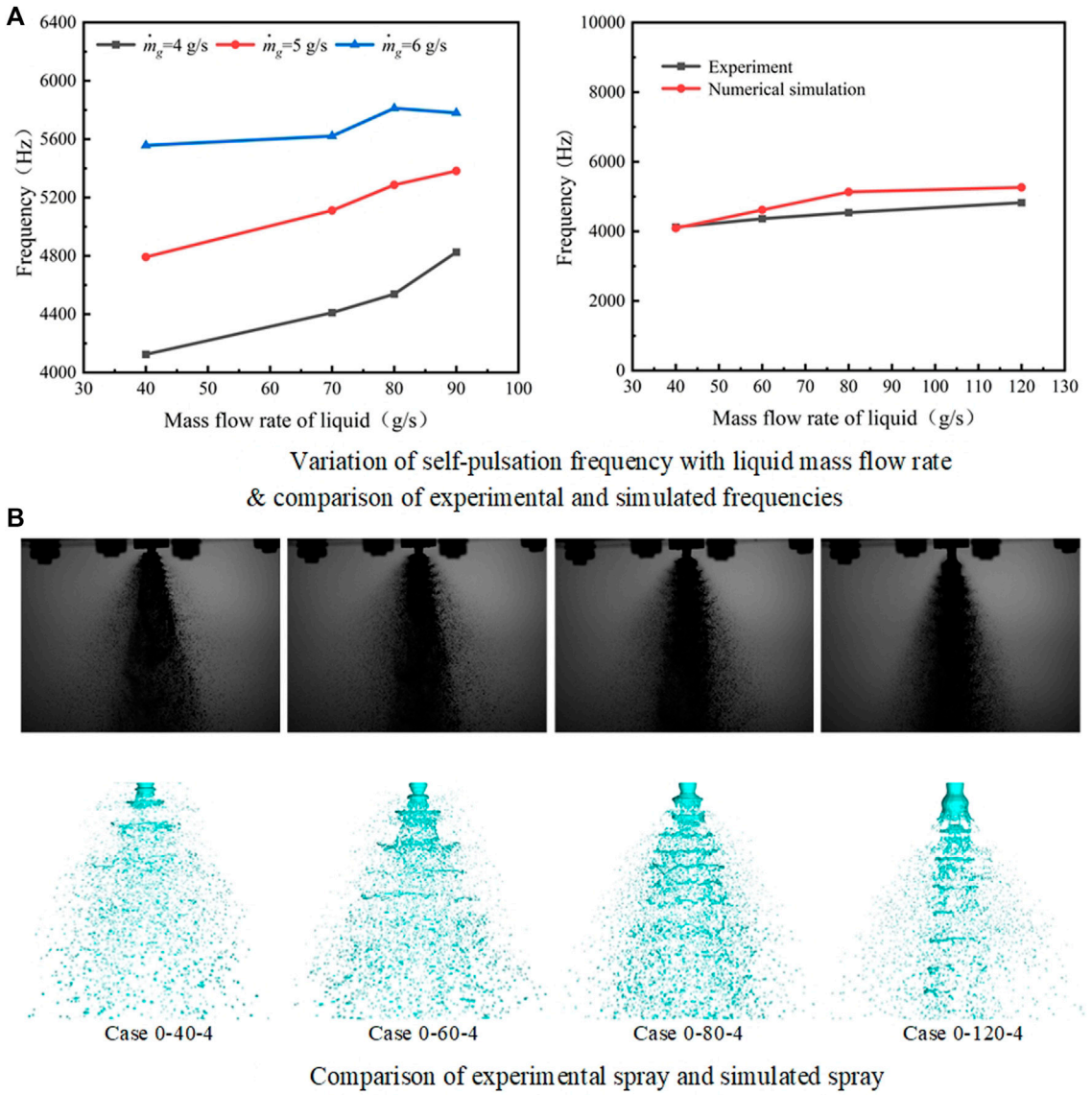

FIGURE 8 | Variation of the self-pulsation frequency with $\dot{m}_l$ and comparison of experimental and simulated frequencies and spray images.

aperture injector tended to shrink toward the central axis shortly after it flowed out of the injector outlet. As the liquid sheet underwent contraction, the "neck" and "shoulder" sections of the spray formed gradually at 2/4T. As the "neck" section blocked the central gas channel, gas accumulation occurred in the inner side of the annular liquid film and caused the pressure inside the annular liquid film to rise. The pressure difference between the

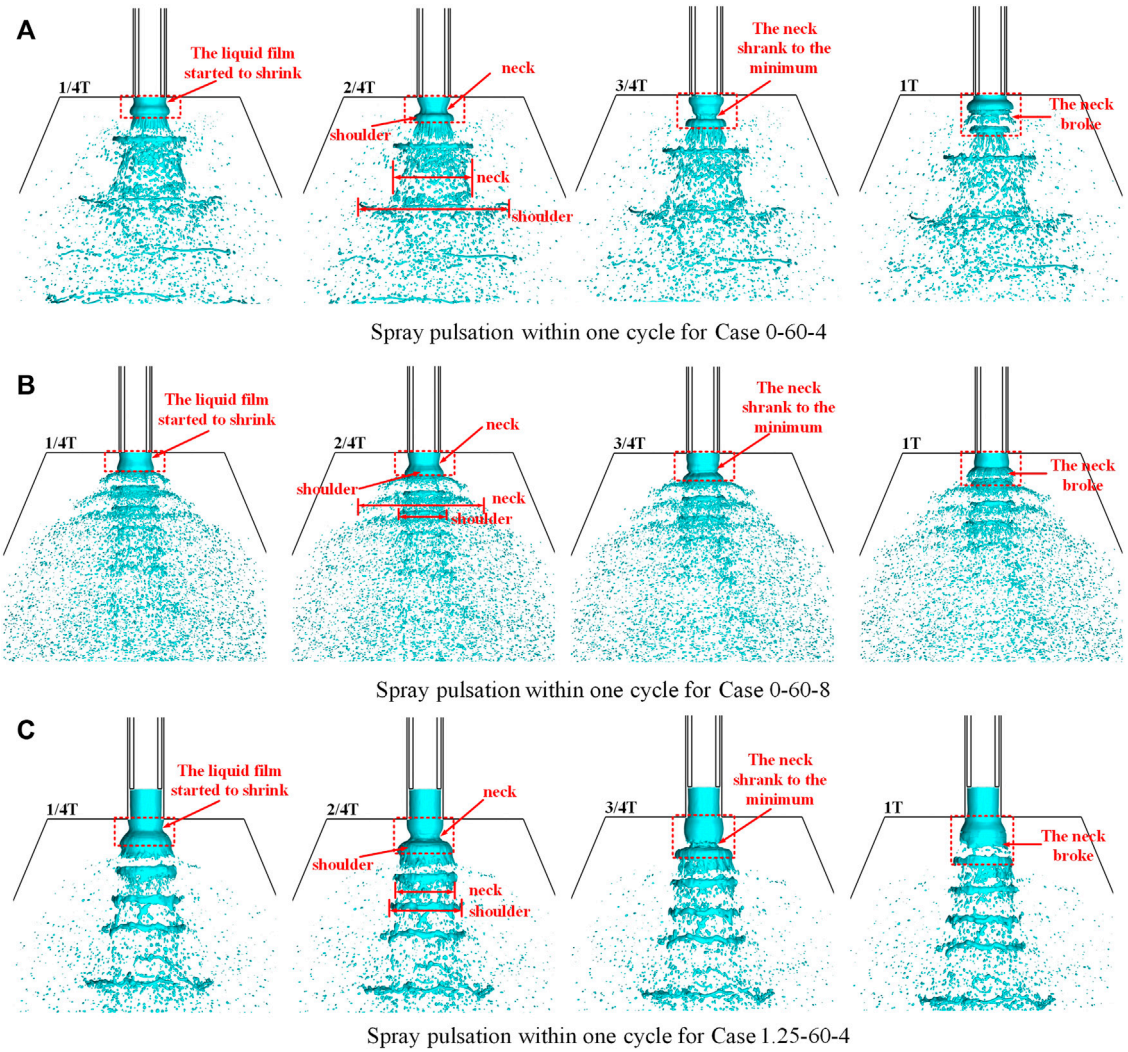

FIGURE 9 | Spray pulsation within one cycle for cases 0-60-4, 0-60-8, and 1.25-60-4.

inside and outside of the liquid film began to reverse. When the "neck" section shrank to its minimum size, the pressure difference between the inside and outside of the liquid sheet attained the maximum value (as shown in **Figure 10B** at 3/4T). Concurrently, the effect of surface tension of the liquid film during contraction caused the downstream liquid film of the "neck" section to become weak. Subsequently, under the combined action of the pressure difference and the impact extrusion of the central gas flow, the "neck" broke, and the gas channel opened (the process was also caused by the combined action of the K-H instability and R-T instability). Then, the spray entered the next pulsation cycle. Substantial momentum was transferred at the "neck" fracture owing to the "breaking out of the liquid film" of the central airflow (as shown in **Figure 9A** at 1T) such that the droplet and liquid block gained a large radial velocity, thus increasing the spray angle. The self-pulsation spray was formed in the shape of a "Christmas tree". The droplet clusters were periodically produced and moved downstream with the spray.

Meanwhile, the flow characteristics during the cycle were evident, as shown in **Figure 10**, which shows the velocity contour, pressure contour, and streamline chart during one cycle of case 0-60-4. As the liquid sheet began to contract, the gas channel at the contraction narrowed at 1/4T, which resulted in an increase in the velocity of the airflow. However, the velocity of the central airflow and the inner part of the liquid film of the annular aperture was reduced by shearing. This resulted in the formation of two counter-swirl reflux zones at the gas injector outlet, with two vortices in opposite directions. The "neck" formation began at 2/4T, and the increasing length of the shearing effect between the central airflow and the inner side of the annular aperture liquid sheet resulted in an increase in the counter-swirl reflux zones. Thus, the two opposite vortices formed between the outlet of the gas

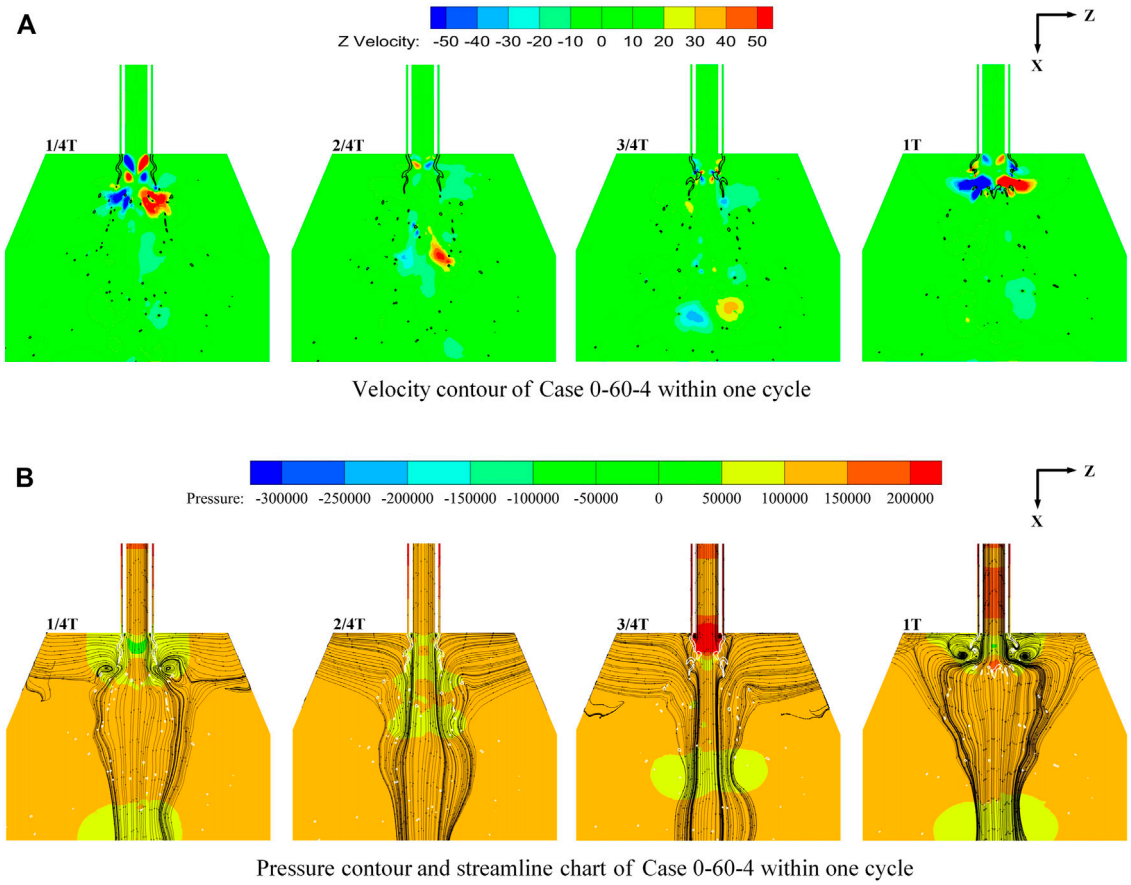

FIGURE 10 | Velocity contour, pressure contour, and streamlines of case 0-60-4 within one cycle (the thick solid line indicates the isoline of the liquid phase volume fraction of 0.25).

injector and the inside of the liquid film increased, and this growth was apparent at 3/4T. Finally, when the "neck" section broke at 1T, the central airflow "broke out of the liquid film" with the opened gas channel. The two vortices in opposite directions formed in the inner part of the "neck" section dissipated rapidly. At the same time, two larger opposing vortices at the "broken" section owing to gas-liquid entrainment and some small and complex vortex systems were generated simultaneously.

When the $\dot{m}_g$ increased, the central airflow was accelerated. The iterative speed of the above-mentioned processes, such as the contraction of the liquid sheet, was accelerated. This resulted in an enhanced frequency of self-pulsations, and a stronger momentum was transferred when the central airflow "broke out of the liquid film". The spray pulsation within one cycle for case 0-60-8 is shown in **Figure 9B**, and its spray pulsation is similar to that of case 0-60-4. However, compared to case 0-60-4, when the "neck" broke at 1T, the action of "breaking out of the liquid film" provided a greater radial velocity to the droplets and liquid blocks at the "neck" for the increase in $\dot{m}_g$. It resulted in the spray width of the "neck" being larger than that of the "shoulder". In other words, compared to case 0-60-4, the comparison of the spray width values for the two above-mentioned values was reversed.

4.3 Self-Pulsation Phenomenon With Recess

The experimental results revealed similar changes in behavior for the injector with and without recess. In other words, when $\dot{m}_g$ was low for a constant $\dot{m}_l$, the phenomenon of self-pulsation occurred and was accompanied by a scream, and the frequency of self-pulsation increased with $\dot{m}_g$ until it subsided. However, for injectors with recess, the frequency of self-pulsation significantly decreased compared to those without recess. The variations in the self-pulsation frequency at different gas mass flow rates for $\dot{m}_l = 40\ g/s$ are illustrated in **Figure 11A**.

The central gas flow in the recess chamber was assumed to have produced the entrainment and ejection functions on the annular aperture liquid sheet. On the one hand, the friction between the gas and liquid hindered the flow of the liquid sheet, which prolonged the period of liquid sheet pulsation, that is, the frequency of self-pulsation decreased. On the other

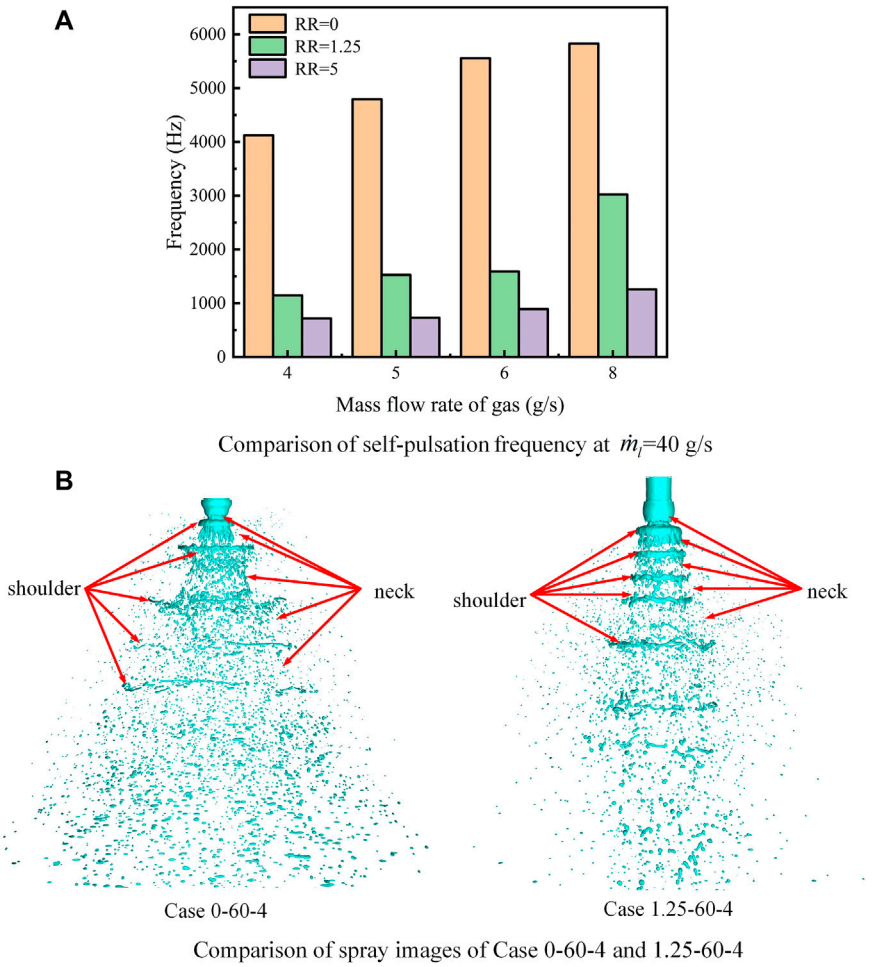

FIGURE 11 | Comparison of the self-pulsation frequency at $\dot{m}_l$ = 40 g/s and comparison of spray images of cases 0-60-4 and 1.25-60-4.

hand, the wall limited the radial velocity of the liquid sheet, which reduced the amplitude of radial pulsation downstream of the outlet, that is, the intensity of self-pulsation decreased. When RR increased, the friction between the gas and liquid further hindered the flow of the liquid sheet. Therefore, the frequency of self-pulsation was further reduced.

Numerical simulations of the injector with recession showed that it also underwent a similar self-pulsation cycle as the injector without a recession, as shown in **Figure 11B**, for the comparison of the spray images of cases 0-60-4 and 1.25-60-4. However, as mentioned earlier, as the recess chamber wall also limited the radial velocity of the liquid sheet, the radial pulsations downstream of the exit amplitude were reduced. This demonstrated that the width difference between the "shoulder" and "neck" of the spray decreased, that is, the spray angle decreased. The spray pulsation process in one cycle of the working condition (frequency of 4,354 Hz obtained from the simulation) is depicted in **Figure 9C**. In this period, the spray pattern was more distinguishable as a "string" shape than a "Christmas tree" shape.

5 CONCLUSION

In this study, the spray characteristics of gas-centered shear coaxial injectors under different operating conditions and RRs were investigated through experiments and numerical simulation methods based on CLSVOF and AMR. The results demonstrated the following.

1) In the case of a constant $\dot{m}_l$, the spray angle showed an opposite variation law for injectors with and without recess. For an injector without recess, the spray angle first stayed almost constant with the variation of $\dot{m}_g$ $(4 \le \dot{m}_g \le 6)$. However, as $\dot{m}_g$ continued to increase, the spray angle dropped linearly. But the spray angle increased with $\dot{m}_g$ for injectors with recess. Moreover, the change in the spray angle with recess was attributed to the second expansion of the central gas flow by the numerical simulation analysis.

2) The experimental results revealed that under certain conditions, the injector without recess produced a self-pulsation phenomenon accompanied by a loud scream, and the self-pulsation frequency increased with $\dot{m}_g$ and $\dot{m}_l$ within

a certain range. Moreover, the "Christmas tree"-shaped spray with the alternating "shoulder" and "neck" sections was obtained in the simulation results in addition to the small error of the frequency between numerical simulation and experiment.

3) The changes of self-pulsation in the injector with recession exhibited a pattern similar to that without recess. However, the self-pulsation frequency for an injector with recess was significantly lower than that without recess. It can be concluded from the analysis results that the friction between the gas and liquid inside the recess chamber hindered the flow of the liquid sheet, which extended the liquid sheet pulsation period, that is, the frequency of self-pulsation decreased. Meanwhile, the radial velocity of the liquid sheet would be restricted by the wall such that its radial pulsations downstream of the outlet amplitude would decrease, that is, the intensity of self-pulsation would be weakened.

4) The self-pulsation mechanism was initially explored through the numerical simulation. The self-pulsation of the injector was possibly the result of the combined action of the pressure difference between the inside and outside of the liquid sheet, the surface tension of the liquid sheet, and the impact extrusion of the central airflow. The self-pulsation spray was shaped like a "Christmas tree" for the injector without recess, whereas the spray was shaped like a "string" for the injector with recess. It was caused by the recess chamber wall to limit the radial velocity of the liquid sheet, and then, the width difference between the "shoulder" and "neck" of the spray and the radial pulsations downstream of the exit amplitude could be further reduced.

DATA AVAILABILITY STATEMENT

The original contributions presented in the study are included in the article/Supplementary Material; further inquiries can be directed to the corresponding authors.

AUTHOR CONTRIBUTIONS

GY mainly contributed to experiments, data processing, and writing; CW and XY were the main contributors to the experiment; JC and XB contributed primarily to data processing; Su and Tong provided financial support for the experiment.

FUNDING

The study was supported by the National Natural Science Foundation of China (No. 12002386).

ACKNOWLEDGMENTS

The authors would like to express their sincere acknowledgment for support from the National Natural Science Foundation of China (No. 12002386).

REFERENCES

Arthur, D., and Vassilvitskii, S. (2007). "K-means++: The Advantages of Careful Seeding, SODA '07," in Proceedings of the Eighteenth Annual ACM-SIAM Symposium on Discrete Algorithms (Philadelphia, PA: Society for Industrial and Applied Mathematics).

Bazarov, V. G., and Yang, V. (1998). Liquid-propellant Rocket Engine Injector Dynamics. *J. Propuls. Power* 14, 797–806. doi:10.2514/2.5343

Bazarov, V. (1998). "Non-linear Interactions in Liquid-Propellant Rocket Engine Injectors," in 34th AIAA/ASME/SAE/ASEE Joint Propulsion Conference and Exhibit (Cleveland, OH: AIAA).

Bazarov, V. (1995). "Self-pulsations in Coaxial Injectors with Central Swirl Liquid Stage," in 31st AIAA/ASME/SAE/ASEE Joint Propulsion Conference and Exhibit (San Diego, CA: AIAA).

Chu, W., Li, X., Tong, Y., and Ren, Y. (2020). Numerical Investigation of the Effects of Gas-Liquid Ratio on the Spray Characteristics of Liquid-Centered Swirl Coaxial Injectors. *Acta Astronaut.* 175, 204–215. doi:10.1016/j.actaastro.2020.05.050

Chu, W., Ren, Y., Tong, Y., Li, X., Jiang, C., and Lin, W. (2021). Numerical Study of Effects of Backpressure on Self-Pulsation of a Liquid-Centred Swirl Coaxial Injector. *Int. J. Multiph. Flow* 139, 103626. doi:10.1016/j.ijmultiphaseflow.2021.103626

Eberhart, C. J., and Frederick, R. A. (2017). Details on the Mechanism of High-Frequency Swirl Coaxial Self-Pulsation. *J. Propuls. Power* 33, 1418–1427. doi:10.2514/1.b36216

Eberhart, C. J., Lineberry, D. M., and Jr Frederick, R. A. (2013). "Detailing the Stability Boundary of Self-Pulsations for a Swirl-Coaxial Injector Element," in 49th AIAA/ASME/SAE/ASEE Joint Propulsion Conference (San Jose, CA: AIAA).

Eberhart, C., Lineberry, D., and Frederick, R. (2012). "Propellant Throttling Effects on Self-Pulsation of Liquid Rocket Swirl-Coaxial Injection," in 48th AIAA/ASME/SAE/ASEE Joint Propulsion Conference & Exhibit (Atlanta: AIAA). doi:10.2514/6.2012-4204

Hardalupas, Y., and Whitelaw, J. H. (1994). Characteristics of Sprays Produced by Coaxial Airblast Atomizers. *J. Propuls. Power* 10, 453–460. doi:10.2514/3.23795

Hautman, D. J. (1993). Spray Characterization of Liquid/gas Coaxial Injectors with the Center Liquid Swirled. *At. Spr.* 3, 373–387. doi:10.1615/atomizspr.v3.i4.20

Huang, J., Cai, W., Wu, Y., and Wu, X. (2022). Recent Advances and Applications of Digital Holography in Multiphase Reactive/nonreactive Flows: a Review. *Meas. Sci. Technol.* 33, 022001. doi:10.1088/1361-6501/ac32ea

Kang, Z. T., Li, X. D., Mao, X. B., and Li, Q. L. (2018). Review on Gas Liquid Shear Coaxial Injector in Liquid Rocket Engine. *Acta Aeronautica Astronautica Sinica* 39, 6–25. doi:10.7527/S1000-6893.2018.22221

Kim, B.-D., Heister, S. D., and Collicott, S. H. (2005). Three-dimensional Flow Simulations in the Recessed Region of a Coaxial Injector. *J. Propuls. Power* 21, 728–742. doi:10.2514/1.12651

Kim, B.-D., and Heister, S. D. (2004). Two-phase Modeling of Hydrodynamic Instabilities in Coaxial Injectors. *J. Propuls. Power* 20, 468–479. doi:10.2514/1.10378

Kulkarni, V., Sivakumar, D., Oommen, C., and Tharakan, T. J. (2010). Liquid Sheet Breakup in Gas-Centered Swirl Coaxial Atomizers. *J. Fluids Eng.* 132, 011303. doi:10.1115/1.4000737

Li, J. N., Lei, F. P., Zhou, L. X., and Yang, A. L. (2019). Effects of Misaligned Impingement on Atomization Characteristics of Impinging Jet Injector. *J. Aerosp. Power* 34, 2280–2293.

Luo, T. Q. (2017). *Fluid Mechanics*. Beijing: China Machine Press, 224.

Nunome, Y., Sakamoto, H., Tamura, H., Kumakawa, A., Amagasaki, S., and Inamura, T. (2007). "An Experimental Study of Super-pulsating Flow on a Shear Coaxial Injector with a Recessed Inner Post," in *43rd AIAA/ASME/SAE/ASEE Joint Propulsion Conference & Exhibit* (Cincinnati, OH: AIAA).

Nunome, Y., Tamura, H., Onodera, T., Sakamoto, H., and Inamura, T. (2009). "Effect of Liquid Disintegration on Flow Instability in a Recessed Region of a Shear Coaxial Injector," in *45th AIAA/ASME/SAE/ASEE Joint Propulsion Conference & Exhibit* (Denver, CO: AIAA).

Siddharth, K. S., Panchagnula, M. V., and Tharakan, T. J. (2017). Effect of Gas Swirl on the Performance of a Gas-centered Swirl Co-axial Injector. *At. Spr.* 27, 741–757. doi:10.1615/atomizspr.2017019923

Tsohas, J., and Heister, S. D. (2011). Numerical Simulations of Liquid Rocket Coaxial Injector Hydrodynamics. *J. Propuls. Power* 27, 793–810. doi:10.2514/1.47761

Wang, K., Yang, G. H., Li, P. F., Zhang, M. Q., and Zhou, L. X. (2016). Numerical Simulation of Internal Flow Process in Pressure Swirl Injector. *J. Rocket Propuls.* 42, 14–20. doi:10.3969/j.issn.1672-9374.2016.04.003

Wang, L., Fang, B., and Wang, G. C. (2021). Process of Pressure Swirl Injector Atomization Based on Large Eddy Simulation. *J. Propuls. Technol.* 42, 1855–1864. doi:10.13675/j.cnki.tjjs.190392

Wu, Y. C., Zhao, X. X., Zhang, H. Y., Lin, X. D., and Wu, X. C. (2022). Discrimination and Measurement of Droplet and Ice Crystal by Combining Digital Inline Holography with Interferometric Particle Imaging with Single Color Camera. *IEEE Trans. Instrum. Meas.*, 0018–9456. doi:10.1109/tim.2022.3147333

Xu, S. (2016). *Experimental Study on Spray Characteristic of Gas-Liquid Centred Coaxial Swirling Injectors*. Changsha: National University of Defense Technology.

Yang, L.-J., and Fu, Q.-F. (2012). Stability of Confined Gas-Liquid Shear Flows in Recessed Shear Coaxial Injectors. *J. Propuls. Power* 28, 1413–1424. doi:10.2514/1.b34560

Yang, L. J., Ge, M. H., Zhang, M. Z., Fu, Q. F., and Cai, G. B. (2006). Spray Characteristics of Recessed Gas-Liquid Coaxial Swirl Injector. *J. Propuls. Power* 2, 1332–1339. doi:10.13675/j.cnki.tjjs.2006.04.001

Conflict of Interest: The authors declare that the research was conducted in the absence of any commercial or financial relationships that could be construed as a potential conflict of interest.

Publisher's Note: All claims expressed in this article are solely those of the authors and do not necessarily represent those of their affiliated organizations, or those of the publisher, the editors, and the reviewers. Any product that may be evaluated in this article, or claim that may be made by its manufacturer, is not guaranteed or endorsed by the publisher.

NOMENCLATURE

d_o inner diameter of the outer injector (unit: mm)

d_g inner diameter of the inner injector (unit: mm)

d_t outer diameter of the inner injector (unit: mm)

L_r recessed length (unit: mm)

RR recess ratio

$\dot{m}$ mass flow rate (unit: g/s)

μ viscosity coefficient (unit: Pa·s)

p pressure (unit: Pa)

ρ density (unit: Kg/m^3)

g gravitational acceleration vector (unit: m/s^2)gas

F additional volume force vector (unit: N)

U velocity vector (unit: m/s)

T_L temperature (unit: K)

T symbol of period

k_{eff} effective heat transfer coefficient (unit: W/m·K)

I unit tensor

J_j diffusive flow of the component j

S_h volumetric heat source term

h_j enthalpy of the component j (unit: J)

T_{L0} reference temperature (unit: K)

μ_0 reference viscosity coefficient (unit: Pa·s)

Subscripts

g gas

l liquid

Advantages of publishing in Frontiers

OPEN ACCESS
Articles are free to read for greatest visibility and readership

FAST PUBLICATION
Around 90 days from submission to decision

HIGH QUALITY PEER-REVIEW
Rigorous, collaborative, and constructive peer-review

TRANSPARENT PEER-REVIEW
Editors and reviewers acknowledged by name on published articles

Frontiers
Avenue du Tribunal-Fédéral 34
1005 Lausanne | Switzerland

Visit us: www.frontiersin.org
Contact us: frontiersin.org/about/contact

REPRODUCIBILITY OF RESEARCH
Support open data and methods to enhance research reproducibility

DIGITAL PUBLISHING
Articles designed for optimal readership across devices

FOLLOW US
@frontiersin

IMPACT METRICS
Advanced article metrics track visibility across digital media

EXTENSIVE PROMOTION
Marketing and promotion of impactful research

LOOP RESEARCH NETWORK
Our network increases your article's readership